Rishi Gupta · Min Sun · Svetlana Brzev ·
M. Shahria Alam · Kelvin Tsun Wai Ng ·
Jianbing Li · Ashraf El Damatty ·
Clark Lim   *Editors*

Proceedings of the Canadian Society of Civil Engineering Annual Conference 2022

Volume 2

Springer

Lecture Notes in Civil Engineering

Volume 348

Lecture Notes in Civil Engineering (LNCE) publishes the latest developments in Civil Engineering—quickly, informally and in top quality. Though original research reported in proceedings and post-proceedings represents the core of LNCE, edited volumes of exceptionally high quality and interest may also be considered for publication. Volumes published in LNCE embrace all aspects and subfields of, as well as new challenges in, Civil Engineering. Topics in the series include:

- Construction and Structural Mechanics
- Building Materials
- Concrete, Steel and Timber Structures
- Geotechnical Engineering
- Earthquake Engineering
- Coastal Engineering
- Ocean and Offshore Engineering; Ships and Floating Structures
- Hydraulics, Hydrology and Water Resources Engineering
- Environmental Engineering and Sustainability
- Structural Health and Monitoring
- Surveying and Geographical Information Systems
- Indoor Environments
- Transportation and Traffic
- Risk Analysis
- Safety and Security

To submit a proposal or request further information, please contact the appropriate Springer Editor:

- Pierpaolo Riva at pierpaolo.riva@springer.com (Europe and Americas);
- Swati Meherishi at swati.meherishi@springer.com (Asia—except China, Australia, and New Zealand);
- Wayne Hu at wayne.hu@springer.com (China).

All books in the series now indexed by Scopus and EI Compendex database!

Rishi Gupta · Min Sun · Svetlana Brzev ·
M. Shahria Alam · Kelvin Tsun Wai Ng ·
Jianbing Li · Ashraf El Damatty · Clark Lim
Editors

Proceedings of the Canadian Society of Civil Engineering Annual Conference 2022

Volume 2

Editors
Rishi Gupta
Department of Civil Engineering
University of Victoria
Victoria, BC, Canada

Min Sun
Department of Civil Engineering
University of Victoria
Victoria, BC, Canada

Svetlana Brzev
Department of Earthquake Engineering
The University of British Columbia
Vancouver, BC, Canada

M. Shahria Alam
The University of British
Columbia-Okanagan Campus
Kelowna, BC, Canada

Kelvin Tsun Wai Ng
University of Regina
Regina, SK, Canada

Jianbing Li
Environmental Engineering Program
University of Northern British Columbia
Prince George, BC, Canada

Ashraf El Damatty
The University of Western Ontario
London, ON, Canada

Clark Lim
Department of Civil Engineering
The University of British Columbia
Vancouver, BC, Canada

Conference Committee Members

Volume 1

Dr. Rishi Gupta (Chair)
Dr. Svetlana Brzev (Technical Co-chair)
Dr. Min Sun (Technical Co-chair)
Dr. Jianbing Li (Cold Regions Specialty Chair)
Dr. Kelvin Tsun Wai Ng (Environmental Specialty Chair)

Volume 2

Dr. Rishi Gupta (Chair)
Dr. Svetlana Brzev (Technical Co-chair)
Dr. Min Sun (Technical Co-chair)
Dr. Ashraf El Damatty
Dr. Ahmed Elshaer

Volume 3

Dr. Rishi Gupta (Chair)
Dr. Svetlana Brzev (Technical Co-chair)
Dr. Min Sun (Technical Co-chair)
Dr. Ashraf El Damatty (Structural Specialty Co-chair)
Dr. Ahmed Elshaer (Structural Specialty Co-chair)
Dr. Shahria Alam (Material Specialty Chair)
Dr. Clark Lim (Transportation Specialty Chair)

Volume 4

Dr. Rishi Gupta (Chair)
Dr. Svetlana Brzev (Technical Co-chair)
Dr. Min Sun (Technical Co-chair)
Dr. Ashraf El Damatty (Structural Specialty Co-chair)
Dr. Ahmed Elshaer (Structural Specialty Co-chair)
Dr. Shahria Alam (Material Specialty Chair)
Dr. Jianbing Li (Cold Regions Specialty Chair)
Dr. Kelvin Tsun Wai Ng (Environmental Specialty Chair)

Contents

Timber Structures

Concrete Structures

Structural Analysis

Analysis and Design of Bridges

Existing Structures and Study Cases

About the Editors

Dr. Rishi Gupta is a Professor in the Department of Civil Engineering at the University of Victoria. He leads the Facility for Innovative Materials and Infrastructure Monitoring (FIMIM) at UVic. He received both a masters and a Ph.D. in Civil Engineering from the University of British Columbia. His current research is focused on studying smart self healing cement-based composites containing supplementary cementitious materials and fiber reinforcement. His areas of interest include development of sustainable construction technologies, structural health monitoring, and non-destructive evaluation of infrastructure. He has more than 20 years of combined academic and industry experience. His industry experience includes working as the Director of Research of Octaform Systems Inc in Vancouver.

Rishi is a Fellow of Engineers Canada, the Canadian Society of Senior Engineers, and a past chair of the EGBC's Burnaby/New West branch. He is the past Chair of the international affairs committee of the Canadian Society of Civil Engineering (CSCE). He is a long standing member of the American Concrete Institute and is also a voting member of several subcommittees of ASTM C 09.

Dr. Min Sun is an Associate Professor and the Director of Undergraduate Program in the Civil Engineering Department at the University of Victoria (UVic). His research interests lie primarily in the field of structural engineering. His past research activity has included the development of design rules for hollow structural section connections and fillet welds, which have been incorporated into Canadian and American national steel design standards. From 2018 to 2020, he was the Western Region VP of the Canadian Society for Civil Engineering (CSCE). In 2019, he received the Faculty Award for Excellence in Teaching at UVic. Before joining UVic, he worked as a structural designer at Read Jones Christoffersen.

Dr. Svetlana Brzev is currently an Adjunct Professor at the Department of Civil Engineering, University of British Columbia. She has more than 35 years of consulting and research experience related to structural and seismic design and retrofitting of masonry structures in Canada and several other countries. Her research has been focused on seismic behaviour and practical design and construction issues related

to masonry structures. She has served as a member of the Technical Committee responsible for developing current Canadian masonry design standard CSA S304 since 2009 and is a member of the Technical Committee 250/SC8/WG1 responsible for developing Eurocode 8 provisions for seismic design of masonry buildings. She has been actively involved in several international initiatives related to promoting safe housing in seismically active regions, such as the EERI-sponsored World Housing Encyclopedia and Confined Masonry Network. Dr. Brzev served as a Director and Vice-President of EERI, a Director of the Masonry Society, and is currently a Director of the International Association for Earthquake Engineering. Dr. Brzev has co-authored two books related to design of masonry structures and a textbook on design of reinforced concrete structures and numerous papers and publications.

Dr. M. Shahria Alam is a Professor of Civil Engineering and the Tier 1 Principal's Research Chair in Resilient and Green Infrastructure in the School of Engineering at The University of British Columbia (UBC)'s Okanagan campus. He is serving as the founding Director of the Green Construction Research and Training Center (GCRTC) at UBC. Dr. Alam is the Vice President (Technical Program) of the Canadian Society for Civil Engineering (CSCE) and Chair of the Engineering Mechanics and Materials Division of CSCE. He received his Ph.D. in Civil/Structural Engineering from Western University in 2008. His research interests include smart and recycled materials and their structural engineering applications. He has published more than 350 peer-reviewed articles in these areas. He is the recipient of more than forty national and international awards including three best paper awards. Currently, Dr. Alam is serving as an Associate Editor of *ASCE's Journal of Bridge Engineering* and *Journal of Materials in Civil Engineering.*

Dr. Kelvin Tsun Wai Ng major fields of interest are in sustainable waste management system, disposal facility design, and data-driven waste policy. Kelvin has over 120 publications, and his projects have been supported by NSERC, Mitacs, CFI, Innovation Saskatchewan, Ministry of Environment, and other national and provincial sponsors. Kelvin has received both research and teaching awards, including six RCE Education for Sustainability Recognition Awards (2018–2022), Elsevier's Top Reviewer Award—Waste Management (2021), Saskatchewan Innovation Challenge (2019), McMaster Engineering Top 150 Alumni for Canada's Sesquicentennial (2017), and the University of Regina President's Award for Teaching Excellence (2017). Provincially, he has been appointed by the Ministry of Environment in Saskatchewan to serve on the Solid Waste Management Advisory Committee. Kelvin has been serving on the Association of Professional Engineers and Geoscientists of Saskatchewan (APEGS) Award Committee since 2017. Currently, he is chairing the APEGS Awards Committee. Kelvin is the Environmental Division Chair for Canadian Society for Civil Engineering and has organized and chaired/co-chaired a number of conferences, including the CSCE General Conference in 2015, and four CSCE Environmental Specialty Conferences in 2019, 2020, 2021, 2022. Currently, he is organizing the 2023 CSCE Environmental Specialty Conference at Moncton.

Dr. Jianbing Li is a professor and professional engineer in the Environmental Engineering program at the University of Northern British Columbia (UNBC). He received his Ph.D. degree in environmental systems engineering from the University of Regina. He has research interests in environmental pollution control, petroleum waste management, contaminated soil and groundwater remediation, environmental modelling and decision analysis, environmental risk assessment, and oil spill response. He has produced more than 300 publications in international journals and conferences, including over 200 refereed journal publications, with an h-index of 45 (Google Scholar). His research has been supported by various organizations, including Natural Science and Engineering Research Council of Canada (NSERC), Fisheries and Oceans Canada (DFO), Natural Resources Canada (NRCan), BC Ministry of Forests, and Geoscience BC. He obtained the 2013 Northern BC Business and Technology Award (Collaborative Research Award with Husky Energy), the 2010, 2014 and 2019 UNBC Research Excellence Award, and the 2013 UNBC Achievement Award in Professional Practice and Mentorship. Dr. Li was nominated for the 2022 and 2023 CUFA BC Ehor Boyanowsky Academic of the Year Award. He served as a member of NSERC's Research Tool and Instruments Selection Committee for Civil, Industrial and Systems Engineering in 2016–2021, and the Committee Chair for the 2021 competition. He is also a member of NSERC's Discovery Grant Evaluation Group for Civil, Industrial and Systems Engineering (EG1509) (2022–2025). He has been a member of the Academic Examiners Subcommittee with Engineers and Geoscientists BC since 2017. He has served as the co-director of the UNBC/UBC environmental engineering program for 4 years (2013–2017). He served as a guest editor for seven international journals, and is currently an Associate Editor or Editorial Board member of seven journals. He is the inaugural Chair of the Northern British Columbia Section of Canadian Society for Civil Engineering (CSCE). Dr. Li was named a CSCE Fellow in 2022.

Dr. Ashraf El Damatty, Professor and Chair of the Department of Civil and Environmental Engineering, Western University. He is a Fellow of the Canadian Academy of Engineering, the Engineering Institute of Canada, and the Canadian Society of Civil Engineering (CSCE). He is a Research Director at the WindEEE Research Institute and Editor-in-Chief of the *Journal of Wind and Structures*. He holds honorary Professorship titles at four international universities. He obtained B.Sc. and M.Sc. from Cairo University, Egypt, Ph.D. from McMaster University, and MBA from University College London, UK. He is the founder of the CSCE Steel Structures Committee and served for five years as the Chair of the CSCE Structures Division. He has written more than 250 publications, supervised more than 60 graduate students and has been invited as keynote speaker in 14 countries. He received several awards including the Alan Yorkdale Award by ASTM, Best Paper Award at the Canadian Conference on Effective Design, Honourable Mention in 2014 Casimir Gzowski Medal, 2015 CSCE Whitman Wright Award, 2016 CSCE Horst Leipholz Medal, Western University Faculty Scholar Award, 2018 Professional Engineers of Ontario Medal of Research and Development, 2021 Pratley Award for Best Paper on Bridges, and the 2021 Western Engineering Award for Excellence in Research,

Western University. He is an international leader in the interdisciplinary field of Wind and Structural Engineering. His research has influenced the international codes and the Engineering practice worldwide. It resulted in the first specifications in the world for downburst and tornado loading on transmission line structures that was recently incorporated into the guidelines of the ASCE.

Clark Lim has over three decades of experience in public, private, and academic sectors, specializing in analytical methods and information systems for transportation applications. As a consultant, he advises senior officials on policy, technology, and governance matters, where he utilizes an evidence-based and technically progressive approach to establish sound policy frameworks. In the mid-1990's, he was part of the team that established TransLink, the Greater Vancouver Transportation Authority, where he was also the Project Manager of the Evergreen Rapid Transit Line planning and consultation process. At UBC Clark is currently an Adjunct Professor in the Department of Civil Engineering where he has taught transportation engineering and planning to senior undergraduate and graduate students since 2006. His previous research at UBC focused on intelligent transportation systems for freight, and the impact quantification of the 2010 Winter Olympic Games. Currently he is researching the effects of hybrid working on transportation policies, the impacts of ride-hailing trips through big data methods, and developing tools to measure sustainability and diversity-equity-inclusion indices for corporate boards.

Design Codes and Provisions

Canadian Seismic Design Considerations for Outriggers Used in High-Rise Buildings

Tobber Lisa, Dehghani Saeed, and Amiri Amirhossein

Abstract A damped outrigger system is an effective structural scheme that has been realized in Canadian construction in the past decade for resisting seismic and wind loads. These outriggers increase the stiffness of reinforced concrete core walls, reduce the moment demand within the walls, and add additional energy dissipation. Essentially, the outrigger system acts as a rotational spring providing additional moment resistance and rotational stiffness, which leads to lower drifts and displacements. Although the outrigger systems demonstrate desirable seismic performance, no seismic design procedures exist within Canadian building codes. In this study, a comprehensive parametric analysis is done, providing empirical relations for the dynamic response of outrigger buildings. Prototype outrigger-wall buildings are designed with the proposed design methods, and the challenges of designing these systems are discussed in detail. This study is a step towards new seismic design guidelines for outrigger buildings in Canada.

Keywords Seismic design · Outriggers · High-rise buildings

1 Introduction

Driven by small building sites, engineers are designing more tall buildings are being constructed which require smaller and as a result more slender reinforced concrete (RC) core walls. However, the dynamic characteristics of tall and slender buildings result in large displacements and accelerations under wind and seismic excitation. These large deformations can cause damage to the structural and non-structural elements of a building. Windstorms and earthquakes also generate large forces in the form of overturning moment and shears, which must be resisted by a lateral force resisting system. Controlling the lateral response of tall buildings to earthquake

T. Lisa (✉) · D. Saeed · A. Amirhossein
University of British Columbia, Kelowna, Canada
e-mail: Lisa.Tobber@ubc.ca

Fig. 1 Damped outrigger
system concept
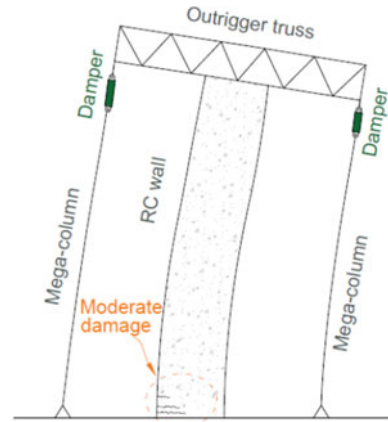
and wind excitation is a well-studied topic and has resulted in many practical and
innovative solutions—one of which is a damped outrigger system.

An outrigger system consists of stiff girders or trusses that couple the RC core
wall to exterior columns, as shown in Fig. 1. An outrigger system adds a rotational
stiffness to the RC core wall, reducing lateral displacements and core moment at
the base of the wall. The addition of dampers within the outrigger system allows for
added energy dissipation, further enhancing the lateral response of these buildings
under earthquake loads.

Over the past two decades, researchers have investigated the performance of
damped outrigger-wall systems [9–11, 14, 16, 18]. Overall, the current literature
shows that the use of outriggers in tall buildings is an effective way to increase the
overall performance of the structure. Generally, the optimal location for an outrigger
with hysteretic dampers is at 60–80% of the building height. However, the outrigger
is often located at the roof for ease of construction and architectural purposes.

Despite the growing research into damped outriggers for seismic design, these
systems have only recently been adopted in practice for seismic applications. For
example, in 2015, RJC designed the MNP Tower (1021 W Hastings) with a roof-top
outrigger that has dampers in the form of buckling restrained braces. This damped
outrigger building was the first of its kind in Canada. Despite the rising popularity of
damped outrigger buildings in Canada, there is currently no seismic design guidance.
In this paper, we study the behaviour of outrigger shear wall buildings and compare
that to conventional shear walls. Based on these results, we have developed empirical
design equations and recommend avenues for future research.

2 Outrigger Stiffness

The outrigger system consists of mega-columns, outrigger dampers, and outrigger trusses or beams. Mega-columns and outrigger dampers primarily resist axial loads, having a low shear resistance, and can therefore be idealized as a rotational spring (where the spring rotational stiffness is k_o, and the yield moment is $M_{o,y}$). The yield of the outrigger dampers, which are assumed to have symmetric elastic–plastic behaviour, provides the only nonlinearity in the outrigger system. The remaining outrigger columns and the beams are capacity-designed to remain elastic. Hence, the yield moment of the equivalent spring consists of the damper yield force ($f_{o,y}$) multiplied by the length of the outrigger truss or beam (L_o), and the result is given in Eq. 1

$$M_{o,y} = f_{o,y} L_o \tag{1}$$

The rotational spring can be calculated by assuming the outrigger beam behaves like a beam connected to two springs in series. The first spring in series has the stiffness of the damper (k_d) while the other represents the stiffness of the column (k_c). The equivalent rotational stiffness (k_o) of an outrigger beam is can then be determined using Eq. 2.

$$k_o = \left[\frac{2L_s}{G_o A_v L_o} + \frac{L_s^2}{3E_o I_o L_o} + \frac{2}{k_{\mathrm{com}} L_o^2} \right]^{-1} \tag{2}$$

where k_{com} is the axial stiffness of the column (k_c), and the damper (k_d) in series $k_{\mathrm{com}} = (1/k_c + 1/k_d)^{-1}$; I_o is the moment of inertia of the outrigger beam; L_s is span between the wall and the mega-column; υ is Poisson ratio of the outrigger material; E_o is the elastic modulus of the outrigger material; and L_o is the length of the outrigger beam. In these calculations, the equivalent beam is assumed to have a rectangular cross section with a shear area of $A_v = \frac{5}{6} A_{o,g}$ and a shear modulus of $G = \frac{E_o}{2(1+\upsilon)}$, where $A_{o,g}$ is the gross area of outrigger beam.

It may not always be efficient to use a beam as an outrigger system. For instance, steel beams are limited in the sizes availability, and it would be difficult to obtain the high stiffness required by outrigger systems. As an alternative, designers may use RC beams; however, the RC beams add additional weight and utilize a significant amount of space. As such, large steel outrigger trusses may be used. Furthermore, in some cases, the wall may extend into the truss. This is common when the outrigger is located near mid-height of the building. In this case, the determination of the rotational stiffness assumes that wall is rigid, relative to the truss. Figure 2 shows the configuration where the wall extends into the truss system. Equation 3 shows the derived equation for rotational stiffness for an outrigger truss with a rigid wall.
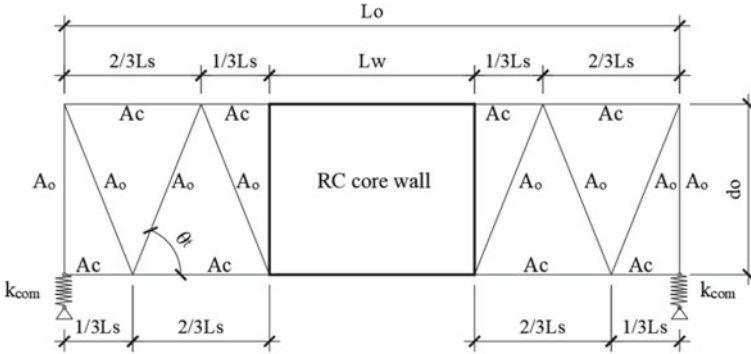
Fig. 2 Outrigger roof truss configuration

$$k_o = \left(\frac{38 L_s}{3 E_s A_c (\tan^2 \theta_t) L_o^2} + \frac{6 d_o}{A_o E_s (\sin^3 \theta_t) L_o^2} + \frac{2 d_o}{A_o E_s L_o^2} + \frac{2}{k_{com} L_o^2} \right)^{-1} \tag{3}$$

where E_s is the steel elastic modulus, $A_o =$ area of the diagonal vertical truss, $A_c =$ area of the top and bottom chords, $L_w =$ length of the wall, $d_o =$ outrigger depth, and $\theta_t =$ angle of inclination of the inside diagonal truss (see Fig. 2).

3 Static Response of Outrigger-Wall System

In the lateral design of outrigger buildings, it is important to understand the portion of total overturning moment that is taken by the outrigger and the wall base. Using a simple model, where an outrigger system is modelled as a rotational spring, the wall is modelled as a Euler–Bernoulli beam, the lateral load is represented as an inverted triangular loading distribution, and the ratio of outrigger moment (M_o) to wall base moment (M_b) can be determined using the Eq. 4.

$$\beta_m = \frac{M_o}{M_b} = \frac{(a^3 - 6a + 8)}{8} \alpha_f \tag{4}$$

where β_m is the ratio of outrigger moment (M_o) to wall base moment (M_b), a is the ratio of the height of the outrigger to the total height of the building, which is a unitless parameter between 0–1; and α_f is a relative stiffness parameter (Eq. 5), which is a unitless parameter between 0–1. For a cantilever wall with no outrigger, $\alpha_f = 0$. Contrastingly, for an infinitely rigid outrigger, $\alpha_f = 1$.

$$\alpha_f = \left(\frac{1}{\frac{E_c I_w}{a k_o H} + 1} \right) \tag{5}$$
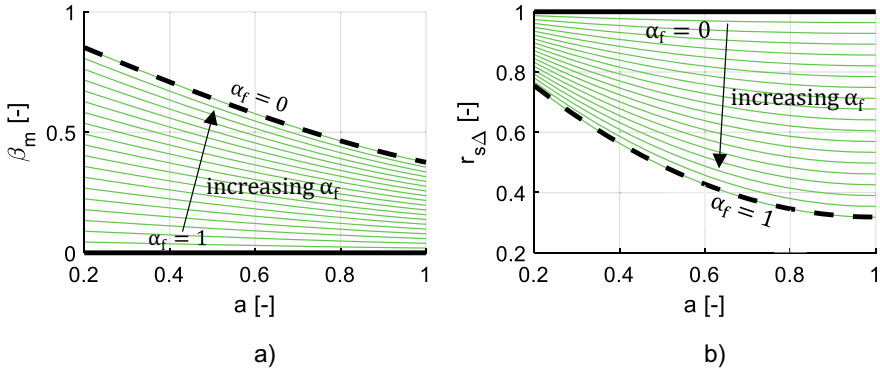
Fig. 3 a Moment distribution of outrigger and **b** roof displacement ratio of outrigger system

where I_w is the moment of inertia of the core wall; H is the height of the core wall; and E_c is the elastic modulus of reinforced concrete.

Figure 3a shows β_m for a range of α_f and a. As shown, a rigid outrigger ($\alpha_f = 1$) positioned lower down the wall ($a \rightarrow 0$) will take the highest portion of overturning moment. Furthermore, a rigid outrigger located at the roof, which is a common practice, can only take a maximum of ~38% of the overturning moment. Finally, the portion of moment which is taken by the outrigger is less sensitive to α_f near the roof than near the base.

Assuming the same inverted triangular static loading is applied, the ratio ($r_{s\Delta}$) of the outrigger system roof displacement (Δ_o) to the cantilevered wall system without an outrigger (Δ_w) can be determined. The value $r_{s\Delta}$ is critical in understanding the displacement savings using an outrigger system compared to a wall without an outrigger. The calculation of $r_{s\Delta}$ is shown in Eq. 6.

$$r_{s\Delta} = \frac{\Delta_o}{\Delta_w} = 1 - \frac{5}{22} a\alpha_f(2 - a) \tag{6}$$

Figure 3b shows $r_{s\Delta}$ for a range of α_f and a. As shown, the outrigger is most effective at a = 1, where a rigid outrigger ($\alpha_f = 1$) gives a 70% reduction in displacements. Additionally, Fig. 3b shows that displacements are more sensitive to outrigger stiffness at high locations in the building. Hence, there is more benefit to adding stiffness to the outrigger near the top of the building rather than at the bottom.

4 Dynamic Response of Outrigger-Walls

The static response of an outrigger systems, described in the previous section, shows impressive efficiency in terms of resistance to lateral loads. The relations discussed previously are useful when static loads are assumed in design, or where dynamic

a)

b)
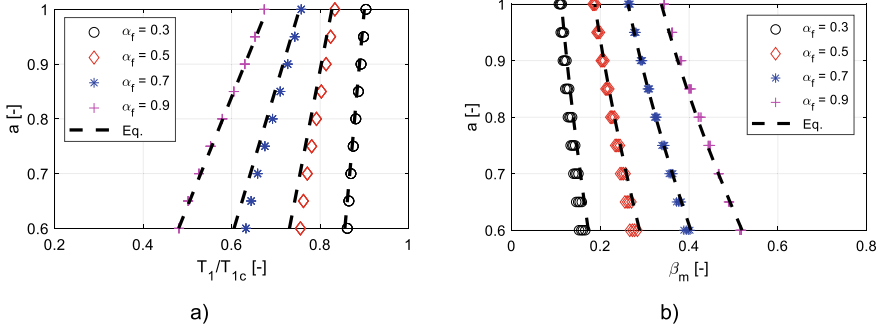
Fig. 4 **a** Fundamental period from model and **b** Moment distribution factor from dynamic analysis

loads are simplified to static loads, such as wind loads or equivalent static force procedures. However, in seismic design of tall buildings, the dynamic response must be understood. To investigate the dynamic elastic behaviour of outrigger systems, modal response spectrum analysis was conducted using distributed mass and stiffness models. The elastic dynamic response of these models was determined, and empirical equations developed are described here-in.

Natural periods of vibration are critical design parameters in earthquake engineering. Eigenvalue analysis was conducted on a range of models, and the fundamental periods were determined. Figure 4a shows the period of the buildings, normalized to the fundamental period of a system without an outrigger ($T_{n_{\alpha_f=0}}$). Interestingly, adding an infinitely rigid outrigger (i.e.,$\alpha_f = 1$) to the RC wall system can cause a maximum reduction in the fundamental period of only ~38%, which implies that increasing section sizes in the outrigger may have a limited effect on the system's performance.

Based on these trends, Eq. 7 is recommended to estimate the natural period of an outrigger system. Figure 4a shows that Eq. 7 has a reasonable approximation of the natural period of the system.

$$T_n \approx \left(1 - 0.36\alpha_f\right)T_{n_{\alpha_f=0}} \tag{7}$$

where $T_{n_{\alpha_f=0}}$ is the natural period of the system without an outrigger (i.e., $\alpha_f = 0$) and is estimated using Eq. 8

$$T_{n_{\alpha_f=0}} \approx 1.85\sqrt{\frac{W * H^3}{g * E_c I_w}} \tag{8}$$

where W is the total weight of the building.

The moment distribution for the outrigger system under dynamic loading is similar to the distribution using static loading. Figure 4b shows β_m both using the dynamic analysis and Eq. 4. As shown, Eq. 4 shows a reasonable estimate of the dynamic

a) C_0 factor　　　　　　　　b) Mass participation
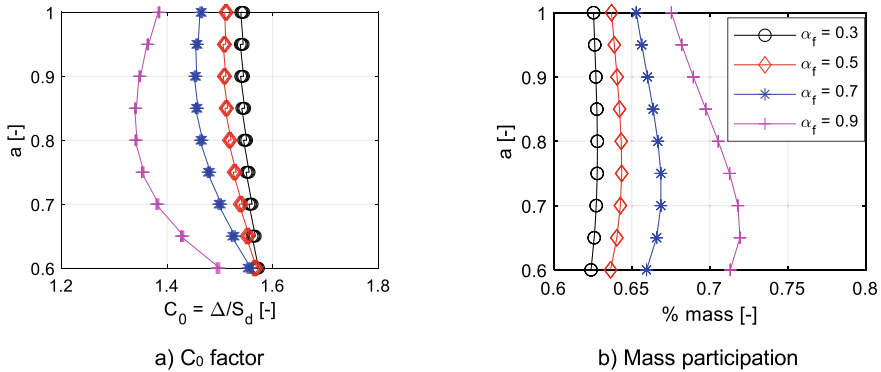
Fig. 5 **a** C_0 factor and **b** Mass participation

moment ration. Implying that the moment distribution is a first-mode dominated response.

The factor C_0 is used to relate the elastic displacement of a multiple degree of freedom (MDOF) system to a single degree of freedom (SDOF) system. Figure 5a shows C_0 as it relates to a and α_f. As shown, C_0 has a dependency on the relative stiffness factor (α_f), where a higher α_f results in a lower C_0. Additionally, there is more variance in the response for lower α_f than for higher. This response is likely due to the rigid outrigger driving a more dominant first-mode response.

Figure 5b shows the modal mass participation of first-mode response for each model. As shown, a high α_f results in a more significant modal mass contribution from the first mode. Furthermore, outriggers located at 70% the building height result in the highest first-mode dominated response.

5　Design of RC Walls in Canada

In design practice, high-rise buildings are typically designed for seismic demands following the National Building Code of Canada (NBCC). Typical high-rise buildings are simplified to equivalent elastic numerical models where the demands are estimated using model response spectrum method (MRSM) scaled to a minimum base shear determined using NBCC requirements. This method assumes that the nonlinear system's displacements are equal to the displacements from an equivalent elastic system. Hence, for a single degree of freedom (SDOF) system, the design displacements are determined by using an estimate of the structural period (T_n) to determine the spectral displacements (S_d) from the design spectrum. The corresponding design base shear is determined from the design spectral acceleration (S_a) reduced by a seismic force reduction factor (R). In the NBCC 2015, R is a combination of a ductility modification factor (R_d) and a force modification factor (R_o). According to the NBCC 2015, ductile RC shear walls use a ductility modification

factor of $R_d = 3.5$ and a force modification factor of $R_o = 1.6$, resulting in an $R = 5.6$.

According to the NBCC, 2015, structures that are taller than 60 m or which have period greater than 2.0 s must use dynamic analysis procedure to determine the seismic demands. Dynamic analysis consists of modal response spectrum method (MRSM), numerical integration linear time history method (NILTHM), or nonlinear time-history analysis (NLTHA). NLTHA is not readily accepted in industry due to the costly peer-review process; however, it is gaining more popularity as tall buildings become increasingly more complex. MRSM is the most prevalent method used by practicing engineers due to its efficiency.

It is well recognized that the extensive concrete cracking and reinforcement yielding in an RC core wall under strong earthquake shaking results in a more flexible response than the elastic behaviour using gross section properties [1]. This nonlinear behaviour is captured in design through the use of equivalent elastic models, which use an effective rigidity ($E_c I_{\text{eff}}$) to account for the additional displacements due to the nonlinear behaviour (ACI, 2016; [5]). For cantilever RC shear walls, the ACI, 2016 assumes the effective rigidity is equal to 50% of the gross rigidity ($E_c I_g$). In the Canadian Standard A23.3 [5], the effective rigidity ranges from 50 to 100% of the gross rigidity.

Like the conventional RC shear wall, it is expected outrigger-wall building will have a softer response under NLTHA than what is obtained from an elastic model with gross section properties. However, unlike the conventional RC core wall, where the lower rigidity is solely due to the RC wall's damage, the other systems have a combination of some wall damage and the inelastic response of the dampers. In leu of more sophisticated analysis, it is assumed that all systems utilize a $\alpha_w = 0.5$. For the systems which include an outrigger, it is assumed that the nonlinear distribution is the same as the elastic distribution of force. As a result, in leu of more sophisticated analysis, the outrigger stiffness is reduced by 0.5.

6   Design Plastic Mechanism

In typical cantilever walls, the energy dissipating mechanism is plastic hinging. Plastic hinging is a region of the wall which is designed for yielding of reinforcing steel and energy dissipation. In CSA A23.3, the length of the plastic hinge is conservatively determined using Eq. 9. To ensure a consistent ductile response within the plastic hinge region, the vertical reinforcing ratio must stay constant over the length of the plastic hinge.

$$l_p = 0.5l_w + 0.1h_w \tag{9}$$

where L_p is defined as the length of the plastic hinge region, l_w is the length of the longest wall (in the hinge region) in the direction considered, and h_w is the wall's height.

Fig. 6 Outrigger damper free-body diagram
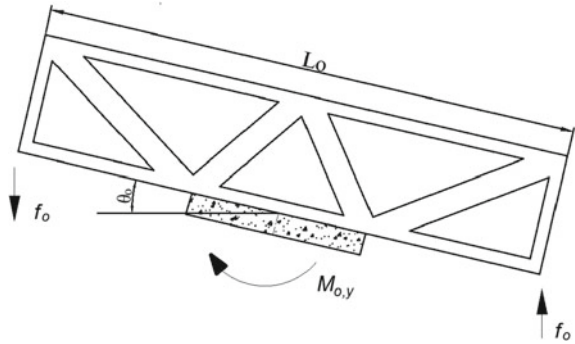
To ensure a wall has adequate ductility within the plastic hinge region, the inelastic rotational capacity of the wall, θ_{ic}, must be greater than the inelastic rotational demand, θ_{id}. For $R_d = 3.5$, the inelastic rotational demand at the base of a wall, θ_{id}, is determined using Eq. 10.

$$\theta_{id} = \frac{\left(\Delta_f R - \Delta_f \gamma_w\right)}{(h_w - l_w/2)} \geq 0.004 \tag{10}$$

where $\Delta_f R$ is the design displacement, and $\Delta_f \gamma_w$ is the elastic portion of the displacement.

The outrigger plastic mechanism is yielding of the dampers within the outrigger. The outrigger damper design forces are determined by resolving the outrigger moment into axial demands in the dampers. Figure 6 shows the free-body diagram of the outrigger system.

Based on equilibrium, the damper forces in the outrigger can be determined using Eq. 11. Similar to determining ductility demand in the wall, the rotational demand (δ_{oid}) in the outrigger is determined by Eq. 12.

$$f_o = \frac{M_{o,y}}{L_o} \tag{11}$$

$$\delta_{oid} = \delta_{fo} R - \gamma_w \delta_{fo} \tag{12}$$

where θ_{fo} is the rotational demand taken from the linear dynamic analysis, δ_{fo} is the factored deformation in the outrigger, and γ_w is the overstrength factor.

7 Capacity Design Procedure

Canadian design, the plastic hinge region is designed to have sufficient reinforcement to generate enough resistance against the factored moment from the dynamic analysis. As shown in Fig. 7a, the overstrength factor, γ_w, is taken as $M_{f,h}/M_{r,h}$, where $M_{f,h}$ and $M_{r,h}$ are the factored moment and moment resistance at the top of the plastic hinge, respectively. This overstrength factor is applied to the factored moment for the remaining of the wall to obtain the moment demand.

An outriggered wall also forms a plastic hinge region near the base, but the moment demand at the outrigger depends on the overstrength of the outrigger system, γ_o. The design process for the plastic hinge region is the same as the conventional core. The overstrength factor, γ_w, is obtained at the top of the plastic hinge region. There are currently no recommendations on the capacity design methods of outrigger-wall systems. In this study, the moment demand at the outrigger is taken as $\gamma_o M_{f,o}$, where $M_{f,o}$ is the factored moment at the outrigger. In between the outrigger and the top of the plastic hinge region, the moment demand is linearly interpolated against elevation as shown in Eq. 13.

a) CW

b) OW
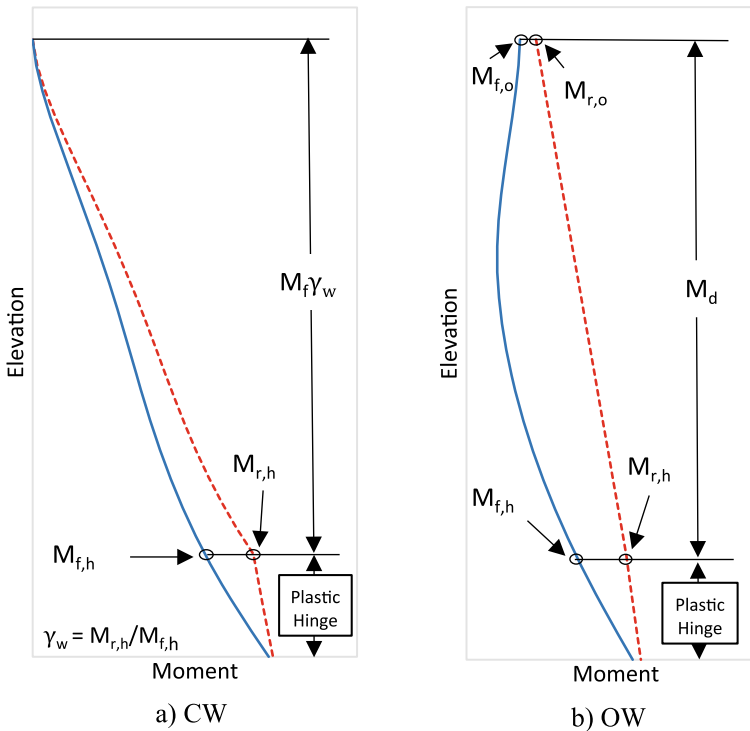
Fig. 7 Capacity design envelop

$$M_d = (M_{r,o} - M_{r,h})/(h_w - l_p) \times (h - l_p) + M_{r,h} \qquad (13)$$

where $M_{r,o}$ is the moment resistance at outrigger; $M_{r,h}$ is the moment resistance at the top of the plastic hinge region; and h is the height where the moment demand is to be calculated.

8 Prototype Buildings Design

Using the design procedure described in Sect. 6–7, a 24-story prototype building was designed with an outrigger and without an outrigger. The building was assumed to be located in Vancouver, Canada, with site class C according to the 2015 National Building Code of Canada. Figure 8 shows the geometry of the prototype building. The core wall has a dimension of 9250 mm × 9250 mm. The thickness of the webs and flanges are 990 mm and 580 mm, respectively. There are two opening to the centre of the core, each with a dimension of 2480 mm. The cross section of the wall is constant for all floors. The designed concrete compressive strength (fc') is 60 MPa, and the designed yielding stress of steel reinforcements is 400 MPa. Four mega-columns each with a dimension of 1250 mm × 1250 mm are placed at the end of the outrigger. The seismic mass of the prototype building 725,770 kg for each floor. It was assumed that wall sustained a gravity load of 1550 KN per floor. The modulus of elasticity was assumed to follow the [5] which is shown in Eq. 14.

$$E_c = 3300\sqrt{f_c'} + 6900[\text{MPa}] \qquad (14)$$

9 Elastic Modelling and Eigenvalue Analysis

The design demands are determined using elastic models built in ETABS. All buildings are modelled as fixed base, and as a result, only two unique elastic models are created: (1) a fixed base cantilever wall without an outrigger, called the cantilever wall (CW), and (2) a fixed base cantilever wall with an outrigger, called the outrigger wall (OW). The floors are modelled using slabs which are meshed for diaphragms and mass distribution. A distributed mass of 964.6 kg/m^2 is applied to the floor. Walls utilize automated meshing. Columns are pin connected and mass-based non-iterative p-delta effect is applied to the model. This study is limited to the effects of two-dimensional response, as such only the X, Z, and RZ degrees of freedom are considered.

The nonlinear effects to obtain displacement estimates are accounted for by using an effective rigidity (EI$_{\text{eff}}$ = 0.5EI$_g$). The outrigger systems use the same effective stiffness as the wall (i.e., the outrigger beam, columns, and dampers all use and effective stiffness). This is to ensure the same distribution of forces as the elastic

Elevation and plan layout of prototype building
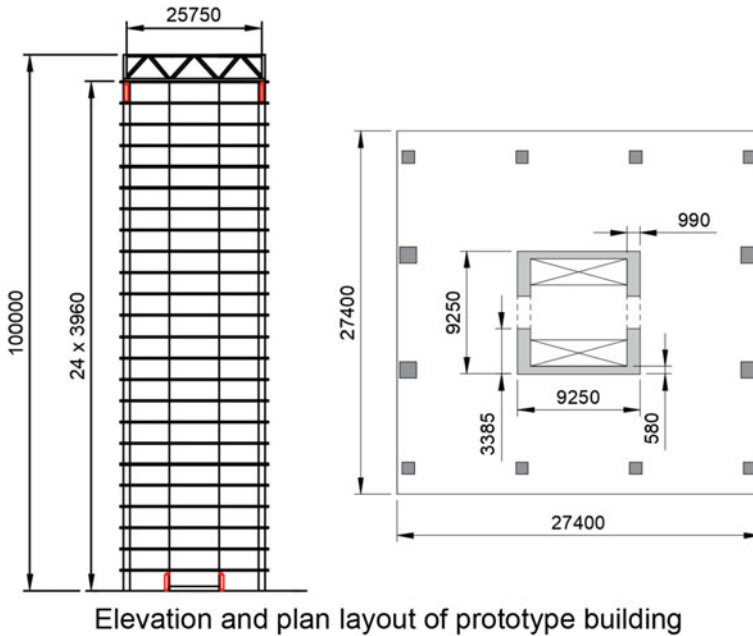
Fig. 8 Elevation and plan layout of prototype building

system. Table 1 shows the natural periods and the modal mass participation of the cantilever wall with and without the outrigger. As shown, the outrigger system has about 4% more mass participation in the first mode than the fixed base wall. On the other hand, the second mode and the third mode are 3% and 1% less modal mass participation, respectively, when compared with the fixed base models. The outrigger systems first, second, and third mode periods are 22, 10, and 5% reduction when compared with the fixed base system.

Figure 9 shows the different mode shapes for the first, second, and third modes for the fixed base wall with and without the outrigger. As shown, the first-mode displaced shape of the OW has a more double curvature response when compared to CW. The displaced shapes of the second and third modes are similar between the CW and OW.

Figure 10 shows the inter-story drift ratio (ISDR) for the first, second, and third modes for the fixed base wall with and without the outrigger. The OW has a peak

Table 1 Periods and mass participation

Mode	Natural periods			Mass participation		
	1	2	3	1	2	3
Outrigger wall (OW)	2.74	0.52	0.21	0.67	0.17	0.06
Cantilever wall (CW)	3.51	0.58	0.22	0.63	0.20	0.07
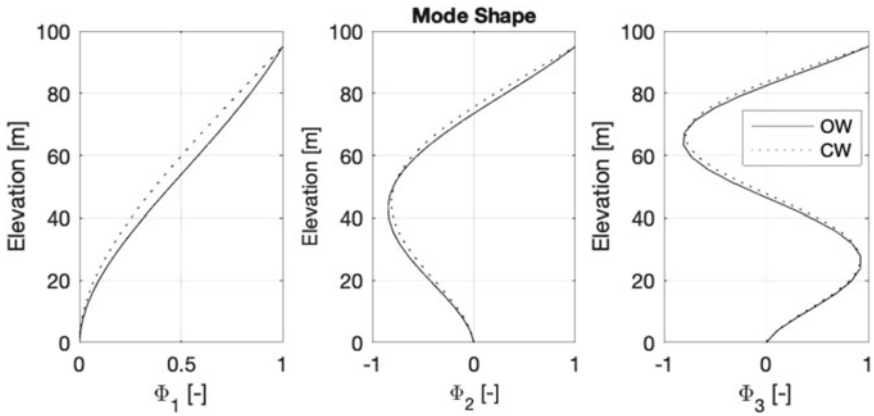
Fig. 9 Eigenvalue response of displaced shape

inter-story drift at the 15th story, while the CW has a peak ISDR over the top four stories. The second and third mode show peak ISDR near the top story.

Figure 11 shows the comparison between the shear modal behaviour. The first modes have almost identical shear distributions, emphasizing the outriggers limited effect on shear forces in the structure.

Figure 12 shows the comparison between the moment behaviour. As shown, the first-mode moment for the CW is maximum at the base and zero at the top of the building. On the other hand, while the outrigger building has peak first-mode moment at the base, it has a first-mode moment in the opposite direction at the roof. The implication of having zero moment near the 60th story can result in drastically reduced moment demands when designing the outrigger system.
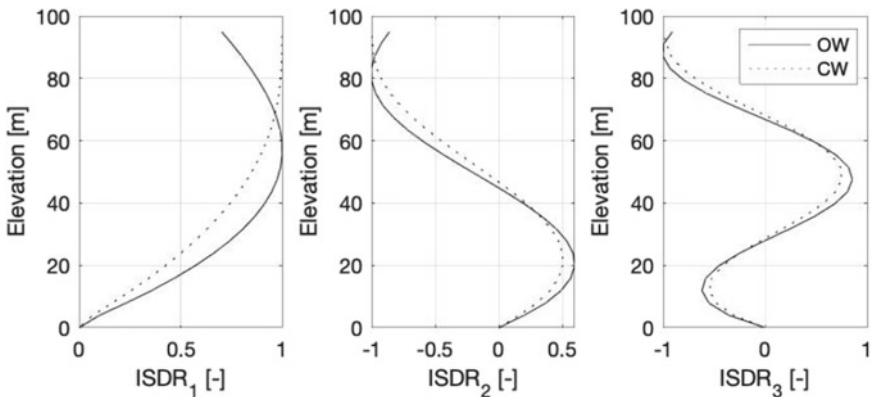
Fig. 10 Eigenvalue response of ISDR
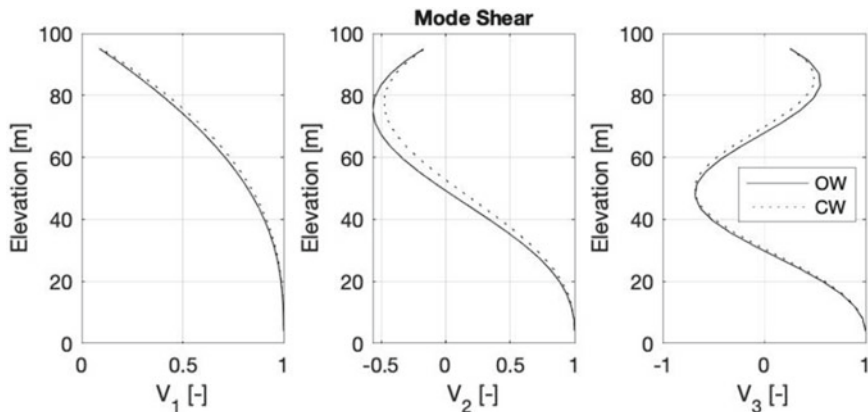
Fig. 11 Eigenvalue response of shear
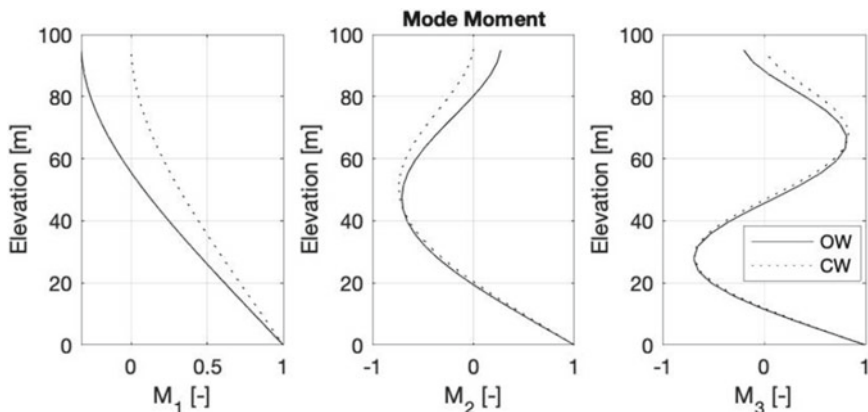
Fig. 12 Eigenvalue response of moment

10 Model Response Spectrum Method (MRSM)

Modal response spectrum analysis was completed using ETABS. The first five modes were combined using the complete-quadratic-combination (CQC) method and 5% damping. The design spectrum displacement and acceleration spectrums are shown in Fig. 13. To eliminate the effects of amplified displacements due to linear interpolation, an acceleration spectrum determined through interpolating the displacement spectrum was used to determine the demands from ISDR and displacements.

Table 2 summarizes the main results from the MRSM scaled to the NBCC base shear. As shown, the addition of the outrigger gives an increase in base shear of 7% which can be attributed to the lower natural period of the OW compared to the CW. Interestingly, the OW moment is only 3% less than the CW moment. This reduction
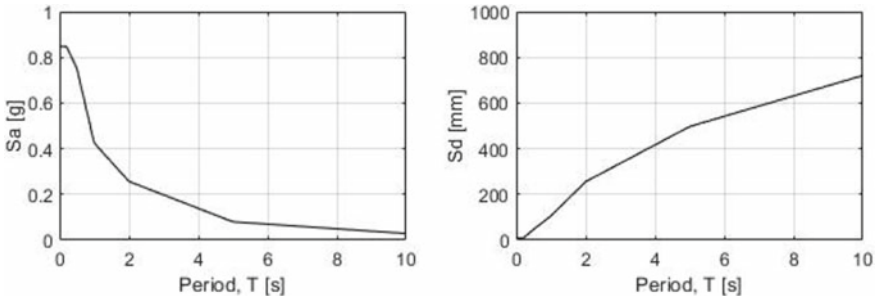
Fig. 13 Design spectrum

is smaller than would be expected by the same outriggered system under static loads, as the lower period results in higher force demands, thereby decreasing the outrigger efficiency for moment reduction. However, the outrigger shows a major advantage when comparing displacements and drifts, boasting a decrease in ISDR of 24% and reduction in roof-drift-ratio (RDR) of 18%.

Figure 14 shows the story plots for displacements, ISDR, moment, and shear determined using MRSM. The OW building has similar displacements compared to the CW for over half the building height. However, there are notable difference between displacements in each building at the roof. In the upper half of the building, the OW displaced shape curves back near the roof, drastically reducing displacements compared to the CW building.

Like the displacements, ISDR is similar between OW and CW until Story 8, at which point the CW building has high ISDR while the OW reduces in magnitude with increased elevation.

The moment diagrams are expectedly different between the OW and CW. An important observation is the near elimination of the higher mode moments of the OW building at 60% of the building height. The OW has low moment demands in the same location that the CW has amplified moment demand. This is due to the first-mode response of the outrigger being zero at this location, resulting in the modal combination to have no contribution from the first, most significant, mode.

The shear distribution of the CW building has a similar shape as the OW building. However, the OW building has higher magnitude of shear due to the lower fundamental period.

Table 2 Global responses

	Base shear	Outrigger moment	Base moment	Inter-story drift ratio	Roof drift ratio	M_v
	V/W	$M_o/W/H$	$M_b/W/H$	ISDR	RDR	M_v
OW (%)	4.26	0.56	1.74	0.84	0.65	1.12
CW (%)	3.97	–	1.79	1.11	0.78	1.14
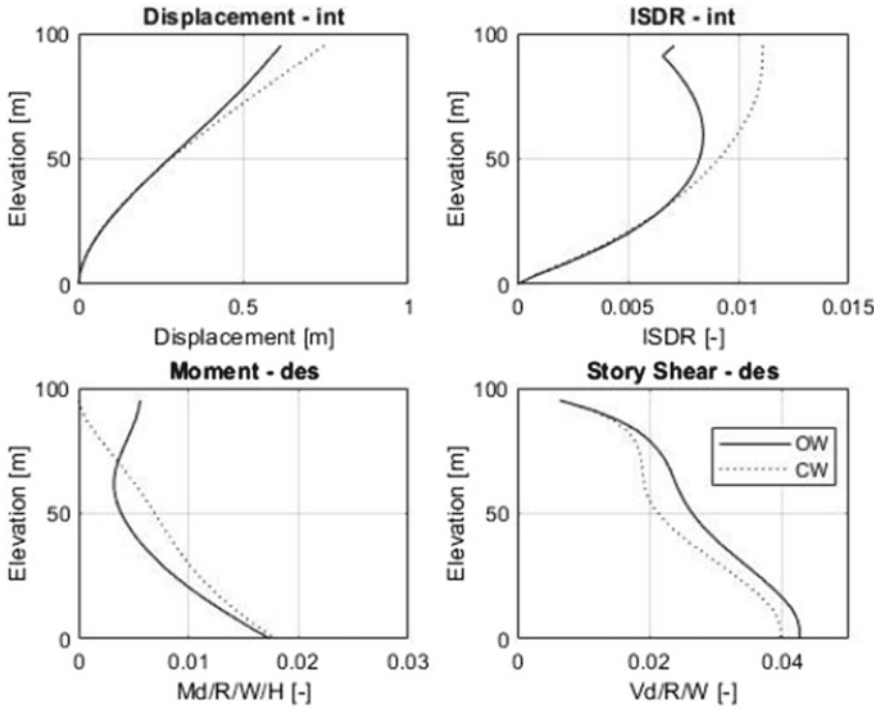
Fig. 14 Global modal response spectrum analysis

The length of the plastic hinge is calculated to be 14 m; however, as per typical practice, the hinge length is increased to the bottom of the stories, so the CW proto-types are designed for the first four stories. The CW and OW reinforcements were designed such that the resistance was greater than the demand. The capacity design process described in Sect. 7 was implemented, and the corresponding rebar is shown in Table 3.

11 Summary and Conclusions

In this study, a comprehensive parametric analysis is completed to provide empirical relations for the dynamic response of outrigger buildings. These parameter studies are used to develop a practical seismic design guideline for outrigger systems. Prototype outrigger-wall buildings are designed with the proposed methods. These prototype buildings are located in a high seismicity region of Canada (Vancouver).

Table 3 Summary of concentrated reinforcement

Story	CW	OW
24		
23		
22		
21		
20		
19		
18		
17		
16		
15		
14		
13		
12		16-20M
11		
10		
9		
8		
7	12-20M	
6		
5		
4		
3		
2	18-20M	18-20M
1		

20M@200mm V.E.F
20M@200mm H.E.F

Zone reinforcing (Table)

15M@250mm V.E.F
15M@250mm H.E.F

20-20M@200mm V.E.F
20M@200mm H.E.F
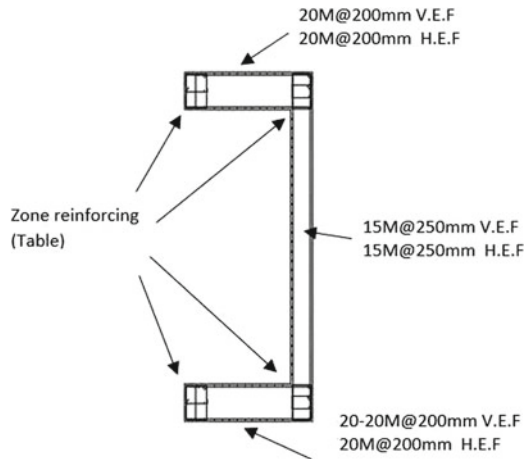
The following conclusions were identified:

- The natural period is depending highly on the relative stiffness factor α_f. Where an infinitely rigid outrigger (i.e., $\alpha_f = 1$) would only result in about 38% reduction in fundamental period if compared to a system without an outrigger (i.e., $\alpha_f = 0$).
- The modal mass participation shows that higher relative outrigger stiffness results in a more dominate first-mode response.
- The ratio between roof displacement to spectral displacement $\left(C_0 = \frac{\Delta_r}{S_d} \right)$ decreases with an increase in α_f.
- Roof displacements are almost entirely governed by the first-mode response regardless of spectral shape.
- Inverted triangular static distribution gives a satisfactory estimate of the displacements
- When scaling to NBCC base shear, the base moment in the outrigger building is comparable to the conventional building due to the lower natural period of the outrigger building.

Modal response spectrum analysis shows minimum moment at 60% of the height of the building for a roof-top outrigger. It is important to note that further research should be completed on a range of building heights to identify the impact of outrigger design decisions on the nonlinear response.

References

1. Adebar P, Ibrahim A, Bryson M (2007) Test of high-rise core wall: effective stiffness for seismic analysis. ACI Struct J 104(5) https://doi.org/10.14359/18857
2. Adebar P, DeVall R, Mutrie J (2017) Evolution of high-rise buildings in Vancouver, Canada. Struct Eng Int 27(1):7–14, , Informa UK Limited. Crossref, https://doi.org/10.2749/101686617x14676303588670
3. American Society of Civil Engineers. ASCE (2016) Minimum design loads for buildings and other structures (ASCE/SEI 7–16)
4. American institute of steel construction (AISC) (2016) Seismic provisions for structural steel buildings (ANSI/AISC 341–16)
5. Group, CSA (2014) CSA A23.1–14/A23.2–14: concrete materials and methods of concrete construction. Toronto, Ontario
6. Building Code Requirements for Structural Concrete (ACI 318–16): An ACI Standard; Commentary on Building Code Requirements for Structural Concrete (ACI 318R-16). American Concrete Institute (2016)
7. Ghodsi T, Ruiz JF, Massie C, Chen Y (2010) PEER/ SSC tall building design case history no. 2. Struct Des Tall Special Build 19(1–2):197–256
8. Hall JF (2006) Problems encountered from the use (or misuse) of Rayleigh damping. Earthquake Eng Struct Dynam 35(5):525–545. https://doi.org/10.1002/eqe.541
9. Huang B, Takeuchi T (2017) Dynamic response evaluation of damped-outrigger systems with various heights. Earthq Spectra 33(2):665–685. https://doi.org/10.1193/051816eqs082m
10. Lin PC, Takeuchi T, Matsui R (2018) Seismic performance evaluation of single dampedoutriggersystem incorporating buckling-restrained braces. Earthquake Eng Struct Dyn. https://doi.org/10.1002/eqe.307
11. Morales-Beltran M, Turan G, Dursun O, Nijsse R (2018) Energy dissipation and performance assessment of double damped outriggers in tall buildings under strong earthquakes. Struct Design Tall Spec Build 28(1):e1554. https://doi.org/10.1002/tal.1554
12. National research council of Canada (NRCC) (2015) National building code of Canada 2015. National Research Council of Canada, Ottawa, Ontario, Canada
13. Natural Resources Canada (NRCAN). Earthquake map of Canada. Retrieved from https://earthquakescanada.nrcan.gc.ca/historic-historique/caneqmap-en.php (Accessed 31 Dec 2020)
14. Smith RJ, Willford MR (2007) The damped outrigger concept for tall buildings. Struct Des Tall Special Build 16(4):501–517
15. Sritharan S, Aaleti S, Henry RS, Liu K-Y, Tsai K-C (2015) Precast concrete wall with end columns (PreWEC) for earthquake resistant design. Earthquake Eng Struct Dynam 44(12):2075–2092. https://doi.org/10.1002/eqe.2576
16. Xing L, Zhou Y, Aguaguiña (2018) Optimal vertical configuration of combined energy dissipation outriggers. Struct Design Tall Special Build. https://doi.org/10.1002/tal.1579
17. Yang TY, Atkinson J, Tobber L, Tung DP, Neville B (2020) Seismic design of outrigger systems using equivalent energy design procedure. Struct Design Tall Special Build 29(10). https://doi.org/10.1002/tal.1743
18. Zhou Y, Zhang C, Lu X (2016) Seismic performance of a damping outrigger system for tall buildings. Struct Control Health Monitor 24(1). https://doi.org/10.1002/stc.1864

Evaluation of the AISC Seismic Design Method for Steel-Plate Concrete Shear Walls

Gharavi Ali, Asgarpoor Masoumeh, Epackachi Siamak, Mirghaderi Seyed Rasoul, and Imanpour Ali

Abstract Steel-plate concrete (SC) shear walls are used as the lateral-load resisting system in high-rise buildings as they can offer faster construction and reduced construction cost compared with their conventional reinforced concrete counter-parts. This paper aims to predict the moment capacity of SC shear walls using the finite element analysis method and evaluate the current method by the AISC Seismic Provisions. Numerical parametric study of SC walls is used to develop a predictive equation for the moment capacity of such walls. The numerical analyses are then used to evaluate the method currently prescribed by the AISC Seismic Provisions. It is shown that the AISC design equation may not accurately predict the moment capacity of SC walls and should be improved.

Keywords AISC · Seismic design · Shear walls

1 Introduction

Steel–Concrete (SC) composite shear walls consist of plain infill concrete covered by steel faceplates on both sides. Tie rods are used as connectors between two steel face-plates to prevent their buckling, and shear-headed studs attach the concrete to steel faceplates to develop composite action between them [9], see Fig. 1.

G. Ali · A. Masoumeh
Sharif University of Technology, Tehran, Iran

E. Siamak (✉)
Amirkabir University of Technology, Tehran, Iran
e-mail: Epackachis@aut.ac.ir

M. S. Rasoul
University of Tehran, Tehran, Iran

I. Ali
University of Alberta, Alberta, Canada

Fig. 1 SC wall configuration [9]
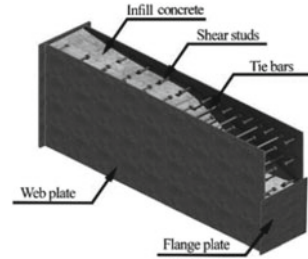
To obtain the moment capacity of SC walls, Kurt et al. proposed equations to calculate the moment capacity of double skin plate SC walls without boundary elements using parametric studies in LS-DYNA, based on tested squat walls [8]. They recommended the use of yield moment capacity, M_y, for walls with an aspect ratio of 0.5, and use of plastic moment capacity, M_p, for walls with an aspect ratio larger than 1.5, and interpolation with consideration of wall thickness for walls with an aspect ratio between 0.5 and 1.5. The yield moment capacity, M_y, corresponds to the yielding of steel under tension with its specified minimum yield strength, F_y, and the first yield in steel under compression with strength, F_y, also considering linear elastic distribution for concrete under compression with the maximum compressive stress equal to 0.7 f_c'. The plastic moment capacity, M_p, corresponds to the full minimum yield strength of steel, F_y, on both tension and compression parts and rectangular Whitney block with compressive stress equal to 0.85 f_c', for concrete under compression. The methodology presented by Kurt et al. was validated for only double skin plate shear walls with limited design variables [8]. The standard AISC 341-16 recommends the use of yield moment capacity, M_y, for SC walls without boundary elements and the use of plastic moment capacity, M_p, for SC walls with boundary elements [1]. For calculation of M_p in AISC 341-16, use of f_c' instead of 0.85 f_c' is recommended. Epackachi et al. conducted a set of monotonic numerical studies in LS-DYNA on SC walls, considering different design variables, including aspect ratio, axial compression ratio, slenderness ratio, reinforcement ratio, axial compression ratio, infill concrete compressive strength, and minimum yield strength of steel faceplates [5]. They considered three values for each design variable and used the design of experiment (DOE) method to reduce the number of analyses effectively. Considering the interaction of shear and axial loading, they proposed an equation for calculating the moment capacity of SC walls with respect to mentioned design variables. The equation proposed by Epackachi et al. was complex and limited to walls without end plates and boundary elements. Moreover, Eapackachi et al. show that all SC walls, including squat and slender are flexural-critical [5].

A robust FE model is required before conducting a large number of numerical analyses, which provides a dataset for the development of predictive equations for the moment capacity of SC walls. Asgarpour et al. presented a comprehensive validation study for numerical modeling of different shapes of SC walls tested in the literature [3]. For modeling the infill concrete, the Winfrith material model is used in LS-DYNA, as it was shown to be an appropriate material model for capturing the fundamental characteristics of concrete in past studies [2, 3, 4, 6, 7]. All assumptions

of numerical modeling used in this paper, including material modeling, the element selected, and interactions are included in [3] and not repeated here for brevity.

Although some efforts have been made for proposing an accurate equation for the moment capacity of SC walls, further investigation is needed for developing an equation for the moment capacity of SC walls, which would be applicable for a variety of SC walls, considering different design variables, especially the wall shape and has an easy-to-use formulation, which is the primary goal of this study. In this paper, a simple and accurate formulation is implemented for SC walls with four cross-sectional shapes, including double skin rectangular, rectangular with end plates, rectangular with boundary elements, and flanged SC walls, considering six design variables, including aspect ratio, slenderness ratio, reinforcement ratio, axial load ratio, infill concrete compressive strength, and minimum yield strength of steel faceplates.

2 Predictive Equation Development

A six design variables that significantly affect the local and global response of SC walls are: aspect ratio, H/L_w, reinforcement ratio, A_s/A_g, slenderness ratio, S/t_s, axial load ratio, $P_u/(A_s F_y + A_c f_c')$, yield strength of the steel faceplates, F_y, and concrete compressive strength, f_c'. This study selects three values (min, max, and mean values used in practice) for each design parameter. The values in the parentheses are coded values indicating low (-1), intermediate (0), and, high (1) values of the design parameters. The values of the design parameters are summarized in Table 1. Based on the AISC 341-16, identical dimensions (10 mm diameter) and properties are assumed for the connectors, i.e., tie rods for all models. However, the distance between tie rods is considered an important design variable.

In this study, four cross-section shapes are considered for SC walls, including double skin plates SC wall (DS-SC wall), double skin plates with end plates SC wall (DSE-SC wall), SC wall with boundary elements (BE-SC wall), and flanged SC wall (FBE-SC wall), see Fig. 2. Based on the number of design variables and considering three values for each shape, 729 analyses need to be conducted for walls with each cross-sectional shape. To effectively consider the effects of design

Table 1 Levels of the design variables

Variable	Low	Intermediate	High
Aspect ratio (AR)	0.5 (-1)	1 (0)	3 (1)
Reinforcement ratio (RR) [%]	4 (-1)	6 (0)	10 (1)
Slenderness ratio (SR)	15 (-1)	25 (0)	40 (1)
Axial load (AL) [%]	0 (-1)	10 (0)	20 (1)
Yield strength of the steel faceplates (SS) [MPa]	235 (-1)	350 (0)	460 (1)
Concrete compressive strength (CS) [MPa]	27.5 (-1)	42 (0)	55 (1)
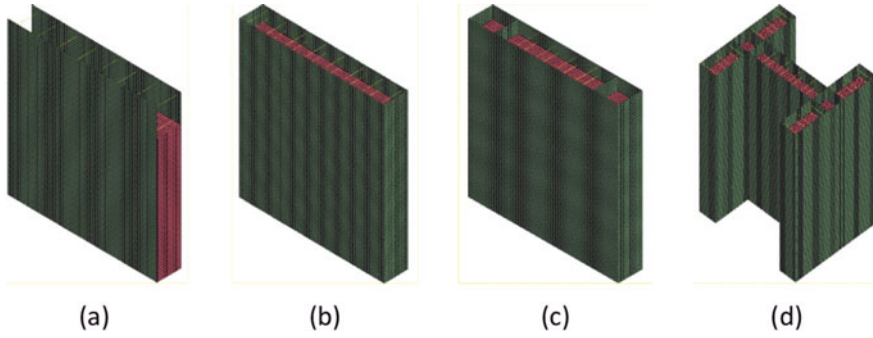
Fig. 2 Four cross-section shapes: **a** Double skin plates SC wall (DS-SC wall), **b** Double skin plates with end plates SC wall (DSE-SC wall), **c** SC wall with boundary elements (BE-SC wall), **d** Flanged SC wall (FBE-SC wall)

variables on the moment capacity of SC walls, a design of experiments (DOE) is used, which reduces the number of analyses from 729 to 88. In the FE models, fixed restraints are considered for the bottom of the SC walls, and lateral load is applied at the top monotonically. Then, the moment capacity of each model is monitored as the corresponding peak lateral load multiplied by its height.

Equations 1–3 are developed to calculate the moment capacity of SC walls considering six design variables and four configurations. Based on Eq. 1, moment capacity of SC walls is based on plastic moment capacity introduced by AISC 341-16 formulation and is modified to consider the effect of these design variables. To identify the importance of each design variable on the moment capacity of SC walls, their coefficient of variation (COV) is determined first. Then, the design variable with the largest COV is eliminated, and the accuracy of the revised equation is evaluated. Although design variables considered in equations significantly impact the accuracy of proposed equations, their importance is different. For instance, the importance of reinforcement ratio is less than other design variables for BE-SC Wall (see Table 2), but it is not ignorable.

$$M_n = \lambda M_P^\gamma \tag{1}$$

$$\lambda = \frac{c\lambda_1^{\alpha_1}}{\lambda_2^{\alpha_2}\lambda_3^{\alpha_3}\lambda_4^{\alpha_4}\lambda_5^{\alpha_5}} \tag{2}$$

$$\lambda_1 = \frac{h}{l_w}; \quad \lambda_2 = \frac{S}{t_s}; \quad \lambda_3 = \frac{A_s}{A_g}; \quad \lambda_4 = \frac{f_y}{f_c'}; \quad \lambda_5 = (1 - N), \quad N = \frac{P_u}{f_c'A_c + f_yA_s} \tag{3}$$

Table 2 Parameter values for Eqs. (1–3)

Shape	c	γ	α_1	α_2	α_3	α_4	α_5
DS-SC wall	6.63	0.83	0.15	0.17	0.08	0.13	0.82
DSE-SC wall	2.04	0.95	0.18	0.09	0.10	0.15	0.44
BE-SC wall	3.50	0.90	0.18	0.04	0.004	0.19	0.65
FBE-SC wall	3.99	0.84	0.54	0.09	0.10	0.14	0.35

3 Evaluation of the Proposed Equation

AISC 341-16 design method for SC walls does not consider the effects of design variables including aspect ratio, slenderness ratio, reinforcement ratio, axial load ratio, and cross-sectional shape on the moment capacity of SC walls. The simple plastic stress distribution method might not lead to an accurate prediction of the actual moment capacity of SC walls. To investigate whether and to what extent ignorant of these design variables changes the results, the moment capacity based on the proposed equation and AISC 341-16 methodology is compared with all cross-sectional shapes, as shown in Fig. 3. The black and red points in Fig. 3 depict the moment capacity values based on the proposed equation and AISC 341-16 method, respectively. The more the predicted values get closer to the bisector line, shown as a dashed line, the more accurate that formulation is. The proposed equation in this study predicts the actual moment capacity of all SC walls with high accuracy and low dispersion. Among four studied cross-sectional shapes, the AISC 341-16 method results in the minimum and maximum errors in DSE-SC and FBE-SC walls, respectively. Figure 3a shows that the AISC 341-16 method underestimates the moment capacity of rectangular SC walls without boundary elements. In particular, in the models with a high aspect ratio, low reinforcement ratio, and high axial load ratio, the moment capacity of the walls is much higher than M_y and close to $2M_y$ in some cases. It is concluded that the use of M_y in DS-SC walls leads to reasonable results only for low aspect ratio walls, moderate values for slenderness ratio and reinforcement ratio, and zero axial load value.

Figure 3b–d show that the AISC 341-16 method overestimates the moment capacity of most SC walls with rectangular end plates and boundary elements and, in particular, flanged walls, which leads to nonconservative results. As shown in Fig. 3b, DSE-SC walls with low aspect ratios have the maximum errors, exhibiting up to 50% overestimating the effects in DSE-SC walls with low aspect ratios and high axial load ratios. Figure 3c shows that AISC 341-16 design equation overestimates the capacity of BE-SC walls with low aspect ratios and underestimates that of walls with a high axial load ratio.

It is inferred that the use of M_p in the walls with end plates and boundary elements leads to reasonable results only for high aspect ratio walls, moderate values for slenderness ratio and reinforcement ratio, and zero axial load value. In general, AISC 341-16 method resulted in a less accurate prediction of the moment capacity
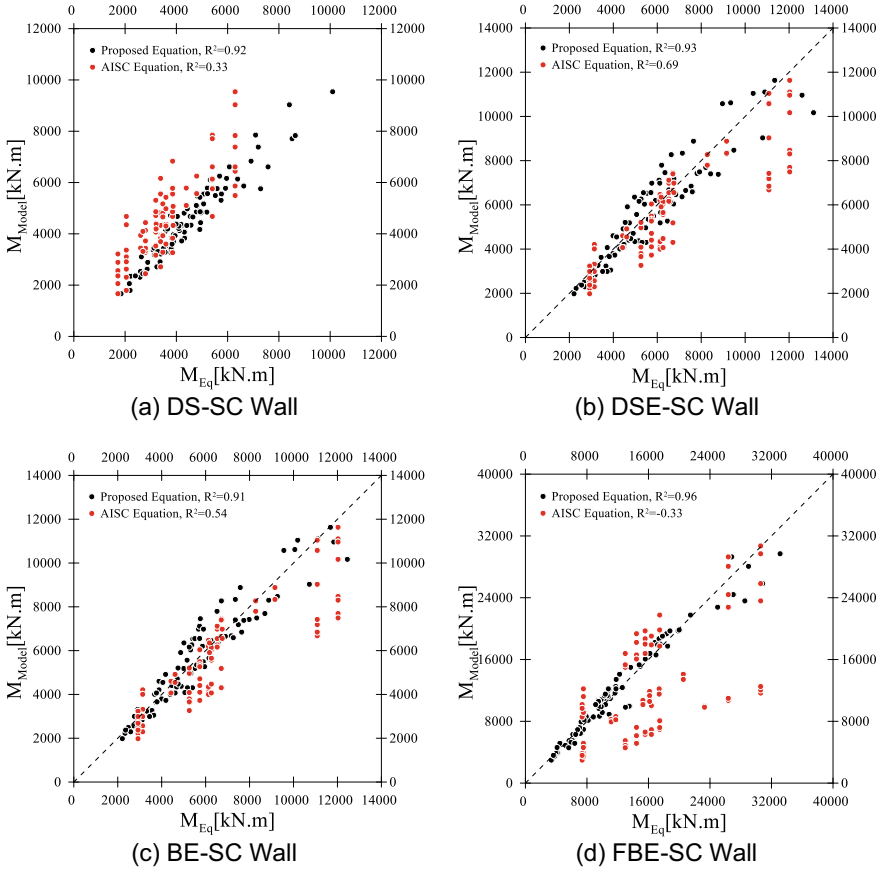
Fig. 3 Calculated moment capacity based on the proposed equation and AISC 341-16

for the studied here, suggesting the importance of considering different key design variables in the design of the moment capacity of SC walls.

4 Conclusions

A new equation was developed to predict the moment capacity of Steel–Concrete (SC) shear walls using the results of extensive numerical analyses performed in LS-DYNA. The proposed equation was then used to evaluate the current AISC 341-16 design equation. A perfect prediction of the SC wall moment capacity was obtained using the proposed equation. It was also confirmed that the AISC 341-16 method might underestimate the moment capacity of DS-SC walls, in particular when the wall has a high aspect ratio and high axial load ratio, while it may overestimate the

moment capacity of DSE-SC walls, BE-SC walls, and BE-SC walls, in particular those with low aspect ratio. Further numerical simulations and experimental testing are required to improve seismic design provisions used to design SC walls.

References

1. AISC (2016) Seismic provisions for structural steel buildings (AISC 341–16). In.
2. Asgarpoor M, Gharavi A, Epackachi S (2021a) Investigation of various concrete materials to simulate seismic response of RC structures. In Structures, 1322–51. Elsevier
3. Asgarpoor M, Gharavi A, Epackachi S, Mirghaderi SR (2021) Finite element analysis of rectangular and flanged steel-concrete shear walls under cyclic loading. Struct Design Tall Spec Build 30:e1863
4. Epackachi S, Nguyen NH, Kurt EG, Whittaker AS, Varma AH (2015) In-plane seismic behavior of rectangular steel-plate composite wall piers. J Struct Eng 141:04014176
5. Epackachi S, Whittaker AS, Aref A (2017) Seismic analysis and design of steel-plate concrete composite shear wall piers. Eng Struct 133:105–123
6. Epackachi S, Whittaker AS, Varma AH, Kurt EG (2015) Finite element modeling of steel-plate concrete composite wall piers. Eng Struct 100:369–384
7. Gharavi A, Asgarpoor M, Epackachi S (2022) Evaluation of plasticity-based concrete constitutive models under monotonic and cyclic loadings. Struct Design Tall Spec Build 31:e1919
8. Kurt EG, Varma AH, Booth P, Whittaker AS (2016) In-plane behavior and design of rectangular SC wall piers without boundary elements. J Struct Eng 142:04016026
9. Shafaei S, Varma AH, Seo J, Klemencic R (2021) Cyclic lateral loading behavior of composite plate shear walls/concrete filled. J Struct Eng 147:04021145

Reliability Assessment of Concrete-Filled RHS Beam-Column Design Provisions

Fatemeh Rahbarimanesh and Kyle Tousignant

Abstract Revisions were recently proposed to the way in which concrete-filled hollow structural section members are handled in CSA S16. These revisions were based on previous research, comparisons to experiments, and an approximate first-order reliability method analysis of the new and existing provisions. Herein, this topic is further expanded by using Monte Carlo simulations (MCS) to evaluate the reliability of design rules for concrete-filled rectangular hollow section (RHS) beam-columns. A representative set of ten concrete-filled RHS members is analysed with variations in wall slenderness, effective length, and loading eccentricity. Using MCS, reliability indices (β^+) are determined over a range of live-to-dead load ratios. The β^+ values are compared to the code-specified target of $\beta^+ = 3.0$ in Annex B of CSA S16.

Keywords Concrete-filled RHS · Beam-column design

1 Introduction

Over the last two decades, American and European design provisions for concrete-filled hollow structural sections (HSS) under static loading (in AISC 360 and Eurocode 4, respectively) have evolved to permit the use of larger tube sizes, slenderer cross sections, and longitudinal steel reinforcing bars. In contrast, the design provisions in Canada for concrete-filled HSS (in CSA S16 Clause 18.2) [8] have remained relatively constant and limited in scope.

Recently, following the completion of CIDECT Design Guide No. 4, 2nd edition (on concrete-filled HSS under static, impact, blast, seismic and fire loading) [21], Tousignant and Packer [18, 19] conducted a review of the design rules in CSA S16 Clause 18.2 [8], which led to proposed changes in its scope (i.e., material and cross-sectional classification limitations) and several provisions (i.e., for compressive

F. Rahbarimanesh · K. Tousignant (✉)
Dalhousie University, Dalhousie, Canada
e-mail: kyle.tousignant@dal.ca

resistance, flexural resistance, and beam-columns). An overview of these proposed changes is given in Tousignant and Packer [20].

The proposed changes by Tousignant and Packer [18, 19] to the CSA S16 design formulae for the compressive resistance and bending resistance of concrete-filled HSS were supported, in part, by approximate first-order reliability method analyses that utilized data from over 450 tests to determine their inherent safety indices over a range of design scenarios [18, 19]; however, the impact of these proposed changes on the reliability of the beam-column interaction equation(s) (in Clause 18.2.4) was not directly assessed.

In this paper, Monte Carlo simulations (MCS) are used to extend the above work by re-analysing data from Tousignant and Packer [18, 19] and the corresponding database [17] to determine inherent reliability indices (β^+) for the concrete-filled rectangular hollow section (RHS) beam-column design provisions proposed by Tousignant and Packer [19]. Section 2 presents an overview of the current rules and the proposal; Sects. 3–5 discuss the MCS approach; and Sect. 5.2 summarizes the results. The conclusions of this research study are presented in Sect. 6.

2 Design Provisions for Concrete-Filled RHS Beam-Columns

2.1 CSA S16:19

The current design rules for concrete-filled RHS beam-columns (in CSA S16:19 Clause 18.2.4) apply to members with 20 MPa $\leq$ concrete strength (f_c') $\leq$ 40 MPa, and sections with flat width-to-thickness ratios (b_{el}/t) that meet the limits in Table 1. These limits are intended to ensure that the RHS can undergo complete plastification.

Provided that these limits are met, concrete-filled RHS beam-columns can be proportioned according to Eq. (1):

$$\frac{C_f}{C_{rc}} + \frac{\beta\omega_1 M_f}{M_{rc}\left(1 - \frac{C_f}{C_{ec}}\right)} \leq 1.0 \quad \text{and} \quad \frac{M_f}{M_{rc}} \leq 1.0 \tag{1}$$

Table 1 Limits for concrete-filled RHS elements in axial or flexural compression

Action	Element	Limit(s)	
		CSA S16:19	Proposed
Axial compression	Flanges	$1350/\sqrt{F_y}$	$1350/\sqrt{F_y}$
	Webs	$1350/\sqrt{F_y}$	$1350/\sqrt{F_y}$
Flexural compression	Flanges	$1350/\sqrt{F_y}$	$1010/\sqrt{F_y}$
	Webs	$1350/\sqrt{F_y}$	$1340/\sqrt{F_y}$

where C_f = factored compressive force; M_f = factored moment; C_{rc} = compressive resistance; M_{rc} = moment resistance; ω_1 = coefficient to determine the equivalent uniform bending effect (found in CSA S16:19 Clause 13.8.6); C_{ec} = Euler buckling strength; and β = coefficient for bending.

In Eq. (1), C_{rc} is taken as

$$C_{rc} = \frac{\tau\phi A_s F_y + \tau'\alpha_1\phi_c A_c f'_c}{(1 + \lambda^{2n})^{\frac{1}{n}}} \quad \text{with} \quad \lambda = \sqrt{\frac{C_p}{C_{ec}}} \quad \text{and} \quad C_{ec} = \frac{\pi^2 E I_e}{(KL)^2} \quad (2)$$

where A_s and A_c = cross-sectional area of steel and concrete; ϕ and ϕ_c = resistance factor for steel and concrete (= 0.9 and 0.65, respectively); τ = confinement reduction factor for steel (= 1.0 for concrete-filled RHS); τ' = confinement enhancement factor for concrete (= 1.0, again, for concrete-filled RHS); α_1 = ratio of average stress in rectangular stress block to f'_c (= $0.85 - 0.0015 f'_c \geq 0.73$); n = column curve parameter (= 1.80); λ = non-dimensional slenderness parameter; $C_p = C_{rc}$ computed with $\phi = \phi_c = 1.0$ and $\lambda = 0$; and EI_e = effective elastic flexural stiffness of the composite column, taken as:

$$EI_e = EI_s + \frac{0.6 E_c I_c}{1 + C_{fs}/C_f} \quad (3)$$

where I_s and I_c = moment of inertia of the steel and concrete areas, respectively, as computed with respect to the centre of gravity of the cross section; E = modulus of elasticity of steel; E_c = modulus of elasticity of concrete (found in CSA S16:19 Clause 3); C_{fs} = sustained axial load on the column; and C_f = total axial load on the column.

M_{rc} in Eq. (1) is taken as

$$M_{rc} = C_r e + C'_r e' \quad (4)$$

with (4)

$$C_r = \frac{\phi A_s F_y - C'_r}{2} \quad \text{and} \quad C'_r = 1.18\alpha_1\phi_c a(b - 2t) f'_c \quad (5)$$

$$C_r + C'_r = T_r = \phi A_{st} F_y \quad (6)$$

where C_r = compressive resistance of steel above the neutral axis (NA); C_r' = compressive resistance of concrete above the NA (over the depth of the concrete compression zone, a); e = lever arm between C_r and T_r; T_r = tensile resistance of steel below the NA (with an area of A_{st}); and e' = lever arm between C_r' and T_r (Fig. 1).
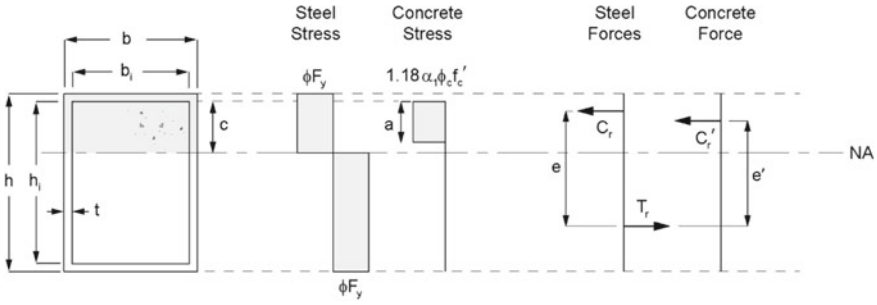
Fig. 1 Stress and force diagrams for concrete-filled RHS, simplified to a box section (CSA S16:19)

In the 2009 [6] and later editions of CSA S19, the depth of the concrete compression zone, a, relative to the depth of the neutral axis (c, in Fig. 1) was no longer specified. The value of c, however, is determined through the equilibrium of resistances to satisfy Eq. (6).

The coefficient β in Eq. (1) is taken as

$$\beta = \frac{C_{\text{rco}} - C_{\text{rcm}}}{C_{\text{rco}}} \tag{7}$$

where $C_{\text{rco}} = C_{\text{rc}}$ calculated with $\lambda = 0$ and $C_{\text{rcm}} = 1.18\alpha_1\phi_c A_c f_c{'}$.

It is important to note that in the 2019 edition of the standard [8], changes were made to the β values for unfilled HSS beam-columns in Clauses 13.8.3 and 13.8.4. The rationale for the new values chosen was based on designing the members for plastic behaviour [10, 14].

2.2   Tousignant and Packer [18, 19]

The study by Tousignant and Packer [18, 19] resulted in several proposed changes to CSA S16 Clause 18.2 that cover its scope (i.e., material limitations), the classification of cross sections, and provisions for compressive resistance, bending resistance, and axial compression plus bending.

Tousignant and Packer [18] recommended to adopt rounded ranges of 20 MPa $\leq f_c{'} \leq 70$ MPa for normal-weight concrete and 20 MPa $\leq f_c{'} \leq 40$ MPa for lightweight concrete in CSA S16. Although the former limit is slightly more restrictive than the current limit in CSA S16 for concentrically loaded columns ($f_c{'} \leq 70$ MPa versus $f_c{'} \leq 80$ MPa), the validated wider range of application for beam-columns is valuable considering that nearly all columns, in practice, are subjected to combined loading.

Tousignant and Packer [18] also recommended to replace the current b_{el}/t limit(s) for plastic design in CSA S16 Clause 18.2.1 (see Sect. 2.1) with the proposed limits

in Table 1 of this paper. Despite being more restrictive again (in some cases), these limits are met by nearly all RHS in the CISC Handbook [4].

A modification to the C_{rc} equation (Eq. 2) was also proposed—to cater to the use of longitudinal steel reinforcing bars; i.e.:

$$C_{rc} = \frac{\tau \phi A_s F_y + \tau' \alpha_1 \phi_c A_c f_c' + \phi_r A_r F_{yr}}{(1 + \lambda^{2n})^{\frac{1}{n}}}$$

(8)

where A_r = cross-sectional area of longitudinal reinforcement and ϕ_r = resistance factor for steel reinforcing bars. A new lower limit of 0.75 for α_1 was proposed as a consequence of adopting the upper limit of $f_c' = 70$ MPa discussed previously.

For consistency, it was also recommended that the expression for EI_e (Eq. 3) be modified to

$$EI_e = EI_s + \frac{0.6 E_c I_c}{1 + C_{fs}/C_f} + EI_r$$

(9)

where I_r = moment of inertia of the reinforcing bar areas, as computed with respect to the centre of gravity of the cross section.

Tousignant and Packer [19] proposed a modification to the equation for M_{rc} in CSA S16 (Eq. 4) which aimed to make it clearer, as well as to provide for the use of longitudinal steel reinforcing bars; i.e.:

$$M_{rc} = Z\phi F_y - 2t\left(\frac{h_i}{2} - a\right)^2 \phi F_y + \frac{Z_c}{2}\phi_c f_c - \frac{b_i}{2}\left(\frac{h_i}{2} - a\right)^2 \phi_c f_c + M_{rr}$$

(10)

where $f_c = 1.18\alpha_1 f_c'$; Z = plastic modulus of the steel section alone; and $h_i = d - 2t$ (where d = overall depth of hollow section). The depth of the concrete compression zone, a, was also explicitly defined:

$$a = \frac{h_i}{2} - \frac{\left(A_g - A_s\right)\phi_c f_c - 2\phi_r F_{yr}\left(A_{src} + A_{srb} - A_{srt}\left(1 - \phi_c f_c/\phi_r F_{yr}\right)\right)}{8t\phi F_y + 2b_i\phi_c f_c}$$

(11)

where A_g = gross cross-sectional area of composite section; A_{srt}, A_{src}, and A_{srb} = area of reinforcing bars in the top, central, and bottom region, respectively, where only the top region is located above the neutral axis; and Z_c = plastic modulus of the area inside the HSS (concrete plus reinforcing bars), taken as

$$Z_c = \frac{b_i h_i^2}{4} - 0.429 r_i^2 h_i + 0.192 r_i^3$$

(12)

where $b_i = b - 2t$ (b = overall width of hollow section); $r_i = t$; and:
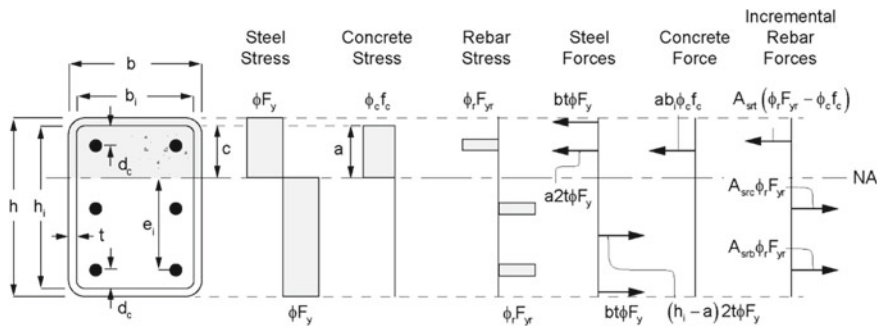
Fig. 2 Stress and approximate force diagrams for concrete-filled RHS (proposed)

$$M_{\mathrm{rr}} = \phi_r F_{yr} \left[A_{\mathrm{srt}}(a - d_c)\left(1 - \phi_c f_c / \phi_r F_{\mathrm{yr}}\right) + A_{\mathrm{src}}\left(\frac{h_i}{2} - a\right) + A_{\mathrm{srb}}(h_i - a - d_c) \right] \tag{13}$$

where d_c = distance from the inside face of the RHS to the centre of the closest adjacent reinforcing bar (Fig. 2). The term M_{rr} reflects the incremental contribution to the moment resistance gained by adding steel reinforcing bars.

With respect to beam-columns, Tousignant and Packer [19] made several recommendations for consistency. In addition to using the previously discussed C_{rc} and M_{rc} equations (Eqs. (8) and (10), respectively) in Eq. (1), subject to the proposed f_c' and b_{el}/t limits (20 MPa $\le f_c' \le$ 70 MPa for normal-weight concrete, and Table 1, respectively), they proposed two possible approaches to determine β:

1. Approach (i): using Eq. (7); and
2. Approach (ii): using "$\beta = 0.85$ for square and circular hollow structural sections, and 1.0 for all other hollow structural sections".

Approach (i) was shown to give similar statistics to the existing CSA S16 method, and Approach (ii) was believed to be more conservative. Approach (ii) is in accord with the changes made for unfilled HSS beam-columns in Clauses 13.8.3 and 13.8.4 of CSA S16:19 [8] (see Sect. 2.1).

3 Scope of Analysis

Herein, the two approaches proposed by Tousignant and Packer [19] for design of concrete-filled RHS beam-columns [Approaches (i) and (ii), above] are evaluated by using MCS to simulate various design scenarios for characteristic members, without reinforcement, over a range of live-to-dead load (L/D) ratios. Reliability indices (i.e., β^+-values) are then obtained and compared to the target value of $\beta^+ = 3.0$ spelled out in Annex B of CSA S16:19 [8].

The reliability indices (β^+) determined herein are based on comparisons of the member resistance (R) and load effect (S) distributions, assuming perfect design (see Sect. 5.1), whereby the safety margin (G) is given by Eq. (14):

$$G = \ln(R) - \ln(S) \tag{14}$$

and, hence, a failure event occurs when $G < 0$.

The probabilistic method used by the Authors relates the probability of failure (i.e., the probability that $G < 0$) to the mean and standard deviation of G (G_m and σ_G, respectively) using a safety/reliability index (β^+), defined as [15]:

$$\beta^+ = \frac{G_m}{\sigma_G} \tag{15}$$

β^+ can be viewed simply as the number of standard deviations between G_m and the failure condition, for which targets are given in design codes (e.g., [1, 8]).

To account for uncertainty in design, R and S are modelled herein as random variables with probability distributions obtained by randomly sampling from the resistance and load effect parameter distributions in Tables 2 and 3.

For each design scenario, a possible resistance and load effect are determined, and this process is repeated 1×10^6 times to approximate the distributions of R and S (from which G, G_m, σ_G, and β^+ can then be determined). The basic random variables in Tables 2 and 3 were taken from the literature and are assumed to be log-normally distributed in general accordance with CSA S408-11 [5]. The symbols δ and V in Tables 2 and 3 denote the bias coefficients (i.e., the means of actual-to-nominal values) and corresponding coefficients of variation (COVs), respectively.

The bias coefficient (δ) and V for F_y in Table 2 were taken from [22] which, in turn, came from the database of [12]. The values for f_c' are in accord with those used by [3] which, in turn, are based on [2]. Since both F_y and f_c' reflect minimum specified strengths in CSA standards [8, 9], their distributions were truncated to

Table 2 Bias coefficients and COVs for resistance parameters (excluding the professional factors)

Parameter	δ	V	References
F_y	1.178	0.086	[22]
f_c'	1.270	0.122	[3]
E	1.00	0.019	[11]
b or h	1.00	0.002	[11]
t	0.975	0.025	[11]

Table 3 Bias coefficients and COVs for load effect parameters

Parameter	δ	V	References
Live load	0.78	0.32	[16]
Dead load	1.05	0.10	[16]

limit the selection of bias coefficients (for F_y and f_c') to a minimum of 1.0. The bias coefficients and COVs for E, b, h, and t in Table 2 were obtained from Kennedy and Gad Aly [11].

The additional parameters required to calculate the resistance of concrete-filled RHS beam-columns (e.g., E_c, A_s, A_c, I_s, and I_c) were calculated as required from the values of f_c', b, h, and t obtained after randomly sampling from the above distributions. All other variables were assumed to be deterministic, including the outside RHS corner radius ($r = 2t$), concrete density ($\rho_c = 2400$ kg/m^2), and effective length (KL). The bias coefficients and COVs for load effects in Table 3 were obtained from [16].

In addition to the above, the probability distribution of R is a function of the so-called "professional factor", which accounts for imperfect nominal resistance design equation(s). The δ and V values for the professional factor(s) used herein were derived from a large database of experiments on concrete-filled RHS column and beam-column members (see Sect. 4).

4   Database of Tests

A database of tests was extracted from [17] and screened to include only specimens that met the proposed new limits of validity (for b_{el}/t and f'_c) discussed in Sect. 2.2. Further screening was performed to remove experiments with $F_y < 300$ MPa and $F_y > 450$ MPa to reflect the range of typical measured HSS yield strengths available in Canada.

For the remaining experiments with loading eccentricity (e) > 0, the nominal predicted compressive strength in the presence of bending (C_n) was calculated for Approaches (i) and (ii) by rearranging Eq. (1) with instances of C_f and M_f replaced by C_n and $C_n \times e$, respectively. It was necessary in calculating C_n to assume that $r = 2t$ and $\rho_c = 2400$ kg/m^2 in accord with above. The bias coefficient(s) for the professional factor was then taken as the average of the actual (experimental) strength (C_a) divided by C_n over all tests. The results (δ and V values) are provided in Table 4, which shows that Approach (ii) produces higher C_a/C_n values, on average, but is less precise than Approach (i).

Figure 3a,b compares the ratios of C_a/C_n for beam-column tests from the database with values of e and KL from the corresponding experiments. It can be deduced from these plots that the ratio of C_a/C_n decreases somewhat for both approaches as KL

Table 4 Bias coefficients and COVs for the professional factor(s)

	n	Approach (i)		Approach (ii)	
		δ	V	δ	V
Beam-columns (e > 0 mm)	48	1.17	0.19	1.44	0.24
Columns (e = 0 mm)	181	1.27	0.16	1.27	0.16
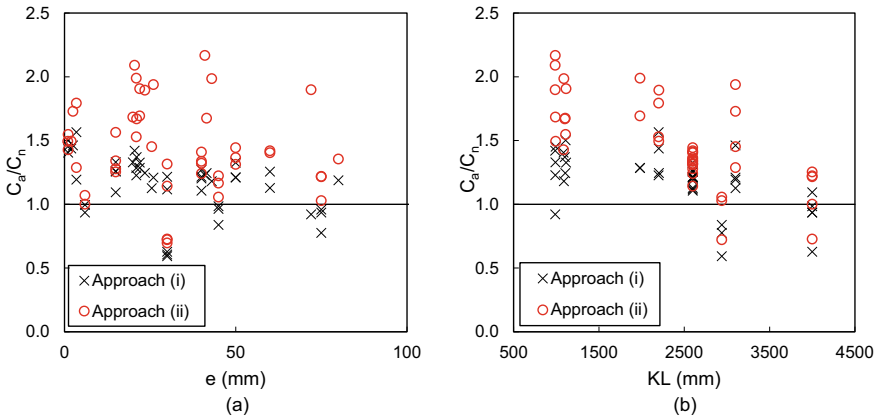
Fig. 3 Comparison of 48 concrete-filled RHS beam-column tests to predictions

goes up. Nonetheless, both approaches [(i) and (ii)] maintain a reasonable level of accuracy over the full range(s) of each variable.

A similar re-analysis was performed of the [17] database to determine professional factor statistics for concentrically loaded RHS members with $e = 0$, which are designed according to Eq. (8). The values of δ and V determined as part of this study are presented in Table 4, which agree with those given by Tousignant and Packer [18].

5 Monte Carlo Simulations

5.1 Procedure

A representative set of ten concrete-filled RHS members was next formulated to cover a range of KL/r and $8 \leq b_{el}/t \leq 44$. (The maximum b_{el}/t was selected to be within the proposed limits of Table 1). Each member was further analysed under an axial load applied at three different values of e (= 0, 50, 100 mm) to produce corresponding ratios of M_f/C_f, as well as for a range of L/D ratios from 0 to 3. In all analyses performed, the nominal strengths of steel and concrete were taken as F_y = 350 MPa and f'_c = 40 MPa, respectively (representative of CSA G40 HSS and regular-strength concrete in Canada) [7], and the column length KL was varied to produce KL/r between 40 and 90. Nominal properties of the representative members are summarized in Table 5.

Reliability indices were determined using Eq. (15) for each of the ten concrete-filled RHS members (times 3 eccentricities, 10 KL/r values, 18 L/D ratios, and two approaches—for a total of 10,800 design scenarios) using the CSA S16 resistance factors of $\phi = 0.9$ and $\phi_c = 0.65$, and load factors of $\alpha_D = 1.25$ and $\alpha_L = 1.50$ when

Table 5 Representative members for Monte Carlo simulation

Member ID	h (mm)	b (mm)	t (mm)	b_{el}/t
1	304.8	304.8	12.70	20
2	304.8	304.8	6.35	44
3	254.0	254.0	12.70	16
4	254.0	254.0	6.35	36
5	203.2	203.2	12.70	12
6	203.2	203.2	6.35	28
7	177.8	177.8	12.70	10
8	177.8	177.8	6.35	24
9	152.4	152.4	12.70	8
10	152.4	152.4	6.35	20

live plus dead load governs (i.e., when L/D $\geq$ 0.135), and $\alpha_D = 1.40$ when dead load only governs (i.e., when L/D < 0.135) [13].

Hence, for each scenario:

1. The factored resistance of the member was determined using the nominal values of material and geometrical properties discussed above.
2. Random samples were drawn from the probability distributions for resistance parameters in Table 2.
3. The sampled values were multiplied by their nominal counterparts.
4. The nominal member resistance was computed using the corresponding parameter values.
5. A random sample was drawn from the probability distribution(s) for the professional factor(s) in Table 4.
6. The nominal member resistance (Step 4) was multiplied by the professional factor to obtain the final (unfactored) resistance.
7. The nominal dead and live loads required for perfect design (utilization ratio = 1.0) were determined for the governing load case.
8. Random samples were drawn from the probability distributions for load effect parameters in Table 3.
9. The sampled values were multiplied by their nominal counterparts, and the results were summed together, if necessary, to obtain the final (unfactored) load effect.

Steps 1–9 were repeated 1×10^6 times for each for the 10,800 design scenarios, and the resulting distribution(s) of R and S, for each scenario, was used to determine G, G_m, σ_G, and β^+. Figure 4 shows typical plots of R and S distributions obtained by completing 1×10^6 iterations of Steps 1–9 for Member 5 in Table 5, using Approach (i) with $e = 50$, KL/$r = 65.0$, and L/D = 1.0. It can be seen, therein, that both distributions are approximately log-normal.
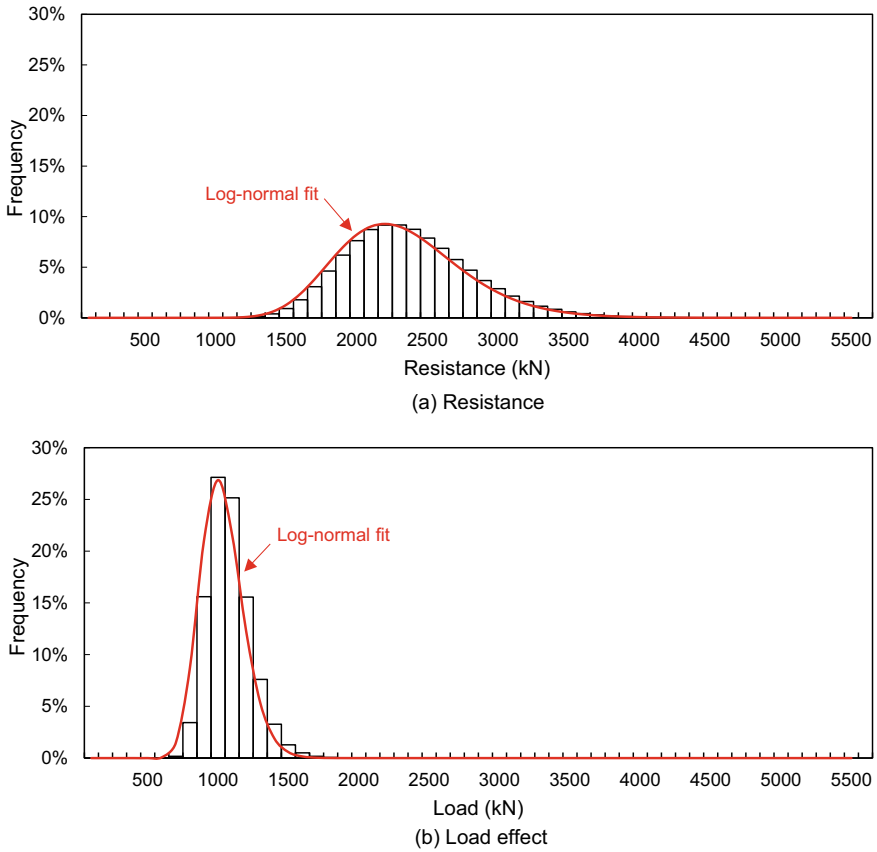
Fig. 4 Resistance and load effect distributions for Member 5, using Approach (i) with $e = 50$, KL/$r = 65.0$, and L/D = 1.0

5.2 Results

The results of the MCS analysis (i.e. plots of β^+ versus L/D) are shown in Fig. 5a–d. Specifically, Fig. 5a,b illustrates the effect of e on β^+, and Fig. 5c,d illustrates the effect of KL/r. Each of the three curves in Fig. 5a,b and each of the six curves in Fig. 5c,d have been calculated by taking the average β^+ value over all ten connections at a given L/D ratio.

For Approach (i), when e = 0 mm (Fig. 5a), β^+ ranges from 3.96 to 4.49 and remains well above the target of $\beta^+ = 3.0$ in Annex B of CSA S16:19 [8]. It is important to note that, for these columns, the professional factor statistics in the last row of Table 4 were used. When $e > 0$ mm (and hence, when axial load plus moment interaction is considered), Approach (i) yields β^+ values between 3.13 and
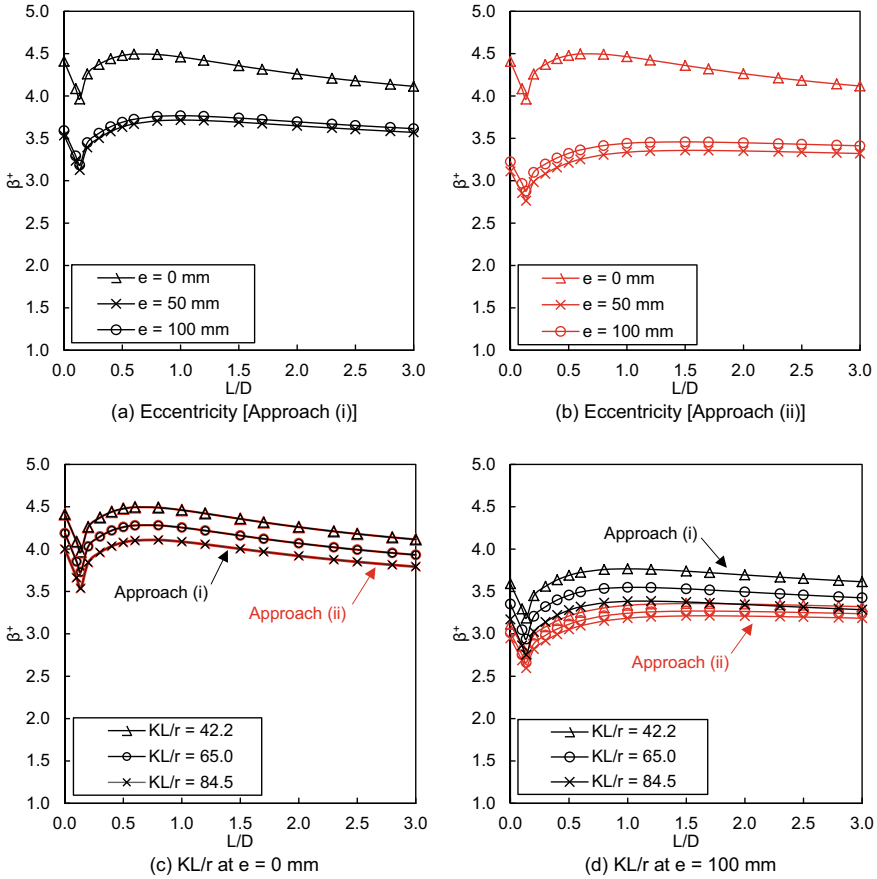
Fig. 5 Effects of various parameters on reliability index

3.77, which are again greater than 3.0. There is very little difference in the β^+ values obtained when $e = 50$ mm and $e = 100$ mm.

For Approach (ii), when e $= 0$ mm (Fig. 5b), β^+ ranges from 3.96 to 4.49 [i.e., the same as above—as expected—since the only difference between Approaches (i) and (ii) is the method for calculating β, which is not required for concentrically loaded columns]. When e > 0 mm, on the other hand, β^+ ranges from 2.76 to 3.46. This is slightly lower than for Approach (i) because the increase in bias for Approach (ii) (higher δ, in Table 4) is coupled with a decrease in precision (i.e., higher V). Nonetheless, the resulting ranges of β^+ are still greater than 2.6, on average, for all L/D ratios considered. This value of 2.6 is the minimum reliability index currently expected in North American codes [1]. Over the practical range of $1 \le$ L/D ≤ 3 for steel members [16], all β^+ values, for both approaches, exceed 3.0.
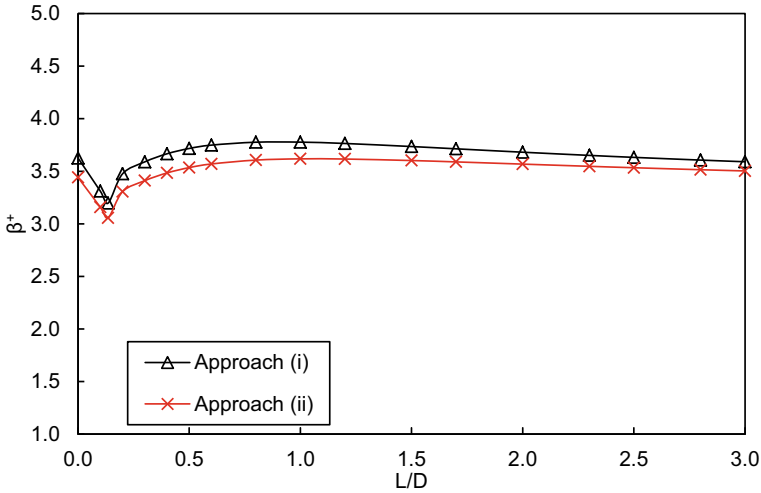
Fig. 6 Overall reliability index versus L/D [both approaches]

Figure 5c shows (for concentrically loaded columns) that β^+ decreases as KL/r increases in accord with the general trend illustrated in Fig. 3b. Figure 5d shows a similar trend, but for beam-columns with $e = 100$ mm.

An "overall" β^+ was computed at each L/D ratio by taking the average β^+ value obtained across all members, eccentricities, and effective lengths. The results [i.e., $3.20 \le \beta^+ \le 3.78$ for Approach (i), and $3.06 \le \beta^+ \le 3.62$ for Approach (ii)] are shown in Fig. 6, which illustrates that β^+ is always greater than 3.0. Based on the above, it can be concluded that the approach(es) proposed by Tousignant and Packer [19] for design of concrete-filled RHS beam-columns obtains a level of safety commensurate with CSA S16 [8].

6   Conclusions

Reliability indices were determined for ten concrete-filled RHS beam-column members over a range of KL/r and $8 \le b_{el}/t \le 44$. Simulations (using MCS) were performed for each member, considering three different loading eccentricities (e = 0, 50, and 100 mm), 10 KL/r values, 18 L/D ratios, and two design approaches [i.e., Approaches (i) and (ii), in Sect. 2.2, which were proposed by Tousignant and Packer [19]. In total, 10,800 design scenarios were covered, and 10.8×10^9 simulations were performed.

The following conclusions can be made from the results:

- For Approach (i), β^+ ranges from 3.20 to 3.78, on average, with is greater than the target value of $\beta^+ = 3.0$ (CSA 2019). For some scenarios (i.e., some columns,

with some values of e and KL/r), β^+ falls below 3.0, but remains above 2.6, which is the minimum value expected in North American codes [1];

- For Approach (ii), β^+ ranges from 3.06 to 3.62 on average, which is—again—greater than the target value of 3.0. For some scenarios, β^+ falls (again) below 3.0, but remains above 2.6.
- When $1 \leq L/D \leq 3$ is considered, which is the common range for steel members, both approaches [(i) and (ii)] produce $\beta^+ \geq 3.0$ across all scenarios considered.

The findings of this research provide evidence to support the use of either approach [(i) or (ii)] for the design of concrete-filled RHS beam-columns within the above parameter ranges in CSA S16.

References

1. AISC. 2016. *Specification for structural steel buildings.* AISC 360–16, American Institute of Steel Construction, Chicago, IL, USA.
2. Bartlett FM, MacGregor JG (1996) Statistical analysis of the compressive strength of concrete in structures. ACI Mater J 93(2):158–168
3. Bartlett FM (2007) Canadian standards association standard A23.3-04 resistance factor for concrete in compression. Can J Civ Eng 34:1029–1037
4. CISC (2021) Handbook of steel construction, 12th edn. Canadian Institute of Steel Construction, Toronto, ON, Canada
5. CSA (2001) Limit states design of steel structures. CAN/CSA S16–01, Canadian Standards Association, Toronto, ON, Canada
6. CSA (2009) Design of steel structures. CSA S16–09, Canadian Standards Association, Toronto, ON, Canada
7. CSA (2018) General requirements for rolled or welded structural quality steel/structural quality steel. CSA G40.20–13/G40.21–13 (R2018), Canadian Standards Association, Toronto, ON, Canada
8. CSA (2019a) Design of steel structures. CSA S16:19, Canadian Standards Association, Toronto, ON, Canada
9. CSA (2019b) Design of concrete structures. CSA A23.3:19, Canadian Standards Association, Toronto, ON, Canada
10. Essa HS, Kennedy DJL (2000) Proposed provisions for the design of steel beam-columns in S16–2001. Can J Civ Eng 27:610–619
11. Kennedy DJL, Gad Aly M (1980) Limit states design of steel structures—performance factors. Canadian J Civil Eng 7:45–77
12. Liu J (2016) Updates to expected yield stress and tensile strength ratios for determination of expected member capacity in the 2016 AISC seismic provisions. Eng J 53(4):215–228
13. National Research Council of Canada (NRC) (2020) NBCC 2020 Part 4. National building code of Canada. NRC, Ottawa, ON, Canada
14. Pillai US (1974) Beam-columns of hollow structural sections. Can J Civ Eng 1(2):194–198
15. Ravindra MK, Galambos TV (1978) Load and resistance factor design for steel. J Struct Div 104(9):1337–1353
16. Schmidt BJ, Bartlett FM (2002) Review of resistance factor for steel: resistance distributions and resistance factor calibration. Can J Civ Eng 29:109–118

17. Thai S, Thai HT, Uy B, Ngo T (2019) Concrete-filled steel tubular columns: test database, design, and calibration. J Constr Steel Res 157:161–181
18. Tousignant K, Packer JA (2022) Concrete-filled hollow structural sections. I: Materials, cross-section classification, and concentrically loaded columns. Canadian J Civil Eng 49(3):368–383
19. Tousignant K, Packer JA (2022) Concrete-filled hollow structural sections II: Flexural members, beam columns, tension, and shear. Canadian J Civil Eng 49(3):384–400
20. Tousignant K, Packer JA (2022c) CSA S16:24—changes to concrete-filled HSS. In: Proceedings, 49th annual conference, Canadian Society for Civil Engineering: STR076–1—STR076–11
21. Xi Q, Packer JA (2021) Assessing the probabilistic assumptions behind structural reliability via simulation. In: Proceedings, 49th annual conference, Canadian society for civil engineering: STR230–1—STR230–10
22. Zhao X.L., Packer JA, Wang YC, McCormick JP (2019) Design guide for concrete-filled hollow section columns under static, impact, blast, seismic and fire loading. CIDECT Final Report 16H-4/19, Comité International pour le Développement et l'Étude de la Construction Tubulaire, Geneva, Switzerland

Reliability Assessment of Canadian Design Provisions for Single-Sided Fillet Welds

Thomas Justin and Tousignant Kyle

Abstract An experimental program was conducted at Dalhousie University to test single-sided fillet welds in cruciform connections subjected to branch axial tension. The connections varied the fillet weld size and branch-plate thickness to investigate the effects of these parameters on weld strength. Using the ultimate loads at weld rupture, an approximate first-order reliability analysis was performed, and the inherent safety index (β^+) of current (CSA S16:19) design provisions for single-sided fillet welds was determined. Results are compared to those from previous finite-element analyses on single-sided fillet welds in hollow structural section connections. The current provisions, which prohibit the use of the directional strength-increase factor for single-sided fillet welds, are shown to meet the target safety index of β^+ = 4.0 across all tests.

Keywords Canadian design provisions · Single-sided fillet welds · Reliability assessment

1   Introduction

In CSA S16 [9], fillet welds other than those that are single-sided and connected to an element in tension can be designed using a directional strength-increase factor (DSIF) $(1.00 + 0.50\sin^{1.5}\theta)$. This factor is based principally on testing of lapped splice and cruciform connections with fillet welds on both sides of a plate loaded in tension (Fig. 1a, b) [3, 19, 21, 24, 25, 26, 11, 18].

However, unlike their two-sided counterparts, single-sided fillet welds are inherently subjected to eccentric loading, and thus prone to local bending and rotation

T. Justin
COWI North America, North America, Canada

T. Kyle (✉)
Dalhousie University, Dalhousie, Canada
e-mail: kyle.tousignant@dal.ca

(a) Lapped splice connection,   (b) Cruciform connection, welded   (c) Cruciform connection, with a
    welded on both sides   on both sides   single-sided fillet weld
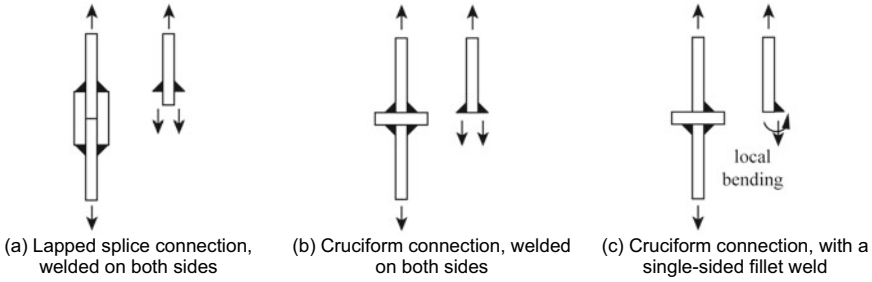
Fig. 1 Fillet-welded connections

about the weld toe (see Fig. 1c). When this occurs, it leads to opening of the root
notch, which can subject the weld to additional stress and reduce its capacity [2, 13].

Experiments and numerical finite-element (FE) analyses on single-sided fillet
welds around the ends of tension-loaded hollow structural sections (HSS) have
confirmed that bending about the weld axis occurs in such situations [29, 33]. This
is the rationale behind CSA S16's ban of the DSIF for single-sided fillet welds.
However, the "single-sided weld effect" (i.e., the reduction in strength relative to
two-sided welds) was shown to be more severe for fillet welds to rectangular HSS
than fillet welds to round HSS, giving rise to other questions, such as the effect of
fillet weld size, connected element thickness, and restraint against rotation at the
weld root [which depends on the connected element shape (linear vs. curved)] on
fillet weld strength.

Herein, the results from 18 weld-critical tests on single-sided fillet weld connec-
tions (Fig. 1c) are presented and compared to previous finite-element analysis results
on fillet-weld-critical HSS-to-rigid plate connect-ions conducted by [33]. Inherent
reliability indices (β^+) are then calculated using (i) an approximate first-order reli-
ability method (FORM) analysis and (ii) a so-called expanded separation factor
approach [20, 30]. The results are compared to one another and to the target value
of $\beta^+ = 4.0$ (for welded joints) specified in Annex B.4 of CSA S16 [10].

2 Background

2.1 Double-Sided Fillet Welds

Since the 1930s, extensive theoretical and experimental studies have been carried
out to investigate the effect of loading angle (θ) on the strength and ductility of fillet
welds.

Butler and Kulak [3] tested 23 fillet-welded lap joints with $\theta = 0°$, 30°, 60°, and
90°, the results of which indicated that the ratio of the strength of transverse fillet
welds ($\theta = 90°$) to longitudinal fillet welds ($\theta = 0°$) equalled 1.44. A later study by

Kato and Morita [19], which used a theoretical model for fillet weld strength, found the DSIF to be 1.46. [16, 17] developed a simple formula that took both the weld geometry and ultimate strength of the weld metal into consideration to determine its strength for a given θ. The proposed formula was validated against experimental results reported by [3], and the corresponding DSIF was found to be 1.41.

Miazga and Kennedy [24] tested an additional 42 fillet-welded lap joints with θ varying in 15° increments from 0° to 90°. Their results showed that values of the DSIF varied between 1.36 and 1.63, based on weld size. Miazga and Kennedy [24] proposed an analytical model to predict fillet weld strength as a function of θ, where for transverse fillet welds, the implied DSIF was 1.5. The model was extended by [21], which gave birth to the modern DSIF: $1.00 + 0.50\sin^{1.5}\theta$.

Ng et al. (2002) and [22] extended the applicability of the $1.00 + 0.50\sin^{1.5}\theta$ factor to fillet welds in both lap-splice and cruciform connections made using the flux-cored arc welding (FCAW) process (previous research had been done on connections made using a shielded-metal arc welding process). [18] then extended it to fillet welds in cruciform connections with large, transverse root notches.

2.2 Single-Sided Fillet Welds

In the early 2000s, [5] carried out an experimental program on the performance of single-sided fillet welds in "H-shape" steel members, testing two types of specimens: shear specimens (with welds loaded at an angle of $\theta = 0°$ to their axis) and tension specimens (with welds loaded at $\theta = 0°$ to their axis). [5] found that the tension specimens exhibited reduced strength due to the inherent eccentricity of the applied load with respect to centre of gravity of the weld in the connection.

Packer et al. [29] later reported the results of 33 tests on weld-critical HSS-to-rigid end-plate connections, which varied tube size, tube profile (rectangular vs. round), and fillet weld throat dimension (t_w). These tests were expanded by [33], who added 73 FE results to the database with further variations in parameters. These studies found, principally, that if the DSIF was used, the CSA S16 fillet weld design provisions at the time (in Clause 13.13.2.2 of CSA S16-14) [6] did not meet the target safety index of $\beta^+ = 4.0$ at failure. As discussed in Sect. 1, the "single-sided weld effect" (i.e., the reduction in strength relative to two-sided welds) was shown to be more severe for fillet welds to rectangular HSS than fillet welds to round HSS.

In a recent European study, [34] examined the effect of applied bending moments due to loading eccentricity on the capacity of single-sided fillet welds in plate-to-box section connections. [34] found that, in some cases, tensile stresses on the root side of the weld due to bending plus tension (i.e., opening of the root notch) led to unexpected failure. A simplified expression for the fillet weld resistance when subjected to an eccentric load was derived based on the provisions of EN 1993–1-8 [13].

Other practical examples of single-sided fillet welds include restrained lap joints and unstiffened seated connections (Figs. C-J2.3 and 10–7, respectively, of the AISC Manual) [1].

3 Fillet Weld Design Provisions in CSA S16

The fillet weld design provisions in CSA S16:19 [10] are principally based on the research by [3], Kato and Morita [19, 21, 24–26] on lapped splice and cruciform connections, welded on both sides.

For connections made with a matching electrode, Clause 13.13.2.2 permits the factored resistance for the direct shear and tension- or compression-induced shear of a fillet weld (V_r) to be taken as:

$$V_r = 0.67\phi_w A_w X_u \tag{1}$$

where ϕ_w = resistance factor for weld metal (= 0.67); A_w = weld effective throat area (= $t_w \times l_w$, where l_w = weld length); and X_u = strength of matching electrode.

A new addition to Clause 13.13.2.2 in S16 [10] stated that, "for cases other than single-sided fillet welds connected to an element in tension, the above resistance may be multiplied by the following factor":

$$(1.00 + 0.50 \sin^{1.5} \theta) \tag{2}$$

CSA S16-14 [6] and earlier editions of the standard did not distinguish between single- and double-sided welds. On the other hand, CSA W59-18 [7] states that "single fillet and single partial joint penetration groove welds shall not be subjected to bending about the longitudinal axis of the weld if it produces tension at the root of the weld".

4 Recent Tests at Dalhousie University

Eighteen weld-critical cruciform connections with nominally concentric branches and single-sided fillet welds were designed and tested at Dalhousie University. The specimens varied in fillet weld throat and leg sizes (t_w, l_v, and l_h) and connected element (branch-plate) thickness (t_b) (see Fig. 2). The specimens were fabricated from plate material conforming to CSA G40.21 Grade 350W [8] and welded, using the FCAW process, with a matching flux-cored (E491T) electrode wire from a single heat. The measured dimensions are summarized in Table 1, wherein the Specimen ID (Column 1) is based on nominal dimensions t_b and t_w (e.g., S6-S-0 denotes a specimen with $t_b = 6.4$ mm and a comparatively "small" weld throat). The trailing 0
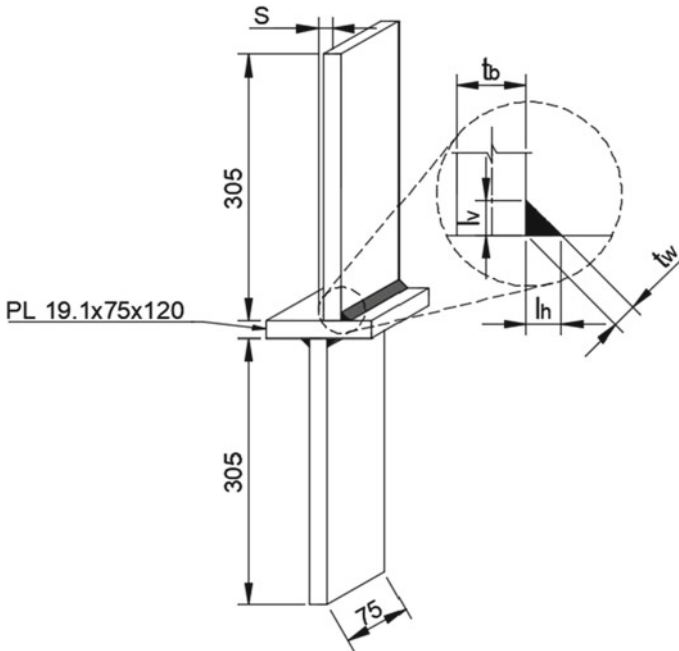
Fig. 2 Schematic diagram of single-sided fillet weld connection specimens

denotes the nominal offset (S). Measured offsets (following fabrication) are reported in Table 1.

As shown in Fig. 2, each specimen was comprised of two 305-mm long vertical steel branch-plates welded to a rigid, 19.1-mm thick horizontal plate with a nominal width of 75 mm. The top, vertical branch-plate in each specimen was connected to the horizontal plate through a single-sided fillet weld that was designed to be "critical" (i.e., to fail). The bottom, vertical branch-plate was connected through two, larger fillet welds, one on each side, that were designed to remain intact during the testing.

4.1 Weld Geometric Properties

Geometric properties of the welds were carefully measured—after (as well as before) testing—by cross-sectioning, polishing, macro-etching, and digitizing the broken weldments at five locations along their length ($5 \times 18 = 90$ cross sections in total), and scaling off the digital weld profiles in AutoCAD. In Table 1, the dimensions l_v and l_h are the average weld leg sizes based upon the smallest triangle that could be inscribed into the weld. The dimension t_w is the average weld throat based on the shortest distance from the root to the face of the diagrammatic fillet weld, in accord with CSA W59 [7].

Table 1 Measured cross-sectional properties of single-sided fillet weld connection specimens

Specimen ID	t_b (mm)	S (mm)	l_v (mm)	l_h (mm)	t_w (mm)	l_w (mm)
S6-S-0	6.41	+ 1.1	4.43	4.03	3.17	75.0
S6-M-0	6.42	+ 0.9	5.54	3.84	3.52	76.2
S6-L-0	6.35	+ 1.1	6.10	4.68	4.04	73.8
S9-XS-0	9.63	+ 1.2	3.78	2.80	2.38	74.3
S9-S-0	9.57	+ 1.2	4.98	3.26	2.76	75.8
S9-M-0	9.64	+ 1.5	5.60	4.58	3.70	79.4
S9-L-0	9.62	+ 0.9	5.82	6.30	4.82	72.1
S9-XL-0	9.62	+ 1.1	8.16	6.78	5.68	75.2
S9-XXL-0	9.58	+ 1.6	8.36	7.44	6.00	74.9
S14-XS-0	15.93	−0.6	2.76	2.46	1.84	72.7
S14-S-0	15.90	−0.4	4.90	3.22	2.72	74.7
S14-M-0	15.88	−0.5	6.14	4.52	3.74	78.7
S14-L-0	15.90	+ 0.8	7.24	7.26	5.20	73.5
S14-XL-0	15.88	+ 0.6	10.18	8.82	6.70	76.5
S14-XXL-0	15.90	+ 1.5	12.16	11.08	8.42	71.5
S20-S-0	19.47	+ 2.8	9.76	8.76	6.86	77.5
S20-M-0	19.46	+ 3.5	13.16	11.90	9.74	74.5
S20-L-0	19.41	+ 3.0	14.66	13.06	10.00	75.5

4.2 Weld Metal Material Properties

To determine the material properties of the welds, three all-weld-metal tensile coupons (TCs), made during fabrication (with the same electrode coil), were cut, and tested in accordance with AWS D1.1 [2]. Stress versus strain curves for the all-weld metal TCs are presented in Fig. 3. The average measured yield strength (F_y, determined by the 0.2% strain offset method) and ultimate strength (X_u) are summarized in Table 2. Additional parameters obtained from the tests (i.e., ε_y = yield strain; ε_f = rupture strain; and E = Young's modulus) are also provided therein.

The rupture strains in Table 2 (which correspond to the x-ordinates of the "X" symbols in Fig. 3) were measured by joining the fractured pieces of the TC back together, remeasuring the gauge length, and dividing the difference between the original and final gauge lengths by the original value.

4.3 Test Procedure and Instrumentation

The single-sided fillet weld connection specimens (Fig. 2) were tested in the Heavy Structures Lab at Dalhousie University using a 2-MN Instron Universal Testing

Fig. 3 Stress versus strain curves for all-weld-metal TCs
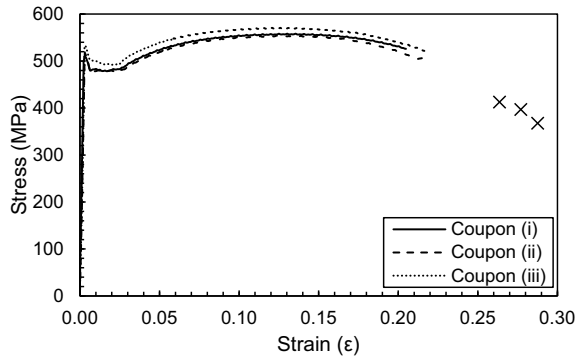
Table 2 Average measured material properties of the as-laid welds

Coupon ID	F_y (MPa)	X_u (MPa)	ε_y (mm/mm)	ε_f (mm/mm)	E (GPa)
(i)	502	558	0.00435	0.288	196.8
(ii)	497	554	0.00499	0.264	166.3
(iii)	514	571	0.00501	0.277	169.6
Average	504	561	0.00479	0.276	177.6

Machine. During testing, tension load on the branch-plate(s) and strain adjacent to the single-sided fillet weld (on both sides of branch-plate) were measured. A digital image correlation (DIC) technique was also used in conjunction with the strain gauges to verify the uniformity of loading along the weld length. While not quantitively addressed herein, the SGs and DIC showed that the welds were uniformly loaded along their length and bending about/opening of the weld root notch occurred but was minimal—similar to what was shown in the previous studies by [29] and [33].

4.4 Results

All 18 specimens failed by rupture along a plane through the weld. Figure 4a, b shows typical weld failures overlaid with DIC results for specimens S14-L-0 and S20-S-0. For use in the following section, Table 3 compares the actual strengths of the welds (V_a) with predicted nominal strengths ($V_n = V_r/\phi_w$) calculated according to Eq. (1), with and without using the DSIF. In Table 3, V_n is calculated according to both methods by using the measured values of t_w and l_w (from Table 1) and $X_u = 561$ MPa (from Table 2). The average actual-to-predicted weld strength (also known as the bias coefficient for the professional factor δ_P) and the corresponding coefficient of variation (V_P) are also presented. These statistics are used in the reliability analyses, in Sect. 6.

(a) S14-L-0   (b) S20-S-0
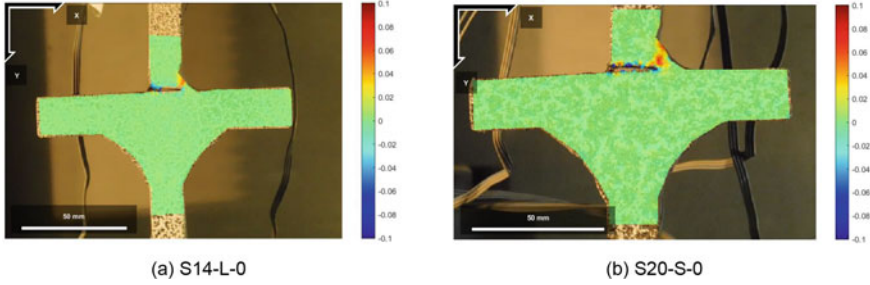
Fig. 4 Typical weld failures and DIC results for xy-axis (shear) strain

5 Previous Finite-Element Work

In addition to the above, FE analysis results from [33] on fillet-weld-critical HSS connections are re-evaluated herein. This additional data comprises 21 "tests" on single-sided fillet welds in rectangular HSS-to-rigid end-plate connections (denoted RHS) and 20 "tests" on single-sided fillet welds in round HSS-to-rigid end-plate connections (denoted CHS). The professional factor statistics (δ_P and V_P) from these tests, extracted from [33], are summarized in Table 4. Those from the current study (denoted CC) are also repeated there, for ease of comparison. It is interesting to note that fillet welds in the CC-series connections have remarkably similar statistics to those in the RHS-series connections.

6 Reliability Assessment

6.1 FORM Analysis

To determine the ranges of β^+ inherent in the forgoing CSA S16 design approach (see Sect. 2), an approximate FORM analysis was conducted using Eq. (3) [27, 31]:

$$\beta^+ = \frac{1}{\sqrt{V_R^2 + V_S^2}} \ln\left[\frac{\delta_R}{\phi}\left(\frac{\alpha_D + \alpha_L(L/D)}{\delta_D + \delta_L((L/D))}\right)\right] \tag{3}$$

where δ_R = bias coefficient for the resistance; V_R = coefficient of variation (COV) of δ_R; α_D and α_L = load factors for dead and live loads, respectively [= 1.25 and 1.5, per NRC [28]]; δ_D and δ_L = bias coefficients for dead and live loads, respectively; and V_S = COV of the total load effect, taken as [8]:

$$V_S = \frac{\sqrt{(\delta_D V_D)^2 + (\delta_L V_L(L/D))^2}}{\delta_D + \delta_L(L/D)} \tag{4}$$

Table 3 Test results

Specimen ID	w/ DSIF			w/o DSIF		Specimen ID	w/ DSIF			w/o DSIF	
	V_a (kN)	V_n (kN)	V_a/V_n	V_a (kN)	V_a/V_n		V_a (kN)	V_n (kN)	V_a/V_n	V_a (kN)	V_a/V_n
S6-S-0	110.5	133.9	0.82	89.3	1.24	S14-XS-0	56.8	75.4	0.75	50.3	1.13
S6-M-0	121.2	151.2	0.80	100.8	1.20	S14-S-0	96.8	114.6	0.85	76.4	1.27
S6-L-0	122.3	168.1	0.73	112.1	1.09	S14-M-0	143.6	165.9	0.87	110.6	1.30
S9-XS-0	95.9	99.7	0.96	66.5	1.44	S14-L-0	155.2	215.5	0.72	143.7	1.08
S9-S-0	104.4	118.0	0.89	78.6	1.33	S14-XL-0	203.7	289.0	0.70	192.7	1.06
S9-M-0	133.7	165.6	0.81	110.4	1.21	S14-XXL-0	208.3	339.4	0.61	226.3	0.92
S9-L-0	139.0	195.9	0.71	130.6	1.06	S20-S-0	222.2	299.7	0.74	199.8	1.11
S9-XL-0	171.8	240.8	0.71	160.5	1.07	S20-M-0	258.7	409.1	0.63	272.7	0.95
S9-XXL-0	171.3	253.4	0.68	168.9	1.01	S20-L-0	278.0	393.1	0.71	262.1	1.06
						Average (δ_p):	0.76				1.14
						COV (V_P):	0.12				0.12

Table 4 Professional factor statistics for single-sided fillet weld connection specimens

Connection type	n	w/ DSIF		w/o DSIF	
		δ_P	V_P	δ_P	V_P
CC	18	0.76	0.12	1.14	0.12
RHS	21	0.76	0.09	1.14	0.09
CHS	20	0.85	0.06	1.28	0.06
All	59	0.79	0.10	1.19	0.10

where V_D and V_L = COV of the live and dead load, respectively.

Equation (3) incorporates the effects of live and dead load through the non-dimensional live-to-dead load ratio, L/D, which is considered over the range of 1 $\leq$ L/D $\leq$ 3. This is the typical range for components in steel buildings [12, 31].

The bias coefficient, δ_R, and the corresponding COV, V_R, are derived by assuming that the resistance is a multiplicative of four independent random variables with a bias coefficient and COV given by [15, 31]:

$$\delta_R = \delta_G \delta_M \delta_P \delta_d \quad \text{and} \quad V_R = \sqrt{V_G^2 + V_M^2 + V_P^2 + V_d^2} \tag{5}$$

where δ_G, δ_M, δ_P, and δ_d = bias coefficients of the geometric, material, professional, and discretization factor, respectively, and V_G, V_M, V_P, and V_d = associated COVs. In the context of this paper, δ_G incorporates variability in the weld throat size; δ_M incorporates variability in electrode strength; δ_P incorporates variability in the accuracy of Eq. (1) (used to calculate V_n); and δ_d incorporates the effect of specifying discreet/commonly used weld sizes that are generally in excess of the minimum required for strength.

Bias coefficients and COVs for dead and live load used in this work were taken as $\delta_D = 1.05$, $\delta_L = 0.90$, $V_D = 0.10$, and $V_L = 0.27$ [23], with a target of $\beta^+ = 4.0$, for connection design, in accordance with with Annex B.4 of CSA S16:19 [10]. A resistance factor of $\phi = 0.67$ was adopted for fillet welds per CSA S16:19 Clause 13.1.

The parameters δ_M and V_M were taken as 1.12 and 0.077, respectively, based on a large database of 672 tests performed on all-weld-metal TCs [21], and the parameters δ_G and V_G were taken as 1.13 and 0.16, respectively, to reflect common "fabrication errors" that result in the variability of weld geometry [4], as well as errors in measurement [32]. The bias coefficient for the discretization factor, δ_d (= 1.09), and the associated COV (= 0.062), were adopted from the same work. The resulting values of δ_R and V_R according to Eq. (5) are summarized in Table 5.

In the following section, inherent β^+ values are calculated and compared to the target value of $\beta^+ = 4.0$ for the current (CC-series) tests, as well as the RHS- and CHS-series tests, over the range of 1 $\leq$ L/D $\leq$ 3. The results are shown graphically in Fig. 5 and numerically in Table 6. It is worth noting that the discontinuities in the

Table 5 Resistance statistics for single-sided fillet weld connection specimens

Connection type	w/ DSIF		w/o DSIF	
	δ_R	V_R	δ_R	V_R
CC	1.06	0.22	1.59	0.22
RHS	1.06	0.21	1.59	0.21
CHS	1.18	0.20	1.78	0.20
All	1.10	0.22	1.65	0.22

curves in Fig. 5 are due to the intersection of the two factored load combinations that in NRC [28] that were considered [i.e., 1.4D (dead load only) and 1.25D + 1.5L].

As shown in Table 6, for CC-series specimens with the DSIF applied, β^+ ranges from 2.97 to 3.06 (when $\phi = 0.67$ and $1 \leq L/D \leq 3$) which does not meet the target value of $\beta^+ = 4.0$. Without the DSIF, β^+ ranges from 4.33 to 4.61, which exceeds the target value of $\beta^+ = 4.0$. For RHS-series specimens, with the DSIF applied, β^+ ranges from 3.08 to $3.21 \leq 4.0$ (again, when $\phi = 0.67$ and $1 \leq L/D \leq 3$). Without the DSIF, β^+ ranges from 4.49 to 4.84. These results are, again, remarkably similar to those for the CC-series specimens. For CHS-series specimens, β^+ ranges from 3.58
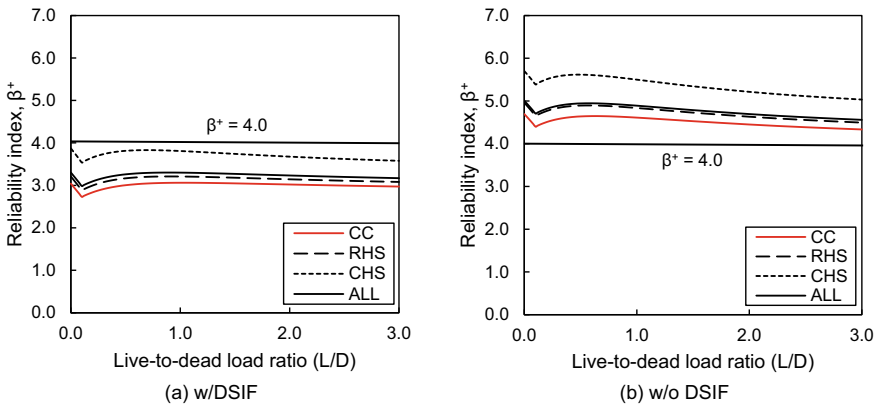
Fig. 5 β^+ (for target $\phi = 0.67$) versus L/D

Table 6 Summary of β^+ values obtained using the FORM approach for $1 \leq L/D \leq 3$

Connection type	β^+	
	w/ DSIF	w/o DSIF
CC	2.97–3.06	4.33–4.61
RHS	3.08–3.21	4.49–4.84
CHS	3.58–3.81	5.03–5.50
All	3.17–3.30	4.56–4.89

Table 7 Summary of β^+ values obtained using the ESF approach

Connection type	β^+	
	w/ DSIF	w/o DSIF
CC	3.41	5.35
RHS	3.54	5.56
CHS	4.22	6.38
All	3.67	5.67

to $3.81 \leq 4.0$ when the DSIF is applied. Without the DSIF, β^+ ranges from 5.03 to $5.50 \geq 4.0$.

When observing all specimens combined, with the DSIF applied, β^+ ranges from 3.17 to 3.30, which does not meet the target value of $\beta^+ = 4.0$. Without the DSIF, β^+ ranges from 4.56 to $4.89 \geq 4.0$. Hence, the current (CSA S16:19) provisions in Clause 13.13.2.2 that prohibit the DSIF for single-sided fillet welds to elements in tension can be considered to be appropriate.

6.2 Separation Factor Method

It may be interesting to compare the above results from the FORM analysis to another largely utilized reliability analysis procedure termed the "expanded separation factor" (or ESF) approach. In doing so, β^+ and ϕ values are calculated according to Eq. (6), which considers the statistical variation of the resistance independently of the load effects [14, 30]:

$$\beta^+ = -\ln\left(\frac{\phi}{\phi_{\beta^+}\delta_R}\right)(\alpha_R V_R)^{-1} \tag{6}$$

where $\phi_{\beta+}$ = recursive adjustment factor = $0.0062(\beta^+)^2 - 0.131\beta^+ + 1.338$, and α_R = coefficient of separation, taken as 0.55 [30]. The results (which are discrete values of β^+ and ϕ, rather than ranges) are shown in Table 7. By comparing Tables 6 and 7, one can see that the ESF method with the $\phi_{\beta+}$ adjustment factor yields less conservative results than the FORM analysis. Regardless, the same conclusion—that the current (CSA S16:19) provisions in Clause 13.13.2.2 that prohibit the DSIF for single-sided fillet welds to elements in tension are appropriate—can be drawn.

7 Conclusions

This paper has presented the results of 18 tests on single-sided fillet welds in cruciform connections. The results were compared to previous FE analysis results on fillet-weld-critical HSS-to-rigid plate connections conducted by [33], and inherent reliability

indices (β^+) were calculated using (i) an approximate FORM analysis and (ii) a so-called expanded separation factor (ESF) approach [20, 30].

The following conclusions can be made:

- Single-sided fillet welds in cruciform connections exhibit similar strength(s) (on average) to those in RHS connections. These welds are, in turn, weaker than those in CHS connections. This can be attributed to the difference in restraint against rotation at the weld root caused by the shape of the connected element (linear versus curved).
- For concentrically loaded cruciform connections with single-sided welds, weld strength and weld size are inversely proportional (see Tables 1 and 3). This can be attributed to the so-called weld size effect [29].

According to the FORM analysis conducted herein, the current fillet weld design provisions in CSA S16:19 Clause 13.13.2.2, which prohibit the use of the directional strength-increase factor (DSIF) for single-sided fillet welds, meet/exceed the target safety index of $\beta^+ = 4.0$ specified in Annex B.4 of CSA S16 [10] for all tests considered. This finding is further supported by the results of the ESF approach.

References

1. American Institute of Steel Construction (AISC) (2016) ANSI/AISC 360–16. Specification for structural steel buildings. AISC, Chicago, IL, USA
2. American Welding Society (AWS) (2020) AWS D1.1/D1.1M:2015. Structural welding code – Steel, 23rd edn. AWS, Miami, FL, USA
3. Butler LJ, Kulak GL (1971) Strength of fillet welds as a function of direction of load. Welding Res Suppl Welding J 50(5):231–234
4. Callele LJ, Driver RG, Grondin GY (2009) Design and behavior of multi-orientation fillet weld connections. AISC Engineering Journal 46(4):257–272
5. Chen Y, Shen ZY, Zheng Q, Chen C (2001) Experimental study on the performance of single weld joints in H-shaped steel members. Int J Steel Struct 1(3):201–211
6. Canadian Standards Association (CSA) (2014) CSA S16–14. Design of steel structures. CSA, Toronto, ON, Canada
7. Canadian Standards Association (CSA) (2018a) CSA W59–18. Welded steel construction (metal arc welding). CSA, Toronto, ON, Canada
8. Canadian Standards Association (CSA) (2018b) CSA G40.20–13/G40.21–13 (R2018). General requirements for rolled or welded structural quality steel / Structural quality steel. CSA, Toronto, ON, Canada
9. Canadian Standards Association (CSA) (2019a) CSA S16:19. Design of steel structures. CSA, Toronto, ON, Canada
10. Canadian Standards Association (CSA) (2019b) CSA S6:19. Canadian highway bridge design code. CSA, Toronto, ON, Canada
11. Deng K, Grondin GY, Driver RG (2006) Effect of loading angle on the behaviour of fillet welds. AISC Eng J 43(1):9–23

12. Ellingwood B, Galambos TV, MacGregor JG, Cornell CA (1980) Development of a probability based load criterion for American national standard A58. National Bureau of Standards, Gaithersburg, MD, USA
13. European Committee for Standardization (CEN) (2005) EN 1993–1–8:2005. Eurocode 3: Design of steel structures—Part 1–8: Design of joints. CEN, Brussels, Belgium
14. Fisher JW, Galambos TV, Kulak GL, Ravindra MK (1978) Load and resistance factor design criteria for connectors. ASCE J Struct Division 104(9):1427–1441
15. Galambos TV, Ravindra MK (1977) The basis for load and resistance factor design criteria of steel building structures. Can J Civ Eng 4:178–189
16. Kamtekar AG (1982) A new analysis of the strength of some simple fillet welded connections. J Constr Steel Res 2(2):33–45
17. Kamtekar AG (1987) The strength of planar fillet weld groups subjected to a shearing force applied outside their planes. J Constr Steel Res 4:163–199
18. Kanvinde AM, Gomez IR, Roberts M, Fell BV, Grondin GY (2009) Strength and ductility of fillet welds with transverse root notch. J Constr Steel Res 65:948–958
19. Kato B, Morita K (1974) Strength of transverse fillet welded joints. Welding Res Suppl Welding J 59s–64s
20. Kennedy DJL, Gad Aly M (1980) Limit states design of steel structures—performance factors. Can J Civ Eng 7:45–77
21. Lesik DF, Kennedy DJ (1990) Ultimate strength of fillet welded connections loaded in plane. Can J Civ Eng 17(1):55–67
22. Li C, Grondin GY, Driver RG (2007) Reliability analysis of concentrically loaded fillet welded joints. Structural Engineering Report 271. University of Alberta, Edmonton, AB, Canada
23. MacPhedran I, Grondin GY (2011) A simple steel beam design curve. Can J Civ Eng 38(2):141–153
24. Miazga GS, Kennedy DJL (1989) Behaviour of fillet welds as a function of the angle of loading. Can J Civ Eng 16(4):583–599
25. Ng AKF, Deng K, Grondin GY, Driver RG (2004) Behaviour of transverse fillet welds: experimental program. AISC Eng J 41(2):39–54
26. Ng AKF, Deng K, Grondin GY, Driver RG (2004) Behaviour of transverse fillet welds: parametric and reliability analyses. AISC Eng J 41(2):55–67
27. Nowak AS, Lind NC (1979) Practical bridge code calibration. ASCE J Struct Eng 105(12):2497–2510
28. National Research Council of Canada (NRC) (2020) NBCC 2020 Part 4. National building code of Canada. NRC, Ottawa, ON, Canada
29. Packer JA, Sun M, Tousignant K (2016) Experimental evaluation of design procedure for fillet welds to hollow structural sections. ASCE J Struct Eng 142(5):0416007–1–04016007–12
30. Ravindra MK, Galambos TV (1978) Load and resistance factor design for steel. ASCE J Struct Division 104(9):1337–1353
31. Schmidt BJ, Bartlett FM (2002) Review of resistance factor for steel: resistance distributions and resistance factor calibration. Can J Civ Eng 29:109–118
32. Thomas JH (2021) Design of single-sided fillet welds under transverse loading. MASc Thesis. Dalhousie University, Halifax, NS, Canada
33. Tousignant K, Packer JA (2017) Numerical investigation of fillet welds in HSS-to-rigid end-plate connections. ASCE J Struct Eng 143(12):04017165–1–04017165–16
34. Tuominen N, Björk T, Ahola A (2018) Effect of bending moment on capacity of fillet welds. In: Proceedings, Tubular Structures XVI. Taylor and Francis Group, London, UK

CSA S16:24—Changes to Concrete-Filled HSS

Tousignant Kyle and Packer Jeffrey

Abstract This paper presents an overview of proposed changes to design provisions for concrete-filled hollow structural section (HSS) members in CSA S16—"Design of Steel Structures". It contains background information on the general characteristics of concrete-filled HSS, as used in Canada, justification for the proposed changes to CSA S16, and references to the research on which the proposed changes are based. Particular emphasis is given to material limitations, cross-section classifications, and provisions for the design of concrete-filled HSS under axial compression, flexure, and combined loading. The potential use of steel reinforcing bars has been introduced, which brings CSA S16 Clause 18.2 more into line with peer standards such as AISC 360 and Eurocode 4.

Keywords Concrete-filled HSS · CSA

1 Introduction

Since the mid-1990s, there has been limited research in Canada on concrete-filled hollow structural section (HSS) members under static loading, and revisions to Clause 18.2 (on concrete-filled HSS) of CSA S16—"Design of Steel Structures" [16] have been minimal. Meanwhile, in peer standards, such as AISC 360 [2] and Eurocode 4 [9], provisions for concrete-filled HSS under static loading have evolved to accommodate the use of ever-increasing tube sizes, light-weight concrete, and longitudinal steel reinforcing bars.

During the 2019 CSA S16 code cycle, Working Group 8 (responsible primarily for Clause 15: Trusses and Clause 18: Composite columns) focused its efforts on revisions to Clause 15; however, the shortcomings of Clause 18.2, particularly with

T. Kyle (✉)
Dalhousie University, Dalhousie, Canada
e-mail: kyle.tousignant@dal.ca

P. Jeffrey
University of Toronto, Toronto, Canada

regard to the exclusion of steel reinforcing bars, were made apparent. At the same time, an international survey of design procedures for composite HSS columns and beam-columns was being initiated, so modernization of Clause 18.2 was deferred to the 2024 code cycle. The international survey resulted in CIDECT Design Guide No. 4, 2nd edition [28], but only covered design recommendations to American, European, Australian, and Chinese standards.

Tousignant and Packer [25, 26] hence reviewed the rules in CSA S16 for design of concrete-filled HSS under static loading, compared them to peer standards (AISC 360 and Eurocode 4), and evaluated them against a database of over 450 tests. The result of this study was a lengthy proposal for changes to CSA S16 Clause 18.2 that cover its scope (i.e., material limitations), the classification of cross-sections, and provisions for compressive resistance, bending resistance, and axial compression and bending, as well as tension, and shear. This paper provides a commentary on CSA S16:19 Clause 18.2 [16], which identifies its limitations, and discusses the proposed changes.

2 Scope

Currently, CSA S16 Clause 18.2 applies to composite members consisting of steel HSS completely filled with concrete, provided that the concrete strength is within specified limits (see Sect. 2.2), and the flat width-to-thickness ratio (b_{el}/t) of rectangular hollow section (RHS) walls or outside diameter-to-thickness ratio (D/t) of circular hollow sections (CHS) does not exceed the limits for plastic design (see Sect. 3).

2.1 HSS

The intent of Clause 18.2 is for design using manufactured HSS made to CSA G40 (in Class C or Class H) [15], ASTM A500 Grade B/C [5], or ASTM A1085 [4]. The relative availability of these alternatives varies around Canada, as described in Tables 6–8 of the CISC Handbook [10]. It is important to note that in the CISC Handbook [10], as in design, section properties for ASTM A500 sections are computed using a design wall thickness (t) of 0.90 times the nominal wall thickness. The yield stress (F_y) for all ASTM A500 Grade C HSS shapes has been harmonized to 345 MPa [5].

2.2 Concrete

Currently, the scope of CSA S16 Clause 18.2 covers concrete strengths ($f_c{}'$) between 20 and 80 MPa for concentrically loaded columns and 20 MPa $\leq f_c{}' \leq$ 40 MPa

for columns subjected to axial compression and bending [16]. AISC 360–16, on the other hand, limits the application of their provisions to concrete-filled HSS having 21 MPa $\leq f_c' \leq$ 69 MPa for normal-weight concrete and 21 MPa $\leq f_c' \leq$ 41 MPa for light-weight concrete. The lower limit of 21 MPa for all concrete densities and the upper limit of 41 MPa for light-weight concrete are to encourage the use of good quality, readily available, grades of structural concrete [2].

Given the consideration of different concrete densities by AISC, it has been recommended to adopt rounded ranges of 20 MPa $\leq f_c' \leq$ 70 MPa for normal-weight concrete and 20 MPa $\leq f_c' \leq$ 40 MPa for light-weight concrete in CSA S16. Although the former limit is slightly more restrictive than the current limit in CSA S16 for concentrically loaded columns ($f_c' \leq$ 70 MPa versus $f_c' \leq$ 80 MPa), the validated wider range of application for beam-columns is valuable considering that nearly all columns, in practice, will be subjected to combined loading. The upper limit of 70 MPa for normal-weight concrete is also in accordance with CSA S16 Clause 18.3 for partially encased composite columns.

It is recommended that a higher sand and cement content can be used in concrete mixes intended for composite columns to ensure adequate plasticity. Cementitious grouts, plasticizers, and self-consolidating concretes are acceptable, but the use of additives that can cause corrosion of steel (e.g., calcium chloride) should be avoided [18]. The maximum aggregate size should also be reduced (especially, if reinforcing bars are placed inside the HSS). Recommendations for this can be found in [18]. For manufactured HSS covered by Clause 18.2 (not very large tubular members), mechanical shear connectors are not required between the HSS and the concrete.

2.3 Reinforcing Bars

Unlike other national standards in the USA [2], Europe [9], Australia (Standards [24], and China [21]), CSA S16 does not cater to the use of longitudinal steel reinforcing bars in concrete-filled HSS strength calculations. They are, however, catered to in strength calculations for partially encased and encased composite columns (Clauses 18.3.2 and 18.4.2, respectively) [16]. For these members, there is no limit on the specified yield stress of reinforcing steel (F_{yr}) that can be used for design calculations.

In AISC 360–16 [2], an upper limit of 550 MPa is set on F_{yr} to be in accordance with ACI 318 (2014). Eurocode 4 [9], on the other hand, imposes no restrictions. The Canadian concrete standard (CSA A23.3:19) [17] has an upper limit of 500 MPa on F_{yr}, although the most common strength used in Canada is still 400 MPa. Accordingly, it is recommended that F_{yr} not exceeds 500 MPa for design calculations in accordance with the recommendations below.

The HSS size will also dictate the potential for inclusion of longitudinal steel reinforcing bars. For concrete filling on site, a minimum outside HSS dimension of 200 mm is recommended. The gap between reinforcing bars/stirrups and the HSS inside wall should also be at least 1.5–2 times the maximum aggregate size, with a maximum concrete cover between 25 and 50 mm.

3 Cross-Section Classification

CSA S16 Clause 18.2 covers concrete-filled HSS with Class 1 and 2 sections (i.e., cross-sections that can undergo complete plastification). These currently include RHS with flat width-to-thickness ratios (b_{el}/t) and CHS with outside diameter-to-thickness ratio (D/t) defined in Tables 1 and 2 for elements under axial compression and flexural compression, respectively. These limits date to at least the 1994 edition of the CSA standard [11] and are larger than those for unfilled HSS because the concrete delays inward buckling of the HSS wall.

Similar limits to those in CSA S16 exist in AISC 360–16 [2] for so-called non-compact sections under axial compression and compact sections under flexural compression. AISC's limits, which are also defined in Tables 1 and 2, are based on the more recent work of [7, 8].

For elements in concrete-filled RHS under axial compression, CSA's current limit of $b_{el}/t = 1350/\sqrt{F_y}$ is in good agreement with AISC's ($1340/\sqrt{F_y}$). However, for concrete-filled CHS, CSA's current limit of $D/t = 28,000/F_y$ is considerably more conservative than AISC's ($38,000/F_y$).

For elements in concrete-filled RHS under flexural compression, AISC logically considers two different local buckling cases (for flanges and webs), which CSA does not. CSA's sole limit ($1350/\sqrt{F_y}$ according to Clause 19.2.1.1 or $700/\sqrt{F_y}$ according to the Commentary) is based on the scope of tests performed in the early 1990s by [22]. For concrete-filled CHS, CSA's current limit of $D/t = 28,000/F_y$ is unconservative.

It was recommended to replace the current limits in CSA S16 Clause 18.2.1 by extending Tables 1 and 2 of CSA S16 (which cover the similar limits for local buckling of steel sections); i.e.:

Table 1 Limits for elements in axial compression

Shape	Specification	Limit
RHS	CSA S16	$1350/\sqrt{F_y}$
	AISC 360	$1340/\sqrt{F_y}$
CHS	CSA S16	$28,000/F_y$
	AISC 360	$38,000/F_y$

Table 2 Limits for elements in flexural compression

Shape	Specification	Element	Limit
RHS	CSA S16	Walls	$1350/\sqrt{F_y}$
	AISC 360	Flanges	$1010/\sqrt{F_y}$
		Webs	$1340/\sqrt{F_y}$
CHS	CSA S16		$28,000/F_y$
	AISC 360		$18,000/F_y$

For compression elements in members subject to axial compression (CSA S16 Table 1):

- Concrete-filled rectangular hollow sections: $b_{el}/t \leq 1350/\sqrt{F_y}$.
- Concrete-filled circular hollow sections: $D/t \leq 38{,}000/F_y$.

For compression elements in members subject to flexure or combined flexure and compression (CSA S16 Table 2):

- Flanges of concrete-filled rectangular hollow sections: $b_{el}/t \leq 1010/\sqrt{F_y}$.
- Webs of concrete-filled rectangular hollow sections: $h_{el}/t \leq 1340/\sqrt{F_y}$.
- Concrete-filled circular hollow sections: $D/t \leq 18{,}000/F_y$.

The above limits are met by nearly all HSSs in the CISC Handbook (CSA 2021) to which Clause 18.2 applies, despite being more restrictive in some cases. Specific HSS that does not meet the above-proposed limits is listed in Tousignant and Packer [25] and should not be used in conjunction with the plastic design method in CSA S16. However, the alternate methods given in AISC 360–16 Sections I2.2 and I3.4 (e.g., strain compatibility, elastic stress) could be applied.

4   Compressive Resistance

According to CSA S16:19 Clause 18.2.2, the factored compressive resistance of a composite concrete-filled hollow structural section (C_{rc}) is taken as:

$$C_{rc} = \frac{\tau \phi A_s F_y + \tau' \alpha_1 \phi_c A_c f_c'}{(1 + \lambda^{2n})^{\frac{1}{n}}}, \tag{1}$$

where A_s and A_c = cross-sectional area of steel and concrete; ϕ and ϕ_c = resistance factor for steel and concrete ($= 0.9$ and 0.65, respectively); τ = confinement reduction factor for steel (due to tensile hoop stresses that develop to confine the concrete); τ' = confinement enhancement factor for concrete; α_1 = ratio of average stress in rectangular stress block to f_c' ($= 0.85 - 0.0015 f_c' \geq 0.73$); n = column curve parameter ($= 1.80$); and λ = non-dimensional slenderness parameter:

$$\lambda = \sqrt{\frac{C_p}{C_{ec}}}, \tag{2}$$

where $C_p = C_{rc}$ computed with $\phi = \phi_c = 1.0$ and $\lambda = 0$, and:

$$C_{ec} = \frac{\pi^2 E I_e}{(KL)^2} \quad \text{with} \quad E I_e = E I_s + \frac{0.6 E_c I_c}{1 + C_{fs}/C_f}, \tag{3}$$

where I_s and I_c = moment of inertia of the steel and concrete areas, respectively, as computed with respect to the center of gravity of the cross-section; E = modulus of elasticity of steel; E_c = modulus of elasticity of concrete, as defined in CSA S16 Clause 3; C_{fs} = sustained axial load on the column; and C_f = total axial load on the column.

In Eq. (1), $\tau = \tau' = 1.0$, except for CHS with a height-to-diameter ratio (L/D) of less than 25 for which:

$$\tau = \frac{1}{\sqrt{1 + \rho + \rho^2}} \quad \text{and} \quad \tau' = 1 + \left(\frac{25\rho^2\tau}{D/t}\right)\left(\frac{F_y}{\alpha_1 f_c'}\right) \quad \text{with} \quad \rho = 0.02(25 - L/D). \tag{4}$$

The above expression for C_{rc} was first introduced in CSA S16-01 [12]. It is based on simply superimposing the contributions of the concrete and HSS and applying a reduction factor, based on λ, using the same form of the column curve found elsewhere in the code (e.g., Clause 13.3). The non-dimensional slenderness parameter (λ) of the composite section depends on the effective elastic flexural stiffness of the composite column (EI_e) which in turn depends on the elastic flexural stiffness of steel column (EI_s) and a flexural stiffness of concrete modified to account for creep under sustained loads. The value of the exponent n in Eq. (1) was taken as 1.80 to provide the best fit with experimental results.

The triaxial load effect on the concrete due to the confining effect of the walls of CHS is based on work by [27]. The triaxial effects increase the failure load of the concrete ($\tau' > 1.0$) and decrease the capacity of the steel section ($\tau < 1$) because the steel is in a biaxial stress state.

In S16-09 [13], the standard introduced a value of $\phi_c = 0.65$ in place of the earlier 0.60 and $\alpha_1\phi_c f_c'$ in place of $0.85\phi_c f_c'$. Reasons for these changes are described by [6]. In S16-14 [14], the lower limit for α_1 was changed to 0.73, which is currently the lowest possible value because the scope of Clause 18.2 covers concrete strengths up to f_c' 80 MPa.

Unlike other national steel standards (see Sect. 2.3), as well as other parts of the standard (i.e., Clauses 18.3.2 and 18.4.2), Clause 18.2.2 does not cater to the use of longitudinal steel reinforcing bars, which are beneficial to strength and often included to improve fire endurance. It was therefore recommended to revise the C_{rc} expression (Eq. 1) to:

$$C_{rc} = \frac{\tau\phi A_s F_y + \tau'\alpha_1\phi_c A_c f_c' + \phi_r A_r F_{yr}}{(1 + \lambda^{2n})^{\frac{1}{n}}}, \tag{5}$$

where A_r = cross-sectional area of longitudinal reinforcement and ϕ_r = resistance factor for steel reinforcing bars. A new lower limit of 0.75 for α_1 was also proposed as a consequence of adopting the upper limit of $f_c' = 70$ MPa for normal-weight concrete discussed in Sect. 2.2.

For consistency, a modification to the expression for EI_e in Eq. (3) is also required:

$$\mathrm{EI}_e = \mathrm{EI}_s + \frac{0.6 E_c I_c}{1 + C_{\mathrm{fs}}/C_f} + E I_r, \qquad (6)$$

where I_r = moment of inertia of the reinforcing bar areas, as computed with respect to the center of gravity of the cross-section.

These modifications were supported by a first-order reliability method (FORM) analysis that utilized results from hundreds of tests on concrete-filled HSS columns falling within the b_{el}/t, D/t, and $f_c{}'$ limits discussed previously. For concrete-filled HSS members without longitudinal reinforcing, reliability indices obtained from the FORM analysis using Eq. (5) and the revised limits are similar to those obtained using the current (CSA S16:19) provisions.

5 Bending Resistance

According to CSA S16:19 Clause 18.2.3, the factored bending resistance of a composite concrete-filled hollow structural section (M_{rc}) is taken as:

$$M_{\mathrm{rc}} = C_r e + C_r' e', \qquad (7)$$

where C_r = compressive resistance of steel above the neutral axis (NA); $C_r{}'$ = compressive resistance of concrete above the NA (over the depth of the concrete compression zone, a); e = lever arm between C_r and T_r, where T_r = tensile resistance of steel below the NA; and e' = lever arm between $C_r{}'$ and T_r (Fig. 1).

The current model is based on the work of [22], who showed that fully plastic stress blocks are developed in the steel and concrete when Class 1 and 2 sections are used. In the proposed model, stress blocks in the steel had an intensity of F_y, and stress blocks in the concrete had an intensity of $f_c{}'$. [22] noted that steel restrained the concrete, increasing its compressive resistance to the full value of $f_c{}'$ rather than $0.85 f_c{}'$, as used in reinforced concrete theory.
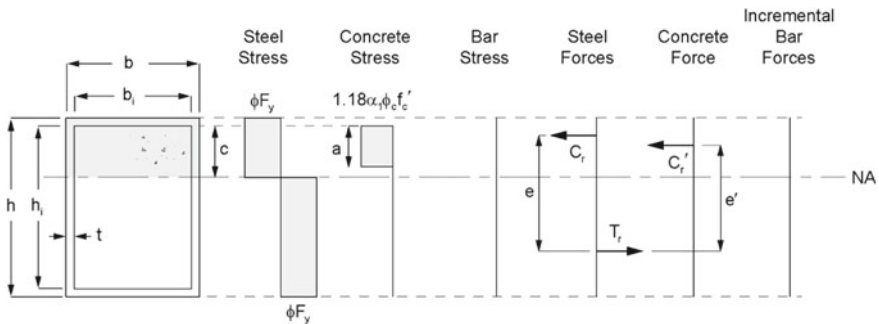
Fig. 1 Stress and force diagrams for concrete-filled RHS, simplified to a box section (CSA S16:19)

Equations are given for C_r and $C_r{'}$ in CSA S16:19 Clause 18.2.3 that are, generally, the product of the stress intensities and geometries (of steel and concrete). CSA S16-01 [12] and earlier editions of the standard noted (in Clause 18.2.3) that a was to be taken as 0.85 times the concrete depth to the neutral axis (= 0.85c); however, in 2009 and later editions, the definition of a was removed. Similarly, these more recent editions reflect a concrete stress block intensity of $\alpha_1\phi_c f_c{'}$ versus $f_c{'}$ as originally proposed by [22].

Tousignant and Packer [26] have shown that omitting the RHS rounded corners—as done in the $C_r{'}$ equation for RHS in CSA S16:19—is unconservative and, for CHS, questioned the need for a recursive (or iterative) function to determine M_{rc}. The existing M_{rc} expression also does not cater to the use of longitudinal steel reinforcing bars. Hence, new formulae, based on the integration of fully plastic stress blocks in the steel, concrete, and rebar, if present—including rounded RHS corners, were proposed.

These equations were derived by assuming that the concrete stress block extends the full depth to the NA (i.e., $a = c$), as is now common practice [2] (Figs. 2 and 3). The location of the NA and M_{rc} are determined by finding equilibrium of forces and moments, respectively, that are generated by resistances, for consistency with the approach used in CSA A23.3:19 [17] and elsewhere in CSA S16.

(a) For concrete-filled RHS:

$$M_{\mathrm{rc}} = Z\phi F_y - 2t\left(\frac{h_i}{2} - a\right)^2\phi F_y + \frac{Z_c}{2}\phi_c f_c - \frac{b_i}{2}\left(\frac{h_i}{2} - a\right)^2\phi_c f_c + M_{\mathrm{rr}},$$

(8)

where $f_c = 1.18\alpha_1 f_c{'}$; Z = plastic modulus of the steel section alone; $h_i = d - 2t$ (where d = overall depth of hollow section); and:
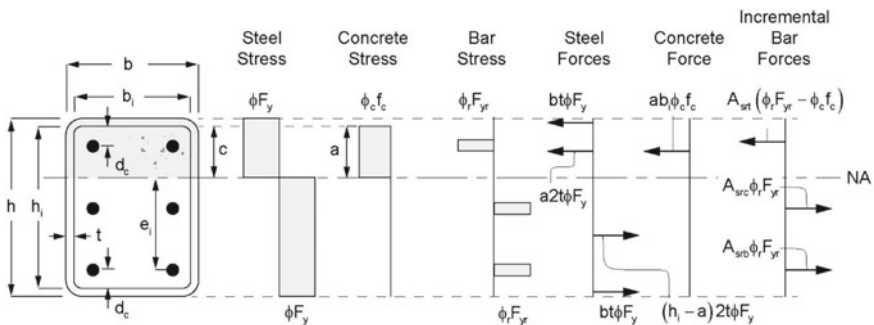
Fig. 2 Stress and approximate force diagrams (after simplifying to a box section as in Fig. 1) for concrete-filled RHS (proposed)
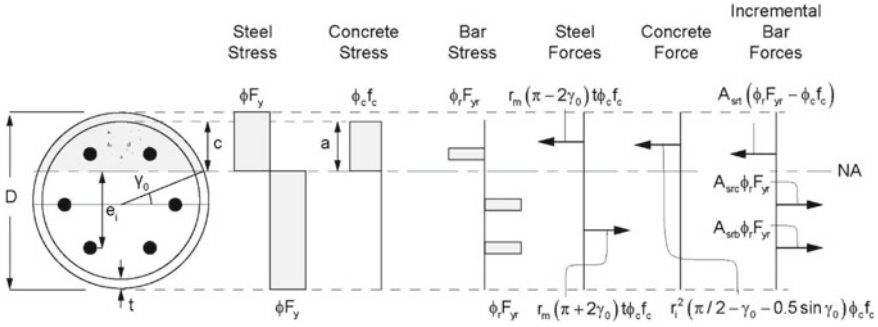
Fig. 3 Stress and force diagrams for concrete-filled CHS (proposed)

$$a = \frac{h_i}{2} - \frac{(A_g - A_s)\phi_c f_c - 2\phi_r F_{yr}(A_{src} + A_{srb} - A_{srt}(1 - \phi_c f_c/\phi_r F_{yr}))}{8t\phi F_y + 2b_i\phi_c f_c}, \quad (9)$$

where A_g = gross cross-sectional area of composite section; A_{srt}, A_{src}, and A_{srb} = area of reinforcing bars in the top, central, and bottom regions, respectively, where only the top region is located above the neutral axis; and Z_c = plastic modulus of the area inside the HSS (concrete plus reinforcing bars):

$$Z_c = \frac{b_i h_i^2}{4} - 0.429 r_i^2 h_i + 0.192 r_i^3, \quad (10)$$

where $b_i = b - 2t$, where b = overall width of hollow section; $r_i = t$; and:

$$M_{rr} = \phi_r F_{yr}\left[A_{srt}(a - d_c)(1 - \phi_c f_c/\phi_r F_{yr}) + A_{src}\left(\frac{h_i}{2} - a\right) + A_{srb}(h_i - a - d_c)\right], \quad (11)$$

where d_c = distance from the inside face of the hollow structural section to the center of the closest adjacent reinforcing bar (Fig. 2). For concrete-filled RHS within the scope of Clause 18.2, lateral torsional buckling is not a governing limit state.

For concrete-filled RHS members without longitudinal reinforcing, the above approach provides a similar level of reliability to CSA S16 and AISC 360–16.

(b) For concrete-filled CHS:

$$M_{rc} = 4\phi F_y t r_m^2 \cos \gamma_0 + \frac{2}{3}\phi_c f_c r_c^3 \cos^3 \gamma_0 + M_{rr}, \quad (12)$$

where:

$$r_m = \left(\frac{D - t}{2}\right) \quad \text{and} \quad r_c = \left(\frac{D - 2t}{2}\right), \quad (13a)$$

where D = outside diameter of hollow section.

$$\gamma_0 = \frac{\pi r_c^2 \phi_c f_c + \phi_r F_{yr}\left(A_{src} + A_{srb} - A_{srt}\left(1 - \phi_c f_c / \phi_r F_{yr}\right)\right)}{8 t r_m \phi F_y + 3 r_c^2 \phi_c f_c}. \tag{13b}$$

and

$$M_{rr} = \frac{A_{sr}}{n}\left(\phi_r F_{yr} \sum_{i=1}^{n} e_i - \phi_c f_c \sum_{i=1}^{n_t} e_i\right), \tag{14}$$

where γ_0 = angular location of the neutral axis; A_{sr} = total area of steel reinforcing bars; n = number of steel reinforcing bars; and e_i = absolute distance from the ith steel reinforcing bar to the neutral axis (Fig. 3). The depth of the neutral axis from the inside face of the CHS can be taken as $r_c(1-\sin\gamma_0)$.

Equation 13b is similar in principle to the one used in the AISC Manual [3] to determine the location of the NA, and the remaining expressions are based on work by [19]. For concrete-filled CHS members without longitudinal reinforcing, the above approach provides a similar level of reliability to CSA S16 while avoiding recursion.

6 Axial Compression and Bending

In CSA S16:19 Clause 18.2.4, composite concrete-filled HSS required to resist both bending moments and axial compression is proportioned analogously to members conforming to Clause 13.8.2, so that:

$$\frac{C_f}{C_{rc}} + \frac{\beta \omega_1 M_f}{M_{rc}\left(1 - \frac{C_f}{C_{ec}}\right)} \leq 1.0 \quad \text{and} \quad \frac{M_f}{M_{rc}} \leq 1.0, \tag{15}$$

where C_f = factored axial load; M_f = factored moment; β = coefficient for bending in beam-columns; and ω_1 = coefficient to determine equivalent uniform bending effect in beam-columns. Although not stated explicitly in CSA S16:19 Clause 18.2.4, ω_1 is found in Clause 13.8.6.

The rightmost inequality in Eq. (15) is intended to prevent a dangerous situation that can arise for beam-columns under low axial loads, in which the leftmost inequality allows for an increase in M_{rc}. In Eurocode 4, this increase is only permitted when M_f results from an eccentricity in C_f.

β is taken as:

$$\beta = \frac{C_{rco} - C_{rcm}}{C_{rco}}, \tag{16}$$

where $C_{rco} = C_{rc}$ calculated with $\lambda = 0$, and $C_{rcm} = 1.18\alpha_1\phi_c A_c f_c{}'$ (which is defined as the factored compressive resistance that can coexist with M_{rc} when all the cross-section is in compression).

In the 2019 edition of the standard [16], changes were made to the β values for unfilled beam-columns in Clauses 13.8.3 and 13.8.4. The rationale for the new values chosen was based on designing the members for plastic behavior [20, 23]. This philosophy was used previously, in CSA S16-14 for Class 1 and 2 I-shaped members and in earlier editions of CSA S16 (e.g., CSA S16.1–94 Appendix F) [11] for some HSS. The β values from Clauses 13.8.3 and 13.8.4 for Class 1 and 2 unfilled RHS and CHS subjected to uniaxial bending are presented in Table 3.

Tousignant and Packer [26] made several recommendations for Clause 18.2.4 to: spell out the value (or location) of ω_1 (recall, it is currently not noted); more clearly state the need to check cross-sectional strength, overall member strength, and/or lateral torsional buckling strength; adopt the previously discussed C_{rc} and M_{rc} expressions, which permit the use of longitudinal steel reinforcing bar; and adopt—as an alternative—the β values in Table 3, for consistency with Clauses 13.8.3 and 13.8.4. It is important to note that the β values in Table 3 are almost universally conservative for concrete-filled HSS [26].

With respect to the latter recommendation, two approaches were given:

- Approach (i): utilizing the recommended C_{rc} and M_{rc} expressions with β calculated by using the current approach, i.e., Eq. (16).
- Approach (ii): utilizing the recommended C_{rc} and M_{rc} expressions with "$\beta = 0.85$ for square and circular hollow structural sections, and 1.0 for all other hollow structural sections".

Considering the results of over 50 tests on concrete-filled RHS beam-columns and 25 tests on concrete-filled CHS beam-columns (all falling within the b_{el}/t, D/t, and $f_c{}'$ limits discussed previously), Approach (i) was shown to give similar statistics to the existing CSA S16 method, and Approach (ii) was shown to be more conservative but produce similar statistics to the interaction method described for beam-columns in AISC 360 [2].

In addition, it was recommended to spell out that the value of ω_1 is defined in Clause 13.8.6 and to extend the analogy of unfilled steel beam-columns to concrete-filled HSS by stating the manner in which cross-sectional strength and overall (in-plane) member strength must be checked when using Eq. (15); i.e., that "the capacity of the member shall be examined for cross-sectional strength (members in braced frames only) and overall member strength, in the manner specified in Clause 13.8.2".

Table 3 Coefficients for uniaxial bending in HSS beam-columns

Shape	Reference	Coefficient (β)
RHS	Classes 1 and 2 square RHS (Clause 13.8.3)	0.85
	All other RHS (Clause 13.8.4)	1.00
CHS	Class 1 and 2 CHS (Clause 13.8.3)	0.85

As discussed in Sect. 5, lateral torsional buckling strength need not be checked as it is not a governing limit state for round, square, or rectangular concrete-filled HSS.

7 Tension Resistance

For the tensile resistance (T_r) of concrete-filled HSS, it was proposed that T_r is taken, conservatively, as that of the steel section alone in accordance with Clause 13.2. The corresponding provisions in AISC 360–16 allow T_r to be taken as the sum of the resistance of the steel section plus reinforcing bars, in which case special detailing may be required to reliably transfer tension force from the HSS to the reinforcement. For T_r, at present, CSA S16 is noticeably silent.

8 Shear Resistance

The shear resistance (V_r) of concrete-filled HSS is covered, at present, by Clause 13.4.1.3 [16]. Clause 13.4.1.3 was introduced in the 2009 edition of the standard and is intended for CHS members only. A more general expression that applies to both CHS and RHS members was hence proposed; i.e.:

$$V_r = 0.66\phi A_v F_y, \tag{17}$$

where $A_v = A_s/2$ for CHS members and $A_s(d/(b + d))$ for RHS members, with the applied shear force in the direction of d, and A_s = area of hollow section. The dimensions b and d are the overall width and depth of the rectangular hollow section, respectively.

Equation 17 is based on the shear resistance of the HSS alone, ignoring any contribution from concrete and/or reinforcing bars. The inelastic limit stress of $0.66F_y$ corresponds to shear deformations into the strain-hardening range, which will occur in HSS webs that are internally supported by concrete.

While stirrups/ties are beneficial to allow for placement of the longitudinal reinforcing bars, they are not required for shear capacity.

9 Summary

The foregoing paper has summarized the rationale for proposed changes to Clause 18.2 (on concrete-filled HSS) of CSA S16:19—Design of Steel Structures [16]. A draft of CSA S16:24 will be available for public review in Spring 2023, finalized in Fall 2023, and published in May 2024. The reader is referred to companion papers by

Tousignant and Packer [25, 26] for illustrative design examples covering concrete-filled RHS and CHS under axial compression, flexure, and combined loading.

References

1. ACI (2014) Building code requirements for structural concrete and commentary. ACI 318–14, American Concrete Institute, Farmington Hills, MI, USA
2. AISC (2016) Specification for structural steel buildings. AISC 360–16, American Institute of Steel Construction, Chicago, IL, USA
3. AISC (2017) Steel construction manual, 15th edn. American Institute of Steel Construction, Chicago, IL, USA
4. ASTM (2015) Standard specification for cold-formed welded carbon steel hollow structural sections (HSS). ASTM A1085/A1085M-15, American Society for Testing and Materials International, West Conshohocken, PA, USA
5. ASTM (2021) Standard specification for cold-formed welded and seamless carbon steel structural tubing in rounds and shapes. ASTM A500/A500M-21a, American Society for Testing and Materials International, West Conshohocken, PA, USA
6. Bartlett FM (2007) Canadian standards association standard A23.3-04 resistance factor for concrete in compression. Can J Civ Eng 34:1029–1037
7. Bradford MA, Loh HY, Uy B (2002) Slenderness limits for filled circular steel tubes. J Constr Steel Res 58(2):243–252
8. Bradford MA, Wright HD, Uy B (1998) Local buckling of the steel skin in lightweight composites induced by creep and shrinkage. Adv Struct Eng 2(1):25–34
9. CEN (2004) Design of composite steel and concrete structures—Part 1–1: General rules and rules for buildings. EN 1994–1–1, European Committee for Standardization, Brussels, Belgium
10. CISC (2021) Handbook of steel construction, 12th edn. Canadian Institute of Steel Construction, Toronto, ON, Canada
11. CSA (1994) Limit states design of steel structures. CAN/CSA-S16.1–94, Canadian Standards Association, Toronto, ON, Canada
12. CSA (2001) Limit states design of steel structures. CAN/CSA S16–01, Canadian Standards Association, Toronto, ON, Canada
13. CSA (2009) Design of steel structures. CSA S16–09, Canadian Standards Association, Toronto, ON, Canada
14. CSA (2014) Design of steel structures. CSA S16–14, Canadian Standards Association, Toronto, ON, Canada
15. CSA (2018) General requirements for rolled or welded structural quality steel / Structural quality steel. CSA G40.20–13/G40.21–13 (R2018), Canadian Standards Association, Torontpo, ON, Canada
16. CSA (2019a) Design of steel structures. CSA S16:19, Canadian Standards Association, Toronto, ON, Canada
17. CSA (2019b) Design of concrete structures. CSA A23.3:19, Canadian Standards Association, Toronto, ON, Canada
18. Dutta D, Wardenier J, Yeomans N, Sakae K, Bucak Ö, Packer JA (1998) Design guide for fabrication, assembly, and erection of hollow section structures. CIDECT Design Guide No. 7, Comité International pour le Développement et l'Étude de la Construction Tubulaire and TÜV-Verlag GmbH, Köln, Germany
19. Elchalakani M, Zhao XL, Grzebieta RH (2001) Concrete-filled circular steel tubes subjected to pure bending. J Constr Steel Res 57:1141–1168
20. Essa HS, Kennedy DJL (2000) Proposed provisions for the design of steel beam-columns in S16–2001. Can J Civ Eng 27:610–619

21. GB (2014) Technical code for concrete filled steel tubular structures. GB50936–2014, China Architecture & Building Press, Beijing, China
22. Lu YQ, Kennedy DJL (1994) The flexural behaviour of concrete-filled hollow structural sections. Can J Civ Eng 21:111–130
23. Pillai US (1974) Beam-columns of hollow structural sections. Can J Civ Eng 1(2):194–198
24. Standards Australia (2017) Composite structures – Composite steel-concrete construction in buildings. AS/NZS 2327:2017, Standards Australia, Sydney, Australia
25. Tousignant K, Packer JA (2022a) Concrete-filled hollow structural sections. I: Materials, cross-section classification, and concentrically loaded columns. Canadian J Civil Eng, in press
26. Tousignant K, Packer JA (2022b) Concrete-filled hollow structural sections. II: Flexural members, beam columns, tension, and shear. Canadian J Civil Eng, in press.
27. Virdi KS, Dowling PJ (1976) A unified design method for composite columns. Memoirs IABSE 36:11
28. Zhao XL Packer JA, Wang YC, McCormick JP (2019) Design guide for concrete-filled hollow section columns under static, impact, blast, seismic and fire loading. CIDECT Final Report 16H-4/19, Comité International pour le Développement et l'Étude de la Construction Tubulaire, Geneva, Switzerland

Canadian Design Recommendations for Diagonally Reinforced Coupling Beams Using a New Comprehensive Database

Amirhossein Amiri, Tobber Lisa, and Jeremy Atkinson

Abstract Diagonally reinforced concrete coupling beams used in coupled walls are prevalent in the Canadian construction industry. In Canadian design, these beams act as seismic fuse elements that dissipate a substantial amount of earthquake energy exerted in core walls. The detailing of these beams is critical in ensuring high-energy dissipation and sufficient ductility. The Canadian Concrete handbook (CSA A23.3–14) provides engineers with guidelines to calculate the shear strength, stiffness, and ductility capacity of coupling beams. This paper presents a new comprehensive database of the hysteretic response of 51 diagonally reinforced coupled beams. With this new database, we identified trends between detailing choices and the hysteretic response and compared these trends with current Canadian codes. Specifically, the shear strength, initial stiffness, and strength loss have been examined and discussed. Overall, this study demonstrates that providing full beam confinement, as opposed to only confining the diagonal reinforcing, is a suitable method for seismic design.

Keywords Reinforced coupling beams · New comprehensive database

1 Introduction

Reinforced concrete coupled wall systems (hereafter referred to as *coupled walls*) are widely used structural systems to resist lateral loads in tall buildings. In this system, a series of concrete wall segments are connected by coupling beams to form an inter-connected wall assembly. The seismic response of coupled walls depends strongly on the nonlinear behavior of the coupling beams joining adjacent wall segments.

A. Amiri · T. Lisa (✉)
School of Engineering, University of British Columbia, Kelowna, Canada
e-mail: lisa.tobber@ubc.ca

J. Atkinson
Structural Engineer with Kor Structural, Vancouver, Canada

Coupling beams significantly enhance the structure's overturning resistance, stiffness, and energy dissipation compared with isolated wall piers. The construction technique used for the beam varies, but the two most common schemes utilize either diagonal reinforcing or longitudinal beam reinforcing.

Diagonal coupling beams, introduced by Paulay and Binney in 1974, are equipped with a group of diagonal bars at both the top and the bottom of the beam's section forming an "x" shape over the length of the beam. Additional longitudinal bars are provided in the corners and sides of the beams to anchor ties and provide crack control. Based on previous experimental programs, the application of diagonal layouts in coupling beams instead of conventional longitudinal reinforcing has led to higher energy dissipation and ductility.

Several experimental programs regarding diagonally reinforced coupling beams (DRCBs) with different test setups were conducted previously each of which included a number of specimens with different geometry, reinforcement arrangement, and detailing. Additionally, some databases about DRCBs have been collected concentrating on specific design parameters, i.e., [14] collected a comprehensive database regarding the initial stiffness of diagonally reinforced coupling beams. However, these databases either did not include an adequate number of studied specimens (for instance [20] or they focused only on a specific designing parameter. In this study, an up-to-date and comprehensive database is collected to derive empirical equations for designing purposes based on Canadian design provisions and instructions.

In this paper, the Canadian detailing and design equations for coupling beams are compared with experimental data from a newly developed database of 51 diagonally coupling beams which is presented in Sect. 3. This analysis provides insights into the coupling beam shear strength, stiffness, and ductility, which are presented in Sect. 4.

2 Design Provisions for Diagonally Reinforced Coupling Beams

2.1 CSA A23.3 Design Provisions

In Canada, coupled walls are designed and detailed according to the CSA A23.3–19 and the National Building Code (NBC) [23]. Figure 1 shows a typical layout for diagonally reinforced coupling beams in Canada and some of the geometric limitations of the design. According to the CSA A23.3, the width (b_w) and height (h) of the coupling beam should not exceed the pier wall's thickness (t_w) and two times the clear length of the coupling beam (L), respectively. It is required that each group of diagonal bars includes at least four bars. Moreover, CSA A23.3–19 requires that the minimum embedment length of diagonal bars into the pier walls at each end should be at least 1.5 L_d, where L_d is the development length of bars.

The design force and deformation demand in coupled wall systems are typically determined using the linear dynamic method in the NBC. As the coupling beams
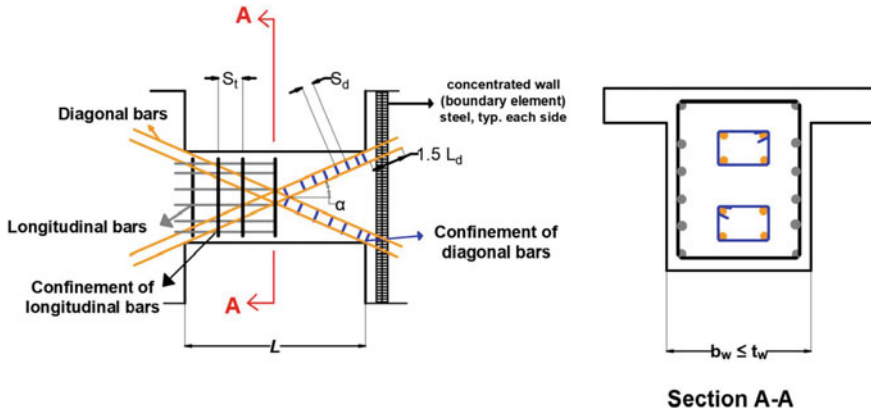
Fig. 1 General CSA A23.3 provisions for diagonally reinforced coupling beams

deform in an earthquake, they will crack, and their stiffness will degrade. For the purpose of linear dynamic analysis, an effective cracked section stiffness is accounted for by applying stiffness modification factors to the finite elements used to model the beams. The effective shear area and the effective moment of inertia are shown in Eqs. 1 and 2, respectively.

$$A_{ve} = \alpha_s A_g \tag{1}$$

$$I_{eff} = \alpha_f I_g \tag{2}$$

where A_g is the beam's gross area, and I_g is the beam's gross moment of inertia. The CSA A23.3–19 recommends modifying coupling beams' shear area and moment of inertia by using $\alpha_s = 0.45$ and $\alpha_f = 0.25$, respectively.

$$V_n = 2A_{S,d} \times f_{y,d} \times \sin \alpha \tag{3}$$

where $A_{S,d}$ is the total area of the diagonal bars at the top or bottom of the beam's section, $f_{y,d}$ is the yielding strength of diagonal bars, and α is the inclination angle between the diagonal bars and the beam longitudinal axis.

To prevent the diagonal bars from buckling, the bundles of diagonal bars are required to be tied by crossties and hoops. The spacing of these diagonal ties is determined using Eq. 4 based on CSA A23.3–14 clause 21.5.8.2.4.

$$S_d \leq \min\{6d_b, 24d_{tie}, 100\text{mm}\} \tag{4}$$

where S_d is the diagonal tie spacing, d_b is the diagonal bars' diameter (mm), and d_{tie} is the hoops or crossties' diameter (mm).

Fig. 2 Crew of five insert #11 (35 M) diagonal bars through wall boundary elements and into a diagonal coupling beam

For most typical applications in tall buildings, beams will use 10 M ties and 20 M or larger diagonal bars, so the 100 mm spacing governs.

It is worth noting that in American codes [21], (i.e., ACI 318–19) designers have the option of either providing confinement around the diagonals or confining the entire beam cross section. However, there are currently no clauses within the CSA A23.3–19 that allow such a design [22]. Confining the entire beam cross section was introduced in ACI 318–08 in light of the results from [14]. This option is often preferred by fabricators because it can simplify the installation of diagonal reinforcing, which is a considerable challenge in heavily reinforced walls (see Fig. 2).

2.2   ACI 318–19 Design Provisions

The ACI requirements for full beam confinement (clause 18.10.7.4d) include minimum reinforcing ratio related to beam geometry and materials (Eq. 5), and maximum spacing between tie legs (S_t) in all three spatial directions (Eq. 6). Spacing between tie legs perpendicular to the longitudinal axis must be less than 200 mm and engage a longitudinal peripheral bar. The peripheral bars are not intended to embed into the adjacent wall piers.

Table 1 ACI 318–19 includes requirements for coupling beams with diagonal confinement

Diagonal requirements	
Diagonal bar group width	$\geq \frac{b_w}{2}$
Diagonal bar group height	$\geq \frac{b_w}{5}$
Total cross-sectional area of transverse reinforcement within the spacings	$A_{sh} \geq \max\left\{0.09 s_t b_c \frac{f'_c}{f_{yt}}, 0.3 s_t b_c \left(\frac{A_g}{A_{ch}} - 1\right) \frac{f'_c}{f_{yt}}\right\}$
Beam requirements	
Beam tie spacing	$S_t \leq \min\left\{\frac{A_v}{0.002 b_w}, 300 \, \text{mm}\right\}$
Longitudinal reinforcement	$A_{s,\text{long}} \geq 0.002 b_w s \, \& \, s \leq 300 \, \text{mm}$

[*]where A_v is the area of transverse reinforcement; $A_{s,\text{long}}$ is the peripheral longitudinal reinforcement total area, and s is the spacing between longitudinal bars.

$$\rho = \frac{A_{sh}}{s_t \times b_c} \geq \max\left\{0.09 \frac{f'_c}{f_{yt}}, 0.3\left(\frac{A_g}{A_{ch}} - 1\right) \frac{f'_c}{f_{yt}}\right\} \tag{5}$$

where ρ is the minimum reinforcing ratio, b_c is the confined beam width, A_{sh} is the total cross-sectional area of transverse reinforcement (including crossties) within spacing S_t and perpendicular to b_c; A_g is the overall beam cross-section area; A_{ch} is the confined beam cross-section area, and f_{yt} is the yield strength of the transverse bars.

$$S_t \leq \min\{150 \text{mm}, 6d_b\} \tag{6}$$

It is also interesting to note that for beams with diagonal confinement, ACI 318–19 includes requirements on the size of the diagonal group of bars, minimum number of confining ties, and minimum beam reinforcing in clause 18.10.7.4c. A minimum area of ties around the diagonal often results in significantly more ties than A23.3 would require. These requirements provide more explicit detailing constraints than A23.3 and are summarized below (Table 1).

3 Specimen Database

The experimental data from 51 diagonal coupling beam specimens were collected and a database was developed. The studied specimens were tested between 1974 and 2020. Each specimen underwent cyclic loading until failure was observed, or underwent cyclic loading then was loaded monotonically until failure (like Paulay et al., 1974 and Adebar et al., 2001). Various factors were considered in selecting each specimen, including aspect ratio (*L/h*); axial restraint (AR); embedment of longitudinal bars (ELB); and diagonal ties.

Aspect ratio (*L/h*) is considered an essential factor in coupling beams design. The database considers specimens with aspect ratios between 1 and 5, as shown in Fig. 3a. Based on the experimental testing, coupling beams with a low aspect ratio, (i.e., *L/h* < 2) behave like stocky beams with high shear deformation and a dominant shear failure mode. On the other hand, coupling beams with higher aspect ratios, (i.e., *L/h* > = 2) act like slender beams, where higher flexural deformation and more flexural yielding are observed.

The embedment of longitudinal bars (ELB) into the pier walls in coupling beams is not recommended by Canadian design codes. However, numerous experiments were completed where the longitudinal reinforcing extended significantly into the wall. The embedment allows for this longitudinal reinforcing to develop strength and, therefore, affects the cyclic response. Figure 3b shows the number of specimens within the database with this embedded longitudinal reinforcing.

Axial restraint (AR) refers to tests that attempt to restrain the coupling beam from any longitudinal movement. In this study, the inclusion of slabs is considered an axial restraint, as slabs were included in numerous experiments, (i.e., [14], Ishikawa et al. 1996 [3]). In some studied experimental programs, the researchers used prestressed or posttensioned bars to create axial forces prior to loading the specimens, acting like axial restraints ([6], [14], Brian [17]). Another method of axial restraint considered
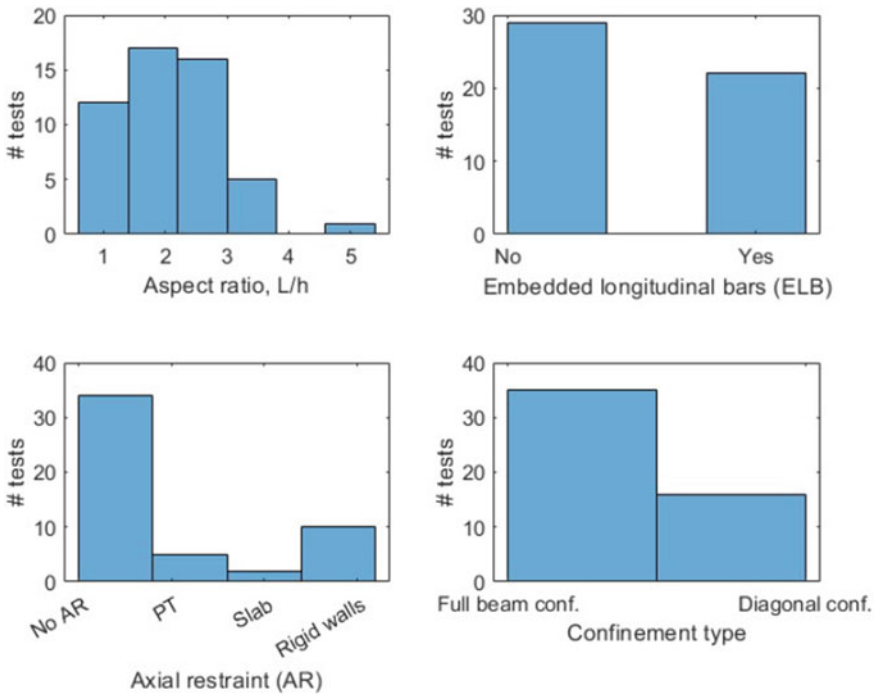
Fig. 3 Characteristics of coupling beams in the database

in the database, and the most rigid, is by preventing the testing setup from axial movement (Kwan et al., 2002, [12, 13], Han et al. [19]). Figure 3c shows the different types of axial constraints within the database.

The majority of tests utilized "beam confinement," where ties are only provided in the beam, and no ties are provided along the diagonal rebars. While the Canadian code does not provide guidance for this type of detail, the data from these tests are included in this analysis. Figure 3d shows the number of tests for each type of confinement.

Table 2 summarizes the authors, specimen names, geometry, materials, and reinforcement details. In these Tables, S_d and S_t are the spacing of the diagonal ties and the beam ties, respectively.

4 Analysis of the Normalized Experimental Data

To systemically study all of the data in the database, each critical parameter was normalized to important Canadian design parameter. In this regard, the backbone parameters shown in Fig. 4 were examined and compared with assumptions used in Canadian design. Specifically, we looked at the initial stiffness (K_i), the maximum shear strength (V_{max}), and the rotation corresponding to the shear strength of 0.8Vmax ($\theta_{80\%}$).

Inelastic rotational capacity is one of the most important factors in the seismic design of reinforced concrete elements. It represents the ability of the element to deform while maintaining strength. In this study, the degradation rotation ($\theta_{80\%}$) is taken as the rotation when the force on the experimental backbone degrades to 80% of the peak shear force. This parameter was used as an indicator of the inelastic rotational capacity. Further loading beyond this point would exhibit a significantly degraded shear capacity, and the beams would be in a severely damaged state.

The following sections compare the experimental response of each specimen with Canadian design practice. In this study, the backbone in both the positive and negative directions was assessed, and the maximum absolute values were selected in the analysis.

4.1 Maximum Shear and Overstrength

The maximum observed shear force and overstrength of coupling beams are important for capacity design and nonlinear modeling. Overstrength was determined as the ratio between the maximum observed shear force (V_{max}) and the nominal shear force (V_{ne}) calculated per Eq. 3 using reported material strength. Figure 5 shows the range of calculated overstrength for all specimens, axial restraint (AR), embedded longitudinal bars (ELB), both AR and ELB, and neither AR nor ELB.

Table 2 Specimens database

Author	Name	L/h	ELB	AR	Sd mm	St mm	α °	b_w mm	h mm	f'c Mpa	Diagonals #	Name	fy, Mpa
L/h < 2													
[1]	Beam 316	1.29	No	None	None	150	36	152	787	33	4	#7	288
											3	#8	287
	Beam 317	1.29	No	None	100	150	36	152	787	51	4	#7	306
											3	#8	270
	Beam 395	1.03	No	None	100	150	20	152	991	36	4	#7	259
											3	#8	289
Ishikawa and Kimura [3]	1	1.78	Yes	None	None	90	17.5	300	450	42	4	D22	523
	2	1.78	Yes	None	None	90	17.5	300	450	46	6	D22	523
	3	1.78	Yes	None	None	90	17.5	300	450	45	6	D22	523
	4	1.78	Yes	Slab	None	90	17.5	300	450	48	6	D22	523
	5	1.78	Yes	None	None	45	17.5	300	450	27	6	D22	523
	6	1.78	Yes	None	None	25	17.5	300	450	51	6	D22	523
	7	1.78	Yes	None	None	90	17.5	300	450	52	6	D22	523
	8	1.78	Yes	None	None	90	17.6	300	450	45	8	D19	387
[5]	P07	1.5	Yes	Rigid	None	120	28.5	150	400	54	8	#3	566
	P12	1.5	Yes	Rigid	150	120	28.5	150	400	42	8	#3	566
[7]	D30	1.136	No	None	60	275	30	300	880	33	8	20-M	456
[8]	CCB11	1.17	Yes	None	60	140	35.8	120	600	37.8*	12	T8	517
[11]	S1	1	Yes	None	75	75	36	200	600	41	8	D13	450
[12]	CB-1	1	Yes	Rigid	None	150	30	200	600	44	4	D16	474

(continued)

Table 2 (continued)

Author	Name	L/h	ELB	AR	Sd mm	St mm	α °	bw mm	h mm	f'c Mpa	Diagonals #	Name	fy, Mpa
[15]	CB10-1	1	Yes	None	None	100	26	250	500	35	8	D25	486
[17]	CC-16d$_b$	1.136	No	None	320	300	30	300	880	38	8	20 M	457
	MD-10d$_b$	1.136	No	None	200	300	30	300	880	42	8	20 M	457
	MD-8d$_b$	1.136	No	None	160	300	30	300	880	43	8	20 M	457
	D-6d$_b$	1.136	No	PT	120	300	30	300	880	45	8	20 M	457
[18]	CB1A	1.89	No	PT	None	76.2	18	250	460	44	12	#7	434
[20]	CB1	1.89	No	None	None	76.2	18	254	457	41	12	#7	434
L/h > 2													
[2]	C6	2.5	No	None	None	33.8	19	102	169	18.1	1	#4	408
	C8	5	No	None	None	33.8	9.5	102	169	23.9	1	#4	433
[4]	LX7L	2.8	Yes	None	None	80	12.9	240	350	37.7	8	D16	528
	NX7L	2.8	Yes	None	None	80	12.9	240	350	38.1	8	D16	528
[6]	K1	2.74	No	PT	100	244	12.3	305	445	35.6	8	30-M	464
[9]	CB-2	3	Yes	None	None	110	14.6	300	500	35.6	4	25 M	461
[10]	N-1	2.5	Yes	None	None	150	19.3	200	400	54	8	D16	476
	N-2	2.5	Yes	None	None	100	19.3	200	400	51	8	D16	459
[13]	DCB1	2.57	Yes	None	76	76	13	254	356	37.6	4	#8	431
	DCB2	3	No	None	51	51	13	254	305	55.3	4	#7	477
[14]	CB24F	2.4	No	None	None	76	15.7	305	381	47.2	12	#7	482

(continued)

Table 2 (continued)

Author	Name	L/h	ELB	AR	Sd mm	St mm	α °	bw mm	h mm	f'c Mpa	Diagonals #	Name	fy, Mpa
	CB24D	2.4	No	None	63.5	63.5	15.7	305	381	47.2	12	#7	482
	CB24F-RC	2.4	No	Slab	None	76	15.7	305	381	50.4	12	#7	482
	CB24F-PT	2.4	No	PT	None	76	15.7	305	381	49.9	12	#7	482
	CB24F-1/2-PT	2.4	No	PT	None	152.4	15.7	305	381	48.2	12	#7	482
	CB33F	3.33	No	None	None	76	12.3	305	457	47.2	12	#7	482
	CB33D	3.33	No	None	63.5	63.5	12.3	305	457	47.2	12	#7	482
[15]	CB20-1	2	Yes	None	None	100	16	300	500	52.1	8	D29	466
[16]	CB30DA	3	Yes	None	150	200	8.8	300	500	39.7	8	#10	464
	CB30DB	3	Yes	None	None	100	8.8	300	500	38.4	8	#10	464
Whan [19]	T1002.0	2	No	Rigid	None	120	20.4	250	525	44	8	D22	477
	T772.0	2	No	Rigid	None	170	20.4	250	525	43	8	D22	477
	T502.0	2	No	Rigid	None	250	20.4	250	525	43	8	D22	477
	T302.0	2	No	Rigid	None	300	20.4	250	525	43	8	D25	481
	T1003.5	3.5	No	Rigid	None	110	8.9	250	300	43	8	D25	481
	T50-3.5	3.5	No	Rigid	None	250	8.9	250	300	44	8	D25	481
	T30-3.5	3.5	No	Rigid	None	500	8.9	250	300	44	8	D25	481

* Value is calculated cylinder strength based on cube test
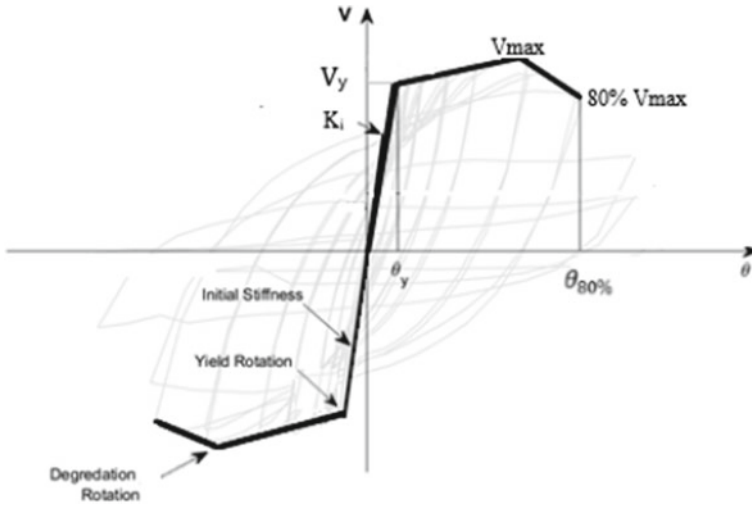
Fig. 4 Backbone curve for coupling beam models
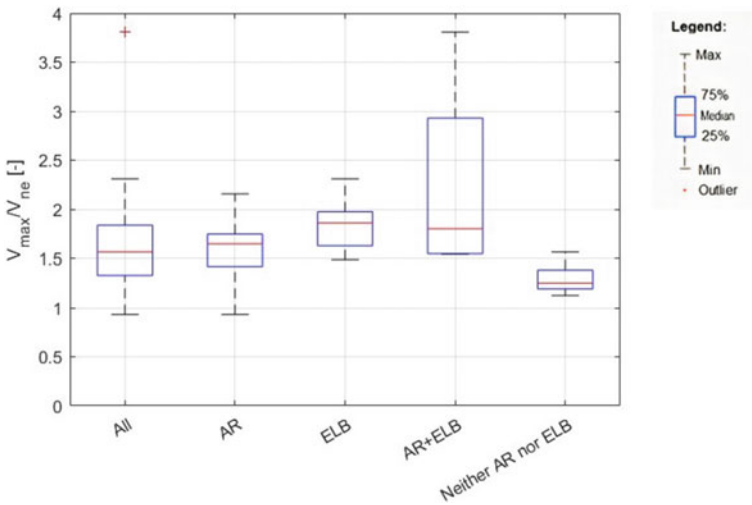
Fig. 5 Range of overstrength for specimens with different characteristics: (i) All specimens, (ii) Axial restrained (AR), (iii) Embedded longitudinal bars (ELB), (iv) Both AR and ELB, and (v) Neither AR nor ELB

The median overstrength for all specimens was approximately 1.55. AR or ELBs contribute to higher median overstrength, ranging from 1.6 for AR only (13 specimens) to 1.8 for ELB only (19 specimens). For the four specimens with AR and ELB, the median overstrength was 1.7, but the variability was large. For example, some specimens had an overstrength exceeding 3.0. When neither AR nor ELB was

present (15 specimens), the median overstrength was approximately 1.25. In short, both AR and ELB are observed to increase the overstrength.

4.2 Effect of Embedded Longitudinal Bars

In order to investigate the effect of embedded longitudinal bars in the shear strength of specimens, a new term of shear strength named "V_t" is introduced. Based on Eq. 7, V_t equals the summation of nominal shear force calculated per Eq. 3 and the shear force corresponding to the flexural resistance (V_{me}), calculated per Eq. 8. To obtain V_{me}, it is required to calculate the nominal moment capacity (M_n). Flexural capacity of coupling beams (M_n) is obtained by using Eq. 9.

$$V_t = V_{me} + V_{ne} \tag{7}$$

$$V_{me} = \frac{2M_n}{L} \tag{8}$$

$$M_n = A_{sl} f_{yl}(d - d') \tag{9}$$

where A_{sl} is the total area of longitudinal bars, f_{yl} is the yield strength of longitudinal bars, and d and d' are the effective depths of longitudinal bars in tension and compression zones, respectively.

Figure 6 illustrates the effect of embedded longitudinal bars on the shear strength of specimens. In this figure, the ratio of V_{max} over V_t is shown in the vertical axis. Different types of specimens in terms of mechanical features were described in the horizontal axis.

As was expected, the median overstrength of specimens without axial restraint and without embedded longitudinal bars is the same as the one plotted in Fig. 5. On the other hand, the median overstrength is equal to 1.25 and 1.3 for ELB and AR + ELB, respectively. Hence, V_t is a reasonable method of estimating the shear force of coupling beams which have embedded longitudinal reinforcing.

4.3 Effect of Axial Restraint

The presence of axial restraint impacts the behavior of coupling beams significantly. Generally, axial restraints would result in higher strength and lower elongation of coupling beams. In this regard, Fig. 7 shows the overstrength of specimens equipped with no axial restraint, and different types of axial restraints, namely prestressed rods (PT), slab, and rigid walls.
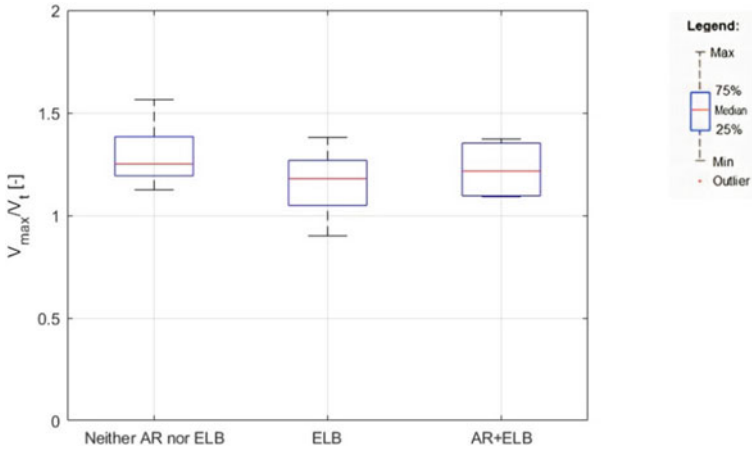
Fig. 6 Range of overstrength including the impact of embedded longitudinal bars for specimens with different characteristics: (i) All specimens, (ii) Axial restrained (AR), (iii) Embedded longitudinal bars (ELB), (iv) Both AR and ELB, and v) Neither AR nor ELB
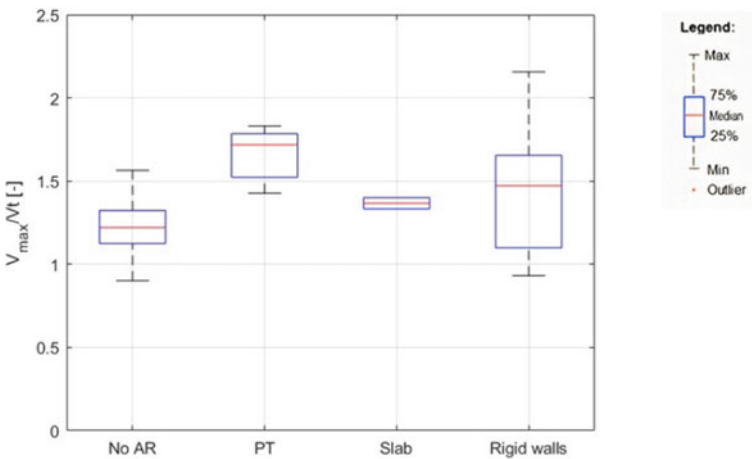
Fig. 7 Range of overstrength including the impact of embedded longitudinal bars for specimens with different types of axial restraint: (i) No axial restraint, (ii) Prestressed rod, (iii) Slab, iv) Rigid walls

According to Fig. 7, specimens without any axial restraints have median overstrength of 1.25. The median overstrength in specimens with slabs is equal to 1.4. This additional overstrength is attributed to the larger compression block provided by the slab. Specimens restrained in the axial direction with PT rods had a median overstrength of about 1.75. This PT overstrength is due to the additional compression load induced by the PT which the calculation of V_t does not account for. Finally,
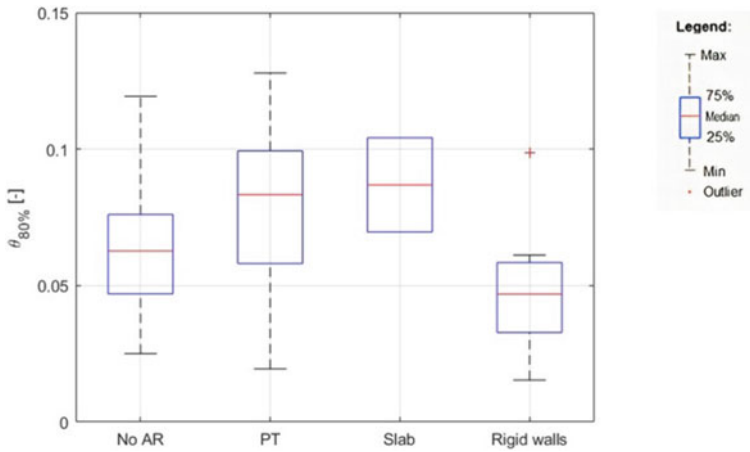
Fig. 8 Range of degradation rotation ($\theta_{80\%}$), for specimens with different types of axial restraint: i) No axial restraint, ii) Prestressed rods, iii) Slab, iv) Rigid walls

the overstrength provided by rigid walls is approximately 1.5. The cause of this overstrength is likely due to contributions from the experimental setup.

Figure 8 depicts the value of degradation rotation ($\theta_{80\%}$) for specimens with different types of axial restraint. According to this figure, the median $\theta_{80\%}$ for specimens with PT rods and slabs is almost 8%, exceeding the median $\theta_{80\%}$ of specimens without axial restraint by about 30%. In the case of the PT, this additional ductility is likely provided by the PT closing cracks and restricting excessive elongation. Similarly, the slab specimens provide added resistance to degradations.

Specimens with rigid axial restraint has the lowest amount of median $\theta_{80\%}$ which is equal to 4.9%. It is anticipated that the rigid restraint provided by the test setup does not permit the cracks to close effectively, resulting in early strength loss.

4.4 Effect of Diagonal Tie Spacing on $\theta_{80\%}$

Figure 9a, b shows $\theta_{80\%}$ of beams with diagonal ties compared with the ratio of diagonal tie spacing (S_d) to the spacing calculated according to the CSA A23.3 (Eq. 4) for L/h < 2 and L/h ≥ 2, respectively. Figure 9 also exhibits the ductility capacity provided by CSA A23.3, which is 0.04 radians (red line). CSA A23.3 requires designers to consider the minimum inelastic ductility demand of coupling beams equal to this value through their design procedures.

Overall, Fig. 9 depicts that there is little correlation between diagonal tie spacing and ductility. A number of specimens with L/h < 2 exhibited ductility's which are lower than the CSA A23.3 limit, even those where the S_d was less than the $S_{d, CSA}$.
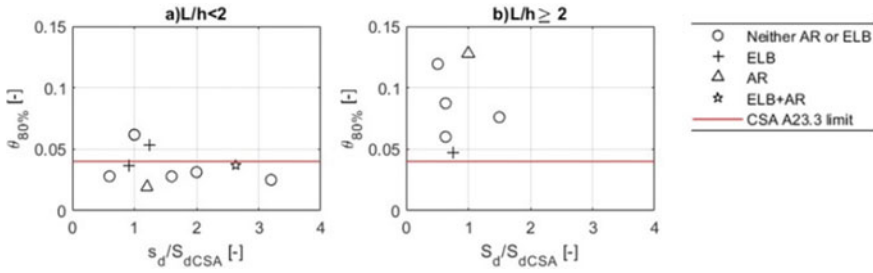
Fig. 9 Degradation rotation ($\theta_{80\%}$) versus diagonal tie spacing for specimens with **a** L/h < 2 and **b** L/h ≥ 2

On the other hand, all specimens are shown in Fig. 9b with L/h ≥ 2 and diagonal ties result in high $\theta_{80\%}$, satisfying the CSA A23.3–19 minimum acceptable value.

4.5 Effect of Beam Tie Spacing on $\theta_{80\%}$

Figure 10a, c show $\theta_{80\%}$ of beams with full confinement compared with the ratio of beam tie spacing (S_t) to half of the beam depth (h/2) for L/h < 2 and L/h ≥ 2, respectively. Figure 10b, d illustrate of beams with diagonal confinement compared with the ratio of beam tie spacing (S_t) to half of the beam depth (h/2) for L/h < 2 and L/h ≥ 2, respectively. For reference, the minimum ductility capacity provided by CSA A23.3, which is 0.04 radians is shown in Fig. 10.

According to Figs. 10a, c, it can be observed that decreasing the beam tie spacing, (i.e., increasing the confinement of the overall beam) increases $\theta_{80\%}$. Furthermore, it is visible that most of the specimens with full beam confinement layouts have an amount of $\theta_{80\%}$ between 0.04 and 0.1.

Figure 10b shows that for specimens with L/h < 2, increasing the beam tie spacing in beams that have diagonal ties results in a decrease of $\theta_{80\%}$. This result implies that beam tie spacing is also a critical variable in the ductility capacity of diagonally reinforced coupling beams, and guidance should be provided to designers.

4.6 Effect of the Transverse Reinforcement Ratio (ρ_V)

Transverse reinforcement ratio (ρ_v), which is calculated by Eq. 10, is recognized as an important design factor.

$$\rho_v = \frac{A_v}{b_w s_t} \tag{10}$$
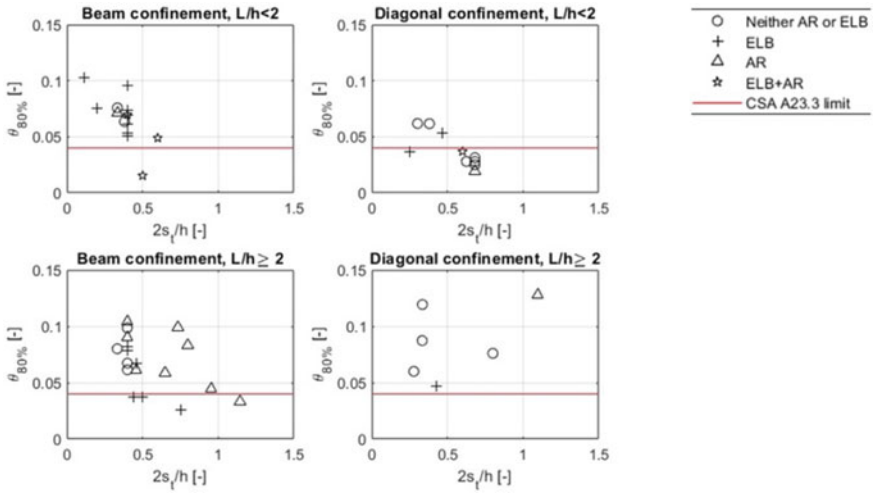
Fig. 10 Degradation rotation ($\theta_{80\%}$) versus beam tie spacing for specimens with **a** Beam conf. layout and L/h < 2, **b** Diagonal conf. and L/h < 2, **c** Beam conf. layout and L/h $\geq$ 2, **d** Diagonal conf. and L/h $\geq$ 2

Figure 11a, c show $\theta_{80\%}$ of beams with full beam confinement compared with ρ_v for L/h < 2 and L/h $\geq$ 2, respectively. Figure 11b, d illustrates $\theta_{80\%}$ of beams with diagonal confinement compared with ρ_v for L/h < 2 and L/h > = 2, respectively.
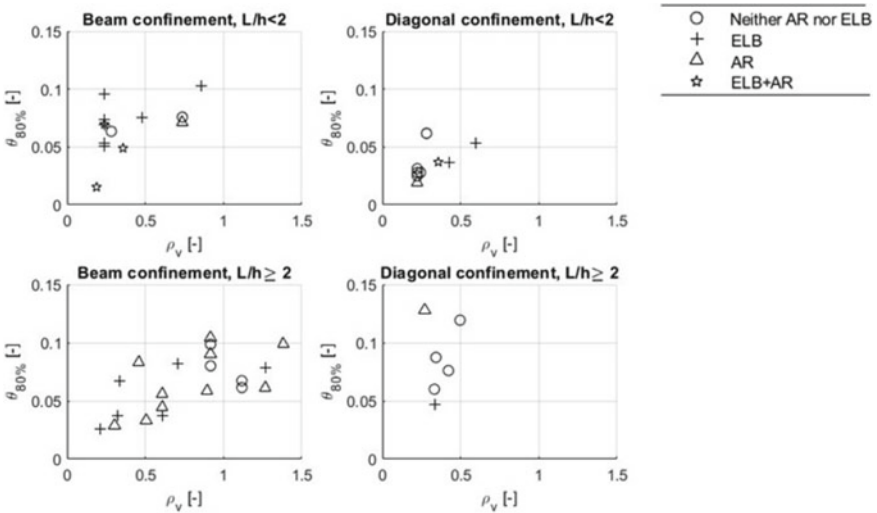
Fig. 11 Degradation rotation ($\theta_{80\%}$) versus beam tie spacing ratio for specimens with **a** Beam conf. layout and L/h < 2, **b** Diagonal conf. and L/h < 2, **c** Beam conf. layout and L/h $\geq$ 2, **d** Diagonal conf. and L/h $\geq$ 2

Based on Figs. 11a, c, it could be concluded that the more amount of transverse reinforcement ratio in the coupling beams with full beam confinement layout would result in more $\theta_{80\%}$. However, according to Figs. 11b, d, it seems that the amount of transverse reinforcmenet ratio does not impact the degradation rotation of the coupling beams with diagonal confinement layout.

4.7 Initial Stiffness (K_i)

The initial stiffness of the coupling beam (K_i) is important when utilizing the dynamic analysis to determine seismic demands on the structure. It is also a critical parameter in determining structural period and developing appropriate models for performance-based design.

The initial stiffness of a coupling beam can be determined by summing the flexural deformation (Δ_F) and shear deformation (Δ_S). The total displacement of a coupling beam (Δ_T) is calculated using Eq. 11.

$$\Delta_T = \frac{V_y}{K_i} = \Delta_F + \Delta_S \tag{11}$$

where V_y is the applied shear force; K_i is the initial stiffness; Δ_F is the flexural deformation (shown in Eq. 12), and Δ_S is the shear deformation (shown in Eq. 13).

$$\Delta_F = \frac{V \times L^3}{E_c \times I_{\text{eff}}} \tag{12}$$

$$\Delta_S = \frac{V \times L}{G_c \times A_{\text{ve}}} \tag{13}$$

where I_{eff} is the effective moment of inertia (Eq. 2), A_{ve} is the effective shear area (Eq. 1); E_c is the elastic modulus of reinforced concrete $\left(E_c = \left(3300\sqrt{f_c'} + 6900 \right) \left(\frac{\gamma_c}{2300} \right)^{1.5} \right)$; f_c' is the compression strength of concrete; γ_c is the concrete density factor which is equal to 2300 kg/m³ in this study; G_c is the shear modulus of reinforced concrete; $G_c = \frac{E_c}{2(1+\nu)}$, and ν is Poisson ratio which has been chosen to 0.25 in this study.

By substituting Eqs. 12 and 13 into Eq. 11 the initial stiffness of the coupling beam is determined and presented in Eq. 14.

$$K_i = b_w \times E_c \times C_K \tag{14}$$

where C_k is a unitless parameter shown in Eq. 15.

$$C_K = \frac{\alpha_f . \alpha_s}{2(1+\nu) . \alpha_f . \left(\frac{L}{h} \right) + \alpha_s . \left(\frac{L}{h} \right)^3} \tag{15}$$

Fig. 12 C_K values based on various amounts of α_f and α_s
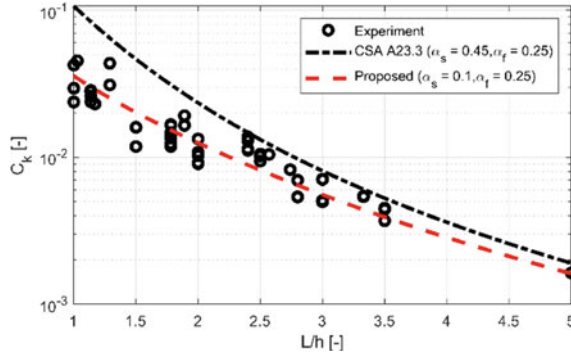
Using the unitless parameter C_K, the experimental results were compared with the effective cracking parameters used by the CSA A23.3–19. In this comparison, the experimental C_K values were determined using Eq. 16.

$$C_K = \frac{K_i, \exp}{b_w E_c} \tag{16}$$

where $K_{i,\exp}$ is the initial stiffness obtained from experiment's results.

Figure 12 shows the effective stiffness parameters $\alpha_s = 0.45$ and $\alpha_f = 0.25$ recommended by CSA A23.3–19, the experimental values, and a new recommendation value of $\alpha_s = 0.1$ and $\alpha_f = 0.25$.

Based on the results shown in Fig. 12, the code equation appears to be an upper bound of the stiffness of coupling beams. However, the proposed values exhibit almost comprehensive coverage over the stiffness of coupling beams.

5 Conclusions

The behavior of diagonally reinforced coupling beams is a critical factor in the seismic performance of coupled wall systems, commonly used in seismically active areas worldwide. The coupling beam elements provide significant energy dissipation over the structure's height and induce large forces into the wall piers. With the increasing use of nonlinear time-history analysis as an assessment and design tool, accurate understanding of structural elements is an important research effort. The discussions in this paper, as well as the empirical relations, can help inform engineers in both performances-based design and assessment.

Some of the key conclusions from this paper are:

- Axial restraint and embedded longitudinal bars can considerably increase the overstrength of the coupling beam. The median amount of overstrength varied from 1.6 for axially restrained, 1.8 for embedded longitudinal bars, and 1.7 for

beams with both axially restraint beams and embedded longitudinal bars. These overstrengths will be significantly higher than those employed in typical capacity design using A23.3–19 recommendations.

- The effect of embedded longitudinal bars should not be neglected in calculating the overstrength in specimens with this characteristic. The median overstrength of specimens without axial restraint and without embedded longitudinal bars is equal to 1.25. This ratio is equal to 1.25 and 1.3 for ELB and AR + ELB, respectively.
- The median amount of overstrength in which the effect of embedded longitudinal bars is considered to be around 1.75 for specimens with slab. This value was equal to 1.4 and roughly 1.5 for specimens that were restrained in an axial direction with PT rods and rigid walls, respectively.
- The median value of ($\theta_{80\%}$) for specimens with PT rods or slabs is almost the same and equal to 8%. This value equals 7% for specimens without any axial restraint. In the specimens with rigid axial restraint, the median value of $\theta_{80\%}$ is equal to 4.9%.
- Full beam confinement is an effective approach that could be implemented for diagonally reinforced coupling beams. It has been observed that by using this type of confinement, the inelastic rotation capacity $\theta_{80\%}$ can meet the existing A23.3 requirements and, in some cases, will outperform the diagonal confinement approach.
- $\theta_{80\%}$ would increase by incrementing transverse reinforcement ratio (ρ_v) in specimens with full beam confinement layout. However, in specimens with diagonal confinement layouts, the enhancement of ρ_v would not significantly impact the value of $\theta_{80\%}$.
- The suggested modification factors for decreasing the shear area and gross moment of inertia of coupling beams by CSA A23.3–19 ($\alpha_s = 0.45$ and $\alpha_f = 0.25$) results in a high initial stiffness which could be considered an upper bound of the studied specimens. We found that $\alpha_s = 0.1$ and $\alpha_f = 0.25$ are reasonable estimates based on the studied specimens.

References

1. Paulay T, Binney JR (1974) Diagonally reinforced coupling beams of shear walls. Special Publ 42:579–598
2. Barney GB, Shiu KN, Rabbit BG, Fiorato AE, Russell HG, Corley WG (1980) Behavior of coupling beams under load reversals (RD068.01B). Portland Cement Association, Skokie, IL
3. Ishikawa Y, Kimura H (1996) Experimental study on seismic behavior of R/C diagonally reinforced short beams. In: Proceedings of the 11th World Conference on Earthquake Engineering, Paper (No. 1386)

4. Sonobe Y, Kanakubo T, Fujisawa M, Tanigaki M, Ökamoto T (1995) 41 Structural performance of concrete beams reinforced with diagonal frp bars
5. Galano L, Vignoli A (2000) Seismic behavior of short coupling beams with different reinforcement layouts. ACI Struct J 97:876–885
6. Gonzalez E (2001) Seismic response of diagonally reinforced slender coupling beams (Doctoral dissertation, University of British Columbia)
7. Dugas DG (2002) Seismic response of diagonally reinforced coupling beams with headed bars
8. Kwan AKH, Zhao ZZ (2002) Cyclic behaviour of deep reinforced concrete coupling beams. Proc Inst Civil Eng-Struct Build 152(3):283–293
9. Zhou J (2003) Effect of Inclined reinforcement on the seismic response of coupling beams, M. Eng. Thesis, McGill University. Montreal
10. Shimazaki K (2004) De-bonded diagonally reinforced beam for good repairability. In: 13th World conference on earthquake engineering, Paper (vol 3173)
11. Canbolat BA, Parra-Montesinos GJ, Wight JK (2005) Experimental study on seismic behavior of high-performance fiber-reinforced cement composite coupling beams. ACI Struct J 102(1):159
12. Yun HD, Kim SW, Jeon E, Park WS, Lee YT (2008) Effects of fibre-reinforced cement composites' ductility on the seismic performance of short coupling beams. Mag. Concrete Res. 60(3):223–233
13. Fortney PJ, Rassati GA, Shahrooz BM (2008) Investigation on effect of transverse reinforcement on performance of diagonally reinforced coupling beams. ACI Struct J 105(6):781
14. Naish D, Fry A, Klemencic R, Wallace J (2013) Reinforced concrete coupling beams-part I: testing. ACI Struct J 110(6):1057
15. Lim E, Hwang SJ, Wang TW, Chang YH (2015) An Investigation on the Seismic Behavior of Deep Reinforced Concrete Coupling Beams. ACI Struct J 113. https://doi.org/10.14359/51687939
16. Lim E, Hwang SJ, Cheng CH, Lin PY (2016) Cyclic tests of reinforced concrete coupling beam with intermediate span-depth ratio. ACI Struct J 113(3)
17. Howard B (2017) Seismic response of diagonally reinforced coupling beams with varied hoop spacings. McGill University, Montreal, Canada
18. Poudel A, Lequesne RD, Lepage A (2018) Diagonally reinforced concrete coupling beams: effects of axial restraint. University of Kansas Center for Research, Inc
19. Han SW, Kim S, Kim T (2019) Effect of transverse reinforcement on the seismic behavior of diagonally reinforced concrete coupling beams. Eng Struct 196:109307. https://doi.org/10.1016/j.engstruct.2019.109307
20. Ameen S, Lequesne RD, Lepage A (2020) Diagonally reinforced concrete coupling beams with grade 120 (830) High-Strength Steel Bars'. ACI Struct J 117(6)
21. American Concrete Institute (2020) Building code requirements for structural concrete (ACI 318–19): An ACI Standard; commentary on building code requirements for structural concrete (ACI 318R-19)
22. Design of Concrete Structures (2019) Toronto, Ontario: CSA Group
23. National Building Code of Canada, 2015 (2018) Ottawa, Ont.: National Research Council Canada

Steel Structures

Behaviour of Beam–Column Connection of Modular Steel Buildings

Elhadary Mostafa and Elshaer Ahmed

Abstract Prefabricated modular structures are becoming more popular in the construction industry, where structural components are prepared off-site leading to accelerating the construction phase. The prefabrication process can eliminate any unpredicted variables, ensure high-quality control, and reduce environmental waste. Modular steel structures have been widely adopted over the last few decades to create structures consisting of repetitive units in houses, tall buildings, and bridges, in addition to being useful for temporary structures. The lateral load (e.g., wind or earthquake) performance of modular structures relies on the interconnections between modules to ensure robustness and structural integrity, instead of the need for an additional structural system. Although volumetric modular structures have been widely used where the entire three-dimensional module is constructed off-site, this type of module is not ideal for transportation. Moreover, the transportation and lifting process of these units can lead to the risk of damaging structural and non-structural members. Alternatively, panels (i.e., two-dimensional modules) can be manufactured off-site and then assembled using bolted connections on-site to avoid limitations of transportation. The current study aims to assess the mechanical performance of beam–column connection for steel modular structures under monotonic loading. Different pretensioning forces have been examined to investigate their impact on connection performance.

Keywords Wind load · Modular construction · Low-rise buildings · Aerodynamics · Beam–column connection · Finite element modelling · Failure criterion

E. Mostafa (✉) · E. Ahmed
Department of Civil Engineering, Lakehead University, Thunder Bay, Canada
e-mail: mabdelh3@lakeheadu.ca

1   Introduction

Modular construction has become popular and promoted across the construction industry. Recently, it has attracted significant attention from engineers because of increasing labour costs in traditional construction methods and global environmental problems. Modular construction permits the building to be manufactured in factory conditions in a highly effective way, then be transported to the construction site and to be an assembly to form a complete structure. Modular construction has more technical advantages over the traditional construction method, including faster construction, less environmental waste around on-site construction, fewer workers on-site, and better-quality control [5, 7, 11]. Various materials can be used on modules units such as timber, concrete, and steel. However, the steel modules are more suitable in robust seismic and wind behaviour and premanufactured buildings due to their long span, lightweight, more flexible architecture design, and more accessible assembly on-site than timber- and concrete-framed modules [8]. Modular steel structures are widely used for low-rise buildings as an alternative to traditional on-site construction such as in residential structures, hotels, hospitals, and schools, as they are suitable for architectural and structural layouts with repetitive modules [6]. This concept was recently adopted in a post-disaster hospital that accommodates 1000 patients, which was built in 10 days in Wuhan, China, as a response to the COVID-19 pandemic [17, 18]. Their popularity has been extended to mid-to-high-rise buildings [13] in high seismicity and wind regions to satisfy the urban construction demand. Modular units are classified into two categories according to their load transferring mechanism, which are (i) frame-supported modules where loads are transferred through edge beam to corner columns and (ii) wall-bearing modules in which loads are transferred through the side walls. The compression resistance of the walls is crucial, and the wall-bearing module is mainly limited to an approximately four-story-high building [14]. The frame-supported module is more suitable for med-to-high-rise building and commonly used in modular construction [2]. Despite several advantages, most modular construction applications have a limitation due to the lack of strong design guidelines for modular structural system joining techniques [19] and installation considerations, including transportation, crane capacity, and connecting access space at the site. The modules can be cracked during the lifting process by cranes. In addition, the vibration of transportation can propagate the cracks and cause damage to non-structural components; the intensity of the damage increases with the roughness of the road [3]. Moreover, the transportation route and method can restrict the weight and dimensions of large modules, and their transportation can be costly and complex [15]. The space between modules units can represent a problem in assembly because walls and floors of adjacent units reduce the space, so workers are an obstacle to accessing the connection points [2, 20]. The structural system of modular steel construction is crucial to ensure structural stability and integrity, which can be categorized into three types according to their lateral force-transferring mechanism, which are (i) stacked module structure, (ii) module-concrete core hybrid structure, and (iii) module-moment frame hybrid structure. Recently, studies focused on the

stacked module structure, where the individual units are connected on-site to form an entire building. In the stacked module structure, connections are classified into three groups: module foundation, intra-module, and inter-module. In the latter connection, i.e., the connection between modules, lateral loads (e.g., wind and seismic) are typically transferred through bolted connections. Intra-module connections, i.e., the connection within the module, are typically beam-to-column welded connections. Module-foundation connections are usually built (e.g., in-situ concrete footing, piles) before modules are transported to the site, depending on the ground conditions and construction site. Module-foundation connections are important because lateral loads can cause overturning and slip failure.

Modular steel construction requires a high-performance inter-connection system to ensure an efficient load transfer mechanism in both vertical and horizontal directions. However, it is challenging to resist gravity and lateral load forces efficiently due to the discontinuities in the lateral force resisting structural components [2]. Many studies have focused on the above challenge to enhance the structural performance of modular steel construction. Chen et al. [1] proposed a plug-in device and a group of long bolts to transfer load between modules units, which eliminates the need for on-site welding or an opening in the structural element (i.e., columns and beams) and provides enough workspace for multi-unit connections. Hwan et al. [4] developed a steel bracket, which allowed all modules units to be connected by hollow cube through bolts. The study carried out an experimental programme to investigate the performance of steel brackets under different loading conditions such as bending and shear loading. It was found that the connection failed in a ductile manner without any evidence of plate failure. Lee et al. [9] proposed a ceiling-bracket-type welded to the column in accordance with stiffener type and the bracket thickness. The study carried out cyclic tests on full-scale specimens to investigate the seismic performance of the inter-module steel connection. It was noted that the proposed modular joint can maintain 80% of the seismic capacity of the beam, and the initial stiffness was increased with a higher bracket thickness and number of stiffeners. [16] developed a self-Interlocking modular connection to improve the integrity and general stability of the module's units. This study carried out numerical analysis using two different loading approaches, the first approach applied horizontal loads, and the second approach removed one module support and checked for redundancy. This connection is considered a suitable solution for a limited workspace site during the installation process. Ma et al. [12] proposed a novel modular connection using in-build components and long tightening bolt groups, which pass through multi-columns and connect modular units horizontally and vertically. This connection can eliminate the four-unit workspace challenge, so an experimental study on the T-joint was conducted to investigate its structure performance under monotonic static loading. It was concluded that the bolted connection is preferred to inter-module connection as it is less site work and the possibility of dismantling. However, the connection encountered a brittle failure due to the failure of weld fracture in the intra-module beam-to-column connection. The intra-module beam is typically welded to the column directly in the factory, so special attention should be given to the weld quality to limit the risk of weld fracture.

It is well known that developing proposed inter-module connections is one of the main challenges that obstruct the progress of modular steel construction. This paper aims to investigate the load-bearing mechanism of inter-modular beam-to-column connection under quasi-static monotonic load. A numerical analysis was performed on a long-bolt modular connection using Implicit software LS-DYNA and validated with [12] experimental results available in the literature review. A case study is performed on specimen T1 using different pretension loads to investigate their influence on the overall response and column continuity.

2   Numerical Model Description

A three-dimensional finite element model of modular beam-to-column connection is developed using LS-DYNA software and validated with the experimental results of [12]. Details of the connections including geometry, nonlinear contact, and material properties are provided in this section. The exploded view of components of the T-joint, extracted from the proposed FE model, is shown in Fig. 1. The experimental test specimen T1 dimensions are summarized in Table 1. As shown in Fig. 2, boundary conditions applied on the FE model replicate that from the experimental test, where columns are restrained by fixed support, beams are laterally restrained in the x-direction, and applied loading point in the Y-direction with a moment lever arm of 1.25 m. All components of the specimen are produced from Q345b mild steel, and grade 12.9S M16 high-strength bolts are used to bolt the units [10]. The bolts had a yield strength of 1080 MPa and are preloaded by 100 kN by a torque wrench. Isotropic elastic–plastic material model is used for steel within the material library to accommodate the large-strain behaviour in the post-failure region, where Poisson ratio (υ) for steel is defined as 0.3, and Young's modulus (E) is defined through the material property. The true stress–strain curve of both Q345b mild steel and grade 12.9S high-strength bolt is shown in Fig. 3. The von Mises yield surface is used in the classical metal plasticity model. All model components are modelled using eight-node 3D solid elements with a reduced integration, which contains hourglass model control to avoid shear self-locking. As shown in Fig. 4, several mesh densities are used in the FE model, where parts within the connection such as: (i) in-build component, (ii) tightening bolts, (iii) side plate, (iv) endplate, and (v) columns near the bolt holes are discretized using a fine mesh of 4 mm. Inflation layers are used around the bolt holes to better capture the distribution of stresses. Cold-formed steel (CFS) beams are discretized using a fine mesh of 5 mm, and two layers of smaller mesh are used to model profiles thickness. Moreover, a coarse mesh of 10 mm is used to discretize parts far away from the connection region. The contacts between connection components (i.e., frictional components) are modelled by using surface-to-surface-mortar contact, and penalty formulation with a friction coefficient of 0.4 is used to define all the tangential responses for all contact surfaces. The contacts between end plates with columns (i.e., welded components) are modelled using surface-to-surface-mortar-tied contact. The bolt clearance of 2 mm is modelled to
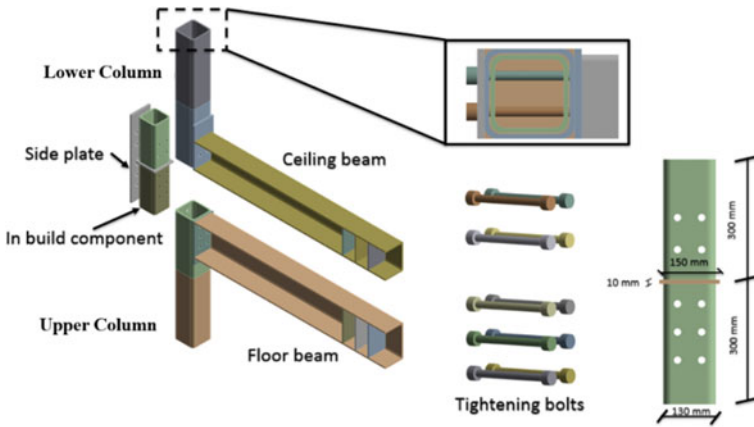
Fig. 1 Explode view of the T-joint [12]

Table 1 Experimental test specimen specification

Specimen No.	Floor beam (mm)	Ceiling beam (mm)	Column (mm)	Stiffener
T1	C250*140*10	C200*140*10	□150*150*8	None

capture the actual bolt behaviour mechanism after releasing bolt pretension load. In the FE model, the load is applied through two time intervals; in the first time interval, a pretension load of 100 kN is applied at the shank of the bolt using initial stress of 490 MPa around the bolt shank. While in the second time interval, displacement boundary motion is applied in Y-direction at the bottom of the floor beam as shown in Fig. 2. The pretension phase is performed in the FE model by dynamic analysis using Newmark time integration, while the loading phase is performed using implicit analysis.

3 Numerical Model Validation

Figure 5 compares the moment–rotation curve between the FE model of the current study and experimental results of [12], where rotation is calculated by subtracting the rotation of the columns from the average beams rotations, while the moment is calculated by multiplying the applied force a lever arm of 1.25 m. It can be noticed from the moment–rotation curve of the proposed FE model that a good agreement is achieved between the current FE model and the experimental results in the linear and nonlinear regions. It is also noticed that many sudden drops and gain behaviour of the moment capacity are captured by the proposed model similar to the experimental test. The latter behaviour is caused by the gap between in build component and columns, and bolt clearance. The specimen T1 failed in the experimental test due to a slip failure
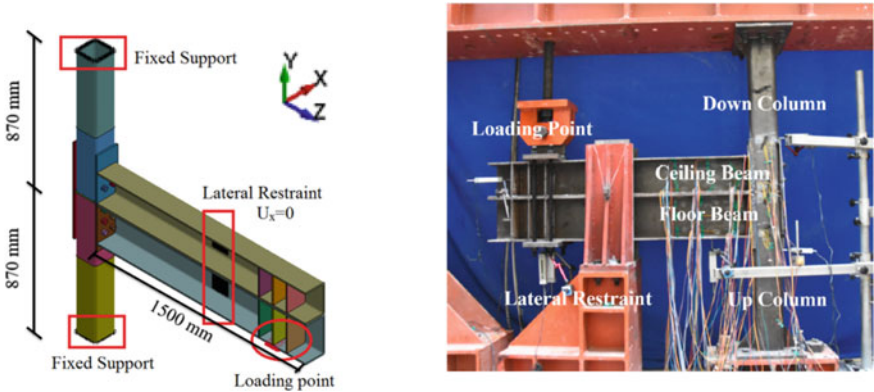
Fig. 2 FE Model boundary condition of specimen T1
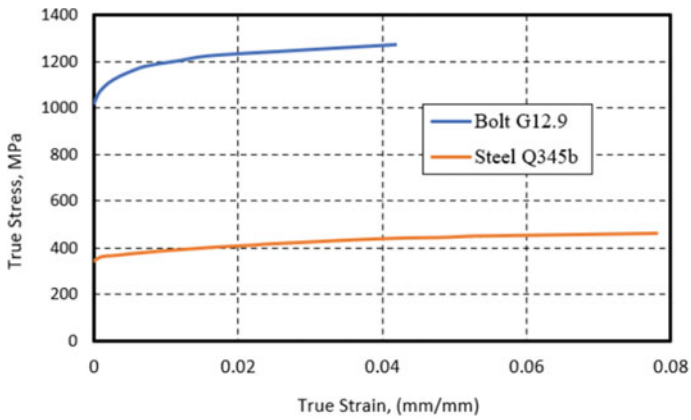
Fig. 3 True stress–strain for specimens' steel
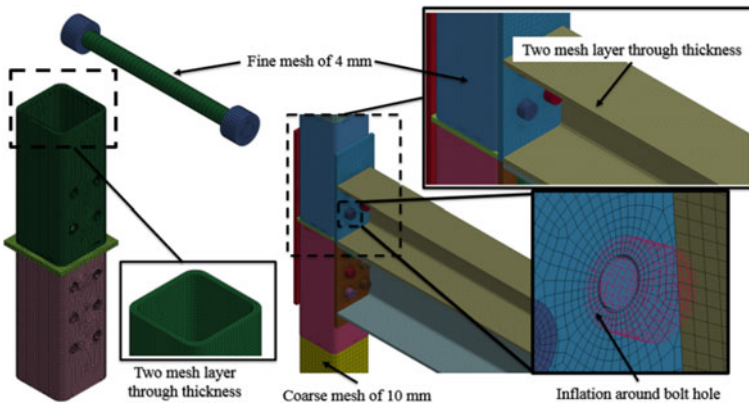
Fig. 4 Mesh configuration for the FE model
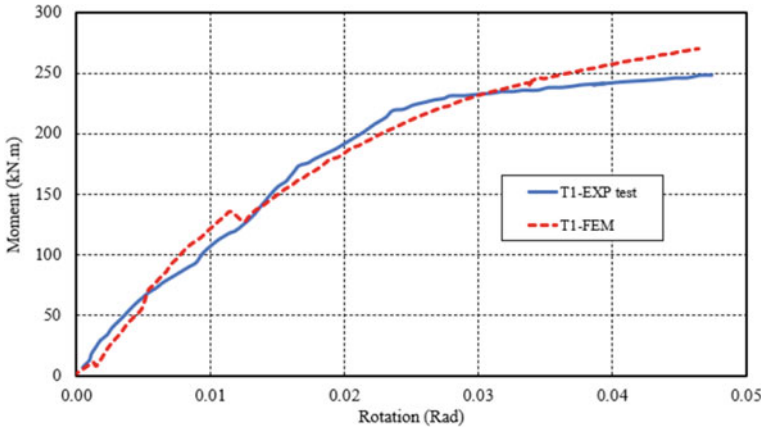
Fig. 5 Moment–rotation curve comparison between proposed FE and experimental result [12]

that happens between the upper and lower columns, and this failure is well captured by the proposed FE model, as shown in Fig. 6. Figure 7 shows different deformation phenomena at other components of the specimen T1, where local buckling occurs at the tension flange of both columns that contribute to the overall rotation of the beams. While the side plate fails by local buckling at the middle location because of the horizontal movement of columns in the opposite direction related to each other at the beginning of the loading process, as shown in Fig. 6. The rotation of the columns leads to significant stress demand on in build component, especially at the middle part because it restricts the joint movement between upper and lower columns. The long tightening bolts are subjected to high deformation during the pretension phase because of the over-pretension force of 100 kN. The stress magnitudes of different bolts are not equal as bolts at the tension region are the critical ones, and they are subjected to higher prying force and failed by twisting, as shown in Fig. 8. In conclusion, the bolts, in-build component, and side plate have significant influence to guarantee higher connection behaviour.

4 Study Case

Based on the validation of the FE model, a case study is performed on specimen T1 to highlight the influence of bolt pretension and snug tightening on the overall T-joint response. Two different cases of bolt pretension are studied, where the first case is bolt load of 90 kN, which is the minimum value mentioned by the Canadian code for steel structures S16-14, and the second case is snug tightening, which is considered 0.1 of the applied pretension load. The bolt pretension causes the previous yielding of the CFS beam endplate before applying load at the beam, as shown in Fig. 9. The latter yielding causes weakness of the connection moment resistance at the initial
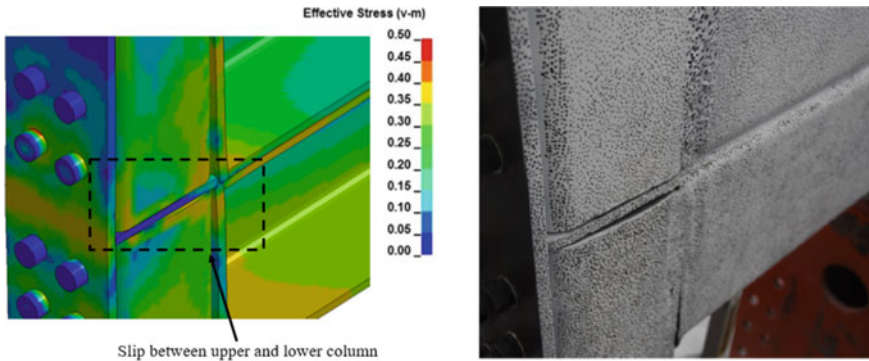
Fig. 6 Slippage between upper and lower column
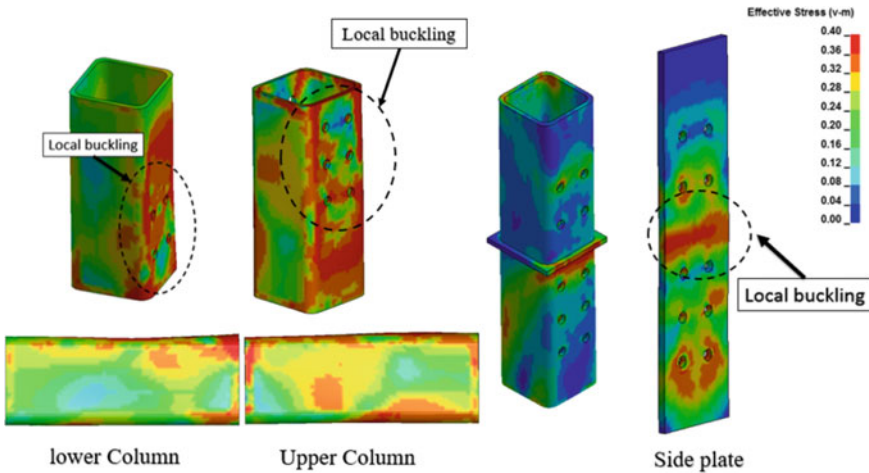
Fig. 7 Stress distribution of columns, side plate, in-build component at the failure phase

loading stage. Even in nonlinear regions, the pretension bolt load does not affect the plastic moment resistance, as shown in Fig. 10. However, the snug-tightening bolt load achieves high moment resistance at the initial stages and does not cause excuses rotation of the columns as the column rotation is restricted by the in-build component and side plate rigidity.
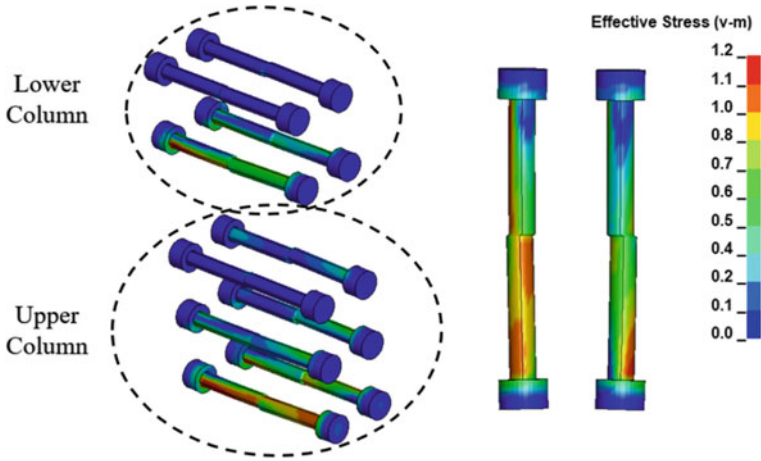
Fig. 8 Stress distribution on bolts
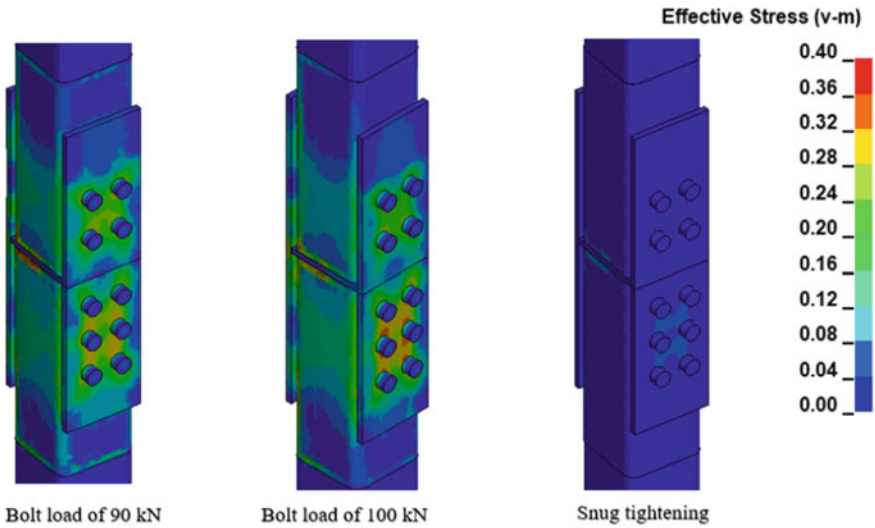
Fig. 9 Effect of pretension on cold-formed steel sections
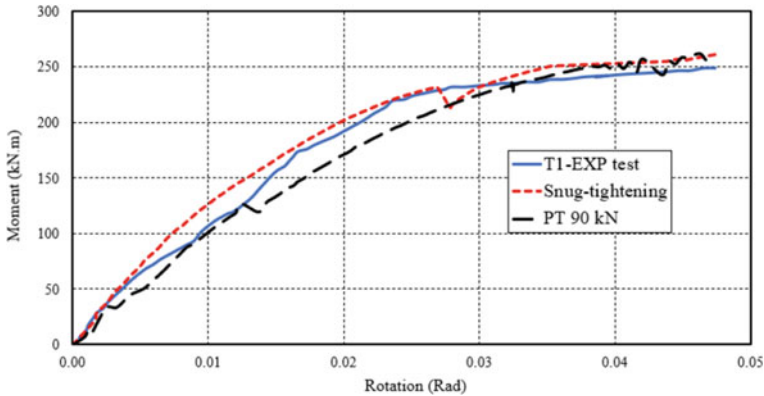
Fig. 10 Moment–rotation relation between bolt pretension and snug-tightening model

5 Conclusion

Modular steel construction has great potential in the construction industry such as hospitals, hotels, and dormitories. Various inter-module connection types have been examined for practices, and further research is required to understand the load transferring mechanism and satisfy the installation and transportation conditions. Upon these challenges, a numerical analysis is performed to investigate the load-bearing mechanism of beam-to-column long bolt connection in modular steel building and validated with the experimental results available in the literature. A case study was performed on the influence of bolt pretension on the connection capacity and rotation, two different cases of bolt load were studied, where the first case is bolt load of 90 kN, and the second case is snug-tightening bolt load of 10 kN. It was found the pretension led to yield the beam endplate and weakness the connection moment resistance at the initial stages, and it does not affect plastic connection capacity. It was also found that large deformation happens at the middle part of the in-build component and side plate where the upper and lower columns are connected. The tension flange of the columns is deformed contributing to the overall rotation of the beams. Moreover, the long tightening bolts in the tension region were deformed significantly. Therefore, special attention should be given to the connection geometries.

References

1. Chen Z, Liu J, Yu Y (2017) Experimental study on interior connections in modular steel buildings. Eng Struct 147:625–638. https://doi.org/10.1016/j.engstruct.2017.06.002
2. Ferdous W, Bai Y, Ngo TD, Manalo A, Mendis P (2019) New advancements, challenges and opportunities of multi-storey modular buildings—a state-of-the-art review. Eng Struct. https://doi.org/10.1016/j.engstruct.2019.01.061

3. Godbole S, Lam N, Mafas M, Fernando S, Gad E, Hashemi J (2018) Dynamic loading on a prefabricated modular unit of a building during road transportation. J Build Eng 18:260–269. https://doi.org/10.1016/j.jobe.2018.03.017

4. Hwan Doh J, Ho NM, Miller D, Peters T, Carlson D, Lai P (2017) Steel Bracket Connection on Modular Buildings. J Steel Struct Construct 02. https://doi.org/10.4172/2472-0437.1000121

5. Kamali M, Hewage K (2016) Life cycle performance of modular buildings: a critical review. Renew Sustain Energy Rev. https://doi.org/10.1016/j.rser.2016.05.031

6. Kim J-Y, Lee J-K (2014) A basic study on the application of modular construction - focused on the analysis of case study. J Korean Housing Assoc 25:39–46. https://doi.org/10.6107/JKHA.2014.25.4.039

7. Lawson RM, Ogden RG, Bergin R (2012) Application of modular construction in high-rise buildings. J Archit Eng 18:148–154. https://doi.org/10.1061/(asce)ae.1943-5568.0000057

8. Lawson RM, Steel construction institute (1999) Modular construction using light steel framing: an architect's guide. Steel Construction Institute

9. Lee S, Park J, Shon S, Kang C (2018) Seismic performance evaluation of the ceiling-bracket-type modular joint with various bracket parameters. J Constr Steel Res 150:298–325. https://doi.org/10.1016/j.jcsr.2018.08.008

10. Li D, Uy B, Wang J, Song Y (2020) Behaviour and design of high-strength Grade 12.9 bolts under combined tension and shear. J Construct Steel Res 174:106305. https://doi.org/10.1016/J.JCSR.2020.106305

11. Lopez D, Froese TM (2016) Analysis of costs and benefits of panelized and modular prefabricated homes. In: Procedia Engineering. Elsevier Ltd, pp 1291–1297. https://doi.org/10.1016/j.proeng.2016.04.166

12. Ma R, Xia J, Chang H, Xu B, Zhang L (2021) Experimental and numerical investigation of mechanical properties on novel modular connections with superimposed beams. Eng Struct 232. https://doi.org/10.1016/j.engstruct.2021.111858

13. Mark Lawson R, Richards J (2010) Modular design for high-rise buildings. Proc Inst Civ Eng Struct Build 163:151–164. https://doi.org/10.1680/STBU.2010.163.3.151/ASSET/IMAGES/SMALL/STBU163-151-F21.GIF

14. Ogden R, Goodier C (n.d) Mark Lawson design in modular construction

15. Schoenborn JM, Jones JR, Schubert RP, Hardiman TE (2012) A case study approach to identifying the constraints and barriers to design innovation for modular construction

16. Sharafi P, Mortazavi M, Samali B, Ronagh H (2018) Interlocking system for enhancing the integrity of multi-storey modular buildings. Autom Constr 85:263–272. https://doi.org/10.1016/j.autcon.2017.10.023

17. Suleiman M, Elshaer A, Billah M (2021a) Covid-19 modular construction

18. Suleiman M, Elshaer A, Billah M, Bassuony M (2021b) Propagation of mouth-generated aerosols in a modularly constructed hospital room. Sustainability (Switzerland) 13. https://doi.org/10.3390/su132111968

19. Thai HT, Ngo T, Uy B (2020) A review on modular construction for high-rise buildings. Structures. https://doi.org/10.1016/j.istruc.2020.09.070

20. Ye Z, Giriunas K, Sezen H, Wu G, Feng DC (2021) State-of-the-art review and investigation of structural stability in multi-story modular buildings. J Build Eng. https://doi.org/10.1016/j.jobe.2020.101844

Strengthening Shear-Damaged Reinforced Concrete Beams Using Iron-Based Shape Memory Alloys

Miguel González-Góez, Trevor D. Hrynyk, and Eugene Kim

Abstract Advanced steel reinforcement technologies are key to enabling more durable and resilient concrete infrastructure in the face of rapidly growing demands, accelerating climate change, and extreme hazards. However, solutions for improving the performance of concrete elements in shear have historically relied on passive means where the reinforcement is only engaged after diagonal or transverse concrete cracking has occurred. This paper presents a numerical investigation on the use of prestressed iron-based shape memory alloys (Fe-SMA) to strengthen shear-damaged reinforced concrete (RC) members. Firstly, a numerical model based on test data from the literature involving large-scale shear-critical RC beams is developed using the program VecTor2. A parametric analysis is then conducted to determine the effects of externally bonded prestressed Fe-SMA on the shear response by varying the Fe-SMA and steel transverse reinforcement volume, the level of prestressing and the bidirectionality of SMA. The main focus of the analysis is on ultimate capacity and crack closing. The results of this study indicate that RC beams retrofitted using Fe-SMA exhibit reduced shear cracking and increased shear capacities.

Keywords Shear-damaged reinforced concrete · Iron-based shape · Memory alloys

1 Introduction

As a result of growing traffic demands and structural degradation accelerated by climate change, there is a critical need for continued advancement of concrete repair and strengthening technologies to enable extended bridge service life. The 2019 Canadian Infrastructure Report Card indicates that over 10% of the nation's bridges are in poor or very poor condition, and that number is forecast to grow in the coming

M. González-Góez (✉) · T. D. Hrynyk · E. Kim
Department of Civil and Environmental Engineering, University of Waterloo, Waterloo, Canada
e-mail: m32gonza@uwaterloo.ca

decades. In response, several retrofit strategies involving externally bonded materials have been developed for reinforced concrete (RC) structures such as fibre-reinforced polymers (FRPs) and near-surface mounted (NSM) steel components. Although many techniques have been developed for enhancing the in-service flexural performance and durability of RC members under flexure-dominated loading scenarios (e.g., the application of prestressing to reduce concrete cracking), comparatively fewer practical options are available to mitigate transverse, or shear, crack development in RC bridge elements. In addition to that, most transverse strengthening techniques are passive in nature and are only engaged after significant damage development. Alternatively, active transverse reinforcement strategies could be used to induce compressive stresses within the surrounding concrete and, as a by-product, potentially close, or at least reduce the widths of, existing cracks and prevent further shear-related concrete damage from occurring, thus enhancing member durability, maintaining member stiffness, and potentially increasing member shear resisting capacity.

The objective of this study is to numerically examine the effectiveness of Fe-SMA as an active strengthening method in shear-damaged RC beams. An experimental specimen presented in the literature and involving a full-scale conventional RC pier cap element was modelled using the nonlinear finite element analysis (NLFEA) software program VecTor2 [16]. Prestressed Fe-SMA elements were introduced in the model to simulate the addition of transverse reinforcement strengthening, and a parametric analysis was performed to investigate the influence of various SMA reinforcement parameters that are expected to play key roles on strengthened component shear resisting performance: (i) the Fe-SMA reinforcement ratio, (ii) the level of SMA prestressing, (iii) the orientation of the simulated SMA retrofit, and (iv) the presence of conventional internal transverse reinforcement (i.e., steel stirrups). The findings of this paper provide insight, generated by way of numerical modelling, into the shear resisting performance of RC components employing novel active shear-strengthening techniques and also illustrate cost-effective modelling strategies that can be utilized to investigate other, or similar, shear retrofits.

2 Shape Memory Alloys

Shape memory alloys (SMAs) are a class of smart materials that undergo phase transformations under mechanical and thermal loading. SMAs possess two unique thermomechanical properties: (1) superelasticity, which is the ability to recover its shape after large nonlinear strains, and (2) shape memory effect, which allows prestrained (i.e., predeformed) SMAs to fully recover plastic deformations and return to their original shape by increasing their temperature. Use of the shape memory effect for prestressing and active confinement has already been demonstrated in numerous research studies using nickel-titanium (Ni–Ti) SMA, which is the most widely available commercially [4, 11]. However, the cost of Ni–Ti is arguably prohibitive for most real-world structural engineering applications; thus, to date, it has primarily
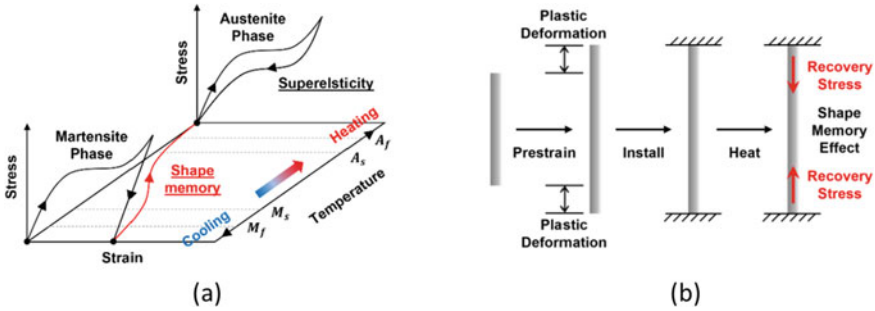
Fig. 1 **a** Thermomechanical behaviour of SMA and **b** SMA prestressing concept

been heavily utilized in other fields (e.g., medical devices, aerospace materials), but the exploration of its use for structural applications has generally been limited to specialized, and highly localized, connection regions. In contrast, iron-based SMAs (Fe-SMAs) are cheaper and easier to machine, opening the possibility of fabricating low-cost structural devices. Although Fe-SMAs do not possess superelastic properties, their shape memory effect can produce high recovery stresses (>300 MPa) at reasonable temperatures (~200ºC) which can actively confine or prestress structural members. By installing prestrained Fe-SMA strips in the transverse direction then activating the shape memory effect, an active pressure can be introduced to help close cracks and apply a confining stress in the concrete. Figure 1 illustrates the shape memory effect and the SMA prestressing concept.

Previous research has evaluated the potential of Fe-SMAs for strengthening RC structures. Soroushian et al. [12] first demonstrated the potential for Fe-SMA shear strengthening by using externally mounted Fe-SMA rods to restore the load carrying capacity of a shear-damaged RC beam. Rojob and El-Hacha [9] proposed a prestressing technique with Fe-SMAs for enhancing the flexural behaviour of RC beams and found significant increases in flexural capacity and ductility of the tested beams. In recent years, several experiments have been conducted with addition of Fe-SMA transverse reinforcement. Cladera et al. [2] presented a series of experiments on real-scale RC beams strengthened with Fe-SMA strips that showed shear strength increases on the order of 30% and delayed shear crack development as a result of the active confining stress. Czaderski et al. [3] developed a shear retrofit method using externally installed Fe-SMA stirrups and found that the transverse prestressing increased the cracking load and reduced the widths of shear cracks. The results obtained from both of these studies show that Fe-SMA prestressing is a promising retrofit strategy for mitigating concrete damage and improving the performance of shear-deficient RC components. However, the methods explored to date are not overly practical, requiring highly invasive installation procedures and anchorages, as well as lacking generally protection against environmental deterioration.

3   Preliminary Validation and Benchmark Analysis

VecTor2 [16] is a RC-dedicated NLFEA program. Cracked concrete material modelling is based on the on the formulations of the Disturbed Stress Field Model (DSFM) [14], which is an extension of the Modified Compression Field Theory (MCFT) [15]. The program is suitable for the analysis of two-dimensional RC membrane structures subjected to quasi-static or dynamic loading. A total load, secant stiffness-based, solution procedure is used and provides stable solutions for all stages of response, making VecTor2 particularly appealing for the analysis of shear-sensitive structures that tend to exhibit abrupt changes in material stiffness and response and are often governed by highly brittle failure mechanisms. Second-order effects and other concrete and reinforcement-related mechanisms that are not inherently accounted for in the formulations of the DSFM (e.g., concrete confinement and dilatation, plain concrete tension softening, concrete and steel hysteretic responses) are considered in the analysis, making the program suitable for a broad range of RC elements and analysis scenarios. In this paper, NLFEA of large-scale beam-type elements are carried-out using VecTor2. The geometry and reinforcement details of the beams are based on those from the testing program reported in Jirsa et al. [7] and [10], which entailed the testing of RC bridge pier cap girders strengthened with carbon fibre-reinforced polymer shear retrofits. In the present study, an experimental control test specimen referred to as D-U-VN-HN* was used as a benchmark for assessing relative performance of Fe-SMA shear retrofitted components and also for validating the overall suitability of the finite element meshing, material models employed, and analysis strategy.

An illustration showing the control beam geometry and reinforcement detailing is summarized in Fig. 2. The beam was constructed with a square cross section measuring 813 by 813 mm, and a total length of roughly 8.4 m. The beam was designed such that the test span region (see Fig. 2) would govern the capacity of the member and would be controlled by shear failure mechanisms. Two-legged 16-mm diameter stirrups were placed at a spacing of 457 mm, resulting in a shear reinforcement ratio of 0.11% within the test span, which is on the order of recommended minimum shear reinforcement requirements in modern North American provisions [1]. 11 US No. 11 bars were provided as longitudinal flexural reinforcement on both the tension and compression sides of the cross section resulting in a flexural tension and compression reinforcement ratio of 1.9%. The beam was tested using a skew-symmetric loading configuration that produced an inflection point at the midspan of the test span region, thus resulting in a double-curvature bending scenario. Additional details regarding the beam geometry and reinforcement, and the testing procedure used in the experimental program, are available in Jirsa et al. [7].
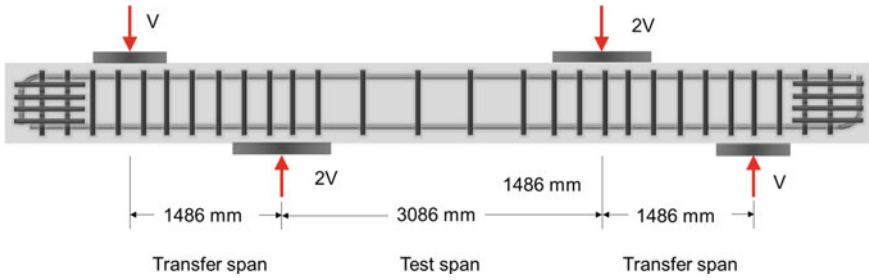
Fig. 2 Jirsa et al. [7] double-curvature control beam

3.1 Modelling Approach

Figure 3 presents the two-dimensional finite element mesh developed for the Jirsa et al. [7] RC control beam. In total, the finite element mesh consisted of 1,266 rectangular finite elements that were used to represent different reinforced concrete material types, steel bearing plates, and load/support interface regions. Flexural longitudinal reinforcement was modelled explicitly using 408 truss bar finite elements that were assumed to be perfectly bonded with the surrounding concrete. All transverse reinforcement was modelled in a smeared sense, using different RC material types to represent the different transverse reinforcement ratios provided over the length of the beam. The analysis was performed in a displacement-controlled manner, with equal and opposite displacements applied at the interior load bearing locations, and a roller and pin support reaction were provided at the two exterior bearing locations. Note that self-weight of the RC beam was neglected.

All user-definable material models and analysis parameters corresponded with VecTor2's default modelling options. More specifically, no effort was made to parametrically define models or refine analysis results, and user input was limited to the definition of the concrete and steel reinforcement materials properties, which were specified to match those reported in Jirsa et al. [7]. For reference, the concrete material
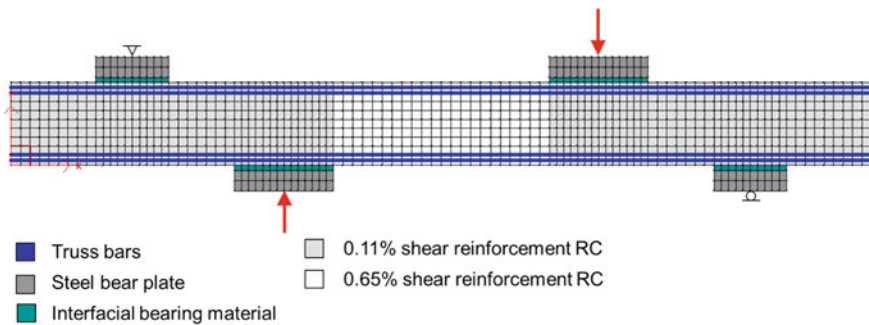
Fig. 3 VecTor2 two-dimensional model

was defined with a cylinder strength of 31 MPa and a maximum nominal aggregate size of 25 mm. Flexural reinforcement was assigned a yield strength of 420 MPa and a modulus of elasticity of 200,000 MPa. Shear reinforcement was assigned a yield strength of 400 MPa and a modulus of elasticity of 200,000 MPa.

3.2 Validation for Benchmark RC Beam

To validate the effectiveness of the meshing and behavioural models employed, results in the form of applied shear versus loading point displacement are presented in Fig. 4 and compared to the reported experimental data. From the figure, it can be seen that the shear capacity is estimated within 5% of that reported. Further, it can be seen that the finite element model developed was generally capable of capturing all aspects of the reported response ranging from the post-cracking shear stiffness, the capacity of the RC beam, and the brittle shear-governed failure mode encountered.

4 Parametric Study

In this section, a parametric study is performed to investigate the impacts of introducing externally bonded Fe-SMA retrofit to shear-damaged RC beams. The base geometry is the based on the pier cap test beam described in Sect. 3. Parameters selected to investigation include the amount of transverse Fe-SMA reinforcement in the test span, the level of Fe-SMA prestressing, the presence of existing internal transverse reinforcement, and addition of longitudinally oriented Fe-SMA within the web region of the beam and in the amount of 0.10%. Table 1 summarizes the parameters considered in the study.

(a) computed shear force-displacement response   (b) reported and computed damage at ultimate
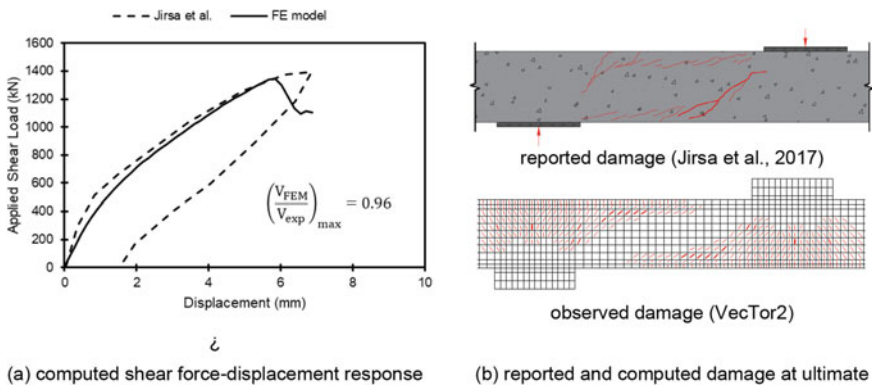
Fig. 4 Results for Shekarchi et al. RC control beam

Table 1 Summary of parameters considered

Prestress level (MPa)	Fe-SMA reinf ratio (%)	Fe-SMA direction	Existing shear reinf ratio
266	0.10	Vertical only	No. Reinf
399	0.20	Vertical + Horizontal	Min = 0.083%[a]
	0.30		
	0.40		

[a]Computed according to clause 11.2.8.1, CSA A23.3:19

To simulate the presence of initial shear damage that would prompt the need for shear retrofitting, and to subsequently estimate the effectiveness of the different Fe-SMA retrofits, the NLFEA was performed in three phases: (1) *initial loading*: a seed model of the RC beam was first loaded up to approximately 85% of the peak capacity to induce shear damage/distress in the RC component (see Fig. 5a), (2) *unloading*: the beam was then unloaded to 50% of the initially applied load (see Fig. 5b), (3) *retrofit and reloading*: at this point, prestressed Fe-SMA reinforcement was added within the previously defined test span region (see Fig. 2) as smeared reinforcement and the analysis was resumed until failure was estimated to occur (see Fig. 5c). Figure 5 presents a schematic view of the three-phase progression of analyses performed.

The Fe-SMA was added to the model as smeared reinforcement in the test span of the beam (see highlighted region in Fig. 6). Shape Memory Alloy (type 2) material from the VecTor2 library was used to define the constitutive models governing the response of the Fe-SMA retrofit and its associated material properties were defined to match those reported by [6] (yielding stress = 463 MPa, ultimate tensile strength = 863 MPa, and modulus of elasticity = 133,000 MPa). The Fe-SMA behaviour is shown in Fig. 7.
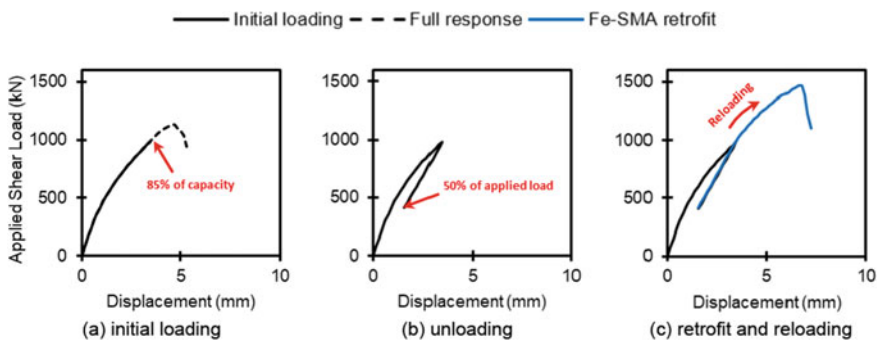
Fig. 5 NLFEA loading phases
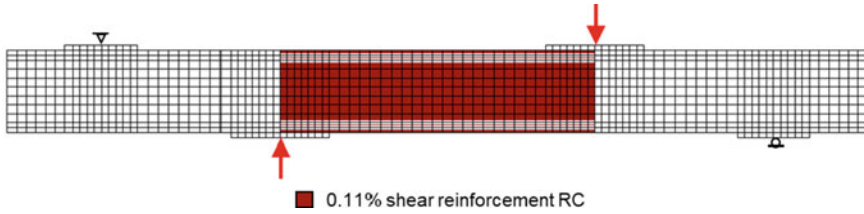
Fig. 6 VecTor2 mesh with smeared Fe-SMA retrofit

Fig. 7 Fe-SMA
stress–strain response [6]
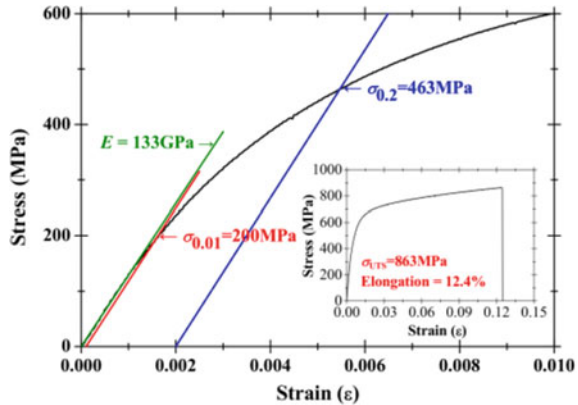
5 Results and Discussion

The analyses were performed using four different finite element seed models to represent the varying levels of internal transverse reinforcement and the different directions/orientations of external Fe-SMA reinforcement. The seed models were denoted as VN, VT, BDN, and BDT where V = vertical Fe-SMA, BD = bidirectional Fe-SMA, N = No transverse reinforcement, and T = minimum transverse reinforcement.

5.1 Shear Response

Figure 8 presents the applied shear versus displacement results before and after Fe-SMA retrofits were incorporated into the models. It can be observed that as the external shear reinforcement ratio (ρ_v) is increased, shear capacity and displacement at peak shear resistance increased. A slight increase is also obtained by way of the transverse prestressing applied via the Fe-SMA; however, when contrasted with the impact of shear reinforcement ratio, increase the level of Fe-SMA prestressing from 286 to 399 MPa is estimated to be less significant to shear capacity. The

post-retrofit stiffness was found to follow the unloading curve of the seed models and exhibited only marginal softening after reaching and exceeding previous load levels. Results pertaining to shear capacity and corresponding shear strength gains compared to seed model analyses without any form of shear retrofit are summarized in Table 2. Maximum estimated shear strengths were 1135 kN for the models without internal transverse reinforcement (VN, BDN) and 1293 kN for models with transverse reinforcement (VT, BDT).

Additional models were developed to further investigate the impact of different shear reinforcement prestressing levels on the shear response of the beam. Figure 9 presents computed shear force–displacement responses for the VN seed model with a Fe-SMA shear retrofit of 0.10%, and Table 3 summarizes the shear capacities obtained for the different retrofits. Five different Fe-SMA prestressing levels were considered: 0, 133, 266, 333, and 399 MPa. From the data presented, it can be seen that the prestressing level does indeed enhance the shear resisting performance of the beam by way of delaying stiffness degradation and by increasing shear capacity.
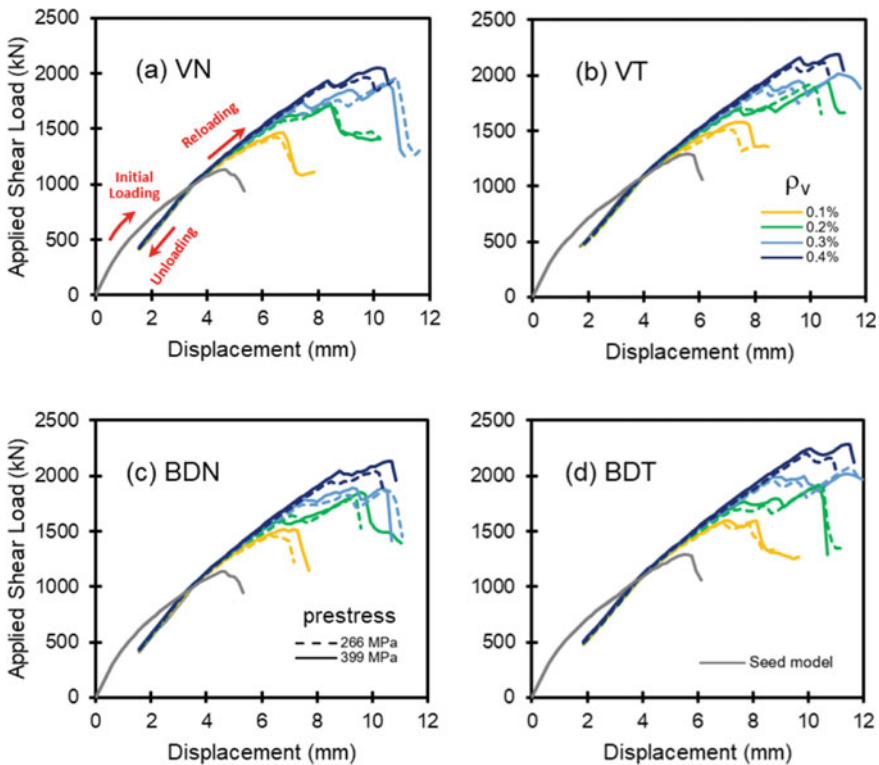
Fig. 8 Shear response

Table 2 Peak shear capacities and retrofit strength gains

Seed model	Prestressing level (MPa)	Fe-SMA reinforcement ratio							
		0.1%	0.2%	0.3%	0.4%	0.1%	0.2%	0.3%	0.4%
		Peak shear (kN)				Peak shear increase (%)			
VN	266	1429	1736	1962	2102	26	53	73	85
	399	1466	1716	1908	2013	29	51	68	77
VT	266	1509	1924	2012	2169	17	49	56	68
	399	1581	1943	2012	2190	22	50	56	69
BDN	266	1459	1800	1873	2078	29	59	65	83
	399	1516	1849	1893	2134	34	63	67	88
BDT	266	1583	1910	2070	2204	22	48	60	70
	399	1601	1919	2018	2285	24	48	56	77
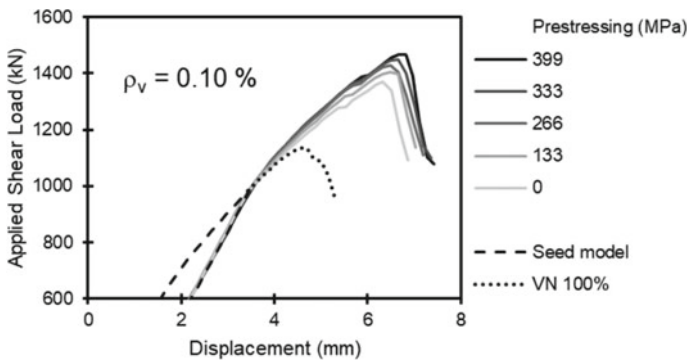
Fig. 9 Influence of prestressing level (VN seed model)

Table 3 Peak shear capacity and influence of prestressing level

Prestressing (MPa)	0	66.5	133	199	266	333	399	465	532
Equivalent prestrain ($\times 10^{-3}$)	0	0.5	1.0	1.5	2.0	2.5	3.0	3.5	4.0
Shear capacity (kN)	1370	1386	1406	1420	1429	1450	1466	1475	1475
Shear strength increase (%)	21	22	24	25	26	28	29	30	30

5.2 Crack Closing Potential

Figure 10 shows the computed crack closing response of a single finite element that is estimated to occur as a result of clamping action developed by way of the active prestressing. The selected element was located at one of the shear cracks of the seed model before retrofit, as shown in Fig. 11. The effectiveness of the Fe-SMA retrofits in closing shear cracks is clearly evident in even the lowest volume of external
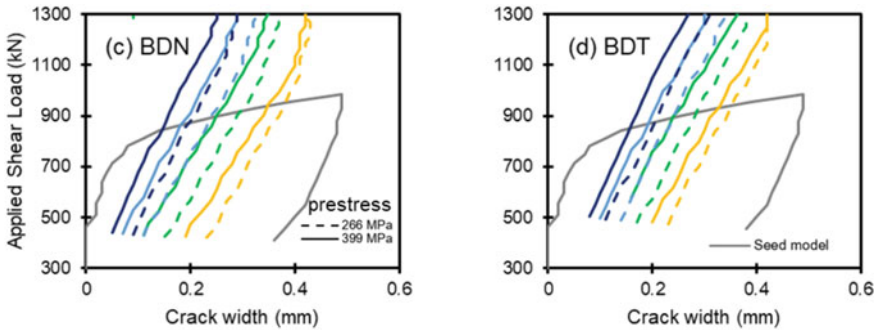
Fig. 10 Crack width in a single element
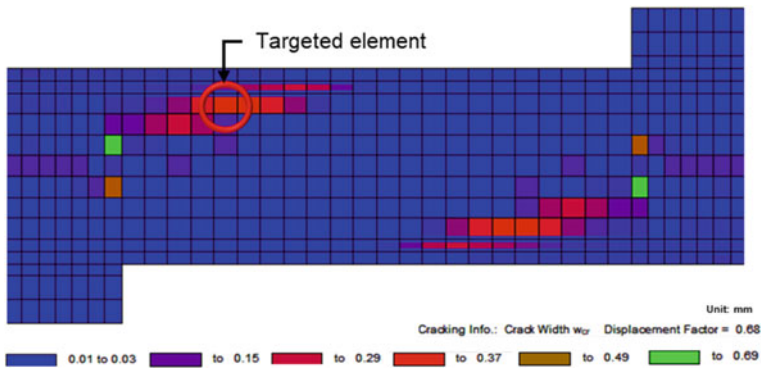
Fig. 11 Crack widths in test span before prestressed Fe-SMA addition

reinforcement. As the reinforcement ratio increases, shear crack widths are reduced by up to 88%.

The influence of prestressing level on the cracking reduction is clearly apparent in Fig. 11, with estimated shear crack widths being significantly smaller for retrofits employing higher prestressing levels (e.g., 399 MPa). Moreover, a major benefit of introducing transverse prestressing in the RC beams is the potential that cracking may be better-controlled and mitigated such they are closed and remain small, under routine service load levels. Overall, the findings of these numerical results indicate that the presence of externally bonded Fe-SMA retrofits is able to provide significant improvements in the shear resisting performance of large-scale RC beams. However, further experimental research is required to establish the viability of the proposed method and to explore different bonding techniques to incorporate Fe-SMA into the surface of the concrete.

6 Conclusions

A numerical study was conducted to evaluate the influence of several parameters on the shear resisting performance of RC beams. The results of this investigation showed that the presence of prestressed iron-based shape memory alloys on the surface of the beams can provide several improvements, which are summarized as follows:

- Iron-based shape memory alloy (Fe-SMA) retrofits were estimated to provide stiffness and strength improvements in damaged RC components as a result of the transverse prestressing induced by way of the active retrofit strategy.
- In the same manner as expected with similar retrofit methods involving passive techniques, the shear capacity of damaged shear-critical beams was estimated to increase as more transverse reinforcement was provided. Combinations of large shear reinforcement ratios with high levels of transverse prestressing provided the largest shear strength gains.
- The additional of prestressed Fe-SMA retrofits were estimated to reduce (i.e., close) shear crack widths and mitigate the development of subsequent shear crack width growth.

References

1. American Association of State Highway and Transportation Officials (2019) AASHTO LFRD bridge design specifications
2. Cladera A, Montoya-Coronado LA, Ruiz-Pinilla JG, Ribas C (2020) Shear strengthening of slender reinforced concrete T-shaped beams using iron-based shape memory alloy strips. Eng Struct 221. https://doi.org/10.1016/j.engstruct.2020.111018
3. Czaderski C, Shahverdi M, Michels J (2021) Iron based shape memory alloys as shear reinforcement for bridge girders. Construct Build Mater 274. https://doi.org/10.1016/j.conbuildmat.2020.121793
4. El-Tawil S, Ortega-Rosales J (2004) Prestressing concrete using shape memory alloy tendons. ACI Struct J 101(6):846–851
5. Federation of Canadian Municipalities (2019) The 2019 Canada Infrastructure report card
6. Hong K, Lee S, Han S, Yeon Y (2018) Evaluation of Fe-based shape memory alloy (Fe-SMA) as strengthening material for reinforced concrete structures. Appl Sci (Switzerland) 8(5). https://doi.org/10.3390/app8050730
7. Jirsa JO, Ghannoum WM, Kim CH, Sun W, Shekarchi WA, Alotaibi NK, Pudleiner DK, Zhu J, Liu S, Wang H (2017) Use of carbon fiber reinforced polymer (CFRP) with CFRP anchors for shear-strengthening and design recommendations/quality control procedures for CFRP anchors. https://library.ctr.utexas.edu/ctr-publications/0-6783-1.pdf
8. Montoya-Coronado LA, Ruiz-Pinilla JG, Ribas C, Cladera A (2019) Experimental study on shear strengthening of shear critical RC beams using iron-based shape memory alloy strips. Eng Struct 20. https://doi.org/10.1016/j.engstruct.2019.109680
9. Rojob H, El-Hacha R (2017) Self-prestressing using iron-based shape memory alloy for flexural strengthening of reinforced concrete beams. ACI Mater J 114(2):523–532. https://doi.org/10.14359/51689455
10. Shekarchi WA (2016) Shear behavior of reinforced concrete bridge pile cap girders strengthened with carbon fiber reinforced polymer (CFRP) strips and CFRP anchors

11. Shin M, Andrawes B (2010) Experimental investigation of actively confined concrete using shape memory alloys. Eng Struct 32(3):656–664. https://doi.org/10.1016/j.engstruct.2009.11.012
12. Soroushian P, Ostowari K, Nossoni A, Chowdhury H (2001) Repair and strengthening of concrete structures through application of corrective posttensioning forces with shape memory alloys 1770:20–26. https://doi.org/10.3141/1770-03
13. Standards Council of Canada (2019) CSA A23.3:19, Design of concrete structures
14. Vecchio FJ (2000) Disturbed stress field model for reinforced concrete: formulation. J Struct Eng 126(9):1070–1077. https://doi.org/10.1061/(ASCE)0733-9445(2000)126:9(1070)
15. Vecchio FJ, Collins MP (1996) The modified compression-field theory for reinforced concrete elements subjected to shear. ACI J 83(22):219–231
16. Wong PS, Vecchio FJ, Trommels H (2013) VecTor2 and Formworks user's manual 2nd edition

Steel Beam-To-Column Connection Fire Design

Jeanneret Chloe, Martins-Robalino Austin, Gales John, Genikomsou Aikaterini, and Kotsovinos Panagiotis

Abstract With architectural styles changing and the knowledge of fire behaviour constantly evolving, it is important to continue advancing the field of fire safety engineering to ensure that the existing and expanding infrastructure is safe and resilient. Within the National Building Code of Canada and subsequent provincial and material design standards, there exists flexibility for designers to consider more advanced computational practices that can optimize the fire protection design. These clauses permit alternative design solutions to be used when they can be proven to be equivalent or superior to the prescriptive design. This, however, can be hard to implement regarding structural fire designs as the Authorities Having Jurisdiction (AHJs) typically do not have the fire education and resources to evaluate and compare a design. Alternative solutions, especially for structural fire design, allow for economic and material savings. A performance-based solution is able to check for all possible scenarios and optimize the fire protection, reducing the environmental impact of the design by reducing the need for excess fire protection, which can be toxic and have negative life cycle analysis impacts. The connections are known as the most vulnerable part of a steel-framed building construction. A preliminary series of fire tests were undertaken at York University's Fire Resiliency Lab, with different methanol pool fire durations, to understand the deformation behaviour of a simple steel post-and-beam frame and how the forces and heat are dissipated into the connections. With an accurate understanding of the thermal forces created by a localized fire, the design of connections would be able to dissipate the large forces that occur through ductile connections. The tests demonstrated how connections and the remaining structure behave intrinsically when exposed to thermal forces, such as displacements and rotations.

J. Chloe (✉) · M.-R. Austin · G. John
York University, Toronto, Canada
e-mail: chloej96@yorku.ca

G. Aikaterini
Queen's University, Kingston, Canada

K. Panagiotis
Arup, London, UK

1 Introduction

The current design methods for structures in fire in Canada are purely prescriptive, which results in designs often being either underdesigned or overdesigned. The current predominant method of fire design in Canada uses the CAN/ULC-S101-14 standard fire [30] in its prescriptive approach. This temperature–time curve assumes uniform burning and homogeneous temperature conditions throughout the compartment regardless of the compartment size, as well as other assumptions that are no longer valid as the standard was first codified in 1917 and is unrepresentative of contemporary fire dynamic theory [10]. Using such a curve can result in the building response not being entirely representative of reality, resulting in potentially unconservative or even overly conservative and wasteful designs. Within the National Building Code of Canada [4] and subsequent provincial and material design standards, there exists flexibility for a designer to consider more advanced computational practices that can optimize the fire protection design. These clauses permit alternative design solutions to be used when they can be proven to be equivalent or superior to the prescriptive design. Alternative solutions in structural fire design can provide greater architectural freedom due to alternative protection and design solutions which can result in economic and material savings. Using performance-based design can also help reduce the environmental impact of the design by optimizing the fire protection and reducing the need for excess fire protection, which can be toxic and have high cradle-to-grave impact. They also have the ability to demonstrate to a practitioner the life safety, economy and robustness benefits available with various fire solutions, as multiple different fire scenarios would be considered. This ensures that the designed structures are resilient. However, structural fire designs can be computationally intensive, and training regarding fire design in Canada is limited.

Steel structures are very common, and the behaviour of their beams and columns during fire events has been extensively studied. The behaviour of steel beam-to-column connections within these structures under thermal loading, however, is not well understood. When exposed to a fire, the members within steel structures expand during heating and contract in cooling, inducing large forces upon the connections. To ensure resiliency, steel connections, such as beam-to-column connections, must be able to withstand the loading that would be induced due to fire. The behaviour of beam-to-column connections under thermal loading is currently not well understood, limiting the current design to being overly conservative rather than using a performance-based solution [9].

There has been limited experimental studies into the behaviour of beam-to-column connections under fire exposure, mainly due to the high cost of fire tests. The majority of the research is focused on modelling, using the limited experiments as forms of validation [18, 22, 24]. A large portion of the previous fire tests, dating early 2000s and earlier, were focused on understanding moment-rotation characteristics of end-plate

connections [1, 2, 15, 16, 27, 28, 32, 34]. The largest, in compartment size, experimental study utilized the Cardington steel structure to perform a large-scale test. This experiment, reported by Wald et al. [31], examined the temperatures selected structural elements, including the connections, would reach using a fuel load of 40 kg/m2 of wooden cribs evenly distributed across the compartment. The structure did not experience collapse; however, some local buckling and fractures occurred, some during the cooling stage. Details about the connection forces or specific behaviours were not discussed. An experimental programme examining semi-rigid steel moment connections was undertaken by Mao et al. [17], leading to modelling. The National Institute of Standards and Technology (NIST) in the United States conducted a series of four experiments on long-span steel–concrete composite floor beam to measure the axial loads created by the thermal exposures [5]. Two major experimental research programmes were also undertaken at the University of Sheffield and the University of Manchester examining connection behaviour, summarized in [33]. The first programme comprised of isolated connection tests at high temperatures [14, 35–37], while the second programme undertook fire tests on structural subassemblies [8, 33]. The full research undertaken by this team until 2012 was summarized by Burgess et al. [3].

Due to the limited knowledge regarding beam-to-column connections, an experimental programme based on a case study building located in London, UK, known as the Scalpel, was conducted. This building is a 38-storey skyscraper with a unique layout causing many angled facades, shown in Fig. 1, designed in accordance with the Eurocode (UK) building standards. This building was ideal for examining the forces that are generated within connections since the uncommon geometry resulted in the buildings having inclined columns. The Scalpel has become recognized for its fire design, performed by ARUP UK, which has created a precedent in the UK for using the travelling fire methodology. The case study provided a baseline of a real, built structure and allowed for the investigation of similar physical responses that could be expected within a similar building. The experiments planned as part of this research project begin to address the need for large-scale experiments to validate complex and detailed modelling of structures under thermal exposure.

2 Methodology

2.1 Experimental Setup

Through a collaboration with ARUP UK, a beam-to-column setup within the Scalpel was identified to be used for a case study analysis. The original setup, however, had dimensions much larger than could be tested and therefore needed to be scaled down while ensuring that the scaled version would behave the same as the original configuration. The sections were therefore scaled to a quarter scale while keeping

Fig. 1 The Scalpel in London, UK, with its angled facades (photograph captured by author)

the relative rotational stiffness constant. The relative rotational stiffness was defined as the ratio of the stiffness of the beam to the stiffness of the column.

A series of three preliminary fire experiments of various thermal exposure durations were undertaken within York University's Fire Resiliency Lab to produce a conceptual framework. The focus within these experiments was on identifying the thermal distribution into the connections when a steel beam was subjected to a localized fire at its centre, as well as the deformations observed due to thermal expansion within the beam and connections. Based upon the scaling to keep the same behaviour, the experimental setup used a W410 × 85 beam and two HSS406 × 406 × 16 columns, conserving a representative connection stiffness. This setup is shown in Fig. 2.

The connections between the beam and columns were designed by Benson Steel Ltd, a steel manufacturer located near Toronto, ensuring that the connections would be designed as is currently done in Canada. Due to their brittle behaviour, shear tab connections were selected for this experimental series. Additional connections will be examined in further studies. Since the beam-to-column setup was scaled using relative stiffness, the connection forces could not be taken from the design of the Scalpel. The scaling ratio from the relative stiffness was also not applicable to the forces directly. Instead, the connection forces were assumed to be 95% of the capacity of the beam member (the lesser of shear and moment capacities). The connection forces were calculated using ambient conditions, unlike the connections in the Scalpel, which would have considered the increased capacities induced by a fire event. This was done since it is representative of design performed in Canada, where a prescriptive design is used, and the connection fire capacities are not considered.
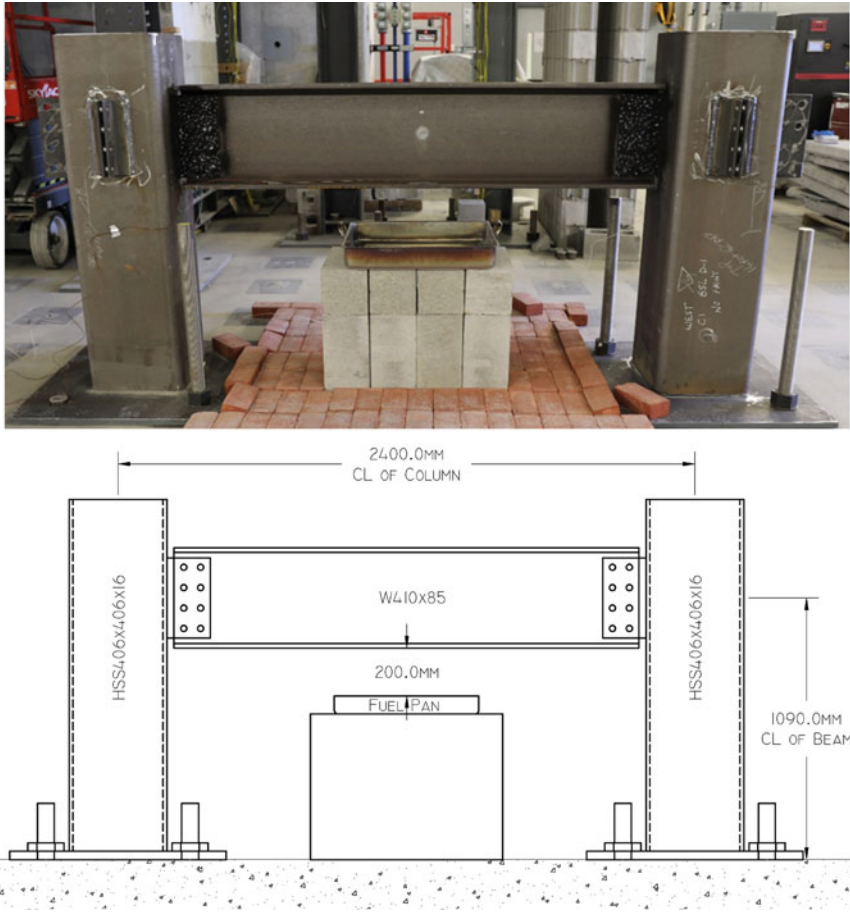
Fig. 2 Beam-to-column connection experimental setup

2.2 Instrumentation

The deformations were recorded using digital image correlation, and narrow spectral illumination was used on the images captured at the centre span to filter out the flames from the photographs. This method is described in [13, 25] and allows visual observation of strains and deflections within the flame area, such as the lower flange at the centre of the span. Narrow-spectrum illumination is a technology developed by NIST and refined at York University where high-intensity blue LEDs illuminate a target and selective colour filters are used to filter light bands above blue. This then allows see through fire measurement [13]. Three Canon EOS 5Ds (Mark IV) 30.4 MPx cameras were used to capture the movements within the experimental setup. The connections which were far enough from the pool fire were painted black with
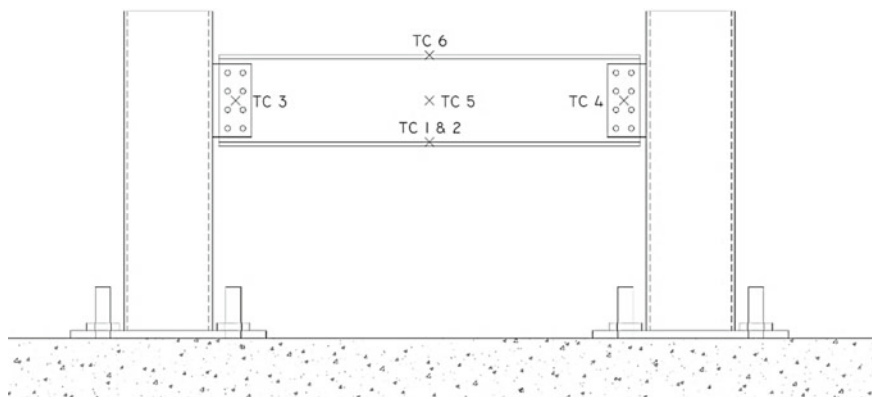
Fig. 3 Thermocouple location on experimental setup

white speckles to provide a high-contrast pattern to facilitate DIC analysis. The DIC analysis for multiple locations along the experimental setup was performed used the GeoPIV RG software [29]. The procedure for measuring strains and deformations is achieved through post-processing where pre-recorded imagery is compared and contrasted using the software to discern minute changes that can then be calculated manually as strain or deflections. Following best practices as defined by Gales et al. [11], error is minimized. This DIC technique has been shown to be accurate for monitoring displacements in [7, 20].

Six K-type thermocouples were used to record the steel temperatures at set points within the experimental setup. Each thermocouple was attached to the steel using ceramic fibre wool and aluminium tape padding, following the methodology described in [12]. This is to shield the thermocouple from the influences of surrounding heat and allow it to record the actual temperature of the steel. The location of each of the thermocouples is illustrated in Fig. 3. These locations allowed for the understanding of the thermal gradients that would occur throughout the depth and span of the beam during thermal exposures.

2.3 Thermal Exposures

To ensure that the experiment was realistic, a form of localized heating was needed. A pool fire resembles as close as possible a pool fire where the connectors may not be exposed to fire. It also inflicts both radiative and convective heating, which is more similar to a real fire compared to other thermal exposures. The beam would also be heated upon multiple faces, creating a realistic heat distribution within the steel beam. It should be acknowledged that a pool fire is not a realistic exposure; however, it does allow for a controlled observational study of the structural system under

an exposure that can be repeated. This type of exposure, combined with narrow-spectrum illumination, was previously used by Nicoletta et al. [21] and Chorlton et al. [7]. These studies used similar setups consisting of methanol pool fires and narrow-spectrum illumination to monitor material deformations and behaviours, and this technique has allowed for repeatable results in creating a representative fire exposure of near 700 °C.

Three different thermal exposures were used to identify the behaviour within the experimental setup. These included a short, a medium and a long methanol pool fire, which created temperatures in excess of 700 °C. Each exposure was then allowed to cool, naturally, until all steel temperatures were measured to be below 100ºC. Due to the soot production of other fuels such as acetone or kerosene, it was decided to use methanol, which produces the least soot. The research by Chorlton et al. [7] describes the process used to determine the most suitable fuel type and volume used in these experiments.

For each fire exposure, the specified amount of fuel was placed in a 0.48 m × 0.6 m pan, located 200 mm below the centre of the beam, to create the desired fire exposure. This created an incident heat of the order of 700–800 °C, as characterized in [19]. For the short, medium and long experiments, 4, 8 and 16 L were used, respectively. This resulted in overall exposure times of 12 min, 20 mi and 38 min, respectively. As each experiment reached different steel temperatures, they required different cooling periods, which were recorded as 39 min, 47 min and 106 min, respectively.

3 Results

3.1 Temperature Distribution

As shown in Fig. 3, the thermocouples were placed along the beam and connections to obtain an understanding of the thermal distribution that would occur due to a localized fire. Figure 4 plots the temperatures recorded with the thermocouples. Some experimental errors occurred during testing, including a thermocouple detaching (TC5 in the long experiment after 80 min). The detached thermocouple recorded the air temperature for approximately 30 min before it was noticed, after which it was reattached to the web of the beam. The air temperature segment of the data was omitted from the graph; however, it is assumed that the web would have cooled in a similar fashion to the previous experiments, following the decrease in temperature observed throughout the beam.

From Fig. 4, it can be observed that the temperature distribution within the beam behaves as expected. The pool fire would have reached temperatures of around 700 °C, as demonstrated by previous pool fire studies using the same configuration [7, 20]. This temperature is illustrated as the upper bounds of the figures and indicates the degree of heat transfer observed. The bottom flange and web above the pool fire saw rapid increases in temperatures as the pool fire reached steady state;
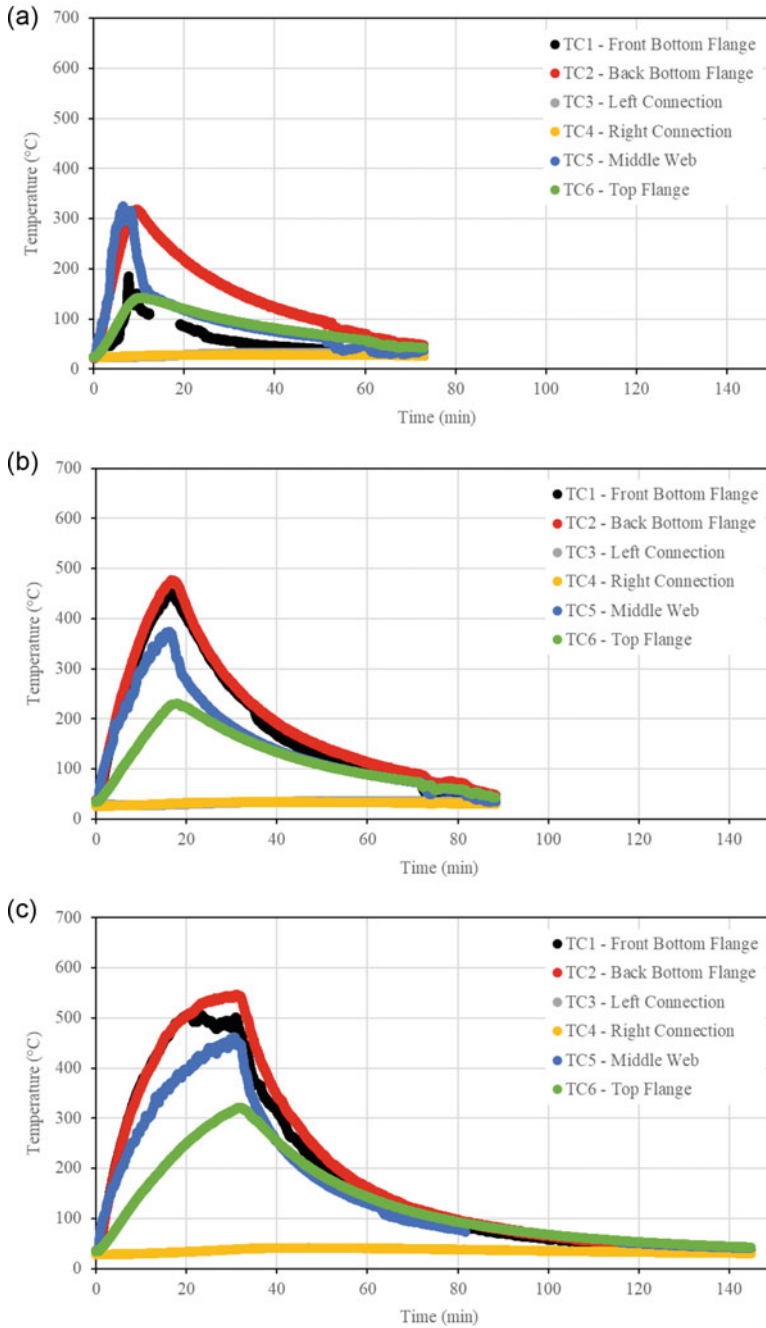
Fig. 4 Temperature distribution through the experimental setup for **a** short, **b** medium and **c** long thermal exposures

however, the beam never reached the fire temperature, although this might have been possible with a longer exposure. The top flange heats up at a slower rate, as it was outside the reach of the flames, relying on heat transfer through the web and the hot air convection to heat up.

The connections, located approximately 950 mm away from the centre of the pool fire, experienced minimal temperature increases. The maximum connection temperatures recorded were 33 °C, 37 °C and 43 °C for the short, medium and long experiments, respectively. The peaks in the connection temperatures occurred after the fire was already extinguished, illustrating the delay in the heating of the connections due to heat transfer through the beam. The low connection temperatures are related to the experimental setup and should not be utilized as proof of low connection temperatures within real fire scenarios. The experimental setup applied a short thermal exposure to the centre of the beam, which does not capture all possible scenarios a structure may experience.

Rapid cooling is observed immediately after the thermal exposure, with the hot steel rapidly losing heat to the surrounding cool air. The cooling rate reduces as the temperature difference decreases. Within the short and medium graphs, some abnormal temperature rates are observed which can be attributed to the water misting applied to aid in cooling. The misting was not applied on the long test to prevent any temperature disruption. The temperatures measured are what would be expected from heating from one side and indicate that the connectors themselves are not fire exposed taking only thermal loading from the beam itself as is intended in this experimental procedure.

3.2 Centre Span Deflection

The deflections at the centre span of the beam were recorded using digital image correlation (DIC) with narrowband illumination technologies. Using the GeoPIV RG software [29], points were selected at the upper edge of the top flange and lower edge of the bottom flange located along the centreline of the beam. No paint was applied within this area due to the uncertainty of the behaviour of the paint at such high temperatures—potentially releasing toxic fumes that may not be fully extracted by the exhaust system without harming researchers. In future tests, different paint configurations designed for high-temperature testing may be considered. Traditional deflection measurements were not used as there was still a degree of substantial heat above the beam which could have influenced the connecting cords. This would cause the deflection metres themselves to thermally expand and give false measurements. Errors occurred within the DIC tracking at the centre span due to the heat radiation distorting the image. This haze induced some data static, resulting in the need to splice the data. This was done using the methodology described and validated in [19].

The recorded deflections are shown in Fig. 5 for all the three tests. It should be noted that the time, shown on the x-axis, is different for the graphs of each test.

The deflection, y-axis, however, was kept the same to allow comparison between experiments. The deflections of both the top and bottom flanges of the beam were recorded to capture the thermal bowing that would occur, as well as the thermal expansion that would occur predominantly within the bottom flange. This can be seen to occur within all the three tests, with a difference of approximately 1.5 mm occurring.

The maximum deflections were seen to occur around the peak temperatures experienced within the beam. These were recorded in Table 1, for each test. As Fig. 5 illustrates, there was some noise in the data, which can be explained by the haze distorting the image. The values included in Table 1 are therefore calculated using a rolling average, with a period of 5, to remove overestimations of the deflection. Figure 5 also illustrates that an upward camber is created within the beam as it cools down. This upward is minimal, remaining below 2 mm at the centre of the span for all tests. This type of behaviour occurs within the experiments as the beam was unloaded. The maximum upward camber for each test is also included in Table 1.

4   Discussion

The experiments described herein were the first experiments to assume realistic rigidity or restraint within the experimental setup. The majority of the limited experiments in literature examined other behaviours experienced within connections without considering the restraint of a real structure. The experiments described herein were based upon a real structure and, while they were scaled down, this was done in a manner to ensure that the rigidity and restraint that would be demonstrated within the case study structure would remain between the frame elements.

The recorded thermocouple data demonstrate the repeatability of a methanol pool fire. From Fig. 4, it can be seen that the steel within the flaming region (on the lower web) consistently followed the same increase between all the three tests. This demonstrates the consistent thermal exposure generated by a methanol pool fire, even when different volumes of fuel are used. The recorded temperatures were also compared to a hand-calculation model, described within the Eurocodes for steel temperatures during uniform thermal exposures. The comparison illustrated that the hand calculations are conservative compared to the experimental results; however, this may be due to the localized heating used.

The deflection measurements demonstrated that unloaded beams exposed to temperatures below 700 °C for short durations experience no permanent thermal degradation. Instead, a slight upward camber is observed due to the uneven cooling that occurs within the assembly. This type of upward camber would not be expected within a structure after a fire. Had the beam been loaded, which would be more likely within a structure, there would have been creep (plastic) deformations that would have occurred in addition to this upward camber, resulting in the camber not being observable. It is therefore not possible for a typical structure to have a final upward deflection after fire, and this camber is a result of the experimental setup.
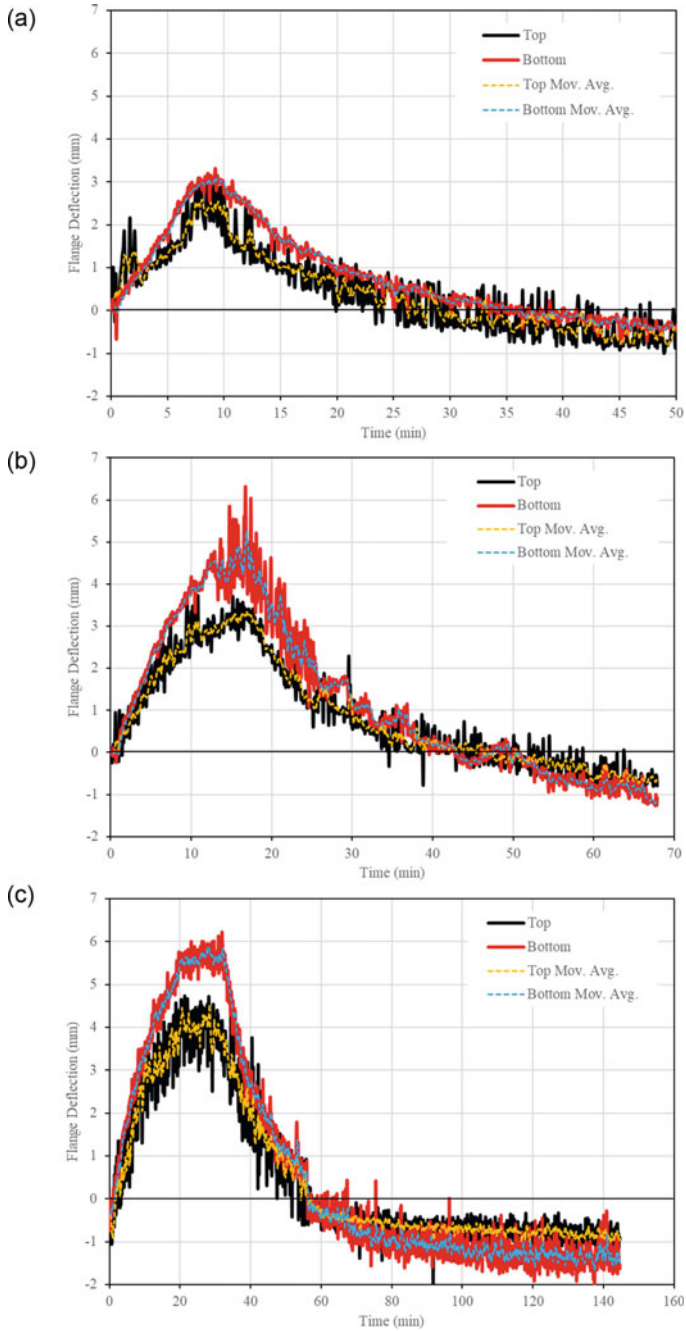
Fig. 5 Deflections at the centre span of the experimental setup for **a** short, **b** medium and **c** long thermal exposures

Table 1 Averaged maximum deflection and upward cambers for each thermal exposure and flange

Thermal exposure	Flange	Maximum deflection (mm)	Maximum upward camber (mm)
Short	Top	2.6	0.8
	Bottom	3.1	0.5
Medium	Top	3.3	0.7
	Bottom	5.3	1.2
Long	Top	4.5	1.0
	Bottom	5.9	1.7

The outward deflections of the columns, as well as other movement within the connections, were also recorded using DIC. These data were not discussed within this paper as it is under development. The outward deflection of the columns will be used to determine the restraining forces being generated within these experiments. There has been limited experimental studies to date that validated the large connection forces experienced due to thermal exposure [5, 6, 23]. To date, the scale of the forces being generated into connections has largely relied on theoretical knowledge. Typically, forces within the range of 1 MN are used for a steel frame building exposed to standard, parametric and travelling fires [26]. The experimental results will be a preliminary step to validate the forces currently used within design, identifying representative forces that could possibly be generated within a steel frame structure.

Additional studies are needed to examine various different configurations of this experimental setup, which would allow for the validation of computational modelling and the forces currently used within fire connection design. This would include experiments with different pool fire locations, different thermal exposures and different connection types. Additional experiments using the current setup are currently underway to ensure the repeatability of the results observed. Future works should include the validation of a finite element analysis model using the experimental series, which would then allow for the undertaking of a parametric study.

5   Conclusion

Practitioners are in need of tools which facilitate the improvement of connection design in order to create resilient infrastructure that can resist thermal loading. When a realistic experimental design is used, it allows for accurate forces and behaviours to be generated. This generates greater understanding of this area which requires additional research. In a fire scenario, the thermal expansion and contraction of beams inflict large restraining forces horizontally on the connections. An experimental programme of three pool fire experiments of various thermal exposures was undertaken to produce preliminary validations of structural fire modelling. The realistic rigidity and stiffness of the experimental setup allowed for accurate forces and behaviours to be generated,

expanding the understanding of the forces and deformations that occur in steel beam-to-column connections. The thermal distribution, centre span deflections and column rotations were recorded during the experiments, using thermocouples and digital image correlation combined with narrow-spectrum illumination. The experimental program outlined above is a preliminary and conceptual research program, which is needed to generate a framework for further testing which will lead to analytical tools and guidance regarding steel connections in fire being developed.

The movement towards alternative solutions and performance-based design in Canada requires more robust codes that include innovations and research progress illustrative of Canadian and international design. The research herein has demonstrated the need to further study the behaviour of steel beam-to-column connections, to ensure safe and resilient infrastructure if exposed to fire.

References

1. Al-Jabri KS, Burgess I, Lennon T, Plank RJ (2005) Moment-rotation-temperature curves for semi-rigid joints. J Constr Steel Res 61:281–303
2. Al-Jabri KS, Lennon T, Burgess I, Plank RJ (1998) Behaviour of steel and composite beam-column connections in fire. J Constr Steel Res 46:308–309
3. Burgess I, Davison JB, Dong G, Huang SS (2012) The role of connections in the response of steel frames to fire. Struct Eng Int: J Int Assoc Bridge Struct Eng (IABSE) 22(4):449–461. https://doi.org/10.2749/101686612X13363929517811
4. Canadian Commision on Building and Fire Codes (2015) National building code of Canada. In: 14th Editi. National Research Council of Canada, Ottawa
5. Choe L, Ramesh S, Grosshandler W, Hoehler M, Seif M, Gross J, Bundy M (2020) Behavior and limit states of long-span composite floor beams with simple shear connections subject to compartment fires: experimental evaluation. J Struct Eng 146(6):04020088. https://doi.org/10.1061/(ASCE)ST.1943-541X.0002627
6. Choe L, Ramesh S, Hoehler M, Seif M, Bundy M, Reilly J, Glisic B (2019) Compartment fire experiments on long-span composite-beams with simple shear connections part 2: Gaithersburg, MD
7. Chorlton B, Forrest B, Gales J, Weckman B (2020) Performance fo type X gyptsum board on timber to non standard fire exposure. Fire Mater 1–16. https://doi.org/10.1002/fam.2822
8. Dai XH, Wang YC, Bailey CG (2010) A simple method to predict temperatures in steel joints with partial intumescent coating fire protection. Fire Technol 46:19–35
9. Emberley R, Nicolaidis A, Fernando D, Torero J (2016) Changing failure modes of cross-laminated timber. Structures in Fire 643–650

10. Gales J, Chorlton B, Jeanneret C (2021) The historical narrative of the standard temperature–time heating curve for structures. Fire Technol 57(2):529–558. Springer US. https://doi.org/10.1007/s10694-020-01040-7

11. Gales J, Green M (2015) Optical characterization of high temperature deformation in novel structural materials. In: Proceedings of the 14th international conference on fire and materials. San Francisco, CA, pp 626–640

12. Gales J, Hartin K, Bisby LA (2016) Structural fire performance of contemporary post-tensioned concrete construction. Springer Briefs in Fire, p 91

13. Gatien S, Young T, Hoehler M, Gales J (2019) Application of narrow-spectrum illumination and image processing to measure surface char formation in lateral ignition and flame spread tests. Fire Mater 43:358–364. https://doi.org/10.1002/fam.2706

14. Hu Y, Davison J, Burgess I, Plank R (2008) Experimental study on flexible end plate connections in fire. Eurosteel, (September):3–5

15. Lawson RM (1990) Behaviour of steel beam-to-column connections in fire. Struct Eng 68:263–271

16. Leston-Jones LC, Lennon T, Plank RJ, Burgess I (1997) Elevated temperature moment-rotation tests on steelwork coneections. In: Proceedings of the ICE—structures and buildings, pp 410–419

17. Mao CJ, Chiou YJ, Hsiao PA, Ho MC (2009) Fire response of steel semi-rigid beam-column moment connections. J Constr Steel Res 65:1290–1303. https://doi.org/10.1016/j.engstruct.2015.01.053

18. Morovat MA, El Ghor AH, Hantouche EG (2018) Time-dependent response of flush endplate connections to fire temperatures. J Struct Eng 144(4):04018023. https://doi.org/10.1061/(asce)st.1943-541x.0002006

19. Nicoletta B (2020) Thermal performance of unloaded spiral strand and locked-coil cables for bridge infrastructure. York University

20. Nicoletta B, Gales J, Kotsovinos P, Weckman B (2021) Experimental thermal performance of unloaded spiral strand and locked coil cables subject to pool fires. Struct Eng Int 1–19. https://doi.org/10.1080/10168664.2021.1881943

21. Nicoletta B, Watson S, Chorlton B, Gales J, Kotsovinos P (2020) Experimental study of unloaded structural steel stay-cables under fire exposure. In: 11th international conference on structures in fire. Brisbane, Australia

22. Rahnavard R, Thomas RJ (2018) Numerical evaluation of the effects of fire on steel connections; part 1: simulation techniques. Case Stud Therm Eng 12:445–453. https://doi.org/10.1016/j.csite.2018.06.003

23. Ramesh S, Choe L, Hoehler M, Grosshandler W, Gross J (2018) Design and construction of long-span composite beam specimens for large structural-fire tests. Structures congress 2018. American Society of Civil Engineers, Reston, VA, pp 151–162

24. Safari P, Broujerdian V (2020) Strategies to increase the survivability of steel connections in fire. Structures 28:2335–2354. https://doi.org/10.1016/j.istruc.2020.10.033

25. Smith C, Hoehler M (2018) Imaging through fire using narrow-spectrum illumination. Fire Technol 54:1705–1723. https://doi.org/10.1007/s10694-018-0756-5

26. Smith M, Gales J (2018) Connection behaviour in contemporary canadian buildings subjected to real fires. In: SFPE performance based design conference, p 6

27. Spyrou S, Davison JB, Burgess I, Plank RJ (2004) Experimental and analytical investigation of the "compression zone" component within a steel joint at elevated temperatures. J Constr Steel Res 60:841–865

28. Spyrou S, Davison JB, Burgess I, Plank RJ (2004) Experimental and analytical investigation of the "tension zone" components within a steel joint at elevated temperatures. J Constr Steel Res 60:867–896

29. Stanier, S., Take, A., Blaber, J., and White, D. 2015. Improved image-based deformation measurement for geotechnical applications. GeoPIV-RG 2015. Canadian Geotechnical Journal,.

30. Underwriters Laboratories of Canada (2014) CAN/ULC-S101–14: standard method of fire endurance tests of building construction materials
31. Wald F, Simões da Silva L, Moore DB, Lennon T, Chladná M, Santiago A, Beneš M, Borges L (2006) Experimental behaviour of a steel structure under natural fire. Fire Saf J 41(7):509–522. https://doi.org/10.1016/j.firesaf.2006.05.006
32. Wang WY, Li GQ, Dong YL (2007) Experimental study and spring-component modelling of extended end-plate joints in fire. J Constr Steel Res 63:1127–1137
33. Wang YC, Davison JB, Burgess IW, Plank RJ, Yu HX, Dai XH, Bailey CG (2010) The safety of common steel beam/column connections in fire. Struct Eng 88(21):26–35
34. Yang KC, Chen SJ, Ho MC (2009) Behavior of beam-to-column moment connections under fire load. J Constr Steel Res 65:1520–1527
35. Yu H, Burgess IW, Davison JB, Plank R (2009a) Tying capacity of web cleat connections inf fire. Part 1: test and finite element simulation. Eng Struct 31(3):651–663
36. Yu H, Burgess IW, Davison JB, Plank RJ (2009b) Experimental investigation of the behaviour of fin plate connections in fire. J Construct Steel Res 65(3):723–736. Elsevier Ltd. https://doi.org/10.1016/j.jcsr.2008.02.015
37. Yu H, Burgess IW, Davison JB, Plank RJ (2011) Experimental and numerical investigations of the behavior of flush end plate connections at elevated temperatures. J Struct Eng 137(1):80–87. https://doi.org/10.1061/(ASCE)ST.1943-541X.0000277

Behavioral Improvement of Steel Plate Shear Walls with Rectangular Openings

Mohammad Sabouri-Ghomi, Anjan Bhowmick, and Saeid Sabouri-Ghomi

Abstract This research investigates the behavior of steel plate shear walls with a rectangular opening. A rectangular opening on the infill plate is often required to accommodate door or window or other utility system to pass through the shear wall. However, steel plate shear walls with rectangular openings are not adequately studied, and there are not many design provisions available for them. In this research, finite-element analyses were carried out on unstiffened models with different sizes of a rectangular opening. A decrease in the shear strength of the panel was observed in all models. Large out-of-plane deformations were also observed around the opening due to the early buckling of the infill plate. As a solution to this problem, stiffeners were attached to the models and the models were analyzed again. Various arrangements of stiffeners were considered for the models and the effectiveness of each arrangement on preventing the deformation of the opening was studied. The results showed that attaching stiffeners to the plate is an effective method to prevent the out-of-plane deformation of the opening as well as increase the shear strength of the panel. Based on the obtained results, recommendations for the best stiffener arrangement that is most effective in preventing the overall deformation around the opening are presented.

1 Introduction

Steel plate shear wall (SPSW) is an effective lateral load resisting system used in moderate-to-high seismic region. This system has been shown to have high strength and stiffness and large energy dissipation capacity [3–5, 9, 10, 17]. Both American [1] and Canadian steel design standard (CSA S16-14) have adopted SPSW system. One

M. Sabouri-Ghomi · A. Bhowmick (✉)

Department of Building, Civil and Environmental Engineering, Concordia University, Montreal, QC, Canada

e-mail: anjan.bhowmick@concordia.ca

S. Sabouri-Ghomi

Department of Civil Engineering, K.N. Toosi University of Technology, Tehran, Iran

137

of the important advantages of a steel plate shear wall system (SPSW) is the option to provide openings on the infill plate. Rectangular openings are regularly required by architectural design for nonstructural elements such as windows or doors. Despite the common need for such an option, this type of SPSW has not been studied thoroughly, especially in the case of rectangular openings. The current Canadian standard [8] does not provide any provisions for steel plate shear walls with openings. Studying this option and providing structural engineers with the required guidelines can help the SPSW system to reach its true potential as a reliable lateral load resisting system.

Studies on the effects of openings on SPSW systems began in 1992. Roberts and Sabouri-Ghomi [14] conducted a series of experimental tests on steel plate shear walls with a circular opening at the center of the plate. Their results showed a reduction in shear stiffness and strength of the panels when openings are introduced to the panel. Based on the results, a conservative linear reduction factor was suggested to calculate the shear strength and stiffness of perforated panels.

$$V_{\mathrm{op}} = V_p(1 - D/b) \tag{1}$$

In this equation, V_p is the strength of the solid panel and V_{op} is the strength of the panel with opening, b is the length of the panel and D is the diameter of the opening.

Numerical studies also confirm the reduction of shear strength of SPSWs with openings. Purba and Bruneau [13] studied a single-storey SPSW with a series of small circular perforations. Their study showed the same effect on the shear strength of the panel and they calibrated the linear reduction factor for the specific form of perforations. Numerical and experimental studies on this type of regularly placed perforations were also conducted by other researchers [2, 12, 18, 19]. Design recommendations were provided by the authors for this type of special perforation. Investigations by [6] and [7] on a number of single-storey and multi-storey finite-element models with circular perforations also proposed reduction factor that can approximately predict the strength of the plate with circular perforations.

One of the known methods to improve the behavior of the system is using stiffeners. Stiffened steel plate shear walls are proven to have higher shear strength, stiffness and energy dissipation capacity. Results from experimental studies by [15] showed these effects. They also provided a design criteria for stiffeners to prevent the global buckling of the plate and force it into local buckling mode [16]. This mode occurs when the buckling takes place in the sub panels of the plate created by stiffeners. Seismic performance of stiffened SPSWs was studied by [11], and their results revealed that the currently used force modification factors in seismic design for unstiffened plates can also be used for stiffened SPSWs.

2 Finite-Element Model for Steel Plate Shear Walls

In this research, several finite-element models with different features were analyzed using ABAQUS software. In order to make sure the modeling approach was correct, a model was created based on a previous experimental study on stiffened SPSW [15]. The length, height and thickness of the infill plate in the experiment were 1410 mm, 960 mm and 2 mm, respectively. Four stiffeners with a width of 60 mm and a thickness of 4 mm were attached to the plate. The test model was subjected to cyclic loading at the top. To model the frame, infill plate and stiffeners, 4-node general-purpose shell (S4R) element was used. The top beam was restrained against out-of-plane displacement and the base of the model was fixed to the ground. Similar to the experiment, cyclic loading was applied to the two ends of the top beam. Since the geometry of the model is not complex, a structured mesh control was assigned to the model. A mesh sensitivity study was conducted and finally a global mesh size of 40 mm was selected for all elements (beams, columns and infill plates) of the SPSW model. Figure 1 shows the model and the meshing and Fig. 2 shows the results. A comparison of the results shows good agreement between the FEA and experiment.

Fig. 1 Finite-element model and the mesh created for validation
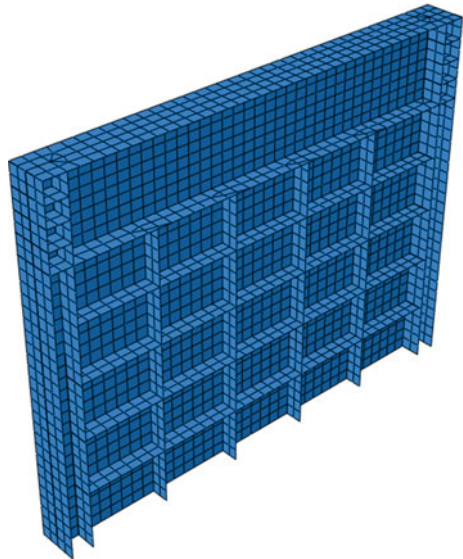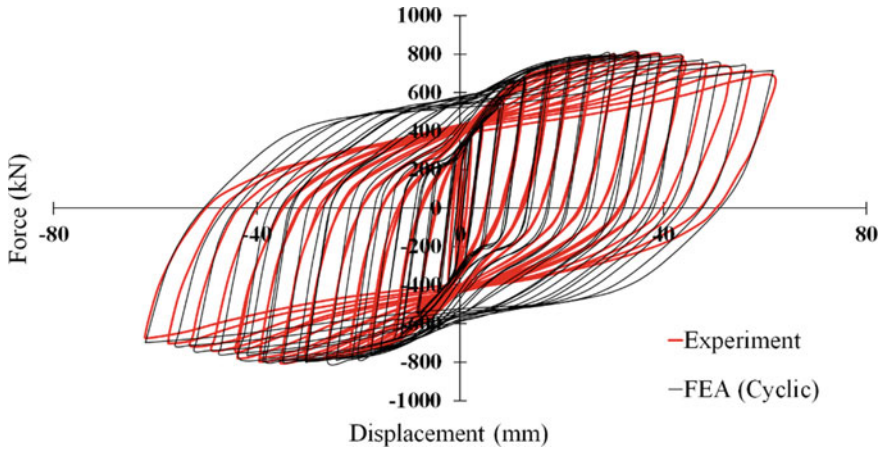
Fig. 2 Cyclic shear force displacement plots for validation

3 Analysis of Unstiffened SPSWs with a Centrally Placed Rectangular Opening

In order to understand the fundamental behavior of steel plate shear walls with rectangular openings, five finite-element models with different opening sizes were analyzed. The infill plate in these models is unstiffened and a rectangular opening is placed in the center of the plate. The material properties for the plate and boundary elements are shown in Table 1. All models have an identical plate and boundary frame sizes that are presented in Table 2.

Nonlinear pushover analysis was conducted on each model with a target drift of 4%. A model without an opening was also analyzed for comparison purposes. Before each analysis, eigenvalue buckling analysis was conducted on the model, and then according to the results, an out-of-plane displacement was applied to the models as an imperfection to initiate buckling in the plate.

Table 1 Material properties for the FE models

Element	Yield stress (MPa)
Infill plate	250
Stiffeners	250
Columns	350
Beam	350

Table 2 Plate dimensions and frame sections for the finite-element models

Plate height (m)	Plate width (m)	Plate thickness (MM)	Column section	Beam section
3.8	6	3	W360 × 262	W460 × 193

The results of the six FE analyses are shown in Table 3 and Fig. 3. Table 3 presents the name of each model, opening dimensions and the maximum value of out-of-plane displacement around the opening (U3) obtained from FE analysis. Figure 3 compares the obtained pushover curves for the models. As expected, decrease in shear strength and initial stiffness can be observed in all models. As the opening size increases, these parameters decrease more significantly. In the model with the smallest opening, the shear strength is around 94% of the solid model. In the model with the largest opening, shear strength drops to around 41% of the panel without opening. Calculating the reduction factor in Eq. 1 for this model by assuming D as the diameter of the rectangular opening will also result in a value equal to 0.41, which shows that using the reduction factor will lead to correct results.

As shown in Table 3, large out-of-plane deformations take place around the opening due to early buckling of the infill plate. Figure 4 shows model Unstf-Op40% as an example. It is also observed that the amount of out-of-plane deformation is increased as the size of the opening is increased.

Table 3 Opening dimensions and the obtained maximum value of out-of-plane displacement around the opening of the unstiffened models

Model name	Opening length (mm)	Opening height (mm)	Maximum U3 around the opening (mm)
Unstf-Op10%	600	380	120
Unstf-Op20%	1200	760	115
Unstf-Op30%	1800	1140	176
Unstf-Op40%	2400	1520	191
Unstf-Op50%	3000	1900	209
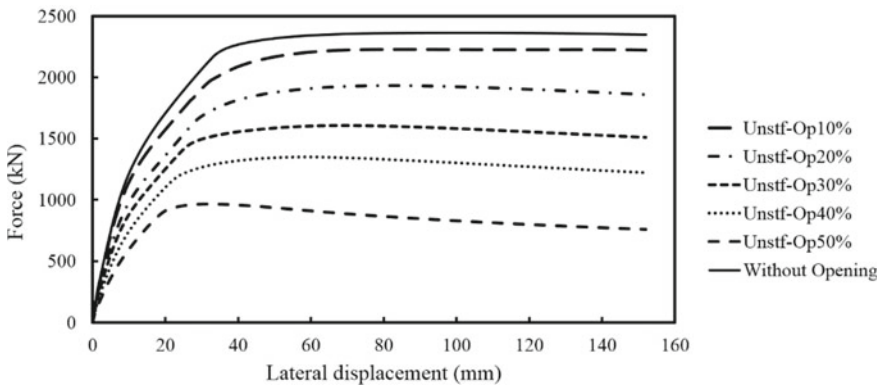
Fig. 3 Comparison of pushover curves for the unstiffened FE models with different opening sizes
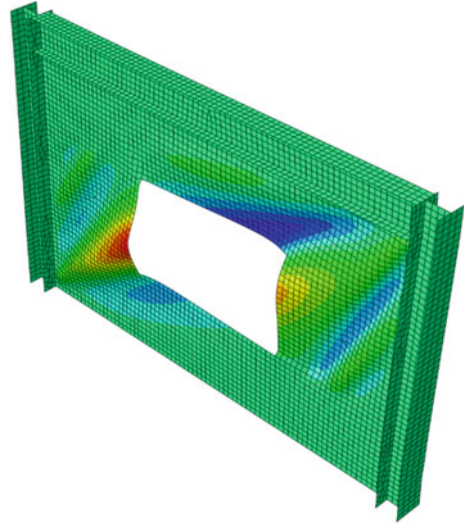
4   Analysis of Stiffened SPSWs with a Centrally Placed Rectangular Opening

The objective of this part of the study was to prevent the deformation around the opening and improve the behavior of the system. As discussed before, using stiffeners can prevent the global buckling of the plate; therefore, adding stiffeners to the infill plate was the selected solution for this purpose. The number of required stiffeners and their arrangement around the opening are investigated in this part. Four different stiffener arrangements are considered for this purpose. These arrangements are presented in Fig. 5. The goal of these arrangements was to use as few stiffeners as possible and improve the behavior of the plate without heavily reinforcing it.

For all the arrangements, stiffeners were attached to both sides of the infill plate. Similar to the unstiffened models, five FE models with different opening sizes were analyzed for each type of arrangement. For all the models, the width and thickness
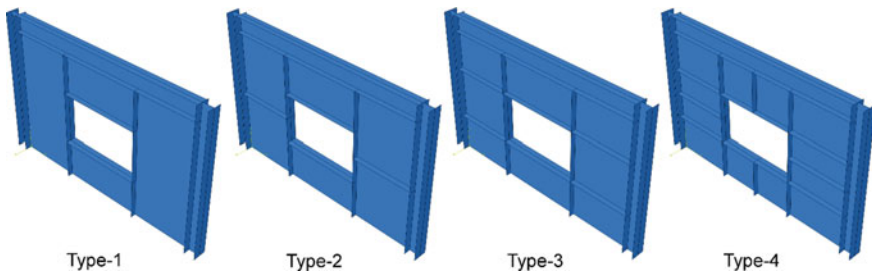
Fig. 5 The four different types of stiffener arrangements considered for the study

of the stiffeners on each side were, respectively, 120 and 7 mm. The dimensions for stiffeners were acquired by selecting an initial size and then gradually increasing it until the global buckling was prevented. The results of the analyses are presented in Table 4.

It is evident from the results that adding stiffeners to the system has a significant effect on the out-of-plane deformation around the opening. In all four of the considered arrangements, the out-of-plane deformation significantly decreased compared to the unstiffened models. The results show that in almost all models the amount of out-of-plane deformation is limited to under 10 mm. Figure 6 shows an example of deformation for each of the considered types.

Although all the four types of arrangements are found to be very effective in preventing the out-of-plane deformation around the opening, type-4 was found to provide the best results. In addition to this, type-4 was also found to be most effective in limiting the in-plane deformation around the opening. Therefore, the type-4 arrangement was selected as the best arrangement for this study. This arrangement has two full vertical and two full horizontal stiffeners covering the four sides

Table 4 Opening dimensions and the obtained maximum out-of-plane displacement around the opening of the stiffened models

Model name	Opening length (mm)	Opening height (mm)	Maximum U3 around the opening (mm)
Type1-Op10%	600	380	4.6
Type1-Op20%	1200	760	1.9
Type1-Op30%	1800	1140	1.3
Type1-Op40%	2400	1520	2.6
Type1-Op50%	3000	1900	6.4
Type2-Op10%	600	380	1.1
Type2-Op20%	1200	760	1.2
Type2-Op30%	1800	1140	3.5
Type2-Op40%	2400	1520	2.3
Type2-Op50%	3000	1900	16.5
Type3-Op10%	600	380	1.2
Type3-Op20%	1200	760	0.4
Type3-Op30%	1800	1140	5.1
Type3-Op40%	2400	1520	0.2
Type3-Op50%	3000	1900	3
Type4-Op10%	600	380	0.2
Type4-Op20%	1200	760	2.7
Type4-Op30%	1800	1140	2.3
Type4-Op40%	2400	1520	0
Type4-Op50%	3000	1900	4.2
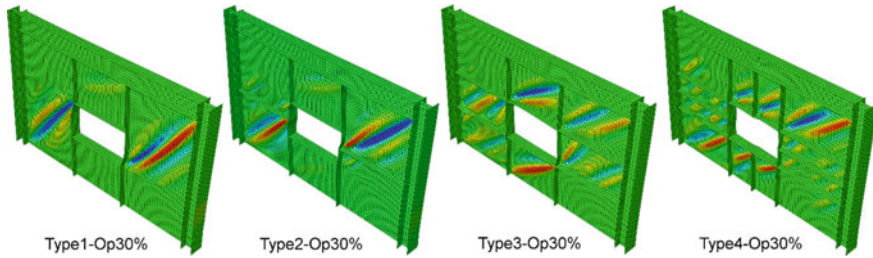
Fig. 6 Examples of deformation for each of the considered arrangements

of the opening and four short stiffeners placed at the middle of each side of the opening. Figure 7 shows the comparison between the pushover curves for the selected arrangement, unstiffened plates and the plate without opening.

As it is observed in the figure, adding the stiffeners will improve the behavior of the system significantly. Shear strength and stiffness are increased in stiffened plates;
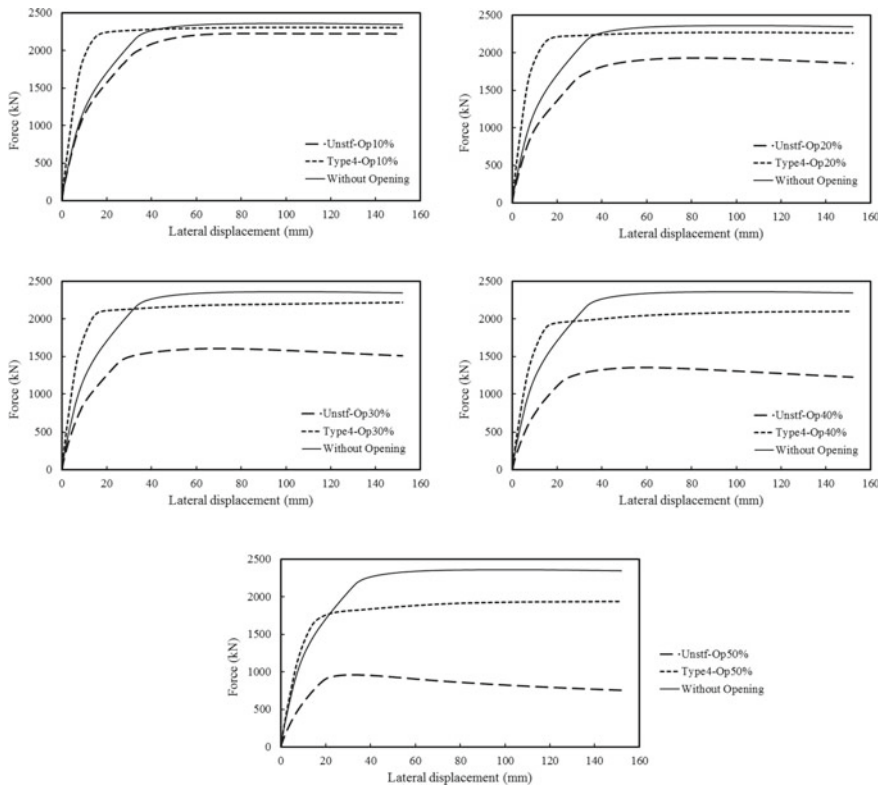
Fig. 7 Comparison between the pushover curves for the stiffened and unstiffened plates with the same opening size

therefore, the negative effects due to having an opening are reduced when stiffeners are installed on the infill plate. The positive effect of using stiffened plates becomes much more apparent when the size of the opening increases. In the plate with the largest opening, attaching stiffeners increased the shear strength of the plate from 41% to around 82% of the solid plate. It also limited the amount of out-of-plane displacement around the opening from more than 200 mm to less than 5 mm.

5　Conclusions

A series of finite-element analyses were performed on unstiffened and stiffened steel plate shear walls with rectangular openings. Five different sizes for openings were considered. The results for unstiffened plates showed a decrease in shear strength and stiffness especially in models with larger openings. In addition to this, large out-of-plane deformations were observed around the openings due to the buckling of the infill plates.

Attaching stiffeners to the infill plate is proposed as a solution to reduce the negative effects of rectangular openings. Four different configurations of stiffeners were studied and the one providing the best results was found. This solution uses four full stiffeners and four short stiffeners to prevent the buckling of the plate. It was observed that using this type of stiffeners would limit the out-of-plane deformation around the opening to lower than 5 mm. Additionally, using this arrangement increased the shear strength and stiffness of infill plates with rectangular openings significantly.

References

1. AISC 341–16 (2016) Seismic provisions for structural steel buildings. American Institute of Steel Construction, Chicago, IL
2. Barua K, Bhowmick AK (2019) Nonlinear seismic performance of code designed perforated steel plate shear walls. Steel Compos Struct 31(1):85–98
3. Bhowmick AK, Driver RG, Grondin GY (2008) Nonlinear seismic analysis of steel plate shear walls considering strain rate and P-Delta effects. J Constr Steel Res 65(5):1149–1159
4. Bhowmick AK, Grondin GY, Driver RG (2010) Performance of type D and Type LD steel plate walls. Can J Civ Eng 37(1):88–98
5. Bhowmick AK, Driver RG, Grondin GY (2011) Application of indirect capacity design principles for seismic design of steel-plate shear walls. J Struct Eng 137(4):521–530
6. Bhowmick A (2014) Seismic behavior of steel plate shear walls with centrally placed circular perforations. Thin-Walled Struct 75:30–42
7. Bhowmick AK, Grondin G, Driver R (2014) Nonlinear seismic analysis of perforated steel plate shear walls. J Constr Steel Res 94:103–113

8. CSA (2014) CAN/CSA-S16–14 limit states design of steel structures. Mississauga, ON, Canada: Canadian Standards Association
9. Dhar MM, Bhowmick A (2016) Seismic response estimation of steel plate shear walls using nonlinear static methods. Steel Compos Struct 20(4):777–799
10. Driver RG, Kulak G, Kennedy DJL, Elwi A (1998) Cyclic test of four-story steel plate shear wall. ASCE J Struct Eng 124(2):112–120
11. Farahbakhshtooli A, Bhowmick AK (2019) Seismic collapse assessment of stiffened steel plate shear walls using FEMA P695 methodology. Eng Struct 200:109714
12. Farahbakhshtooli A, Bhowmick AK (2021) Nonlinear seismic analysis of perforated steel plate shear walls using a macro-model. Thin-Walled Struct 166:108022
13. Purba R, Bruneau M (2009) Finite-element investigation and design recommendations for perforated steel plate shear walls. J Struct Eng 135(11):1367–1376
14. Roberts T, Sabouri-Ghomi S (1992) Hysteretic characteristics of unstiffened perforated steel plate shear panels. Thin-walled Struct 14:139–151
15. Sabouri-Ghomi S, Sajjadi SRA (2012) Experimental and theoretical studies of steel shear walls with and without stiffeners. J Constr Steel Res 75:152–159
16. Sabouri-Ghomi S, Kharrazi MH, Mam-Azizi SED, Sajadi RA (2008) Buckling behavior improvement of steel plate shear wall systems. Struct Design Tall Spec Build 17(4):823–837
17. Thorburn L, Kulak G, Montgomery C (1983) Analysis and design of steel shear wall systems. Structural engineering report 107, Department of Civil Engineering, University of Alberta, Canada
18. Vian D, Bruneau M, Purba R (2009) Special perforated steel plate shear walls with reduced beam section anchor beams. II: analysis and design recommendations. J Struct Eng 135(3):221–228
19. Vian D, Bruneau M, Tsai KC, Lin YC (2009) Special perforated steel plate shear walls with reduced beam section anchor beams. I: experimental investigation. J Struct Eng 135(3):211–220

Design and Assessment of Steel Pipe Rack Moment Connections with Emphasis on Web Doubler Plates

Hana Chaya, Ali Imanpour, Robert Driver, and Brett Morgan

Abstract This paper illustrates design and detailing of steel moment connections in pipe racks and evaluates the response of the connection under expected loading scenarios, using the component-based finite element method with emphasis on the web doubler plates. Several alternative designs with emphasis on web doubler plate details are proposed with the objective of improving fabrication efficiency of pipe rack moment connections in the shop. The alternatives focus mainly on using doubler plates singly or in pairs, and the corresponding dimensions with different weld types. The findings confirm that design and fabrication of modular pipe rack moment connections can be enhanced using two-sided reduced doubler plates fillet-welded to the column web, provided that a set of thresholds are defined to limit the application of such detail based on the forces induced in the connection.

Keywords Steel pipe rack · Moment connections · Web doubler plates

1 Introduction

Pipe-supporting structures, commonly referred to as pipe racks, are heavy steel structures used extensively in refineries, chemical plants, and oil sands facilities in Canada. Due to similar loading conditions along the network, they are often broken into repetitive volumetric modules that can be prefabricated off-site and shipped to the construction site for assembly. Modularization can reduce the fabrication and construction costs even though the tonnage typically increases by about 30% [6]. The beams and columns of the modules are often made of wide-flange shapes. They carry the anticipated loads using a gravity load-resisting system combined with concentrically braced frames and moment-resisting frames [7, 8] to resist lateral loads. As

H. Chaya (✉) · A. Imanpour · R. Driver
University of Alberta, Edmonton, Canada
e-mail: hchaya@ualberta.ca

B. Morgan
WF Steel & Crane, Nisku, Canada

opposed to building applications, beam-to-column moment connections in pipe rack modules often involve multiple stiffeners designed to resist complex combinations of torsion, axial forces, and both strong- and weak-axis moments, in addition to serving as the connection points for attachments. This complexity tends to lead to expensive connection details and labour-intensive tasks. Moreover, web doubler plates are often required to transfer flexural bending from the beam to the column when the thickness of the column web is not sufficient to carry the moments in the connection through panel shear, which further complicates the connection detail and increases the fabrication cost of already costly connections.

This paper first illustrates the design of a prototype beam-to-column moment connection with emphasis on the web doubler plates typically used in steel pipe racks in the province of Alberta. Potential alternative details are then illustrated. The stress distributions in the doubler plates of the baseline detail plus four design alternatives are finally evaluated using the component-based finite element approach under loading scenarios expected in steel pipe rack structures.

2   Moment Connections in Steel Pipe Racks

The fabrication of steel pipe racks involves labor-intensive tasks, including cutting, drilling, fitting, welding, crane operations, and assembly. Complex connections are expected in such structures to resist permanent loads such as gravity plus other potential loading scenarios such as hydraulic and wind that could arise during the life of the structure. Other loads that factor into the design of pipe racks' connections include thermal loads resulting from contraction or expansion due to the changes in ambient temperature during operation, anchor loads that arise from the restraints to displacements or rotations imposed during operating conditions, friction loads which can result from sliding pipes, erection loads, and impact loads [6]. As such, stiffeners and complex welding details are used in the connection of modules, which leads to substantial added costs to the fabrication of pipe racks. Beam-to-column moment connections in pipe racks often involve multiple stiffeners designed to resist torsion, weak-axis bending, and additional attachments, which lead to expensive connection details since the complex connection details can significantly impact fabrication costs and scheduling.

Despite the extensive use of heavy pipe-supporting structures in Canada, particularly in natural resource development regions such as Alberta, limited information and guidelines are available in practice for design and detailing of their connections given that pipe racks involve various complex loading conditions and design considerations [9]. In lieu of a unified design procedure, steel fabricators typically develop their own design methods and spreadsheets, which may lack technical justifications or lead to uneconomical fabrication processes [6]. Additional and updated design guides with the knowledge of all the parameters and design mechanisms are needed so that consistent design methods can be used throughout the industry [9].

Fig. 1 Typical pipe rack beam-to-column connection detail
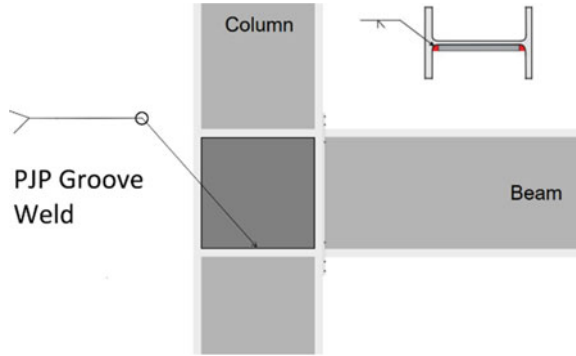
3 Current Design Practice

3.1 Connection Components

To transfer the demands, including bending, axial force and shear, from beams to the column in pipe racks, welded end plate beam-to-column connections, as shown in Fig. 1, are typically used. Web doubler plates are required when the thickness of the column web is not sufficient to transfer the beam moment, which induces a large shear in the column web. Groove welds are typically used to attach the web doubler plates to the column radius in the connection region, as shown in Fig. 1. The detail and type of weld can vary from fabricator to fabricator because of the challenges associated with the implementation of such welds in the K-region of the column section. The industry partner of this study (WF Steel & Crane) uses a detail that can be treated as a PJP weld due to the welding position and the lack of surface preparation and inspection.

3.2 Pipe Rack Moment Connection Design

The structural design of the pipe rack moment connection shown in Fig. 2 is illustrated here. The design is performed in accordance with the provisions of the Canadian steel design standard CSA S16, AISC 360-16, AISC Design Guides 4, 13, 16, and Australian Steel Institute Design Guide (DG) 11. The beam and column consist of wide-flange sections conforming to 350 W steel with the yield strength $F_y = 350$ MPa. The selected sections for the beam and column are a W310 × 79 and a W250 × 73, respectively.

Four load cases representing various loading conditions were evaluated and the design steps under the most critical load case are presented. The load case includes a strong-axis moment, a weak-axis moment, a shear force, and an axial force applied at the face of the column. The connection design loads are presented in Table 1.

End plate: 260x3/4"x510 Gr.300W
Flange weld: 8 FW/490 - Web weld: 6 FW/490
Bolts: 10 x 1" A325PT/N in 2 cols. at 130 gauge
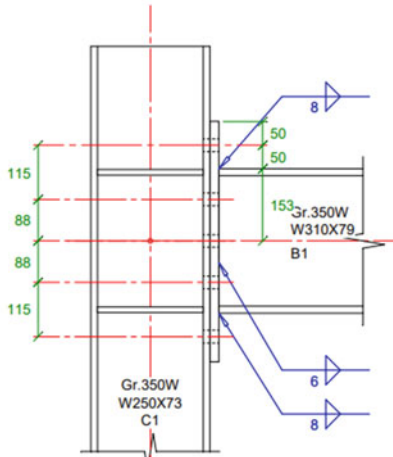
Stiffeners:
Top: 120x1/2"x224.6 Gr.300W - Weld=6 FW/490 Side=full End=full
Web doubler one side: 203x3/8"x260 Gr.300W CJPGW all around
Btm.: 120x1/2"x224.6 Gr.300W - Weld=6 FW/490 Side=full End=full

Plates: 34.5 kg
Bolts: 9.2 kg
Welds: 1.4 kg

Fig. 2 End plate moment connection used in pipe rack structure

Table 1 Connection design loads		Design loads	
Axial tension in the flanges	P_{uft}	701.7 kN	
Axial tension in the web	P_{uwt}	48.7 kN	
Axial compression in the flanges	P_{ufc}	550.4 kN	
Axial compression in the web	P_{uwc}	0 kN	
Connection design moment	M_{uw}	17.6 kN m	
Connection design shear	V_{uw}	250.0 kN	
End plate design moment	M_{ueq}	229.1 kN m	
Column web panel shear	V_{up}	706.3 kN	
Stiffener design tension	P_{uts}	267.5 kN	

The design steps for the connection of Fig. 2 are as follows:

Step (1)   Design the beam web fillet following S16 Clause 13.13.2.2:

$$V_r = 0.67\phi_w A_w X_u \left(1.00 + 0.5 \sin^{1.5} \theta\right)$$
$$V_r = 931.7\,\text{kN} > P_{uft} = 701.7\,\text{kN}$$
$$V_r = 931.7\,\text{kN} > P_{ufc} = 550.4\,\text{kN} \tag{1}$$

where V_r is the factored weld resistance for direct shear and tension- or compression-induced shear. A_w is the area of the fillet weld, X_u is the

weld ultimate tensile strength, and θ is the angle of the weld segment axis with respect to the line of action of the applied force [8].

Step (2) Check the bolt tensile strength to carry the applied moment following AISC DG4 2.7:

$$M_{np} = n P_t \sum_{i=1}^{N} h_i$$

$$M_{np} = 365.2 \, \text{kNm} > M_{ueq} = 229.1 \, \text{kNm} \tag{2}$$

where M_{np} is the nominal connection moment strength for the limit state of bolt fracture with no prying action, n is the number of bolts in each row, N is the number of bolt rows, h_i is the distance from the centreline of the compression flange to the centreline of the bolt row, and P_t is the bolt tensile strength [2].

Step (3) Check the bolt shear strength under the applied shear force following AISC DG4 3.17:

$$R_n = \phi n_b F_v A_b$$

$$\phi R_n = 561.8 \, \text{kN} > V_{uw} = 250 \, \text{kN} \tag{3}$$

where ϕR_n is the bolt shear strength, $\phi = 0.75$, n_b is the number of bolts at the compression flange (the bolt shear rupture strength of the connection is conservatively assumed to be provided by the bolts at the compression flange), and F_v is the nominal shear strength of the bolts [1, 2].

Step (4) Check the bolt bearing/tear-out failure at the end plate and column flange under the applied shear following AISC DG4 3.18:

$$R_n = (n_i)\phi R_n (\text{Inner Bolts}) + (n_o)\phi R_n (\text{Outer Bolts})$$

$$\phi R_n = 2090.3 \, \text{kN} > V_{uw} = 250 \, \text{kN} \tag{4}$$

where ϕR_n is the end plate bolt bearing strength, n_i is the number of inner bolts (bolts between the beam flanges shown in Fig. 2), n_o is the number of outer bolts (bolts above and below the beam flanges shown in Fig. 2), R_n is equal to $\min[1.2 L_c t F_u, 2.4 d_b t F_u]$ for each bolt, L_c is the clear distance in the direction of the force between the edge of the hole and the edge of the adjacent hole or edge of the material, t is the end plate or column flange thickness, F_u is the specified minimum tensile strength of the end plate or column flange material, and d_b is the diameter of the bolt [2].

Step (5) Check the end plate yield strength following the plastic mechanism method specified in AISC DG4 Table 3.1 (Fig. 3):

$$\phi M_{pl} = \phi_b F_{yp} t_p^2 Y_p$$

| Geometry | Yield-Line Mechanism | Bolt Force Model |
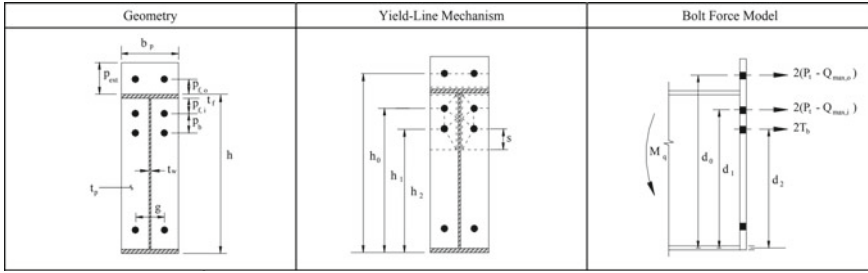
Fig. 3 Plastic yield line analysis of unstiffened end plate moment connections (AISC Design Guide 16)

$$\phi M_{pl} = 234.1 \,\text{kNm} > M_{ueq} = 229.1 \,\text{kNm} \qquad (5)$$

where ϕM_{pl} is the nominal connection strength for the limit state of end plate yielding, $\phi_b = 0.9$, F_{yp} is the end plate material yield strength, t_p is the end plate thickness, and Y_p is the yield line parameter as shown in Fig. 3 [4].

Step (6) Calculate the end plate no-prying thickness under the applied moment following AISC DG4 3.7:

$$t_{p\,\text{Req'd}} = \sqrt{\frac{1.11\phi M_{np}}{\phi_b F_{yp} Y_p}}$$

$$t_{p\,\text{Req'd}} = 25 \,\text{mm} > t_p = 19 \,\text{mm, bolt prying occurs} \qquad (6)$$

where $t_{p\,\text{Req'd}}$ is the required end plate thickness, $\phi = 0.75$, $\phi_b = 0.9$, and M_{np} is the no-prying moment for bolt strength [2].

Step (7) Check bolt rupture following AISC DG16 [4] as given in Fig. 3 and Table 2:

$$\phi M_n = 281.8 \,\text{kN} > M_{ueq} = 229.1 \,\text{kN}$$

where ϕM_n is the nominal connection strength for the limit state of bolt rupture with prying action, P_t is the bolt tensile strength, T_b is the bolt pretension force, $Q_{\max,i}$ is the maximum possible bolt prying force in the tension bolts between the beam flanges, $Q_{\max,o}$ is the maximum bolt prying force in tension bolts outside the beam flanges, and w' is the effective width of the end plate per bolt minus the bolt hole diameter.

Step (8) Check the horizontal shear yield strength of the extended portion of the end plate under the applied shear force in accordance with AISC DG4 3.12:

$$\phi R_n = \phi 0.6 F_{yp} b_p t_p$$

Table 2 Bolt rupture strength of unstiffened end plate moment connections (Adapted from AISC Design Guide 16)

End plate yield	$\phi M_n = \phi_b M_{pl} = \phi_b F_{yp} t_p^2 Y$
	$Y = \dfrac{b_p}{2}\left[h_1\left(\dfrac{1}{p_{f,i}}\right) + h_2\left(\dfrac{1}{s}\right) + h_0\left(\dfrac{1}{p_{f,o}}\right) - \dfrac{1}{2} \right]$
	$+ \dfrac{2}{g}\left[h_1\left(p_{f,i} + 0.75 p_b\right) + h_2\left(s + 0.25 p_b\right) \right] + \dfrac{g}{2}$
	$s = \frac{1}{2}\sqrt{b_p g}$ Note: Use $p_{f,i} = s, if p_{f,i} > s$
	$\phi_b = 0.90$
Bolt rupture w/prying action	$\phi M_n = \phi M_q$
	$= \max \begin{vmatrix} \phi\left[2\left(P_t - Q_{\max,o}\right)d_0 + 2\left(P_t - Q_{\max,i}\right)d_1 + 2T_b d_2\right] \\ \phi\left[2\left(P_t - Q_{\max,o}\right)d_0 + 2T_b\left(d_1 + d_2\right)\right] \\ \phi\left[2\left(P_t - Q_{\max,i}\right)d_1 + 2T_b\left(d_0 + d_2\right)\right] \\ \phi\left[2T_b\left(d_0 + d_1 + d_2\right)\right] \end{vmatrix}$
	$\phi = 0.75$
Bolt rupture no prying action	$\phi M_n = \phi_b M_{pl} = \phi[2P_t(d_0 + d_1 + d_2)]$ $\phi = 0.75$

$$\phi R_n = 802.4\,\text{kN} > V_{uw} = 250\,\text{kN} \tag{7}$$

where ϕR_n is the shear yielding resistance in kN, $\phi = 0.9$, and b_p is the width of the end plate [2].

Step (9)   Check the shear rupture resistance of the extended portion of the end plate under the applied shear force following AISC DG4 3.13:

$$\phi R_n = \phi 0.6 F_{up} A_n$$
$$\phi R_n = 953.7\,\text{kN} > V_{uw} = 250\,\text{kN} \tag{8}$$

where ϕR_n is the shear rupture resistance, $\phi = 0.75$, F_{up} is the minimum tensile strength of the end plate, A_n is the net area of the end plate [3].

Step (10)   Check the flexural yielding limit state of the column flange under the applied bending moment as per AISC DG4 3.21:

$$\phi M_{cf} = \phi_b F_{yc} Y_c t_{fc}^2$$
$$\phi M_{cf} = 151.2\,\text{kNm} > M_{ueq} = 229.1\,\text{kN} \tag{9}$$

where ϕM_{cf} is the unstiffened column flange yielding strength, $\phi_b = 0.9$, F_{yc} is the specified yield stress of column flange material, Y_c is the unstiffened column flange yield line mechanism parameter, and t_{fc} is the column flange thickness [2].

Step (11) Check the unstiffened column web yielding at both beam tension and compression flanges under the applied tension load in the flange following AISC DG13 2.2-11:

$$\phi R_n = 1.0 \times \left[C_t \left(6k + 2t_p \right) + N \right] F_y t_w$$
$$\phi R_n = 750.4 \, \text{kN} > P_{uft} = 701.7 \, \text{kN}$$
$$\phi R_n = 750.4 \, \text{kN} > P_{ufc} = 550.4 \, \text{kN} \qquad (10)$$

where ϕR_n is the local web yielding strength, t_w is the column web thickness, F_y is column specified minimum yield strength, k is the distance from the outside face of the column flange to the web toe of the flange-to-web fillet, N is the beam flange thickness plus $2w$ in mm for a directly welded moment connection, w is the leg size of the fillet weld or groove weld reinforcement used, and $C_t = 0.5$ if the distance from the column end to the closer face of the beam tension flange is less than the column depth and $C_t = 1.0$ otherwise [3].

Step (12) Check the local web crippling strength under the applied compression load in the flange as per AISC DG13 2.2-12:

$$\phi R_n = 0.75 \times 135 C_t t_w^2 \left(1 + N_d \left(\frac{t_w}{t_f} \right) \right) \sqrt{\frac{F_y t_f}{t_w}}$$
$$\phi R_n = 660.2 \, \text{kN} > P_{ufc} = 550.4 \, \text{kN} \qquad (11)$$

where ϕR_n is the column web crippling strength, $C_t = 0.5$ if the distance from the column end to the closer face of the beam compression flange is less than half the column depth and $C_t = 1.0$ otherwise, t_f is the column flange thickness, and $N_d = 3N/d_c$ if the distance from the column end to the closer face of the beam tension flange is either (1) greater than or equal to half the column depth or, (2) less than $d_c/2$ and N/d_c is less than or equal to 0.2, and $N_d = (4N/d_c - 0.2)$ otherwise [3].

Step (13) Check the column web buckling strength following AISC DG13 2.2-13:

$$\phi R_n = 0.9 \times \frac{4100 C_t t_w^3 \sqrt{F_y}}{h}$$
$$\phi R_n = 596.2 \, \text{kNm} > P_{ufc} = 550.4 \, \text{kN} \qquad (12)$$

where ϕR_n is the column web buckling strength and $h = d_c - 2k$ (AISC Design Guide 13 2003).

Step (14) Check the unstiffened column web yielding at both beam tension and compression flanges as per AISC DG13 2.2-1 and 2.2-2:

$$\phi R_v = \begin{cases} 0.9 \times 0.6 F_y d_c t_w & P_u \leq 0.4 P_y \\ 0.9 \times 0.6 F_y d_c t_w \left(1.4 - \frac{P_u}{P_y}\right) & P_u > 0.4 P_y \end{cases}$$

$$\phi R_v = 815.3 \,\text{kN} > 706.3 \,\text{kN} \tag{13}$$

where ϕR_v is the panel zone shear strength, P_u is the column required axial strength, and P_y is the column axial yield strength, which is equal to the column yield strength multiplied by the area of the column web [3].

Step (15) Check the transverse stiffener yielding at the beam tension flange following ASI DG 11, 12.2:

$$\phi R_{fts} = 0.9 A_s f_{ys}$$
$$\phi R_{fts} = 720.1 > P_{uts} = 267.5 \,\text{kN} \tag{14}$$

where ϕR_{fts} is the stiffener's yield strength, A_s is the total cross-sectional area of stiffeners, and f_{ys} is the yield stress of the stiffener [5].

Step (16) Check the stiffened column flange bending strength at the beam tension flange under the applied moment following AISC DG4 Table 3.4:

$$\phi M_{cf} = \phi_b F_{yc} t_{fc}^2 Y_{cs}$$
$$\phi M_{cf} = 232.3 \,\text{kNm} > M_{ueq} = 229.1 \,\text{kNm} \tag{15}$$

where ϕM_{cf} is the stiffened column flange bending strength, $\phi_b = 0.9$, F_{yc} is the specified yield stress of column flange material, Y_{cs} is the stiffened column flange yield line mechanism parameter, and t_{fc} is the column flange thickness [2].

The critical limit state among the 16 checks performed here was the stiffened column flange strength, check 16, with a utilization ratio of 99%. Table 3 summarizes the dimensions and weld sizes of the connection plates and stiffeners of the connection of Fig. 2.

4 Alternative Designs

Several alternative connection designs with the focus on the column doubler plate detail are proposed here to improve the economy of doubler plates in steel pipe racks. These details are based on the proposed details in past studies, e.g. steel moment-resisting frames under seismic loads, and the discussion with WF Steel & Crane. The proposed details include (1) doubler plates fillet-welded to the column web (Fig. 4a); (2) continuous doubler plates with fillet welds connecting the plate to the column web (Fig. 4b); (3) doubler plates offset from the column web so that the doublers can act both as transverse stiffeners and web plates (Fig. 4c); (4) diagonal stiffener

Table 3 Summary of the connection dimensions for the bolted moment end plate connection

	Dimensions (mm)	Weld size (mm)	Steel grade/ electrode (MPa)
Flange weld	499	8	490
Web weld	277	6	490
Top stiffener	120 × 13 × 224.6	6	300
Bottom stiffener	120 × 13 × 224.6	6	300
Web doubler (×1)	203 × 9.5 × 260	CJPGW	300
End plate	260 × 19 × 510	–	300
Bolts	10 25.4 mm-bolts in 2 columns		825

welded to the column web (Fig. 4d); and (5) reduced-size doubler plates welded to the column web using fillet welds (Fig. 4e). In addition to these details, one potential solution to eliminate the need for doubler plates is to use columns with high strength steel. The proposed connection details in Fig. 4 are expected to offer a favourable solution by avoiding PJP welds in the connection and improving productivity in the shop, while maintaining the load-carrying capacity and stability of the connection. It is significant to note that unlike moment-resisting frames in building applications, where increasing the column section size to one with a thicker web can help avoid the need for doubler plates, using a larger column size in pipe racks often results in a less economical design because of the large number of similar or identical modules in a project.
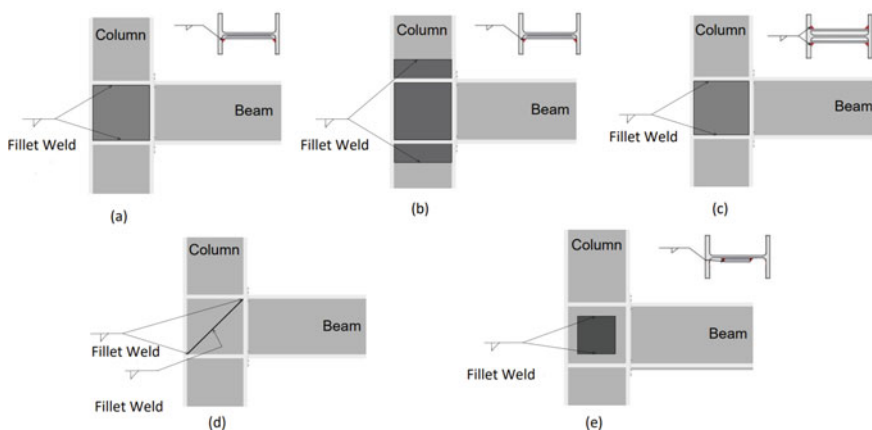
Fig. 4 Proposed beam-to-column connection details

5 Connection Response Evaluation

The Idea StatiCa programme [13], which is a structural design software package developed to analyze and design connections, is used to evaluate the baseline web panel zone detail (detail 1) shown in Fig. 1 and four design alternatives (detail 2–3) as shown in Fig. 4a, e, and (detail 4–5) which are double-sided versions of Fig. 4a, e. In these details, the web doubler plates were made using (1) complete joint penetration groove welds (CJPGW) in lieu of PJP welds (Fig. 1); (2) fillet welds to the column, stiffeners (Fig. 4a); and (3) fillet welds to the column web only via the application of reduced-width doubler plates (Fig. 4e and a double-sided version of it). Table 4 gives the dimensions of the doubler plates used in each of these designs. The alternative designs are assessed to determine whether the complex PJP-welded doubler plate can be replaced by a simpler and more efficient detail.

A tentative loading scenario representing those expected in a pipe rack connection is applied to compare the responses of each connection relative with the others using von Mises stress distributions. This comparison provides an insight into their performance and, in particular, the local effects that may dominate the panel zone response. The loading involves a 150 kN m moment, 150 kN shear, and 100 kN axial load applied at the face of the column, as shown in Figs. 5, 6, 7, 8, and 9. The numerical models of the connections representing details 1–5 developed in Idea StatiCa are shown in Figs. 5, 6, 7, 8 and 9, respectively. The results of the analysis for detail 1 show the occurrence of the largest von Mises stress of 315 MPa in the column web in the corner of the panel zone. The equivalent stress distributions in the reduced one-sided doubler plate and regular one-sided doubler plate connected using fillet welds are shown in Figs. 6 and 7, respectively. Figure 8 shows the second alternative design where a regular doubler plate is used on both sides of the column web using PJP welds all around. Figure 9 presents the connection improved using two-sided reduced doublers fillet-welded to the column web. Table 5 gives the parameters used to reproduce details 1–5 in Idea StatiCa.

The material model used to define the stress–strain response of steel is an elastic–plastic material model with a small strain hardening amplitude with respect to the elastic stiffness of steel. The nonlinear behaviour of the material follows the von Mises yield criterion [11]. Eight finite elements were used per cross-section height in the analysis [11]. Denavit and Truman-Jarell [11] showed by comparing the response of an extended end plate moment connection simulated using the component-based finite element method with that obtained from the traditional methods that the

Table 4 Doubler plate dimensions for the studied connection design alternatives

Doubler plate	Regular one-sided	Reduced one-sided	Regular two-sided	Reduced two-sided
Length (mm)	203	168	203	164
Thickness (mm)	10	10	5	5
Width (mm)	207	196	201	174
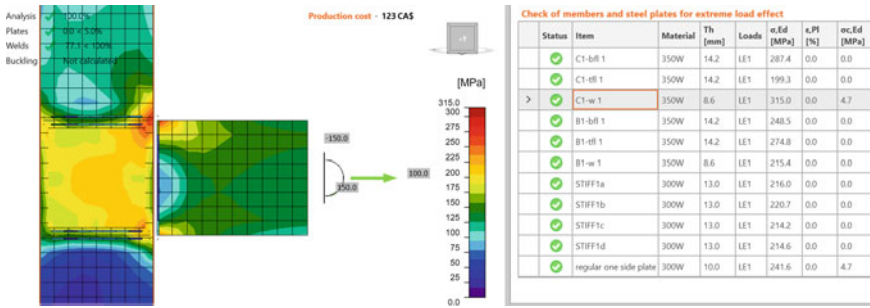
Fig. 5 von Mises stress distributions of detail 1 (one-sided regular doubler plate with PJP welds all around)

Check of members and steel plates for extreme load effect (Production cost - 123 CA$)

Status	Item	Material	Th [mm]	Loads	σ,Ed [MPa]	ε,Pl [%]	σc,Ed [MPa]
✓	C1-bfl 1	350W	14.2	LE1	287.4	0.0	0.0
✓	C1-tfl 1	350W	14.2	LE1	199.3	0.0	0.0
> ✓	C1-w 1	350W	8.6	LE1	315.0	0.0	4.7
✓	B1-bfl 1	350W	14.2	LE1	248.5	0.0	0.0
✓	B1-tfl 1	350W	14.2	LE1	274.8	0.0	0.0
✓	B1-w 1	350W	8.6	LE1	215.4	0.0	0.0
✓	STIFF1a	300W	13.0	LE1	216.0	0.0	0.0
✓	STIFF1b	300W	13.0	LE1	220.7	0.0	0.0
✓	STIFF1c	300W	13.0	LE1	214.2	0.0	0.0
✓	STIFF1d	300W	13.0	LE1	214.6	0.0	0.0
✓	regular one side plate	300W	10.0	LE1	241.6	0.0	4.7

Fig. 6 von Mises stress distributions of detail 2 (one-sided regular doubler plate with fillet welds all around)

Check of members and steel plates for extreme load effect (Production cost - 101 CA$)

Status	Item	Material	Th [mm]	Loads	σ,Ed [MPa]	ε,Pl [%]	σc,Ed [MPa]
✓	C1-bfl 1	350W	14.2	LE1	289.0	0.0	0.0
✓	C1-tfl 1	350W	14.2	LE1	206.8	0.0	0.0
> ✓	C1-w 1	350W	8.6	LE1	315.1	0.1	13.3
✓	B1-bfl 1	350W	14.2	LE1	250.9	0.0	0.0
✓	B1-tfl 1	350W	14.2	LE1	275.2	0.0	0.0
✓	B1-w 1	350W	8.6	LE1	218.5	0.0	0.0
✓	STIFF1a	300W	13.0	LE1	222.4	0.0	0.0
✓	STIFF1b	300W	13.0	LE1	224.8	0.0	0.0
✓	STIFF1c	300W	13.0	LE1	215.8	0.0	0.0
✓	STIFF1d	300W	13.0	LE1	215.6	0.0	0.0
✓	regular one side fillet weld	300W	10.0	LE1	179.0	0.0	13.3

Fig. 7 von Mises stress distributions of detail 3 (one-sided reduced doubler plate with fillet welds all around)

Check of members and steel plates for extreme load effect (Production cost - 102 CA$)

Status	Item	Material	Th [mm]	Loads	σ,Ed [MPa]	ε,Pl [%]	σc,Ed [MPa]
> ✓	C1-bfl 1	350W	14.2	LE1	282.1	0.0	0.0
✓	C1-tfl 1	350W	14.2	LE1	204.9	0.0	0.0
✓	C1-w 1	350W	8.6	LE1	315.2	0.1	6.3
✓	B1-bfl 1	350W	14.2	LE1	253.5	0.0	0.0
✓	B1-tfl 1	350W	14.2	LE1	276.5	0.0	0.0
✓	B1-w 1	350W	8.6	LE1	220.1	0.0	0.0
✓	STIFF1a	300W	13.0	LE1	237.5	0.0	0.0
✓	STIFF1b	300W	13.0	LE1	232.9	0.0	0.0
✓	STIFF1c	300W	13.0	LE1	226.0	0.0	0.0
✓	STIFF1d	300W	13.0	LE1	221.0	0.0	0.0
✓	reduced one side plate	300W	10.0	LE1	211.4	0.0	6.3

capacity design capabilities of IDEA StatiCa provide conservative results and the web panel-zone strength from IDEA StatiCa is similar to the strength from the AISC Specification when the effect of inelastic panel-zone deformations on frame stability is accounted for in the analysis to determine required strengths [11]. The
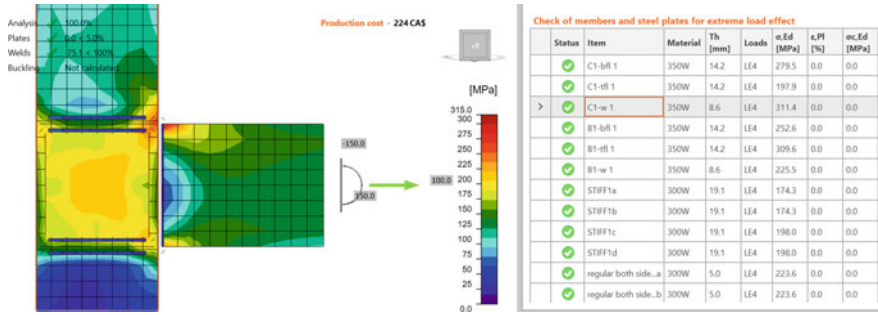
Fig. 8 von Mises stress distributions of detail 4 (two-sided regular doubler plates with PJP welds all around)
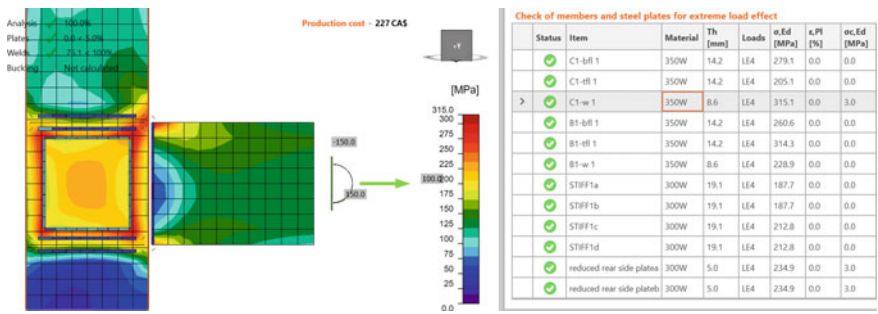
Fig. 9 von Mises stress distributions of detail 5 (two-sided reduced doubler plates with fillet welds all around)

Table 5 Summary of the connection parameters and dimensions for the welded moment connection used in Idea *StatiCa models*

	Details 1, 2, 3	Details 4, 5
Beam section	W250 × 73	W250 × 73
Column section	W250 × 73	W250 × 73
Steel grade (MPa)	350	350
Flange weld size (mm)	8	12
Web weld size (mm)	8	8
Weld electrode (MPa)	490	490
Top stiffener dimensions (mm)	122 × 13 × 224.6	122 × 19 × 224.6
Bottom stiffener dimensions (mm)	122 × 13 × 224.6	122 × 19 × 224.6
Stiffener weld (mm)	6	12
Stiffener steel grade (MPa)	300	300

traditional calculation methods in this verification were based on recommendations provided in AISC Design Guide 4 and requirements for load and resistance factor design provided in the AISC Specification (2016), whereas the component based finite element method (CBFEM) results were obtained from IDEA StatiCa Version 21.0 [11].

The analysis results show that the maximum stress in the column web remained fairly similar when reduced doubler plates or two-sided doubler plates are used (in the order of 1% difference), but the distribution of the stresses in the web show higher stress values around the doubler plate when reduced doublers are used. The maximum stress in the doubler plates decreases from 242 to 223 MPa when using two-sided web doublers with PJP welds and from 242 to 235 MPa when using fillet welds, due to a more uniform distribution of resulting stresses in two plates compared with a single one-sided doubler plate. The results show that reducing the dimension of doubler plates can be considered as a viable solution to improve fabrication of pipe rack moment connection provided that a set of thresholds are defined to limit the application of such detail based on the forces induced in the connection.

6 Conclusion and Future Work

Steel moment connections in pipe rack modules are designed to transfer bending moments, shear forces, and axial forces, which produce a complex stress condition in the column web and often result in an expensive detail that makes the connection fabrication a labour-intensive task in the shop. The use of doubler plates and stiffeners is often required in such connections to improve panel zone strength and stability [10]. The design of a welded end plate beam-to-column moment connection, part of a pipe rack structure, is first illustrated. Three design alternatives with the focus on the column doubler plate and weld types were introduced in addition to the baseline detail (with PJP welds) currently used in practice. The results obtained from the component-based finite element simulation of the baseline detail and four alternative details confirmed that two-sided reduced doubler plates fillet-welded to the column web can represent a viable alternative for modular pipe rack structure connections to enhance fabrication efficiency in the shop provided that a set of thresholds are defined to limit the application of such detail based on the forces induced in the connection. However, further analyses, as well as a mechanics-based verification, are required.

Future studies should investigate the proposed design alternatives using a continuum finite element model to track stresses and observe yielding in the connection, and in particular in the web panel zone. The selected connection detail to improve the fabrication efficiency should be evaluated using full-scale laboratory testing.

References

1. American Institute of Steel Construction (AISC) (2016) Specification for structural steel buildings (ANSI/AISC 360–16). IL, USA
2. American Institute of Steel Construction. Design Guide 4 (2004) Extended end-plate moment connections seismic and wind applications, 2nd edn
3. American Institute of Steel Construction. Design Guide 13 (2003) Wide-flange column stiffening at moment connections (Print)
4. American Institute of Steel Construction. Design Guide 16 (2002) Flush and extended multiple-row moment end-plate connections (Print)
5. Australian Steel Institute. Design Guide 11 (2009) Welded beam to column moment connections—17 design capacity tables
6. Bedair O (2015) Rational design of pipe racks used for oil sands and petrochemical facilities. Practice Period Struct Des Constr 20(2):04014029. https://doi.org/10.1061/(ASCE)SC.1943-5576.0000224
7. Canadian Institute of Steel Construction (CISC) (2021) Handbook of steel construction, 12th edn. Ontario, Canada
8. Canadian Standards Association (CSA) (2019) Design of steel structures (CAN/CSA-S16), Ontario, Canada
9. Drake RM, Walter RJ (2010) Design of structural steel pipe racks. AISC Eng J (4th Quarter)
10. Gupta U (2013) Cyclic loading analysis of doubler plate attachment details for steel moment resisting frames
11. IDEA StatiCa Connection Theoretical Background (2009–2022) Available from https://www.ideastatica.com/support-center/general-theoretical-background
12. IDEA StatiCa Extended End-Plate Moment Connections (AISC). Available from https://www.ideastatica.com/support-center/extended-end-plate-moment-connections-aisc
13. IDEA StatiC (2021) IDEA StatiCa connection. V. 20.1.5115,1 IDEA StatiCa. Windows 2021

Development of Unique Test Bed for Assessing Stability Response of Steel Cantilevered Girders

Maha Essa, Vahab Esmaeili, Ali Imanpour, and Robert Driver

Abstract Cantilever-suspended-span construction, also known as the Gerber system, is a popular framing scheme used for roofs of large single-storey buildings in North America. Despite their advantages and widespread application, collapses of Gerber roofs have made it clear that there are stability issues implicit in these systems that are not reflected as part of a unified design method. It is, therefore, necessary to understand the complex stability response of these systems—which can benefit greatly from the results of full-scale physical testing of overhanging girders. This paper outlines the development of a test bed for evaluating the stability response of overhanging girders and an experimental plan for the stability assessment of Gerber systems, which represents a part of an ongoing comprehensive research project at the University of Alberta. The primary criteria for the selection of the test specimens are first introduced. A finite-element model is then utilized to highlight the importance of those criteria through several numerical simulations. The key considerations of the test setup design, including the loading and lateral bracing conditions as well as restraints at column locations, are discussed. Simulating proper boundary conditions is of crucial importance in the experimental study of overhanging girders. The results reveal that the existence or absence of bottom chord extensions for secondary members, typically open-web steel joists, is a key design consideration for the test setup and can be highly influential in the stability response of the Gerber system.

Keywords Test bed · Stability response · Steel cantilevered girders

1 Introduction

Cantilever-suspended-span construction, also known as the Gerber system, is a common roof framing scheme for large single-storey buildings in North America. This system, shown in Fig. 1, consists of a series of simply supported girders in

M. Essa (✉) · V. Esmaeili · A. Imanpour · R. Driver
University of Alberta, Edmonton, AB, Canada
e-mail: essa@ualberta.ca

Fig. 1 Gerber system in a
single-storey building in
Edmonton, AB

the principal framing direction that extend beyond the column as cantilevers, with
open-web steel joists (OWSJs) as the secondary framing members. Drop-in spans
are supported in alternate bays at the cantilever ends. The continuity between adja-
cent bays results in lower magnitudes of positive moment by introducing negative
moments at the supports. As a result of the balanced moments, Gerber girders allow
for a more efficient design—where lighter and shallower girders are adequate to carry
the same loads as compared to simply supported spans. Furthermore, the system
avoids costly and complex moment connections, making it faster to erect, and results
in lower deflections than those seen in conventional roof girders [11].

Despite the advantages and widespread application of the Gerber system in steel
buildings in North America, current steel design standards in Canada and the United
States [1, 5] provide little guidance on the design of Gerber systems—especially with
regard to the effect of the interaction between the cantilever and the back span on
lateral–torsional buckling (LTB) of the system. The prediction of the LTB response
in this system relies on the consideration of a variety of parameters, including
loading and bracing conditions. The effects of these parameters can be realized from
the results of full-scale physical testing of overhanging girders subject to different
bracing and loading conditions. This paper outlines the development of a unique
test bed for evaluating the stability response of overhanging girders used in Gerber
systems. The experimental data obtained from these tests will be used to further
validate a comprehensive finite-element model for overhanging girders developed
as part of an ongoing research project at the University of Alberta [7]. The accurate
validation of this model will be instrumental in developing a practical design method
in the framework of the Canadian steel design standard for cantilevered girders.

2 Gerber Stability Database

As part of the larger research project, a comprehensive finite-element model [7] has
been developed in the *Abaqus* programme [6] for overhanging girders. In addition to
global buckling limit state, the possibility of distortional buckling—where the girder
cross-section undergoes distortion and deflection simultaneously—greatly influences

the flexural capacity of overhanging girders [9]. The finite-element model is capable of considering such buckling modes, as well as material and geometric nonlinearities, initial geometric imperfections, and residual stresses.

Figure 2 shows the configuration of a typical overhanging girder considered in this study. In this figure, P_b refers to the point loads on the back span coming from OWSJs; P_{max} and P_{min} represent the larger and smaller point loads at the cantilever tips, respectively; L_b denotes the length of the back span; L_c is the length of the cantilever; s represents the joist spacing; n equals the number of point loads on the back span plus 1; M_{max}^l is the local maximum bending moment along the back span; $M_{F_{max}}$ and $M_{F_{min}}$ signify the bending moments at the two supports; and κ_1' and κ_2' are defined as $\frac{M_{max}^l}{M_{F_{max}}}$ and $\frac{M_{F_{min}}}{M_{F_{max}}}$, respectively.

A total of 266 overhanging girders, including 245 single-overhanging girders and 21 double-overhanging girders, are considered in the numerical simulation. These include seven standard steel wide-flange sections (W-shapes), which conform to both CSA G40.21 Grade 345WM [4] and ASTM A992 [2]. The cross-sectional properties and class [5] of the selected cross-sections are presented in Table 1. For all the girders, the length of the back span, L_b, is 9.0 m and the length of the cantilever, L_c, and joist spacing, s, are both equal to 1.8 m.

In Table 1, $b/2t$ represents the flange slenderness ratio, where b is the overall width of the flange and t denotes its thickness; h/w is the web slenderness ratio, where h is the clear depth of the web and w denotes its thickness; I_x/I_y is an index of the difference between the strong- and weak-axis geometric stiffnesses of the girder; and d is the depth of the section.
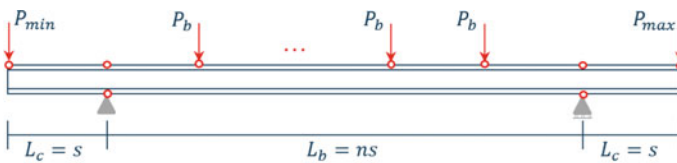
(a) Configuration
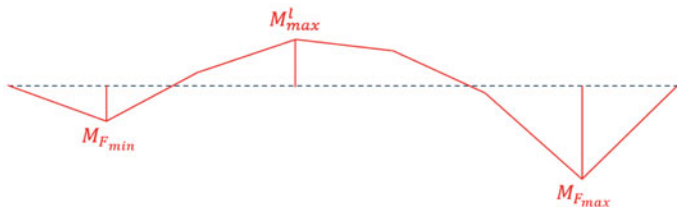
(b) Bending moment diagram

Fig. 2 Typical overhanging girder (symbol red circle represents point of lateral support)

Table 1 Geometrical properties of selected cross-sections

Cross-section	Flange class	Web class	$\frac{b}{2t}$	$\frac{h}{w}$	$\frac{I_x}{I_y}$	$\frac{L_b}{d}$
W410 × 85	1	1	5.0	34.8	17.5	22
W460 × 52	1	1	7.0	56.4	33.4	20
W460 × 60	1	1	5.8	53.6	32.0	20
W460 × 97	1	1	5.1	37.5	19.5	19
W460 × 144	1	1	6.4	31.5	8.7	19
W530 × 66	1	1	7.2	56.4	41.0	17
W530 × 82	2	1	7.9	52.8	23.5	17
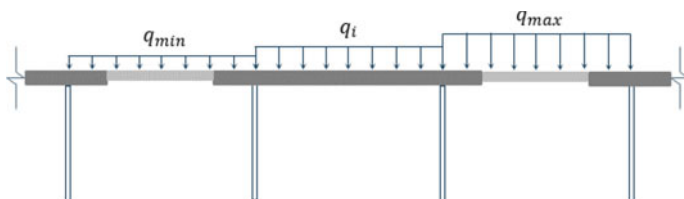
Fig. 3 Typical roof framing under a schematic load pattern

Figure 3 shows a typical roof framing under a schematic load pattern. This highlights the importance of considering pattern loading in the study, which can occur due to phenomena such as moving live loads or drifting snow.

In Fig. 3, q_i refers to the distributed load on the back span bay; q_{max} and q_{min} represent the larger and smaller distributed loads on the adjacent bays, respectively; and κ_1'' and κ_2'' are defined as q_i/q_{max} and q_{min}/q_{max}, respectively. To develop the Gerber stability database, the following range is considered for κ_1'':

$$\kappa_1'' = \{2.00, 1.60, 1.30, 1.00, 0.77, 0.63, 0.50\} \tag{1}$$

κ_2'' is equal to zero for single-overhanging girders considered in this study.

While the finite-element model has been validated using available test results [7], the experimental test programme outlined in this paper will evaluate experimentally a wider range of Gerber girders by varying configuration (single or double overhang), loading scheme, and cross-section to achieve a better representation of the stability of such girders. The data from these tests will then be used to further validate the numerical model.

3   Test Specimen Selection Criteria and Matrix

The finite-element model described earlier is used to evaluate the influence of various parameters on the lateral–torsional buckling capacity of steel cantilevered girders. These parameters include configuration (single or double overhang), cross-sectional properties, loading conditions, and lateral bracing conditions. The parameters with the highest influence according to the numerical simulations [7] are to be considered so as to select test specimens, which will expand on the existing cantilever test database provided by [8].

The specimens are categorized into five distinct groups according to the restraint conditions on the cantilever and back span, as shown in Fig. 4, with the following identifiers:

Fig. 4   Test specimen loading and restraint conditions

- $C(T) – B(T)$: cantilever tip is laterally restrained at the top flange and back span is laterally restrained at the top flange;
- $C(U) – B(T)$: cantilever tip is unbraced and back span is laterally restrained at the top flange;
- $C(U) – B(TB)$: cantilever tip is unbraced and back span is laterally restrained at both the top and bottom flanges;
- $C(TB) – B(T)$: cantilever tip is laterally restrained at both the top and bottom flanges and back span is laterally restrained at the top flange; and
- $C(TB) – B(TB)$: cantilever tip is laterally restrained at both the top and bottom flanges and back span is laterally restrained at both the top and bottom flanges.

3.1 Configuration

While the tests performed by [8] were limited to only single-overhanging girders, this experimental study will incorporate both single and double-overhanging girders. In practice, both configurations are used in the Gerber system depending on the location of the cantilever segment in the structural layout. While end spans typically consist of single-overhanging girders, interior spans typically consist of girders that run continuously over two columns in a double-overhanging configuration then connecting to drop-in segments on either end. It is therefore important to understand the stability response of both configurations of overhanging girders.

The proposed test specimen configurations consisted of single-overhanging girders with a total length of 10.8 m and double-overhanging girders having a total length of 12.6 m. This length includes the lengths beyond the support centreline and cantilever tip load centreline.

The numerical model was used to assess the effects of different L_b/d ratios on the nominal capacity of the girder, M_n, for both single and double-overhanging girders. This was achieved by varying κ_1'' values, namely, 0.625, 1, and 1.6. The results of the analyses for Group $C(T) – B(T)$ are shown in Fig. 5.

The configuration is seen to have a significant impact on the capacity of the system, with the additional cantilever on the double-overhanging girders having the ability to either increase or decrease the moment capacity depending on the load pattern ratios. The smaller capacities seen for double-overhanging girders are a result of smaller κ_1' values for the same κ_1'' values as a single-overhanging girder. Furthermore, the peaks in the chart correspond to the sections in Table 1 with smaller I_x/I_y values (W410 $\times$ 85, W460 $\times$ 97, and W460 $\times$ 144), and are consequently stronger than the rest of the sections in terms of weak-axis bending. It is therefore crucial to investigate both configurations to fully capture the stability response of Gerber systems.

(a) $\kappa_1'' = 0.625$

(b) $\kappa_1'' = 1$

(c) $\kappa_1'' = 1.6$
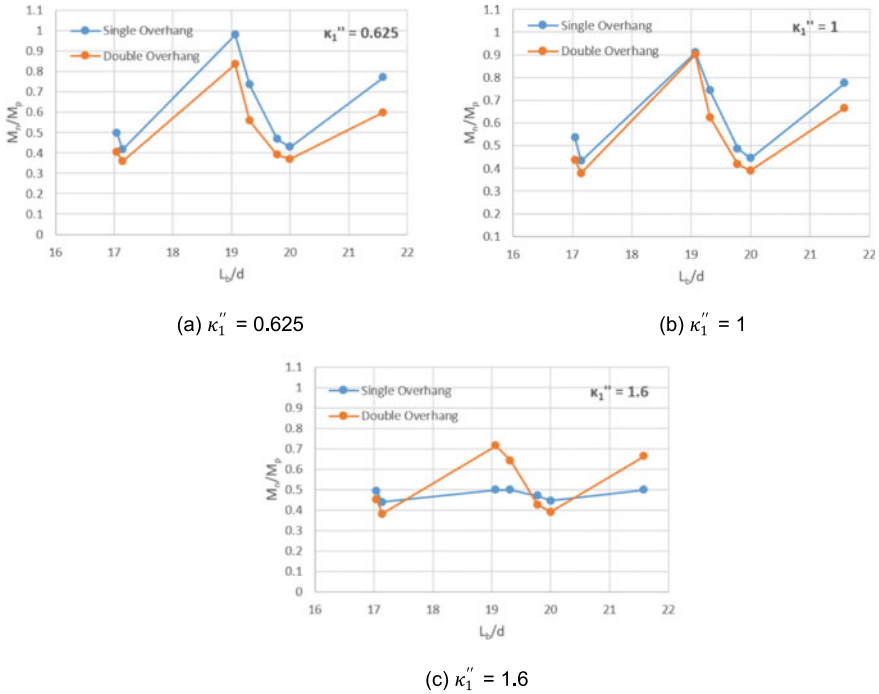
Fig. 5 Effect of configuration on nominal capacity for the $C(T) - B(T)$ group

3.2 Cross-Sectional Properties

The experimental programme performed by [8] was limited to two cross-sections, W360 × 39 and W310 × 39, both of which are considered in today's Gerber construction practice as shallow and light, but were primarily selected to meet the laboratory constraints. To expand on this, the proposed test matrix of this experimental study includes three new cross-sections: W410 × 85, W310 × 44.5, and W460 × 113. The W410 × 85 section complies with the Class 1 section width-to-thickness ratio limits, and the W310 × 44.5 and W460 × 113 profiles meet Class 2 section requirements.

The selection of these three cross-sections was based on the results of the numerical simulations [7] that show that dimensionless parameters $b/2t$ (flange width-to-thickness ratio or local slenderness ratio) and I_x/I_y (ratio of moments of inertia) are particularly influential on the lateral–torsional buckling capacity of cantilever girders. The nominal values of both parameters for each cross-section is presented in Table 2.

Numerical simulation results can be used to realize the significance of cross-sectional properties on the nominal flexural capacity, M_n, of overhanging girders. Figure 6 shows the variation of the nominal capacity as I_x/I_y changes for the $C(T) - B(T)$ group.

Table 2 Flange local slenderness ratio and ratio of moments of inertia for selected wide-flange sections

Gerber girder	$\frac{b}{2t}$	$\frac{I_x}{I_y}$
W410 × 85	4.97	17.5
W310 × 44.5	7.41	11.6
W460 × 113	8.09	8.78

(a) $\kappa_1'' = 0.625$

(b) $\kappa_1'' = 1$

(c) $\kappa_1'' = 1.6$
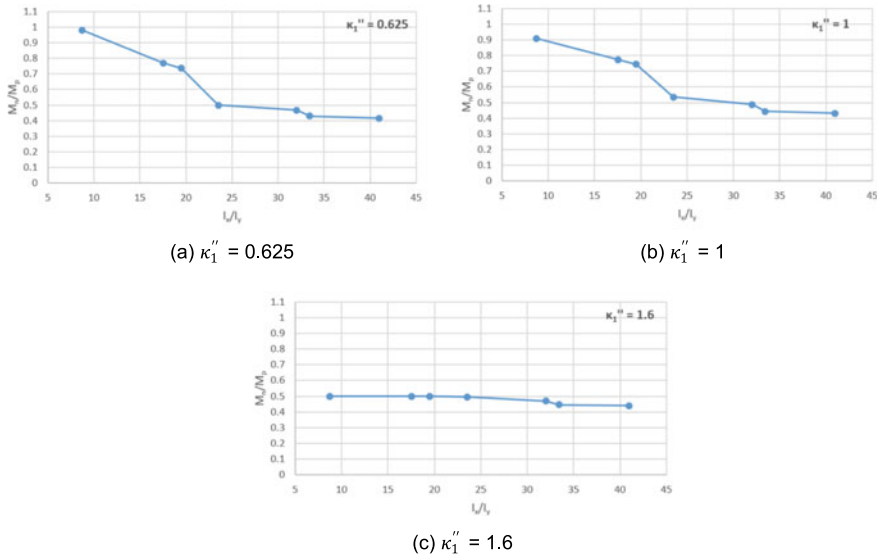
Fig. 6 Effect of cross-sectional properties on the flexural capacity of cantilevered girders for the $C(T) - B(T)$ group

As seen in the numerical simulation results, the capacities of the sections are greatly influenced by the cross-sectional properties. Increasing the $\frac{I_x}{I_y}$ ratio indicates that the moment of inertia about the weak-axis, I_y, is decreasing relative to the moment of inertia about the strong axis, I_x. This causes the system to be more susceptible to lateral–torsional buckling, which explains the decrease in capacity as this ratio increases and highlights the importance of testing various cross-sections.

3.3 Loading Condition

Another parameter that was identified from the numerical simulations as having a high impact on the stability of the system, particularly the stability of the back span, is the shape of the bending moment diagram. This is quantified by the ratio $\kappa_1' = M_{\max}^l / M_{F_{\max}}$, where $M_{\max}^l$ is the local maximum bending moment on the back span, and $M_{F_{\max}}$ is the bending moment at the support. Due to the continuity of the

Table 3 Variation of κ_1''' and κ_1' considered in test programme

κ_1'''	κ_1'
0.80	− 1.90
0.50	− 1.00
0.31	− 0.44

girder over the column, the negative moment at the column causes the bottom flange of the girder to go into compression. The length of the bottom flange under compression and the location of inflection points depends on the bending moment gradient, and therefore the loading condition. For this reason, it is important to evaluate the system under pattern loading. This is reproduced in the proposed experimental study by testing the girders under different load ratios. The loading of the test specimens involve four point loads at 1.8-m intervals on the 9 m-long back span plus a point load applied at the tip of the 1.8 m-long cantilever. A distinct load of P_{max} will be applied on the cantilever tip in each of the tests of all test specimen groups. The load on the back span, P_b, will then be varied in each of the tests with respect to P_{max} until a desired κ_1' ratio is achieved, as shown in Table 3. This is quantified by the ratio $\kappa_1''' = P_b/P_{max}\kappa_1'$, which can take on three values: 0.80, 0.50, or 0.31. Table 3 summarizes the variation of κ_1''' considered in the tests and their corresponding κ_1' values.

Numerical simulation results showed the influence of different load patterns, quantified by κ_1'' in the context of the numerical simulations, on the nominal flexural capacity of the girder. Figure 7 shows this effect for the three cross-sections in the C(T)–B(T) group.

For a single-overhanging girder, increasing the κ_1'' value represents increasing the load on the back span compared to the load on the cantilever. Referring to the numerical results, increasing κ_1'' past a value of 1.00 (corresponding to a higher load on the back span than on the cantilever) leads to a rapid decrease in the moment capacity of the section. Therefore, loading conditions are of crucial significance when investigating the capacity of an overhanging girder, and therefore various loading conditions have been included in the selection criteria of the test matrix.

3.4 Lateral Bracing Condition

The cantilever portion of a Gerber system can be subject to various bracing conditions in the real world, which is being simulated in this experimental study by including the test specimen groups introduced earlier (Fig. 4). The Gerber stability database confirmed that different bracing conditions at the cantilever tip, as well as the presence of a bottom chord extension on secondary members off the column line, have a significant impact on the capacity of the system.

(a) W460×144

(b) W410×85

(c) W530×82
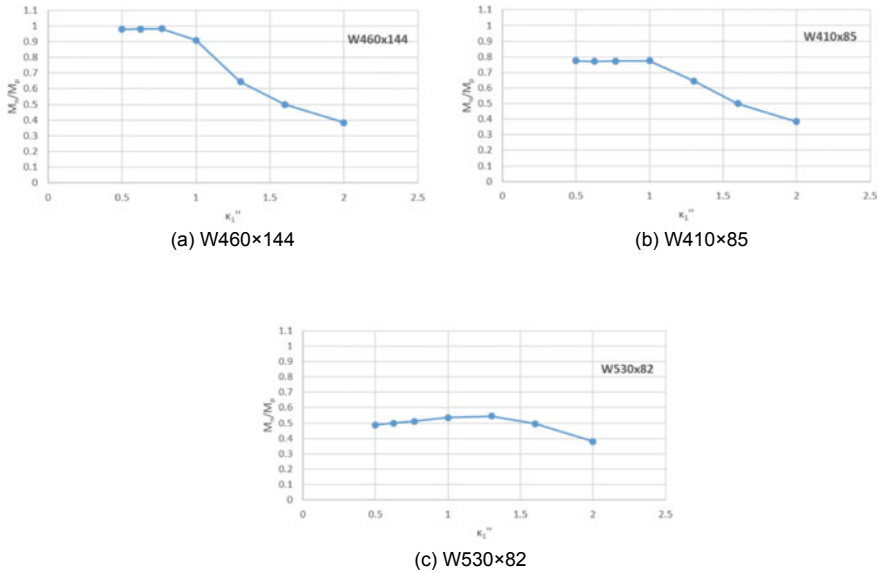
Fig. 7 Effect of load pattern on nominal flexural capacity for the C(T)–B(T) group

The numerical model was used to analyse the effect of different L_b/d ratios on the nominal flexural capacity of the girder, M_n, for the test specimen groups as shown in Fig. 8. This was achieved by varying $\kappa_1^{''}$ values, namely, 0.625, 1, and 1.6.

The numerical results showed that the models with bottom chord extensions at the bracing location off the column line exhibit a significantly higher capacity compared to the models where only the top flange is braced along the entire back span. Due to the variation in capacity with varying bracing conditions, the inclusion of various lateral bracing conditions in the test matrix is essential.

4 Test Bed Design

The experimental test programme described in this paper consists of 15 W410 × 85 single-overhanging girders. The ongoing design of the test setup is being done by paying consideration to minimizing incidental restraint, which can have a significant impact on the results of large-scale experimental testing by resulting in capacities higher than what would have been obtained under the intended restraint [15]. The test setup design considerations are based largely on the recommendations of the Structural Stability Research Council (SSRC) Technical Memorandum No. 9 on flexural testing [15]. Models have been prepared in *Revit* [3] for each of the five test specimen groups. Figure 9 shows the overall test setup for the C(T)–B(T) case. In this figure, the blue member is the test specimen, and the load frame, bracing system and

(a) $\kappa_1'' = 0.625$

(b) $\kappa_1'' = 1$

(c) $\kappa_1'' = 1.6$
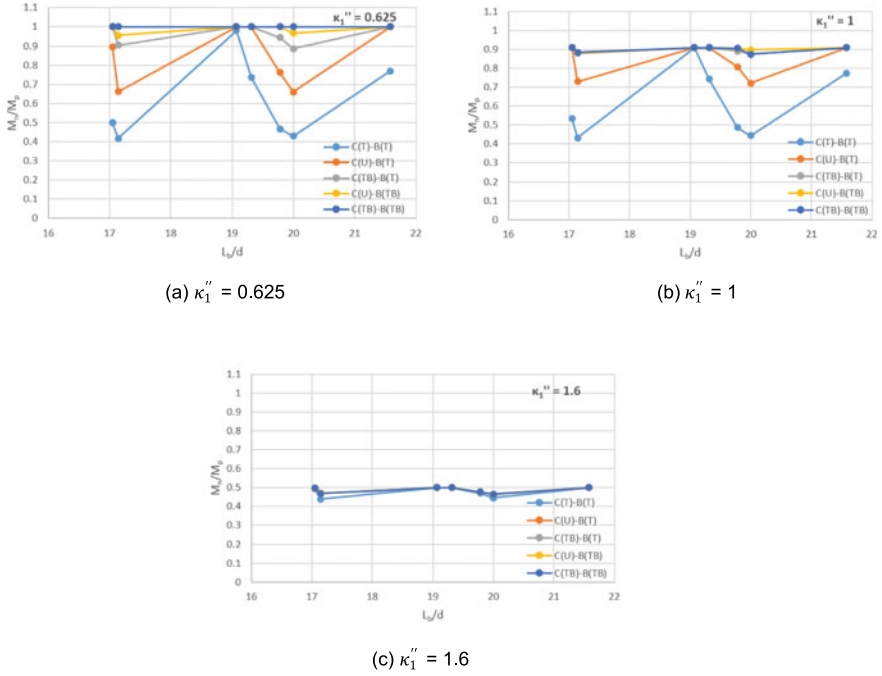
Fig. 8 Effect of lateral bracing condition on flexural capacity of single-overhanging girders

supports are shown in grey. This section describes the loading, support, and bracing details of the test setup to simulate those anticipated in a typical Gerber system.

Fig. 9 Model of test setup for C(T)–B(T) case (test specimen shown in blue)
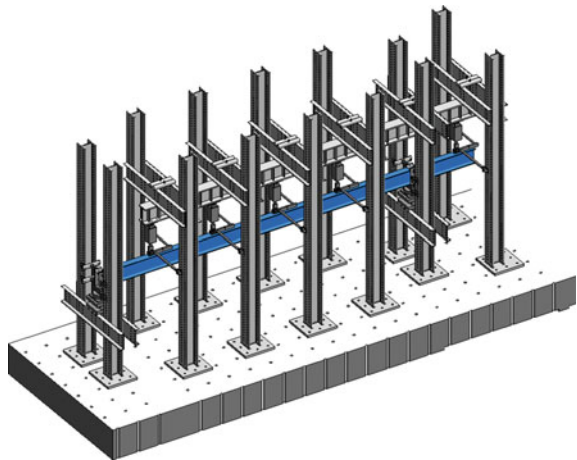
4.1 Physical Simulation of Loading Conditions

The loading of the test specimens involve four point loads at 1.8-m intervals on the 9 m-long back span plus a point load applied at the tip of the 1.8 m-long cantilever. The gravity load is applied using a hydraulic actuator, which generates the concentrated load on test specimen. On one end, the hydraulic actuators are connected to a stiff reaction frame composed of a distributing beam connected to 2.7 m-long MC 460 × 86 channels, which subsequently span across two 6 m-tall columns on either side of the girder. At the opposite end, the actuator is connected to a semi-cylindrical bearing with its axis aligned with the longitudinal axis of the girder, which accommodates cross-section twist and sits on the top flange of the girder. This configuration is used at the load application points on both the back span and the cantilever in the test specimen groups where the cantilever tip is braced.

For the C(U)–B(T) and C(U)–B(TB) test specimen groups, where the cantilever tip is unbraced, a different gravity load application mechanism is employed which is composed of: (1) gravity load simulator (GLS), (2) hydraulic actuator, and (3) load collar. This configuration is shown in Fig. 10.

The gravity load simulator (GLS) is a mechanism designed to allow an applied load to remain vertical on a test specimen as the loaded structure undergoes sidesway [14]. Under an applied load provided by a hydraulic actuator, the GLS is able to move laterally by approximately 140–225 mm in either direction from its equilibrium position while keeping the hydraulic actuator vertical [10]. Therefore, employing the GLS at the cantilever tip when it is unbraced will effectively eliminate incidental restraint in the lateral direction while continuing to apply a vertical gravity load.
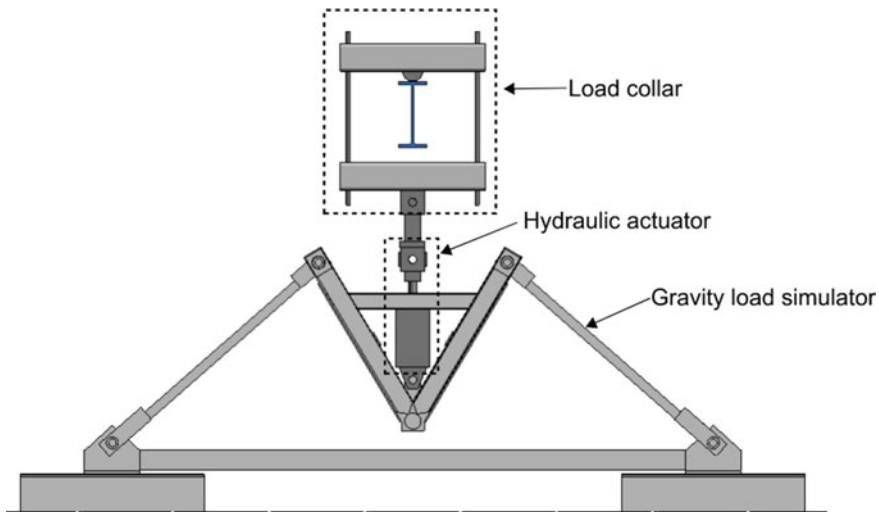
Fig. 10 Gravity load mechanism at an unbraced cantilever tip

The load collar, which surrounds the girder and is then connected to the hydraulic actuator through a yoke and tension rod, applies the load generated by the hydraulic actuator to the top flange of the girder. A semi-cylindrical bearing is also employed as part of the load collar in order to accommodate twisting of the cross-section.

4.2 Physical Simulation of Column Locations

Column locations in a typical Gerber frame are simulated in this experimental test setup at the supports. Identical configurations are used at the support fixtures at each end of the back span, resulting in the girder being simply supported. This means that the specimen is free to displace longitudinally and warp but is prevented from twisting and displacing laterally or vertically. To achieve this support condition, the specimen will rest on a set of rollers, a load cell, and a knife edge, as shown in Fig. 11. The rollers allow the girder to undergo longitudinal displacement, the knife edge allows the girder to pivot in-plane, and the load cell measures the reaction forces. These elements are supported on a pair of MC 460 × 86 channels spanning between two columns situated on either side of the girder.

Achieving a torsionally pinned boundary condition requires allowing the girder to warp, while preventing it from twisting. This is done by bringing in four lateral braces at each support, two which bear against the top flange and two against the bottom flange, effectively preventing cross-section twist and lateral movement of the girder. Furthermore, the girder is allowed to warp and displace longitudinally by equipping the lateral braces with rollers. The strength and stiffness requirements
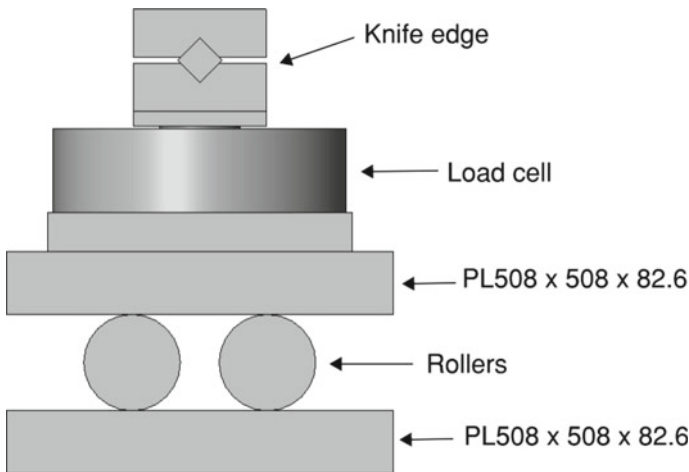
Fig. 11 Conceptual support detail

specified in Appendix 6 of AISC 360-16 [1] for girder point bracing are used to design lateral and torsional braces.

4.3 Physical Simulation of Lateral Bracing Conditions

Lateral bracing is used in flexural testing of girders to prevent out-of-plane movement. Since the girder is expected to deflect vertically along the back span and cantilever, in order to avoid incidental restraint it is important to use a lateral bracing mechanism that allows for free vertical movement while simultaneously restraining movement in the direction perpendicular to the girder web. Therefore, a conventional threaded rod, used at the supports as explained in Sect. 4.2, would not be appropriate for use at the load points. The lateral bracing condition in the test setup makes use of a Watt's linkage (Fig. 12), a type of brace which restrains lateral displacement while allowing for free translation in the longitudinal and vertical directions. The Watt's linkage has been used in previous lateral–torsional buckling tests [12–14]. As shown in Fig. 12, the Watt's linkage consists of two levers. One end of the lever is pin-connected to a column on one side of the girder (points A and B in Fig. 12), while the other end is pin-connected to a coupler (member CD in Fig. 12). The coupler includes a 1 ¼ in. diameter hole in the middle, through which the brace is pinned and welded to the flange of the girder being restrained.

Depending on the test specimen group, lateral bracing at various points along the back span may be provided to either the top flange only or both the top and bottom flanges. In cases where only the top flange is laterally restrained, only a single Watt's linkage would be used at the brace point, with the coupler connected to the top flange of the girder. For instance, a Watt's linkage would be connected to both the top and bottom flanges when simulating a bottom chord extension of a joist, effectively restraining the lateral movement of both flanges while allowing the girder to deflect vertically.

In the case of the cantilever tip, the load point may also be completely unbraced. The use of a gravity load simulator at the cantilever tip allows for a continuous gravity
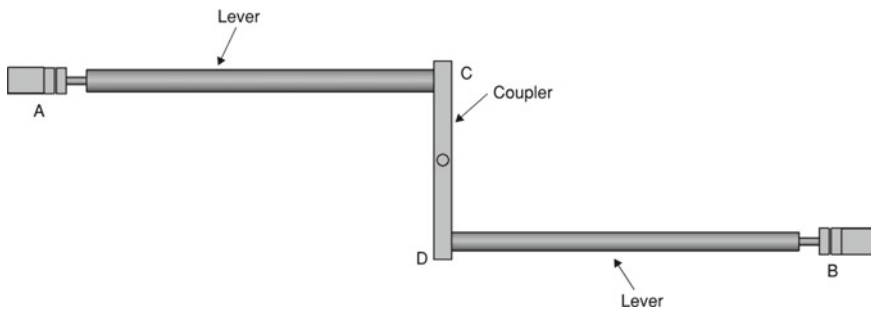
Fig. 12 Watt's linkage for lateral bracing

load application while allowing the specimen to undergo free lateral movement in either direction of its equilibrium position. By using the gravity load simulator in the C(U)–B(T) and C(U)–B(TB) groups, it is possible to apply an increasing point load while allowing the girder to deflect vertically and laterally, producing an unbraced cantilever tip. Meanwhile, Watt's linkages are still used at the brace points on the back span to restrain the top or bottom flange, as required.

5 Summary and Conclusions

An experimental test programme for evaluating the stability response of single-overhanging girders that aims to minimize incidental restraints and properly simulate the loading conditions, supports, and bracing conditions commonly used in Gerber construction is presented. A numerical database of the Gerber system developed in the companion study was used to select the test specimens and design the test setup. The experimental data obtained from the physical tests will be used to validate a comprehensive finite-element model which can predict the lateral–torsional buckling capacity for any arbitrary overhanging girder. This will be instrumental in proposing future design equations to be used in the design of Gerber girders.

References

1. American Institute of Steel Construction (AISC) (2016) Specification for structural steel buildings (ANSI/AISC 360-16). Chicago, IL
2. American Society for Testing and Materials (ASTM) (2020) Standard specification for structural steel shapes. ASTM A992/A992M-20, ASTM, West Conshohocken, PA
3. Autodesk Inc. (2022) Revit architecture 2022 user's guide, Version 2022, San Rafael, CA
4. Canadian Standards Association (CSA) (2013) General requirements for rolled or welded structural quality steel/structural quality steel. CSA G40.20-13/G40.21-13 (reaffirmed 2018), CSA, Toronto, ON
5. Canadian Standards Association (CSA) (2019) Design of steel structures. CSA S16-19, CSA, Toronto, ON
6. Dassault Systèmes (2017) Abaqus/standard user's manual. Version 2017, Vélizy-Villacoublay, France
7. Esmaeili V, Imanpour A, Driver RG (2021) Stability of gerber systems with top-flange bracing. In: Proceedings of the annual stability conference. Structural Stability Research Council (SSRC). Louisville, KY
8. Essa HS, Kennedy DJ (1993) Distortional buckling of steel beams. Structural engineering report no. 185. University of Alberta, Edmonton, AB

9. Essa HS, Kennedy DJ (1994) Design of cantilever steel beams: refined approach. J Struct Eng 120(9):2623–2636
10. Ji D, Driver RG, Imanpour A (2019) Large-scale lateral–torsional buckling tests of welded girders. Steel centre engineering report no. 015. University of Alberta, Edmonton, AB
11. Rongoe J (1996) Design guideline for continuous beams supporting steel joist roof structures. NASCC Proc
12. Slein R, Buth JS, Latif W, Kamath AM, Alshannaq AA, Sherman RJ, Scott DW, White DW (2020) Large-scale experimental lateral-torsional buckling tests of welded I-section members. In: Annual stability conference. Atlanta, GA, 1–20
13. Smith MD, Turner AK, Uang CM (2013) Experimental study of cyclic lateral–torsional buckling of web tapered I-beams. Department of Structural Engineering, University of California, San Diego, CA
14. Yarimci E, Yura JA, Lu LW (1967) Techniques for testing structures permitted to sway. Fritz laboratory reports (paper 112), Bethlehem, PA
15. Ziemian RD (2010) Guide to stability design criteria for metal structures. Structural Stability Research Council (SSRC), Wiley, Hoboken, NJ

A Metaheuristic-Based Methodology to Minimize the Concentration of Lateral Displacements in Low-Rise Steel Concentrically Braced Frames Subjected to Seismic Loading

Bardia Mahmoudi and Ali Imanpour

Abstract This paper proposes a new methodology to evaluate the seismic performance of multi-storey Concentrically Braced Frames (CBFs) and to minimize the concentration of frame nonlinear lateral displacements. A three-storey concentrically braced frame with chevron bracing is first selected. An optimization tool is then developed to study drift concentration under seismic loading. This tool leverages a fully parametric design script interacting with the *OpenSees* programme to generate a large number of potential frame designs analysed under ground motion accelerations and to iteratively update the frame design using the PSO algorithm until minimum drift concentration is achieved. Preliminary results of the proposed methodology and future direction of the research are finally presented.

Keywords Lateral displacements · Low-rise steel concentrically braced frames · Seismic response

1 Introduction

Steel Concentrically Braced Frames (CBFs) are widely used as the lateral load-resisting system of multi-storey buildings. Under lateral seismic loads, the lateral roof displacement may not be distributed evenly between the storeys as their braces experience nonlinear response through tensile yielding and buckling, resulting in the concentration of lateral inelastic displacements in one or some of the storeys. This stems from a poor performance of CBFs in redistributing inelastic demands along their height mainly due to inherent poor hysteretic response of diagonal braces when buckling in compression, which significantly reduces storey shear resistance, thus

B. Mahmoudi (✉) · A. Imanpour

Department of Civil and Environmental Engineering, University of Alberta, Edmonton, AB, Canada

e-mail: bardia1@ualberta.ca

discouraging yielding to develop in adjacent floors [20, 29, 32, 54, 60]. This response is compared to an ideal uniform lateral displacement response in Fig. 1 for a three-storey steel CBF with chevron bracing. As shown in Fig. 1a, a desirable response involves brace tensile yielding and compression buckling in all the storeys, resulting in a uniform distribution of lateral displacements over the height of the frame, whereas the frame in real-life under earthquake loading may experience concentration of lateral deformation as shown in Fig. 1b (e.g. in the first storey) due to the elastic response of tension-acting braces in some of the storeys (e.g. Storeys 2 and 3), leading to soft or weak storey behaviour. The concentration of lateral deformations become more critical in tall CBFs, those with heavy gravity loads imposing large P-Δ effects, and the CBFs located in high seismic regions such as Vancouver or Victoria, BC [28, 44, 53, 56].

Several design parameters can influence the distribution of the lateral frame displacement under seismic loads. Past numerical studies have shown the number of storeys, distribution of seismic mass along the frame height, column orientation and splices, brace demand-to-capacity ratios, lateral stiffness offered by adjacent gravity columns, bracing configuration (e.g. X-bracing, chevron, diagonal), bracing system (e.g. tension–compression, tension-only), brace slenderness ratio within each storey and its variation over the storeys can affect seismic behaviour of concentrically braced frames [28, 52, 54].
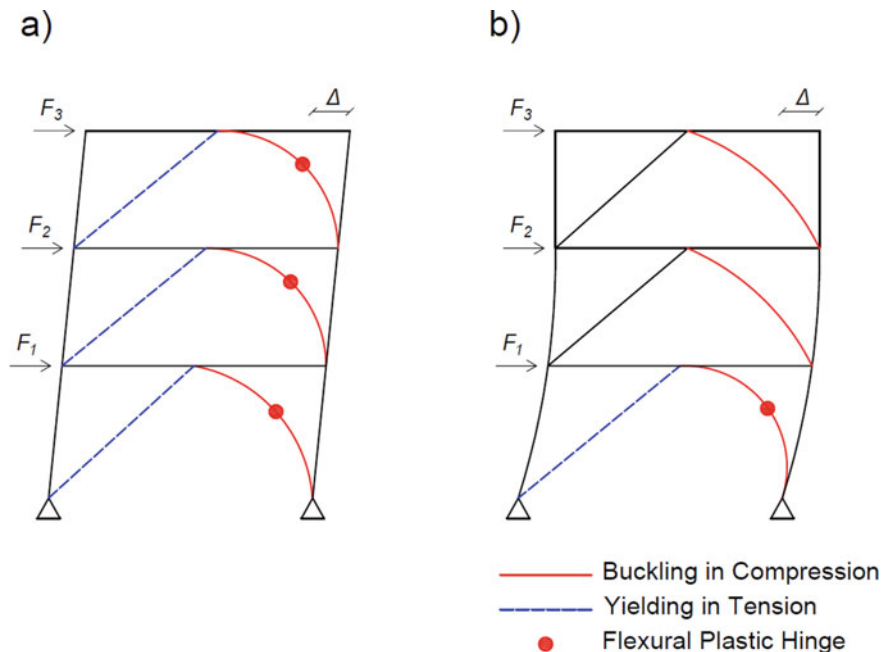
Fig. 1 Comparison of concentrically braced frames lateral deformation distributions: **a** uniform lateral deformation distribution, **b** damage concentration in storey 1

A number of mitigation techniques have been evaluated and proposed by various researchers in the past to reduce the concentration of lateral deformations in steel CBFs. These techniques include (1) rigid truss or strong-back systems tied to the CBF where the CBF acts as the energy dissipation system and the rigid truss is intended to remain essentially elastic forcing the CBF to undergo uniform lateral deformations during inelastic response [14, 33–35, 43, 54–56, 62], (2) innovative bracing members such as buckling-restrained braces (BRBs) instead of conventional braces [2, 3, 12, 19, 21, 26, 27, 38, 45–47, 51, 57, 59, 61], (3) moment-resisting frame (MRF) used in addition to the CBF to engage frame action [13, 16, 25, 62], (4) zipper or vertical tie bar systems [24, 49, 66], (5) two-storey X (split-X) system aiming at developing a 2-storey collapse mechanism [54], (6) rocking systems [4, 18, 22, 37, 41, 48, 58, 63, 64, 7–9, 30, 42, 65].

An alternative design solution to tackle damage concentration in CBFs and achieve a more uniform seismic response is to adjust brace selection, in particular, the brace slenderness parameter $\lambda = KL/r(F_y/\pi^2 E)^{1/2}$ where K is the effective length factor, L is the brace length, r is the radius of gyration of the brace cross-section, F_y is the steel yield stress, and E is Young's modulus of steel. Lacerte and Tremblay [28] developed a method for the selection of braces in Split-X concentrically braced frames such that they attain smooth variations of the post-buckling shear resistance over the frame height. In this method, braces having relatively low slenderness and post-buckling resistance were selected to help the propagation of inelastic deformations in several storeys under major seismic events producing a large lateral displacement at the roof level (in the order of 2% roof drift). This method was verified for systems up to 12 storeys and showed that it can avoid soft storey mechanisms and achieve more stable global response. Drift concentration in 1–8 storey X-braced frames designed as tension–compression or tension-only system was mitigated by limiting brace slenderness to 2.65 and designing the columns for an in-plane demand equal to 20% of the plastic moment capacity of the section in addition to the axial compression forces arising from brace axial resistances and gravity loads [52]. Imanpour et al. [20] proposed a design method for multi-tiered concentrically braced frames experiencing significant drift concentration in one of the braced tiers under seismic-induced deformation demands, leading to column yielding and instability. The method involved new strength and stiffness requirements for columns, which engage column flexural stiffness to force tensile yielding in adjacent braces under seismic loading.

Although various approaches have been proposed in the past to tackle the poor seismic performance of steel CBFs when it comes to the distribution of nonlinear lateral deformations over the frame height and reducing CBF vulnerability to damage concentration and dynamic instability, they lack taking into account inclusive design parameters (e.g. number of storeys, brace slenderness ratio, column orientation, brace demand-to-capacity ratios, bracing configuration and system) affecting the seismic response of CBFs. To this end, this study proposes and implements a metaheuristic optimization tool to overcome the challenges associated with investigating the influence of various design scenarios, which can become computationally intensive, and to develop a design strategy to efficiently achieve a uniform distribution of lateral inelastic deformations under seismic loading. The proposed optimization tool is

developed by linking a fully parametric numerical model of multi-storey CBF, a three-storey chevron braced frame presented in this paper, to the optimization algorithm, which generates a large number of potential frames by varying the influential parameters pertaining to brace design and then updates each frame's members until damage concentration is minimized. This results in a number of candidate frame designs, which are subsequently classified into a small number of groups as final design alternatives using clustering algorithms.

2   Research Methodology

To measure and evaluate concentration of lateral deformation in CBFs, the Drift Concentration Ratio (DCR) is defined as the maximum standard deviation of storey drifts recorded under a given ground motion record. The frame that possesses the smallest DCR is then considered as the one achieving a nearly uniform distribution of lateral displacements over the height. However, finding the frame with the minimum DCR in a large set of frames generated to evaluate damage concentration would be a challenging task if traditional mathematical methods, which require computing derivatives of a function with respect to its variables, were to be used because the DCR cannot be expressed as a continuous and differentiable function of the design variables or the loading input, e.g. ground motion acceleration. Metaheuristic optimization algorithms, which have been developed based on evolutionary behaviour of species in nature, can be implemented instead [50]. The essence of such methods lies on their capability to locate global optimum of a function just by evaluating its value at different points over function's domain, which in the context of this study can help assess design parameter patterns in CBFs, contributing to a better understanding and quantification of such parameters and their impact on minimizing the concentration of frame lateral nonlinear deformations. The Particle Swarm Optimization (PSO) algorithm [23], which is a single objective metaheuristic optimization algorithm vastly used in various engineering disciplines, will be exploited in this study to overcome the challenge of finding the CBF design with the minimum DCR by bypassing a more complex assessment involving the combination of a large number of design variables. The key steps of the iterative process adopted here to minimize the objective function, i.e. the DCR, with respect to its variables, i.e. brace cross-sections, taking advantage of the PSO algorithm are summarized below:

1. *Generate random population*: A set of random particles with a population of *N*, i.e. first generation, is created by assigning random values to variables associated with the problem. Each particle returns a specific value for the objective function defined for the optimization problem and by inspecting these values, different particles can be ranked against each other.

2. *Objective function evaluation*: Particles defined in Step 1 are subject to various constraints with a feasible space. The selected algorithm forces these constraints to the particles using a penalty function. If a particle satisfies all the constraints,

the value of its objective function remains the same. Otherwise, the particle would get penalized by a multiplier implicit in its objective function to increase its value such that it cannot compete with feasible solutions of the generation when they are ranked based on their objective function.

3. *Particle updating by adjusting their velocity*: Once the set is sorted in accordance with the particle objective functions, the algorithm updates particles inside the generation by adjusting their variables using a velocity term v leading to a new set of solutions, i.e. the next generation. The algorithm then attempts to find the objective function's global minimum by generating a new set of particles and guiding them towards the global optimum. To update the location of particle i in generation t, x_i^t, and obtain the adjusted location in generation $t + 1$, x_i^{t+1}, using the velocity parameter v_i^{t+1}, Eqs. 1 and 2 can be used as follows:

$$x_i^{t+1} = x_i^t + v_i^{t+1} \tag{1}$$

$$v_i^{t+1} = wv_i^t + c_1 r_1 \left(x_{pb}^t - x_i^t \right) + c_2 r_2 \left(x_{gb}^t - x_i^t \right) \tag{2}$$

where inertia factor w and trust constants c_1 and c_2 are selected depending on the optimization problem and determine whether the particle should move towards its local best record or the global best record [40]. Factors r_1 and r_2 take random values between 0 and 1 in each iteration, which helps formulate randomness within the algorithm and search the entire feasible domain of the problem instead of getting trapped in local optima zones. It is recommended to set $w = 0.7298$ and $c_1 = c_2 = 1.4962$ in order to improve the algorithm's convergence rate [10]. It is worth noting that v_i^t can be taken as zero in the first generation.

A particle's velocity is a function of three parameters, (1) its velocity in the previous generation, v_i^t, (2) the location of personal best of that particle, x_{pb}^t, representing the coordinate in which particle i has recorded the smallest value it could obtain for the objective function after being modified for t generations, and (3) the location of global best, x_{pb}^t, being the coordinate of the smallest value achieved for the objective function by comparing the results of all particles after t generations. Figure 2 shows the interaction between these three parameters.

4. *Approaching optimum solution*: As Steps 2 and 3 are repeated, the algorithm tries to find the best solutions of each generation and improves them in subsequent generations. This process eventually converges to the optimum solution provided that a sufficient number of iterations are conducted. The algorithm should then terminate creating new generations and bypass performing Steps 2 and 3 by either setting a total number of generations before the algorithm started generating solutions, or verifying the convergence at each iteration by comparing the best solutions of the last two generations with each other (if the difference between the objective function values corresponding to these two solutions is less than the specified tolerance it means the algorithm can no longer find a more optimal solution and it should stop generating new solutions). The drawback associated with the latter is that the algorithm may get stuck around a local optimum and

Fig. 2 Particle updating through the adjustment of velocity
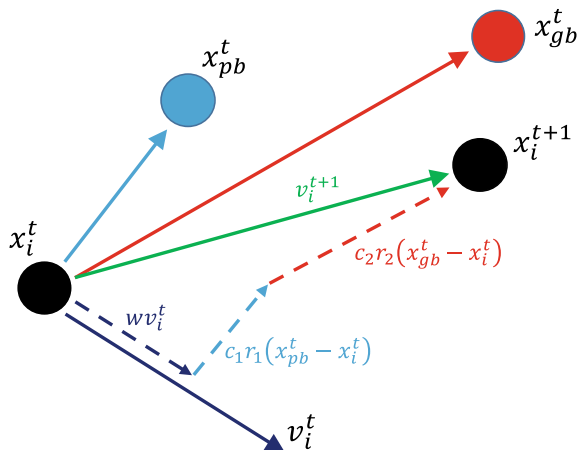
terminating the loop, which performs Steps 2 and 3, may not let the randomness considered in velocity of particles help the algorithm discover new regions in the domain that may contain more optimal solutions.

3   Model Building

A three-storey model building was used to illustrate the proposed methodology developed to assess and minimize damage concentration in steel CBFs under seismic loading. The building selected is an office building located in Vancouver, BC on site Class C. The building measures 45 m × 45 m in the plan as shown in Fig. 3a. Four Moderately Ductile (Type MD) concentrically braced frames with chevron bracing located on the perimeter of the building are considered to resist lateral seismic loads in each direction of the building. One of the CBFs as shown in Fig. 3b is evaluated in this study. Columns are continuous along the height and are pinned at their base.

The loading calculation was performed in accordance with 2015 National Building Code of Canada [39]. The summary of gravity loads, including dead load, live load, snow load, and exterior wall load, are given in Table 1.

Lateral seismic loads were calculated using the equivalent static force procedure. The seismic-induced forces in the braces were then used to select brace cross-sections from ASTM A1085 Hollow Structural Sections (HSSs) following the Canadian steel design standard CSA S16:19 [5] provisions assuming a demand-to-capacity ratio of 0.5 or higher, which are considered as candidate braces to be fed into the algorithm as the optimization variables. An effective length factor $K = 0.9$ taking into account the effect of end connections was used to obtain the brace factored axial resistance. Braces with a broad range of demand-to-capacity and slenderness ratios help thoroughly investigate design alternatives. The candidate brace cross-sections are presented in Table 2.
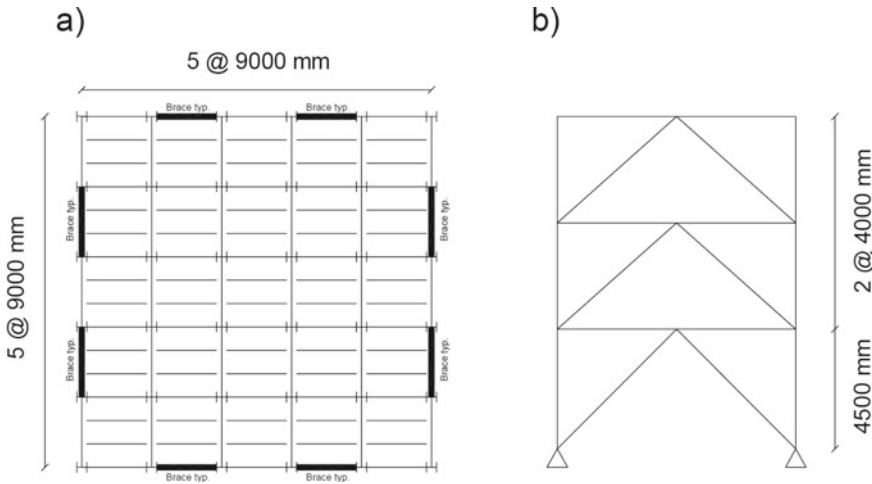
Fig. 3 **a** Plan view of building; **b** elevation view of frame

Table 1 Summary of gravity loads

Location	Source	Load kPa
Roof	Dead	1.35
	Snow	1.64
Floor	Dead	4.6
	Live	2.4
Exterior wall	Dead	1.5

The column and beams of the CBF are then sized with W-shape sections selected from ASTM A992 steel with the yield strength of 345 MPa following the capacity design principles. The CSA S16:19 provision associated with the reduction of the probable tensile resistance of the tension-acting braces in chevron braced frames lower than 4 storeys is ignored in this study to isolate the effect of the brace characteristics on the frame response.

Brace gusset plate connections were designed under probable axial tension and compression loads of the braces following the recommendations by [11].

4 Numerical Model

A fibre-based model of the frame was developed in the *OpenSees* programme [36]. The numerical model of the frame is shown in Fig. 4a. Columns, beams, and braces were modelled using nonlinear force-based beam-column elements with

Table 2 Candidate brace cross-sections for three-storey chevron CBF

Storey	Brace section	Area (mm²)	KL/r	λ	Demand/capacity
3	HSS 5 × 5 × 1/4	2961.28	111.19	1.47	0.73
	HSS 5 × 5 × 5/16	3652.80	112.70	1.49	0.61
	HSS 5 × 5 × 3/8	4245.15	114.97	1.52	0.54
	HSS 4.5 × 4.5 × 1/4	2638.70	124.05	1.64	0.97
	HSS 4.5 × 4.5 × 5/16	3219.35	126.32	1.67	0.82
	HSS 4.5 × 4.5 × 3/8	3761.28	128.59	1.70	0.72
	HSS 4 × 4 × 1/2	4103.22	153.55	2.03	0.89
2	HSS 7 × 7 × 3/8	6180.63	79.42	1.05	0.63
	HSS 7 × 7 × 1/2	7999.98	81.69	1.08	0.50
	HSS 6 × 6 × 3/8	5212.89	93.79	1.24	0.91
	HSS 6 × 6 × 1/2	6683.86	96.82	1.28	0.74
1	HSS 8 × 8 × 1/2	9290.30	74.88	0.99	0.56
	HSS 7 × 7 × 3/8	6180.63	83.96	1.11	0.96
	HSS 7 × 7 × 1/2	7999.98	86.23	1.14	0.77
	HSS 7 × 7 × 5/8	9612.88	87.74	1.16	0.65

fibre discretization of the cross-section. Beams, columns, and braces were modelled according to recommendations by [17].

Shear-tab connections connecting beams to columns were modelled as pin-ended members. Relatively rigid elastic beam-column elements were used to model the portions of beams, columns, and braces that intersect with each other as shown in Fig. 4b. To reproduce brace out-of-plane buckling, assumed in design, gusset plate
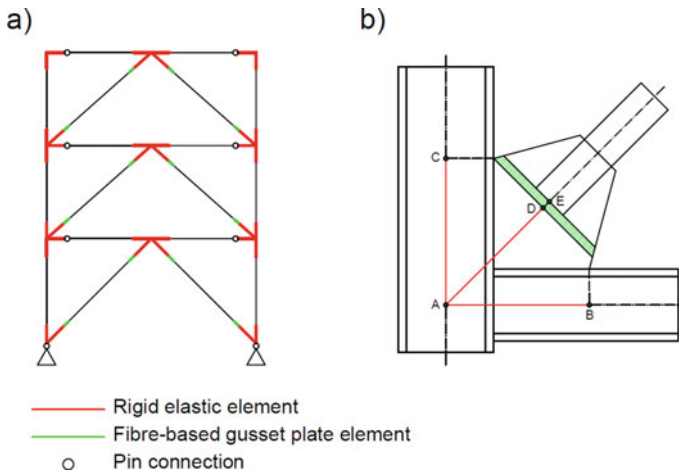
Fig. 4 Fibre-based numerical model of the frame: **a** three-storey CBF; **b** gusset plate connection

connections were modelled using a separate nonlinear beam-column element with fibre discretization of the gusset plate within the theoretical plastic hinge area, DE, shown in Fig. 4b, i.e. 2*t* offset where *t* is the gusset plate thickness.

All members were modelled using the *Steel02* material with properties recommended by [1]. The yield stress for brace cross-sections was set equal to 460 MPa, while the yield stress of 345 MPa was used for the rest of frame members.

To perform NonLinear Response History Analysis (NLRHA), masses were lumped at the mid-point and two ends of each beam. A leaning column, not shown in Fig. 4a, was modelled to account for P-Δ effects. Viscous damping was created using Rayleigh damping method consisting of initial stiffness of the frame CBF and seismic mass; the damping ratio ξ was set to 2% of critical damping.

5 CBF Design Optimization

5.1 *Proposed Optimization Tool*

An optimization tool was developed to improve the seismic response of steel CBFs by encouraging a uniform distribution of lateral deformations along the frame height. This tool was established by linking the PSO algorithm with the parametric *OpenSees* model of the CBF and incorporating a parametric design script capable of automatically designing beams, columns, and gusset plates. In the DCR minimization process shown in Fig. 2, the numerical model of CBF design alternatives plays the role of particles optimized by PSO algorithm, brace cross-sections are the optimization variables, *OpenSees* is the function evaluator to obtain objective function values, i.e. DCR, for each particle, and *m* is the total number of generations to be assessed by the optimization tool. Figure 5 details the steps followed by the automated tool developed to evaluate and minimize the drift distribution in steel CBFs. These steps are as follows:

1. First generation of frames is created by randomly selecting three brace cross-sections from the candidate brace list for each frame.
2. Beams and columns are sized using the lightest section available to carry brace probable tensile and compressive resistances plus gravity loads. This process is performed by a parametric design script.
3. Once beam, column, and brace sections are determined, gusset plate dimensions are calculated using the design script. Since the design script is directly implemented in the optimization tool, no penalty function is required for the PSO algorithm as all generated particles (i.e. braced frames) already belong to the feasible domain by satisfying all limit states addressed by design provisions.
4. Each frame is then modelled in *OpenSees* based on the selected beams, columns, braces, and gusset plates generated by the design script.
5. The NLRHA is performed using the numerical model in *OpenSees* for each frame and the respective DCR values are recorded.
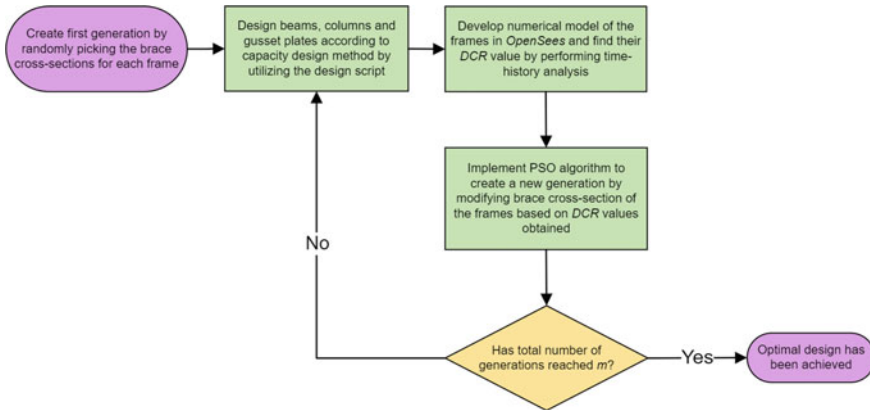
Fig. 5 Optimization workflow

6. At the end of each generation, the PSO algorithm modifies brace cross-sections for each frame based on DCR values obtained and creates a new generation.
7. Steps 2 to 6 are repeated until the termination criteria is met (i.e. number of generations analysed reaches m).
8. Last generation represents a potential set of design alternatives owing to the fact that all its particles have evolved generation by generation and possess relatively smaller DCR values compared to results obtained in previous generations. x_{gb}^m containing brace cross-sections of the frame with best performance (i.e. least DCR value) among all frames is reported as the optimum design.

5.2 Clustering

In order to further investigate and gain better understanding of the correlation between drift concentration and key attributes of brace cross-sections selected in the design stage, frames with desirable seismic performance obtained from the optimization tool can be classified into different groups based on the properties of their structural members and their lateral response features. K-means algorithm [31] is utilized to cluster the frames into k groups. The steps taken by this algorithm to partition the optimized frames are demonstrated in Fig. 6 and detailed below:

1. k random points in the domain of clustering problem are selected as centroids of clusters.
2. Euclidian distance between each particle (i.e. frame) and all centroids is measured. Frames will be assigned to the nearest centroid and form a cluster with it. Centroids remaining with no particles assigned to them are eliminated and the algorithm attempts to cluster the data into k-n groups, n being the number of centroids unable to attract any particles to their clusters.
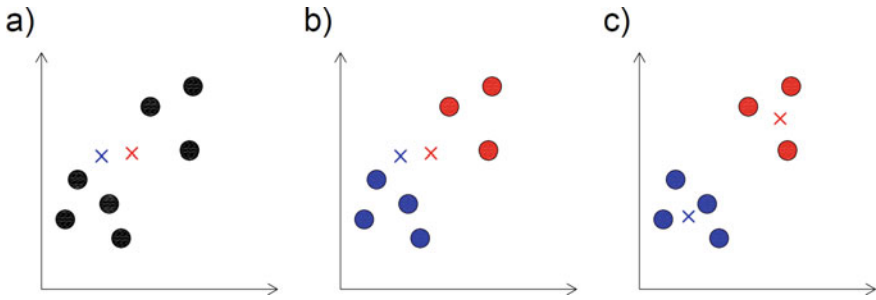
Fig. 6 K-means algorithm steps for clustering: **a** selection of random centroids, **b** particle assignment to centroids, **c** centroid adjustment

3. Each centroid's location is adjusted by moving it to the mean point of the particles inside the cluster it represents.
4. By repeating Steps 2 and 3, clusters are modified until particles assigned to each centroid do not change anymore.

Final clusters' shape is highly sensitive to the initial location of centroids. It is therefore suggested that this algorithm is performed on optimized frames multiple times until clusters with least variation between their particles are achieved. Finally, the closest particle to the centroid in each cluster can be reported as its representative.

6 Conclusions

This paper introduced a new methodology to address damage concentration in three-storey steel CBFs by implementing a metaheuristic optimization algorithm, namely the drift concentration ratios under lateral seismic loads are minimized. The proposed methodology is summarized as follows:

- A design script capable of sizing CBF braces, beams, columns, and gusset plates was developed and linked to a fully parametric numerical model constructed in the *OpenSees* programme.
- The PSO algorithm used in the proposed optimization tool generates numerous CBFs and modifies them iteratively with the objective of minimizing their DCR when the frame is subjected to earthquake ground motion accelerations.

- Candidate frames obtained from the optimization process with the respective least DCR value are finally grouped into different clusters using the K-means algorithm.

Although the current proposed methodology facilitates the seismic design of steel CBFs and assists structural designers to select safer structures less prone to concentration of lateral displacements under seismic loading, additional aspects of braced frame optimization need to be analysed as described below:

- The numerical model of shear-tab connections can be improved using elements with pinching material instead of assuming pin connections between beams and columns to account for the additional lateral stiffness and flexural strength provided by these connections towards the frame lateral response.
- Other steel CBF configurations such as Split-X (two-storey X) braced frames, which offer a more favourable solution when compared to chevron or V-bracing configuration, owing lesser unbalanced seismic load applied at the storey beam mid-span.
- Currently the optimization tool only varies brace cross-sections and the influence of beams and columns on the frame lateral response is evaluated indirectly. The number of optimization variables can be increased by creating separate optimization variables pertaining to beam and column sections to help take advantage of beam and column selections on controlling drift concentration.
- Other optimization algorithms such as genetic algorithm [15] or jEDE [6] can be used to discover most suitable algorithms for structural applications and achieve the algorithm with higher convergence rate and lesser function evaluation compared to the one used in this study.
- Multi-objective optimization can be implemented to account for other design parameters such as total weight of structure and its correlation with lateral response.
- Unsupervised algorithms capable of partitioning optimization results to different groups can be used to alleviate the need of determining the number of clusters k beforehand.

References

1. Ashrafi A, Imanpour A (2021) Seismic response of steel multi-tiered eccentrically braced frames. J Constructional Steel Res 181
2. Chen CC, Chen SY, Liaw JJ (2001) Application of low yield strength steel on controlled plastification ductile concentrically braced frames. Can J Civ Eng 28(5):823–836
3. Clark PW, Aiken ID, Kasai K, Kimura I (2004) Large-scale testing of steel unbonded braces for energy dissipation. In: Structures congress 2000: advanced technology in structural engineering, vol 103, pp 1–5

4. Clough RW, Huckelbridge AA (1977) Preliminary experimental study of seismic uplift of a steel frame. Earthquake Engineering Research Center, Report No. UCB/EERC-77/22
5. CSA (2019) CSA S16:19, design of steel structures. Canadian Standard Association, Toronto, ON, Canada
6. Cubukcuoglu C, Ekici B, Tasgetiren MF, Sariyildiz S (2019) Optimus: self-adaptive differential evolution with ensemble of mutation strategies for grasshopper algorithmic modeling. Algorithms 12(7):141
7. Deierlein G, Krawinkler H, Ma X, Eatherton M, Hajjar J, Takeuchi T, Kasai K, Midorikawa M (2011) Earthquake resilient steel braced frames with controlled rocking and energy dissipating fuses. Steel Constr 4(3):171–175
8. Eatherton MR, Hajjar JF (2014) Hybrid simulation testing of a self-centering rocking steel braced frame system. Earthquake Eng Struct Dynam 43(11):1725–1742
9. Eatherton MR, Ma X, Krawinkler H, Deierlein GG, Hajjar JF (2014) Quasi-static cyclic behavior of controlled rocking steel frames. J Struct Eng 140(11):04014083
10. Eberhart RC, Shi Y (2001) Particle swarm optimization: developments, applications and resources. Proc IEEE Conf Evolut Comput ICEC 1:81–86
11. Ebrahimi S, Mirghaderi SR, Zahrai SM (2019) Proposed design procedure for gusset plate dimensions and force distribution at its interfaces to beam and column. Eng Struct 178:554–572
12. Fahnestock LA, Sause R, Ricles JM (2006) Analytical and large-scale experimental studies of earthquake-resistant buckling-restrained braced frame systems. ATLSS Engineering Research Center, Report No. 06-01
13. Foutch DA, Goel SC, Roeder CW (1987) Seismic testing of full-scale steel building—part I. J Struct Eng 113(11):2111–2129
14. Ghersi A, Neri F, Rossi PP, Perretti A (2000) Seismic response of tied and trussed eccentrically braced frames. Proc Third Int Conf STESSA 2000:495–502
15. Goldberg DE (1989) Genetic algorithms in search, optimization and machine learning, 1st edn. Addison-Wesley Longman Publishing Co., Boston, MA, USA
16. Hassan OF, Goel SC (1991) Modeling of bracing members and seismic behavior of concentrically braced steel structures. Department of Civil Engineering, The University of Michigan, Ann Arbor, Michigan, Report No. UMCE 91-1
17. Hsiao PC, Lehman DE, Roeder CW (2012) Improved analytical model for special concentrically braced frames. J Constr Steel Res 73:80–94
18. Huckelbridge AA (1977) Earthquake simulation tests of a nine story steel frame columns allowed to uplift. Earthquake Engineering Research Center, Report No. UCB/EERC-77/23
19. Iami K, Yasui N, Umezu Y (1997) Development of tube-in-tube type FLD bracing member (force limiting device) and its impulsive analysis. In: Proceedings of the 1997 Structural Stability Research Council (SSRC), pp 515–533
20. Imanpour A, Tremblay R, Davaran A, Stoakes C, Fahnestock LA (2016) Seismic performance assessment of multitiered steel concentrically braced frames designed in accordance with the 2010 AISC seismic provisions. J Struct Eng 142(12):04016135
21. Iwata M, Kato T, Wada A (2000) Buckling-restrained braces as hysteretic dampers. In: Proceedings of the third international conference STESSA 2000, pp 33–38
22. Kelly JM, Tsztoo DF (1977) Earthquake simulation testing of a stepping frame with energy-absorbing devices. NZ Soc Earthquake Eng Bull 10(4):196–207
23. Kennedy J, Eberhart R (1995) Particle swarm optimization. In: Proceedings of ICNN'95—international conference on neural networks, vol 4, pp 1942–1948
24. Khatib IF, Mahin SA, Pister KS (1988) Seismic behavior of concentrically braced steel frames. Earthquake Eng Res Center 1:1–238
25. Kiggins S, Uang CM (2006) Reducing residual drift of buckling-restrained braced frames as a dual system. Eng Struct 28(11):1525–1532
26. Kim J, Choi H (2004) Behavior and design of structures with buckling-restrained braces. Eng Struct 26(6):693–706
27. Ko E, Tajiran F, Kimura I (2001) Building a safer future with unbonded brace. In: First international conference on steel & composite structures, Pursuan, Korea, pp 1549–1556

28. Lacerte M, Tremblay R (2006) Making use of brace overstrength to improve the seismic response of multistorey split-X concentrically braced steel frames. Can J Civ Eng 33(8):1005–1021
29. Lai J-W, Mahin SA (2015) Strongback system: a way to reduce damage concentration in steel-braced frames. J Struct Eng 141(9):04014223
30. Ma X, Deierlein G, Eatherton M, Krawinkler H, Hajjar J, Takeuchi T, Kasai K, Midorikawa M, Hikino T (2010) Large-scale shaking table test of steel braced frame with controlled rocking and energy dissipating fuses. In: 9th US National and 10th Canadian conference on earthquake engineering 2010, including papers from the 4th international tsunami symposium, vol 3, pp 1914–1923
31. MacQueen J (1967) Some methods for classification and analysis of multivariate observations. Proc Fifth Berkeley Symp Math Stat Probab 1:281–296
32. MacRae GA, Kimura Y, Roeder C (2004) Effect of column stiffness on braced frame seismic behavior. J Struct Eng 130(3):381–391
33. Mahin S, Lai JW (2008) An innovative approach to improving the seismic behavior of steel concentric braced frames. University of California, Berkeley, Proposal for SEAONC special projects initiative
34. Mar D (2010) Design examples using mode shaping spines for frame and wall buildings. In: 9th US National and 10th Canadian conference on earthquake engineering 2010, including papers from the 4th international tsunami symposium, vol 2, pp 1290–1299
35. Martini K, Amin N, Lee PL, Bonowitz D (1990) The potential role of non-linear analysis in the seismic design of building structures. In: Proceedings of Fourth US National conference on earthquake engineering, pp 67–76
36. McKenna F, Fenves G, Scott M (2000) Open system for earthquake engineering simulation. Pacific Earthquake Engineering Research Center (PEER)
37. Midorikawa M, Azuhata T, Ishihara T, Wada A (2006) Shaking table tests on seismic response of steel braced frames with column uplift. Earthquake Eng Struct Dynam 35(14):1767–1785
38. Morino S, Kawaguchi J, Shimokawa H (1996) Hysteretic behavior of flat-bar braces. Proc Int Conf Adv Steel Struct 2:1127–1132
39. NRC (2015) National Building Code of Canada (NBCC). Associate Committee on the National Building Code, Ottawa, ON, Canada
40. Perez RE, Behdinan K (2007) Particle swarm approach for structural design optimization. Comput Struct 85(19–20):1579–1588
41. Pollino M, Bruneau M (2010) Seismic testing of a bridge steel truss pier designed for controlled rocking. J Struct Eng 136(12):1523–1532
42. Pollino M (2015) Seismic design for enhanced building performance using rocking steel braced frames. Eng Struct 83:129–139
43. Popov EP, Ricles JM, Kasai K (1992) Methodology for optimum EBF link design. In: Proceedings of the 10th world conference on earthquake engineering, pp 3983–3988
44. Redwood RG, Lu F, Bouchard G, Paultre P (1991) Seismic response of concentrically braced steel frames. Can J Civ Eng 18(6):1062–1077
45. Rezai M, Prion H, Tremblay R, Bouatay N, Timler P (2000) Seismic performance of brace fuse elements for concentrically steel braced frames. In: Proceedings of the third international conference STESSA 2000, pp 39–46
46. Sabelli R (2001) Research on improving the design and analysis of earthquake-resistant steel-braced frames. NEHRP professional fellowship report. EERI
47. Sabelli R, Mahin S, Chang C (2003) Seismic demands on steel braced frame buildings with buckling-restrained braces. Eng Struct 25(5):655–666
48. Sause R, Ricles JM, Roke DA, Chancellor NB, Gonner NP (2010) Seismic performance of a self-centering rocking concentrically-braced frame. In: 9th US National and 10th Canadian conference on earthquake engineering 2010, including papers from the 4th international tsunami symposium, vol 2, pp 1280–1289
49. Stavridis A, Shing PB (2010) Hybrid testing and modeling of a suspended zipper steel frame. Earthquake Eng Struct Dynam 39(2):187–209

50. Torres A, Mahmoudi B, Darras AJ, Imanpour A, Driver RG (2022) Achieving an optimized solution for structural design of single-storey steel buildings using generative design methodology. In: Proceedings of the Canadian society of civil engineering annual conference 2021, CSCE21 structures track, vol 2, pp 301–312
51. Tremblay R, Degrange G, Blouin J (1999) Seismic rehabilitation of a four storey building with a stiffened bracing system. In: Proceedings of 8th Canadian conference on earthquake engineering, pp 549–554
52. Tremblay R (2000) Influence of brace slenderness on the seismic response of concentrically braced steel frames. In: Proceedings of the third international conference STESSA 2000, pp 527–534
53. Tremblay R, Lacerte M (2002) Influence of the properties of bracing members on the seismic response of concentrically braced steel frames. In: Proceedings of the 12th European conference on earthquake engineering, paper 481
54. Tremblay R (2003) Achieving a stable inelastic seismic response for multi-story concentrically braced steel frames. Eng J 40(2):111–129
55. Tremblay R, Merzouq S (2004) Dual buckling restrained braced steel frames for enhanced seismic response. In: Proceedings of passive control symposium, pp 89–104
56. Tremblay R, Poncet L (2004) Improving the seismic stability of concentrically braced steel frames. In: Proceedings—annual stability conference, structural stability research council, pp 19–38
57. Tremblay R, Bolduc P, Neville R, DeVall R (2006) Seismic testing and performance of buckling-restrained bracing systems. Can J Civ Eng 33(2):183–198
58. Tremblay R, Poirier L, Bouaanani N, Leclerc M, Rene V, Fronteddu L, Rivest S (2008) Innovative viscously damped rocking braced steel frames. In: Proceedings of the 14th world conference on earthquake engineering, paper no. 05-01-0527
59. Tsai KC, Lai JW, Chen CH, Hsiao BC, Weng YT, Lin ML (2004) Pseudo dynamic tests of a full scale CFT/BRB composite frame. In: Proceedings of the 2004 structures congress—building on the past: securing the future, pp 1241–1250
60. Uriz P, Mahin SA (2008) Toward Earthquake-resistant design of concentrically braced steel-frame structures. Pacific Earthquake Engineering Research Center, PEER Report 2008/08
61. Watanabe A, Hitomi Y, Saeki E, Wada A, Fujimoto M (1988) Properties of brace encased in buckling-restraining concrete and steel tube. Proc Ninth World Conf Earthquake Eng 4:719–724
62. Whittaker AS, Uang C-M, Bertero VV (1990) An experimental study of the behavior of dual steel systems. Earthquake Engineering Research Center, University of California, Berkeley, CA. Report UCB-EERC-88/14
63. Wiebe L, Christopoulos C, Tremblay R, Leclerc M (2013a) Mechanisms to limit higher mode effects in a controlled rocking steel frame. 1: Concept, modelling, and low-amplitude shake table testing. Earthquake Eng Struct Dyn 42(7):1053–1068
64. Wiebe L, Christopoulos C, Tremblay R, Leclerc M (2013b) Mechanisms to limit higher mode effects in a controlled rocking steel frame. 2: large-amplitude shake table testing. Earthquake Eng Struct Dyn 42(7):1069–1086
65. Wiebe L, Christopoulos C (2014) R = 100? Toward codification of controlled rocking steel braced frames. In: NCEE 2014—10th U.S. National conference on earthquake engineering: frontiers of earthquake engineering. Earthquake Engineering Research Institute
66. Yang C-S, Leon RT, DesRoches R (2008) Pushover response of a braced frame with suspended zipper struts. J Struct Eng 134(10):1619–1626

Influence of Open-Web Steel Joists on Stability of Gerber Girders

Zamir Datoo, Vahab Esmaeili, Robert Driver, and Ali Imanpour

Abstract In this chapter, the validity of the assumption that open-web steel joists provide rigid lateral restraints, but negligible torsional restraints, to the main girder is evaluated. With this end in view, the potential stiffness components at the ends of joists are quantified through the linear elastic analysis of the 16K5 open-web steel joist. The estimated joist stiffnesses are used to define the load response of equivalent discrete rotational springs that are then incorporated into a high-fidelity numerical model of the main girder, which considers initial out-of-straightness, residual stresses, material and geometric non-linearities, and cross-sectional distortions. Non-linear buckling analyses are then performed to account for the way restraints afforded by the joists influence the buckling resistance of the main girder. The results reveal that open-web steel joists tend to have sufficient axial stiffness and strength to restrain the lateral movement of the main girder at the top-flange level. It can also be concluded that the current design procedures may be conservative as a result of overlooking the beneficial effect of torsional restraints due to open-web steel joists.

Keywords Open-web steel joists · Gerber girders · Stability

1 Introduction

Gerber framing, which is a cantilever-suspended-span system, is a popular choice of structural system for roofs of large single-storey steel buildings in North America, such as supermarkets, warehouses, and big-box stores. It is a type of cantilever-suspended-span construction that consists of overhanging girders and drop-in segments connected between the cantilever tips, as shown in Fig. 1. This system has many benefits such as lighter girders as compared to framing using simple spans in each bay, simple and repeatable connections, and reduced deflections due to the continuity at the column locations [4]. However, the girders are complex to analyse

Z. Datoo (✉) · V. Esmaeili · R. Driver · A. Imanpour
University of Alberta, Edmonton, AB, Canada
e-mail: zdatoo@ualberta.ca

accurately, which can make them difficult to design and detail properly and lead to inconsistent application of design requirements by designers. Moreover, collapses of this system have brought attention to the fact that there is little guidance provided to designers by modern steel design standards. One aspect that influences the girder behaviour is the benefits that the secondary framing members, usually Open-Web Steel Joists (OWSJs), provide to the overall girder stability. It is generally assumed that the OWSJs constitute a discrete lateral bracing system at the top flange of the main girder, an assumption that implicitly neglects any torsional restraint that these members may provide by means of the flexural stiffness of their top chords and the semi-rigid connection to the girder flange at the OWSJ shoe.

Essa and Kennedy [9] concluded that torsional restraints significantly enhance the stability of the girder. Therefore, analysing the torsional restraint that the OWSJs provide, as well as correctly applying that restraint to the girder, is very important in design. Most design procedures currently neglect the effect of torsional restraint provided by OWSJs, which may be overly conservative given the stability benefit they provide to the system.
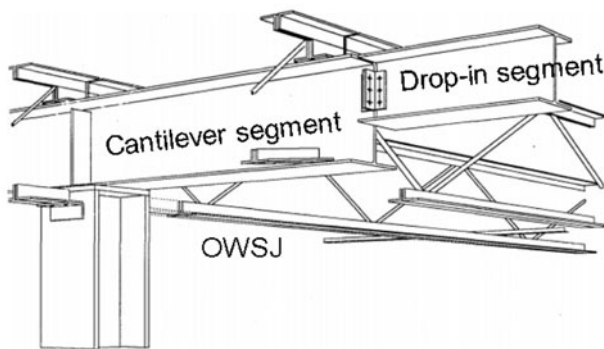
(a) Configuration (CISC, 1989)

(b) Application

Fig. 1 Gerber roof framing system

When OWSJs are welded to the top flange of a girder, the top flange is restrained with respect to twist at these points. Essa and Kennedy [9] proposed a representation of the effective continuous torsional restraint delivered to the bottom flange of the girder, which can be in compression over much of the span, through its web using a spring model with an equivalent stiffness, K_e:

$$\frac{1}{K_e} = \frac{1}{K_w} + \frac{1}{K_f} + \frac{1}{K_b} + \frac{1}{K_j} \tag{1}$$

where K_w represents the bending stiffness of the web; and K_f is the effective torsional stiffness of the girder flange. The influence of these terms can readily be incorporated directly into a finite-element model of the Gerber girder. K_b is the distribution of the in-plane bending stiffness of the OWSJs along the girder; K_j, is the moment–rotation stiffness of the joist-to-girder connection. Milner [10] suggests that K_j be equal to infinity for welded connections, although this neglects any deformation of the connection materials.

The importance of Eq. (1) is illustrated by considering a restrained girder under uniform negative moment, M with lateral braces at the top flange along its length, L, at a spacing s, as shown in Fig. 2. The critical elastic moment under these conditions is [8]:

$$M_{cr} = \frac{GJ}{d} + \frac{2n^2\pi^2 EC_w}{dL^2} + \frac{K_e L^2}{n^2\pi^2 d} \tag{2}$$

The first term in Eq. (2) is associated with the Saint-Venant torsional resistance of the cross-section, the second term represents the effect of warping, and the third term is focused on the torsional restraints coming from the OWSJs. This shows the role that these torsional restraints play in increasing the moment capacity of a girder. Therefore, if the K_e term is equal to zero, it means that the torsional restraints provided by the bracing system are not being relied upon to stabilize the compression flange and increase the moment capacity of the girder.
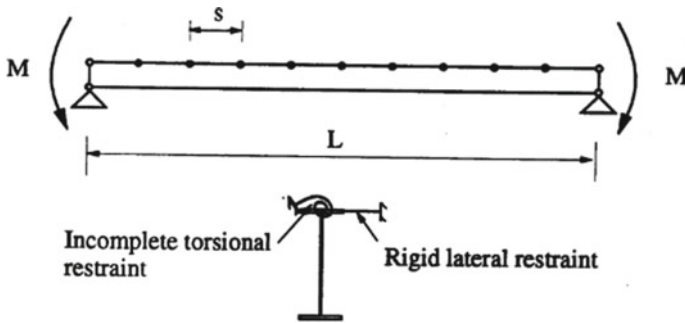
Fig. 2 Cantilevered system under uniform negative moment [8]

Avci and Murray [2] investigated the effects of the addition of a bottom chord
extension on the flexural stiffness of OWSJs. Using analytical and experimental
studies, they found that the flexural stiffness of the OWSJ increased significantly
when a bottom chord extension was installed. Therefore, a bottom chord extension
can both increase the torsional restraint and provide full lateral restraint at the bottom
flange of the girder.

Previous research has shown that the bracing conditions provided by the OWSJs
are important for the overall stability of the Gerber system, as they may affect the
stability of the main girder. This chapter, therefore, aims to investigate the validity of
the current design procedures, which assume that the OWSJs provide lateral bracing
at the top flange and negligible torsional restraint. In order to do this, the stiffness
components at OWSJ ends are quantified through a linear elastic analysis. These
stiffnesses are then included as a pair of springs in the finite-element model of the
main girder. The influence of the OWSJ restraints is then assessed through non-linear
buckling analyses of the main girder with and without the torsional restraints. Finally,
the extent to which the inelastic domain needs to be considered in characterizing the
brace behaviour in future work is evaluated.

2   Numerical Simulation of OWSJ

In order to investigate the properties of the OWSJs, the two-dimensional (2D) finite-
element model of an OWSJ was constructed in the S-Frame program [11]. The
purpose of this model is to determine the lateral and flexural stiffnesses of different
OWSJs under a variety of loading conditions. These stiffnesses can then be incorpo-
rated as a pair of springs into the finite-element model of the girder to examine its
effect on the entire system. A translational spring is used to represent flexible lateral
restraints and a rotational spring to represent flexible torsional restraints. As a means
of indirect validation of the model behaviour, a numerical model of the 16K5 OWSJ
specimen tested by [3] was developed. This OWSJ is shown in Fig. 3.
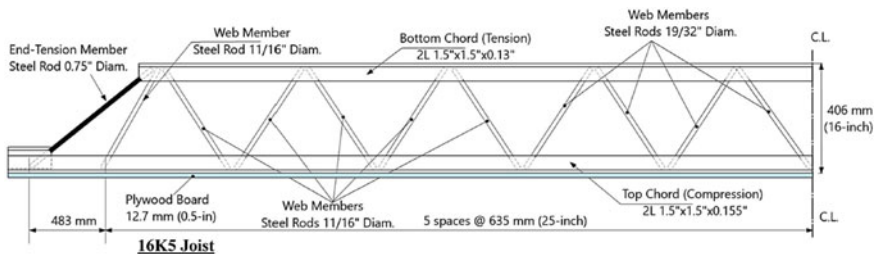
Fig. 3 16K5 OWSJ used for model validation [3]

2.1 Member Types, Releases, and Support Conditions

In order to create an accurate model, it is important to correctly define the member types that make up the OWSJ. In a typical OWSJ, the role of the diagonal web members is to resist shear. Since they do so mainly through axial force and not moment, the web members were initially defined as truss members in the software. In contrast, the continuous top and bottom chords of the OWSJ are designed to carry the bending moment from the loads applied to the top chord, in addition to axial force that develops to resist bending of the overall member. The induced axial force in the top chord is typically compression arising from the uniformly-distributed loads, whilst the bottom chord experiences tensile forces. To account for both axial force and moment, the top and bottom chords were defined as beam elements. Another important modelling assumption is the member releases to ensure the OWSJ transfers the load as would be expected. Pin-pin connections were utilized between the web members and chords to ensure no transfer of moment. Although this is the initial definition of the members, a variety of cases were analysed to observe differences when the definitions of these members were altered. The global support conditions of the OWSJ have been modelled as a simple pin-roller system.

2.2 Member Sizes and Definition

The web members of the OWSJ consist of circular steel rods, whereas the chords are steel double angles, as shown in Fig. 3. For the web members, the software allows the use of circular sections. For the 16K5 OWSJ, the slenderness ratios of the web members increase towards the middle of the span, as can be seen by the decreasing diameters identified in Fig. 3. For the top and bottom chords, the double angles were simulated using equivalent tee sections.

2.3 Material Properties

The first phase of the assessment of the OWSJ behaviour considers only the linear elastic domain, and the elastic modulus of steel was input as 200 GPa and Poisson's ratio was 0.3. All of the sections that make up the OWSJ were considered to meet the requirements of CSA G40.21 Grade 345WM [5] and ASTM A992 [1] steel.

3 Model Validation

The 16K5 OWSJ model is validated by comparing its load response to test results reported by [3]. They conducted experimental tests on OWSJs and compared them to an assumed elastic–perfectly plastic resistance function used for the design of OWSJs. The purpose of this test was to examine the failure mechanisms of OWSJs under static loading conditions. The key assumptions of the 16K5 S-Frame model are verified in the linear elastic range by comparing the load response to the elastic component of the elastic–perfectly plastic resistance function. In order to calculate the elastic stiffness under a uniformly-distributed load, the following relationships were utilized [13]:

$$K = \frac{384 E I_j}{5 L^3} \tag{3}$$

$$I_j = 2.6953 w_{\text{allow}} L^3 10^{-5} \text{ mm}^4 \tag{4}$$

where K is the elastic flexural stiffness of the OWSJ (total force, uniformly applied, per unit of mid-span deflection); E is the elastic modulus of the OWSJ steel; I_j is the OWSJ moment of inertia; L is the span length, taken as the "design length" [12]; and w_{allow} is the allowable uniformly-distributed load to meet the mid-span deflection limit of 1/360 times the span length. The OWSJ allowable load as obtained from the SJI data (2015) is used in Eq. (4) to find the moment of inertia of the OWSJ. The elastic flexural stiffness value is then obtained using Eq. (3). Finally, the elastic flexural stiffness, K, is reduced by 15% to account for shear deformation [12] and divided by the span to determine the slope of the distributed load–displacement curve in the linear elastic region, which is found to be 181 N/mm/m for a 16K5 OWSJ.

To validate the S-Frame model in the linear elastic range, the stiffness of the 16K5 OWSJ model was found. This was done by applying a uniformly-distributed load along the top chord of the OWSJ and observing the deflection at mid-span. Since a normalized value was considered here using a linear elastic analysis, the exact value of the distributed load was not important. Therefore, a linear elastic analysis was run with a 100 kN/m uniformly-distributed load, as shown in Fig. 4. The vertical mid-span deflection was then considered to compute the flexural stiffness value. The deflection diagram is shown in Fig. 5.

To obtain the stiffness value, the uniformly-distributed load was divided by the vertical mid-span deflection as shown in Eq. (5):
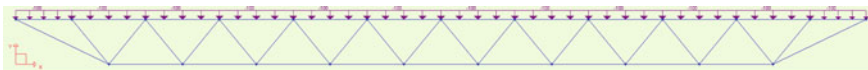
Fig. 4 S-frame loading for model validation
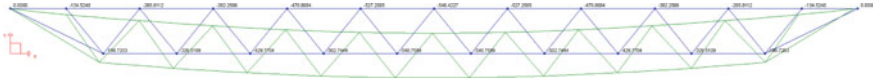
Fig. 5 Deflection under 100 kN/m uniformly-distributed load

$$S = \frac{w}{\Delta_y} = \frac{100 \text{ N/mm}}{0.546 \text{ m}} = 183 \text{ N/mm/m} \tag{5}$$

where S is the slope of the distributed load–displacement curve in the linear elastic region; w is the uniformly-distributed load; and Δ_y is the vertical mid-span deflection. The value of 183 N/mm/m from the model is about 1% different from the value obtained using Eqs. (3) and (4). This provides confidence that the model is responding accurately in the linear elastic range.

4 Stiffnesses of OWSJs as Applied to Main Girder

4.1 Axial Stiffness of OWSJ

The axial stiffness of the OWSJs indicates the degree of lateral restraint provided to the Gerber girder. This is extremely important, as it indicates the level of translational bracing at the girder top flange. If this restraint is effectively infinite, it means that the girder is unable to move laterally at the locations of the OWSJs. By adding a bottom chord extension, restraint can be applied to the bottom flange of the girder. The OWSJs are typically bolted or field-welded to the girders in the Gerber roof framing system [4]. In order to determine this lateral stiffness, the finite-element model of the Gerber girder [6] was utilized. From this analysis, the maximum force experienced by any of the bracing members when assumed infinitely stiff was applied to the OWSJ model at the roller, as shown in Fig. 6.

From the linear elastic analysis, the horizontal deflection of the OWSJ was determined, as shown in Fig. 7.
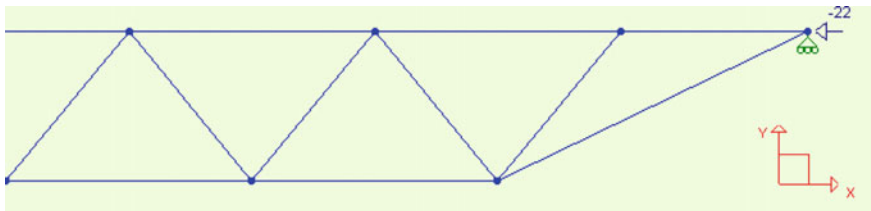
Fig. 6 Axial loading of OWSJ
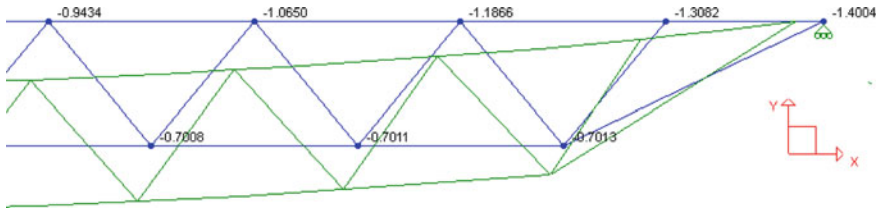
Fig. 7 Horizontal deflection of 16K5 OWSJ under axial load

Under this loading, the OWSJ deflected 1.4 mm at the roller support. Dividing the axial force by the deflection, a lateral stiffness value is obtained:

$$K_{\text{LAT}} = \frac{P}{\Delta_x} = \frac{22\,\text{kN}}{1.4\,\text{mm}} = 15.7\,\text{kN/mm} \tag{6}$$

where K_{LAT} is the lateral stiffness; P is the axial load; and Δ_x is the horizontal deflection. Such a large value of K_{LAT} suggests that the initial assumption of rigid lateral restraints is valid, but further analysis of the girders with braces modelled with this numerically-derived stiffness may reveal that the brace forces increase marginally from the original value used. It is important to note that the stiffness of the roof diaphragm is neglected in the analysis, so it is likely that the girder deflection will be smaller.

4.2 Flexural Stiffness of OWSJ

To establish the torsional restraint provided to the top flange of the girder, a linear elastic analysis is run in order to find the flexural stiffness of the OWSJ. Three cases were analysed to determine the most suitable modelling approach. The first case consisted of the web members represented as truss members and the top and bottom chords being beam members, as shown in Fig. 8. In addition, the truss members were pin-connected between webs and chords, whilst the chords were rigidly connected at the panel points. The effect of these conditions was such that the web members could not carry any moment.

In the second case, shown in Fig. 9, the translational and rotational Degrees-of-Freedom (DOFs) of the end diagonals, simulated using beam elements, were
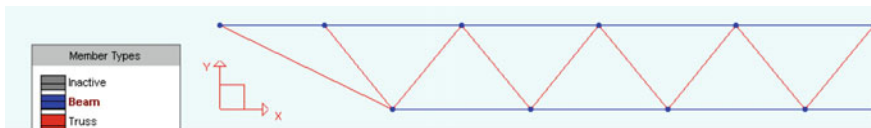
Fig. 8 Restraint case 1
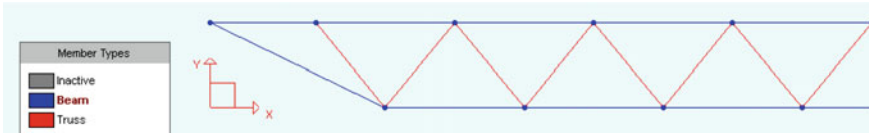
Fig. 9 Restraint case 2
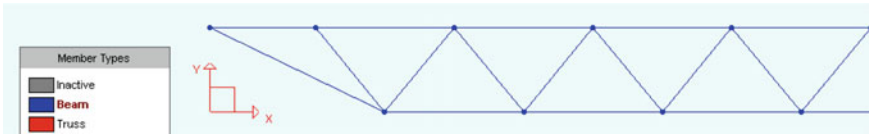
Fig. 10 Restraint case 3

restrained to the top chord, whilst the other web elements were unchanged. This allowed the end diagonals to resist moment, whilst the rest of the web members still were pinned.

Finally, the third case consisted of all members defined as beam elements and being restrained in all DOFs to each other, as shown in Fig. 10. This allowed the consideration of a rigidly-connected OWSJ where any element was able to develop moment.

In order to develop a flexural stiffness value, opposing unit moments were applied at the two ends of the OWSJ, as shown in Fig. 11. The end rotation of the OWSJ was then obtained at the same points for all of the cases.

Furthermore, the three cases shown in Figs. 8, 9 and 10 were analysed by assuming the moment acted at one end of the OWSJ only, as shown in Fig. 12. This produced six cases in total.

By dividing the end moment by the rotation, a flexural stiffness value of the OWSJ is obtained. This process is shown in Eq. (7) for Case 1 with moment applied at both ends. The moment diagram for this scenario is shown in Fig. 13, and the corresponding deformation diagram is shown in Fig. 14.

The flexural stiffness at the end of the OWSJ, K_{FLEX}, is:

Fig. 11 End moments applied at both ends

Fig. 12 End moments applied at one end
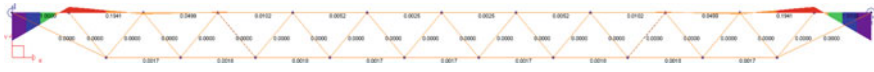
Fig. 13 Moment diagram for case 1 under moments at both ends
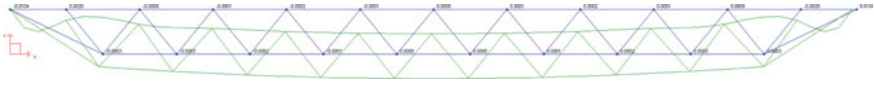
Fig. 14 Deformations for case 1 with moment at both ends

Table 1 Summary of results for flexural stiffness, K_{FLEX} (kN m/rad) of 16K5 OWSJ

Moment applied at both ends			Moment applied at one end		
Case 1	Case 2	Case 3	Case 1	Case 2	Case 3
96	100	102	98	103	104

$$K_{FLEX} = \frac{M}{\theta} = \frac{1\,\mathrm{kN\,m}}{0.0104\,\mathrm{rad}} = 96\,\mathrm{kN\,m/rad} \tag{7}$$

where M is the moment at the support; and θ is the corresponding rotation. The same process was used for the other cases, and the summary of the results is shown in Table 1.

The values of rotational stiffness varied by less than 7% across all cases considered. For this reason, the value of 100 kN·m/rad was considered to be sufficiently accurate, as it is close to the average of all results. This value was represented in the finite-element model through the use of flexible torsional springs, as discussed in Sect. 5.

5 Numerical Simulation of Main Girder

A total of 216 single-overhanging girders using 24 standard steel W-shapes, representing the most common cross-sections utilized in Gerber construction, were considered covering a broad range of geometric properties. All cross-sections, which conform to both CSA G40.21 Grade 345WM [5] and ASTM A992 [1], are either Class 1 or 2 so that the plastic moment represents the upper bound flexural capacity. In order to numerically simulate the main girder, a finite-element model [6] capable of considering material and geometric non-linearities, initial geometric imperfections, and residual stresses were employed. An elastic–perfectly plastic stress–strain curve was considered for the material with a yield stress of 345 MPa. Details of the selected girders are described by [7]. With regard to the joist-to-girder connection, the top flange of the girder was assumed to be full laterally restrained, whereas the torsional

Table 2 Statistical indices associated with normalized maximum effects in OWSJ at joist-to-girder connections of cases with torsional restraints

	Normalized maximum moment[a]	Normalized maximum axial force[b]
Maximum	3.67	0.16
Minimum	0.12	0.00
Mean	1.20	0.06
Coefficient of Variation (CoV)	65%	67%

[a] With respect to the yield moment of the OWSJ
[b] With respect to the yield axial force of the OWSJ

restraint was simulated as a linear rotational spring with a stiffness of 100 kN·m/rad for half of the cases and the torsional restraint is neglected for the other half.

The results obtained from the numerical simulations of the main girder reveal that, amongst 216 girders, 139 cases undergo inelastic lateral–torsional buckling and the other 77 cases reach their fully-plastic flexural capacity. Table 2 presents the statistical indices associated with the normalized maximum effects in the OWSJ at the joist-to-girder connections of the cases with torsional restraints. The moments are normalized by the yield moment of the OWSJ chord, 1.0 kN·m, and the axial forces are normalized by the yield axial force, 198 kN. Furthermore, the finite-element results show that the maximum moment resisted by the OWSJs exceeds the yield moment of the top chord in 51 cases out of the 108 with torsional restraints, indicating that elastic rotational springs may not provide a good representation of the restraint afforded to the girders in all cases. Nevertheless, there is evidence of a tangible benefit to accounting for the rotational stiffness at the OWSJ ends, and further study is warranted. Table 3 summarizes the results associated with the 57 cases in which the maximum moments developed by the torsional restraints do not exceed the yield moment of the OWSJ top chord, along with the same girders without torsional restraints.

Table 3 Effect of torsional restraints on the nominal moment resistance of overhanging girders

	w/o torsional restraints	w/ torsional restraints[a]
Number of cases of inelastic lateral–torsional buckling	33	25
Number of cases where girder becomes fully plastic.	24	32
$\left(\frac{\text{Nominal Moment Resistance}}{\text{Plastic Moment of Section}}\right)_{mean}$	0.46	0.55

[a] For cases in which the maximum moments developed by the rotational spring torsional restraints do not exceed the yield moment of the top chord

6 Conclusions and Future Work

OWSJs play an important role in the stability response of the Gerber system. They can benefit the girder by making them less vulnerable to lateral–torsional buckling. This chapter focuses on the lateral and flexural stiffness components of the OWSJs and how they can be used to examine the stability of the main girder.

Through the linear elastic analysis of the OWSJ and the inclusion of the stiffness values in the finite-element model, the following conclusions are drawn:

- OWSJs appear to provide full lateral restraint to the girder at the top flange owing to their relatively high axial stiffness.
- Current design procedures for Gerber girders may be overly conservative by neglecting the torsional restraint provided by the flexural stiffness of OWSJs.

The S-Frame model has been validated only in the linear elastic range, but the results from the finite-element model of the girder indicate that—in some cases—the loads experienced by the 16K5 OWSJ will result in flexural yielding. Therefore, the next step is to investigate the non-linear behaviour of the OWSJs. Once this has been completed, the final output from the S-Frame model will be a bi-linear moment–rotation curve characterizing the flexural stiffnesses in both the elastic and inelastic regions. The backbone curve of the OWSJ will then be implemented in the finite-element model of the Gerber girders using non-linear rotational and translational springs and be used to evaluate the non-linear buckling response of Gerber system.

References

1. American Society for Testing and Materials (ASTM) (2020) Standard specification for structural steel shapes. ASTM A992/A992M-20, ASTM, West Conshohocken, PA
2. Avci O, Murray T (2012) Effect of bottom chord extensions on the static flexural stiffness of open-web steel joists. J Perform Constr Facilit 26(5):620–632
3. Bondok DH, Salim HA, McClendon MA (2017) Static resistance of open web steel joist roof trusses for blast response analysis. J Perform Construct Facilit 31(6), 04017106:1–10
4. CISC (1989) Roof framing with cantilever (Gerber) girders & open web steel joists. Canadian Institute of Steel Construction, Markham, ON
5. Canadian Standards Association (CSA) (2013) General requirements for rolled or welded structural quality steel/structural quality steel. CSA G40.20-13/G40.21-13 (reaffirmed 2018), CSA, Toronto, ON
6. Esmaeili V, Imanpour A, Driver RG (2021) Stability of Gerber systems with top-flange bracing. In: Proceedings of the annual stability conference, structural stability research council. Louisville, KY

7. Esmaeili V, Imanpour A, Driver RG (2022) Numerical assessment of design procedures for overhanging steel girders. In: Proceedings of the CSCE annual conference, Whistler, BC
8. Essa HS, Kennedy DJL (1993) Distortional buckling of steel beams. Structural engineering report no. 185. Department of Civil Engineering, University of Alberta, Edmonton, AB
9. Essa HS, Kennedy DJL (1995) Design of steel beams in cantilever-suspended span construction. J Struct Eng 121(11):1667–1673
10. Milner HR (1977) The design of simple supported beams braced against twisting on the tension flange. Civ Eng Trans 19(1):84–91
11. S-Frame Software Inc. (2017) S-frame analysis quick start guide. Version 2017. Richmond, BC
12. Steel Joist Institute (SJI) (2015) Standard specifications load tables and weight tables for steel joists and joist girders, 44th edn. Myrtle Beach, SC

Macro-Block and DEM-Based Probabilistic Analysis to Predict In-Plane Structural Behavior of URM Pier–Spandrel Systems

Bora Pulatsu, Semih Gonen, Paulo B. Lourenço, and Kagan Tuncay

Abstract In the last several decades, computational modeling of unreinforced masonry buildings has been a subject of interest in the field of structural and conservation engineering. Different computational modeling techniques are being used by researchers and practitioners at various levels of complexity. However, most studies only focus on a single method, and they fail to compare different approaches. In this context, the present study aims to discuss both practice-oriented simplified macro-block analysis and advanced computational models based on the discrete element method (DEM). They are utilized to predict the structural behavior of a pier–spandrel system subjected to lateral forces. Moreover, the variability of the structural behavior and capacity of the system is explored by explicitly addressing uncertainties in the material properties. Probabilistic analyses considering the spatial variation of the material parameters are carried out using Monte Carlo simulations. The results show that considering spatial and non-spatial material properties in the advanced model improves our understanding of their effect on structural behavior and capacity. Specifically, two input parameters, joint tensile strength and friction angle, revealed a considerable effect on the load-carrying capacity of the pier–spandrel system. The results also indicate advantageous features of different approaches.

Keywords Probabilistic analysis · In-plane structural behavior · URM pier–spandrel systems

B. Pulatsu (✉)
Department of Civil and Environmental Engineering, Carleton University, Ottawa, Canada
e-mail: bora.pulatsu@carleton.ca

S. Gonen
Civil Engineering and Energy Technology, Oslo Metropolitan University, Oslo, Norway

P. B. Lourenço
Institute of Sustainability and Innovation in Structural Engineering, University of Minho, Braga, Portugal

K. Tuncay
Civil Engineering, Middle East Technical University, Ankara, Turkey

1 Introduction

Accurate estimation of the structural performance of historic buildings plays a crucial role in achieving sustainable conservation plans and preventing unexpected and dangerous collapses. In this regard, both simplified and advanced computational tools become important in seismic and damage assessments by providing valuable information about the capacity and behavior of historic buildings. However, developing a systematic approach to capture the collapse mechanism of masonry structures is challenging due to the complexity of the problem and inherited uncertainties in the material properties.

Masonry structures can be built with various construction techniques and materials. Typically, clay bricks, stone, or adobe blocks are used as masonry units, and cement or lime-based mortar is utilized as a binding material. The macro-behavior of masonry constructions is directly influenced by its constituents (e.g., unit, mortar, and unit–mortar interface) and the construction quality [3]. Hence, it is essential to have a good understanding of its construction technique (workmanship), geometrical features of structural elements (e.g., walls, arches, domes), and material characteristics to provide accurate estimations about the structural behavior of masonry buildings. It is expected that different unit and mortar combinations (such as weak brick—strong joint or strong brick—weak joint) alter the damage progression and crack pattern in masonry constructions, as noted in early studies [27, 30]; hence, it influences the deformability and capacity of the overall structure [21, 26, 29]. In this regard, computational models addressing these factors can provide valuable insights in predicting the structural performance and determining the influence of proposed interventions plans. As witnessed in the recent and past earthquakes, lack of knowledge in the mechanics of masonry structures and erroneous interventions may cause severe detrimental effects and failures in masonry buildings [1, 2].

This research aims to simulate the structural behavior of an unreinforced masonry pier–spandrel system, which typically exists in many residential and historic buildings, by considering the effect of vertical stress and uncertainties in the material properties. Strong brick—weak joint combination is assumed throughout the analyses, representing the general case for heritage structures. First, computational models are validated by comparing to recent experimental findings presented by Howlader et al. [7]. Then, probabilistic analyses are performed, considering the spatial and non-spatial variation in the material properties of the structure. Furthermore, predefined rigid macro-blocks, depicted from DEM-based simulations, are utilized to apply upper-bound kinematic limit analysis. The results and computational procedures are discussed in the following sections.

2 Computational Procedure: Discrete Element Method

The advanced structural analysis of masonry constructions can be grouped as continuum- and discontinuum-based approaches. In the former strategy (also referred to as the macro-modeling approach), the composite masonry is represented as a homogenous continuum, where no distinction is made about the constituents of masonry (e.g., see [4, 20, 24, 32]). On the contrary, the latter replicates the discontinuous nature of masonry explicitly in the numerical formulation to obtain failures at the joints acting as weak planes in the structure. In this regard, the employed modeling strategy, so-called discrete element method (DEM), falls into the category of discontinuum-based analysis, where the masonry units are described as distinct rigid blocks (expanded up to the half-thickness of the mortar joints), and the influence of mortar joints is considered via zero-thickness interfaces as illustrated in Fig. 1. Hence, the brickwork assemblage is simulated using the group of rigid blocks that interact along their boundaries, using the adopted point contact hypotheses (Fig. 1).

Briefly, DEM relies on integrating the equations of translational and rotational motion for each rigid block center of mass, written in Eqs. 1 and 2, respectively. The new translational ($\dot{u}^{t+}$) and rotational (ω^{t+}) velocities are obtained via the central difference method, in which the block velocities are evaluated at the mid-intervals of the time step (Δt, $t^+ = t + \Delta t/2$, $t^- = t - \Delta t/2$). The quasi-static solutions are obtained adopting Cundall's local damping formulation, proportional to the unbalanced force (ΣF) for translation motion and unbalanced moment (ΣM) for rotational motion and controlled by a non-dimensional factor (λ, the default value is 0.8). Note that the unbalanced force includes the sum of the contact forces, self-weight, and applied forces, whereas the unbalanced moment consists of the sum of moments produced by contact and applied forces [5].

$$\dot{u}_i^{t+} = \dot{u}_i^{t-} + \frac{\Delta t}{m}\left(\Sigma F_i^t - \lambda \left|\Sigma F_i^t\right| \mathrm{sgn}\left(\dot{u}_i^{t-}\right)\right) \tag{1}$$

$$\omega_i^{t+} = \omega_i^{t-} + \frac{\Delta t}{I}\left(\Sigma M_i^t - \lambda \left|M_i^t\right| \mathrm{sgn}\left(\omega_i^{t-}\right)\right) \tag{2}$$
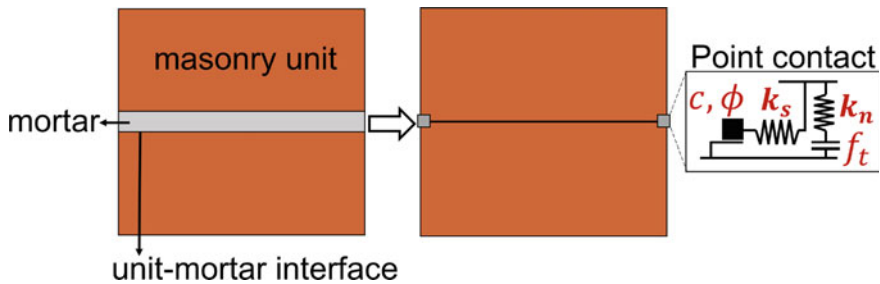
Fig. 1 Representation of brickwork assemblage in DEM and point contact model (illustrated in 2D)
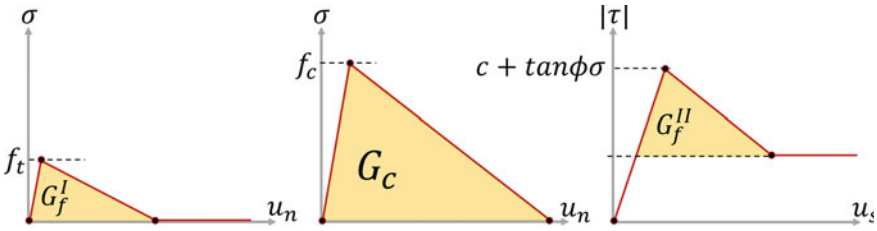
Fig. 2 Contact constitutive laws in tension, compression, and shear

where m, I, and $\text{sgn}(\cdot)$ are block mass, the moment of inertia, and sign function ($\text{sgn}(\gamma) = 1$, if $\gamma \geq 0$; else $\text{sgn}(\gamma) = -1$). Then the new velocities are utilized to update the position of each rigid block centroid (hence the block vertices) after computing the displacement and rotation increments ($\Delta u_i = \dot{u}_i^{t+}\Delta t$, $\Delta \theta_i = \dot{\omega}_i^{t+}\Delta t$, respectively). The new block positions are further employed to compute associated contact forces, which are the function of relative block displacements [12, 17]. It is important to note that only the initial configuration of the contact points is utilized; therefore, no new contact pairs are detected during the analysis. As shown in Fig. 1, force transfer at the point contacts is controlled by the orthogonal springs, working in the normal and shear directions. Through this research, fracture-energy-based contact constitutive laws are utilized that are implemented to better capture the unit-mortar-interface (bond) behavior in post-peak regime in tension, shear, and macro-behavior of masonry in compression (readers are referred to the reference studies for further details [28, 31]). The elastic response at the contact points is governed by the normal (k_n) and shear (k_s) stiffnesses, whereas nonlinear behavior is described by the tension (f_t) and compression (f_c) strength in the normal direction, cohesion (c) and friction angle (ϕ) in the shear directions. Bi-linear contact stress–displacement behaviors are adopted in tension, compression and shear regimes based on the defined fracture energies (G_f^I, G_f^{II}, and G_c, , respectively), as illustrated in Fig. 2. Therefore, fundamental failure modes of brickwork assemblages are captured at the contact points via the adopted contact stress–displacement laws.

The computed contact stresses are multiplied with the associated contact area to get forces, later employed in the equations of motions as explained earlier. The outlined explicit dynamic solution procedure is executed through the pseudo-time domain by satisfying the critical time step criteria ($\Delta t < \Delta t_{\text{critical}}$) to obtain stable solutions simulating collective mechanics of discrete rigid blocks [11]. All computational models are solved using a commercial three-dimensional discrete element code, 3DEC, developed by ITASCA. The adopted contact models are written in C++ and compiled as dynamic link library (DLL) into 3DEC. In the next section, a validation of the proposed modeling strategy is presented using the most recent test results for the in-plane behavior of an unreinforced pier–spandrel system.

3 Validation of Macro-Block and DEM-Based Solutions

A benchmark study presented by [14] is utilized to validate the proposed discontinuum-based modeling strategy and the simplified macro-block analysis. In addition, the results of deterministic discrete element models are discussed and compared with simplified macro-block solutions.

3.1 Pier–Spandrel Test—[14]

The benchmark study was performed by [14] to better understand the in-plane response of perforated unreinforced masonry walls under different vertical loads. The designed test setup consists of two piers and an arch spandrel constructed as double wythe thick masonry (thickness of 0.23 m). The height of the structure is 2.4 m, and the spanning distance is 0.97 m between two piers. For a detailed description of the specimen geometry, readers are referred to the reference study [14]. Low-strength solid bricks with a lime-rich cement-lime mortar mix were used during the construction.

Two different vertical precompression levels (0.2 and 0.5 MPa) were applied to the piers before imposing lateral displacements to the loading beams, as demonstrated in Fig. 3. The piers equally shared the vertical loads and kept constant during the test (see Fig. 3).

Fig. 3 Illustration of the test setup
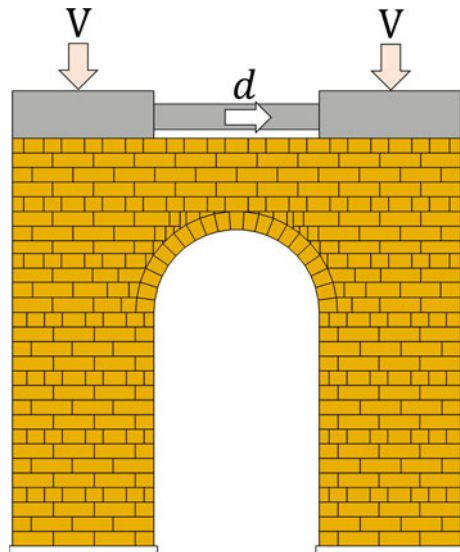
3.2   Discrete Element Modeling: Deterministic Analysis

In the DEM-based model, identical geometrical properties are used to generate rigid blocks representing the pier-spandrel system and loading beams. The contact properties are defined based on the experimental findings reported in the benchmark study and well-known empirical formulations given in the literature (if applicable). The elastic modulus of masonry (consisting of low-strength bricks and lime-based mortar) is predicted based on the mean compression strength of masonry prism, given as 7 MPa by [14], using the empirical relationship of $E_{\text{masonry}} \approx 225 f_c$, which usually varies between the lower bound of $200 f_c$ and upper bound of $350 f_c$ [33, 34]. Then, the estimated elastic modulus is employed to compute contact stiffness, $k_n = E_{\text{masonry}}/h$, where h indicates the vertical joint spacing (0.086 m). Bond tensile strength, cohesion and joint friction angle are directly taken from the experimental results [14]. The related fracture energies are estimated based on the suggested ductility index values and empirical relations available in the literature [19, 25]. The contact properties are given in Table 1.

The nonlinear quasi-static analyses are performed, imposing lateral displacement to the loading beam once the static equilibrium is reached under the vertical pressure and self-weight. The sum of shear forces between the support block and the piers is recorded during the analyses. The obtained force–displacement curves and associated crack patterns, both for 0.2 and 0.5 MPa vertical pressures, are presented in Fig. 4. An excellent agreement is observed between the numerical and experimental force–displacement curves. As shown in Fig. 4a, b, the results undoubtedly exhibit the positive impact of the vertical pressure on the lateral resistance of the pier–spandrel system. The deformation starts as a pier rocking, followed by diagonal cracks at the spandrel. It is noted that high vertical pressure (0.5 MPa) yields more cracks on the arch spandrel than low vertical pressure (0.2 MPa), which can be observed in Fig. 4c, d. However, both vertical pressures yield similar behavior in terms of global mechanisms.

Notwithstanding, the force–displacement behaviors and corresponding failure mechanisms are obtained through quasi-static analysis in discrete element models, while cyclic loads were applied in testing. Therefore, the difference in the loading conditions may yield variations in the crack pattern, as shown in Fig. 4d, where damaged piers are not obtained in the numerical models. Overall, a good agreement is found between discontinuum-based analysis and experiment.

Table 1   Contact properties defined in discrete element model

k_n, k_s (GPa/m)	f_t (MPa)	f_c (MPa)	c, ϕ (°)	G_f^I (N/m)	G_f^{II} (N/m)	G_c (N/m)
18, 0.4 k_s	0.1	7	1.5 f_t, 36.5	0.03 f_t	85	1.6 f_c
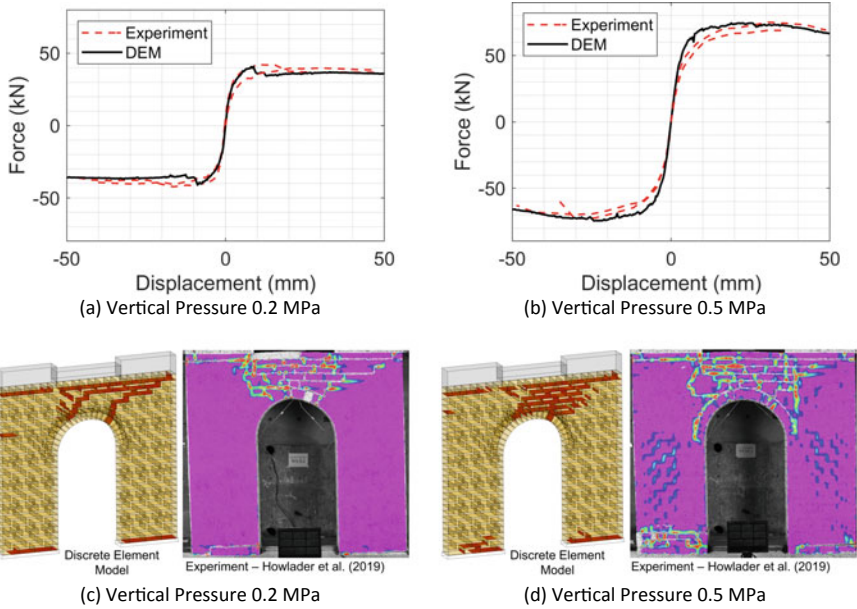
Fig. 4 DEM versus experiment—comparisons of the force–displacement behavior and damage state at the ultimate displacement (red color indicates cracks (openings and/or sliding) at the joints in DEM)

3.3 Simplified Macro-Block Analysis

In this section, failure mechanisms, obtained from the discrete element model, are employed to generate rigid macro-blocks, considering Heyman's material model for masonry, which assumes no tensile strength, no sliding failure, and infinite compression capacity [13]. Once the macro-blocks are depicted from discrete element models, the lateral load multiplier (λ) is computed through the use of the virtual work principle. The workflow is illustrated in Fig. 5. De Luca et al. [6] presented a similar workflow considering a continuum setting based on the finite element analysis and post-processing the stress field to position the plastic hinges. Alternatively, the present study interprets the explicit joint failures (in other words, cracks) to locate plastic hinges and associated crack paths developing within the discontinuous medium.

The results obtained from DEM-mediated macro-blocks align with the experimental findings and discrete element models, as shown in Fig. 6. However, it is also noted that macro-block solutions may provide lower capacity, as obtained for 0.2 MPa vertical pressure since it considers no rotational restriction at the top of the pier–spandrel system. This simplification may not be completely satisfied in testing and can be addressed in discrete element modeling because both loading beams sitting on top of the piers are connected.
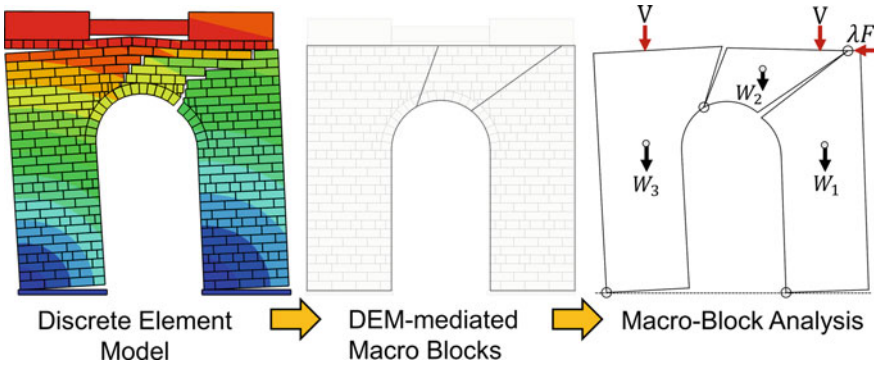
Fig. 5 Discontinuum-based workflow to define macro-block mechanism
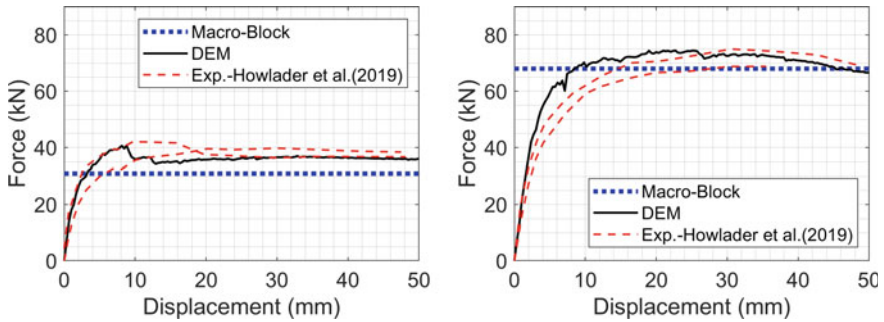
Fig. 6 Comparison of the experimental findings and DEM-based solutions with macro-block analysis (left: vertical pressure 0.2 MPa; right: vertical pressure 0.5 MPa)

4 Spatial and Non-spatial Probabilistic Analysis

Masonry properties are probabilistic due to the inherent variability in its constituents and uneven material degradation [9]. Further uncertainties also appear in the numerical modeling when considering the loading, boundary conditions, and geometry of the analyzed structure. The research community has recognized this phenomenon, and probabilistic assessment of masonry structures has recently been employed for various structural typologies [7, 8, 10, 15, 22, 23]. While such studies showed the importance of probabilistic modeling in predicting structural performance, they also demonstrated a further need for quantifying the uncertainties included in the analysis. Therefore, this study considers the variability of the mechanical properties in a pier–spandrel system to investigate the effect of these uncertainties on structural behavior and capacity.

4.1 Data Preparation

Two types of parameters (random and dependent) are considered in the probabilistic analyses, in which joint tensile strength ($f_{t,j}$), joint friction angle (ϕ_j), masonry compressive strength (f_c), and elasticity modulus (E) are taken as random variables. Note that the mean values and the coefficient of variations (CoV) of the assigned distributions are determined in agreement with the benchmark study, given in Table 2. On the other hand, the dependent parameters are fully correlated with the random variables, and their mean and CoV are the multiples of the random variables. For example, the cohesion is computed following relationship $c_j = 1.5 f_{t,j}$ while the fracture energies are calculated using simple formulations given in Table 2. A normal distribution is defined for all parameters except the joint tensile strength, which has a lognormal distribution following the pertinent literature [18, 23].

The statistical distributions and their parameters defined previously are used to derive the sample values for Monte Carlo simulations (MCS). Sampling of the parameter values is done using the Latin Hypercube Sampling (LHS) method [35]. During sampling, 70% correlation is defined between the elastic modulus and compressive strength of masonry, according to a recent study [16]. For the non-spatial analyses, where uniform material properties are considered throughout the structure, 150 samples of each parameter are generated. In other words, one value for each modeling parameter is generated in each realization of the Monte Carlo simulations, and that value is assigned to all the joints. In the spatial analyses, each one of the 948 joints in the analyzed structure is assigned a different value in each of the 150 Monte Carlo simulations. Therefore, the modeling parameters change throughout the structure in a single MCS. The sufficient number of MCS is determined by tracking the variation of the mean value of the maximum lateral force ($\overline{F}_{\max}$). As shown in Fig. 7, $\overline{F}_{\max}$ stabilizes after 70 simulations.

Table 2 Variables, their associated distributions, and parameters

Random variable	Probability distribution	Mean (μ)	Coefficient of variation (CoV)
f_t (MPa)	Lognormal	0.10	0.30
ϕ (degrees)	Normal	36.5	0.15
f_c (MPa)	Normal	7.0	0.07
E (GPa)	Normal	1.5	0.10
Dependent variable	*Relationship*		
c	$1.5 f_{t,j}$		
$G_{f,I}$	$0.03\ f_{t,j}$		
G_C	$1.6\ f_c$		

Fig. 7 Variation of the
average maximum lateral
force against the total
number of simulations
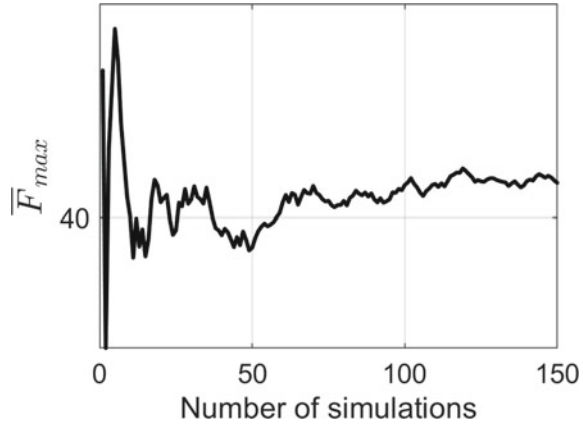
4.2 Results

The results of the stochastic analyses are presented in the form of lateral force–displacement curves in Figs. 8 and 9 and summarized in Table 3. Note that Figs. 8 and 9 reveal both spatial and non-spatial analyses when the vertical pressure is 0.2 MPa and 0.5 MPa, respectively. In both figures, it is evident that the variability of the results decreases in the spatial analysis, leading to more consistent behavior. Ironically, the results show more variability when the modeling properties are uniformly distributed throughout the structure.

Furthermore, another salient feature of the graphs is the increase in the lateral load capacity of the pier–spandrel system with the increasing vertical pressure. Specifically, for the analyzed structure, increasing the vertical pressure from 0.2 to 0.5 MPa almost doubles the capacity. It can also be stated that the variability of
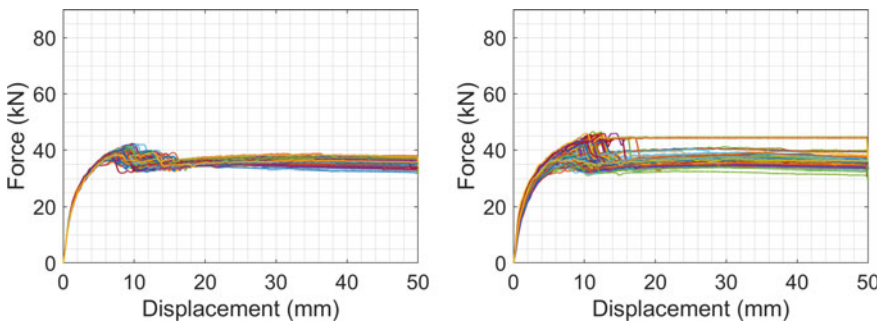
Fig. 8 Force–displacement curves obtained from spatial (left) and non-spatial (right) probabilistic analyses under 0.2 MPa vertical pressure
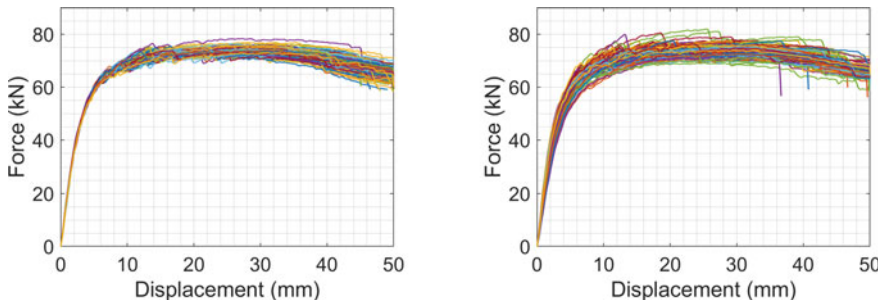
Fig. 9 Force–displacement curves obtained from spatial (left) and non-spatial (right) probabilistic analyses under 0.5 MPa vertical pressure

Table 3 Summary of the stochastic analyses in terms of the lateral force capacity

Vertical pressure (MPa)	Non-spatial		Spatial	
	F_{max} (kN)		F_{max} (kN)	
	Mean	CoV	Mean	CoV
0.2	40.32	0.084	39.93	0.027
0.5	74.97	0.028	74.20	0.014

the results decreases for both spatial and non-spatial analyses as the vertical pressure increases. Finally, it should be noted that in both cases, the results yield similar failure mechanisms to those shown in Fig. 4.

The correlation between the modeling parameters and the lateral force capacity of the pier–spandrel system is also investigated. The Pearson product–moment correlation coefficient, $\rho_{x,y}$, which quantifies a linear statistical correlation between two random variables (x, y) is used. This correlation coefficient ranges between 0 and 1, indicating zero and full correlation, respectively. Figure 10 indicates the change in the lateral force capacity of the structure with respect to the change in the joint tensile strength and friction angle for different vertical pressures. While a linear relationship between the force capacity and joint tensile strength is found in Fig. 10a, it is not possible to infer such a relationship for the joint friction angle. Indeed, the correlation coefficients between the change in the lateral force capacity and the joint tensile strength and friction angle are $\rho = 0.90$ and $\rho = 0.30$, respectively. Moreover, as can be interpreted from Fig. 10b, the correlation coefficient for the joint tensile strength decreases to 0.49 ($\rho = 0.49$) while it increases to 0.76 ($\rho = 0.76$) for the joint friction angle. These outcomes are not only peculiar observations, but they also comply with the physics of the structural system, where the shear behavior becomes more dominant as the vertical pressure increases on the piers. As for the compressive strength and elasticity modulus of the masonry, no significant linear correlation between these parameters and the change in the lateral capacity is observed.

Another interesting observation is the limits of the change in the lateral capacity of the system, which is $\pm 20\%$ when the vertical pressure is 0.2 MPa and $\pm 10\%$
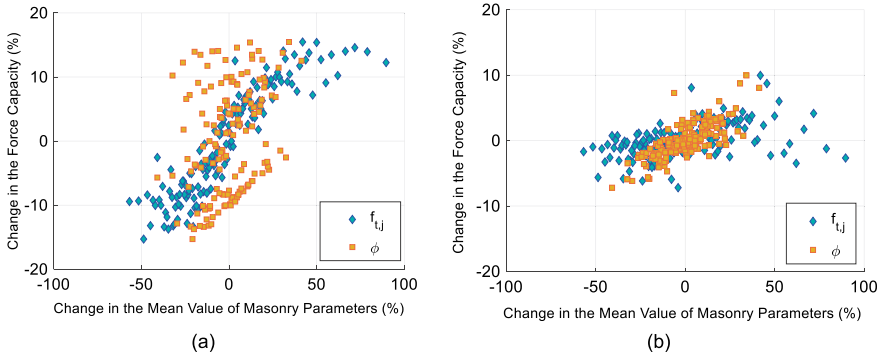
Fig. 10 Change in the mean value of the masonry parameters versus the change in the lateral force capacity for **a** vertical stress = 0.2 MPa and **b** vertical stress = 0.5 MPa

when the vertical pressure is 0.5 MPa. This also confirms the previous observations presented in Table 3.

5   Conclusions

This research investigates the in-plane behavior of a pier–spandrel system using the discrete element method. A DEM-mediated simplified macro-block solution is suggested to predict the lateral load-carrying capacity. Additionally, validated discontinuum models are utilized to better understand the effect of the material properties on the behavior and lateral load-carrying capacity of the structure. Specific conclusions are drawn as follows.

1. The results suggest that discontinuum-based analysis of strong brick—weak joint masonry assemblages can be accurately captured via the proposed approach, which can also be utilized as a tool to predefine the macro-block mechanisms.
2. In unreinforced pier-spandrel systems, the damage mechanisms vary considerably depending on the vertical pressure, in which a more spread crack pattern is observed for higher vertical pressures. Moreover, it is observed that the lateral load capacity increased by 90% when the vertical pressure is raised from 0.2 to 0.5 MPa.
3. Spatial and non-spatial stochastic analyses yielded similar results in terms of the average maximum load; however, the spatial stochastic analysis resulted in less variation in the lateral load capacity of the system.
4. It is demonstrated that for higher vertical stresses, the shear behavior dominates the response of the pier-spandrel system. This phenomenon is observed and quantified using the correlation coefficients between the change in the mean value of joint friction angle and tensile strength and the lateral force capacity of the system.

5. This research also shows that DEM-mediated macro-block solutions provide close predictions with computational models and experimental findings, indicating that they can be considered alternative preliminary solutions in practice over computationally demanding numerical tools.

References

1. Augenti N, Parisi F (2010) Learning from construction failures due to the 2009 L'Aquila, Italy, Earthquake. J Perform Constr Facil 24(6):536–555
2. Borri A, Corradi M (2019) Architectural heritage: a discussion on conservation and safety. Heritage 2(1):631–647
3. Borri A, Corradi M, Castori G, De Maria A (2015) A method for the analysis and classification of historic masonry. Bull Earthquake Eng 13(9):2647–2665
4. Ciocci MP, Sharma S, Lourenço PB (2018) Engineering simulations of a super-complex cultural heritage building: Ica Cathedral in Peru. Meccanica 53(7):1931–1958
5. Cundall PA, Detournay C (2017) Dynamic relaxation applied to continuum and discontinuum numerical models in geomechanics. In: Rock mechanics and engineering. CRC Press, pp 57–102
6. De Luca A, Giordano A, Mele E (2004) A simplified procedure for assessing the seismic capacity of masonry arches. Eng Struct 26(13):1915–1929
7. Gonen S, Pulatsu B, Soyoz S, Erdogmus E (2021) Stochastic discontinuum analysis of unreinforced masonry walls: lateral capacity and performance assessments. Eng Struct 238:112175
8. Gonen S, Soyoz S (2021) Reliability-based seismic performance of masonry arch bridges. Struct Infrastruct Eng: 1–16
9. Gonen S, Soyoz S (2021) Investigations on the elasticity modulus of stone masonry. Structures 30:378–389
10. Gooch LJ, Masia MJ, Stewart MG (2021) Application of stochastic numerical analyses in the assessment of spatially variable unreinforced masonry walls subjected to in-plane shear loading. Eng Struct 235:112095
11. Hart R, Cundall PA, Lemos JV (1988) Formulation of a three-dimensional distinct element model—part II. Mechanical calculations for motion. Int J Rock Mech Min Sci Geomech 25(3):117–125
12. Hart R, Cundall PA, Lemos JV (1988) Formulation of a three-dimensional distinct element model-Part II. Mechanical calculations for motion and interaction of a system composed of many polyhedral blocks. Int J Rock Mech Min Sci 25(3):117–125
13. Heyman J (1966) The stone skeleton. Int J Solids Struct 2(2):249–256, IN1–IN4, 257–264, IN5–IN12, 265–279
14. Howlader MK, Masia MJ, Griffith MC (2019) Cyclic in-plane testing of simulated Australian historical perforated URM walls. In: Dillon PB, Fonseca FS (eds) 13th North American Masonry conference. The Masonry Society, Salt Lake City, pp 1615–1627
15. Isfeld AC, Stewart MG, Masia MJ (2021) Stochastic finite element model assessing length effect for unreinforced masonry walls subjected to one-way vertical bending under out-of-plane loading. Eng Struct 236:112115
16. Jafari S, Rots JG, Esposito R (2021) A correlation study to support material characterisation of typical Dutch masonry structures. J Build Eng 45:103450
17. Lemos JV (2007) Discrete element modeling of masonry structures. Int J Archit Heritage 1(2):190–213
18. Li J, Stewart MG, Masia MJ, Lawrence SJ (2016) Spatial correlation of material properties and structural strength of masonry in horizontal bending. J Struct Eng 142(11):04016112

19. Lourenço PB (2009) Recent advances in masonry structures: micromodelling and homogenisation. In: Multiscale modeling in solid mechanics: computational approaches, pp 251–294
20. Lourenço PB, Rots JG, Blaauwendraad J (1998) Continuum model for masonry: parameter estimation and validation. J Struct Eng 124(6):642–652
21. Malomo D, DeJong MJ, Penna A (2019) Influence of bond pattern on the in-plane behavior of URM piers. Int J Archit Heritage: 1–20
22. Müller D, Förster V, Graubner C-A (2017) Influence of material spatial variability on required safety factors for masonry walls in compression. Mauerwerk 21(4):209–222
23. Parisi F, Augenti N (2012) Uncertainty in seismic capacity of masonry buildings. Buildings 2(3):218–230
24. Pelà L, Cervera M, Roca P (2013) An orthotropic damage model for the analysis of masonry structures. Constr Build Mater 41:957–967
25. Van der Pluijm R (1993) Shear behavior of bed joints. In: 6th North American masonry conference, The Masonry Society, Philadelphia, pp 125–136
26. Pulatsu B, Bretas EM, Lourenço PB (2016) Discrete element modeling of masonry structures: validation and application. Earthquakes Struct 11(4):563–582
27. Pulatsu B, Erdogmus E, Lourenço PB, Lemos JV, Hazzard J (2020) Discontinuum analysis of the fracture mechanism in masonry prisms and wallettes via discrete element method. Meccanica 55(3):505–523
28. Pulatsu B, Erdogmus E, Lourenço PB, Lemos JV, Tuncay K (2020) Simulation of the in-plane structural behavior of unreinforced masonry walls and buildings using DEM. Structures 27:2274–2287
29. Pulatsu B, Gencer F, Erdogmus E (2020c) Study of the effect of construction techniques on the seismic capacity of ancient dry-joint masonry towers through DEM. Euro J Environ Civ Eng: 1–18
30. Pulatsu B, Gonen S, Erdogmus E, Lourenço PB, Lemos JV, Hazzard J (2020d) Tensile fracture mechanism of masonry wallettes parallel to bed joints: a stochastic discontinuum analysis. Modell Int Open Access J Modell Eng Sci 1(2):78–93
31. Pulatsu B, Gonen S, Erdogmus E, Lourenço PB, Lemos JV, Prakash R (2021) In-plane structural performance of dry-joint stone masonry walls: a spatial and non-spatial stochastic discontinuum analysis. Eng Struct 242:112620
32. Saloustros S, Pelà L, Roca P, Portal J (2015) Numerical analysis of structural damage in the church of the poblet monastery. Eng Failure Anal 48:41–61
33. Segura J, Pelà L, Roca P (2018) Monotonic and cyclic testing of clay brick and lime mortar masonry in compression. Constr Build Mater 193:453–466
34. Segura J, Pelà L, Roca P, Cabané A (2019) Experimental analysis of the size effect on the compressive behaviour of cylindrical samples core-drilled from existing brick masonry. Constr Build Mater 228:116759
35. Stein M (1987) Large sample properties of simulations using latin hypercube sampling. Technometrics 29(2):143–151

Numerical Assessment of Design Procedures for Overhanging Steel Girders

Vahab Esmaeili, Ali Imanpour, and Robert G. Driver

Abstract In the design of roof structures for large single-storey buildings, it is common practice to extend the primary girders of alternate bays beyond the columns to support the girders in the other bays, the span of which is adjusted to balance the moment distribution along the girder line. This structural system, typically with open-web steel joists constituting the secondary members, is commonly known as Gerber construction. Despite the common use of the Gerber system, concerns have arisen about how designers evaluate the stability of overhanging girders, as contemporary steel design standards remain mostly silent on how to take into account the interaction between the back span and the cantilever. The main objective of this paper is to provide new insights into the stability response and design of overhanging girders. Commonly used design procedures for overhanging girders used to assess the limit state of lateral–torsional buckling are first discussed. A finite-element model capable of considering material and geometric nonlinearities, residual stresses, initial out-of-straightness, and cross-sectional distortions is then utilised to obtain the buckling resistances of a practical range of overhanging girders. It is assumed that the back span is under top-flange loading, and open-web steel joists provide only lateral restraints to the main girder. Three different restraint conditions are considered at the cantilever tip: free, lateral restraint at the top flange, and lateral restraint at both the top and bottom flanges. Finally, the results are compared to the predictions of available design procedures. The results suggest that the current methods may lead to overly conservative or unconservative predictions, as they either overlook the role of interaction between the back span and the cantilever or miscalculate the beneficial effect of top-flange bracing on the stability of the back span under reverse-curvature bending.

Keywords Design procedures · Overhanging steel girders

V. Esmaeili (✉) · A. Imanpour · R. G. Driver
University of Alberta, Edmonton, AB, Canada
e-mail: vahab@ualberta.ca

1   Introduction

Cantilever-suspended-span construction, with overhanging girders considered to be the main components, is a popular roof framing scheme for large single-storey buildings in North America. The beauty of this system is that it enjoys more balanced moment distributions than its conventional counterpart with simply supported girders, thereby reducing the peak positive moments by allowing negative moments to develop at the column locations. In addition, simpler connections and ease of erection are among the comparative merits of such a structural system [2]. Nevertheless, a lack of consensus on the appropriate means of stability design of overhanging girders, considering the interaction between their individual segments, has consistently been a matter of concern among structural designers. There have also remained many unanswered questions on the way overhanging girders benefit from the restraints provided by the secondary members such as open-web steel joists (OWSJs).

In an effort to develop a design method for overhanging girders, [11] proposed the notional effective length concept, in which the back span and the cantilever segment are of the same length. The cantilever tip is assumed to be laterally restrained at the shear-centre level, whereas the back span is free of loads and restraints between the supports. The proposed method neglects to account for the effect of the back span bay dimension on the stability of the overhanging girder. In order to address this issue, [10] recommended considering the length of the back span as the minimum allowable effective length of the cantilever. However, the concept of effective length was adopted by the Structural Stability Research Council (SSRC) guide [8] without implementing the above-mentioned limitation.

An interaction method was proposed by [13] so as to obtain the elastic buckling resistance of a double-overhanging girder with equal cantilevers. It was assumed that the girder was unable to move laterally at the two supports. With regard to the loading condition at the cantilever tips, top-flange and shear-centre loadings were investigated. In this method, the buckling resistances of the back span and the cantilever are first estimated separately. The back span is assumed to be under a free-to-warp condition at the two ends, whereas the cantilever is considered built-in at the support. Eventually, the overall capacity of the double-overhanging girder is obtained considering the interaction between the adjacent segments. For the cases with top-flange loading at the tip, this method tends to overestimate the buckling resistance of the system [7].

Another interaction method was proposed by [7] in order to calculate the critical elastic moment of overhanging girders when the cantilever segment is more critical than the back span. It was assumed that no restraints were provided to the back span between the column locations. Additionally, both top-flange and shear-centre loadings were considered at the cantilever tip. In this method, the critical elastic moments associated with the individual segments under a free-to-warp condition at the supports are calculated. Interaction equations were provided for the cases with two different restraint conditions at the cantilever tip: free and laterally restrained

at the top-flange level. For the case where the cantilever tip is laterally restrained at both the top- and bottom- flange levels, the design procedures presented in the SSRC guide [8] or by [12] can be utilised. Furthermore, the overall buckling resistance of the overhanging girder can be taken as the buckling resistance of the back span if the back span is more critical [13].

The stability response of girders with reverse-curvature bending was investigated by [14] with the aim of finding the actual unbraced length of the girder with top-flange bracing under negative bending moments. It was recommended that the point of contraflexure could not generally be considered a braced point. Several lateral–torsional buckling (LTB) modification factors were also proposed to account for special cases of girders with reverse-curvature bending, including cases free between the supports and those with continuous bracing of the top flange. Furthermore, girders restrained at one flange were scrutinised, focusing on lateral and torsional bracings and composite construction.

Esmaeili et al. [6] further investigated the effect of top-flange bracing on the stability of girders with reverse-curvature bending, which are representative of the back span bay of a typical overhanging girder. The elastic buckling resistances associated with the back spans of 19,200 different single-overhanging girders with top-flange bracing under free-to-warp conditions were obtained through the finite-element method and compared to the predictions of prevailing design methods. The current LTB modification factors were found to be excessively either conservative or unconservative. An artificial intelligence (AI)-based model was also proposed for predicting the elastic buckling resistance of the back span of a typical single-overhanging girder with top-flange bracing under free-to-warp conditions.

From the presented literature review, it can be deduced that crucial questions have yet to be addressed in regard to the way current design methods account for the interaction buckling of overhanging girders and the actual effect of restraints afforded by secondary members. This paper is aimed at the performance assessment of commonly used design procedures for overhanging girders. To achieve this, a practical range of single-overhanging girders is first numerically simulated and analysed considering material and geometric nonlinearities as well as initial imperfections. The back span is assumed to be under top-flange loading, and only lateral restraints are considered to be provided to the girder by OWSJs. Also, three distinct restraint conditions are considered at the cantilever tip: free, lateral restraint at the top flange, and lateral restraint at both the top and bottom flanges. Finally, the results are compared to the predictions by current design procedures.

2 Scope of Numerical Simulations

Figure 1 depicts the configuration of a typical single-overhanging girder, along with its bending moment diagram, and presents the relevant load and geometric variables.
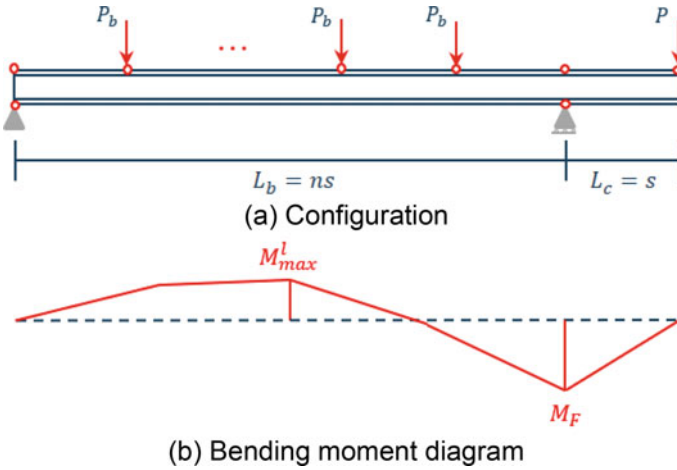
Fig. 1 Typical single-overhanging girder (symbol red circle represents point of lateral support)

In Fig. 1,

- P_b refers to the point loads on the back span arising from the end reactions of OWSJs;
- P represents the point load at the cantilever tip;
- L_b denotes the length of the back span;
- L_c is the length of the cantilever;
- s represents the joist spacing;
- n equals the number of point loads on the back span plus 1;
- $M^l_{\max}$ is the local maximum bending moment along the back span;
- M_F signifies the (negative) bending moment at the fulcrum;
- κ' is defined as the ratio between $M^l_{\max}$ and M_F, including sign.

A total of 1699 single-overhanging girders using 24 standard steel W-shapes, representing the most common cross-sections utilised in Gerber construction, are considered. The selected sections conform to CSA G40.21 Grade 345WM [4], which is aligned with ASTM A992 [1]. The W-shapes considered, along with the class of each [5], are presented in Table 1.

Herein lies the main modelling features:

- Lateral deflections and twisting are prevented at support locations (fork supports).
- Warping deformation is allowed at support locations.
- Torsional restraints afforded to the girder by OWSJs are neglected.
- Restraints afforded and loads delivered to the girder by OWSJs are defined as follows:

    - For the back span, loads and lateral restraints are applied at the top-flange level.

Table 1 W-shapes considered and classes of cross-sectional elements

Cross section	Class		Cross section	Class		Cross section	Class	
	Flange	Web		Flange	Web		Flange	Web
W410 × 39	2	2	W530 × 82	2	1	W690 × 152	1	1
W410 × 60	1	1	W530 × 138	1	1	W760 × 134	2	2
W410 × 85	1	1	W610 × 92	1	1	W760 × 147	1	1
W460 × 52	1	1	W610 × 125	1	1	W760 × 161	1	1
W460 × 60	1	1	W610 × 155	2	1	W840 × 176	1	1
W460 × 97	1	1	W610 × 241	1	1	W840 × 193	1	1
W460 × 144	1	1	W690 × 125	1	1	W920 × 201	1	1
W530 × 66	1	1	W690 × 140	1	1	W920 × 223	1	1

- Three different restraint conditions are considered at the cantilever tip: (1) free, (2) lateral restraint at the top flange—as shown in Fig. 1—and (3) lateral restraint at both top and bottom flanges.
- For restraint condition (1), the point load at the cantilever tip comes from the adjacent drop-in segment and is applied at the shear-centre level.
- For restraint conditions (2) and (3), the point load at the cantilever tip comprises both joist and drop-in segment reactions and is conservatively applied at the top-flange level.

Considering the above-mentioned criteria, Table 2 summarises all the possible loading and restraint conditions (LRCs) considered, and Fig. 2 depicts the three configurations.

To illuminate the inclusiveness and practicality of the set of girders considered, the statistical indices associated with the contributing variables are reported in Table. Figures 3 and 4 demonstrate the relative frequency distribution for the length of back span and joist spacing, along with their mean values and coefficients of variation.

In Table 3,

- $\frac{b}{2t}$ signifies the flange slenderness ratio, where b is the overall width of the flange and t denotes its thickness;
- $\frac{h}{w}$ is indicative of the web slenderness, where h denotes the clear depth of the web and w is its thickness;

Table 2 Loading and restraint conditions (LRCs)

	Cantilever tip	
	Restraint condition	Loading condition
LRC 1	Condition (2)	Top flange
LRC 2	Condition (1)	Shear centre
LRC 3	Condition (3)	Top flange
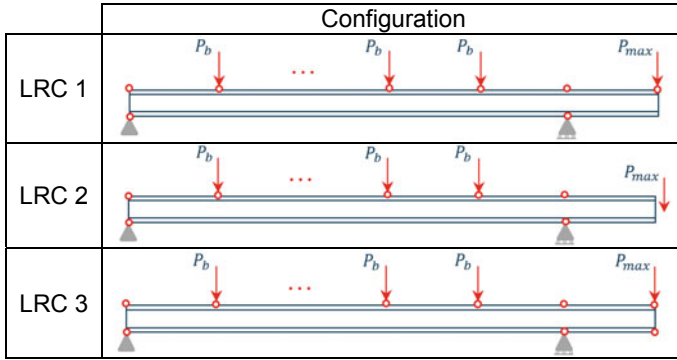
Fig. 2 Configurations for single-overhanging girders
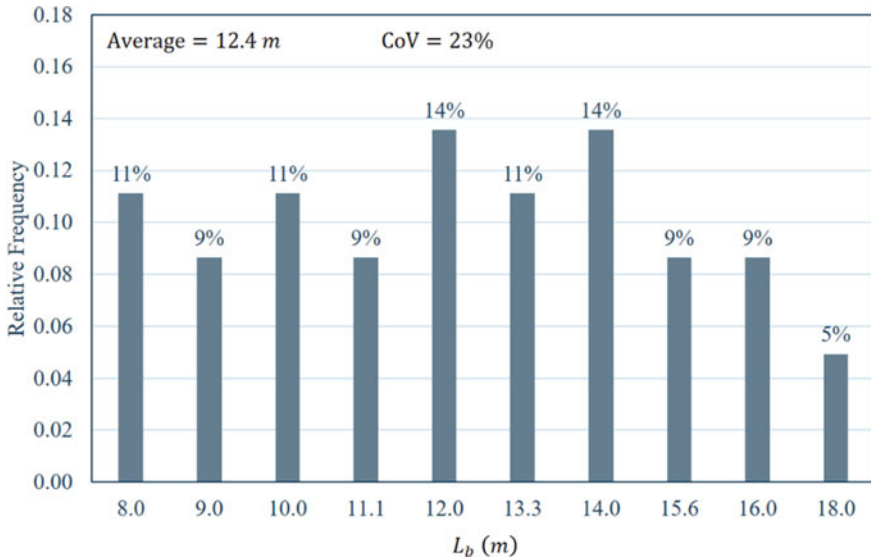
Fig. 3 Relative frequency distribution for length of back span, L_b

- $\frac{I_x}{I_y}$ represents the ratio of the strong- and weak-axis geometric stiffnesses of the girder;
- $\frac{d}{b}$ is the overall cross-sectional aspect ratio of the girder, where d is the depth of the section and b is the width of the flange;
- $X = \frac{\pi}{L_b}\sqrt{\frac{EC_w}{GJ}}$ is principally a torsional parameter reflective of the ratio between the warping and St. Venant torsional stiffnesses;
- $\frac{L_b}{d}$ is the ratio between the length of the back span and the overall depth of the section;
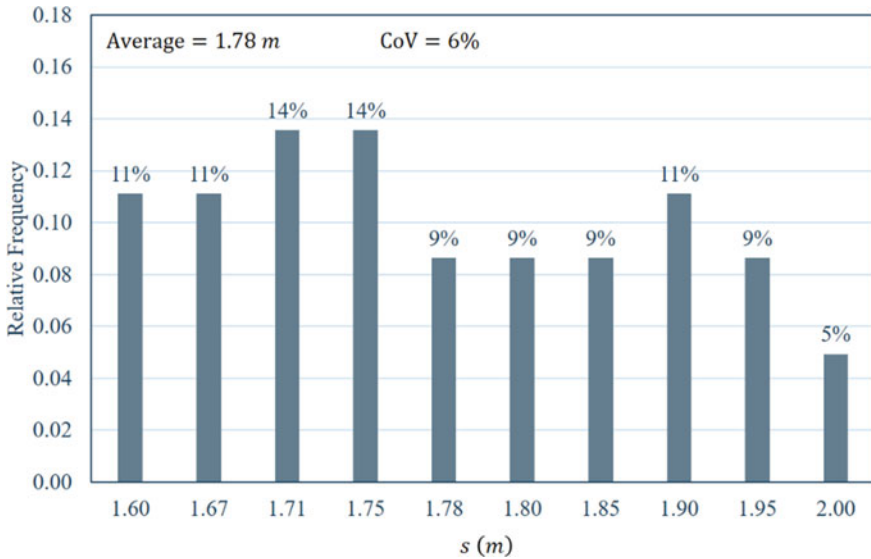
Fig. 4 Relative frequency distribution for joist spacing, s

Table 3 Statistical indices associated with the contributing variables

	$L_b(m)$	$s(m)$	$\frac{b}{2t}$	$\frac{h}{w}$	$\frac{I_x}{I_y}$	$\frac{d}{b}$	X	$\frac{L_b}{d}$	$\frac{L_b}{r_y}$
Maximum	18.0	2.00	8.5	60.4	45.2	3.4	1.1	22	347
Minimum	8.0	1.60	4.5	31.5	8.7	1.7	0.4	15	119
Mean	12.4	1.78	6.8	49.7	27.1	2.7	0.7	19	240
Coefficient of variation (CoV) (%)	23	6	16	18	33	15	18	10	21

- $\frac{L_b}{r_y}$ is the ratio between the length of the back span and the radius of gyration of the section about its weak axis.

It is important that a broad variety of load patterns be considered in the evaluation of the existing design procedures. To establish a criterion for measuring this factor, a typical roof framing under a schematic load pattern is considered—as shown in Fig. 5.
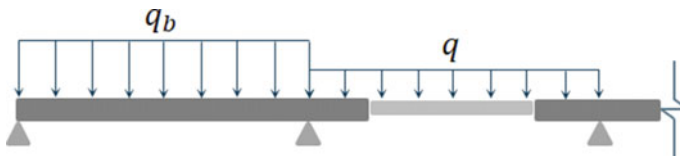
Fig. 5 Typical roof framing under a schematic load pattern

Fig. 6 Residual stress
pattern proposed by
Galambos and Ketter [9]
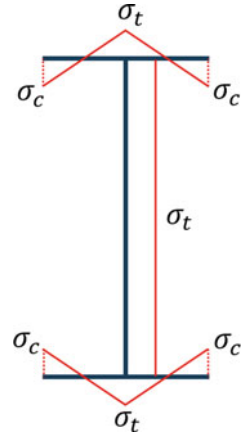
In Fig. 5, q_b refers to the intensity of the uniformly distributed load on the back span bay; q represents the uniformly distributed load on the adjacent bay; and κ'' is defined as the ratio between q_b and q. To ensure that the dataset includes the most commonly used load patterns, the following range is considered for κ'':

$$\kappa'' = \{2.00, 1.60, 1.30, 1.00, 0.77, 0.63, 0.50\} \tag{1}$$

For the purpose of numerical simulation, the finite-element model developed by [6]—which is capable of considering material and geometric nonlinearities and imperfections—is adopted. An elastic–perfectly plastic stress–strain curve is considered for the material with an elastic modulus and a yield stress of 200 GPa and 345 MPa, respectively. Moreover, a parabolic sweep with the maximum out-of-straightness of $L_b/1000$ along the back span is used to introduce initial geometric imperfections into the numerical model. In order for the residual stresses to be incorporated, the pattern proposed by Galambos and Ketter [9]—as shown in Fig. 6—is employed.

In Fig. 6,

- $\sigma_c = 0.3F_y$ represents the maximum compressive stress at the flange tips, where F_y signifies the specified minimum yield stress of steel;
- $\sigma_t = \frac{bt}{bt+w(d-2t)}\sigma_c$ is the maximum tensile stress throughout the web and at the flange-web intersection.

To distinguish between various types of instability, the maximum internal bending moment, the maximum compressive stress, and deformations throughout the girder are monitored during analysis. Therefore, if no local instabilities are captured, three different scenarios are possible:

- The girder becomes unstable as a result of plastic hinge formation as soon as the maximum internal bending moment reaches the plastic moment of the section, M_p.

- The instability of the girder is classified as inelastic buckling if the compression flange is partly yielded at the buckling stage.
- The instability of the girder is classified as elastic buckling if the compression flange is not yielded at the buckling stage.

3 Existing Design Methods

For the design of overhanging girders, it is standard practice to first obtain the buckling resistances of their individual segments, i.e. the back span and the cantilever segment, separately. Afterwards, the buckling resistance of the entire system is calculated either considering or neglecting the interaction between the individual segments.

3.1 Back Span

The back span of overhanging girders typically experiences both positive and negative bending moments. Considering the different bracing conditions at the top and bottom flanges along the back span, its adequacy under these two moments needs to be evaluated in different ways.

3.1.1 Under Maximum Positive Moment

The capacity of the back span under the maximum positive moment can be checked based on the procedure CSA S16-19 (2019) proposes for the bending capacity of laterally unsupported members. To do this, the critical elastic moment of the back span at the point of maximum positive moment is calculated as:

$$M_{cr_b}^+ = \frac{\omega_2 \pi}{s} \sqrt{E I_y G J + \left(\frac{\pi E}{s}\right)^2 I_y C_w} \tag{2}$$

where E and G are the elastic modulus and shear modulus of steel, respectively; I_y is the moment of inertia about the weak axis of the cross section; J and C_w represent the St. Venant torsional constant and warping torsional constant, respectively; s is the joist spacing representing the unbraced length as the top flange is under compression; and ω_2 is a coefficient to account for various moment gradients along the unbraced segment and is calculated using the following equation:

$$\omega_2 = \frac{4M_{\max}}{\sqrt{M_{\max}^2 + 4M_a^2 + 7M_b^2 + 4M_c^2}} \leq 2.5 \tag{3}$$

In Eq. (3), M_a, M_b, and M_c are the absolute values of moments at the quarter point, centreline, and three-quarter point of the unbraced segment, respectively; $M_{\max}$ is the absolute value of the maximum moment in the unbraced segment.

3.1.2 Under Maximum Negative Moment

The capacity of the back span under the maximum negative moment can be evaluated in two different ways. The first approach is to use the same procedure as for the back span under the maximum positive moment, considering the full length of the back span as the unbraced length. Therefore, the critical elastic moment of the back span at the point of maximum negative moment is calculated as:

$$M_{cr_b}^- = \frac{\omega_2 \pi}{L_b} \sqrt{E I_y G J + \left(\frac{\pi E}{L_b} \right)^2 I_y C_w} \tag{4}$$

where L_b is the length of the back span. The reason that L_b is considered to be the unbraced length is that the bottom flange is partly under compression, but no lateral restraints are provided to the bottom flange between the two supports. Additionally, the point of contraflexure—where the bending moment is zero—could not generally be considered a point of lateral support.

The second approach is to replace ω_2 with an LTB modification factor proposed by [14], which is calculated as:

$$C_{b-\mathrm{YH}} = 3.0 - \frac{2}{3} \left(\frac{M_1}{M_o} \right) - \frac{8}{3} \left[\frac{M_{CL}}{(M_o + M_1)} \right] \tag{5}$$

in which M_o is the (negative) moment at the end of the back span that gives the largest compressive stress in the bottom flange; M_1 is the moment at the other end of the back span; M_{CL} is the moment at the centreline of the back span, including sign; and $(M_o + M_1)$ is taken equal to M_o if M_1 is positive and causes tension on the bottom flange.

3.2 Cantilever

In order to check the adequacy of the cantilever segment, the notional effective length—as defined by [10]—is utilised. In this approach, the critical elastic moment of the cantilever segment—under its actual loading and restraint conditions—is assumed to be equal to that of a notional simply supported girder of identical section under uniform moment. Thus, the critical elastic moment of the cantilever is calculated as:

$$M_{cr_c} = \frac{\pi}{kL_c}\sqrt{EI_yGJ + \left(\frac{\pi E}{kL_c}\right)^2 I_y C_w}$$ (6)

where L_c signifies the length of the cantilever; k is referred to as effective length factor and is determined based on the loading and restraint conditions of the cantilever, as presented in Table 4.

A different set of effective length factors was proposed by the Canadian Institute of Steel Construction [2] as specified in Table 5.

Table 4 Effective length factors, k, proposed by [10]
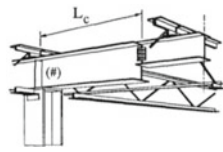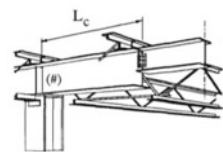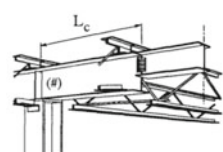
Restraint condition	Loading condition at tip	
	Top flange	Others
	2.5	1.0
	2.5	0.9
	1.2	0.7

Table 5 Effective length factors, k, proposed by the CISC [2]

Condition[a]	Restraints	k
		1.5–2.5
		1.0–1.5
		0.8–1.0

[a] Lateral restraint is provided to bottom flange at the root of cantilever by OWSJ bottom chord extension

3.3 Interaction Method

For an overhanging girder, due to the interaction between its adjacent segments during buckling, the less critically loaded segment restrains the more critically loaded one [7]. When the back span is more critical, the overall buckling resistance of the overhanging girder can be taken as the buckling resistance of the back span alone [13]. However, when the cantilever is more critical and its tip is either free or laterally restrained at the top-flange level only, the critical elastic moment of the overhanging girder at the point of maximum negative moment is determined as [7]:

$$M_{\mathrm{cr}}^- = M_{\mathrm{cr}_c} + F_I\big(M_{\mathrm{cr}_b}^- - M_{\mathrm{cr}_c}\big) \tag{7}$$

where

- $M_{\mathrm{cr}_b}^-$ refers to the critical elastic moment of the back span at the point of maximum negative moment and can be calculated based on Eq. (4) through either ω_2 (Eq. 3) or $C_{b-\mathrm{YH}}$ (Eq. 5);
- M_{cr_c} denotes the critical elastic moment of the cantilever at the point of maximum negative moment and is calculated as specified in Table 6;
- F_I is referred to as interaction factor and is calculated as specified in Table 7.

For the case where lateral restraints are provided to both the top and bottom flanges at the cantilever tip, the following steps need to be taken [12]:

- The critical elastic moment of the cantilever is calculated as:

$$M_{\mathrm{cr}_c} = \frac{1.75\pi}{L_c}\sqrt{EI_yGJ + \left(\frac{\pi E}{L_c}\right)^2 I_y C_w} \tag{8}$$

- The stiffness of the back span, the restraining segment, is defined as:

Table 6 Critical elastic moment of cantilever segment, M_{cr_c} [7]

Loading condition	M_{cr_c}
Top flange	$1.5\frac{GJ}{d}$
Shear centre	$\frac{4}{L_c}\sqrt{EI_yGJ}$

Table 7 Interaction factors, F_I, proposed by [7]

Restraint condition	Interaction factor (F_I)
	$-0.08 + 0.18\frac{L_b}{L_c} - 0.009\left(\frac{L_b}{L_c}\right)^2$
	$0.064 + 0.162\frac{L_b}{L_c} - 0.009\left(\frac{L_b}{L_c}\right)^2$

$$\alpha_b = \frac{3EI_y}{L_b}\left(1 - \frac{M_{cr_c}}{M_{cr_b}^-}\right) \tag{9}$$

- The stiffness of the cantilever, the critical segment, is computed as:

$$\alpha_c = \frac{3EI_y}{L_c} \tag{10}$$

- The stiffness ratio for the root of the cantilever is calculated as:

$$G_{Root} = \frac{\alpha_c}{\alpha_b} \tag{11}$$

- Assuming infinity as the stiffness ratio for the cantilever tip, G_{Tip}, implying it is free to rotate about the weak axis and warp, the effective length factor for interaction method—k_I—is determined from Fig. 7.
- Using the following equation, the critical elastic moment of the overhanging girder at the point of maximum negative moment is obtained:

Fig. 7 Nomograph for effective length factors of columns in continuous frames with sidesway prevented [3]
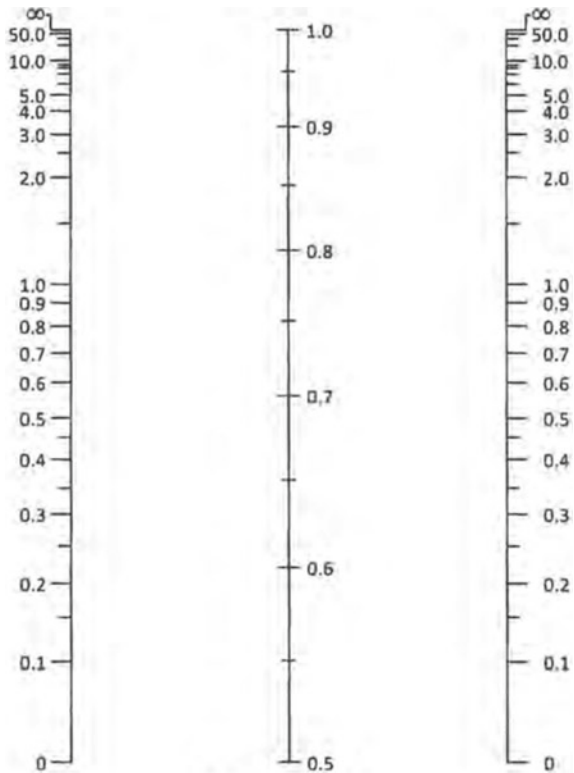
$$M_{\text{cr}}^- = \frac{1.75\pi}{k_I L_c} \sqrt{EI_y GJ + \left(\frac{\pi E}{k_I L_c}\right)^2 I_y C_w} \tag{12}$$

3.4 Ultimate Capacity

Having the critical elastic moments of the individual segments, the following steps are taken to finalise the design:

- M_{cr}^+, the critical elastic moment of the overhanging girder at the point of maximum positive moment, is set to $M_{\text{cr}_b}^+$ (Eq. 2).
- For methods considering the interaction between the back span and the cantilever, M_{cr}^-—the critical elastic moment of the overhanging girder at the point of maximum negative moment—is obtained from Eqs. (7) or (12) based on the restraint condition at the cantilever tip.
- For methods neglecting the interaction between the back span and the cantilever, M_{cr}^- is taken as the lesser of $M_{\text{cr}_b}^-$ and M_{cr_c}.
- M_n^+, the nominal capacity of the overhanging girder at the point of maximum positive moment, is determined as [5]:

$$M_n^+ = \begin{cases} M_{\text{cr}}^+ & M_{\text{cr}}^+ \leq 0.67 M_p \\ 1.15 M_p \left[1 - \frac{0.28 M_p}{M_{\text{cr}}^+}\right] \leq M_p & M_{\text{cr}}^+ > 0.67 M_p \end{cases} \tag{13}$$

- M_n^-, the nominal capacity of the overhanging girder at the point of maximum negative moment, is calculated as [5]:

$$M_n^- = \begin{cases} M_{\text{cr}}^- & M_{\text{cr}}^- \leq 0.67 M_p \\ 1.15 M_p \left[1 - \frac{0.28 M_p}{M_{\text{cr}}^-}\right] \leq M_p & M_{\text{cr}}^- > 0.67 M_p \end{cases} \tag{14}$$

- M_n, the overall nominal capacity of the overhanging girder, is then computed as:

$$M_n = \begin{cases} M_n^- & \frac{M_n^+}{M_n^-} \geq |\kappa'| \\ \frac{M_n^+}{|\kappa'|} & \frac{M_n^+}{M_n^-} < |\kappa'| \end{cases} \tag{15}$$

It is noteworthy that M_n is nominally the maximum moment the overhanging girder can resist at the location of maximum negative moment, that is, the fulcrum.

4 Performance Assessment of Existing Design Procedures

Based on the design methods utilised for checking the adequacy of the individual segments of the overhanging girder and the decision as to whether or not the interaction between the individual segments is to be taken into account, the designer could adopt any of the design procedures presented in Table 8.

In order to evaluate the performance of the above-mentioned design procedures, for each girder from the 1,699 cases previously defined for the numerical simulation, the nominal capacity—taken at the fulcrum—is obtained from a finite-element analysis (FEA) and introduced as $M_{n-\text{FEA}}$. The nominal capacity of each case is also calculated based on the six design procedures specified in Table 8. Afterwards, the performance of each design procedure is evaluated for each of the LRCs of single-overhanging girders through the information summarised in Tables 9 and 10. In Table 9, the mean normalised moments for each of the LRCs of single-overhanging girders obtained from the FEAs are presented. Additionally, the mean ratio between the nominal capacities obtained from the FEAs and those calculated using each of the six design procedures specified in Table 8 is reported in Table 10—along with the associated coefficient of variation—for each type of instability separately.

From Tables 9 and 10, the following observations emerge:

- Under LRC 1,

  - a few girders (4.4%) buckle elastically;
  - the mean value of $\frac{M_{\text{max}-\text{FEA}}}{M_p}$ is equal to 0.80—representing a quite inclusive range of girders that undergo inelastic buckling;

Table 8 Existing design procedures for overhanging girders

Procedure		$M_{\text{cr}_b}^+$	$M_{\text{cr}_b}^-$	M_{cr_c} or M_{cr}^-
1	S16/S16/IM	S16-19 (2019)	S16-19 (2019)	Interaction method
2	S16/YH/IM	S16-19 (2019)	[14]	Interaction method
3	S16/S16/KN	S16-19 (2019)	S16-19 (2019)	[10]
4	S16/S16/CISC	S16-19 (2019)	S16-19 (2019)	CISC [2]
5	S16/YH/KN	S16-19 (2019)	[14]	[10]
6	S16/YH/CISC	S16-19 (2019)	[14]	CISC [2]

Table 9 Mean normalised moments for different LRCs based on FEAs

	$\left(\frac{M_{n-\text{FEA}}}{M_p}\right)_{\text{mean}}$	$\left(\frac{|\kappa'|M_{n-\text{FEA}}}{M_p}\right)_{\text{mean}}$	$\left(\frac{M_{\text{max}-\text{FEA}}}{M_p}\right)_{\text{mean}}^{\text{a}}$
LRC 1	0.49	0.73	0.80
LRC 2	0.61	0.85	0.94
LRC 3	0.66	0.88	0.98

[a] $M_{\text{max}-\text{FEA}} = \max\left(M_{n-\text{FEA}}, |\kappa'|M_{n-\text{FEA}}\right)$

Table 10 FEA/design ratios for existing design procedures

LRC 1

Instability type		Elastic		Inelastic		Plastic	
Number of cases		25		427		115	
Procedure		Mean	CoV (%)	Mean	CoV (%)	Mean	CoV (%)
1	S16/S16/IM	1.52	26	1.86	26	1.24	23
2	S16/YH/IM	0.83	11	0.82	17	1.00	0
3	S16/S16/KN	1.26	33	1.70	28	1.19	22
4	S16/S16/CISC	1.26	33	1.70	28	1.19	22
5	S16/YH/KN	0.81	15	0.82	19	1.00	0
6	S16/YH/CISC	0.64	8	0.79	21	1.00	0

LRC 2

Instability type		Elastic		Inelastic		Plastic	
Number of cases		9		353		204	
Procedure		Mean	CoV (%)	Mean	CoV (%)	Mean	CoV (%)
1	S16/S16/IM	1.88	23	2.29	35	1.46	37
2	S16/YH/IM	1.01	5	0.98	4	1.01	3
3	S16/S16/KN	1.88	23	2.29	35	1.46	37
4	S16/S16/CISC	1.88	23	2.29	35	1.46	37
5	S16/YH/KN	1.01	5	0.98	4	1.01	3
6	S16/YH/CISC	1.02	4	0.98	5	1.01	3

LRC 3

Instability type		Elastic		Inelastic		Plastic	
Number of cases		0		301		265	
Procedure		Mean	CoV	Mean	CoV (%)	Mean	CoV (%)
1	S16/S16/IM	–	–	2.48	43	1.76	45
2	S16/YH/IM	–	–	1.05	14	1.04	7
3	S16/S16/KN	–	–	2.48	43	1.76	45
4	S16/S16/CISC	–	–	2.48	43	1.76	45
5	S16/YH/KN	–	–	1.05	14	1.04	7

Table 10 (continued)

LRC 3							
Instability type		Elastic		Inelastic		Plastic	
Number of cases		0		301		265	
Procedure		Mean	CoV	Mean	CoV (%)	Mean	CoV (%)
6	S16/YH/ CISC	–	–	1.05	14	1.04	7

- the accuracy of the considered design procedures mostly depends on the method used for the calculation of $M_{\mathrm{cr}_b}^-$;
- the procedures using the S16 method to calculate $M_{\mathrm{cr}_b}^-$ tend to be overly conservative;
- in the procedures using the S16 method to calculate $M_{\mathrm{cr}_b}^-$ without considering the interaction between the back span and the cantilever, M_{cr_c} can never affect the ultimate capacity of the overhanging girder owing to the conservatism of the S16 method;
- the procedures using $C_{b-\mathrm{YH}}$ to calculate $M_{\mathrm{cr}_b}^-$ tend to be unconservative—yet practically accurate for the cases reaching their fully plastic capacity;
- considering the interaction between the back span and the cantilever could make the design procedure even more conservative when the S16 method is employed to calculate $M_{\mathrm{cr}_b}^-$;
- using the CISC's effective length factors rather than Kirby and Nethercot's to calculate M_{cr_c} could make the design procedure even more unconservative when $C_{b-\mathrm{YH}}$ is utilised to calculate $M_{\mathrm{cr}_b}^-$.

- Under LRC 2,

    only a very few girders (1.6%) experience elastic buckling;
    the mean value of $\frac{M_{\mathrm{max-FEA}}}{M_p}$ is quite close to 1.0—which means, for the cases going under inelastic buckling, very large portions of the most critical compression flanges yielded;
    the accuracy of the design procedures solely depends on the method used for the calculation of $M_{\mathrm{cr}_b}^-$;
    the procedures using the S16 method to calculate $M_{\mathrm{cr}_b}^-$ tend to be overly conservative—i.e. more conservative than those under LRC 1;
    the procedures using $C_{b-\mathrm{YH}}$ to calculate $M_{\mathrm{cr}_b}^-$ are sometimes unconservative—yet quite accurate.

- Under LRC 3,

    none of the girders undergoes elastic buckling;
    the mean value of $\frac{M_{\mathrm{max-FEA}}}{M_p}$ is practically equal to 1.0—which means even the cases experiencing inelastic buckling tend to verge on plastic hinge formation;
    the accuracy of the design procedures solely depends on the method used for the calculation of $M_{\mathrm{cr}_b}^-$;

the procedures using the S16 method to calculate $M_{\mathrm{cr}_b}^-$ tend to be overly conservative—i.e. more conservative than those under LRC 2;

the procedures using $C_{b-\mathrm{YH}}$ to calculate $M_{\mathrm{cr}_b}^-$ are mostly unconservative—yet quite accurate.

5 Summary and Conclusions

A set of 1699 single-overhanging girders was analytically investigated considering material and geometric nonlinearities, residual stresses, initial geometric imperfections, and cross-sectional distortions. As a result of open-web steel joists, the concentrated loads and lateral restraints were applied at the top-flange level—at discrete locations along the back span. Three different restraint conditions were considered at the cantilever tip: free, lateral restraint at the top flange, and lateral restraint at both the top and bottom flanges. The results reveal that existing design procedures may lead to overly conservative or unconservative predictions, as a result of neglecting the interaction between the back span and the cantilever or miscalculating the effect of top-flange bracing on the stability of the back span under reverse-curvature bending. Furthermore, the level of conservatism could differ significantly for different loading and restraint conditions at the cantilever tip, as well as different potential types of instability. It can also be concluded that the method used for calculating the critical elastic moment of the back span at the point of maximum negative moment could dramatically affect the accuracy of the design procedure.

References

1. American Society for Testing and Materials (ASTM) (2020) Standard specification for structural steel shapes. ASTM A992/A992M-20, ASTM, West Conshohocken, Pennsylvania, USA
2. Canadian Institute of Steel Construction (CISC) (1989) Roof framing with cantilever (gerber) girders and open-web steel joists. CISC, Markham, Ontario, Canada
3. Canadian Institute of Steel Construction (CISC) (2017) Handbook of steel construction, 11th edn. CISC, Markham, Ontario, Canada

4. Canadian Standards Association (CSA) (2013) General requirements for rolled or welded structural quality steel/structural quality steel. CSA G40.20-13/G40.21-13 (reaffirmed 2018), CSA, Toronto, Ontario, Canada
5. Canadian Standards Association (CSA) (2019) Design of steel structures. CSA S16-19, CSA, Toronto, Ontario, Canada
6. Esmaeili V, Imanpour A, Driver RG (2021) Stability of gerber systems with top-flange bracing. In: Proceedings of the annual stability conference. Structural Stability Research Council (SSRC). Louisville, Kentucky, USA
7. Essa HS, Kennedy DJL (1994) Design of cantilever steel beams: refined approach. J Struct Eng 120(9):2623–2636
8. Galambos TV (1998) Guide to stability design criteria for metal structures. Structural Stability Research Council (SSRC), Wiley, New York, USA
9. Galambos TV, Ketter RL (1959) Columns under combined bending and thrust. J Eng Mech Div 85(2):1–30
10. Kirby PA, Nethercot DA (1979) Design for structural stability. In: Constrado Nomographs. Granada Publishing, London, United Kingdom
11. Nethercot DA (1973) The effective lengths of cantilevers as governed by lateral buckling. Struct Eng 51(5):161–168
12. Schmitke CD, Kennedy DJL (1985) Effective lengths of laterally continuous, laterally unsupported steel beams. Can J Civ Eng 12(3):603–616
13. Trahair NS (1983) Lateral buckling of overhanging beams. In: Instability and plastic collapse of steel structures. Granada Publishing, London, United Kingdom
14. Yura JA, Helwig TA (2010) Buckling of beams with inflection points. In: Proceedings of the annual stability conference. Structural Stability Research Council (SSRC), Orlando, Florida, USA, 761–780

Seismic Behaviour of Steel Wide-Flange Columns in Ductile Moment-Resisting Frames Considering Base Plate Flexibility

Omid Moammer, Ali Imanpour, and Robert Tremblay

Abstract This paper aims to examine the seismic behaviour of steel wide-flange columns in steel ductile moment-resisting frames considering the deformations of the base plate and anchor rods. A prototype MRF is first designed in accordance with the Canadian steel design standard (CSA S16-19) seismic provisions. A continuum finite element model of the interior first-storey column isolated from the prototype frame is then developed together with the base footing and connection. The flexibility of the adjoining beams at the top end of the column is also considered in the numerical model. The capability of the model components in reproducing the cyclic response of the wide-flange column and its base conditions are then calibrated against available experimental test data. Special attention is placed on the cyclic response of the anchor rods and base plate. The seismic response of the columns of the prototype frame is finally examined using the corroborating finite element model under realistic seismic demands obtained from the two-dimensional concentrated plasticity-based numerical model of the frame subjected to representative earthquake ground motions. The results from the finite element analyses confirm that base flexibility can influence the inelastic cyclic response and the stability of first-storey MRF columns. Furthermore, the proposed numerical modelling technique can be used in future studies to properly simulate the inelastic seismic response of the column base plate, anchor rods, and footing for the purpose of MRF response evaluation.

Keywords Wide-flange columns · Steel moment-resisting frames · Nonlinear modelling · Seismic behaviour · Base flexibility

O. Moammer (✉) · A. Imanpour
Department of Civil and Environmental Engineering, University of Alberta, Edmonton, AB, Canada
e-mail: moammer@ualberta.ca

R. Tremblay
Department of Civil, Geological and Mining Engineering, Polytechnique Montréal, Montreal, QC, Canada

1 Introduction

Steel moment-resisting frames (MRFs) are used commonly as a lateral load-resisting system of multi-storey buildings in high-seismic areas. MRFs, in particular those part of low- and mid-rise buildings, are made of wide-flange beams and columns. In Canadian design practice, the MRF column base connections include embedded and exposed connections. Embedded base connections are ideally considered to be fixed and are suitable for mid-rise and high-rise buildings with relatively large columns. Exposed column base connections act as a suitable and economical solution for low- and mid-rise buildings in which bending moments at the column bases are relatively lower. Greater rotational flexibility is expected in exposed column base connections compared to their embedded counterpart, which suggests that they cannot be considered as fully restrained in analysis and design [30]. Past experimental studies and post-earthquake observations confirmed that column base connections can influence the seismic performance of MRF columns and, in turn, the system [2, 4, 9, 13, 15, 28, 33, 34]. Furthermore, analytical studies performed on MRF base connections showed that base flexibility can affect the plastic mechanism of the structure, affecting ductility, strength, seismic demand, and stability [22, 36].

Exposed column base connections have been the subject of extensive research in the past. References [9, 15, 33] studied experimentally the seismic response of exposed base connections under axial load and strong axis bending. The observed failure modes included plate yielding, anchor rod yielding, weld fracture, and crushing of grout. Lee et al. [24] investigated the influence of weak axis bending on the base connection response using numerical simulations and showed that ratio between the strength of the column, base plate, anchor rods, and grout controls the response of the connection. Lee et al. [25] tested four specimens under cyclic loading history and reported cracks at the column flange tips after 1% drift, which had unnoticeable influence on strength degradation, even up to 5% drift. Choi et al. [7] studied the effect of biaxial bending on the seismic behaviour of column base connections using six square hollow structural section (HSS) specimens. The results confirmed the occurrence of pinching behaviour owing to anchor rod yielding when thick base plate was used, and due to base plate yielding in the case of thin base plate. Bajer et al. [3] studied experimentally and numerically four base connections under biaxial and uniaxial bending conditions in the presence of a constant axial compression load. The observed failure modes for the specimens under biaxial bending and axial load involved anchor rod rupture at around 10% drift. Seco et al. [31] investigated experimentally the effect of the base plate thickness and axis of bending on the performance of column base connections and reported anchor rod and base plate yielding as the observed failure modes. A total of 32 column base specimens were tested under biaxial bending and axial compression to provide insight into the effect of the base plate thickness, anchor rod diameter, and axial force level on the failure modes as well as strength and stiffness of exposed base column connections [8]. Pan et al. [30] studied six specimens with four internal anchor bolts representing a pinned base column connection under strong and weak axis bending and showed that under

strong axis bending punching shear failure of the column flanges and anchor rods governed the behaviour, whereas anchor rod pullout dominated the response in the specimens under weak axis bending.

Extensive research effort has been put in the past decade to study the cyclic response of wide-flange steel columns located in the first storey of MRFs with base plastic hinging [12, 35]. In these test programs, the flexibility of the base connection was ignored, although some of these specimens were tested taking into account the flexibility provided by the storey beam [11, 12, 35]. It was shown in other test programs that the flexibility of the column base connection can affect the column failure mode and the amplitude of column axial shortening, which in turn affects the column seismic stability [10, 20]. The evaluation of the seismic response of embedded base connections showed that they possess limited inherent flexibility although cracks were observed in concrete base. The evaluation of the interaction between steel wide-flange MRF columns and their embedded base connections showed that base flexibility can lead to a more satisfactory seismic response by delaying the formation of plastic hinges at the column bases [18–20].

Although the nonlinear response and stability of wide-flange steel columns under seismic load effects have been investigated extensively in the past, the influence of the deformations occurring in column base connections including the base plate, anchor rods, and concrete footing were typically ignored in the past studies. This poses a question about the influence of column base condition on the seismic performance and stability of such columns, which has not been well comprehended yet. This paper aims at examining the nonlinear response of the steel wide-flange columns including the base connection under seismic-induced demands. Once the corroborated finite element model of the column isolated from a five-storey steel MRF is developed including its base connection, footing, and the flexibility of storey beams, the history of the axial load, rotation and displacement demands obtained from a nonlinear response time history analysis of the frame under a representative earthquake ground motion acceleration are imposed to the column FE model. The results obtained from the analysis of the column with base connections are then compared to those featuring an identical column, but with fixed base and flexible top end condition to characterize the effect of column base connection on the seismic response of MRFs with exposed base plates.

2 Description of Experimental Database

In this study, the experimental program performed by Gomez et al. [15] who examined the seismic performance of exposed column base connections under axial compression and flexure was selected to develop and verify the numerical model of the wide-flange column with the base connection. The experimental test setup is presented in Fig. 1. This test program involved testing seven large-scale column base connections with W8 × 48 columns with flange width-to-thickness ratio of 5.92 and web width-to-thickness ratio of 21.25, welded to the centre of the base plate with partial
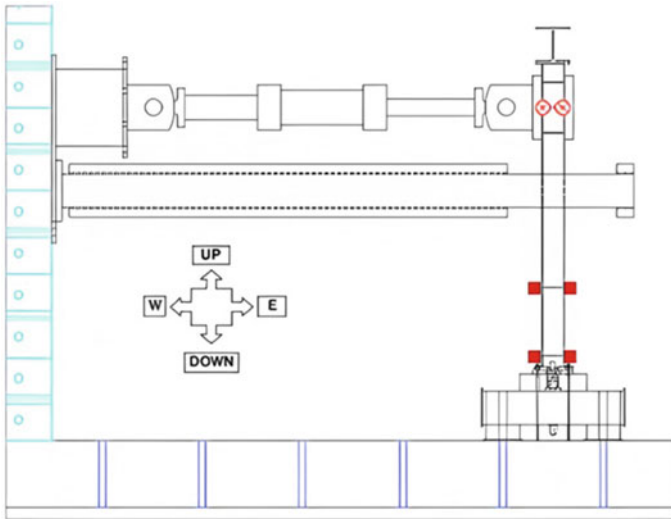
Fig. 1 Experimental test setup by Gomez et al. [15]

joint penetration welds plus reinforcing fillet welds. The base plates measured 355 × 355 mm and three different thicknesses were studied: 25.4, 38.1, and 50.8 mm, The anchor rods were ASTM F1554 Gr. 36 or Gr. 105 with a diameter of 20 mm. The depth of the grout pad and concrete footing were 50.8 and 609.6 mm, respectively, in all the tests. The column height was 2.35 m measured from the upper side of the base plate, which approximately represents 2/3 of the height of a typical first-storey column in steel MRFs. The column was oriented such that the applied lateral displacement imposed strong axis bending. The top end of the column was braced out of plane, and the maximum lateral displacement reached 246 mm, which corresponded to 10.6% storey drift ratio.

In the current study, Test 1 and 2 specimens, which were geometrically identical, were selected. Test 1 specimen was loaded monotically subjected to a maximum drift ratio of 10.6%, while a linearly stepwise-incrementing cyclic displacement protocol following the SAC loading protocol [23] was used for the second specimen. No axial load was applied to the specimens. In Test 1, the response remained elastic up to a storey drift of 1% drift, followed by yielding of the plate, as revealed by flaking of the paint on the plate, and anchor rod yielding. Damage to the grout initiated at a drift ratio of 3%, leading to a drop in the flexural strength of the connection at 8% drift ratio. The weld connecting the corner of the column flange to the base plate fractured at a drift ratio of approximately 4%. The response in Test 2 was dominated by pinching due to the gap produced by yielding and cumulated permanent elongation of the anchor rods under cyclic loading. Damage in grout initiated at 2% drift ratio, leading to extensive crushing due to compressive action of base plate on grout at the end of the experiment. The anchor rods and the base plate yielded at drift ratios of 1 and 3%, respectively. The test stopped after the rupture of one the anchor rods at a

drift ratio of 7%, which led to a 56% drop in the flexural strength of the connection. It is worth mentioning that no fracture in the column to base plate welds was reported in this test. Refer to Gomez et al. [15] for additional details about the experiments.

3　Seismic-Induced Demands in Steel MRFs

3.1　MRF Design

A five-storey office building located on a Class C site (firm ground) in Vancouver, British Columbia (Seismic Category 4) was selected in this study. The plan view and elevation of the selected building are shown Fig. 2. The live and dead loads of typical floors are 4.6 kPa and 2.4 kPa, respectively, and the dead load and snow load at the roof level are 3.4 kPa and 1.64 kPa, respectively. The weight of the exterior walls was set equal to 0.6 kPa. The seismic loading was performed in accordance with the provisions of the upcoming 2020 National Building Code (NBC) of Canada [29] using the modal response spectrum analysis method. The importance factor is $I_E = 1.0$ and the higher mode factor $M_v = 1.0$. The lateral load-resisting system of the building consists of ductile MRFs in the long direction and ductile buckling-restrained braced frames (BRBFs) in the short direction (Fig. 2). One of the two MRFs was designed for this study. The ductility-related and overstrength-related force modification factors of the ductile MRF are $R_d = 5.0$ and $R_o = 1.5$. The period of the first mode of vibration of the MRF is 2.1 s. The seismic weight of the structure is 18883 kN which led to a total lateral seismic load of 951 kN for strength design and 632 kN for the lateral deflection check.

The MRF was designed in accordance with the seismic provisions of the Canadian steel design standard S16-19 [5]. The beams and columns are made of ASTM A992 wide-flange sections with specified and expected yield strengths of F_y 345 MPa and $R_y F_y$ 385 MPa, respectively. The modulus of elasticity of steel is $E = 200$ GPa. Further details about the design of steel MRFs can be found in [21].

3.2　Design of Column Base Plate

The exposed column base connection for the interior MRF column studied here (Fig. 2a) was designed in accordance with AISC steel design Guide 1 [14] and CSA S16-19 [5]. The detail of the base plate is shown in Fig. 3. The base plate is made of ASTM A572 Gr. 50 steel and is 88.9 mm-thick. Washer plates are also made of the same steel material with 12.7 mm thickness. In total, there are eight anchor rods, 38.1 mm in diameter and made of F1554 Gr. 105 steel. It is assumed that a shear lug welded underneath the base plate carries the shear force induced in the base connection and anchor rods are only designed under tension. The embedment
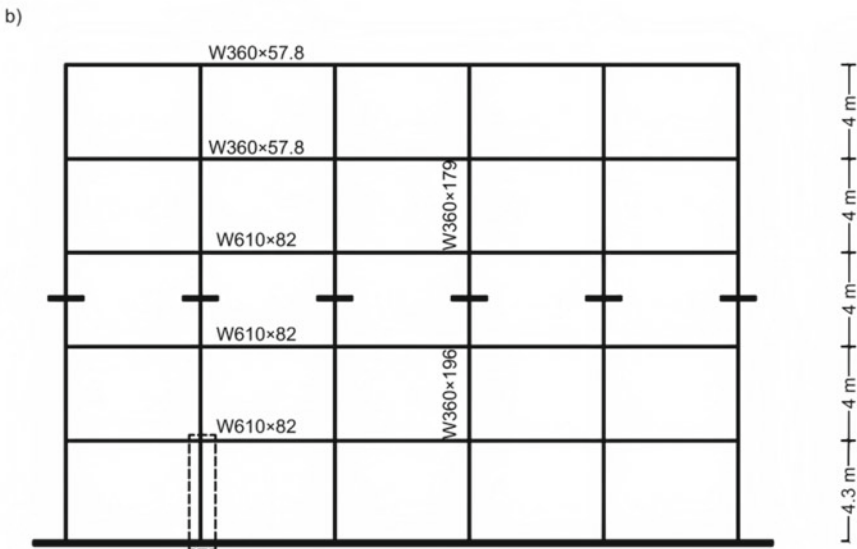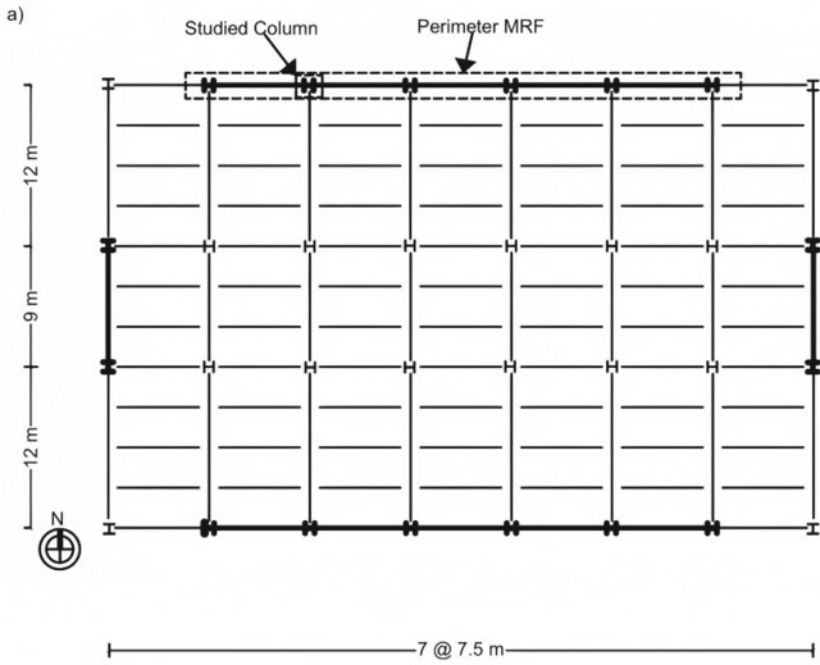
Fig. 2 Selected five-storey building **a** plan view, **b** prototype steel MRF
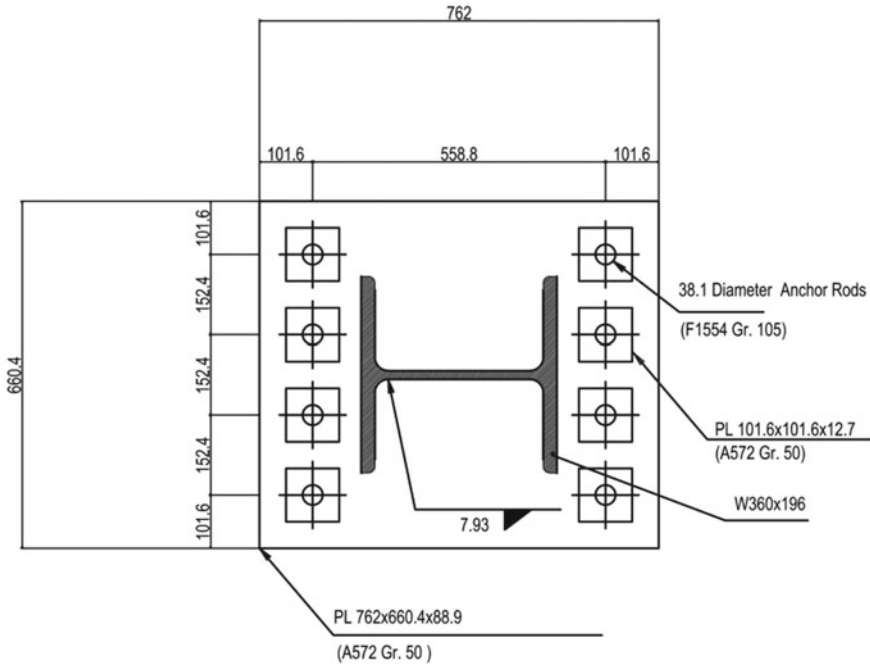
Fig. 3 Details of the column base plate (dimensions in mm)

length of the anchor rods is limited to one metre, benefitting supplemental shear reinforcement for restraining concrete breakout.

3.3 Concentrated Plasticity-Based Model

A two-dimensional (2D) model of the selected MRF (Fig. 2b) was constructed in OpenSees using nonlinear zero-length springs assigned at the ends of beams and columns plus elasticBeamColumn elements joining their end springs. The nonlinear cyclic properties of zero-length springs were based on the Ibarra Medina Krawinkler (IMK) deterioration model [27]. The nonlinear response of the IMK springs assigned to the column bases was modified as recommended by [26] to account for the influence of the column axial force and end conditions on its cyclic response. The panel zone was modelled using the parallelogram model with a nonlinear trilinear flexural spring along with rigid elements [16]. The columns were assumed to be fixed at their bases. A leaning column made of truss elements with relatively high axial stiffness was included to impose P-Delta effects from the gravity columns tributary to the selected MRF. That column was connected to the MRF at each storey using a relatively rigid truss element to simulate a rigid floor diaphragm response. Lumped

masses were assigned to the top nodes of the columns to reproduce the seismic mass of the building associated with the MRF. The Rayleigh damping method with mass and stiffness proportional damping corresponding to a critical damping ratio of 2% in the first and second vibration modes was used to reproduce the classical damping matrix of the structure [37]. Refer to [21] for additional details regarding the concentrated plasticity-based model of the MRF.

In a well-designed MRF, out of plane bracing through floor slab or point bracing is provided to the beam which ensures that the weak axis flexure remains almost elastic. The modelling approach in which elastic properties are assumed for weak axis flexure of MRF beams should not significantly influence the in-plane response of the frame examined in this paper. In this context, 2D frame analysis is sufficient to obtain displacement demands at top of the column which is subsequently imposed in detailed 3D finite element analysis.

3.4 First-Storey Column Deformation Demands

Nonlinear Response History Analysis (NLRHA) of the MRF was performed under the 2003 Tokachi-Oki, Kitami N-S, interface subduction earthquake record scaled to match the design response spectrum for the site following the guidelines of the NBC Commentary J. Under the selected ground motion record, no collapse was observed, and the profile of the peak storey drifts over the frame height is shown in Fig. 4. In the first-storey, the maximum inter-storey drift reached 2.7%. The time histories of horizontal displacement and rotation at the top of the selected first-storey interior column are presented in Fig. 5a, b, respectively. As indicated, these results were obtained assuming fixed base conditions for the columns.

Fig. 4 Profile of peak storey drift ratios

a)

b)
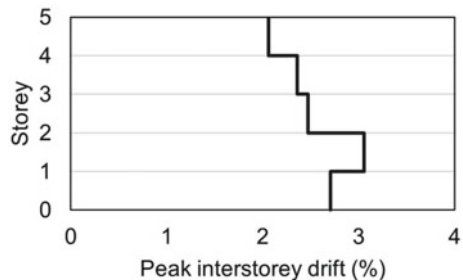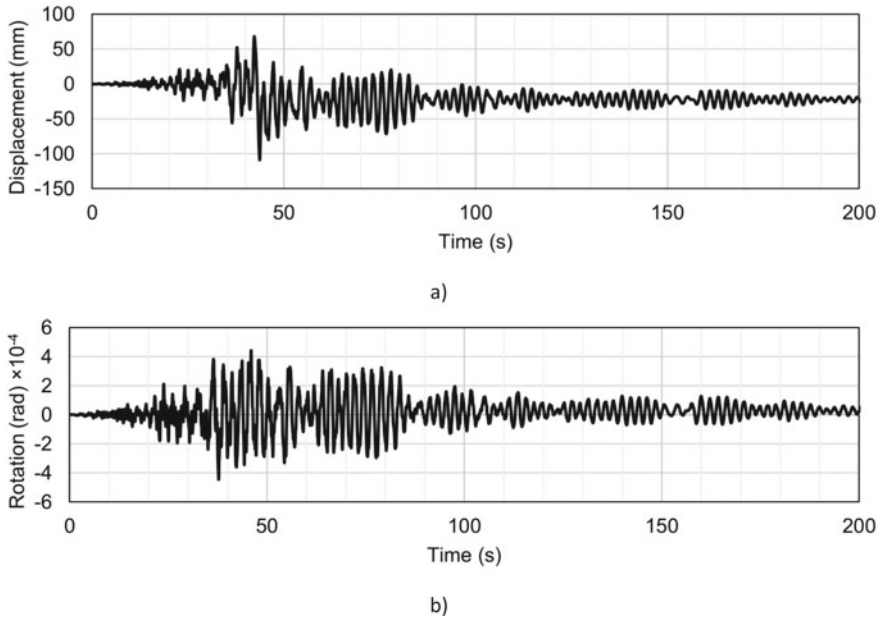
Fig. 5 Seismic-induced demands at top of the interior first-storey column under the 2003 Tokachi-Oki, Kitami N-S earthquake: **a** in-plane displacement history, **b** strong axis rotation history

4 Influence of MRF Column Base Conditions on the Column Response

4.1 Finite Element Model Development

The detailed three-dimensional (3D) model of the exposed column base connection was created in the ABAQUS program [1]. The finite element model of the column is shown in Fig. 6. In the model, footing, base plate, anchor rods, and columns were constructed using solid hexahedral (C3D8R) elements to explicitly simulate the thickness of base plate, grout pad, concrete pedestal, and column flanges. A total of almost 60,000 elements were used. The wide-flange column can also be made of Shell S4R elements to reduce computational cost while properly capturing local buckling. The base nodes of the column were tied in all degrees-of-freedom (DOFs) to the base plate nodes at the intersection of the column and base plate. All nuts were tied to the washers, and the washers themselves were tied to the anchor rods. The base of the footing was fixed in all DOFs, while the top end of the column was braced against out of plane deformation.

The numerical surface-to-surface contact properties having tangential and normal behaviour was used to simulate the interaction between the components of the column base connection and footing. The contact properties included steel to steel, steel to

Fig. 6 Detailed finite
element model of the column
and base connection
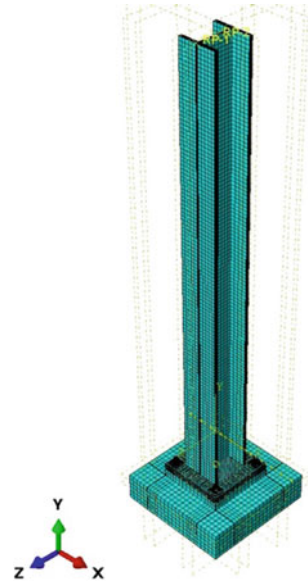
concrete, anchor rods to concrete, anchor rods to grout, and anchor rods to base
plate. In steel-to-steel contact, hard contact was defined with tangential behaviour
and isotropic friction using the penalty method with the coefficient of friction of 0.8.
Note that hard contact definition allows for separation, which is expected between
the washers and the base plate, as was observed in the test program by Gomez et al.
[15]. The coefficient of friction in steel to concrete contact was assumed as 0.45.
Steel-to-steel contact was used between the top washer and the base plate, as well
as between the bottom washer and the base plate. Steel-to-concrete contact was
considered between the base plate and the grout and between the bottom washer and
the grout. Interaction between the anchor rods and the concrete, grout, and base plate
was simulated using a soft contact with the linear formulation. The elastic stiffness (E)
of concrete, grout, and steel were used as contact stiffness for anchor rods to concrete,
anchor rods to grout, and anchor rods to base plate contact properties, respectively.
The tangential behaviour of the anchor rods to concrete and anchor rods to grout
contact properties was ignored, which is consistent with the observation by Gomez
et al. [15]. The tangential behaviour of anchor rods to concrete and anchor rods to
grout was therefore ignored in the model owing to the fact that anchor rods tend to
de-bond from concrete at the beginning of loading in the test as reported by Gomez
et al. [15]. The tangential behaviour of the anchor rods to base plate was also ignored.
This assumption aligns with the design assumptions as the size of the anchor rod
holes exceeds the anchor rod diameter, which will eliminate friction between the
sides of anchor rods and the base plate.

Material nonlinearity in the base plate steel was incorporated through the
Maxwell–Huber–Hencky–von Mises yield criterion with associated flow rule. The
nonlinear cyclic behaviour of the steel material was reproduced using the Voce and
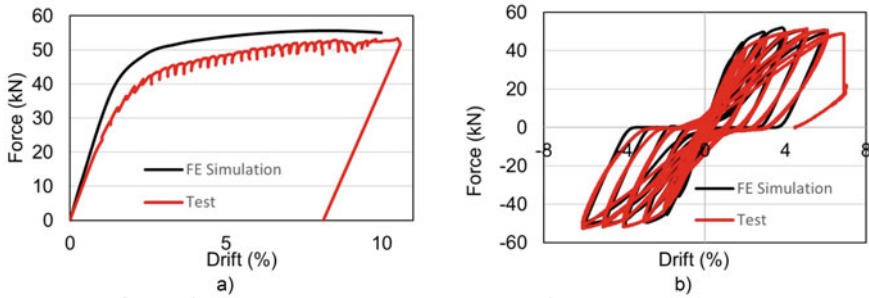
Fig. 7 Column force–displacement responses obtained from the experiment as compared to numerical predictions: **a** test 1 and **b** test 2

Chaboche plasticity model that features combined isotropic/kinematic hardening [6, 11, 17] with three back stress curves to match the ancillary test data provided by Gomez et al. [15]. Concrete and grout materials were assumed to remain elastic for simplicity and were modelled using the modulus of elasticity reported by Gomez et al. [15], i.e. $E_c = 24.13$ kN/mm^2 and $E_g = 20.68$ kN/mm^2, respectively [32].

4.2 Model Validation

In Fig. 7a, b, the force—displacement responses obtained from the FE model for Test 1 and 2 specimens are compared to those measured in the experimental program. Overall, very good correlation could be obtained between the predictions and the test results. The pinching response in the cyclic response (Fig. 7b) is mainly attributed to the cumulated permanent elongation of anchor rods, which prevented them from being engaged in tension after each load reversal until the base plate became in contact with the washer and nut. The elongation of the anchor rods during load reversal is illustrated in Fig. 8. Crushing of the grout was ignored in the model, as the grout was only assigned linear elastic response. However, this assumption had minor impact on the magnitude of the forces in the monotonic and cyclic tests because the force–displacement response of the column was dominated by the anchor rod and base plate yield mechanisms.

4.3 Column Response

The horizontal displacement and rotation time histories of Fig. 5 were applied at the top end of the finite element model of the selected interior first-storey column for two base conditions: fully fixed and with the base connection of Fig. 3. No global instability of the column was observed in the analyses. The comparison of
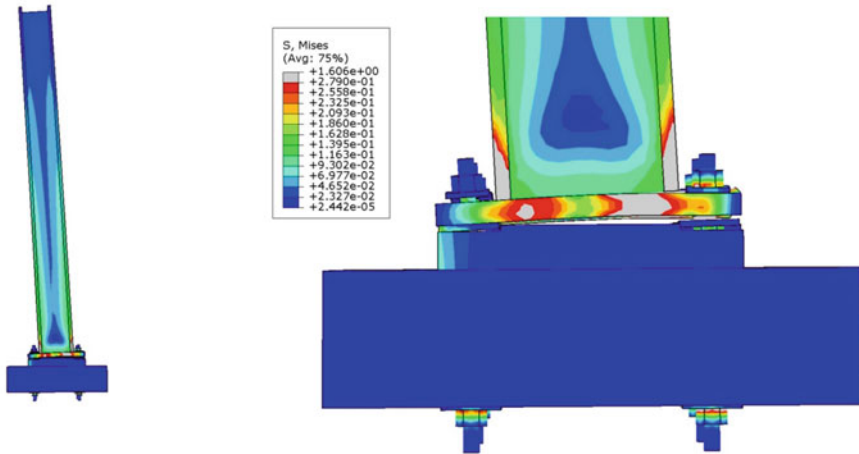
Fig. 8 Deformed shape and von Mises stress distributions of the column base at 7% drift ratio showing the elongation of the anchor rods during the load reversal under cyclic loading protocol (stresses are in kN/mm^2; grey zones represent yielding)

the lateral force—chord rotation and base moment—chord rotation responses of the columns with fully fixed base condition and with the base connection are presented in Fig. 9a, b, respectively. The flexural stiffness of the column with the realistic base condition is approximately 30% lower than that of the column with fully fixed condition. Moreover, the nonlinear response of the column was significantly affected when more realistic base condition was considered. In particular, limited nonlinear response was observed and column flexural yielding was limited to only few large drift excursions experienced during the ground motion. This behaviour can stem from the flexibility induced by the flexural yielding of the base plate and the plastic elongation of the anchor rods.

The deformed shape and von Mises distributions of the columns with fully fixed and realistic base conditions at the maximum drift ratio (2.7%) are shown in Figs. 10 and 11. As shown, although the extend of flexural yielding is almost the same, less severe local buckling at the base plastic hinge location accompanied by lower axial shortening was observed when realistic base conditions were considered.
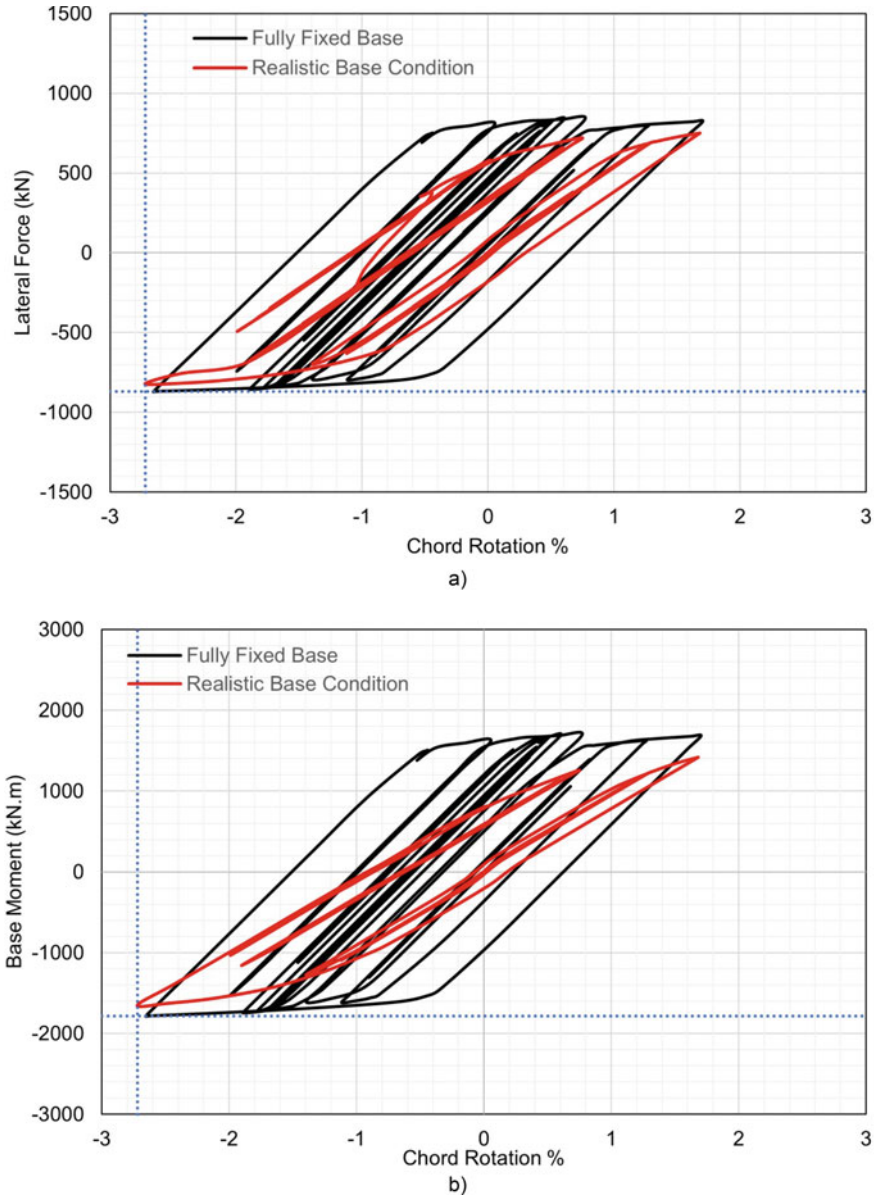
Fig. 9 Responses of the column with fully fixed base condition and the column with realistic base condition under the 2003 Tokachi-Oki, Kitami N-S earthquake: **a** lateral force—chord rotation, **b** base moment—chord rotation
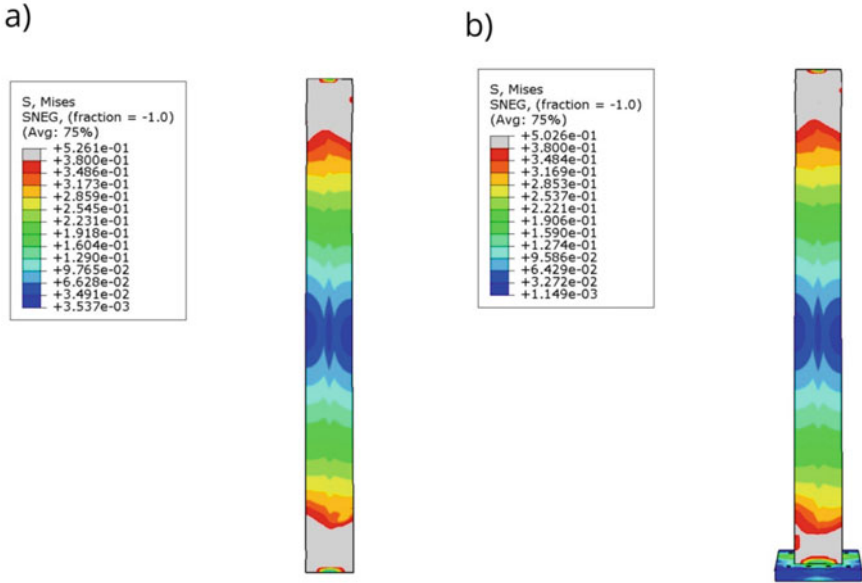
Fig. 10 Deformed shape and von Mises stress distributions of the interior first-storey MRF column at 2.7% drift ratio under the 2003 Tokachi-Oki, Kitami N-S earthquake looking at the column web: **a** column with fully fixed base condition, **b** column with realistic base condition
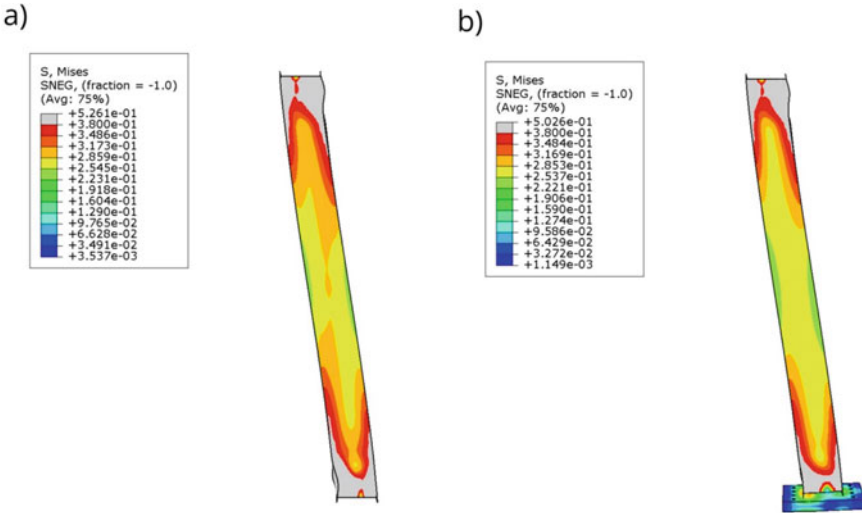
Fig. 11 Deformed shape and von Mises stress distributions of the interior first-storey MRF column at 2.7% drift ratio under the 2003 Tokachi-Oki, Kitami N-S earthquake looking at the column flange: **a** column with fully fixed base condition, **b** column with realistic base condition

5 Conclusion

The objective of this study was to evaluate the effect of the column base conditions on the nonlinear cyclic response of steel wide-flange columns with exposed column base connections located in the first storey of steel ductile MRFs. A detailed finite element model of the column and its base connection was developed in ABAQUS and calibrated against past experimental test data. The nonlinear cyclic response of the columns with a fully fixed base condition and with realistic base connection condition was examined under seismic-induced demands obtained from NLRHA of the MRF subjected to a ground motion record from a severe interface subduction earthquake. The key findings of this study can be summarized as follows:

- A detailed continuum-based finite element model of an MRF column base including the base plate, anchor rods, grout, and footing concrete was developed and tied to the first-storey column shell-based model to study the column cyclic response taking into account realistic base conditions. Numerical modelling recommendations were proposed.
- The experimentally observed pinching response of exposed column base connections due to cumulated permanent elongation of the anchor rods could be accurately reproduced using the proposed numerical model.
- The cyclic inelastic response of the exposed column base connection is mainly controlled by yielding of the anchor rods and the base plate.
- Realistic base conditions that account for the deformations of the base plate, anchor rods, grout, and footing concrete can significantly affect the nonlinear cyclic response and the severity of local buckling of wide-flange columns located in the first storey of steel MRFs.
- The flexural stiffness of the column was reduced by approximately 30% when considering realistic base conditions. Moreover, the magnitude of the flange and web local buckling at the base plastic hinge locations appreciably decreased.
- Realistic base conditions can significantly affect the displacement response of the first storey of MRFs and the demand on the columns in that storey under seismic loading.

Future studies should evaluate the flexibility of the column base for deeper wide-flange columns preferred in the construction of steel MRFs. Moreover, realistic base conditions of wide-flange MRF columns should be factored in when analysing the structural response under seismic loading.

References

1. Abaqus G (2020) Abaqus 6.14.1. Dassault Systemes Simulia Corporation, Providence, RI, USA
2. Astaneh A, Bergsma G, Shen JH (1992) Behavior and design of base plates for gravity, wind and seismic loads. In: Proceedings of the national steel construction conference, 209–14. AISC Chicago, IL
3. Bajer M, Vild M, Barnat J, Holomek J (2014) Influence of selected parameters on design optimization of anchor joint. In: 12th international conference on steel, space and composite structures, pp 28–30
4. Burda JJ (1999) Studies of seismic behavior of steel base plates. University of Nevada, Reno
5. Canadian Standards Association (2019) CSA S16: 19. Design of Steel Structures, Toronto, Canada
6. Castro e Sousa AD, Suzuki Y, Lignos D (2020) Consistency in solving the inverse problem of the voce-chaboche constitutive model for plastic straining. J Eng Mech 146 (9):04020097
7. Choi J-H, Ohi K (2005) Evaluation on interaction surface of plastic resistance for exposed-type steel column bases under biaxial bending. J Mech Sci Technol 19(3):826–835
8. Cloete R, Roth CP (2021) Column base connections under compression and biaxial moments: experimental and numerical investigations. J Constr Steel Res 184:106834
9. DeWolf JT, Sarisley EF (1980) Column base plates with axial loads and moments. J Struct Div 106(11):2167–2184
10. Elkady A, Güell G, Lignos DG (2020) Proposed methodology for building-specific earthquake loss assessment including column residual axial shortening. Earthquake Eng Struct Dynam 49(4):339–355
11. Elkady A, Lignos DG (2015) Analytical investigation of the cyclic behavior and plastic hinge formation in deep wide-flange steel beam-columns. Bull Earthquake Eng 13(4):1097–1118
12. Elkady A, Lignos DG (2018) Full-scale testing of deep wide-flange steel columns under multi-axis cyclic loading: loading sequence, boundary effects, and lateral stability bracing force demands. J Struct Eng 144(2):4017189
13. Fahmy M, Stojadinovic B, Goel SC (1999) Analytical and experimental behavior of steel column bases. In: Proceedings of 8th Canadian conference on earthquake engineering. Canadian Association for Earthquake Engineering, Ottawa, ON, Canada
14. Fisher JM, Kloiber LA (2006) Steel design guide 1-base plate and anchor rod design. AISC, pp 801–806
15. Gomez I, Deierlein G, Kanvinde A (2010) Exposed column base connections subjected to axial compression and flexure
16. Gupta A (1999) Seismic demands for performance evaluation of steel moment resisting frame structures. Stanford University
17. Hartloper AR, de Castro e Sousa A, Lignos DG (2021) Constitutive modeling of structural steels: nonlinear isotropic/kinematic hardening material model and its calibration. J Struct Eng 147(4):04021031
18. Inamasu H, Kanvinde AM, Lignos DG (2019) Seismic stability of wide-flange steel columns interacting with embedded column base connections. J Struct Eng 145(12):04019151
19. Inamasu H, Lignos DG (2022) Finite element modeling and behavior of dissipative embedded column base connections under cyclic Loading. J Constr Steel Res 189:107063
20. Inamasu H, Lignos D, Kanvinde A (2018) Influence of embedded steel column base strength on earthquake-induced residual deformations. In: Proceedings of the 16th European conference on earthquake engineering
21. Islam A, Imanpour A (2022) Stability of wide-flange columns in steel moment-resisting frames: evaluation of the Canadian seismic design requirements. Bull Earthquake Eng: 1–27
22. Kanvinde AM, Grilli DA, Zareian F (2012) Rotational stiffness of exposed column base connections: experiments and analytical models. J Struct Eng 138(5):549–560
23. Krawinkler H, Gupta A, Medina R, Luco N (2000) Development of loading histories for testing of steel beam-to-column assemblies. Stanford University

24. Lee D-Y, Goel SC, Stojadinovic B (2008a) Exposed column-base plate connections bending about weak axis: I. Numerical parametric study. Int J Steel Struct 8(1):11–27
25. Lee D-Y, Goel SC, Stojadinovic B (2008b) Exposed column-base plate connections bending about weak axis: II. Experimental study. Int J Steel Struct 8(1):29–41
26. Lignos DG, Hartloper AR, Elkady A, Deierlein GG, Hamburger R (2019) Proposed updates to the ASCE 41 nonlinear modeling parameters for wide-flange steel columns in support of performance-based seismic engineering. J Struct Eng 145(9):04019083
27. Lignos DG, Krawinkler H (2010) Deterioration modeling of steel components in support of collapse prediction of steel moment frames under earthquake loading. J Struct Eng 137(11):1291–1302
28. Myers AT, Kanvinde AM, Deierlein GG, Fell BV (2009) Effect of weld details on the ductility of steel column baseplate connections. J Constr Steel Res 65(6):1366–1373
29. National Research Council (2020) User's guide—NBC 2020 structural. Canadian Commission on Buildings and Fire Codes, National Research Council of Canada
30. Pan J, Huang R, Xu J, Wang P, Wang Z, Chen J (2021) Behavior of exposed column-base connections with four internal anchor bolts under seismic loading. Structures 34:105–119
31. Seco LD, Silva MC, Hjiaj M, Neves LC (2021) Column base-plates under biaxial bending moment. Eng Struct 231:111386
32. Singh G, Woods J (2022) 2D and 3D numerical modelling of exposed steel base plate connections under cyclic loading. Can J Civ Eng
33. Thambiratnam DP, Paramasivam P (1986) Base plates under axial loads and moments. J Struct Eng 112(5):1166–1181
34. Tremblay R, Filiatrault A, Timler P, Bruneau M (1995) Performance of steel structures during the 1994 Northridge earthquake. Can J Civ Eng 22(2):338–360
35. Uang C-M, Ozkula G, Harris J (2015) Observations from cyclic tests on deep, slender wide-flange structural steel beam-column members. In: Proceedings of the SSRC annual stability conference
36. Zareian F, Kanvinde A (2013) Effect of column-base flexibility on the seismic response and safety of steel moment-resisting frames. Earthq Spectra 29(4):1537–1559
37. Zareian F, Medina RA (2010) A practical method for proper modeling of structural damping in inelastic plane structural systems. Comput Struct 88(1–2):45–53

Seismic Performance Comparison of Moderately Ductile and Conventional Construction Steel Concentrically Braced Frames

Anirban Kundu, Lydell Wiebe, and Georgios P. Balomenos

Abstract Steel concentrically braced frames (CBFs) are widely used as a seismic force resisting system (SFRS) in Canada because of their efficiency in resisting seismic loads. Several different approaches can be taken to design CBFs according to the Canadian Steel Design Standard CSA S16:19. These approaches range from moderately ductile (Type MD) CBFs, which require special detailing considerations and limits on local and member slenderness to promote the intended ductile response, to conventional construction (Type CC), which requires higher seismic design forces but has more relaxed detailing requirements. While these construction types have been defined in CSA S16:19 for many years, few studies have compared the seismic performance of frames designed using these different sets of requirements. To address this research gap, this paper compares designs for the same archetype structure using both Type MD and Type CC CBFs. Both frame types are designed according to CSA S16:19 and subsequently modelled using the advanced earthquake simulation software OpenSees. Thereafter, the models are subjected to a multiple stripe analysis (MSA) using a set of ground motions prescribed in FEMA P-695, to assess their seismic performance. A close look at the inter-storey drift time history during a typical ground motion record reveals the sequential occurrence of the different damage states, while the statistics of the inter-storey drift ratio demonstrates that the Type CC design leads to more variable performance. Finally, storey-by-storey fragility curves are developed for both construction types to compare the seismic performance.

Keywords Seismic performance · Steel structures · Numerical modelling · Concentrically braced frames · Conventional construction · Moderately ductile concentrically braced frame · Multiple stripe analysis

A. Kundu (✉) · L. Wiebe · G. P. Balomenos
Department of Civil Engineering, McMaster University, Hamilton, Canada
e-mail: kundua6@mcmaster.ca

1 Introduction

Concentrically braced frames (CBFs) are widely used as a lateral force resisting system for their inherent strength and stiffness, which make them efficient, economical, and practical to meet the force and deformation requirements of building codes. The lateral force is resisted by the tension and compression of opposing braces. During severe, infrequent earthquakes, braces yield in tension and buckle in compression, and the post-buckling behaviour of the brace is associated with formation of a hinge at mid-length, as well as significant cyclic load and end rotational demand on the gusset plate [11]. To promote the intended brace behaviour, modern seismic codes place limits on the global and local slenderness ratios of brace sections for the most ductile CBFs (e.g., Type MD CBFs in [7]). Meanwhile, other framing elements are required to be capacity protected to remain elastic when the braces reach their probable post-buckling and post-yielding strengths. Also, the connections of the braces to the framing elements must be designed and detailed properly so that the ductile failure mechanism is concentrated only in the brace. The most critical detailing parameters include adequate rotational capacity in the gusset plate at the brace ends, as well as adequate weld strength and toughness (hereafter referred to as a "demand critical weld") at the gusset plate interface and brace-to-gusset connection. A recent extension of this approach is the balanced design procedure (BDP), where a preferred sequence is promoted for the different yielding and failure mechanisms in an effort to maximize the overall ductility [22].

When such design requirements are not followed, the consequences can include loss of strength and stiffness of the brace module at low drift demands, leading to a premature and unintended system failure mechanism. Such behaviour is expected for CBFs built prior to modern seismic ductility design provisions, referred to as non-ductile CBFs (NCBFs) [25]. Alternatively, modern seismic codes generally allow lower ductility CBFs to be designed for higher seismic forces as a means to avoid the above-mentioned complexities of ductile designing while also avoiding unintended failure modes. For example, the US standard (ASCE/SEI 7-22 2022) has categories for "*system not specifically detailed for seismic resistance*" ($R = 3$) and ordinary CBF (OCBF, $R = 3.25$), while the Canadian standard [7] has categories for limited ductility (LD) CBFs and conventional construction (CC). While a relatively high ductility-related reduction factor ($R_d = 3.0$) allows Type MD CBFs to be designed with a relatively low base shear, Type CC CBFs are designed with a comparatively lower value of R_d (1.5), leading to a higher base shear but without the need for rigorous seismic detailing. CSA S16:19 prescribes a further 50% increase in the connection demand for Type CC design when the expected connection failure mode is not ductile. Although there are some limitations to the use of Type CC, such as excluding it for post-disaster buildings [20] there are few limitations on designing or detailing. This ease of design makes it convenient for a designer to use Type CC design as a seismic force resisting system (SFRS), particularly in regions of low or moderate seismicity. On the other hand, these relaxations may make the seismic performance of Type CC design less predictable. The behaviour might be expected

to be similar to the NCBFs due to the following reasons: (i) CSA S16:19 implies a preference for ductile connections but does not define how to do this; (ii) lack of adequate rotational clearance at the brace ends could cause fracture of the interface welds, leading to the complete loss of connection strength and hence the total brace module [24], and (iii) absence of limitations for local and global slenderness ratio in the braces, which might lead to premature fracture of them. The difference between Type MD and Type CC CBFs in both seismic design loads and expected nonlinear response leads to uncertainty about their relative performance overall.

The seismic performance of Type CC CBFs was studied by [6] in two phases. First, the ductility capacity of a typical bolted brace connection was evaluated experimentally. Based on the force and deformation ductility capacity found in first phase, a set of buildings was designed and analysed numerically with varying design parameters such as location (Vancouver and Montreal), building height, storey height, bracing configuration, etc. Among the set, two buildings from Vancouver were chosen for incremental dynamic analysis. The study suggested that connections need to be designed with demand related to $R_d R_o$ less than 1 to avoid any height limit, but buildings with a height of 15.6 m or less would provide adequate protection against collapse if ductile connections are used, the building is located on Site Class C, and a split-X or chevron configuration is used. In the USA, experimental testing of one-storey, single-diagonal-configuration bracing systems was performed at the University of Washington to investigate the behaviour of Special CBFs (SCBFs), which are the most ductile CBF system according to the AISC Seismic Provisions (ANSI/AISC 341-16 2016), as well as NCBFs, under a quasi-static loading protocol. The behaviour of SCBFs was experimentally demonstrated by [10, 15, 16, 21]. Subsequently, the same frame configuration was used by [4, 14, 27, 28] to investigate the behaviour of the CBFs designed non-seismically, along with various types of connection and their behaviour after retrofit. Based on the results from these experimental tests, an improved numerical approach was developed to model the gusset plate connection for both SCBFs (which are similar to Type MD CBFs, as per CSA S16:19) [12], as well as NCBFs [24].

A few other studies are also important in the context of seismic behaviour of non (or low)-ductile CBFs. [23] tested six full-scale Type CC I-shaped brace specimens with bolted end connections in two different configurations to connect the brace to the gusset plate. The test indicated that the Type CC brace specimens could achieve storey drift ratios of 1–2%, even though capacity design provisions were not incorporated in their design. Significant contributions to ductility capacity came from yielding and buckling of the gusset plate and lap plate, together with bolt bearing, and friction associated with bolt slip. Based on the findings of [23], a component-based numerical modelling approach was proposed by [29], which takes into account the considerable contribution of gusset plate yielding and bolt hole elongation to overall deformation capacity. Two full-scale, two-storey, low-ductility CBFs, one with seismic detailing as per the AISC Seismic Provisions (ANSI/AISC 341-16 2016) for an ordinary concentrically braced frame (OCBF) with $R = 3.25$ and another with no seismic detailing ($R = 3$), were tested by [5]. The study evaluated failure mechanisms, post-elastic frame behaviour, reserve capacity, and overall

collapse performance. A detailed seismic performance assessment of low-ductility CBFs, in the context of US design standard, was conducted by [26].

Building on these past studies of the performance of CBFs, this study develops a storey-wise collapse-based fragility assessment considering three damage states. First, a pair of 3-storey CBFs are designed according to Clauses 27.5 (Type MD, R_d = 3, R_o = 1.3) and 27.12 (Type CC, R_d = 1.5, R_o = 1.3) of [7], using seismic force demands calculated as per the National Building Code [20]. Next, numerical models are developed to capture fracture in the brace for both Type CC and MD CBF, as well as fracture of the gusset plate interface weld in the case of Type CC CBF. A suite of 44 ground motions is then chosen based on the [9] and scaled based to the design spectrum. The seismic performance is investigated first for a single ground motion at design ground motion (DGM) level earthquake. Next, a series of nonlinear response history analyses (NLRHA) are conducted in OpenSees [19] under the framework of multiple stripe analysis [3]. Finally, the fragility curves obtained from both the design types are compared.

2   Specimen Design

Figure 1 shows the three-storey office building that was considered in this study, located in Victoria, BC, and having a total height of 12.5 m, with a plan dimension of 36 m × 36 m and bay lengths of 9 m in each direction. The gravity loads are shown in Table 1. The prototype building was equipped with two braced bays in each exterior frame. The brace configuration was split-X cross bracing at the first two stories and chevron at the top storey. Site Class C was considered with an importance factor of 1. The design spectrum was calculated based on the hazard level for a 2% probability of exceedance in 50 years, noted as the design ground motion (DGM) as per the [20]. The R_d for Type MD design is 3, whereas for Type CC it is 1.5. For the Type MD design, the base shear was 7075 kN, whereas it was 14,150 kN for Type CC design. The modelled fundamental period of the Type MD CBF was 0.35 s, whereas for the Type CC CBF, it was 0.33 s. The designed member dimensions are provided in Table 2.

As $I_E S_a(0.2) > 0.45$, the connection demand was amplified by 50% of the factored brace force demand [7]. To differentiate from the Type MD design, capacity-based designing details were not followed in the Type CC design, including:

- In the case of Type MD design, the beams were designed for the factored gravity load along with an unbalanced vertical force demand generated due to the difference between the expected post-buckling capacity of the compression braces and the expected yielding capacity of the tension braces. This unbalanced demand was also considered in designing the shear tab connections at the beam ends. In Type CC design, this unbalanced vertical force demand was not considered when designing the beam. Likewise, the shear tab connection at the end of the beam was designed for the factored gravity load only.

Fig. 1 Floor plan and the elevation of the building
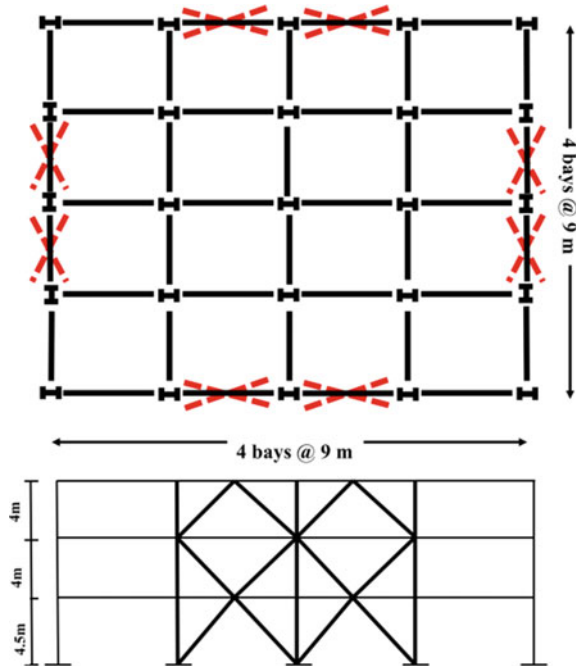
Table 1 Gravity loads

	Load (kPa)			
	Dead	Live	Snow	Cladding
Roof	3.5	1.0	1.64	1.5
Floor	4.9	2.4	–	

Table 2 List of designed members

St	Type MD			Type CC		
	Beam	Column	Brace	Beam	Column	Brace
3	W610 × 341	W310 × 415	HSS127 × 127 × 13	W410 × 46	W360 × 134	HSS203 × 203 × 7.9
2	W460 × 97		HSS152 × 152 × 13	W460 × 60		HSS254 × 254 × 9.5
1	W610 × 415		HSS178 × 178 × 16	W460 × 60		HSS254 × 254 × 16

- The global slenderness ratio of the braces in Type MD CBF was limited to a minimum of 70, which was not required in Type CC CBF design.
- For Type MD CBFs, the width-to-thickness ratio of the HSS cross section was limited to $330/\sqrt{F_y}$ (for $KL/r \leq 100$, , which was the case for each brace in this current study). This restriction in local slenderness was not required for Type CC design.
- When calculating the demand on the column in Type MD CBF, the probable tensile and compressive capacity of the braces were considered, as per capacity design principles. Also, an additional moment of 0.2ZFy (as mentioned in clause 27.5.5.3 (b) of [7]) was applied. Conversely, in the case of Type CC CBF, the vertical component of the factored force induced by the braces was considered based on the linear elastic analysis under the applied seismic loads, and no additional moment was considered.
- For Type MD CBF, the demand in the connection was calculated based on the probable strength of the brace. For Type CC, this demand was calculated as 1.5 times the factored brace design force.
- None of the clearance criteria (neither linear 2tp nor elliptical 8tp) was fulfilled for the Type CC design.

Although the Type MD CBF was designed for half the base shear of Type CC CBF, other restrictions resulted in a much larger beam section (Table 2), especially in the first and third floors, to accommodate the unbalanced vertical demand mentioned above. The column section within the SFRS was also larger for the Type MD design compared to Type CC. The braces in Type MD design are stockier, having a higher global slenderness but lower local slenderness ratio compared to Type CC.

3   Numerical Modelling

To capture the overall seismic behaviour of the CBF system, it is important to accurately model several key features, including yielding in tension, buckling and post-buckling of the brace in compression, rotational deformations and yielding of the gusset plates, and local yielding of the beams and columns adjacent to the gusset plates. Although a well-designed Type MD CBF seldom reaches fracture of the braces or gusset plate, for Type CC, these are paramount modelling requirements. A schematic of the frame modelled in OpenSees [19] is shown in Fig. 2, where fibre-discretized distributed-plasticity-based beam–column elements were used for the defining the braces, beams, and columns, while concentrated-plasticity springs were used to define the gusset plate connections.

Sixteen nonlinear displacement-based beam–column elements were used along the length of the brace with an initial camber of 1/500 of the total length, in a sinusoidal shape, to initiate the buckling behaviour of the brace. Four integration points were considered for each element. The cross section of the HSS brace was discretized using four fibres across the thickness and depth in each direction, following the
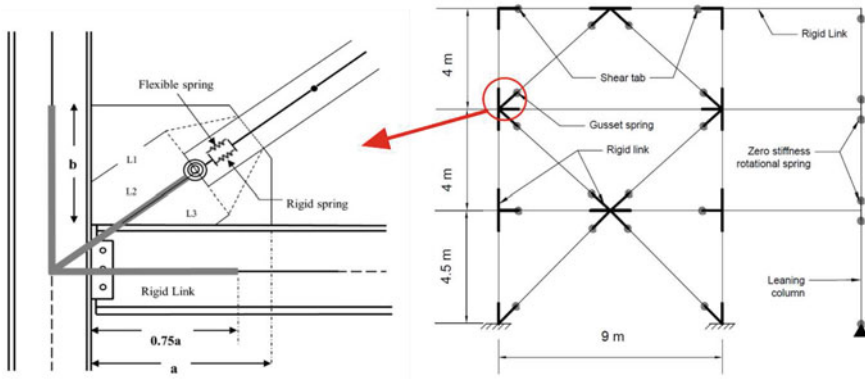
Fig. 2 Schematic diagram and numerical modelling details of the connection

approach recommended by [12]. Force-based nonlinear beam–column elements with four integration points were used for beams and columns along with fibre cross sections. To improve convergence during dynamic analysis in OpenSees, the beams were modelled with multiple elements, but without any imperfection, unlike the braces. A Giuffre–Menegotto–Pinto model with the Steel02 material was used to model all the constitutive elements for all members [12, 24].

The gusset plate connection was simulated by using a zero-length nonlinear, concentrated, out of plane, rotational spring Hsiao et al. 2012), at the end of the brace in the axial direction where the rigid link ends (Fig. 2). Steel02 material was used as a constitutive model for the spring. The flexural stiffness (K) and strength (F_y^{rot}) of the rotational spring are provided in Eqs. (1) and (2) respectively, as follows:

$$K = \frac{E}{L_{\text{avg}}} \left(\frac{W_w t^3}{12} \right) \tag{1}$$

$$F_y^{\text{rot}} = \frac{W_w t^2 F_{y,\text{gusset}}}{6} \tag{2}$$

where E is Young's modulus of steel, W_w is the Whitmore width defined by a 45° projection angle, L_{avg} is the average of $L1$, $L2$ and $L3$ as shown in Fig. 2, and t is the thickness of the gusset plate. The post-yield stiffness was taken as 1% of the initial stiffness. The rigid zones extend from the work point to the edge of gusset plate, except along the horizontal beam, where they extend to 75% of the gusset dimension. The shear tab (shown in Fig. 2) was modelled as per [18], as described by [8].

3.1 Fracture Modelling

The maximum strain-based fracture model developed by [13] and modified by [24] was used, where a fracture-material "wrapper" is used over the parent material. The fracture-material monitors the strain of the underlying parent material and initiates fracture of individual brace fibres based on the maximum strain range (MSR) between tension and compression. When the fracture criterion is reached, the strength and stiffness of the fibre are reduced by the wrapper to nearly zero. Conceptually, the fibre is removed from the section at that location, and the progressive fracture of the fibres leads to complete brace fracture. The MSR is a function of local as well as global slenderness ratio and strength of the material and is given by the following equation from [24]:

$$\text{MSR} = 0.554 \left(\frac{b}{t} \right)^{-0.75} \left(\frac{L_c}{r} \right)^{-0.47} \left(\frac{E}{F_y} \right)^{0.21} \left(\frac{\delta_{c,\max}}{\delta_{t,\max}} \right)^{0.068} \tag{3}$$

The above equation indicates that braces with a higher $\frac{b}{t}$ ratio lead to lower MSR, resulting in reduced fracture life. Ductile CBFs (e.g., Type MD in CSA S16:19) delay this behaviour by employing stockier cross sections. This factor creates a substantial difference in the fracture life in between braces in Type MD and Type CC design.

Another prevalent mode of failure in Type CC design is the gusset plate interface weld fracture, which leads to complete loss of strength provided by the brace module. This part of the connection is subjected to in-plane deformation due to the opening and closing of the beam–column joints, as well as out-of-plane deformation due to buckling of the brace. This is accommodated in ductile CBFs (Type MD in CSA S16:19 or SCBFs in AISC 341-16) by providing a clearance for brace end rotation along with demand critical welds. Conversely, in Type CC CBF, the connection was designed for an amplified force demand instead of applying this special ductile detailing. Shortcomings in the connection details of Type CC CBF in the modern code CSA S16:19 are like that of the NCBFs. So, the interface weld fracture was modelled with a rotational limit, θ_f (Eq. 4), proposed by [24]. The limit was employed on a zero-length rotational spring (shown in Fig. 2) defined for the gusset plate, proposed by [12]. The limit is a function of demand to capacity ratio for the interface weld (DCR$_{\text{gpw}}$) and the clearance provided at the end of the brace:

$$\theta_f = 0.11 \left(\frac{L_{\text{clear}}}{t_p} \right)^{0.33} \text{DCR}_{\text{gpw}}^{-0.57} \leq 0.257 \, \text{rad} \tag{4}$$

where L_{clear} is the thickness of the elliptical clearance provided, and t_p is the thickness of the gusset plate. DCR$_{\text{gpw}}$ was calculated according to the balanced design approach, proposed by [22], which was based on the tensile capacity of the plate and the weld, given by the following equation:

$$DCR_{gpw} = \frac{(RyFy)_p t_p}{0.9\sqrt{2}F_{EXX}w_p} \tag{5}$$

Type CC design was not expected to meet any of the criteria for clearance or demand critical welds. In most cases, the elliptical clearance factor ($\frac{L_{clear}}{t_p}$ in Eq. 3) was much lower than the prescribed value (i.e., 8, as per [7, 17]), near 1 or 2 or even less than that [25]. Therefore, to maintain uniformity and ease in modelling, $\frac{L_{clear}}{t_p}$ was taken as 1 when defining the model for all the gusset plates of Type CC, and in most of the cases the DCR was more than 1. The rotational spring was connected to the brace by a set of two parallel springs, one rigid and another one flexible. Once the amount of rotation in the gusset plate spring exceeds θ_f, the rigid spring (Fig. 2) was removed, causing all the axial resistance of the brace to be lost.

3.2 Model Validation

The numerical modelling approach was validated based on two experimental programs conducted at the University of Washington. Figure 3 shows the validation of the modelling approach for a ductile CBF (equivalent to Type MD CBF in this study) based on a frame tested by [15]. The gusset plate was modelled with the rotational spring suggested by [12]. No rotational limit was implemented as discussed in Sect. 3.1, assuming that the demand critical weld and adequate clearance for out-of-plane rotation is provided. The brace fracture was modelled by the MSR material proposed by [24]. In the case of Type CC, the overall approach was the same, except with the addition of gusset plate interface weld fracture. Figure 4 shows the validation of this model based on a frame tested by [4]. The sudden drop of strength is attributed to the gusset plate interface weld fracture, which was modelled as discussed in Sect. 3.1. Two other modes of damage, namely brace-to-gusset weld fracture and axial yielding of the gusset plate, were also considered during the validation against the test result from [4]. However, for the sake of simplicity, these two modes were omitted while modelling the prototype buildings for the current study because, during the validation, failure occurred due to the gusset plate interface weld and brace fracture at a much earlier stage than developing the capacity of the brace-to-gusset weld and axial yielding of the gusset plate, indicating that the two omitted damage modes were not as dominant compared to the modelled ones.

4 Ground Motion Selection and Scaling

A suite of 22 ground motions, each having two horizontal components, was selected and scaled according to FEMA P695 (2009). This ground motion record set was then collectively scaled at various increments, from one-third to two times the DGM (2%

Fig. 3 Validation of the numerical model for type MD (experimental results from [15])
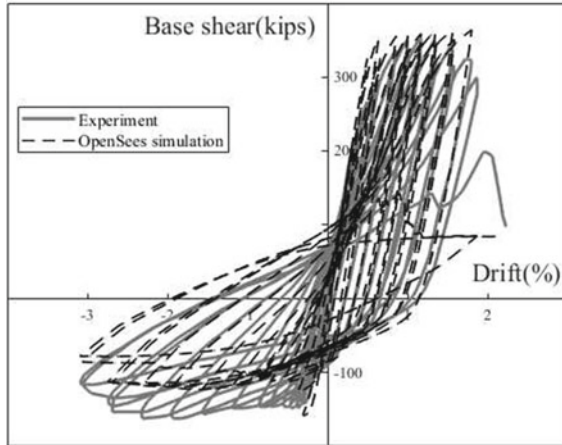
Fig. 4 Validation of the numerical model for type CC (experimental results from [4])
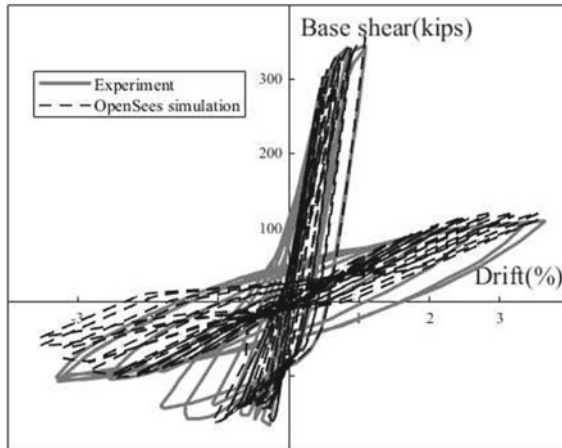
probability of being exceeded in 50 years, as per the [20]). The scaled spectra of all records, the corresponding median spectrum, and the target spectrum are shown in Fig. 5. Figure 5 also shows the spectrum for the Imperial Valley ground motion, which is used in Sect. 5.1. The median of the scaled spectra matches the target spectrum at the fundamental period of the structure but underestimates the target at longer periods.
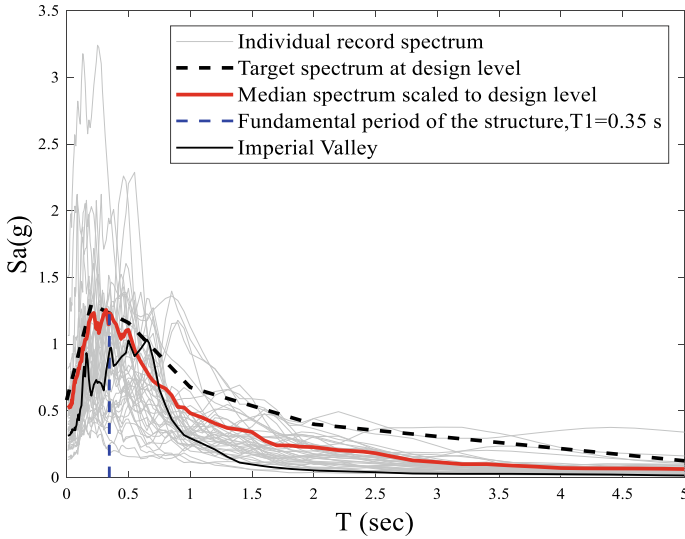
Fig. 5 Scaling according to FEMA P-695

5 Results and Discussion

5.1 Response to a Single Ground Motion

Figure 6 shows the inter-storey drift ratio (IDR) of the three floors of the Type MD CBF, subjected to the single record (Imperial Valley) at the DGM level. As discussed earlier, brace fracture was the only failure mode in the Type MD CBF. In both Types MD and CC, the onset of the brace fracture was captured by monitoring the stress–strain behaviour of the extreme fibre of the brace element, and hence, the "brace fracture" does not mean the complete fracture of the brace but rather the onset of fracture at the extreme fibre. Sequential occurrence of the different damage states for Type MD is shown Fig. 6. In the current study, several damage states were considered: (i) buckling or yielding of the braces (grouped as DS1), (ii) the onset of the brace fracture and gusset plate fracture (grouped as DS2); and (iii) probable collapse (DS3), where the maximum inter-storey drift exceeds 5% [11]. None of the six braces initiated fracture during the earthquake, and the storey drift was reasonably similar at all levels but slightly larger at the second storey, which is consistent with the average results discussed in Sect. 5.2.

Figure 7 shows the storey drift history for the Type CC CBF, subjected to the same ground motion with the same scaling. For this frame, the right brace buckled first, followed by the left brace. After a few seconds, the right brace fractured, causing an excessive rotational demand at the gusset plate that immediately led to fracture of the gusset plate interface weld, and thus the whole brace module lost its strength. A much higher value of IDR is observed in the top storey compared to the bottom
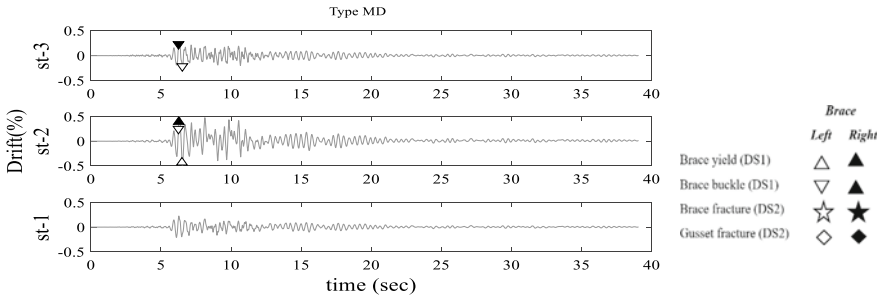
Fig. 6 Inter-storey drift ratio for three stories, showing the sequential damage states for type MD during Imperial Valley

storeys. Figure 8 demonstrates the force–deformation hysteresis of the right brace of the top storey. Any further brace fracture or gusset plate interface weld fracture was not observed in the left brace, while the middle of the third-floor beam deflected severely (more than 150 mm) both upward and downward. This severe deflection at the middle of the beam prevented the left brace from developing forces that would lead to any further damage mode. For comparison, in the case of the Type MD CBF, the deflection of the third-floor beam was limited to 2.5 mm and only in downward direction.
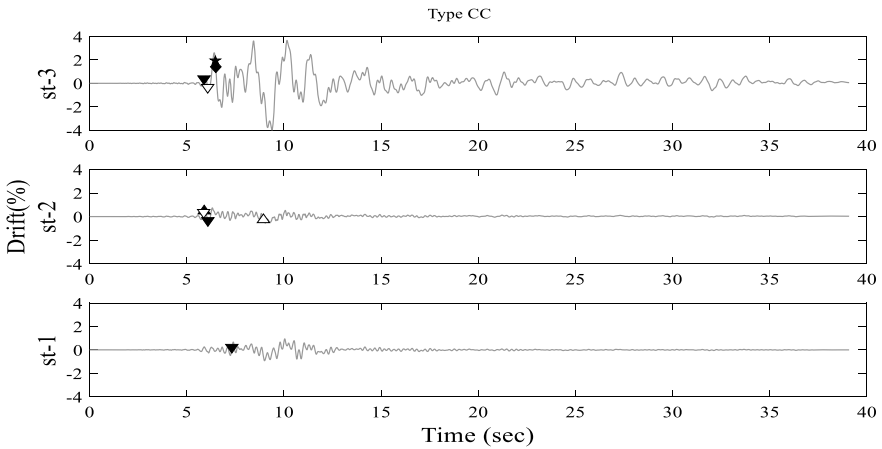
Fig. 7 Damage states shown on the inter-storey drift ratios for the type CC during the Imperial Valley ground motion

Fig. 8 Force deformation hysteretic behaviour of the third storey right brace
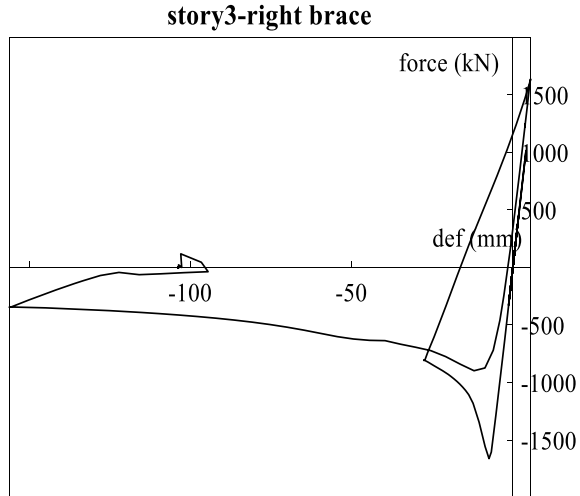
5.2 Response to the Suite of Ground Motions at DGM Level

Figure 9 shows the mean and mean + standard deviation of the IDR for both frame types at the DGM level earthquake. In case of the Type MD design, the mean IDR of each storey is within a similar range and much lower compared to that of the Type CC design. In the case of Type CC design, the IDR at the top storey level is generally much higher than at the bottom two storeys. Also, the top storey shows a much higher dispersion relative to the mean IDR. The Type CC CBF was designed for a much higher base shear than the Type MD CBF, with the braces intended to be nearly elastic. However, the beams in the Type CC CBF were not capacity protected for the unbalanced vertical force after brace buckling, and the top beam was most vulnerable in this regard, having no bracing above to mitigate the effect of the chevron bracing in the third storey. As was seen for one typical case in Sect. 5.1, after fracturing one of the braces in the third storey, the third-floor beam often yielded and deformed vertically, preventing the remaining brace from exhibiting its intended nonlinear response and resulting in a very high IDR at the top storey (Fig. 9).

In case of the Type CC CBF, DS2 comprises two different modes of failure: (i) when the brace started fracturing prior to the gusset plate and (ii) when gusset fracture happened first. There was no case where the brace started fracturing but did not eventually lead to a gusset plate interface weld fracture. Conversely, in some cases the gusset plate interface weld fractured first, which immediately detached the brace module from the frame and did not allow the brace fracture to take place. The distribution of these two modes of failure is described in Table 3. While the contribution of "gusset fractured first" is less compared to "brace fracture started first," it is not negligible.

Fig. 9 Average trend of the storey drift ratio in type MD and CC
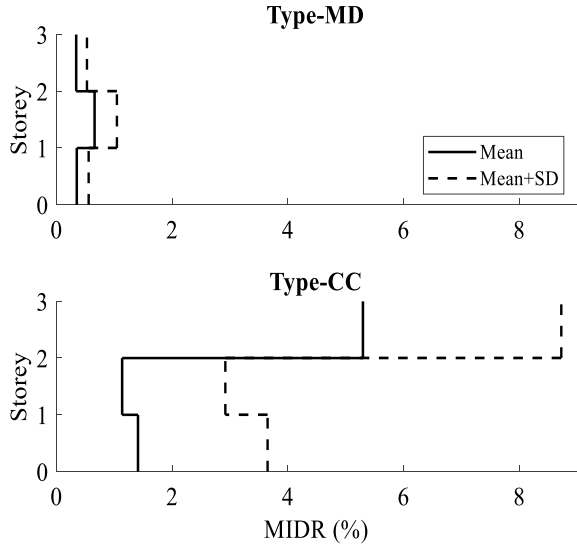
Table 3 Distribution of two types of fracture mechanics in DS2 of Type CC; all entries represent the number of occurrences out of 44 EQs

IM	Storey	Brace fracture started first	Gusset fractured first
0.33DGM	1	0	0
	2	0	0
	3	4	2
0.67DGM	1	0	1
	2	1	0
	3	24	8
DGM	1	2	8
	2	5	1
	3	28	8
1.5DGM	1	16	13
	2	20	1
	3	32	7
2.0DGM	1	34	8
	2	28	0
	3	34	9

5.3 Multiple Stripe Analysis

Multiple stripe analysis (MSA) was conducted, where dynamic analysis was performed with the suite of 44 ground motions at a variety of intensity measure
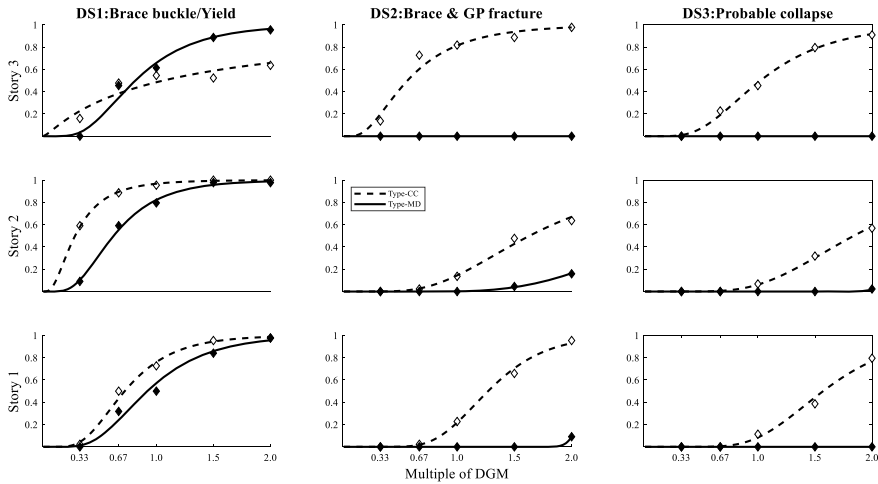
Fig. 10 Fragility curve drawn over the separate storey level, for three different damage states considered

(IM) levels and the number of occurrences or exceedances of any damage state was noted at each IM level. In the current study, five IM levels were considered: 0.33, 0.67, 1.0, 1.5, and 2.0 times the DGM. Considering the three damage states discussed earlier, the fragility curves were fitted using a lognormal distribution based on the maximum likelihood estimation method [3]. Figure 10 shows the fragility curves drawn over the three storey levels to understand the behaviour of the system, such as drift accumulation or the variation in the number of different fracture mechanisms over the storey levels.

Figure 10 demonstrates that the probability of reaching DS1 (brace buckles or yields) is similar for both designs at the first storey, whereas Type CC CBF shows higher probability of failure than the Type MD CBF at the second storey. A well-designed Type MD shows a similar fragility curve at all storeys, whereas the Type CC design shows a lower probability of reaching DS1 than the Type MD design at the top storey for intensities at and above the DGM, but higher probabilities of reaching DS1 at other storeys and intensities. In the case of the Type MD design, the probability of exceeding DS2 and DS3 is zero for almost all cases. Conversely, the probability of the Type CC CBF reaching or exceeding DS2 or DS3 in at least one level is 50% or higher for all intensities at or above the DGM. Overall, at DS1, the performance of the two design types is comparable, but a significant difference in failure probability is noticed at DS2 and DS3.

6 Conclusion

A pair of CBF systems was designed based on the provisions for Type MD and Type CC in CSA S16:19. The CBFs were modelled numerically in OpenSees to capture both brace fracture and gusset plate interface weld fracture, and the seismic performance was compared. First, the sequential occurrence of damage states observed during NLRHA of a typical record at the DGM level was discussed. The IDRs at different storey levels of the Type MD CBF were generally similar, whereas for the Type CC design, the IDR was much higher at the third storey because of the yielding and deflection of the top floor beam due to the unbalanced vertical force demand after brace buckling. Overall, the mean and dispersion of IDR were much higher for the Type CC design than for the Type MD design, especially at the top storey. Considering three levels of damage states, storeywise fragility curves were drawn. At DS1, the performance of the two types of design was comparable. However, the probability of exceeding DS2 and DS3 was much higher for the Type CC CBF than for the Type MD CBF. This suggests that, while both designs equally satisfied the building code requirements, the risk of both seismic loss and collapse with the Type CC design was significantly higher than for the Type MD design. Further study is needed to determine whether this result is true more generally for other buildings and types of connections, as well as how various design parameters affect the seismic fragility of the structure.

References

1. ANSI/AISC 341-16 (2016) Seismic provisions for structural steel buildings. American Institute of Steel Construction, Chicago, Illinois
2. ASCE/SEI 7-22 (2022) Minimum design loads and associated criteria for buildings and other structures. American Society of Civil Engineers
3. Baker JW (2015) Efficient analytical fragility function fitting using dynamic structural analysis. Earthq Spectra 31(1):579–599
4. Ballard R (2015) Impact of connection type on performance of non-seismic concentrically braced frames. Thesis submitted in partial fulfillment of the requirements of Master of Science, Dept. of Civil Engineering, University of Washington
5. Bradley CR, Fahnestock LA, Hines EM, Sizemore JG (2017) Full-scale cyclic testing of low-ductility concentrically braced frames. J Struct Eng 143(6):04017029
6. Castonguay PX (2009) Seismic performance of concentrically braced steel frame of the conventional construction catagory. Thesis submitted in partial fulfillment of the requirements of a Master's degree in applied sciences, Dept. of Civil Engineering, Ecole Polytechnique De Montreal
7. CSA S16:19 (2019) Design of steel structures. Canadian Standards Association, Toronto, Ont., Canada

8. Elkady A, Lignos DG (2015) Effect of gravity framing on the overstrength and collapse capacity of the steel frame building with perimeter special moment frames. Earthquake Eng Struct Dynam 44:1289–1307
9. FEMA P-695 (2009) Quantification of building seismic performance factors. Prepared by Applied Technology Council. Prepared for Federal Emergency Management Agency
10. Herman D (2007) Further improvements on and understanding of special concentrically braced frame systems. Thesis submitted in partial fulfillment of the requirements of Master of Science, Dept. of Civil Engineering, University of Washington
11. Hsiao PC, Lehman DE, Berman JW, Roeder CW, Powell J (2014) Seismic vulnerability of older braced frames. J Perform Constr Facil 28(1):108–120
12. Hsiao PC, Lehman DE, Roeder CW (2012) Improved analytical model for special concentrically braced frames. J Constr Steel Res 73:80–94
13. Hsiao PC, Lehman DE, Roeder CW (2013) A model to simulate special concentrically braced frames beyond brace fracture. Earthquake Eng Struct Dynam 42:1–6
14. Johnson MM (2014) Seismic evaluation of bolted connections in non-seismic concentrically braced frames. Thesis submitted in partial fulfillment of the requirements of Master of Science, Dept. of Civil Engineering, University of Washington
15. Johnson SM (2005) Improved seismic performance of special concentrically braced frames. Thesis submitted in partial fulfillment of the requirements of Master of Science, Dept. of Civil Engineering, University of Washington
16. Kotulka BA (2007) Analysis for a design guide on gusset plates used in special concentrically braced frames. Thesis submitted in partial fulfillment of the requirements of Master of Science, Dept. of Civil Engineering, University of Washington
17. Lehman DE, Roeder CW, Herman D, Johnson S, Kotulka B (2008) Improved seismic performance of gusset plate connections. J Struct Eng 134(6):890–901
18. Liu J, Astaneh-Asl A (2004) Moment-rotational parameters for composite shear tab connections. J Struct Eng 130(9):1371–1380
19. McKenna FT (1997) Object-oriented finite element programming framework for analysis, algorithm and parallel computing. Ph.D. thesis, Dept. of Civil Engineering, University of California, Berkeley
20. NBC (2015) National building code of Canada. National Research Council of Canada. Canadian Commision on Building and Fire Codes
21. Powell JA (2009) Evaluation of special concentrically braced frames for improved seismic performance and constructability. Thesis submitted in partial fulfillment of the requirements of Master of Science, Dept. of Civil Engineering, University of Washington
22. Roeder CW, Lumpkin EJ, Lehman DE (2011) A balanced design procedure for special concentrically braced frame connections. J Constr Steel Res 67(11):1760–1772
23. Rudman A, Tremblay R, Rogers CA (2021) Conventional I-shape brace member bolted connections under seismic loading: laboratory study. J Constr Steel Res 184
24. Sen AD, Roeder CW, Lehman DE, Berman JW (2019) Nonlinear modeling of concentrically braced frames. J Constr Steel Res 157:103–120
25. Sen AD, Sloat D, Ballard R, Johnson MM, Roeder CW, Lehman DE, Berman JW (2016) Experimental evaluation of the seismic vulnerability of braces and connections in older concentrically braced frames. J Struct Eng 142(9):04016052
26. Sizemore JG, Fahnestock LA, Hines EM, Bradley CR (2017) Parametric study of low-ductility concentrically braced frames under cyclic static loading. J Struct Eng 143(6):04017032
27. Sloat D (2014) Evaluation and retrofit of non-capacity designed braced frames. Thesis submitted in partial fulfillment of the requirements of Master of Science, Dept. of Civil Engineering, University of Washington
28. Swatosh MA (2016) Seismic evaluation and retrofit of concentrically btraced frames. Thesis submitted in partial fulfillment of the requirements of Master of Science, Dept. of Civil Engineering, University of Washington
29. Wang C, Tremblay R, Rogers CA (2021) Component-based model for bolted brace connections in conventional concentrically braced frames. Eng Struct 247

Timber Structures

Investigating the Influence of Openings on the Mechanical Performance of Cross-Laminated Timber Shearwalls

Mohammadreza Khajehpour, Daniele Casagrande, and Ghasan Doudak

Abstract The suitability of using cross-laminated timber (CLT) shearwalls to resist seismic loading has been extensively investigated in recent years, mainly due to their ability to dissipate energy through controlled yielding mechanisms in mechanical connections. A considerably different behaviour and failure mechanisms are expected when window and door openings are incorporated into the shearwall, resulting in significant deformation and possible premature brittle failure mode in the CLT panel. This is particularly critical in the case where the opening is directly cut out of the wooden panel, allowing for structural continuity between the wall segments and the lintel beam element or parapet. An alternative way to introduce openings in a CLT shearwall is by joining separate lintel and parapet elements to the wall segments using connections that usually do not allow for any moment continuity between those timber elements. Regardless of the construction techniques, designers usually assume the segmented method due to its simplicity. The effect of lintel beam height and parapet height on the failure mechanism and mechanical properties of single-storey CLT shearwall with multiple openings has been investigated in this paper by using a valid finite-element (FE) model. The influence of the construction techniques and the potential benefit that could be achieved in design by cutting the openings rather than assembling separated elements during the manufacturing process are investigated and discussed.

Keywords Influence of openings · Mechanical performance · Cross-laminated timber shearwalls

M. Khajehpour (✉) · G. Doudak
University of Ottawa, Ottawa, Canada
e-mail: mkhaj098@uottawa.ca

D. Casagrande
National Research Council of Italy, Trento, Italy

1 Introduction and Literature Review

The use of cross-laminated timber (CLT) shearwalls to resist lateral loads has increased significantly in recent years due to their high strength and in-plane stiffness and ability of the wall to dissipate energy through boundary connections between panels, as well as between panels and foundation [9, 17]. Several studies have been conducted on single-panel CLT shearwalls with different types of connections in order to establish their performance as a function of the wall-to-floor connection behaviour [2, 8, 9, 19, 20]. Studies on multipanel CLT shearwalls have demonstrated the ability of such systems to dissipate significant amount of energy by additionally engaging the vertical joints between the panels [7, 11, 16].

The fabrication process of CLT shearwalls with openings typically yields two construction methods, namely, segmented shearwalls (SSW) and monolithic shearwalls (MSW). In the SSW method, the wall consists of assembling different lintel beams, parapets (i.e. segments below windows) and wall panels together with connections, as shown in Fig. 1a. From a design perspective, it is generally assumed that the connections between the various wood segments do not allow for moment continuity and as such the wall is idealized as two cantilevers while ignoring the contribution of the segments above and below the openings. In the MSW method, the shearwall is assumed to consist of a single continuous CLT panel (Fig. 1b), where the potential effects of the openings are recognized to be significant while acknowledging the importance of the continuity of the CLT panels around the openings. Despite the common use of CLT panel with openings, the fact that such segments are disregarded in design standards (e.g. CSA O86), the potential benefit of incorporating them in the analysis of the building may be lost.

Research on CLT shearwalls with openings has been relatively scarce and limited to establishing the effect on in-plane stiffness and load-bearing capacity caused by the openings (e.g. [15]). Casagrande et al. [3] carried out full-scale experimental test on CLT shearwalls with single opening and reported brittle bending or net shear failure in the lintel beam. Mestar et al. [14] investigated the kinematic behaviour of CLT shearwall and reported that the kinematic behaviour is highly influenced by the lintel beam and parapet due to interaction between the shearwall elements. Dujic
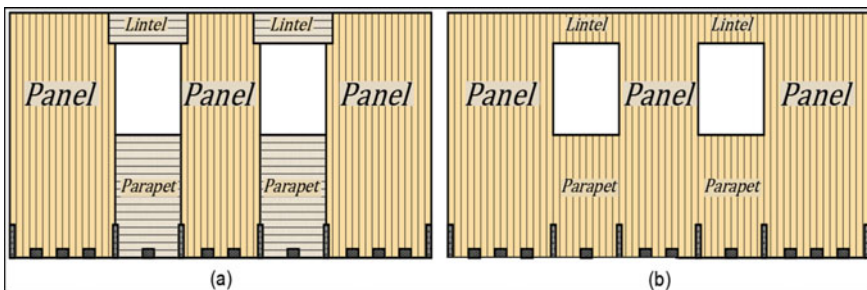
Fig. 1 CLT shearwall with assembling segments (**a**), with the opening cut out of the panel (**b**)

et al. [5] carried out numerical analysis on a single-storey shearwall with openings, incorporating the friction between the CLT panel and the base. Key findings from this study include the effect of the dimension and layout of the openings on the load-bearing capacity and stiffness of the shearwall. It was reported that opening areas up to 30% of the total wall area did not seem to produce significant effect on the peak load, while the effect on the stiffness was very significant. This could be attributed to failure occurring in the hold-down and angle bracket connections prior to development of any significant stresses in the CLT panel. Equivalent frame model was developed by Mestar et al. [13] to represent the elastic behaviour of CLT shearwall with opening. A finite-element model based on 2D elements was developed by Khajehpour et al. [10] to establish the behaviour of multi-storey MSW CLT shearwalls with single door or window openings. Variables investigated in the study included parapet height, lintel beam dimensions and gravity load.

A clear omission in the reviewed literature is notably research related to MSW with multiple openings. The current study addresses this gap in knowledge by numerically investigating single-storey CLT shearwalls with two openings and incorporates the effect of segments above and below the openings on the failure mechanism, stiffness and capacity of the CLT shearwall. The impact of including such continuity is also compared to design assumptions where SSW idealization is commonly made.

2 Numerical Analysis

Single-storey CLT shearwalls with two openings are analyzed using SAP2000 [4]. The focus of the current study is on establishing the effect of lintel beam and parapet heights by investigating different wall configurations and construction methods. The type of mechanical anchors and size of segments are chosen based on their common availability in construction. The values for shearwall height (H) and length (L), length of side wall segments (L_S), distance between the opening (O_D), lintel's length (L_L) and vertical load (q) are provided in Table 1.

The reference case in the comparisons consists of lintel beam height and parapet height of 0.4 m and 1.2 m, respectively. Other configurations with varying heights of lintel beam and parapet segment are presented in Figs. 2 and 3, respectively.

The panel segments are assumed to be attached to their base using AE116 angle brackets connected with eighteen 3½ inch (89 mm) spiral nails [ETA-06/0106. 2021] and WHT620 hold-downs with fifty-five 4.0 * 60 mm annular-ringed shank nails [ETA-11/086. 2015]. The distance between the mechanical anchors is assumed to be constant and equals to 400 mm. The nonlinear behaviour of the hold-downs and angle brackets used in the model is represented in Fig. 4 as tri-linear curves. These idealized curves were developed based on experimental tests conducted by [2, 20].

The thickness and layout of the CLT panel is assumed constant in all models and equals to 105 mm (i.e. 35 mm for each ply). The modulus of elasticity parallel to grain (E_0) and the in-plane shear modulus (G_0) of laminations are taken as 730 MPa and 11,700 MPa, respectively, in accordance with NS-GT6 (2020). The mean value

Table 1 Values of geometrical dimensions adopted in the analyses

Parameter	Symbol	Values
Height of CLT panel	H [m]	3.2
Total length of the CLT shearwall	L [m]	6.4
	L_S [m]	1.6
Length of side wall segments	O_D [m]	1.2
	H_L [m]	1.2; 0.8; 0.4*; 0.2; 0
Distance between openings	L_L [m]	1.0
	H_P [m]	1.6; 1.2*; 0.8; 0.4; 0.2; 0
Lintel's height	q (kN/m)	15.0
Lintel's length		
Parapet's height		
Vertical load		

* Reference value
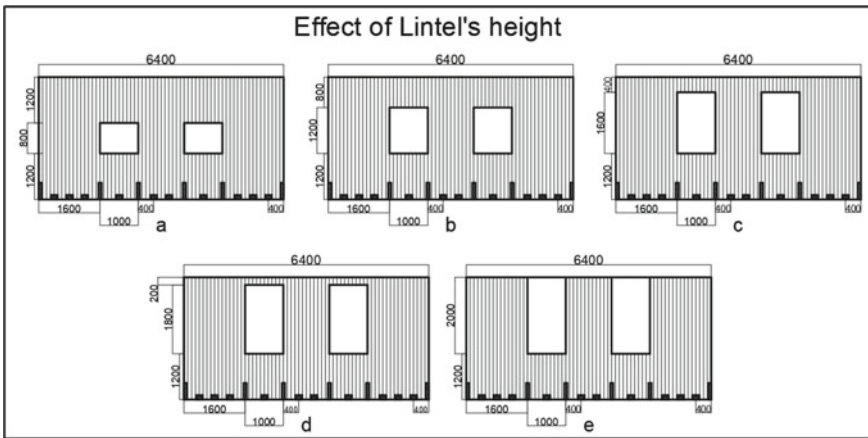
Fig. 2 Analyzed configurations with different lintel's height
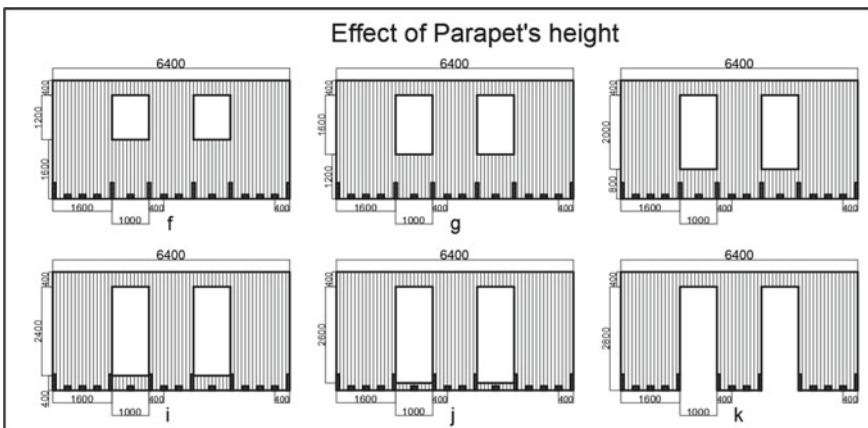
Fig. 3 Analyzed configurations with different parapet's height
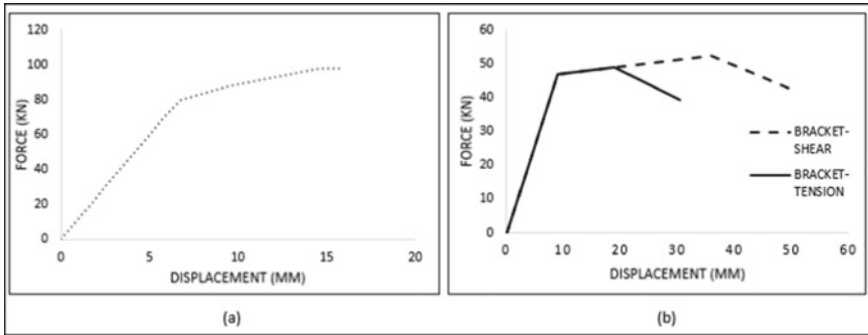
Fig. 4 Nonlinear behaviour of hold-down (**a**) and angle brackets (**b**)

of the tensile strength parallel to grain (f_t), compressive strength parallel to grain (f_c), in-plane net-shear strength $(f_{v,r})$ and torsional strength $(\tau_{T,r})$ are taken as 26.6 MPa, 33.2 MPa, 11.1 MPa and 3.5 MPa, respectively, as reported in [3].

2.1 Finite-Element Modelling

The CLT elements are modelled using four-node quadrilateral area elements. Such elements have been shown to represent a reasonable balance between the accuracy and modelling efficiency of CLT shearwalls. A meshing size equal to 50 mm in both directions was selected based on a mesh sensitivity. Angle brackets and hold-downs were modelled as nonlinear two-directional and one-directional springs, respectively. Gap elements were used to model the contact between the CLT panel and the base. When lintel beams are omitted in a wall mode, truss elements having zero and very high stiffness in vertical and horizontal directions, respectively, were used (Fig. 5).
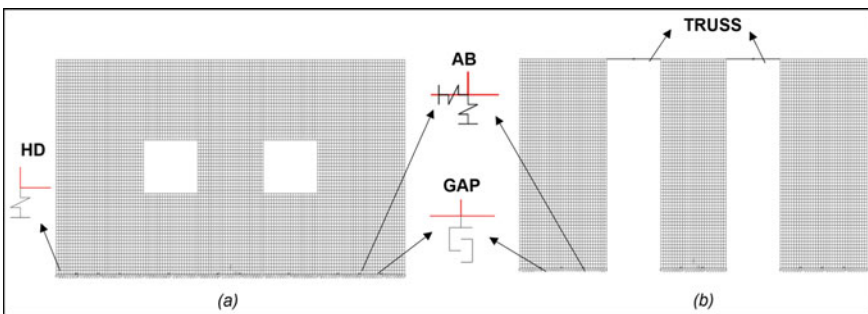
Fig. 5 Numerical model for a single-storey CLT shearwall with two-window openings for MSW (**a**) and SSW shearwall (**b**)

According to [1], the effective values of modulus of elasticity in the vertical ($E_{\text{eff},v}$) and horizontal ($E_{\text{eff},h}$) directions, as well as the in-plane shear modulus (G_{eff}), can be used to characterize the material properties of the CLT panel, as illustrated in Eqs. 1 and 2.

$$E_{\text{eff},v} = \frac{E_0 \cdot t_v + E_{90} \cdot t_h}{t_{\text{CLT}}}$$

$$E_{\text{eff},h} = \frac{E_0 \cdot t_h + E_{90} \cdot t_v}{t_{\text{CLT}}} \tag{1}$$

$$G_{\text{eff}} = \frac{G_0}{1 + 6 \cdot \alpha \cdot \left(\frac{t_{\text{mean}}}{w}\right)^2} \tag{2}$$

where t_{CLT} is the total thickness of the CLT panel, t_V and t_h are the total thickness of the vertical and horizontal layers, respectively, w is the width of the laminations, t_{mean} is the mean thickness of laminations and α is calculated as shown in Eq. 3 [1] for a 3-ply panel.

$$\alpha = 0.535 \cdot \left(\frac{t_{\text{mean}}}{w}\right)^{-0.795} \tag{3}$$

2.2 Failure Verification in the CLT Panel

In order to determine the failure conditions in the CLT panel, the axial (σ_h and σ_v) and shear (τ) stresses of all area elements need to be verified. Bogensperger et al. [1] presented the representative volume sub-element (RVSE) method to calculate the in-plane axial and shear strength in the panels. The method presents an equation to calculate the ideal nominal shear stress (τ_0), as shown in Eq. 4.

$$\tau_0 = \frac{v}{\sum_{i=1}^{n} t_{\text{RVSE},i}} \tag{4}$$

where v is the in-plane internal shear force per unit length, $t_{\text{RVSE},i}$ is the thickness of the ith RVSE (Table 2) and n is the number of the RVSE layers, which is equal to 2 for a 3-ply CLT panel.

Table 2 Ideal thickness of RVSEs for three-layer CLT panel

RVSE	Thickness
#1	$t_{\text{RVSE},1} = \text{Min}\,(2\,t_1, t_2)$
#2	$t_{\text{RVSE},2} = \text{Min}\,(2\,t_2, t_3)$

Verification in terms of effective shear stress τ_V and maximum torsional stresses τ_T in the glue interface was performed using Eq. 5 [1].

$$\begin{cases} \tau_V = 2 \cdot \tau_0 \le f_{v,r} \\ \tau_T = 3 \cdot \tau_0 \cdot \frac{\max(t_{\text{RVSE},i})}{w} \le \tau_{T,r} \end{cases} \tag{5}$$

where, $f_{v,r}$ and $\tau_{T,r}$ are the effective shear strength and torsional strength, respectively.

The verification in terms of horizontal σ_x and vertical σ_z axial stresses is performed according to Eq. 6.

$$\sigma_x = \frac{n_x}{t_x} \le \begin{array}{ll} f_t & \text{if} \quad \sigma_x \ge 0 \\ f_c & \text{if} \quad \sigma_x < 0 \end{array}$$

$$\sigma_z = \frac{n_z}{t_z} \le \begin{array}{ll} f_t & \text{if} \quad \sigma_z \ge 0 \\ f_c & \text{if} \quad \sigma_x < 0 \end{array} \tag{6}$$

where n_x and n_z are the in-plane axial internal force per unit length and t_x and t_z are the total thickness of laminations along with the horizontal and vertical directions, respectively. f_t and f_c are the tensile and compressive axial strength of the laminations, respectively.

3 Results

It should be noted that although not presented in this paper, the proposed numerical method presented has been validated against experimental test results reported by [8] for shearwalls with and without openings. The results are reported in the study by Khajehpour et al. [10], where it was concluded that the proposed methodology provided an acceptable representation of the failure mechanism, stiffness and peak load of the CLT shearwalls.

3.1 Effect of Lintel Height (H_L)

In order to establish the influence of the lintel height on the behaviour of the CLT shearwall, five different analysis cases (Fig. 2) were carried out with varying lintel heights while keeping the parapet height unchanged (i.e. equal to 1200 mm). Table 3 presents the failure mechanism and ratios of peak load and lateral stiffness. Figure 6 presents the ratio of the lateral stiffness (R_K) and peak load (R_F) of each model in comparison to those obtained from the reference case with 400 mm lintel height.

The results obtained from the analysis and presented in Fig. 6 show that for walls with lintel heights of 800 mm or higher, the dominant failure mode is a shear failure in the angle brackets, while for lintel heights less than 400 mm, the failure mode

Table 3 Effect of lintel height on failure mode

	Model	H_L (mm)	Failure mode	F_{max} (kN)	R_F	K (kN/mm)	R_K
a	DW1.4LH1.2P1.2	1200	ABS	576.1	1.39	28.12	1.63
b	DW1.4LH0.8P1.2	800	ABS	576.1	1.39	26.23	1.52
c	DW1.4LH0.4P1.2	400	AL	491.8	1.19	20.3	1.18
d	DW1.4LH0.2P1.2	200	NS	460.2	1.11	18.37	1.06
e	DW1.4LH0P1.2	0	NS	413.7	–	17.26	–

* *ABS* shear failure of the angle brackets; *AL* axial failure in the lintel beam; *NS* net shear failure
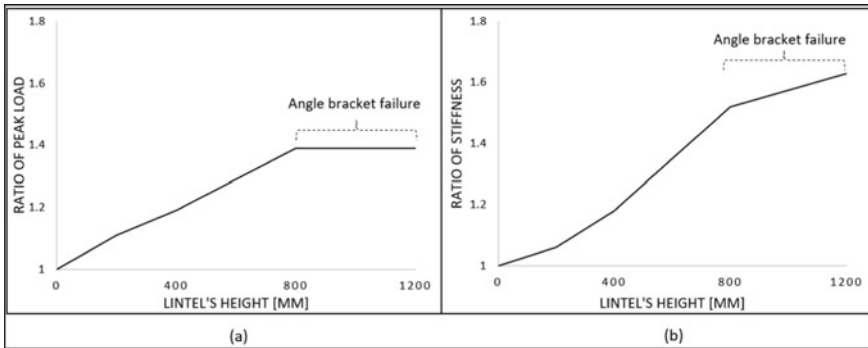
Fig. 6 Ratio of peak load (**a**) and lateral stiffness (**b**) for the models with different values of lintel's height

tends to be governed by bending and net shear failure. A significant increase in both peak load and lateral stiffness is observed with increasing the lintel height. Beyond the 800 mm height, the peak load appears to have a constant value and the stiffness increase is significantly reduced. This can be attributed to the shift in failure mode from that predominantly in the CLT panel to one that occurs in the angle brackets.

3.2 Effect of Parapet Height (H_P)

Six CLT shearwalls were modelled and analyzed in order to investigate the effect of the parapet height on the behaviour of the CLT shearwall, assuming same lintel height (equal to 400 mm). It can be noted from Fig. 3 that some of the studied configurations seem less likely to appear in construction (e.g. configuration J); however it is included in this analysis to obtain a complete picture of the behaviour. The results from the sensitivity analysis are reported in Table 4. As expected, having a very small parapet, as the case in configuration J, only adds slightly to the stiffness of the wall but it has no effect on the ultimate strength (i.e. does not alter the failure mechanism).

Table 4 Effect of parapet's height on failure mode

	Model	H_P (mm)	Failure mode	F_{max} (kN)	R_F	K (kN/mm)	R_K
f	DW1.4LH0.4P1.6	1600	ABS	576.1	2.27	24.67	2.17
g	DW1.4LH0.4P1.2	1200	AL	491.8	1.94	20.3	1.78
h	DW1.4LH0.4P0.8	800	AL	427.7	1.68	17.46	1.53
I	DW1.4LH0.4P0.4	400	AL	344.9	1.36	14.19	1.25
j	DW1.4LH0.4P0.2	200	AL	254.5	1.00	12.97	1.14
k	DD1.4LH0.4P0	0	AL	254	–	11.38	–

* *ABS* shear failure of the angle brackets; *AL* axial failure in the lintel beam; *NS* net shear failure
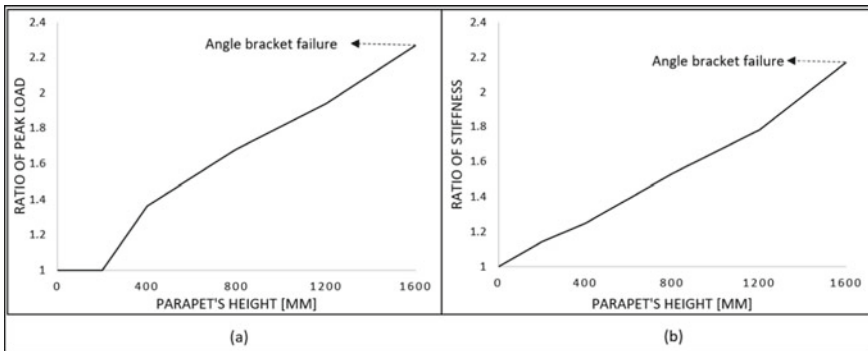
Fig. 7 Ratio of peak load (**a**) and lateral stiffness (**b**) for the models with different values of parapet height

It can be observed from Fig. 7 that the strength and stiffness of the wall is almost linearly related to the height of the parapet. This is likely due to the consistent failure mode in the CLT panel as noted in Table 4. The capacity and stiffness of the wall more than doubles from configurations K to F. Only at very large values of parapet heights does the failure mode shift to that and mechanical anchors (angle brackets). This observation further emphasizes the need for verification of panel failure in CLT shearwalls with openings.

3.3 Comparison Between MSW and SSW Behaviour

In this section, a comparison between the mechanical behaviour of CLT shearwalls assuming monolithic (MSW) and segmented (SSW) configuration is presented and discussed.

For all the configuration presented in Sect. 3.1, the ratio between the lateral stiffness (ρ_K) and peak load (ρ_F) obtained from MSW and that obtained from the SSW

models is calculated and presented in Table 5 for different values of lintel and parapet heights.

The results presented in Table 5 and Fig. 8 clearly highlight the importance of the assumption made during analysis and design of the CLT shearwall with regard to the connection between the wall segments and the lintel beam and parapet. The difference obtained when the openings are cut from the panel (i.e. MSW) and from joining the segments (SSW) is very significant, with ratios reaching values of 2.5 and 3.5 for peak loads and stiffness, respectively. This finding may encourage manufacturers to consider using the MSW method in their fabrication process, but more importantly, it should encourage designers to avoid using simplified analysis assumptions by considering an MSW wall as SSW only to facilitate the analysis process.

Table 5 Ratio of peak load and lateral stiffness of MSW models in comparison to SSW models

	Model	H_L (mm)	H_P (mm)	Failure mode	F_{max} (kN)	ρ_F	K (kN/mm)	ρ_K
a	DW1.4LH1.2P1.2	1200	1200	ABS	576.1	2.58	28.12	4.11
b	DW1.4LH0.8P1.2	800	1200	ABS	576.1	2.58	26.23	3.83
c	DW1.4LH0.4P1.2	400	1200	AL	491.8	2.20	20.3	2.96
d	DW1.4LH0.2P1.2	200	1200	NS	460.2	2.06	18.37	2.68
e	DW1.4LH0P1.2	0	1200	NS	413.7	1.85	17.26	2.52
f	DW1.4LH0.4P1.6	400	1600	ABS	576.1	2.58	24.67	3.60
g	DW1.4LH0.4P1.2	400	1200	AL	491.8	2.20	20.3	2.96
h	DW1.4LH0.4P0.8	400	800	AL	427.7	1.91	17.46	2.55
I	DW1.4LH0.4P0.4	400	400	AL	344.9	1.54	14.19	2.07
j	DW1.4LH0.4P0.2	400	200	AL	254.5	1.14	12.97	1.89
k	DD1.4LH0.4P0	400	0	AL	254	1.14	11.38	1.66
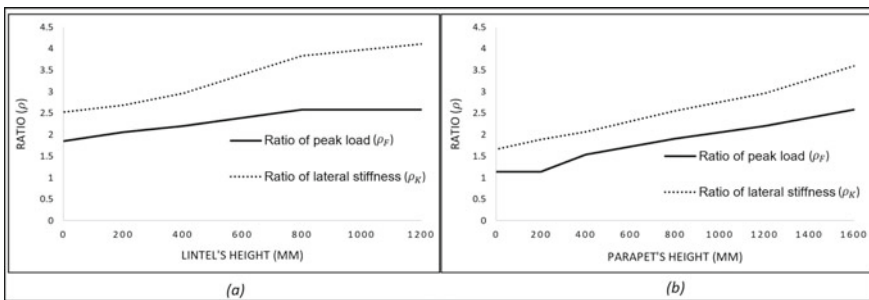
Fig. 8 Ratio of peak load ρ_F and lateral stiffness ρ_K as a function of lintel's height (**a**) and parapet's height (**b**)

4 Conclusions

Based on the analysis conducted in this study, it can be observed that CLT segments above and below the openings have significant effects on the failure mechanism, wall capacity and lateral stiffness. It was also found that even when the load-bearing capacity of the shearwall remained constant due to failure in boundary connections, the lateral stiffness of the wall was still affected by the change in wall geometry. A key finding that affects design assumption is that omitting the contribution of the CLT segments above and below the door and window openings in a monolithic shearwall configuration may result in significant impact on the analysis and design of the CLT wall, with ratios in the magnitude of 2.5 and 3.5, for peak loads and stiffness, respectively.

References

1. Bogensperger T, Moosbrugger T, Silly G (2010) Verification of CLT-Plates under loads in plane. In: World conference of timber engineering, WCTE
2. Casagrande D, Polastri A, Sartori T, Loss C, Chiodega M (2016) Experimental campaign for the mechanical characterization of connection systems in the seismic design of timber buildings. In: Word conference on timber engineering (WCTE 2016)
3. Casagrande D, Fanti R, Doudak G. Polastrci A (2021) Experimental and numerical study on the mechanical behaviour of CLT shearwalls with openings. Constr Build Mater 298(6):123858
4. CSI.SAP2000 (2017) Integrated software for structural analysis and design. Computers and Structures Inc., Berkeley, California
5. Dujic B, Klobcar S, Zarnic R (2007) Influence of openings on shear capacity of wooden walls. Presented at meeting Forty of the International council for research and innovation in building and construction. Working commission W18-Timber structures. Slovenia, Aug 2007
6. Gavric I, Ceccotti A, Fragiacomo M (2011) Experimental cyclic tests on cross-laminated timber panels and typical connections. In: Proceedings of 14th ANIDIS conference, Politecnico di Bari, Italy
7. Gavric I, Fragiacomo M, Ceccotti A (2013) Capacity seismic design of X-LAM wall systems based on connection mechanical properties. In: International council for research and innovation in building and construction, working commission W18-Timber structures. 46th conference, CIB-W18/46-15-2
8. Gavric I, Fragiacomo M, Ceccotti A (2015) Cyclic behaviour of typical metal connectors for cross-laminated (CLT) structures. Mater Struct March 48:1841–1857. https://doi.org/10.1617/s11527-014-0278-7
9. Izzi M, Polastri A, Fragiacomo M (2018) Investigating the hysteretic behavior of cross-laminated timber wall systems due to connections. J Struct Eng 144(5). https://doi.org/10.1061/(ASCE)ST.1943-541X.0002022
10. Khajehpour M, Casagrande D, Doudak D (2022) The role of lintels and parapets on the mechanical performance of multi-storey cross laminated timber shearwalls with openings. Eng Struct 255:113912
11. Li M, Lam F (2015) Lateral behaviour of cross-laminated timber shear walls under reversed cyclic loads. In: Tenth Pacific conference on earthquake engineering. Sydney, Australia
12. Liu J, Lam F (2018) Experimental test of coupling effect on CLT angle bracket connections. Eng Struct 178:P586–P602
13. Mestar M, Doudak G, Caola M. Casagrande D (2020) Equivalent-frame model for elastic behaviour of cross-laminated timber walls with opening. Constr Build Mater 298:123858

14. Mestar M, Doudak G, Polastri A, Casagrande D (2021) Investigate the kinematic modes of CLT shear-walls with openings. Eng Struct 228:111475
15. Moosbrugger T, Guggenberger W, Bogensperger T (2006) Cross-laminated timber wall segments under homogeneous shear—with and without openings. Paper presented at the WCTE 2006, 9th world conference on timber engineering, Portland, Oregon, United States
16. Nolet V, Casagrande D, Doudak G (2019) Multipanel CLT shearwalls: an analytical methodology to predict the elastic-plastic behaviour. Eng Struct 179:640–654. https://doi.org/10.1016/j.engstruct.2018.11.017
17. Pei S, van de Lindt J-WG, Popovski M, Berman JW, Dolan JD, Ricles J et al (2016) Cross laminated timber for seismic regions: progress and challenges for research and implementation. J Struct Eng 142(4). https://doi.org/10.1061/(ASCE)ST1943-541X.0001192
18. Shen YL, Schneider J, Tesfamariam S, Stiemer SF, Mu ZG (2013) Hysteresis behaviour of bracket connection in cross-laminated-timber shear walls. Constr Build Mater 48:980–991
19. Tomasi R, Sartori T (2013) Mechanical behaviour of connections between wood framed shear walls and foundations under monotonic and cyclic load. Constr Build Mater 44(2013):682–690
20. Yinlan S, Schneider J, Stiemer SF, Xueyong R (2019) Failure modes and mechanical properties of bracket anchor connections for cross-laminated-timber. In: MATEC web of conferences 275,01011, ACEM2018 and SBMSI

Wave Propagation Techniques for the Condition Assessment of Timber Structures: A Review

Sanaz Ajabshir, Rishi Gupta, Conroy Lum, and Mohammad-Sadegh Mazloomi

Abstract Several deteriorating mechanisms such as moisture, biological degradation, delamination, and photochemical degradation can significantly affect the design life of timber structures. Undetected damage sharply augments the associated maintenance costs and, in extreme cases, results in the complete failure of timber structures. With a focus on sustainability in the construction industry, the demand for timber as a construction material has grown exponentially in the last decade. Hence, it has become imperative to not only characterize the behavior of timber structures under different circumstances but also to timely detect any progressive damage within the structures. This paper is focused on evaluating the existing state of art on wave propagation-based acoustic emission and ultrasonic methods for damage evaluation of timber structures. This paper reviews the test results of small timber specimens monitored within the laboratory environment as well as large structures that underwent real-time monitoring. The paper entails the details of the existing gaps in the area of use of wave propagation techniques for monitoring timber structures and also proposes possible solutions to cover those gaps.

Keywords Wave propagation · Timber structures

1 Introduction

Timber is a prevalent construction material all over the world, and it is being used in more and more construction projects as a result of the considerable technological advancements and improvements that have enabled this success [50]. The fact that wood has been utilized as a construction material for thousands of years has resulted in a lot of expertise (mainly in-field). Nonetheless, the use of wood in the most

S. Ajabshir · R. Gupta (✉)
Department of Civil Engineering, University of Victoria, Victoria, BC, Canada
e-mail: guptar@uvic.ca

C. Lum · M.-S. Mazloomi
FPInnovations, Vancouver, Canada

recent architectural and engineering projects, as well as the development of current standardization criteria for wood construction (Eurocode 8, Design of structures for earthquake resistance), necessitates the development of a scientific background that goes beyond current knowledge.

A variety of deterioration factors, including moisture, biological degradation, delamination in layered timber members, photochemical degradation, chemical degradation, and thermal degradation, may cause damage to timber structures. Undetected and gradual deterioration to timber structures often results in a decrease in the life cycle of the structure and, as a result, increased maintenance costs, as well as the collapse of the structure in severe circumstances. For example, the total estimated average annual bridge failure rate in North America is between 87 and 222, with an expected value of 128, out of which 12% are timber bridges (Lee et al. 2003).

An optimum structural monitoring system would allow for early damage detection (in terms of degradation, overloads, spatial variability, cracks, etc.), the assurance of structural serviceability throughout its service life, and the development of reasoned and less expensive maintenance strategies during the life of the structure. This has prompted the development and investigation of new non-destructive methods (NDTs) for the structural health monitoring of timber structures, which serves as a first step toward the diagnosis of damage and the determination of structural safety for timber structures (Yeomans et al. 2014).

Several researchers have explored different NDTs including wave propagation techniques such as acoustic emission, ultrasonic methods, radiographic methods such as X-ray and gamma rays; fiber-optic methods such as the use of fiber Bragg grating; and vibration-based methods. Although some of these techniques are promising, more research is needed to be done in this area. This is predominantly because timber has: (1) a complex chemical structure with cellulose, lignin, and other extraneous compounds; (2) longitudinally aligned tubular fiber structure; (3) viscoelasticity; (4) hygroscopicity with an abundance of water-attracting hydroxyl groups; and (5) anisotropicity (Palma and Steiger 2020).

This is further complicated by the fact that diverse sources of wood need a specific NDT to be calibrated for every new configuration, in addition to the use of a single NDT for condition assessment (Desch and Dinwoodie 1996). This study provides an overview of wave propagation non-destructive testing NDT techniques including ultrasonic and acoustic emission.

2   Wave Propagation-Based Technique

Wave-based techniques are non-destructive methods for characterization and monitoring of wood that are based on analyzing the reaction of the material to wave fields of numerous variables [38]. Due to the sensitivity to the wood microstructure and its internal defects, wave-based approaches have been extensively used for structural evaluation and damage diagnosis of timber structures, where they effectively provide adequate quantitative and qualitative assessment [15].

The wave propagation method is more commonly referred to as an acoustic method, which is based on the propagation of stress waves (elastic or sonic stress waves) through structural elements and has been widely used in the characterization of timber and wood-based elements for many years [7, 23, 40], specifically for identifying the initiation of failure (e.g., by analyzing acoustic emissions), detecting discontinuities (e.g., fractures and delaminations in bonded timber elements using ultrasonic techniques), and estimating mechanical and physical properties based on empirical correlations between them and stress wave characteristics (e.g., calculation of static modulus of elasticity based on wave velocity) [23, 42].

There are two main acoustic methods: analysis of acoustic emissions and ultrasonic methods, both of which will be covered in-depth in this article.

2.1 Ultrasonic

Among the numerous non-destructive techniques NDTs for timber assessment (such as radioscopy, vibration methods, probing, and sounding) [44], sonic/ultrasonic wave propagation is regarded as the most common for evaluating and predicting the elastic properties (strength and stiffness) of wood and wood products (Sharma and Shukla 2012), having been used to wood since the 1950s [31]. The majority of ultrasonic inspection applications for wood members have been directed at evaluating product quality in a manufacturing environment, rather than assessing the in situ state of members in wood structures [13].

The ultrasonic technique is an active method [29], in which predefined stress waves are generated on the monitored element with the objective of finding defective timber materials. Additionally, it will offer information for periodic evaluation of wood structural components to identify the level of deterioration, allowing for the replacement or reinforcement of damaged elements to prevent structural collapse [22, 27, 29, 44]. This approach has received extensive popularity in the field of quality control and material inspection due to a number of benefits it offers over traditional testing procedures, including reduced time and cost, as well as accurate and consistent results ([2, 44]; Sharma and Shukla 2012). The ultrasonic technique of assessing timber structures is based on the physical principle that any wave causes the oscillation of the particles of the medium in which it propagates. This results in the particles oscillating about their equilibrium location with decreasing amplitude as wave energy is lost ([53]; Branco 2017).

Stress waves, in fact, travel faster through sound and high-quality wood than they do through degraded and low-quality wood, since voids, cracks, and decay attenuate and redirect stress waves, resulting in increased transmission times (Sharma and Shukla 2012) [14, 35, 45]. This concept is illustrated in Fig. 1.

The ideal frequency range for analyzing the mechanical properties of wood is between 20 and 500 kHz, due to the considerable attenuation at higher frequencies [53]. The factors that influence the propagation or transmission of ultrasonic waves in wood are the physical properties of the substrate, geometrical characteristics of the species (macro and microstructures), conditions of the medium (temperature,
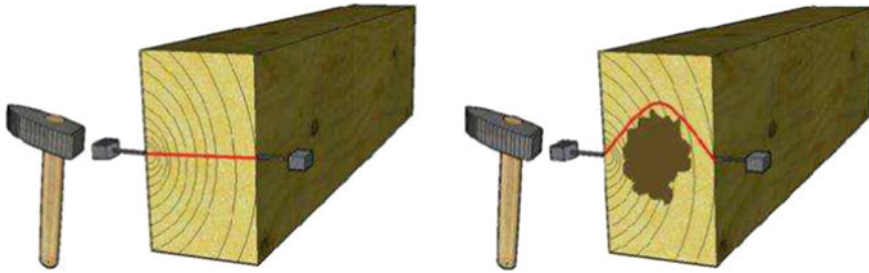
Fig. 1 Stress wave propagation in sound timber (left) and decayed timber (right) [10]

humidity), and the procedure utilized to take the measurements (frequency and sensitivity of the transducers, their size, and the position and dynamic characteristics of the equipment) [12, 39].

For research objectives, ultrasonic evaluation may be used in two fields: sound wood and decayed wood. Sound wood is a method for determining wood strength using longitudinal ultrasonic transmission speeds (Sandoz 1989) [1], and decayed wood is a method for quantifying the degradation status of wooden structures under restoration using ultrasonic transmission speeds perpendicular to the grain and wood density (kg/m^3) [41, 57].

While applying ultrasonic techniques for evaluation of timber structures is fast and simple to use, it does need more precision to attain the best results. For instance, it can only demonstrate significant flaws and cannot offer quantitative data. To provide a quantitative measure of the travel of sound in timber, different NDT testing methods have been developed that record and analyze the propagation of sound waves. Additionally, the stress wave transmission technique has limited sensitivity. A single-pass stress wave measurement can only detect internal degradation of more than 20% of the total cross-sectional area. To increase the reliability of the inspection and determine the degree and position of any internal decay, it would be prudent to take multiple measurements in various directions at the same cross section, particularly in suspicious areas. Identifying degradation with ultrasonic techniques can be accomplished via the use of two signal characteristics: ultrasonic pulse velocity and ultrasonic-guided wave [17, 26, 34, 49].

2.1.1 Ultrasonic Pulse Velocity

Ultrasonic pulse velocity is by far the most common way to measure timber sections. This is done by measuring the time of flight of the stress wave to figure out the wave transmission velocity [10, 36].

The ultrasonic pulse velocity technique is used to determine the velocity of an ultrasonic pulse passing through a solid material. The equipment consists of an emitter (generating transducer) from which ultrasonic pulses are transmitted, a receiver (or receiving transducer) from which the pulses are received, and a device for indicating the time of travel between the transmitter and the receiver (Fig. 2).

An ultrasonic pulse is generated by rapidly changing the voltage between a transmitter and a piezoelectric transformation element, causing them to vibrate at their fundamental frequency. The transducer is put in contact with the material so that the vibrations are transferred to the material. Vibrations propagate through the material and are detected by the receiver. The wave velocity is determined by the amount of time required for the pulse to transit the measured distance between the transmitter and receiver [6, 11, 12 , 26, 49, 57].

$$V1 = L * 10/t \tag{1}$$

where $V1$ = pulse velocity (km/s); L = path length (cm); t = transit time (ms); and 10 = constant to adjust the units.

Ultrasonic pulse velocity measurements can be conducted either parallel or perpendicular to the grain. The arrangement of the probe can be adjusted and measured in the following three ways, depending on accessibility and the desired path of stress wave travel the arrangement of the probe can be measured in the following 3 ways (Fig. 3): (a) direct: the receiver and the transmitter are opposite to each other on either side of the cube; (b) semi-direct: the transmitter and the receiver are on any two perpendicular faces of a cube; and (c) indirect (surface) transmission: the receiver and the transmitter are on the same face of a cube [15, 17].

Fig. 2 PUNDIT UPV testing instrument [33]. The pulse velocity can be determined from the following equation:
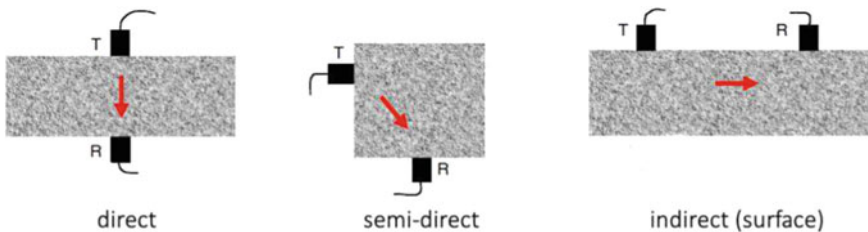
Fig. 3 The arrangement of probe of pulse velocity measurement: (a) direct, (b) semi-direct, (c) indirect (surface) transmission [55]

The most sensitive arrangement is direct transmission, whereas the least sensitive is indirect transmission. There is a way of measuring the path length for each of the available transducer arrangements. For direct transmission, the path length is defined as the distance between the transducers; for semi-direct transmission, the path length is commonly defined as the distance between the transducers' centers. Each arrangement is suitable for a variety of purposes. For instance, in situations where the surface quality of the material is critical in comparison to its overall quality, such as in the event of a destructive accident such as a fire, it has been proposed to arrange transducers in an indirect path [5, 9, 22], but generally speaking, by combining different wave paths in direct or indirect transmission, it is possible to observe the structure's interior damage pattern through tomography algorithms [8].

Specific gravity and compressive strength of wood parallel to the grain are proportional to pulse-velocity data. External stresses seem to have little influence on velocity, and internal voids, fractures, and discontinuities diminish the velocity.

The pulse velocity measured perpendicular to the grain along the span length of a flexural part may be utilized to identify degradation and estimate the reserved load-carrying capacity. The use of ultrasonic pulse velocity for assessing decay in timber structures has a broad variety of applications and benefits. Several studies, for example, have revealed a good relationship between ultrasonic velocity and specific gravity and the mechanical properties of wood (Sharma and Shukla 2012; [12]). The sensitivity of this technique to determining moisture content in the wood also makes it useful for assessing the lumber stiffness of standing trees [56]. In addition, ultrasonic wave timing inspection techniques are employed to evaluate internal defects caused by decay in standing trees [25]. However, the location of defects does not affect ultrasonic velocity [6, 40], which makes ultrasonic wave velocity testing appropriate for smaller timber structure sizes (Dackermann 2007), [25, 47].

2.1.2 Ultrasonic-Guided Wave (GW)

Ultrasonic-guided waves are regarded as one of the most effective and reliable techniques that provide adequate quantitative and qualitative evaluation (15; Ehrhart and Bockenheimer 2010). The guided wave propagation technique has been extensively utilized in several sectors for material characterization and damage detection, and it can also be used to predict the mechanical properties of wood materials. In general, GWs are composed of many forms of vibrations referred to as wave modes. Normally, they are dispersed in character. This implies that the signal's various frequency components travel at different speeds along the structure. As a result, the signal expands during propagation. Dispersion curves illustrate the relationship between the speed of wave modes and frequency. These may be shown as phase velocity, group velocity, or wavenumber plotted as a function of frequency [43].

Technically in timber-based structures, the reflection and transmission ratios for various quantities of internal damage are estimated using guided wave signals in forward and backward scattering directions [37]. A boundary must be defined in guided wave propagation. As a consequence of a boundary along with a thin plate or

interface, we may envisage a range of distinct waves reflecting and mode converting within a structure and superimposing with sections of constructive and destructive interference, which eventually results in well-guided wave packets that can travel through the structure (Rose 2002).

The GW technique can meet the requirements for timber damage detection in a multitude of sectors. The primary advantage of using guided ultrasonic waves is that their properties, such as wave velocity and amplitude, are proportional to the mechanical properties of the propagation medium [17, 32]. Additionally, the low attenuation of waves and their high frequency make it simple to evaluate massive timbers [10], and it is very sensitive to various forms of damage [58]. The guided wave method is able to identify changes in material properties caused by environmental variables such as moisture contents ([17]; Faithi 2021) and UV aging [32]. Recently, guided waves have been utilized to determine the moisture-dependent viscoelastic properties of timber, including shear storage, shear loss, and loss factor [17].

Nevertheless, guided wave propagation is not yet widely used in complicated structures, such as timber [51, 52]. The orthotropic nature of wood presents various evaluation issues. Apart from geometry, where the actual three-dimensional wave equation becomes difficult to solve, dispersion, attenuation, and distortion seem to provide significant difficulties when analyzing the findings [52].

Although the guided wave technique has the potential to provide a robust damage evaluation in timber, little attention has been devoted to its application for damage detection in timber attributed to the material anisotropy and inhomogeneity (Harb and Yuan 2016) [16], and detecting inconspicuous internal damages caused by internal decay or insect attack has remained crucial.

2.2 Acoustic Emission (AE)

Acoustic emission (AE) is a non-destructive technique pioneered by Kaiser over sixty years ago [3] that enables the evaluation and assessment of the structural health and the prediction of the progression of damage from its initiation in order to optimize timber structure maintenance operations. Furthermore, AE enables continuous monitoring of the structure response to mechanical or environmental constraints. Additionally, AE allows the early detection and localization of acoustic sources, as well as the characterization and identification of various damage mechanisms (6, 48). AE is the only non-destructive testing technique that can be used to monitor defects during manufacturing. Other conventional NDT techniques include interrupting the line to evaluate the materials. Despite ultrasonic or radiographic techniques, AE does not need external energy; the test object generates the acoustic emission [24].

AE testing is a real-time passive monitoring approach ([20]; McLaskey et al. 2009) that basically relies on two critical components: a material deformation that serves as the source and transducers that receive the stress waves generated from the source. This technique involves the attachment of piezoelectric transducers to a structure. These sensors convert mechanical energy, such as elastic waves, to an

electric impulse, which is transferred to the AET computer through wired or wireless connection (Fig. 4). The test does not discover preexisting flaws but rather monitors the emergence of flaws in a structure when it is subjected to increasing or continual stress. However, preferably, the test would identify defects while also describing their development rate when the stress level grows or the stress condition persists over time [48, 54] (Ono 2014). Rather than an external excitation source, the elastic wave is formed by a rapid redistribution of stress caused by localized damage. As a result, the location of sources of acoustic energy may be determined.

AE will identify pathological defects that might lead to the failure of part or all of the structure if the stress application replicates the circumstances that the test structure is expected to undergo in real operation (Beattie 2013).

Fundamentally, two kinds of AE monitoring systems are available: global and local. Global monitoring assists in determining the integrity of a complete structure, while local monitoring focuses on a single region of damage [21]. AE monitoring may also be classified into long-term and short-term monitoring, depending on the period of the needed monitoring. Long-term monitoring is often used in situations when the timber structures are new or need monitoring as a follow-up after a routine inspection. Short-term monitoring is more precise and is often the result of a brief investigation to determine the structure's integrity state (Nasir and Cai 2010).

The amount of emission detected and the location of emission sources will be determined by the structure design and the materials utilized to construct it (Hamstad 1986; Wadley et al. 2013). The detection range of the AE is less than 1 kHz and has been reported at frequencies up to 100 MHz. When rapid stress-releasing events occur, stress waves begin at 0 Hz and typically decay at a pace of a few MHz ([7, 24]; Drouillard 1990).

The characteristics of the acoustic emission signal are dependent on the form of the wave source (crack propagation, friction deformation, etc.) and the material properties. The most often utilized parameters for describing AE signals are as follows: (1) AE amplitude: the AE signal's maximum amplitude, (2) AE count: the number of times an AE signal exceeds a preset threshold level during the test, and (3) AE count rate: the number of counts within a given time interval [18, 19] (Diakhate et al. 2017).

There are different parameters that affect the detection of AE: (1) sensors, (2) piezoelectricity, (3) size effects, (4) couplants, (5) the influence of temperature, (6) sensor sensitivity—effects of cables, (7) sensor sensitivity—effect of preamplifier

Fig. 4 Acoustic emission testing [28]
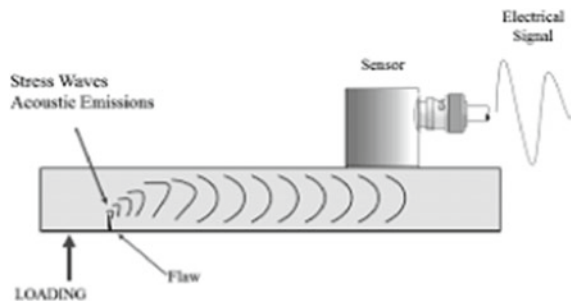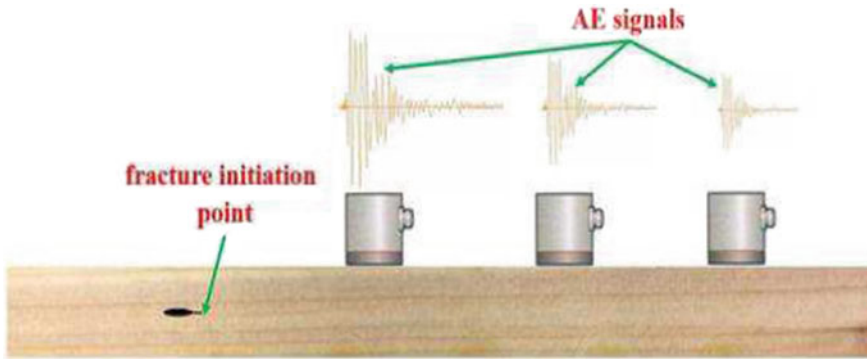
Fig. 5 Attenuation of acoustic emission signals during propagation (Zhao et al. 2020)

noise, and (8) sensor calibration [3, 54]. Acoustic emission monitoring has usually been employed to research the behavior of small- scale wood specimens but has more recently been used to structural-sized timber elements [24, 36]. The detection volume may encompass the whole specimen, depending on the number of sensors and their distance from the source of acoustic emissions, and can be used to locate the source by measuring the time it takes for the acoustic emissions to reach various sensors [59, 46]. It must be mentioned that since it is difficult to distinguish actual AE signals from background noise during measurement [20, 24], the level of acoustic activity in the item being tested, the background noise, and the signal attenuation must all be addressed when selecting a sensor [4].

However, a review of the literature on the AE approach indicates that several difficulties have been identified when utilizing this technique, necessitating more exact implementation. In general, the signal emanating from the source of the damage travels a considerable distance before being detected by the AE sensor. The AE sensor receives an attenuated signal that does not accurately represent the signal's intensity at the site of the damage (Fig. 5) (Zhao et al. 2020). Its high heterogeneity results in very high wave distortion. Multiple reflections and other wave propagation processes significantly modify the form of the wave, making subsequent analysis very complicated and unreliable. To resolve this issue, all AE data processing must be performed on a very small window of the signal, shortly after the threshold is crossed, and encompassing just one cycle of the waveform. This action mitigates the influence of reflections and other propagation phenomena to a great extent [30, 38].

3 Conclusion

This paper delved into the common NDT methods that are based on wave attenuation techniques to evaluate the condition of timber members. Various methods are explained, their pros and cons are explained, and comparisons were made between methods where applicable. Ultrasonic, ultrasonic pulse velocity, ultrasonic (GW), and AE are discussed in detail. Ultrasonic pulse velocity and ultrasonic (GW) are

used to assess the decay in timber since a single-pass stress wave measurement can only identify internal decay of more than 20% of the member's cross-sectional area. Finally, AE facilitates continuous monitoring of the timber member under mechanical or environmental constraints. It is the only NDT method that can be applied to detect flaws and imperfections in the course of timber manufacturing. The classification offered in this paper can help engineers and researchers select an appropriate NDT technique for evaluating timber structure conditions.

References

1. Arriaga F, Íñiguez G, Esteban M, Fernández-Golfín JI (2006) Structural Tali timber (*Erythrophleum ivorense* A. Chev., *Erythrophleum suaveolens* Brenan.): assessment of strength and stiffness properties using visual and ultrasonic methods. Holz Als Roh Werkst 64:357–362
2. Beall F C (2002) Overview of the use of ultrasonic technologies in research on wood properties. Wood Science and Technology, 36(3): 197–212. https://doi.org/10.1007/s00226-002-0138-4
3. Beattie A G (1983) Acoustic emission, principles and instrumentation (SAND-82-2825). Sandia National Labs, Albuquerque, NM (USA). https://www.osti.gov/biblio/6309755
4. Behnia A, Chai HK, Shiotani T (2014) Advanced structural health monitoring of concrete structures with the aid of acoustic emission. Constr Build Mater 65:282–302
5. Benedetti A (1998) On the ultrasonic pulse propagation into fire damaged concrete. Struct J 95B: 259–271
6. Brozovsky J, Zach J (2008) An Assessment of the Condition of Timber Structures
7. Bucur V (2006) Acoustics of Wood (2nd edition). Journal of The Acoustical Society of America, 119. https://doi.org/10.1121/1.2197787
8. Chai HK, Aggelis DG, Momoki S, Kobayashi Y, Shiotani T (2010) Single-side access tomography for evaluating interior defect of concrete. Constr Build Mater 24:2411–2418. https://doi.org/10.1016/j.conbuildmat.2010.03.003
9. Cioni P, Croce P, Salvatore W (2001) Assessing fire damage to R.C. elements. Fire Saf J 36:181–199. https://doi.org/10.1016/S0379-7112(00)00050-3
10. Dackermann U, Crews K, Kasal B, Li J, Riggio M, Rinn F, Tannert T (2014) In situ assessment of structural timber using stress-wave measurements. Materials and Structures, 47(5): 787–803. https://doi.org/10.1617/s11527-013-0095-4
11. Darmono Ma'arif F, Widodo S, Nugroho M S (2019) Determination of Modulus of Dynamic Elasticity of Wood Using Ultrasonic Pulse Velocity Testing. IOP Conference Series: Earth and Environmental Science, 366(1): 012015. https://doi.org/10.1088/1755-1315/366/1/012015
12. de Oliveira FGR, Candian M, Lucchette FF, Luis Salgon J, Sales A (2005) A technical note on the relationship between ultrasonic velocity and moisture content of Brazilian hardwood (*Goupia glabra*). Build Environ 40:297–300
13. Emerson P, Kainz F, McLean R (1998) Nondestructive Evaluation Techniques for Timber Bridges
14. Emerson P, McLean F, Pellerin R (2002) Ultrasonic inspection of large bridge timbers. 52:8
15. El Najjar J, Mustapha, S (2020) Understanding the guided waves propagation behavior in timber utility poles. Journal of Civil Structural Health Monitoring, 10(5): 793–813. https://doi.org/10.1007/s13349-020-00417-0
16. Fang Y, Lin L, Feng H, Lu Z, Emms GW (2017) Review of the use of air-coupled ultrasonic technologies for nondestructive testing of wood and wood products. Comput Electron Agric 137:79–87
17. Fathi H, Nasir V, Kazemirad S (2020) Prediction of the mechanical properties of wood using guided wave propagation and machine learning. Construction and Building Materials, 262: 120848. https://doi.org/10.1016/j.conbuildmat.2020.120848
18. Farhidzadeh A, Salamone S, Singla P (2013) A probabilistic approach for damage identification and crack mode classification in reinforced concrete structures. J Intell Mater Syst Struct

19. Ghaib M, Shateri M, Thomson D, Svecova D (2018) Study of FRP bars under tension using acoustic emission detection technique. J Civ Struct Health Monit 8
20. Grosse C U, Ohtsu M, Aggelis D G, Shiotani T (2021) Acoustic Emission Testing: Basics for Research–Applications in Engineering. Springer Nature. Google-Books-ID: EYk4EAAAQBAJ
21. Holford K M, Carter D C (1999) Acoustic Emission Source Location. Key Engineering Materials, 167–168:162–171. https://doi.org/10.4028/www.scientific.net/KEM.167-168.162
22. Karaiskos G, Deraemaeker A, Aggelis DG, Hemelrijck DV (2015) Monitoring of concrete structures using the ultrasonic pulse velocity method. Smart Mater Struct 24:113001
23. Kasal B, Lear G, Tannert T (2011) Stress waves. In: Kasal B, Tannert T (eds) Situ assessment structural timber state art report RILEM technical communication. 215-AST, Springer Netherlands, Dordrecht, pp 5–24
24. Kawamoto S, Williams R S (2002) Acoustic emission and acousto-ultrasonic techniques for wood and wood-based composites: A review. Gen. Tech. Rep. FPL-GTR-134. Madison, WI: U.S. Department of Agriculture, Forest Service, Forest Products Laboratory. 16:134. https://doi.org/10.2737/FPL-GTR-134
25. Kazemi-Najafi S, Shalbafan A, Ebrahimi G (2009) Internal decay assessment in standing beech trees using ultrasonic velocity measurement. Eur J For Res 128:345–350
26. Krause M, Dackermann U, Li J (2015) Elastic wave modes for the assessment of structural timber: ultrasonic echo for building elements and guided waves for pole and pile structures. J Civ Struct Health Monit 5:221–249
27. Kot P, Muradov M, Gkantou M, Kamaris GS, Hashim K, Yeboah D (2021) Recent advancements in non-destructive testing techniques for structural health monitoring. Appl Sci 11:2750
28. Lee A, Wang G, Ternowchek S, Botten S F (2014) Structural Health Monitoring on Ships Using Acoustic Emission Testing
29. Lynnworth L (1989) Ultrasonic measurements for process control. https://www.semanticscholar.org/paper/Ultrasonic-measurements-for-process-control-Lynnworth/0c11ff7d0475fdf986a7ed3ce12a6094f432da34
30. Martínez-Jequier J, Gallego A, Suárez E, Juanes FJ, Valea Á (2015) Real-time damage mechanisms assessment in CFRP samples via acoustic emission Lamb wave modal analysis. Compos Part B Eng 68:317–326
31. Morales Conde MJ, Rodríguez Liñán C, Rubio de Hita P (2014) Use of ultrasound as a nondestructive evaluation technique for sustainable interventions on wooden structures. Build Environ 82:247–257
32. Nasir V, Fathi H, Kazemirad S (2021) Combined machine learning–wave propagation approach for monitoring timber mechanical properties under UV aging. Struct Health Monit 20:2035–2053
33. Ndagi A, Umar A A, Hejazi F, Jaafar M S (2019) Non-destructive assessment of concrete deterioration by ultrasonic pulse velocity: A review. IOP Conference Series: Earth and Environmental Science, 357(1):012015. https://doi.org/10.1088/1755-1315/357/1/012015
34. Nobile L, Nobile S (2015) Some Recent Advances of Ultrasonic Diagnostic Methods Applied to Materials and Structures (Including Biological Ones). Physics Procedia, 70: 681–685. https://doi.org/10.1016/j.phpro.2015.08.080
35. Papandrea SF, Proto AR, Cataldo MF, Zimbalatti G (2020) Comparative evaluation of inspection techniques for decay detection in urban trees. Environ Sci Proc 3:14
36. Peterson M L (1998) Evaluation of Wood Products Based on Elastic Waves. In R. E. Green (Ed.), Nondestructive Characterization of Materials VIII (pp. 561–566). Springer US. https://doi.org/10.1007/978-1-4615-4847-8_88
37. Raghavan A (2007) Guided-wave structural health monitoring [Thesis]. http://deepblue.lib.umich.edu/handle/2027.42/77498 . Accepted: 2010-07-12T15:23:00Z
38. Rescalvo FJ, Valverde-Palacios I, Suarez E, Roldán A, Gallego A (2018) Monitoring of carbon fiber- reinforced old timber beams via strain and multiresonant acoustic emission sensors. Sensors 18:1224
39. Rivera-Gómez C, Galán-Marín C (2013) In situ assessment of structural timber elements of a historic building by Moisture content analyses and ultrasonic velocity tests. International Journal for Housing Science and Its Applications, 37: 33–42

40. Riggio M, Sandak A, Sandak J (2012) In-situ assessment of structural timber using selected wave-based NDT methods. J Herit Conserv
41. Rodríguez Liñán C, Morales Conde MJ, Rubio de Hita P, Pérez Gálvez F (2011) Inspección mediante técnicas no destructivas de un edificio histórico: oratorio San Felipe Neri (Cádiz). Inf Constr 63:13–22
42. Rose J L (2000) Guided wave nuances for ultrasonic nondestructive evaluation. IEEE Transactions on Ultrasonics, Ferroelectrics, and Frequency Control, 47(3): 575–583. https://ieeexplore.ieee.org/document/842044. Accepted: 2014-12-01T07:09:39Z
43. Rose J L (2004) Ultrasonic Guided Waves in Structural Health Monitoring. Key Engineering Materials, 270–273: 14–21. https://doi.org/10.4028/www.scientific.net/KEM.270-273.14
44. Ross R J, Pellerin R F (1994) Nondestructive evaluation of wood: Proceedings of the 3rd Materials Engineering Conference. Infrastructute, 1233–1241
45. Rudnicki M, Wang X, Ross RJ, Allison RB, Perzynski K (2017) Measuring wood quality in standing trees—a review, U.S. Department of Agriculture, Forest Service, Forest Products Laboratory, Madison, WI
46. Sachse W, Yamaguchi K, Roget J (1991) Acoustic emission: current practice and future directions. ASTM International
47. Santoni A, Schoenwald S, Van Damme B, Fausti P (2017) Determination of the elastic and stiffness characteristics of cross-laminated timber plates from flexural wave velocity measurements. J Sound Vib 400:387–401
48. Scruby C B (1987) An introduction to acoustic emission. Journal of Physics E: Scientific Instruments, 20(8): 946. https://doi.org/10.1088/0022-3735/20/8/001
49. Shaji T, Somayaji S, Mathews MS (2000) Ultrasonic pulse velocity technique for inspection and evaluation of timber. J Mater Civ Eng 12:180–185
50. Smith I, Frangi A (2008) Overview of Design Issues for Tall Timber Buildings. Structural Engineering International, 18(2): 141–147. https://doi.org/10.2749/101686608784218833
51. Subhani M, Li J, Samali B (2013) A comparative study of guided wave propagation in timber poles with isotropic and transversely isotropic material models. J Civ Struct Health Monit 3:65–79
52. Subhani M M (2014) A study on the behaviour of guided wave propagation in utility timber poles [Thesis]. https://opus.lib.uts.edu.au/handle/10453/30350
53. Tanasoiu V, Miclea C, Tanasoiu C (2002) Nondestructive testing techniques and piezoelectric ultrasonics transducers for wood and built in wooden structures. Journal of Optoelectronics and Advanced Materials, 4
54. Tonolini F, Sala A, Villa G (1987) General review of developments in acoustic emission methods. Int J Press Vessels Pip 28:179–201
55. Ultrasonic Testing of Concrete |FPrimeC. (2023, July 18). FPrimeC Solutions Inc. https://www.fprimec.com/ultrasonic-testing-of-concrete
56. Wessels C, Malan F, Rypstra T (2011) A review of measurement methods used on standing trees for the prediction of some mechanical properties of timber. Eur J For Res 130
57. Wilcox W (1988) Detection of early stages of wood decay with ultrasonic pulse velocity. Forest Products Journal. https://www.semanticscholar.org/paper/Detection-of-early-stages-of-wood-decay-with-pulse-Wilcox/00e63e1c9c7fd738c578db4efc899eb1a95dc1bd
58. Wu J, Ng CT, Fang H (2022) Internal damages detection for structural timber members using low- frequency anti-symmetric guided wave. Constr Build Mater 322:126355
59. Yapar O, Basu PK, Volgyesi P, Ledeczi A (2015) Structural health monitoring of bridges with piezoelectric AE sensors. Eng Fail Anal 56:150–169

Behaviour of Heavy Timber Members Subjected to Sequential Shocktube-Simulated Blast Loads

Damian Oliveira, Christian Viau, and Ghasan Doudak

Abstract This paper presents the results of an experimental programme investigating the effects of repeated dynamic blast loading on the behaviour of glued-laminated timber (glulam) beams and cross-laminated timber (CLT) panels. The specimens were subjected to a total of eight dynamic four-point bending tests using the University of Ottawa Shock Tube Test Facility. Control specimens were subjected to a single blast load causing failure, in order to document the load–displacement behaviour without the risk of inducing damage accumulation. Other specimens were then subjected to multiple blast loads, to investigate the effect of repetitive loading on the bending stiffness and capacity, as well as damage accumulation. Post-peak behaviour was found to vary significantly between glulam and CLT specimens, which greatly affected how the specimens performed when subjected to multiple blast loads. The outcome of this study is expected to contribute to knowledge base for heavy timber members subjected to blast loads in situations where exposure to multiple shock waves is probable, such as shock wave reflection emanating from nearby buildings, or during research testing where the timber element is considered for multiple tests.

Keywords Heavy timber members · Sequential shocktube-simulated · Blast loads

D. Oliveira
Canadian Wood Council, Ottawa, Canada

C. Viau (✉)
Carleton University, Ottawa, Canada
e-mail: christian.viau@carleton.ca

G. Doudak
University of Ottawa, Ottawa, Canada

1 Introduction and Literature Review

Recent interest in sustainable design has resulted in timber products being increasingly considered for a variety of construction projects. This has especially been the case for engineered wood products, such as glued-laminated timber (glulam) and cross-laminated timber (CLT), due to their enhanced structural properties, rapid onsite assembly, and aesthetically pleasing characteristics [4]. Recent research effort on the dynamic response of timber structures have been undertaken with emphasis on extending their application to that of tall structures. This is in direct response to the adoption of building code regulations, (e.g. Ontario Building Code) allowing for mid- and high-rise structures made completely or partially out of timber. This trend is expected to increase the risk of potential damage and failure associated with extreme events on these types of structures, particularly those constructed using engineered wood products such as CLT and glulam, as they are the principal building materials for such structures, due to their increasing prevalence in construction projects.

High strain rate effects occurring in structural members subjected to blast loads have been studied using simulated blast loading. Recent work focussing on the characterization of these effects has been conducted using idealized simply-supported boundary conditions, in order to isolate the material behaviour. Through comparisons between static and dynamic test results of visually-graded studs [3] and light-frame stud walls [5, 6, 11, 12, 16], it was determined that the modulus of rupture was significantly affected by high strain rates, with an average increase in the order of 40%. Similarly, experimental testing on full-scale glulam members was carried out by Lacroix and Doudak [7] to investigate suitable dynamic increase factors (DIF) for glulam members. The study found that specimens which featured continuous or aligned finger joints across the member width did not experience an increase in flexural strength, while specimens without continuous joints demonstrated a dynamic increase of 14%. No notable increases in stiffness were found and the response of all tests was reported to be linear elastic until failure, with no significant post-peak resistance. Poulin et al. [10] conducted an experimental investigation of the static and dynamic out-of-plane behaviour of CLT panels, and proposed an average DIF of 1.28 on the flexural strength with no observable strain rate effect for panel stiffness.

The effects of typical and retrofitted connections on the performance of glulam and CLT assemblies were also investigated, including bolted connections [8, 14], self-tapping screws [1], bearing angles [13], and innovative energy-absorbing connections designed to optimize the energy absorbed during a blast or impact event [15]. In the majority of these studies, specimens were subjected to multiple blast loads prior to the final test, where the specimen was loaded to failure. These typically entailed loading the specimens or assemblies to a certain percentage of their known capacity, to obtain elastic test data. For example, a glulam specimen tested by Viau and Doudak [15] was subjected to a total of seven blast loads, six of which were assumed to have had elastic response, however this assumption could not be verified.

Testing protocols involving repeated loading in experimental testing are typically utilized for reasons of cost or consistency within a certain experimental test matrix.

For example, a connection test, where different types of connections are investigated but the same load-bearing timber specimen is used in order to eliminate variability of the wood component in the assembly. The assumption that repeated loading does not have an influence on the behaviour of wood and does not cause any form of damage accumulation is an important research topic that has yet to be investigated thoroughly in the literature. An alternative to avoid this issue altogether is to only implement ultimate shots as to avoid errors associated with repeated loading, however, this may lead to increase in cost and complexity in the analysis and may require a significant increase in the number of tests to be conducted. The current study aims to fill this research gap by investigating the progression of damage and resulting effect on the dynamic resistance prevalent in mass timber elements when subjected to repeated simulated blast loading.

2 Experimental Programme and Test Setup

A total of eight dynamic tests were conducted on two CLT panels and two glulam beams for the purpose of evaluating the effect to sequential loading on the load–displacement behaviour of the specimens. The five-ply CLT panels were fabricated with spruce-pine-fir (SPF) lumber and had a total thickness of 175 mm. The panel lay-up consisted of laminates in alternating orthogonal directions, with the outer and centre laminates having the wood grain aligned in the longitudinal direction. The panels were of E1 grade [2], and measured 445 mm in width and 2500 mm in length, respectively. The glulam specimens consisted of 86 mm by 178 mm 24F-ES grade and measured 2500 mm in length. At the time of testing, the average moisture contents of the CLT and glulam specimens were determined to be 15% and 14%, respectively. A summary of the experimental programme and specimens is given in Table 1. The glulam and CLT tests conducted in this study were identified with the prefix "LAM" and "CLT", respectively, followed by a subscript and superscript. The subscript identifies whether the specimen was subjected to only one failure shot (F) or repeated loading (R), and the superscript provides information on the sequential identifier of the reported shot for specimens subjected to multiple shots. For example, CLT_R^3 refers to the third blast test of the CLT specimen subjected to repeated tests.

Specimens CLT_F and LAM_F were each subjected to a single blast load causing complete failure, in order to establish a baseline for dynamic material strength and behaviour, as well as compare them with existing analytical methods and published test results. The remaining specimens (CLT_R and LAM_R) were loaded within their respective elastic range and subsequently exposed to increasing blast loads until complete failure occurred. The intent of this methodology was to investigate possible damage accumulation and generate multiple data points to be used in the documentation of the effects of repeated loading, as well as to validate analytical methods that include damage accumulations [9].

Table 1 Experimental test matrix

Specimen type	Test ID	Testing protocol
CLT	$CLT_F{}^1$	Baseline failure shot
	$CLT_R{}^1$	Elastic, 95% of peak
	$CLT_R{}^2$	Failure of middle longitudinal laminate
	$CLT_R{}^3$	Progression of crack propagation
Glulam	$LAM_F{}^1$	Baseline failure shot
	$LAM_R{}^1$	Elastic, 40% of peak
	$LAM_R{}^2$	Elastic, 90% of peak
	$LAM_R{}^3$	Failure shot

The experimental testing was conducted at the University of Ottawa Shock Tube Test Facility, a state-of-the-art test facility capable of simulating the dynamic pressure effects of far-field blast explosions on structural and non-structural components. The shock tube consists of an end-frame, expansion section, diaphragm, and driver. The maximum reflected pressure that the shock tube is capable of generating is 100 kPa, and the generated blast wave can have a positive phase up to 70 ms. Depending on the combination of pressure and impulse to be applied to the test specimen, the thickness and quantity of aluminium foils, separating the diaphragm section from the driver and expansion sections, can be modified as required. Once the desired driver pressure is reached, the section between the foils is promptly drained, resulting in the rupture of both foil sets, and thus a release of compressed air as a shockwave. As shown in Fig. 1, a load transfer device (LTD) was used in order to convert the uniform pressure wave from the shock tube to two concentrated loads applied to the test specimens. The two load-transfer beams consisted of steel I-beams rigidly bolted to the LTD. A clear span of 2235 mm (88 in.) was consistently utilized throughout testing, based on the geometrical dimensions of the shock tube. Idealized simply-supported boundary conditions were provided by using sets of notched plates and pins that would transfer the load to the reaction load cells. Linear-variable differential transducers (LVDTs), strain gauges, and piezoelectric pressure sensors were used to measure the displacement-, strain-, and pressure-time histories, respectively. All test instrumentation was connected to a high-speed data acquisition system, with a sampling rate of up to 100,000 samples per second. High-speed video cameras recording at 2000 frames per second were also utilized to better document the dynamic behaviour of the specimens.
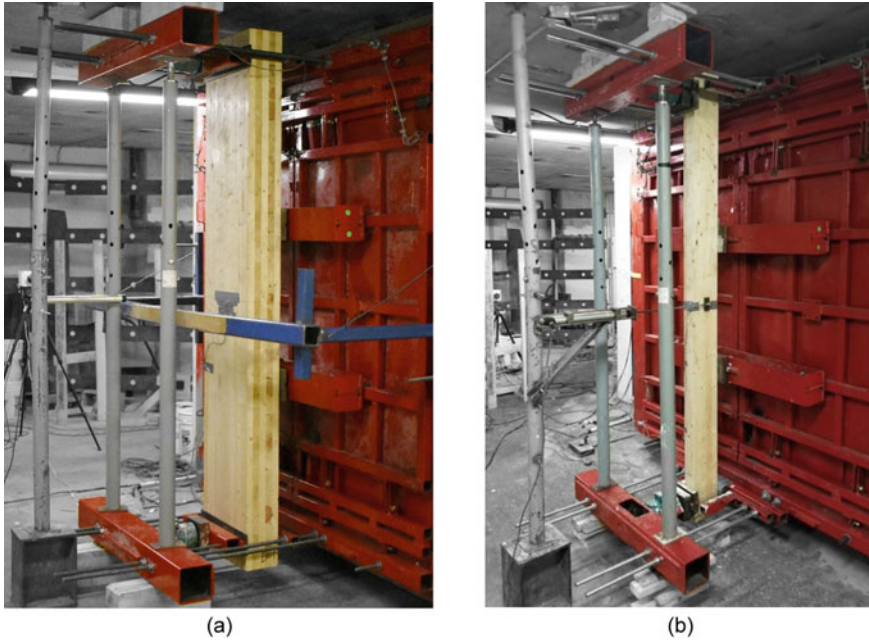
Fig. 1 Experimental test setups for: **a** CLT; **b** Glulam

3 Experimental Results and Discussion

3.1 Dynamic Behaviour of CLT Specimens

Specimen CLT_F was observed to fail in flexure, with splintering failures in the wood fibres initiating in the outermost tension ply and limited wood crushing in the outermost compression ply. Rolling shear cracks were observed to occur in the transverse layers simultaneously with or shortly after flexural failure occurred. A representative example of the progression of this failure is shown in Fig. 2.

Specimen CLT_R was subjected to a total of three shots. The first shot ($CLT_R{}^1$) caused minor flexural failures in the outermost tension laminates, as well as rolling shear damage in the panel's transverse plies, as shown in Fig. 3a, b, respectively. The second test conducted on the specimen ($CLT_R{}^2$) caused significant propagation of the rolling shear cracks initiated in the previous shot to be extended, as illustrated in Fig. 3b, c.

Finally, the specimen was subjected to a third and final shot ($CLT_R{}^3$), causing the rolling shear cracks previously developed during shots $CLT_R{}^1$ and $CLT_R{}^2$ to propagate further, as well as flexural failure of the innermost tension laminate. Significant rolling shear deformations occurred before the start of the flexural fracture. Compared with the previous two tests, the panel had noticeably more permanent deformations.

Fig. 2 Progression of failure
in CLT: **a** Failure initiation;
b Transverse crack
development

(a)   (b)

(a)   (b)   (c)
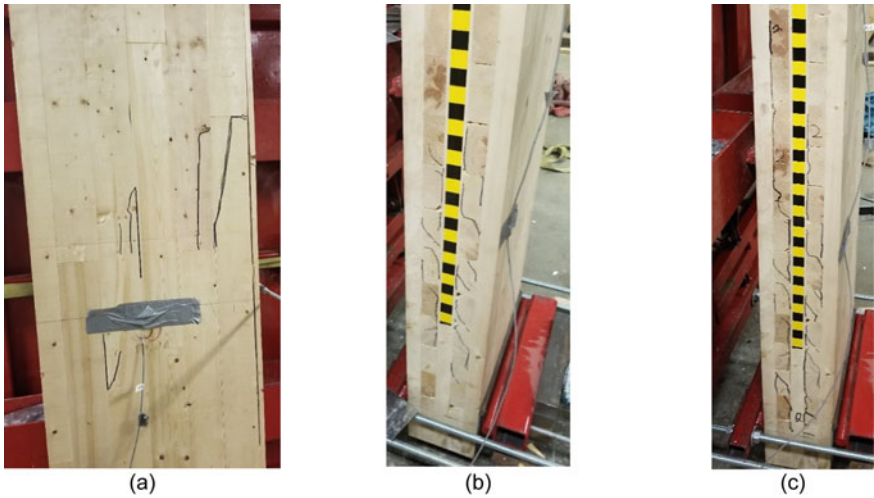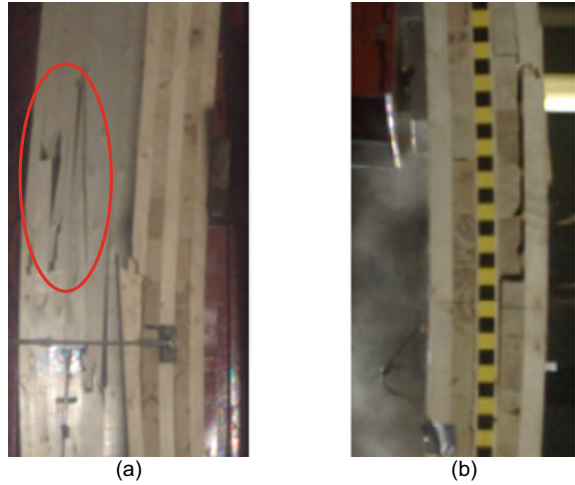
Fig. 3 **a** Minor damage following $CLT_R{}^1$; **b** Rolling shear damage following $CLT_R{}^1$; **c** Further propagation of cracks following $CLT_R{}^2$

The development of failure during $CLT_R{}^3$ is depicted in Fig. 4. Although this failure mechanism has been observed in previous studies [10, 13], the investigations have been limited to panels subjected to a single shot causing failure.

Fig. 4 Failure development during CLT$_R$[3]: **a** Flexural response and expansion of cracks; **b** Failure of inner laminate

(a)　　　　(b)

3.2 Dynamic Behaviour of Glulam Specimens

As expected, the general behaviour of the glulam specimens differed significantly from that observed in the CLT members, primarily due to the absence of the cross-laminations. Linear-elastic behaviour was observed in the glulam specimens, with no significant post-peak resistance. The failure of each specimen was initiated in the region between the load application points at a knot or other natural defect on the tension side. Specimen LAM$_F$, which was subjected to a single failure shot, experienced flexural failure characterized by tension-side cracking, as shown in Fig. 5a. In the case of such crack development, degradation in both stiffness and strength was expected after the shot, apparent when consulting the experimental test data for the specimen (Fig. 5b), where the point of flexural failure characterized by the sudden drop in tension-side strain can be observed. However, sufficient wood material remained in the cross section for the specimen to rebound back to its initial position, as observed in the specimen's displacement–time history (Fig. 5b).

While no damage could be observed following LAM$_R$[1], it was observed that limited superficial cracks developed following LAM$_R$[2], as shown in Fig. 6. However, these cracks were found to have insignificant effect on the response of the specimen in the subsequent shot (LAM$_R$[3]) and were likely caused by natural defects already present within the specimen, and only became apparent following the elastic shots. In the final shot, LAM$_R$[3], whereby the specimen was loaded to failure, it was observed
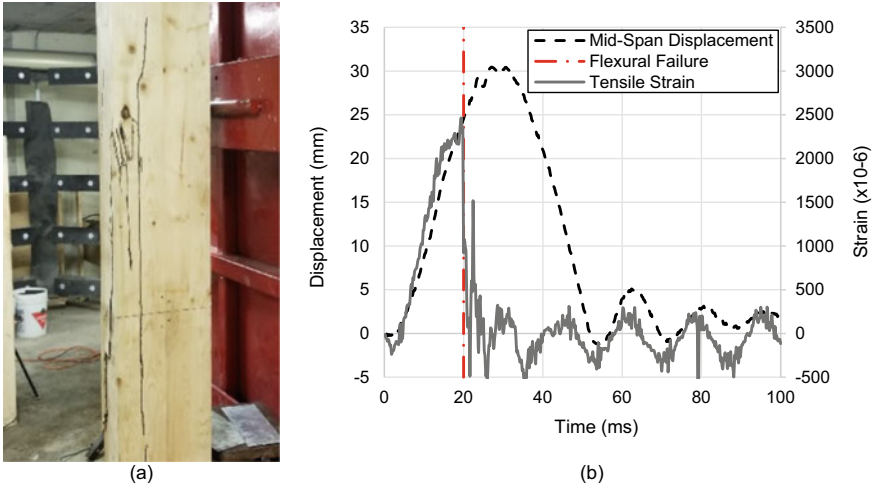
Fig. 5   Results of LAM$_F$[1]: **a** Flexural failure; **b** Displacement–time history

(via video-review) that failure initiation occurred at the superficial cracks that formed in the previous elastic shots.
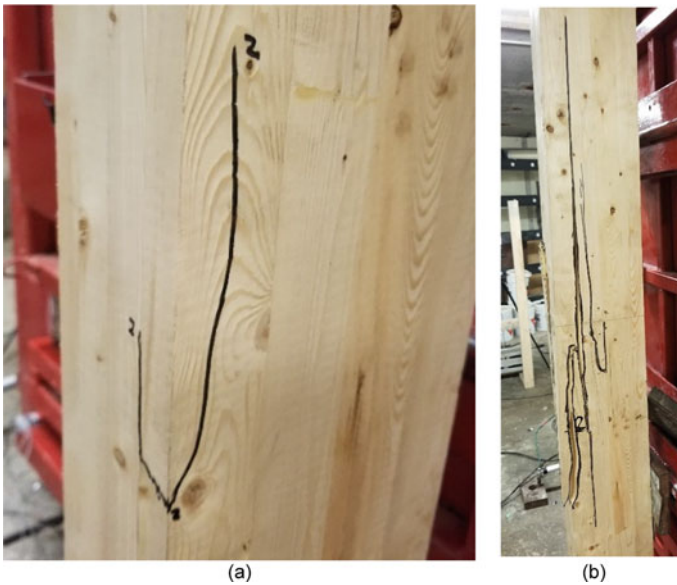
Fig. 6   Results of glulam testing: **a** Superficial cracking (LAM$_R$[2]); **b** Flexural failure (LAM$_R$[3])

3.3 Effect of Sequential Loading on the Resistance Curves

The results obtained from specimen CLT_R present a unique opportunity to investigate whether the model generally adopted for CLT could be used when the member is exposed to multiple shots. As shown in Fig. 7a, the typical "staircase" shaped resistance curve was observed among both CLT specimens, consistent with observations made in previous studies on blast-loaded CLT panels [10]. The results demonstrate that the backbone envelop curve is primarily driven by the longitudinal plies. When overlaying the measured resistance curves of CLT specimens subjected to repeated loading (Fig. 7a), it can be observed that the behaviour tends to follow the backbone envelope curve. This is an important finding, as it suggests that the response of a structural member subjected to multiple blast loads can be described by considering the theoretical resistance curve already established for elements subjected to a single failure shot. This finding would allow designers to "trace" the level of damage and estimate the reserved capacity in a given structural member. This emphasizes that the response to subsequent loading can be modelled by developing a methodology whereby the extent of prior damage is tracked. In situations where the panel is unloaded, and then reloaded in a subsequent shot, the rebound stiffness may be approximately the same as the degraded stiffness measured in the next test.

The observations for the glulam specimens tended to be more predictable and simpler to evaluate. No stiffness degradation was observed during the specimen
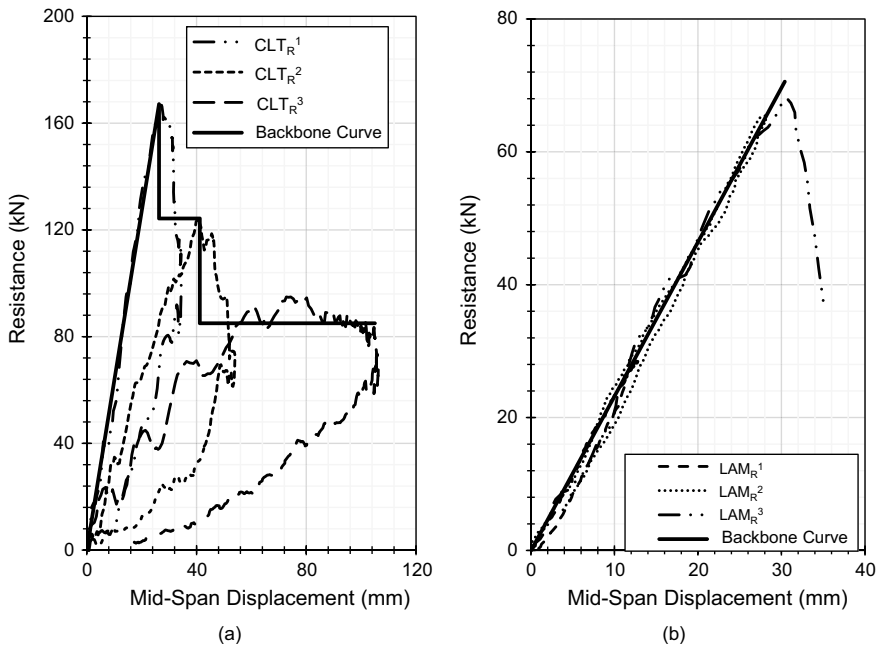
Fig. 7 Resistance curves: **a** CLT specimens; **b** Glulam specimens

rebounds, as well as during any sequential reloading from a second or third shot, for specimens that responded elastically to the applied blast load, as illustrated in Fig. 7b.

4 Conclusions

A total of eight dynamic shock tube tests were performed on two CLT and two glulam full-scale specimens under idealized simply-supported boundary conditions in order to investigate the potential effects of repeated blast loading on the load–displacement relationship. Both CLT and glulam members failed in flexure. Due to the presence of transverse layers, prominent rolling shear damage was observed in the CLT specimens, corroborating previous research on CLT panels. Based on the obtained experimental resistance curves, it was determined that damage accumulation occurring in the CLT panels could be characterized by the backbone curve established in the literature when the elements are subjected to one shot causing failure. For both material types, no damage or stiffness degradation could be observed when the specimens were loaded within their elastic regime, even in cases where superficial damage was observed. These findings confirm that the use of timber specimens within research setting where multiple loading regiments are to be applied to the same member, can in fact be performed without consideration for preliminary loss of capacity or stiffness, if the specimen is loaded within the elastic range. These findings can also be applied to assess the remaining blast resistance of timber structures already subjected to blast or impact loading if the approximate level of loading is known.

References

1. Côté D, Doudak G (2019) Experimental investigation of cross-laminated timber panels with realistic boundary conditions subjected to simulated blast loads. Eng Struct 187:444–456
2. CSA (2019) Engineering design in wood. CSA O86. CSA Group, Mississauga, ON
3. Jacques E, Lloyd A, Braimah A, Saatcioglu M, Doudak G, Abdelalim O (2014) Influence of high strain-rates on the dynamic flexural material properties of spruce–pine–fir wood studs. Can J Civ Eng 41(1):56–64
4. Kuzmanovska I, Gasparri E, Monné DT, Aitchison M (2018) Tall timber buildings: emerging trends and typologies. In: Conference paper WCTE 2018—world conference on timber engineering, Seoul, South Korea, 20–23 Aug
5. Lacroix D, Viau C, Battelli E, Doudak G (2021) Enhancing the performance of light-frame wood studs using glass fibre-reinforced polymers. Eng Struct 245:112973
6. Lacroix DN, Doudak G (2015) Investigation of dynamic increase factors in light-frame wood stud walls subjected to out-of-plane blast loading. J Struct Eng 141(6):04014159
7. Lacroix DN, Doudak G (2018) Determining the dynamic increase factor for glued-laminated timber beams. J Struct Eng 144(9):04018160
8. McGrath A, Doudak G (2021) Investigating the response of bolted timber connections subjected to blast loads. Eng Struct 236:112112

9. Oliveira D, Viau C, Doudak G (2022) Modelling of heavy timber members subjected to sequential shocktube-simulated blast loads. In: CSCE 2022 annual conference, Canadian Society for Civil Engineering, Whistler, BC, 25–28 May

10. Poulin M, Viau C, Lacroix DN, Doudak G (2018) Experimental and analytical investigation of cross-laminated timber panels subjected to out-of-plane blast loads. J Struct Eng 144(2):04017197

11. Viau C, Doudak G (2016) Investigating the behavior of light-frame wood stud walls subjected to severe blast loading. J Struct Eng 142(12):04016138

12. Viau C, Doudak G (2016) Investigating the behaviour of typical and designed wall-to-floor connections in light-frame wood stud wall structures subjected to blast loading. Can J Civ Eng 43(6):562–572

13. Viau C, Doudak G (2019) Behaviour and modelling of cross-laminated timber panels with boundary connections subjected to blast loads. Eng Struct 197:109404

14. Viau C, Doudak G (2021) Behavior and modeling of glulam beams with bolted connections subjected to shock tube-simulated blast loads. J Struct Eng 147(1):04020305

15. Viau C, Doudak G (2021) Energy-absorbing connection for heavy-timber assemblies subjected to blast loads-concept development and application. J Struct Eng 147(4):04021027

16. Viau C, Lacroix DN, Doudak G (2016) Damage level assessment of response limits in light-frame wood stud walls subjected to blast loading. Can J Civ Eng 44(2):106–116

Experimental Investigation of Performance of Perforated Steel Plate as Structural Fuse for Mass Timber Seismic Force Resisting Systems

Hossein Daneshvar, Carla Dickof, Thomas Tannert, and Chui Ying Hei

Abstract Design of tall timber buildings in high seismic regions is still a challenge mainly due to lack of ductile connections, as a main component of Seismic Force Resisting System (SFRS). There are different methods to dissipate energy during major earthquakes including dissipation through yielding of steel material by going through plastic deformations, also called hysteresis energy dissipation. Under the induced seismic motions, such dissipative elements are intended to undergo excessive deformation whilst the rest of the structure remain intact with minimum damage. In this research, the focus is on the perforated steel plates as a dissipating energy device, also called seismic fuses, to enhance seismic performance of mass timber buildings during extreme earthquakes. Whilst the previous tests performed on such fuses demonstrated the potential of the concept to be used as different types of connections in the mass timber SFRS, their behaviour in cyclic loading can be improved. This chapter presents part of an extensive experimental study on perforated plate connections focusing on investigating the effect of various parameters such as number of rows of perforations, shape of perforations, size of perforations, steel plate thickness, and the steel link length between adjacent perforations. Thirty tests were performed in total, including 15 monotonic and 15 cyclic tests. Preliminary comparisons are made between the obtained hysteresis responses and their corresponding envelope curves versus the associated monotonic responses. It is shown that the ellipse and stagger patterns possess the largest ultimate displacement and stiffness, respectively. In addition, no significant enhancement is observed by adding more than four rows using a 5 mm perforation link size. Results of the perforated plate tests have shed light on the behaviour of the connection made of this plate type which will assist with

H. Daneshvar (✉) · C. Y. Hei
Department of Civil and Environmental Engineering, University of Alberta, Edmonton, Canada
e-mail: hossein.daneshvar@ualberta.ca

C. Dickof
Fast + Epp, Vancouver, Canada

T. Tannert
Wood Innovation and Design Centre, University of Northern British Columbia, Prince George, Canada

317

the design of future test program on full-size mass timber connections consisting of such fuses.

Keywords Cross-Laminated Timber (CLT) shear walls · Timber Braced Frame (TBF) · Ductile connections · Structural fuse · Perforated steel plate connection · Seismic Force Resisting System (SFRS) · Link size

1 Introduction

There is global interest towards high-rise mass timber buildings in the past decade as part of the global trend to use biomaterials for designing sustainable structural systems. Whilst the use of mass timber elements in the gravity load-resisting systems of buildings is well-established, their application as the primary material for the Seismic Force Resisting System (SFRS) requires more investigation. This is mainly due to brittle nature of wood failure, in general, and the necessity of having ductile connections. Timber Braced Frames (TBF) and Cross-Laminated Timber (CLT) shear walls are two common mass timber lateral load-resisting systems, shown in Fig. 1. End Brace Connections (EBC) within TBF (Fig. 1a) and Panel-to-Panel Connections (PPC) and Hold-Downs (HD) within CLT shear walls (Fig. 1b) are potential locations for providing local ductility, which leads to global ductility of the SFRS. Conventional dowel-type fasteners are the most common type of connector employed by designers in different types of connections in TBF and CLT shear walls. Such fasteners e.g., bolts, screws, and nails can behave in a ductile manner if designed properly. Different design parameters of such connections, including their capacity and failure mode prediction, are presented in many timber design standards, including CSA O86-19 (CSA 2019), based on the so-called European Yield Model [14]. However, the damage imposed on the timber elements and dowel-type fasteners might impose significant economic loss and interruption in the continuous serviceability of the structure after major seismic events. Consequently, connection types that can be replaced after major earthquakes, without significant damage in the mass timber elements, are needed and appreciated by practitioners and owners. Perforated plates accompanied by capacity protected dowel fasteners are one plausible solution at the EBC, PPC, and HD locations, as shown in Fig. 1c, d. The dominant failure mechanism is shear yielding at the location of perforation zones; whilst the rest of the structural elements are capacity protected to ensure that they are undamaged. As can be seen, in the Fig. 2, the fuses can be replaced after a major event, whilst the dowel fasteners and the timber elements remain almost undamaged.

The performance of the perforated plate connections, which is a modified version of Holz-Stahl-Komposit (HSK)™, is discussed in a few research articles including the one presented by Bathon et al. [3, 4]. A HD connection with a glued-in perforated steel plate as a designated shear yield area was investing bated by Zhang et al. [22] and Eatherton et al. [13]. Ma [18] used butterfly shear fuses in self-centred steel braced frames. Blomgren et al. [5] and Morrell et al. [19] attempted to use a
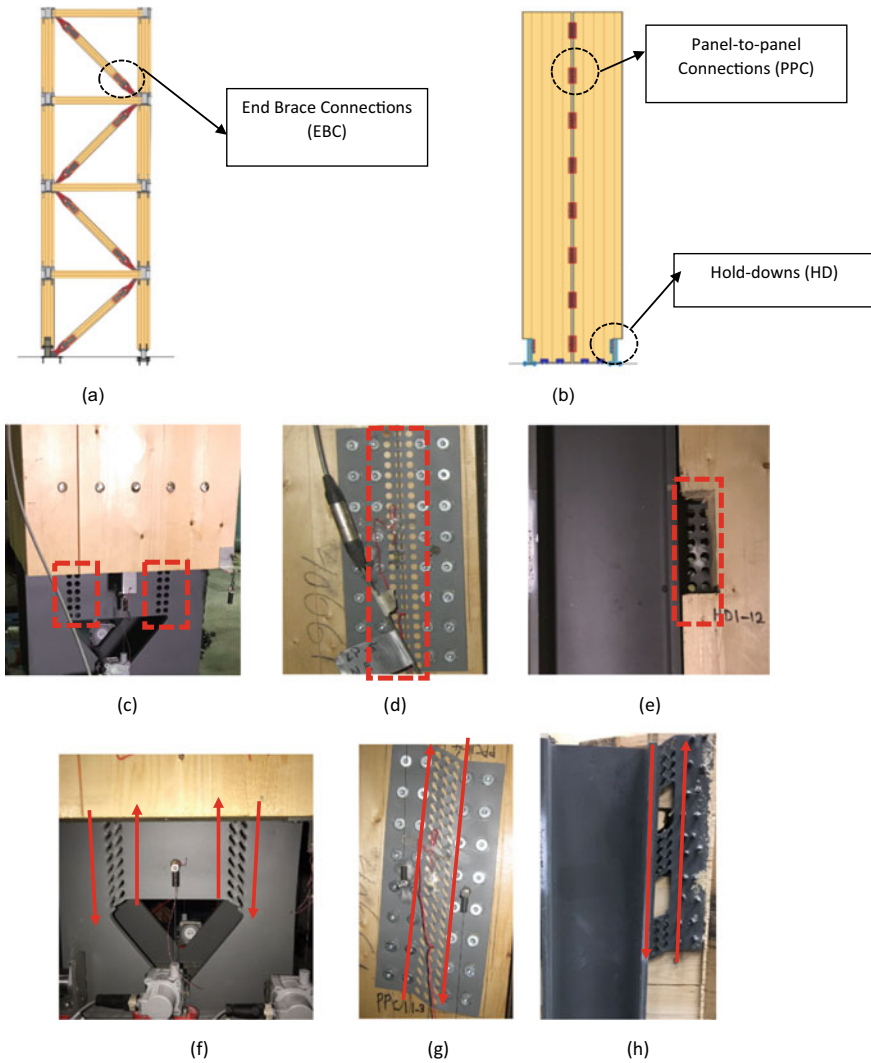
Fig. 1 Mass timber SFRS: **a** TBF; **b** CLT shear walls and their pertinent connections with illustrations of using perforated fuses for: **c** EBC, **d** PPC, **e** HD; yielding of perforated fuses mainly in shear to dissipate energy **f** EBC, **g** PPC, **h** HD

similar fuse concept for panel-to-panel connections in CLT shear wall structures and have registered their fuse system as a proprietary connection. Another study, also inspired by the perforated plate concept, is a project to design a CLT shear wall holddown using self-drilling dowels as fasteners but with diamond-shaped perforations [20]. The intended outcome was that the diamond cut-outs would form diagonal yield lines, increasing the yield area, as opposed to vertical yield lines from circular
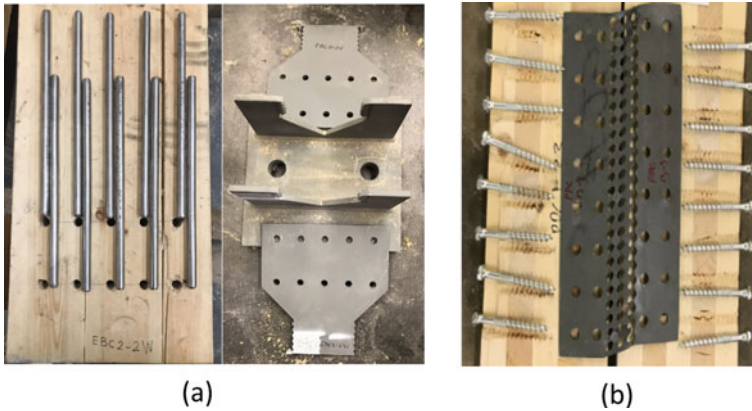
Fig. 2 Replaceability of the fuses after cyclic tests to the failure simulating major seismic events **a** EBC; **b** PPC

perforations. One major disadvantage of the diamond shape cut-out over the circular perforation was a larger stress concentration and consequently, higher probability of fatigue-like crack initiation under cyclic loading. Similarly, the research by Kobori et al. [15], Chan and Albermani [7], Chan et al. [8, 9], Teruna et al. [21], Lee et al. [16], Ahmadie Amiri et al. [1], and Li [17], can provide insight into the use of perforated plate connections as a source of energy dissipation in timber systems, even though these studies focused on steel structures. Daneshvar et al. [10, 11] extended the work of [22] by replacing the adhesive with dowel-type fasteners. The results showed that perforated steel plates can be reliably designed to fail in a ductile manner with a desired yield and ultimate strength. In a recent work, Daneshvar et al. [12] demonstrated that stiff and strong connections in combination with a perforated steel plate resulted in seismic fuse behaviour during cyclic tests, with large open hysteretic loops, unlike traditional dowel-type fasteners. Despite the predictable and scalable ultimate capacity and deformability as well as desired failure modes of connections in monotonic tests, their performance in cyclic behaviour requires more investigation. This chapter presents the interim results of an extensive experimental study on the perforated plate connections, focusing on investigating the effects of various parameters such as the number of rows of perforations, shape of perforations, size of perforations, steel plate thickness, and the steel link length between adjacent perforations, to understand and potentially enhance the performance of such fuses subjected to monotonic and cyclic loading.

2 Experimental Program

A total of 60 perforated specimens were tested, in 30 tests (two plates per test to keep the experiments symmetric). The perforation arrangement and attributes of 30 types of specimens are summarized in Table 1 and Fig. 3. All perforated plates were made up of CSA G40.21 300W steel material. The perforations were water jet cut, although drilled holes were also allowed. The specimen labels explain the plate configuration and loading type following this convention: perforation size—number of (no.) of rows (S: staggered pattern)—centre to centre (C/C) distance of the perforations—plate thickness—loading type the specimen tested upon [monotonic (M) vs. cyclic (C)]. For instance, specimen 10-3-15-6.4-C refers to a 6.4 mm thick plate with 3 rows of 10 mm perforations, C/C 15 mm and tested in cyclic loading. As can be seen in Table 1 and Fig. 3, the perforation arrangements differed in terms of number of rows (lines of perforation parallel to the loading direction), link size (row spacing), perforation size (hole diameter), perforation shape (circular versus ellipse), pattern (regular versus staggered) as well as plate thickness. The link element, defined as clear distance between two adjacent perforations, is considered the fundamental unit of such a connection system whose attributes determine the performance of the whole system. Three link sizes of 5 mm, 10 mm, and 15 mm were considered, whilst the two perforation sizes of 10 mm and 15 mm were investigated. Also, the number of rows were limited to 3–5 rows. The nominal plate thickness was 6.4 or 9.5 mm.

The monotonic tests were displacement-controlled and performed on the first set of each specimen type (with a minor deviation reported in the Table 1) at a rate of 2 mm/min. Cyclic tests were performed in the same test setup, based on the ASTM E2126 standard method B [2]. This method uses a displacement-controlled loading procedure involving cycles grouped in phases of incrementally increasing displacement levels. There are two patterns in this loading protocol: the first being five fully reversed cycles up to 10% of the ultimate displacement obtained from the monotonic test and the second pattern consisting of phases of three fully reversed cycles of equal amplitude (called a step), starting at 20% of the ultimate displacement with a step-wise increase of 20% until specimen failure. Figure 4 illustrates the two patterns within the discussed loading schedule. Due to uncertainties in post-peak behaviour of the specimens, also negligible expected post-peak deformation [12], the ultimate displacement at the peak load obtained from the monotonic test was used as the reference displacement for the cyclic loading tests of the associated specimen type.

A 1.5 MkN capacity Universal Testing System (UTS) was used in the test program. The machine was capable of static and low-frequency cyclic loads. The applied load was measured by an internal 5000kN load cell. High-capacity test fixtures were designed to meet the test requirements. It consists of two stiffened plate girders (called blue beams), and three stub columns, as shown in Fig. 5. The bottom of the blue beams was anchored to the strong floor via an adaptor, whilst the top beam was bolted to the loading actuator. The middle stub column was restrained in the vertical direction, whilst the outer stub columns were moving vertically to apply

Table 1 Testing matrix

Test no	Test label	Main parameter under investigation	Plate			Perforation		
			Length (mm)	Thickness (mm)	No. of rows	Size (mm)	End distance (mm)	Link size (mm)
1	10-3-15-6.4C	No. of rows of perforations	365	6.4	3	10	5	5
2	10-3-15-6.4M		365	6.4	3	10	5	5
3	10-4-15-6.4C		365	6.4	4	10	5	5
4	10-4-15-6.4 M		365	6.4	4	10	5	5
5	10-5-15-6.4C		365	6.4	5	10	5	5
6	10-5-15-6.4 M		365	6.4	5	10	5	5
7	10-3-20-6.4R-C	No. of rows of perforations / link size	270	6.4	3	10	10	10
8	10-3-20-6.4R-M		270	6.4	3	10	10	10
9	10-4-20-6.4C		370	6.4	4	10	10	10
10	10-4-20-6.4 M		370	6.4	4	10	10	10
11	10-3-25-6.4R-C		265	6.4	3	10	15	15
12	10-3-25-6.4R-M		265	6.4	3	10	15	15
13	10-4-25-6.4R-M-1		265	6.4	4	10	15	15
14	10-4-25-6.4R-M-2		265	6.4	4	10	15	15
15	15-3-20-6.4C	Perforation size	365	6.4	3	15	5	5
16	15-3-20-6.4 M		365	6.4	3	15	5	5
17	15-3-25-6.4C		385	6.4	3	15	10	10
18	15-3-25-6.4 M		385	6.4	3	15	10	10
19	10E-3-15-6.4C	Perforation shape	365	6.4	3	10 × 14	5	5
20	10E-3-15-6.4 M		365	6.4	3	10 × 14	5	5
21	10E-3-20-6.4R-C		270	6.4	3	10 × 14	10	10
22	10E-3-20-6.4R-M		270	6.4	3	10 × 14	10	10
23	10-3S-15-6.4C	Perforation pattern	360	6.4	3	10	5.3	11.2
24	10-3S-15-6.4M		360	6.4	3	10	5.3	11.2
25	10-3S-20-6.4C		370	6.4	3	10	10.3	18.3
26	10-3S-20-6.4M		370	6.4	3	10	10.3	18.3
27	10-3-15-9.5C	Plate thickness	260	9.5	3	10	5	5
28	10-3-15-9.5M		260	9.5	3	10	5	5
29	10-3-20-9.5C		270	9.5	3	10	10	10
30	10-3-20-9.5C-2		270	9.5	3	10	10	10
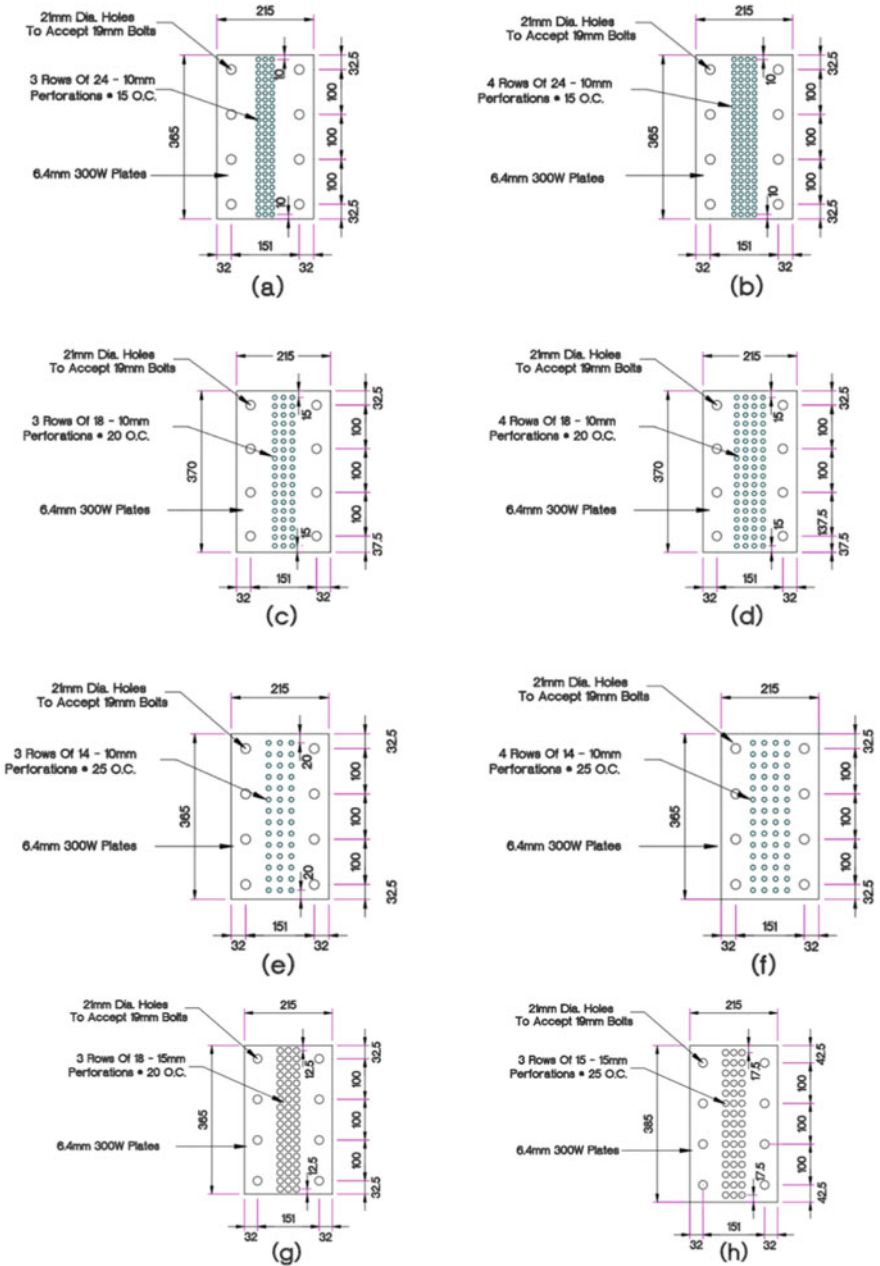
Fig. 3 Specimens **a** 10-3-15-6.4; **b** 10-4-15-6.4; **c** 10-3-20-6.4; **d** 10-4-20-6.4; **e** 10-3-25-6.4; **f** 10-4-25-6.4; **g** 15-3-20-6.4; **h** 15-3-25-6.4; **i** 10E-3-15-6.4; **j** 10E-3-20-6.4; **k** 10-3S-15-6.4; **l** 10-3S-20-6.4; **m** 10-3-15-9.5; **n** 10-3-20-9.5; **o** 10-5-15-6.4
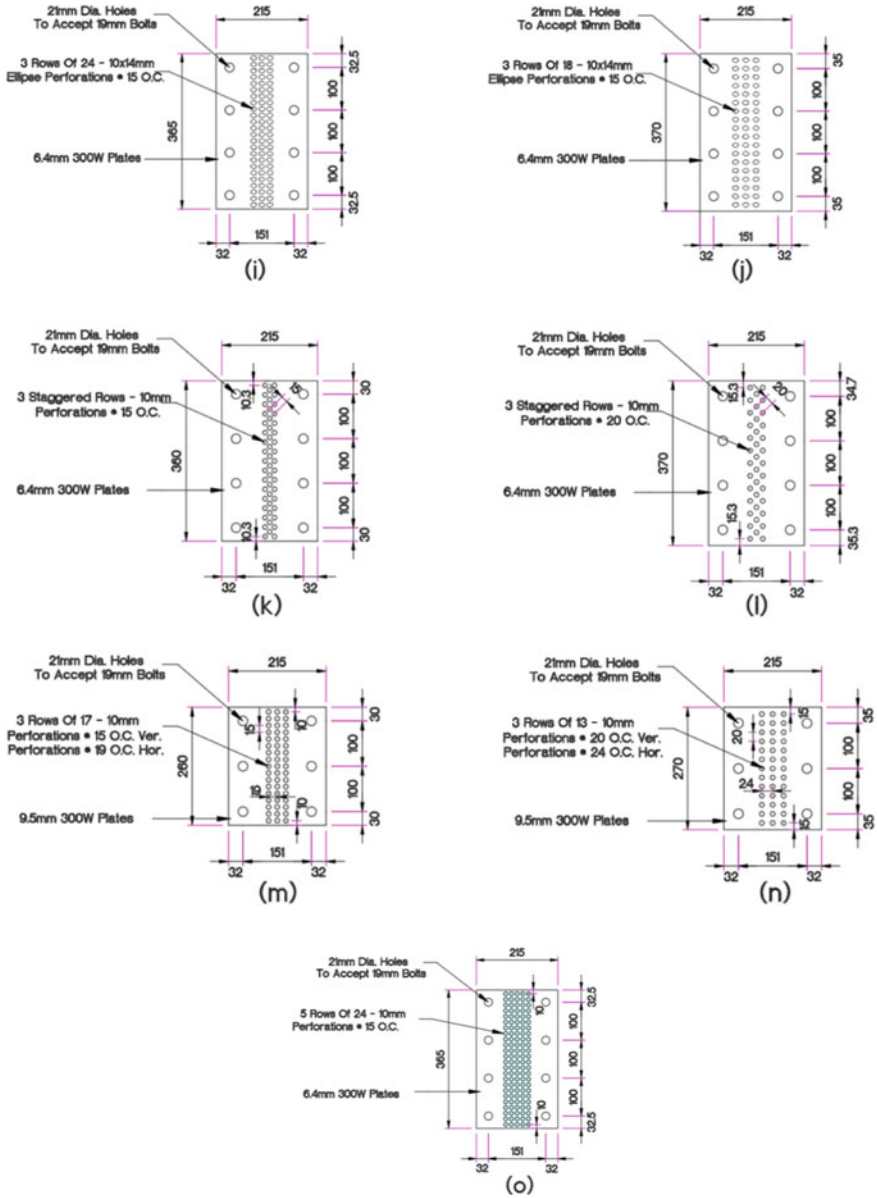
Fig. 3 (continued)
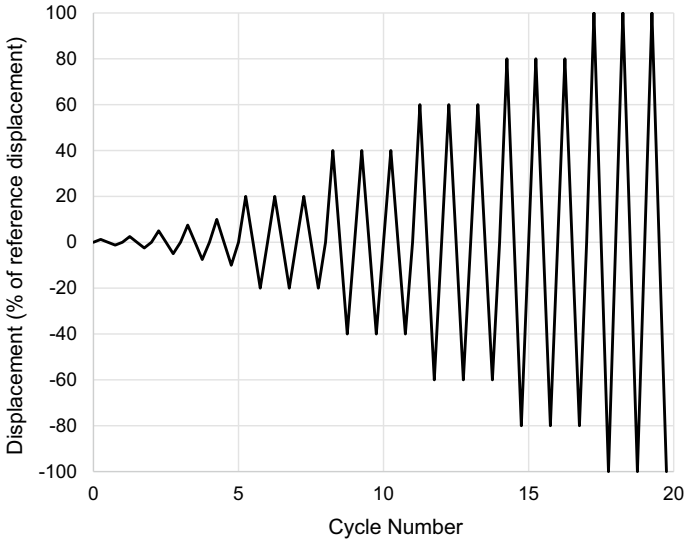
Fig. 4 Cyclic displacement schedule according to ASTM E2126 standard method B [2]

the displacement to each plate through the top girder. The specimens were installed amongst the stub columns using eight angles. The connection of these angles to the stub columns was designed to be slip critical using high-strength bolts to facilitate the installation of specimens in between six linear potentiometers, with a measurement range of 100 mm, were installed to record the response of the different components of the specimens and the setup, as shown in the Fig. 6. The pure deformations at perforation zones are of particular interest. Based on the abbreviations shown in Fig. 6, the average perforation deformations can be calculated using Eq. (1).

perforation deformation

$$= \frac{((S - M - \text{BOT}) - (S - F - \text{BOT})) + ((N - M - \text{BOT}) - (N - F - \text{BOT}))}{2}$$

(1)

During the cyclic tests, the difference of the measurements reported by two linear potentiometers installed on the North specimen was employed as a feedback signal to control the displacement cycles according to the ASTM E2126 Method B procedure [2]. It was noted that the actual displacements differed somewhat from the programmed protocol. However, additional evaluation revealed that the measured (actual) peaks are within 4% of the programmed peak values, which is deemed acceptable for the study.

(a)   (b)
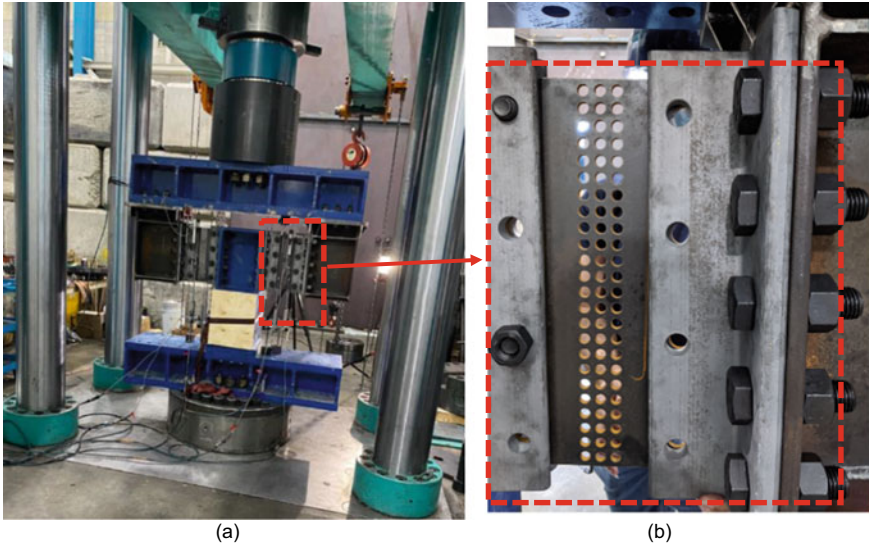
Fig. 5 **a** Test setup and **b** specimen installed
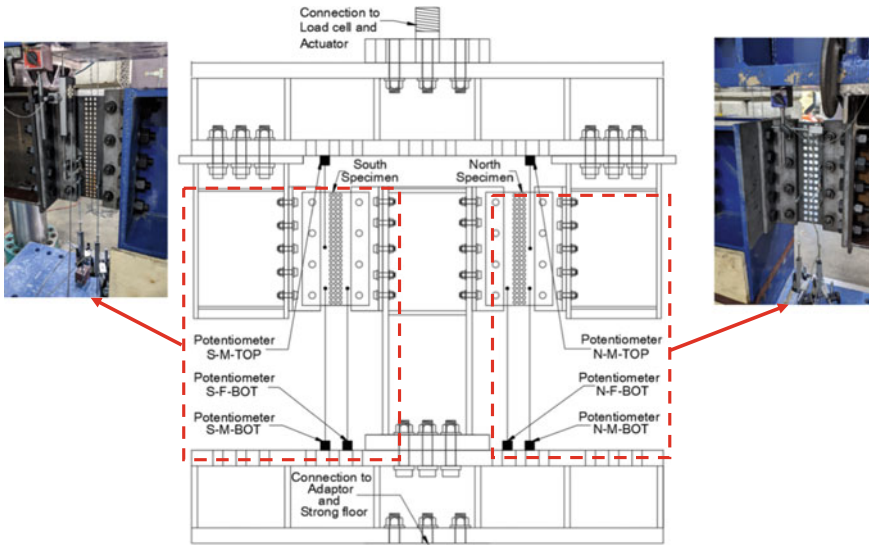
Fig. 6 Instrumentation

3 Test Results

Figures 7 and 8 show sample failure modes of the specimens in monotonic and cyclic loadings. Overall, the desired failure mode of ductile shear yielding of link elements was confirmed by the tests. However, the failure modes of the cyclic specimens exhibited complexities that will require further investigation. In general, the dominant failure mode under cyclic loading was a low cycle fatigue-type rupture of fuses, which reduced the total number of cycles the fuse can survive, similar to the previous study [12]. In particular, the staggered specimens that failed due to a rupture of the link elements, as shown in Fig. 8, deformed significantly out-of-plane. This makes the prediction of their behaviour difficult based on in-plane shear yielding assumption. In addition, the symmetric deformed shapes observed in the majority of the monotonic tests, (e.g., Fig. 7), were not observable in the cyclic failed specimen (e.g., Fig. 8). In this chapter, results from a preliminary analysis of the results are presented, whilst a more detailed analysis of the results to generate a better understanding of the behaviour is ongoing.

Specimen 10-3-15-6.4-M was used as the reference pattern for this study. As can be seen in Fig. 9a, the stroke of the UTS shows a larger deformation compared to the deformation measured with the potentiometers installed on both specimens (approximately 8 mm of difference). This confirms the decision to not rely on the UTS stroke for such measurements. In addition, as shown in Fig. 9b, the responses of the south and north specimens were almost the identical. As a result, the average deformation calculated based on the Eq. (1) was deemed appropriate. Similarly, equal sharing of forces between the two specimens were observed in the majority of the monotonic tests performed, except in the latest stage of loading prior to failure. The reference specimen, 10-3-15-6.4-M, reached a peak load of 645.1 kN at the perforation deformation of 26.7 mm whilst it failed slightly after reaching an ultimate deformation of 28.5 mm. Unfortunately, specimen 10-3-15-6.4-C was damaged due
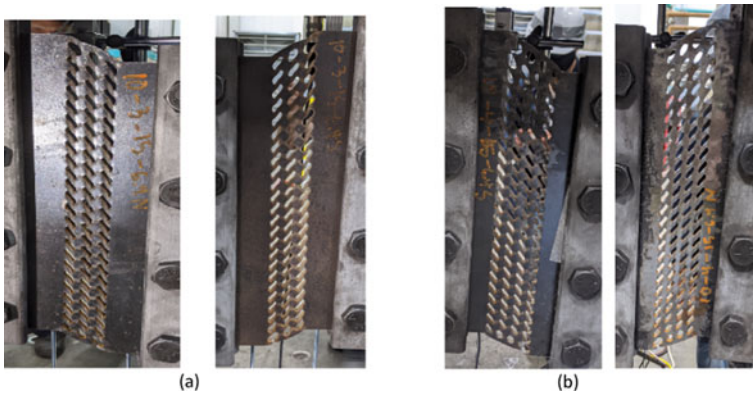
Fig. 7 Deformed shapes of south and north specimens in monotonic tests **a** 10-3-15-6.4M; **b** 10-4-15-6.4M
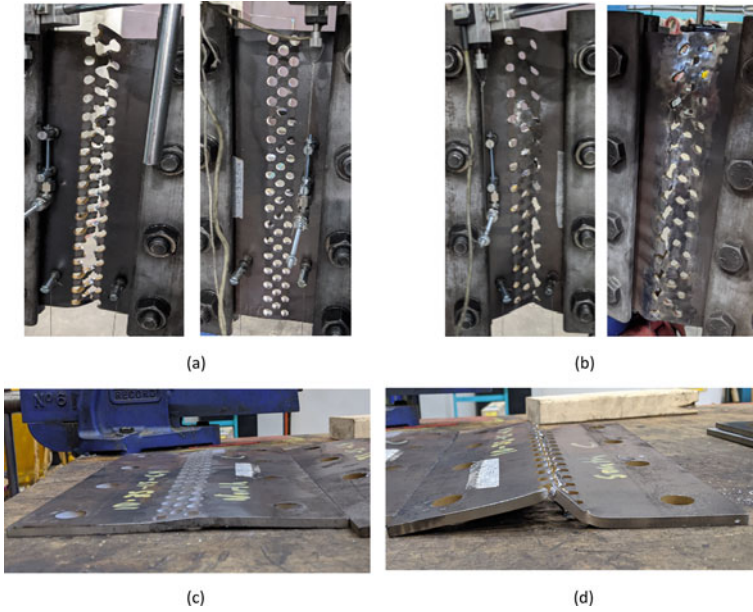
Fig. 8 Sample in-plane deformed shapes of south and north specimens in cyclic tests **a** 10-3S-15-6.4 and **b** 10-3S-20-6.4; out-plane deformation of 10-3S-15-6.4 specimen **c** north, and **d** south specimens

to a mistake in the load application. Therefore, no cyclic data was available for this configuration.

The load-deformation curves for the selected additional tests performed are shown in the Fig. 10. Based on the obtained hysteresis curves, the envelope curves (i.e., constructed by connecting the peak load of the first cycle of each phase of the load-displacement hysteresis loops) were produced and compared with the corresponding
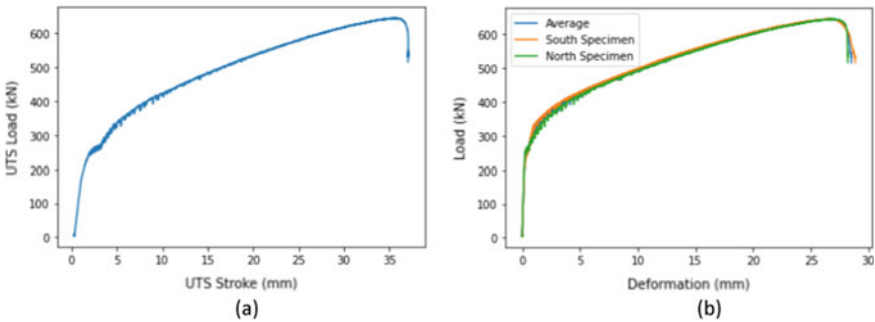
Fig. 9 Load-deformation response of 10-3-15-6.4-M: **a** UTS load and stroke; and **b** UTS load and potentiometer deformations of south and north specimens

monotonic responses. A visual comparison of Fig. 10a–l reveals that, within the scope of the configurations considered in this study there is a significant reduction in the ultimate deformation of the connections in cyclic loading regardless of their patterns (with the exception of 10-3S-20-6.4). The ellipse perforation type (i.e., 10E-3-20-6.4) demonstrated the highest ultimate deformations, both in the cyclic and monotonic deformations, whilst stagger patterns (i.e., 10-3S-15-6.4 and 10-3S-20-6.4) manifested less deformation compared to other configurations. The ultimate displacement achieved in cyclic loads is about 40–50% of the corresponding monotonic deformations caused by a low cycle fatigue-type rupture of fuses. As a result, it is important to re-examine the testing protocol adopted for the cyclic loading and to investigate if the premature fatigue-type of failure can be suppressed by employing other applicable loading regimes (i.e., investigating the effect of number of cycles and their amplitude on the performance of the fuse). Detailed analysis of the results is ongoing.

4   Summary and Conclusions

Thirty tests were performed in total. These included 15 monotonic and 15 cyclic tests on perforated fuses. Preliminary comparisons were made amongst the obtained hysteresis curves and their corresponding envelope curves versus the associated monotonic responses. It was shown that the ellipse and stagger patterns possess the largest ultimate displacement and stiffness, respectively. The ultimate displacement achieved in cyclic loads was about 40–50% of the corresponding monotonic deformations caused by premature low cycle fatigue-type rupture of steel at the fuses. As a result, within the scope of the configuration considered, the reduced ultimate deformation under cyclic loading remains a technical challenge that needs to be addressed if this type of seismic fuse is to be installed in SFRS, despite the promising potential of the ellipse pattern. Results of the perforated plate tests performed have provided insight into the behaviour of the connections made by these plates that will also influence a testing matrix for future cyclic tests of the full-size mass timber connections containing such fuses. Particularly, it is suggested that impacts of the cyclic testing protocol on load-deformation hysteresis response and mode of failure, particularly the fatigue-type rupture, should be further investigated.
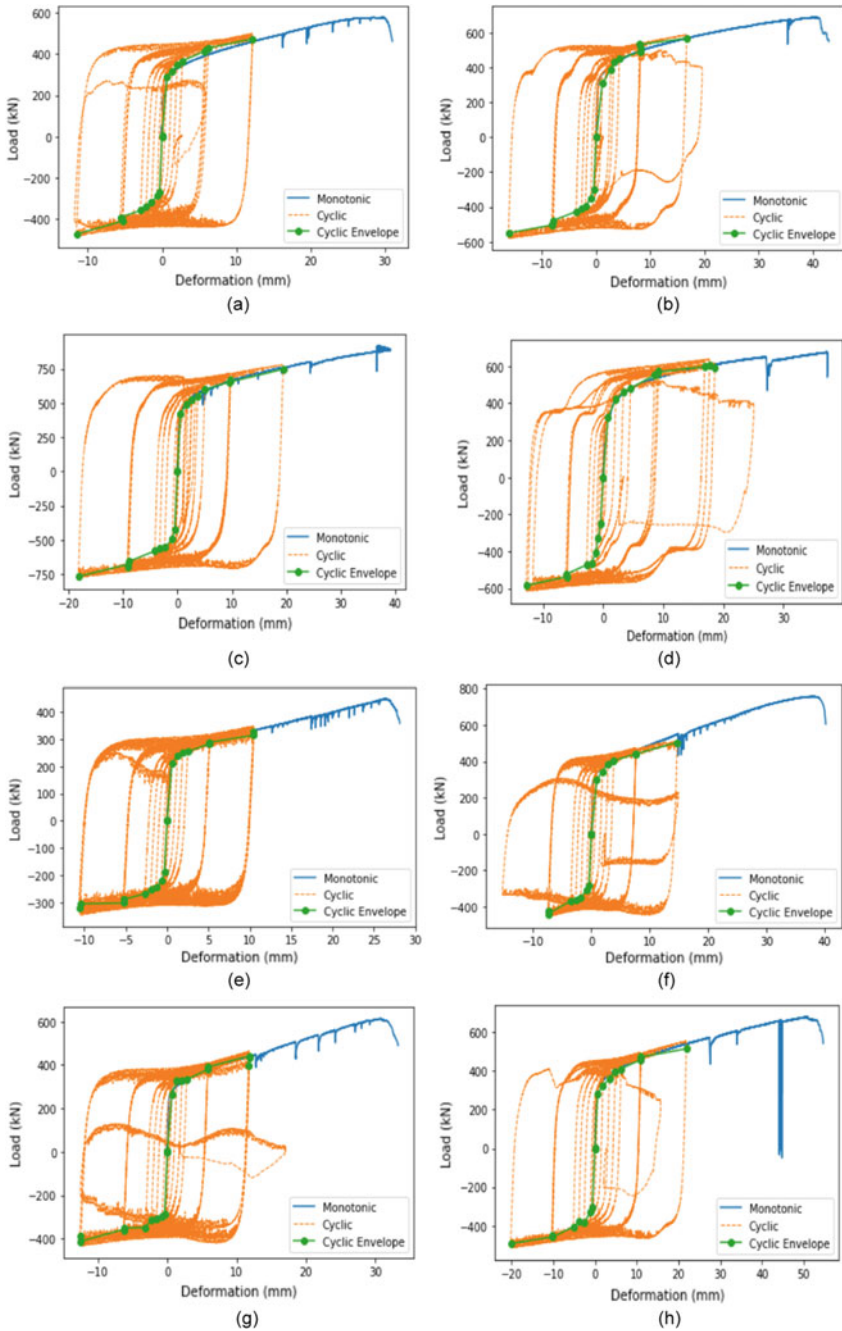
Fig. 10 Load-deformation curves for specimens **a** 10-4-15-6.4; **b** 10-3-20-6.4; **c** 10-4-20-6.4; **d** 10-3-25-6.4; **e** 15-3-20-6.4; **f** 15-3-25-6.4; **g** 10E-3-15-6.4; **h** 10E-3-20-6.4; **i** 10-3S-15-6.4; **j** 10-3S-20-6.4; **k** 10-3-15-9.5; **l** 10-5-15-6.4
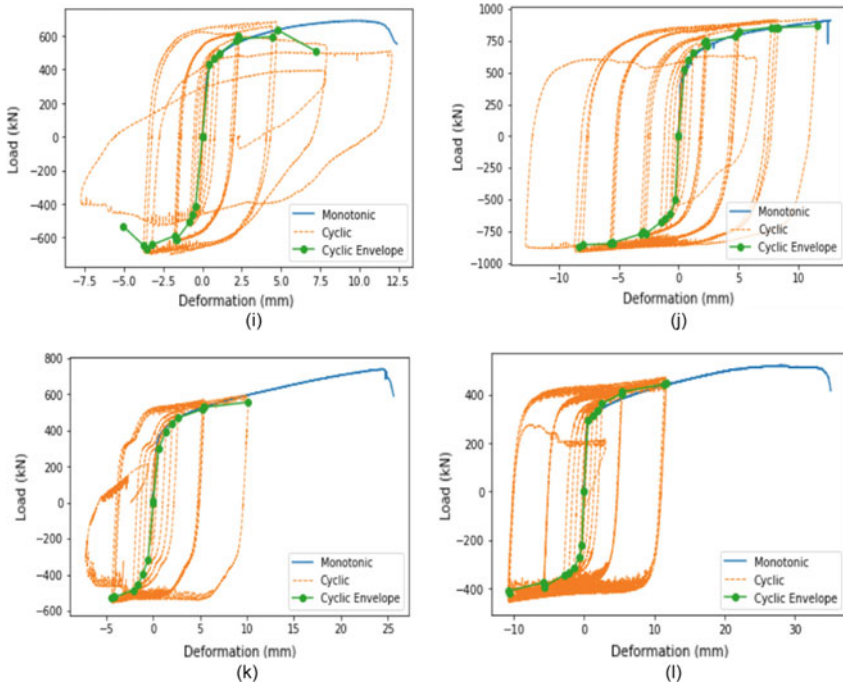
Fig. 10 (continued)

References

1. Ahmadie Amiri H, Najafabadi E, Estekanchi H (2018) Experimental and analytical study of block slit damper. J Constr Steel Res 141:167–178
2. ASTM E2126 (2018) Standard test methods for cyclic (reversed) load test for shear resistance of vertical elements of the lateral force resisting systems for buildings. ASTM International, West Conshohocken, Pennsylvania, United States
3. Bathon L, Bletz-Mühldorfer O, Schmidt J, Diehl F (2014a) Fatigue performance of adhesive connections for wooden wind towers. In: Materials and joints in timber structures. Springer, Dordrecht, Netherlands, pp 375–380
4. Bathon L, Bletz-Mühldorfer O, Schmidt J, Diehl F (2014b) Fatigue design of adhesive connections using perforated steel plates. In: Proceedings of the world conference on timber engineering. Quebec City, Quebec, Canada, pp 996–1001

5. Blomgren HE, Pei S, Powers J, Dolan JD, Wilson A, Morrell I, Jin Z (2018) Cross-laminated timber rocking wall with replaceable fuses: validation through full-scale shake table testing. In: WCTE 2018: world conference on timber engineering. Seoul, Republic of Korea.

6. Canadian Standards Association (CSA) (2019) Engineering design in wood. CSA Standard 086-19, Toronto, Ontario, Canada

7. Chan RWK, Albermani F (2008) Experimental study of steel slit damper for passive energy dissipation. Eng Struct 30(4):1058–1066

8. Chan RWK, Albermani F, Williams M (2009) Evaluation of Yielding shear panel device for passive energy dissipation. J Constr Steel Res 65(2):260–268

9. Chan RWK, Albermani F, Kitipornchai S (2013) Experimental study of perforated yielding shear panel device for passive energy dissipation. J Constr Steel Res 91:14–25

10. Daneshvar H, Niederwestberg J, Dickof C, Spencer J, Letarte JP, Chui YH (2019a) Seismic performance of end brace connections in ductile braced timber frame. In: Proceedings of INTER2019, Tocoma, Washington, United States

11. Daneshvar H, Niederwestberg J, Dickof C, Letarte J-P, Chui YH (2019b) Cross-laminated timber shear walls in balloon construction: seismic performance of steel connections. In: Proceedings of modular and offsite construction conference, Banff, Alberta, Canada

12. Daneshvar H, Niederwestberg J, Dickof C, Jackson R, Chui YH (2022) Perforated steel structural fuses in mass timber lateral load resisting systems. Eng Struct 257:114097

13. Eatherton M, Hajjar J, Deierlein G, Krawinkler H, Billington S, Ma X (2008) Controlled eocking of steel-framed buildings with replaceable energy-dissipating fuses. In: Proceedings of the 14th world conference on earthquake engineering, Beijing, China

14. Johansen KW (1949) Theory of timber connectors. (9):249–262. Zurich, Publication of the International Association of Bridges and Structural Engineering

15. Kobori T, Miura Y, Fukuzawa E, Yamada T, Arita T, Takenake Y, Fukumoto T (1992) Development and application of hysteresis steel dampers. In: Proceedings of the 10th world conference on earthquake engineering, Rotterdam, Netherlands, pp 2341–2346

16. Lee CL, Ju YK, Min JK, Lho SH, Kim SD (2015) Non-uniform steel strip dampers subjected to cyclic loadings. Eng Struct 99:192–204

17. Li T (2018) Experimental testing and numerical modelling of honeycomb structural fuse. MASc thesis, Department of Civil Engineering, University of British Columbia, Vancouver, British Columbia, Canada

18. Ma X (2011) Seismic design and behavior of self-centering braced frame with controlled rocking and energy dissipating fuses. Ph.D. thesis, Stanford University, Stanford, California, United States

19. Morrell I, Phillips A, Dolan J, Blomgren H-E (2018) Development of an inter-panel connector for cross-laminated timber rocking walls. In: Proceedings WCTE 2018: world conference on timber engineering, Seoul, South Korea

20. Nicholas JH (2019) Pilot study of a high capacity ductile seismic holddown for cross laminated timber. MASc thesis, Department of Civil Engineering, Montana State University, Bozeman, Montana, United States

21. Teruna D, Majid T, Budiono B (2015) Experimental study of hysteretic steel damper for energy dissipation capacity. In: Advances in civil engineering, Article ID 631726

22. Zhang X, Popovski M, Tannert T (2018) High-capacity hold-down for mass-timber buildings. Constr Build Mater 164:688–703

Long-Span CLT-Glulam Composite Flooring System Connected with Bamboo-Based Shear Connectors: Feasibility of Design for Assembly

Yue Diao and Cristiano Loss

Abstract Composite flooring systems built with CLT-glulam ribs have a higher strength-to-weight ratio compared to the concrete-steel composites; thus, it can result in an economical solution for spans over 12 m. In practice, the lack of studies on the structural performance of such CLT-glulam composites often leads to the over-size of the floor members. In addition, shear connectors design is crucial and drives to the structural efficiency of the floor assembly. In this paper, the long-span CLT-glulam composite flooring system is assembled using bamboo-based shear connectors. Similar to conventional mortise-tenon joints, this new connection method can minimize the required number of connectors and installation time. Modular design is incorporated in the flooring system, serving the North American mass timber construction market. The design method of the flooring system is based on the theory of composite beams with partial interaction. Design assumptions covering effective width, joint efficiency, and components configuration are discussed under ultimate limit state and serviceability limit states. Four bamboo-based shear connector prototypes with different tenon profiles are given. The optimized timber components and connectors for a 12-m span floor are implemented. Individual load-slip response of bamboo-based shear connectors is investigated by means of modeling each component with a solid-type finite element (FE) model. Results show that bamboo-based shear connectors have high stiffness values and can transfer shear force between the timber members efficiently. Based on the stress distribution analysis, discussion on the mechanical behavior and floor's bending resistance is also included. Compared to common hardwood shear keys, bamboo connectors have advantages in terms of material and structural efficiency.

Keywords Long-span CLT-glulam composite · Flooring system · Bamboo-based shear connectors

Y. Diao · C. Loss (✉)
Sustainable Engineered Structural Solutions Laboratory, University of British Columbia, Vancouver, BC, Canada
e-mail: cristiano.loss@ubc.ca

1   Introduction

1.1   Mass Timber Construction

Cross-laminated timber (CLT) and other mass timber products bring new possibilities to use wood as a structural material. Nowadays, it is not uncommon for a 10-story residential or commercial buildings to have bearing elements made of wood. Alongside the environmental, social, and economic benefits, such a lightweight structure makes it very competitive in terms of structural design and eventually project investment for an open-space commercial project. The behavior of timber in fire has been largely studied and so protection strategies for mass timber products [13]. Other intrinsic properties, such as the aesthetic and biophilic nature of exposed wood members, make timber public projects more attractive to tourism and can lead to the increasing of government revenue [20].

With increasing research and case studies on mass timber structures, the height limitation on common timber structures in national and provincial building codes is loosening. For instance, in the *National Building Code of Canada* (NBCC) [26], the encapsulated mass timber construction is allowed to be built up to 12-story, indicating a new era of mass timber construction in Canada and beyond.

1.2   Mass Timber Composite Flooring Systems

CLT was conceived as a panelized product to complement the range of engineered wood products (EPWs). Such high-quality solid wood products can be used in a variety of structural applications, such as flooring and wall systems. However, as long-span floor components of mass timber buildings, composite flooring systems can provide better structural performance compared to single CLT members in bending, allowing for cost cuts. Studies on CLT-glulam ribbed flooring systems aroused interest worldwide: Gu [16], Negrão and Jorge [25], Masoudnia et al. [22], and Thiel and Brandner [30]. Research also included the development of box-type CLT composite timber flooring systems [6]. Special interests also ascended to the development of the new connection systems [18].

The behavior of the connection system drives the structural efficiency of timber composite flooring systems. In CLT-glulam composite systems subjected to bending moment, shear forces are generated between the panels and the ribs. The adhesive connection has an almost rigid behavior, and thus the full composite action is assumed. The design of such system is regulated in Eurocode 5 as glued composite members [4]. When timber members are mechanically connected, i.e., using metal fasteners as the connection system, partial composite action can be assumed. For this latter, Möhler [23] proposed an approximate solution, i.e., known as the gamma method, and included in Annex B of Eurocode 5 [4]. It is a simplified method that

introduces gamma factor to represent the joint efficiency. Moreover, the basic assumption is that only the shear deformation of the connection is accounted, while the shear deformation of timber components is assumed negligible.

1.3 Building Environment and Carpentry Joint in Timber Constructions

The adoption of metal fastener and adhesive connections for timber building design took off after the first industrial revolution [31]. Behavior of standardized products has been studied for decades, and architects, engineers, and builders have been engaged well with manufacturers in developing such technology.

With the advancement of digital fabrication technologies in the wood industry (e.g., computer numerically controlled (CNC) machines, robots, etc.), research for wood-based connection systems and carpentry joints is getting traction. Studies on rounded dovetail joints (Tannert 2016), multiple tenon connections [7], and castellated joints [3, 14] have demonstrated the high stiffness and load-carry capacity of carpentry joints applied in modern timber frame and mass timber structures. More recently, the possibility of using engineered wood products, e.g., Beech plywood and LVL, as shear connectors along the edge of CLT panels has been investigated [27] and [28]. On the other hand, there is a growing interest in the development of bamboo and bamboo-based composites as building materials [11]. In fact, experiment results show that bamboo products offer comparable or better mechanical properties compared to their counterparts [29].

1.4 Research Scope

In terms of carpentry joints, although the German National Annex of Eurocode 5 has included specific provisions for tenon design, design rules are typically applied for particular sized fixed tenons rather than shear connectors. Furthermore, no design guidelines are available for bamboo-based shear connectors used in timber composite systems.

This research aimed to provide a bamboo-based connection system for long-span mass timber composite flooring systems assembled in prefabricated floor elements. To the best of the authors' knowledge, this is the first study in Canada to investigate the potential of the design of CLT-glulam ribbed floor assembly applying bamboo as shear connectors.

2 CLT-Glulam Module Design

2.1 Design Loads

The proposed CLT-glulam ribs composite flooring system is intended for office-type buildings, where vertical bearing elements are placed within large open-space grids. The flooring system is designed in accordance with *NBCC* 2020 [26]. Uniformly distributed loads include a 2.4 kPa live load, self-weight of the floor, and a 1.2 kPa added dead load to simulate a concrete topping (having a non-structural function). The floor is assumed to be simply supported. Material strength check is made assuming all possible load combinations describing the most unfavorable effect. Only the short-term static structural performance of the flooring system is accounted for within this paper.

2.2 Floor Configuration

Figure 1 shows the modular structure of the CLT-glulam ribs composite flooring system for a 12 m span. The design considers common wood product types and sizes in North America (e.g., common CLT width is 2.4 m). CLT panels are in SPF with grade E1M5, in 3-ply or 5-ply arrangement. The major direction of CLT panel is designed to be parallel with the longitudinal axis of glulam beams. Unbalanced Douglas-fir 24f-E glulam is chosen for the composite system. The width of the glulam beams is set as 175 mm. Single CLT-glulam module can be assembled at the factory, and multiple modules can be jointed on site. The design is based on one T-beam section consisting of a CLT flange and one glulam rib web.
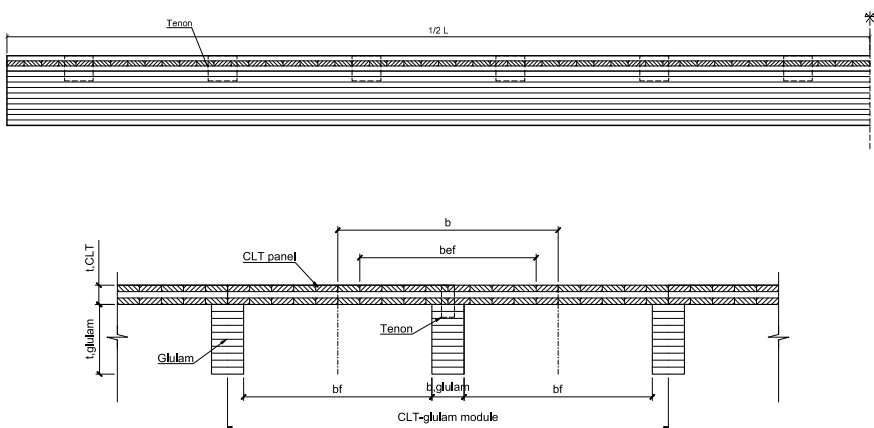
Fig. 1 Modular design of CLT-glulam ribs composite flooring systems

2.3 Floor Design Under Full Composite Action

The shear deformation of the flange results in the nonuniform distribution of the longitudinal strains along the flange width. This phenomenon is known as shear lag. To account for shear lag, the effective width approach can be used. Models to evaluate the effective width of timber slabs are covered in Eurocode 5 [4] (Method 1 of Table 1), Swedish timber structures design books [10] (Method 2 of Table 1), a new revision of Eurocode 5 embedded with Bogensperger theory of equivalent in-plane shear modulus [2, 5] (Method 3 of Table 1), the theoretical formula for stressed skin panels [24] (Method 4 of Table 1), and formula adopted from bridge engineering [22] (Method 5 of Table 1). However, these models are either not updated for CLT panels or not valid for long-span composite systems over 9 m.

Assuming a CLT panel with 1200 mm in width and glulam beams with 175 mm in width, resulting in a clear space of 1025 mm (b_f), Table 1 shows the effective width of the CLT-glulam system evaluated following different methods.

Method 1 provides an upper boundary of effective width where in this case, the full width of the flange can be considered. The calibration factors in the method 3 were referred to [8]. The equivalent material properties of CLT panels used for method 4 were based on modal test results from [15]. A recent experimental study on the CLT-glulam systems [21] shows that an effective width of 80% of the original flange width is a more precise assumption. This is close to the results calculated by using method 4 and 5. Accordingly, in current research, the effective width of 3-ply CLT panels and 5-ply CLT panels were chosen as 960 mm.

The transformed cross-section approach was used in the calculation of the bending stiffness of the composite beam, following Eq. 1.

$$b'_{\text{glulam}} = \frac{E_{\text{glulam}}}{E_{\text{CLT}}} \times b_{\text{glulam}} \tag{1}$$

where b_{glulam} is the original glulam width; b'_{glulam} is the transformed glulam width; E_{glulam} is the modulus of elasticity of glulam; E_{CLT} is the modulus of elasticity of CLT panels based on [19] and is employed as reference.

Performed-based checks at ultimate and serviceability limit states were based on objective-based design requirements of NBCC 2020. Cross-section sizes of the slab and beams were optimized for minimal structural weight.

Table 1 The effective width results using different prediction models

CLT lay-up	Grade	Method 1 EC 5 (OSB)	Method 2 Advance OSB	Method 3 New EC5	Method 4 Möhler	Method 5 Bridge engineering
3-ply	E1M5	1200	992.71	612.16	989.06	/
5-ply	E1M5	1200	992.71	617.99	/	943.12

Note Unit in mm

2.4 Floor Design with Partial Composite Action

The gamma method included in the Eurocode 5 was used to size the elements of the flooring module, assuming calculated stiffness of the bamboo-based shear connectors used to join the slab to the beams. The gamma value was calculated using Eq. 2.

$$\gamma_i = \frac{1}{1 + \frac{\pi^2 E_i A_i}{l^2 k_{\text{core}}}} \tag{2}$$

where γ_i is the gamma value of the ith layer; E_i is the modulus of elasticity of the ith layer; A_i is the cross-sectional area of the ith layer; l is the span; k_{core} is the shear stiffness of the connection.

If mechanical fasteners are at constant spacing, k_{core} is calculated using Eq. 3.

$$k_{\text{core}} = \frac{k \times n}{s} \tag{3}$$

where k is the slip modulus of the individual connector; n is the number of connectors used along the span; s is the spacing between connectors.

The effective bending stiffness is calculated using Eq. 4.

$$(EI)_{\text{ef}} = \sum_i^n \left(E_i b_i \frac{t_i^3}{12} + \gamma_i E_i A_i a_i^2 \right) \tag{4}$$

where b_i is the width of the ith layer; t_i is the thickness of the ith layer; A_i is the cross-sectional area of the ith layer; a_i is the distance between the neutral axis and the centroid of the ith layer.

The deflection of partially connected flooring system is calculated using Eq. 5.

$$\Delta = \frac{5wl^4}{384(EI)_{\text{ef}}} \tag{5}$$

The recommended deflection limits under the service load combinations are $l/180$ and $l/360$ for 1.0 DL + 1.0 LL (Combo 1) and 1.0 LL (Combo 2), respectively. For a 12-m span flooring system, the maximum allowable deflections are 66.67 mm and 33.33 mm for combo 1 and combo 2, respectively.

2.5 Tenon Design

Figure 2 illustrates the mortise-tenon design. The material used for tenons is parallel strand bamboo (PSB). The width of the tenon is set as 70 mm which is 40% the total
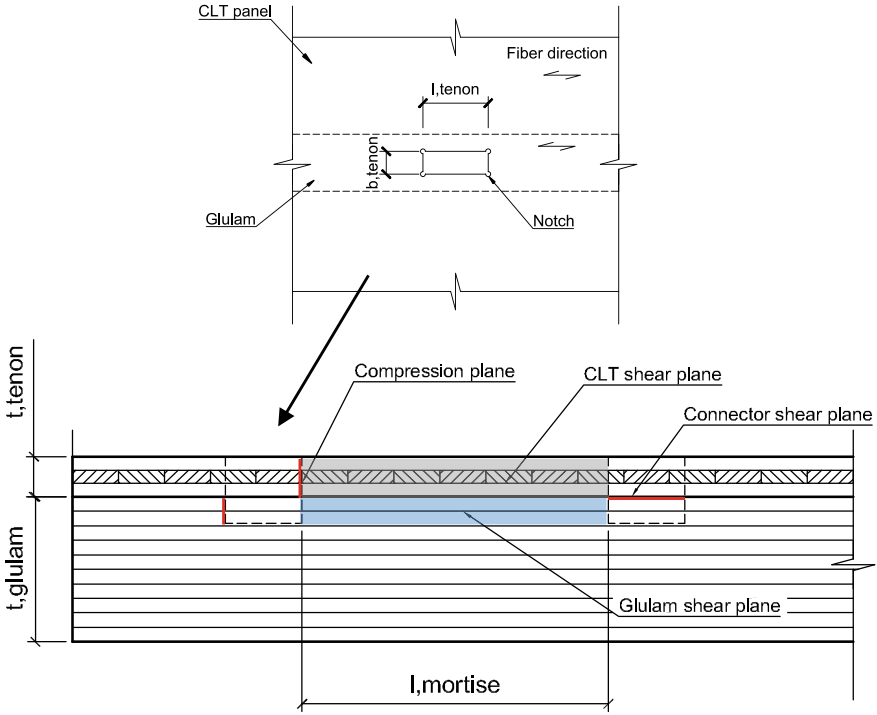
Fig. 2 Mortise-tenon design

width of glulam. Meanwhile, notches have been added to the mortise, i.e., on CLT panel and glulam ribs, to avoid local failure at the corners when installing.

Shear and compression failure can be expected depending on the geometry of the joint. The strength resistances of each component are expressed by Eqs. 6–8.

$$F_{R,\text{tenon}} = \min \begin{cases} F_{R,\text{tenon},c,\text{CLT}} = b_{\text{tenon}} \times t'_{\text{tenon}} \times f_c \\ F_{R,\text{tenon},c,\text{glulam}} = b_{\text{tenon}} \times t'_{\text{tenon}} \times f_c \\ F_{R,\text{tenon},v} = b_{\text{tenon}} \times l_{\text{tenon}} \times f_v \end{cases} \quad (6)$$

$$F_{R,\text{CLT}} = \min \begin{cases} F_{R,\text{CLT},c} = F_{R,\text{CLT},c,0} = b_{\text{tenon}} \times t_{\text{CLT},0} \times f_{c,\text{CLT},0} \\ F_{R,\text{CLT},v} = F_{R,\text{CLT},v,0} = 2 \times l_{\text{mortise}} \times t_{\text{CLT},0} \times f_{v,\text{CLT}} \end{cases} \quad (7)$$

$$F_{R,\text{glulam}} = \min \begin{cases} F_{R,\text{glulam},c} = b_{\text{tenon}} \times t'_{\text{tenon}} \times f_{c,0} \\ F_{R,\text{glulam},v} = F_{R,\text{glulam},v} = 2 \times l_{\text{mortise}} \times t'_{\text{tenon}} \times f_v \end{cases} \quad (8)$$

where $F_{R,\text{tenon}}$, $F_{R,\text{CLT}}$, and $F_{R,\text{glualm}}$ represent the resistance from single bamboo-based tenon, CLT and glulam, respectively. Only the longitudinal layer of CLT panel is considered in the calculation of the strength resistance of the CLT panel.
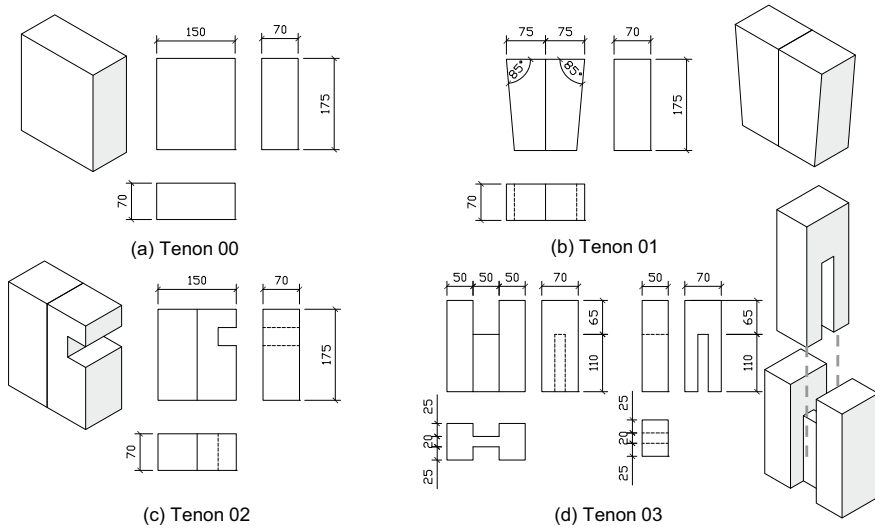
Fig. 3 Four bamboo-based tenon prototypes: **a** Tenon 00: original rectangular design; **b** Tenon 01: two-piece tenon with wedge profile; **c** Tenon 02: two-piece tenon with groove cut; **d** Tenon 03: two-piece tenon with half-tenons

The strength values of CLT and glulam were obtained from CSA O86:19 [9], while mechanical properties of PSB were taken from [17]. Bamboo-based tenons were placed with their faces perpendicular to the shear force direction. The length of tenons was in the range of 100–300 mm to inhibit brittle shear failure of wood members.

Four bamboo-based tenon prototypes were developed. Each solution had a specific shape as shown in Fig. 3, while dimensions of the tenon prototypes, i.e., length, width, and depth, were similar. Tenon 00 of Fig. 3a was manufactured as one piece of rectangular PSB. Tenon 01 of Fig. 3b was a two-piece wedged tenon assembly. Tenon 02 of Fig. 3c was a two-piece tenon assembly with one of the tenons had a groove cut. Tenon 03 of Fig. 3d was a tenon assembly consisting of two pieces of half-tenons.

3 Modeling Method

Numerical models of the four tenon prototypes were built in ANSYS Workbench [1]. The material properties of CLT panels and glulam were obtained from the Wood Handbook [12] referring to Table 5–1 for elastic properties, Table 2 for Poisson ratios. Material properties of bamboo tenon were obtained from [17]. The elastic properties of materials are listed in Table 2.

Table 2 Elastic properties of materials used in models

Member	Species	E_L	E_T	E_R	G_{LR}	G_{LT}	G_{RT}	μ_{LR}	μ_{LT}	μ_{RT}
		Mpa	Mpa	Mpa	Mpa	Mpa	Mpa	/	/	/
CLT panel	Spruce, Sitka	12,320	529.76	960.96	788.48	751.52	36.96	0.372	0.467	0.435
Glulam	Douglas-fir	14,960	748	1017.28	957.44	1166.88	104.72	0.292	0.449	0.39
Tenon	PSB	11,890	3066	3066	1361	1361	746	0.411	0.411	0.115

The global coordinate system is assigned with the *x*-axis, the longitudinal fiber direction, with *y*- and *z*-axis the radial and the tangential fiber directions, respectively. Glulam was modeled as one unite orthotropic material using the global coordinate system. CLT panels were modeled as three layers of orthotropic material bonded together. The top and bottom layers of CLT panels were in alignment to the global coordinate system. A local coordinate system was created with the global *y*-axis as the longitudinal fiber direction, the global *x*-axis, and the global *z*-axis as the radial and tangential fiber directions, respectively. The local coordinate system was assigned to the transverse layer of the CLT panel. The orientation of the tenon fiber was parallel to the global *y*-axis.

Figure 4 shows the as-built model of one-meter-long composite floor module. SOLID186 element was used with total elements number in the range of 13,256–13,506 depending on tenon profiles. The meshing size was set as 20 mm. Mesh quality was checked, with an average element quality of 0.9. Contact elements were used between mortise and tenon. The frictional factor was set as 0.5 for wood-to-wood friction [1].

The boundary conditions were applied to mimic monotonic push-out shear tests, see Fig. 5. The top surface of the CLT panel and the bottom surface of the glulam was restrained against out-of-plane displacements, and one end of the CLT panel was fixed. A 100 kN force was applied at one end of the glulam. To capture the load-slip response at specific applied force levels, i.e., 20, 40, 60, 80, and 100 kN, the results were calculated in 5 steps under static structural analysis. The contact elements were used, and the deformation on members was expected to occur; thus, the large deflection was turned on.

4 Results and Discussion

4.1 Stress Distribution

Figure 6 shows the von Mises stress distribution contours of four bamboo-based tenon models at 100 kN. Shear force is transmitted from the glulam to the CLT panel through the width of the tenon. There are more stress concentrations at the corner of the glulam and the CLT panel. The maximum stress appears on the left side of the

SOLID 186

Associated Target Surfaces

Contact Elements

Surface of Solid/Shell Element

Conta 174 (paired with Targe 170)
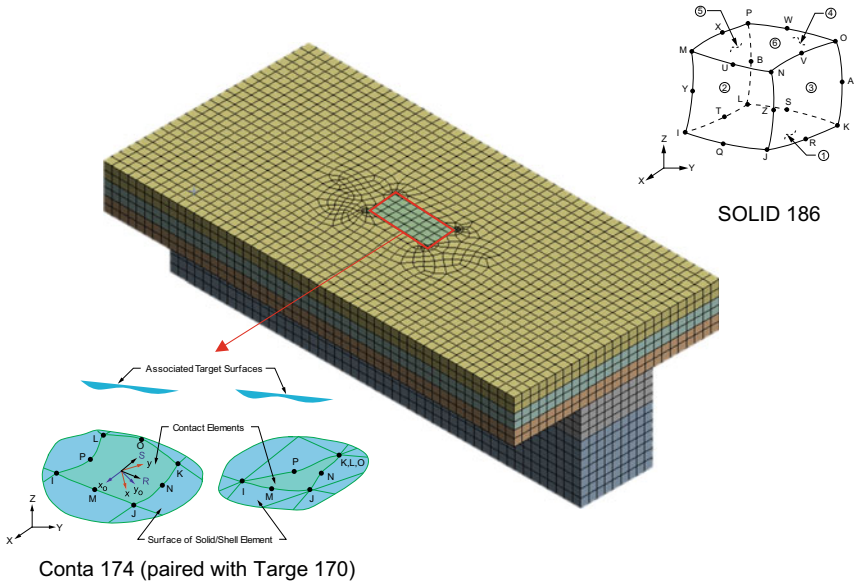
Fig. 4 Model in ANSYS workbench

CLT panel

Tenon

Glulam

Apply force
(surface effect)

Free displacement along X-axis
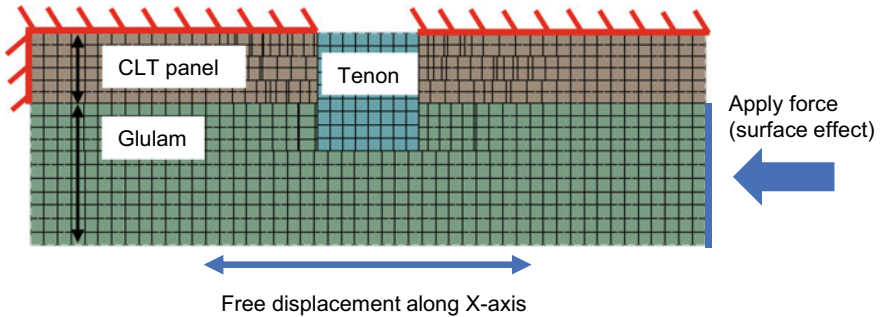
Fig. 5 Boundary conditions and the applied force

tenon at the interface. Slips between tenon parts were observed when applying two-piece assembly (Tenon01 and Tenon02). The stress distribution is slightly different among tenon prototypes. The wedged tenon has a clear stress distribution area in the upper layer of the CLT panel (Tenon01). Stress concentration is found in the tenon groove (Tenon02). When using the half-tenon assembly (Tenon03), the stress distribution is similar to the rectangular tenon (Tenon00); however, more significant deformation is observed on the glulam corner.

(a) Tenon 00

(b) Tenon 01

(c) Tenon 02

(d) Tenon 03
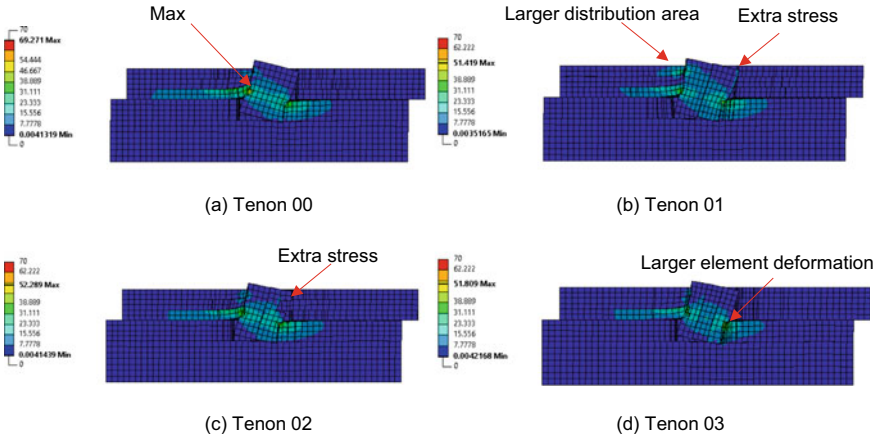
Fig. 6 Von Mises stress distribution contour

4.2 Extracted Load-Slip Response of Shear Connectors

The displacement at the opposite end of the glulam and the reaction forces from boundary conditions were collected and plotted as load-slip responses curves see Fig. 7. The stiffness results are close among prototypes, with an average value of 43.06 kN/mm. This latter is slightly higher than the average stiffness value of 32.89 kN/mm of LVL shear keys studied by Schmidt and Blaß [28].

The wedged tenon prototype has a different load-slip response at the initial stage compared to its relatives. Slipping and more significant rotation occurred on the tenon, see Fig. 8b.

Fig. 7 Load-slip responses

Moved slightly in the negative direction   Larger rotation

Slight slip between tenon assembly

(a) Tenon 00   (b) Tenon 01
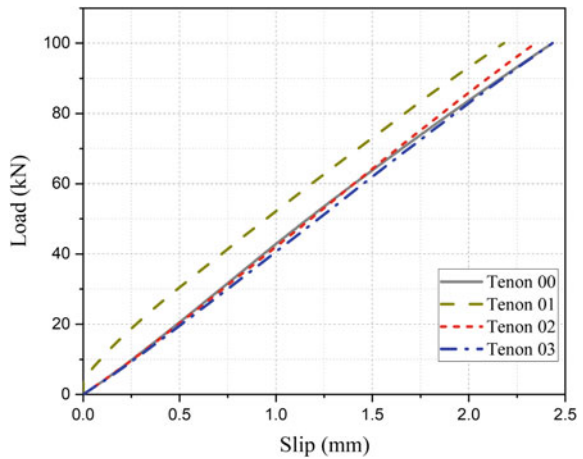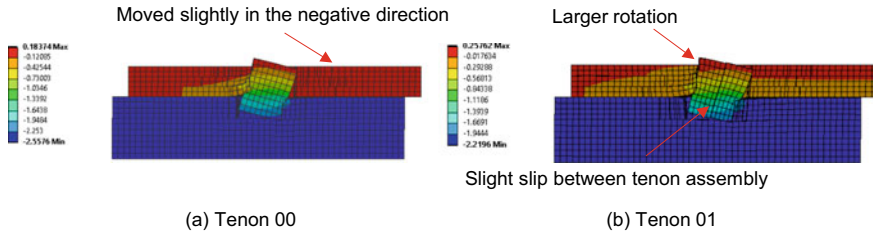
Fig. 8 Directional deformation contour

4.3 Floor Configuration for the Long-Span Application

Four composite floor configurations were designed in full composite action. Normal stress and shear stress results under full composite action are listed in Tables 3 and 4, respectively. Table 5 shows the mid-span deflection under different service load combinations.

The stress results show that the stress on timber components largely depends on the depth of glulam rather than the CLT panel configuration. Meanwhile, although all four types of floor configurations can meet the structural requirements, the deflection results are different. This indicates that the flexural performance under service loads governs the long-span composite flooring system design. It also aligns with other studies on the timber composite flooring system [25].

Table 3 Normal stress results

Floor configuration	Glulam depth	$\sigma_{CLT,center}$	$\sigma_{CLT,top}$	$\sigma_{glulam,center}$	$\sigma_{glulam,bottom}$
	(mm)	(Mpa)	(Mpa)	(Mpa)	(Mpa)
3-ply CLT panel system	342	4.49	7.10	7.56	17.27
	380	4.07	6.11	6.16	14.63
5-ply CLT panel system	342	2.73	5.51	7.67	15.28
	380	2.51	4.73	6.34	13.09

Table 4 Shear stress results

Floor configuration	Glulam depth	τ_{max}	$\tau_{interface}$	Shear flow
	(mm)	(Mpa)	(Mpa)	(N/mm)
3-ply CLT panel system	342	0.88	0.86	150.81
	380	0.80	0.78	136.61
5-ply CLT panel system	342	0.87	0.87	153.05
	380	0.80	0.80	140.59

Table 5 Deflection results

Floor configuration	Glulam depth	$\Delta_{1.0DL+1.0LL}$	$\Delta_{1.0LL}$
	(mm)	(mm)	(mm)
3-ply CLT panel system	342	58.37	21.41
	380	45.80	16.71
5-ply CLT panel system	342	45.43	15.57
	380	36.26	12.36

In addition, 3-ply CLT panel ribbed with 380 mm deep glulam and 5-ply CLT panel ribbed with 342 mm deep glulam, have the same structural depth and close mid-span deflections; however, the volume of one module of 3-ply CLT panel system and 5-ply CLT panel system is 4.62 m^3 and 6.48 m^3, respectively. As a result, the 3-ply CLT panel flooring system saves 28.66% of the material. Therefore, the 3-ply CLT panel floor configuration is a more economical solution for long-span applications.

4.4 The Joint Efficiency of Tenons

Table 6 lists the calculated stiffness values via finite element analysis and the corresponding gamma values. The gamma value indicates that the proposed tenon connection can provide sufficient stiffness for the composite system, in which case a near full composite action can also be assumed.

A comparison of mid-span deflection under full composite action assumption ($\gamma = 1$), partial composite action ($\gamma = 0.87$), and no composite action ($\gamma = 0$) is listed in Table 7. With no composite action, the 3-ply-based composite flooring system cannot satisfy the deflection requirement under $1.0\,DL + 1.0\,LL$ load combination. On the contrary, the fully connected system can meet the structural demand under the same load combination. Therefore, long-span composite systems with composite action are structurally more efficient. Moreover, the mid-span deflection results between the full and partial composite actions are close, with a difference of 4.3%.

Table 6 Stiffness results and corresponding gamma values

	(Unit)	Tenon 00	Tenon 01	Tenon 02	Tenon 03
k	(N/mm)	43.03	44.07	43.34	41.78
γ	/	0.87	0.87	0.87	0.87

Table 7 Deflection of the composite system at different composite level

Floor configuration	b_{flange}	b_{ef}	γ	Shear flow	$\Delta_{1.0DL+1.0LL}$	$\Delta_{1.0LL}$
	(mm)	(mm)	/	(N/mm)	(mm)	(mm)
3-ply system	1200	960	1	136.61	45.80	16.71
	1200	960	0.87	123.92	47.77	17.43
	1200	0	0	0.00	67.00	24.44

5 Conclusion

The following conclusions can be drawn:

- Compared to 5-ply CLT-glulam composite flooring systems, 3-ply CLT-glulam composite flooring systems require less material in achieving similar bending moment resistance; therefore, they are recommended for long-span applications;
- The numerical results show an average stiffness value of 43.06 kN/mm for bamboo-based tenons. The current investigated changes have no significant effect on the stiffness results. However, effect of manufacturing and installation tolerances on the behavior of connectors should be next studied;
- The interaction between mortise and tenon, i.e., between CLT panels and bamboo-based shear connectors, reduces the stress concentration on the interface;
- The proposed bamboo-based connection system is able to provide sufficient stiffness to the CLT-glulam composite flooring system. Although the partial composite action is assumed in design, the gamma value above 0.87 of such connection provides similar deflection results as the fully connected ones, suggesting simplifications as per full composite action.

Further work will include the optimization of the tenon design for fabrication and structural performance, testing of CLT-glulam joints with bamboo-based tenons and validation of the assumptions through full-scale bending tests of long-span timber composite floors.

References

1. Ansys® Academic Research Mechanical, Release 2021 R1, Ansys Innovation Courses, Contact Mechanics, ANSYS, Inc.
2. Bogensperger T, Moosbrugger T, Silly G (2010) Verification of CLT-plates under loads in plane. In: Proceedings of 11th world conference on timber engineering (WCTE2010), pp 885–898

3. Brown JR, Li M, Sarti F (2021) Structural performance of CLT shear connections with castellations and angle brackets. Eng Struct 240:112346. https://doi.org/10.1016/j.engstruct.2021.112346
4. CEN (2014) EN 1995-1-1:2004/AC:2006/A1:2008/A2:2014, Eurocode 5: design of timber structures—Part 1–1: General—common rules and rules for buildings. European Committee for Standardization (CEN), Brussels, p 2014
5. CEN (2018) CEN/TC 250/SC 5 N 892: M515 SC5.T1 phase 1 final deliverables—SC5.T1 final document of prEN 1995-1-1 on CLT. Brussels
6. Chen Y, Lam F (2013) Bending performance of box-based cross-laminated timber systems. J Struct Eng 139:04013006. https://doi.org/10.1061/(ASCE)ST.1943-541X.0000786
7. Claus T, Seim W (2018) Development of the multiple tenon timber connection based on experimental studies and FE simulation. Eng Struct 173:331–339. https://doi.org/10.1016/j.engstruct.2018.06.102
8. Christovasilis IP, Brunetti M, Follesa M, Nocetti M, Vassallo D (2016) Evaluation of the mechanical properties of cross laminated timber with elementary beam theories. Constr Build Mater 122:202–213
9. CSA Group (2019) CSA O86-19. Engineering design in wood. CSA Group, Toronto, Ontario, Canada
10. Design of Timber Structures, 2:2016 (ed) (2016) Swedish Forest Industries Federation
11. De Flander K, Rovers R (2009) One laminated bamboo-frame house per hectare per year. Constr Build Mater 23(1):210–218
12. Forest Products Laboratory (2021) Wood handbook—wood as an engineering material, U.S. ed
13. Frangi A, Fontana M, Hugi E, Jübstl R (2009) Experimental analysis of cross-laminated timber panels in fire. Fire Saf J 44:1078–1087. https://doi.org/10.1016/j.firesaf.2009.07.007
14. Gamerro J, Bocquet JF, Weinand Y (2020) Experimental investigations on the load-carrying capacity of digitally produced wood-wood connections. Eng Struct 213:110576. https://doi.org/10.1016/j.engstruct.2020.110576
15. Gsell D, Feltrin G, Schubert S, Steiger R, Motavalli M (2007) Cross-laminated timber plates: evaluation and verification of homogenized elastic properties. J Struct Eng 133:132–138. https://doi.org/10.1061/(ASCE)0733-9445(2007)133:1(132)
16. Gu M (2017) Strength and serviceability performance of southern yellow pine cross-laminated timber (CLT) and CLT-glulam composite beam. Dissertation for the Degree Doctor of Philosophy Civil Engineering. Clemson University
17. Huang D, Bian Y, Zhou A, Sheng B (2015) Experimental study on stress–strain relationships and failure mechanisms of parallel strand bamboo made from phyllostachys. Constr Build Mater 77:130–138. https://doi.org/10.1016/j.conbuildmat.2014.12.012
18. Jacquier N, Girhammar UA (2014) Tests on glulam–CLT shear connections with double-sided punched metal plate fasteners and inclined screws. Constr Build Mater 72:444–457. https://doi.org/10.1016/j.conbuildmat.2014.08.095
19. Karacabeyli E, Gagnon S (2020) Canadian CLT handbook. FPInnovations, Pointe-Claire, QC
20. Kesik T, Martin R (2021) Mass timber building science primer. Univerity of Toronto, CA, Mass Timber Institution
21. Kleinhenz M, Just A, Frangi A (2021) Experimental analysis of cross-laminated timber rib panels at normal temperature and in fire. Eng Struct 246:113091. https://doi.org/10.1016/j.engstruct.2021.113091
22. Masoudnia R, Hashemi A, Quenneville P, Asce M, Engineer S, Ipenz G (2018) Predicting the effective flange width of a CLT slab in timber composite beams. J Struct Eng 144(7):04018084
23. Möhler K (1956) Über das Tragverhalten von Biegeträgern und Druckstäben mit zusammengesetzten Querschnitten und nachgiebigen Verbindungsmitteln. Doctoral dissertation
24. Möhler K, Abdel-Sayed G, Ehlbeck J (1963) Zur berechnung doppelschaliger, geleimter Tafelelemente. Holz als Roh-und Werkstoff 21(8):328–333
25. Negrão J, Jorge L (2016) CLT structure for long span floors and roofs—optimizing the cross-section properties. In: 41st IAHS world congress: sustainability and innovation for the future. Albufeira, Algarve, Portugal, p 10

26. NRC (2020) National building code of Canada. National Research Council, Ottawa, Ont
27. Robeller C (2015) Integral mechanical attachment for timber folded plate structures
28. Schmidt T, Blaß HJ (2016) Contact joints in engineered products. In: WCTE 2016—world conference on timber engineering, p 8
29. Sharma B, Gatóo A, Bock M, Ramage M (2015) Engineered bamboo for structural applications. Constr Build Mater 81:66–73. https://doi.org/10.1016/j.conbuildmat.2015.01.077
30. Thiel A, Brandner R (2016) ULS design of CLT elements—basics and some special topics. In: Cross laminated timber—a competitive wood product for visionary and fire safe buildings: proceedings of the joint conference of COST actions FP1402 & FP1404 KTH building materials, 10 Mar 2016, p 23
31. Dangel U (2016) Turning point in timber construction: a new economy. Birkhäuser

Comparative Life-Cycle Assessment (LCA) Analysis of Timber and Reinforced Concrete Multi-story Buildings. State-of-the-Art Review

Laura Corti, Giuseppe Di Nunzio, and Giovanni Muciaccia

Abstract Being the building sector responsible of 30–40% of total greenhouse gases' emissions and being some administrations (e.g., EU and Canada) targeting net-zero carbon emissions by 2050, a proper assessment of building sustainability is no more an option but an essential requirement. To the scope, Life-Cycle Assessment (LCA) analysis results an unavoidable tool to be adopted during building design process: by carrying out targeted sensitivity analysis on different aspects (e.g., materials, geometry, construction techniques), the optimal solution may be identified. To the scope, LCA cradle-to-grave analysis should include all the processes involved in building construction, use and decommissioning, in order to provide relevant and robust results through a comprehensive approach. Existing literature is reviewed highlighting, for those aspects that generally represent standardized analysis steps, items that naturally involve uncertainties in their estimation. Strengths and weaknesses in current estimation procedures are identified and discussed, to the scope of guaranteeing the reliability of Life-Cycle Assessment as a tool to evaluate sustainability of building works. It is found that Operational Energy Use phase (commonly referred to as B6) is generally disregarded or estimated as a given constant value, disregarding that operational energy, which contributes in a significant way to GWP emissions of the whole structure, may be highly influenced by the specific material or construction system. Additionally, other phases of stage B should require specific attention as seismic strengthening, service life extension, renovation, considering their remarkable contribution to emissions and their high values of embodied energy. Finally, such aspects also impact on End-of-Life (D) Phase, which again is analyzed by low-standardized methods.

Keywords Life cycle assessment · Timber and reinforced concrete · Multistorey buildings

L. Corti (✉) · G. Di Nunzio · G. Muciaccia
Department of Civil and Environmental Engineering, Politecnico di Milano, Milan, Italy
e-mail: laura.corti@polimi.it

1   Introduction

The evaluation of environmental impact of man-made products in terms of emissions plays a key role in the current context of climate change. Such issue gains an even more key role if considering that the building sector is responsible of nearly 40% of greenhouse gases emissions and 50% of extracted materials [1]. Considering that climate change, unfortunately, is not stopping, the implementation of measures to mitigate catastrophic effects is urgent and cannot be postponed. Within this framework, the use of Life-Cycle Assessment (LCA) analysis during early design phase of a building is the tool to quantitatively assess materials, energy and related environmental impact [2, 3].

A solution that in the last years is receiving more attention may lie in timber (or hybrid timber-concrete) buildings [4], as many advantages are provided, starting from reduced construction times [5], lower values of embodied carbon [6, 7] and better behavior in case of seismic action [8]. To prove the effective sustainability of such solution, it is necessary to quantify the benefits of a timber vs. conventional reinforced concrete buildings: comparative LCA seems to be the eligible tool to compare different proposals, by assessing emissions for each phase and detecting strengths and weaknesses of each construction system. A building is then analyzed according to the scheme presented in Table 1, where life stages are individually treated.

Nowadays, assessment of (comparative) LCA is provided with some common guidelines with regard to more straightforward stages, while other steps of the analysis are less standardized [10]: One of the aims of this paper is the identification of LCA shortcomings through analysis of targeted literature dealing with comparative LCA between timber and RC buildings. Moreover, comparison of quantitative outcomes of papers presenting comparative LCA is provided, in order to weight methodological uncertainties and environmental impact of every stage.

2   Methods

The proposed methodology considers first a literature review, aiming to collect a database concerning comparative LCA of timber and RC multi-story buildings. Selection criteria are: the existence of a comparison between timber and RC buildings, a focus on current open issue of LCA methodology (when applied to such construction system) and a comprehensive assessment of different LCA stages.

Papers including explicit numerical estimations in terms of comparative LCA are selected and summarized and weights of each stage is presented. This type of analysis provides multiple benefits: Not only numerical outcomes can be directly compared, but methodological shortcomings can also be identified. In particular, concerning the first task, comparisons among buildings with different structural system are carried out, where results from LCA analysis support identification of specific criticalities

Table 1 LCA stages according to [9]

Building Life-Cycle Assessment stages according to [9]

Product			Construction		Use stage						
A1	A2	A3	A4	A5	B1	B2	B3	B4	B5	B6	B7
Raw material supply	Transport	Manufacturing	Transport	Construction	Use	Maintenance	Repair	Replacement	Refurbishment	Operational energy use	Operational water use

Benefits and loads beyond the system boundary

Building Life-Cycle Assessment stages according to [9]

End of life				D
C1	C2	C3	C4	
Deconstruction Demolition	Transport	Waste processing	Disposal	Reuse–Recovery–Recycling potential

from environmental point of view. On the other hand, comprehension of less investigated stages is the key for a further step where methodological weaknesses are thoroughly explored. It is worth mentioning the key role covered by comparative LCA [11]: This tool is more powerful than LCA, as it provides information to compare building relatively, even if through more cumbersome and longer procedures; it is fundamental to carry out the analysis with similar buildings that, apart from obvious and necessary differences (e.g., the structural system, the construction techniques, the maintenance routines), make the comparison profitable and reliable.

The second step deals in a more specific way with LCA challenges. Since benefits of comparative LCA are highlighted, it is necessary to focus on critical stages that still need to be deeply investigated or that are difficult to be examined with standard procedures [12, 13]. Finally, stages, where methodological weaknesses are tougher than strengths and their environmental burden is significant, are analyzed in specific sections, where historical reasons of limited investigations are provided and the most recent solutions are examined.

It is worth stressing that results are summarized in terms of Global Warming Potential (GWP, measured in kg CO_2 eq.), not accounting for other impact indicators (as, e.g., ozone depletion, acidification, eutrophication) as it is the most widespread and internationally employed index [14, 15] and so a wider comparison among existing literature results is feasible. In this way, even if outcomes in terms of GWP are representative for several impact indicators, some effects on the environment are not considered.

3   Results

In this chapter, findings of the research are outlined, following the method explained in the previous section.

3.1   Comparison of Stages' Weights in Comparative LCA Analysis and Identification of Critical Steps

In order to provide a profitable review of comparative LCA analysis, Table 2 reports, for some selected articles, a brief description of their scopes and of their main outcomes.

After highlighting the main focus of each paper, a quantitative summary of each stage is carried out, as presented in Table 3. Whenever data are not available, a bar line is inserted and the relevant phase is simply disregarded in the final computation. However, such phase should represent a significant environmental burden, and such aspect is addressed later in Sect. 3.2.

Table 2 References for summary of LCA stages' weights according to literature

References	Brief description	Results
[16]	Comparison of a CLT building with an equivalent RC one located in Portland (USA) through a complete cradle-to-grave LCA analysis and a specific focus on stage D	Stage D is the key point for the CLT building, where negative values of emissions in terms of kg CO_2 eq. are recorded. On the other hand, during construction phases, timber manufacturing produces higher values of CO_2 emissions
[17]	Comparison of steel and mass timber buildings with two different heights in Seattle (USA). In this case, stage B is disregarded, while a special focus is devoted to stage D	Timber sustainability is treated in a critical way: This material cannot be considered more sustainable a priori, as, e.g., forest regrowth and appropriate End-of-Life directives should be followed
[18]	Comparison of two solutions concerning residential building in Auckland (NZ): Light steel and light timber frames are analyzed considering a comprehensive cradle-to-grave LCA analysis	Both the two buildings ensure high environmental performance, in particular when stage D is accounted for: This outcome confirms that even more traditional buildings may have a lower impact when End-of-Life phase is properly addressed
[19]	Comparisons of RC and CLT solutions located in Chongqing (CN), focusing just on stage A, with investigations on phase A4, in particular for timber when it is imported from abroad	The predominant environmental impact comes from phases A1–A3 for both the two buildings, and in broad terms, the CLT solution results better environmentally efficient (GWP is 25% less than RC building)
[20]	Comparison of hybrid (timber and concrete) building with two equivalent ones made respectively by concrete and timber, located in Helsinki (FI) in a comprehensive cradle-to-grave LCA analysis	Integration of hybrid solution allows investigation of an intermediate step between RC and timber frames: even if the overall most convenient performance is associated with timber building, the hybrid one exhibits excellent performances in A, C and D stages. In this way, more rational use of wood in hybrid buildings is assessed
[21]	Comparison of two solutions for multi-story residential buildings, the first one in MT and the other one in RC in Santiago (CL), disregarding stages B (apart from B6) and C	System boundaries extend from raw material extraction to building use, with special addressing to stage D for MT solution; in this case, operational energy use is studied, with a remarkable lower value for the timber building. Stage D (carbon stock) is considered in such a way that A-to-D LCA analysis in MT case exhibits negative values of GWP
[22]	Comparison of RC and CLT equivalent buildings located in Northern Italy (IT), in general terms	CLT solution exhibits the lowest environmental impact, as a result of several advantages gained during all the life-cycle phases, as long as a correct forest management in the site where wood is sourced, is provided

<div align="right">(continued)</div>

Table 2 (continued)

References	Brief description	Results
[23]	Comparison of five solutions for apartment buildings in Czech Republic (CZ): two hybrid (timber-concrete) solutions, CLT, RC and masonry	Results are reported concerning the overall analysis, by classifying the CLT solution as the most environmentally friendly but considering that it is not allowed by Czech fire regulations, the two hybrid options result the less impactful in terms of GWP
[24]	Comparison of RC and CLT solutions for high-rise residential buildings in Vancouver (CA), considering in general terms A, B (except B6 and B7) and C stages	Results confirm expectations in terms of lower impact of MT solution, whereas some difficulties arise from limited literature on LCA applied to CLT structures and absence of a common method for energy accountings
[25]	Comparison of four solutions for three-story university building in Nelson (NZ): RC, steel, timber and low-energy timber	The two timber buildings exhibit the lowest overall environmental impact, with valuable lower values also regarding operational energy use. The same analysis is carried out also in a future scenario, where significant improvements are foreseen concerning the End-of-Life stage for all solutions
[26]	Comparison of MT and RC solutions for single-family houses in Montevideo (UY) in a comprehensive cradle-to-grave LCA analysis	In this assessment, timber carbon stock is accounted in stage A, so it exhibits a CO_2 emission and more in general lowers environmental impact compared to the equivalent RC building. The timber solution on the other hand exhibits tougher footprint concerning B2–B4 stages, due to more frequent needing, for e.g., maintenance and replacement
[27]	Comparison of CLT and RC options for apartment buildings in Trondheim (NO), disregarding C stage	In this case, considering A-to-C stages, the CLT building exhibits greater emissions compared to the RC solution, while, when stage D is also accounted, the situation is reversed
[28]	Comparison of RC and CLT for apartment buildings in Trondheim (NO), disregarding stages B (except for B6), C and D	Outcomes highlight better performance of CLT building, mainly thanks to lower impact during the Product (A1_A3) stage
[29]	Comparisons of conventional RC—commercial building in Melbourne (AU)—and timber—commercial and residential building in London (GB) adapted for Australian code due to unavailability of a real case—solutions. In this case, just stage A is considered	Timber building shows lower environmental impact for every stage studied (A1, A2, A3, A5), but it is worth highlighting that transportation would need a more precise assessment, related to real-case investigations

Table 2 (continued)

References	Brief description	Results
[30]	Comparison of three solutions for mid-rise commercial buildings in Seattle (USA): two hybrid CLT (respectively, with fireproofing and charring design) and RC options are assessed for a cradle-to-gate analysis	Although two hybrid CLT solutions perform the best environmental results, it is worth mentioning that just for stage A4 the RC building exhibits significantly lower values of emissions thanks to the fact that difficulties linked, e.g., with fixed routes are avoided, due to short distance to the construction site

Stage A is generally the most thoroughly developed, as the large number of papers focusing on such analysis confirm. Both for RC and timber buildings, the product stage is the more significant, as its weight is generally at least 80% of the total, with many cases rising to 90%. It is noted that the construction process stage of timber building, which includes transport to the construction site, may be significantly heavier than the same stage in a common RC building; this issue should be carefully considered for each specific case, as the site where the building is located plays a key role [19, 31]. In order to clarify this concept, it is worth considering [20], where in the former case timber is from the same region, while in the latter it is imported from abroad. A deeper investigation on A4 stage is presented in Sect. 3.2.1.

Works dealing with a deeper investigations and comparisons concerning stage B are very limited, mainly for two reasons: (1) B6 and B7 stages are often considered constant as they are defined independent on the structural system and (2) stages B2–B5, when accounted, are never computed all and separately, possibly due to their costly and time-consuming features. Concerning stage B the most evident observation is the almost totally dependence on the operational energy use (B6) stage (B6 and B7 are generally considered jointly, with the exception of one case [18], where B7 was analyzed separately). It is known that operational energy use has a very strong impact in terms of environmental burden, but on the other hand due to abovementioned issues in B2–B5 stages, the real weight of the package B2–B5 stages is actually unknown. Stages B2–B5 and B6–B7 are examined in Sect. 3.2.2 and Sect. 3.2.3, respectively; stage B1 is not analyzed due to its lower environmental impact, with respect to other stages of phase B.

Concerning stages C and D, it is not possible to provide detailed surveys as for previous stages, due to lack of data; so more general remarks are provided. Stage C has not a crucial weight and no evident differences are recorded between timber and RC buildings. Even if it is not straightforward to distinguish weight of every single phase, there is an established market that sets precise requirements which must be followed, e.g., for disposal, collecting specific data, for the specific case, does not represent an issue. On the other hand, stage D exhibits great variability in terms of kg CO_2 eq. subtracted from the environment by timber: so the absence of common rules and standardized procedures is a true, as it will be discussed in Sect. 3.2.4. Furthermore, the potentially positive impact of a proper evaluation of this stage is

Table 3 LCA stages' weights according to literature

| # | Type | % contribution of each LCA stage (GWP—CO$_2$ eq.) | | | | | | | | | | | | | | | | | Total (A to C) (10^6 kg CO$_2$ eq.) | Total (A to D) (10^6 kg CO$_2$ eq.) |
		A1	A2	A3	A4	A5	B1	B2	B3	B4	B5	B6	B7	C1	C2	C3	C4	D		
[16]	RC	7.14	0.08	with A1	0.31	0.29	–	0.13	–	with B2	–	91.76	–	0.38	0.1	with C1		0.03	2.55E + 01	2.55E + 01
	MT	5.10	0.14		0.06	0.20	–	0.24	–		–	93.23	–	0.39	0.09			−4.18	2.51E + 01	2.40E + 01
[17]	Five-story S	90.00			6.00		–							4.00				−5.27	1.35E + 00	1.28E + 00
	Five-story MT	83.00			9.00		–							8.00				−112	9.99E−01	−1.41E−01
	Twelve-story S	90.00			6.00		–							4.00				−3	4.59E + 00	4.46E + 00
	Twelve-story MT	83.00			9.00		–							8.00				−103	3.15E + 00	−8.40E−02
[18]	LT	15.97			3.40		–	8.06	–	with B2	–	57.77	10.50	4.43				−5.13	1.39E−01	1.32E−01
	LS	27.44			18.25		–	8.65	–		–	49.33	10.90	1.59				−9.01	2.59E−01	2.39E−01
[19]	CLT	86.68			11.80	1.56	–	–	–	–	–	–	–	–	–	–	–	–	7.80E−02	–
	RC	85.44			11.62	2.93	–	–	–	–	–	–	–	–	–	–	–	–	1.04E−01	–
[20]	Hybrid	31.05			0.88	2.85	3.96					58.57	–	2.70				−12.91	1.30E + 00	1.13E + 00
	RC	31.71			1.06	2.87	3.97					58.24	–	2.22				−9.36	1.29E + 00	1.17E + 00
	MT	24.12			0.42	3.05	5.13					63.62	–	3.67				−20.25	1.22E + 00	9.69E−01
[21]	MT	68.48			2.90	5.11	–	–	–	–	–	23.32	–	–	–	–	–	−309	1.84E−01	−3.85E−01
	RC	45.77			1.27	0.20	–	–	–	–	–	52.82	–	–	–	–	–	–	4.96E−01	–
[22]	CLT	–	–	–	–	–	–	–	–	–	–	–	–	–	–	–	–	–	1.84E−01	–
	RC	–	–	–	–	–	–	–	–	–	–	–	–	–	–	–	–	–	2.82E−01	–
[23]	Hybrid 1	–	–	–	–	–	–	–	–	–	–	–	–	–	–	–	–	–	3.30E + 00	–

(continued)

Table 3 (continued)

#	Type	% contribution of each LCA stage (GWP—CO₂ eq.)																	Total (A to C) (10⁶ kg CO₂ eq.)	Total (A to D) (10⁶ kg CO₂ eq.)
		A1	A2	A3	A4	A5	B1	B2	B3	B4	B5	B6	B7	C1	C2	C3	C4	D		
	Hybrid 2	–	–	–	–	–	–	–	–	–	–	–	–	–	–	–	–	–	3.45E+00	–
	RC	–	–	–	–	–	–	–	–	–	–	–	–	–	–	–	–	–	4.02E+00	–
	Masonry	–	–	–	–	–	–	–	–	–	–	–	–	–	–	–	–	–	3.87E+00	–
	CLT	–	–	–	–	–	–	–	–	–	–	–	–	–	–	–	–	–	2.25E+00	–
[24]	CLT	–	89				–	3				–	–	8				–	–	–
	RC	–	93				–	1				–	–	6				–	–	–
[25]	RC	13.20			0.93	–	–	2.66	–	–	–	82.07	–	1.14	–	–	–	–	2.90E+00	–
	S	17.20			0.69	–	–	2.64	–	–	–	83.88	–	-4.44	–	–	–	–	2.88E+00	–
	MT	1.24			0.64	–	–	2.87	–	–	–	88.53	–	6.71	–	–	–	–	2.65E+00	–
	MT low e	0.60			0.64	–	–	1.92	–	–	–	70.46	–	8.36	–	–	–	–	2.13E+00	–
[26]	RC	17.47			3.74	4.92	–	11.45			–	55.84	–	2.13	2.33	–	2.14	–	8.42E-01	–
	MT	–13.00			5.09	6.02	–	41.57			–	56.61	–	0.40	0.60	–	2.73	–	4.77E-01	–
[27]	CLT	37.07			–	0.23	-2.80	–	–	17.49	–	48.26	–	–	–	–	–	-50.59	4.29E+00	2.12E+00
	RC	46.27			–	0.30	-6.35	–	–	13	–	46.88	–	–	–	–	–	-13.91	3.31E+00	3.31E+00
[28]	RC	39.01			1.45	–	–	–	–	–	–	59.34	–	–	–	–	–	–	1.90E+00	–
	CLT	33.59			2.89	–	–	–	–	–	–	63.44	–	–	–	–	–	–	1.66E+00	–
[29]	RC	58.13	14.16	6.67	with A2	21.04	–	–	–	–	–		–	–	–	–	–	–	8.96E+00	–
	MT	49.07	15.95	6.79	with A2	28.19	–	–	–	–	–		–	–	–	–	–	–	6.08E+00	–
[30]	Hybrid CLT 1	75			6	19	–	–	–	–	–	–	–	–	–	–	–	–	3.57E+00	–
	Hybrid CLT 2	86			6	8	–	–	–	–	–	–	–	–	–	–	–	–	3.51E+00	–

(continued)

Table 3 (continued)

#	Type	% contribution of each LCA stage (GWP—CO_2 eq.)																Total (A to C) (10^6 kg CO_2 eq.)	Total (A to D) (10^6 kg CO_2 eq.)
		A1	A2	A3	A4	A5	B1	B2	B3	B4	B5	B6	B7	C1	C2	C3	C4	D		
	RC	92			1	7	–	–	–	–	–	–	–	–	–	–	–	–	4.82E + 00	–

Fig. 1 Investigation on
phases weights of stage A
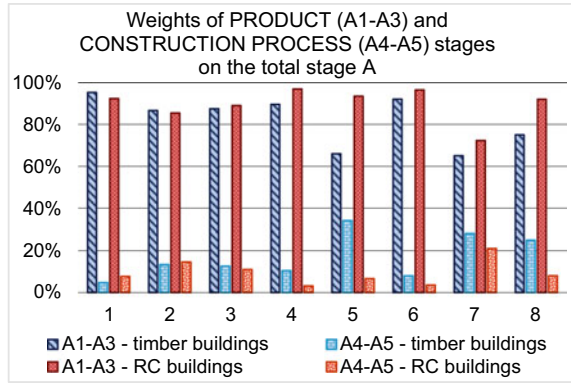
also a function of decisions taken during the construction stage and—even before—
at the level of choice of raw materials (in particular for timber it is crucial to consider
its origin and be aware of reforestation regulations [32]). It is worth mentioning that
benefits originated in this stage are not always evident through a cradle-to-grave
analysis, whereas they are better evaluated in a cradle-to-cradle analysis.

Figure 3 aims to provide a comprehensive overview of the role of each stage, by
providing individual weights. It is noticed how total emissions evaluated as kg CO_2
eq. are always governed by the Use (B) stage, followed by Product and Construction
Process (A) stage. Concerning timber buildings, stage B assumes an even more
important role, as their maintenance is considerably more expensive with respect to
an equivalent RC building in order to guarantee an adequate service life. The very low
impact of stage C is confirmed, while methodological problems affecting stage D do
not allow accurate evaluations, apart from a remarkable impact for timber buildings.

Fig. 2 Investigation on
phases weights of stage B
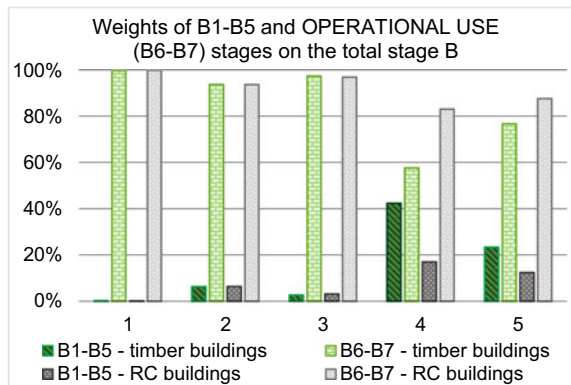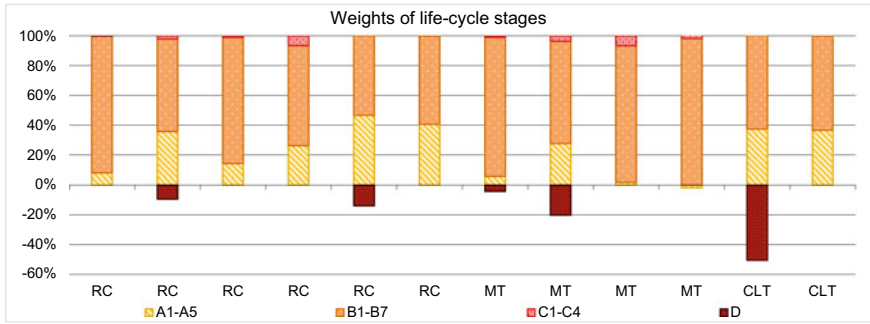
Fig. 3 Comparison of life-cycle stages' impact (indicator: GWP—kg CO_2 eq.)

3.2 Examination of LCA Critical Stages

Some of intrinsic LCA criticalities were addressed in Sect. 3.1; the following ones will deal with a more detailed assessment of strengths and weaknesses of each stage. Strength and weaknesses are identified with reference to methodological procedures, also accounting for the findings of Sect. 3.1 as regards environmental impact: In this way, the focus is targeted on those stages that, jointly with lacks in the existence of consistencies of standardized evaluation procedures, are characterized by high values of GWP emissions.

Table 4 is the benchmark that points out the most important features of every stage, and it introduces detailed discussion of following Sections.

3.2.1 Stage A4

This phase generally plays a marginal role if compared to other stages (e.g., B6), but it might be relevant, especially for timber buildings, when wood is imported from abroad or in general in all the cases where the materials are not locally produced [38]. So, when distance from extraction point to construction site becomes considerable, the practice of deepening this phase should be implemented. First of all, the need for specific data is extremely crucial, with additional information concerning the planned itinerary, different transport systems, in order to carry out comparisons with other phases of stage A. It may result that Transport stage emissions are higher that its Product stage [39], so in these cases it may be beneficial to develop furtherly the analysis and to investigate alternative solutions. According to [31] in Table 5, the information to be provided in case of long travel distances is listed.

3.2.2 Stages B2, B3, B4, B5

These stages are often evaluated jointly, with the result of providing unclear feedbacks that are difficult to be associated with a specific phase. From the authors' perspective, these steps should be distinguished, as different approaches are required. For

Table 4 LCA stages—strengths and weaknesses

Stage	Strengths (known parameters and established procedures)	Weaknesses (unknown parameters and low-standardized methods)
A1—Raw material supply A2—Transport A3—Manufacturing	• Data provided in the Bill of Materials (BoM)	• Transportation data are generally unknown
A4—Transport	• Distance extraction point—construction site	• Transportation data are generally unknown (e.g., transport systems, shipment from abroad) • Assumptions made on best guesses and most likely scenarios [9]
A5—Construction-installation process	• Use of equipment and machinery is well-established	• Whenever (rarely) information is not available scenarios are adopted
B1—Use	• Data related to this phase require a little effort	• Difficulties due to non-unique methodology • Lack of data, as emissions during use are disregarded or accounted, e.g., in EoL phase
B2—Maintenance	• Scheduled maintenance is generally well defined • Not significant weight over short (e.g., 50 years) lifespans [33]	• Great discrepancies as results of different calculation methods, building energy performance and assumptions on future scenarios [33] • Need for clarity on distinction among stage B phases
B3—Repair	• Number of repair situations that will arise during building life are accounted through formulation of potential scenarios	• Uncertainties due to unpredictable damages • Need for quantification of repair materials, energy consumption and broken components management [34]

(continued)

Table 4 (continued)

Stage	Strengths (known parameters and established procedures)	Weaknesses (unknown parameters and low-standardized methods)
B4—Replacement	• Scheduled maintenance is generally well defined • Not significant weight over short (e.g., 50 years) lifespans [33]	• Great discrepancies as results of different calculation methods, building energy performance and assumptions on future scenarios [33] • Uncertainties linked with the studied period about elements to be maintained or replaced
B5—Refurbishment	• Recent interest for this stage	• Necessity to focused studies on B5 stage (often included in B2, B3 or B4 stages) [35] • Uncertainties due to unpredictable issues • Necessity for studies on building retrofitting (e.g., seismic strengthening)
B6—Operational energy use B7—Operational water use	• Sensitivity analysis performed in the early design phase allows comprehension of parameters affecting operational energy and water uses	• Often disregarded as considered independent on the structural system or at least treated as constant inputs • Need for accurate local data and parameters
C1—Deconstruction demolition C2—Transport C3—Waste processing	• Specific data are usually not difficult to be collected	• Difficulties in predicting accurate future scenarios [36]
C4—Disposal	• Generally precise technical requirements are established thanks to existing market	• It may suffer of lack of data as sometimes the system boundary is set at stage C2 or C3
D—Reuse, recovery, recycling potential	• Precise assessment allows new chances for waste	• Simplified assumptions • Lack of data and methodologies [37] • Effective implementation of reuse or recycling procedures

Table 5 Transportation information to be provided in case Transport stage (A4) is relevant

From	To	Distance	Transportation system	# Means of transport
City (country)	City (country)	[km]	E.g., ship [km] + truck [km]	E.g., containers [#] + trucks [#]

instance, when considering Repair and Replacement, the former deals with unexpected management of damaged portions, while the latter is generally a planned action to be scheduled for such components whose building life is shorter than service life of the entire building. Hence, these two stages should be analyzed through separate approaches, possibly providing for Repair more than one future scenario (as causes and consequences of damages may be different) [33].

It is also worth addressing Refurbishment on its own as different interpretations exist for this phase: this stage encompasses stages B2–B3 and it may involve a portion or the complete building. In particular, in existing standards, the second option is not thoroughly addressed [40], even if some recent researches suggested refurbishment as a valuable alternative to demolition and reconstruction, so treating this stage as stage A plus stage C (in order to take into account waste processing of the old building) [34, 41–43].

In broad terms, these stages are strictly linked with the foreseen structural behavior, function of choices taken during the design process: In this way, the early design phase plays a key role in determination of measures to be adopted during building life [9]. In conclusions, a lack of literature dealing with experimental investigations is found for these stages: currently, stage B5 is never accounted in the papers reported in Table 2, revealing need for common rules to guarantee comparable methods.

3.2.3 Stages B6 and B7

Difficulties related to these stages are complex as different issues are simultaneously faced:

- Stage B6 is generally taken into account (Table 3), even if it is generally the result of many assumptions and approximations considered as independent on the building structural properties [16]. Recent studies proved that also in this case, the early design phase assumes a crucial role in guarantying low operational energy emissions [44, 45], even if some optimization should be accurately planned in order to avoid counter-productive environmental effects [46, 47].
- Operational Energy Use in comparative LCA analysis is occasionally assumed as a constant value for buildings with different structural frames (e.g., for RC and timber buildings) [16]. Most of the case studies consider structural differences and non-structural components [18, 20] that actually lead to some gaps which are generally around 5%, even if they may result much more relevant, as in [21], where timber and RC buildings are investigated and their B6 stage weighs respectively 23% and 53% on the total A-to-C building emissions
- On the other hand, stage B7 is rarely considered (just in one study case—[18]—Operational Water Use has been assessed from papers selected in Table 2) for different reasons, as lack of awareness on the relevance of such stage [12], lack of specific assessment data [16] and the fact that B7 it currently not accounted as an indicator of environmental impact [15]. Actually, also in this case, if considering

environmental impact of a building in broader terms and to make LCA analysis an even more complete tool toward sustainability [48], stage B7 should not be disregarded at all, taking into account reduction of water consumption, decrease of wastewater treatment through methods based on site-specific data [49].

- Stage B6 holds an undeniable leading role in contribution to building emissions, as results collected in Table 3 confirm: Its percentage on the overall GWP emissions is approximately 75%, with several peaks of more than 90%; it is fundamental to consider data as precise as possible, because even minor inaccuracies turn out to be eventually not negligible [50].

In light of these outcomes, also considering a more recent conception of buildings' sustainability by overpassing LCA traditional boundaries, sensitivity and uncertainty analyses should be carried out to estimate consequences and impact of different parameters [51].

3.2.4   Stage D

This step is generally considered as an optional one, outside of conventional system boundaries (Table 1), reflected in the limited number of papers (Table 3) addressing it (only 6 out of 15). So, Beyond Life stage suffers of simplified assumptions and lack of data, also due to realistic difficulties in predicting methods and practices which will be available at the end of building service life, at least 50 years after building construction [17]. Nonetheless, an adequate assessment of this stage may contribute to diminish building emissions in a consistent way, in particular it is the key to correctly compare timber and RC buildings, as great advantages for the first one arise from this stage [52, 53].

Moreover, stage D is the starting point for step forward from cradle-to-grave LCA analysis to cradle-to-cradle assessment to truly assess the sustainability of the entire process, with a continuity in Reuse, Recovery and Recycling potential between old and new buildings. Waste recycling from building End-of-Life, apart from economical workability, provides environmental benefits that involve not just the building in demolition [54], but also impacts on parameters hard to encase in traditional LCA as, e.g., avoided landfilling of materials preventing land use [55] and resource consumption avoidance by raw material extraction and processing [56].

In conclusion, a more integrate use of LCA is desirable, where this tool is adopted in a broader and more comprehensive way accounting for every factor that may result in an environmental benefit or drawback.

4 Discussion and Conclusions

This review paper provides a state-of-the-art of current milestones in comparative LCA analysis, focusing on phases deemed critical both in terms of applied methodology and environmental impact. The obtained results emphasize that through a wise timber use, a greater sustainability may be achieved by adopting a timber-based solution. A key role is played by stage D, where effective benefits are detectable in case an accurate planning is carried out; on the other hand, when these solutions are not accounted during the early design phase, they will hardly be implemented later, due to technical difficulties, e.g., in disassembling the building without damaging members to be reused.

Considering stages B2–B5, they generally weigh naturally more in a timber than in a conventional RC building: Careful planning of maintenance and replacement over the lifespan is the key to guaranteeing not only structural safety, but also to avoid an excessive increase environmental cost of this stage.

This study allows an overview of several literature investigations from different countries, so considering different local specific data: standardization of some procedures is the key to guarantee reliable comparisons, while exploiting LCA flexibility; sensitivity analysis should be the tool to analyze influence of different parameters and to be aware of their prominence, envisaging future research in this direction.

Some open problems requiring deeper investigations still persist: Simplified approaches should be adopted only after careful evaluation, (eventually applying sensitivity analysis), as well as a more diffuse assessment of stage D will allow greater accuracy in a cradle-to-cradle LCA analysis. Additionally, when dealing with the issue of repair, indirect effects should be also considered; in fact, is structural robustness should be guaranteed to cope with unexpected events that may induce exceptional loading demand, the environmental impact in stage A unavoidably increases.

A very similar issue is found when considering durability, with reference to both the structure and specific equipments or components. The main output of these stages is in close relationship with stage A: to some extent, they can be seen as inversely proportional, since through a wise and forward-looking use of materials or a specific construction method in stage A, the environmental impact of stages B2–B5 can be strongly reduced. Once more, results of multi-parametric sensitivity analysis are the key: research on the impact of the structural scheme on simplicity of reuse is envisaged, where the role of LCA in assessing sustainability of a specific solution is prominent.

References

1. Gervasio H, Dimova HS (2018) Environmental benchmarks for buildings. Publications Office of the European Union
2. Sharma A, Saxena A, Sethi M, Shree V, Varun G (2010) Life cycle assessment of buildings: a review. Renew Sustain Energy Rev.
3. Hájek P, Fiala C, Kyncˇlová M (2011) Life cycle assessments of concrete structures—a step towards environmental savings. Struct Concr (1)
4. Gosselin A, Blanchet P, Lehoux N, Cimon Y (2017) Main motivations and barriers for using wood in multi-story and non-residential construction projects. BioResources (1)
5. Mirdad AH, Daneshvar H, Joyce T, Chui YH (2021) Sustainability design considerations for timber-concrete composite floor systems. In: Advances in civil engineering
6. Dias A, Skinner J, Crews K, Tannert T (2015) Timber-concrete-composites increasing the use of timber in construction. Eur J Wood and Wood Prod
7. Rosati G, Zasso B, Altomare E (2014) Analysis of embodied energy and CO_2 in buildings structures under seismic action: wood, reinforced concrete, steel. In: Recent advances in civil engineering and mechanics
8. Fragiacomo M, Dujic B, Sustersic I (2011). Elastic and ductile design of multi-storey crosslam massive wooden buildings under seismic actions. Eng Struct 33(11):3043–3053
9. Gervasio H, Dimova S (2018) Model for Life Cycle Assessment (LCA) of buildings. Publications Office of the European Union
10. Rodriguez BX, Simonen K (2017) Comparison of methodologies for whole building life cycle assessment: a review
11. Abouhamad M, Abu-Hamd M (2020) Life cycle environmental assessment of light steel framed buildings with cement-based walls and floors. Sustainability (24)
12. Nwodo MN, Anumba CJ (2019) A review of life cycle assessment of buildings using a systematic approach. Build Environ
13. Trigaux D, Allacker K, Debacker W (2021) Environmental benchmarks for buildings: a critical literature review. Int J Life Cycle Assess (26)
14. Klöpffer W (1997) Life cycle assessment. from beginning to the current state. Environ Sci Pollut Res (4)
15. Kellenberger D (2010) Comparison of European LCA-based building assessment and design tools. Wellington
16. Chen Z, Gu H, Bergman RD, Liang S (2020) Comparative life-cycle assessment of a high-rise mass timber building with an equivalent reinforced concrete alternative using the athena impact estimator for buildings. Sustainability (11)
17. Allan K, Phillips AR (2021) Comparative cradle-to-grave life cycle assessment of low and mid-rise mass timber buildings with equivalent structural steel alternatives. Sustainability (6)
18. Dani AA, Roy K, Masood R, Fang Z, Lim JBP(2021) A comparative study on the life cycle assessment of New Zealand residential buildings. Buildings (12)
19. Chen CX, Pierobon F, Jones S, Maples I, Gong Y, Ganguly I (2022) Comparative life cycle assessment of mass timber and concrete residential buildings: a case study in China. Sustainability (14)
20. Rinne R, Ilgın HE, Karjalainen M (2022) Comparative study on life-cycle assessment and carbon footprint of hybrid, concrete and timber apartment buildings in Finland. Int J Environ Res Public Health (19)
21. Felmer G, Morales-Vera R, Astroza R, González I, Puettmann M, Wishnie M (2022) A life-cycle assessment of a low-energy mass-timber building and mainstream concrete alternative in Central Chile. Sustainability 14
22. Pittau F, Dotelli G, Arrigoni A, Habert G, Iannaccone G (2019) Massive timber building vs. conventional masonry building. A comparative life cycle assessment of an Italian case study. IOP Conf Ser Earth Environ Sci

23. Ryklová P, Mančík Š, Lupíšek A (2019) Environmental benefits of timber-concrete prefabricated construction system for apartment buildings—a simplified comparative LCA study. IOP Conf Ser Earth Environ Sci
24. Abolghassem Tehrani M, Froese TM (2017) A comparative life cycle assessment of tall buildings with alternative structural systems: wood vs. concrete. In: CSCE/CRC international construction specialty conference
25. Buchanan A, John S, Love S (2013) Life cycle assessment and carbon footprint of multistorey timber buildings compared with steel and concrete buildings. NZ J For 4
26. Soust-Verdaguer B, Llatas C, Moya L (2020) Comparative BIM-based life cycle assessment of Uruguayan timber and concrete-masonry single-family houses in design stage. J Clean Prod
27. Andersen JH, Rasmussen NL, Ryberg MW (2021) Comparative life cycle assessment of cross laminated timber building and concrete building with special focus on biogenic carbon. Energy Build
28. Eliassena AR, Faanesb S, Bohne RA (2019) Comparative LCA of a concrete and steel apartment building and a cross laminated timber apartment building
29. M. Sandanayakea, W. Lokugeb, G. Zhangc, S. Setungec and Q. Thushar, "Greenhouse gas emissions during timber and concrete building construction - A scenario based comparative case study," *Sustainable Cities and Society,* no. 38, 2017.
30. Pierobon F, Huang M, Simonen K, Ganguly I (2019) Environmental benefits of using hybrid CLT structure in midrise nonresidential construction: an LCA based comparative case study in the U.S. Pacific Northwest. J Build Eng (26)
31. Hemmati M, Messadi T, Gu H (2021) Life cycle assessment of cross-laminated timber transportation from three origin points. Sustainability (1)
32. Ramage MH, Burridge H, Busse-Wicher M, Fereday G, Reynolds T, Shah DU, Wu G, Yu L, Fleming P, Densley-Tingley D, Allwood J, Dupree P, Linden PF, Scherman O (2017) The wood from the trees: the use of timber in construction. Renew Sustain Energy Rev
33. Francart N, Widström T, Malmqvist T (2021) Influence of methodological choices on maintenance and replacement in building LCA. Int J Life Cycle Assess (26)
34. Årskog V, Fossdal S, Gjørv OE (2004) Life-cycle assessment of repair and maintenance systems for concrete structure. In: Proceedings of the international workshop on sustainable development and concrete technology
35. Vilches A, Garcia-Martinez A, Sanchez-Montanes B (2017) Life cycle assessment (LCA) of building refurbishment: a literature review. Energy Build
36. Giorgi S, Lavagna M, Campioli A (2018) Life cycle assessment of building end of life. In: Life cycle thinking in decision-making for sustainability: from public policies to private businesses
37. Delem L, Wastiels L (2019) The practical use of module D in a building case study: assumptions, limitations and methodological issue. In: IOP conference series: earth and environmental science
38. Ryberg MW, Ohms PG, Møller E, Lading T (2021) Comparative life cycle assessment of four buildings in Greenland. Build Environ
39. Passarelli R, Koshihara M (2017) "CLT panels in Japan from cradle to construction site gate: global warming potential and freight costs impact of three supply options. Int Wood Prod J (2)
40. Di Bari R, Belleri A, Marini A, Horn R, Gantner J (2020) Probabilistic life-cycle assessment of service life extension on renovated buildings under seismic hazard. Buildings (10)
41. Pittau F, Giacomel D, Iannaccone G, Malighetti L (2019) Environmental consequences of refurbishment versus demolition and reconstruction: a comparative life cycle assessment of an Italian case study. J Green Build (4)
42. Palacios-Munoz B, Peuportier B, Gracia-Villa L, López-Mes B (2019) Sustainability assessment of refurbishment vs. new constructions by means of LCA and durability-based estimations of buildings lifespans: a new approach. Build Environ
43. Ghose A, Pizzol M, McLaren SJ (2017) Consequential LCA modelling of building refurbishment in New Zealand - an evaluation of resource and waste management scenarios. J Cleaner Prod

44. Kovacic I, Reisinger J, Honic M (2018) Life cycle assessment of embodied and operational energy for a passive housing block in Austria. Renew Sustain Energy Rev
45. Tushar Q, Bhuiyan MA, Zhang G (2021) Energy simulation and modeling for window system: a comparative study of life cycle assessment and life cycle costing. J Cleaner Prod
46. Zhao S, Lavagna M, De Angelis E (2017) The role of life cycle assessment (LCA) and energy efficiency optimization during the early stage of building design. In: XI Convegno della Rete Italiana LCA VI Convegno dell'Associazione Rete Italiana LCA
47. Oregi X, Hernandez P, Gazulla C, Isasa M (2015) Integrating simplified and full life cycle approaches in decision making for building energy refurbishment: benefits and barriers. Buildings (5). https://doi.org/10.3390/buildings5020354
48. Berger M, Finkbeiner M (2010) Water footprinting: how to address water use in life cycle assessment? Sustainability
49. Assessment of operational water use in complete LCA, Oct 2012. [Online]. Available: https://www.eebguide.eu/eebblog/?p=3618. Accessed 2022
50. Anand CK, Amor B (2016) Recent developments, future challenges and new research directions in LCA of buildings: a critical review. Renew Sustain Energy Rev
51. Buyle M, Braet J, Audenaert A (2013) Life cycle assessment in the construction sector: a review. Renew Sustain Energy Rev
52. Hart J, D'Amico B, Pomponi F (2021) Whole-life embodied carbon in multistory buildings. J Ind Ecol
53. Peng Z, Lu W, Webster CJ (2021) Quantifying the embodied carbon saving potential of recycling construction and demolition waste in the Greater Bay Area, China: Status quo and future scenarios. Sci Total Environ
54. Krause K, Hafner A (2019) Relevance of the information content in module D on circular economy of building materials. In: 6th International symposium on life-cycle civil eEngineering, IALCCE 2018
55. Blengini GA (2009) Life cycle of buildings, demolition and recycling potential: A case study in Turin, Italy. Build Environ
56. Wastiels L, Van Dessel J, Delem L (2013) Relevance of the recycling potential (module D) in building LCA: a case study on the retrofitting of a house in Seraing. In: SB13 sustainable building conference, Graz

Concrete Structures

Deflection of Reinforced Concrete Flexural Members with Axial Load

Peter H. Bischoff

Abstract Deflection of reinforced concrete flexural members (beams and slabs) is typically computed with an effective moment of inertia I_e that accounts for tension carried by the concrete between cracks (tension stiffening) and the variation of stiffness along the member length. The ACI 318-19 Building Code Requirements for Structural Concrete has adopted an expression for I_e different from the expression used for the past fifty years or so by earlier editions of ACI 318 and other codes and standards. CSA A23.3-19 Design of Concrete Structures and S6-19 Canadian Highway Bridge Design Code are both considering adoption of the new expression used by ACI 318-19 for reinforced concrete. This paper extends the approach used to develop the new expression for I_e to compute deflection for flexural members with axial load. The approach is applicable to flexural members with low axial load such as load bearing walls and can be extended to compute deflection of columns and prestressed members that are cracked under service load.

Keywords Reinforced concrete · Deflection · Axial load

1 Introduction

Deflections of reinforced concrete flexural members such as beams and slabs, are typically computed with an effective moment of inertia I_e to account for tension carried by the concrete between cracks (called tension stiffening) and the variation of stiffness along the member length. The ACI 318-19 Building Code Requirements for Structural Concrete [2] has adopted [4, 5] expression for I_e. This new expression for I_e is different from the old expression based on [8] approach used for the past fifty years or so by earlier editions of ACI 318 and other codes and standards. The ACI 318–19 expression for I_e is given by

P. H. Bischoff (✉)
University of New Brunswick, Fredericton, Canada
e-mail: bischoff@unb.ca

$$I_e = \frac{I_{\mathrm{cr}}}{1 - \left(\frac{2/3M_{\mathrm{cr}}}{M_a}\right)^2 \left(1 - \frac{I_{\mathrm{cr}}}{I_g}\right)} \quad \text{for } M_a > 2/3M_{\mathrm{cr}} \tag{1}$$

For $M_a \leq 2/3M_{\mathrm{cr}}$, $I_e = I_g$. The cracking moment $M_{\mathrm{cr}} = f_r I_g/y_t$, f_r equals the concrete modulus of rupture (defined by ACI 318 as $0.62\sqrt{f_c'}$ in MPa), and y_t is the distance from the centroidal axis of the uncracked section to the tension face. The moment of inertia of the uncracked transformed section I_{tr} is approximated with the moment of inertia I_g of the gross concrete section, I_{cr} is the moment of inertia of the cracked transformed section, and M_a is the service load moment at the critical section. A reduced cracking moment of $2/3M_{\mathrm{cr}}$ accounts for early age loading and tensile stresses that develop in the concrete from restraint to shrinkage by the internal reinforcement [13].

AASHTO LRFD Bridge Design Specifications [1] is planning to adopt the expression used by ACI 318-19 for reinforced concrete [3], while A23.3 Design of Concrete Structures [9] and the S6 Canadian Highway Bridge Design Code [10] are also considering adoption.

This paper extends the ACI 318-19 expression for I_e to compute deflection of flexural members with an additional eccentric axial compressive load. The proposed approach is applicable to flexural members with low axial load such as load bearing walls and can be extended to compute deflection of prestressed members [6] and columns that are cracked under service load. Deformation is computed for service loads assuming linear elastic behaviour and P-Δ effects are not considered.

2   Behaviour Under Combined Loading

Expressions are derived for deflection of a flexural member (beam, slab or wall) subjected to transverse (lateral or out-of-plane) loading combined with an axial compressive load P having an eccentricity e measured from the top (compressive) face of a member as shown in Fig. 1. The axial load P is considered constant while the moment M^* from transverse loading is variable. The total or combined moment M is computed about the centroid of the uncracked section, such that

$$M = M^* + P(e + y_{\mathrm{tr}}) \tag{2}$$

and y_{tr} is the location of the uncracked centroid relative to the top (compressive) face of the member.

Figure 2 plots the moment curvature response of a flexural member subjected to the combined loading described. The response is presented for two sets of axes, one corresponding to the total moment M in the member (from transverse loading and the eccentric axial load) and the other corresponding to the moment M^* from transverse loading only. The latter would be applicable for a prestressed concrete member where the eccentric axial force P from the prestressing is an internal force
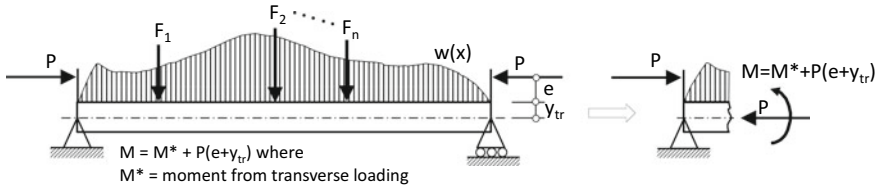
Fig. 1 Flexural member subjected to transverse (lateral) loads and eccentric axial load

Fig. 2 Moment curvature response of a flexural member with combined loading from transverse loads and an eccentric axial load ($e > -y_{tr}$)
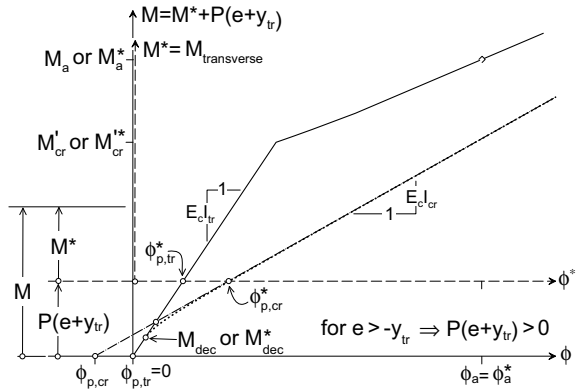
(but with a corresponding eccentricity $e \leq -y_{tr}$), while the former is applicable for an external axial force acting on the member (such as a wall subjected to eccentric vertical axial loads and out-of-plane lateral loads from wind or seismic forces). P-Δ effects are not considered.

Notice how the cracked section response is initially nonlinear (shown by the dotted line beginning at M_{dec} or M_{dec}^* in Fig. 2) but converges quickly to the fully cracked $E_c I_{cr}$ response that is shifted relative to the uncracked $E_c I_{tr}$ response. The $E_c I_{cr}$ response does not start off at the origin, as expected for a member without axial load. Neither does the $E_c I_{tr}$ response relative to the M^* axis. For $M = 0$, the curvature of the uncracked response $\phi_{p,tr}$ equals zero, while the curvature of the cracked response $\phi_{p,cr}$ is negative as indicated in Fig. 2. The curvatures of the uncracked and cracked response when $M^* = 0$ are defined as $\phi_{p,tr}^*$ and $\phi_{p,cr}^*$ respectively and are both positive. These curvatures correspond to the curvature values from the eccentric axial force which is considered constant in the analysis.

Figure 3 shows the section forces acting on an uncracked rectangular member, which are used to define the curvature values $\phi_{p,tr}$ and $\phi_{p,tr}^*$ that arise from the eccentric axial force relative to the centroid of the uncracked transformed section. Once again, the flexural member is subjected to transverse (lateral) loading and an eccentric axial load P with eccentricity e measured from the top (compressive) face of the member as defined in Figs. 1 and 3. The curvature ϕ_{tr} of the uncracked section is expressed as
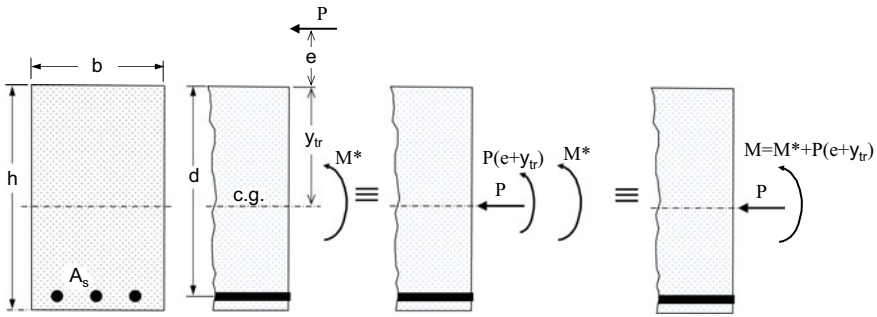
Fig. 3 Section forces for uncracked member under combined (moment plus axial) loading

$$\phi_{\mathrm{tr}} = \frac{M}{E_c I_{\mathrm{tr}}} = \frac{M^* + P(e + y_{\mathrm{tr}})}{E_c I_{\mathrm{tr}}} \tag{3}$$

where the moment M is defined by Eq. 2, I_{tr} is the moment of inertia of the uncracked transformed section, and E_c is the elastic modulus of concrete. Setting $M = 0$ gives the curvature of an uncracked section $\phi_{p,\mathrm{tr}} = 0$ corresponding to the total (combined) moment M being equal to zero. Alternatively, setting the moment from transverse loads $M^* = 0$ gives a corresponding curvature $\phi^*_{p,\mathrm{tr}} = P(e + y_{\mathrm{tr}})/E_c I_{\mathrm{tr}}$ for an uncracked section (see Fig. 2).

For the fully cracked section shown in Fig. 4, the moment is now computed about the centroid of the cracked section (equal to the neutral axis for a fully cracked section). The section forces acting on a cracked member are used to define the curvature values $\phi_{p,\mathrm{cr}}$ and $\phi^*_{p,\mathrm{cr}}$ that arise from the eccentric axial force relative to the centroid of the cracked transformed section. The curvature ϕ_{cr} of a fully cracked section is defined as

$$\phi_{\mathrm{cr}} = \frac{M^* + P(e + y_{\mathrm{cr}})}{E_c I_{\mathrm{cr}}} = \frac{M + P(y_{\mathrm{cr}} - y_{\mathrm{tr}})}{E_c I_{\mathrm{cr}}} \tag{4}$$
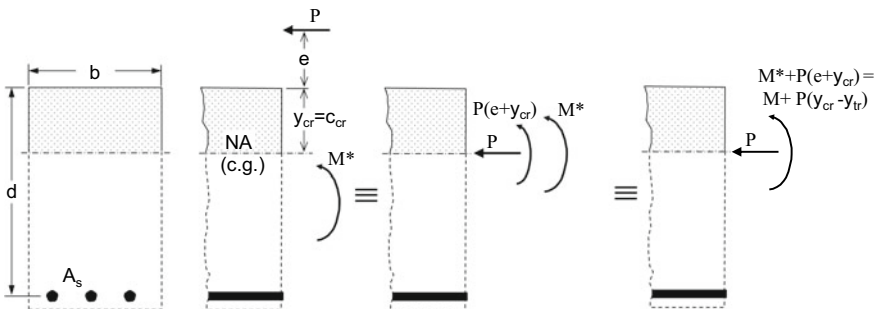
Fig. 4 Section forces for fully cracked member under combined (moment plus axial) loading

where I_{cr} is the moment of inertia of the fully cracked transformed section and y_{cr} is the location of the cracked centroid (or neutral axis location c_{cr} in this case for a fully cracked section) measured from the top (compressive) face of the section. Setting $M = 0$ gives $M^* = -P(e + y_{tr})$ from Eq. 2, which is then substituted into Eq. 4 to give $\phi_{p,cr} = P(y_{cr} - y_{tr})/E_c I_{cr}$. Alternatively, setting $M^* = 0$ gives a corresponding curvature $\phi_{p,cr}^* = P(e + y_{cr})/E_c I_{cr}$ of a cracked section (see Fig. 2).

3 Model Development

3.1 Axial Load with Positive Eccentricity (Relative to Centroid of the Uncracked Section)

Figure 2 is used as the basis for developing expressions to compute the deflection of a member under combined flexure plus axial loading. Full details of the derivation are provided in the Appendix for two options. One of these options (Option 2) is recommended for practical reasons as presented below. Both options give the same results.

For moment expressed in terms of the combined moment M defined by Eq. 2, the curvature ϕ_a for a service load moment M_a is defined as

$$\phi_a = \frac{M_a}{E_c I_e} + \phi_{p,e} \tag{5}$$

where

$$I_e = \frac{I_{cr}}{1 - \beta_{ts}\left(\frac{M_{cr}'}{M_a}\right)\left(1 - \frac{I_{cr}}{I_{tr}}\right)} \tag{6}$$

and

$$\phi_{p,e} = \beta_{ts}\phi_{p,tr} + [1 - \beta_{ts}]\phi_{p,cr} \text{ with } \phi_{p,tr} = 0 \text{ and } \phi_{p,cr} = P(y_{cr} - y_{tr})/E_c I_{cr} \tag{7}$$

The cracking moment M_{cr}' accounts for tensile stresses that develop in the concrete from restraint to shrinkage and for compressive stresses in the concrete arising from the axial compressive load. M_{cr}' is defined as

$$M_{cr}' = \frac{2}{3}M_{cr}\left[1 + \frac{3}{2}\frac{(P/A_{tr})}{f_r}\right] \tag{8}$$

where A_{tr} is the area of the uncracked transformed section. Using 2/3 of the cracking moment $M_{cr} = f_r I_{tr}/y_t$ accounts for early age loading and the tensile stresses that develop in the concrete from restraint to shrinkage caused by the internal

reinforcement [13]. The cracking moment M'_{cr} applies to the combined moment M which includes the moment $P(e + y_{tr})$ from the eccentric axial force (refer to Eq. 2 and Fig. 3). Hence, for the moment M^* from transverse loading only, $M'^*_{cr} = M'_{cr} - P(e + y_{tr})$.

The axial load P has a limit defined by Eq. 9a when the eccentricity $e > K_t - y_{tr}$, to avoid cracking on the flexural tension side when the moment from lateral loads $M^* = 0$. In other words, the member is assumed to be uncracked when the eccentric axial force acts alone. When $e \leq K_t - y_{tr}$, there is no limit on P as the member does not crack on the flexural tension face from the eccentric axial force alone. Alternatively, the eccentricity is limited by Eq. 9b for a given axial load P to avoid cracking when no transverse loads are applied.

$$P \leq \frac{2/3M_{cr}}{e + y_{tr} - K_t} \text{ when } e > K_t - y_{tr}, \text{ with } K_t = \frac{S_b}{A_{tr}} \text{ and } S_b = I_{tr}/y_t \quad (9a)$$

$$e \leq 2/3(M_{cr}/P) + K_t - y_{tr} \quad \text{for } P > 0 \quad (9b)$$

The tension stiffening factor β_{ts} is defined relative to the decompression moment M_{dec} [6] corresponding to zero stress at the tension face of the member (refer to the Appendix for details).

$$\beta_{ts} = \frac{M'_{cr} - M_{dec}}{M_a - M_{dec}} \text{ and } M_{dec} = (P/A_{tr})\frac{I_{tr}}{y_t} \quad (10)$$

Setting $P = 0$ leads to Eq. 1 for I_e as defined by ACI 318-19 for the default case of a member with flexure only. $P = 0$ gives $M'_{cr} = 2/3M_{cr}$, $M_{dec} = 0$, $\beta_{ts} = M'_{cr}/M_a$, and $\phi_{p,tr} = \phi_{p,cr} = 0$; assuming $I_{tr} \approx I_g$ then leads to $I_e = I_{cr}/[1 - (2/3M_{cr}/M_a)^2(1 - I_{cr}/I_g)]$ and $\phi_{p,e} = 0$. Hence $\phi_a = M_a/E_c I_e$ in this case.

For moments defined in terms of the moment M^* from transverse loading only, the curvature ϕ^*_a corresponding to a service load moment M^*_a is defined as

$$\phi^*_a = \frac{M^*_a}{E_c I^*_e} + \phi^*_{p,e} \quad (11)$$

where

$$I^*_e = \frac{I_{cr}}{1 - \beta^*_{ts}\left(\frac{M'^*_{cr}}{M^*_a}\right)\left(1 - \frac{I_{cr}}{I_{tr}}\right)} \quad (12)$$

$$\phi^*_{p,e} = \beta^*_{ts}\phi^*_{p,tr} + (1 - \beta^*_{ts})\phi^*_{p,cr} \quad (13)$$

with $\phi^*_{p,tr} = P(e + y_{tr})/E_c I_{tr}$ and $\phi^*_{p,cr} = P(e + y_{cr})/E_c I_{cr}$

Fig. 5 Flexural member response under combined loading for a concentric axial load ($e = -y_{tr}$)
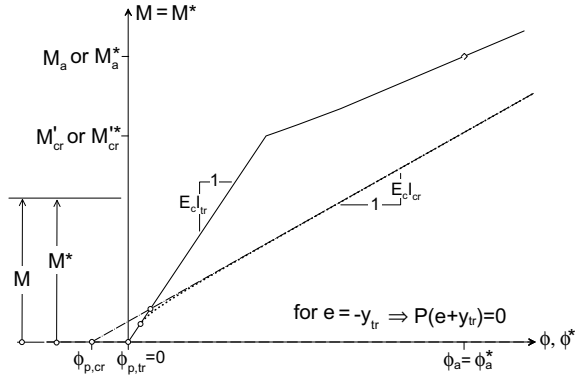
$$M_{cr}^{'*} = M_{cr}^{'} - P(e + y_{tr}) = \frac{2}{3}M_{cr}\left[1 + \frac{3}{2}\frac{(P/A_{tr})}{f_r}\right] - P(e + y_{tr}) \qquad (14)$$

$$\beta_{ts}^* = \frac{M_{cr}^{'*} - M_{dec}^*}{M_a^* - M_{dec}^*} \text{ and } M_{dec}^* = (P/A_{tr})\frac{I_{tr}}{y_t} - P(e + y_{tr}) \qquad (15)$$

3.2 Concentric Axial Loading (Relative to Centroid of the Uncracked Section)

Figure 5 plots the moment curvature response for a flexural member with the axial load applied at the centroid of the uncracked transformed section. In other words, the axial load is concentric (with $e = -y_{tr}$) to give $M = M^*$ as defined by Eq. 2, $\phi = \phi^*$, $\phi_{p,tr}^* = \phi_{p,tr} = 0$, and $\phi_{p,cr}^* = \phi_{p,cr} = P(y_{cr} - y_{tr})/E_c I_{cr}$. This approach is applicable for deformation of columns with axial load and moment acting at the centroid of the cross-section. An alternative option for deformation described in the Appendix (Option 1) is somewhat comparable to a CEB model developed by Favre and Koprna for a flexural member with an axial compressive load applied at the centroid of the uncracked section [11, 12].

3.3 Axial Load with Negative Eccentricity (Relative to Centroid of the Uncracked Section)

Figure 6 plots the moment curvature response for a flexural member with the axial load applied below the centroid of the uncracked transformed section. In this case, $e < -y_{tr}$ and $P(e + y_{tr}) < 0$. Notice how the M and M^* axes are flipped when compared

Fig. 6 Flexural member response under combined loading for an axial load with negative eccentricity $(e < -y_{tr})$
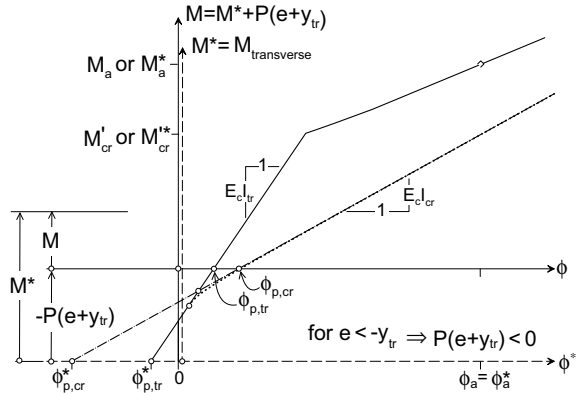
with Fig. 2. For this case, the $M^* - \phi^*$ response is comparable to a prestressed concrete member as described by Bischoff[6].

3.4 Limitations

Development of the proposed model for computing deformation assumes the cracked section response $E_c I_{cr}$ lies below the cracking moment M'_{cr} as shown in Figs. 2, 5 and 6. However, increasing the axial load P has the effect of shifting the $E_c I_{cr}$ response upwards until it eventually lies above M'_{cr} for $P > 2/3 M_{cr} \eta / (y_{tr} - y_{cr} - K_t \eta)$, with $K_t = S_b/A_{tr}$, $S_b = I_{tr}/y_t$ and $\eta = 1 - I_{cr}/I_{tr}$. Bischoff's [6] work with prestressed concrete has shown that the proposed approach is still applicable for this case when using the tension stiffening factor β_{ts} or β_{ts}^* as defined by Eqs. 10 and 15.

4 Summary

An approach that incorporates tension stiffening in a realistically consistent manner is developed to compute service load deformation of a flexural member under combined loading, with the moment arising from transverse (lateral) loads acting together with an eccentric axial compressive load. The proposed approach separates the deformation arising from flexure from that caused by the axial force. Deformation from the moment (M or M^*) is computed with an effective moment of inertia I_e or I_e^* based on the same rationale used by ACI 318-19 to computed deflection of flexural members. Deformation from the axial compressive load is computed with an effective curvature value $\phi_{p,e}$ or $\phi_{p,e}^*$. Account is also taken of the effect that tensile stresses in the concrete from restraint to shrinkage and compressive stress from the axial compressive force have on the cracking moment. Deformation can be computed relative to

the total moment from the transverse loads plus the moment from the eccentric axial force or for the moment from transverse loads only. The approach can be extended to compute deformation of prestressed flexural members and columns that are cracked under service loads.

List of Symbols

A_s	area of reinforcing steel
A_{tr}	transformed area of uncracked section
b	width of rectangular section
c_{cr}	neutral axis depth of cracked transformed section
c'_{cr}	neutral axis depth of partially cracked transformed section
d	effective depth of reinforcing steel
e	eccentricity of axial compressive force relative to the top (compressive) face of the member
E_c	elastic modulus of concrete
E_s	elastic modulus of reinforcing steel
f'_c	compressive strength of concrete
f_r	concrete modulus of rupture
F	transverse (lateral) forces
h	height of rectangular section
I_{cr}	moment of inertia of the cracked transformed section
I_e, I_e^*	effective moment of inertia (relative to the M and M^* axes respectively)
I_{e1}, I_{e1}^*	effective moment of inertia using Option 1 (relative to the M and M^* axes respectively)
I_{e2}, I_{e2}^*	effective moment of inertia using Option 2 (relative to the M and M^* axes respectively)
I_g	moment of inertia of the gross concrete section (approximation for I_{tr})
I_{tr}	moment of inertia of the uncracked transformed section
k_{cr}	ratio of neutral axis depth to effective depth for a cracked transformed section
k'_{cr}	ratio of neutral axis depth to effective depth for a partially cracked transformed section
K_t	kern value ($= S_b / A_{\mathrm{tr}}$)
M, M^*	total or combined moment from the transverse loads plus the eccentric axial force; moment from transverse loading only
M_a, M_a^*	service load moment (relative to the M and M^* axes respectively)
M_{cr}	cracking moment with no shrinkage or axial load ($= f_r I_{\mathrm{tr}} / y_t$)
M'_{cr}, M'^*_{cr}	cracking moment accounting for axial compressive force and tensile stresses from restraint to shrinkage (relative to the M and M^* axes respectively)
M_{dec}, M_{dec}^*	decompression moment (relative to the M and M^* axes respectively)
$M_{\mathrm{transverse}}$	moment from transverse lateral loads defined as M^*

M_1, M_1^*	intersection point of the uncracked and cracked section response (relative to the M and M^* axes respectively)
$\Delta M_{cr}, \Delta M_{cr}^*$	tension stiffening moment at cracking (relative to the M and M^* axes respectively)
n	modular ratio (E_s/E_c)
P	axial compressive force
S_b	section modulus value to bottom (tension) face ($= I_{tr}/y_t$)
y_{cr}	centroid location of the cracked section relative to the top (compression) face
y_t	distance from the centroidal axis of the uncracked section to the tension face
y_{tr}	centroid location of the uncracked section relative to the top (compression) face
w	distributed load
β_{ts}, β_{ts}^*	tension stiffening factor (relative to the M and M^* axes respectively)
η	$1 - I_{cr}/I_{tr}$
Δ	lateral deflection used to describe $P - \Delta$ effects
ϕ, ϕ^*	curvature (relative to the M and M^* axes respectively)
ϕ_a, ϕ_a^*	curvature at service load moment (relative to the M and M^* axes respectively)
ϕ_{cr}	curvature of a fully cracked section
$\phi_{p,e}, \phi_{p,e}^*$	effective curvature from the axial force P (relative to the M and M^* axes respectively)
$\phi_{p,e1}, \phi_{p,e1}^*$	effective curvature from the axial force P using Option 1 (relative to the M and M^* axes respectively)
$\phi_{p,e2}, \phi_{p,e2}^*$	effective curvature from the axial force P using Option 2 (relative to the M and M^* axes respectively)
$\phi_{p,cr}, \phi_{p,cr}^*$	curvature of a cracked section from the axial force P (relative to the M and M^* axes respectively)
$\phi_{p,tr}, \phi_{p,tr}^*$	curvature of an uncracked section from the axial force P (relative to the M and M^* axes respectively)
ϕ_{tr}	curvature of an uncracked section
ϕ_1, ϕ_1^*	curvature corresponding to M_1 and M_1^* respectively
ρ	reinforcement ratio A_s/bd.

Appendix: Deformation Derivation for a Cracked Member Under Combined Loading

Figure 7 (based on Fig. 2) is used to derive the expressions for deformation presented in this paper for a flexural member subjected to combined loading from flexure plus axial load, where the moment equals the moment M^* from transverse loading plus the moment $P(e + y_{tr})$ from the eccentric axial load. Expressions are presented

Fig. 7 Moment curvature response of a flexural member under combined loading
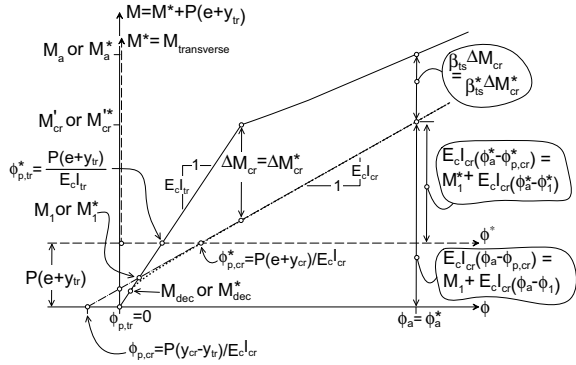
with respect to the total moment $M = M^* + P(e + y_{tr})$ and the moment M^* from transverse loading only.

Derivation begins with a few basic definitions that include the tension stiffening moment at first cracking (ΔM_{cr} equal to ΔM_{cr}^*), tension stiffening moment ($\beta_{ts}\Delta M_{cr}$ equal to $\beta_{ts}^*\Delta M_{cr}^*$) at the service load moment (M_a or M_a^*) which is defined by a tension stiffening factor (β_{ts} equal to β_{ts}^*), intersection point of the uncracked $E_c I_{tr}$ and cracked $E_c I_{cr}$ responses (characterized by M_1 and ϕ_1 or M_1^* and ϕ_1^*), and the decompression moment (M_{dec} or M_{dec}^*) defined by zero tensile stress at the bottom face of the member. $\eta = 1 - I_{cr}/I_{tr}$ in these definitions.

$$\Delta M_{cr} = \eta\left(M_{cr}' - M_1\right) = \eta M_{cr}' + \left(\phi_{p,cr} - \phi_{p,tr}\right)E_c I_{cr} \text{ equal to}$$

$$\Delta M_{cr}^* = \eta\left(M_{cr}'^* - M_1^*\right) = \eta M_{cr}'^* + \left(\phi_{p,cr}^* - \phi_{p,tr}^*\right)E_c I_{cr}$$

$$M_1 = \left(\phi_{p,tr} - \phi_{p,cr}\right)E_c I_{cr}/\eta \text{ and}$$

$$\phi_1 = \phi_{p,cr} - \left(\phi_{p,cr} - \phi_{p,tr}\right)/\eta \text{ with } \phi_{p,tr} = 0 \text{ or}$$

$$M_1^* = \left(\phi_{p,tr}^* - \phi_{p,cr}^*\right)E_c I_{cr}/\eta \text{ and } \phi_1^* = \phi_{p,cr}^* - \left(\phi_{p,cr}^* - \phi_{p,tr}^*\right)/\eta$$

$$M_{dec} = (P/A_{tr})\frac{I_{tr}}{y_t} \text{ or } M_{dec}^* = (P/A_{tr})\frac{I_{tr}}{y_t} - P(e + y_{tr})$$

The curvature of the uncracked section ($\phi_{p,tr}$ or $\phi_{p,tr}^*$) from axial load, and the curvature of the cracked section ($\phi_{p,cr}$ or $\phi_{p,cr}^*$) from axial load are defined in the main text of the paper as

$$\phi_{p,tr} = 0 \text{ and } \phi_{p,tr}^* = \frac{P(e + y_{tr})}{E_c I_{tr}}$$

$$\phi_{p,\text{cr}} = \frac{P(y_{\text{cr}} - y_{\text{tr}})}{E_c I_{\text{cr}}} \text{ and } \phi^*_{p,\text{cr}} = \frac{P(e + y_{\text{cr}})}{E_c I_{\text{cr}}}$$

The cracking moment M'_{cr} or M'^*_{cr} is also defined in the main text of the paper as

$$M'_{\text{cr}} = \frac{2}{3} M_{\text{cr}} \left[1 + \frac{3}{2} \frac{(P/A_{\text{tr}})}{f_r} \right] \text{ or } M'^*_{\text{cr}} = \frac{2}{3} M_{\text{cr}} \left[1 + \frac{3}{2} \frac{(P/A_{\text{tr}})}{f_r} \right] - P(e + y_{\text{tr}})$$

Two alternatives (Option 1 and Option 2) are presented for deformation of the cracked section. Both give the same curvature. The second alternative (Option 2) is presented in the main text of the paper as it is considered more practical. See [6] for an explanation related to prestressed concrete.

For Option 1 (refer to Fig. 7):

$$M_a = M_1 + E_c I_{\text{cr}}(\phi_a - \phi_1) + \beta_{\text{ts}} \Delta M_{\text{cr}}$$

$$\therefore \phi_a = \frac{(M_a - M_1)}{E_c I_{\text{cr}}} \left[1 - \frac{\beta_{\text{ts}} \Delta M_{\text{cr}}}{(M_a - M_1)} \right] + \phi_1$$

using $\Delta M_{\text{cr}} = \eta \left(M'_{\text{cr}} - M_1 \right)$ and $\phi_1 = \phi_{p,\text{cr}} - \left(\phi_{p,\text{cr}} - \phi_{p,\text{tr}} \right)/\eta$

$$\phi_a = \frac{(M_a - M_1)}{E_c I_{\text{cr}}} \left[1 - \beta_{\text{ts}} \left(\frac{M'_{\text{cr}} - M_1}{M_a - M_1} \right) \eta \right] + \phi_{p,\text{cr}} - \left(\phi_{p,\text{cr}} - \phi_{p,\text{tr}} \right)/\eta$$

$$\therefore \phi_a = \frac{(M_a - M_1)}{E_c I_{e1}} + \frac{\phi_{p,\text{tr}} + \phi_{p,\text{cr}}(\eta - 1)}{\eta} \text{ with } I_{e1} = \frac{I_{\text{cr}}}{1 - \beta_{\text{ts}} \left(\frac{M'_{\text{cr}} - M_1}{M_a - M_1} \right) \eta} \text{ and } \phi_{p,\text{tr}} = 0$$

Now, setting $\phi_a = M_a / E_c I_{e1} + \phi_{p,e1}$

gives $\phi_{p,e1} = \beta_{\text{ts}} \left(\frac{M'_{\text{cr}} - M_1}{M_a - M_1} \right) \phi_{p,\text{tr}} + \left[1 - \beta_{\text{ts}} \left(\frac{M'_{\text{cr}} - M_1}{M_a - M_1} \right) \right] \phi_{p,\text{cr}}$ with $\phi_{p,\text{tr}} = 0$

Finally, $\beta_{\text{ts}} = \frac{M'_{\text{cr}} - M_{\text{dec}}}{M_a - M_{\text{dec}}} \cong \frac{M'_{\text{cr}} - M_1}{M_a - M_1}$ for $M_1 \leq M'_{\text{cr}}$ corresponding to $P \leq \frac{2/3 M_{\text{cr}} \eta}{(y_{\text{tr}} - y_{\text{cr}} - K_t \eta)}$
Using the alternative M^* axis for Option 1,

$$M^*_a = M^*_1 + E_c I_{\text{cr}} \left(\phi^*_a - \phi^*_1 \right) + \beta^*_{\text{ts}} \Delta M^*_{\text{cr}}$$

$$\therefore \phi^*_a = \frac{\left(M^*_a - M^*_1 \right)}{E_c I_{\text{cr}}} \left[1 - \frac{\beta^*_{\text{ts}} \Delta M^*_{\text{cr}}}{\left(M^*_a - M^*_1 \right)} \right] + \phi^*_1$$

using $\Delta M^*_{\text{cr}} = \eta \left(M'^*_{\text{cr}} - M^*_1 \right)$ and $\phi^*_1 = \phi^*_{p,\text{cr}} - \left(\phi^*_{p,\text{cr}} - \phi^*_{p,\text{tr}} \right)/\eta$

$$\phi_a^* = \frac{(M_a^* - M_1^*)}{E_c I_{cr}} \left[1 - \beta_{ts}^* \left(\frac{M_{cr}^{'*} - M_1^*}{M_a^* - M_1^*} \right) \eta \right] + \phi_{p,cr}^* - \left(\phi_{p,cr}^* - \phi_{p,tr}^* \right)/\eta$$

Setting $\phi_a^* = M_a^*/E_c I_{e1}^* + \phi_{p,e1}^* \phi_a^* = M_a^*/E_c I_{e1}^* + \phi_{p,e1}^*$

$$\text{with } I_{e1}^* = \frac{I_{cr}}{1 - \beta_{ts}^* \left(\frac{M_{cr}^{'*} - M_1^*}{M_a^* - M_1^*} \right) \eta}$$

$$\text{gives } \phi_{p,e1}^* = \beta_{ts}^* \left(\frac{M_{cr}^{'*} - M_1^*}{M_a^* - M_1^*} \right) \phi_{p,tr}^* + \left[1 - \beta_{ts}^* \left(\frac{M_{cr}^{'*} - M_1^*}{M_a^* - M_1^*} \right) \right] \phi_{p,cr}^*$$

with $\beta_{ts} = \dfrac{M_{cr}^{'*} - M_{dec}^*}{M_a^* - M_{dec}^*} \cong \dfrac{M_{cr}^{'*} - M_1^*}{M_a^* - M_1^*}$ for $M_1^* \leq M_{cr}^{'*}$ corresponding to

$$P \leq \frac{2/3\eta M_{cr}}{(y_{tr} - y_{cr} - \eta K_t)}$$

For Option 2 (refer to Fig. 7): presented in the main text of the paper

$$M_a = E_c I_{cr}(\phi_a - \phi_{p,cr}) + \beta_{ts}\Delta M_{cr}$$

$$\therefore \phi_a = \frac{M_a}{E_c I_{cr}} \left[1 - \frac{\beta_{ts}\Delta M_{cr}}{M_a} \right] + \phi_{p,cr}$$

$$\text{using} \Delta M_{cr} = \eta M_{cr}^{'} + \left(\phi_{p,cr} - \phi_{p,tr} \right) E_c I_{cr}$$

$$\phi_a = \frac{M_a}{E_c I_{cr}} \left[1 - \beta_{ts} \left(\frac{M_{cr}^{'}}{M_a} \right) \eta \right] + \beta_{ts}\phi_{p,tr} + (1 - \beta_{ts})\phi_{p,cr}$$

Now, setting $\phi_a = M_a/E_c I_{e2} + \phi_{p,e2}$

$$\text{gives } I_{e2} = \frac{I_{cr}}{1 - \beta_{ts} \left(\frac{M_{cr}^{'}}{M_a} \right) \eta} \text{ and}$$

$$\phi_{p,e2} = \beta_{ts}\phi_{p,tr} + (1 - \beta_{ts})\phi_{p,cr} \text{ with} \phi_{p,tr} = 0 \text{ and } \beta_{ts} = \frac{M_{cr}^{'} - M_{dec}}{M_a - M_{dec}}$$

Using the alternative M^* axis for Option 2,

$$M_a^* = E_c I_{cr}(\phi_a^* - \phi_{p,cr}^*) + \beta_{ts}^*\Delta M_{cr}^*$$

$$\therefore \phi_a^* = \frac{M_a^*}{E_c I_{cr}} \left[1 - \frac{\beta_{ts}^* \Delta M_{cr}^*}{M_a^*} \right] + \phi_{p,cr}^*$$

using $\Delta M_{cr}^* = \eta M_{cr}^{'*} + \left(\phi_{p,cr}^* - \phi_{p,tr}^* \right) E_c I_{cr}$

$$\phi_a^* = \frac{M_a^*}{E_c I_{cr}} \left[1 - \beta_{ts}^* \left(\frac{M_{cr}^{'*}}{M_a^*} \right) \eta \right] + \beta_{ts}^* \phi_{p,tr}^* + \left(1 - \beta_{ts}^* \right) \phi_{p,cr}^*$$

Setting $\phi_a^* = M_a^* / E_c I_{e2}^* + \phi_{p,e2}^*$

$$\text{gives } I_{e2}^* = \frac{I_{cr}}{1 - \beta_{ts}^* \left(\frac{M_{cr}^{'*}}{M_a^*} \right) \eta}$$

$$\text{and } \phi_{p,e2}^* = \beta_{ts}^* \phi_{p,tr}^* + \left(1 - \beta_{ts}^* \right) \phi_{p,cr}^*$$

$$\text{with } \beta_{ts}^* = \frac{M_{cr}^{'*} - M_{dec}^*}{M_a^* - M_{dec}^*}$$

For Section Analysis

The cracked section response is not only shifted relative to the uncracked $E_c I_{tr}$ response, but starts off nonlinear as shown by the dotted line in Figs. 2 and 7, although the response does converge to the fully cracked $E_c I_{cr}$ response as $Pd/M^* \to 0$ and $Pe/M^* \to 0$ with increasing moment. The nonlinearity results from the presence of an axial compressive force and gives an actual moment of inertia of the partially cracked section I_{cr}' greater than I_{cr} but less than I_{tr}. I_{cr}' is computed relative to the centroidal axis of the partially cracked section and is not coincident with the neutral axis location; whereas I_{cr} is computed relative to the neutral axis of the fully cracked section, which does coincide with the centroidal axis as for a flexural member without axial load. I_{cr}' eventually converges to I_{cr} under increasing moment as the neutral axis depth c_{cr}' approaches c_{cr}.

For a rectangular section with tension reinforcement only, the neutral axis depth c_{cr}' of a partially cracked section is defined as

$c_{cr}' = k_{cr}' d \geq c_{cr}$ which requires solution of a cubic equation for k_{cr}' given by

$$\frac{Pd}{M^*} \left(k_{cr}' \right)^3 + 3 \left[1 + \frac{Pe}{M^*} \right] \left(k_{cr}' \right)^2 - 6n\rho \left[1 + \frac{P(e+d)}{M^*} \right] \left[1 - k_{cr}' \right] = 0$$

Recall that M^* is the moment from external loading, e is the eccentricity measured from the top (compressive) face of the member, and d is the effective depth of the tension reinforcement.

For concentric axial loading with $e = -y_{tr}$, where the axial load acts at the centroid of the uncracked section located at y_{tr} from the compressive face

$$\frac{Pd}{M^*}\left(k_{cr}'\right)^3 + 3\left[1 - \frac{Py_{tr}}{M^*}\right]\left(k_{cr}'\right)^2 - 6n\rho\left[1 + \frac{P(d - y_{tr})}{M^*}\right]\left[1 - k_{cr}'\right] = 0$$

and for a prestressed concrete member with $e = -d$ where P is the axial force from the prestressing steel

$$\frac{Pd}{M^*}\left(k_{cr}'\right)^3 + 3\left[1 - \frac{Pd}{M^*}\right]\left(k_{cr}'\right)^2 - 6n\rho\left[1 - k_{cr}'\right] = 0$$

where d is now the effective depth of the prestressing steel. Refer also to [7] for more explanation regarding the neutral axis location for a cracked prestressed flexural member.

For a flexural member with no axial load ($P = 0$), the cubic equation for k_{cr}' simplifies to the classic equation used to determine the neutral axis location of a reinforced (nonprestressed) member with a rectangular cross-section and tension reinforcement only.

$$0.5(k_{cr})^2 + n\rho k_{cr} - n\rho = 0 \rightarrow k_{cr} = \sqrt{(n\rho)^2 + 2n\rho} - n\rho \text{ with } c_{cr} = k_{cr}d$$

References

1. AASHTO (2020) AASHTO LRFD bridge design specifications, 9th edn. American Association of State Highway and Transportation Officials (AASHTO), Washington, D.C.
2. ACI Committee 318 (2019) Building code requirements for structural concrete (ACI 318-19) and commentary (ACI 318R-19). American Concrete Institute (ACI), Farmington Hills, MI
3. Bayrak O (2022) Details on several upcoming changes to the AASHTO LRFD bridge design specifications: deflection calculations and stress limits. Aspire Concr Bridge Mag Winter 2022:62–63
4. Bischoff PH (2005) Revaluation of deflection prediction for concrete beams reinforced with steel and FRP bars. J Struct Eng ASCE 131(5):752–767
5. Bischoff PH (2020) Comparison of existing approaches for computing deflection of reinforced concrete. ACI Struct J 117(1):231–240
6. Bischoff PH (2022) Deformation model for reinforced and cracked prestressed concrete. ACI Struct J 119(1):243–254
7. Bischoff PH, Naito CJ, Ingaglio JP (2018) Immediate deflection of partially prestressed concrete flexural members. ACI Struct J 115(6):1683–1693
8. Branson DE (1965) Instantaneous and time-dependent deflections of simple and continuous reinforced concrete beams. HPR Report No. 7, Part 1, Alabama Highway Department, Bureau

of Public Roads, Montgomery, AL. Department of Civil Engineering and Auburn Research Foundation, Auburn University, Aug 1963

9. Canadian Standards Association (CSA) A23.3 (2019a) Design of concrete structures (A23.3:19). CSA Group, Rexdale (Toronto), ON
10. Canadian Standards Association (CSA) S6 (2019b) Canadian highway bridge design code (S6:19). CSA Group, Rexdale (Toronto), ON
11. Comité Euro-International du Béton (CEB) (1985) CEB design manual on cracking and deformations. Swiss Federal Institute of Technology (EPFL), Lausanne, Switzerland
12. Espion B, Halleux P (1988) Moment curvature relationship of reinforced concrete sections under combined bending and normal force. Mater Struct 21(5):341–351
13. Scanlon A, Bischoff PH (2008) Shrinkage restraint and loading history effects on deflection of flexural members. ACI Struct J 105(4):498–506

Behaviour of GFRP-RC Slender Circular Columns Subjected to Eccentric Loads

S. M. Hasanur Rahman and Ehab El-Salakawy

Abstract Slender circular concrete columns carry less loads compared to their short counterparts due to their geometrical configuration or slenderness ratio. Due to corrosion, conventional steel-reinforced concrete (RC) columns cannot keep the structural integrity in harsh environmental for their entire design service life. In recent years, the non-corrodible fibre-reinforced polymer (FRP) bars have been established as an internal reinforcement for RC structures. However, current design codes and guidelines do not allow the contribution of FRP bars in slender columns, exceeding a slenderness ratio of 22 and bent in single curvature. The lack of code provisions drew the need for investigation on the behaviour of slender columns. This study aimed at experimentally investigating the behaviour of circular columns with a slenderness ratio of 45. The results of two glass FRP-RC slender columns with a length of 4000 mm and a diameter of 355 mm, loaded with an eccentricity-to-diameter ratio of 8.5%, are reported. The test parameter of the study was the longitudinal reinforcement ratio (1.2 and 3.5%). It was found that the column with higher reinforcement ratio carried 13.7% more load and had 35% less deflection compared to its counterpart with less reinforcement. Moreover, the column with higher reinforcement ratio showed more deformable failure mechanism, which can be attributed to the improved confinement resulted from the large number of longitudinal bars.

Keywords GFRP · Circular columns · Eccentric loads

1   General

Circular concrete columns are found in bridge structures, parking garages, foundation piles and secant walls in earth retaining structures. The columns in such structures withstand different types of loads like vehicle weight, wind load, earthquake load and lateral ice or earth pressure. Due to the loading pattern, the columns are very

S. M. H. Rahman · E. El-Salakawy (✉)
Department of Civil Engineering, University of Manitoba, Winnipeg, Canada
e-mail: ehab.el-salakawy@umanitoba.ca

often subjected to both axial and eccentric loads. Currently, most columns are steel-reinforced concrete (RC) columns, which fail to keep the structural integrity when the steel bars corrode in severe environmental conditions. Conversely, glass fibre-reinforced polymer (GFRP)-RC columns are not susceptible to corrosion. Excellent resistance to corrosion, high strength-to-weight ratio, electromagnetic neutrality, and transparency to radio frequencies, high fatigue resistance, and high service life in corrosive environment are considered some of GFRP's important characteristics [2].

In recent years, there has been a significant amount of research towards the use of GFRP bars as internal reinforcement in compression members, for example, under concentric loads [9], and under eccentric loads [3–6, 10, 12]. Most of these studies were limited to the slenderness ratio of approximately 20, in which the second-order effect of deflection was very little. Regarding slender columns, some researchers [11, 15] studied rectangular columns while others [3, 6, 13] investigated circular columns. None of the studies, except for [13], had a slenderness ratio greater than 33.

From the geometrical perspective, stiffness being inversely proportional to length, a slender column carries less axial load than a shorter counterpart. Also, under the same axial load, a slender column is prone to more second-order moments due to excessive lateral deflection, which raises a concern that a slender column may not reach the material failure. Therefore, to have a better understanding of the behaviour of slender columns, an experimental investigation was conducted under axial loading with eccentricities.

2 Experimental Programme

2.1 Test Specimens and Material Properties

Two columns, C1.2 and C3.5, were constructed with normal-weight, ready-mix concrete, sand-coated GFRP bars, and spirals. At the time of concrete pouring into the formworks, standard concrete cylinders (100×200 mm) were sampled according to the provisions of the CSA A23.1-19/A23.2-19 [8]. Concrete cylinders were tested on the day of column testing, and the average compressive strength was found to be 43 MPa. Both column specimens were reinforced with GFRP bars in the longitudinal direction and GFRP spirals in the transverse direction and were cast vertically to simulate the regular construction practice. Two longitudinal reinforcement ratios (1.2 and 3.5%) were used in this study. The specimen ID consists of one letter "C" referring to column followed by one number presenting the reinforcement ratio, as shown in Table 1.

Two different sizes of GFRP straight pultruded bars (No. 16 and No. 19) and size No.10 GFRP spirals were employed to prepare the reinforcement cages. The reinforcement configuration of both columns met the minimum requirements of the CSA S806-12 (R2017) [7]. The mechanical properties of the reinforcing bars and

Table 1 Details of test columns

Column ID	Concrete compressive strength (MPa)	Eccentricity, e (mm)	Longitudinal reinforcement		Transverse reinforcement		
			No. of bars	ρ_f (%)	Size	Pitch (mm)	ρ_{fs} (%)
C1.2	43	30	6 No. 16	1.21	No 10	85	1.12
C3.5			12 No. 19	3.46			

Table 2 Properties of GFRP bars and spirals

Size (type)	Nominal diameter (mm)	Nominal area (mm²)	Elastic tensile modulus (GPa)	Tensile strength (MPa)	Tensile strain at failure (%)
No. 16 (Bar)	15.9	199	64	1580	2.47
No. 19 (Bar)	19.1	285	63	1465	2.32
No. 10 (Spiral)	9.5	71	54	594	1.10

spirals are shown in Table 2, which were collected from the material compliance certificate provided by the manufacturer [14].

2.2 Instrumentations and Testing Procedure

Lateral displacement, strains in concrete, longitudinal bars and spirals were the primary concerns of the experimental programme. Most of the instrumentation was concentrated around the column mid-section (mid-height), which is the critical section in both compression and tension sides. A total of three LVDTs were mounted perpendicular to the column longitudinal axis at the quarter length. To measure strains at the concrete critical section, a concrete strain gauge was attached to the compression surface. Two strain gauges to the outermost tension and compression GFRP bars and one to immediately next bar to it were attached to take tensile and compressive strains. Two strain gauges were secured in both the tension and compression side of spiral located at the mid-section of the specimens. Also, a PI-gauge was installed on concrete compression surface over a span of 200-mm length to take the strain readings. The instrumentation is shown in Fig. 1.

For both columns, C1.2 and C3.5, a 5000-kN capacity hydraulic machine was used to apply a displacement-controlled load at a rate of 0.25 mm/minute. The loading was stopped once the load-carrying capacity of the column dropped by 50%.
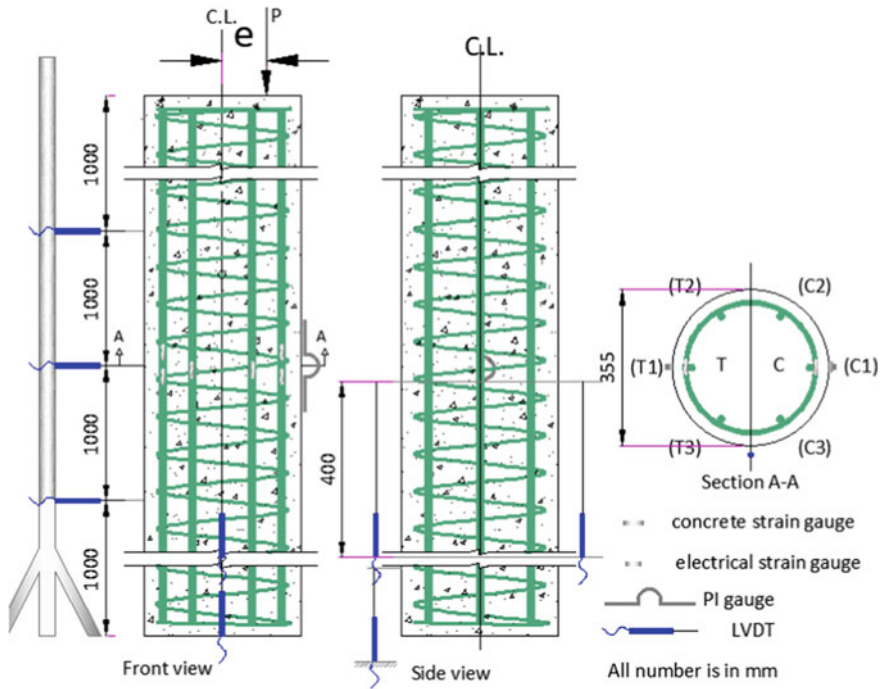
Fig. 1 Instrumentation of test column

3 Test Results and Discussion

3.1 General Behaviour and Failure Modes

The behaviour of both columns can be best described by three stages of structural responses. The first stage is the nonlinear elastic behaviour up to peak load, while the second stage is up to the peak load. The third stage is the descending part or the decline of load-carrying capacity. Column C3.5 showed elastic behaviour with no cracks appeared until the peak load was achieved while column C1.2 had the first visible crack at approximately 97% of the peak load. Immediately before reaching the peak load, column C1.2 began to have a couple of tension cracks at the mid-height. Concrete crushing, and subsequently concrete cover spalling off, in the compression side of column C1.2 resulted in a sudden and significant reduction of load-carrying capacity. The nature of post-peak behaviour indicated a compression failure of column C1.2 as shown in Fig. 2. On the other hand, column C3.5 had also similar behaviour in the first stage of response; however, at the peak load it had some vertical cracks appeared at the mid-height in the compression side. Similar observations were reported by other researchers for columns with small eccentricities [1, 5, 6]. These vertical cracks started to widen and spread over a large area and ultimately led to

Fig. 2 Failure modes of the columns

C1.2		C3.5	
Front view	Side view	Front view	Side view
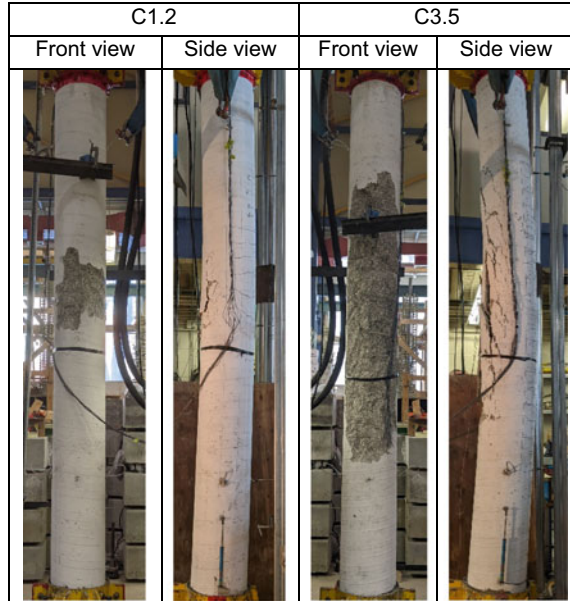
concrete cover spalling off. The post-peak resistance to loading shown by column C3.5 defined a progressive compression failure. At the end of testing both columns, a visual inspection of compression area and GFRP bars and spirals was conducted; however, no evidence of bar crushing on the compression side was found. Also, no rupture of bar or spiral was observed at any location.

3.2 Evaluation of Load Resistance and Strains

The effect of increasing reinforcement ratio from 1.2 to 3.5% was evaluated in terms of load–deflection response, compressive and tensile strains in GFRP bars, concrete and spirals. Since column C1.2 and C3.5 had same eccentricity-to-diameter ratio (e/D) of 8.5% and slenderness ratio (λ) of 45, both columns behaved similarly up to the peak load, as shown in Fig. 3. A certain degree of nonlinearity near the peak load in Fig. 3 can possibly be attributed to the geometric nonlinearity and concrete cracks in the compression side. In terms of load-carrying capacity, column C3.5 carried 13.7% more load compared to its counterpart C1.2. In the ascending loading branch, column C3.5 showed stiffer resistance to deflection compared to column C1.2. For example, at load of 2000 kN, column C1.2 underwent lateral deflection of 8.5 mm while C3.5 deflected by 6.3 mm, i.e. 35% less deflection. This can be attributed to the higher amount of longitudinal reinforcement, which contributed to the increased flexural stiffness of column C3.5. One more noticeable difference was that column C3.5

Fig. 3 Axial load and lateral deflection relationship
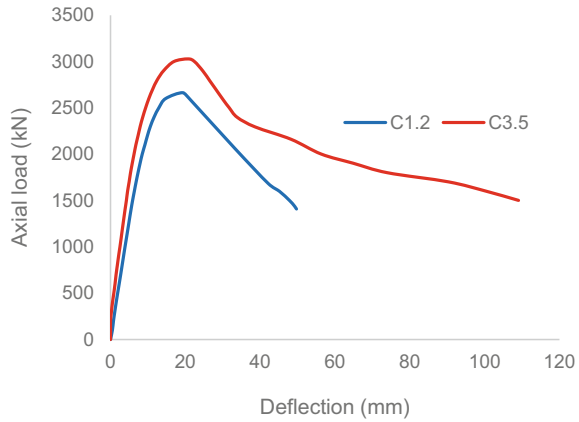
had longer descending branch, which could be credited to increased confinement of concrete core contributed by the 12 longitudinal bars.

Figure 4 demonstrates the strains profile of GFRP bars located in both compression and tension side of C1.2 and C3.5. As both columns were subjected to axial load with a small *e/D* ratio of 8.5%, all bars experienced compressive stresses for almost the whole loading history regardless of the position of the bar in the cross-sectional area. The GFRP bar strains at peak load from tension side of column C1.2 and C3.5 were 540 and 160 με, respectively, whereas the strains from compression side were −3150 and −2490 με, respectively. The higher amount of reinforcement also contributed to limiting the bar strains observed above. It is worth mentioning that no longitudinal bars ruptured or crushed before ending the test for both columns. The maximum recorded compressive strain was −12,050 με, which accounted for more than 50% of the ultimate strains of the GFRP bar.

With the increasing load, concrete and spiral strains were plotted in Fig. 5. Concrete compressive strains in C1.2 and C3.5 reached −2550 and −3060 με, respectively. The spiral tensile strains at the peak load of C1.2 and C3.5 were 1380

Fig. 4 Strains in compression and tension bars
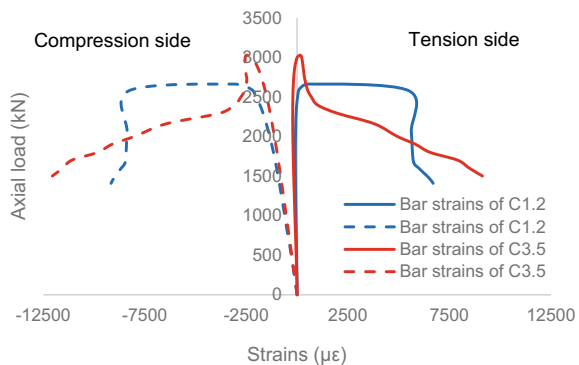
Fig. 5 Strains in concrete and spiral
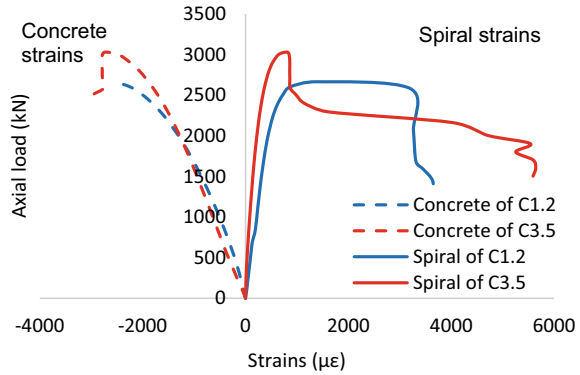
and 800 µε, respectively. However, with higher concrete confinement under higher axial stress in C3.5, the spiral action was activated due to the passive pressure of concrete core mobilization and exceeded the strains of its counterpart C1.2. At the end of testing, the spiral tensile strains in C3.5 were recorded to be 5590 µε (49% of ultimate capacity) as opposed to 3650 µε in C1.2, which contributed to have a progressive collapse of column C3.5 or, in other words, more deformable failure.

3.3 Second-Order Effect

Both columns, C1.2 and C3.5, experienced axial load–deflection (P-Δ) effects up to peak loads. At any specific load in the ascending branch, C1.2 had higher deflection compared to C3.5, so did higher secondary moments. However, the larger amount of reinforcement in column C3.5 increased the load-carrying capacity, which is the reason that both primary and secondary moments were 13.7 and 21.5% higher compared to column C1.2, as listed in Table 3.

In Table 3, P_n = nominal peak load, δ_n = lateral deflection at the mid-section at peak load, M_{n1} = nominal primary moments corresponding to initial eccentricity e, M_{n2} = nominal secondary moments corresponding to lateral deflection.

Table 3 Secondary moments of the test columns

Column ID	e (mm)	P_n (kN)	δ_n (mm)	M_{n1} (kN-m) $P_n \times e$	M_{n2} (kN-m) $P_n \times \delta_n$	M_n (kN-m) $M_{n1} + M_{n2}$
C1.2	30	2664	19.3	79.9	51.5	131.4
C3.5	30	3028	20.7	90.8	62.6	153.4

4   Conclusions

Based on the test results and discussion above, the following findings can be concluded:

a. Both columns showed nonlinear elastic resistance to loading up to the peak load. Column C3.5 had a progressive compression failure characterized by longer descending loading branch.
b. The effect of increasing the longitudinal reinforcement from 1.2 to 3.5% on the load–deflection relationship was pronounced as indicated by 13.7% more load-carrying capacity and 35% reduced deflection.
c. Up to the peak load, column C1.2 experienced more second-order moments caused by excessive deflection at the same loading level; however, in the post-peak load, column C3.5 had higher secondary moments.

References

1. Abdelazim W, Mohamed HM, Afifi MZ, Benmokrane B (2020) Proposed slenderness limit for glass fiber-reinforced polymer-reinforced concrete columns based on experiments and buckling analysis. ACI Struct J 117(1):241–254
2. ACI Committee 440 (2015) Guide for the design and construction of structural concrete reinforced with FRP bars (ACI 440.1R-15). American Concrete Institute, Farmington Hills, MI
3. Almomani M, Mahmoud K, El-Salakawy E (2022) Experimental investigation of large-scale eccentrically loaded GFRP-reinforced high-strength concrete columns. J Comp Constr ASCE 26(2):04021072
4. Almomani M, Mahmoud K, El-Salakawy EF (2022) Effect of slenderness ratio on GFRP-reinforced HSC columns. ACI Struct J 119(2):287–299
5. Barua S, El-Salakawy E (2020) Performance of GFRP-reinforced concrete circular short columns under concentric, eccentric, and flexural loads. J Compos Constr ASCE 24(5):04020044
6. Barua S, Mahmoud K, El-Salakawy E (2021) Slender GFRP-RC circular columns under concentric, eccentric, and flexural loads: experimental investigation. J Bridge Eng ASCE 26(7):04021033
7. Canadian Standards Association (CSA) (2017) Design and construction of building structures with fiber-reinforced polymers. CSA S806-12 (R 2017), Canadian Standards Association, Toronto, ON, Canada
8. Canadian Standards Association (CSA) (2019) Concrete materials and methods of concrete construction/Test methods and standard practices for concrete. CSA A23.1-19/A23.2-19, Canadian Standards Association, Toronto, ON, Canada
9. De Luca A, Matta F, Nanni A (2010) Behavior of full-scale glass fiber-reinforced polymer reinforced concrete columns under axial load. ACI Struct J 107(5):589–596

10. Guerin M, Mohamed HM, Benmokrane B, Nanni A, Shield CK (2018) Eccentric behavior of full-scale reinforced concrete columns with glass fiber-reinforced polymer bars and ties. ACI Struct J 115(2):489–499
11. Khorramian K, Sadeghian P (2019) Behavior of slender GFRP reinforced concrete columns. In: Structures congress, Orlando, Fl, 24–27 Apr.
12. Hadhood A, Mohamed HM, Benmokrane B (2017) Experimental study of circular high-strength concrete columns reinforced with GFRP bars and spirals under concentric and eccentric loading. J Comp Constr ASCE 21(2):04016078
13. Hales TA, Pantelides CP, Reaveley LD (2016) Experimental evaluation of slender high-strength concrete columns with GFRP and hybrid reinforcement. J Comp Constr ASCE 20(6):04016050
14. Pultrall Inc. (2021) Pultrall.com, Canada. https://www.pultrall.com/en/index.asp
15. Xue W, Peng F, Fang Z (2018) Behavior and design of slender rectangular concrete columns longitudinally reinforced with fiber-reinforced polymer bars. ACI Struct J 115(2):311–322

Feasibility of Using Powder Actuated Fasteners in Carbon Nanofibre Ultra-High Performance Fibre Reinforced Concrete

B. T. Forrest, R. El-Hacha, and J. Michels

Abstract Powder actuated fasteners (PAFs) are recognized as a safe and cost-effective fastening technique of non-structural elements to masonry, steel, and concrete. A novel flexural post-tensioning technique uses PAFs to anchor iron shape memory alloy (Fe-SMA) strips to strengthen reinforced concrete (RC) structures. The technique is being explored for strengthening ultra-high performance fibre reinforced beams (UHPFRC). However, there is no data on the fastening performance of UHPFRC. The objective of this experiment was to investigate the feasibility of using PAFs to anchor an Fe-SMA strip to UHPFRC beams by comparing the pull-out strength to a reference study with conventional concrete. The capacity of various anchorage configurations was evaluated with thirteen specimens. The key variables were the number of fasteners, fastening spacing, and length. Tension was applied using a hydraulic pulling system until anchor failure. Four, six, and eight-fastener configurations (22 mm long) with 50 mm spacing resisted a pull-out load of 35kN, 130kN, and 144kN, respectively, which exceeds results from the reference study that used 45-mm-long fasteners. In addition, more cost savings are possible as no pre-drilling was required in this investigation. Group effects were observed at a fastener spacing of 25 mm. However, the results varied significantly and the UHPFRC blocks rotated during testing, so the load-slip could not be reported. As the popularity of UHPFRC increases, having fastening performance data for PAFS will enable its advantages to be exploited. From this investigation, PAFs could be a suitable candidate. More tests for repeatability and increased confidence are recommended, and new applications are proposed.

Keywords Powder-actuated fasteners · Carbon nanofiber · Ultra high performance fiber reinforced concrete

B. T. Forrest (✉) · R. El-Hacha
University of Calgary, Calgary, Canada
e-mail: benjamin.forrest@ucalgary.ca

J. Michels
Re-Fer AG, Schwyz, Switzerland

1 Introduction

Builders and designers are constantly looking for ways to improve field installation cost and time. Powder actuated fasteners (PAF) are recognized as a safe and cost-effective means of fastening into various base materials such as steel, concrete, and masonry. Many applications exploit the ease of fastening with PAFs, such as fastening partition walls, cold-formed steel, wood sill plates, steel deck attachment, and plumbing or electrical components. The fasteners use energy from either compressed gas, battery power or powder cartridges to propel the fastener through the material. In addition, PAFs save time and cost relative to mechanical and adhesive anchors as there is often no requirement for pre-drilling, need to clean out drilled holes, and need to install and wait for adhesives to set or requirement to tighten mechanical anchors.

An emerging technique for strengthening reinforced concrete (RC) beams uses PAFs to anchor external unbonded post-tensioning tendons to the concrete. The technique exploits the shape memory effect of iron-based shape memory alloy (Fe-SMA) strips. When the tendon is heated, it generates internal stress (recovery stress), which post-tensions the concrete structure at the anchors [1, 2]. The PAF anchoring system was compared to others using bolts or clamping plates. It was selected as the most practical system citing comparable pull-out capacity and less slip [3].

The effectiveness of using PAFs to anchor the Fe-SMA for the novel post-tensioned strengthening technique was demonstrated in the literature and has also been proven in the field [1, 4, 5] for strengthening RC structures. A recent study was conducted to improve the performance of girders using Fe-SMA strips and carbon nanofibre ultra-high performance fibre reinforced concrete (CNF-UHPFRC) [6]. The Fe-SMA strips were also anchored using PAFs. However, to the best of the authors' knowledge, there are no reports of using these fasteners in ultra-high performance concrete (UHPFRC) in the literature. Hilti's documentation limits technical fastening data to concretes with compressive strengths less than 55 MPa [7]. Through consultation with Hilti representatives, the limitation comes from a declining fastening performance with increased concrete strength for two reasons. A longer fastener has more tendency to bend due to a denser matrix, and higher strength concrete is generally more brittle, resulting in a greater tendency for surface spalling. Additionally, a fastener gets holding power from concrete which opens as the fastener is driven through and closes back on the fastener shaft. High-strength concrete is generally stiffer and has less tendency to close back on the fastener. The more inelastic response, combined with increased surface spalling and cracking, results in less fastener withdrawal resistance. As compensation, with longer fasteners or higher strength concretes, Hilti recommends pre-drilling holes in the concrete to reduce surface material and allow deeper penetration without bending or deflecting.

CNF-UHPFRC, by contrast, has no large aggregates and is less brittle due to the presence of steel fibres. As well, since the fastening performance with this specific UHPFRC was unknown, attempts to fasten without pre-drilling were made. Eliminating the need to pre-drill would further reduce installation time and cost, making

this strengthening technique more attractive and practical in the field. In this investigation, feasibility tests were conducted to investigate the fastening performance of PAFs in UHPFRC. This investigation aims to evaluate the feasibility of using PAFs to anchor Fe-SMA strips to CNF-UHPFRC. This objective is reached with two sub-objectives. First, the required power configuration to properly fasten the Fe-SMA strip into CNF-UHPFRC was evaluated based on a visual quality inspection. Second, various anchorage configurations were evaluated in a pull-out test to determine the pull-out strength and slip of the Fe-SMA relative to a CNF-UHPFRC block. This article explains the experimental set-up to achieve each sub-objective, followed by the results and a discussion on the fastening performance and observations during the experiments. Finally, new applications derived from the findings of this investigation are proposed, followed by the main conclusions drawn and recommendations for future research.

2   Experimental Set-up

The materials, test objectives, and set-up in the investigation are summarized in this section.

2.1   Materials

The alloy composition for the Fe-SMA strips used in this investigation was Fe-17Mn-5Si-10Cr-4Ni-1(V, C) (mass%) which is the same alloy used in similar tests and case studies for strengthening RC beams [1–3, 5, 8, 9]. The 1.5 mm thick strips are 120 mm wide.

The base material in this investigation was a proprietary mix of CNF-UHPFRC. In contrast to other UHPFRC blends, this mix can be mixed on-site using standard concrete mixing equipment and does not require complex curing regimes. The mix consisted of a blend of premix (cement and fine aggregates), a proprietary paste (dispersed carbon nanofibres), water, and steel fibres. The steel fibres (0.2 mm diameter) were 13 mm long with a tensile strength of 2500 MPa. The specimens for the penetration tests consisted of 300-mm-long rectangular prisms with a 75 mm-by-75 mm cross section and 150-mm-deep cylinders with a diameter of 75 mm. For the batch used in this investigation, the mass percentage of premix, paste, water, and fibres was 86%, 1%, 7%, and 6%, respectively. Compression strengths were determined with standard compression tests (ASTM C39M-21) performed on the cylinders. The average compressive strength of the mix was found to be 122 MPa and 124 MPa at the age of 28 and 53 days (day of the anchorage tests), respectively. The tension properties were determined following the inverse analysis method specified in CSA S6:19 Annex 8.1 for tension softening fibre reinforced concrete (TSFRC). The average cracking, specified post-cracking, and ultimate post-cracking strength

were 10.2 MPa, 3.13 MPa, and 0.1 MPa, respectively. The crack associated with the specified and ultimate post-cracking strength was 0.5 mm and 2.2 mm, respectively.

2.2 Penetration Tests

The objective of these tests was to determine a suitable fastening length and power configuration for fastening the Fe-SMA strip to the UHPFRC beam. The direct fasteners are available in multiple shank lengths (22, 27, and 40 mm) and shank types (universal or premium). The power configuration was regulated by cartridge level and fastening tool power setting. The cartridge levels and penetration power are given in Table 1. Due to the dense matrix and presence of steel fibres of CNF-UHPFRC, level 5 and 6 cartridges were used in this investigation (red and black colour, respectively). In addition to the cartridge level, a tool setting regulates the power by increasing or decreasing stand-off from the fastening surface. The tool used in these experiments is the DX-5 shown in Fig. 2, and the power settings are in increments of 0.5 and range from 1 to 4. Rectangular prisms (300 mm × 75 mm × 75 mm) and cylinders (150 mm × 75 mm) were used for testing the fastening quality. Initially, the tests were conducted without Fe-SMA to observe any negative effects such as damage from spalling or cracking. Following those tests, small tabs of Fe-SMA were added to find the correct power configuration to fasten the tabs to the cylinders. The quality of fastening was determined by a visual inspection following guidelines in Hilti's technical documentation. It was characterized as a fastening which is neither overdriven nor underdriven, with no evidence of damaged CNF-UHPFRC or Fe-SMA material. The longer fasteners have more withdrawal resistance; however, the risk of deflection or bending is increased. Compared to the universal fasteners, the premium fasteners are made from a stronger material, less prone to bending. Premium fasteners were selected through consultations with senior Hilti codes and standards representatives. Additionally, anchorage capacity would be evaluated for the shortest fasteners without pre-drilling to establish minimum performance data for this feasibility study. Ten tests using the 22 mm fastener length were designed to meet the objectives of this ancillary test. The test set-up and parameters are given in Table 2.

2.3 Anchorage Tests

Following the penetration tests, the objective of the anchorage tests was to investigate the pull-out strength of the anchorage design to determine the feasibility of using PAFs to anchor Fe-SMA strip to CNF-UHPFRC beams. Similar pull-out tests on conventional concrete blocks in a reference study reached pull-out loads of 45–110 kN depending on the configuration of the fasteners. Since the anchorage will be used in a similar application on CNF-UHPFRC beams, the fastening method would be

Table 1 Cartridge level (and corresponding colour) recommended by fastener manufacturer*

Base material	Recommended Cartridge level
Solid concrete blocks	2
Concrete (2000 psi, 13 MPa)	2, 3
Concrete (4000 psi, 27 MPa)	3, 4, 4.5
Concrete (6000 psi, 41 MPa)	4, 4.5, 5, 6
Steel	5, 6

* After [7]

Cartridge colours correspond to levels

They are 2—White, 3—Green, 4—Yellow, 4.5—Blue, 5—Red, 6—Black

Table 2 Penetration test results (22-mm-long fasteners)

Test no.	Base material	Fe-SMA present?	Fastener status (length in mm O/U)	Specimen status	Cartridge colour	Tool power setting
P1	P	No	NF	D	Red	1
P2	P	No	NF-U (+16.5)	D	Red	1
P3	Cy	No	NF-O (−3.2)	Cr	Red	4
P4	Cy	No	NF-O (−2.8)	Cr	Red	3
P5	Cy	No	NF-O (−1.9)	Cr	Red	2
P6	Cy	No	NF-U (+1.3)	Cr	Red	1
P7	Cy	Yes	NF-U (+1.4)	Cr	Red	2
P8	Cy	Yes	NF-PU	Cr	Red	3
P9	Cy	Yes	F	Cr	Red	2.5
P10	Cy	Yes	F	Cr	Red	3

P—Rectangular prism (300 mm long, 75 mm wide, 75 mm deep)

Cy—Cylinder (150 mm long, 75 mm diameter)

F—Fastened, NF—Not fastened, O—Over, U—Under, PU—Fastener pull-out

D—Destroyed, Cr—Cracked

considered feasible if similar values are achieved in this investigation. For the base material, 300-mm-long CNF-UHPFRC blocks with the same cross section of the beams were constructed and installed in a steel reaction frame. A 600 mm length of Fe-SMA plate was then fastened to the block using various anchorage configurations shown in Fig. 1. The changing parameters were primarily the fastener spacing and the number of fasteners. The other end of the Fe-SMA plate was connected to a hydraulic pulling system via a bolted connection shown in Fig. 3. A hydraulic jack, shown in Fig. 4, engaged the pulling system, and a load cell was used to monitor the load. The reaction frame is shown in Fig. 3. It consisted of a large steel beam (yellow) bolted to the 75 mm thick concrete floor. Additional braces (red) and a heavy steel plate clamped to two channels (red) bolted to the floor were provided to resist CNF-UHPFRC block movement. The flanges and web of the stiff column (red) shown in
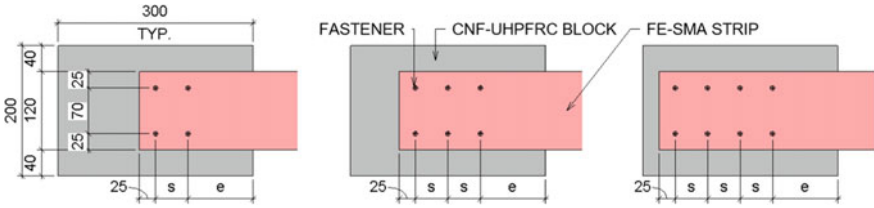
Fig. 1 Various anchorage configurations investigated in the anchorage tests. s—fastener spacing, e—edge distance

Fig. 4 were stiffened to prevent buckling. The pull-out test consisted of switching on the hydraulic pump, which began applying tension to the pull-out system and anchorage. The pull-out load was increased uniformly until the anchorage connection failed. Two video cameras recorded the failure, one recorded the experiment from an oblique angle above the specimen to capture the experiment overall. The other was positioned aligned with the top surface of the CNF-UHPFRC blocks to observe the failure mechanism of the anchors.

Fig. 2 Hilti DX-5 tool shown here was used for fastening all powder actuated fasteners in this investigation
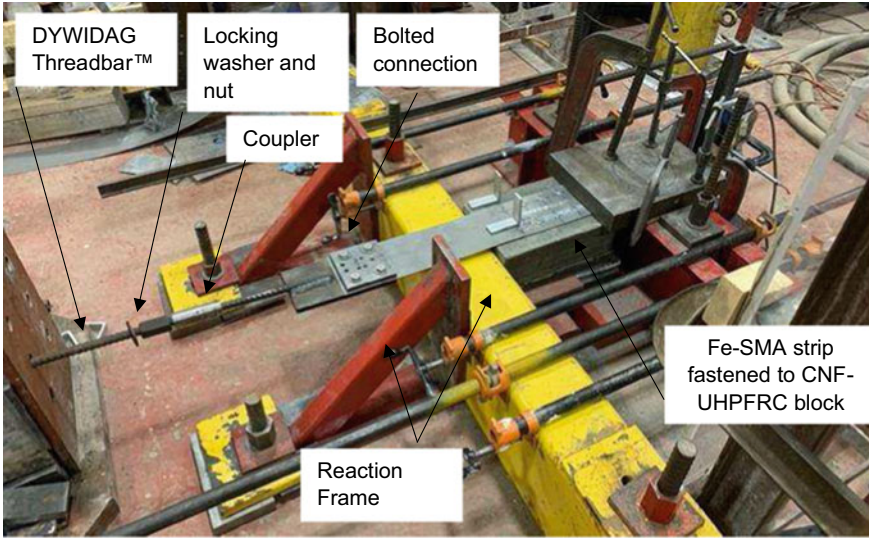
Fig. 3 Anchorage tests set-up showing reaction frame, pulling system, Fe-SMA strip fastened to the CNF-UHPFRC block, and deflectors for the lasers

Fig. 4 Hydraulic jack and load cell for recording the force from the pulling system

3 Results and Discussion

3.1 Penetration Tests

A suitable power configuration for the DX-5 was found to be with a level five cartridge and a power setting of 2.5. A summary of the results is presented in Table 2. Initially, shallow, 75-mm-deep CNF-UHPFRC prisms were used. However, they were destroyed after fastening as shown in Fig. 5. To prevent shattering, the base material was changed to deeper cylinders (150 mm). Although none of the cylinders shattered, some surface material at the fastener spalled, exposing some steel fibres and forming large cracks. Some spalling was expected. It is reasonable to think the

amount of spalling was reduced by the presence of steel fibres. The cracking was attributed to the small distances from the fastener to the edge of CNF-UHPFRC. Although a structural concern, larger edge distances will be provided in the actual anchorage tests and CNF-UHPFRC beam, so it was not considered to hinder the feasibility of the fastening method. With the specimens remaining intact after fastening, a bracketing technique suggested by Hilti's technical documentation was followed to find the appropriate cartridge level and power setting, starting with red cartridges and the lowest setting. If proper fastening was not achieved, the power setting was increased. Black cartridges would be used if proper fastening could still not be achieved. Black cartridges were not used since proper fastening occurred with red cartridges. With red cartridges and a tool setting of 1, the fastener in test P2 was under-fastened. Increasing the tool setting to 4 resulted in over-fastening for test P3. The tool setting was incrementally lowered for tests P4 and P5, resulting in less over-fastening each time until the fastener was under-fastened once again in test P6 with a tool setting of 1. Increasing the tool setting back to 2 in test P7 under-fastened the fastener is interesting since the same power setting over-fastened the fastener in test P5. This is likely attributed to how the tool was positioned and held during fastening and is evidence of the sensitivity of fastening to the operator's technique. A good fastening was observed in tests P9 and P10, although surface cracks were produced as mentioned earlier using a power setting of 2.5 and 3. The power cartridge level and tool setting for the 22-mm-long nails were selected as a red cartridge with a tool setting of 2.5 (Figs. 6 and 7).

Fig. 5 Image showing destroyed rectangular prism after fastening test P2

Fig. 6 Image showing spalled surface material, exposed steel fibres and large cracks after test P3

Fig. 7 Images of all the specimens following the penetration tests showing the destroyed and cracked specimens with and without Fe-SMA

3.2 Anchorage Tests

The results of thirteen tests are given in Table 3. As expected, there was no evidence of surface cracks in the larger CNF-UHPFRC specimens due to larger edge distances

compared to the cylinder specimens in the penetration tests. Inconsistent results occurred in test A1-A3 due to improperly fastened fasteners. Since the fasteners were under-fastened, increased power was required. Once a new power configuration was selected, improper fastenings occurred less frequently. The configuration for four, six, and eight fasteners at 50 mm o.c. achieved a maximum pull-out capacity of 48.9, 47.6, and 145kN, respectively. For comparison, the eight-fastener configurations in the reference study [3] achieved a maximum pull-out capacity of 118kN. This is interesting since the fasteners used in the reference study were longer (45 mm vs 22 mm), and the concrete was pre-drilled prior to fastening. This finding supports the potential for time and cost savings using PAFs with CNF-UHPFRC. Group effects appeared to hinder the capacity when the fastener spacing was reduced to 25 mm. Looking at tests A6 and A7, reducing the fastening spacing from 50 to 25 mm reduced the maximum pull-out capacity by 46%. When the photos of these specimens after testing are reviewed, shown in Fig. 8, there is evidence of overlapping failure cones (indicated with dotted circles) which supports the reduction in pull-out capacity.

Overall, there was a correlation between the number of fasteners and the pull-out capacity; however, there was a significant variation of results for each group of fasteners which appears to correlate with the number of proper fastenings. Determination of a proper fastening was conducted by a visual inspection and characterized by a fastening which is neither over nor underdriven, with no damage visible on the Fe-SMA strip or surrounding CNF-UHPFRC. As discussed earlier, the variation

Table 3 Anchorage test results

Test no	No. fasteners	No. proper fastenings[a]	Edge distance e, (mm)	Cartridge-tool setting	Fastener length (mm)	Fastener spacing s, (mm)	Pull-out load (kN)
A1	4	3	100	Red-2.5	22	100	61.6
A2	4	3	100	Red-4	22	100	34.5
A3	4	2	100	Red-4	22	50	13.4
A4	4	3	50	Black-4	22	50	35.2
A5	4	2	100	Black-2.5	22	50	44.3
A6	4	4	50	Black-2.5	22	50	48.9
A7	4	4	50	Black-2.5	22	25	22.3
A8	4	0	100	Black-4	40[b]	100	47.8
A9	4	0	100	Black-4	27[b]	100	35.5
A11	6	6	100	Black-2.5	22	50	47.8
A10	8	8	75	Black-2.5	22	50	144.6
A12	8	8	75	Black-2.5	22	50	131.0
A13	8	7	75	Black-2.5	22	50	90.6

[a] Proper fastenings are based on a visual inspection and are characterized by a fastening which shows good seating on the Fe-SMA plate as per manufacturer recommendations
[b] All fasteners were under-fastened

Fig. 8 Side by side images of the CNF-UHPFRC block after the pull-out test A6 (left) and A7(right). Dotted lines are added to point out the extent of the failure cones

in fastening performance was attributed mainly to the way the tool was held and positioned during fastening. Only five out of thirteen tests (A6, A7, A10, A11, and A12) had all proper fastenings, highlighting the importance of proper handling by the operator. For instance, looking at tests A12 and A13, there was a 31% reduction in pull-out capacity when one of the fasteners was improperly fastened. As well, it is almost impossible to remove the fastener and install a new one in its place without damaging the surrounding Fe-SMA and CNF-UHPFRC, so additional fasteners are required as compensation which changes the anchorage configuration and failure path. Additional tests and practice by the operator are recommended to reduce the number of improper fastenings.

The power configuration was changed from that selected in the penetration tests. Test A1 had one under-fastened fastener, so the power setting was increased to 4 for subsequent tests. Both A2 and A3 also had under-fastened fasteners, so black cartridges were used. A tool setting between 2.5 and 4 was selected in a trial-and-error process until proper fastenings were achieved with a good frequency with a tool setting of 2.5. Note a consistent tool setting was arrived at after 11 tests. This supports the need for the operator to become familiar with the operation, cartridge level, and tool setting prior to using the fastening method for better results.

Two tests, A8 and A9, were attempted with longer fasteners (40 mm and 27 mm, respectively) to observe the fastening quality. The 40 mm fasteners were under-fastened by almost 20 mm, and the 27-mm-long fasteners were marginally under-fastened by 5 mm. Regardless, even using the highest power configuration available (black cartridge, setting 4), the fasteners were still under-fastened. Therefore, the pre-drilling technique recommended by the manufacturer should be employed when these larger fasteners are used. The pre-drilling method is explained in the technical guide and consists of drilling a pilot hole in the base material. The fastener is then placed in the pilot hole and fastened using the fastening tool. The pre-drilling technique should reduce the tendency for surface material to spall and the fastener to bend or deflect when being driven through the concrete. Therefore, it is reasonable to believe larger fastening capacities will be achieved with longer fasteners as long as the pre-drilling method is employed.

Reviewing the footage from the tests, all experiments failed by a pry-out mechanism, one of the typical failure mechanisms for anchors in concrete. Therefore, the final configuration tested was with eight fasteners at 50 mm spacing. This configuration was tested three times (A10, A12 and A13). However, in test A13, only seven out of eight fasteners were fastened properly, resulting in a significant reduction in pull-out capacity evident in Table 3. Regardless, this anchorage configuration met the objective by achieving greater pull-out strengths compared to the reference study for the same configuration in tests A10 and A12. This supports PAFs being a feasible anchorage method for fastening a Fe-SMA strip into a CNF-UHPFRC beam (Figs. 9 and 10).
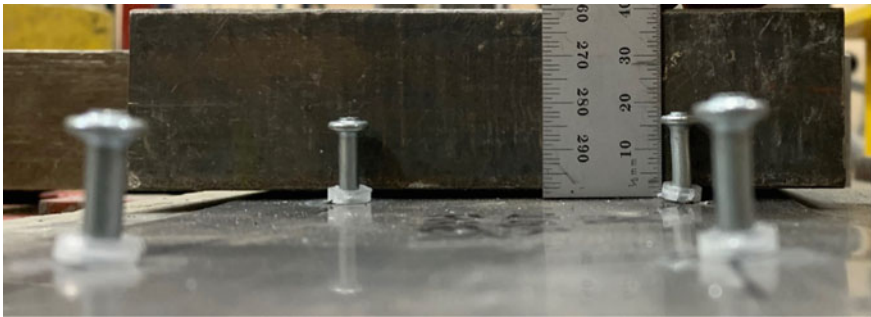
Fig. 9 Surface image of test A8 showing four under-fastened fasteners (40 mm fastener, no pre-drilling)

Fig. 10 Surface image of test A9 showing four slightly under-fastened fasteners (27 mm fastener, no pre-drilling)

4 Potential Applications

The findings of this investigation are related to anchoring the Fe-SMA strip to CNF-UHPFRC beams. However, it has impacts on fastening any material to CNF-UHPFRC as well, which opens the door for new applications proposed in this section.

Failure of reinforced concrete strengthening techniques can be governed by the concrete failing at the anchors. This type of failure is characterized by a pry-out which occurred in this investigation and shear or crushing of the concrete in the vicinity of the anchors. Replacing conventional concrete at the anchors with CNF-UHPFRC is a promising solution to increase the capacity of the anchors. The steel fibres, coupled with enhanced tensile and compressive strengths of CNF-UHPFRC, should minimize surface spalling and cracking, allowing anchors to resist more force compared to anchors in conventional concrete structures. It would be interesting to compare the anchorage performance of anchors installed in conventional concrete to those of RC structures replaced with UHPFRC at the location of the anchors.

The use of CNF-UHPFRC is more prevalent in bridges today than ever before. As UHPFRC is substituted for conventional concrete, it will be necessary to fasten non-structural components to UHPFRC, such as plumbing and electrical components. Perhaps a more significant application could be the attachment of guard rails and fences. There may be an opportunity for substantial time and cost savings if PAFs are used as anchors when fastening into CNF-UHPFRC, as it could eliminate the need for pre-drilled baseplates. Even if the entire bridge is not constructed with UHPFRC, a portion of the concrete could be substituted with CNF-UHPFRC at the guard rails. It would be interesting to investigate the performance of PAFs for anchoring guard rails to CNF-UHPFRC.

5 Conclusion

The feasibility tests in this investigation were devised to evaluate the fastening performance of Hilti PAFs in CNF-UHPFRC since it is not reported in the literature or from the manufacturer. Ten penetration tests were conducted to determine an appropriate power configuration by varying the DX-5 tool setting. Initially, the tests were performed without Fe-SMA to observe any damage. There appeared to be minimal spalling, likely due to the presence of steel fibres. Proper fastenings were achieved with red cartridges and a tool setting of 2.5; however, the CNF-UHPFRC cylinders used were cracked, attributed to small edge distances.

In the anchorage tests, the same power configuration resulted in under-fastened fasteners due to the larger edge distances and no energy was lost when the base material cracked. Therefore, the power configuration was increased to black cartridges with a tool setting of 2.5. Thirteen tests were conducted to determine an anchorage configuration that could support comparable pull-out capacities of a reference study

where PAFs were used to anchor an Fe-SMA strip to conventional concrete. However, in contrast to the reference study, shorter fasteners were used (22 mm vs 45 mm) without pre-drilling the base material to investigate the minimum capacity from this fastening method. The following are the key findings of the anchorage tests:

- The anchorage configuration selected is eight, 22-mm-long fasteners spaced at 50 mm;
- This configuration resisted a pull-out load of 145 kN which exceeds that from the reference study by 23%;
- Group effects appeared to govern the capacity when at a spacing of 25 mm o.c. evident with overlapping failure cones; and
- Steel fibres within the CNF-UHPFRC likely resulted in less spalling at the surface.

The findings are based on a limited number of tests for each anchorage configuration. The resulting pull-out capacities varied significantly, which was attributed to improper fastenings. It is recommended, in addition to the operator getting familiar with the tool operation and power configuration, at least five specimens for each anchorage configuration should be investigated for repeatability and to increase confidence in the fastening method with CNF-UHPFRC. It would be interesting to compare the pull-out capacity of PAFs in CNF-UHPFRC and compare the results to those in conventional concrete.

Specifically, PAFs could be used for all the same applications for which it is already recognized as a safe and efficient means of fastening, such as fastening cold-formed steel, partition walls and plumbing or electrical components. It is likely installation cost and time could be improved by eliminating the need for pre-drilling and using shorter fasteners relative to those used in conventional concrete while still achieving a similar pull-out capacity. Potential new applications such as improving strengthened concrete structures by substitution of conventional concrete with CNF-UHPFRC at the anchors or installing guard rails and fencing on bridges were proposed. The findings are significant as the need for time, and cost-effective fastening methods is unlikely to diminish as more concrete products are substituted with UHPFRC.

References

1. Schranz B, Michels J, Shahverdi M, Czaderski C (2019) Strengthening of concrete structures with iron-based shape memory alloy elements: case studies. In: Proceedings of the SMAR 2019—fifth conference on smart monitoring assessment and rehabilitation of civil structures, Potsdam, Germany

2. Michels J, Shahverdi M, Czaderski C (2017) Flexural strengthening of structural concrete with iron-based shape memory alloy strips. Struct Concr 19(3):876–891
3. Schranz B (2017) Strengthening of reinforced concrete structures with iron-based shape memory alloy strips. Universität für Bodenkultur Wien, Vienna
4. re-fer AG, referenzen | referenzobjekte. Retrieved 21 Feb 2022, from https://www.re-fer.eu/referenzen/
5. Forrest BT, El-Hacha R, Michels J (2021) Flexural strengthening of reinforced concrete structures using iron-based shape memory alloys: case studies (IN PRESS). In: Proceedings of the eighth international conference on advanced composite materials in bridges and structures, Sherbrooke, Canada, Springer
6. Forrest BT, El-Hacha R, Michels J (2022) Improving the flexural performance of girders with carbon-nanofibre, ultra, high-performance, fibre-reinforced concrete post-tensioned with iron-based shape memory alloy strips (SUBMITTED). In: Proceedings of the Canadian society for civil engineers 2022 annual conference, Whistler, Canada
7. Hilti Volume 1: Direct fastening technical guide, ed 21
8. Strieder E et al (2019) Strengthening of reinforced concrete beams with externally mounted sequentially activated iron- based shape memory alloys. Materials 12(3)
9. Mercier J, Basile B, Hallopeau X, Michels J, Tourneur C, AG R-f (2019) Structural concrete strengthening with Fe-SMA strips: case study with specific control after activation. In: Proceedings of the SMAR 2019—fifth conference on smart monitoring assessment and rehabilitation of civil structures, Potsdam, Germany

Evaluation of Concrete Constitutive Models for Finite Element Simulation of Dam Shear Keys

Mario Freitas, Mahdi Ben Ftima, Pierre Léger, and Najib Bouaanani

Abstract   Three-dimensional performance-based structural assessment of concrete dams subjected to floods and earthquakes requires an accurate estimation of inter-monolith-relative displacements. These displacements could be limited by the presence of shear keys, used in many concrete gravity and arch dams' contraction joints as interlocking mechanisms for transferring shear forces between adjacent monoliths. The key shear strength that could be mobilized is a function of several parameters that control the load–displacement response and failure mechanisms: friction, cohesion, key geometry, confinement pressure, etc. The influence of these parameters is not well understood. This paper first presents an evaluation of five concrete constitutive models implemented in three commercially available general-purpose finite element software packages for numerically simulating the behavior of plain concrete shear keys (ABAQUS, LS-Dyna, ATENA). First, a brief review of each model is presented, including their theoretical formulations, required inputs, advantages, and limitations. Experimental data on shearing of trapezoidal shear keys, available from the literature, are used to evaluate the performance of each constitutive model. The study is then extended to different shear key geometries. It is shown that the load–displacement responses, ultimate shear capacities, failure mechanisms, and post-peak softening behavior can be accurately predicted by a well-calibrated LS-Dyna Concrete Surface Cap Model. It is also shown that the geometry and the boundary conditions, with either unrestrained or restrained lateral shear dilatancy, can greatly influence the failure mechanisms and consequently the shear key load-bearing capacity and residual strength.

Keywords   Concrete constitutive models · Finite element simulation · Dam shear keys

M. Freitas (✉) · M. Ben Ftima · P. Léger · N. Bouaanani
Polytechnique Montréal, Montréal, Canada
e-mail: mario-raul.freitas@polymtl.ca

1   Introduction

Shear keys are present in the contraction joints of many existing concrete gravity dams (Figs. 1a, b). These shear keys were initially designed considering a bidimensional (2D) behavior and little consideration for seismic loads. Empirical estimates of the shear capacity of shear keys are based on friction and cohesion resistances developed along the joint [6]. However, evidence of three-dimensional (3D) behavior of shear keys subjected to seismic loads has been presented in the literature [2, 5, 8, 11, 20, 24]. Thus, the actual behavior and capacity of shear keys under seismic load may significantly differ from those assumed in design.

Shear keys have been considered in finite element analyses of concrete dams by many authors. However, due to the significant difference in scale between the shear keys and the dam, detailed modeling of the key geometry would result in unrealistically fine meshes. Most authors simplify the keyed joints as high-stiffness linear springs, ignoring slipping and failing of the keys [14, 16, 23]. Other authors consider the possibility of failure of the shear keys by computing the shear stress in the joint and comparing it to the estimated key strength. Once the shear stress exceeds this estimate, the key is assumed failed and only frictional resistance is left [1, 10, 12]. Simplified shear key geometries, substituting the detailed shear keys with fewer larger keys has also been proposed [9, 21]. However, these models do not capture the local nonlinear response of shear keys, neither they consider the interactions with multiaxial loading, including effects of bending moment and torsion (Figs. 1c, d).
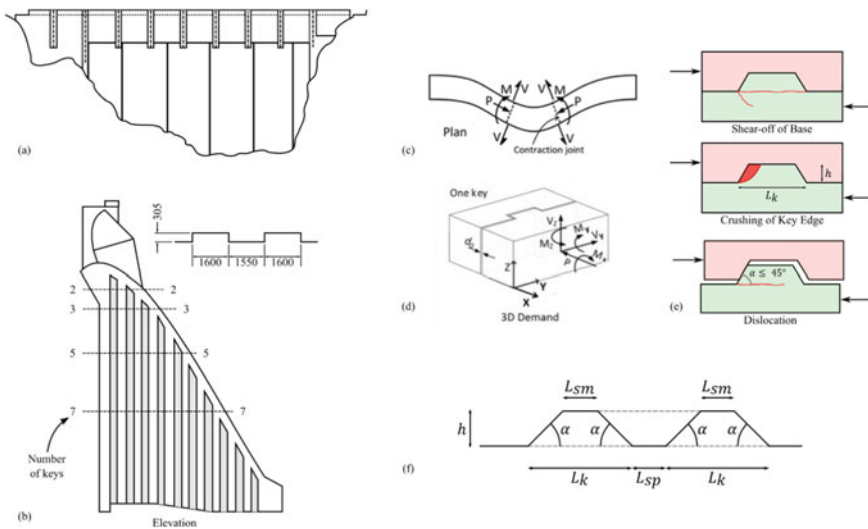
Fig. 1   Shear keys in gravity dams: **a** profile of a gravity dam, **b** elevation section of a spillway with shear keys, **c** contraction joint loads, **d** 3D demand on shear keys, **e** shear key failure mechanisms (adapted from Lacombe, and Pommeret [15]), **f** geometric parameters of shear keys

In this study, a comparison between the constitutive models (i) Continuous Surface Cap Model (CSCM/LS-Dyna) (Murray, 2007), (ii) Karagozian and Case Concrete (KCC/LS-Dyna) [17], (iii) Concrete Damage Plasticity (CDP/ABAQUS) [7], (iv) "Endommagement Progressif Multiaxial Tridimensionnel" (user-defined subroutine—EPM3D/ABAQUS) [18], and (v) StahlBETonAnalyse (SBETA/ATENA) [4] is performed. The goal of the comparison is to evaluate which constitutive model best captures the nonlinear response of concrete shear keys. Experimental data from Zhou et al. [25] and Jiang et al. [13] are used to validate the constitutive models. Then, parametric variation of the key geometry is performed to study the possible failure mechanisms and the influence of geometry in the key loading response (Figs. 1e, f).

2 Evaluation of Concrete Constitutive Models for Shear Keys

2.1 Experimental Data on Shear Keys

Experimental data from Zhou et al. [25] and Jiang et al. [13] are used for the assessment of the concrete constitutive models. These experimental tests were chosen from the literature because they present levels of confinement and concrete compressive strength that are closer to what we expect to find in dams. Zhou et al. [25] tested specimens with one and three shear keys under confinement pressures of 1.0, 2.0, and 4.5 MPa. They use a labeling scheme such as M1-D-K1-1, where M1 stands for monotonic load with 1 MPa of confinement pressure, D stands for dry joint, K1 stands for one shear key, and the last digit represents the number of the specimens (Table 2). Jiang et al. [13] tested specimens with one key under 1.0 MPa (K1-01) and 2.0 MPa (K1-02) of confinement pressure. The geometry of their specimens is shown in Fig. 2.
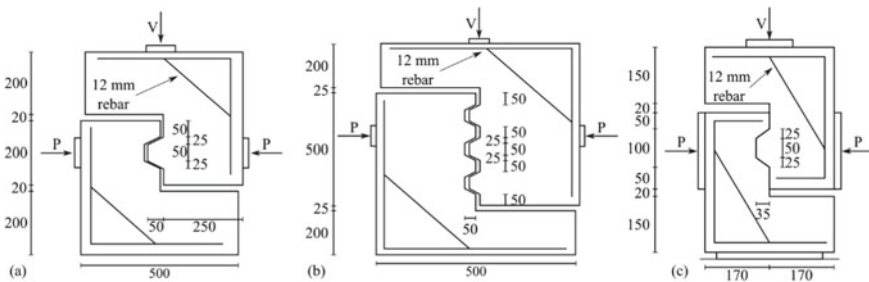
Fig. 2 Shear key experimental tests (dimensions in mm): **a** M1-D-K1, M2-D-K1, and M4.5-D-K1, **b** M1-D-K3, **c** K1-01 and K1-02

2.2   Numerical Modeling of Shear Keys

Three numerical models of shear keys tested by Zhou et al. (Figs. 3a, b) and by Jiang et al. (Fig. 3c) were developed to study the constitutive models. The mesh for these models was created in ABAQUS and exported to LS-Dyna. Thus, simulations with both software used the same mesh. For ATENA, the model had to be rebuilt from scratch.

The simulations are divided into two steps. In the first step, a horizontal confinement pressure P is applied. In the second step, a displacement-controlled shearing load V is applied at a single point on the top and in the middle of the loading plate (Fig. 3). The confinement pressure is kept constant through the entire shearing process. No additional pressure due to dilation is developed because the Poisson's effect is not restrained.

The numerical models in ABAQUS and LS-Dyna use 3D solids' elements with a single element in the depth direction. The ATENA model is 2D. The confinement pressure is applied as pressure on the side of the male shear key. The back of the entire model is restricted in the z-direction. The base of the female shear key on the Zhou models (Figs. 3a, b) and the base of the vertical support plate on the Jiang model (Fig. 3c) are restrained in the y-direction (vertical). A lateral restraint is imposed on the section of the female shear key opposite to the section where the confinement pressure is applied.

2.2.1   CSCM

CSCM is a concrete constitutive model developed for dynamic applications in roadside safety structures. This model presents a smooth intersection between its shear failure surface and a hardening cap. CSCM, which requires 46 material parameters, includes an initialization routine where the default parameters are generated based on the compressive strength and aggregate size input. Using default parameters, CSCM presents a smooth post-peak response, the displacement at ultimate strength is well
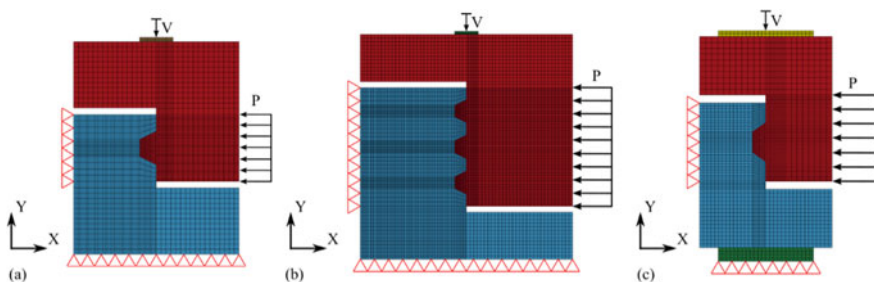
Fig. 3 Shear key finite element models: **a** M1-D-K1, M2-D-K1, and M4.5-D-K1, **b** M1-D-K3, **c** K1-01 and K1-02

estimated compared to the experimental data (Fig. 4a), and the damage observed in the simulation is similar to what is expected from the literature (Fig. 4d). Moreover, the finite element solution is very stable. However, it overestimates the shear resistance of the keys (Fig. 4a). Thus, in an attempt to calibrate this model to the load-response curves from experimental data, we studied the following constitutive model parameters: (i) the flag that enables or disables cap retraction (IRETRC), which controls the position of the hardening cap and shape of the yield surface, (ii) the aspect ratio of the cap surface (R), which controls the shape of the intersection between the shear surface and the cap, (iii) the maximum plastic volume compaction (W), which controls the hardening of the yield surface, and (iv) the parameter controlling erosion (deletion) of elements (ERODE).

The first attempts to calibrate CSCM were manual, varying one parameter at a time. First, the erosion of damaged elements was activated. When the EROSION parameter is set to a value between 0 and 1.0 (not including 1.0), the erosion of elements is deactivated. When set to 1.0, elements that reach 0.99 damage are deleted from the model. When set to a value above 1.0, elements that reach 0.99 damage and have a strain greater than 1.0—EROSION are deleted. Inclusion of erosion prevents excessive deformation of damaged elements and makes the model more stable. However, because eroded elements are not capable of resisting any additional load (both in tension and compression), once erosion of elements happens, the structure starts to lose strength (Fig. 4a) and a large crack in the structure may lead to a large portion of the model being eroded (Fig. 4d). Thus, the choice of the ERODE parameter is an exercise of balance between the stability of the model and response accuracy. Values of the parameter ERODE greater than 1.0 can improve model stability while preventing large erosion of elements.

When cap retraction is activated (IRETRC = 1), the shear capacity of the shear key significantly decreases to values smaller than the experimental data. However, the post-peak behavior resembles the experimental results, with a similar softening slope and some residual strength different than zero (Fig. 4a).

The default value of the cap surface aspect ratio parameter R is 5. Murray (2007) states that this is value which is "typical and is commonly used by the developer to fit concrete with $f_c' = 45$ MPa". Increasing this parameter to R = 8, R = 9, or R = 10 can increase the shear capacity and changes the post-peak behavior, making it closer to the experimental data (Fig. 4b).

The maximum plastic volume compaction parameter W is associated with the porosity of the air voids in concrete. The default value for this parameter is 0.05 (5% of air void porosity) [19]. Increasing this parameter to 10 or 20% significantly increases the shear capacity but for the most part does not affect the post-peak behavior (Fig. 4c).

The damage patterns for some of the parameter combinations used herein are shown in Fig. 4d. Based on this parametric analysis, it was estimated that the best estimation of the experimental data is obtained with ERODE of 1.1, cap retraction enabled, R of approximately 9, and W of approximately 10%.

After performing the manual calibration, the optimization module LS-OPT from LS-Dyna was used to perform an automatic calibration based on the minimization
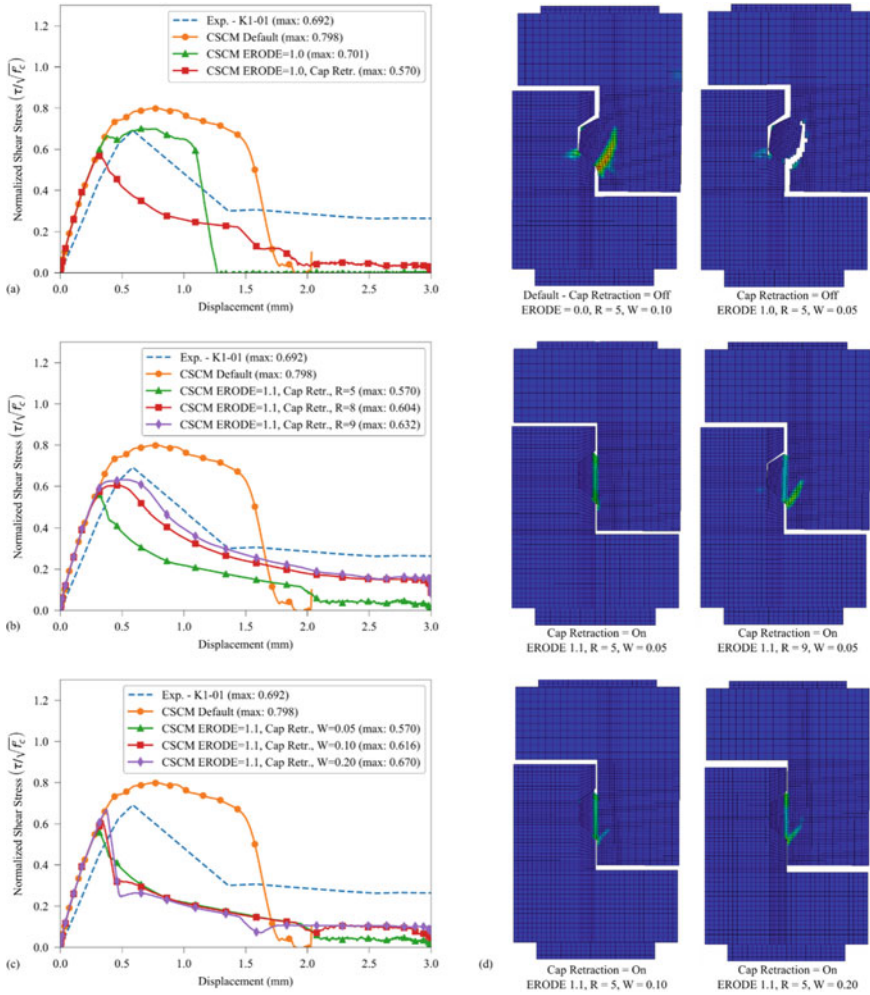
Fig. 4 CSCM manual calibration: **a** element erosion and cap retraction, **b** cap ellipticity parameter R, **c** maximum volume compaction parameter W, **d** damage patterns

of the area between the experimental data and the response obtained numerically. The same parameters studied in the manual calibration are passed to LS-OPT. Three iterations with 16 simulations for each shear key model (K1-01 and K1-02) are performed. A linear meta-model is built and the point selection method used is D-optimal [22] (Fig. 5).

The optimal values for the calibration parameters obtained are $R = 9.023$, $W = 0.105$, ERODE $= 1.067$ and cap retraction activated. These values agree with those obtained in the manual calibration.
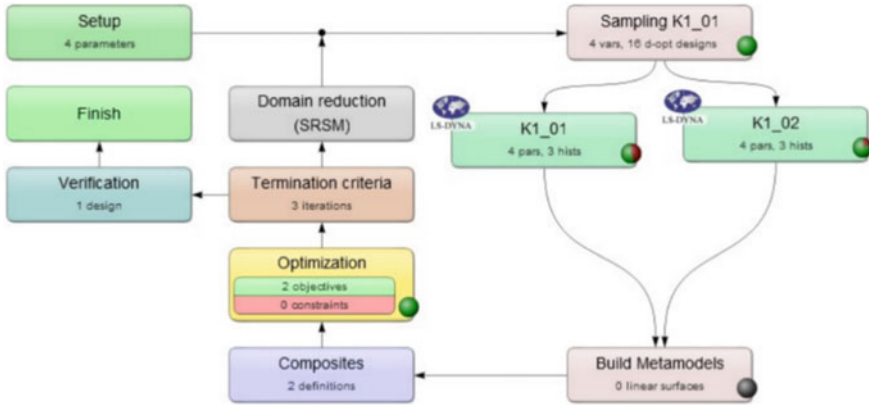
Fig. 5 LS-OPT curve fitting workflow

Using this calibration, we checked the shear response for all the [25] and Jiang et al. [13] shear key models that were studied during the selection of constitutive models. The difference in maximum shear strength between the calibrated CSCM model and the experimental data varied from 8 to 15% (Fig. 6). For most cases, the calibrated post-peak responses resembles well the experimental data. However, for the case with three shear keys, the calibrated response does not capture the sequential failure of shear keys.

2.2.2 KCC

KCC is a constitutive model in LS-Dyna, that requires 50 parameters. KCC uses a set of three shear failure surfaces according to the phase of the loading: (i) an initial yield surface for the elastic phase, (ii) a maximum failure surface for the peak strength response, and (iii) a residual failure surface for the post-peak (residual strength) response. It requires only the uniaxial compressive strength f_c' as an input parameter. Other material parameters, if not provided, are initialized with default values based on f_c'.

KCC presented a very good estimate of the shear strength, but it presents a very brittle response after the peak strength (Fig. 7a). Moreover, the models always presented excessive displacement after reaching peak strength, making the simulation unstable. Thus, the post-peak behavior of the key cannot be captured with this model. Attempts to calibrate this model included changing the parameter b3 (which controls the volumetric plastic strain) and adding damping equivalent to 1 and 10% of the critical damping ζ_c. However, those changes did not affect the brittle behavior of the model.
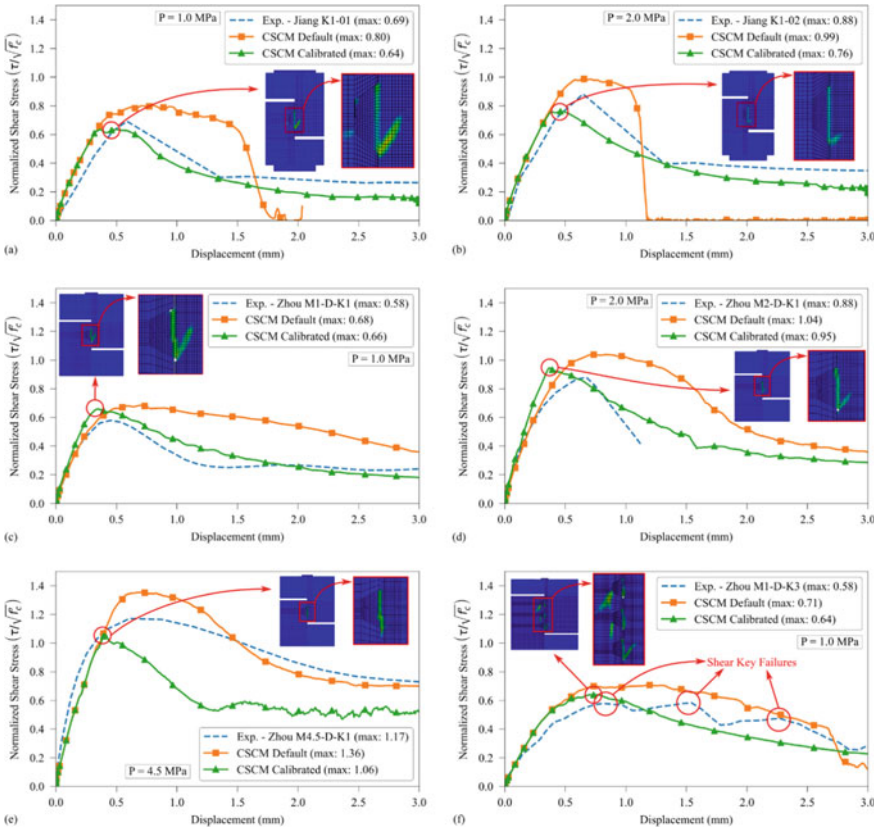
Fig. 6 CSCM calibrated response: **a** K1-01, **b** K1-02, **c** M1-D-K1, **d** M2-D-K1, **e** M4.5-D-K1, **f** M1-D-K3
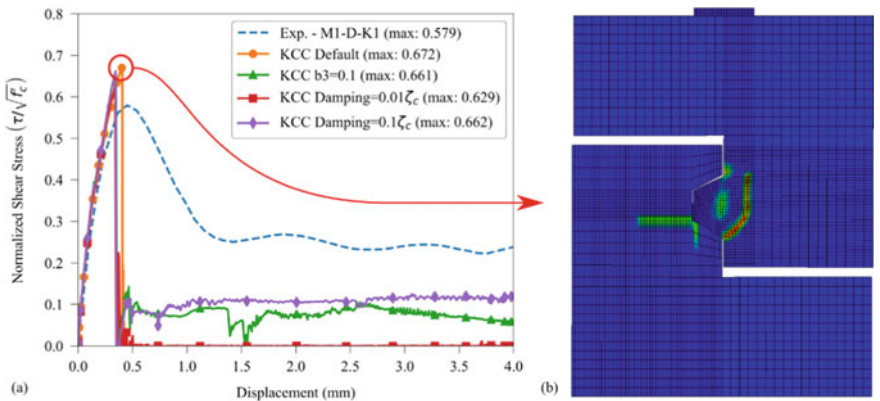
Fig. 7 KCC: **a** normalized shear stress–displacement response, **b** damage pattern

2.2.3 Concrete Damage Plasticity

CDP is a concrete constitutive model in ABAQUS with an isotropic damage formulation. It requires the definition of the compressive plastic behavior (hardening and softening) in terms of yield stress and inelastic strain, as well as the definition of the tensile softening in terms of yield stress and fracture energy. The default parameters for CDP were defined using the recommendations in Dassault [7], the Hognestad model for the compressive behavior, and a linear softening for the tensile behavior. Using those parameters, the shear capacity with CDP is greatly underestimated (Fig. 8a).

Alternatively, setting an elastic compressive behavior increases the shear strength to values that are closer to the experimental data (Fig. 8b). However, for cases with higher confinement pressure, CDP still significantly underestimates the shear strength, even considering elastic compressive behavior (Fig. 8c). Moreover, CDP presented a very brittle behavior, where the shear key loses all or most of its strength immediately after reaching the ultimate strength. In addition to that, the model usually presents excessive deformation soon after reaching the ultimate strength (Fig. 8a), and thus, it cannot capture the post-peak behavior.
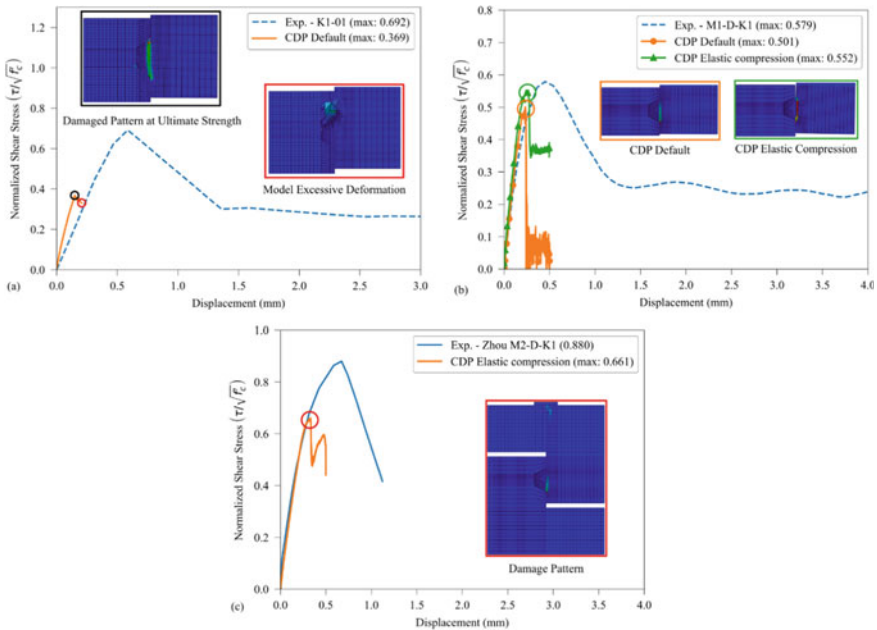
Fig. 8 CDP response: **a** K1-01, **b** M1-D-K1, **c** M2-D-K1
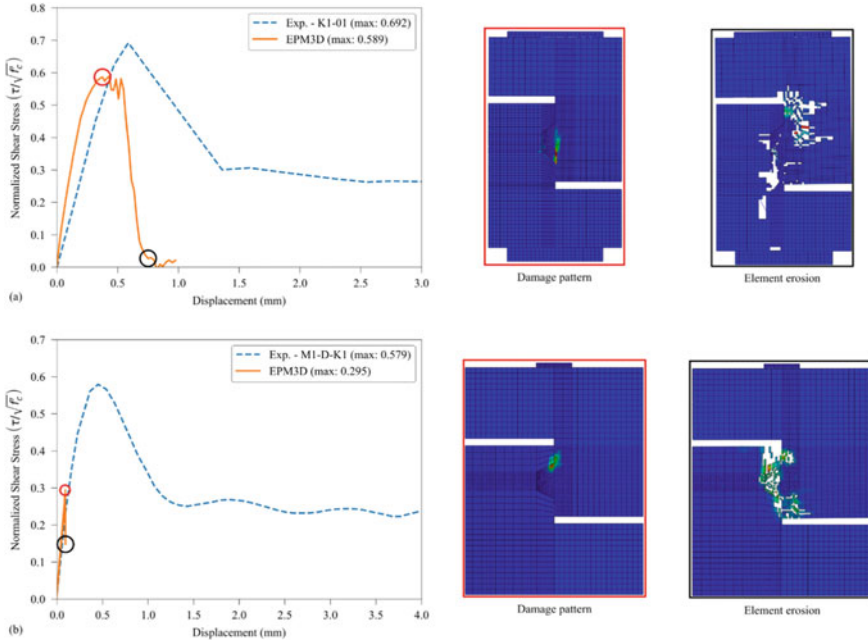
Fig. 9 EPM3D response: **a** K1-01, **b** M1-D-K1

2.2.4 EPM3D

EPM3D is a portable constitutive model implemented as a user-defined subroutine in ABAQUS. The model uses a smeared crack approach and damage softening is modeled as a function of the fracture energy. The damage index is calculated for each principal axis, but the damage parameters in compression and in tension are coupled during the calculation of degraded elastic modulus and tensile residual stress. EPM3D provided reasonably good estimates of the shear key shear strength for the specimen K1-01 (Fig. 9a). However, the model presented a lot of excessive distortion, resulting in the erosion of a large number of elements. This caused a premature failure in model M1-D-K1, greatly underestimating the shear capacity, and it also happened in the post-peak of model K1-01. Thus, the solution with this model was not stable for the application in shear keys.

2.2.5 SBETA

SBETA is a concrete constitutive model available in ATENA with two smeared crack models available: (i) a fixed crack direction model and (ii) a rotated crack direction model. In the fixed crack model, the direction of the crack is constant throughout the loading and defined by the principal stress direction at the moment of crack initiation,
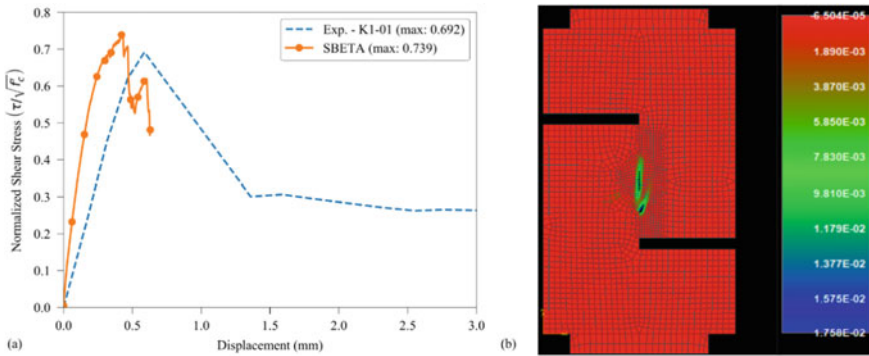
Fig. 10 SBETA: **a** normalized shear stress–displacement response, **b** maximum principal strain and cracks

representing the material axis of orthotropy. In the rotated crack model, the crack follows the direction of principal stress throughout the loading, and thus, no shear strain occurs on the crack plane. A single model of the K1-01 specimen was built on ATENA. SBETA was used with a rotated smeared crack model and otherwise default parameters. This model provides a good estimate of the shear capacity (Fig. 10a) and it captures the expected cracking pattern, with a diagonal crack at the beginning and shearing of the base after that (Fig. 10b). However, similarly to most models, it was very brittle and did not capture the post-peak behavior of the shear keys.

2.3 Comparison of Constitutive Models

From the assessment of the five constitutive models tested herein, the calibrated CSCM was the only model that simultaneously provides a good estimate of the shear capacity and a post-peak response that was comparable to the experimental data. The displacement at peak load was also similar to the experimental data. The accurate estimation of the shear capacity and the displacement at ultimate capacity tell the point of cracking initiation. The shape of the softening curve and the area under the response diagram relate to the fracture energy of the shear key. The residual post-peak strength indicates that the shear keys are capable of resisting load even after cracking. These characteristics are essential for a nonlinear analysis of the complete response of concrete dam shear keys and could only be captured with CSCM.

CDP greatly underestimated the shear capacity, and its brittle behavior did not allow for capturing the post-peak response. Thus, CDP would not be recommended for analysis of concrete shear keys. EPM3D, KCC and SBETA provided a good estimate of the shear capacity, but they did not capture the post-peak behavior. These models could be used in a more traditional analysis, where the shear keys are assumed to provide no additional resistance once the key fails. A comparison of the response
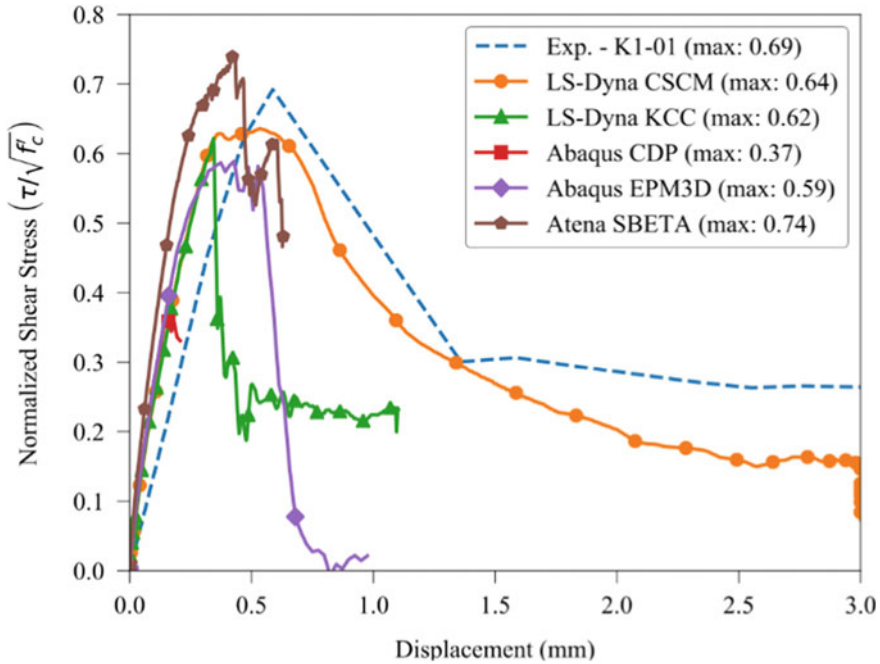
Fig. 11 Comparison of constitutive models' load response for specimen K1-01

of model K1-01 using the best calibration obtained for each constitutive model is presented in Fig. 11 and illustrates these recommendations.

3 Trapezoidal and Rectangular Shear Keys

3.1 Model Description

In this section, parametric analyses of the geometry of trapezoidal shear keys are performed. The geometries used are based on Table 1, respecting the range of angle α and ratios L_k/h and L_k/L_{sm} observed in existing dams. A trapezoidal shear key with $L_k = 160$ cm, $L_{sm} = 114$ cm, $\alpha = 60°$, and $h = 40$ cm was used as the starting point. Then, the angle α was changed, maintaining h, L_k, and L_{sp} constant, to generate new geometries in parametric analysis of the shear key angle. Similarly, a parametric variation of the shear key depth was performed varying h while maintaining α, L_k, and L_{sp} constant for a trapezoidal and a rectangular shear key (Table 3). The boundary conditions are the same as those used in the evaluation of constitutive models. Analyses were performed with confinement pressures $P = 0$. MPa and $P = 1$ MPa. The finite element models for a trapezoidal, a rectangular, and a triangular

Table 1 Shear key geometry in existing dams

Dam (type)	Shear key shape	L_k (cm)	L_{sm} (cm)	h (cm)	α	L_k/h	L_k/L_{sm}
Ruskin (PG)	Rectangular	160	160	30	90.00°	5.33:1	1.00
Chute Bell (PG)	Rectangular	60	60	30	90.00°	2.00:1	1.00
Waitaki (PG)	Trapezoidal	166	–	30	–	5.03:1	–
Morrow Point (VA)	Trapezoidal	76	15	15	26.57°	5.07:1	5.00
Ste. Marguerite 3 (PG)	Trapezoidal	60	40	20	63.43°	3.00:1	1.50
Waneta (PG)	Trapezoidal	106	61	15	33.69°	7.07:1	1.74
Nam Ngum 5 (VA)	Trapezoidal	80	20	15	26.57°	5.33:1	4.00
Zhang, 2014 dam (VA)	Trapezoidal	260	180	40	45.00°	6.50:1	1.40

Table 2 Experimental tests on shear keys

Author	Specimen name	f_c' (MPa)	Confining stress P (MPa)	Number of keys	Shear capacity (kN)
[13]	K1-01	41.5	1.0	1	89.7
	K1-02	41.5	2.0	1	113.9
[25]	M1-D-K1	38.7	1.0	1	193.0
	M2-D-K1	56.2	2.0	1	335.0
	M4.5-D-K1	37.1	4.5	1	375.0
	M1-D-K3	35.7	1.0	3	446.0

shear key used in these analyses are shown in Fig. 12. The triangular shear key is the extreme case of a trapezoidal key with $L_{sm} = 0$ cm.

3.2 Parametric Analysis of Geometry

When no confinement pressure is considered ($P = 0$ MPa), shear keys with $\alpha \leq 45°$ fail by dislocation. Because dilation is unrestricted, the male shear keys with $\alpha \leq 45°$ move away from the female block, losing contact and not producing any frictional forces. This results in zero-shear capacity (Fig. 13a). When $P = 1$ MPa is considered, the male and female blocks remain in contact and some shear resistance is developed. However, keys with $\alpha < 45°$ still fail by dislocation (Fig. 13b).

For keys with $\alpha > 45°$ and $P = 0$ MPa, the failure mechanism is the shearing-off of the base. This failure mechanism is also observed for $\alpha \geq 45°$ and $P = 1$ MPa. However, for $P = 0$ MPa, the crack developed at the base is diagonal and curved

Table 3 Geometry of shear keys for parametric variations

L_k. (cm)	L_{sp}(cm)	L_{sm}(cm)	α	h (cm)	h/L_k
Variation of key angle					
160	160	0	26.6°	40	1/4
160	160	40	33.7°	40	1/4
160	160	80	45.0°	40	1/4
160	160	114	60.0°	40	1/4
160	160	160	90.0°	40	1/4
Variation of depth (trapezoidal)					
160	160	0	60.0°	20	1/8
160	160	90	60.0°	40	1/4
160	160	114	60.0°	60	3/8
160	160	137	60.0°	80	1/2
Variation of depth (rectangular)					
160	160	160	90.0°	20	1/8
160	160	160	90.0°	40	1/4
160	160	160	90.0°	60	3/8
160	160	160	90.0°	80	1/2
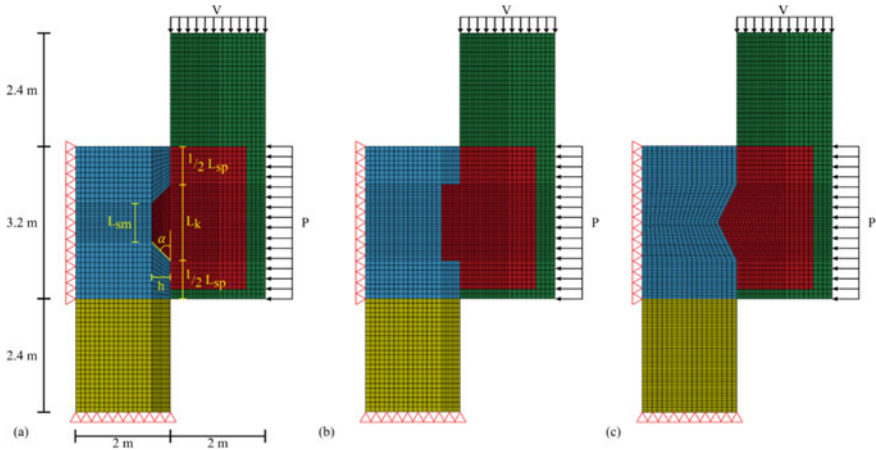
Fig. 12 Finite element models for geometry parametric variations: **a** trapezoidal model, **b** rectangular model, **c** triangular model

(Fig. 13a), while for $P = 1$ MPa, the crack is vertical (Fig. 13b). This happens because the lateral movement (dilation) of the male block creates tension in a direction perpendicular to the crack being formed. Because the lateral movement is much larger in the case with $P = 0$ MPa, the crack assumes a diagonal orientation.
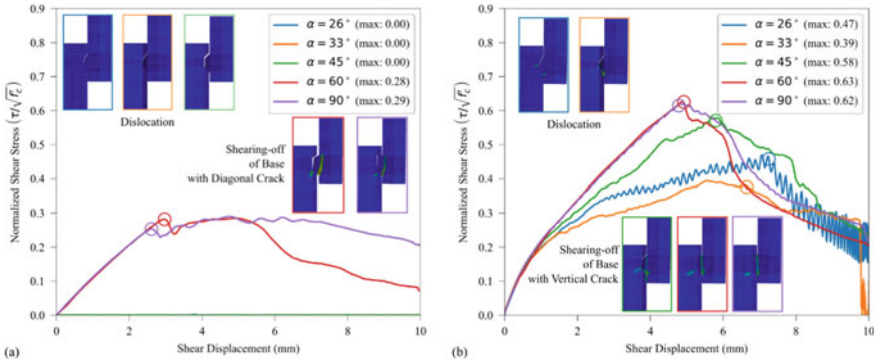
Fig. 13 Shear key angle—load response and failure mechanisms: **a** $P = 0$ MPa, **b** $P = 1$ MPa

Increasing the confinement pressure from $P = 0$ MPa to $P = 1$ MPa increases the shear capacity by 117%. For $P = 1$ MPa, and increasing the angle α also increases the shear capacity. However, the difference in shear capacity from $\alpha = 45°$ to $\alpha = 60°$ is only 8% and increasing again to $\alpha = 90°$ does not increase the shear capacity.

The variation of the shear key depth presented similar failure mechanisms with the addition of the crushing of the key edge for shallow shear keys ($h = 20$ cm) with $P = 1$ MPa (Figs. 14b, d). The triangular shear keys (trapezoidal keys with $L_{sm} = 0$) failed by dislocation both for $P = 0$ MPa (Fig. 14a) and $P = 1$ MPa (Fig. 14b). However, for $P = 1$ MPa, the full shear capacity is developed, while for $P = 0$ MPa, no frictional force is developed due to loss of contact. The results show that within the same failure mechanism, the variation of the key depth does not significantly change the shear capacity. However, from crushing of the key edge to shearing-off of base for $P = 1$ MPa, there is a 34% increase in shear capacity.

4 Conclusions

Among the five constitutive models that were tested, LS-Dyna CSCM proved to be the most versatile, stable, and accurate for modeling the response of concrete shear keys. The calibration of CSCM yielded an estimation of the shear capacity that deviates by no more than 15% from the reference experimental data used as benchmarks. The post-peak behavior of the calibrated CSCM model resembles the experimental data in most cases. The failure mechanism and crack formation, identified from the damage contour plots, are consistent with the literature and the experimental data.

Three failure mechanisms were observed from the parametric variation of geometry: (i) dislocation, (ii) crushing of the shear key edge, and (iii) shearing-off of the key base. Dislocation was observed for trapezoidal shear keys with an angle $\alpha \leq 45°$ for $P = 0$ MPa and $\alpha < 45°$ for $P = 1$ MPa. Crushing of the shear key edge was
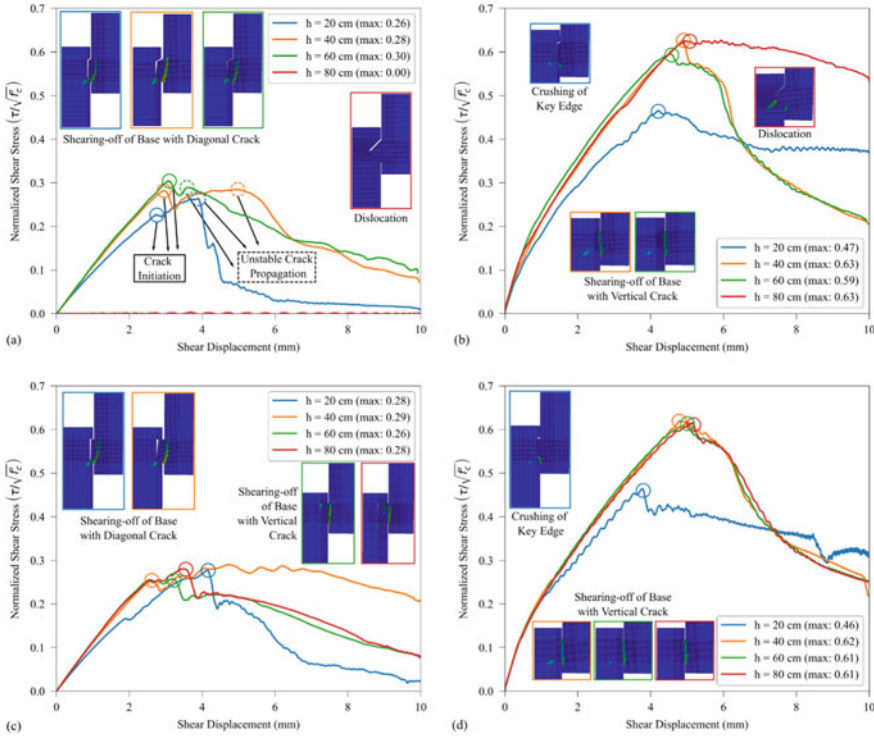
Fig. 14 Shear key depth—load responses and failure mechanisms: **a** trapezoidal shear keys with $P = 0$ MPa, **b** trapezoidal shear keys with $P = 1$ MPa, **c** rectangular shear keys with $P = 0$ MPa, **d** rectangular shear keys with $P = 1$ MPa

observed for shallow shear keys with $h = 20$ cm ($h/L_k = 1/8$), which is consistent with Bakhoum [3]. Shearing-off of the key base was observed in two different variations: with a diagonal crack and with a vertical crack. The diagonal crack was observed for $P = 0$ MPa because the frictional forces due to the lateral movement (free dilation) create tension in a diagonal direction perpendicular to the crack. When $P = 1$ MPa, the lateral displacement is much smaller, and the crack formed is vertical. Each failure mechanism presented significantly different shear capacities. However, within the same failure mechanism, increasing the shear key depth does not significantly increase the shear capacity and increasing the shear key angle for trapezoidal keys only increased the shear capacity up to $\alpha = 60°$.. These results help understanding the effect of key geometry in the possible failure mechanisms and their impact on the shear key capacity and load–displacement response. This will aid to predict the shear strength contribution and assess the residual displacement of shear keys in existing structures in need of safety reassessments.

References

1. Amos P, Black J, Dungar R, Walker J (2014) Utilising the curved footprint of an 80 year old gravity dam to aid performance during extreme earthquakes. In: 34th Annual USSD conference, San Francisco, California, pp 177–194
2. Azmi M, Paultre P (2002) Three-dimensional analysis of concrete dams including contraction joint non-linearity. Eng Struct 24(2002):757–771. https://doi.org/10.1016/S0141-0296(02)000 05-6
3. Bakhoum MM (1991) Shear behaviour and design of joints in precast concrete segmental bridges. Doctoral dissertation, Massachusetts Institute of Technology, Cambridge, Massachusetts
4. Consulting C (2015) ATENA program documentation—user's manual for Atena 2D. Czech Republic, Prague
5. Chopra AK (2020) Earthquake engineering for concrete dams. Wiley, Hoboken, NJ
6. Curtis DD, Lum KKY (2008) Estimated strength of shear keys in concrete dams. In: CDA 2008 annual conference, Winnipeg, MB, Canada, pp 17–28
7. Dassault Systèmes (2014) Abaqus 6.14—Abaqus/CAE user's guide. Providence, Rhode Island
8. Dowdell DJ, Fan BH (2004) Practical aspects of engineering seismic dam safety—case study of a concrete gravity dam. In: 13th World conference on earthquake engineering, Vancouver, B.C., Canada
9. Du C, Jiang S, Jiangsu N (2010) Nonlinear dynamic responses of arch dam with shear keys. Math Comput Appl 15(5):828–833
10. Ghiasian M, Ahmadi MT (2015) Efficient 3D boundary element dynamic analysis of discontinuities. Eng Anal Boundary Elem 50(2015):320–328. https://doi.org/10.1016/j.enganabound. 2014.09.006
11. Guerra A (2007) Shear key research project literature review and finite element analysis. Report No. DSO-07-05. USBR, Denver, Colorado
12. Gunn RM (2005) The design of shear keys for large arch dams in seismic regions. In: 73rd Annual meeting of ICOLD, Tehran, Iran
13. Jiang H, Chen L, Ma ZJ, Feng W (2015) Shear behavior of dry joints with castellated keys in precast concrete segmental bridges. J Bridg Eng 20(2):1–12. https://doi.org/10.1061/(asce)be. 1943-5592.0000649
14. Jiang S, Du C, Yuan J (2011) Effects of shear keys on nonlinear seismic responses of an arch-gravity dam. Sci China Technol Sci 54(1):18–27. https://doi.org/10.1007/s11431-011-4613-8
15. Lacombe G, Pommeret M (1974) Les Joints Structuraux dans les Constructions en Grands Panneaux Prefabriques. Annales de I.T.B.T.P., Gros-Oeuvre No 18, Paris, France
16. Løkke A, Chopra AK (2019) Direct-finite-element method for nonlinear earthquake analysis of concrete dams including dam–water–foundation rock interaction. Report No. 2019/02. Pacific Earthquake Engineering Research Center, Berkeley, California
17. Malvar LJ, Crawford JE, Wesevich JW, Simons D (1997) A plasticity concrete material model for DYNA3D. Int J Impact Eng 19(9–10):847–873
18. Massicotte B, Ben Ftima M (2017) EPM3D-v3—a user-supplied constitutive model for the nonlinear finite element analysis of concrete structures. École Polytechnique de Montréal, Montreal

19. Murray YD (2007) Users manual for LS-DYNA concrete material model 159. U.S. Department of Transportation
20. NZSOLD (2015) New Zealand dam safety guidelines
21. Qiu Y-X, Wang J-T, Jin A-Y, Xu Y-J, Zhang C-H (2021) Simple models for simulating shear key arrangement in nonlinear seismic analysis of arch dams. Soil Dyn Earthq Eng 151(2021):1–25. https://doi.org/10.1016/j.soildyn.2021.107006
22. Stander N, Basduhar A, Roux W, Liebold K, Eggleston T, Goel T, Craig K (2020) LS-OPT user's manual—a design optimization and probabilistic analysis tool for the engineering analyst. LSTC, Livermore, California
23. Toyoda Y, Shiojiri H, Ueda M, Tsunekawa K (2004) Dynamic analysis of an existing arch dam including joint non-linearity and dam-waterfoundation rock interaction. In: 13th World conference on earthquake engineering, Vancouver, BC
24. Wang G, Wang Y, Lu W, Yu M, Wang C (2017) Deterministic 3D seismic damage analysis of Guandi concrete gravity dam: a case study. Eng Struct 148(2017):263–276. https://doi.org/10.1016/j.engstruct.2017.06.060
25. Zhou X, Mickleborough N, Li Z (2005) Shear strength of joints in precast concrete segmental bridges. ACI Struct J 102(1):3–11

Effect of Connection Type and Reinforcement Ratio on the Shear Capacity of Embedded Plates in Reinforced Concrete

Caine Smithaniuk and Douglas Tomlinson

Abstract Recent research at the University of Alberta emphasized the lack of consideration in Annex D for the effect of reinforcement on anchorage capacity, as well as the treatment of combined loading for common shear-type connections. Conservatism in design and confusion for designers are manifestations of the current limitations of the design standard. There is currently no practical approach, codified or otherwise, that can accurately describe the behaviour of embedded plates in reinforced concrete. An experimental program was conducted to evaluate the effects of various reinforcement layouts and two different connection types (shear tab and double angle) on the load/displacement response of precast embedded plates, with the goal of better understanding their behaviour. This research aims to propose more practical, straightforward design guidelines for designers to use in the future when calculating the capacity of anchorages in reinforced concrete. Results from this test program will provide additional context to previously standardized embedded plate design tables, and further streamline the design of these connections. The test results will also contribute to a greater body of work that is trending towards more accurate estimates of anchorage capacities in reinforced concrete. There are few test programs that have been dedicated to the behaviour of embedded plates in reinforced concrete, and this is one of the first to consider the reinforcement layout as an independent variable.

Keywords Shear capacity · Embedded plates · Reinforced concrete

1 Introduction

Embedded plates are commonly used to connect steel and reinforced concrete members. These plates typically consist of a rectangular steel baseplate with headed studs welded to one side and steel connections (e.g. shear tab) welded to the other

C. Smithaniuk · D. Tomlinson (✉)
University of Alberta, Edmonton, Canada
e-mail: dtomlins@ualberta.ca

side (Fig. 1a). Plates are secured to formwork such that concrete is poured and cures around them. The baseplate is flush with the face of concrete and then allows a steel member to be anchored to concrete via bolts or welds. There are many locations where embedded plates are used including cases where the plate is in a concrete beam. In this case, the plate is loaded primarily in shear perpendicular to a free edge (Fig. 1b). For this case, concrete breakout often governs design. From a structural standpoint, it is beneficial to keep the plates far from the concrete edge but the plate location is often dictated by constraints other than capacity, such as architectural requirements that limit member depth. The Canadian design standard for concrete, A23.3:19 [6] includes provisions for anchorage to concrete in Annex D that dictate the design capacity of anchorage systems including embedded plates. Annex D gives conservative estimates of breakout strength since it considers concrete to be unre-inforced. This assumption is carried over from the theory that Annex D is based on, the concrete capacity design (CCD) method [7], which was developed from best fit curves from anchor tests in unreinforced concrete. There is a modification factor in Annex D that seems to account for reinforcement, but is more accurately described as a factor that accounts for additional capacity gained from concrete being uncracked, since reinforcement mitigates the harmful effects of cracks in unrein-forced concrete. The capacity of specific reinforcing bars can be substituted for the concrete breakout strength entirely provided that they meet certain proximity and development requirements, but the addition of concrete and reinforcement strength is not currently permitted in the standard.

Though a few recent studies estimated anchorage capacity in reinforced concrete [9, 12], most research used for Annex D provisions is from single anchor tests that may not be representative of anchorages with multiple anchor rows. Most tests are also loaded under pure shear using uplift restraints that prevent rotation [8, 11]. In reality, anchorages like embedded plates often use multiple anchor rows with load applied eccentrically through shear connections. Tests with combined shear and tension loads may not represent loads applied to shear connections, which are subject to shear and moment generated by the load eccentricity combined with fixity present due to
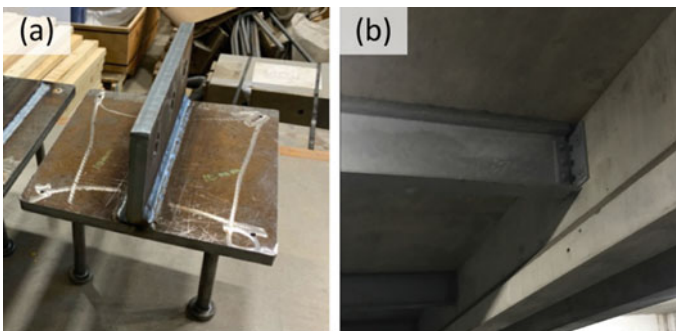
Fig. 1 a Plate prior to concrete casting, **b** Post-installed anchorage on a concrete beam loaded in shear towards the free edge

connection stiffness. The objectives of this study are to (1) study the behaviour of embedded plates as a whole, rather than just headed anchors or embedded plates under pure shear, in concrete containing various levels of reinforcement; and (2) investigate the effects of connection flexibility on concrete breakout strength in typical embedded plates. The embedded plates were loaded in shear perpendicular to a free edge, with the load applied at a fixed eccentricity through a shear tab or a double angle connection detail.

2 Test Program

2.1 Plate and Block Description

Embedded plates with two connection details (shear tab and double angle, see Fig. 2) placed at an edge distance of 150 mm to the centre of the nearest stud row were loaded in shear towards the concrete edge. Connection details were selected because they are both common shear-type connections with different load-rotation behaviours while still being classified as simple, or pinned, connections. The shear tab design standardized by Chin [5] is more rigid than the double angle connection, where the angles are only connected to the baseplate at the weld along their toe, which allows the outstanding leg to "flex" away from the baseplate. These plates were selected as they are consistent with the four stud embedded plate (4SEP) proposed by Chin [5] as part of an effort to standardize embedded plates for design, fabrication, and construction economy. 4SEP includes four welded headed studs with a shank diameter of 16 mm and an effective embedment of 150 mm that were welded to a $250 \times 250 \times 16$ mm thick baseplate.

The double angle connection is comprised of two L102 $\times$ 76 $\times$ 7.9 mm angles with the short leg welded to the baseplate along their toe. Load was applied through three 22 mm ASTM A325 bolts at an eccentricity of 65 mm from the baseplate. This eccentricity was selected to be consistent with typical gauge lengths used in construction. The second connection is a 16 mm thick shear tab with three 22 mm holes at an eccentricity of 65 mm from the face of the baseplate. The shear tab is welded to the baseplate using a continuous 10 mm weld on both sides, while the angles are welded continuously along their toe with a 6 mm weld. The shear tab is the same length as the baseplate (250 mm), while the angles are 230 mm long to

Fig. 2 Embedded plates
with double angle (left) and
shear tab connection (right)
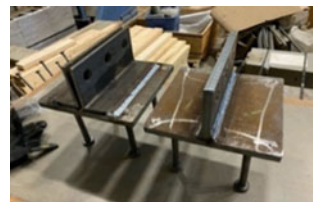
leave room for weld returns on either end. This is a necessary feature for the angles, since it is expected that there will be significant plastic hinging near the weld, and returns help to preclude weld tearout.

Two $1750 \times 1750 \times 400$ mm concrete blocks were cast with four embedded plates cast in each block at the centre of each edge (Fig. 3b). Block dimensions were selected such that the supports would not interact with expected shear breakout cones based on the stud spacing and distance from the block edge to the furthest anchors. The block depth was selected to represent a width could be found in typical reinforced concrete beam. Reinforcement, described as stirrups since they act to resist shear forces from each plate, was placed in a grid consisting of 10 M bars with spacings of 175 mm, 215 mm, or 250 mm on centre (Fig. 3a). Perimeter reinforcement, analogous to longitudinal reinforcement in beams, comprised two 15 M bars in most tests. One test had four 20 M bars as perimeter reinforcement while another had no perimeter bars at all. Drawings of each block is shown in Fig. 4.

The goal of six of these tests was to examine the effects of stirrup density and connection type on plate response. A spacing of 250 mm was chosen as a baseline to match [5] tests. Chin [5] concluded that even with minimal reinforcement, embedded plates distribute load to all studs, rather than relying only on studs in the row furthest
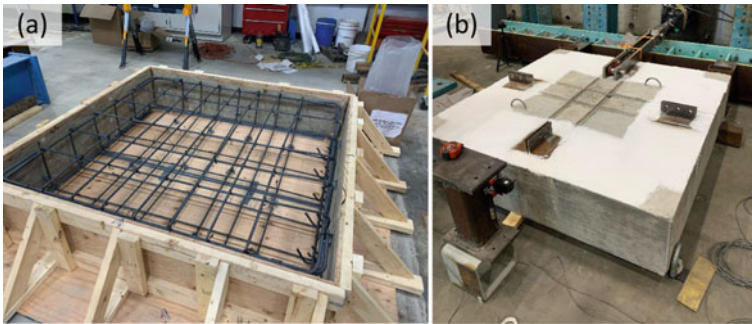
Fig. 3 **a** Reinforcement cage prior to embed placement and concrete pour, **b** Cast block
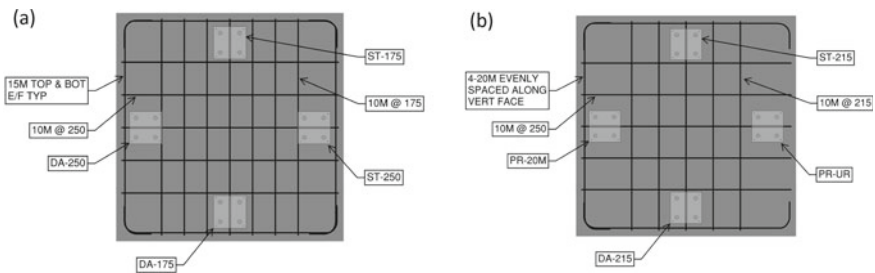
Fig. 4 Plan drawing of block used for **a** ST-175, DA-175, ST-250, DA-250 and **b** ST-215, DA-215, PR-20M, and PR-20M

from the edge. In all eight of their tests, Chin [5] found that the load exceeded the critical stud capacity, despite multiple tests having a stud spacing to edge distance ratio greater than or equal to 0.6, which ACI 318-14 gives as the maximum value, where multiple rows of anchors can be considered to contribute to shear capacity. When this ratio is less than 0.6, it is increasingly likely that breakout cones form from the front studs and these studs will no longer be able to carry any load. While this behaviour was noted in [5] tests, the modest reinforcement present was able to tie the initial breakout cone to the rest of the breakout body and allow multiple rows of anchors to carry the shear load. The smallest stirrup spacing (175 mm) was selected because expressions from Sharma et al. [12] suggest that the concrete breakout capacity at this spacing coincides with the stud shear capacity. The remaining two tests focus on assessing the perimeter reinforcement contribution. PR-20M, which includes four 20M perimeter bars, provides a level of reinforcement more representative of what could be found on the tension face of a reinforced concrete beam. A23.3 permits a 20% increase in the concrete breakout strength if at least one 15 M bar is provided as edge reinforcement, but it is possible that increasing this reinforcement further may have a beneficial effect.

Table 1 summarizes the test matrix. Tests are identified using a two-term description. The first two letters establish that the embedded plate utilizes a shear tab (ST), a double angle (DA) connection, or is a test that investigates perimeter reinforcement (PR). Note that the two PR tests used shear tab connections. The second term in the test ID is the stirrup centre-to-centre spacing in mm for most tests. For example, DA-175 indicates that this test uses a double angle connection with 10 M stirrups at 175 mm spacing. For the two tests where perimeter reinforcement (PR) is varied, the second term specifies the perimeter bar details. PR-UR is the test without perimeter reinforcement while PR-20 M contains four 20 M perimeter bars. The baseplate size and thickness, and the stud size, length, and layout, are all consistent with the four stud embedded plate (4SEP) that was proposed by Chin [5].

Table 1 Test matrix

Test ID[a]	Stirrup spacing (mm)	Perimeter reinforcement	Connection type
ST-250	250	2–15M	Shear tab
DA-250	250	2–15M	Double angle
ST-215	215	2–15M	Shear tab
DA-215	215	2–15M	Double angle
ST-175	175	2–15M	Shear tab
DA-175	175	2–15M	Double angle
PR-UR	250	None	Shear tab
PR-20M	250	4–20M	Shear tab

[a] All tests had an edge distance of 150 mm and used a four stud embedded plate

2.2 Materials

Three concrete cylinders and three modulus of rupture beams were tested as per ASTM C39 [2] and ASTM C78 [3] 35 days after casting. The average compression strength was 40.6 MPa with a standard deviation of 3.2 MPa. The average rupture strength was 4.4 MPa with a deviation of 0.4 MPa.

Three samples were taken from each of the three reinforcement bar sizes and tested as per ASTM A370 [4]. The average yield strength of the 10 M bars was 458 MPa with a standard deviation of 1.8 MPa. The average yield strength of the 15 M bars was 450 MPa with a standard deviation of 2.6 MPa. The average yield strength of the 20 M bars was 401 MPa with a standard deviation of 0.5 MPa.

Lastly, three studs were tested as per ASTM A370 [4] to determine their yield and ultimate strength. The average yield strength of the studs was 419 MPa with a standard deviation of 3.8 MPa. The average ultimate strength of the studs was 506 MPa with a standard deviation of 3.3 MPa.

2.3 Test Set-up and Instrumentation

Plates were loaded using a hydraulic jack anchored to the strong wall as shown in Fig. 5. The actuator was connected to the embedded plate using two 25 mm thick steel bars. The concrete block beared against two supports resting on a transfer beam that spanned between two columns were bolted to the strong floor. The clear span between the supports on the block was 1400 mm, which left room for the predicted breakout cone width of 1050 mm. A tie down strap at the far end of the block was secured to the strong floor to prevent block uplift during the tests.

Instrumentation is shown in Fig. 5a, b. Two cable transducers were connected to the baseplate to measure displacement in the direction of the applied load. Two clinometers measured rotations with one placed on the baseplate and the other placed on the wide flange section that applied the load to the embedded plate. LVDTs were placed on each side of the block to capture movement as the specimen was pulled into bearing by the loading arm. A Canon Rebel T6i DSLR camera was placed above the specimen to capture photos for digital image correlation (DIC) of the surface of the block. DIC results are beyond the scope of this document, but time-lapse photos from this camera were used to better understand the response of the connection. All sensors collected data at 2 Hz, while the DSLR camera captured photos at 0.33 Hz.

Prior to testing to failure, a pre-load of around 30 kN was applied to pull the block tight to the supports. This load was large enough to move the block against the reaction beams but was well below the load at which any damage (e.g. cracking) occurred for all tests. After setting the block, load removed, then the connections were loaded until failure. The loading rate was controlled manually and averaged 0.7 kN/ s from 30% of peak load up to the peak load. After the peak load, loading continued at an average of 2.8 mm/min. For tests that failed by concrete breakout, load was
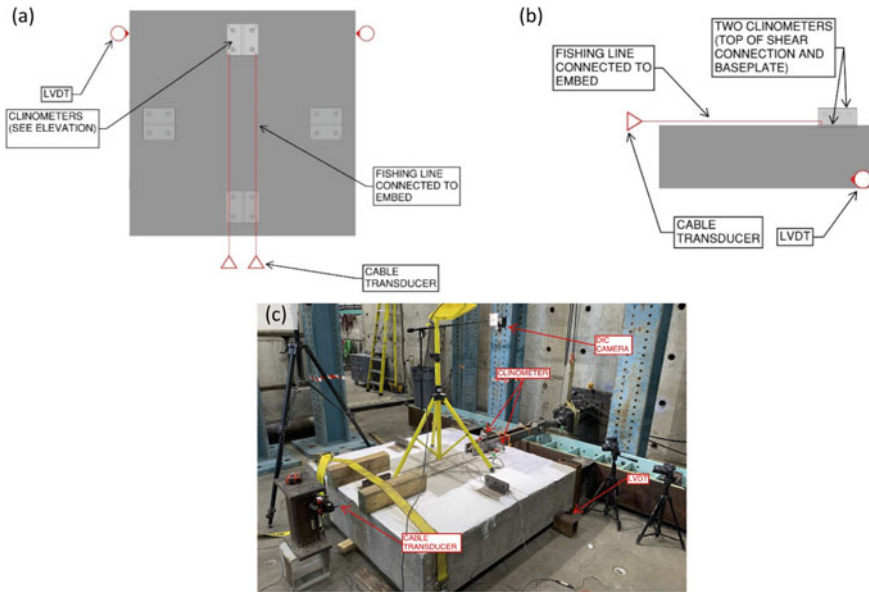
Fig. 5 Test set-up and instrumentation **a** Plan view, **b** Elevation view, **c** Photo of test specimen in place

applied until it dropped below 50% of peak, or when displacement exceeded 25 mm, which was well past peak load for all tests. For tests that failed by weld rupture (DA-175 and DA-250), the load dropped suddenly when the welds failed, and the specimen was immediately unloaded.

2.4 Loading Arm

A focal point of this program was to assess how load is applied to the plate and this influence on connection behaviour. Many programs consider pure shear or tension loading but typical shear connections, where there are combined loads and rotations, are not as straightforward. Moment is transferred due to load eccentricity and partial fixity in the connection itself. Sharma et al. [10] tested plates with vertical restraint. This enabled them to study how reinforcement affects capacity for systems under pure shear. Sharma et al. [11] mentioned that the plates under shear without uplift restraint requires further investigation. They theorized that without uplift restraint that failure may be a combination of shear and tension breakout, since moments cause a prying effect that reduces shear capacity. The extent that tension reduces shear capacity is often estimated using tension-shear interaction expressions. However, these expressions are intended for combined shear and pure tension loads, not moments. For cases of eccentric shear, tension is only applied in studs furthest from the edge, and

Fig. 6 Depiction of the test set-up used by Chin [5]. Note pin supports at front and back of the jack
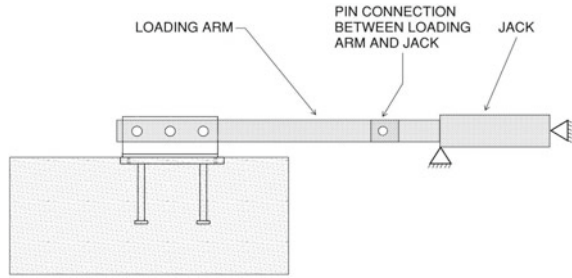
the compressive force underneath the front edge of the plate provides benefit by preventing the tension breakout cone from fully developing.

Chin [5] noted that moments developed in plates with loading arms bolted directly to shear tabs. They placed a pedestal underneath the jack that prevented the jack from rotating about its rear pin support (Fig. 6). In theory, these constraints provide perfect uplift restraint, but in reality play in the bolt holes and bending of the loading arm allowed for notable rotation in the plate.

If a similar method of load application were used in this test program, it would prevent the two types of shear connector under consideration from behaving differently. To address this, a W310 × 67 stub was bolted to the shear connection with three 22 mm ASTM A325 bolts and the loading arm applied the load to the wide flange stub through a clevis. The intent of this connection was to decouple the rotation of the embedded plate from the loading arm, which would allow the more flexible angles to rotate up and away from the baseplate, while the shear tab would remain rigid. The first four tests (ST-250, DA-250, ST-175, DA-175) were completed using this pinned detail. For the last four tests (ST-215, DA-215, PR-20 M, PR-UR) the connection was modified to eliminate the pin at the embedded plate, and the loading arms were instead bolted directly to the shear tab or double angles (Fig. 7) because of some undesirable responses in the first four tests, discussed later. The bolted connection at the embedded plate is analogous to what was used by Chin [5]. However, a key difference was that there was no pedestal placed under the front of the hydraulic jack, so the jack was able to rotate freely, and by extension the loading arm.
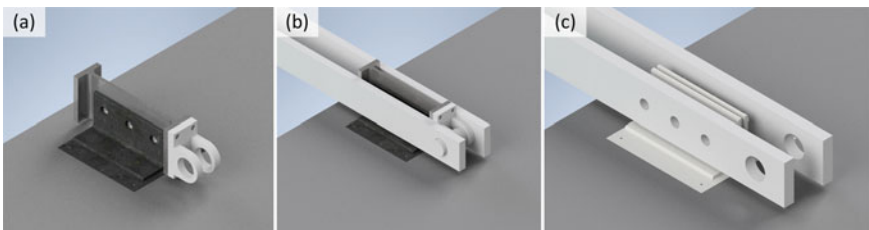
Fig. 7 Rendered image of plate with **a** W stub and clevis plate, **b** With W stub, clevis plate, and loading arms and **c** Loading arms modified to include bolts to connect loading arms to embedded plate

3   Results and Discussion

Table 2 summarizes results for all eight tests, and the load–displacement curves are shown in Fig. 8. The net plate displacement was calculated by averaging LVDT readings that recorded specimen displacement and subtracting that from the average value of the two cable transducers measuring the displacement of the embedded plate. ST-250 was stopped earlier than other tests due to excessive cracking that unexpectedly extended into areas that may conflict with breakout cones of other tests in the same block. Inspection of the block following this test suggested that cracks were superficial at the points where they crossed into the breakout cones of subsequent tests, and therefore it is not believed that they had a significant effect on the behaviour of the adjacent plates. The load displacement curves for ST-215, DA-215, and PR-UR were truncated at 20 mm of net plate displacement, which was well beyond peak load, and there were no notable changes in behaviour past this point. Figure 8b includes the curves for DA-175 and DA-250, which failed suddenly due to weld rupture and these tests stopped and unloaded immediately following this failure.

The load–displacement curves for all eight tests show a stiff, linear response up to 100–150 kN, followed by a decrease in stiffness, followed by a second essentially linear response up until around peak load. Although there is some variability in stiffness between 50 and 150 kN between tests, this is not attributed to parameters examined in this test program. It was noted that for some tests, although the bottom

Table 2   Test results

Test ID	Loading arm	Peak load (kN)	Net displacement at peak load (mm)	Baseplate rotation at peak load (rad)	Connection rotation at peak load (rad)	Failure mode
ST-250	Pinned	277	6.71	0.013	0.017	Concrete breakout
DA-250	Pinned	231	4.48	0.006	0.053	Weld rupture
ST-215	Fixed	278	4.40	0.011	0.013	Concrete breakout
DA-215	Fixed	276	4.72	0.009	0.024	Concrete breakout
ST-175	Pinned	287	7.01	0.022	0.022	Concrete breakout
DA-175	Pinned	230	2.49	0.007	0.038	Weld rupture
PR-UR	Fixed	276	6.18	0.010	0.019	Concrete breakout
PR-20 M	Fixed	254	2.69	0.003	0.008	Concrete breakout
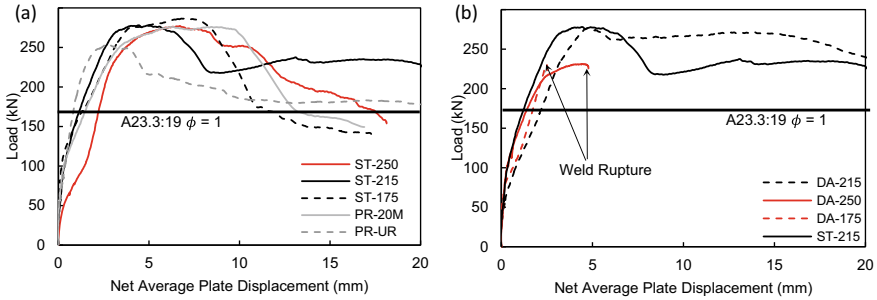
Fig. 8 Load versus net plate displacement curves for **a** Tests with shear tabs and **b** Tests with double angles, plus ST-215 for reference. Capacity predictions from A23.3:19 with material reduction factors taken as 1.0 also shown

of the block directly beared against supports, that a small gap between supports and the top of the block existed. Since uplift restraint at the back of the block was not fully rigid, the block could rotate about the bottom corner of the front face until the top of the front face came into contact with the supports. Although LVDTs were connected to the block to account for translation, these LVDTs were located at the bottom of the block, and did not measure rotation-induced displacement at the top of the block. The test most affected by this issue was ST-250. ST-250 exhibited what appears to be a loss in stiffness greater than any other test at around 50 kN, and then the stiffness increases again around 100 kN. From comparing time-lapse videos of this test to the load–displacement curve, it is clear that the block rotated, and that this rotation occurred predominantly between 50 and 100 kN. However, beyond this point, the test continued to the peak load with a stiffness consistent with the other tests and is expected to not affect total capacity. Further quantification of these findings will be completed when DIC results are presented in future.

Another factor that may impact the stiffness is how the failure surfaces from previous tests may interfere with bearing on either side of the breakout cone. Although breakout cones were contained to the predicted region of approximately 450 mm from either side of the embed, excessive cracking from behind some embeds propagated beyond this region towards supports on either side of the block. When subsequent tests were conducted, there was deformation in regions near the bearing supports that contributed to increased displacements. To that end, variation in stiffness leading up to peak load was not necessarily indicative of actual differences in connection stiffness. This conclusion is consistent with observations from other test programs that have looked at embedded plates in reinforced concrete. Sharma et al. [10] found that the initial stiffness also remained constant regardless of the amount of reinforcement present.
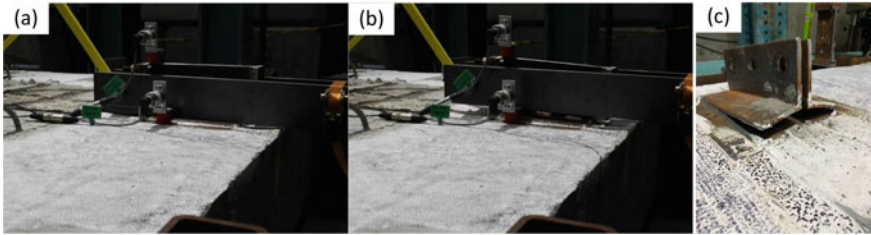
Fig. 9 Side view of DA-250 **a** At the beginning of the test and **b** Just before weld rupture, **c** Weld rupture on double angle connection

3.1 Loading Arm Effect and Weld Rupture

The first four tests (ST-250, DA-250, ST-175, and DA-175) were conducted with the fully pinned connection described in Sect. 2.3. Though this method of load application has an inherent destabilizing effect, other test programs show such small rotations up to peak load that it was not expected to cause any issues. However, in these tests the pinned connection resulted in cases where the eccentricity of the shear load alone was enough to cause a combination of shear and tension concrete breakout that can be best described as a pryout effect that would be most representative of a cantilever. The pinned connection had an unfortunate and significant impact on the behaviour of double angle connections. The double angles did not have sufficient stiffness to prevent extreme rotation, and they pried off the baseplate via weld rupture for both DA-250 and DA-175. Figure 9 shows DA-250 at the beginning of the test (a), and the instant before the welds ruptured (b), where there is very little shear deformation, but a large rotation of the W310 × 67 that was applying the load to the double angles.

For the last four tests (ST-215, DA-215, PR-20M, and PR-UR), the loading scheme was modified by drilling three holes in the loading arms that were used to bolt them directly to the shear tab or double angles (Fig. 7). The intent of this change was to provide restraint to prevent the remaining double angle test (DA-215) from failing by weld rupture. This change was also expected to reduce the severity of pryout effects on all remaining tests. Although successful in preventing weld rupture in DA-215, the remaining tests still exhibited a pryout effect consistent with the first four tests completed with the original pin connection.

3.2 Concrete Breakout Failure

Six of the eight tests failed in concrete breakout (Fig. 10). For the six tests that failed by concrete breakout, nonlinear behaviour began at around 90% of the peak load. For the two tests that failed via weld rupture, there is a distinct difference between DA-175 and DA-250. For DA-175, the more heavily reinforced test, the
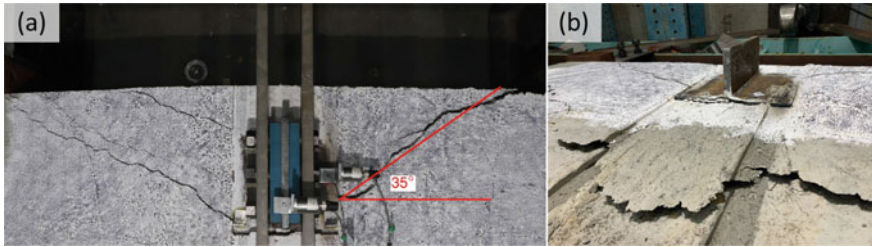
Fig. 10 **a** Typical shear breakout cone for anchorage (ST-215 shown) and **b** ST-250 breakout cone. Note shear breakout forming from the plate and the tension breakout extending past the back of the plate

load–displacement curve had no plateau, but rather continued linearly until failure. In contrast, DA-250 exhibited a small plateau prior to weld rupture.

In all tests the first crack to propagate from the plate to the concrete edge originated close to the first row of studs at around 150 mm from the edge of the concrete. In some cases, superficial cracks opened at the front corners of the embedded plate, but as the load increased the primary shear breakout cone formed from the first row of studs. Pictures from the DIC camera (such as Fig. 10a) were taken in plane view and captured shear breakout cones but tension breakout cones are best seen from other angles (Fig. 10b).

3.3 Considerations for Anchor Group Design

Tests that failed by concrete breakout greatly exceeded the shear breakout strength if calculated using only the front anchor row (52 kN), despite reductions from moment prying effects. The peak load also exceeded the shear strength of two studs (166 kN) in all tests, which indicates that load was carried by both rows of anchors. ACI 318 permits designers to consider multiple rows of anchors if the anchor row spacing to front anchor edge distance ratio is less than 0.6. This would require an edge distance to the nearest studs of 250 mm for the tested plates since the row spacing was 150 mm. However, for these tests this ratio was equal to one; ACI 318 suggests that multiple rows of anchors could not carry shear in this case. Since the peak load exceeds the shear strength of two anchors, both anchor rows participated in resisting applied load. This effect is attributed to reinforcement in the concrete. During the tests, a smaller shear breakout cone first formed from the front studs just before peak load and as load plateaued a second breakout cone formed from the back studs. In unreinforced concrete, once the first cone formed the front studs would be unable to carry any load. However, reinforcement anchors the breakout body to the rest of the member, so even after breakout cones form from the front studs, they are still tied to the rest of the member and front studs are still able to carry shear load. Figure 11 shows that the back studs exhibited both bending and shear deformations. There was no discernible

Fig. 11 Back stud of DA-215 which yielded due to bending, but also experienced notable shear deformation just below the weld that connected it to the baseplate

deformation of the stud, where the weld connects the stud to the baseplate but just below this area the shear deformation is significant. This is consistent with [1] who indicated that local increases in strength around welds cause failures to preferentially take place in weaker, unaffected metal just beyond the weld.

3.4 Load-Rotation Behaviour

Despite the pryout failures that were observed, baseplate rotations were not any more significant than tests from [5], where shear breakout was the dominant failure mode due to the rotational restraint from the loading arm and jack. Chin [5] load-rotation curves show near constant stiffness followed by a non-linear region where rotations increase and load gradually increases as peak load is approached. Similar behaviour was seen in load–displacement curves indicating that load is redistributing and reinforcement is yielding. Contrast that with Fig. 12 where there is no nonlinear region to suggest yielding prior to peak load. The lack of rotational restraint allowed the plates to pry up and away from the concrete rather than being forced to displace laterally which would better engage reinforcement. This behaviour is evident in the post-peak behaviour, where rotations in excess of 0.1 rad were recorded, while [5] only saw 0.08, with most tests rotating less than 0.06 rad. Figure 13 shows rotations measured within the connection. Shear tabs were rigidly connected to the baseplate, so the rotation of the shear tabs was very similar to baseplate rotation. For DA-250 and DA-175 which failed by weld rupture, Fig. 13b shows the double angle connection with the pinned loading arm connection was very flexible, so angles rotated until they were pried off of the baseplate, while the baseplate rotation remained small. DA-215 was the only double angle test completed with the bolted loading arm, and in comparing Fig. 13a, b up to peak load, connection and baseplate rotations were very different (the connection rotation was around three times that of the baseplate). In situations where a certain amount of rotation is forced on the connection, the more flexible double angle detail would transfer less moment to the embedded plate which would increase the shear capacity of the anchorage.
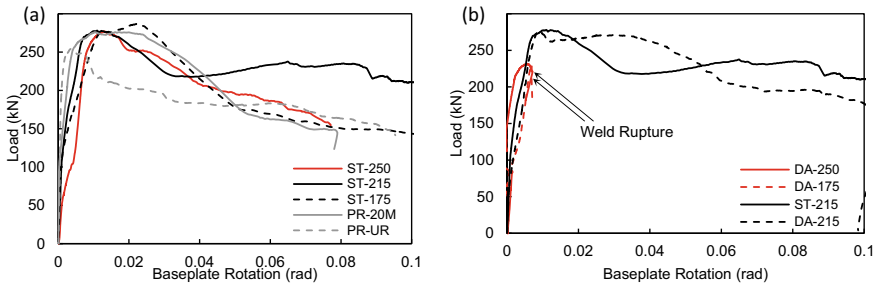
Fig. 12 Load versus base plate rotation **a** Tests with shear tabs and **b** Tests with double angles, plus ST-215 for reference
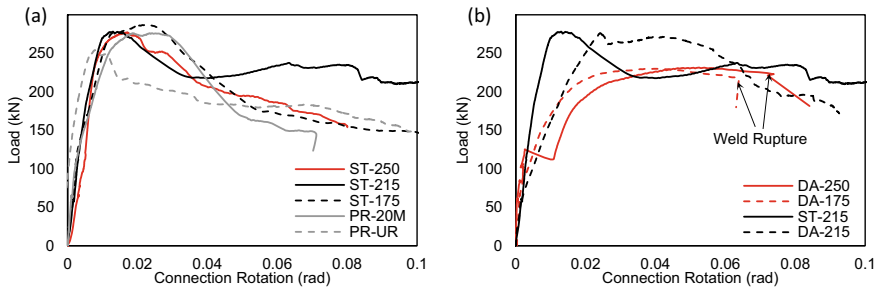
Fig. 13 Load versus connection rotation **a** Tests with shear tabs and **b** Tests with double angles, plus ST-215 for reference

3.5 Comparison with A23.3:19

Predictions from CSA A23.3 are shown for two different cases in Fig. 14. The first (case 1) is how designers would usually calculate breakout strength. This includes a leading coefficient of $k_{v,5\%} = 0.58$, the material resistance factor set to 0.65, and $\Psi_{c,V}$ taken as 1.2 for all tests except PR-UR, where it is taken as 1.0. $k_{v,5\%}$ is empirically derived by Fuchs et al. [7] and is reduced from a nominal value of around 1.0 to account for cracked concrete and the 5% fractile adjustment. The 5% fractile adjustment results in a probability of 95% that the actual breakout strength exceeds the calculated capacity. Although the concrete was uncracked, which permits $\Psi_{c,V}$ to be taken as 1.4, concrete cracking is a complex problem that warrants caution, and for that reason designers consulted on this project indicated that a value of 1.0 is usually assumed. The second case (case 2) is intended to be a closer-to-true prediction of anchorage capacity, meaning that material resistance factors were set to one, $\Psi_{c,V}$ is 1.4 since the concrete is uncracked, and the nominal leading coefficient, $k_{v,50\%} = 1.0$, is used to estimate breakout capacity. Note that A23.3 allows designers to use $k_{v,5\%} = 0.66$ for welded headed studs, but the authors were unable to find any supporting evidence for this clause, even after looking through references in

Fig. 14 Comparisons of the test results with predictions from CSA A23.3
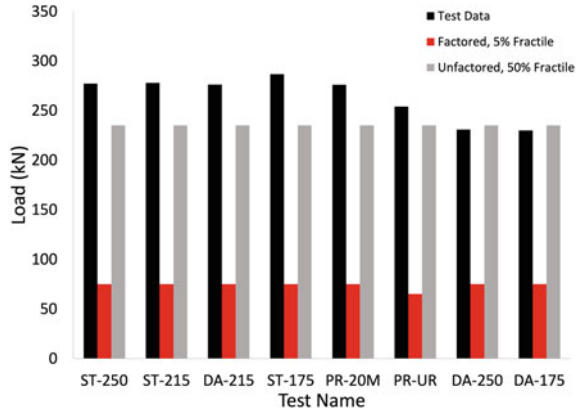
commentary from ACI 318–19's anchorage to concrete provisions which are what Annex D of A23.3 is based on. In both cases, the allowable shear capacity was calculated through an iterative process that involves first calculating the tension and shear breakout strengths separately, since these were the governing failure modes.

All six tests that failed by concrete breakout greatly outperformed the case (1) code predictions, with an average test-to-predicted ratio of 3.75. Even if the material resistance factor is taken as unity, the average test-to-predicted ratio is 2.43. The gross underestimation of the breakout strength is primarily attributed to the use of the 5% fractile by the design standard, as well as the choice of $\Psi_{c,V}$. The 5% fractile adjustment reduces the calculated capacity by approximately 25%, and the choice of $\Psi_{c,V}$ can reduce the predicted capacity by 14–29%, for a total reduction of 53–64%.

4 Conclusion

A full-scale test program was conducted to evaluate the effects of reinforcement density and connection type on precast embedded plates loaded in shear towards a free edge. Stirrup spacings were varied between 250 and 175 mm, and the shear-type connections were shear tabs and double angles. Two additional tests compared the behaviour of tests with varying amounts of perimeter reinforcement oriented perpendicular to the applied load.

All eight tests greatly outperformed A23.3:19 predictions of concrete breakout, including the two tests that failed by weld rupture. Six of the eight tests failed in a combination of shear and tension breakout. The severity of the tension breakout failure depended on the amount of reinforcement and was a result of a loading system that permitted free rotation of the embedded plates, which contrasted other test programs that provided uplift restraint to force a pure shear load. The embedded plates exhibited significant rotation and pryout behaviour due to the eccentricity of the shear force alone.

Future work should consider a means of applying the load in a manner consistent with load-rotation curves for common connections. Achieving this in a full-scale test program would be elaborate, but would provide valuable information on this complex response that could be used to validate finite element models for parametric studies that examine load-rotation behaviour, reinforcement layouts, and edge distances.

References

1. Anderson N, Meinheit D (2000) Design criteria for headed stud groups in shear: Part 1—steel capacity and back edge effects. PCI J 45:46–75
2. ASTM (2018) C39-18: standard test method for compressive strength of cylindrical specimens. ASTM International, West Conshohocken, PA
3. ASTM (2018) C78-18: standard test method for flexural strength of concrete (using simple beam with third-point loading). ASTM International, West Conshohocken, PA
4. ASTM (2019) A370-19: Standard test methods and definitions for mechanical testing of steel products. ASTM International, West Conshohocken, PA
5. Chin I (2021) Standardization and testing of embedded plates for design, fabrication, and construction economy. M.S. thesis, University of Alberta
6. Canadian Standards Association (2019) CSA A23.3:19 design of concrete structures. Canadian Standards Association, Ontario, Canada
7. Fuchs W, Eligehausen R, Breen J (1995) Concrete capacity design (ccd) approach for fastening to concrete. ACI Struct J 92(1):73–94
8. Grosser P (2012) Load-bearing behavior and design of anchorages subjected to shear and torsion loading in uncracked concrete. Ph.D. thesis, University of Stuttgart
9. Park YM, Kim TH, Kim DH, Kang CH, and Lee, J-H (2017) Breakout shear strength of cast-in-place anchors using shaking table tests. Proceedings of the Institution of Civil Engineers-Structures and Buildings, 170(12), 939–950
10. Sharma A, Eligehausen R, Asmus J (2017a) Experimental investigation of concrete edge failure of multiple-row anchorages with supplementary reinforcement. Struct Concr 18(1):153–163
11. Sharma A, Eligehausen R, Asmus J (2017b) A new model for concrete edge failure of multiple row anchorages with supplementary reinforcement. Struct Concr 18(6):893–901
12. Sharma A, Eligehausen R, Asmus J (2018) Analytical model for anchorages with supplementary reinforcement under tension or shear forces. Story. In: High tech concrete: where technology and engineering meet. Springer International, pp 974–982

Collapse Fragility Functions for Squat Reinforced Concrete Shear Walls with Different Design Parameters

Ahmed Akl and Mohamed Ezzeldin

Abstract Earthquake-related disasters are unpredictable in nature, thus leading to catastrophic consequences if structures are not adequately designed to mitigate such risks. Recent research studies have shown poor seismic performance demonstrated by buildings that had squat reinforced concrete shear walls as their main seismic force-resisting systems. This performance is mainly due to the complex nonlinear behavior, governed mainly by shear, as well as the wide range of design parameters of such walls. As such, developing seismic collapse fragility functions for such walls is still needed to link the probability of structural collapse occurrence to a ground motion intensity level. In this respect, the objective of this study is to conduct incremental dynamic analysis for squat reinforced concrete shear walls with different geometrical configurations and design parameters, and then use the analysis results to develop seismic collapse fragility functions in order to facilitate the quantification of the seismic collapse risk. To achieve this objective, OpenSees is used to develop numerical models that simulate the seismic response of different walls, designed with several configurations under different gravity load levels. The developed collapse fragility functions can be used to assess the adequacy of the design in mitigating seismic risks and eventually can be implemented by the different design standards to ensure the robustness and effectiveness of their design methodology.

Keyword Collapse fragility · Squat reinforced concrete shear walls

A. Akl (✉) · M. Ezzeldin
McMaster University, Hamilton, Canada
e-mail: akla1@mcmaster.ca

M. Ezzeldin
e-mail: ezzeldms@mcmaster.ca

447

1   Introduction

Earthquakes can cause a lot of devastation to cities and countries as the occurrence of such events cannot be predicted, and therefore, structural systems are not fully immune to them. For instance, this year marks eleven years since the costliest natural disaster of all time occurred, namely the Great East Japan Earthquake in 2011 and the following Fukushima Daiichi nuclear accident [1]. Earthquakes have also caused tremendous economic losses all over the world. For example, earthquake events are estimated to have resulted in 520 billion dollars in losses during the last 50 years, thus constituting the highest share (about 47%) of the total losses caused by all natural disasters throughout the same period [2]. This has necessitated the need for intense evaluation of the performance of structural systems under seismic loading.

Squat reinforced concrete shear walls (SRCWs) have been generally used in various low-rise buildings as the main seismic force-resisting system. For example, shear walls used in residential and office buildings, parking structures, industrial as well as nuclear facilities [3, 4] provide sufficient lateral stiffness and resistance against service-level earthquakes. Furthermore, such walls are capable of providing adequate ductility capacity in case of beyond service-level earthquakes, thus protecting non-ductile members against collapse and subsequently limiting the overall damage that the structure can sustain [5]. SRCWs are generally characterized by having a complex nonlinear behavior as a result of the flexure-shear interaction [6]. Despite such unique behavior, most relevant building codes and design standards do not designate distinctive seismic performance factors for squat walls. Furthermore, recent research studies have demonstrated that the performance of SRCWs was poor and has not been adequately quantified [7] to allow for proper seismic performance assessment. In addition, the recent study by ref. [8] showed that low response modification factors (i.e., $R < 6$ for low and high axially loaded walls, respectively) should be used for SRCWs to achieve an acceptable seismic performance that is capable of satisfying the safety criteria of the FEMA P695 [9].

In this regard, the main purpose of the current paper is to assess the performance of SRCWs with different configurations and design parameters (e.g., seismic performance factors, axial loads, and aspect ratios). The assessment is based on the results obtained from incremental dynamic analyses which are subsequently used to perform probabilistic seismic collapse risk assessments. In this respect, an OpenSees [10] model is used to simulate the nonlinear behavior of such walls. Afterward, 18 wall archetypes are designed and evaluated with different seismic performance factors (i.e., $R = 2$, $R = 3$, and $R = 6$) using 44 earthquake records provided by the FEMA P695 [9]. Subsequently, the obtained results are used to develop collapse fragility functions that can be utilized to indicate the performance level of such walls. These functions are expected to provide insight to engineers about essential parameters (e.g., the level of damage and the corresponding repair costs) that can help stakeholders in the decision-making process.

2 Numerical Model

A numerical model capable of adequately capturing the nonlinear behavior of SRCWs is crucial to the accuracy and precision of the probabilistic seismic collapse risk assessment. This is because the SRCW is a structural system of a unique behavior that is mainly governed by shear or shear/flexure interaction. Hence, the SFI-MVLEM element [11], available in *OpenSees*, was used to simulate the behavior of such walls. The element is capable of capturing the shear-flexure interaction [12] with reasonable accuracy [6, 13, 14]. Additionally, the model showed good agreement with the behavior of experimentally tested squat walls with aspect ratios of less than two [8]. Hence, the model was decided to be suitable herein for conducting incremental dynamic analysis in order to develop the intended collapse fragility functions.

The SFI-MVLEM model is considered a typical example of the macroscopic-based modeling approach, which is well known for its ability to properly capture the global behavior of structures while optimizing the computational demands. Generally, the model consists of a number of RC panels (*m*) connected by a rigid element located at the top and bottom edges of the element. The element is then replicated vertically to represent a wall height with a total number of (*n*) elements placed on top of one another, as shown in Fig. 1. The number of panels (*m*) was found to produce the most accurate results when selected to lie within the range of 5 and 10, while the number of elements placed vertically (*n*) should be estimated based on the plastic hinge length formula by ref. [15], as presented in equation [12].

$$L_p = 0.143\,L_w + 0.072(M/V) \tag{1}$$

Fig. 1 Schematic of the numerical model (based on [11])
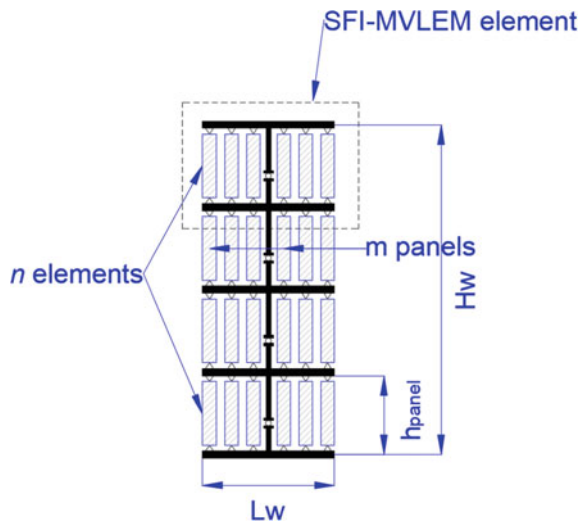
where L_p is the plastic hinge length, L_w is the wall length, and M/V is the moment-to-shear ratio. Further details about the model parameters and their effects on the model results can be found in [11].

3 Wall Design Requirements and Configurations

Due to the broad spectrum of the available design applications of SRCWs, only a small portion was incorporated in the current study. Specifically, rectangular cantilever low-aspect-ratio reinforced concrete walls in a regular building layout, typically found in industrial and parking structures, were assumed. In this study, three building types were implemented; (1) 1-story buildings whose walls are named "A1," (2) 2-story buildings whose walls are named "A2," (3) 1-story double-height buildings whose walls are named "A3." As shown in Fig. 2 as an example for the 1-story buildings, each building had four walls, two walls in each of the building's main directions, to provide seismic resistance. The building design parameters included the building's floor plan dimensions ($L \times W$), wall aspect ratios (H_w/L_w), wall dimensions ($L_w \times H_w \times t_w$), and tributary area (i.e., indicated in the figure). Single-story buildings (i.e., A1 and A3) had a wall height, H_w, equal to 4.00 m and 6.00 m, respectively, while the first and second stories of the two-story buildings were 3.60 m and 4.00 m high, respectively. The thicknesses of the walls ranged between 250 and 400 mm thick, which was selected in order to induce high shear stresses on such walls (i.e., $8\sqrt{f'_c}$, where f'_c denotes the specified compressive strength of concrete), thus representing a realistic loading case for low-rise walls. Moreover, the walls had aspect ratios ranging from 0.30 to 1.50 to cover a wide range of squat wall archetypes. Two levels of axial loads were considered in this study: (1) a low axial load level with average axial stress of 0.075 f'_c; and (2) a high axial load level with average axial stress of 0.20 f'_c. A total of 18 walls were considered herein, where the name of each wall refers to the design parameters used in developing this archetype, as presented in Table 1. The first letter indicates the type of the building, A1, A2, and A3, representing single-story, two-story and single-story with double-height buildings, respectively. The second letter indicates the response modification factor value used in the design of this wall: $R = 2$, 3, and 6. Finally, the last letter indicates the level of axial load applied to the wall when conducting the analyses, where letters L and H refer to low and high axial load levels, respectively.

All walls were designed based on the forces calculated according to the equivalent lateral force procedure of the ASCE7-16 [16]. All walls were assumed to act as cantilevers with concentrated masses placed at the floor levels with the base assumed to be fixed to induce more seismic shear demands [7]. The approximated fundamental period (T_a) was calculated as presented in Eq. 2 following the ASCE7-16 [16] formula, where h_w is the building height. Consequently, (T_a) was used to calculate the value of the code-based fundamental period as shown in Eq. 3, taking into consideration the upper and lower limits imposed by the ASCE7-16 [16], where (C_u) is the upper limit on the calculated period, and T is the structural fundamental period.
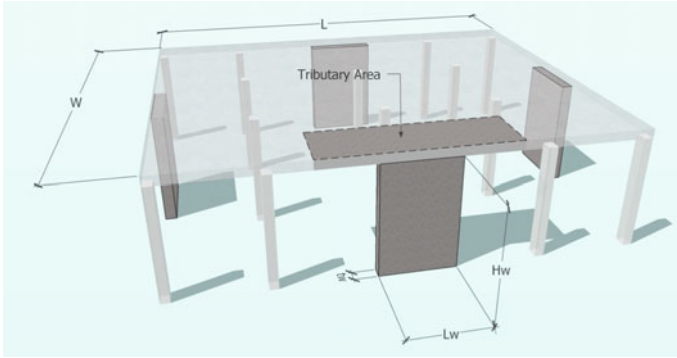
Fig. 2 Typical floor configuration

Table 1 Floor plan and walls dimensions

Archetype	Number of floors	Plan dimensions (m × m (ft × ft))	L_w m (ft)	tw m (in)	H_w/L_w
A1-R6-L	1	122 × 107 (400 × 350)	7.95 (26)	0.25 (10)	0.50
A2-R6-L	2	85 × 73 (280 × 240)	7.60 (25)	0.25 (10)	1.00
A3-R6-L	1	85 × 85 (280 × 280)	4.00 (13)	0.25 (10)	1.50
A1-R3-L	1	122 × 107 (400 × 350)	9.90 (33)	0.40 (16)	0.40
A2-R3-L	2	85 × 73 (280 × 240)	9.85 (32)	0.35 (14)	0.80
A3-R3-L	1	85 × 85 (280 × 280)	6.70 (22)	0.30 (23)	0.90
A1-R2-L	1	122 × 107 (400 × 350)	13.50 (44)	0.40 (16)	0.30
A2-R2-L	2	85 × 73 (280 × 240)	12.95 (42)	0.40 (16)	0.60
A3-R2-L	1	85 × 85 (280 × 280)	8.65 (28)	0.35 (14)	0.71
A1-R6-H	1	122 × 107 (400 × 350)	7.95 (26)	0.25 (10)	0.50
A2-R6-H	2	85 × 73 (280 × 240)	7.60 (25)	0.25 (10)	1.00
A3-R6-H	1	85 × 85 (280 × 280)	4.00 (13)	0.25 (10)	1.50
A1-R3-H	1	122 × 107 (400 × 350)	9.90 (33)	0.40 (16)	0.40
A2-R3-H	2	85 × 73 (280 × 240)	9.85 (32)	0.35 (14)	0.80
A3-R3-H	1	85 × 85 (280 × 280)	6.70 (22)	0.30 (23)	0.90
A1-R2-H	1	122 × 107 (400 × 350)	13.50 (44)	0.40 (16)	0.30
A2-R2-H	2	85 × 73 (280 × 240)	12.95 (42)	0.40 (16)	0.60
A3-R2-H	1	85 × 85 (280 × 280)	8.65 (28)	0.35 (14)	0.71

$$T_a = 0.02 \, h_w^{0.75} \tag{2}$$

$$T = C_u T_a \geq 0.25 \text{ s} \tag{3}$$

The seismic response coefficient (C_s) was calculated based on a response acceleration at short periods parameter (S_{DS}) value of 1.0 for the seismic design category Dmax as per [9, 16] recommendations. The base shear was then calculated and distributed based on a response acceleration factor at 1 s (S_{D1}) of 0.6 for the seismic design category Dmax as per Sect. 12.8.3 of the ASCE7-16 [16].

The material properties were assumed to be constant across all archetypes, where a compressive concrete strength of 41 MPa (6.0 ksi) and a yield stress of 420 MPa (60.0 ksi) for reinforcement rebars were assumed. Based on these design parameters, the straining actions were calculated using the design load combinations of the ASCE7-16 [16], and the design was carried out according to the provisions of the ACI318-19 [12]. Subsequently, the corresponding ultimate bending moment and ultimate axial loads were plotted against the acceptable design space defined by the reduced nominal sectional moment capacity and the reduced nominal sectional axial load capacity. The need for boundary elements was also assessed and provided when needed as per the ACI318-19 [12] recommendations. The full reinforcement details are provided in Table 2.

Table 2 Reinforcement details for walls

Archetype	Boundary thickness (mm (in))	Vertical web (%)	Horizontal web (%)	Boundary vertical (%)	Boundary horizontal (%)
A1-R6-L	1270 (50.0)	1.10	0.89	1.71	2.07
A2-R6-L	1700 (67.0)	0.35	1.00	3.13	1.60
A3-R6-L	1270 (50.0)	1.87	1.03	5.54	2.13
A1-R3-L	1524 (60.0)	0.78	1.07	2.08	1.30
A2-R3-L	1450 (57.0)	0.95	1.07	1.94	1.62
A3-R3-L	1525 (60.0)	1.72	1.03	3.88	1.59
A1-R2-L	2030 (80.0)	0.99	1.04	1.60	1.27
A2-R2-L	2285 (90.0)	0.94	0.99	1.35	1.25
A3-R2-L	1780 (70.0)	1.05	1.07	2.85	1.31
A1-R6-H	3680 (145)	2.73	0.89	3.55	2.06
A2-R6-H	2285 (90.0)	1.10	0.89	1.92	2.06
A3-R6-H	1650 (65.0)	1.63	1.03	5.68	2.13
A1-R3-H	4300 (170.0)	0.90	0.92	1.19	1.18
A2-R3-H	2920 (115.0)	0.72	1.03	1.57	1.29
A3-R3-H	2920 (115.0)	0.86	1.00	2.58	1.57
A1-R2-H	5840 (230.0)	0.99	1.04	1.40	1.30
A2-R2-H	3800 (150.0)	0.93	1.07	1.77	1.61
A3-R2-H	3800 (150.0)	1.41	1.05	1.50	1.34

4   Nonlinear Analyses

4.1   Static Pushover Analysis

Pushover analysis is an example of the displacement-based analytical approaches that aim at predicting the strength and deformation capacities of structures. In this study, static pushover analyses were conducted for all archetypes in order to assess their collapse drift ratios to be used in conjunction with the incremental dynamic analysis to obtain the corresponding collapse fragility functions. Throughout the pushover analyses, the seismic loads were distributed vertically at story levels using the corresponding mode shape ordinates as per the ASCE7-16 [16] recommendations. Additionally, a leaning column was incorporated into the model of each archetype to include the effects of the gravity system and the P-delta effects.

4.2   Collapse Criteria

Since OpenSees has some limitations that prevent it from depicting all failure modes adequately, some non-simulated collapse modes have been imposed while post-processing the results. In this study, the following non-simulated modes were considered:

1. Axial Failure: Axial failure was defined as per the formula introduced by ref. [17] to estimate the maximum attained drift ratio before axial loads cause collapse.
2. Steel Buckling/Fracture: A failure strain value of 0.05 was assumed to be capable of inducing steel rebars fracture/buckling. However, since a single rebar buckling/ fracture cannot provoke structural failure, the collapse was assumed to occur when the rebars lying within at least a quarter of the wall length have all failed [18].
3. Sliding Shear: Sliding shear was assumed to occur when the value of base shear reached the value calculated according to the equation by Mattock et al. [19, 20]. This equation includes the effects of both the aggregate interlock and the reinforcement dowel effects.

Finally, a maximum limit for the collapse drift ratio was imposed, which corresponds to a 20% strength degradation as indicated in the static pushover analysis [9]. This limitation ensures reasonable maximum drift ratios capable of guaranteeing life safety.

4.3 Incremental Dynamic Analysis

Incremental dynamic analysis is a nonlinear approach that applies ground motions
with increasing scale factors to the structure until collapse occurs [21]. The set of
ground motions provided by the FEMA P695 [9] was used to carry out the incremental
dynamic analysis in order to conduct a structural collapse assessment. The set consists
of 22 pairs of ground motions (44 in total) that were all captured at a distance greater
than or equal to 10 km from fault rupture. Figure 3 shows a sample of the obtained
results from the incremental dynamic analysis. Each point on the plot represents the
results obtained from a single nonlinear dynamic analysis for the considered wall
archetype using a single ground motion with a single scale factor. The indicated
ultimate displacement corresponds to the value obtained from the collapse criteria
taking into consideration the non-simulated modes of failure as discussed previously.
The results are then used to plot a collapse fragility function for this wall archetype.

5 Collapse Fragility Functions

Collapse fragility functions are based on cumulative distribution functions that link
the probability of structural failure to the seismic level intensity of the ground motions
using the incremental dynamic analysis. Collapse fragility curves can provide insights
to engineers about the influence of the different parameters on the overall safety and
robustness of the structural system under seismic loading. The probability of collapse
can be expressed mathematically, as shown in Eq. (4) [22]:

$$P(C|IM = x) = \Phi\left(\frac{\ln(x/\theta)}{\beta}\right) \tag{4}$$

where $P(C|IM = x)$ is the probability of collapse given an intensity measure (IM),
Φ is the standard normal cumulative distribution function, θ is the collapse median
intensity, and β is the standard deviation of the IM [22]. The collapse fragility func-
tions are developed based on the incremental dynamic analysis results. First, the

ultimate drift ratio was obtained from the static pushover analysis along with the non-simulated modes of failure. Afterward, the value of the ultimate drift ratio was plotted as indicated in Fig. 3, and for each increment of seismic level intensity (i.e., at 0.10 g increments), the number of ground motions resulting in the structural collapse was obtained. Then, this number was used to calculate the probability of structural collapse at this seismic level intensity. This procedure was carried out repeatedly for all the designed walls to obtain the distribution of their collapse probability. Subsequently, the probability of collapse for each archetype was plotted against the corresponding level of seismic intensity to indicate the probability of structural failure at any level of earthquake.

Figures 4 and 5 show the collapse fragility functions for the 18 archetypes. The figures show that the probability of collapse is directly proportional to the response modification factor used in the design. Specifically, as the R-factor decreases, the fragility curves show a general reduction in values which indicates lower probability of collapse values. In other words, the robustness of low-rise structures tends to significantly increase as the value of the used seismic response modification factor decreases, thus yielding higher overall structural performance than those structures designed with relatively higher values of R-factor. For example, as can be seen from Fig. 4b, at a seismic intensity level of 2.0 g, walls A1 subjected to low axial loads have probability of collapse values of 66%, 46%, and 15% when designed using R-factors of 6.0, 3.0, and 2.0, respectively. Similarly, Fig. 4a–d shows the same overall behavior, where the probability of failure decreases as the response modification factor increase. Figure 4a shows a significant drop in the probability of collapse between walls designed with different R-factors, with a drop of about 52% and 80% at a seismic level of 2.5 g between the wall when designed using $R = 6.0$ and $R = 3.0$, and the same wall when designed with $R = 6.0$ and $R = 2.0$, respectively. Hence, indicating an overall gain in structural robustness. Figure 4c and d shows a decrease in the probability of failure as the R-factor increase as well, however, walls designed using $R = 3$ approach a similar probability of failure at very high seismic levels. These fragility curves can be utilized to indicate the expected required level of damage, anticipated casualties, expected replacement/repair costs as well as downtime when such walls are subjected to an earthquake event. Such information can give effective insights that can significantly aid the decision-making process.

Additionally, Fig. 5a, and b shows, as expected, that a higher probability of failure is generally associated with a higher design R-factor. For instance, at a seismic intensity level of 2.0 g, walls have a probability of collapse of 13%, 30%, and 57% for R-factors of 2.0, 3.0, and 6.0, respectively. Likewise, at the same level of seismic intensity, the probability of collapse values for walls experiencing lower axial load levels were 14%, 34%, and 53%, for R-factors of 2.0, 3.0, and 6.0, respectively.

Furthermore, Fig. 6 shows the relationship between different archetypes using the same R-factor. Generally, the figure shows that walls experiencing a higher level of axial loads, reaching 0.20 f'_c A$_g$, tend to have a lower probability of collapse when compared to those subjected to lower axial loads levels (0.075 f'_c A$_g$), where f'_c is the concrete compressive strength and A$_g$ is the wall's gross sectional area. For instance, at a seismic intensity level of 2.5 g, wall archetypes A1, A2, and A3
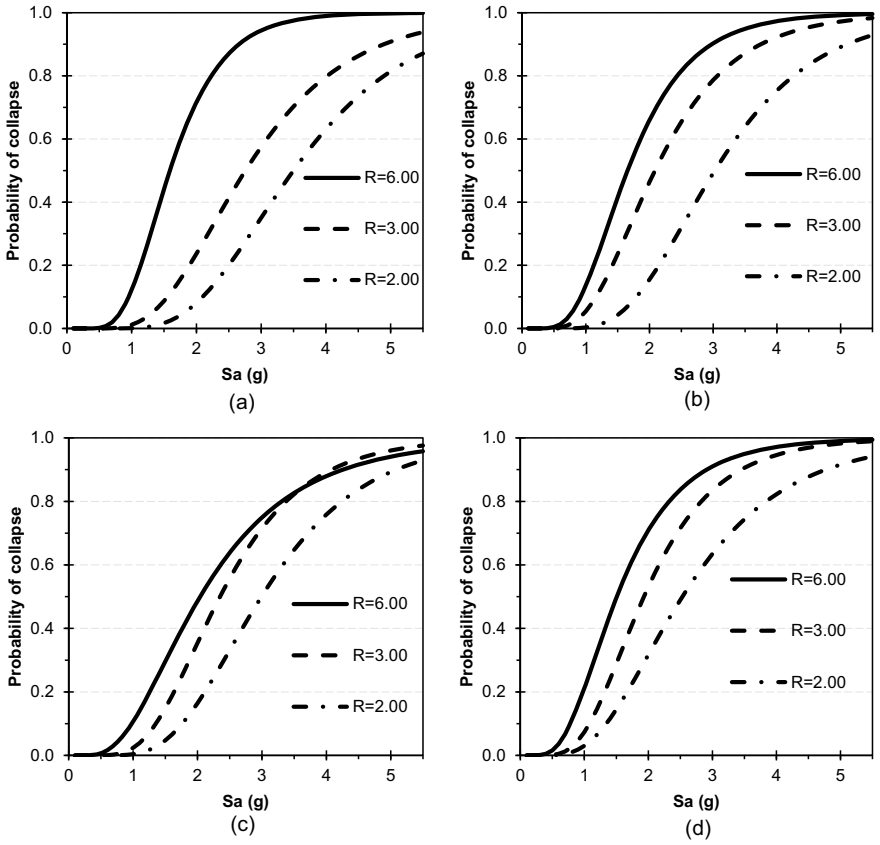
Fig. 4 Collapse fragility functions: **a** A1-H; **b** A1-L; **c** A2-H; **d** A2-L
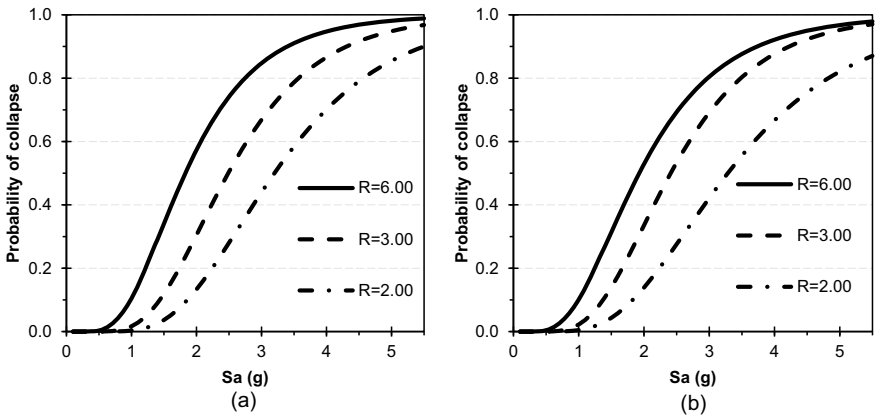
Fig. 5 Collapse fragility functions: **a** A3-H; **b** A3-L

designed for high axial loads with *R*-factor of 2.0 had lower probability of failure values when compared to walls designed for low axial loads by 37%, 13%, and 35%, respectively as shown in Fig. 6c. Similarly, the same behavior is noticed for walls designed using an *R*-factor of 3.0, where the failure probabilities for walls designed with higher axial load, indicated by the dashed lines, are below walls designed for low axial loads, indicated by solid lines as shown in Fig. 6b. However, this behavior is less pronounced in walls designed with *R*-factor of 6.0 as can be seen in Fig. 6a, where the probabilities of failure are similar for one-story walls, with lines almost coinciding, while a lower probability of failure is associated with higher axial loads for two-story walls designed with $R = 6.0$.

6 Conclusions

The current study developed collapse fragility functions for low-aspect-ratio walls with different design configurations in an effort to quantify their seismic collapse risks. In this respect, 18 wall archetypes were designed and detailed using three values of response modification factor, *R*-factor, $R = 6.0$, 3.0, and 2.0. The designed walls were modeled using OpenSees to simulate the seismic response for such walls. Afterward, nonlinear static and dynamic analyses were carried out to develop incremental dynamic analyses plots. Consequently, the plots were used to construct collapse fragility functions for such walls in order to provide a quantitative assessment of the adequacy of the design as well as the ability to mitigate seismic risks.

The collapse fragility functions generally showed an overall improvement regarding seismic performance for walls designed using *R*-factors of 2.0 and 3.0 when compared to walls designed with an *R*-factor of 6.0. Additionally, archetypes subjected to high axial load levels (0.20 f_c' Ag) showed a lower probability of failure when compared to those with low axial load levels (0.075 f_c' Ag), hence indicating higher levels of seismic resilience. The presented collapse fragility functions can be incorporated to denote the anticipated level of damage, expected repair/maintenance costs, downtime, as well as structural performance levels which can give useful insight for engineers and decision-makers.

Fig. 6 Collapse fragility
functions: **a** R6; **b** R3; **c** R2
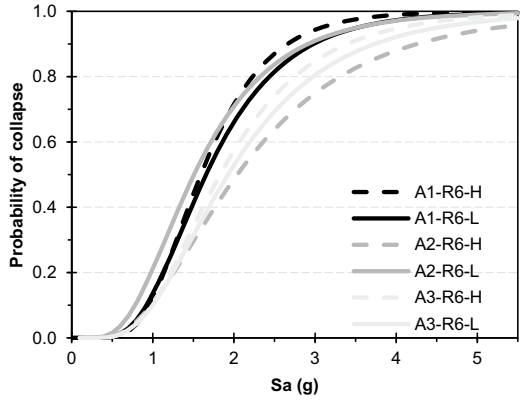
(a)
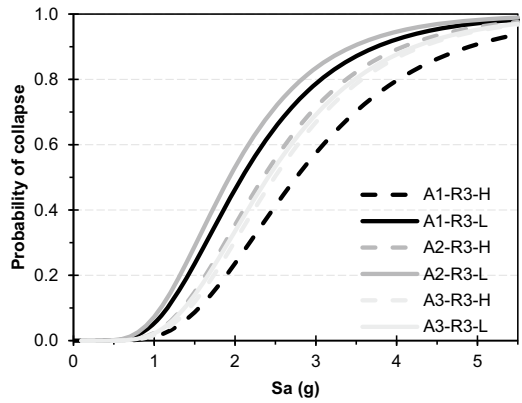
(b)
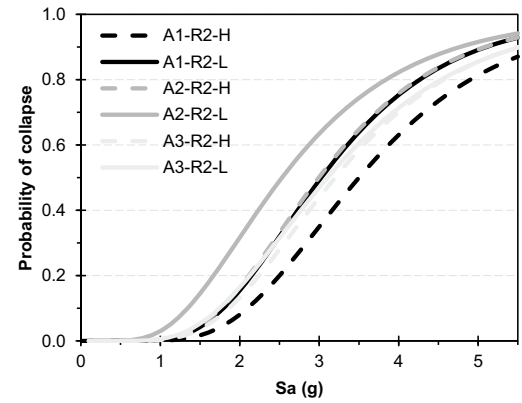
(c)

References

1. Re M (2012) Review of natural catastrophes In 2011: earthquakes result in record loss year. https://www.munichre.com/en/company/media-relations/media-information-and-corporate-news/media-information/2012/2012-01-04-review-of-natural-catastrophes-in-2011-earthquakes-result-in-record-loss-year.html#257855192
2. Centre for Research on the Epidemiology of Disasters (CRED) (2021) EM-DAT database 2021. https://www.emdat.be/database
3. Massone LM, Orakcal K, Wallace JW (2009) Modeling of squat structural walls controlled by shear. ACI Struct J 106(5):646–655
4. Terzioglu T, Orakcal K, Massone LM (2018) Cyclic lateral load behavior of squat reinforced concrete walls. Eng Struct 160:147–160
5. Gulec CK, Whittaker AS (2009) Performance-based assessment and design of squat reinforced concrete shear walls. Report no. MCEER-09-0010, Multidisciplinary center for earthquake engineering research, Buffalo, N.Y., USA
6. Kolozvari K, Orakcal K, Wallace JW (2015b) Shear-flexure interaction modeling for reinforced concrete structural walls and columns under reversed cyclic loading. PEER report no. 2015/12, Pacific earthquake engineering research center, Berkeley, USA
7. Gogus A, Wallace JW (2015) Seismic safety evaluation of reinforced concrete walls through FEMA P695 methodology. J Struct Eng 141(10):1–17
8. Akl A, Ezzeldin M (2021) Seismic collapse risk assessment of low-aspect-ratio reinforced concrete walls. In: Canadian society for civil engineering annual conference. Niagara Falls, Ontario, Canada
9. FEMA (2009) FEMA P695: quantification of building seismic performance factors. Washington, D.C., USA
10. McKenna F, Fenves G, Scott M (2000) OpenSees: open system for earthquake engineering simulation. https://opensees.berkeley.edu/index.php
11. Kolozvari K (2013) Analytical modeling of cyclic shear—flexure interaction in reinforced concrete structural walls. Ph.D. thesis, Department of civil engineering, University of California, Los Angeles, USA
12. ACI (2019) ACI 318-19: building code requirements for structural concrete. Farmington Hills, MI, USA
13. Kolozvari K, Orakcal K, Wallace JW (2018) New opensees models for simulating nonlinear flexural and coupled shear-flexural behavior of RC walls and columns. Comput Struct 196:246–262
14. Pozo JD, Hube MA, Kurama YC (2020) Quantitative assessment of nonlinear macro-models for global behavior and design of planar RC walls. Eng Struct 224:1–17
15. Kazaz I (2013) Analytical study on plastic hinge length of structural walls. J Struct Eng 139(11):1938–1950
16. ASCE (2016) ASCE7-16: Minimum design loads and associated criteria for buildings and other structures. Reston, Virginia, USA
17. Wallace JW, Elwood KJ, Massone LM (2008) Investigation of the axial load capacity for lightly reinforced wall piers. J Struct Eng 134(9):1548–1557
18. Thomsen JH, Wallace JW (2004) Displacement-based design of slender reinforced concrete structural walls—experimental verification. J Struct Eng 130(4):618–630
19. Mattock AH, Johal L, Chow HC (1975) Shear transfer in reinforced concrete with moment or tension acting across the shear plane. PCI J 20(4):76–93
20. Mattock AH, Li WK, Wang TC (1976) Shear transfer in lightweight concrete. PCI J 21(1):20–39
21. Vamvatsikos D, Cornell CA (2002) Incremental dynamic analysis. Earthquake Eng Struct Dynam 31(3):491–514
22. Baker JW (2015) Efficient analytical fragility function fitting using dynamic structural analysis. Earthq Spectra 31(1):579–599
23. Kolozvari K, Orakcal K, Wallace JW (2015a) Modeling of cyclic shear-flexure interaction in reinforced concrete structural walls. I: theory. J Struct Eng 141(5):1–10

Effects of Imperfect Bonding on RC Columns Using Various Bond-Slip Models in Advanced Fiber Beam-Column Element

Shaghayegh Abtahi and Yong Li

Abstract This paper investigates the nonlinear behavior of reinforced concrete (RC) columns while considering imperfect bonding between steel bars and the surrounding concrete (i.e., bond-slip). The objective of this study is to introduce a comprehensive bond-slip material model with quantification of prevailing uncertainties as indicated by experimental data and existing bond-slip models in the literature. This study compares the effect of various bond-slip models on the nonlinear behavior of RC columns to reveal the modeling uncertainty stemming from bond-slip properties. Recognizing such variations in bond-slip behaviors, this paper develops a new model for bond-slip behavior based on the experimental data compiled from the literature. To quantify the prevailing uncertainties in bonding properties, probabilistic models are developed based on the available experimental data through Bayesian linear regression. The bond-slip models are combined with newly implemented fiber beam-column elements to investigate the effect of imperfect bonding between the concrete and steel rebars on the structural behavior. The results reveal the need for considering imperfect bonding in advanced finite element modeling of RC columns. Furthermore, the findings indicate that uncertainties of bonding properties can dramatically influence the nonlinear behavior simulations of RC columns, particularly for RC columns with unhooked steel bars in the anchorage.

Keywords Imperfect bonding · Fiber beam-column element · Bond-slip model

1 Introduction

In the common finite element (FE) modeling approach for reinforced concrete (RC) structures, the bonding between reinforcing steel and the surrounding concrete has been considered to be perfect. Perfect bonding here implies that the deformation

S. Abtahi (✉) · Y. Li

Department of Civil and Environmental Engineering, University of Alberta, Edmonton, Alberta, Canada

e-mail: abtahi1@ualberta.ca

of reinforcing steel is perfectly compatible with the deformation of the surrounding concrete. However, this assumption neglects the experimental observations of failures due to the de-bonding of reinforcement. In general, the experimental tests indicate that the force–deformation behavior of RC columns is characterized by pinched hysteresis with less energy dissipation capabilities than predicted from modeling with the perfect bonding assumption [1, 2]. This observation highlights the need for modeling the bond-slip behavior in RC columns. Different modeling approaches for slippage between rebar and surrounding concrete have been used to address the issue [3–6]. Some approaches, such as using a zero-length element [6] and modifying the stress–strain behavior of steel [3], take into account the effect of bonding implicitly and thus cannot be employed for deteriorated columns (e.g., corroded RC columns) where degraded bond-slip behavior needs to be modeled. As such, this paper adopts a different approach to model bond-slip explicitly [5], albeit with modifications [7]. This approach considers bond-slip by adapting the displacement-based fiber beam-column element with one additional degree of freedom at each rebar node representing the steel movement [5, 7]. The authors [7] enhanced this element by considering the geometrical nonlinearity for both the steel rebars and concrete beam component and implemented it in the open-source finite element software framework, OpenSees [8].

The next step to incorporate the effect of bond-slip into the RC structural modeling is to define a stress-slip relationship (i.e., bond-slip model) for the bonding behavior. Several studies have proposed different patterns with various bonding properties based on the rebar diameter, concrete strength, spacing between rebars, lug properties, loading rate, etc. [4, 9–15]. Among these studies, [10] has one of the pioneering models for bond-slip behavior developed based on several experimental tests and has been used as the basis of many of the other models. Hence, the main purpose of the other studies was to generate the bond-slip properties (i.e., maximum stress and corresponding slip, residual stress and corresponding slip, and the slip range for the plateau in Eligehausen's bond-slip model). However, each of these models was developed based on a certain test dataset, which consisted of a small sample size, and did not take advantage of all the other tests. Although the models have been validated, the effect of deviations among those models on the behavior of RC columns is unclear. In addition, the prevailing uncertainties in the model generation have not been considered. Therefore, this study addresses the requirement to generate a proper model based on all the available experimental realizations for bonding properties, which will be used in the newly developed fiber beam-column element in OpenSees.

In summary, the study first examines the goodness of existing bond-slip models by comparing model predictions with observations derived from experimental tests in the literature. Then, using Bayesian linear regression based on experimental data compiled, a new model is proposed for bonding properties. The proposed properties together with the bond-slip material model newly implemented in OpenSees (i.e., *BondSlip03* [7]) are used with the newly developed element validated through one experimental RC column. Finally, the effect of various bond-slip models is investigated through the static cyclic pushover test for this experimental RC column and a comparison between the force–deformation results.

2 Material Model for Bond-Slip

This section describes the pattern considered for the bond-slip behavior. To fulfill the demonstration of the bond-slip behavior, the bonding properties are required to be introduced. In this regard, this study examines the common models for bond-slip properties in the literature. Each of these models is developed based on a limited set of experimental data. To develop a reliable model that works for all of the cases, a new set of probabilistic models is generated for bonding properties, which capture the prevailing uncertainties through Bayesian linear regression.

2.1 Bond-Slip Pattern

To capture the effect of slippage between steel rebar and surrounding concrete, many studies have proposed different relationships between the bonding stress and the slippage displacement (e.g., [9, 10, 12–15]). The general pattern proposed in all of these studies comprises a nonlinear curve (power-law function) up to the yield point of bond-slip (i.e., at the maximum stress t_1 and the corresponding slip u_1), a plateau until the slip reaches u_2, a softening linear behavior due to the crushing of the concrete between lugs up to the residual friction stress t_3 at slip u_3, and constant residual stress afterward. Among all of these models, one of the common patterns proposed by [10] is considered in this study shown in Fig. 1a. Note that the nonlinearity parameter α is considered equal to 1 in this study. Figure 1b demonstrates the general cyclic behavior of the bond-slip in comparison with the monotonic envelope shown as the dashed line. Under cyclic loading, the bonding behavior follows the monotonic curve described above at the beginning of the loading stage. However, if any unloading occurs, it follows a linear behavior with a relatively high stiffness, which is here considered as 4 times of the secant stiffness corresponding to the point (u_1, t_1) [13], up to the frictional branch. This friction stress is damaged during cyclic behavior based on the energy dissipated by the friction branch only. Afterward, it goes to the reduced monotonic envelope degraded based on a damage factor dependent on the total dissipated energy. The same procedure is followed at each load reversal point. For more details, see [10].

2.2 Bond-Slip Properties Based on the Existing Models

To define the bond-slip behavior for each RC structure, the bonding properties (i.e., t_1, t_3, u_1, u_2, and u_3) are required to be evaluated. For this purpose, there are many models in the literature such as Eligehausen [10], Pochanart [14], Soroushian [15], Monti [4], Lowes [12], Bamonte [9], FIB [11], and Delso [13] models. Based on these models, the bonding properties for well-confined RC structures are described depending on

$$t(u) = t_1 + \frac{t_3 - t_1}{u_3 - u_2}(u - u_2)$$

$$t(u) = t_1 \left(\frac{u}{u_1}\right)^\alpha$$

(a)

(b)
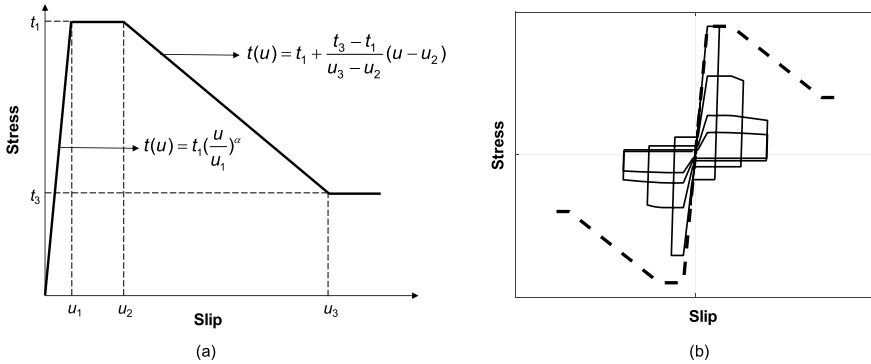
Fig. 1 Schematic bond-slip material behavior: **a** monotonic and **b** cyclic behavior

the rebar diameter, concrete strength, lug properties, and spacing between rebars. Note that according to some experiments [10], there are other factors (e.g., slip rate and external pressure influencing the bonding properties); however, their effects are ignored due to lack of data. To investigate the accuracy of the developed models, a comparison between the experimental data available in the literature and the data produced by these models is conducted in this study. In this regard, 93 data points for t_1, 30 data points for t_3, 64 data points for u_1, 37 data points for u_2, and 59 data points for u_3 are extracted from the available studies including [9, 10, 13–16]. These data points are considered as observations and then, the model predictions for each case are evaluated. The ratio of the observation to the model prediction for each model is shown in Fig. 2a to e for t_1, t_3, u_1, u_2, and u_3, respectively. In each plot, the data points originally used for the corresponding model generation are shown by gray diamonds, and the rest are expressed by black circles. Also, the ratio equal to 1 is presented with a solid black line as a reference; i.e., as the spots are closer to this line, the model is more accurate. In addition, the R-squared (R^2 value for each case is shown in the figure) indicated better model as it gets closer to 1. According to these figures, the level of accuracy of these models is low; more precise and inclusive models are required to reduce the error coming from the model development.

2.3 Probabilistic Model for Bond-Slip Properties

This section focuses on developing a new set of probabilistic models to predict the bond-slip properties, i.e., t_1, t_3, u_1, u_2, and u_3. The experimental data used in this study are derived from previous studies in the literature as described in the previous section [9, 10, 13–16]. To quantify the uncertainty of model parameters, Bayesian linear regression modeling methodology is used instead of classical linear regression [17]. This approach starts with examining a number of functional forms for which the regression analysis calibrates the model parameters. Then, the generated model
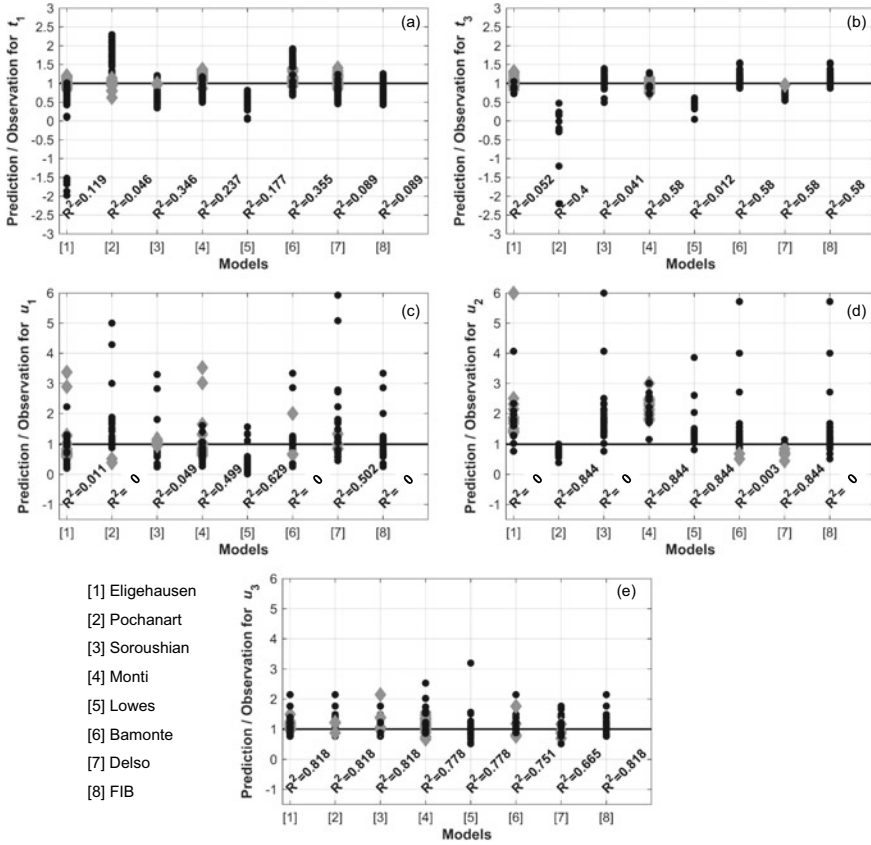
Fig. 2 Ratio of prediction to observation based on eight different models for bond-slip properties: **a** t_1, **b** t_3, **c** u_1, **d** u_2, and **e** u_3

is subjected to diagnostic tests to evaluate the quality of model prediction, normality, and homoscedasticity of model residuals.

The first bonding property considered here is t_1 with 93 realizations from the experimental data. For this parameter, 26 model forms, depending on rebar diameter d_b in mm, concrete strength f_c in MPa, and the ratio of the space between rebar lugs to the lug height S, were examined, which featured various functions of the regressors and regressand including linear and logarithmic. Equation (1) shows the best functional form for t_1 in MPa:

$$t_1 = \sqrt{f_c}\left(d_b^{\theta_1}\exp(\theta_2 S + \theta_3 + \varepsilon)\right) \qquad (1)$$

where θ_1, θ_2, and θ_3 are model parameters and ε is the model error assumed as Gaussian zero mean and standard deviation σ. The first- and second-moment statistics of these parameters (i.e., mean, coefficient of variation (CoV), and correlation

coefficients) are provided in Table 1. In accordance with Bayesian statistics, the θ_i (i = 1, 2, 3) parameters have a joint t distribution. Here, σ has the inverse chi-squared distribution with presented properties in Table 1.

The second bonding parameter is t_3 with 30 data points, for which two candidate model forms are considered to relate this parameter to t_1 linearly. The resulted model is presented in Eq. (2) with model parameter θ_1 with a mean of 0.338 and a CoV of 0.267. The standard deviation of model error ε is distributed with a mean and a CoV equal to 0.761 and 0.136, respectively.

$$t_3 = \theta_1 t_1 + \varepsilon \tag{2}$$

The next bond-slip property considered for regression analysis is u_1 with 64 experimental data points. By considering 14 model forms based on d_b in mm, f_c in MPa, S, and clear spacing between rebars c in mm, regression analysis is conducted, and the best model to describe u_1 is found to be as Eq. (3) with model parameters described in Table 2.

$$u_1 = \theta_1 + \theta_2 d_b + \frac{\theta_3}{\sqrt{f_c}} + \theta_4 \frac{c}{d_b} + \theta_5 S + \varepsilon \tag{3}$$

Similar to the model generated for t_3, a regression analysis is conducted for u_2 to relate it linearly to u_1 with 37 experimental observations. By considering two candidate model forms, Eq. (4) describes the designated model for u_2 with a defined

Table 1 Regression parameters for t_1 model

Parameter	Mean	CoV	Correlation coefficients		
			θ_1	θ_2	θ_3
θ_1	− 0.270	0.162	1.000		
θ_2	0.017	0.306	0.101	1.000	
θ_3	1.845	0.083	− 0.940	− 0.398	1.000
σ	0.228	0.076	–	–	–

Table 2 Regression parameters for u_1 model

Parameter	Mean	CoV	Correlation coefficients				
			θ_1	θ_2	θ_3	θ_4	θ_5
θ_1	− 2.565	0.121	1.000				
θ_2	0.045	0.122	− 0.050	1.000			
θ_3	8.280	0.164	− 0.767	− 0.441	1.000		
θ_4	0.144	0.165	− 0.520	− 0.625	0.641	1.000	
θ_5	0.113	0.126	− 0.389	0.284	− 0.120	− 0.078	1.000
σ	0.382	0.094	–	–	–	–	–

model parameter with a mean of 1.230 and a CoV of 0.310. The mean and CoV of the standard deviation of model error ε are 0.366 and 0.121, respectively.

$$u_2 = \theta_1 u_1 + \varepsilon \qquad (4)$$

The last bonding property considered here is u_3 with 59 experimental data points. To develop a proper model for this property based on f_{c-}, c, and spacing between rebar lugs S_L in mm, 12 candidate model forms are examined. Equation (5) shows the best model to describe u_3 with model properties presented in Table 3. In all of these equations, the deterministic form can be found by inserting mean values for the model parameters.

$$u_3 = \theta_1 + \frac{\theta_2}{\sqrt{f_c}} + \theta_3 c + \theta_4 S_L + \varepsilon \qquad (5)$$

To assess the quality of the model predictions, Fig. 3a–e present the ratio of model predictions to the corresponding observations used in the regression analysis for t_1, t_3, u_1, u_2, and u_3, respectively. The R^2 of the regression analysis is also shown in each plot in addition to the solid black line of the ratio equal to 1 as a reference. Figure 3a shows that the points in this new model for t_1 are closer to the reference line comparing to the other models in the literature, although the R^2 is not very close to 1 for this parameter (i.e., t_1) mainly due to highly scattered and limited number of data points. Figure 3b denotes the same problem for t_3. However, by respectively comparing Fig. 3a and b with Fig. 2a and b, it can be concluded that the generated models for both of these parameters are more precise and inclusive than the existing models. Despite t_1 and t_3, in the other models (i.e., u_1, u_2, and u_3) shown in Fig. 3c–e, the points are quite close to the reference line, and the R^2 values of the regression analysis for all of the models are close to 1 which reaffirms the models are capable to properly predict the bonding properties. Although not shown here for brevity, the normality plot for each of these models shows that the probability distribution of model residuals follows a normal distribution, and also, the residual plots indicate no sign of heteroscedasticity. In summary, the models successfully pass the diagnostics tests of a linear regression model.

Table 3 Regression parameters for u_3 model

Parameter	Mean	CoV	Correlation coefficients			
			θ_1	θ_2	θ_3	θ_4
θ_1	− 10.283	0.119	1.000			
θ_2	62.583	0.108	− 0.791	1.000		
θ_3	0.017	0.169	− 0.429	0.704	1.000	
θ_4	0.702	0.094	0.034	− 0.594	− 0.782	1.000
σ	1.742	0.099	–	–	–	–
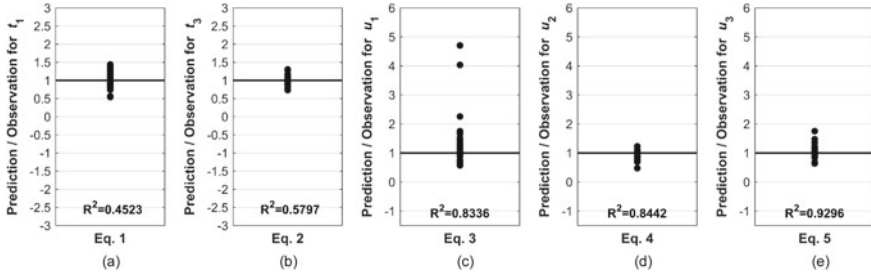
Fig. 3 Ratio of prediction to observation for **a** t_1, **b** t_3, **c** u_1, **d** u_2, and **e** u_3 models

3 Effect of Various Bond-Slip Properties

To investigate the effect of the variation of bond-slip properties on the global behavior of RC columns, an experimental RC column, denoted as Bousias column [18], is considered from the literature. The geometry, sections, and material behaviors of this column are presented in Fig. 4a–e. This column is modeled through the newly implemented *dispBeamColumnBS* element in OpenSees [7], and the bond-slip behavior follows the pattern presented in Fig. 1. The bond-slip properties shown in Fig. 4e are quantified based on the proposed model considering the deterministic forms.

Figure 5 compares the static cyclic pushover results for this column based on the perfect bonding assumption, normal bonding with proposed properties, and experimental data. This figure indicates that using the proposed bond-slip properties in the newly implemented element in OpenSees would lead to closer force–deformation behavior to the experimental results rather than the perfect bonding case. Moreover, it highlights the fact that ignoring the effect of imperfect bonding would remarkably influence the pinching behavior of RC columns.
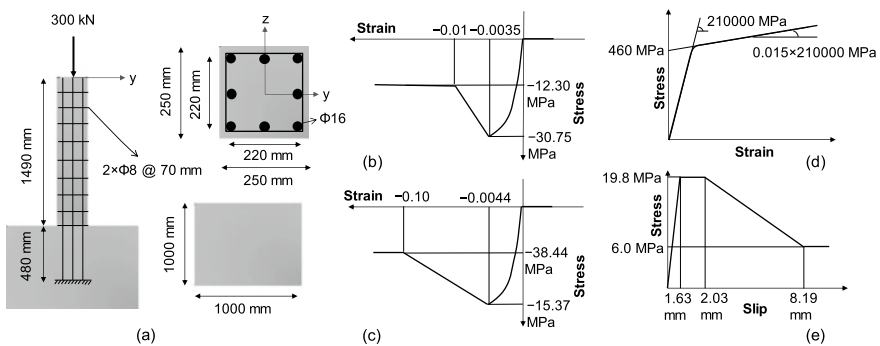
Fig. 4 **a** Geometry and sections, Kent-Scott-Park concrete model for **b** unconfined and **c** confined regions, **d** Giuffre-Menegotto-Pinto steel model, and **e** proposed bond-slip model for Bousias column
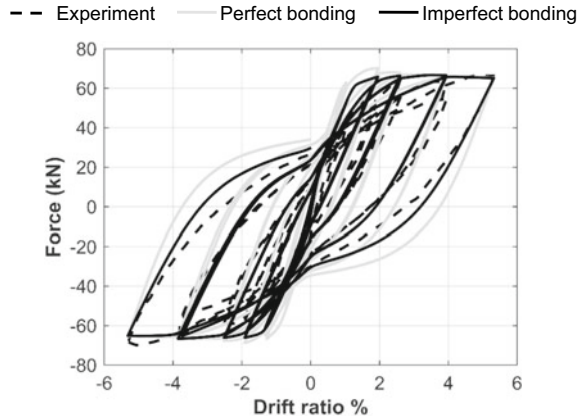
To investigate the effect of various bonding properties on the global response of
the RC column, different bond-slip properties are generated by existing models in
the literature, and the variation effect is investigated through static cyclic pushover
analysis. Based on the structural properties of the Bousias column described in Fig. 4,
the bond-slip parameters are generated based on Eligehausen, Pochanart, Soroushian,
Monti, Lowes, Bamonte, Delso, and FIB models as mentioned before. The monotonic
bond-slip behaviors based on these models are shown in Fig. 6a. These material
models are applied to the Bousias column, and the force–displacement relationships
resulting from the static cyclic pushover analysis are plotted in Fig. 6b for each bond-
slip model. As shown, the results are very close together, and it can be concluded
that the prevailing uncertainties in the properties of the bond-slip behavior do not
significantly affect the global behavior of this column. This is mainly because the
bond-slip did not experience significant nonlinearity here for this column.

Due to significant slippage of rebars at the bottom of the column (i.e., column
footing), one of the important factors affecting the role of bond-slip is the anchorage
condition. In Bousias column, the rebars are hooked in the anchorage; i.e., no slip
occurs where the rebar bends due to its full embedment in the adjoining concrete
member. To investigate the effect of various bonding properties on the static behavior
simulation of RC column with different anchorage conditions, the FE model of
Bousias column with various bonding properties is analyzed here assuming straight
(unhooked) rebars with sufficient and insufficient anchorage lengths. The corre-
sponding FE predictions of force-drift ratio hystereses are presented in Fig. 7a and b
for the case with sufficient anchorage length (i.e., original anchorage length, which
is equal to $30d_b$) and the case with insufficient anchorage length (i.e., $15d_b$), respec-
tively. Comparing Fig. 7a with Fig. 6b reveals that the effect of variations of bonding
properties on the static behavior prediction is more significant when the anchored
rebars are straight (i.e., no hook). In addition, the comparison between Fig. 7a
and b indicates that this effect gets more important when the anchorage length is
insufficient. This observation shows that need to consider uncertainties in bonding
properties in advanced modeling of RC columns.
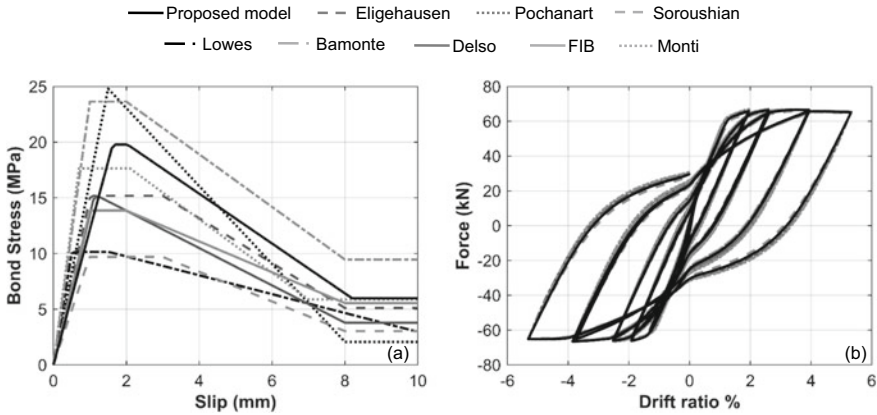
Fig. 6 **a** Force-drift ratio hysteresis comparison between FE predictions and experiment, **b** different monotonic material behavior models for bond-slip, and **c** force-drift ratio hysteresis comparison between FE predictions with nine different sets of bond-slip properties for Bousias column
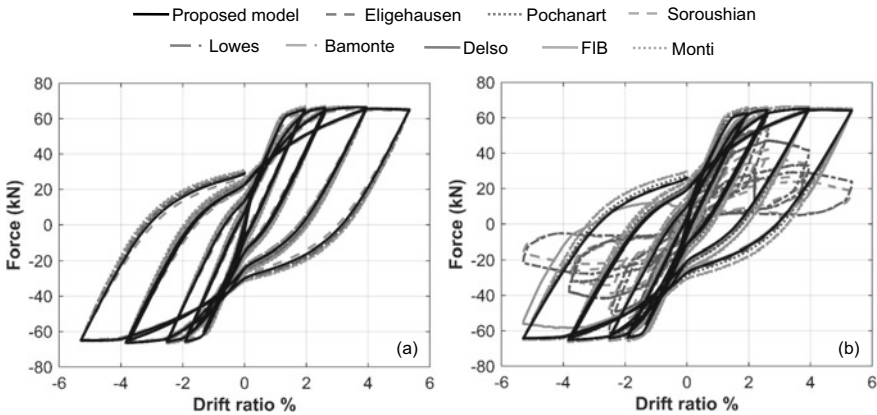
Fig. 7 Force-drift ratio hysteresis comparison between FE predictions with nine different sets of bond-slip properties for Bousias column assuming straight rebars with **a** sufficient and **b** insufficient anchorage lengths

To fulfill the objective of this section, Fig. 8a and b present the probability distribution function (PDF) of t_1 and t_3 for the Bousias column with the shaded gray area, respectively. The mean, mean $\pm$ standard deviation, and mean $\pm 2 \times$ standard deviation are also shown as references. In order to find the level of confidence of each model, the evaluated t_1 and t_3 based on different models are presented in this figure. It can be observed that the resulted values are highly scattered so that for some of them, the presented values lie in the upper and lower tales of the distribution with a small chance to occur. However, as shown in Fig. 6b, these, unlike properties, do not severely affect the global behavior of the column with hooked rebars, while
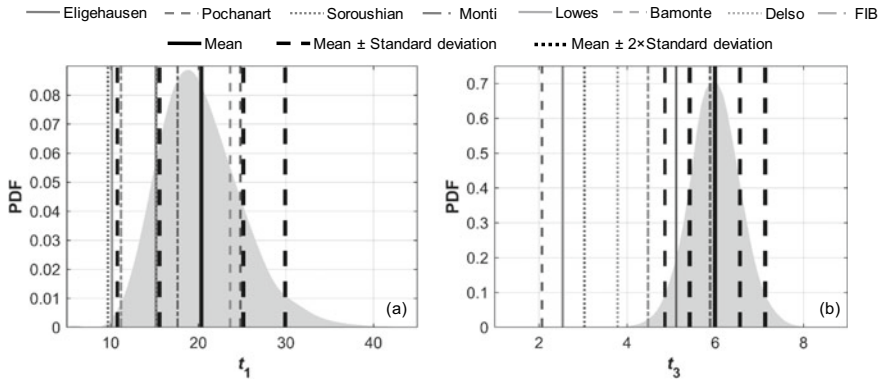
Fig. 8 PDFs for **a** t_1 and **b** t_3 in addition to values based on different models for Bousias column

this effect gets more significant in the case with unhooked rebars and insufficient anchorage length, as presented in Fig. 7. On the other hand, the bonding behavior under deterioration (e.g., corrosion) would be very different. For instance, for a 20% mass loss ratio, t_1 would be decreased by about 75%. In this case, the bonding property is significantly changed and as shown in [7], and it would affect the behavior of the RC columns with different anchorage conditions.

4 Conclusion

This paper addresses the imperfect bond-slip behavior between the reinforcing steel and the surrounding concrete in RC columns at both the material and component levels. While there are several bond-slip models in the literature, each of them was developed based on a dataset for a specific range of geometrical and material properties. As such, a bond-slip material model based on all these data with a large sample size is developed. Additionally, all the existing models are deterministic; i.e., the effect of model uncertainties is not taken into account. Therefore, this study puts forward developing a new set of probabilistic models for bond-slip properties, which allows the further investigation of the effect of model deviations/uncertainty in bond-slip on RC columns at the component level. The bond-slip models are used with a newly implemented fiber beam-column element. It is shown that the incorporation of bond-slip is needed when comparing the cases with imperfect bonding and the case with the perfect bonding. To summarize, the significant contributions of this study can be highlighted as follows: (1) using an inappropriate bonding property prediction model can result in an unrealistic simulation of RC column behavior (e.g., when the steel bars are unhooked in the bar ends), and (2) bonding property variations/ uncertainties have a significant impact on the hysteretic energy dissipation of RC columns with straight (unhooked) steel bars. As a result, it is essential to consider

the pertinent uncertainties of the bonding properties. More RC columns need to be further studied using the newly proposed model to confirm the effect of the modeling uncertainty in bond-slip on FE predictions when dynamic loading is applied.

References

1. Saatcioglu M, Alsiwat JM, Ozcebe G (1992) Hysteretic behavior of anchorage slip in RC members. J Struct Eng, ASCE 118(9):2439–2458
2. Sezen H, Setzler EJ (2008) Reinforcement slip in reinforced concrete columns. ACI Struct J 105(3):280–289
3. Braga F, Gigliotti R, Laterza M, D'Amato M, Kunnath S (2012) Modified steel bar model incorporating bond-slip for seismic assessment of concrete structures. J Struct Eng, ASCE 138(11):1342–1350
4. Monti G, Spacone E (2000) Reinforced concrete fiber beam element with bond-slip. J Struct Eng, ASCE 126(6):654–661
5. Spacone E, Limkatanyu S (2000) Responses of reinforced concrete members including bond-slip effects. ACI Struct J 97(6):831–839
6. Zhao J, Sritharan S (2007) Modeling of strain penetration effects in fiber-based analysis of reinforced concrete structures. ACI Struct J 104(2):133–141
7. Abtahi S, Li Y (2020) Nonlinear behavior of reinforced concrete structures considering bond-slip under corrosion. In: Proceedings of 17th world conference on earthquake engineering, Sendai, Japan
8. Mazzoni S, McKenna F, Scott MH, Fenves GL, Jeremic B (2006) Open system for earthquake engineering simulation, user command-language manual. Pacific Earthquake Engineering Research Center, Berkeley, California, USA
9. Bamonte PF, Gambarova PG (2007) High-bond bars in NSC and HPC: study on size effect and on the local bond stress-slip law. J Struct Eng ASCE 133(2):225–234
10. Eligehausen R, Popov E, Bertero V (1983) Local bond stress-slip relationships of deformed bars under generalized excitations. In: Earthquake engineering research center report. 82/33. University of California, Berkeley, USA
11. FIB (2013) Fib model code for concrete structures 2010. Ernst & Sohn, Berlin, Germany
12. Lowes LN, Moehle JP, Govindjee S (2004) Concrete-steel bond model for use in finite element modeling of reinforced concrete structures. ACI Struct J 101(4):501–511
13. Murcia-Delso J, Shing PB (2015) Bond-slip model for detailed finite-element analysis of reinforced concrete structures. J Struct Eng, ASCE 141(4):04014125
14. Pochanart S, Harmon T (1989) Bond-slip model for generalized excitations including fatigue. ACI Mater J 86(5):465–474
15. Soroushian P, Choi K (1989) Local bond of deformed bars with different diameters in confined concrete. ACI Struct J 86(2):217–222
16. Lundgren K (2000) Pull-out tests of steel-encased specimens subjected to reversed cyclic loading. Mater Struct 33(7):450–456
17. Box GEP, Tiao GC (2011) Bayesian inference in statistical analysis. Wiley, New York, USA
18. Bousias SN, Verzeletti G, Fardis MN, Gutierrez E (1995) Load-path effects in column biaxial bending with axial force. J Eng Mech, ASCE 121(5):596–605

Out-of-plane Unrestrained Thermal Curvatures in Reinforced Concrete Walls During Fire Exposure

M. Lazhari, M. A. Youssef, and S. F. El-Fitiany

Abstract Reinforced concrete (RC) walls support the vertical and lateral loads and act as impediments to prevent fire spread. Fire incidents affect the material properties and induce thermal and transient strains. This paper focusses on the unrestrained thermal curvatures of RC walls, which can affect their structural capacity and induce additional demands on other elements within the building. A comprehensive parametric study was conducted to evaluate the effects of different parameters on the value of the unrestrained thermal curvature, developed during fire exposure. Evaluated parameters are concrete compressive strength, wall cross section, steel ratio, and fire duration. For each of the evaluated cases, the temperature distribution within the wall section was first evaluated and then utilized to evaluate the unrestrained thermal curvature. The wall cross section was found to significantly influence the calculated curvature values. For example, increasing the wall thickness from 200 to 350 mm reduced the thermal curvature by about 52.0%.

Keywords Unrestrained thermal curvatures · Fire exposure · Reinforced concrete walls

1 Introduction

Concrete buildings have historically performed well during fire incidents, as compared to other building materials such as steel and wood. Fire incidents result in elevated temperatures that reduce the mechanical properties of concrete and steel. They also induce thermal and transient strains [1]. When RC walls are heated uniformly in the absence of mechanical loads, concrete exhibits an isotropic expansion usually known as a free thermal strain. However, when the wall structure is

M. Lazhari (✉) · M. A. Youssef · S. F. El-Fitiany
Department of Civil and Environmental Engineering, Western University, London, Canada
e-mail: mlazhari@uwo.ca

M. A. Youssef
e-mail: youssef@uwo.ca

Fig. 1 RC wall cross section
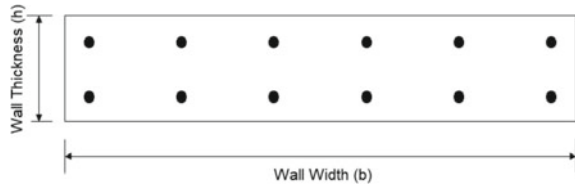
subjected to a transient temperature rise, the temperature distribution within the section becomes nonlinear. Appendix E of ACI 349 [2] provides a method to convert this nonlinear distribution to a linear distribution, which is composed of: (1) a uniform temperature change and (2) a thermal gradient. The unrestrained thermal deformations can then be calculated using this linear distribution [3]. El-Fitiany and Youssef [4] explained that this conversion is resulting from the development of self-induced strains in the concrete section to maintain the plane section concept. El-Fitiany and Youssef [4, 5] then presented a sectional analysis technique, which provided reasonable predictions of the behaviour of RC sections exposed to fire.

Previous studies addressing the unrestrained thermal strains in RC elements are limited. For RC beams exposed to ASTM-E119 fire, El-Fitiany and Youssef [6] conducted a parametric study to predict the unrestrained thermal strains and curvatures. For RC walls, such study does not exists. Thus, this paper aims at evaluating the effect of wall parameters including fire duration, concrete compressive strength, wall cross section, and steel ratio on the wall unrestrained thermal curvature.

2 Study Parameters

A comprehensive numerical study is conducted to examine the effect of fire on the unrestrained thermal curvature of RC walls. Figure 1 shows a typical cross section for the examined walls. Table 1 gives the geometric and mechanical properties of the 32 RC walls examined in this study. The studied parameters are fire duration (t = 0.5 to 2.0 h), concrete compressive strength (f'_c = 30 to 45 MPa), geometry of wall section (h = 0.20 to 0.35 m and b = 2.5 to 4.0 m), and reinforcement ratio (ρ = 0.25 to 2.50%).

3 Analysis Method

The RC walls are assumed to be exposed to a standard fire (ISO 834) on one side only. The temperature distribution within the wall section, Fig. 2a, is then evaluated using the finite difference method. The corresponding thermal strain is nonlinear, Fig. 2b. Self-induced strains, Fig. 2c, are developed in the wall section to maintain the plane section concept. The final equivalent linear thermal strain is shown in Fig. 2d and

Table 1 Geometrical and mechanical properties of considered RC walls

Member	t (hr)	f'_c (MPa)	h (m)	b (m)	ρ (%)
W1	0.5	30	0.2	2.5	0.25
W2					1
W3					2
W4					2.5
W5				3	0.25
W6				3.5	
W7				4	
W8			0.25	2.5	
W9			0.3		
W10			0.35		
W11	1		0.2		
W12	1.5				
W13	2				
W14			0.35	4	2.5
W15	0.5	35	0.2	2.5	0.25
W16	2		0.35	4	2.5
W17	0.5	40	0.2	2.5	0.25
W18	2		0.35	4	2.5
W19	0.5	45	0.2	2.5	0.25
W20			0.35	4	2.5
W21	1				
W22	1.5				
W23	2		0.2		
W24			0.25		
W25			0.3		
W26			0.35	2.5	
W27				3	
W28				3.5	
W29				4	0.25
W30					1
W31					2
W32					2.5
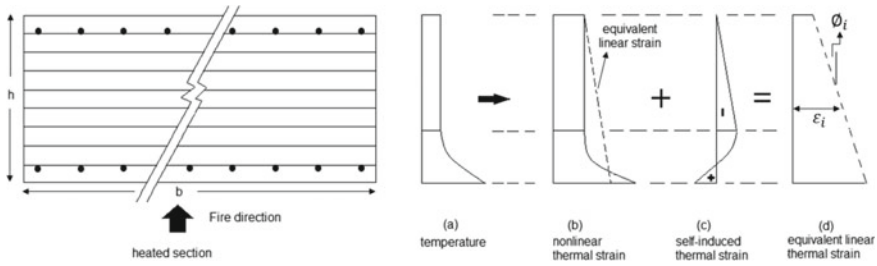
Fig. 2 Thermal strains in RC wall section exposed to fire

is characterized by a strain value at the centroid of the wall of ε_i and curvature $\varnothing_i$. The values of the self-induced thermal strains are calculated by trial and error, such that they are in self-equilibrium and result in a final linear strain distribution. The following sections discuss the effect of each of the considered parameters on the unrestrained thermal curvature $\varnothing_i$.

4 Effect of Fire Duration

The solid curve in Fig. 3 presents the average unrestrained thermal curvatures as a function of fire duration, considering walls W1, W11, W12, and W13, which utilize the minimum values for f_c' (30 MPa), h (0.20 m), b (2.50 m), and ρ (0.25%). On the other hand, the dotted curve provides the unrestrained thermal curvatures considering walls W20, W21, W22, and W3ch utilize the maximum values for f_c' (45 MPa), h (0.35 m), b (4 m), and ρ (2.5%). Clearly, the fire duration is a significant factor affecting the unrestrained thermal curvatures. As the fire duration increases, the temperature gradient through the cross section increases, which increases $\varnothing_i$.
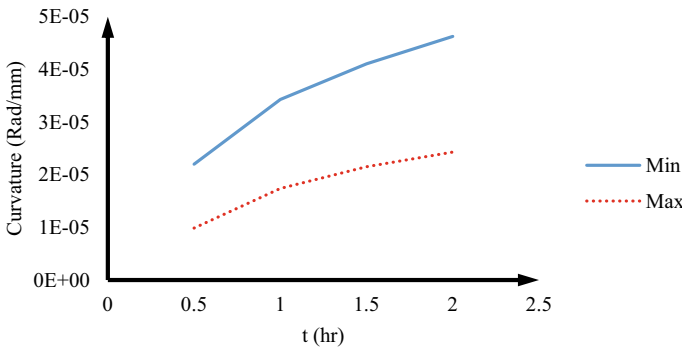
Fig. 3 Effect of the fire duration on $\varnothing_i$
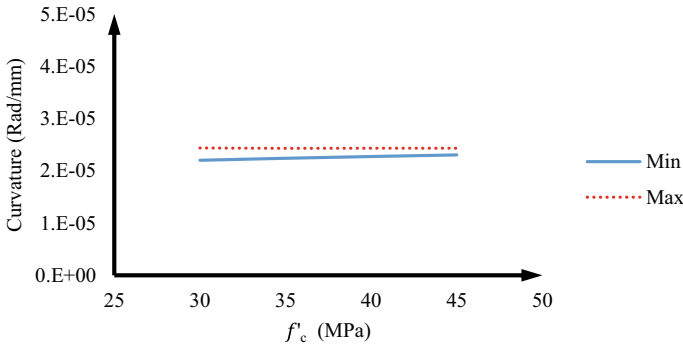
Fig. 4 Effect of the fire f_c' on $\emptyset_i$

5 Effect of Concrete Compressive Strength

The variation of $\emptyset_i$ with f_c' is shown in Fig. 4 considering the minimum values for t (0.5 h), h (0.2 m), b (2 m), and ρ (0.25%), which were used in W1, W15, W17, and W19, as well as the maximum values for t (2 h), h (0.35 m), b (4 m), and ρ (2.5%), which were used for walls W14, W16, W18, and W32. The unrestrained thermal curvature mainly occurs due to thermal strains; thus, the concrete compressive strength does not affect its value.

6 Effect of Wall Thickness

The solid curve in Fig. 5 presents the variation of the average unrestrained thermal curvatures with the wall thickness, considering walls W1, W8, W9, and W10, which utilize the minimum values for t (0.5 h), f_c' (30 MPa), b (2.5 m), and ρ (0.25%). The dotted curve displays the unrestrained thermal curvatures, considering walls W23, W24, W25, and W32 which utilize the maximum values for t (2 h), f_c' (45 MPa), b (4 m), and ρ (2.5%). Increasing the wall thickness from 20 to 350 mm resulted in about 52.0% reduction in unrestrained thermal curvature. This effect can be attributed to the fact that for thicker walls, the fire temperature is only affecting part of wall thickness; thus, the corresponding linear curvature becomes smaller.

7 Effect of Wall Width

The solid curve in Fig. 6 shows the variation of the unrestrained thermal curvature with the wall width, considering walls W1, W5, W6, and W7 which include the minimum values for t (0.5 h), f_c' (30 MPa), h (0.2 m), and ρ (0.25%). Additionally,
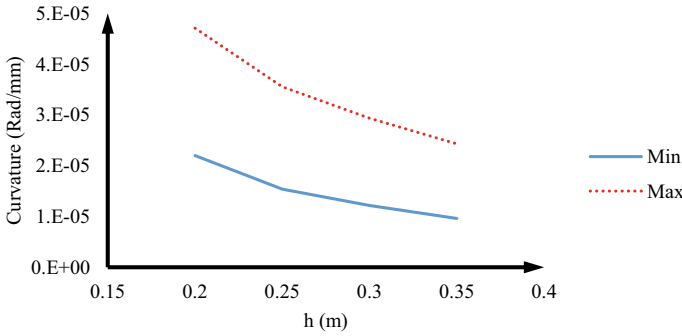
Fig. 5 Effect of the wall thickness on $\emptyset_i$
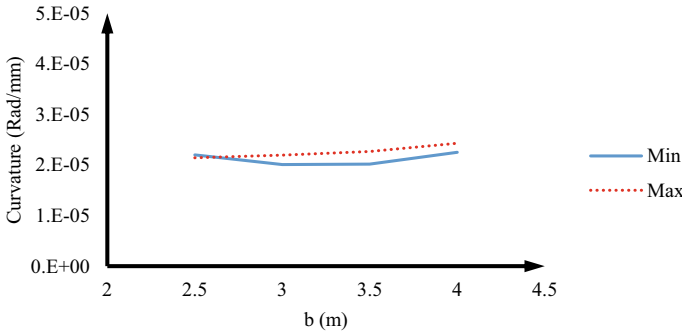
Fig. 6 Effect of the wall width on $\emptyset_i$

the dotted curve presents unrestrained thermal curvatures for W26, W27, W28, and W32 which were assigned the maximum values for t (2 h), f_c' (45 MPa), b (4 m), and ρ (2.5%). The wall width was found to have negligible effect, as the wall is heated uniformly along its width.

8 Effect of Steel Reinforcement

The solid curve in Fig. 7 presents the relationship between the unrestrained thermal curvatures and the steel ratio for W1, W2, W3, and W4, which used the minimum values for t (0.5 h), f_c' (30 MPa), h (0.2 m), and b (2.5 m). Furthermore, the dotted curve shows the unrestrained thermal curvature for W29, W30, W31, and W32 which utilized the maximum values for t (2 h), f_c' (45 MPa), h (0.35 m), and b (4 m). The steel reinforcement ratio was found to have a negligible effect on the wall unrestrained thermal curvatures, as the temperature distribution is controlled by the concrete thermal properties. However, increasing the steel reinforcement for thinner walls was
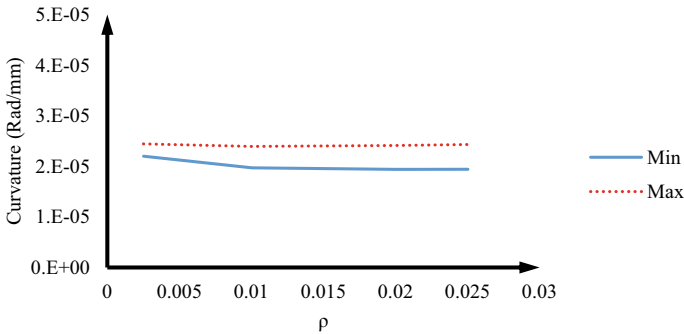
Fig. 7 Effect of the steel ratio on $\emptyset_i$

found to result in a 3 to 5% reduction in wall unrestrained thermal curvatures. This is attributed to the role that the steel bars play in the section equilibrium considering the self-induced strains.

9 Conclusions

Fire incidents result in thermal deformations, which can cause damage to reinforced concrete structures. This paper investigated the effect of the wall parameters: concrete compressive strength, cross section, steel ratio, and fire duration on the unrestrained thermal curvatures. The fire duration and the wall thickness were found to have significant effects on the thermal curvature. Results of the parametric study are being utilized to develop equations to estimate the initial thermal curvature during fire exposure. These equations will help engineers to achieve fire safety by utilizing the performance-based design instead of the traditional prescriptive fire design.

References

1. Lie TT (1992) Structural Fire protection. In: ASCE Manuals and reports on engineering practice, New York, NY, no 78, p 241
2. ACI 349 (2006) Code requirements for nuclear safety-related concrete structures and commentary (ACI 349–06). American Concrete Institute
3. Bae S (2012) Thermally induced uniform strains and curvatures calculated using equivalent linear temperature distributions. Nucl Eng Des 250:42–52
4. El-Fitiany S, Youssef MA (2009) Assessing the flexural and axial behaviour of reinforced concrete members at elevated temperatures using sectional analysis. J Fire Saf 44(5):691–703

5. El-Fitiany SF, Youssef MA (2014) Interaction diagrams for fire-exposed reinforced concrete sections. Eng Struct 70:246–259
6. El-Fitiany SF, Youssef MA (2013) Unrestrained thermal deformations of concrete elements exposed to fire. In: 3rd Specialty conference on disaster prevention and mitigation, Montreal, QC, Canada, DIS-043, p 10

Structural Analysis

Finite Element Study of the Bending and Compression Behavior of Modified Steel-Reinforced Elastomeric Isolators

Rose Noggle and Niel Van Engelen

Abstract One of the most popular technologies in seismic protection is base isolation—the separation of a structure from the ground with a flexible layer that increases the lateral period of the structure in the event of an earthquake. Steel-reinforced elastomeric isolators, one of the most popular bearings in base isolation practice, are often too heavy and costly to use in residential, commercial, and developing world projects. In this paper, the bending and compression behavior of infinite strip-shape bearings with steel removed from the center of each reinforcement layer is studied. The bending and compression moduli, and shear and normal stress distributions of each case were analyzed using finite element modeling. Under compression, the compression modulus decreased, maximum normal stress decreased, and maximum shear stress increased with increasing area removed. Under rotation, the bending modulus decreased, and normal and shear stresses normalized by the moment generally increase with increasing area removed. In every case, reducing the area of the reinforcement caused concentrations of stress under the remaining reinforcement that may require special consideration in bearing design.

Keywords Steel-reinforced elastomeric isolators · Finite element · Bending · Compression

1 Introduction

Base isolation decreases a structure's lateral stiffness at its base, artificially reducing its natural frequency, and thereby reducing the acceleration and inertial forces that could damage the structure during an earthquake [1]. Different types of base isolation systems, including elastomer bearings, friction pendulum and sliding bearings, and

R. Noggle
Worcester Polytechnic Institute, Worcester, MA, USA

N. Van Engelen (✉)
University of Windsor, Windsor, ON, Canada
e-mail: niel.vanengelen@uwindsor.ca

roller bearings, have all been implemented to reduce seismic demand on structures [2]. After base isolated buildings performed exceedingly well in previous earthquakes, application of base isolation technologies has expanded to more countries and cities, including those within the United States, Italy, China, and Japan [3, 4].

A key barrier to wider implementation of base isolation is the high initial cost of seismic bearings. The use of base isolation can dramatically reduce the life-cycle cost of a building due to its high performance in decreasing seismic loads to structures [5]. However, the initial cost of installing seismic isolators can increase the cost of new construction by around 1–5% [5, 6] and of a retrofit by 2–3% [7]. The high cost of base isolation systems is an impediment to implementation in projects where only initial costs are considered [6] or where increased costs are prohibitive.

One of the most popular base isolators is the steel-reinforced elastomeric isolator (SREI) [4]. Elastomeric bearings have a high vertical stiffness to support vertical loads from the structure and a low horizontal stiffness to allow large horizontal displacement under earthquake loading. The high vertical stiffness in SREIs is achieved by including horizontal rigid steel layers that restrict the lateral deformation of each elastomeric layer at the interface between the elastomer and the reinforcement [8]. Due to the incompressibility of the elastomer, the restriction of lateral bulging reduces the ability of the elastomer layers to deform vertically under vertical load, which increases the vertical stiffness.

Most previous research into changing the weight or properties of elastomeric bearings focuses on changing the materials used for reinforcement or elastomer, or on redesigning the shape of the reinforcement. This study addresses the gap in research on the modification of SREIs, as well as the issues of weight-related costs associated with SREIs. In this paper, the effects of reducing the area of steel reinforcement on bearing characteristics were studied with numerical simulations in Abaqus CAE [9].

2 Background

Part of the cost of SREIs comes from the manufacturing process. In this process, the steel reinforcement is cut to the shape of an individual bearing and is then sandblasted, treated with an acid cleaner, and coated with a bonding compound. The steel and elastomer layers are assembled in a mold and compressed under a set pressure and temperature to bond them together by vulcanization [10]. This process is labor-intensive [11] and is not translatable to large-batch production because the materials must be cut to the shape of an individual bearing before vulcanization [12]. These factors make the manufacturing process fairly expensive.

Another part of the cost of SREIs comes from their large weight. The majority of the weight of SREIs lies in their steel end plates and steel reinforcement layers [11]. Most SREIs contain two end plates of about 20 mm thickness and multiple steel reinforcement layers of 1–2 mm thickness. The weight of these bearings sometimes exceeds one tonne [11]. This large weight increases shipping, handling, and installation costs.

The high cost of SREIs has largely limited their use to buildings and structures of critical importance, like hospitals, and buildings containing highly sensitive technology [13]. Because of their high rate of success in minimizing seismic damage to structures that already have them in use, there is a demand for lower-cost seismic bearings for other applications. Such applications include residential buildings and historical buildings, as well as buildings in developing countries where fatalities from earthquakes are higher [2]. To meet this demand, efforts have been made by many researchers to reduce the cost of elastomeric bearings.

2.1   Efforts to Reduce the Cost of Elastomeric Bearings

The most well-researched method of reducing the cost of SREIs is replacing the steel reinforcement in the bearing with carbon fiber sheets, which reduces the weight of the bearing and the need for expensive manufacturing procedures [14]. Fiber-reinforced elastomeric isolators (FREIs) can be produced in large blocks and cut down to shape [15]. For these reasons, manufacturing costs of FREIs are expected to be greatly reduced from those of SREIs.

Many researchers have shown that FREIs offer the same levels of vertical stiffness as SREIs, with a notable increase in flexibility. Among them are [16], who used finite element analysis to study the behavior of unbonded FREIs, which are FREIs that are placed between the structure and foundation without bolting, eliminating the need for the large and heavy steel end plates used for this purpose in bonded FREIs and SREIs. The rollover deformation that unbonded FREIs experience reduces the tensile stresses in elastomeric layers, reducing risk for delamination [16].

Other researchers have made different material substitutions to reduce the manufacturing costs or weight-related costs of elastomeric bearings. For example, Calabrese et al. [11] replaced natural rubber with recycled rubber and steel reinforcement with fiber reinforcement, which reduced the top floor acceleration and acceleration amplification in the test structure compared with a fixed-base structure but increased inter-story drift. Han et al. [17] instead replaced the steel reinforcement with high strength steel mesh in high damping rubber bearings, which improved the shear and seismic isolation performance over that of traditional laminated rubber bearings. In both cases, costs were reduced through the use of less expensive or lighter materials.

2.2   Efforts to Improve Other Properties of Elastomeric Isolators

Researchers have also modified steel bearings in order to improve properties such as damping, stiffness, and performance in non-earthquake loading situations like wind.

To develop a seismic isolator that would provide better protection to structures during earthquakes, [18] used finite element modeling and physical testing to investigate the performance of a new design for an isolator. This design used a rubber core surrounded by steel rings, which slide over each other to create friction damping and increase the vertical stiffness of the bearing. Once the friction force is overcome, the rubber core is allowed to deform. The new system showed increased damping and decreased horizontal stiffness over the original lead core base isolator.

To reduce residual displacement and improve damping behavior, Dezfuli and Alam [19] used shape memory alloy (SMA) wires of varying materials and configurations in their design for rectangular carbon fiber-reinforced high damping rubber bearings (HDRBs). They found that including SMA wires on both tested configurations and materials improved the energy dissipation of both HDRBs and traditional elastomeric bearings, but did not reduce residual displacement. To reduce horizontal stiffness in FREIs, Osgooei et al. [13] studied the lateral responses of bearings with a circle removed from the interior, or semicircles from two opposing exterior edges, of the fiber layers using three-dimensional finite element models. They found that exterior modification resulted in increased peak principal stresses, where interior modification resulted in decreased peak principal stresses. In each case, improvements in bearing properties resulted from changes to the bearing assembly and materials.

3   Methods

To investigate the effects of reducing the steel area in the reinforcement layers on the characteristics of SREIs, five finite element models with varying amounts of steel removed were built in Abaqus CAE [9]. These models were modified from those used in [20] and in other investigations to reflect the use of steel reinforcements and the changes in geometry of the reinforcements [15, 21]. For validation of these models, including the convergence study, please see [20].

3.1   Finite Element Model

The steel reinforcement was defined in the unmodified model as an elastoplastic material with a modulus of elasticity of 200,000 MPa, a Poisson's ratio of 0.3, and a yield stress of 240 MPa, as in [22]. In the modified models, the two separate pieces of the steel reinforcement on each reinforcing layer shown in Fig. 1 are defined as one rigid body using a reference point on the interior edge of the left piece, so that the reinforcement remained in plane for each simulation. The elastomer layers were defined as a hyper elastic material using the Neo-Hookean model for strain energy potential, as in [20], because this model does not require experimental testing to determine material properties. A shear modulus of 0.8 MPa and a bulk modulus of 2000 MPa were used for the Neo-Hookean model. All parts of the bearing were
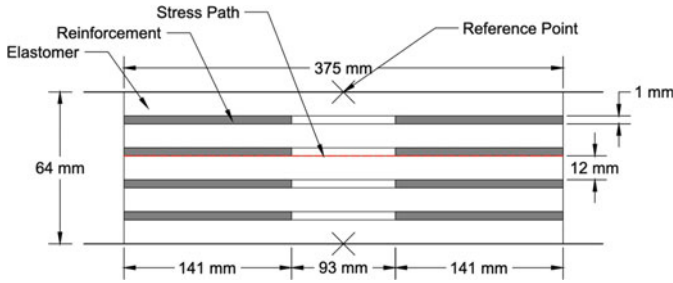
Fig. 1 Geometry of the infinite strip sections modeled—the 25% R model

modeled using four-node bilinear plane strain quadrilateral, hybrid, constant pressure (CPE4H) elements of 1 mm width and height.

The top and bottom connecting plates were modeled as rigid wires with reference points in the center. The bottom plate was constrained for all degrees of freedom, while the motion of the top plate was only constrained laterally. For the compression model, a vertical load was applied to the top plate reference point in the downward direction and was ramped up to 1875 kN (5 MPa). For the bending model, a rotation of 0.01 radian was applied as boundary condition to the top plate. The elastomer layers were tied (bonded) to the connecting plates and the reinforcing layers at all contact points.

3.2 Parametric Study

The infinite strip bearing models each had five elastomer layers with 12 mm thickness and steel reinforcement with 1 mm thickness, for a total bearing height of 64 mm and a total elastomer thickness of 60 mm; the shape factor, defined as the ratio of the loaded area to unloaded area of a single layer of elastomer, was 15.6. The shape factor is a representation of the restraint provided by the reinforcement on the lateral bulging of the elastomeric layers. The bearings were modeled in two dimensions as a section taken across the width of the infinite strip pad, which was 375 mm wide. Five models were made, including one with full reinforcement (unmodified), with decreasing area of steel in the reinforcing layers. The steel area was removed from the center of each layer as shown in Fig. 1, in increments of 25, 50, 75, and 90% of the width. Each model was named for the percentage of steel removed, such that the model with 25% of the reinforcement removed was labeled "25% R". The dimensions of the reinforcement in each model are described in Table 1. Stress distributions were taken along the path shown in red in Fig. 1.

Table 1 Description of reinforcements in each model

Model Name	Width of steel section removed (mm)	Total width of steel section remaining (mm)	Area removed from reinforcement (%)
0% R	0	375	0
25% R	93	282	25
50% R	187	188	50
75% R	281	94	75
90% R	337	38	90

4 Results

The compression modulus of each model was calculated from the applied force and resultant vertical displacement values taken at each step of the compression load ramp, and the bending modulus from the applied rotation and resultant moment at each step of the rotation ramp. The displacements were sampled at the reference point at the top plate in each finite element model. The slopes of the resulting curves were used in combination with Eq. (1) for compression and Eq. (2) for bending to calculate the compression and bending modulus, respectively.

$$F = E_c A \big/ t_r \cdot x \tag{1}$$

$$M = E_b I \big/ t_r \cdot \theta \tag{2}$$

where F represents applied vertical force, E_c is the compression modulus, A is the plan area of the bearing, t_r is the total thickness of all the elastomer layers in the bearing, x is the vertical displacement, M is the reaction moment, E_b is the bending modulus, I is the second moment of area of the top face of the bearing, and θ is the applied angle of rotation.

4.1 Force–displacement, Moment-rotation, and Respective Elastic Moduli

The compression modulus was calculated for each model using the slope of the force–displacement line shown in Fig. 2a using Eq. (1). Figure 2b shows that the compression modulus of the bearing decreases as the steel area removed increases, save for the 25% R model which has a higher compression modulus than the 0% R model by a 1.2% difference. It is unclear why this is the case. The compression moduli for the 0% R to 90% R models are 533, 539, 506, 398, and 258 MPa, respectively. The degree of reduction in the compression modulus generally increases with the

area removed, with a 69.3% difference between 0% R and 90% R. The compression modulus increases by 0.257 MPa per percent removed from 0% R to 25% R, then decreases by 1.33 MPa per percent removed from 25% R to 50% R, 4.31 MPa per percent removed from 50% R to 75% R, and 9.30 MPa per percent removed from 75% R to 90% R.

The bending modulus was calculated for each model using the slope of the moment-rotation line shown in Fig. 3a using Eq. (2). Figure 3b shows that the bending modulus decreases with increasing area removed from the reinforcement, with a 175% difference between 0% R and 90% R. The bending moduli for the 0% R to 90% R models are 142, 102, 51, 17, and 9 MPa, respectively. The downward trend increases from 1.59 MPa per percent removed between 0%R and 25% R to 2.04 MPa per percent removed between 25% R and 50% R. The trend then diverges to a more gradual slope of 1.37 MPa per percent removed from 50% R to 75% R and 0.50 MPa per percent removed from 75% R to 90% R.
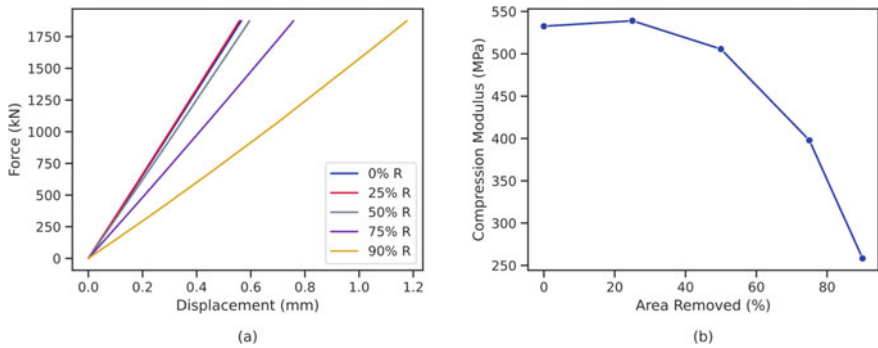
Fig. 2 a Force–displacement relationship and **b** Compression modulus for each model
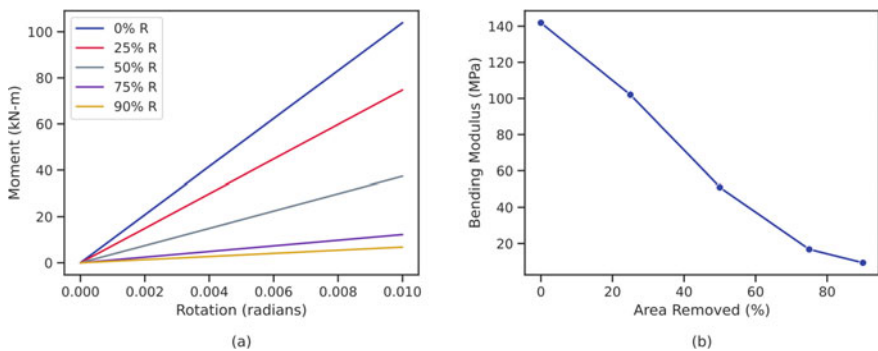
Fig. 3 a Moment–rotation relationship and **b** Bending modulus for each model

4.2   Stress Distributions

4.2.1   Normal Stress Distributions

Normal stresses for each node along the path through the top edge of the middle elastomer layer, marked in Fig. 1, were recorded for each model for the compression and bending analyses at the maximum load for compression and maximum rotation for bending. As shown in Fig. 4, the maximum normal stress decreases as the amount of area removed increases in both the compression and bending cases. In each loading case, the section where the reinforcement has been removed experiences nearly constant normal stress. In the compression case, this section experiences the maximum normal stress.

In the compression case, the maximum normal stress decreases from the 0% R model to the 90% R model: 7.30, 7.05, 6.45, 5.77, and 5.45 MPa, respectively, due to the reduction in the restraint on the elastomeric layers provided by the reinforcement. Both Figs. 4 and 5 show the area of maximum vertical normal stress increasing as the area removed increases. For the compression loading case, the normal stresses in the three principal directions are within -1.43%, as assumed for traditional reinforced bearings based on the pressure solution.

In the bending case, the maximum normal stress decreases with the bending modulus, as the moment required to achieve 0.01 radians rotation decreases. Normalized with maximum bending moment to control for the change in load, the maximum normal stress increases from 0.040 MPa/N•mm in the 0% R model to 0.043 MPa/N•mm in the 25% R model, 0.050 MPa/N•mm in the 50% R model, and 0.056 MPa/N•mm in the 50% R model. It then drops back down to 0.033 MPa/N•mm in the 90% R model. For bending case models 0% R through 90% R, the three principal stresses are within 6.4%, as assumed for traditional bearings.
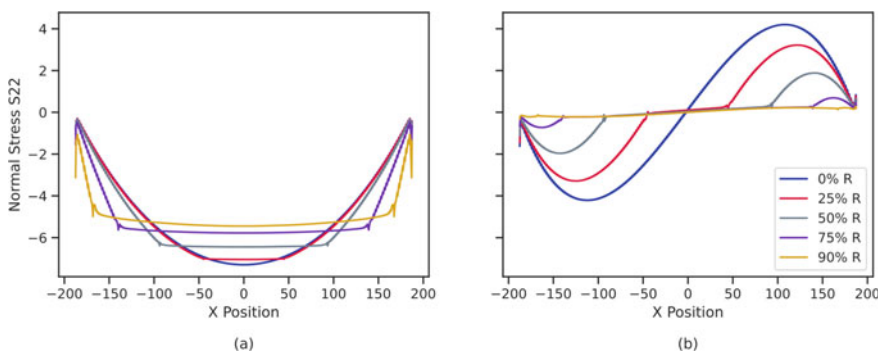
Fig. 4   Normal stress distributions for the **a** Compression and **b** Bending cases of each model (MPa)
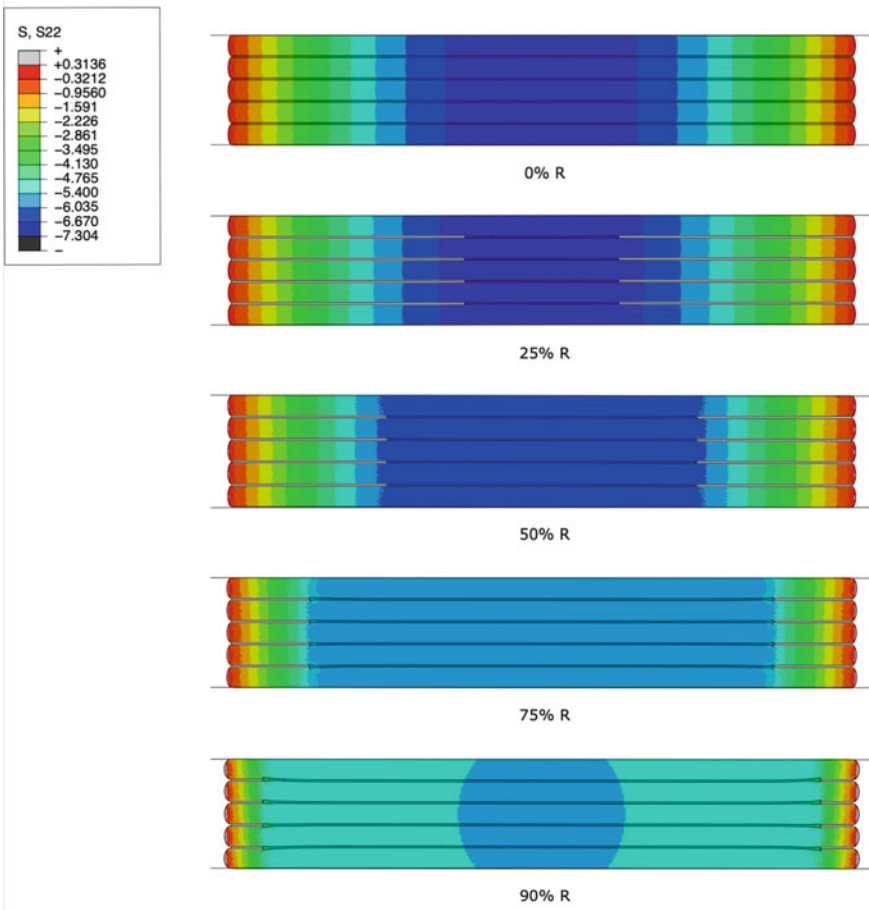
Fig. 5 Normal stress contours for the compression case of each model (MPa)

4.2.2 Shear Stress Distributions

Shear stresses for each node along the path through the top edge of the middle elastomer layer, marked in Fig. 1, were also recorded for the compression and bending analyses for each model. Similar to the normal stresses, the shear stress holds nearly constant at 0.0 MPa for the region of elastomer directly below the section where reinforcement was removed. However, for the compression load cases, the maximum shear stress increases with increasing area removed, starting from 0.445 MPa in the 0% R model, and increasing to 0.448 MPa in the 25% R model, 0.483 MPa in the 50% R model, 0.661 MPa in the 75% R model, and 1.17 MPa in the 90% R model, as shown in Fig. 6. Figure 7 shows the contours of shear stress in the bending cases of three models, and Fig. 8 shows the shear stress contours in the compression cases.

As the area removed increases, the shear stresses are concentrated around the areas of the remaining reinforcement.

In the bending load case, maximum shear stress decreases with increasing area removed as the moment to achieve 0.01 radians rotation decreases. Normalized with maximum bending moment to compensate for the changing load, the maximum shear stress increases from 0.004 MPa/N•mm in the 0% R model to 0.005 MPa/N•mm in the 25% R model, 0.008 MPa/N•mm in the 50% R model, and 0.014 MPa/N•mm in the 75% R model, and then decreases to 0.008 MPa/N•mm in the 90% R model.
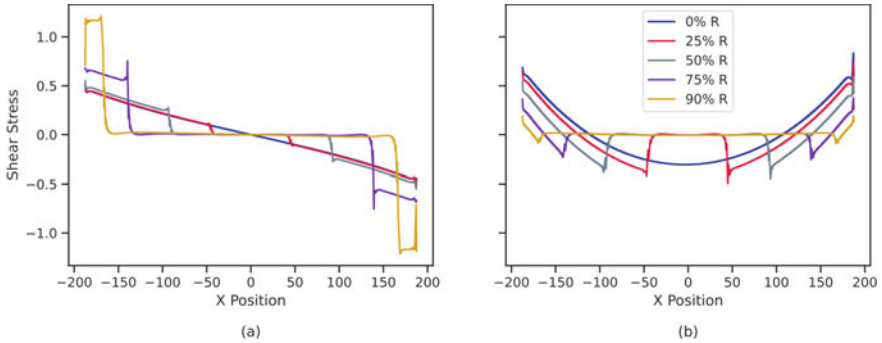
Fig. 6 Shear stress distributions for the **a** Compression and **b** Bending cases of each model (MPa)
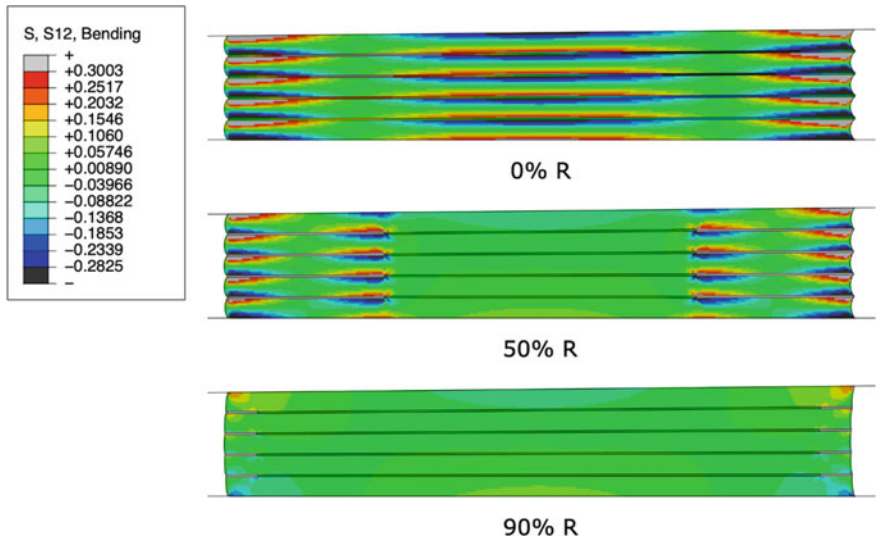
Fig. 7 Shear stress contours for the bending cases of the 0% R, 50% R, and 90% R models (MPa)
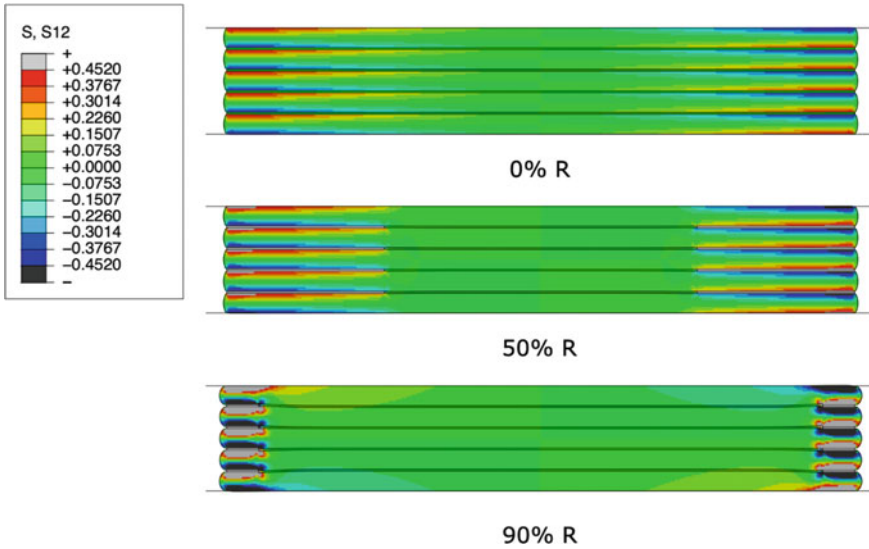
Fig. 8 Shear stress contours for the compression cases of the 0% R, 50% R, and 90% R models (MPa)

5   Conclusions

Reducing the quantity of steel used in SREIs would reduce bearing weight, which could help reduce the costs associated with their use. This would make their inclusion in residential, commercial, and developing-world projects more feasible. Finite element modeling with Abaqus CAE (2020) was used to investigate the compression and bending behaviors of infinite strip-shape SREIs with varying amounts of steel removed from the center of the reinforcement layers. The following trends in bending modulus, compression modulus, normal stress distribution, and shear stress distribution are presented in this paper:

(1)   In the compression cases, compression modulus decreased, the maximum normal stress decreased, and maximum shear stress increased with increasing area removed.
(2)   In the bending cases, bending modulus decreased, and normal and shear stresses normalized with maximum moment generally increase with increasing area removed.
(3)   In every case, reducing the area of the reinforcement caused concentrations of stress around the remaining reinforcement that may require special consideration in bearing design.

Additional work is needed to investigate the same trends in different geometries, and to validate the results of this paper.

References

1. Kelly JM (1986) Aseismic base isolation: review and bibliography. Soil Dyn Earthq Eng 5(4):202–216
2. Matsagar VA, Jangid RS (2008) Base isolation for seismic retrofitting of structures. Pract Period Struct Des Constr 13(4):175–185
3. Clemente P (2017) Seismic isolation: past, present, and the importance of SHM for the future. J Civ Struct Heal Monit 7:217–231
4. Pan P, Ye L, Shi W, Cao H (2012) Engineering practice of seismic isolation and energy dissipation structures in China. SCIENCE CHINA Technol Sci 5(11):3036–3046
5. Dang Y, Han JP, Li YT (2015) Analysis of the seismic performance of isolated buildings according to life-cycle cost. Comput Intell Neurosci 2015:495042–495047
6. Mayes RL, Jones LR, Buckle IG (1990) Impediments to the implementation of seismic isolation. Earthq Spectra 6(2):283–296
7. Kelly JM, Konstantinidis DA (2011) Mechanics of rubber bearings for seismic and vibration isolation. Wiley, Chichester, West Sussex, United Kingdom
8. Angeli P, Russo G, Paschini A (2013) Carbon fiber-reinforced rectangular isolators with compressible elastomer: analytical solution for compression and bending. Int J Solids Struct 50(22–23):3519–3527
9. Simula (2020) Abaqus CAE, Dassault Systemes, PC
10. Pauletta M, Pinzano F, Frappa G, Russo G (2020) Tensile tests for the improvement of adhesion between rubber and steel layers in elastomeric isolators. Appl Sci 10(22):8063–8080
11. Calabrese A, Spizzuoco M, Serino G, Della Corte G, Maddaloni G (2015) Shaking table investigation of a novel, low-cost, base isolation technology using recycled rubber. Struct Control Health Monit 22(1):107–122
12. de Raaf MGP, Tait MJ, Toopchi-Nezhad H (2014) Stability of fiber-reinforced elastomeric bearings in an unbonded application. J Compos Mater 45(18):1873–1884
13. Osgooei PM, Van Engelen NC, Konstantinidis D, Tait MJ (2015) Experimental and finite element study on the lateral response of modified rectangular fiber-reinforced elastomeric isolators (MR-FREIs). Eng Struct 85:293–303
14. Moon BY, Kang GJ, Kang BS, Kim GS, Kelly JM (2003) Mechanical properties of seismic isolation system with fiber-reinforced bearing of strip type. Int Appl Mech 39(10):1231–1239
15. Al-Anany YM, Tait MJ (2015) A numerical study on the compressive and rotational behavior of fiber reinforced elastomeric isolators (FREI). Compos Struct 133:1249–1266
16. Toopchi-Nezhad H, Tait MJ, Drysdale RG (2011) Bonded versus unbonded strip fiber reinforced elastomeric isolators: finite element analysis. Compos Struct 93(2):850–859
17. Han L, Tian S, Dang X, Yuan W, Wei K (2016) Performance of steel mesh reinforced elastomeric isolation bearing: experimental study. Constr Build Mater 121:60–68
18. Talaeitaba SB, Pourmasoud MM, Jabbari M (2018) An innovative base isolator with steel rings and a rubber core. Asian J Civ Eng 20:313–325
19. Dezfuli FH, Alam MS (2013) Multi-criteria optimization and seismic performance assessment of carbon FRP-based elastomeric isolator. Eng Struct 49:525–540
20. Bai J (2020) Lift-off behaviour of fiber-reinforced elastomeric bearings. University of Windsor, PhD diss
21. Konstantinidis D, Kelly JM, Makris N (2008) Experimental investigation on the seismic response of bridge bearings. University of California, Earthquake Engineering Research Center

22. Saedniya M, Talaeitaba SB (2019) Numerical modeling of elastomeric seismic isolators for determining force–displacement curve from cyclic loading. Int J Adv Struct Eng 11(3):361–376

A Review of Structural Behavior and Composite Action Between the Steel Beams and Concrete Slabs

P. Panjehbashi Aghdam, S. Parent, and N. Roy

Abstract The steel–concrete composite construction is known as one of the fast, economical, and eco-friendly methods due to its advantages in terms of saving in weight of steel and concrete. Composite constructions are extensively used in multi-story buildings and medium-span bridge decks. The longitudinal shear transfer between the steel beam and reinforced concrete slab is achieved through various mechanical devices called shear connectors. The mechanical properties of the shear connector, including the strength and stiffness, play a vital role in the composite action of the steel–concrete beam. The stud-type connectors are widely used in composite construction and are subjected to flexural and axial forces when resisting the interface forces by means of dowel action. In a composite slab, the degree of shear connection, the shear strength, and the stiffness of an individual stud can be determined experimentally by conducting push-out tests. Previous studies have conducted flexural tests to investigate the composite interaction in steel–concrete composite beam elements. This paper reviews different types of push-out and flexural tests proposed in the literature to evaluate the characteristics of composite slabs. The paper also provides different approaches to investigate the interaction of composite elements. This research contributes to the field by providing a comprehensive discussion of the advantages and challenges of the experimental methods to perform the push-out and flexural tests and how these two types of tests can cooperatively promote the understanding of the behavior of composite slabs.

Keywords Composite steel–concrete beams · Composite construction · Composite interaction · Shear connector · Flexural behavior · Push-out test · Shear stud

P. P. Aghdam · S. Parent · N. Roy (✉)
Université de Sherbrooke, Sherbrooke, Longueuil, QC, Canada
e-mail: Nathalie.Roy@USherbrooke.ca

1 Introduction

Advancement of material properties and construction technologies, as well as human challenges to the height and span of structures, led to creative innovations in the construction industry, such as composite steel–concrete systems. This is formed by connecting concrete slabs to the supporting steel members in the composite beam/floor system, enhancing its structural performance. Many previous studies have investigated the behavior and design of steel–concrete composite members [1, 2]. Compared with conventional reinforced concrete beams, steel–concrete composite beams have significant bending resistance and stiffness advantages. This is achieved mainly by fully utilizing the steel's material strength, such as high strength, ductility, and ease of erection, and reinforced concrete, such as high rigidity and low cost. The efficiency of a composite beam lies in restraining the slip between the steel beam and concrete slab and enabling shear force transfer between them to ensure the composite action through mechanical action, friction, and adhesion [3]. Mechanical action is provided by different shear connectors that guarantee the transfer of shear forces at the interface between the steel beam and the concrete slab, which are directly related to the bearing capacity of the whole composite beam [4, 5]. If the shear connectors are rigid, the full composite action or the full interaction is achieved [6, 7]. The degree of shear connection and the degree of composite interaction are the two terms used to describe the behavior of shear connectors in a steel–concrete composite beam. The degree of shear connection refers to the equilibrium of forces in a composite beam at the ultimate limit state (ULS). In contrast, the degree of interaction refers to the compatibility of displacements and, more specifically, the shape of the strain profile through the depth of a given section [8]. The degree of shear connection, η, is provided in Eq. (1) and is defined as the ratio of the ultimate shear strength of the interface in a shear span, F_i, to the minimum strength necessary for the section to develop its full flexural capacity at the end of the shear span, F_f.

$$\eta = \frac{F_i}{F_f} \tag{1}$$

This connection can be full, partial, or there can be no connection at all. Figure 1a shows the longitudinal equilibrium of forces at the ULS for a full shear connection (η = 1), partial shear connection ($0 < \eta < 1$), and no shear connection ($\eta = 0$). In design codes, the shear strength of the interface is calculated using the ultimate strength of all shear connectors in the shear span, neglecting friction and bond. It should be noted that the degree of shear connection is independent of the load at any given time. As a result, a beam or girder can be described as having a constant degree of shear connection [9]. Although the degree of shear connection can be defined straightforwardly, the degree of composite interaction, φ, is difficult to define without using differential calculus and complex compatibility equations. Newmark et al. [10] formulated the linear elastic partial-interaction theory, which was later extended, and a simplified equation (Eq. (2)) was proposed [8] based on the ratio of the neutral axis
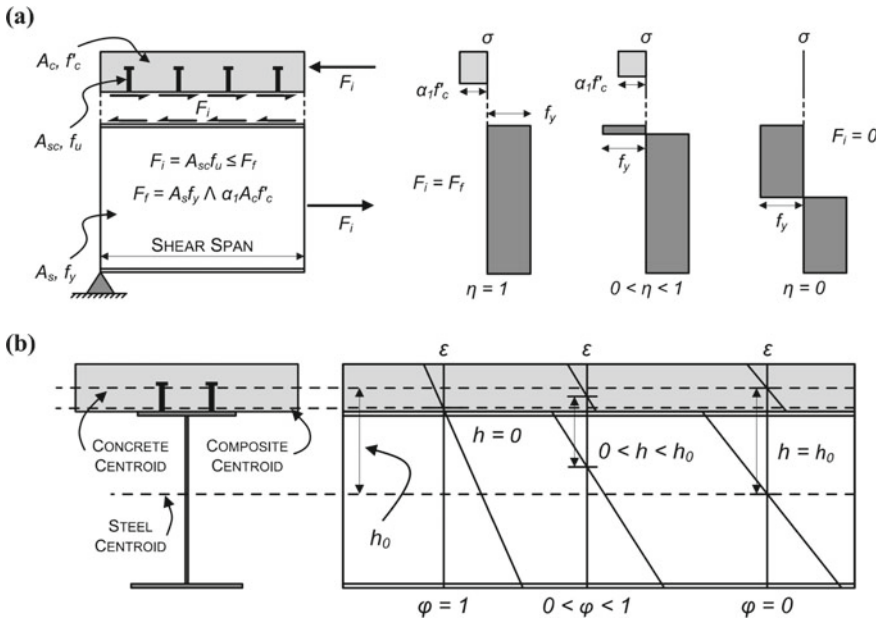
Fig. 1 Degree of **a** Shear connection; **b** Composite action [9]

separation, h, to the maximum neutral axis separation, $h_\circ$.

$$\varphi = 1 - \frac{h}{h_\circ} \tag{2}$$

This maximum neutral axis separation is the distance between the steel and concrete neutral axis in case of non-composite behavior. Figure 1b schematically shows strain profiles in full ($\varphi = 1$), partial ($0 < \varphi < 1$), and no interaction ($\varphi = 0$) cases. Unlike the degree of shear connection, the degree of composite interaction changes with loading history, over the beam's length, and the beam's life.

It is possible to perform both flexural beam tests or push-out tests to establish a stud shear connector's load-slip behavior, nominal shear strength, and stiffness. These tests are characterized by several shear connectors embedded in a small section of the concrete slab and attached to a steel section. The schematic view of a typical push-out and flexural test for a composite beam is shown in Fig. 2a, b. The steel section or the concrete slab is loaded during testing while the other element is held in position. In Fig. 3, the strain profile is shown in the steel and concrete section of the composite beam in flexural and push-out tests. In this figure, the deformed shapes are also illustrated.

Instead of expensive full-scale beam tests, push-out tests are preferred, and specifications such as AISC [11] and Eurocode 4 [12] provide empirical equations based on push test results to calculate the stud shear resistance. The shear stud strength in
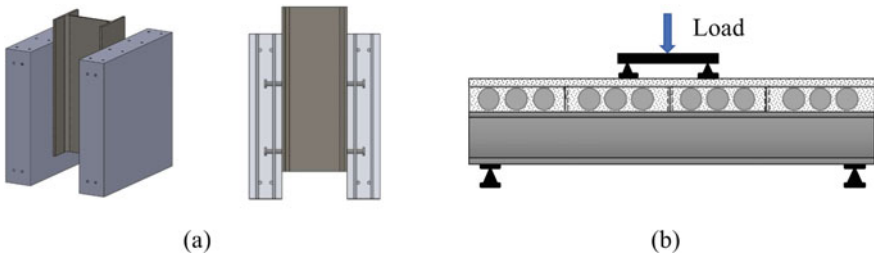
Fig. 2 Typical experimental test of composite beam: **a** Push-out test; **b** Four-node flexural test
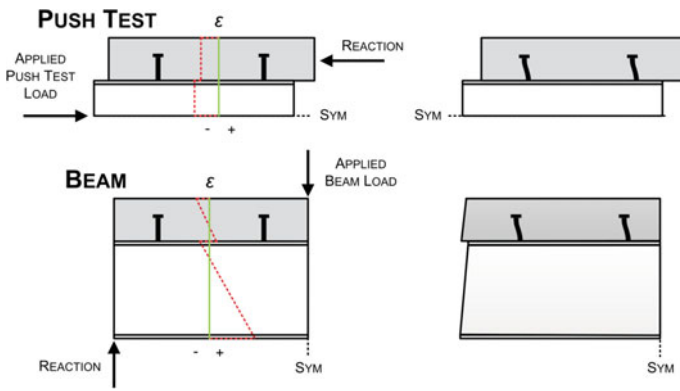
Fig. 3 Strain profiles and deformed shape in: **a** Push-out test; **b** Flexural test [9]

solid reinforced slabs was first determined by [13] and presented in terms of empirical formulas such as Eq. (3) by performing 48 push-out tests.

$$Q_u = 0.5 A_s \sqrt{f_c' E_c} \leq A_s F_{ut} \tag{3}$$

where Q_u is the normal shear stud strength embedded in a solid concrete slab, A_s is the effective cross-sectional area of a stud anchor (mm^2), f_c' is the cylinder compressive strength of concrete (MPa), E_c is the modulus of elasticity of concrete (MPa) and F_{ut} is the ultimate tensile strength of the steel stud (MPa). In a typical push-out test, the cast in situ or precast concrete slabs are attached to the flanges of a steel beam using pre-welded shear studs. The concrete slabs are symmetrically placed at both sides of a steel beam to simulate the actual loading condition and are restrained for any lateral movements during the test procedure. The loading process can be monolithic or cyclic, applied in a displacement or force-controlled mode. In general, failures observed in push-out tests can be categorized into five different modes: (1) stud shearing; (2) concrete pull-out; (3) rib shearing; (4) splitting, and (5) rib punching.

In a composite beam flexural test, the shear studs are welded to the flange of the steel beam, which is set on a bearing plate and roller assembly that restrain the vertical movement and allow rotation at each end. Then, the cast-in-place or precast concrete slabs are placed on the steel beam, and the load is applied through hydraulic pistons to load distribution elements. The loading process can be cyclic or monolithic, with specific increments until a specified midspan displacement or a sudden loss in load-carrying capacity is observed [14]. However, in a composite beam test, the connectors are loaded indirectly from the flexural forces within the beam. The force on a connector is not directly proportional to the load applied to the beam but depends on the stiffness of various components of the composite beam.

Therefore, the main difference between the push-out and beam tests is how the shear forces arise. In the beam test, the externally applied load causes a strain gradient with a discontinuity at the interface (also called "slip strain"). Connectors are subjected to shear force to resist slip accumulation due to the strain discontinuity on the length of the beam. In a push-out test, however, connectors resist shear force because they are part of the load path between the applied load and the balancing reaction at the base of the specimen. The drawback of the load-slip curve obtained from the push-out test is that it does not give a quantitative indication of the composite action that may result from the presence of a connector in a beam. In other words, in a push-out test, the shear forces on individual connectors remain constant relative to one another throughout the test. In contrast, in a beam test, when one shear stud begins to fail and crack, the other neighboring shear studs begin to compensate for the increased shear force, and as a result, the force redistribution is featured. Since the induction of composite action is the primary function of a shear connector, the push-out test fails to evaluate connectors on this basis.

Consequently, to quantify the flexural capacity of the composite steel beam with concrete slab, it is essential to perform both push-out and composite beam tests with complete information on the degree of shear connection and degree of composite interaction. The primary purpose of the current paper is to review different types of push-out and flexural tests proposed in the literature to evaluate the characteristics of composite slabs. The paper also provides different approaches for investigating the interaction of composite elements. This research contributes to the field by providing a comprehensive discussion of the advantages and challenges of the experimental methods to perform the push-out and flexural tests and how these two types of tests can cooperatively promote the understanding of the behavior of composite beams.

2 Literature Review

This section provides an overview of the literature about the previous studies investigating the composite action between the steel beam and concrete slab in composite steel beams. The first subsection of this review investigates the different push-out tests conducted to determine the shear strength of the shear connectors. The second

subsection will highlight recent research on the composite action between the steel beam and the concrete slabs.

2.1 Determining the Shear Strength of Shear Connectors

Shear stud connectors are the essential components of steel–concrete composite structures that transfer the longitudinal shear force at the interface between the steel and concrete [15]. The push-out tests are the preferred method to establish the load-slip behavior, nominal shear strength, and stiffness of a stud shear connector. In the push-out tests, the strain distribution can be measured more easily because the shear connectors are part of the load path between the applied load and balancing reactions at the base of the specimen. Nevertheless, despite the popularity of push-out tests to establish the static and fatigue capacity of shear connectors, the test method and the layout of the specimen have been discussed for several decades. The common challenges and factors investigated by recent studies conducting push-out tests include: (1) the eccentricity between the load and the supports [16], (2) the support conditions; (3) the absence of normal compressive force at the steel–concrete interface; (4) the width and height of the slab, and (5) the number of shear connector rows. Modified push-out tests have been proposed recently to determine the shear strength and stiffness of stud shear connectors under combined shear and tension forces. Generally, the modified push-out test follows the established standard push-out test recommended in EN 1994–1–1 [17], except the concrete-steel interface is inclined to an angle of about 15° from the vertical [18].

Previous experimental, numerical, and theoretical studies indicate that the shear resistance of a stud shear connection in a composite steel–concrete beam depends on the following factors: (1) compressive and tensile strength of the concrete, as well as the elastic modulus; (2) tensile strength of stud shear connectors as well as their shapes and sizes; (3) welding quality of shear studs and dimensions of welding collars at stud roots; (4) arrangements of the shear stud connectors; and (5) sizes and arrangement of steel reinforcement in the vicinity of the shear stud [19, 20].

Different types of shear connectors have been used in composite structures. However, headed studs' popularity stems because they can be installed easily through the cellular steel deck using a welding gun [21]. The behavior of a headed stud shear connector depends on the stud details and the concrete environment, such as concrete properties and reinforcement detailing. Under cyclic loading, the fatigue failure of headed studs is the primary failure mode and should be considered in structural design [22, 23]. Studies have shown that the stud geometry, shear stress range, concrete material properties, stud welding process, and fatigue test methods affect the fatigue performance of the shear connectors [24–27]. Based on these studies, design codes on composite structures have specified fatigue strength curves of headed stud connectors based on nominal shear stress [28]. Wang et al. [29] conducted a total of 96 push-out tests and investigated the interface shear force-slip curves and the failure modes of shear stud groups (SSGs) (Fig. 4). Their results revealed that the
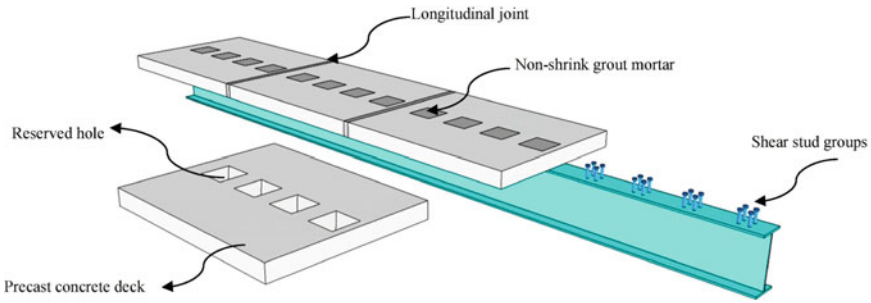
Fig. 4 Shear stud groups on PC composite beam [21]

shear behavior of the SSGs in square reserved holes is more favorable than that in circular reserved holes. They concluded that the shear strength of SSGs in precast (PC) decks is smaller than that in cast-in-place (CIP) decks under monotonic loads, whereas the shear strength of SSGs in PC decks is similar to that in CIP decks under repetitive loads.

Yu-Liang et al. [30] performed nine push-out tests to investigate the mechanical behavior of grouped stud shear connectors embedded in hybrid fiber-reinforced concrete (HFRC), considering the spacing and number of studs. They developed a refined 3D finite element (FE) model of the HFRC incorporating the constitutive model in the ANSYS software. Based on the test and the FE analysis results, an equation was proposed considering the contribution of the steel and polypropylene fiber to estimate the capacity of a single stud. Bonilla et al. [31] developed an accurate nonlinear FE model to study the behavior of headed stud shear connectors welded to the deck in composite beams with profiled steel sheeting. The nonlinear material of the concrete was modeled with damaged plasticity available in ABAQUS software [32]. The FE analyses and the experimental push-out test results were compared with the codified shear resistance of the shear studs calculated using AISC-LRFD [33] and Eurocode 4 [12]. The comparison of the results revealed that the codified shear resistance of stud connectors might not necessarily be conservative.

Sun et al. [34] conducted a series of push-out tests to study the monotonic and cyclic behavior of headed steel stud anchors in composite beams with profiled steel decks by considering profile type, steel deck direction, and load conditions. The results indicated that both monotonic and cyclic responses are affected by the shape of the profile. Tong et al. [35] investigated the shear performance of stud connectors in high-strength steel-UHPC composite beam specimens under static loads considering the diameter and layout of studs. Experimental results indicated that the failure modes of all specimens were stud shank failure, where the diameter of the studs significantly affected their shear performance. Wang et al. [29] investigated the static behavior of large stud shear connectors in steel-UHPC composite structures through 18 push-out specimens. The investigated parameters in their study were the stud diameter, stud aspect ratio, concrete strength, and concrete slab thickness. They resulted that the shear strength, stiffness, and ductility of a stud with a 30 mm diameter

were approximately 15, 45, and 60% higher than those of a stud with a 22 mm diameter, respectively. Also, the stud aspect ratio and concrete slab thickness showed no apparent influence on the static behavior of the test specimens.

Finally, they proposed an empirical equation considering stud diameter to predict the load-slip curve of headed studs as:

$$\frac{P}{P_u} = \frac{S/d_{stud}}{0.006 + 1.02S/d_{stud}} \tag{4}$$

where P is the shear load of stud, S is slip, and, P_u is the maximum shear load.

Souza et al. [36] analyzed the degree of shear connection between hollow core slabs and headed studs connected to the web of the steel beam by performing push-out tests. They found that when the concrete compressive strength is increased, the stress concentration occurs at the base of the stud. Shen and Chung [18] investigated the structural behavior of stud shear connections under combined shear and tension forces. They carried out two series of push-out tests. In the first series, eleven standard push-out tests were performed where the shear connectors only underwent the shear forces. However, in the second series of tests, shear connectors' behavior was studied using modified push-out tests under combined shear and tension forces. The results revealed that when the tension force T_n is smaller than or equal to $0.267*Q_m$, where Q_m is the standard shear resistance, the shear resistance of the shear connection should be reduced with a factor of 0.84 and 0.75.

Lowe et al. [37] performed 15 push-out tests to determine the longitudinal splitting characteristics of a concrete slab in a steel–concrete composite beam with headed shear stud connectors under cyclic and monotonic loads. It was concluded that the transverse compression forces across the base of the studs would increase the capacity of the beam against longitudinal splitting. Zhang et al. [38] conducted an experimental study including six push-out and eight flexural composite beam tests to investigate the transverse reinforcement ratio on the degree of shear connection. They proposed an equation for calculating the longitudinal shear resistance of steel–concrete composite beams with longitudinal double-row studs. Etim et al. [39] performed experimental push-out tests on composite slabs comprising normal and pultruded fiber-reinforced polymer (PFRP) concrete. In the first phase of the test, the effects of the headed shear stud configuration on the load-carrying capacity of the composite slabs were studied. The second phase focused on characterizing the behavior of the composite slab by varying the shear stud diameter. The test results revealed that the dominant failure modes were the FRP plates' bearing, net tension, and shear-out failures. These results differed from those prevalent in the conventional steel–concrete composite, either stud shank failure or concrete pull out.

Ahmed and Tsavdaridis [40] performed a series of push-out tests to study the shear resistance and behavior of the connection systems designed for a prefabricated ultra-shallow flooring system consisting of a T-ribbed lightweight concrete floor and C-channel steel edge beam. The studied connection system was either web-welded shear studs only or combined with horizontally lying steel dowels. Prakash
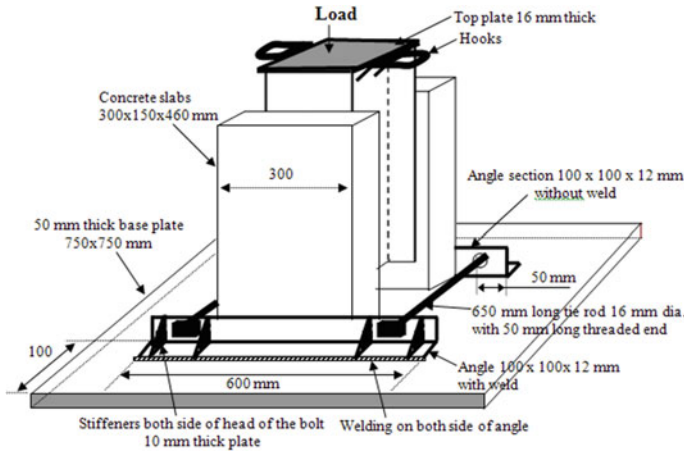
Fig. 5 Schematic illustration of the setup for the modified push-out test [41]

et al. [41] conducted modified push-out tests to determine high-strength steel studs' shear strength and stiffness. The configuration of their test setup is schematically illustrated in Fig. 5. Their experimental study indicated that concrete confinement in the vicinity of the high-strength shear stud connector could significantly enhance concrete's compressive strength and splitting resistance.

Yanez et al. [42] presented a modified push-out test on a joist-type profile to capture the stiffness coefficient when the stud anchor is placed on the weak or strong side relative to the steel deck stiffener. Four different stiffness coefficients were calculated in their experimental study to characterize the overall beam deflection when full-interaction, slip, and shear deformation is considered. They concluded that studs placed on the solid side of the stiffener give better performance when compared with the weak stud position, enhancing deflection values by 5% on average. Table 1 summarizes the previous experimental and numerical studies investigating the load-slip behavior, nominal shear strength, and stiffness of a stud shear connector in steel–concrete composite construction using push-out tests.

2.2 Investigating the Flexural Response of Composite Systems by Bending Tests

The flexural performance and composite action of composite steel beams with concrete slabs have been investigated in previous studies [44–48]. The preferred method for quantifying the composite action between the composite steel beam and the concrete slab is through the bending test, in which shear connectors resist the accumulation of the slip and the externally applied load results in a strain slip with a

Table 1 Summary of the previous push-out tests

Ref	Description of the specimens	Number of tests	Purpose of study	Results
[38]	Composite steel beams connected to the precast (PC) and cast-in-place (CIP) concrete decks with shear stud groups (SSGs)	96	Experimentally investigate the interface shear force-slip curves and the failure modes of the SSGs	The shear behavior of the SSGs in square reserved holes is more favorable than in circular reserved holes. The shear strength of SSGs in PC decks is smaller than that in CIP decks under monotonic loads
[30]	Composite steel beams with SSGs embedded in hybrid fiber reinforced concrete (HFRC)	9	Experimentally and numerically investigate the mechanical behavior of grouped stud shear connectors embedded in HFRC	An equation considering the contribution of steel fiber (SF) and polypropylene fiber (PF) to estimate the capacity of a single stud for grouped stud-HFRC shear connectors was proposed
[35]	Composite steel beams with ultra-high-strength precast concrete (UHPC) slabs	6	Experimentally investigate the shear performance of stud connectors in steel-UHPC composite beam	Failure modes of all the high-strength steel-UHPC push-out specimens were stud shank failure, the diameter of the studs significantly affected their shear performance
[38]	Composite steel beams connected to ultra-high-performance concrete (UHPC) slabs with 22 and 30 mm shear studs	18	Experimentally investigate the static behavior of large stud shear connectors in steel-UHPC composite structures	The shear strength, stiffness, and ductility of a stud with a 30 mm diameter are approximately 15, 45, and 60% higher than a 22 mm diameter

(continued)

Table 1 (continued)

Ref	Description of the specimens	Number of tests	Purpose of study	Results
[36]	Composite steel beams connected to the PCHC slabs by headed shear studs on the web of steel beam	3	Experimentally and numerically analyze the composite action between PCHC slabs and headed studs connected to the web of the steel beam	The concrete compressive strength influences the ultimate capacity and stud forces, as the concrete compressive strength increases, the stress concentration occurs at the base of the stud
[18]	Composite steel beams with solid concrete and composite slabs	11	Experimentally investigate the structural behavior of stud shear connections under combined shear and tension forces with both composite and solid slabs	Provided that the tension force T_n is smaller than or equal to 0.267 of the shear resistance of the shear stud, the shear resistance of the shear stud should be reduced with a factor of 0.84 and 0.75 for the cases of a solid concrete slab and a composite slab, respectively
[43]	Composite steel beams with concrete slabs	6	Investigate the parameters as transverse reinforcement ratio and shear connection degree	Proposed a formula to calculate the longitudinal shear resistance of steel–concrete composite beams with longitudinal double-row studs
[39]	Composite steel beams with slabs comprising of normal density concrete, and pultruded fiber reinforced polymer (PFRP)	6	Experimentally investigate the effects of headed shear stud configuration on the load capacity of the composite slabs, and characterize the behavior of the composite slab by varying the headed stud diameter	Dominant failure modes in the mentioned specimens were the FRP plates' bearing, net tension, and shear-out failures

(continued)

Table 1 (continued)

Ref	Description of the specimens	Number of tests	Purpose of study	Results
[40]	Prefabricated ultra-shallow flooring system (PUSS) consisting of a T-ribbed lightweight concrete floor and C-channel steel edge beam	8	Experimentally study the shear resistance and behavior of the connection system comprised of the web-welded shear studs only or combined with horizontally lying steel dowels	The compressive strength of the concrete significantly influences the ultimate shear strength capacity loads and the failure mode of the connection
[41]	Composite steel beam connected to reinforced concrete slabs with shear studs	4	Experimentally determine the shear strength and stiffness of high-strength steel (HSS) studs	The confinement of the concrete in the vicinity of the HSS stud connector significantly enhances the compressive strength and splitting resistance of concrete, which must be considered while designing concrete slabs for push-out specimens
[42]	Composite steel joists (CSJ)	24	Experimentally predict the linear behavior of the shear connector embedded in a concrete slab with a steel sheet profile considering the stud diameter variation	Deflection is better predicted in partial connection studs on the stiffener's strong side perform better than the weak stud position while enhancing deflection values by 5% on average

discontinuity at the interface. Consequently, bending tests provide a quantitative indication of the composite action that results from the presence of connectors in a beam. Recently, [49] conducted a four-point bending test to investigate the flexural performance of large-scale composite beams composed of a precast UHPC (ultra-high performance concrete) slab connected to the steel girder by large-headed stud clusters embedded with shear pockets. Based on the test results, they proposed a formulation according to a simplified plasticity theory considering the tensile strength of UHPC for predicting the ultimate flexural capacity of the steel-UHPC composite beams. Dar et al. [50] conducted an experimental study on full-scale supported cold-formed steel (CFS) concrete composite beams under four-point monotonic loading to investigate the flexural strength and the degree of shear interaction. They also assessed the performance of various shear connectors in strength, stiffness, and ductility. Baran [51] performed flexural tests and numerical simulations on concrete hollow core panels (PCHC) to understand the effect of concrete topping over the surface of precast concrete hollow core on the flexural response (Fig. 6). Their results demonstrated that significant composite action is developed between the hollow core unit and the topping slab under load levels corresponding to the uncracked state of the cross section. Also, the existence of topping concrete resulted in improvements in the cracking moment and initial stiffness of hollow-core units. Ibrahim et al. [52] investigated the shear-flexural capacity of composite slabs using PCHC units and concrete topping. Their test intended to obtain vertical shear failure considering the effects of surface conditions. Their specimens were subjected to a static three-point bending test on a simple span with roller supports at both ends. The vertical deflection, interface (horizontal) slip and vertical slip (or interface dilation) were measured using potentiometers. Their results revealed that the surface roughness and moisture condition of the PCHC units affect the performance and behavior of composite slabs and the ultimate shear capacity between the PCHC units and the concrete topping.

Zhang et al. [38] performed a three-point bending test on steel-UHPC composite beams with stud and bolt connectors, as shown in Fig. 7. Their results showed that steel-UHPC composite beams exhibited excellent cracking and flexural performance under the hogging moment. Compared with the steel-normal strength concrete
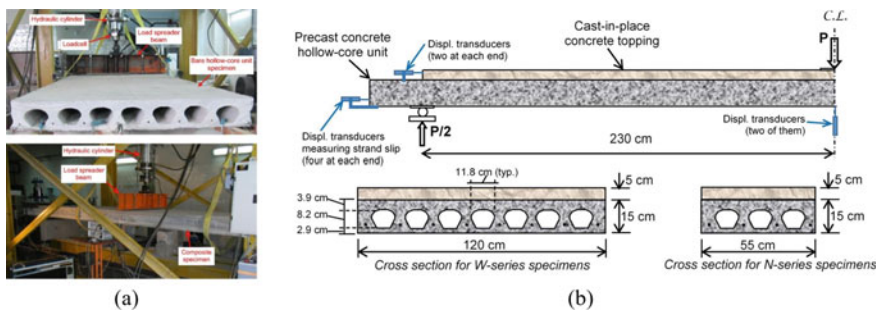
Fig. 6 Specimen cross section, instrumentation, and loading setup details adopted by [51]: **a** On-site photos; **b** Schematic sketch

composite beam, the cracking load and ultimate flexural capacity of steel-UHPC composite beams were increased by around 340 and 26%, respectively. Also, verified by test results, theoretical formulas were proposed in their study to calculate the slip moment, the moment at a crack width of 0.05 mm, and the ultimate moment of the steel-UHPC composite beams under the hogging moment.

As shown in Fig. 8, they calculated the position of the plastic axis of the composite section according to the axial force equilibrium. They predicted the ultimate slip moment (M_{su}) as follows:

$$N_{cr} + N_{rt} + N_{st} + N_{wt} = N_{wc} + N_{sb} \tag{5}$$

$$x = \frac{f_{cr}b_eh_u + f_{ry}A_{rt} + f_{sy}(A_{st} + h_wt_wA_{sb})}{2f_{sy}t_w} + t_2 \tag{6}$$

$$M_{su} = f_{ry}A_{rt}y_1 + f_{cr}b_eh_uy_2 + f_{sy}(A_{st}y_3 + A_{wt}y_4 + A_{wc}y_5 + A_{sb}y_6) \tag{7}$$

where the resultant forces of concrete stress block are N_{cr}, forces of steel reinforcement is N_{rt} , forces of the top flange plate is N_{st}, forces of web in tension is N_{wt}, forces of the web in compression is N_{wc}, and forces of the bottom flange plate of the
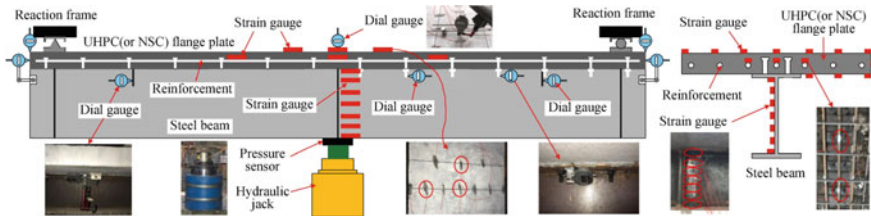
Fig. 7 Flexural test setup and measurements [38]
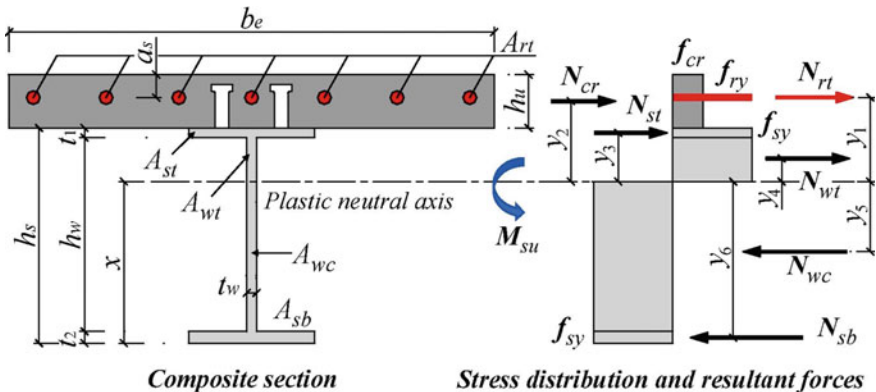
Fig. 8 Analytical model of SU-S under hogging moment at the ultimate state [38]

steel beam is N_{sb}. Also, f_{cr} is the cracking strength of UHPC, and f_{ry} and f_{sy} are the yield strengths of steel reinforcement and steel beam, respectively. As denoted in Fig. 8, A_{rt} is the reinforcement area in tension, A_{st} is the flange area of the steel beam in tension, A_{wt} is the web area of the steel beam in tension, A_{wc} is the web area of the steel beam in compression, and A_{sb} is the flange area of the steel beam in compression.

Qi et al. [53] studied the flexural behavior of steel-ultra high-performance fiber-reinforced concrete (UHPFRC) composite beams by conducting bending tests and an analytical program. They performed four-point bending tests on two large-scale beams, one made of normal-strength concrete (NC) slab and another consisting of a UHPFRC slab. The results showed that using the UHPFRC slab increased the stiffness and improved the crack control capacity of the composite beam. Bandelt et al. [14] conducted an experimental study on the full-scale and component specimens to investigate the flexural response of a girder-slab © composite system. The system combines steel beams, precast hollow core slabs, steel reinforcement, and composite floor assembly for residential and commercial construction applications (Fig. 10). Furthermore, they compared the experimental results with the predicted flexural strength of the system based on two analytical methods: (1) a strain compatibility analysis using principles of displacement-curvature behavior and (2) a simplified plastic composite section analysis. Their results showed that both methods could accurately predict the full-scale specimen's experimental strength but over-predicted the component specimen strength due to the boundary conditions.

Table 2 summarizes previous experimental and numerical studies investigating the composite action between the composite steel beam and concrete slabs using bending tests.
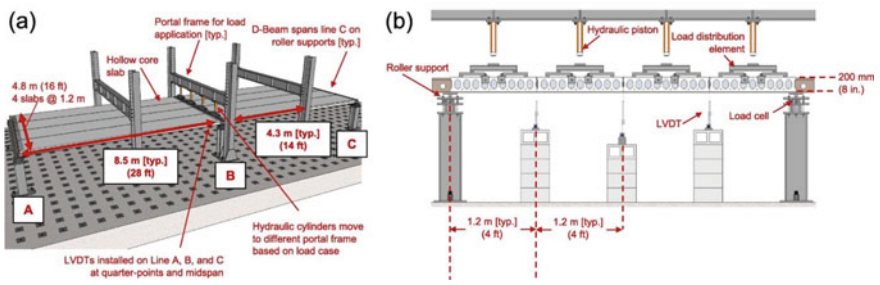
Fig. 9 a Overview of the full-scale composite experimental setup, b Elevation of the composite component specimen [14]

Table 2 Summary of the previous bending tests

Ref	Description of the specimens	Number of tests	Purpose of study	Results
[49]	Composite steel beams connected to the ultra-high-performance concrete (UHPC) slabs by large-headed stud clusters	2	Investigate the flexural performance of composite steel beams with UHPC slabs performing four-point bending tests	A formulation according to a simplified plasticity theory considering the tensile strength of UHPC to predict the ultimate flexural capacity of the steel-UHPC composite beams
[50]	Simply supported cold-formed steel (CFS) concrete composite slab	7	Investigate the flexural strength and the degree of shear interaction of CFS concrete composite slabs performing four-point bending tests	CFS concrete composite slabs structurally perform better than conventional reinforced concrete (RC) slabs
[51]	Precast hollow core concrete (PCHC) slabs	5	Demonstrate the effect of concrete topping placed over the as-cast surface of PCHC units in improving the flexural response	Significant composite action is valid between the PCHC unit and the topping slab under load levels corresponding to the uncracked state of the cross section. Topping concrete improves the cracking moment and initial stiffness of PCHC
[52]	Precast hollow core concrete (PCHC) slabs	2	Investigate the shear-flexure capacity of composite slabs using PCHC units and concrete topping, performing a three-point bending test	The surface roughness and moisture condition of the PCHC units affect the performance and behavior of composite slabs and the ultimate shear capacity between the PCHC units and the concrete topping
[38]	Steel-UHPC composite beams with stud connectors (SU-S) and bolt connectors (SU-B)	5	Investigate the crack resistance, ultimate flexural capacity, failure modes, and of SU-S and SU-B under negative bending moment at the supports	Compared with the steel-normal strength concrete composite beam, the cracking load and ultimate flexural capacity of steel-UHPC composite beams increase by around 340 and 26%, respectively

(continued)

Table 2 (continued)

Ref	Description of the specimens	Number of tests	Purpose of study	Results
[53]	Composite steel beams with ultra-high-performance fiber-reinforced concrete (UHPFRC) slabs	2	Study the flexural behavior of steel-UHPFRC composite beams by performing four-point bending tests	UHPFRC slabs increase the stiffness and improve the crack control capacity of the steel-UHPFRC composite beam
[14]	Composite steel beams with reinforced precast hollow core slabs	1	Investigate the flexural response of a girder-slab © composite system that combines steel beams, precast hollow core slabs, steel reinforcement, and composite floor assembly	Two analytical methods: (1) a strain compatibility analysis using principles of movement-curvature behavior and (2) a simplified plastic composite section analysis, accurately predicting the flexural strength compared with the experimental results

3   Summary and Discussion

The findings of this paper can be summarized below:

- The main difference between the push-out and beam tests is how the shear forces arise. In a push-out test, connectors resist shear force as a part of the load path between the applied load and the balancing reaction at the base of the specimen. The shear forces on individual connectors remain constant relative to one another throughout the test. The drawback of the load-slip curve obtained from the push-out test is that it does not give a quantitative indication of the composite action that may result from the presence of a connector in a beam. In the beam tests, however, connectors are subjected to shear force to resist the slip accumulation due to the strain discontinuity on the length of the beam. When one shear stud begins to fail and crack, the other neighboring studs start to compensate for the increased shear force, and as a result, the force redistribution is featured. In other words, in the push-out test, the degree of shear connection is measured, referring to the equilibrium of forces in a composite beam at the ultimate limit state. It is independent of the loading condition, while the degree of composite interaction refers to the compatibility of displacements and changes with the loading conditions. Typically, performing the flexural tests is costly and requires a relatively complex setup in which controlling the boundary conditions is difficult. On the contrary, push-out tests are easy to perform, requiring the least instrumentation to capture and interpret the results. Consequently, many code provisions interchangeably use the degree of shear connection and composite action for defining design procedures.
- To better understand the behavior of the composite beams, performing both the push-out and flexural beam tests is recommended. The push-out tests establish the load-slip behavior, nominal shear strength, and stiffness of stud shear connectors in composite beams. The beam tests quantify the flexural capacity of the composite beams.
- At the University of Sherbrooke, 11 standard push-out tests and two full-scale flexural tests have been conducted on composite steel beams with precast concrete hollow core (PCHC) slabs. Verified numerical finite element models will follow the research to modify the design equations of clause 17-composite beams, trusses, and joists of the S16-19 [54] design of steel structures for PCHC applications. As a result, the appropriate configuration of the shear studs and the degree of composite action between the PCHC slab and the steel beam connected via cast in situ cover concrete would be quantified. Finally, a new design methodology will be proposed which considers the composite action between the composite steel beams and PCHC slabs.

References

1. Behnam A, Denavit MD (2020) Plastic stress distribution method for predicting interaction strength of steel-concrete composite cross sections. J Constr Steel Res 170:106092. https://doi.org/10.1016/j.jcsr.2020.106092

2. Lai B, Liew JYR (2020) Axial-moment interaction of high strength concrete encased steel composite columns: design recommendation. J Constr Steel Res 170:106136. https://doi.org/10.1016/j.jcsr.2020.106136

3. Hou H et al (2016) Experimental evaluation of flexural behavior of composite beams with cast-in-place concrete slabs on precast prestressed concrete decks. Eng Struct 126:405–416. https://doi.org/10.1016/j.engstruct.2016.07.065

4. Deng W et al (2019) Static and fatigue behavior of shear connectors for a steel-concrete composite girder. J Constr Steel Res 159:134–146. https://doi.org/10.1016/j.jcsr.2019.04.031

5. Zhang Q et al (2018) Internal force transfer effect-based fatigue damage evaluation for PBL shear connector groups. J Constr Steel Res 148:469–478. https://doi.org/10.1016/j.jcsr.2018.06.016

6. Kalibhat MG, Upadhyay A (2020) Numerical study on the deformation behavior of steel concrete composite girders considering partial shear interaction. Structures 23:437–446. https://doi.org/10.1016/j.istruc.2019.10.007

7. Suwaed ASH, Karavasilis TL (2020) Demountable steel-concrete composite beam with full-interaction and low degree of shear connection. J Constr Steel Res 171:106152. https://doi.org/10.1016/j.jcsr.2020.106152

8. Oehlers DJ, Seracino R (2002) A tiered approach to the fatigue assessment of composite steel and concrete bridge beams. Proc Inst Civ Eng Struct Build 1523:249–257

9. Sjaarda M (2018) The fatigue behavior of welded and bolted shear connectors in composite highway bridges

10. Newmark NM, Siess CP, Viest IM (1951) Tests and analysis of composite beams with incomplete interaction. Proc Soc Exp Stress Anal 9(1):75–92

11. American Institute of Steel Construction (2016) Specification for structural steel buildings, ANSI/AISC 360–16. American Institute of Steel Construction, p 676

12. CEN E (2004) Eurocode 4: Design of composite steel and concrete structures. Part 1–1: general rules for buildings. Brussels, Belgium

13. Ollgaard JG, Slutter RG, Fisher JW (1971) Shear strength of stud connectors in lightweight and normal weight concrete. Eng J Amer Inst Steel Constr 8(2):55–64

14. Bandelt MJ et al (2019) Flexural behavior of a composite steel and precast concrete open web dissymmetric framing system. Eng Struct 198(June):109456. https://doi.org/10.1016/j.engstruct.2019.109456

15. Xu X, Zhou X, Liu Y (2020) Behavior of rubber-sleeved stud shear connectors under fatigue loading. Const Build Mater 244:118386. https://doi.org/10.1016/j.conbuildmat.2020.118386

16. Hällmark R, Collin P, Hicks SJ (2019) Post-installed shear connectors: push-out tests of coiled spring pins vs. headed studs. J Constr Steel Res 161:1–16. https://doi.org/10.1016/j.jcsr.2019.06.009

17. BS EN 1994–1–1 (2004) Eurocode 4: design of composite steel and concrete structures. Part 1.1: general rules for buildings

18. Shen MH, Chung KF (2017) Experimental investigation into stud shear connections under combined shear and tension forces. J Constr Steel Res 133:434–447. https://doi.org/10.1016/j.jcsr.2017.02.021

19. Katwal U et al (2020) Load sharing mechanism between shear studs and profiled steel sheeting in push tests. J Constr Steel Res 174:106279. https://doi.org/10.1016/j.jcsr.2020.106279

20. Shen M-h et al (2020) Structural behaviour of stud shear connections in composite floors with various connector arrangements and profiled deck configurations. Eng Struct 210(February):110370. https://doi.org/10.1016/j.engstruct.2020.110370

21. Wang YH et al (2019) Shear behavior of shear stud groups in precast concrete decks. Eng Struct 187(February):73–84. https://doi.org/10.1016/j.engstruct.2019.02.002

22. El-Zohairy A, Salim H, Saucier A (2019) Fatigue tests on steel-concrete composite beams subjected to sagging moments. J Struct Eng, United States 145(5):1–11. https://doi.org/10.1061/(ASCE)ST.1943-541X.0002326

23. Sjaarda M et al (2017) Fatigue behavior of welded shear studs in precast composite beams. J Bridg Eng 22(11):1–11. https://doi.org/10.1061/(ASCE)BE.1943-5592.0001134

24. Higashiyama H et al (2014) Fatigue of headed studs welded with improved ferrules under rotating shear force. J Constr Steel Res 92:211–218. https://doi.org/10.1016/j.jcsr.2013.09.012

25. Qi Y et al (2017) Shear force demand on headed stud for the design of composite steel plate shear wall. Eng Struct 148:780–792. https://doi.org/10.1016/j.engstruct.2017.07.023

26. Xu C, Sugiura K, Su Q (2018) Fatigue behavior of the group stud shear connectors in steel-concrete composite bridges. J Bridg Eng 23(8):1–13. https://doi.org/10.1061/(ASCE)BE.1943-5592.0001261

27. Liu Y et al (2019) Static and fatigue push-out tests of short headed shear studs embedded in Engineered Cementitious Composites (ECC). Eng Struct 182:29–38. https://doi.org/10.1016/j.engstruct.2018.12.068

28. American Association of State Highway and Transportation Officials (2017) LRFD bridge design specifications, 7th edn. AASHTO, Washington, DC

29. Wang J et al (2019) Static behavior of large stud shear connectors in steel-UHPC composite structures. Eng Struct 178:534–542. https://doi.org/10.1016/j.engstruct.2018.07.058

30. Yu-liang H et al (2020) Experimental and numerical analysis of grouped stud shear connectors embedded in HFRC. Constr Build Mater 242:118197. https://doi.org/10.1016/j.conbuildmat.2020.118197

31. Bonilla J, Bezerra LM, Mirambell E (2019) Resistance of stud shear connectors in composite beams using profiled steel sheeting. Eng Struct 187(February):478–489. https://doi.org/10.1016/j.engstruct.2019.03.004

32. Manual AU (2012) Abaqus version 6.12–1 documentation. Dassault Systemes SIMULIA Corporation, Providence, RI, USA

33. Construction AIS (2000) Load and resistance factor design specification for structural steel buildings. American Institute of Steel Construction, Incorporated

34. Sun Q et al (2019) Monotonic and cyclic behavior of headed steel stud anchors welded through profiled steel deck. J Constr Steel Res 157:121–131. https://doi.org/10.1016/j.jcsr.2019.01.022

35. Tong L et al (2020) Static behavior of stud shear connectors in high-strength-steel–UHPC composite beams. Eng Struct 218(May):110827. https://doi.org/10.1016/j.engstruct.2020.110827

36. Souza PT, Kataoka MN, El Debs ALHC (2017) Experimental and numerical analysis of the push-out test on shear studs in hollow-core slabs. Eng Struct 147:398–409. https://doi.org/10.1016/j.engstruct.2017.05.068

37. Lowe D et al (2020) Full scale experiments on splitting behaviour of concrete slabs in steel concrete composite beams with shear stud connection. Structures 23:126–138. https://doi.org/10.1016/j.istruc.2019.10.008

38. Zhang Y et al (2020) Flexural responses of steel-UHPC composite beams under hogging moment. Eng Struct 206:110134. https://doi.org/10.1016/j.engstruct.2019.110134

39. Etim O et al (2020) Shear characterisation of pultruded superstructural FRP-concrete push-outs. Structures 23:254–266. https://doi.org/10.1016/j.istruc.2019.10.004

40. Ahmed IM, Tsavdaridis KD (2020) Shear connection of prefabricated slabs with LWC—part 1: experimental and analytical studies. J Constr Steel Res 169:106016. https://doi.org/10.1016/j.jcsr.2020.106016

41. Prakash A et al (2012) Modified push-out tests for determining shear strength and stiffness of HSS stud connector-experimental study. Int J Compos Mater 2(3):22–31. https://doi.org/10.5923/j.cmaterials.20120203.02

42. Yanez SJ, Dinehart DW, Santhanam S (2017) Composite steel joist analysis using experimental stiffness factor from push-out tests. J Constr Steel Res 137(April):1–7. https://doi.org/10.1016/j.jcsr.2017.04.001

43. Zhang J et al (2020) Experimental and theoretical study on longitudinal shear behavior of steel-concrete composite beams. J Constr Steel Res 171:106144. https://doi.org/10.1016/j.jcsr.2020.106144
44. Chen Y et al (2020) Flexural behavior of composite box girders with corrugated steel webs and trusses. Eng Struct 209:110275. https://doi.org/10.1016/j.engstruct.2020.110275
45. Kabir MI et al (2020) Flexural behaviour of ECC-LWC encased slender high strength steel composite beams. J Constr Steel Res 173:106253. https://doi.org/10.1016/j.jcsr.2020.106253
46. Zhang S, Liu J (2007) Seismic behavior and strength of square tube confined reinforced-concrete (STRC) columns. J Constr Steel Res 63(9):1194–1207. https://doi.org/10.1016/j.jcsr.2006.11.017
47. Zhu J et al (2020) Numerical and theoretical research on flexural behavior of steel-UHPC composite beam with waffle-slab system. J Constr Steel Res 171:106141. https://doi.org/10.1016/j.jcsr.2020.106141
48. Qiao W et al (2020) Flexural properties of new cold-formed thin-walled steel and concrete composite slabs. J Build Eng 31(January):101441. https://doi.org/10.1016/j.jobe.2020.101441
49. Hu Y et al (2020) Flexural performance of steel-UHPC composite beams with shear pockets. Structures 27(February):570–582. https://doi.org/10.1016/j.istruc.2020.05.039
50. Dar MA et al (2020) Comparison of various shear connectors for improved structural performance in CFS concrete composite slabs. Eng Struct 220(June):111008. https://doi.org/10.1016/j.engstruct.2020.111008
51. Baran E (2015) Effects of cast-in-place concrete topping on flexural response of precast concrete hollow-core slabs. Eng Struct. https://doi.org/10.1016/j.engstruct.2015.04.017
52. Ibrahim IS et al (2016) Experimental study on the shear behaviour of precast concrete hollow core slabs with concrete topping. Eng Struct 125:80–90. https://doi.org/10.1016/j.engstruct.2016.06.005
53. Qi J et al (2020) Flexural behavior of steel-UHPFRC composite beams under negative moment. Structures 24(January):640–649. https://doi.org/10.1016/j.istruc.2020.01.022
54. CSA Group, CAN/CSA S16–19 (2019) Design of steel structures. CSA Group, Toronto, Ontario, Canada

Mitigation of Higher Mode Effects in Controlled Rocking Walls

Saeed Dehghani, Lisa Tobber, and Amirhossein Amiri

Abstract Controlled rocking is the method of only attaching the wall-base vertically with energy dissipating devices, such as dampers. This design method is advantageous for walls under cyclic loads as the controlled rocking allows for self-centering capability. However, in tall building systems, a localized plastic response at the wall-base can result in substantial higher mode effects, such as amplified flexural strains at upper floors. The higher mode effect is a challenging issue for designing tall buildings as it can cause undesirable structural behavior under earthquake excitation, and consequently considerable structural and non-structural damage. Recently, several approaches have been employed in order to mitigate the effects of higher modes within the controlled rocking systems. This chapter explores various methods of reducing higher mode effects in controlled rocking tall buildings using a parametric analysis. A range of archetype buildings were studied using both linear and nonlinear time history analysis. Higher modes are mitigated using different outriggers' locations over the height of the building. Analysis showed that outriggers located at the top provided a more desirable response than the mid-height. The results will help the practitioners with the design of controlled rocking high-rise buildings in Canada and worldwide.

Keywords Higher mode effects · Controlled rocking walls

1 Introduction

Rapid urbanization worldwide has created an upsurge in tall building construction, including regions of high-seismicity. Reinforced Concrete (RC) core wall systems are popular structural systems to resist seismic loads due to their low construction

S. Dehghani · L. Tobber (✉) · A. Amiri
University of British Columbia, Kelowna, Canada
e-mail: Lisa.Tobber@ubc.ca

L. Tobber
School of Engineering, University of British Columbia, Okanagan, Canada

costs and versatility in architecture. In Vancouver, one of the most seismically active regions in North America, virtually all high-rise buildings utilize RC core walls as the seismic force-resisting system [1]. RC core walls typically consist of C-shaped walls connected with coupling beams (shown in Fig. 1). This configuration essentially consists of two separate lateral force-resisting systems along each principal axis: the coupled wall system (East–West in Fig. 1) and the cantilever wall system (North–South in Fig. 1).

Conventionally designed RC core walls dissipate the earthquake energy through damage. For example, after the February 2011 Christchurch earthquake, numerous RC walls showed singular large cracks, and further investigation revealed that some vertical bars were fractured. Figure 2a shows one such wall where only one crack is observed at the far corner of the wall, while Fig. 2b shows the fractured reinforcing steel within the wall. These fractures are due to single cracks opening and inducing significant strains across a relatively short unbonded gauge length. The fracturing of this reinforcing steel, particularly in the critical section, is a life safety issue that will require extensive repairs or total demolition [2].

Developing low-damage walls is a crucial step in the creation of earthquake-resilient RC core wall systems. An effective low-damage wall solution is controlled rocking, where walls are only connected vertically to the foundation through dampers. Prior research shows that controlled rocking limits the damage of RC walls for low-rise construction [3–5]. However, previous experimental work is limited to low-rise planar walls without considerations for the cyclic behavior of walls found in high-rise RC core walls (i.e., C-shaped walls, significant gravity loads, and coupled walls). Previous numerical studies by [6–9] show that controlled rocking is a promising solution for reducing damage in high-rise buildings. However, these studies utilize simplified numerical models on a small sample size of buildings. More comprehensive analyses for building characteristics and geometries are needed to understand the limitations of controlled rocking in tall building design. Furthermore, mitigation

Fig. 1 RC core wall plan and isotropic view
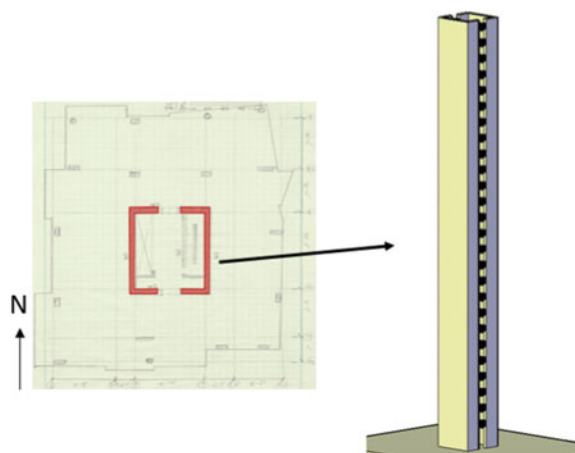
Fig. 2 Damage in RC wall in 2011 Christchurch earthquake [2] **a** crack at far end of the wall and **b** fractured reinforcing steel

measures are needed to control the significant higher mode moments that affect the rocking walls. In 2020, Tobber and Yang proposed using rooftop outriggers with a controlled rocking wall-base. The outrigger is an effective structural system used to provide a rotational stiffness at a pre-defined location and add damping to the wall to dissipate the input energy. This system includes mega-columns to resist the axial loads, outrigger dampers, and trussed beams. By implementing the outrigger system, the wall moment demand would be reduced, which results in the core wall with a smaller cross-section. Although this system could enhance the seismic performance of tall buildings by mitigating the higher mode effects and enabling the first mode to be dominant, the considerable plastic hinges may occur in the wall's base region. In the study by Tobber and Yang, the combination of an outrigger and a controlled rocking wall-base proved effective in reducing higher mode effects. However, their study was limited to using a design procedure that is not currently adopted by Canadian design practice. Furthermore, their study limited the number of prototype buildings evaluated and only applied the outrigger at the roof [10–12].

This chapter explores various methods of reducing higher mode effects in controlled rocking walls using outriggers. A range of archetype buildings is studied using linear and nonlinear time history analysis. Higher modes are mitigated by investigating the effects of varied systems' parameters, including outrigger's location, outrigger's stiffness, outrigger's nonlinear capacities, structural period, structural height, and different rocking wall-base nonlinear behavior. Analysis showed that outriggers located at the top of the structure provided efficient responses for mitigating the higher mode effects. New seismic design recommendations for controlling the higher modes are proposed based on the trends from the parametric studies.

2 Cyclic Response of Controlled Rocking Wall

Through conventional walls, the plastic hinges are formed near the base of the wall. These plastic hinges are formed as cracks develop over a portion of the wall's length. Within each open crack the rebar yields resulting in the energy dissipation. On the other hand, rocking systems are essentially the formation of a single crack at the wall-base. A large singular crack in a conventional wall would result in high strains and non-ductile behavior. As such rocking systems are often fitted with dampers or yielding devices intended to withstand these high demands. Figure 3 shows the mechanism and curvature for the conventional wall and the rocking wall systems. As shown, the conventional wall has a gradual increase in curvature demands, while the rocking system has a spike in the strain at the base [13–15].

Despite the differences between the two systems curvatures, the global force deformation of a rocking wall system and a conventional wall system are similar when exposed to similar loading. For example, Fig. 4 shows two experimental tests. Figure 4a shows a wall test specimen design to represent a high-rise building located in Vancouver BC [16]. On the other hand, Fig. 4b shows a post-tensioned rocking wall panel [3]. In the fixed base system, the energy dissipation (the loops) is primarily attributed to yielding of the wall reinforcing. For the rocking wall system, there is limited energy dissipation and the wall behaves nonlinear elastically before the PT tendon yields [15].

As shown in Fig. 4, both systems give a comparable force–deformation response. The highly pinched responses are due to the high contribution of axial load to the overturning resistance in both the fix base and rocking wall systems. The y-axis in Figs. 4a and b is the moment from the test normalized to the rocking moment, M_{rocking}, calculated using Eq. (1) [15].

$$M_{\text{rocking}} = PL_w/2 \tag{1}$$

where P is the axial load; L_w is the length of the wall; V is the lateral load (base shear); and H is the distance from the base of the wall to the location where the lateral load is applied.

Fig. 3 Comparison of the mechanism and curvature for the conventional wall and the rocking wall systems

a) Conventional Wall   b) Rocking wall
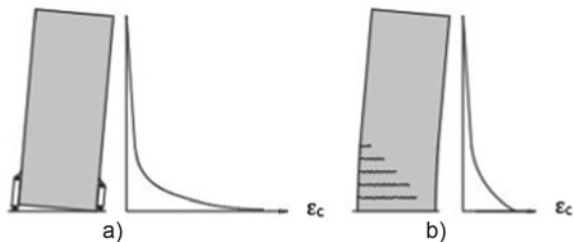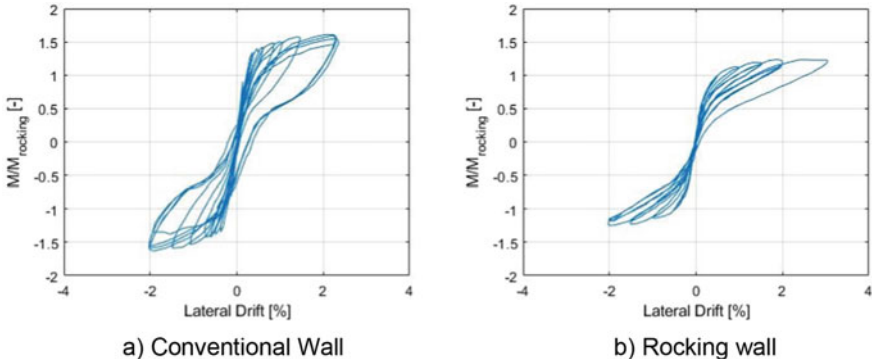
Fig. 4 Nonlinear behavior of conventional wall and rocking wall

3 Proposed System

The proposed system to control the higher mode effects is to use an outrigger system as shown in Fig. 5. In this system, the outrigger may be treated as a rotational hinge with stiffness of k_o and a yielding moment of M_{oy}.

The equivalent rotational spring stiffness is determined based on Eq. (2) [15].

$$k_0 = \frac{E_c I_{wy}}{H\left(\frac{1}{\alpha_f} - 1\right)} \tag{2}$$
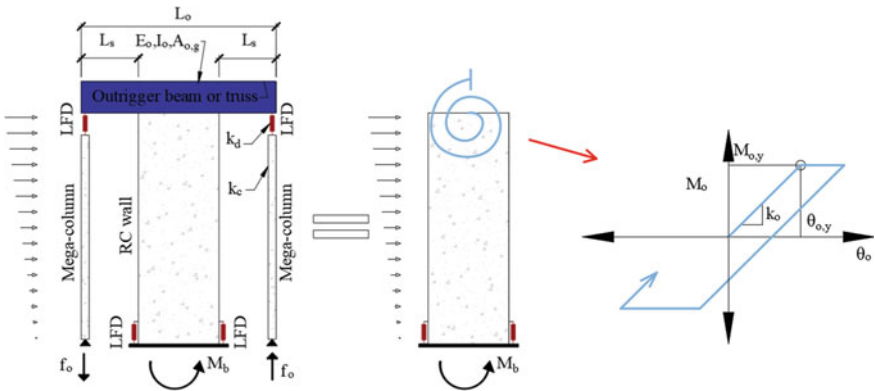
Fig. 5 Behavior of the outrigger system in the controlled rocking wall: **a** outrigger and controlled rocking wall; **b** equivalent outrigger and controlled rocking wall system; **c** force–deformation of equivalent outrigger spring

where E_c is the elastic module of concrete, I_{wy} is moment inertia of core wall about the y-axis of the core wall's centroid, H is the total height of the structure, and α_f is a stiffness factor in the range of [0,1].

4 Design Philosophy

The National Building Code of Canada (NBCC) is usually followed in order to design the tall buildings in the design practice. In this regard, the equivalent elastic model is conducted with the aim of simplifying the numerical modeling, and the linear dynamic methods (i.e., linear time history analysis) are used to determine the demands. The linear dynamic results are scaled to a minimum base shear achieved according to NBCC procedure, and it is assumed that the nonlinear displacements are same as the equivalent elastic displacements. Therefore, the design displacements are calculated via estimating the structural period (T_n) to acquire the spectral displacement (S_d) of a single degree of freedom [17].

As the base shear is calculated from the design spectral acceleration (S_a), it would be reduced by dividing by the seismic force reduction factor (R). The seismic reduction factor is defined in NBCC [17], as the product of ductility modification factor (R_d) and a force modification factor (R_o), which are equal to 3.5 and 1.6, respectively for the reinforced shear wall system ($R = 5.6$) [17].

In this study, the models are subject to linear time history analysis. From this analysis, the moment demands are determined at the controlled rocking points and the outrigger. These yield moments are determined by reducing the elastic moments by the seismic force reduction factors (R). In this study, the RC wall is modeled as elastic, to demonstrate the amplifications due to the higher mode effect.

5 Parametric Study

In this study, a parametric study has been conducted in order to evaluate the seismic behavior of the building type which has a controlled rocking wall-base and an outrigger located at the roof and at mid-height. Three different building geometries, with two different mass sizes were selected for this study. The buildings were assumed to be located in Vancouver, Canada with site class C according to the NBCC [17]. The shear walls were assumed to be flanged and integrated into a core wall, which is common practice in North American high-rise buildings [18]. Table 1 shows the core wall's cross-section geometry of the prototype building. The designed concrete compressive strength $\left(f_c' \right)$ is 60 MPa, and the designed yielding stress of steel reinforcements is 400 MPa. Table 1 shows the properties of the prototype buildings.

The different values for each parameter including three structural heights, two masses, four outrigger stiffness parameters $\left(\alpha_f \right)$, two β, and two outrigger locations

Table 1 Prototype building properties

Parameter	20 Story	30 Story	40 Story	
Mass per floor (kg)	625,000	700,000	625,000	
	927,000	998,000	1,284,000	
Wall cross sectional area (m^2)	14.6	21.7	31.2	
Gross moment of inertia (m^4)	126.2	261.4	545.8	
$E_c I_g$ (kNm^2)	3.36×10^9	7.44×10^9	1.65×10^{10}	

a) Outrigger at top level   b) Outrigger at mid-height
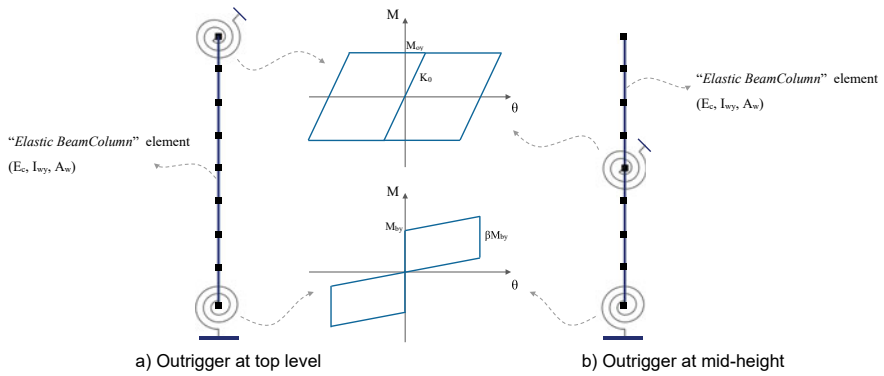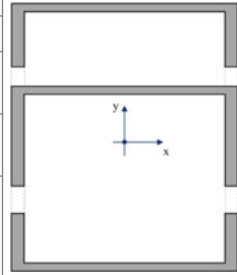
Fig. 6 Schematic of the analysis model

have been considered. The β parameter is ratio of forward to reverse activation moment of the rocking wall-base system, which is shown in Fig. 6. Table 2 shows the list of values for different parameters. It should also be noted that $\alpha_f = 0.0$ is corresponding to the structure without outrigger.

6 Description of Nonlinear Modeling Approach

Two-dimensional finite element analysis models are created for the prototype buildings using OpenSees [19]. Figure 6 shows a schematic of the analysis model. Figure 6a depicts the structure which is equipped with the outrigger at the top level, while Fig. 6b shows the structure with the outrigger located at mid-height. The RC core wall is modeled as elastic beam-column elements, and the demands are checked

Table 2 List of values for
different parameters

Parameter	20 Story	30 Story	40 Story
Outrigger location	Top level	Top level	Top level
	Mid-height	Mid-height	Mid-height
Mass per floor (kg)	625,000	700,000	625,000
	927,000	998,000	1,284,000
R	2	2	2
	4	4	4
	6	6	6
α_f	0.0	0.0	0.0
	0.3	0.3	0.3
	0.6	0.6	0.6
	0.8	0.8	0.8
β	0.5	0.5	0.5
	1.0	1.0	1.0

to ensure whether these elements remain elastic during post-processing. The outriggers are modeled using the "*steel01*" material in OpenSees. The rocking wall-base is modeled using "*self-centering*" materials in OpenSees.

A suite of 15 ground motions were selected from the PEER NGA2 Database [20]. Ground motions were chosen such that moment magnitudes were restricted to a minimum of 5.0 and a maximum of 8.0, and no more than two records from a single event were used. Amplitude scaling was utilized to match the ground motions to the target spectrum between the range of 0.20 and 10 s, to cover the range of periods from the three prototype buildings. The ground motion acceleration spectrums, the mean of the ground motion spectrum and the target spectrum are shown in Fig. 7. The target spectrum has been chosen for the location of Vancouver at the Maximum Considered Event (MCE) hazard level.

Fig. 7 The ground motion
acceleration spectrums, the
mean of the ground motion
spectrum and the target
spectrum
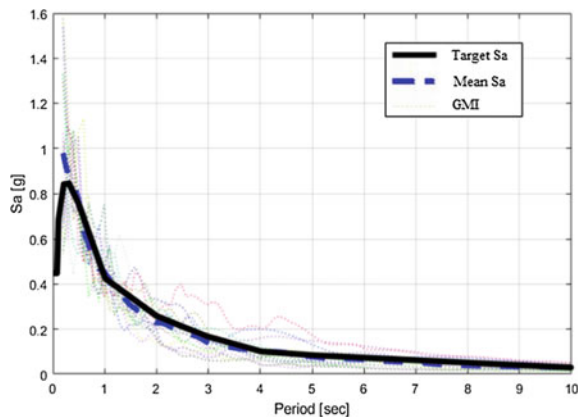
7 Nonlinear Time History Analysis Results

7.1 General Response

The mean distribution of the seismic force and deformation demands throughout the height of the 40-story archetype building, for the cases where $R = 2$ and $R = 6$ and the two locations of the outrigger system are presented in Figs. 8, 9, 10. Each plot shows the mean demand from the suite of ground motions for different values of α_f and β.

As shown in Fig. 8, a stiffer outrigger (i.e., higher values of α_f) results in considerably lower drifts. For example, structures with $R = 6$ show that as α_f increases from 0.01 to 0.8, maximum story drift decreases by ~ 40%. Likewise, higher energy dissipation at the rocking wall-base (i.e., higher values of β), generally results in lower values of peak story drifts. For example, for $R = 6$, drifts corresponding to $\beta = 1.0$ are on average ~ 10% lower than those associated with a β of 0.5. However, at $R = 2$, the change in β does not make a considerable difference in story drifts. Also, at $R = 6$, drift values at levels closer to the base are higher than those associated with $R = 2$, and thus drift profile for higher values of R is more uniform throughout the height of the building.

As shown in Fig. 9, higher values of α_f can significantly reduce moment demands specifically at mid-height levels and thus alleviate higher mode moment effects. Also, the change in β becomes more effective on story moments at higher values of R. At $R = 6$, where outriggers are not employed, the ratio of M/M_{rb}[1] exceeds one throughout several stories from grade to approximately mid-height of the archetypes. However, implementing the outrigger helps mitigate higher mode effects (M/M_{rb} less than one) and the associated amplifications in the seismic demands. For the case where $R = 2$, due to the high flexural capacity of the rocking wall-base, the ratio M/M_{rb} conservatively remains below one for the entire height of the building, which is not ideal from a design standpoint. In addition, it can be observed that the location of the outrigger system plays an integral role in the effectiveness of such systems. Mid-height moments have a higher reduction when the outrigger is at the top compared to the ones where the outrigger is implemented at the mid-height. For example, Figs. 8b and d show that stiffer outriggers at mid-height have increased the M/M_{rb} ratios.

Figure 10 shows the story shear forces for each 40-story archetype with $R = 2$ and $R = 6$. As shown, story shears are lower for higher values of α_f. However, this reduction is not as significant as the changes in drifts and bending moments. Furthermore, the change in β is not as effective on story shear forces as on deflection demands.

---

[1] M_{rb}: The moment demand of rocking base.
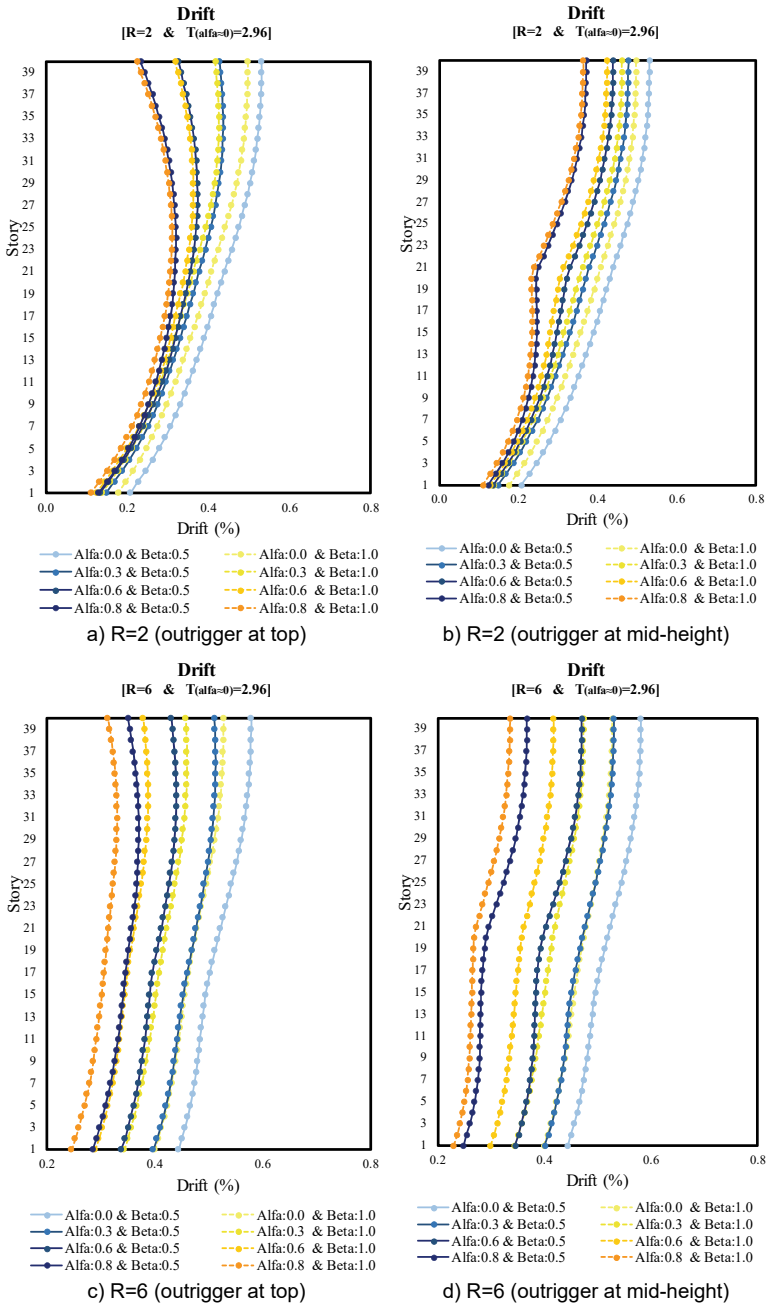
Fig. 8 The distribution of interstory drift ratio over the height for 40-story prototype
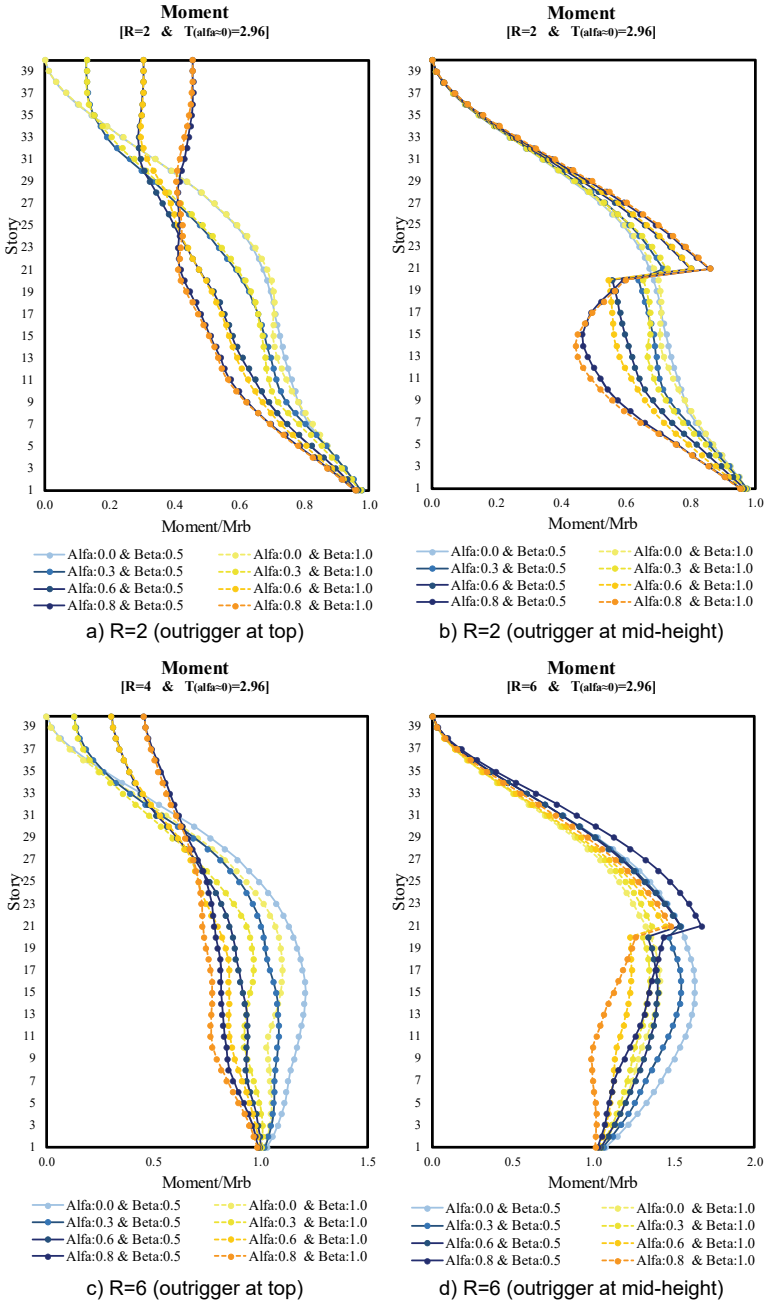
Fig. 9 The distribution of moment over the height for 40-story prototypes
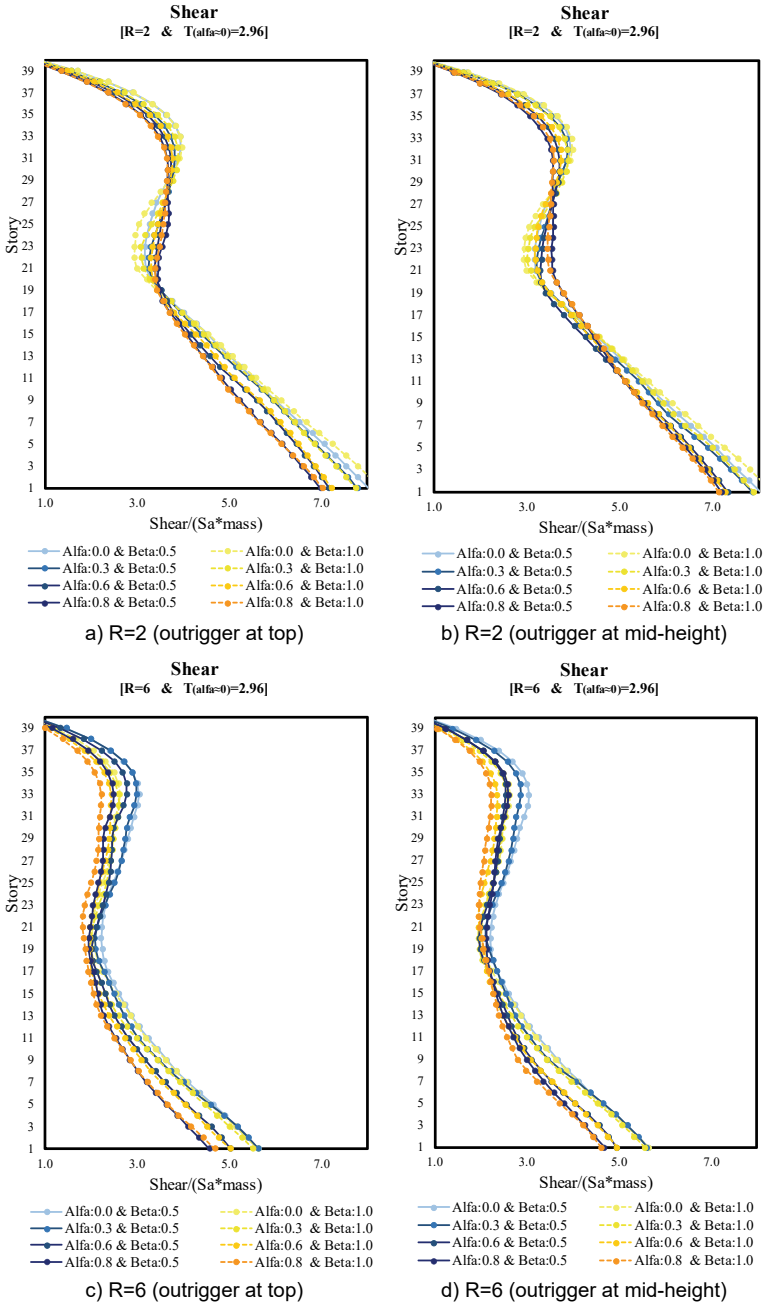
Fig. 10 The distribution of shear over the height for 40-story prototype

7.2 Interstory Drifts

Figure 11 shows the maximum interstory drift ratio for the structures in all scenarios with varied parameters. The ISDR has been determined from nonlinear time history analysis according to Eq. (3).

$$
\text{ISDR} = \max\left\{\text{average}\left\{\max\left\{\text{abs}\{\mathbf{Drift}\}^{(t)}\right\}\right\}^{(e)}\right\}^{(i)}
$$
$$
\text{for } 0 < t < t_{\max}^{(e)}; \ e = 1, 2, \ldots, N_e; \quad i = 1, 2, \ldots, N_S
$$

(3)

where $t_{\max}^{(e)}$ is the duration of the earthquake, N_e is the number of ground motions, and N_S is the number of stories.

Figure 11 shows that maximum story drifts increase as the values of R increase, which is due to higher inelastic deformation demands on the outrigger and the rocking wall-base system. Higher values of β result in significantly lower deflections, due to higher seismic energy dissipation at the base. Likewise, stiffer outriggers can limit the seismic deformations and the associated damages.

For intermediate values of α_f, where outrigger is located at mid-height of the buildings, story drifts are higher than those with outriggers at the top of the buildings. Comparing the plots for buildings of different heights, it can be observed that the change in design parameters (R, α_f, and β) on the seismic response of the archetypes can be more significant for taller structures, which indicates the desirable performance of these structural systems specifically for taller buildings.
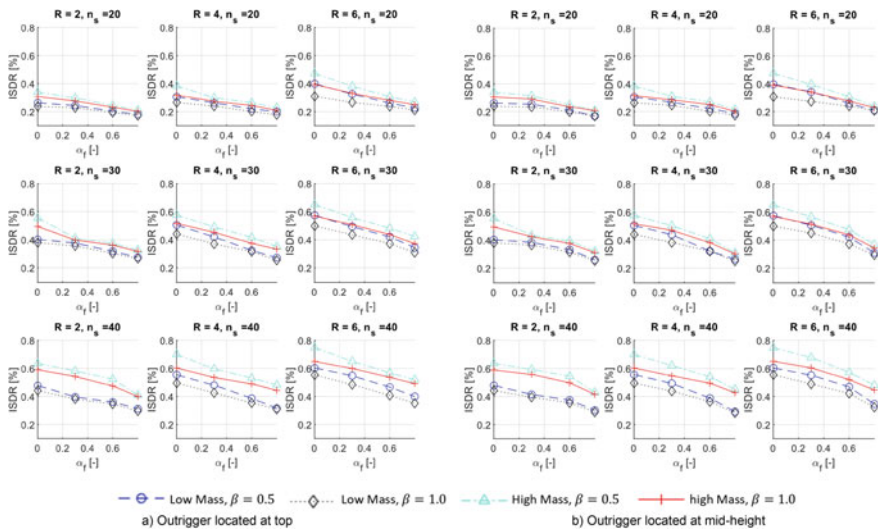
Fig. 11 The maximum ISDR for all scenarios

7.3 Shears

Figure 12 shows the maximum shear ratio for the structures with different parameters. The V_{max} has been determined from nonlinear time history analysis according to Eq. (4).

$$V_{max} = \max\left\{\text{average}\left\{\max\left\{abs\{\mathbf{Shear}\}^{(t)}\right\}\right\}^{(e)}\right\}^{(i)}$$

$$\text{for } 0 < t < t_{max}^{(e)}; \quad e = 1, 2, \ldots, N_e; \quad i = 1, 2, \ldots, N_S \tag{4}$$

where $t_{max}^{(e)}$ is the last time of the earthquake, N_e is the number of ground motions, and N_S is the number of stories.

Figure 12 shows that seismic base shear decreases as R values increase, which is associated with the inelastic behavior of the employed control systems. It can also be observed that for taller buildings (herein the 40-story archetype), the ratio of V_{max}/S_a is considerably higher for heavier buildings when the outrigger system is not implemented (case with $\alpha_f = 0.0$), however, with the increase in α_f, this difference decreases to the point that at $\alpha_f = 0.8$ this ratio is nearly identical for the archetypes with seismic masses of 625 and 1284 tons. The location of the outrigger does not seem to have a considerable effect on seismic base shear.
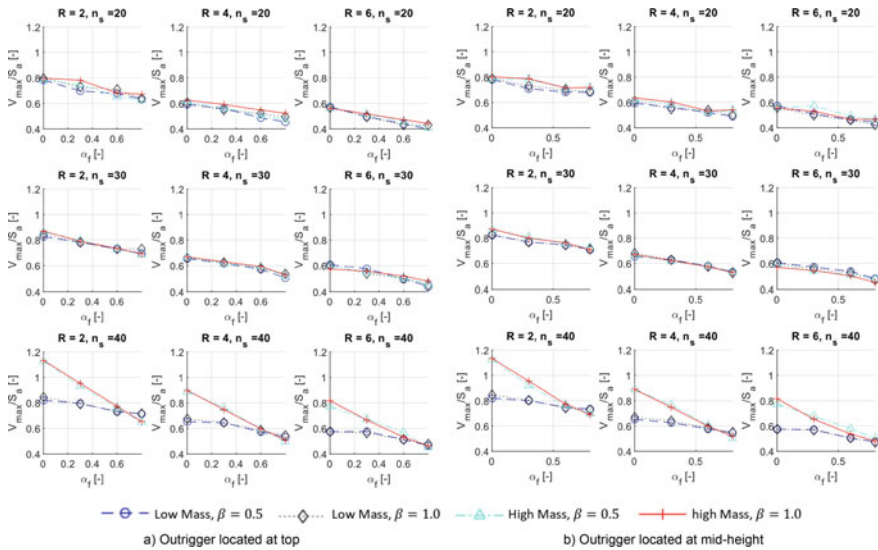
Fig. 12 The maximum shear ratio for all scenarios
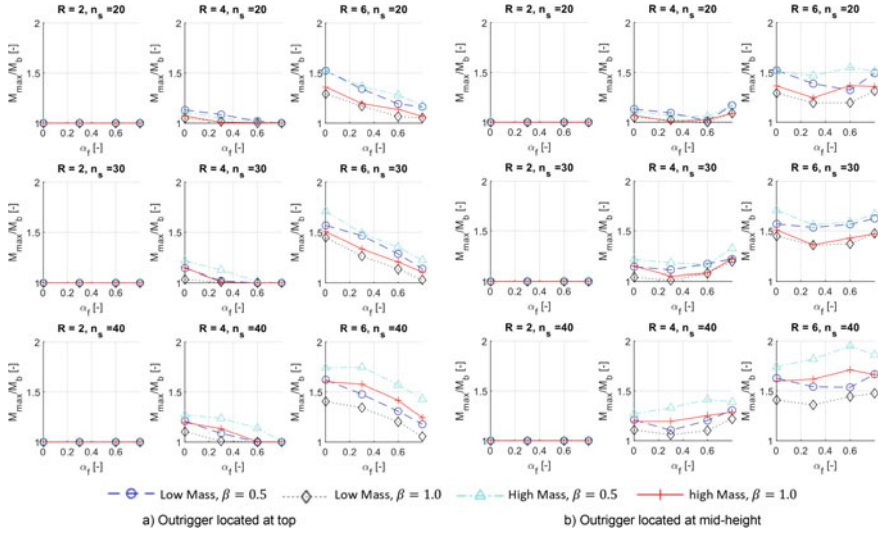
Fig. 13 The maximum moment ratio for all scenarios

7.4 Moments

Figure 13 shows the maximum shear ratio for the structures with different parameters. The M_{max} has been determined from nonlinear time history analysis according to Eq. (5).

$$M_{max} = \max\left\{\text{average}\left\{\max\left\{\text{abs}\{\mathbf{Moment}\}^{(t)}\right\}\right\}^{(e)}\right\}^{(i)}$$
$$\text{for } 0 < t < t_{max}^{(e)}; \quad e = 1, 2, \ldots, N_e; \quad i = 1, 2, \ldots, N_S$$

(5)

where $t_{max}^{(e)}$ is the last time of the earthquake, N_e is the number of ground motions, and N_S is the number of stories.

Figure 13 demonstrates the effect of higher modes on the seismic response of each archetype buildings such that higher exceedance of the ratio M/M_{rb} from one indicates more significant contribution of higher modes to structural seismic response. In general, with increase in the values of R and the resulting decrease in the flexural capacity of the rocking wall-base, higher mode effects would be more considerable. For $R = 2$, higher mode effects are negligible as the higher capacity of the rocking wall-base maintains the M/M_{rb} ratio less than one for the entire building heights, which would be a conservative choice for this design parameter. On the other hand, for cases where $R = 6$, outriggers can alleviate this effect to some extent, i.e., only use of highly stiff outriggers $\left(\alpha_f > 0.8\right)$ can mitigate this effect almost entirely.

For all 20-, 30-, and 40-story archetype buildings, $R = 4$ would be the better choice where at intermediate values of α_f, higher mode effects can be entirely mitigated. It is generally expected that higher mode effects would reduce while using stiffer outriggers. This assumption holds true for buildings with outriggers at the roof elevation however, where outriggers are placed at mid-height, in several cases stiffer outriggers can have a reverse effect on the seismic response of the buildings by amplifying this effect.

8 Summary and Conclusions

In this chapter, a parametric study to investigate the seismic response of RC core wall systems equipped with rocking wall-bases and damped outrigger system has been conducted. For this purpose, varied parameters including three structural heights, two masses, two outrigger locations, four values of α_f, two values of β, three values of R (2, 4, and 6) have been considered to be investigated through the nonlinear time history analysis.

The R parameter has a significant role in amplification of mid-height moments. In this regard, the outrigger and rocking wall-base systems designed with $R = 2$ seem to be highly conservative. On the other hand, the $R = 6$ resulted in a weak outrigger and rocking wall-base system which resulted in mid-height moments which far exceeded the wall-base moment.

The results show that the outrigger location plays an important role in the seismic response. Regarding this, the structures equipped with an outrigger on the top level have more desirable performance than the mid-height location. Furthermore, as was expected, the higher parameters α_f and β values resulted in lower seismic force and deformation demands.

Overall, outriggers have shown to be an effective method in reducing mid-height moments (caused by higher modes) for tall controlled rocking systems. Particularly, systems designed with high seismic force reduction factors (i.e., R).

References

1. Adebar P, DeVall R, Mutrie J (2017) Evolution of high-rise buildings in Vancouver, Canada. Struct Eng Int 27(1):7–14.
2. Buchanan A, Carradine D, Beattie G, Morris H (2011) Performance of houses during the Christchurch earthquake of 22 February 2011. Bull N Z Soc Earthq Eng 44(4):342–357
3. Perez FJ, Sause R, Pessiki S (2007) Analytical and experimental lateral load behaviour of unbonded posttensioned precast concrete walls. J Struct Eng 133(11):1531–1540
4. Xu H (2020) Mechanism and experimental validation of innovative self-centering conical friction damper. In: Open collections. University of British Columbia. Retrieved from https://open.library.ubc.ca/soa/cIRcle/collections/ubctheses/24/items/1.0387456
5. Reinhorn AM, Li C, Constantinou MC (1995) Experimental and analytical investigation of seismic retrofit of structures with supplemental damping: part I-fluid viscous damping devices.

In: NCEER Rep. 95–0028. University of Buffalo, The State University of New York, Buffalo, NY

6. Khanmohammadi M, Heydari S (2015) Seismic behavior improvement of reinforced concrete shear wall buildings using multiple rocking systems. Eng Struct 100:577–589. https://doi.org/10.1016/j.engstruct.2015.06.043

7. Lu Y, Panagiotou M (2014) Three-dimensional cyclic beam-truss model for nonplanar reinforced concrete walls. J Struct Eng 140:04013071. https://doi.org/10.1061/(ASCE)ST.1943-541X.0000852

8. Tong F, Christopoulos C (2020) Uncoupled rocking and shear base-mechanisms for resilient reinforced concrete high-rise buildings. Earthquake Eng Struct Dynam 49(10):981–1006. https://doi.org/10.1002/eqe.3273

9. Wiebe L, Christopoulos C (2009) Mitigation of higher mode effects in base-rocking systems by using multiple rocking sections. J Earthquake Eng 13(S1):83–108

10. Morales-Beltran M, Turan G, Dursun O, Nijsse R (2018) Energy dissipation and performance assessment of double damped outriggers in tall buildings under strong earthquakes. Struct Design Tall Spec Build 28(1):e1554. https://doi.org/10.1002/tal.1554

11. Tobber L, Yang TY (2021) Seismic design and evaluation of controlled outriggered rocking wall (CORW) using equivalent energy design procedure (EEDP). Eng Struct 247:113194

12. Zhou Y, Zhang C, Lu X (2016) Seismic performance of a damping outrigger system for tall buildings. Struct Control Health Monit 24(1):e1864. https://doi.org/10.1002/stc.1864

13. Hashemi A, Zarnani P, Masoudnia R, Quenneville P (2017) Seismic resistant rocking coupled walls with innovative Resilient Slip Friction (RSF) joints. J Constr Steel Res 129:215–226. https://doi.org/10.1016/j.jcsr.2016.11.016

14. Henry R, Ingham J, Sritharan S (2012) Wall-to-floor interaction in concrete buildings with rocking wall systems. In: New Zealand Society of Earthquake Engineering Conference, Christchurch, New Zealand

15. Tobber L (2021) Development of an innovative earthquake-resilient reinforced concrete core wall system. Doctoral dissertation, University of British Columbia

16. Adebar P, Ibrahim A, Bryson M (2007) Test of high-rise core wall: effective stiffness for seismic analysis. ACI Struct J 104(5):549–559. https://doi.org/10.14359/18857

17. National Research Council of Canada (NRCC) (2015) National building code of Canada 2015. In: National research council of Canada, Ottawa, Ontario, Canada

18. Dezhdar E (2012) Seismic response of cantilever shear wall buildings. Doctoral dissertation, University of British Columbia

19. Pacific Earthquake Engineering Research Center (PEER) (2000) Open system for earthquake engineering simulation (OpenSees). Pacific Earthquake Engineering Research Center, University of California, Berkeley, CA

20. Pacific Earthquake Engineering Research Center (PEER) (2018) NGA-West 2 peer ground motion database. Retrieved from https://ngawest2.berkeley.edu/site. Accessed on 1 Jan 2018

Macro Modeling of Steel-plate Concrete Composite Shear Walls in the OpenSees Environment

Masoumeh Asgarpoor, Ali Gharavi, Siamak Epackachi, and Ali Imanpour

Abstract A new macro model is developed in the OpenSees environment to analyze SC shear walls efficiently. The proposed modeling technique benefits from higher accuracy in predicting the response of SC walls compared to similar macro models and lower computational costs. The proposed model is then used to predict the cyclic response of 12 rectangular SC wall specimens with and without boundary elements and end plates, tested under cyclic loading. The results confirm that the initial stiffness, peak strength, displacement at peak strength, and post-peak behavior predicted are in good agreement with test results.

Keywords Steel-plate concrete · Composite shear walls · OpenSees environment

1   Introduction

Steel-plate composite (SC) walls consist of steel faceplates, infill concrete, headed steel studs anchoring the faceplates to the infill, and tie rods connecting the two faceplates through the infill, see Fig. 1. The behavior of SC walls is determined by the nonlinear cyclic responses of steel plates, plain concrete, the bond between the steel faceplates and infill concrete, and connectors (studs and tie rods). Nonlinear responses of structures can be obtained using micro or macro modeling. Finite element modeling enables users to investigate the detailed responses of the structural component. However, this type of analysis needs considerable time and computational effort. On the other hand, macro modeling needs less complex modeling efforts

M. Asgarpoor · A. Gharavi
Sharif University of Technology, Tehran, Iran

S. Epackachi (✉)
Amirkabir University of Technology, Tehran, Iran
e-mail: Epackachis@aut.ac.ir

A. Imanpour
University of Alberta, Alberta, Canada

Fig. 1 SC wall
configuration [12]
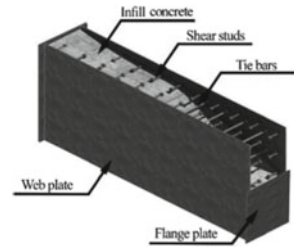
and presents the overall response of structures quickly using simple tools. The level
of accuracy in the macro modeling approach depends on basic assumptions and
material and element models used in the analysis.

There exist three types of macro models for Reinforced Concrete (RC) shear walls,
including the beam-column element model, multiple spring element model, and truss
element model. Given the lack of any macro model for SC walls, the available macro
models can be modified to be used to analyze composite walls. Among three well-
known macro models for RC shear walls, the beam-column element model is the
simplest one where shear-flexure interaction is ignored. Two latest models, namely
"MVLEM model of Kolozvari [1]" and "3D beam-truss model of Lu [2]" consider
shear-flexure interaction, neutral axis fluctuation, and the axial force effect on RC
shear wall responses and are more complicated models.

The first and simplest beam-column model was developed by Clough et al. [3].
This model disregards important features of the experimentally observed behavior
of RC walls, including the variation of the neutral axis of the wall's cross-section
and interaction with the frame members connected to the wall [4]. Following a full-
scale test on a seven-story RC frame-wall building in Tsubaki, Japan, Kabeyasawa
et al. proposed a new macroscopic Three-Vertical-Line-Element Model (TVLEM)
to account for experimentally observed behavior that could not be captured using an
equivalent beam-column model [4]. Vulcano et al. proposed the Multi-Component-
in-Parallel Model (MCPM) to obtain a more refined description of the flexural
behavior of the wall by modifying the geometry of the wall model to account for the
progressive yielding of reinforcement gradually, and using more refined hysteretic
rules based on the actual behavior of the materials and their interactions [5]. Orakal
improved the Multiple-Vertical-Line-Element Model (MVLEM) by adopting refined
constitutive relationships for materials and conducting detailed calibration studies
to investigate the model's effectiveness in predicting inelastic wall response [6].
Massone et al. modified the MVLEM using a shear spring for each uniaxial element,
treated as an RC panel element, with membrane actions, i.e., uniform normal, and
shear stresses applied in the in-plane direction [7]. Therefore, the interaction between
flexure and shear is incorporated at the uniaxial element (fiber) level. Kolozvari
proposed an analytical model that captures the interaction between axial/flexural
and shear responses for RC walls subjected to reversed-cyclic loading [1].

In the nonlinear truss model proposed by Lu, an RC member was idealized by
longitudinal, transverse, and diagonal truss elements [2]. Each element was modeled

as a composite component consisting of concrete and reinforcing bars. The strut-and-tie model was developed as a macroscopic model for the analysis and design of RC members, such as deep beams and corbels. The magnitude and distribution of stresses and strains vary significantly. Compared to the fiber-based nonlinear beam element model, the strut-and-tie model provided an advantage to ignore plane sections remain plane assumption leading to a more accurate representation of RC shear walls, specifically for walls with low to moderate aspect ratios.

There are some numerical investigations on the behavior of reinforced concrete elements under multidirectional loading and SC walls under cyclic loading [8–11]. Previous studies on SC walls have shown that most of these walls are flexure-critical, even those with a low aspect (height-to-depth) ratio. Therefore, a nonlinear beam-column model is used to simulate the cyclic response of SC walls with a wide range of design variables.

2 Experimental Database

This study selected a comprehensive set of test data of SC walls for numerical validation. Details of tested SC walls are presented in Table 1. The cross-sectional shapes are shown schematically in Fig. 2.

3 Numerical Modeling

Displacement-based nonlinear beam-column elements are used for modeling elements in the plastic hinge region of SC walls in OpenSees. The plastic hinge length is estimated based on the work of Asgarpoor et al. [9]. Elastic beam-column elements are used for the rest of the wall elements. Element types used along the height of the SC walls are illustrated in Fig. 3. Confined concrete stress–strain relationships are assumed for sections inside the boundary conditions and wall portions near the endplates. For the other parts, concrete is assumed to be unconfined. Steel faceplates are modeled using equivalent reinforcement with the ability to consider steel buckling between tie bars and fracture.

The concrete elements are modeled with *Concrete02* material model in OpenSees. The model is based on the work of Yassin and Hisham and uses modified Kent-Park model equations [17]. Stiffness degradation at unloading and reloading branches of cyclic loading is simulated while it does not consider strength reduction after each loading cycle. The stress–strain curve and its input parameters are illustrated in Fig. 4a. The input parameters include maximum compressive strength of concrete $\left(f_c'\right)$, concrete strain at maximum strength (ε_{c0}), concrete crushing strength $\left(f_{cu}'\right)$, concrete strain at crushing strength (ε_u), the ratio between unloading slope at ε_u and initial slope (lambda), maximum tensile strength (f_t), and tension softening stiffness (E_{ts}). The initial slope for this model is taken as $2f_c'/\varepsilon_{c0}$.

Table 1 Test specimen configurations

Researcher	Specimen ID	Wall dimension ($H \times L \times T$) (in. $\times$ in. $\times$ in.)	Tie rod/ stud spacing (in.)	Faceplate thickness (in.)	Axial comp. load (klb)	Cross-sectional shape
[13]	SC-1	$60 \times 60 \times 12$	12	0.186	0	Rectangular
	SC-2	$60 \times 60 \times 12$	6	0.186	0	Rectangular
	SC-3	$60 \times 60 \times 9$	9	0.189	0	Rectangular
	SC-4	$60 \times 60 \times 9$	4.5	0.189	0	Rectangular
[14]	SC-5	$60 \times 60 \times 12$	12	0.186	0	Rectangular
	SC-6	$45 \times 60 \times 12$	12	0.186	0	Rectangular
[15]	SC-7	$120 \times 48.6 \times 8$	8	0.312	0	Rectangular with half-round HSS 8.6×0.32 end plates
	SC-8	$120 \times 43.2 \times 6$	8	0.312	0	Rectangular with round HSS 8.6 $\times$ 0.32 boundary elements
[16]	SC-9	$101 \times 50.6 \times 8.4$	5.7	0.196	1645	Rectangular with Box boundary elements
	SC-10	$101 \times 50.6 \times 8.4$	5.7	0.157	1694	Rectangular with Box boundary elements
	SC-11	$101 \times 50.6 \times 8.4$	5.7	0.118	1664	Rectangular with Box boundary elements
	SC-12	$59 \times 29.5 \times 4.92$	3.3	0.118	619.5	Rectangular with Box boundary elements

(a) (b) (c)
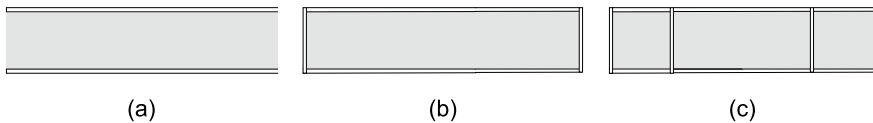
Fig. 2 Cross-sectional shapes for SC walls: **a** rectangular, **b** rectangular with endplates, **c** rectangular with boundary elements

To model steel fibers of the composite cross-section, the reinforcing steel material model is used in OpenSees developed by Kunnath et al. [18]. This material model can consider both steel buckling under compression and fracture to capture strength degradation. Although this material model is developed for modeling reinforcement,
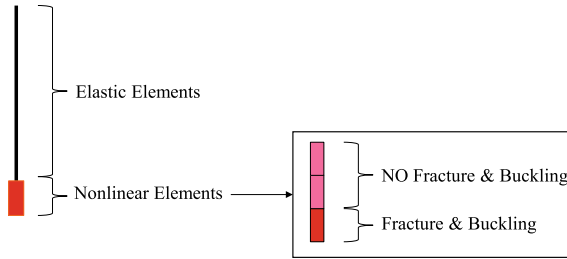
Fig. 3 Element type along the SC wall height
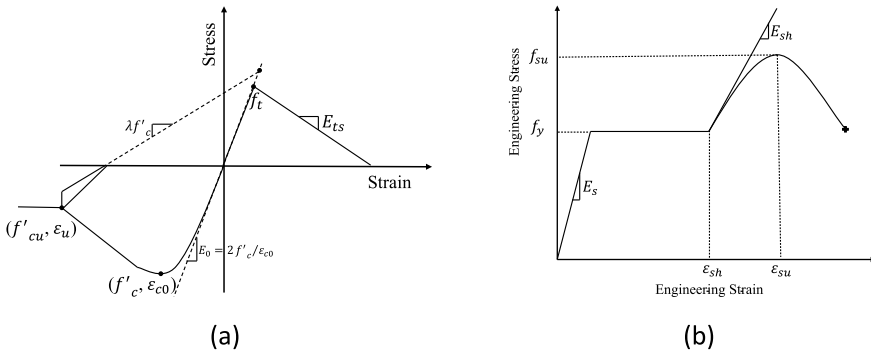
Fig. 4 The stress–strain relationship used for **a** *Concrete02* and **b** Reinforcing Steel

steel faceplate fibers can be simulated using equivalent rebars. The input parameters for this material model include yield strength in tension (F_y), ultimate strength in tension (F_{su}), elastic modulus (E_s), tangent modulus at the onset of strain hardening (E_{sh}), strain corresponding to the onset of strain hardening (ε_{sh}), strain at peak stress (ε_{su}), as shown in Fig. 4b.

Buckling is modeled based on Gomes and Appleton, which has four input parameters, as shown in Fig. 5 [19], including slenderness ratio (I_{sr}), amplification factor for the buckled stress–strain curve (β), buckling reduction factor (r), and buckling constant (γ). The parameter β is an amplification factor that allows the user to scale the buckling curve, which is helpful for adjusting the location of the bifurcation point. To calculate I_{sr}, the length between tie bars is considered. The equivalent rebar diameter should be calculated by equating the radius of gyration of a bar to the radius of gyration of the rectangular steel plate of composite walls. The r factor, ranging from 0.0 to 1.0, is used to adjust a curve between the buckled and unbuckled curves. The γ factor, ranging from 0.0 to 1.0, is the positive stress location where the buckling factor is initiated. This factor was introduced to avoid kinks in the reloading branch. The basic idea is that the stress–strain curves are reduced toward positive stress γf_u.

The Coffin-Manson fatigue and strength reduction model is used to model fracture and strength degradation in cyclic loops [20, 21]. This model includes Coffin-Monson
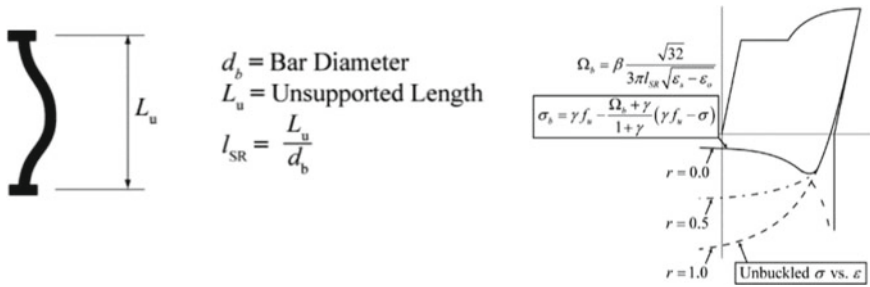
Fig. 5 Buckling parameters [19]

constants (C_f, β) and cyclic strength reduction constant (C_d). The input parameter is best obtained from calibration of test results and is usually constant for a material type, and it typically ranges from 0.5 to 0.7. The parameter C_f is a ductility constant used to adjust the number of cycles to failure. A higher value for C_f will result in a larger number of cycles to failure. The parameter C_d is the strength reduction constant. A larger value for C_d will result in a lower reduction of strength for each cycle.

4 Validation Study

The proposed macro model is validated using 12 SC walls subjected to cyclic loading. The force–displacement responses of the macro model (OpenSees) are compared to experimental results (Test) in Fig. 6. Referring to this figure, the numerical results are in good agreement with test results implying the macro model is robust enough to simulate the cyclic response of different types of SC walls, including rectangular with and without endplates or boundary elements. The pre-peak, peak, and post-peak responses of wall specimens successfully are predicted by the proposed macro model. Numerical simulations can reasonably predict pinching behavior due to the opening and closing of concrete cracks at different load stages. Based on the experimental observations, as the number of loading cycles increases, the stiffness of SC walls decreases due to steel yielding and concrete cracking, leading to a decrease in structural strength and an increase in lateral displacement. The proposed macro model captured the stiffness and strength degradation of SC walls over loading cycles.
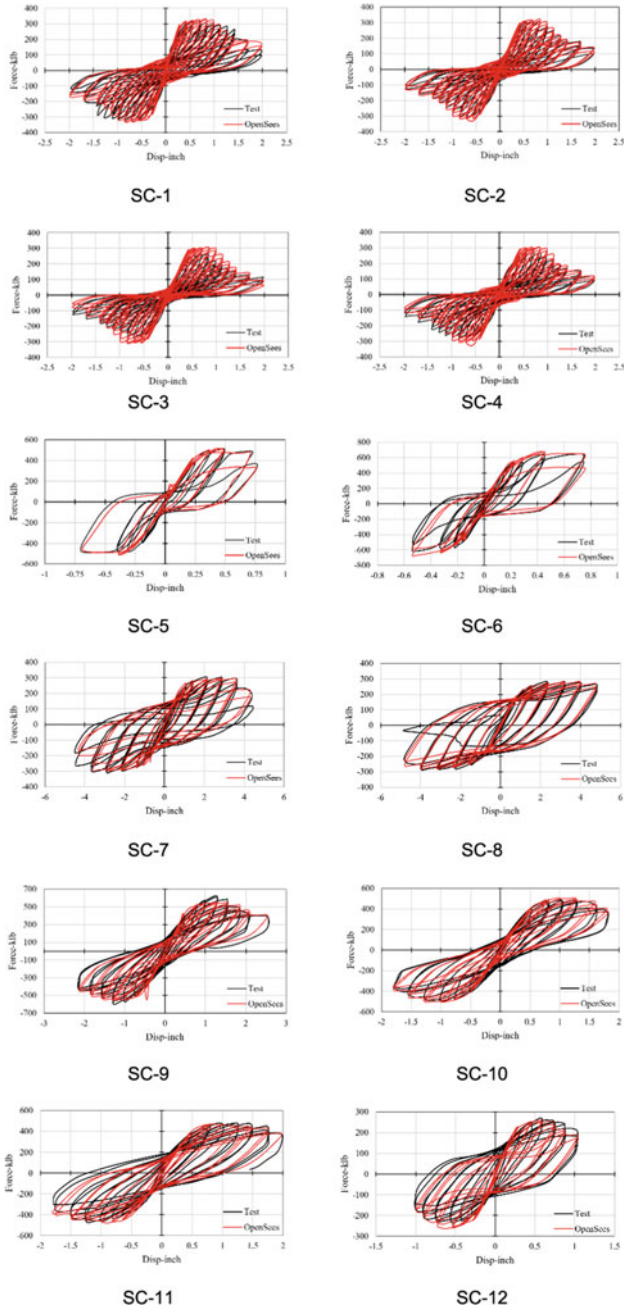
Fig. 6 Force–displacement responses

5   Conclusions

The inability of beam-column elements to capture the shear-dominant response of RC walls motivated many researchers to develop more sophisticated models. However, this study proved that simple beam-column could simulate their behavior under cyclic loading because of the flexural-controlled behavior of all squat and slender SC walls. In this study, a nonlinear beam-column element was implemented to numerically simulate the cyclic response of steel–concrete composite walls in the OpenSees framework. Using *Concrete02* and Reinforcing Steel material models, considering steel buckling and fracture, the behavioral characteristics of SC walls, including strength degradation and pinching, were appropriately reproduced compared to SC walls' experimental test data.

References

1. Kolozvari K, Orakcal K, Wallace JW (2015) Modeling of cyclic shear-flexure interaction in reinforced concrete structural walls. I: theory. J Struct Eng 141:04014135
2. Lu Y, Panagiotou M, Koutromanos I (2016) Three-dimensional beam-truss model for reinforced concrete walls and slabs–part 1: modeling approach, validation, and parametric study for individual reinforced concrete walls. Earthq Eng Struct Dynam 45:1495–1513
3. Clough RW, Benuska KL, Wilson EL (1965) Inelastic earthquake response of tall buildings. In: Proceedings of the third world conference on earthquake engineering, New Zealand
4. Kabeyasawa T, Otani S, Aoyama H (1983) Nonlinear earthquake response analyses of R/C wall-frame structures. Trans Jpn Concr Inst 5:277–284
5. Vulcano A, Bertero VV, Colotti V (1988) Analytical modeling of RC structural walls. In: Proceedings of the 9th world conference on earthquake engineering, pp 41–46
6. Orakcal K (2004) Nonlinear modeling and analysis of slender reinforced concrete walls. University of California, Los Angeles
7. Massone LM, Orakcal K, Wallace JW (2006) Shear-flexure interaction for structural walls. Spec Publ 236:127–150
8. Asgarpoor M, Gharavi A, Epackachi S (2021) Investigation of various concrete materials to simulate seismic response of RC structures. Structures, Elsevier 29:1322–1351
9. Asgarpoor M, Gharavi A, Epackachi S, Mirghaderi SR (2021) Finite element analysis of rectangular and flanged steel-concrete shear walls under cyclic loading. Struct Des Tall Spec Build 30(12):e1863
10. Asgarpoor M, Gharavi A, Epackachi S, Mirghaderi SR (2021) Investigation of concrete constitutive models under monotonic loading. In: 12th International congress on civil engineering (12ICCE), pp 1274–1288
11. Gharavi A, Asgarpoor M, Epackachi S (2021) Evaluation of plasticity-based concrete constitutive models under monotonic and cyclic loadings. Struct Des Tall Spec Build 31(6):e1919
12. Shafaei S, Varma AH, Seo J, Klemencic R (2021) Cyclic lateral loading behavior of composite plate shear walls/concrete filled. J Struct Eng 147:04021145
13. Epackachi S, Nguyen NH, Kurt EG, Whittaker AS, Varma AH (2015) In-plane seismic behavior of rectangular steel-plate composite wall piers. J Struct Eng 141:04014176
14. Kurt EG (2016) Steel-plate composite (SC) walls and their basemat connections: seismic behavior, analysis and design. Purdue University
15. Alzeni Y, Bruneau M (2014) Cyclic inelastic behavior of concrete filled sandwich panel walls subjected to in-plane flexure. University of Buffalo, State University of New York

16. Nie J-G, Hong-Song H, Fan J-S, Tao M-X, Li S-Y, Liu F-J (2013) Experimental study on seismic behavior of high-strength concrete filled double-steel-plate composite walls. J Constr Steel Res 88:206–219
17. Yassin M, Hisham M (1994) Nonlinear analysis of prestressed concrete sructures under monotonic and cyclic loads. University of California, Berkeley
18. Kunnath SK, YeongAe H, Mohle JF (2009) Nonlinear uniaxial material model for reinforcing steel bars. J Struct Eng 135:335–343
19. Gomes A, Appleton J (1997) Nonlinear cyclic stress-strain relationship of reinforcing bars including buckling. Eng Struct 19:822–826
20. Coffin LF (1971) A note on low cycle fatigue laws(plastic strain range-fatigue life behavior as two slope relationship, considering low cycle fatigue laws in terms of crack propagation mode change). J Mater 6:388–402
21. Manson SS (1965) Fatigue: a complex subject—some simple approximations. Exp Mech 5:193–226

Elastic Lateral Torsional Buckling Resistance of Beams Strengthened with Cover Plates Under Pre-existing Loads

Amin Iranpour and Magdi Mohareb

Abstract The present study investigates the elastic Lateral Torsional Buckling (LTB) behavior of flexural steel members of W sections that are strengthened with steel cover plates while under loading. For this purpose, a finite element study is developed to investigate the effect of span, strengthening scenarios where only a portion of beam is strengthened, types and location of loading before and after strengthening, magnitude of pre-strengthening loads, boundary conditions, and load height. Abaqus shell model is used to carefully simulate the full sequence of pre-existing loading application, application of clamping forces to bring into contact the initially straight steel cover plates with the bent configuration of the beam, the rebound arising during the removal of the clamping forces, welding at the interfaces between the cover plates and the flanges, the application of post-strengthening loads up to the point of onset of elastic LTB for the strengthened system as determined by eigenvalue analysis. It is shown that web distortional effects play an important role in reducing the elastic critical moment capacity. Practical recommendations are then provided to suppress distortional effects and maximize the elastic critical moment capacity of the strengthened beams. The study shows that cover plate strengthening is an effective means of increasing the LTB capacity of existing beams. A simplified design equation is then proposed to quantify the post-strengthening critical moment capacity of strengthened beams. The merits and limitations of the equation are identified and discussed.

Keywords Elastic lateral torsional buckling · Finite element analysis · Strengthening · Pre-existing loads

A. Iranpour (✉) · M. Mohareb
University of Ottawa, Ottawa, Ontario, Canada
e-mail: Amin.iranpour@uottawa.ca

1 Introduction and Literature Review

Existing steel structures need to be strengthened when required to withstand oper-
ating loads greater than those for which they were originally designed. Effective
strengthening strategies need to be tailored to suit the failure modes expected under
the expected increase in loads. Elastic lateral torsional buckling (LTB) is a failure
mode that is likely to govern the capacity of wide flange beams with long unbraced
lengths. Under such scenarios, the welding of steel cover plates to both flanges of the
I-beam would be a practical method for strengthening existing steel beams. In most
strengthening scenarios, entirely relieving members from loads before strengthening
might maximize the effectiveness of strengthening. However, the full removal of
existing loads is typically difficult and expensive to achieve. Hence, it is common to
strengthen members while under at least partial loading. The classical LTB theory
(e.g., [1], which forms the basis of LTB provisions in steel design standards (e.g.,
CAN/CSA-S16-19 [2] and ANSI/AISC360 [3]), does not account for the effect of
the loads acting on the member prior to strengthening. Hence, applying it to strength-
ening applications of beams with pre-existing loads is questionable and is subject to
the investigation of the present study.

Studies on the LTB of strengthened beams are scarce. MacCrimmon [4] provided
a procedure to estimate the critical moments for built-up crane runway beams. Hsu
et al. [5] and [6]) investigated the torsional properties of I-beams strengthened with
open-side down channels over the top flanges of wide flange beams in a bit to reliably
evaluate the LTB capacity of the strengthened beams. Pezeshky et al. [7] developed
a generalized thin-walled beam theory for the elastic LTB analysis of wide flange
sections strengthened with any number of cross-sections forming a monosymmetric
assembly. Based on a 3D shell-based Finite Element (FE) modeling, [8] conducted
a parametric study to investigate the elastic LTB capacity of beams with stepped
flanges and proposed simplified procedures to estimate their effective properties.
None of the above studies, however, investigated the effect of loads that may be
acting on the member before the strengthening process.

Liu and Gannon [9, 10] conducted experimental and numerical studies on nine
tests and 93 FE runs to investigate the behavior and capacity of I-beams strengthened
while under load. The authors reported that, while the pre-strengthening load level has
a noticeable effect on the inelastic LTB capacity of the member, its effect is negligible
on its yielding strength. None of the experiments reported however failed in elastic
LTB. Another experimental study on four specimens by [11] confirmed the findings
of [9, 10], where it was found that pre-strengthening load levels adversely affect the
inelastic LTB resistance of strengthened beams. Pham et al. [12] conducted an analyt-
ical investigation on the effect of pre-strengthening loads on the post-strengthening
elastic response of flexural members. The study did not address, however, the LTB
mode of failure.

Within the above context, the present study aims to investigate the elastic LTB
capacity of flexural members that are strengthened while under loads.

2 Statement of the Problem

An unloaded wide flange beam is depicted in Configuration 1 in Fig. 1. Under general transverse loads q_0, it undergoes a transverse deflection V_0 (Configuration 2). While under loading, the beam is to be strengthened using two initially straight plates. To enable the welding of the straight plates to the deflected beam, temporary loads q_t are applied to the plates to bring them into full contact with the flanges along the span. The plates are then clamped to the flanges (Configuration 4) and the temporary loads q_t are removed causing the system to rebound upwards while undergoing a deflection V_r to attain Configuration 5. Welding is then performed at Configuration 5 and additional operating external reference loads q_p are applied to the strengthened beam which brings the system to Configuration 6 by undergoing an additional displacement V_p. The applied reference loads q_p are then gradually increased to λq_p at which the strengthened system attains the state of onset of LTB (Configuration 7), in which λ is an unknown load multiplier to be determined from a buckling analysis. At this state, the system loses its lateral stiffness and has a tendency to buckle in a lateral torsional mode (Configuration 8) under no increase in loads.

It is required to determine the post-strengthening elastic critical moment M_{cr} of the system. For this purpose, the post-strengthening elastic critical moment M_{cr-FEA} is determined based on Finite Element Analysis (FEA) by using shell models in [13] to obtain the FE-predicted critical moments while modeling the full loading and strengthening sequence depicted in Fig. 1.
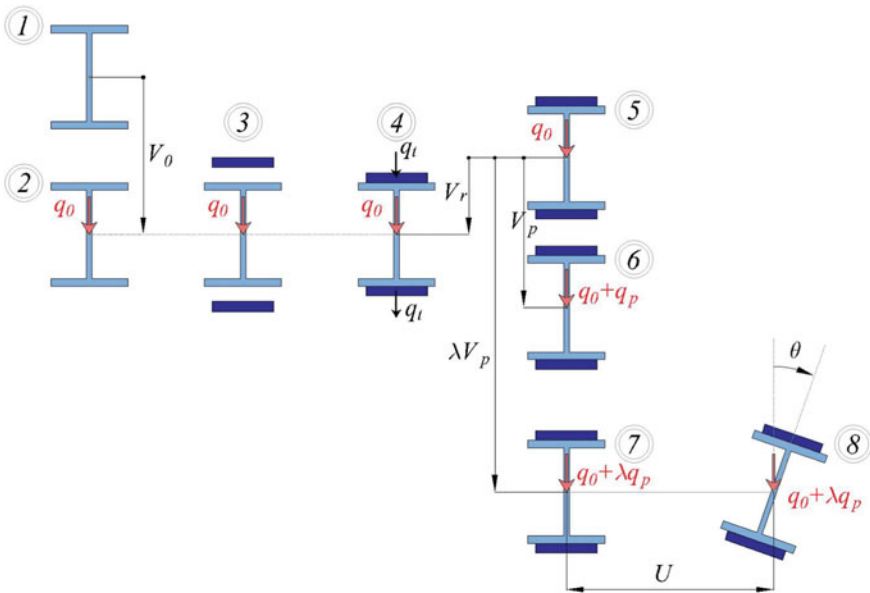
Fig. 1 Loading and strengthening sequence

3   Parametric Study

3.1   Reference Beam

A reference beam spanning 7 m with a W310 × 52 cross-section is simply supported relative to transverse and lateral displacements and relative to twist at both ends. Prior to strengthening, the reference beam is subjected to two point loads (2PLs) at third span points (i.e., $L/3$ and $2L/3$) acting at the shear center of the cross-section. The capacity of the beam prior to strengthening is governed by elastic LTB for yield strength $F_y = 350$ MPa. The magnitude of the pre-strengthening loads applied to the reference beam is taken to correspond to a fraction $\Omega = 75\%$ of the critical moment M_{ua} of the unstrengthened beam as determined from

$$M_{ua} = (\omega_{2-\text{CSA}})_a \frac{\pi}{L} \sqrt{E I_{ya} G J_a + \left(\frac{\pi E}{L}\right)^2 I_{ya} C_{wa}} \tag{1}$$

in which E is the modulus of elasticity, G is shear modulus, L is the beam span, I_{ya} is the weak axis moment, J_a is the Saint–Venant torsional constant, C_{wa} is the warping constant and all subscripts a denote quantities pertaining to the unstrengthened beam. In Eq. (1), $(\omega_{2-\text{CSA}})_a$ is the moment gradient factor according to (CAN/CSA-S6-19 [14]) and is given by

$$(\omega_{2-\text{CSA}})_i = \left(\frac{4M_{\max}}{\sqrt{M_{\max}^2 + 4M_A^2 + 7M_B^2 + 4M_C^2}}\right)_i \quad i = a, b \tag{2}$$

in which $M_{\max}$, M_A, M_B, and M_C are, respectively, the absolute values of the peak moment, the quarter point, midspan, and third-quarter point moments of the unbraced segments and subscript i takes the value $i = a$ to denote values pertaining to the pre-strengthening loads and $i = b$ to denote values pertaining to the post-strengthening loads. The critical moment for the unstrengthened beam as predicted by Eq. (1) is $M_{ua} = 131.6$ kNm. Thus, the point loads corresponding to a fraction $\Omega = 75\%$ of the critical moment M_{ua} induce a peak moment of 0.75×131.6 kNm $= 98.7$ kNm.

The entire span of the reference beam is then strengthened by welding two cover plates $b_p \times t_p = 140$ mm $\times$ 10 mm and subsequently subjected to a post-strengthening loading scenario similar in distribution to the pre-strengthening load (i.e., 2PLs applied at third span points acting at the shear center of the cross-section). It is required to obtain the post-strengthening critical moment for the strengthened section using the Abaqus shell model.

3.2 Finite Element Modeling

3.2.1 Shell Element Model

The S4R element in the Abaqus library [13] was used to mesh the model. The S4R is a four-node shell element with six degrees of freedom per node, with reduced integration, and hourglass control. A mesh study indicated that convergence is attained when an element size of nearly 15 mm is used throughout the beam. The interaction between the cover plates and beam flanges was modeled using the *CONTACT PAIR keyword in Abaqus, with the SMALL SLIDING, TYPE = SURFACE TO SURFACE features. These features enforce a small-sliding formulation between the two surfaces in contact by considering the sliding between the two surfaces as small/negligible relative to the deformations/motion of the structure [13]. In order to prevent penetration between both surfaces, a HARD contact pressure over-closure relationship was defined.

The analysis in Abaqus is performed in three steps; (1) the unstrengthened section was first subjected to the pre-strengthening load while the cover plates were concurrently bent to match the configuration of the bent beam, (2) A ROUGH friction model was activated at the interfaces between the plates and the flanges by using the *FRICTION, ROUGH keyword while suppressing the separation between the two surfaces after contact has been established by using the *SURFACE BEHAVIOR, NO SEPARATION, PRESSURE − OVERCLOSURE = HARD keyword. The use of the above combination of features ensures surfaces to remain fully bonded together, with no separation nor tangential sliding, once they have been brought into contact, even when the contact pressure between them is tensile, and (3) The post-strengthening load is then applied and a linearized eigenvalue buckling analysis is performed, in order to obtain the residual critical moment for the strengthened beam.

3.2.2 Thin-walled Beam Element Model

Given that the Abaqus shell models capture cross-sectional distortion, a thin-walled beam solution that suppresses web distortion is also used for comparison to determine the non-distortional LTB critical moment and provide a basis to quantify the effect of web distortion on the LTB capacity. For this purpose, the LTB-UO program [15] is used. This program is developed based on the formulation by [16] element and will be referred to subsequently as the BG element. The element omits the cross-sectional distortion and computes the elastic LTB capacity of beams under general transverse loading and general boundary conditions.

The FE formulation of the element is developed based on the total potential energy functional Π of a thin-walled beam during buckling. The simplest form of Π, omitting the effects of shear deformation, web distortion, pre-buckling deformation, and load height effects is
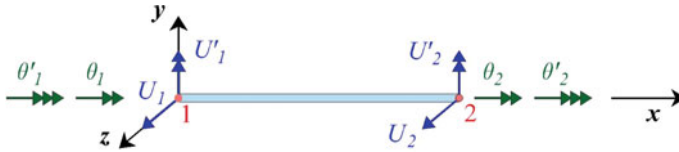
Fig. 2 Degrees of freedom of the BG element employed in the LTB-UO program

$$\Pi = \frac{1}{2} \int_L \left(EI_y U''^2 + EC_w \theta''^2 + GJ\theta'^2 + 2\lambda M\theta U'' \right) dx \qquad (3)$$

in which E is the modulus of elasticity, G is shear modulus, I_y is the weak axis moment of inertia, J is the Saint–Venant torsional constant, C_w is the warping constant, $U = U(x)$ is the lateral displacement, $\theta = \theta(x)$ is the angle of twist, λ is a buckling load multiplier to be determined from an eigenvalue analysis, $M = M(x)$ is the moment distribution under the applied transverse loads. Within the finite element, it is obtained by adopting linear interpolation over the element length L_e, i.e.,

$$M(x) = -M_1\left(1 - x/L_e\right) + M_2\left(x/L_e\right) \qquad (4)$$

in which, M_1 and M_2 are bending moment values at element ends and are obtained from the pre-buckling analysis. The BG element is a two-node thin-walled beam element with four buckling degrees of freedom per node: the lateral displacement U, the rotation about the weak axis U', the angle of twist θ and the warping deformation θ' (Fig. 2).

The lateral displacement $U(x)$ and angle twist $\theta(x)$ within the element are related to the vector of degrees of freedom $\mathbf{d}^T = \left\langle U_1\ U_1'\ U_2\ U_2'\ \theta_1\ \theta_1'\ \theta_2\ \theta_2' \right\rangle$ through

$$U(x) = \mathbf{H}_U^T \mathbf{d}, \qquad (5a)$$

$$\theta(x) = \mathbf{H}_\theta^T \mathbf{d} \qquad (5b)$$

in which the vectors of shape functions are defined by

$$\begin{aligned}
\mathbf{H}_U^T &= \mathbf{H}_U^T(x) \\
&= \left\langle H_1\ -H_2\ H_3\ -H_4\ 0\ 0\ 0\ 0 \right\rangle \\
\mathbf{H}_\theta^T &= \mathbf{H}_\theta^T(x) \\
&= \left\langle 0\ 0\ 0\ 0\ H_1\ H_2\ H_3\ H_4 \right\rangle \\
\left\langle H_1,\ H_2,\ H_3,\ H_4 \right\rangle & \\
&= \left\langle \begin{matrix} 1 - 3\zeta^2 + 2\zeta^3,\ L_e\zeta(1 - \zeta)^2, \\ 3\zeta^2 - 2\zeta^3,\ L_e\zeta^2(\zeta - 1) \end{matrix} \right\rangle, \quad \zeta = x/L_e
\end{aligned} \qquad (6)$$

From Eq. (5)a–b, by substituting into the variational principle in Eq. (3) and evoking the stationarity conditions $(\partial\Pi/\partial\mathbf{d})\delta\mathbf{d} = 0$, one obtains the linearized eigenvalue problem that yields the load multiplier λ corresponding to the state of onset of buckling, i.e.,

$$(\mathbf{k_E} - \lambda\mathbf{k_G})_{8\times 8}\mathbf{d}_{8\times 1} = \mathbf{0}_{8\times 1} \tag{7}$$

in which $\mathbf{k_E}$ is the elastic stiffness matrix and $\mathbf{k_G}$ is the geometric matrix.

It is noted that the total potential energy expression in Eq. (3) forms the basis of the critical moment equation in design standards (e.g., CAN/CSA-S16-19 [2] and ANSI/AISC360 [3]). For example, for a simply supported beam relative to twist and lateral displacement subjected to uniform moment, by assuming the displacement functions $U(x) = A\sin(\pi x/L)$ and $\theta(x) = B\sin(\pi x/L))$, substituting into Eq. (3), taking, evoking the stationary condition (i.e., $\partial\Pi/\partial A = \partial\Pi/\partial B = 0$), expressing the result in a matrix form, and setting to zero the determinant of the matrix of coefficient, one obtains the critical moment equation

$$\lambda M = \pm\frac{\pi}{L}\sqrt{EI_y GJ + \left(\frac{\pi E}{L}\right)^2 I_y C_w} \tag{8}$$

Since the potential energy expression in Eq. (3) omits the cross-sectional distortion, Eq. (8) does not account for distortional effects.

3.3 Design of Parametric Study

An additional 22 cases were investigated by varying the beam span, the strengthening configuration (Fig. 3a), the loading configurations and locations before and after strengthening of the beam (Figs. 3b and 4), the magnitude of the pre-strengthening load, the boundary conditions (Fig. 3c), and the load height. Table 1 provides the input parameters for each case. By varying the span from 7 to 11 and 14 m (Column 2 in Table 1), three values of span to depth ratio L/d are investigated (Column 3).

As shown in Fig. 3a, in addition to the unstrengthened beam, three strengthening schemes are investigated (Column 4 in Table 1): (1) Full Strengthening of the entire beam, (2) End Strengthening through plates located at beam ends, and (3) Midspan Strengthening through plates located at midspan. Seven loading configurations are investigated (Figs. 3b and 4): (1) 1PL: Point load applied at the beam midspan, (2) 2PLs: Two point loads applied at third points, (3) 3PLs: Three point loads applied at quarter points, (4) 4PLs: Four point loads applied at fifth points, (5) UDL: Uniformly distributed load, (6) PL-L/4: Point load applied at L/4, and (7) PL-3L/4: Point load applied at 3L/4. The distributions of pre- and post-strengthening loads are different in some cases as presented in Columns 5 and 7. The magnitude of pre-strengthening
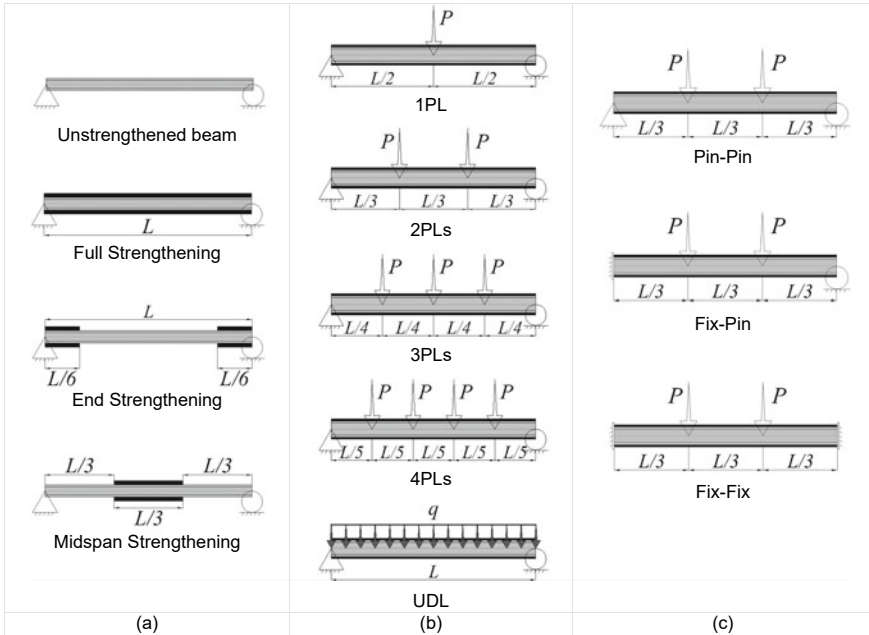
Fig. 3 Variables investigated **a** Strengthening configurations (Runs R, 4, 5 and 6), **b** Loading configurations (Runs R, 7–14), and **c** Boundary conditions (Runs R, 18 and 19)
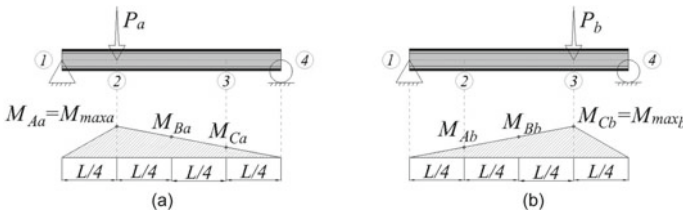
Fig. 4 Location of applied loads and corresponding bending moments for Run 22 **a** prior to strengthening, and **b** after strengthening

loads is taken as a fraction Ω (Column 6) of the critical moment of the unstrengthened beam. As shown in Fig. 3c, three sets of boundary conditions are investigated (Column 8). Column 9 reports the load height of each run. Three scenarios are investigated: (1) SC: Loads are acting at the Shear Center, (2) TF: Loads are acting at the Top Flange, and (3) BF: Loads are acting at the Bottom Flange.

Table 1 Table of runs (effect of stiffeners on critical moment increase)

Run Number	Span L (m)	Span to depth ratio L/d	Strengthening scheme	Loading and boundary conditions					Critical moments (kNm)			Percentage change	
				Pre-strengthening load configuration	Pre-strengthening moment fraction Ω	Post-strengthening load configuration	Boundary conditions	Load height	Unstiffened web	End stiffeners	Ends and midspan stiffeners	$(11-10)/(10)\times100$	$(12-10)/(10)\times100$
(1)	(2)	(3)	(4)	(5)	(6)	(7)	(8)	(9)	(10)	(11)	(12)	(13)	(14)
1	7	22.0	US[a]	2PLs	0.00	2PLs	Pin-Pin	SC	118.7	126.2	126.3	6.3%	6.4%
R	7	22.0	Full[b]	2PLs[e]	0.75	2PLs	Pin-Pin	SC[l]	137.0	175.7	178.1	28.3%	30.0%
2	11	34.6	Full	2PLs	0.75	2PLs	Pin-Pin	SC	95.9	112.8	113.2	17.6%	18.1%
3	14	44.0	Full	2PLs	0.75	2PLs	Pin-Pin	SC	78.1	88.8	89.0	13.6%	13.9%
R	7	22.0	**Full**	2PLs	0.75	2PLs	Pin-Pin	SC	137.0	175.7	178.1	28.3%	30.0%
4	7	22.0	**US**	2PLs	0.75	2PLs	Pin-Pin	SC	20.0	27.5	27.6	37.5%	37.9%
5	7	22.0	**End**[c]	2PLs	0.75	2PLs	Pin-Pin	SC	46.6		See Table 2		
6	7	22.0	**Mid**[d]	2PLs	0.75	2PLs	Pin-Pin	SC	44.3	53.6	54.5	21.1%	23.2%
7	7	22.0	Full	**1PL**[f]	0.75	2PLs	Pin-Pin	SC	148.2	186.3	188.9	25.7%	27.4%
R	7	22.0	Full	**2PLs**	0.75	2PLs	Pin-Pin	SC	137.0	175.7	178.1	28.3%	30.0%
8	7	22.0	Full	**3PLs**[g]	0.75	2PLs	Pin-Pin	SC	144.8	183.5	185.9	26.8%	28.5%
9	7	22.0	Full	**4PLs**[h]	0.75	2PLs	Pin-Pin	SC	139.2	178.0	180.4	27.9%	29.6%
10	7	22.0	Full	**UDL**[i]	0.75	2PLs	Pin-Pin	SC	140.2	179.4	181.8	28.0%	29.7%
11	7	22.0	Full	2PLs	0.75	**1PL**	Pin-Pin	SC	172.3	219.4	222.8	27.3%	29.3%
R	7	22.0	Full	2PLs	0.75	**2PLs**	Pin-Pin	SC	137.0	175.7	178.1	28.3%	30.0%
12	7	22.0	Full	2PLs	0.75	**3PLs**	Pin-Pin	SC	148.4	190.4	193.1	28.3%	30.1%
13	7	22.0	Full	2PLs	0.75	**4PLs**	Pin-Pin	SC	139.9	179.7	182.1	28.4%	30.2%
14	7	22.0	Full	2PLs	0.75	**UDL**	Pin-Pin	SC	141.3	182.0	184.5	28.8%	30.5%
15	7	22.0	Full	2PLs	**0.00**	2PLs	Pin-Pin	SC	237.4	275.9	278.2	16.2%	17.2%
16	7	22.0	Full	2PLs	**0.25**	2PLs	Pin-Pin	SC	203.9	242.5	244.8	18.9%	20.1%
17	7	22.0	Full	2PLs	**0.50**	2PLs	Pin-Pin	SC	170.5	209.1	211.5	22.7%	24.1%
R	7	22.0	Full	2PLs	**0.75**	2PLs	Pin-Pin	SC	137.0	175.7	178.1	28.3%	30.0%
R	7	22.0	Full	2PLs	0.75	2PLs	**Pin-Pin**	SC	137.0	175.7	178.1	28.3%	30.0%
18	7	22.0	Full	2PLs	0.75	2PLs	**Fix-Pin**	SC	398.5		See Table 3		
19	7	22.0	Full	2PLs	0.75	2PLs	**Fix-Fix**	SC	643.0		See Table 4		
20	7	22.0	Full	2PLs	0.75	2PLs	Pin-Pin	**TF**[m]	91.9	130.3	132.3	41.8%	44.0%
R	7	22.0	Full	2PLs	0.75	2PLs	Pin-Pin	**SC**	137.0	175.7	178.1	28.3%	30.0%
21	7	22.0	Full	2PLs	0.75	2PLs	Pin-Pin	**BF**[n]	192.0	229.1	232.0	19.4%	20.9%
22	7	22.0	Full	PL-L/4[j]	0.75	PL-3L/4[k]	Pin-Pin	SC	212.6	267.6	270.4	25.9%	27.2%

[a] US: Unstrengthening beam

[b] Full: Full strengthening scheme

[c] End: End strengthening scheme

[d] Mid: Midspan strengthening scheme

[e] 2PLs: 2 point loads applied at L/3 and 2L/3

[f] 1PL: Point load applied at the beam midspan

[g] 3PLs: 3 point loads applied at L/4, L/2 and 3L/4

[h] 4PLs: 4 point loads applied at L/5, 2L/5, 3L/5 and 4L/5

[i] UDL: Uniformly distributed load

[j] PL-L/4: Point load applied at L/4

[k] PL-3L/4: Point load applied at 3L/4

[l] SC: Shear centre loading

[m] TF: Top flange loading

[n] BF: Bottom flange loading

[o] NA: Not applicable

3.4 Suppressing Web Distortion

Past studies reported that web distortion can significantly affect the LTB capacity of beams with slender webs and stocky flanges in beams with short spans [17, 18]. According to [19], simply supported unstrengthened beams undergoing LTB exhibit maximum distortion at beam ends and midspan. Using transverse stiffeners

to suppress web distortion at these locations was shown to increase the distortional LTB capacity and help approaching the non-distortional LTB capacity. One of the objectives of the present study is to extend the investigation for strengthened beams. Towards this objective, web distortion is suppressed at different locations of shell models by employing kinematic constraints that suppress web distortion between both flanges while coupling the angles of twist of both flanges and the web to emulate the action of a transverse stiffener at the stiffened section while enabling the section to warp freely.

For Run 1 in Table 1, the critical moment is 118.7 kNm (Column 10 in Table 1) when no stiffeners are provided, i.e., web distortion is enabled (Fig. 5b). By suppressing the distortion at the beam ends, cross-sectional distortion decreases (Fig. 5c) and, subsequently, the critical moment increases to 126.2 kNm (Column 11), a 6.3% increase. This value compares to 127.2 kNm based on the non-distortional critical moment obtained using the BG element. Cross-sectional distortion is subsequently suppressed at midspan. The further increase in critical moment observed is a mere 0.10%. It is concluded that suppressing only the beam ends in Run 1 suffices to attain its non-distortional critical LTB moment capacity. This conclusion is also confirmed by observing the web distortion along the beam span as discussed in the following section.

Figure 6 compares the buckled configurations of the top and bottom flanges for Run 1 based on three models: (1) the shell FEA which captures the web distortion along the entire span, (2) the shell FEA with suppressed distortion at both ends, and (3) the non-distortional solution based on the BG element. In all three cases, the buckling modes were normalized with respect to the peak lateral displacement at the top flange. For this reason, the lateral displacements of the top flange in all three models are nearly identical. At the bottom flange, however, the lateral displacement predicted by the shell model which captures web distortion slightly differs from that based on the non-distortional BG model. The difference is attributed to web distortion in the former model. When the cross-sectional distortion is suppressed in the shell model at beam ends, the buckled configuration of the shell model approaches/coincides
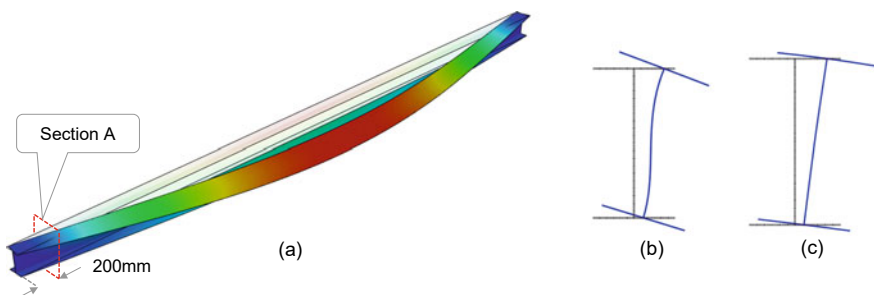
Fig. 5 Run 1 **a** Buckled Configuration, **b** No transverse stiffener provided at beam ends: Distortion takes place at Section A, and **c** Transverse stiffener provided at beam ends: Distortion roughly suppressed at Section A

Top Flange-BG (Non-distortional solution)

- - - - Top Flange-Shell (Distortion suppressed at both ends)

- · - Top Flange-Shell (Distortion allowed)

Bottom Flange-BG (Non-distortional solution)

- - - - Bottom Flange-Shell (Distortion suppressed at both ends)

- · - Bottom Flange-Shell (Distortion allowed)
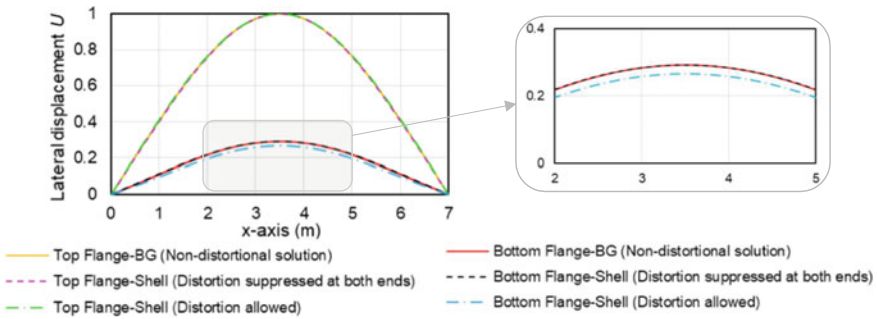
Fig. 6 Comparison of buckled shapes of the top and bottom flanges in Run 1

with that of the non-distortional BG element. Hence, the web distortion in Run 1 can effectively be suppressed by providing end stiffeners. For this reason, the critical moment of Run 1 based on the shell model with end stiffeners, which is 126.2 kNm (Column 11 in Table 1), is very close to that based on the non-distortional solution, which is 127.2 kNm.

Tables 1, 2, 3, 4 summarize the effect of suppressing the cross-sectional distortion at different locations for all models investigated. In all cases, suppressing distortion at midspan was found to have a negligible effect on the critical moment (around 2%).

When the strengthening cover plates are provided at end portions of the beam (e.g., Run 5 and Table 2), the web was found to distort at the location of section change in addition to the beam ends. Suppressing the distortion by providing transverse stiffeners at these locations was found to significantly increase the elastic critical moment capacity (by 75%). Conversely, when the strengthening cover plate is provided in the middle portion of the beam (e.g., Run 6 in Table 1), cross-sectional distortion at the location of section change was found to be negligible.

For beams with fixed end supports (i.e., Runs 18 and 19), maximum distortion was found to take place in the vicinity of the fixed support. As a result, suppressing

Table 2 Effect of stiffeners on critical moment increase in Run 5

Transverse stiffener location		M_{cr-FEA} (kNm)	Percentage change (%)
Unstiffened		46.6	–
End stiffeners		70.6	51.4
Ends + locations of section change		81.6	75.0
Ends + locations of section change + midspan		81.8	75.4

Table 3 Effect of stiffeners on critical moment increase in Fixed-Pinned Beam (Run 18)

Transverse stiffener location		M_{cr-FEA}(kNm)	Percentage change (%)
Unstiffened		399	–
Pinned end		453	13.7
Pinned end + 1 m from fixed end		459	15.1
Pinned end + 1 m from fixed end + midspan		465	16.6

Table 4 Effect of stiffeners on critical moment increase in Fixed–Fixed Beam (Run 19)

Transverse stiffener location		M_{cr-FEA}(kNm)	Percentage change (%)
Unstiffened		643	–
1 m from both fixed ends		675	4.9
1 m from both fixed ends + midspan		686	6.7

cross-sectional distortion at these regions was found to increase the LTB capacity of the beam (Tables 3 and 4).

To exclude the effects of cross-sectional distortion on LTB capacity, and hence maximize the elastic LTB capacity attained, cross-sectional distortion is suppressed at proper locations in all models (beam ends, one meter away from the fixed support, locations of the section change and midspan).

3.5 Effect of Cover Plate Strengthening on the Critical Moment

3.5.1 General

For the reference beam, the post-strengthening critical moment as predicted by the Abaqus shell model is $M_{cr-FEA} = 178.1$ kNm (Column 12 in Table 5). Towards devising a simplified methodology to estimate the post-strengthening critical moments, the following expression is proposed to quantify the additional post-strengthening critical moment M_{cr-m}

$$M_{cr-m} = (\omega_2)_b \frac{\pi}{L} \sqrt{EI_{yb}GJ_b + \left(\frac{\pi E}{L}\right)^2 I_y C_{wb}} - M_0 \tag{9}$$

in which the cross-sectional properties of the strengthened beam are the weak axis moment of inertia I_{yb}, the Saint–Venant torsional constant J_b, the warping constant C_{wb}. In Eq. (9), M_0 denotes the pre-strengthening bending moment value (e.g., $M_0 = M_{Ca} = M_{\max a}/3$ in Fig. 4a) corresponding to the location of the peak post-strengthening moment (e.g., Point 3 in Fig. 4b) and $(\omega_2)_b$ is the moment gradient factor corresponding to the post-strengthening loads which can be obtained in two ways: (1) Setting $i = b$ in Eq. (2), and (2) Using FEA results.

For the reference beam, $(\omega_{2-CSA})_b$ as predicted by Eq. (2) is 1.13 (Column 15 in Table 5). This value is slightly greater than the moment gradient factor obtained from

Table 5 Effect of pre-existing loads on post-strengthening critical moments

Run Number	Span L (m)	Span to depth ratio L/d	Strengthening scheme	Pre-strengthening load configuration	Pre-strengthening moment fraction Ω	Post-strengthening load configuration	Boundary conditions	Load height	Pre-existing moment at location of peak post-strengthening moment M_0	For unstrengthened beam M_u	Post-strengthening predicted by FEA M_{cr-FEA}	Post-strengthening predicted by Eq. [9] M_{cr-m}	M_{cr-m}/M_{cr-FEA}	Predicted by Eq. [2] $(\omega_{2-CSA})_b$	Predicted by FEA $(\omega_{2-FEA})_b$	Strengthening effectiveness [(10)+(12)]/(11)
(1)	(2)	(3)	(4)	(5)	(6)	(7)	(8)	(9)	(10)	(11)	(12)	(13)	(14)	(15)	(16)	(17)
R	7	22	Full	2PLs	0.75	2PLs	PP	SC	98.7	131.6	178.1	186.2	1.05	1.13	1.10	2.10
2	11	35	Full	2PLs	0.75	2PLs	PP	SC	57.1	76.1	113.2	117.0	1.03	1.13	1.11	2.24
3	14	44	Full	2PLs	0.75	2PLs	PP	SC	43.6	58.1	89.0	91.5	1.03	1.13	1.11	2.28
R	7	22	**Full**	2PLs	0.75	2PLs	PP	SC	98.7	131.6	178.1	186.2	1.05	1.13	1.10	2.10
4	7	22	**US**	2PLs	0.75	2PLs	PP	SC	98.7	131.6	27.6	28.1	1.02	1.13	1.09	-
5	7	22	**End**	2PLs	0.75	2PLs	PP	SC	98.7	131.6	81.8	NA	-	1.13	1.07	1.37
6	7	22	**Mid**	2PLs	0.75	2PLs	PP	SC	98.7	131.6	54.5	NA	-	1.13	1.13	1.16
7	7	22	Full	**1PL**	0.75	2PLs	PP	SC	110.4	147.1	188.9	174.6	0.92	1.13	1.10	NA
R	7	22	Full	**2PLs**	0.75	2PLs	PP	SC	98.7	131.6	178.1	186.2	1.05	1.13	1.10	2.10
8	7	22	Full	**3PLs**	0.75	2PLs	PP	SC	98.7	131.6	185.9	186.5	1.00	1.13	1.11	2.16
9	7	22	Full	**4PLs**	0.75	2PLs	PP	SC	98.7	131.6	180.4	186.7	1.03	1.13	1.11	2.12
10	7	22	Full	**UDL**	0.75	2PLs	PP	SC	98.7	131.6	181.8	186.2	1.02	1.13	1.10	2.13
11	7	22	Full	2PLs	0.75	**1PL**	PP	SC	98.7	131.6	222.8	256.5	1.15	1.26	1.38	NA
R	7	22	Full	2PLs	0.75	**2PLs**	PP	SC	98.7	131.6	178.1	186.2	1.05	1.13	1.10	2.10
12	7	22	Full	2PLs	0.75	**3PLs**	PP	SC	98.7	131.6	193.1	210.2	1.09	1.13	1.20	2.22
13	7	22	Full	2PLs	0.75	**4PLs**	PP	SC	98.7	131.6	182.1	192.9	1.06	1.13	1.13	2.13
14	7	22	Full	2PLs	0.75	**UDL**	PP	SC	98.7	131.6	184.5	196.0	1.06	1.13	1.14	2.15
15	7	22	Full	2PLs	**0.00**	2PLs	PP	SC	0.0	131.6	278.2	282.7	1.02	1.13	1.10	2.11
16	7	22	Full	2PLs	**0.25**	2PLs	PP	SC	32.9	131.6	244.8	252.0	1.03	1.13	1.10	2.11
17	7	22	Full	2PLs	**0.50**	2PLs	PP	SC	65.8	131.6	211.5	219.1	1.04	1.13	1.10	2.11
R	7	22	Full	2PLs	**0.75**	2PLs	PP	SC	98.7	131.6	178.1	186.2	1.05	1.13	1.10	2.10
R	7	22	Full	2PLs	0.75	2PLs	**PP**	SC	98.7	131.6	178.1	186.2	1.05	1.13	1.10	2.10
18	7	22	Full	2PLs	0.75	2PLs	**FP**[b]	SC	180.2	240.3	464.6	257.3	0.55	2.07	1.70	2.68
19	7	22	Full	2PLs	0.75	2PLs	**FF**[c]	SC	205.8	274.4	685.8	184.1	0.27	2.36	1.51	3.25
20	7	22	Full	2PLs	0.75	2PLs	PP	**TF**	98.7	131.6	132.3	NA	-	1.13	1.10	1.76
R	7	22	Full	2PLs	0.75	2PLs	PP	**SC**	98.7	131.6	178.1	186.2	1.05	1.13	1.10	2.10
21	7	22	Full	2PLs	0.75	2PLs	PP	**BF**	98.7	131.6	232.0	NA	-	1.13	1.10	2.51
22	7	22	Full	PL-L/4	0.75	PL-3L/4	PP	SC	39.8	159.1	270.4	341.2	1.26	1.37	1.48	NA

[a] PP: Pin-Pin boundary condition (BC) [b] FP: Fix-Pin BC [c] FF: Fix-Fix BC

FEA $(\omega_{2-\text{FEA}})_b$, which is 1.10 (Column 16). FEA predicted values for the moment gradient factor $(\omega_{2-\text{FEA}})_b$ are obtained in three steps: (1) Omitting pre-strengthening loads and analyzing the beam under the post-strengthening loads, (2) Analyzing the same model under the uniform moment, and (3) dividing the critical moment of step 1 by that of step 2, to obtain a more accurate moment gradient factor $(\omega_{2-\text{FEA}})_b$ than that based on the standard.

For the reference beam, the critical moment of the unstrengthened beam due to pre-strengthening loads M_{ua} as predicted by Eq. (1) is 131.6 kNm (Column 11 in Table 5). As discussed, the applied pre-strengthening loads induce a peak moment ΩM_{ua}, which gives $0.75 \times 131.6 = 98.7$ kNm for the reference beam. The peak moments corresponding to pre- and post-strengthening loads occur at the same location since the pre- and post-strengthening loads have the same distribution, so $M_0 = 98.7$ kNm (Column 10). The predicted value of the post-strengthening critical moment using Eq. (9) with $(\omega_{2-\text{FEA}})_b$ is found to be $M_{\text{cr}-m} = 186.2$ kNm (Column 13).

The ratio $M_{\text{cr}-m}/M_{\text{cr}-\text{FEA}}$ is used to assess the accuracy of the predictions of Eq. (9). When pre-strengthening loads are set to zero, $M_{\text{cr}-m}/M_{\text{cr}-\text{FEA}}$ is very close to unity. However, when the beam is under load prior to strengthening, the accuracy of Eq. (9) will vary. For the reference beam, one has $M_{\text{cr}-m}/M_{\text{cr}-\text{FEA}} = 1.05$ (Column 14), indicating that Eq. (9) overpredicts the post-strengthening critical moment by 4.6%. Similar results are obtained for all runs and reported in Table 5.

The ratio of total flexural capacity of the strengthened beam to that of the unstrengthened beam is a possible indicator of the efficiency of strengthening. For the reference beam, the total flexural capacity of the strengthened beam can be obtained by adding the applied pre-strengthening moment to the FEA predicted post-strengthening critical moment (i.e., $M_0 + M_{\text{cr}-\text{FEA}} = 98.7 + 178.1 = 276.8$ kNm). Thus, the strengthening efficiency attained for the reference beam is defined as $(M_0 + M_{\text{cr}-\text{FEA}})/M_{\text{ua}} = 2.1$ (Column 17 in Table 5), suggesting that the addition of the cover plates is an effective means of increasing the elastic LTB resistance for the beam. Column 17 of Table 5 provides the strengthening effectiveness ratio $(M_0 + M_{\text{cr}-\text{FEA}})/M_{\text{ua}}$ for most cases investigated. Since FEA results indicated that $M_0 + M_{\text{cr}-\text{FEA}}$ does not lead to an accurate estimate of the total flexural capacity for Runs 7, 11, and 22, the strengthening effectiveness ratio is not provided for these cases.

3.5.2 Effect of Strengthening Scheme (Runs R and 4–6)

Equation (9) is not applicable to partial strengthening schemes (i.e., end and midspan strengthening schemes). Thus, the post-strengthening critical moments for these scenarios are obtained only by FEA. These values are then normalized by the corresponding value for the unstrengthened beam $M_{\text{cr}-\text{FEA}-\text{US}}$ to quantify the efficiency of partial strengthening schemes. As Fig. 7 indicates, the end strengthening scheme is 50% more effective than the midspan strengthening scheme. By normalizing the mode shapes relative to the peak lateral displacement, it is shown that the fully strengthened beam shows the least twist at beam end (Fig. 8b), followed by the end

Fig. 7 Effect of strengthening schemes on the post-strengthening critical moments normalized relative to the critical moment of the unstrengthened beam
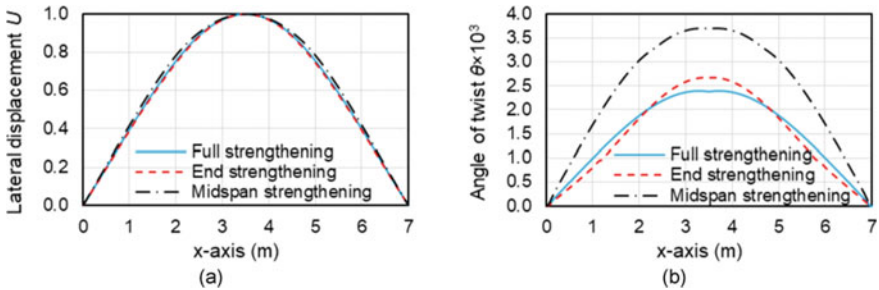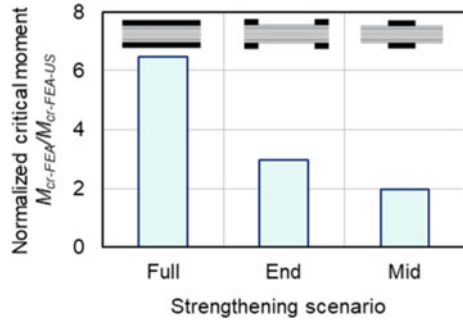
Fig. 8 Normalized mode shapes for Runs R and 4–6 **a** Lateral displacement, and **b** Angle of twist

strengthening scheme, while the largest angles of twist correspond to the midspan strengthening scheme. The rate of variation in the angle of twist represents the warping deformation, and as Fig. 8b indicates, the warping deformation at the ends of the beam with the end strengthening scheme is close to that of the fully strengthened beam. It is concluded that strengthening the ends of the beam can effectively restrain the warping deformation at these locations and provide an effective and economic means of increasing the critical moment.

3.5.3 Effects of Span to Depth Ratio (Runs R, 2 and 3), Pre-strengthening Moment Fraction (Runs R and 15–17) and Loading Configurations and Locations (Runs R, 7–14 and 22)

Values of M_{cr-m} / M_{cr-FEA} for Runs R, 2, 3, and 15–17 in Table 5 show that L/d and Ω lead to a critical moment ratio that is slightly larger than unity, i.e., Eq. (9) overpredicts the post-strengthening critical moment. Conversely, results for Runs R, 7–14 indicate that the loading distribution before and after strengthening influence the accuracy of the predictions of Eq. (9). When the beam is subjected to a midspan point load prior to strengthening and two point loads at third span points after strengthening (Run 7), Eq. (9) is shown to underpredict the critical moment by 8.0%. Conversely, Eq. (9) overpredicts the result by 15% for Run 11. Another

parameter that can significantly alter the inaccuracy of Eq. (9) predictions, is the load distribution before and after strengthening. The results for Run 22 (Table 5) in which the pre-strengthening point load is applied at $L/4$, and post-strengthening point load is applied at $3L/4$ (Fig. 4), show that Eq. (9) overpredicts the critical moment by 26%.

3.5.4   Effect of Boundary Conditions (Runs R, 18 and 19)

As discussed in Sect. 3.2.2, predictive equations for LTB capacity (e.g., Eqs. (1) and (8)) presented in steel design standards (e.g., ANSI/AISC360 2016, CAN/CSA-S6-19 2019) are derived based on the basic case of a simply supported beam in which weak axis rotation and warping deformation are free at both ends. As a result, these equations are expected to underpredict the critical moment of beams with fixed supports (e.g., Runs 18 and 19 in Table 5). Values of M_{cr-m}/M_{cr-FEA} for Runs R, 18 and 19 (Table 5) show that Eq. (9) accurately predicts the critical moments when both beam ends are free to warp and rotate about weak axis (i.e., Pin-Pin boundary condition relative to twist and weak axis rotation). However, by fixing one end of the beam and restraining warping and weak axis rotation at that point, Eq. (9) underpredicts the post-strengthening critical moment by 45%. Furthermore, by fixing both ends of the beam, Eq. (9) underpredicts the critical moment by 73%, due to the fact that the moment gradient coefficient ω_{2-CSA} in Eq. (9) is not intended for such boundary conditions.

3.5.5   Effect of Load Height (Runs R, 20 and 21)

Equation (9) does not account for the load height effect. In this regard, three cases are considered (Runs R, 20 and 21) and their FEA predicted critical moments are normalized to the critical moment of the reference case $M_{cr-FEA-SC}$, in which the load is applied at the shear center. As results indicate, placing downward transverse load on the top flange decreases the critical moment by 26% while placing the load on the bottom flange increases the capacity by 30% (Fig. 9).

4   Summary and Conclusions

The present study investigates the elastic lateral torsional buckling behavior of flexural steel members that are strengthened with steel cover plates while under loading. For this purpose, a finite element study is developed to investigate the effect of span, strengthening scenarios where only a portion of beam is strengthened, types and location of loading before and after strengthening, magnitude of pre-strengthening

Fig. 9 Load height effect on normalized critical moments
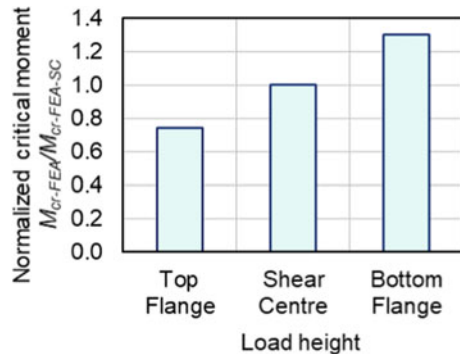
loads, boundary conditions and load height. The following conclusions can be drawn from the present study:

(1). Providing cover plates is an effective means of increasing the LTB resistance of existing steel beams.

(2). End strengthening can be an effective and economic means of strengthening existing steel beams.

(3). While distortional effects tend to have a small/moderate effect on the elastic LTB resistance of most unstrengthened beams, their effect becomes more pronounced in beams strengthened with cover plates. It is thus important to minimize web distortion in strengthened beams by providing transverse stiffeners.

(4). Effective locations for transverse stiffeners include beam ends. Cover plate ends are also shown to be very effective in end strengthening scenarios.

(5). A simplified equation is proposed to estimate the post-strengthening critical moment when distortional effects are suppressed through transverse stiffeners at key locations. The predictions of the equation are in reasonable agreement with finite element results for cases where pre-strengthening and post-strengthening loads have similar distributions. In its present form, the proposed equation is limited to cases of full-strengthening, shear center loading, and beams that are simply supported relative to weak axis rotation and twist.

References

1. Vlasov V (1961) Thin-walled elastic beams. Program for Scientific Translations, Jerusalem, Israel, Israel
2. CAN/CSA-S16–19 (2019) CSA S16: 19, Design of steel structures, Toronto, Canada. In: Canadian standards association
3. ANSI/AISC360 (2016) Specification for structural steel buildings (ANSI/AISC 360–16). American Institute of Steel Construction, Chicago-Illinois
4. MacCrimmon R (2009) Guide for the design of crane-supporting steel structures. Markham, ON, CA
5. Hsu WT, Lue DM, Chen YF (2012) Design aid for moment strength of built-up crane runway girders. Int J Steel Struct 12(3):403–417
6. Hsu WT, Lue DM, Hsiao BT (2009) Numerical approach for torsion properties of built-up runway girders. J Appl Sci Eng 12(4):381–389
7. Pezeshky P, Sahraei A, Rong F, Sasibut S, Mohareb M (2020) Generalization of the Vlasov theory for lateral torsional buckling analysis of built-up monosymmetric assemblies. Eng Struct 221:111055
8. Reichenbach MC, Liu Y, Helwig TA, Engelhardt MD (2020) Lateral-torsional buckling of singly symmetric I-girders with stepped flanges. J Struct Eng 146(10):04020203
9. Liu Y, Gannon L (2009) Experimental behavior and strength of steel beams strengthened while under load. J Constr Steel Res 65(6):1346–1354
10. Liu Y, Gannon L (2009) Finite element study of steel beams reinforced while under load. Eng Struct 31(11):2630–2642
11. Wang Y-Q, Zong L, Zhu R-X, Liu X-Y, Shi Y-J (2015) Behavior of I-section steel beam welding reinforced while under load. J Constr Steel Res 106:278–288
12. Pham PV, Mohareb M, Fam A (2017) Elastic analysis of steel beams strengthened with GFRP plates including preexisting loading effects. J Struct Eng 143(12):04017163
13. Abaqus (2020) Abaqus/CAE user's manual, Dassault Systemes
14. CAN/CSA-S6–19 (2019) Canadian highway bridge design code. In: Canadian standards association
15. Sahraei A, Iranpour A, Mohareb M (2020) User manual for LTB-UO V3.0 (LTB-UO is a computer program for Lateral Torsional Buckling analysis of beams/beam-columns, written at the University of Ottawa), University of Ottawa
16. Barsoum RS, Gallagher RH (1970) Finite element analysis of torsional and torsional–flexural stability problems. Int J Numer Methods Eng 2(3):335–352
17. Liang C, Reichenbach MC, Helwig TA, Engelhardt MD, Yura JA (2022) Effects of shear on the elastic lateral torsional buckling of doubly symmetric I-beams. J Struct Eng 148(3):04021301
18. Pezeshky P, Mohareb M (2018) Distortional lateral torsional buckling of beam-columns including pre-buckling deformation effects. Comput Struct 209:93–116
19. Arizou R, Mohareb M (2021) Design considerations for distortional lateral buckling. J Struct Eng 147(12):04021203

Experimental and Numerical Assessment of the Structural Performance of a Prefabricated Hybrid CLT-steel Floor Module

David Owolabi and Cristiano Loss

Abstract The actualization of optimal structural performance and material efficiency in mass timber construction is often hinged upon hybridizing its structural assembly. This study investigates the out-of-plane static behaviour of a CLT-steel modular composite floor assembly via full-scale bending tests and numerical modelling. The structural performance of the floor assembly and its components under gravity loads are assessed in both ultimate and serviceability limit states. The results show that excellent load-carrying capacity and stiffness are reached, demonstrating that the prototyped floor assembly is a practical low-carbon alternative to steel–concrete composites.

Keywords Prefabricated hybrid CLT-steel floor module · Structural performance

1 Introduction

Hybrid structures are typically employed to provide building systems with efficient design and optimal structural performance [1]. Hybridization can be engaged at the material, element, component or system level. Composite floor systems, for instance, represent a common example of component-level hybridization. In modern timber buildings, steel is commonly used for connectors, restraints and ductile anchor devices. However, timber-steel composite floor technology is still in its infancy with only a handful of existing studies available on their in-plane [2], out-of-plane [3, 4] and vibration behaviour [5, 6], making the implementation of specific design provisions in the next generation of building codes and standards impracticable. In this study, the structural performance of a standardized CLT-steel composite floor module is investigated. The floor prototype leverages both elastic and plastic properties of steel and wood to achieve a structurally efficient prefabricated floor solution.

D. Owolabi · C. Loss (✉)

Sustainable Engineered Structural Solutions Laboratory, University of British Columbia, Vancouver, BC, Canada

e-mail: cristiano.loss@ubc.ca

2　Proposed Hybrid Prefabricated Floor Module

The floor module is a 6-m spanning prefabricated component, consisting of a slender five-ply 85 mm thick CLT panel connected to two 180 mm deep custom-built lightweight cold-formed steel beams (Fig. 1a). The geometry of each beam varies along its length, having an omega-shaped cross-section in the middle (zone 1) and U-shaped profiles at the extremities (zone 2), (Fig. 1b). Perforated steel plates bonded with an epoxy-based grout are used as shear connectors, while self-tapping screws (STS) are installed to minimize the buckling length in the compressed inner regions of the beams (Fig. 1c). Given the faster curing of epoxy-based grout compared with concrete, the ease of installation of screws and the intrinsic lightweight of the modules, the floor module can be prefabricated off-site for quick on-site assembly. Each module is installed by tightening the steel beam ends with high-strength bolts with the desired preload to minimize initial slips. The modules are connected with inclined, fully threaded STS arranged at constant spacing along the edges of the CLT panels. As a result, the floor module is also easily demountable, allowing for end-of-life repurposing of the components in furtherance of sustainability and a circular economic model.

3　Floor Module Design

The floor module was sized assuming a built-up composite section with partial composite action. Stresses in the members and connectors were calculated by solving equilibrium and deformation Newmark's differential equation [7], where materials are assumed linearly elastic and small displacements theory applies. The stresses were checked to comply with their ultimate limit state (ULS) strength requirements stipulated in Eurocode 5 (Committee of European Normalization (CEN) [8]) and Eurocode 3 [9] for wood and steel, respectively. The CLT cross-section depth, spacing of beams, number of shear connectors, shape and thickness of the cold-formed steel beams were defined to force plastic deformation to the steel beams which can progress further to the shear connectors. The CLT panel is capacity-protected to always remain elastic. A deflection limit of $l/300$ as per Eurocode 5 [8], where l is the floor span, was considered under the SLS load combination to check the serviceability limit state performance of the floor. Since the level of discomfort caused by human movement and machines mainly depends on the building's function, vibration check was neglected in the individual floor module design.
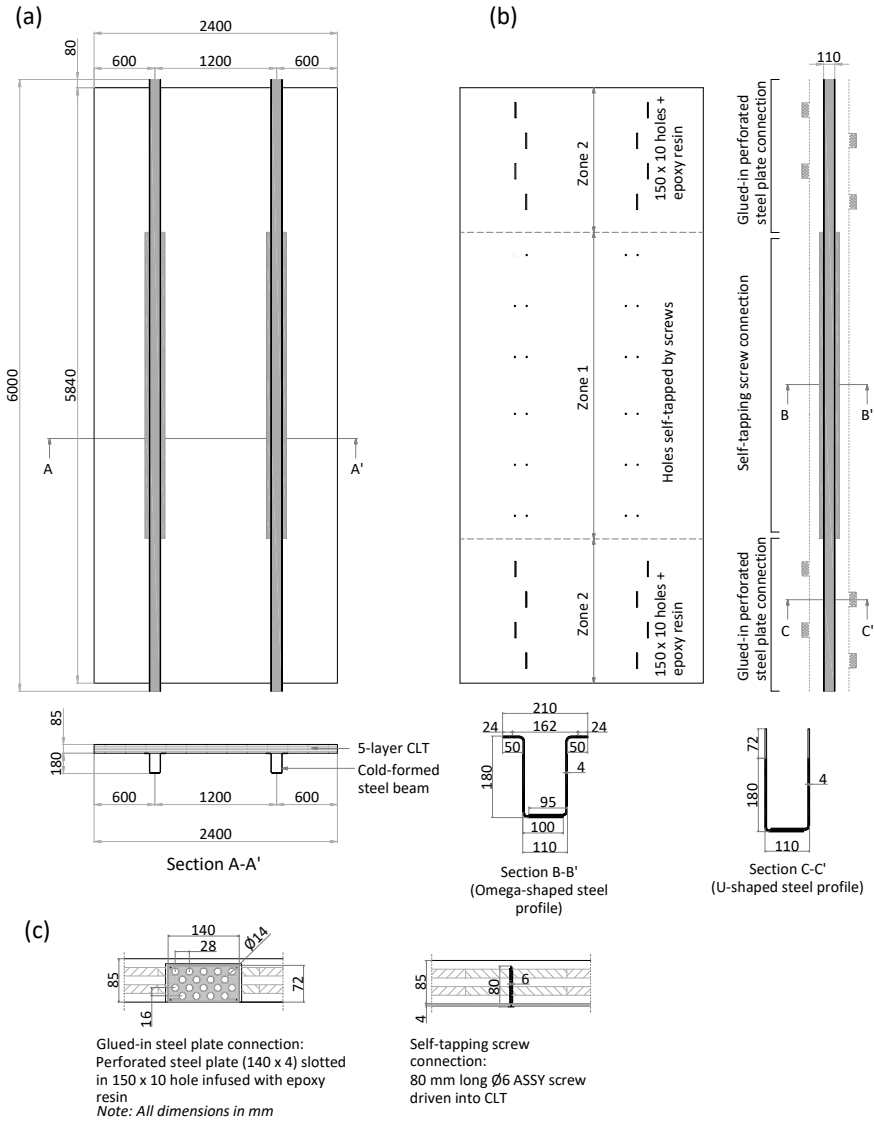
Fig. 1 CLT-steel composite floor module: **a** Fully assembled module; **b** Module components; **c** Slab-to-beam connections

4 Experimental Study

The structural response of the floor module under vertical loads was assessed via six-point bending tests (Fig. 2a). To simulate a uniformly distributed loading condition, a two-level custom-built set-up was adopted. A steel roller was used at each
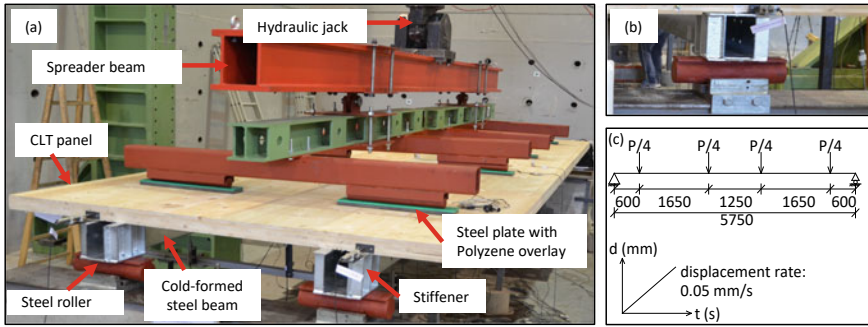
Fig. 2 Composite floor module bending tests overview: **a** Six-point bending test set-up; **b** Simple support detail; **c** Loading protocol

loading point to transmit the load to the floor slab and keep each force centred at the loading position as the floor deflection progressed. Thick steel plates were used to spread the loads from the steel rollers to the CLT slab to prevent localized bearing plastic deformation in the panel. Polyzene sheets were also laid on the steel plates to minimize friction at the roller-plate interface. Simply supported conditions were maintained at the beam ends using auxiliary steel rollers (Fig. 2b). The load was applied through a hydraulic jack at a displacement rate of 0.05 mm/s (Fig. 2c) up to a target mid-span floor deflection of 150 mm.

The floor's bending response was monitored considering each symmetric portion of the double-T cross-section. Linear variable differential transducers (LVDTs) were used to measure the beam-panel slips and floor deflection while strain gauges were installed to measure the local material deformation in the steel and wood. A total of 33 measurement locations were considered to create a robust dataset. The data acquisition system was set to a sampling frequency of 5 Hz. The experiment was conducted in an indoor environment under a controlled air temperature of 20°C and relative humidity between 40 and 55%. Six-point bending tests were also carried out to assess individual elastic properties of the steel beams and CLT panels. The shear connector type in the floor module was previously tested by Loss et al. [10, 11]. Load-slip curves, design parameters and associated failure modes obtained from Loss et al.'s monotonic, cyclic and cyclic-reversed double-shear push-out tests, were adopted within this work.

5 Finite Element Modelling

5.1 Component Model Development

The CLT and steel beams were first modelled and calibrated individually based on the non-destructive component tests data. Each CLT layer was modelled as a single entity using 20-node 3D elements named SOLID186 elements in ANSYS Workbench [12]. Bonded contacts were assigned between the CLT lamella to simulate the glued layers and the support condition was defined with displacement constraints equivalent to a hinge and a roller. Hill's yield criterion [13] was combined with a bilinear isotropic hardening law [14] to capture the orthotropic plasticity of wood. Deflection and strain responses at identical positions as in the experimental set-up were simulated through a monotonic displacement-controlled elastic analysis. A mesh independence study was conducted to ascertain the optimal mesh size for the model by systematically changing the mesh size until a grid-independent result was obtained. The cold-formed steel beams were modelled using SOLID187 elements—10-node 3D elements, while the steel rollers were modelled with SOLID186 elements. Each beam was implemented as a single homogenous solid with hinge and roller supports. The isotropic elastic mechanical properties of the steel beam were defined based on specifications provided by the steel coil manufacturer. The bilinear isotropic hardening law was assigned to the steel beam to define its plastic behaviour, and like in the CLT a mesh independence study was conducted.

5.2 Composite Floor Model Development

The finite element model (FEM) of the composite floor module was developed by assembling the individual FEMs for the CLT panel and cold-formed steel beam (Fig. 3). The STS and grout in the connection systems were modelled with SOLID187 elements. The shear plates, which are part of the steel beams, were bonded to their surrounding grout layers, and the grout layers were subsequently bonded to their adjoining CLT surfaces. Since the STS were only laterally loaded, the withdrawal mechanism of the threaded portions was not considered, and bonded contacts were assigned between the STS and the CLT. The elastic and plastic behaviour of the STS and grout were specified based on experiments carried out by Loss et al. [10, 11]. Nonlinear static analysis was executed with simply supported restraint conditions for the composite floor model. In the analysis, the load was applied stepwise until a mid-span target deflection of 150 mm was reached.
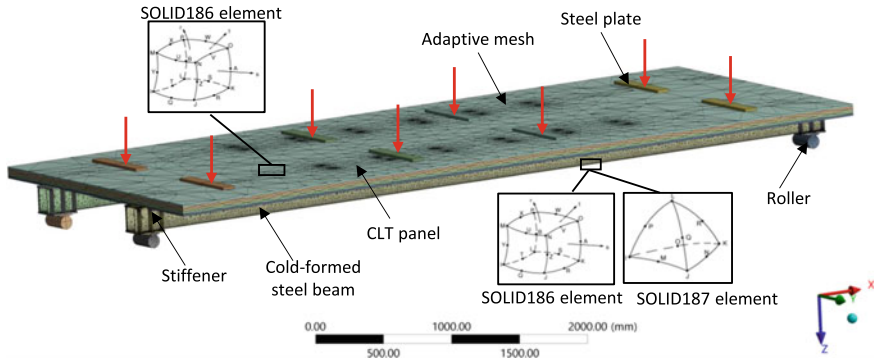
Fig. 3 Finite element model for the composite floor assembly

5.3 Calibration Procedure

Adaptive multiple-objective optimization analyses (MOA) were carried out to calibrate the FEM in ANSYS Workbench [12]. The input values for calibration were the elastic and plastic mechanical properties of wood and steel, set as stochastic variables. Their upper and lower limits were defined so that 90% of the possible elastic and strength values were covered (Table 1). Specifically, these stochastic parameters were the modulus of elasticity (E), tangent modulus (E_t) and yield strength (f_y). The probability density functions (PDF) and coefficients of variation (CoVs) of the stochastic variables were assigned based on the European Probabilistic Model Code (EPMC) (Joint Committee on Structural Safety (JCCS) [15]). A summary of stochastic variables is given in Table 1. Other properties were defined as fixed parameters. The target output variables were strains and deflections recorded at set locations in the experiments. The Pareto-optimal non-dominated solutions returned from the MOA provided a set of candidate values of optimized mechanical properties, from which values producing deformations with the smallest deviation from those experimentally observed were chosen.

6 Results and Discussion

6.1 Out-of-plane Response of the Floor

Table 2 summarizes the mechanical properties of the floor materials and the results of the model calibration. Figure 4a to c show the load–displacement curves of the CLT panel, cold-formed steel beam and floor module while Fig. 4d shows the load-slip monotonic shear response of the shear connector. It can be observed from Fig. 4a to c that the FEM exhibited high accuracy. A slight discrepancy is noticeable along

Table 1 Stochastic parameters for CLT panels and steel beams

Property	CLT panels	Steel beams
CoV of E (%)	0.13	0.03
PDF of E	Log-normal	Log-normal
Range of E (MPa)	9660—14,340[*], 295—445[**]	200,000—220,000
CoV of f_y (%)	0.25	0,07
Distribution of f_y	Log-normal	Log-normal
Range of f_y (MPa)	20.29—44.62[*], 2.41—5.31[**]	354.5—443.89
Range of E_t (MPa)	320—478	2000—2200

[*] longitudinal direction, [**] radial and tangential direction

the curved region of the shear connector's load-slip curve in Fig. 4d, however, this does not compromise the overall simulated behaviour of the floor module shown in Fig. 4c.

The composite floor module exhibited a substantial resistance under out-of-plane loading. Before failure was attained, the proportional limit load (F_Y) detected was thrice the ultimate limit state design load (F_{ULS}). For large deflections in the floor, herein assumed beyond 100 mm in the mid-section, the steel beams suffered severe damage due to shear web buckling while the CLT remained elastic, with no visual damage detected nor material fracture noise during testing. The yield capacity of the composite floor module (343.5 kN) was about five times the characteristic yield load capacity of the steel beam (68.3 kN). The latter was back-calculated from the bending stress relationship $\sigma = My/I$ starting from the declared characteristic yield strength of steel. The mid-span deflection of the floor at service load (F_{SLS}) was equivalent

Table 2 Material properties and calibrated values

Property	CLT panels			Steel beams	Grout
	L	T	R		
E (MPa)	12,000	370	370	210,000[*]	8000
$E_{cal.}$ (MPa)	12,820	350	350	213,060[**]	–
E_t (MPa)	400	–	–	2100[*]	80
E_{t-cal} (MPa)	427	–	–	640[**]	–
f_y (5th %) (Mpa)	21	2.5	2.5	355	70
f_{y-cal} (Mpa)	32.5	3.9	3.9	439.5	–
	LR	LT	RT		
ν	0.42	0.46	0.26	0.3	0.2
τ	4.0	4.0	1.8	–	–

[*] applies to all steel components; [**] applies to steel beam; values for loading plates, rollers and screws were kept constant, *cal.* calibrated value
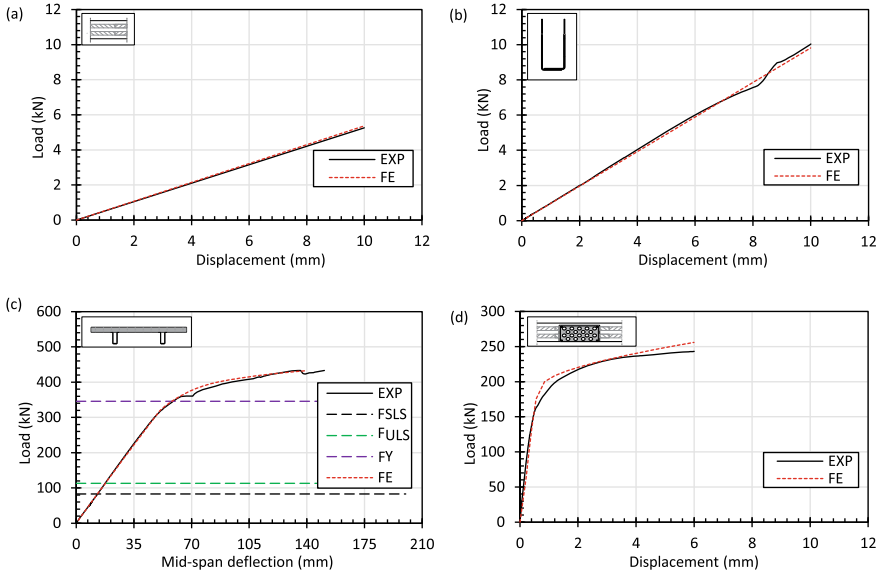
Fig. 4 Load-deformation curves for composite floor components and full assembly: **a** CLT panels; **b** Steel beams; **c** Full assembly; **d** Shear connectors

to span/445, far lower than the recommended limit of span/300 in Eurocode 5 [8]. Also, the effective elastic stiffness of the floor module (6314.8 kN/m) was about six times that of the bare steel beam (1017.4 kN/m) and twelve times that of the CLT panel subjected to six-point bending loading.

6.2 Slip in Beam-slab Interface

Figure 5a shows the wave-like slip distribution at the beam-slab interface. The peak difference between experimental and numerical values was below 20%. Furthermore, the highest slip occurred in the region of the inner connectors and not at the extremities like in composite beams with continuous connectors subjected to uniform gravity loads. This is due to the difference in spacing of connectors in the end regions and the absence of shear connectors in the inner regions of the composite floor assembly. Overall, the shear connectors exhibited high stiffness, providing the composite floor modules with nearly fully composite action under both ultimate and serviceability limit state loading combinations.
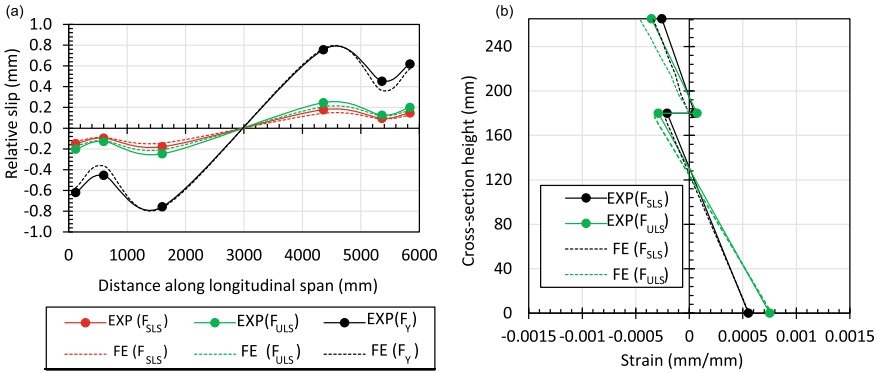
Fig. 5 **a** Beam-panel slip **b** Strain distribution at mid-span cross-section of the composite floor module

6.3 Cross-section Strain Distributions

Figure 5b shows the strain diagrams in the CLT and steel members at the mid-span of the floor module for the ULS and SLS loading conditions. On average, a 15% overestimate was observed in the CLT slab with the finite element strain prediction regardless of the applied load, this error reduces to 5% in the steel beams. The discrepancy resulted from the local variations in the mechanical properties of the CLT lamellae not captured in the model. Also, strain measurements obtained from the strain gauges provided average strains around an area in contrast to the FEM, where the strains are calculated at exact locations. Cross-section strain diagrams showed higher strain across the steel region of the floor module than in the wood region, confirming the floor system's capacity hierarchy of the steel yielding first and the CLT remaining undamaged under static loading conditions.

6.4 Composite Efficiency

The calibrated FEM was further used in studying the composite floor's efficiency under out-of-plane loading by running load–deflection analyses considering different connection scenarios, (i.e. fully rigid and no connection). The floor module's efficiency (E_{ff}) was then estimated using Eq. (1) [16], based on the service load, F_{SLS}.

$$E_{\text{ff}} = \frac{\Delta_{\text{NC}} - \Delta_{\text{SC}}}{\Delta_{\text{NC}} - \Delta_{\text{FC}}} \times 100 \tag{1}$$

where Δ is the mid-span deflection of the composite floor assessed numerically, with subscripts NC and FC referring to no and fully rigid connection scenarios,

respectively, while subscript SC accounts for the effective stiffness of the shear connections used in the study.

An efficiency of 98% was obtained, confirming that the shear stress flow into the individual material sections of the flooring system is optimal. It also indicates that the normal stresses that can be carried in both slab and beams have limits dictated by the weaker material's strength and not the shear connectors.

7 Conclusion

The out-of-plane structural performance of a prefabricated composite double-T-shape composite floor module has been examined. The results provide insight into its bending behaviour and structural performance characteristics such as stiffness, capacity, connection slips, cross-sectional stress and strain distributions and composite efficiency. The findings of this study reveal that:

- The composite floor has very adequate structural capacity. This is evidenced by its yield resistance, which is thrice the ultimate limit state load and its mid-span deflection under serviceability loads which corresponds to span/445, much lower than the limit set in the Eurocode standard for residential floors.
- The shear connectors are characterized by very low slippage resulting in a high degree of composite action and far-greater effective stiffness and strength of the composite floor relative to the bare steel beams.
- The FEM approach is reliable in replicating the material strain, member deformations and overall elasto-plastic behaviour of the floor, with errors lower than 5% on the average at the system scale.
- The floor prototype has the potential to compete as an eco-friendly alternative to mainstream steel–concrete composites.

References

1. Smith I, Frangi A (2014) Use of timber in tall multi-storey buildings. IABSE-SED 13, Zurich, Switzerland
2. Loss C, Frangi A (2017) Experimental investigation on in-plane stiffness and strength of innovative steel-timber hybrid floor diaphragms. Eng Struct 138:229–244

3. Hassanieh A, Valipour HR, Bradford MA (2017) Experimental and numerical investigation of short-term behaviour of CLT-steel composite beams. Eng Struct 144:43–57
4. Loss C, Davison B (2017) Innovative composite steel-timber floors with prefabricated modular components. Eng Struct 132:695–713
5. Chiniforush AA, Makki AM, Dackermann U, Valipour HR, Akbarnezhad A (2019) Vibration behaviour of steel-timber composite floors. Part 1: experimental and numerical investigation. J Constr Steel Res 161:244–257
6. Hassanieh A, Chiniforush AA, Valipour HR, Bradford MA (2019) Vibration behaviour of steel-timber composite floors. Part 2: evaluation of human-induced vibrations. J Constr Steel Res 158:156–170
7. Newmark NM (1959) A method of computation for structural dynamics. J Eng Mech Div 85(3):67–94
8. CEN (2004) EN 1995:1–1: Design of timber structures. Part 1–1: general rules and rules for buildings. CEN, Brussels, Belgium
9. CEN (2005) EN. 1993:1–3: Design of steel structures. Part 1.3: general rules—supplementary rules for cold-formed members and sheeting. CEN, Brussels, Belgium
10. Loss C, Piazza M, Zandonini R (2016) Connections for steel-timber hybrid prefabricated buildings. Part I: experimental tests. Constr Build Mater 122:781–795
11. Loss C, Piazza M, Zandonini R (2016) Connections for steel-timber hybrid prefabricated buildings. Part II: innovative modular structures. Constr Build Mater 122:796–808
12. ANSYS (2021) ANSYS mechanical APDL element reference. ANSYS Inc., USA.
13. Hill R (1998) The mathematical theory of plasticity. Oxford University Press, London, UK
14. Chaboche JA (2008) Review of some plasticity and viscoplasticity constitutive theories. Int J Plast 24(10):1642–1693
15. Joint Committee on Structural Safety (JCCS) (2002) JCSS Probabilistic model code. Part 3: material properties. Retrieved from https://www.jcss-lc.org/jcss-probabilistic-model-code/. Accessed on 3 Mar 2022
16. Gutkowski R, Brown K, Shigidi A, Natterer J (2008) Laboratory tests of composite wood-concrete beams. Constr Build Mater 22(6):1059–1066

Lateral Behavior of a 12-story Modular Building Structure with Vertically Unconstrained Inter-modular Connections, Including a Grouted Slip-resistant Mechanism

Ehsan Bazarchi, Ali Davaran, Charles-Philippe Lamarche, Nathalie Roy, and Serge Parent

Abstract In most industrialized countries, new strategies are being sought to increase the efficiency of manufacturing and construction methods to mitigate the effect of increased labor costs, and the shortage of human resources, on the overall cost of construction projects. Modular building structures have proved to be promising in this regard by enhancing the speed of construction and minimizing on-site activities. In modular building systems, prefabricated volumetric units called "modules" are constructed off-site in a controlled environment and transported to the construction site, where they are assembled using inter-modular connections. Bolted inter-modular connections are generally used to avoid welding on-site. However, because of construction tolerances inherent to bolted connections, the latter are prone to serviceability issues such as slip between the connected elements. For extreme load cases such as earthquakes or wind, the accumulation of inter-story slip displacements/drift can lead to the global instability of the modular building. The inter-modular connections' slip resistance is also crucial because most code provisions do not tolerate any slip under service loads. This study incorporates a grouted slip-resistant mechanism to a basic inter-modular connection concept to prevent slip. Sophisticated nonlinear-static pushover analyses were performed to investigate the lateral behavior of a prototype 12-story modular building, including possible slip effects. The numerical finite element results showed that the proposed grouted mechanism could efficiently control slip displacement in the proposed connection. The lateral displacements of the building were reduced by replacing the basic connections with enhanced connections in the upper six stories.

Keywords Modular building structure · Modular connections · Slip-resistant mechanism

E. Bazarchi · A. Davaran · C.-P. Lamarche (✉) · N. Roy · S. Parent
Université de Sherbrooke, Sherbrooke, QC, Canada
e-mail: Charles-Philippe.Lamarche@USherbrooke.ca

1   Introduction

Modular construction involves assembling a complete structure that comprises prefabricated volumetric units manufactured off-site and installed on-site [1]. Modular building structures (MBS) inherently present significant advantages compared to their conventional counterpart in terms of speed of construction, return on investment, quality, safety, and sustainability, if appropriate construction management strategies are implemented [2, 3]. Some of the constructional advantages of this system were evident during the pandemic when critical situations obliged the hospitals and healthcare organizations to expand the size of their buildings in a very short period of time [4].

Inter-modular connections (IC) are key elements of MBS. ICs typically entail a horizontal component (HC) in one or two directions to link neighboring modules, and a vertical component (VC) for vertically stacked modules [5] (Fig. 1).

The ICs play a critical role in the distribution/transfer of inertial forces of floor and or roof diaphragms within the modules (Fig. 2). The mechanical properties of connections, such as stiffness, strength, and ductility, significantly influence the overall serviceability, strength, safety, and stability of structures [6].

An efficient IC should be structurally resistant, functional, and easy to assemble, requiring the least on-site labor and manufacturing effort possible. Thus, bolted ICs are generally used in the MBS to increase the speed of construction and avoid the use of on-site welding. However, the use of bolted ICs also has some drawbacks. For example, bolted ICs must have suitable tolerances to allow positioning and fastening of the bolts on-site. Providing suitable tolerances and oversized bolt holes can introduce a potential for out of plumb accumulation over multiple stories and a vulnerability to slip displacements under lateral loading [7]. Gunawardena [8] concluded that long slotted holes should be avoided for tall modular buildings due to possible slip accumulation and damage in the columns induced by $P - \Delta$ effects. An accurate understanding of the shear load-slip behavior of IC is particularly important due to the large number of ICs in MBS, which could result in large cumulative displacements over the height of the building [7]. It is important to note that even if the slip would not result in failure or instability of structural components, IC slips cannot be tolerated under service loads [9].

Fig. 1 Illustration of the connection terminology used in MBSs

Connections in MBSs:

⊢ Intermodular connection (IC)

▮ Vertical component (VC)

— Horizontal component (HC)

⌐ Intradmodular connection
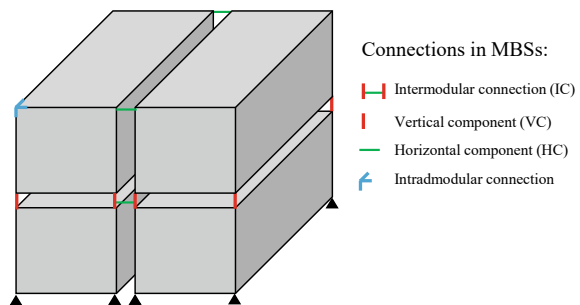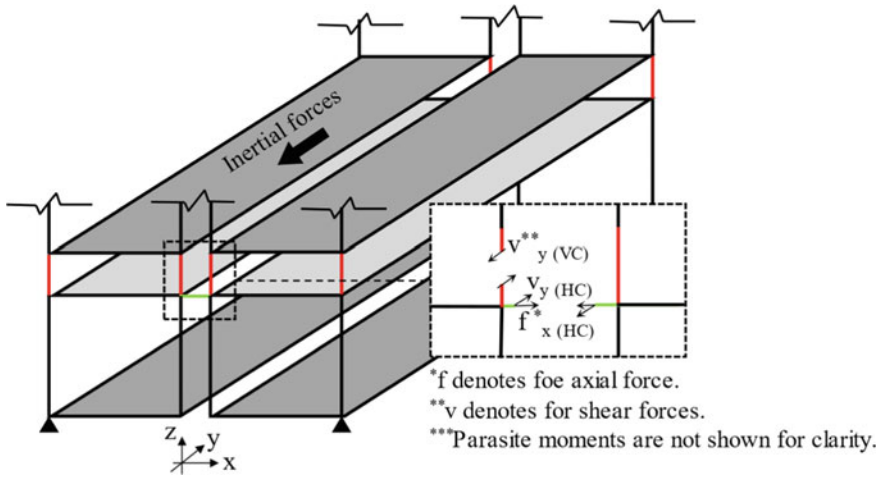
Fig. 2 Transfer of inertial forces of the diaphragm between modules through IC

MBS behaves differently from conventional building systems under gravity and lateral loads (e.g., wind and seismic). The structural behavior of ICs being one of the most contributing factors [10, 11]. Common modeling and design practices might not be suitable for MBSs, and their applicability for MBSs is unknown [12, 13]. For a realistic emulation of the structural behavior of MBSs, simplified IC models incorporated within global models of building structures were proposed in the literature (e.g., [14, 15]). For an efficient implementation of IC into structural MBS models, investigating the twelve degrees of freedom (DOF) (6 DOF for the HC and 6 DOF for the VC) is of paramount importance [14] (Fig. 3).

Portland cement-based grouts have been used in various areas of civil engineering, such as rehabilitation of structures, soil stabilization, and shield tunneling. Grout is a composite material generally consisting of water, cement, and sand. It is typically used to fill voids under machines or other structural elements, seal joints and openings in surfaces, and reinforce existing structures. The use of grouts has been recently introduced to ICs. In the connections proposed by [16], grout was used to resist the uplift in VC of the IC (Fig. 4). In previously proposed ICs, long threaded bolts, self-locking mechanisms, and post-tensioned rods/strands were used to restrain uplift between vertically stacked modules [1, 17, 18].

This study proposes a novel steel connection with a grouted slip-resistant mechanism. This connection is the enhanced version of an uplift-unconstrained connection recently proposed by [20]. The local structural behavior of the basic and enhanced connections is studied herein using volumetric finite element (FE) models. The local behavior of the ICs is introduced by the use of link elements in a sophisticated numerical model of a 12-story prototype MBS with reinforced concrete shear walls as a seismic load resisting system. Nonlinear-static pushover analyses were carried out on the two prototype sub-models: (1) all the ICs are of the "basic" type and; (2) all

Vertical connection components

Horizontal connection components
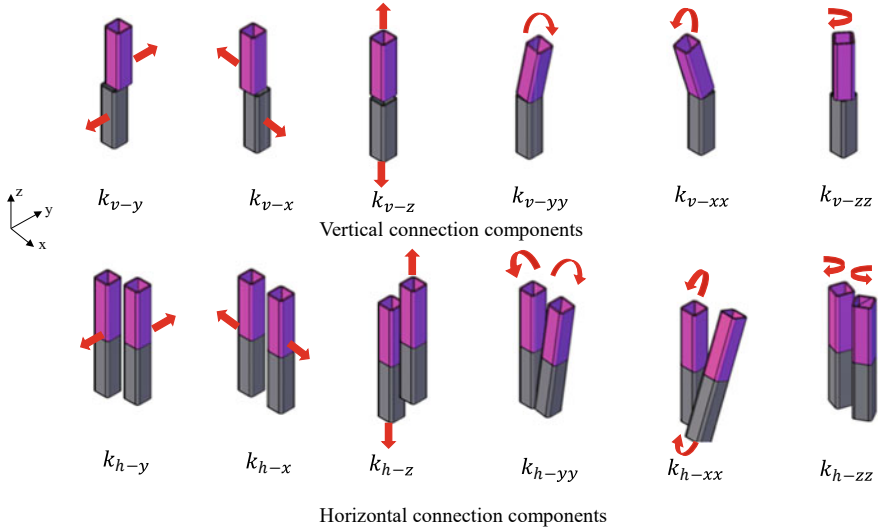
Fig. 3 12 DOFs of the IC (adapted from [14])
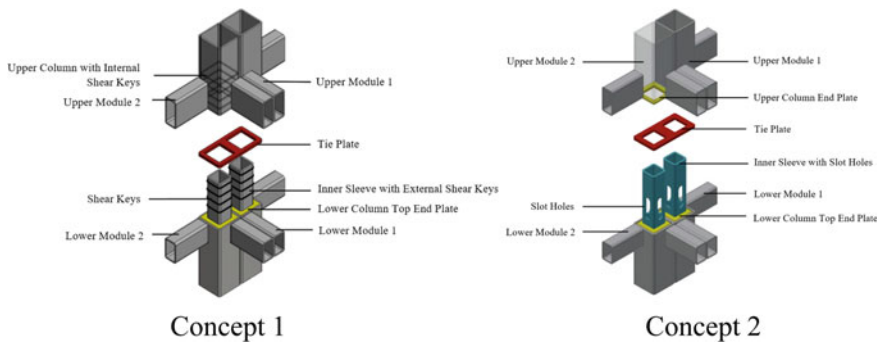
Fig. 4 The connections with grout mechanism [19]

the ICs are of the basic type except the connections of the upper last six stories that are of the "enhanced" type with grout. Finally, the lateral response of both prototype sub-models is compared to one another.

2 Connection with Slip-resistant Grout Mechanism

An uplift-unrestrained IC has been recently proposed for the gravity force resisting modules [20] (Fig. 5a). A perforated tie-plate connecting the columns from adjacent modules acts as the HC in this connection. The vertical connectivity of the stacked
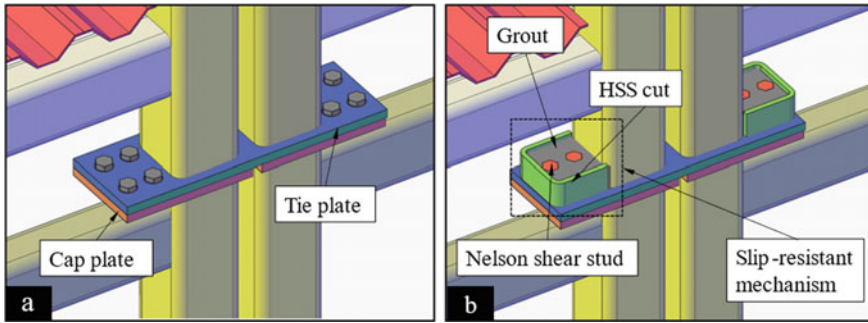
Fig. 5 **a** Basic IC concept; **b** enhanced IC concept with the grouted slip-resistant mechanism

modules is achieved through a male–female mechanism matching the void within HSS columns. Because of the gap tolerance between the inner face of the HSS column and the male–female connection, this connection might be vulnerable to slip under service load at upper story levels of MBSs, where gravity loads carried by the IC decrease with height. As a result, an enhanced form of the basic connection was proposed in which a grouted mechanism is used to block the slip (Fig. 5b). These enhanced connections can be used at selected stories/locations where the possibility of slip exists based upon structural analyses of the MBS. This mechanism consists of a 70 mm deep HSS strip, where one of the flanges was cut and welded at the base of a column (in the factory), and then filled with cement-based grout (on-site). Nelson-type shear studs welded to the tie-plate are embedded within the grouted HSS section strip to ensure an adequate shear force transfer between each story and therefore prevent any slip. Note that implementing the basic connection requires less factory time and on-site activity than the enhanced connection. Consequently, using both types of connections gives more flexibility to designers.

3 Numerical Models

Two scales of numerical models are investigated: (1) *Connection-scale* (local-scale): the structural behavior of the basic and the enhanced IC is investigated numerically using volumetric FE models. Both types of connections are used to capture specific components. FE models developed in [20] calibrated upon experimental tests [21] are used for the basic connections. The calibration procedure is not presented in this paper. Uncalibrated new FE models are used for the slip-resistant connections; (2) *Structural-scale* (global-scale): a beam-element-based structural FE model of a 12 story MBS incorporating "two nodes link" elements (nonlinear springs) to model the behavior of the ICs at the local-scale are used. This structural model is detailed in the following sections.

3.1 Structural Behavior at the Connection-Scale

Investigating the critical behavioral components comprised within the HC's six DOFs and the VC's six DOFs is crucial for accurately modeling the ICs. In the current study, standard advanced modeling techniques widely used by researchers are utilized for modeling some of the critical components/DOFs of both ICs. This methodology aims to reduce the computational efforts necessary to run the numerical models and reduce the number of outputs resulting from the analyses.

3.1.1 Basic Inter-modular Connection

Horizontal Components (HCS) of the Basic Connection

The six DOFs corresponding to the HCs are presented in Fig. 3. The coordinate system is consistent with the one shown in Fig. 2. The basic connection's HC includes a 22.2 mm thick perforated tie-plate attached to the cap plate of the upper part of the HSS of adjacent modules using structural bolts. The rotational components around the x and y-axes were considered unconstrained (k_{h-xx} and k_{h-yy} in Fig. 3). The rotational component around the z-axis (k_{h-zz}) was considered infinitely rigid due to the tie-plate's relatively high in-plane bending stiffness, as recommended by [14]. The translational component in the vertical direction (k_{h-z}) was released due to the low in-plane bending stiffness of the tie-plate around the y-axis. The two last in-plane translational components of the HCs of the basic connection requiring further investigation are the axial and the in-plane shear behavior of the tie-plate connection. The idealized force–displacement behaviors used for both of these components (k_{h-x} and k_{h-y}) are shown in Fig. 6. More details concerning the numerical simulations and the experimental tests can be found in [21].
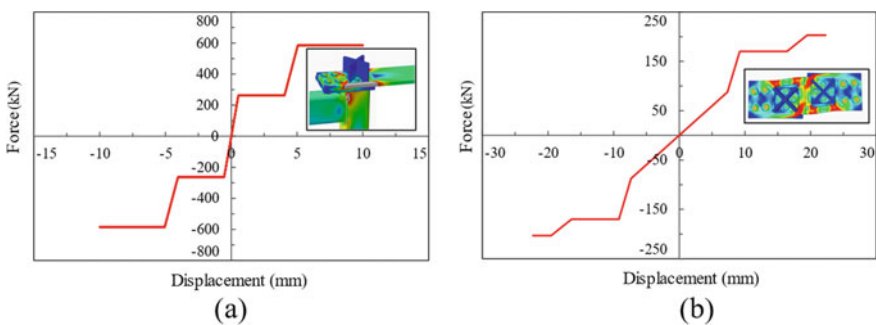
Fig. 6 Force–displacement behavior of the HCs in the x and y dir: **a** k_{h-x}; **b** k_{h-y}
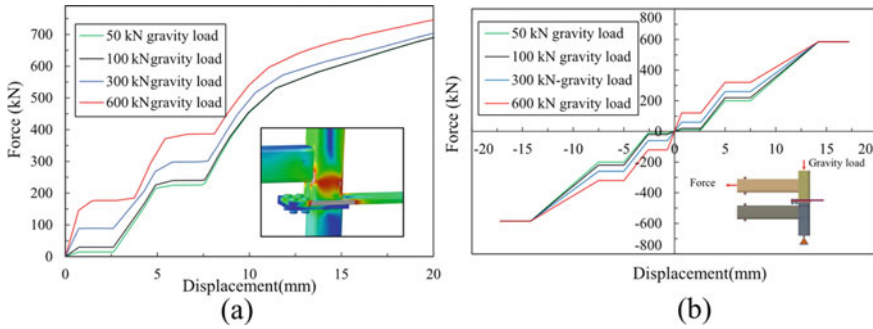
Fig. 7 Shear behavior of the VC (k_{v-x} and k_{v-y}) under different gravity loads: **a** ABAQUS model; **b** simplified models used in the structural models of the MBS

Vertical Components (VCS) of the Basic Connection

The lower part of the corner HSS of upper modules can easily rotate with respect to the plug-in elements due to the gap tolerances between the two components. As a result, no numerical investigations were required to determine the rotational VC components (Fig. 3). Each rotational VC component (k_{v-xx}, k_{v-yy}, k_{v-zz}) were considered unconstrained. The VC cannot prevent the uplift of the upper HSS as dictated by the connection's concept. The shear behavior in both directions (k_{v-x} and k_{v-y}) of the VC is of great importance for accurately emulating the lateral behavior of the MBS. The shear component of the VC includes the slip between the free edge of the top HSS column and the tie-plate before any contact occurs between the upper HSS column and the plug-in element. The results representing the VC's shear behavior obtained from the calibrated numerical model for various gravity loads are shown in Fig. 7a. Note that the numerical model with 50 kN gravity load was calibrated using experimental test results. The related measured friction coefficient between the free edge of the top HSS column and the tie-plate was used to produce the data for the shear behavior of the VC for different gravity loads. Figure 7b shows the simplified behavior used for modeling the VC in the structural model of the MBS.

3.1.2 Enhanced Connection

The component behavior of the HC in the enhanced connection is the same as the basic connection. However, due to the addition of a slip resisting mechanism, the VC of the IC behaves differently compared to the basic connection. Additionally, the grouted mechanism partially blocks the rotation around the *y*-axis in the enhanced connection. As a result, the rotational DOFs cannot be considered perfectly pinned. Numerical analyses were carried out using the ABAQUS software (Dassault [22] to predict the shear and rotational behavior of the VC (k_{v-x}, k_{v-y}, and k_{v-yy}). More details about these numerical models can be found in [21]. Experimental tests were carried out to determine the compression and tensile capacity of the grout. The

compression and tension strength of the grout used for the numerical simulations
are 61, and 3.9 MPa, respectively. The tensile strength was obtained through direct
tensile tests on cylindrical "notched" specimens. The "concrete damaged plasticity"
model of ABAQUS was used to simulate the grout's behavior. This model assumes
that the main two failure mechanisms are the concrete material's tensile cracking and
compressive crushing. In the numerical model, the adopted damage parameters are
summarized in Table 1. The "embedded" constraint was used to model the shear studs
in the grout. Except for the HSS steel floor beam modeled using four nodes (S4R)
shell elements, all other components: HSS columns, HSS strip, Nelson studs, and
grout, were modeled using eight-node linear brick elements with reduced integration
(C3D8R).

The meshed FE model is shown in Fig. 8a. The Von Mises stress contour plot
corresponding to the model intended to capture the shear behavior of the VC is
shown in Fig. 8b (k_{v-x}). Note that the Von Mises contour plot presented in the figure
corresponds to the loading level where the narrow sides of the tie-plate have yielded
in tension in the x-direction.

The Von Mises stress contour plot shown in Fig. 9 corresponds to the loading
case intended to capture the rotational behavior of the enhanced connection (k_{v-yy}).
Because of the asymmetrical geometry of the enhanced connection, the clockwise
and counterclockwise rotational DOFs are investigated separately. For the sake of

Table 1 Damage model parameters used for modeling the grout in ABAQUS

Dilation angle (degree)	Flow eccentricity potential	Ratio of equi-biaxial to uniaxial compressive yield stress (f_{b0}/f_{c0})	Ratio between second stress invariant on the tensile meridian (K)	Viscosity parameter
35	0.1	1.16	0.667	0.007
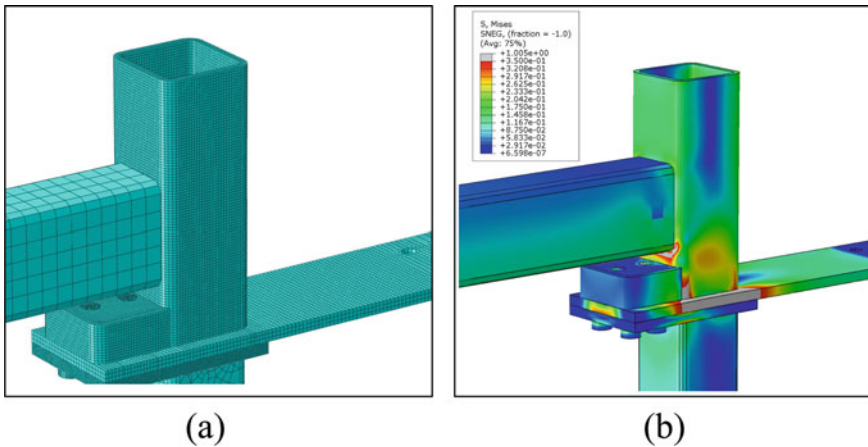
Fig. 8 Numerical model of the enhanced IC intended for capturing the shear behavior of VC:
a meshed model; **b** Von Mises stress contour plot after analysis
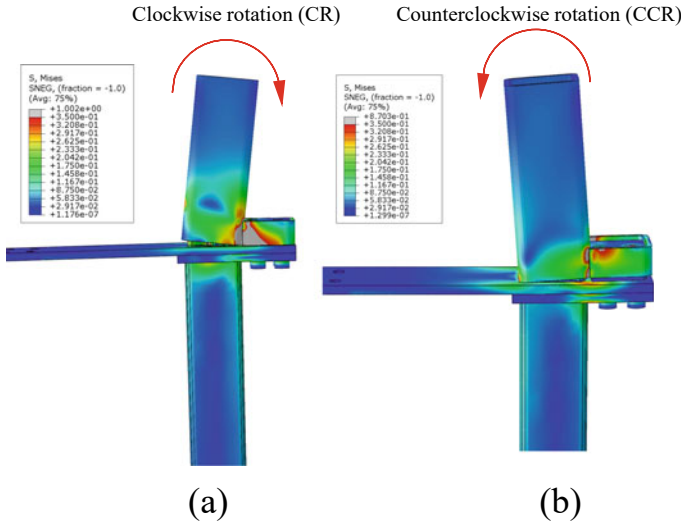
Fig. 9 Von Mises stress contour plots for the rotational behavior of VC: **a** clockwise rotation; **b** counterclockwise rotation

simplicity, it was decided that the most flexible rotational behavior would be used in both directions in the structural MBS models.

The numerical results for the shear and rotational behavior of the VC and the simplified models used in the prototype 12-story building model (presented in the next section) are illustrated in Fig. 10. As shown in Fig. 10a, the grout mechanism fails at a shear force of approximately 400 kN (axial force in the floor beam). After the failure of the grouted mechanism, the shear behavior of the VC connection corresponds to the one obtained from the basic connection model (Fig. 7a). However, in the structural MBS model presented in Sect. 3, the shear demand in any VCs did not exceed the 400 kN threshold. Figure 10b shows that the enhanced connection has a completely different behavior when loaded in the clockwise (CR) or counterclockwise (CCR) directions. The connection exhibits a lower rotational stiffness with higher capacity when loaded in the CCR direction than the CR direction. According to Fig. 10b, a flexural demand of about 33 kN-m is obtained under a 0.025 radians rotation (2.5% story drift).

The shear behavior of the basic and the enhanced connection are compared in Fig. 11. This figure shows that the enhanced connection can control the slip up to a 400 kN shear demand. Once the grouted mechanism fails, the load–displacement behavior of the enhanced connection return to the basic's connection behavior.
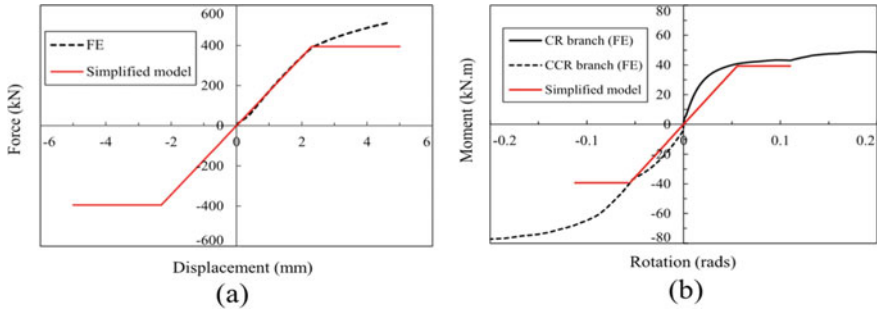
Fig. 10 Behavior of the VC: **a** shear component; **b** rotational component

Fig. 11 Comparison between the behavior of the shear component of the VC in the enhanced and basic connection (gravity load = 50 kN)
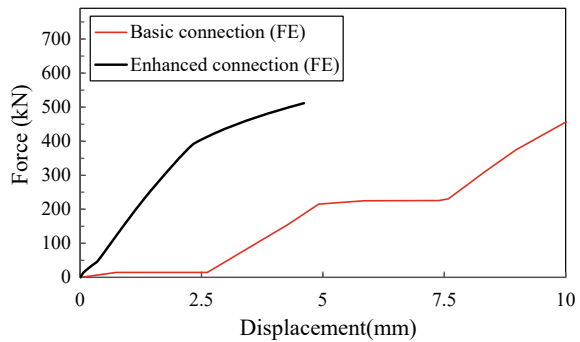
4 Lateral Behavior of the MBS Under Earthquake Loads

The 12-story MBS prototype model presented in Fig. 12a was developed in SAP2000 [23]. The height side by side $21.11 \times 4.14 \times 3.05$ m steel modules vertically stacked up to 12 stories were designed as gravity force resisting modules. RC shear walls were used as a seismic force resisting system (SFRS). Their design was based on over-strength and ductility-related coefficients consistent with the conventional construction type: $R_o = 1.3$ and $R_d = 1.5$) based on CSA-S16-19 [24] and CSA-A23.3–19 [25]. The structure's seismic and wind forces correspond to the city of Gatineau, Quebec [26]. An importance factor of 1.00 was used for the service wind loads. The structure's total height is 41 m. The fundamental period of vibration and the seismic design base shear are 1.64 s and 2275 kN (type C soil type), respectively. Details about the design of the shear walls and the steel members of the modules can be found in [20]. The simplified components' behaviors obtained from the ABAQUS numerical models presented previously were introduced using link elements, as shown in Fig. 12b.

A bare steel deck without concrete topping forms a flexible diaphragm at the floor level of each module. Idealized truss elements are used to consider the diaphragm flexibility in the model. As shown in Fig. 12b, the IC components are introduced
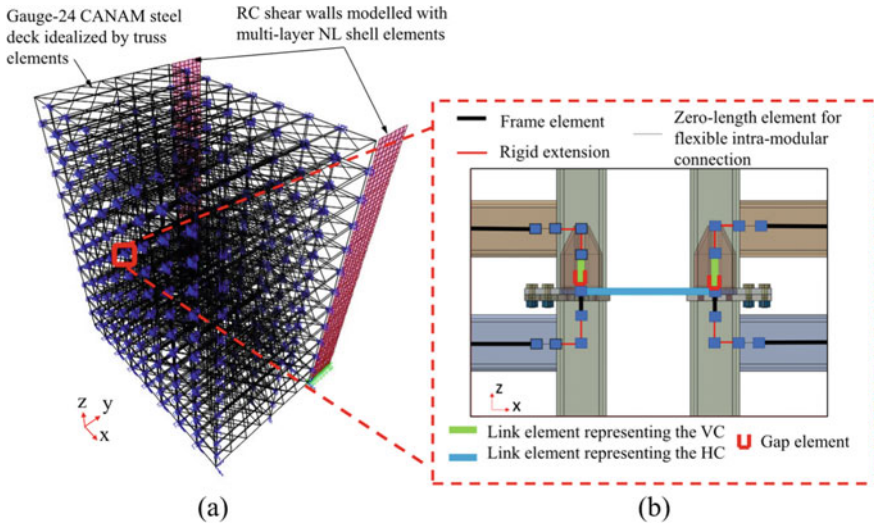
Fig. 12 12-story prototype SAP2000 MBS model: **a** 3D view; **b** details of the connection model

through two different link elements representing the VC and the HC. These links are connected to the beam elements using rigid extensions representing the panel zones. "Gap" elements with "infinite" stiffness under compression forces are defined parallel to the VC link element to capture any uplift in the model during the simulations. Zero-length elements are used to simulate the flexibility of the beam to HSS column connection. The shear component of a VCs is dependent on the column's gravity load. The idealized plan view of the prototype model and tributary areas for interior and exterior columns are presented in Fig. 13 (three per story). As a result, tributary areas for corner and intermediate columns over the 12 levels were necessary. The gravity loads corresponding to the two corner columns with minimum tributary areas at a given story were used to model the two remaining corner columns at the same story. Therefore, two different behaviors were assigned to the shear component of each VCs depending on their location in the building structure (24 in total).
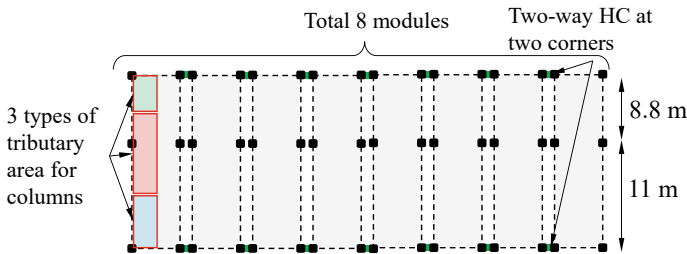
Fig. 13 Plan view of the MBS and typical tributary areas of the columns

5 Nonlinear-static Analyses Results

Nonlinear-static pushover analyses were carried out on two prototype sub-model loaded in the *y*-direction. In the first model (model 1), it was assumed that all the connections were of the basic type. In the second model (model 2), all the connections of the lower six stories were the same as the first model (basic type), and enhanced connections were used in the six upper stories. The pushover curves of these two models are compared in Fig. 14. In both cases, the seismic loads were monotonically applied gradually using the design loading pattern based on the equivalent static design procedure.

In Fig. 14, the base shear corresponding to the service wind and ultimate seismic design conditions are highlighted. In this figure, the pushover curves for the two models closely follow each other. Under service wind load level, the base shear is equal to 1440 kN, accompanied by a total roof displacement of 72.5 and 69.9 mm for models 1, and 2, respectively. The maximum story drifts in both models were under the prescribed limit of $h_s/500$. The difference in the roof displacement between model 1 and model 2 corresponds to shear sliding the VC at the upper story level in model 1 (model with only basic connections). Such behavior under service loading is unacceptable. The sliding was successfully prevented in model 2 using enhanced connections in the upper story levels.

Under ultimate seismic loading conditions, the base shear is equal to 2275 kN, accompanied by a total roof displacement of 139.7 and 135.0 mm for models 1 and 2, respectively. The difference in the roof displacement between model 1 and 2 corresponds to shear sliding the VC at the two upper story levels in model 1 (model with only basic connections). Contrary to the service limit state, the observed sliding is not critical unless the story drift at those levels exceeds $0.025h_s$ prescribed limit. No story drift at any level under the design earthquake loading exceeded the prescribed limit of $0.025h_s$. The sliding was successfully prevented in model 2 using enhanced connections in the upper story levels as in the wind load case.

Fig. 14 Pushover curves of two models: Base shear versus total roof displacement
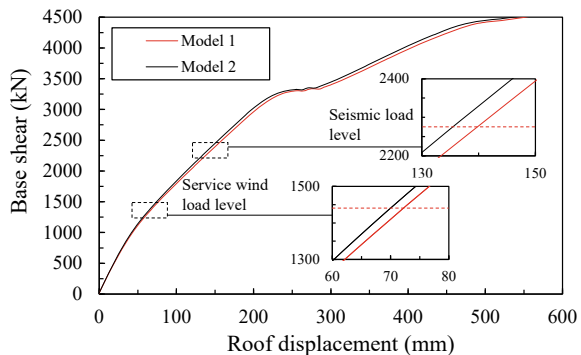
6 Conclusion and Discussion

MBS connections are designed to include gap tolerances to ease the on-site assembly of the modules. The slip accumulated from the gap tolerances makes the MBSs vulnerable to serviceability or instability issues under lateral loads. This study introduces a novel grouted connection to block the potential slip under lateral loads in a recently proposed connection [20]. The components' behavior of the proposed ICs was studied through sophisticated volumetric finite element simulations, and their behavior was implemented into two prototype numerical models of a 12 story MBS in SAP2000. The main findings of the study are as follows:

- By comparing the shear behavior of the VCs of the basic and the enhanced connection, it can be concluded that the enhanced connection can efficiently prevent slip in the connection up to a 400 kN shear demand.
- Upon analysis of the 12-story building under wind loading, it was demonstrated that the new connection could efficiently prevent sliding under service loads.
- More research is needed experimentally to study the behavior and strength of the new connection.
- More sophisticated analyses of MBS, including nonlinear time histories and calibrated connection behavior, are also needed.

References

1. Chen Z, Liu J, Yujie Y (2017) Experimental study on interior connections in modular steel buildings. Eng Struct 147:625–638. https://doi.org/10.1016/j.engstruct.2017.06.002
2. Ferdous W, Bai Y, Ngo TD, Manalo A, Mendis P (2019) New advancements, challenges and opportunities of multi-storey modular buildings—a state-of-the-art review. Eng Struct 183:883–93. https://doi.org/10.1016/j.engstruct.2019.01.061
3. Kamali M, Hewage K (2016) Life cycle performance of modular buildings: a critical review. Renew Sustain Energy Rev 62:1171–1183. https://doi.org/10.1016/j.rser.2016.05.031
4. Gatheeshgar P, Poologanathan K, Gunalan S, Shyha I, Sherlock P, Rajanayagam H, Nagaratnam B (2021) Development of affordable steel-framed modular buildings for emergency situations (Covid-19). Structures 31(February):862–875. https://doi.org/10.1016/j.istruc.2021.02.004
5. Rajanayagam H, Poologanathan K, Gatheeshgar P, Varelis GE, Sherlock P, Nagaratnam B, Hackney P (2021) A-state-of-the-art review on modular building connections. Structures 34(September):1903–1922. https://doi.org/10.1016/j.istruc.2021.08.114

6. Srisangeerthanan S, Hashemi MJ, Rajeev P, Gad E, Fernando S (2020) Review of performance requirements for inter-module connections in multi-story modular buildings. J Build Eng 28:101087. https://doi.org/10.1016/j.jobe.2019.101087
7. Lacey AW, Chen W, Hao H, Bi K (2019) New interlocking inter-module connection for modular steel buildings: experimental and numerical studies. Eng Struct 198(May):109465. https://doi.org/10.1016/j.engstruct.2019.109465
8. Gunawardena T (2016) Behaviour of prefabricated modular buildings subjected to lateral loads
9. Annan CD, Chiza A (2013) Characterization of slip resistance of high strength bolted connections with zinc-based metallized faying surfaces. Eng Struct 56:2187–2196. https://doi.org/10.1016/j.engstruct.2013.08.040
10. Lacey AW, Chen W, Hao H, Bi K (2018) Structural response of modular buildings—an overview. J Build Eng 16:45–56. https://doi.org/10.1016/j.jobe.2017.12.008
11. Lacey AW, Chen W, Hao H, Bi K (2020) Effect of inter-module connection stiffness on structural response of a modular steel building subjected to wind and earthquake load. Eng Struct 213:110628. https://doi.org/10.1016/j.engstruct.2020.110628
12. Annan C-D (2009) Applicability of traditional design procedures to modular steel buildings. University of Western Ontario
13. Gunawardena T, Ngo T, Mendis P (2016) Behaviour of multi-storey prefabricated modular buildings under seismic loads. Earthq Struct 11(6):1061–1076. https://doi.org/10.12989/eas.2016.11.6.1061
14. Chua YS, Richar JYL, Pang SD (2020) Modelling of connections and lateral behavior of high-rise modular steel buildings. J Constr Steel Res 166:105901. https://doi.org/10.1016/j.jcsr.2019.105901
15. Lacey AW, Chen W, Hao H, Bi K (2021) Lateral behaviour of modular steel building with simplified models of new inter-module connections. Eng Struct 236:112103. https://doi.org/10.1016/j.engstruct.2021.112103
16. Dai Z, Pang SD, Liew JYR (2020) Axial load resistance of grouted sleeve connection for modular construction. Thin-Walled Struct 154(February):106883. https://doi.org/10.1016/j.tws.2020.106883
17. Dai XM, Zong L, Ding Y, Li Z-X 2019. Experimental study on seismic behavior of a novel plug-in self-lock joint for modular steel construction. Eng Struct 181:143–164. https://doi.org/10.1016/j.engstruct.2018.11.075
18. Sanches R, Mercan O, Roberts B (2018) Experimental investigations of vertical post-tensioned connection for modular steel structures. Eng Struct 175(August):776–789. https://doi.org/10.1016/j.engstruct.2018.08.049
19. Dai Z, Clarenc TYC, Pang SD, Liew JYR (2021) Experimental study of grouted sleeve connections under bending for steel modular buildings. Eng Struct 243:112614. https://doi.org/10.1016/j.engstruct.2021.112614
20. Bazarchi E, Davaran A, Lamarche C-P, Roy N, Parent S (2020) Nonlinear behaviour of hybrid modular steel structures with reinforced concrete shear walls. In: 17th World conference on earthquake engineering, Sendai, Japan
21. Bazarchi E, Davaran A, Lamarche CP, Roy N, Parent S (2023) Experimental and numerical investigation of a novel vertically unconstrained steel inter-modular connection. Thin-Walled Struct 183:110364
22. Dassault Systèmes (2020) Abaqus Unified FEA
23. CSI (2019) SAP2000 Integrated software for structural analysis and design
24. CSA-S16 (2019) Design of steel structures: CAN/CSA-S16–19. Canadian Standards Association
25. CSA-A23 (2019) Design of concrete structures: CAN/CSA-A23.3–19. Canadian Standards Association
26. NRC (2015) National building code of Canada (NBCC). In: National research council of Canada

Lateral Torsional Buckling Resistance of Gerber Beams Under Gravity and Uplift Loads

R. Arizou and M. Mohareb

Abstract A recent study developed a family of finite elements for determining the elastic buckling strength of beams with wide flange sections. The formulation accounts for web distortion by treating it as a Kirchhoff thin-plate while treating each of the flanges as a Vlasov beam. The solution is equipped with the features needed to model the Gerber beam systems: (1) evoking or eliminating web distortional effects, (2) inserting discrete lateral restraints at any or both flanges at user-specified locations, (3) providing a distortion diagram that characterizes the distribution of web distortion along the span as the beam buckles laterally, and (4) incorporating transverse stiffeners into the model to suppress distortion at user-specified locations. By exploiting these features, a systematic design methodology is developed to optimize the transverse stiffener configuration, thus maximizing the critical moment resistance of Gerber beam systems. A systematic parametric study is then conducted for the problem and recommendations are made for optimizing their lateral torsional buckling resistance under gravity and uplift loading.

Keywords Elastic distortional buckling resistance · Gerber beams

1 Introduction

The Gerber beam system is a structural system that is commonly used for roofs of steel single-storey structures. It consists of a beam spanning between columns (back-span) with cantilever overhangs (cantilever spans). Each of the overhangs is intended to support a beam segment from the adjacent span (suspended span) (Fig. 1). The ease of construction of this system makes it an attractive and economical roofing system for single-storey commercial structures in shopping centres, warehouses, etc.

Historically, the Gerber system was devised by introducing internal hinges between the overhang tips and the suspended span to realize two advantages

R. Arizou (✉) · M. Mohareb
University of Ottawa, Ottawa, ON, Canada
e-mail: Rariz027@uottawa.ca
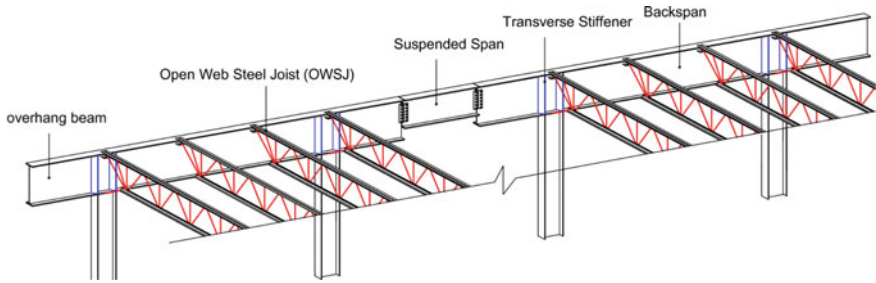
Fig. 1 Gerber system

(a) ensuring the system is statically determinate and hence non-susceptible to the effects of differential settlements, thermal stresses, etc., and (b) optimizing the ratio of cantilever span to back-span such that the maximum negative bending moments at the column location is nearly equal to the maximum positive moment at the middle of the back-span, with the intent of making full usage of the flexural yield resistance of the beam cross-section.

In roof systems, Gerber systems are commonly made of wide flange beams. Regularly spaced open-web steel joists (OWSJ) are connected perpendicular to the axis of the Gerber beams. Loads from the roof system are collected by OWSJs and transmitted to the Gerber beams as point loads applied at joist-to-beam junctions.

At column locations, it is common to connect the top and bottom chords of OWSJs to both flanges of Gerber beams, thus providing lateral bracings at these locations. In between columns, it is more common to connect only the top chord of OWSJ to the top flange of the Gerber beam, thus providing a lateral restraint only to the top flange. Vertical loads acting on the suspended spans are transmitted to the Gerber beams via point loads applied to the overhang tips. Vertical loads can act downward due to the action of gravity forces or upward due to the action of wind uplift and the resulting load combinations of these loads can thus be upward or downward depending on the gravity and wind uplift magnitudes. Typically, Gerber beams are made of wide flange members that bridge relatively long spans. Under gravity or uplift load, they are subjected to major-axis bending moments that alternate between negative and positive values, thus inducing compressive stresses on parts of both flanges within the back-span. When such compression zones in the flanges are laterally unbraced, they become prone to lateral torsional buckling. Also, the cantilever spans of the Gerber system are restrained only partially against warping at the cantilever span roots, which make the use of available design rules for built-in cantilever inapplicable to Gerber systems. Furthermore, there are presently no available methods that reliably capture the interaction between the back-span and cantilever spans when characterizing the lateral torsional buckling capacity of the Gerber system. It is thus of interest to investigate the LTB capacity of the Gerber system in the light of the bracing influence of OWSJs and the arrangement of transverse stiffeners.

2 Literature Review

The Canadian steel design standard (CSA S16:19) identifies three possible modes of failure for flexural members with laterally unsupported segments; material failure, inelastic LTB, or elastic LTB. For beams of Class 1 or Class 2, CSA S16:19, the nominal flexural resistance M_n for the flexural member is given by

$$M_n = \begin{cases} M_P & M_u / M_P \geq 2.15 \\ 1.15 M_P \left(1 - 0.28 M_P / M_u\right) & 2.15 \geq M_u / M_P \geq 0.67 \\ M_u & 0.67 \geq M_u / M_P \end{cases} \qquad (1)$$

in which M_u is elastic critical moment, and $M_P = Z_x F_y$ is the plastic moment where Z_x being the plastic section modulus. When $M_u / M_P \geq 2.15$, the strength of the member is governed by yielding considerations rather than LTB. When $M_u / M_P \leq 0.67$, the member strength is governed by elastic LTB failure, and when $2.15 \geq M_u / M_P \geq 0.67$ the member resistance is governed by inelastic LTB failure. The elastic LTB critical moment M_u provided in standards is based on the thin-walled beam Vlasov theory [1] which assumes that (i) beam cross-section does not distort throughout buckling, (ii) shear deformation within the mid-surface of the section are negligible, and (iii) pre-buckling deformations are negligible, i.e. the sagging configuration of the beam under transverse loads can be approximated by the straight undeformed beam. Based on a modified version of the Vlasov beam theory, CSA S16:19 provides expressions for critical moments for laterally unsupported beam segments restrained at both ends against twist and lateral displacements and for cantilevers with restraints against lateral displacements, weak axis rotation, twist, and warping at the cantilever root and no restraints at the cantilever tip. Additional approximate treatments are provided to account for the effect of load height effects. Examples of advanced analytical solutions incorporating the effect of discrete lateral and rotational restraints include the work of [2–5].

As implicitly recognized in Clause 13.6.2 of CSA S16:19 related to the Gerber system, the solutions presently available in the standard lack the generality required to apply them for the lateral buckling analysis of Gerber systems which involve an interplay between (a) multi-span beam interactions, (b) the offset of loads from the section shear centre, (c) the softening effect of web distortion throughout buckling, (d) the lateral and rotational restraints offered by adjacent spans, nor (e) the beneficial effect of transverse stiffeners. For these reasons, CSA S16:19 broadly recommends more advanced solutions for determining the LTB resistance of Gerber systems.

A non-exhaustive review of available numerical solutions with some of the relevant aspects as identified in Clause 13.6.2 include the work of [6] and [7] who investigated the effect of discrete lateral and/or torsional restraints and load height on lateral buckling of cantilevers. [8] and [9] developed numerical solutions for predicting LTB resistance of beams with lateral and torsional bracing. Since these solutions are based on the Vlasov beam theory, they do not capture web distortional effects.

A family of LTB solutions exists in the literature in which the web is treated with Kirchhoff thin-plate kinematics while flanges are treated with Vlasov/Gjelsvik kinematics. As a result, such models capture the web distortional effect while treating the flanges as a rigid disk within the plane of the cross-section. Among these studies, the effect of discrete rotational and lateral restraints of I-beams was investigated by [10–13]. The common theme in these solutions is that web buckling deformation is characterized by a cubic polynomial distribution of the lateral displacement along the web height. Most recently, [14] developed a finite element solution that accurately characterizes web distortion throughout buckling by assuming the lateral displacement variation along the web to consist of two linear terms (non-distortion modes) and additional Fourier terms (distortional modes). The number of distortional modes in the analysis can be controlled by the analyst to attain the sought degree of accuracy. The solution captures (a) the load height effect, (b) is able to model lateral braces to the top and/or bottom flange, and (c) is able to naturally model the effect of transverse stiffeners that may suppress web distortion at discrete locations along the beam span. These features naturally lend themselves to the modelling of the lateral buckling of Gerber systems and hence the formulation in [14] will be used in the present investigation. A concise overview of the main aspects of the formulation is hence provided in the following section.

3   Overview of Relevant Past Work

3.1   Finite Element Formulation

The main idea of the distortional LTB finite element developed in [14] is provided. A doubly symmetric I-beam with flange width b and thickness t, web height h and thickness t_W is considered. A transverse line load $q(z)$ is applied to the beam whose line of action is defined by the curve $y_q(z)$ from web mid-height. The total potential energy Π during buckling is

$$\Pi = \Pi_W + \Pi_B + \Pi_T + V \tag{2}$$

where Π_W, Π_B, and Π_T denote the total potential energy contributions of web, bottom, and top flanges, respectively, and V denotes the potential energy increase caused by load $q(z)$ undergoing vertical displacement due to web deformation. The web is treated as Kirchhoff thin-plate [15] while flanges are treated as Gjelsvik beams [16]. The total potential energy terms Π_W, Π_B, and Π_T and destabilizing term due to load V due to the load height effect can be expressed in terms of the lateral displacement of web $u(y, z)$ as

$$\Pi_W = \int_0^L \int_{-h/2}^{h/2} \left(\frac{D}{2} \left(\begin{array}{c} u_{,yy}^2 + u_{,zz}^2 + 2\mu\, u_{,yy} u_{,zz} \\ +2\,(1-\mu) u_{,yz}^2 \end{array} \right) \atop -\frac{\lambda}{2} \left(\sigma t_W u_{,z}^2 + 2 t_W \tau u_{,y} u_{,z} \right) \right) dy\, dz \qquad (3a)$$

$$\Pi_B = \frac{1}{2} \int_0^L \left(\begin{array}{c} EI_{yF} u_{,zz}^2 + EC_{wF} u_{,yzz}^2 + GJ_F u_{,yz}^2 \\ -\frac{\lambda}{2} \left(\sigma A_F u_{,z}^2 + \sigma I_{yF} u_{,yz}^2 \right) \end{array} \right)_{y=h/2} dz \qquad (3b)$$

$$\Pi_T = \frac{1}{2} \int_0^L \left(\begin{array}{c} EI_{yF} u_{,zz}^2 + EC_{wF} u_{,yzz}^2 + GJ_F u_{,yz}^2 \\ -\frac{\lambda}{2} \left(\sigma A_F u_{,z}^2 + \sigma I_{yF} u_{,yz}^2 \right) \end{array} \right)_{y=-h/2} dz \qquad (3c)$$

$$V = \frac{\lambda}{2} \int_0^L \int_{y=0}^{y=y_q(z)} q u_{,y}^2 dy\, dz \qquad (3d)$$

where μ is Poisson's ratio, G is the shear modulus, and E is Young's modulus. The normal stress distribution $\sigma(z, y)$ and the shear stress $\tau(z)$ in the web are obtained from a pre-buckling static analysis bases on the conventional Euler–Bernoulli beam. The flexural rigidity of the web is $D = Et_W^3 / 12(1 - \mu^2)$. The sectional properties of a single flange are given by $[A_F, I_{yF}, C_{wF}, J_F] = [bt, b^3 t / 12, b^3 t^3 / 144, bt^3 / 3]$ in which A_F is the cross-sectional area, I_{yF} is the moment of inertia of the flange about the y axis, C_{wF} is the local warping constant, and J_F is the Saint–Venant torsional constant. As a convention, all commas denote the partial derivative of the leading field with respect to the argument coordinate. The web lateral displacement throughout buckling $u(y, z)$ is assumed to take the form

$$u(y, z) = \sum_{i=1,2}^{m} \tilde{u}_i(y) \phi_i(z) \qquad (4)$$

in which the cross-sectional deformation moded $\tilde{u}_i(y)$ are taken as

$$\tilde{u}_i(y) = \begin{cases} (1/2 + \eta) & i = 1 \\ (1/2 - \eta) & i = 2 \\ \cos[\pi(i-2)\eta] & i = 3, 5, 7 \ldots \\ \sin[\pi(i-2)\eta] & i = 4, 6, 8 \ldots \eta = y/h \end{cases} \qquad (5)$$

Each cross-sectional deformation mode $\tilde{u}_i(y)$ is assumed to vary along the longitudinal direction z according to a function $\phi_i(z)$. Functions $\phi_i(z)$ are taken as cubic functions which are related to the nodal degrees of freedom of the element

$$\Delta_i^T = \langle \phi_i(0)\ \phi_{i,z}(0)\ \phi_i(L)\ \phi_{i,z}(L) \rangle \qquad (6)$$

through Hermitian polynomials $\mathbf{H}_{1 \times 4}^T(z)$, i.e.

$$\phi_i(z) = \mathbf{H}_{1 \times 4}^T(z)\mathbf{\Delta}_i \tag{7}$$

in which

$$
\begin{aligned}
&\mathbf{H}_{1 \times 4}^T(z) \\
&= \langle (1 - 3\xi^2 + 2\xi^3)\ L(\xi - 2\xi^2 + \xi^3)\ (3\xi^2 - 2\xi^3)\ L(-\xi^2 + \xi^3) \rangle; \\
&(\xi = z/L)
\end{aligned}
\tag{8}
$$

From Eqs. (5) and (7), by substituting for all modes $i = 1, 2, ..., m$ into From Eq. (2), and then into the total potential energy (Eq. 3a–d), one obtains

$$\Pi = \frac{1}{2}\mathbf{\Delta}^T(\mathbf{K} - \lambda\mathbf{G})\mathbf{\Delta} \tag{9}$$

in which $\mathbf{K}$ and $\mathbf{G}$ are the stiffness and the geometric matrices, and $\mathbf{\Delta}^T = \langle \mathbf{\Delta}_1^T \mid \mathbf{\Delta}_2^T \mid \ldots \mid \mathbf{\Delta}_m^T \rangle$ is the nodal displacement vector for the element. The formulation is shown to yield non-distortional critical moments M_{ND} when only the linear modes are included in the analysis, i.e. $m = 2$, and distortional critical movement M_D accurately when a larger number of modes is taken, i.e. $m \geq 6$.

Other features of the formulation are its natural ability to constrain (a) the lateral displacement at the bottom flange by suppressing the first mode $\tilde{u}_1(y)$, (b) the lateral displacement of the top flange by suppressing the second mode $\tilde{u}_2(y)$, and (c) web distortion by suppressing the distortional modes $\tilde{u}_i(y)$, $i = 3, 4, \ldots, m$ [17] at a given cross-section.

3.2 Quantifying Distortion

Solving Eq. (9) yields the degrees of freedom of the system $\mathbf{\Delta}_3$, $\mathbf{\Delta}_4$, $\ldots$, $\mathbf{\Delta}_m$ corresponding to the distortional modes. Equation (7) yields the corresponding magnitude of the distortional modes $\phi_3(z)$, $\phi_4(z)$, $\ldots$, $\phi_m(z)$ along the span. A web distortion configuration $u_D(y, z)$ is defined by combining distortional modes and their corresponding contributions, i.e.

$$u_D(y, z) = \sum_{i=3, 4}^{m} \tilde{u}_i(y)\phi_i(z) \tag{10}$$

The buckled configuration $u_D(y, z)$ is normalized by the lateral displacement of the top flange, which enables comparing web distortion under various loading conditions. For a given section $z = z^*$ along the span, the web can be subdivided into $s - 1$ segments along the height that are delineated by the points (y_k, z^*), $k = 1, 2, ..., s$. The deviation from the non-distortional modes $i = 1, 2$ at a point (y_k, z^*) on the web is given by $u_D(y_k, z^*)$.

We define the Euclidean Norm

$$\overline{u}_D(z^*) = \sqrt{\sum_{k=1}^{k=s} u_D^2(y_k, \, z_j)} \tag{11}$$

as a distortion indicator that characterizes the magnitude of the distortion at section z^*. The intent of $\overline{u}_D(z^*)$ is to serve as an objective to characterize the relative distortion at various sections along a beam span, e.g. for a given member, the condition $\overline{u}_D(z_1^*) > \overline{u}_D(z_2^*)$ implies more distortion at section z_1^* than in section z_2^*.

4 Reference Beam

Figure 2a shows a Gerber beam with two overhangs. As a reference case, beam cross-section is taken as W410 × 39 ($h = 339$ mm, $b = 140$ mm, $t = 8.8$ mm, $t_W = 6.4$ mm). Yield strength is taken as $F_y = 350$ MPa. The back-span is taken as $L_2 = 7.5$ m and the cantilever spans are taken as $L_1 = 1.5$ m. The overhangs are subjected to uniformly distributed line load w_1, and the back-span and suspended span are both subjected to uniformly distributed line load w_2.

Additional point loads P are applied at overhang tips to represent the effect of loads transferred from the adjacent suspended span through the shear connection connecting the suspended span to the cantilever span. Hence, loads P are taken to act at the section mid-height. Since it is common to have equidistant columns, the suspended spans are taken as $L_2 - 2L_1$ and the effect of a suspended span on a cantilever tip is modelled by a point load $P = (w_1/2)(L_2 - 2L_1)$ applied to the mid-height of the overhang tips.

The back-span is assumed to be laterally restrained at the top flange through five equidistantly spaced OWSJs, which are modelled by suppressing the second mode $\tilde{u}_2(y)$ at these locations. Similarly, the overhang tips are restrained against the lateral displacement at the top flange. As it is common practice to additionally connect the bottom chords of OWSJ to the bottom flange at column location, the bottom flange is restrained at column locations by suppressing also the first mode $\tilde{u}_1(y)$ at column location. Additionally, it is common practice to provide transverse stiffeners at column locations to suppress web distortion at these locations. Thus, all distortional modes $\tilde{u}_i(y), \quad i = 3, 4, \ldots, m$ are suppressed at the column locations
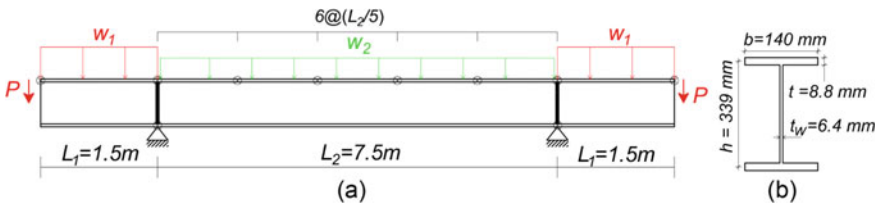
Fig. 2 a Reference Gerber System, and **b** Reference Cross-section

in order to model the effect of transverse stiffeners in suppressing web distortion in these locations.

5   Validation

The model (Fig. 2) was verified against shell FEA results in [17] and experimental results in [14] for simply supported beams. In the following, we expand the verification to include Gerber systems through a comparison against the predictions of shell finite element analysis.

   The reference beam (Fig. 2) is examined under the effect of uniformly distributed loading acting on the back-span and both overhangs of equal magnitude, i.e. $w = w_1 = w_2$. The system is discretized longitudinally using a 105 elements. Buckling analyses are conducted for gravity loading $w > 0$ and for wind uplift loading $w < 0$. Furthermore, a buckling analysis is obtained using the S4R shell finite element, in which the beam is meshed using 350 elements along the span and 16 elements along the flange e width and along the web height.

   For gravity loading, the critical moments predicted by the shell model are 106.4 KNm. This compares to and 116.4 KNm based on the present distortional model, corresponding to a critical moment ratio of 1.09. For uplift loading, the critical moments predicted by the shell model are 357.4 KNm, which compares to and 382.4 KNm based on the present distortional model, corresponding to critical moment ratio of 1.07. The proximity of critical moment ratios to unity indicates is indicative of the ability of the present model to predict the critical moment capacity of Gerber system. Thus, the present model is used in this work for investigating the buckling behaviour of the Gerber systems.

6   Design of Transverse Stiffeners

The case in the previous section is revisited here. The distortional critical moment is obtained using 16 modes of deformation while the non-distortional critical moment is obtained using 2 modes of deformation. The distortion indicator $\overline{u}_D$ is computed for both loading cases at all cross-sections based on Eq. (11), yielding the distortional indicator plot shown in Fig. 3a.

   For gravity loading, one obtains $(M_D)_{\text{gravity}} = 116.4$ KNm and $(M_{\text{ND}})_{\text{gravity}} = 134.3$ KNm. The difference is attributed to distortional effects in the web which are captured in the former model but suppressed in the later model. Also, for wind uplift loading, one obtains $(M_D)_{\text{uplift}} = 382.4$ KNm and $(M_{\text{ND}})_{\text{uplift}} = 489.0$ KNm. The plastic moment for the section is $M_P = 274.9$ KNm.

   The above critical moments correspond to $(M_D / M_{\text{ND}})_{\text{gravity}} = 0.87$ for gravity loading, and $(M_D / M_{\text{ND}})_{\text{uplift}} = 0.78$ for uplift loads. A relatively small ratio
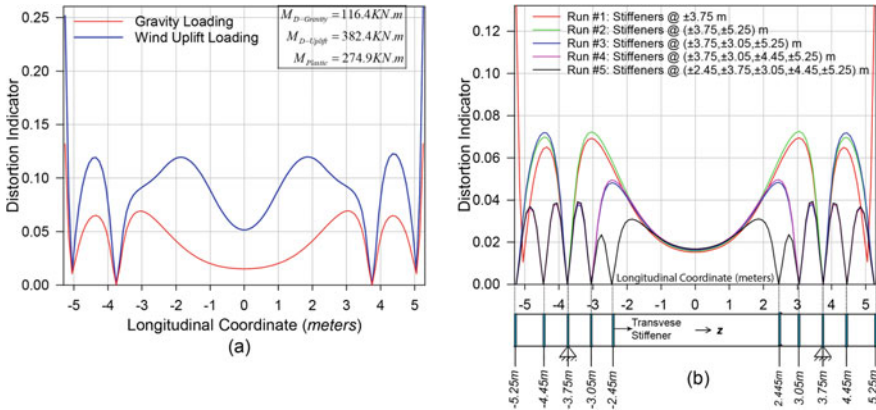
Fig. 3 **a** Distortion indicator obtained for the reference Gerber subjected to uplift and gravity loading, **b** Distortion indicator for various transverse stiffener scenarios

M_D / M_{ND} is indicative of the amount of distortion in the system and flags the potential capacity increase that can be achieved by providing transverse stiffeners that suppress distortion. The above ratios thus suggest a potential increase in critical moment capacity of 13% in the case of gravity loading and by 22% in the case of uplift loading.

However, according to Eq. (1), the nominal moment M_n can be enhanced insofar as the ratios of distortional critical moment to plastic moment $M_u / M_P = M_D / M_P$ does not exceed 0.67. One obtains $(M_D / M_P)_{\text{gravity}} = 0.42 < 0.67$ indicating that the nominal capacity is governed by elastic LTB in this case. The provision of transverse stiffeners to increase the elastic distortional critical moment capacity results in a directly proportional increase in the nominal capacity $M_n = M_D$ in this case.

For uplift loading, one has $(M_D / M_P)_{\text{uplift}} = 1.39$, which lies in the inelastic LTB range $2.15 \geq (M_D / M_P)_{\text{uplift}} \geq 0.67$. The corresponding nominal capacity as given by $M_n = 1.15 M_P (1 - 0.28 M_P / M_u)$ still benefits from an increase in the elastic distortional critical moment $M_u = M_D$ albeit the increase in M_n attained is comparatively less than that achieved by the increase in elastic critical moment M_D. For example, for $(M_D / M_P)_{\text{uplift}} = 1.39$, the nominal capacity ratio is $(M_n / M_P)_{\text{uplift}} = 1.15(1 - 0.28/1.39) = 0.918$. If enough transverse stiffeners are provided so as to increase $M_{D-\text{uplift}}$ by 10%, the ratio $(M_D / M_P)_{\text{uplift}}$ increases to 1.52, which still lies within the inelastic LTB range $2.15 \geq (M_D / M_P)_{\text{uplift}} \geq 0.67$ and the corresponding nominal capacity ratio increases to $(M_n / M_P)_{\text{uplift}} = 1.15(1 - 0.28/1.52) = 0.938$, which corresponds to a 2.2% increase in the nominal inelastic buckling resistance. The provision of transverse stiffeners in this case has a minor effect on increasing the nominal capacity of the system. Thus, in the following discussion, the arrangement of the transverse

stiffeners will be obtained based on gravity loading considerations, rather than uplift loading.

Trial #1: Transverse stiffeners are provided solely at the column locations $z = \pm 3.75$ m. The critical moment ratio as determined from the analysis is found to be $(M_D / M_{ND})_{\text{Gravity}} = 0.86$ and the distortion indicator is found to peak at the overhang tips $z = \pm 5.25$ m (Fig. 3b) suggesting that suppressing distortion (by providing transverse stiffeners at these locations) would reduce distortion in the system.

Trial #2: In addition to providing transverse stiffeners at sections $z = \pm 3.75$ m, transverse stiffeners are added at overhang tips $z = \pm 5.25$ m. The critical ratio is found to increase to $(M_D / M_{ND})_{\text{Gravity}} = 0.89$ and the distortion indicator new peaks are found to occur at $z = \pm 3.05$ m(Fig. 3b). Additional transverse stiffeners are thus provided at these locations for Trial 3. The process is repeated until the condition $(M_D / M_{ND})_{\text{Gravity}} \geq 0.95$ is attained. Table 1 shows the gradual increase in the critical moment ratio attained by the successive addition of stiffeners. Also, Fig. 3b shows the distortion indicator distribution for each trial. In general, the location(s) of peak distortion indicator(s) at Trial i will determine the optimum location of the stiffener(s) in Trial $i + 1$.

7 Parametric Study: Effect of Geometry on Critical Moments

7.1 Model Description

The reference beam (Fig. 4) described in Sect. 4 is examined in this section by assuming that the uniformly loads acting on the overhangs and the back-span to have equal magnitudes, i.e. $w = w_1 = w_2$. The back-span length is $L_2 = 7.5$ m, with two cantilevers each spanning $L_1 = 1.5$ m. The suspended spans are assumed to have the length $L_2 - 2L_1$, and subjected to a uniformly distributed load w. The actions of the suspended spans are modelled by point loads $P = (w/2)(L_2 - 2L_1)$ applied to the mid-height of the overhang tips.

The reference case has the non-dimensional parameters $b/t = 15.90, h/t_W = 52.97, b/h = 0.41, L_2/L_1 = 5.0$, and $L_2/h = 22.1$. A parametric study is conducted by varying one of the five dimensionless parameters ($b/t, h/t_W, b/h,$ L_2/L_1, and L_2/h) and keeping the remaining four parameters unchanged from those of the reference case. Table 2 provides the maximum and minimum values for $b/t, h/t_W$, and b/h obtained by scanning W cross-sections in the Handbook of Steel Construction. In the present parametric study, the selected ranges for non-dimensional parameters overlap with those based from the Handbook of Steel Construction.

A total of 181 geometries were considered. Two types of loading were applied to each geometry: gravity loading $w > 0$ and uplift loading $w < 0$. For each case, the

Table 1 Information obtained from each trial in the proposed design procedure for transverse stiffeners

Trial #	Coordinates (metres)		Distortional LTB critical	Ratio	Terminate?
	Transverse stiffeners	Maximum distortion indicator	Moment $(M_D)_{\text{Gravity}}$ (KNm)	$\left(\frac{M_D}{M_{\text{ND}}}\right)_{\text{Gravity}}$	
1	± 3.75	± 5.25	116.4	0.87	No
2	$\pm 3.75,\ \pm 5.25$	± 3.05	121.1	0.90	No
3	$\pm 3.75,\ \pm 5.25,\ \pm 3.05$	± 4.45	123.8	0.92	No
4	$\pm 3.75,\ \pm 5.25,\ \pm 3.05,\ \pm 4.45$	± 2.45	126.6	0.94	No
5	$\pm 3.75,\ \pm 5.25,\ \pm 3.05,\ \pm 4.45,\ \pm 2.45$	–	127.9	0.95	Yes
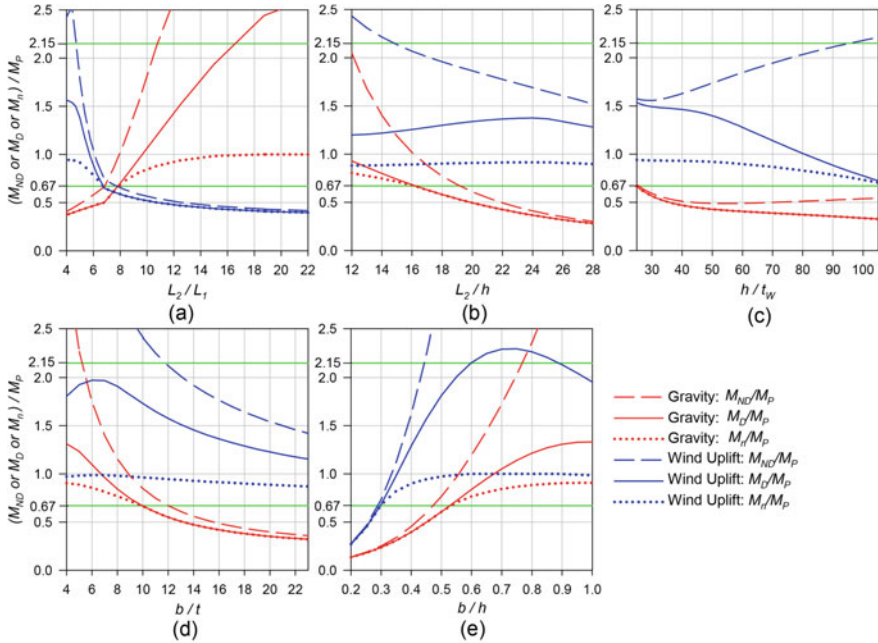
Fig. 4 Gerber system subjected to uplift forces on the reduction of critical moments against variation in **a** back-span to overhang span ratio L_2 / L_1, **b** normalized back-span L_2 / h, **c** web slenderness h / t_W, **d** flange slenderness b / t, and **e** aspect ratio b / h

Table 2 Ranges of non-dimensional parameters used in the parametric investigation

	Parameters				
	h / t_W	b / t	b / h	L_2 / L_1	L_2 / h
Lower bound in CISC database	7.3	3.6	0.2	–	–
Upper bound in CISC database	66	23	1.0	–	–
Lower bound used in this study	25	4	0.2	4	12
Upper bound used in this study	105	24	1.0	22	28

elastic critical moments were obtained by retaining only modes 1 and 2 leading to the non-distortional critical moment M_{ND}. Also, the distortional critical moment M_D was obtained by employing 16 modes. The total number of runs is thus 181 cases $\times$ 2 loading cases $\times$ 2 critical moments = 724 runs. Each geometry is discretized longitudinally at least by 35 elements resulting in convergent solutions.

7.2 Results

Figure 4a–e shows the normalized critical moments M_ND/M_P and M_D/M_P versus the non-dimensional parameters $L_2/L_1, L_2/h, h/t_W, b/t$, and b/h. The difference between the M_ND/M_P and M_D/M_P curves is indicative of the influence of web distortion throughout lateral buckling. The effect of the span ratio L_2/L_1 on the web distortional effect varies according to the type of loading: An increase in L_2/L_1 leads to a decrease in web distortional effects under uplift loads, while a decrease in L_2/L_1 lead to an increase in web distortional effects under gravity loads.

The elastic critical moment of the system is influenced by two factors: (a) the load height effect (since the OWSJ loads act at the top flange and hence are offset from the shear centre, and (b) the bracing height effect (since OWSJ provide lateral restraints at the top flange, i.e. they are offset from the shear centre). In the case of gravity loads, top flange loading is associated with a detrimental destabilizing effect (when compared to shear centre loading or bottom flange loading) while the height of lateral braces at the top flange provided by OWSJs is optimal in increasing the lateral buckling resistance since it restrains the flange that has the larger tendency to buckle laterally. Conversely, in the case of uplift loads, top flange loading is associated with a favourable stabilizing effect (when compared to shear centre loading or bottom flange loading) while the height of lateral braces at the top flange is sub-optimal since it braces the flange that is less prone to buckling laterally.

Figure 4a–e shows that the interplay of the above two factors generally leads to a larger elastic LTB when the system is subjected to uplift loading. The Gerber systems examined in the present study exhibited a larger flexural resistance under uplift than under gravity loading except when $L_2/L_1 \geq 7.5$.

For all geometries considered, all cross-sections considered met Class 2 requirements according to the Canadian steel design standards [18] based on a yield strength $F_y = 350$ MPa. Accordingly, the nominal flexural resistance of the system M_n can be determined by Eq. (1). In the present study, the critical moment resistance of the system is taken as the distortional LTB critical moments, i.e. $M_u = M_D$ since it is more accurate than the non-distortional critical moment M_ND. The border $M_D/M_P = 2.15$ delineating the region of plastic moment failure from inelastic LTB as well as $M_D/M_P = 0.67$ delineating inelastic LTB region from elastic LTB region are both depicted by the horizontal green lines. The dotted lines in Fig. 4a–e depict the normalized nominal flexural resistance M_n/M_P of the system.

It is observed that the nominal flexural resistance of the system under uplift loading is primarily governed by inelastic LTB except when $L_2/L_1 \geq 7.5$ (Fig. 4a) where it is governed by elastic LTB. In (Fig. 4e), the flexural resistance is governed by elastic LTB when $b/h \leq 0.3$, by inelastic LTB when $0.3 \leq b/h \leq 0.6$, and by plastic resistance when $0.6 \leq b/h$.

8   Effect of Number of Lateral Restraints

The previous parametric study was conducted using the reference Gerber system in which the top flange was laterally restrained by the action of OWSJs at six equidistant points between both columns and at the overhang tips. This section examines the effect of increasing the number of lateral restraints provided at the top flange on the buckling resistance of the system. Forty-two elements were used to mesh the reference Gerber system.

   The buckling resistance of two cases is examined: (a) The discrete restraint case defined in the reference Gerber system in which the top flange back-span is laterally restrained at six equidistantly spaced locations, and (b) a continuous restraint case in which the entire top flange is hypothetically assumed to be continuously restrained. This case is intended to simulate the limiting case where a large number of OWSJs fame into the top flange. The reference beam (Fig. 4) described in Sect. 4 is investigated in this section by assuming that the uniformly loads acting on the overhangs and the back-span to have equal magnitudes, i.e. $w = w_1 = w_2$, along with loads $P = (w/2)(L_2 - 2L_1)$ acting on the overhang tips. The beam is discretized by 16 elements. A distortional LTB buckling analysis is then conducted using 16 modes of deformation.

   For uplift loading, the distortional LTB critical moment is found to be $(M_{D-\text{Dis}})_{\text{Uplift}} = 380.2\,\text{KNm}$ for the discrete restraint case. This value increases to $(M_{D-\text{Cont}})_{\text{Uplift}} = 402.0\,\text{KNm}$ for the continuous restraint case, which corresponds to a 5.7% increase. For gravity loading, the distortional LTB critical moment is found to be $(M_{D-\text{Dis}})_{\text{Gravity}} = 116.4\,\text{KNm}$ for discrete restraint case and increases to $(M_{D-\text{Cont}})_{\text{Uplift}} = 119.1\,\text{KNm}$ for continuous restraint case, which corresponds to a 2.3% increase. The minor increase in distortional critical moments suggests that buckling behaviour of the discrete and continuous restraint systems are nearly identical both for uplift and gravity loading. This is confirmed by examining the buckling configurations for the normalized lateral displacement at both flanges, and at web mid-height (Fig. 5). The buckled configurations in both the continuous and discrete restraint cases are nearly identical for both uplift and gravity loadings. These results suggest that the parametric study provided in Sect. 7 would provide valid results if the number of lateral restraints provided by OWSJs to the top flange is increased.

9   Interaction Diagram for Adjacent Bays with Equal Spans and Different Line Loads

In the previous sections, the uniformly distributed load applied to the back-span was taken equal to that acting on the adjacent cantilever and suspended spans, i.e. $w_1 = w_2$. During construction, however, it is conceivable to have different loads acting on adjacent spans. This would occur, for example, after the roof has been fully erected over one span, but prior to roof installation on the adjacent span. The section
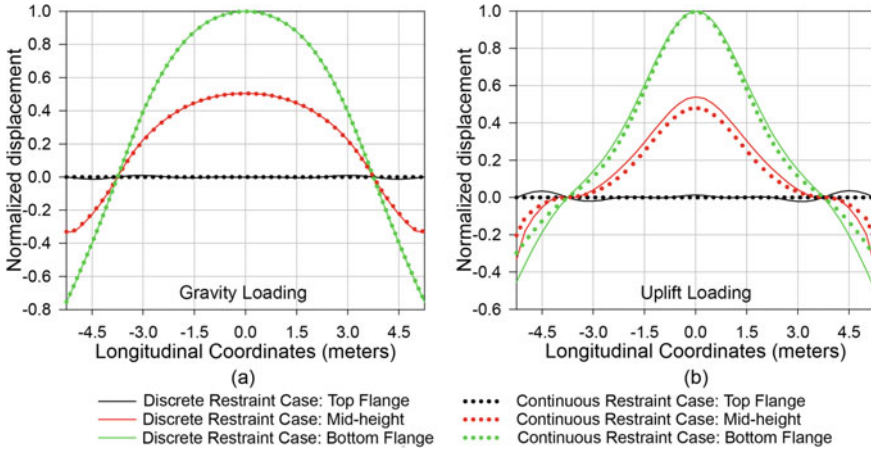
Fig. 5 Normalized buckled configuration for the reference Gerber beam under **a** Gravity loading and **b** Uplift loading

thus investigates the interaction between load levels acting on two adjacent bays with equal spans. When adjacent bays have equal spans, the point loads acting on the overhang tip are $P(w_1) = w_1 / (2L_2 - L_1)$, and the interaction diagram sought relates the independent load parameters w_1 (acting on the overhang and suspended span) to w_2 (acting on the back-span).

Lateral torsional buckling analyses are conducted on the reference beam (Fig. 2) while varying the ratio $\alpha_j = w_1 / w_2$ between the independent loading parameters w_1, w_2. For each loading condition α_j, a non-distortional load combination is determined from the eigenvalue analysis by taking the number of modes $m = 2$. Also, a distortional load combination is determined by setting $m = 16$. The resulting interaction diagrams are depicted in Fig. 6a. In regions where both interaction diagrams are in close proximity, web distortional effects are negligible. Conversely, in regions where the non-distortional buckling interaction diagram is significantly farther from the distortional buckling interaction diagram are indicative of the importance of distortional effects and the use of classical non-distortional solutions in such cases can grossly overestimate the critical moment capacity of Gerber beams.

Also shown in red on the figure is the interaction diagram based on the plastic resistance limit state for various load ratios $\alpha_j = w_1 / w_2$. Depending on the relative load magnitudes w_1 / w_2 acting on both spans, the peak moment may occur either at the midspan section of the back-span or at the supporting columns. The shape of the plastic interaction diagram accounts for both scenarios while equating the peak moment within the beam to the plastic flexural resistance of the section. Since the bending moment at the support depends only on load w_1, the horizontal red lines indicate the region of the interaction curve where the maximum moment occurs at the support.
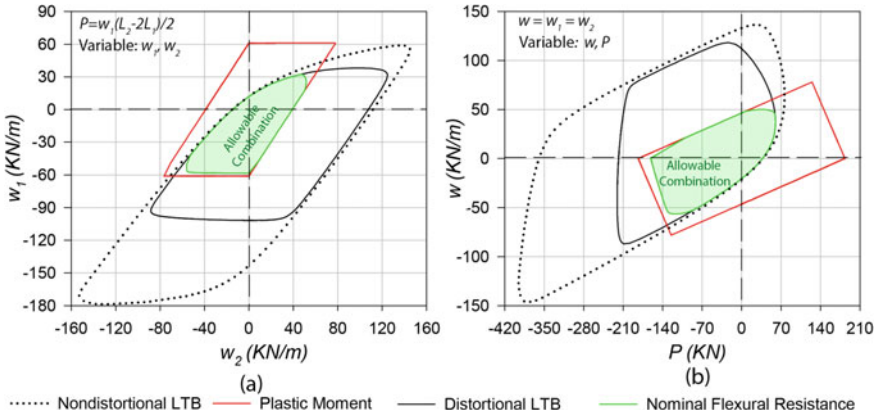
Fig. 6 Interaction diagrams for **a** Adjacent bays with equal spans with different line loads (w_1, w_2) and **b** Tip point load P independent of line load magnitude w

Lastly, the area bounded by the green line depicts the nominal flexural resistance M_n as computed by Eq. (1) by using the distortional LTB critical moment $M_u = M_D$ and section plastic moment M_P. As expected, this area lies within the intersection of the buckling interaction diagram and the plastic interaction diagram. Regions where the green line coincides with the plastic interaction diagram (in red), indicate that material failure governs the capacity of the system (i.e. $M_D/M_P \geq 2.15$). Regions where the green line coincides with the distortional interaction diagram (the solid black line), indicate that the resistance of governed by elastic LTB (i.e. $M_D/M_P \leq 0.65$). The remaining portion of the nominal interaction diagram corresponds to an inelastic LTB mode of failure (i.e. $2.15 \geq M_D/M_P \geq 0.65$). A load combination ($w_1$, w_2) lying within the area bound by the nominal resistance interaction diagram is deemed to be safe.

Within the area bound by nominal resistance interaction diagram in Fig. 6a, the second quadrant where $w_1 > 0$, $w_2 < 0$ (gravity loading on adjacent span + uplift loading on back-span) is associated with a particularly weak nominal resistance. Particular attention is needed when treating such loading combinations.

10 Interaction Diagram for Adjacent Bays with Different Spans and Equal Line Loads

In the previous sections, the load P acting at the cantilever tips to represent the effect of cantilever span on the Gerber system was taken as $P = (w_1/2)(L_2 - 2L_1)$. In some practical situations, load P can have different values. This will occur, for example, when the spacing between columns supporting the Gerber beam system is non-uniform. To investigate the resistance such Gerber systems, the uniformly

distributed load applied to the back-span is taken equal to that acting on the adjacent cantilever and suspended spans, i.e. $w = w_1 = w_2$ while the tip load P is taken to vary independently of w. The interaction relation between point load P and the uniformly distributed load w is investigated for the reference beam.

In a manner similar to Sect. 8, four interaction diagrams are generated based on elastic non-distortional buckling analysis, elastic distortional buckling analysis, plastic resistance, and the nominal flexural resistance M_n as computed by Eq. (1) by using the distortional LTB critical moment $M_u = M_D$. Within the area bound by the nominal resistance interaction diagram in Fig. 6b, the fourth quadrant where $P > 0$, $w < 0$ is associated with a particularly weak nominal moment resistance. Gerber systems subjected to load combinations in this quadrant are particularly prone to buckling and special care is needed if/when Gerber systems are subjected to such load combinations.

11   Summary and Conclusions

The present study adopted a recently developed finite element formulation to investigate the lateral torsional buckling behaviour of Gerber systems. A non-dimensional parametric study is conducted on the effect of various geometric parameters on the distortional and non-distortional LTB capacity of Gerber systems. The main findings of the present study are:

- Web distortional effects can significantly reduce the elastic lateral torsional buckling resistance of Gerber systems.
- The reduction in elastic LTB resistance in the Gerber system becomes pronounced with an increase in span ratio L_2 / L_1, web slenderness h / t_W, and aspect ratio b / h, and with a decrease in the normalized back-span to depth ratio L_2 / h and flange slenderness b / t.
- The parametric study showed when the loading direction shifts from the gravity to uplift loads a Gerber system with a specific geometry exhibit primarily increased buckling capacity. However, for Gerber systems with large back-span length relative to the overhang length $(L_2 / L_1 \geq 7.5)$, the buckling capacity is increased when uplift loading is applied.
- The flexural resistance of the Gerber system geometries investigated in the present study under uplift loads are primarily governed by inelastic LTB except when the span ratio $L_2 / L_1 \geq 7.5$.in which case, elastic LTB governs the resistance. Also, the section aspect ratio b / h was shown to play an important role on the governing failure mode: the flexural resistance is governed by elastic LTB when $b / h \leq 0.3$, by inelastic LTB when $0.3 \leq b / h \leq 0.6$, and by plastic resistance when $0.6 \leq b / h$.
- The study successfully exploits the distortion indicator to identify the optimum locations for transverse stiffeners needed to suppress the web distortion in Gerber systems. It is observed that maximum distortion tends to take place at the tip

of overhangs suggesting that providing stiffeners at these locations is optimal to maximize the elastic lateral torsional buckling resistance.

- The interaction diagrams developed in the present study suggest that the elastic LTB resistance of Gerber systems is particularly weak for loading scenarios involving loads acting in opposite directions (e.g. when gravity loads acting on part of the Gerber system and uplift acting on the remaining part). The buckling strength under these conditions is found to be relatively small and highly sensitive to the magnitudes of the applied load.

References

1. Vlasov VZ (1961) Thin-walled elastic beams. National technical information service
2. Lee HE, Nguyen CT, Moon JH, Joo HS (2011) Lateral-torsional buckling of discretely-braced i-girder. Procedia Eng 14:264–271. https://doi.org/10.1016/j.proeng.2011.07.032
3. Nguyen CT, Moon J, Le VN, Lee H-E (2010) Lateral–torsional buckling of I-girders with discrete torsional bracings. J Constr Steel Res 66(2):170–177. https://doi.org/10.1016/j.jcsr.2009.09.011
4. Valentino J, Trahair NS (1998) Torsional restraint against elastic lateral buckling. J Struct Eng 124(10):1217–1225. https://doi.org/10.1061/(ASCE)0733-9445(1998)124:10(1217)
5. Mohammadi E, Hosseini SS, Rohanimanesh MS (2016) Elastic lateral-torsional buckling strength and torsional bracing stiffness requirement for monosymmetric I-beams. Thin-Walled Struct 104:116–125. https://doi.org/10.1016/j.tws.2016.03.003
6. Kitipomchai S, Dux PF, Richter NJ (1984) Buckling and bracing of cantilevers. J Struct Eng 110(9):2250–2262. https://doi.org/10.1061/(ASCE)0733-9445(1984)110:9(2250)
7. Wang CM, Kitipornchai S, Thevendran V (1987) Buckling of braced monosymmetric cantilevers. Int J Mech Sci 29(5):321–337. https://doi.org/10.1016/0020-7403(87)90115-9
8. McCann F, Gardner L, Wadee MA (2013) Design of steel beams with discrete lateral restraints. J Constr Steel Res 80:82–90. https://doi.org/10.1016/j.jcsr.2012.09.011
9. Nguyen CT, Joo H-S, Moon J, Lee H-E (2012) Flexural-torsional buckling strength of I-girders with discrete torsional braces under various loading conditions. Eng Struct 36:337–350. https://doi.org/10.1016/j.engstruct.2011.12.022
10. Pezeshky P, Mohareb M (2018) Distortional lateral torsional buckling of beam-columns including pre-buckling deformation effects. Comput Struct 209:93–116. https://doi.org/10.1016/j.compstruc.2018.08.010
11. Pezeshky P, Sahraei A, Mohareb M (2017) Effect of bracing height on lateral torsional buckling resistance of steel beams. In: 6th International conference on engineering mechanics and materials, Vancouver
12. Pezeshky P, Sahraei A, Mohareb M (2019) Distortional lateral torsional buckling analysis of beams with overhangs. J Struct Eng 145(3):04018266. https://doi.org/10.1061/(ASCE)ST.1943-541X.0002271
13. Ronagh HR, Bradford MA (1994) Some notes on finite element buckling formulations for beams. Comput Struct 52(6):1119–1126. https://doi.org/10.1016/0045-7949(94)90178-3
14. Arizou R, Mohareb M (2021) Design considerations for distortional lateral buckling. J Struct Eng 147(12):04021203. https://doi.org/10.1061/(ASCE)ST.1943-541X.0003167
15. Reddy JN (2006) Theory and analysis of elastic plates and shells. CRC Press LLC, Bosa Roca
16. Gjelsvik A (1981) The theory of thin-walled bars, vol 49. Wiley, New York, USA

17. Arizou R (2020) Distortional lateral torsional buckling of doubly symmetric wide flange beams. University of Ottawa, Civil Engineering
18. Canadian Standards Association (2019) Design of steel structure CSA S16:19. CSA Group, Toronto, Ontario, Canada

Comparison Between the Results of Strip Loads Surcharge and Undefined Uniform Load on External Stability of a T-Shape Modular Retaining Wall

S. Haji Ghasemali and S. Mirmirani

Abstract The T-shape retaining wall element, T-WALL, is a precast modular gravity wall system designed mainly for heavy highway, railway, waterway, and site development applications. It is composed of structurally reinforced, monolithic T-shape precast concrete units and a granular backfill. The surcharge for designing retaining walls supporting highways is usually a uniform load. In case of the railway application, the surcharge on top of the wall is represented by one or multiple strip loads located at different distances from the wall facing. This paper demonstrates the comparison between the results of modeling the surcharge as a single or multiple strip load and undefined uniform load on lateral stress applied to the retaining wall. Then, the sliding and overturning forces of modular elements are investigated at each level separately.

Keywords Strip loads surcharge · Undefined uniform load · T-shape modular retaining wall

1 Introduction

The concrete T-shape units, T-WALL®, consist of a facing panel and a stem that extends into the backfill. Individual units have a rectangular facing and the stem that comes in various lengths. As shown in Fig. 1, the stem length generally decreases course by course from bottom to the top, reducing the required quantity for select backfill as compared to Mechanically Stabilized Earth (MSE) retaining wall systems.

The facing section can be treated with an architectural finish to provide a pleasing appearance to the finished structure. The stem varies in length according to the wall design.

The configuration of the live loads on the wall depends on the application of the structure itself. The two main applications for T-Wall structures are in the roadway

S. H. Ghasemali (✉) · S. Mirmirani
Reinforced Earth Company Ltd., Mississauga, ON, Canada
e-mail: shajighasemali@recocanada.com
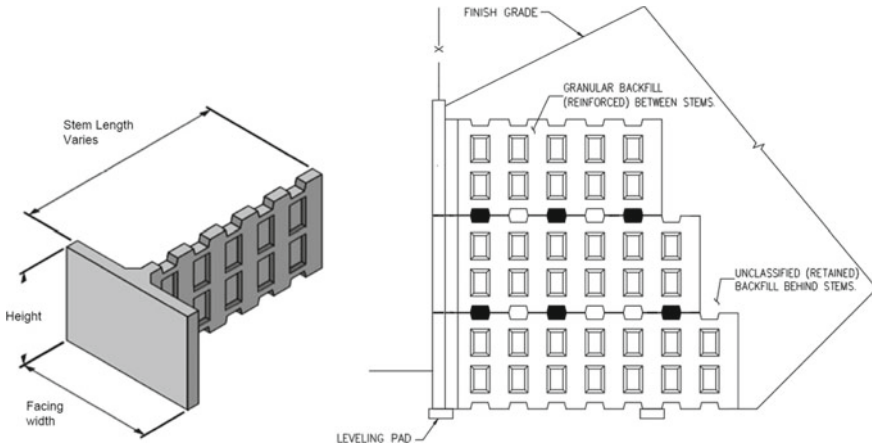
Fig. 1 Typical T-WALL unit and section

and railway markets. The typical live loads for roadway applications are represented by a uniform surcharge load (q) on top of the wall. In this case, the additional vertical or lateral stress due to the surcharge is constant with the depth.

For the retaining walls supporting railway tracks, lateral pressure due to the surcharge is computed considering elasticity theory from Boussinesq [3].

While some authors reported acceptable agreement between experimental results and the elastic theory [6] [4] and [7], others observed significant differences between the elastic theory and field measurements, which attained in some cases 200% [5, 8, 9]. The disparity between the experimental results and the elastic theory could be attributed to several factors such as the nonlinear behavior of the soil and the efficiency of the experimental system.

This paper investigates the comparison between the results of Boussinesq theory and regular undefined uniform load (UUL) on external stability and lateral force applied to the retaining wall.

2   Lateral Pressure Distribution

2.1   Boussinesq Theory

Surcharge load causes a lateral pressure to act on the system in addition to the basic earth pressure.

Based on the Boussinesq theory, the lateral stress applied to the retaining wall as shown in Fig. 2 is calculated using Eq. 1 (AREMA 2016):

$$\sigma_x = Ps = \frac{2q}{\pi}\left(\beta + \text{Sin}\beta\text{Sin}^2\alpha - \text{Sin}\beta\text{Cos}^2\alpha\right) \tag{1}$$

q: Strip load

The Boussinesq method assumes a linear–elastic homogeneous isotropic half-space for the soil media.

The distribution of the lateral pressure applied on a typical T-WALL section using Boussinesq model is shown in Fig. 3. Where the back of prefabricated modulus forms a stepped surface, the earth pressure is calculated on a plane surface (rigid block) drawn from the upper back corner of the top module to the lower back heel of the bottom module using Coulomb earth pressure theory [1].

In Fig. 3:

F_s: Lateral earth force applied on plane surface.
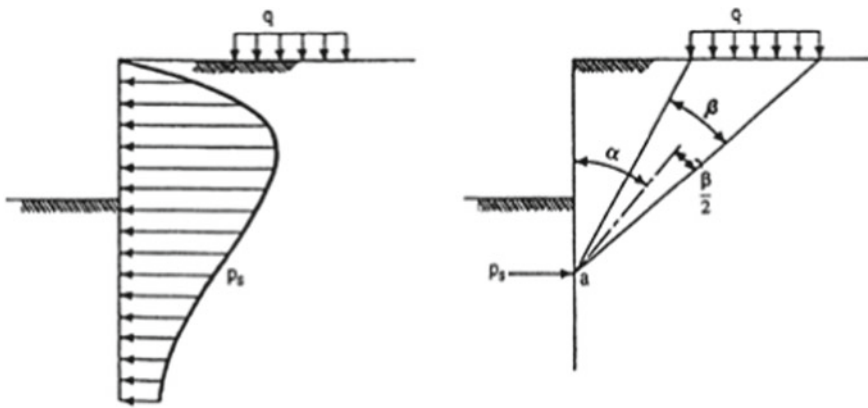
Fig. 2 Pressure distribution for strip load [2]
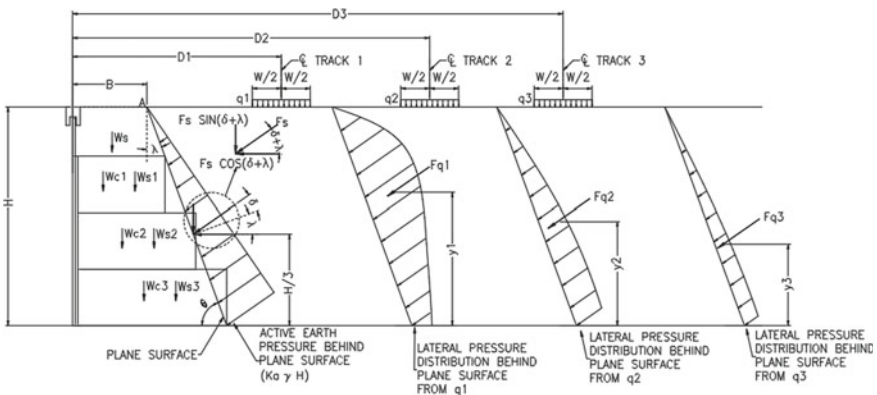
Fig. 3 Boussinesq model for the strip load lateral pressure distribution

F_{qi}: Lateral force due to track i applied on plane surface.

y_i: Vertical distance from the centroid of lateral force due to track i applied on plane surface to bottom of wall.

θ : Angle from plane surface to horizontal line.

λ: Angle from plane surface to vertical line.

δ : Wall friction angle.

W: Tie length.

2.2 Undefined Uniform Surcharge (UUL)

Uniform surcharge loads will exert a rectangular pressure distribution on the back of retaining wall as shown in Fig. 4. In this case, the lateral stress is calculated based on Eq. (2).

$$\sigma_x = k_a q \qquad\qquad (2)$$

In Fig. 4:

K_a: Active earth pressure coefficient.

q: Uniform surcharge load.

The distribution of the lateral pressure applied on a typical T-WALL section is shown in Fig. 5.

In Fig. 5:

F_q: Lateral force due to uniform load applied on plane surface.

Fig. 4 Distribution of lateral stress for the uniform surcharge
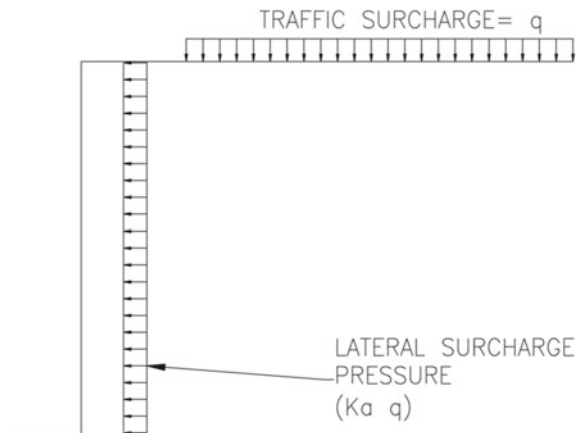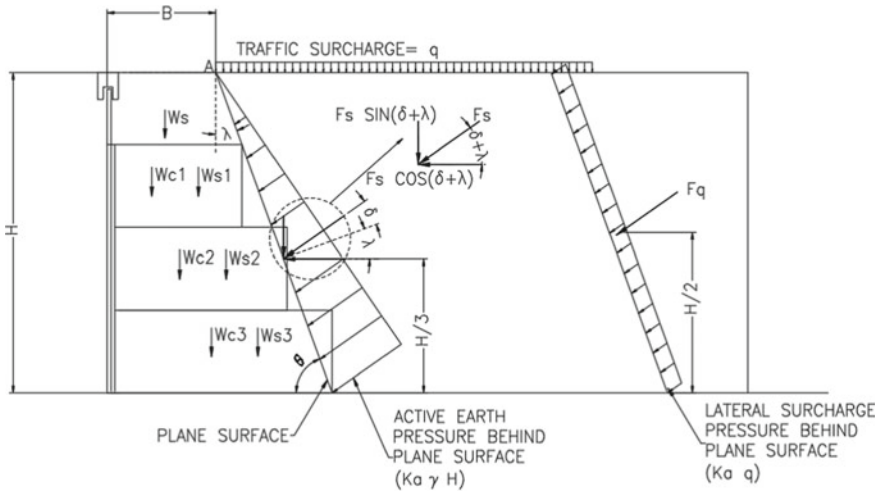
Fig. 5 Uniform load pressure distribution

3 Analytical Model

To compare the results between Boussinesq theory and UUL on external stability, the wall section shown in Fig. 6 is studied.

The strip load is calculated based on Cooper-E80 surcharge as per AREMA [2] as shown in Eq. 3:

$$q = \frac{\text{MAX} \cdot \text{Axle load (Kips)}}{\text{Axle spacing (ft)} \times \text{Tie length (ft)}} = \frac{80}{5 \times 8} = 2K_s f = 95.8 \text{ kN/m}^2 \quad (3)$$

The selected shapes are the typical geometry used in routine designs. Table 1 shows the backfill parameters used in this research.

4 Analysis and Results

4.1 Surcharge Lateral Force

Figure 7 shows the change of lateral surcharge force in the height of wall for the two different models of surcharge. It is seen that the lateral pressure calculated by UUL model is less up to 4 m wall height and then gets higher as the height increases which is 72 percent more than Boussinesq model at the full height of the wall. The reason is that the lateral surcharge pressure in the UUL model is constant in the wall height (Fig. 4), which result a linear distribution for the lateral force, and it will increase as
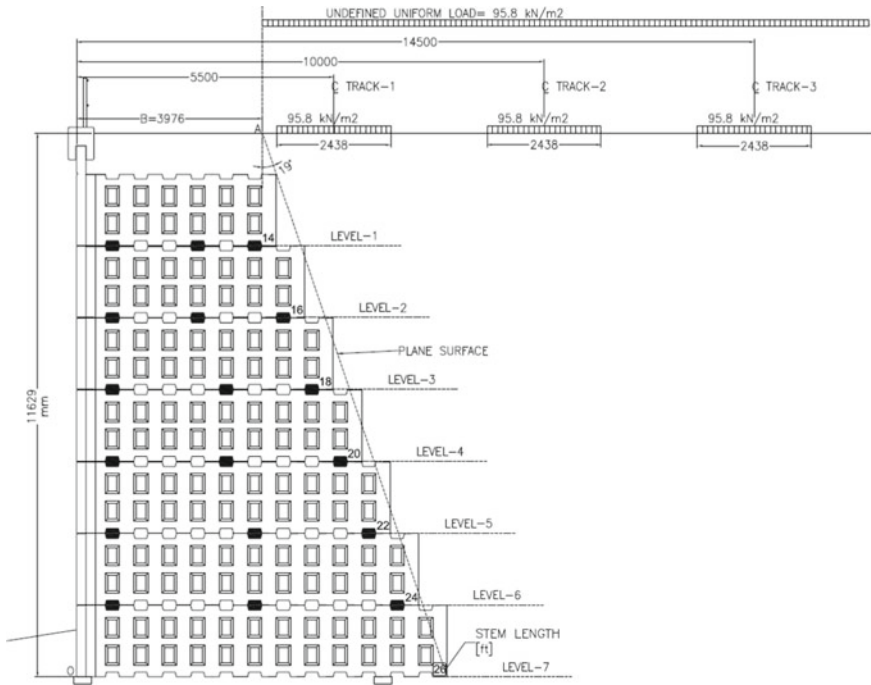
Fig. 6 Studied T-WALL section

Table 1 Backfill parameters

	Unit weight (kN/ m³)	Soil internal friction angle (°)	Wall friction angle (°)
Granular backfill between stems	22	35	23.33
Foundation and retained backfill behind stems	20	30	20

the height of the wall increases; while in the Boussinesq model, the lateral surcharge pressure dissipates at the lower depths as shown in Fig. 2, which cause a constant lateral force (not increasing with depth).

4.2   External Stability

The lateral pressure will cause sliding or overturning of the rigid block at each level. Therefore, T-WALL units must have sufficient strength to resist against sliding and overturning at each level.
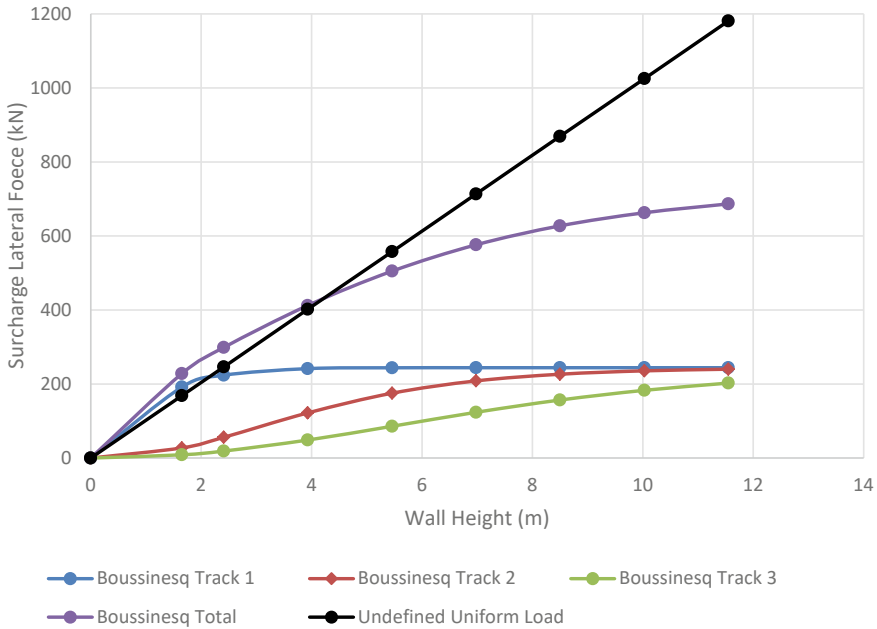
Fig. 7 Surcharge lateral force distribution in the wall height

To calculate the factor of safety for sliding (SF_s) and overturning (SF_O), the driving force (F_f) and the resisting force (F_r) should be identified at each level of T-WALL units. Driving forces are the horizontal component of lateral earth pressure and lateral surcharge pressure, and the resisting forces are the weight of the rigid block and vertical component of the lateral pressures. Then, the factor of safety for the sliding and overturning are obtained using Eqs. (4 and 5), respectively.

$$\text{SF}_s = \frac{F_f}{F_r \times \mu_f} \tag{4}$$

F_f: Driving force.
F_r: Resisting force.
μ_f : Friction factor

$$\text{SF}_o = \frac{M_f}{M_r} \tag{5}$$

M_f and M_r are driving and resisting moment taken about point O shown in Fig. 6 at the base or at each level of T-Wall units.

Figure 8 shows the factor of safety for sliding, at each level of T-Wall units. In level 1, the SF_s calculated by Boussinesq model is less than SF_s obtained from UUL model as in the Boussinesq model, the lateral surcharge pressure is higher in the
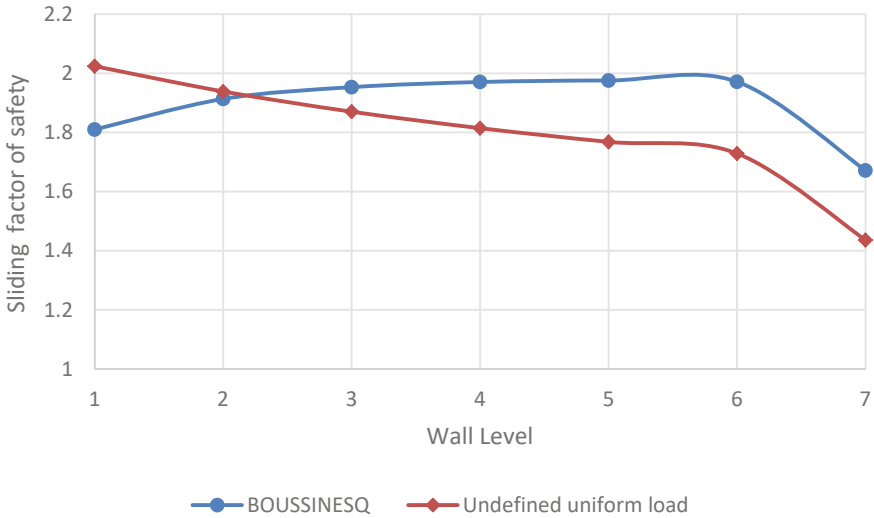
Fig. 8 Sliding factor of safety at each level of T-wall units

zones which are closer to the top of wall (Fig. 2); therefore, the driving force will be higher. In level 2, the SF_s obtained from two models are approximately the same, while after level 2 the SF_s calculated by Boussinesq model is more than UUL model due to dissipation of lateral surcharge pressure in the lower wall depth.

The factor of safety for overturning, SF_O, at each level of T-Wall units is shown in Fig. 9. It is seen that for levels 1 to 5 of the wall, the SF_O for the Boussinesq model is less than SF_O for the UUL model and for the level 6 and 7 the SF_O are the same using both models. These results are reasonable as the driving moment calculated in Boussinesq model is more than UUL model due to higher moment arm (distance from centroid of lateral surcharge force to the wall base) calculated in the Boussinesq model.

Figure 10 shows the moment arm location at each level of the unit. Since in Boussinesq model the lateral surcharge pressure is higher in the areas closer to the top of the wall, therefore the centroid of the lateral force is closer to the top of wall compared to the UUL model. It is more significant in the lower level of wall as seen in Fig. 10.
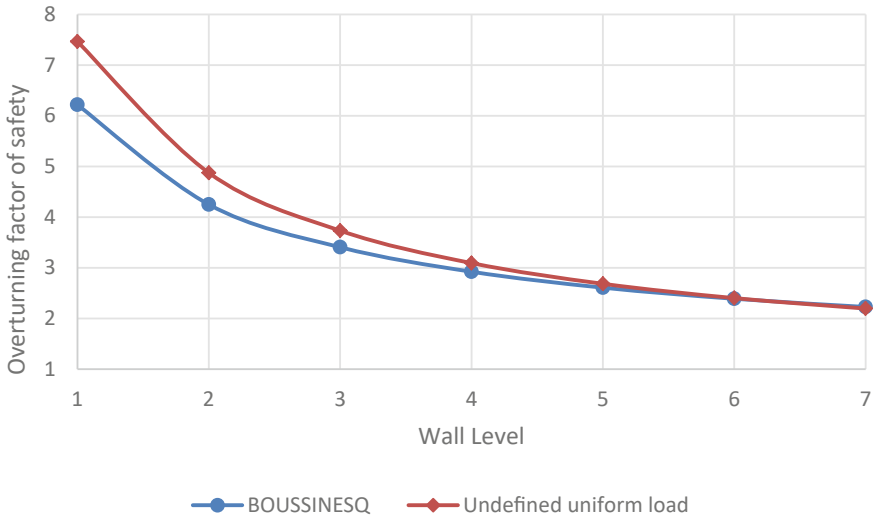
Fig. 9 Overturning factor of safety at each level of T-wall units
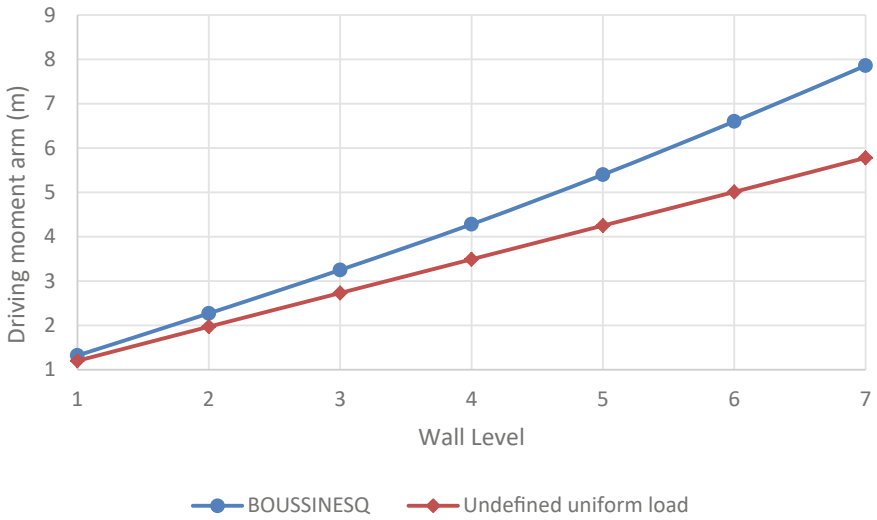
Fig. 10 Location of driving moment arm at each level of T-wall units

5   Conclusion

Based on geometry of wall studied in this study, it could be concluded that

- For the upper T-WALL units up to 4 m depth, the total lateral surcharge force applied on the rigid block (behind the stems) calculated based on Boussinesq model is higher compared to undefined uniform load model, while for the lower level T-WALL units the result is opposite.
- Calculating the factor of safety for the sliding based on undefined uniform load model is conservative for the T-WALLs higher than 4 m. For the wall shorter than 4 m depth, the Boussinesq model is recommended.
- Calculating the factor of safety for the overturning based on undefined uniform load is not conservative for the T-WALLs less than 10 m high. A Boussinesq model is recommended in this case.

References

1. American Association of State Highway and Transportation Officials (AASHTO) (2020)
2. American Railway Engineering and Maintenance of way Association (AREMA) (2016)
3. Boussinesq J (1885) Applications des potentiels à l'étude de l'équilibre et mouvement des solides elastiques. Gauthier-Villard, Paris
4. Nilsson RN, Oost IH (1996) Visco-elastic analysis of full-scale pavements: Validation of VEROAD, Transportation Research Record 1539, TRB, National Research Council, Washington, DC, USA
5. Sadeq M, Shahrour I (2007) Use of the Boussinesq solution in geotechnical and road engineering: influence of plasticity, C.R. Mecanique 335:516–520
6. Siddharthan RV, Yao J, Sebaaly P (1996) Field verification of a moving load model for pavement response, Transportation Research Record 1540, TRB, National Research Council, Washington, DC, USA
7. Ullidtz P (1987) Pavement analysis. Elsevier Science, Amsterdam
8. Ullidtz P, Askegaard V, Sjölin FO (1996) Normal stresses in a granular material under FWD loading, Transportation Record 1540, TRB, National Research Council, Washington, DC, USA
9. Zhang W, Ullidtz P, Macdonald R (1998) Pavement subgrade performance study, part II: Modeling pavement response and prediction pavement performance, Report 87, Danish Road Institute, Roskilde, Denmark

Seismic Analysis and Structural Dynamics

Non-linear Finite Element Analysis of GFRP-RC Circular Columns Subjected to Simulated Earthquake Loading

Yasser M. Selmy, Amr E. Abdallah, and Ehab F. El-Salakawy

Abstract Currently, there is a scarcity of available experimental data on the seismic performance of glass fiber-reinforced polymer (GFRP)-reinforced concrete (RC) columns. For better understanding of the behavior of such columns, a non-linear finite element analysis was carried out using a commercial software. The constructed finite element model (FEM) was validated against previous experimental results of GFRP-RC circular columns. The validation process included the hysteretic behavior, crack patterns, and ultimate loads. The FEM was capable of simulating hysteresis behavior of the tested columns by considering the cyclic behavior of reinforcement, the non-linear behavior of concrete, the confinement provided by transverse reinforcement, and the reduction of compressive strength due to concrete cracking. In addition, the bond-slip relationship between reinforcing bars and surrounding concrete were incorporated. The validated FEM was utilized to investigate the effect of spiral pitches and column concrete compressive strengths. The FEM agreed well with the experimental results on the identification and propagation of the damage, and the mechanism of failure. Improvement in the lateral load capacity was observed by increasing the concrete compressive strength. On the other hand, the spiral pitch had a marginal effect on drift capacities.

Keywords Non-linear analysis · GFRP-RC circular columns · Earthquake loading

1 Introduction

Reinforced concrete (RC) columns are often utilized as part of seismic force-resisting systems. Understanding the behavior of columns during earthquake excitations is essential to the safety of the whole structure. Due to its desirable properties, particularly its non-corrodible nature, fiber-reinforced polymers (FRPs) are being widely accepted as a viable alternative to traditional steel reinforcement in RC structures.

Y. M. Selmy · A. E. Abdallah · E. F. El-Salakawy (✉)
Department of Civil Engineering, University of Manitoba, Winnipeg, MB, Canada
e-mail: ehab.el-salakawy@umanitoba.ca

However, because of the linear-elastic stress–strain relationship of FRP up to failure as well as the lower strain capacity and elastic modulus compared to steel, many concerns were raised about the performance of FRP-RC structures in earthquake-prone areas. Compared to other types of FRPs, glass FRP (GFRP) reinforcement is more economical and has adequate strain capacity, thus, it is more attractive to infrastructure applications.

While structural members such as slabs, beams, and flat plates have been well discussed and refined within current design provisions [1, 4, 12, 13], the design requirements of FRP-RC columns are being established at a slower rate as a result of paucity of experimental data, particularly for those tested under simulated seismic loading. FRP is not recommended as a primary reinforcement in compression members according to the ACI 440.1R-15 [4] guidelines. Moreover, FRP can be implemented in RC columns according to both Canadian standards, CSA S806-12 [12], and AASHTO LRFD code [1] although its load-bearing capacity is ignored. The Canadian Highway Bridge Design Code, CSA S6-19 [13], on the other hand, allows FRP to be used in compression members up to a maximum compressive strain of 2000 $\mu\varepsilon$.

As a result, recent research studies, utilizing GFRP reinforcement as a main rein-forcement, have focused on several parameters influencing the behavior of GFRP-RC columns under various loading configurations, such as axial concentric [18, 9, 10], eccentric [7, 10], and seismic loading [2, 3, 6, 20, 24]. These studies concluded that stable hysteretic responses were observed for GFRP-RC columns examined under uni-directional reversed-cyclic loads with considerable amounts of energy dissipation.

Despite the significant research committed to understanding the seismic behavior of GFRP-RC columns, the affecting parameters remain not fully comprehended. Non-linear finite element analysis can be employed concisely in the analysis of RC structures to obtain a reliable and complete intuitive understanding of such behavior. Only a few numerical studies on columns internally reinforced with FRP have been published [15, 21, 23], all were established on evaluating the performance of FRP-RC columns under different schemes of monotonic loads. In this study, using the software package ATENA/GiD [11], three-dimensional (3D) finite element models (FEMs) were constructed. The results of the tested columns by Abdallah and El-Salakawy [2, 3] were used to validate the FEMs. Utilizing the validated FEMs, the influence of concrete strength and transverse reinforcement ratio on the seismic response of GFRP-RC circular columns was explored.

2 Summary of the Experimental Study

2.1 Specimens Details and Material Properties

The experimental study involved eight full-scale GFRP-RC circular columns subjected to constant axial load and unidirectional cyclic lateral reversals. The specimens had 350-mm diameter, 1,750-mm shear span, and were reinforced with six GFRP longitudinal bars and No.10 GFRP spirals. A rigid steel-RC footing with dimensions of 1400 × 900 × 600 mm was constructed for each column to ensure appropriate fixity (Fig. 1). The mechanical parameters of the GFRP reinforcement employed in this study are summarized in Table 1. More details about the material properties or tested specimens can be found elsewhere [2, 3].
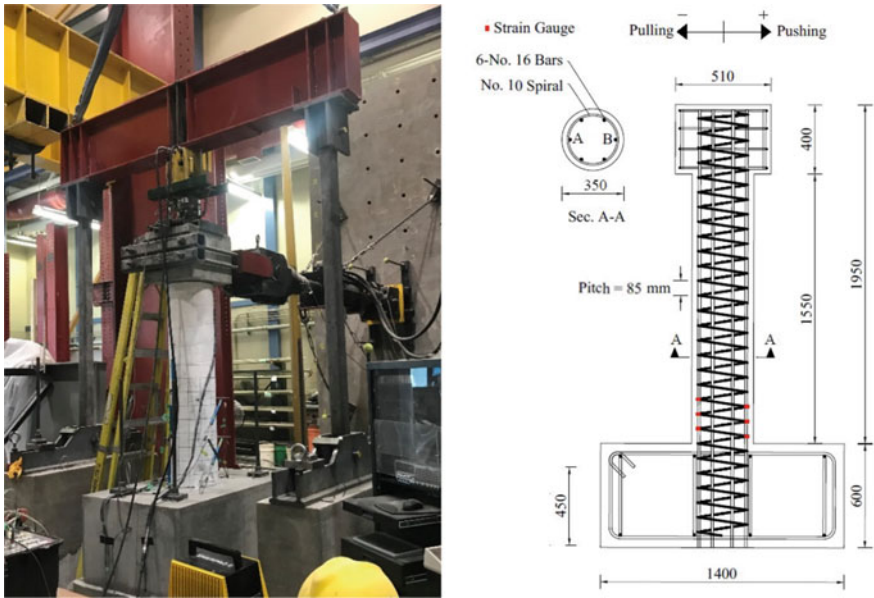
Fig. 1 Specimens and testing configuration (dimensions in mm)

Table 1 GFRP reinforcing bars material properties

Bar type	Nominal diameter (mm)	Area (mm^2)	Modulus of elasticity (GPa)	Tensile strength (MPa)	Ultimate strain (%)
No. 16	15.9	197.9	65.7	1711	2.60
No. 10 (Spirals)	9.5	71.0	58.4	1376	2.36

2.2   Test Setup and Loading Procedure

The test configuration is presented in Fig. 1. Using a hinged frame supporting a hydraulic jack, the axial load was applied to the column head, permitting the entire system to move in lockstep with the simulated cyclic drift reversals. Dywidag bars were used to ensure the fixation of the footings to the laboratory's floor.

The proper axial load was gradually applied on the column, then the simulated seismic load was implemented in two successive phases: a load-controlled phase to mimic the column at first cracking and service, followed by cyclic lateral displacement steps, as per ACI 374.1-05 [5]. Additional information can be found elsewhere [2, 3].

3   Numerical Modeling

3.1   Material Modeling

3.1.1   Concrete Constitutive Modeling

The concrete is modeled by 3D eight node brick elements. A built-in fracture-plastic model accessible in ATENA/GiD [11] was employed to incorporate the fracture and plastic concrete behavior models. Crack model with fixed crack direction was employed. In addition, as suggested by CEB-FIP Model Code 1990, the tension-stiffening factor, c_{ts}, was set to 0.4. Furthermore, a zero unloading factor was used in this investigation to approximate fracture closure when the load was reversed [16, 17, 22]. The formulas for computing the concrete constitutive parameters are summarized in Table 2.

3.1.2   Reinforcement Modeling

The GFRP reinforcement (i.e., bars and spirals) were modeled as a one-dimensional truss element. The multi-linear constitutive law, which varied linearly from zero to the ultimate strength of the GFRP material, f_{Fu}, was used to define the stress–strain

Table 2 Input concrete parameters

Parameter	Formula
Tensile strength f_t'	$f_t' = 0.27\left(f_{cu}'\right)^{2/3}$
Fracture energy G_F	$G_F = 0.000025 f_t' \; [\text{MN}/\text{m}]$
Initial elastic modulus E	$E_c = \left(6500 - 19.8 f_c'\right)\sqrt{f_c'}$

relationship of GFRP reinforcement. Table 1 shows the properties of the GFRP reinforcement that were utilized in the FEMs. The behavior of reinforcing GFRP under cyclic loading was incorporated using Menegotto and Pinto's [19] constitutive model. The columns' head and footing were reinforced with a 1 and 3% reinforcement ratio, respectively, using a smeared crack model.

A bond stress-slip constitutive model is proposed based on experimental findings by Alves et al. [8], however a perfect bond was proposed for the transverse reinforcement because no signs of slippage were recorded in the experimental tests by Abdallah and El-Salakawy [2, 3].

3.2 Geometry, Boundary Conditions and Loading Procedure

Figure 2 shows the five primary components of the FEMs: the column, footing, column head, longitudinal and transverse reinforcement, and loading and supporting steel plates. To ensure strain compatibility, rigid contact surfaces were created among each two adjacent components. An element mesh sized of 50 and 100-mm was used to mesh the column and the rest of model (i.e., footing and head), respectively. Moreover, at a general mesh size of 50 mm, four-node tetrahedral elements were employed for the bearing steel plates (i.e., loading and supporting plates).

To mimic the effect of post-tensioning on the footing, steel supporting plates were employed, which were restrained in all the global degrees of freedom. To eliminate local stress concentrations, flat plates having a thickness of 25-mm were employed at the load positions. In the FEMs, all steel plates were modeled as 3D solid elastic

(a) macro elements   (b) elements meshing   (c) discrete reinforcement
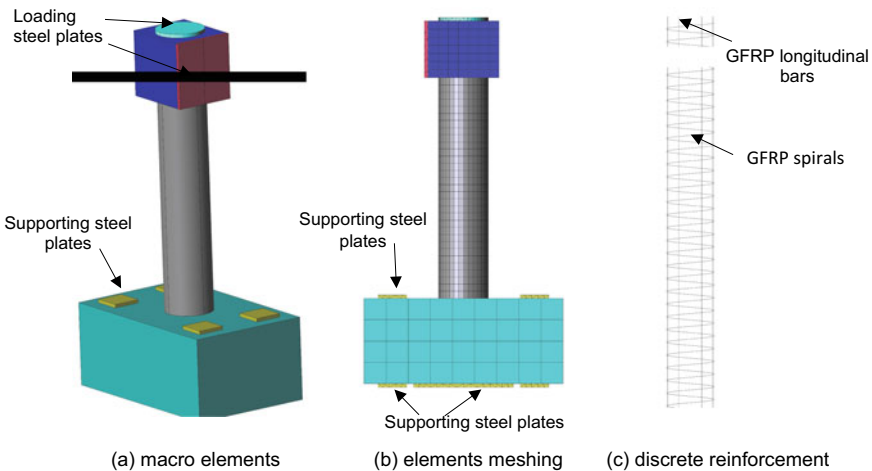
Fig. 2 FEM model details

materials with no yielding, to eliminate the potential of early failure, with an elastic modulus of 200 GPa and a Poisson's ratio of 0.3.

The axial force was employed first, in twenty load-controlled increments, then sustained throughout the entire analysis process. The cyclic drift reversals were then implemented. Each drift cycle consisted of a series of 1.0-mm displacement-controlled steps. The typical Newton–Raphson iterative approach, which is included in ATENA/GiD, was employed in the FEMs. In addition, as advised by earlier research, the convergence error of 1.0% was adopted [14, 16].

3.3 Validation of Finite Element Models

The outcomes of the FEMs were validated against six GFRP-RC specimens tested by Abdallah and El-Salakawy [2, 3]. The validation procedures were carried out in terms of hysteretic response and initial stiffness. Generally, the experimental and FEM results were in good agreement. An example of this form of agreement is illustrated by Fig. 3a, b for specimen GN-5.0-0.2-85. With an error of less than 10%, all FEMs were able to predict the measured failure drifts and lateral load capacity. In addition, as demonstrated in Fig. 3c, d, the FEMs could accurately predict the stiffness degradation and the spalling region, respectively, of the test specimens.

(a) hysteretic behavior

(b) lateral load-drift envelope

(c) stiffness degradation

(d) spalling region at failure
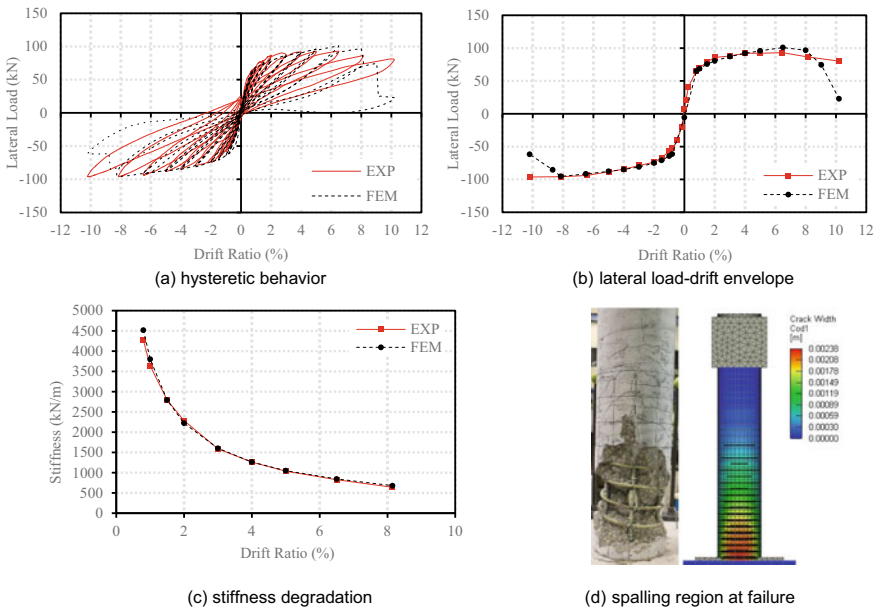
Fig. 3 Test and corresponding FEM results for GN-5.0-0.2-85 specimen

3.4 Parametric Study

The specimens in this investigation were assigned a four-character alphanumeric code, with initial character, G, denoting GFRP reinforcement. The second letter stood for concrete compressive strength. The third number indicated the column aspect ratio (shear span-to-depth ratio). Furthermore, the fourth integer denoted the ratio of the applied axial load, P, to the column's unconfined axial capacity, P_o. Finally, the spiral pitch was symbolized by the fifth number. For example, G30-5.0-0.2-85 refers to a GFRP-RC column with an aspect ratio of 5.0 under axial load equals to 20% of the unconfined axial capacity and spiral pitch of 85 mm.

3.4.1 Effect of Concrete Strength

The influence of different concrete strengths, ranging from 30 to 90 MPa, was evaluated using two sets of FEMs with 85 and 100-mm spiral pitches. As expressed in Fig. 4a, improvement in both lateral load resistance and stiffness was achieved by increasing concrete compressive strength improved both lateral load and stiffness, however this led to compromising drift capacity. Furthermore, increasing the concrete strength by up to 40 MPa enhanced the column's lateral load capacity and stiffness without altering its drift for the 85 mm spiral pitch, which meets the standards provided by the Canadian standard, CSA S806-12 [12].

For the spiral pitch of 100 mm, as shown in Fig. 4b, a slight increase in concrete strength, such as 10 MPa, would result in a significant deterioration of hysteretic response and lower deformability. This emphasizes the significance of the maximum spiral pitch limit of one-fourth the column's gross diameter, as specified by the Canadian standard CSA S806-12 [12]. Figure 5 reveals that when concrete strength increases, stiffness initially increases, however there is a significant stiffness degradation.
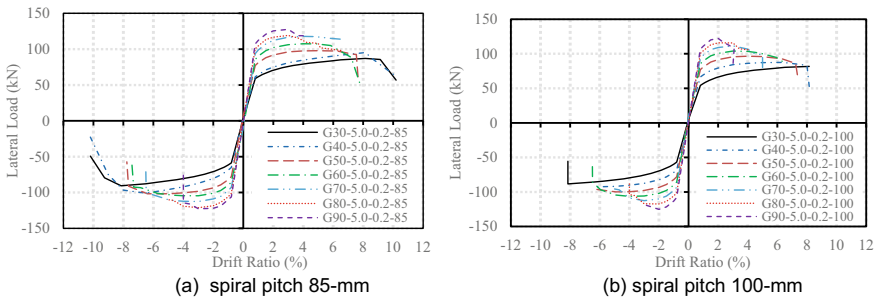
Fig. 4 Lateral load-drift relationship envelopes obtained from FEMs considering several concrete strengths
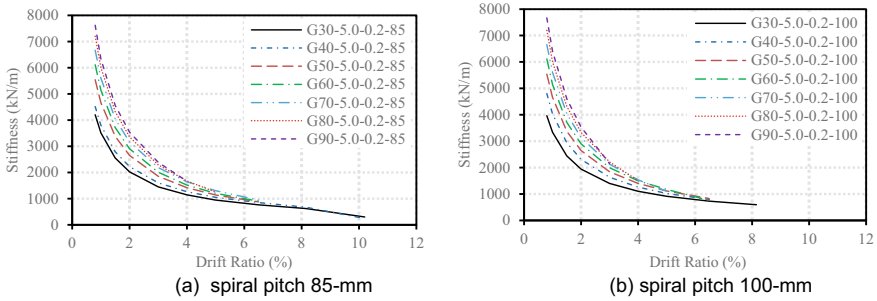
Fig. 5 Stiffness degradation obtained from FEMs considering several concrete strengths

3.4.2 Effect of Spiral Pitch

The effect of volumetric ratio of spiral reinforcement was evaluated in this study by exploring various spiral pitches for different concrete strengths: 30, 60, and 90 MPa. As indicated in Fig. 6a, at low concrete strength, 30 MPa, an increase in the spiral pitch from 85 to 130 mm resulted in a 13 and 36% reduction in lateral load capacity and in failure drift, respectively. On contrary, when the spiral pitch was increased by the same amount for concrete with a strength of 60 MPa, the lateral load dropped by just 6%, while the failure drift decreased by 51%, (Fig. 6b). Similarly, an increase in the spiral pitch from 50 to 100 mm reduced failure drift by 36 and 61%, respectively, for high concrete strengths of 60 and 90 MPa, as shown in Fig. 6b, c. This demonstrates that, at high concrete compressive strengths, lowering the spiral pitch could be more effective in enhancing columns' deformability.

As shown in Fig. 7a, regardless of the spiral pitch, it was observed that all FEMs with the same concrete strength of 30 MPa was comparable in terms of stiffness degradation. When the spiral pitch is increased for columns with comparatively high compressive strengths of 60 and 90 MPa, there is a higher strength deterioration for FEMs after 2.0% drift ratio. (Fig. 7b, c).

4 Conclusions

1. Lateral load capacity of circular GFRP-RC columns, hysteretic response, and stiffness were significantly enhanced when increasing concrete compressive strength.
2. The higher concrete strength came at the expense of column deformability and drift capacity. The loss in drift capacity was more pronounced when spiral pitches were larger.
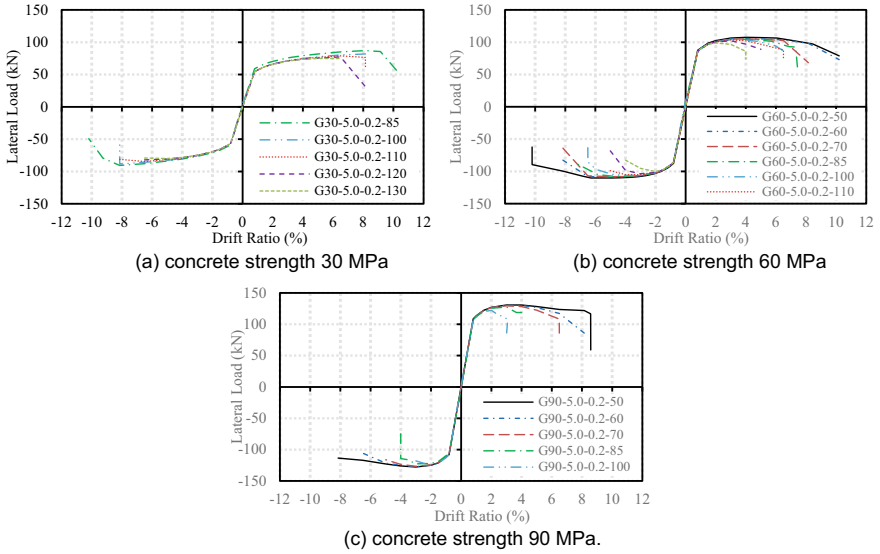
Fig. 6 Lateral load-drift envelopes obtained from FEMs considering various spiral pitches
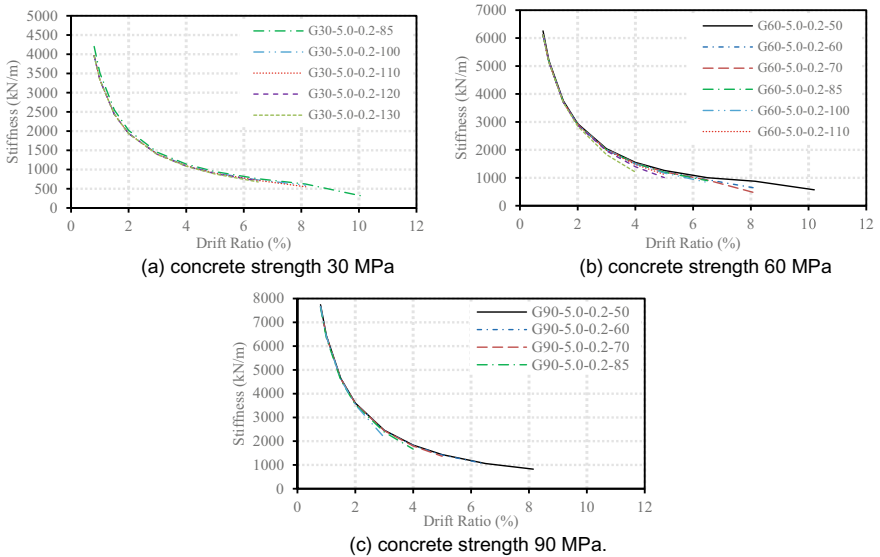
Fig. 7 Stiffness degradation obtained from FEMs considering various spiral pitches

3. Reduction of the spiral pitch enhanced columns' drift capacity. This enhancement was more significant at lower concrete compressive strength. With an increase in the spiral pitch from 85 to 130 mm, the failure drift was reduced by 36 and 51% for columns having a concrete strength of 30 and 60 MPa, respectively.
4. For columns having high concrete strengths of 60 and 90 MPa, a higher stiffness degradation was observed by employing larger spiral pitch, whereas increasing spiral pitch from 85 to 130 mm barely affected the stiffness for the columns with a concrete strength of 30 MPa.

References

1. AASHTO (2018) AASHTO LRFD bridge design guide specifications for GFRP–reinforced concrete, 2nd edn. Washington, DC
2. Abdallah AE, El-Salakawy EF (2021) Seismic behavior of high-strength concrete circular columns reinforced with glass fiber-reinforced polymer bars. ACI Struct J 118(5):221–234
3. Abdallah AEM, El-Salakawy EF (2021) Confinement properties of GFRP-reinforced concrete circular columns under simulated seismic loading. ASCE, J Comp Construct 25(2):04020088
4. ACI (2015) Guide for the design and construction of structural concrete reinforced with FRP bars, ACI 440.1R-15. American Concrete Institute (ACI), Detroit, MI, 88 pp
5. ACI (2019) Acceptance criteria for moment frames based on structural testing and commentary. ACI 374.1-05" (R2019). American Concrete Institute (ACI), Detroit, MI, 9 p
6. Ali M, El-Salakawy EF (2016) Seismic performance of GFRP-reinforced concrete rectangular columns. ASCE, J Comp Const 20(3):04015074
7. Almomani M, Mahmoud K, El-Salakawy EF (2022) Experimental investigation of large-scale eccentrically loaded GFRP-reinforced high-strength concrete columns. ASCE, J Comp Construct 26(2):1–13
8. Alves J, El-Ragaby A, El-Salakawy EF (2011) Durability of GFRP bars' bond to concrete under different loading and environmental conditions. ASCE, J Comp Const 15(3):249–262
9. Barua S, El-Salakawy E (2020) Performance of GFRP-reinforced concrete circular short columns under concentric, eccentric, and flexural loads. ASCE, J Comp Const 24(5):04020044
10. Barua S, Mahmoud K, El-Salakawy E (2021) Slender GFRP-RC circular columns under concentric, eccentric, and flexural loads: experimental investigation. ASCE, J Bridge Eng 26(7):1–13
11. Červenka V, Červenka J, Pryl D, Janda Z (2020) ATENA manual for ATENA-GiD interface, June, 139
12. CSA (2017) Design and construction of building structures with fibre-reinforced polymers. CSA S806-12 (R 2017). Canadian Standards Association, Toronto, ON, Canada, 208 p
13. CSA (2019) Canadian highway bridge design code, CSA-S6-19. Canadian Standards Association, Toronto, ON, Canada, 1092 p
14. El-Gendy MG, El-Salakawy EF (2021) Finite-element analysis of FRP-reinforced concrete slab–column edge connections subjected to reversed-cyclic lateral loads. ASCE, J Comp Const 25(1):04020082

15. Elchalakani M, Karrech A, Dong M, Mohamed Ali MS, Yang B (2018) Experiments and finite element analysis of GFRP reinforced geopolymer concrete rectangular columns subjected to concentric and eccentric axial loading. Structures 14(April):273–289
16. Ghomi SK, El-Salakawy E (2018) Seismic behavior of exterior GFRP-RC beam-column connections: analytical study. ASCE, J Comp Const 22(4):04018022
17. Hosseini F, Gencturk B (2019) Structural assessment of bridge columns with engineered cementitious composites and Cu-Al-Mn superelastic alloys. Constr Build Mater 203:331–342
18. De Luca A, Matta F, Nanni A (2010) Behavior of full-scale glass fiber-reinforced polymer reinforced concrete columns under axial load. ACI Struct J 107(5):589–596
19. Menegotto M, Pinto PE (1973) Method of analysis of cyclically loaded RC plane frames including changes in geometry and nonelastic behavior of elements under normal forces and bending. Preliminary Rep. No. *13*, IABSE, Zurich, Switzerland, 15–22
20. Naqvi S, El-Salakawy E (2017) Lap splice in GFRP-RC rectangular columns subjected to cyclic-reversed loads. ASCE, J Comp Construct 21(4):04016117
21. Raza A, Rehman A, Masood B, Hussain I (2020) Finite element modelling and theoretical predictions of FRP-reinforced concrete columns confined with various FRP-tubes. Structures 26(May):626–638
22. Selmy YM, Ye F, El-Salakawy EF (2021) Seismic performance of GFRP-RC rectangular columns: numerical study. Proc Inter Struct Eng Const 8(1):STR-49-1-STR-49-6
23. Tahir M, Wang Z, Wei Z, Jameel R (2021) Numerical and analytical modeling of FRP-reinforced concrete columns subjected to compression loading. Australian J Struct Eng Taylor & Francis 22(2):96–109
24. Tavassoli A, Liu J, Sheikh SA (2015) Glass fiber-reinforced polymer-reinforced circular columns under simulated seismic loads. ACI Struct J 112(1):103–114

Aftershock Record Selection Criteria for Structural Vulnerability Assessments

Eugene Kim and Bianca Angheluta

Abstract After a major earthquake, sizeable aftershocks can continue for weeks and cause considerable impact to recovery, but aftershocks are largely overlooked in engineering practice. Numerous research studies have considered the response of structures under mainshock-aftershock (MS-AS) sequences, but there is lack of validation for the artificially generated sequences used in these studies and no standardized method exists for selecting aftershock motions for consideration. This study examines three different aftershock selection criteria adopted in the literature (replicate, random, and generalized Omori's law) and assesses the validity of artificially generated near-field MS-AS sequences, by comparing the cumulative damage potential against real sequences from Northridge (1994), Livermore (1980), and Mammoth Lakes (1980). An elastic-perfectly plastic (EPP) single-degree-of-freedom (SDOF) model is used to compare the peak ductility demand for the different selection methods. The results highlight how poorly selected aftershock ground motions can severely misrepresent the risk and offer insight on key ground motion and sequence characteristics that are crucial for accurately representing aftershock hazards. The generalized Omori's law could potentially be used to generate representative MS-AS sequences for shallow near-field earthquakes, but additional work is needed to further investigate the influence of earthquake parameters on the inelastic response potential of aftershocks and ultimately develop a practical and reliable ground motion selection scheme or framework to support structural assessments and decision-making under aftershock hazards.

Keywords Aftershock record · Vulnerability assessment

E. Kim (✉) · B. Angheluta
University of Waterloo, Waterloo, ON, Canada
e-mail: kekim@uwaterloo.ca

1   Introduction

In regions with complex fault systems, the occurrence of multiple earthquakes in
succession, including foreshocks, mainshocks, and aftershocks occurs due to cumu-
lative stresses in the fault which are not entirely released after a mainshock [1, 8].
More notably, large mainshocks can generate substantial aftershocks such as the
magnitude 6.0 aftershock which was felt only one minute after the magnitude 6.7
Northridge earthquake in 1994 [12]. These observations can be explained through
three empirical scaling laws: the Gutenberg-Richter's law, Omori's law, and Bath's
law which statistically relate mainshocks and aftershocks.

Gutenberg-Richter frequency magnitude scaling describes the number of occur-
rences of an earthquake over a magnitude threshold. Omori's law describes the
temporal decay of aftershocks, giving the occurrence rate of aftershocks over time.
Bath's law states that the difference between the magnitude of the mainshock and
largest aftershock is equal to 1.2, meaning large mainshocks are more likely to
produce large aftershocks [13]. These large aftershocks have the potential to cause
significant damage to structures due to the accumulation of damage caused by
multiple earthquakes, making it important to consider structures under multiple
earthquakes in vulnerability assessments [1].

Before vulnerability assessments for structures under aftershock excitation can be
conducted, appropriate ground motions must first be selected, and MS-AS sequences
then generated. Whereas standardized methods already exist for selecting main-
shock ground motion records, a variety of mainshock-aftershock (MS-AS) sequence
generation methods have been previously used in vulnerability assessments. Four
common methods used in the literature for generating MS-AS sequences are: (1)
as-recorded aftershocks, (2) replicate mainshock, and (3) pairing a mainshock with
another randomly selected mainshock, and (4) pairing a mainshock with an earth-
quake record selected based on generalized Omori's law. The replicate, random, and
Omori's law generation methods are often used because there is little to no after-
shock data available for given mainshock, making it impossible to use as-recorded
sequences [3, 8, 11, 12]. However, these artificially generated sequences may not
be representative of true MS-AS sequences, significantly over or underestimating
the true risk. This paper assesses the applicability of artificially generated MS-AS
sequences for shallow crustal, near-field earthquakes by comparing the peak ductility
demand with 44 natural MS-AS records from California. Results show that while the
replicate and random methods significantly overestimate the inelastic damage poten-
tial of aftershocks, aftershocks selected based on the generalized Omori's law could
adequately represent natural MS-AS sequences. The current study will be further
expanded upon in the future to develop a rational and practical aftershock selection
method.

2 Aftershock Sequence Generation Methods

2.1 As-Recorded

When sufficient records are available for both mainshocks and aftershocks, the natural MS-AS sequences of an earthquake can be used in vulnerability assessments. In this case, one aftershock is paired with its corresponding mainshock. Using as-recorded sequences when possible is preferred since it takes into consideration how the ground motion characteristics of mainshocks and aftershocks, such as magnitude, amplitude, frequency content, and duration differ [1, 5].

Recent studies have aimed to establish relationships for frequency content parameters between mainshocks and aftershocks such as predominant period and response spectra. Statistical relationships explored between the predominant periods of mainshocks and aftershocks for a given earthquake find that they are weakly positively and that predominant periods of mainshocks were found to be longer than aftershocks, suggesting frequency content between mainshocks and aftershocks differ correlated [2, 4, 11, 12].

It has also been found that the response spectra shapes for mainshocks and aftershocks within a sequence differ. Comparing response spectra shapes from 90 records, Goda [4] found that aftershock response spectra consistently plot below those of mainshocks and had a different shape, specifically, aftershock response spectra decreased more rapidly at long periods. Ruiz-Garcia and Negrete-Manriquez [11] reported similar findings when comparing the mainshock and aftershock response spectra at three different stations from the 1994 Northridge earthquake, with the response spectra of the aftershock plotting below that of the mainshock and displaying a different shape. Using as-recorded sequences when possible takes into consideration the ways mainshocks and aftershocks differ in terms of frequency content and how their magnitude and occurrence rate can be related through empirical scaling laws. Sufficient aftershock records may, however, not always be available if there is low station density where the earthquake occurred, resulting in the need to generate artificial sequences. In these cases, consistency of artificial selections with empirical scaling laws and frequency content should be considered [4].

2.2 Replicate Sequences

Generating MS-AS sequences using the replicate method simply involves repeating the time history of a mainshock as the aftershock. Mainshock records may be repeated exactly with no scaling, such was done by Ruiz-Garcia and Negrete-Manriquez [11] and Ruiz-Garcia [12]. Replicate records may also be appropriately scaled but methods for scaling are widely varied. Li and Ellingwood [5] used the Gutenberg-Richter law to predict the magnitude of an aftershock and scaled the mainshock down to have the determined magnitude value. Li et al. [6] used a scaling factor defined as the ratio

between the damage state of a building due to a mainshock and the fundamental period of the building. A limitation of the replicate case, particularly with no scaling, is that it does not consider how frequency content and other parameters, such as magnitude, differs between mainshocks and aftershocks, since the exact mainshock is repeated.

Goda [4] found that when replicate sequences were applied to a two story wood-frame structure where the mainshock and aftershock had the same response spectra, the two story wood-frame structures had a reduced seismic capacity and accumulated more damage when compared with as-recorded sequences where response spectra shaped differed [4]. In particular, Goda [4] attributed higher inter-story drift observed in the replicate analysis to the repetition of the frequency content. If the mainshock initially causes significant damage to a structure, it results in much more significant damage accumulation when it is repeated which may significantly exaggerate the risk in true MS-AS sequences [4, 5, 11, 12].

2.3 Random Sequences

Random sequences are typically generated by randomizing a set of mainshock records from different stations, for a given earthquake, and assigning them as aftershocks for each mainshock record. Although the mainshocks are used as aftershocks, this method attempts to account for the varied frequency content characteristics observed between mainshocks and aftershocks, as the frequency content in each record will vary between stations, even for the same mainshock due to site conditions and distance to the epicenter of an earthquake [4–6, 11, 12].

Ruiz-Garcia and Negrete-Manriquez [11] and Ruiz-Garcia [12] note that in some cases, if a randomly selected mainshock which covers the fundamental period of a structure is used as an aftershock, it could cause more damage than the replicate or as-recorded methods. Although this is not a common occurrence, they oppose the general agreement that the random case is a more appropriate MS-AS sequence generation method than the replicate case, indicating that neither method is perfect in simulating as-recorded sequences. This additionally suggests that it is critical to consider the frequency content of the mainshocks and aftershocks used to generate artificial sequences to avoid overestimations of ductility demand or other damage criteria.

2.4 Generalized Omori's Law

Goda [3] proposed a method of generating MS-AS sequences using generalized Omori's law, which was developed by Shcherbakov [13] and combines Gutenberg-Richter', Bath's, and Omori's laws. Generalized Omori's law [1] describes the rate of occurrences, r, of aftershocks with magnitudes greater than m

$$r(t, m) = \frac{dN(\geq m)}{dt} = \frac{(p-1)c^{p-1}10^{(m_{ms} - \Delta m^* - m)}}{(t+c)^p} \qquad (1)$$

where b, c, and p are region specific parameters, t is the time elapsed since the mainshock in days, m_{ms} is the magnitude of the mainshock, and Δm^* is the difference between the magnitudes of the mainshock and largest aftershock as described by Bath's law.

To verify the applicability of this scaling law, Shcerbakov [13] studied the accuracy of the generalized Omori's law using four California earthquakes (Landers, Northridge, Hector Mine, and San Simeon). A good correlation between aftershock data used and predicted values from generalized Omori's law was found; however, earthquakes with unusually large aftershocks were less accurately approximated by this scaling model [13].

Using generalized Omori's law, Goda [3] developed [2] to generate aftershock magnitudes, m_{as}

$$m_{as} = -\log_{10}\left[10^{-bM_{min}} - (1-u) \times \left(10^{-bM_{min}} - 10^{-bM_{max}}\right)\right]/b \qquad (2)$$

where u is the sample rate from the standard uniform variate, U, b, and p are region specific parameters, and M_{min} and M_{max} are the minimum and maximum magnitudes for aftershocks. This calculated aftershock magnitude, along with a predefined criteria for selecting aftershocks including site class, was then used to select records which would be used as artificial aftershocks for a given mainshock. Specifically, this method was used to select aftershocks for both near and far field Japanese earthquakes. Vulnerability assessments performed with sequences using the generalized Omori's law for the Japanese earthquakes were found to produce similar ductility demands to as-recorded sequences for a SDOF model. The assessment results along with the method's consideration of relationships between mainshocks and aftershocks according to empirical scaling laws which indicates the methods applicability [3]. In this paper, record selection using generalized Omori's law will be performed for the Northridge, Livermore, and Mammoth Lakes earthquakes for near-field stations.

3 Data

To generate as-recorded, replicate, random and Omori's law sequences for the current study, strong motion data was obtained from the PEER NGA-West2 database. Mainshocks and aftershocks records from three earthquakes, Northridge (1994), Livermore (1980), and Mammoth Lakes (1980), and their recording stations were selected based on the following criteria: (1) aftershocks with moment magnitude greater than 4.0, (2) earthquake included data for three or more stations which recorded both the mainshock and aftershock(s), (3) stations were considered near-field (<50 km from epicenter), 4) stations were located on site class C or D. Northridge, Livermore,

and Mammoth Lakes stations were all located on site class C or D, so selecting aftershocks with these same site classes maintains consistency. All earthquakes were purposefully chosen from the same region to maintain the same b, c, and p parameters in Omori's law. For California, Reasenberg and Jones [10] recommend values of $b = 0.91$, $c = 0.05$, and $p = 1.08$. Table 1 lists all the earthquakes and stations which provided records used in this study. Records with ID 1–22 are mainshocks and their corresponding aftershocks from the Northridge (1994), Livermore (1980), and Mammoth Lakes (1980) earthquakes. These records were used to generate the as-recorded, replicate, and random sequences assessed in the study. Records with ID 23–42 are records which were selected to generate sequences based on generalized Omori's Law. Both horizontal components of each record were used to generate the MS-AS sequences, resulting in a total of 194 collected records.

As-recorded sequences were generated by pairing a mainshock with each of its aftershocks at a given station, ensuring that corresponding horizontal components were paired. Replicate sequences were generated by directly repeating the same mainshock record back-to-back with no scaling. Finally, to generate the random pairs, the mainshock records for an earthquake were randomized then paired with other mainshocks from the same earthquake. In this case, records from differing stations were paired which meant mainshock and artificial aftershock records could be recorded from varying horizontal components.

MS-AS sequences based on generalized Omori's law were generated in a two-step process. Using [2] an aftershock magnitude value was determined for Northridge, Livermore, and Mammoth Lakes using the same b, c, and p parameters specified by Reasenberg and Jones [10]. Records with this calculated magnitude value were then searched for to act as an aftershock. Additional criteria for selection included earthquakes from the California region, and earthquakes having the same fault mechanism as the mainshock, near-field events, stations located on site classes C or D. These criteria were selected so that selected records emulated potential aftershocks in terms of empirical scaling laws and frequency content.

4 Peak Ductility Demand

To assess and compare the cumulative damage potential of the natural and artificial MS-AS sequences, an elastic-perfectly plastic (EPP) single-degree-of-freedom (SDOF) model with 5% critical damping was created in OpenSees [7] and the peak ductility demand was evaluated for strength reduction factors $R = 2$, $R = 4$, and $R = 6$. Within each sequence, the system was allowed to undergo 20 s of free vibration at the end of each earthquake excitation for it to return to rest before the next input excitation was applied. Figure 1 shows a typical displacement response time history and hysteretic response for a system with natural period $T = 0.5$ s and $R = 2$.

In the case shown in Fig. 1, the peak ductility demand of 2.6 occurred during the mainshock excitation, meaning the aftershocks did not cause additional inelastic damage to the system. For the as-recorded sequences, the earthquakes were always

Table 1 Selected earthquake records

ID	Earthquake	Station name	Moment magnitude	Hypocentral depth (km)	Epicentral distance (km)	Vs30 (m/s)
1	Northridge-01, 02, 06	Arleta—Nordhoff Fire Station	6.7, 6.1, 5.3	17.5, 6.0, 13.1	11.1, 6.6, 3.4	297.71
2	Northridge-01, 02, 03, 04, 05, 06	Castaic—Old Ridge Route	6.7, 6.1, 5.2, 5.9, 5.1, 5.3	17.5, 6.0, 6.0, 9.8, 11.3, 13.1	40.7, 35.0, 25.1, 27.0, 21.5, 40.1	450.28
3	Northridge-01, 02, 03, 04, 05, 06	Elizabeth Lake	6.7, 6.1, 5.2, 5.9, 5.1, 5.3	17.5, 6.0, 6.0, 9.8, 11.3, 13.1	53.0, 44.2, 41.5, 47.0, 42.7, 48.6	326.19
4	Northridge-01, 05, 06	Jensen Filter Plant Generator	6.7, 5.1, 5.3	17.5, 11.3, 13.1	13.0, 19.7, 9.3	525.79
5	Northridge-01, 02, 06	LA—Baldwin Hills	6.7, 6.1, 5.3	17.5, 6.0, 13.1	28.2, 32.0, 26.9	297.07
6	Northridge-01, 02, 06	LA—Century CC North	6.7, 6.1, 5.3	17.5, 6.0, 13.1	20.2, 24.6, 19.5	277.98
7	Northridge-01, 02, 04, 05, 06	LA—City Terrace	6.7, 6.1, 5.3	17.5, 6.0, 13.1	11.1, 6.6, 3.4	297.71
8	Northridge-01, 02, 06	LA—Hollywood Stor FF	6.7, 6.1, 5.3	17.5, 6.0, 13.1	23.6, 25.0, 20.1	316.46
9	Northridge-01, 02, 03, 06	Newhall—Fire Sta	6.7, 6.1, 5.2, 5.3	17.5, 6.0, 6.0, 13.1	20.3, 13.0, 9.1, 18.1	269.14
10	Northridge-01, 02, 03, 04, 05, 06	Pacoima Kagel Canyon	6.7, 6.1, 5.2, 5.9, 5.1, 5.3	17.5, 6.0, 6.0, 9.8, 11.3, 13.1	19.3, 11.1, 22.5, 31.0, 11.7, 29.9	508.08
11	Northridge-01, 06	Rinaldi Receiving Sta	6.7, 5.3	17.5, 13.1	10.9, 5.5	282.25
12	Northridge-01, 06	Sylmar—Converter Sta East	6.7, 5.3	17.5, 13.1	13.6, 9.0	370.52
13	Northridge-01, 03, 06	Tarzana—Cedar Hill A	6.7, 5.2, 5.3	17.5, 6.0, 13.1	5.4, 21.3, 9.6	257.21
14	Mammoth Lakes-01, 02, 03, 04, 05, 06, 10, 11	Convict Creek	6.1, 5.7, 5.9, 5.7, 5.7, 5.9, 5.3, 5.3	9.0, 14.0, 16.0, 5.0, 4.7, 14.0, 3.0, 4.5	1.4, 8.6, 5.9, 2.8, 9.4, 12.0, 8.9, 9.8	382.12
15	Mammoth Lakes-01, 02, 03, 04, 05, 06	Long Valley Dam (Upr L Abut)	6.1, 5.7, 5.9, 5.7, 5.7, 5.9	9.0, 14.0, 16.0, 5.0, 4.7, 14.0	12.7, 20.1, 11.5, 14.2, 16.9, 14.0	537.16
16	Mammoth Lakes-01, 02	Mammoth Lakes H. S	6.1, 5.7	9.0, 14.0	10.9, 3.5	346.82
17	Livermore-01, 02	Antioch—510 G St	5.8, 5.4	12.0, 14.5	17.8, 31.5	304.68

(continued)

Table 1 (continued)

ID	Earthquake	Station name	Moment magnitude	Hypocentral depth (km)	Epicentral distance (km)	Vs30 (m/s)
18	Livermore-01, 02	APEEL 3E Hayward CSUH	5.8, 5.4	12.0, 14.5	30.8, 29.6	517.06
19	Livermore-01, 02	Del Valle Dam (Toe)	5.8, 5.4	12.0, 14.5	26.8, 13.1	403.37
20	Livermore-01, 02	Fremont—Mission San Jose	5.8, 5.4	12.0, 14.5	37.3, 27.9	367.57
21	Livermore-01, 02	San Ramon—Eastman Kodak	5.8, 5.4	12.0, 14.5	17.1, 16.6	377.51
22	Livermore-01, 02	San Ramon Fire Station	5.8, 5.4	12.0, 14.5	16.7, 21.7	384.47
23	Lytle Creek	Cedar Springs Pumphouse	5.3	8	22.5	477.22
24	Lytle Creek	Colton—So Cal Edison	5.3	8	31.5	301.95
25	Lytle Creek	Devil's Canyon	5.3	8	20.4	667.13
26	Lytle Creek	LA—Hollywood Stor FF	5.3	8	76.2	316.46
27	Lytle Creek	Lake Hughes #1	5.3	8	93.2	425.34
28	Lytle Creek	Puddingstone Dam (Abutment)	5.3	8	31.7	421.44
29	Lytle Creek	Wrightwood—6074 Park Dr	5.3	8	13	486
30	Whittier Narrows-02	Alhambra—Fremont School	5.3	8	4.4	549.75
31	Whittier Narrows-02	Altadena—Eaton Canyon	5.3	13.3	13	375.16
32	Whittier Narrows-02	Downey—Co Maint Bldg	5.3	13.3	16.2	271.9
33	Whittier Narrows-02	Inglewood—Union Oil	5.3	13.3	23.7	316.02
34	Whittier Narrows-02	LA—116th St School	5.3	13.3	20.5	301
35	Whittier Narrows-02	LA—Baldwin Hills	5.3	13.3	24.4	297.07
36	Whittier Narrows-02	LA—Hollywood Stor FF	5.3	13.3	22	316.46
37	Humbolt Bay	Ferndale City Hall	5.8	10	73.5	219.31
38	Northwest Calif-03	Ferndale City Hall	5.8	10	56	219.31

(continued)

Table 1 (continued)

ID	Earthquake	Station name	Moment magnitude	Hypocentral depth (km)	Epicentral distance (km)	Vs30 (m/s)
39	Livermore-01	APEEL 3E Hayward CSUH	5.8	12	30.8	517.06
40	Livermore-01	Antioch—510 G St	5.8	12	17.8	304.68
41	Livermore-01	Del Valle Dam (Toe)	5.8	12	26.8	403.37
42	Livermore-01	Fremont—Mission San Jose	5.8	12	37.3	367.57
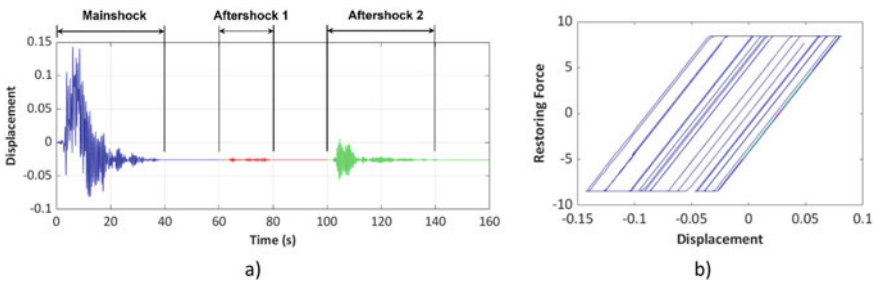
Fig. 1 Response from as-recorded sequence 13 (Northridge: Tarzana–Cedar Hill A) **a** Displacement response **b** Hysteretic response

simulated in the order of occurrence. Some events only had one aftershock record while others had as many as eight that satisfied the selection criteria described in the previous section. All artificially generated sequences were limited to a single aftershock.

5 Results and Discussion

5.1 As-Recorded Sequences

Results from the as-recorded MS-AS sequences are plotted in Fig. 2. Figure 2a shows the average normalized acceleration response spectra in which the spectral acceleration from each earthquake is normalized by its peak ground acceleration (PGA), Fig. 2b shows the probability of the peak response in the MS-AS simulation being greater than from the mainshock excitation alone ($P(\mu_{MSAS} > \mu_{MS})$), and Fig. 2c, d show the cumulative probability distribution function of the peak ductility demand for $R = 2$ and $R = 4$, respectively.
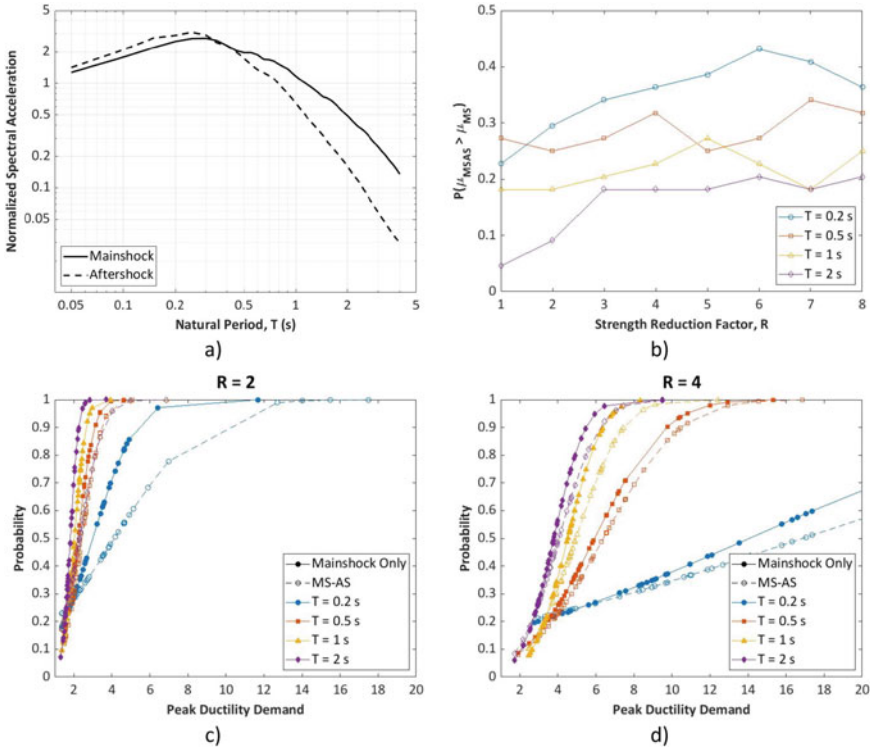
Fig. 2 Results from the as-recorded MS-AS sequences **a** Average normalized acceleration response spectra (5% damping) **b** Probability of inelastic response due to MS-AS sequence exceeding mainshock response **c** Cumulative probability distribution function of the peak ductility demand for $R = 2$ **d** Cumulative probability distribution function of the peak ductility demand for $R = 4$

From the normalized response spectra, it can be seen that both the mainshocks and aftershocks have high short-period spectral content as would be expected from near-field records. Aftershocks generally have lower spectral content in the long-period range which is mainly attributable to the fact that aftershocks have lower magnitude. The characteristics of the normalized spectra are carried over to the inelastic demand. Overall, it can be seen in Fig. 2b that the probability of the cumulative MS-AS response, exceeding the peak response due to the mainshock only is greater for short natural periods. The probability gradually increases from a range of 0.05–0.27 for systems with $R = 1$, which remain linear elastic during the mainshock to between 0.09 and 0.43 with increasing R. These observations suggest systems with shorter period and higher R are generally affected more severely by aftershocks.

The potential for increased inelastic demand from aftershock is also clearly evident in the cumulative probability distribution functions in Figs. 2c, d. In general, for both $R = 2$ and $R = 4$, the peak mainshock ductility demand decreases with increasing

natural period, and aftershocks tend to cause more incremental damage to shorter period systems.

5.2 Artificial Sequences

The averaged normalized response spectra and the probability of MS-AS peak ductility demand exceeding the mainshock demand are shown in Fig. 3 for the random and generalized Omori's law sequences.

As explained above, the random sequences were generated by pairing the mainshock from earthquakes 1–22 in Table 1 with a random mainshock record from the same earthquake. As a result, the mainshock and aftershock acceleration response spectra are identical to each other and to the mainshock spectrum for the as-recorded
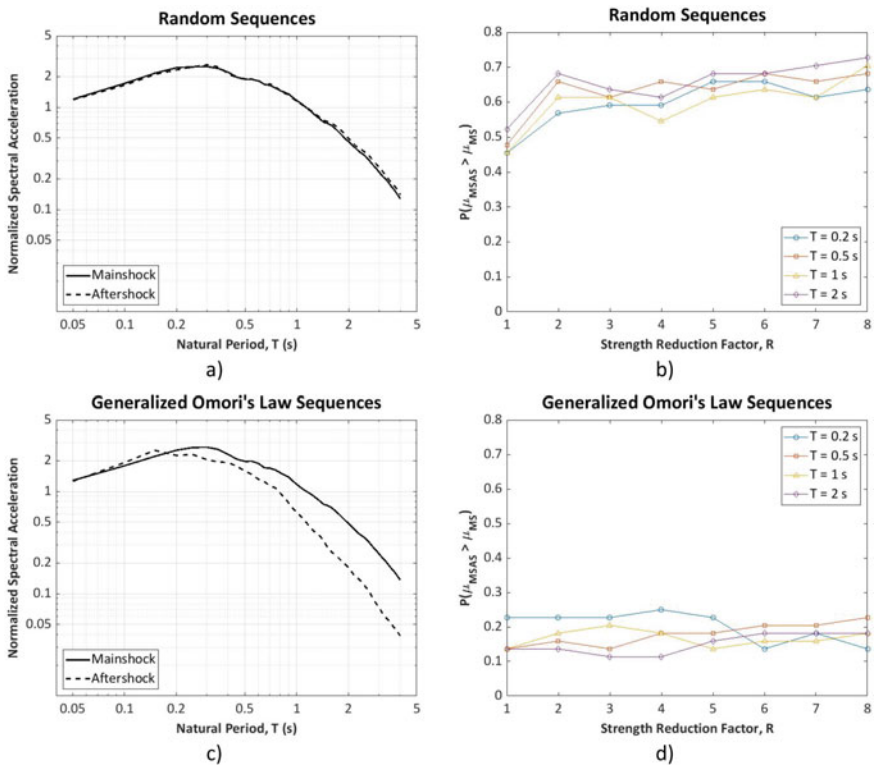
Fig. 3 **a** Average normalized acceleration response spectra for random sequences (5% damping) **b** Probability of inelastic response due to MS-AS sequence exceeding mainshock response for random sequences **c** Average normalized acceleration response spectra for generalized Omori's law sequences (5% damping) **d** Probability of inelastic response due to MS-AS sequence exceeding mainshock response for generalized Omori's law sequences

sequences. As can be seen in Fig. 3a, random MS-AS sequences are significantly more likely to generate higher ductility demands than the mainshock only. In terms of the overall population, random sequences yield results very similar to replicate analysis. Both the replicate and random sequence methods excessively overstate the nonlinear response potential of aftershocks.

In contrast, the average normalized response spectrum for aftershocks selected based on generalized Omori's law is comparable with the as-recorded spectrum in Fig. 2a. The generalized Omori's law yielded aftershocks with relatively low spectral content in the short-period range, but the overall spectral shape closely matches the natural spectrum. Comparing the relative probability plot in Fig. 3d to the as-recorded sequences in Fig. 2b, Omori's law sequences appear to yield comparable results at longer periods but underestimate the damage potential of aftershocks at short periods. From the cumulative probability distribution of the peak ductility demand plotted in Fig. 4, Omori's law sequences do indeed closely reproduce the peak ductility distributions of as-recorded sequences at for $T = 1$ s and $T = 2$ s. However, at shorter periods, Omori's law sequences yielded some very high peak ductility demands. It is reasonable to expect high peak ductility demands for low period systems with high strength reduction factors but in this case, Omori's law simply generated more such cases than the natural sequences.

The current study focused on simply assessing the validity of the replicate, random, and generalized Omori's law-based MS-AS sequence generation methods against real recorded sequences. However, a larger sample size of natural sequences and a more comprehensive investigation are needed to determine how aftershock inelastic response potential is affected by earthquake size, intensity, and frequency content. Furthermore, the EPP hysteretic model is too simplistic to accurately capture the damage accumulation process. These issues will be addressed in a future study.

6 Conclusions

Aftershocks are largely overlooked in engineering practice, but large aftershocks have the potential to cause considerable additional damage to structures and impede the recovery process. The impact of MS-AS sequences has been studied in numerous research studies, but there is lack of validation for the artificially generated sequences used in these studies, and no standardized method exists for selecting aftershock motions for consideration. In this study, the validity of three artificial MS-AS sequence generation methods were assessed against natural as-recorded sequences: replicate sequences, random sequences, and sequences based on generalized Omori's law. The primary focus was on whether these artificial sequences accurately represent the ductility demand in shallow near-field MS-AS sequences. A simple EPP SDOF system was used to quantify the peak ductility demand in the artificially generated sequences to 44 real MS-AS sequences, recorded from the 1980 Livermore earthquake, 1980 Mammoth Lakes earthquake, and 1994 Northridge earthquake. Results showed that the replicate and random methods for generating MS-AS
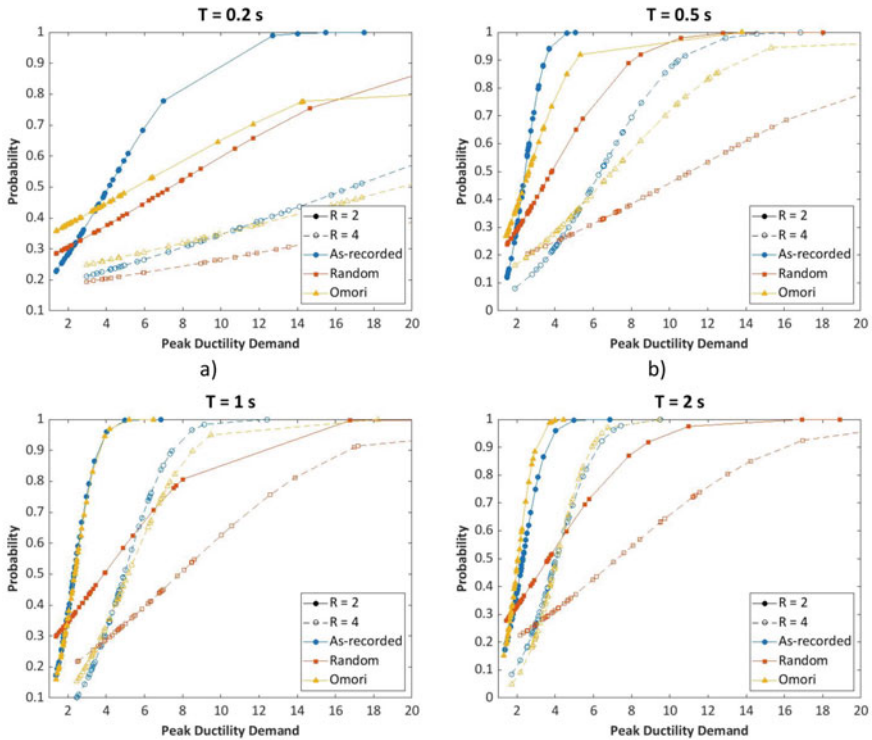
Fig. 4 Cumulative probability distributions of the peak ductility demand for as-recorded, random, and for generalized Omori's law MS-AS sequences **a** $T = 0.2$ s **b** $T = 0.5$ s **c** $T = 1$ s **d** $T = 2$ s

sequences significantly overestimate the damage potential of aftershocks. The generalized Omori's law shows some promise for selecting aftershock records for shallow near-field earthquakes, particularly for systems with longer fundamental natural periods but a larger sample size and a more comprehensive investigation are needed to characterize the effect of earthquake characteristics on aftershock inelastic response potential and develop rational and practical guidelines for considering aftershocks in seismic analyses.

References

1. Abdelnaby AE (2018) Fragility curves for RC frames subjected to Tohoku mainshock-aftershocks sequences. J Earthquake Eng 22(5):902–920
2. Di Sarno L, Pugliese F (2021) Effects of mainshock-aftershock sequences on fragility analysis of RC buildings with ageing. Eng Struct 232:111837
3. Goda K (2012) Nonlinear response potential of mainshock-aftershock sequences from Japanese earthquakes. Bull Seismol Soc Am 102(5):2139–2156

4. Goda K (2015) Record selection for aftershock incremental dynamic analysis. Earthquake Eng Struct Dynam 44:1157–1162
5. Li Q, Ellingwood BR (2007) Performance evaluation and damage assessment of steel frame buildings under main shock–aftershock earthquake sequences. Earthquake Eng Struct Dynam 36(3):405–427
6. Li Y, Song R, Van De Lindt J (2014) Collapse fragility of steel structures subjected to earthquake mainshock-aftershock sequences. J Struct Eng 140(12):04014095
7. McKenna F, Scott MH, Fenves GL (2010) Nonlinear finite-element analysis software architecture using object composition. J Comput Civ Eng 24(1):95–107
8. Omranian E, Abdelnaby AE, Abdollahzadeh G (2018) Seismic vulnerability assessment of RC skew bridges subjected to mainshock-aftershock sequences. Soil Dyn Earthq Eng 114:186–197
9. PEER NGA (2021) Pacific Earthquake Engineering Research Center PEER strong motion database. Retrieved from https://ngawest2.berkeley.edu/. Last accessed 03/03/2022
10. Reasenberg PA, Jones LM (1989) Earthquake hazard after a mainshock in California. Science 243:1173–1176
11. Ruiz-Garcia J, Negrete-Manriquez JC (2010) Evaluation of drift demands in existing steel frames under as-recorded far-field. Eng Struct 33(2):621–634
12. Ruiz-Garcia J (2012) Mainshock-aftershock ground motion features and their influence in building's seismic response. J Earthquake Eng 16(5):719–737
13. Shcherbakov R, Turcotte D, Rundle J (2005) Aftershock Statistics. Pure Appl Geophys 162:1051–1076

Impact of Ground Motion Selection on the Seismic Performance Assessment of Buckling-Restrained and Shape Memory Alloy Braces

Emad Abraik, Iqbal Asif, and Alam Shahria

Abstract This paper presents the seismic evaluation of three-story buildings located in Los Angeles, California, which has been designed according to the 2005 ASCE 7 and AISC 341. A three-dimensional (3D) model for buckling-restrained brace (BRB) and superelastic shape memory alloy (SE-SMA) buildings are developed, and the seismic response is assessed under different ground motion selections, which are scaled by utilizing the risk-targeted maximum considered earthquake scenario (MCEr). The time history analysis results indicate the need for considering the 3D numerical model for the seismic evaluation of buildings. Additionally, the SE-SMA building results show residual displacement and brace-deformation damage lower than that of the BRB building under different ground motion selections using the ASCE 41 procedure. NF ground motions have a significant impact on the evaluation performance of BRB and SE-SMA buildings, and thus, a conservative retrofit solution can be developed.

Keywords Ground motion · Seismic engineering · Buckling-restrained · Shape memory alloy · Self-centering · Retrofit

1 Introduction

The poor seismic performance (e.g., limited ductility and energy dissipation and large residual deformation) of conventional braced frames in severe earthquakes has led researchers to introduce alternative types of braces [18], including buckling-restrained braces (BRBs), tension braces, and self-centering braces. The BRB steel braces are prevented from buckling by the surrounding concrete, and this design

E. Abraik (✉) · I. Asif

Department of Civil Engineering, University of Northern British Columbia, Prince George, BC, Canada

e-mail: eabraik@uwo.ca

E. Abraik · A. Shahria

School of Engineering, The University of British Columbia, Endowment Lands, BC, Canada

can dissipate symmetric energy in both tension and compression. However, BRB's lower initial and post-yield stiffness led to story mechanisms (i.e., soft story) in multi-story buildings [14], resulting in severe damage combined with considerable residual deformations.

Recent investigation in resilient infrastructures has been aiming to develop self-centering seismic resisting systems that can minimize to damage probability and economic losses and increase functional recovery speed following an earthquake [13]. Considerable research efforts have been made in developing self-centering lateral resisting systems based on superelastic shape memory alloy (SE-SMA). The novel material exhibits an extraordinary ability to recover large strain upon unloading. This unique behavior led researchers to investigate its use in several seismic applications, such as base isolations, dampers [22], and steel frame connections [23]. The results of these studies prove that the use of SE-SMA materials has improved structural seismic performance during and after seismic events. Several efforts have been directed to utilize the SE-SMA material in reinforced concrete (RC) structures, including RC beam–column joints [26], RC bridge columns [24], RC moment frames [5], and RC shear walls [2–5]. The results of these studies demonstrated a superior seismic behavior and the ability of SE-SMA material to reduce the main shock seismic effects.

In steel structures, the material has been introduced as an alternative solution for the conventional and BRB braces. Asgarian and Moradi [11] conducted a study that used a short segment of SE-SMA in each brace. The seismic performance of the system has been compared to the one using BRBs. The results indicated that combining the SE-SMA in the steel brace can lead to reducing the inter-story drift ratio (IDR) and residual inter-story drift ratio (RIDR). Moradi et al. [18] compared the seismic performance of four stories' buildings equipped with either BRBs or SE-SMA braces. The study indicated that the SE-SMA braces could be more beneficial than the BRBs under severe ground motions. Vafaei and Eskandari [25] confirmed the SE-SMA braces' superior seismic performance when the system was subjected to near-field (NF) ground motions [12]. Miller et al. [20] investigated the cyclic response of SE-SMA braces. The experimental results showed a stable hysteretic response with large energy dissipation and self-centering ability. Following this concept, Nazari-mofrad and Shokrgozar [21] conducted a performance evaluation of steel braces with SE-SMA braces. The results of SE-SMA braces showed an improvement in ductility with a negligible residual displacement compared to the BRB structures. Abraik [6] recently investigated the torsional implication response of SE-SMA braces. A reduction of the inter-story drift (IDR) as compared to the SE-SMA and BRB braces was noted. Although prior publication research provided a sufficient understanding of BRB and SE-SMA braces' behavior, evaluating steel buildings with SE-SMA braces considering different ground motion selections using the three-dimensional (3D) model has not yet been explored.

The objective of this paper is to comparatively evaluate the seismic response of BRB and SE-SMA brace buildings. Ground motions are selected to represent different characteristics, including near-field and far-field location. A 3D

nonlinear time history analysis procedure is used to conduct the seismic performance assessment using the ASCE 41 (2017).

2 Building Design

2.1 BRB Building

A three-story BRB-braced frame office building was designed by Forwll/Elsesser Engineers, Inc. with occupancy category II and importance factor $I = 1$ [5]. The building has been designed according to the provisions of the International Building Code [15], ASCE 7 (2005), and the AISC 341 (2005) using the Equivalent Lateral Force Method. The building is assumed to be located in Los Angeles, CA (latitude: 34.00 N, longitude: 118.2 W), on stiff soil (site class D with shear wave velocity Vs30 = 180–360 m/s. The BRB building was designed with a force reduction factor $R = 8$ and a drift ratio limit of 2.0%. The characteristic yield strength of steel was assumed to be 345 MPa for frame members and 318 MPa for brace members. The building layouts are 55 m × 36.6 m in the plan, with story heights of 4.57 m and column spacing of 9.15 m in each direction. The lateral loads are carried by a single-braced bay on each side of the building perimeter, while the remaining elements were designed to resist gravity loads only, as shown in Fig. 1. Table 1 lists the steel sections for all design frame members of the building. The total gravity load considered for seismic mass includes the self-weight of frame members, 3.11–3.21 kPa dead load, including self-weight and superimposed load per floor, and 0.96 kPa for cladding around the building exterior. Thus, each story's seismic weight was computed as 7962 kN, 7957 kN, and 8304 kN at the first, second, and roof levels, respectively.

2.2 SMA Building

In previous studies, a common design approach is to use short SE-SMA segments connected to the frame through rigid elements, as shown in Fig. 2. The SE-SMA braces were considered buckling-restrained by assuming that the SE-SMA bars are encased in grouted tubes and unbonded, allowing them to undergo compressive loading without buckling. The reason to use short SE-SMA segments is that SE-SMA has a lower modulus of elasticity than conventional steel. The SE-SMA cross-section area (ASMA) is designed to provide the same axial strength of the steel area (AS), and the SE-SMA segment length (LSMA) is calculated to provide the same initial axial stiffness of the original steel bracing length (LS). As a result, both the conventional steel and the SE-SMA frame designs had the same natural frequency. Based on these considerations, the following relations are derived [1, 6]:
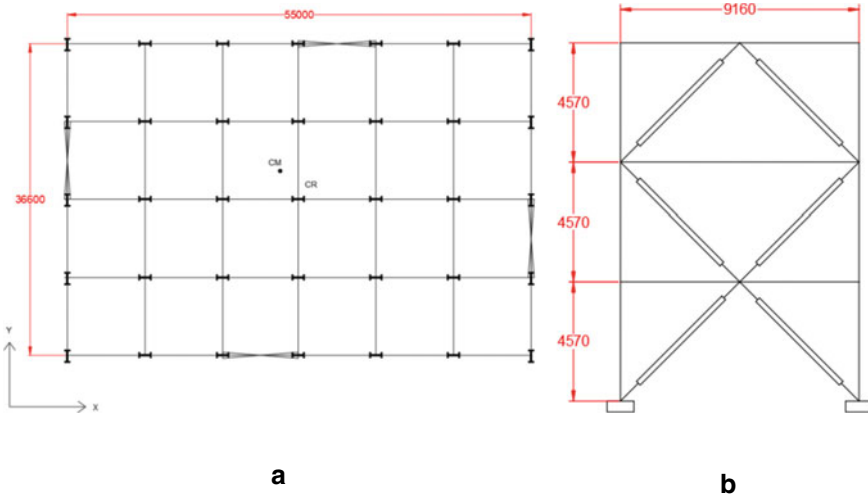
Fig. 1 **a** Plan view of the building; **b** elevation (all dimensions in mm)

Table 1 Members' section details

Story	Column	Girder	BRB area (mm^2)	SMA area (mm^2)
1	W12X120	W18X76	8448	7070
2	W12X120	W18X76	7680	6427
3	W12X65	W18X76	6144	5142

$$A_{SMA} = \frac{F_y}{f_{y-SMA}} A_s, \tag{1}$$

$$L_{SMA} = \frac{F_y}{f_{y-SMA}} \cdot \frac{E_{SMA}}{E_s} \cdot L_s, \tag{2}$$

where f_{y-SMA}, E_{SMA}, and E_s are the yielding stress of SE-SMA, modulus of elasticity of SE-SMA, and modulus of elasticity of steel, respectively.

3 Numerical Model

Three-dimensional models of both buildings (i.e., BRB and SE-SMA braces) were developed in the Open System for Earthquake Engineering Simulation (OpenSees) platform (2013). The mass center at each story was shifted by 5% of the plan dimension in both directions, shown in Fig. 1a, to account for accidental torsion, as required by ASCE 7 (2016). All columns were modeled using force-based nonlinear elements
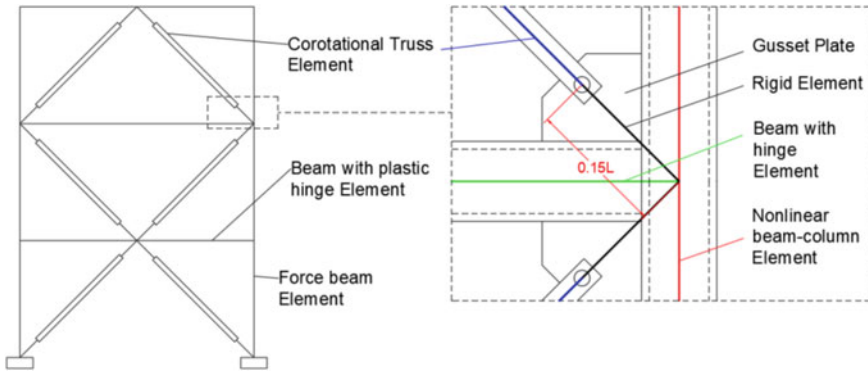
Fig. 2 Numerical model details

Table 2 SE-SMA bars parameters used in the numerical model

Material	Parameter	Value
NiTi SE-SMA (55.9% nickel and 44.1% titanium)	Austenite yield strength, f_{y-SMA} (Mpa)	380
	Austenite modulus, K_1 (Mpa)	36,459
	Post-yield stiffness, K_2 (Mpa)	1724
	Recoverable strain, ε_r	7.0%
	Lower plateau stress factor, β	0.55%

that model the spread of plasticity across the element to account for moment–axial force interaction at each analysis step. All beams of both buildings were modeled using a nonlinear frame element that combines finite length 'plastic hinge' regions at the element ends with an interior elastic region (i.e., beam with plastic hinge elements), as shown in Fig. 2. A steel material using the Giuffre, Pinto, and Menegotto steel model (Steel02) was used with a strain hardening ratio of 3%. The braced bay and gravity columns were fixed and pinned at the base, respectively. The braces were modeled with an effective length of 0.7L, where L is the full diagonal length between beam–column intersection centerlines. The SMA material was made using self-centering material. Table 2 lists the material parameters used in the numerical model.

4 Ground Motion Selection

The near-field (NF) and far-field (FF) ground motions might be defined as ground motions occurring near and far from the earthquake faults. Two main criteria are used to distinguish between them: (1) the source distances of NF ground motions are less than 20 km; and (2) the ratio of PGV and PGA is greater than 0.2 [17]. Several
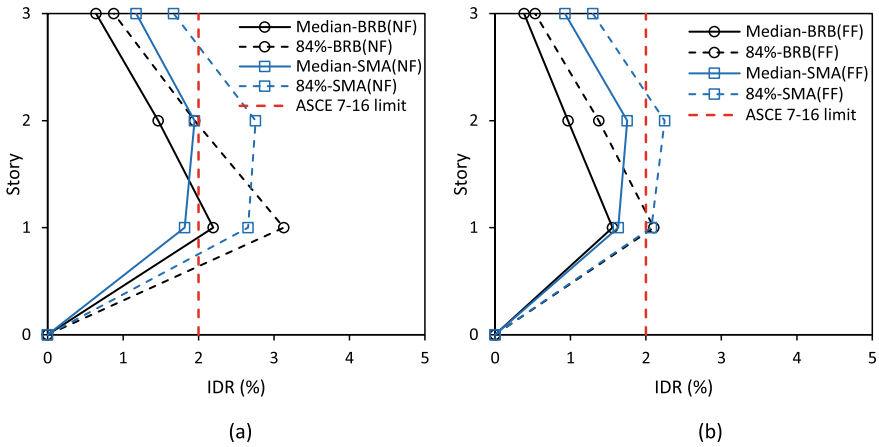
Fig. 3 IDR at CM for **a** NF; **b** FF

other assumptions were also applied to the selected records, including both buildings which are assumed to be site in soil class D with earthquake magnitude range from 6.0 to 8.0, the distance range from 10 to 100 km, and the maximum scale factor of 5 as upper scale limit.

Figure 3 compares the median and the 84th percentile of IDR demand of both buildings subjected to NF and FF ground motions. The statistical values (median and 84th percentile) under the NF level are larger than that of the FF ground motions by a factor of 1.5 and 1.3 on average for the BRB and SE-SMA building, respectively. Comparing the two buildings, the 84th percentile IDR results of both buildings have exceeded the ASCE 7 (2016) limit. Additionally, the results indicate that the BRB building exhibits higher IDR in the first story even for median IDR. This IDR, however, is effectively reduced in the upper stories in comparison to the SE-SMA building, which has an almost uniform IDR along with the building height.

Regarding the RIDR response, shown in Fig. 4, it is clear that both buildings are below the DS2 limit proposed by the FEMA P-58-1 [16] under the FF ground motions level. The BRB building's 84th percentile static data violate the DS2 limit along with the building height under the NF ground motions level.

5 Seismic Assessment Based on ASCE 41-17

The ASCE 41 (2017) standard is provided by the American Society of Civil Engineering to conduct seismic evaluation and retrofit of existing buildings. The standard includes performance objectives and seismic hazards, seismic performance evaluation procedures, and retrofit evaluation.
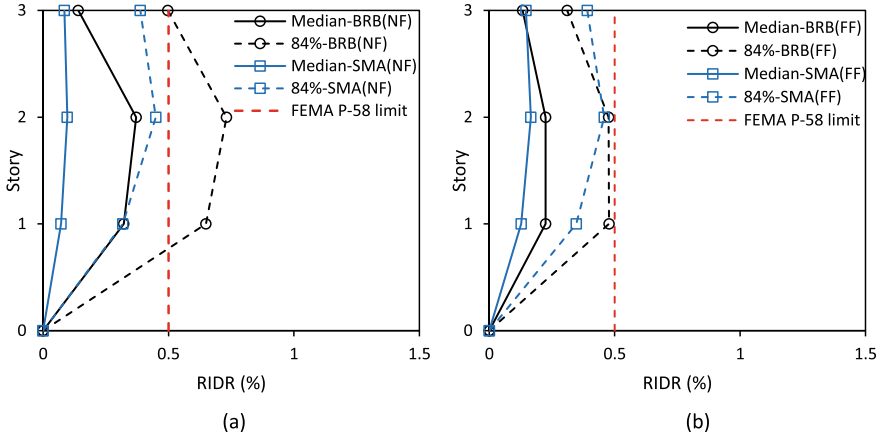
Fig. 4 RIDR at CM for **a** NF; **b** FF

Figure 5 illustrates the seismic evaluation of the brace members along the building height. The figure plots the ratio of 84th percentile peak rotation normalized to the brace's expected strength. As shown, the SE-SMA braces have sufficient capacities for remaining below the plastic capacity limit induces by different ground motion selections. A significant variation is observed along the BRB building height with values exceeding the BRB brace plastic capacity under LD and NF ground motions. The difference in brace responses between the two considered systems is attributed to the delay of yielding displacement, area of SE-SMA, and SE-SMA material's yielding strength. Figure 6 plots the residual deformation (θres) along the building height as a ratio to their yielding rotation (θy). The θres/θy ratio of all BRB braces induced by different ground motion selections except for FF sets exceeds 1.0 at the bottom level. All braces' seismic performances under a different ground motion for the SE-SMA building are better than those seen in the BRB building and remain elastic after the seismic events.

Evaluations of beams' and columns' response for both buildings are condensed in Fig. 7 under 84th percentile statistic data. The results utilize the plastic deformation capacity (i.e., the ratio of the peak deformation, θ to the plastic deformation, θ_p) as the acceptance criteria for the seismic assessment. The beams' seismic evaluation for both buildings is the same regarding the difference in ground motion selections mainly because of beams' low axial force demand. As for columns, the results indicate that all columns at upper stories successfully pass the assessment criteria with θ/θ_p values below 1.0, providing a sufficient margin of safety under different ground motion selections. For columns at the base level, the θ/θ_p remains below 1.0 under SD and FF ground motion selection. As expected, the high energy obtained from the LD and NF ground motions led to sustained higher axial load demand and large brace axial deformations, combined with large moments. Results are more critical for both buildings when assessing the base columns under NF ground motions.
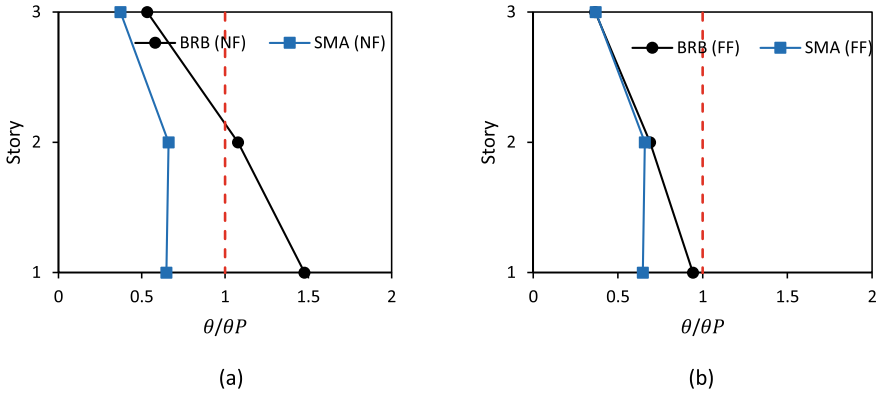
Fig. 5 Evaluation of the braces under: **a** NF; **b** FF ground motions
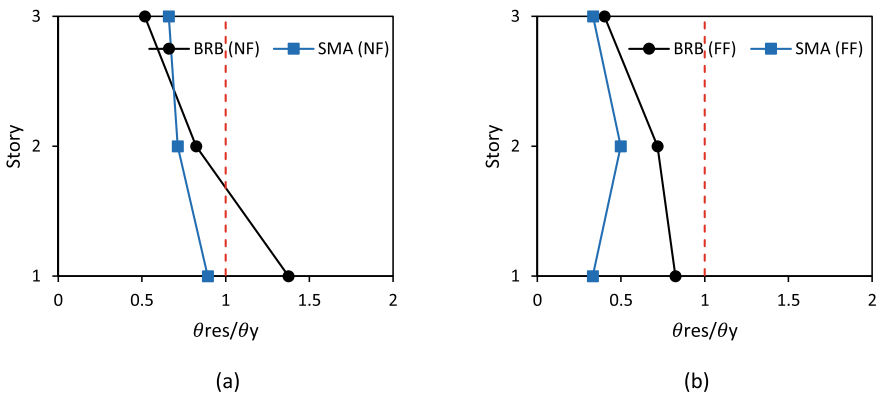
Fig. 6 Evaluation of the braces residual rotation under **a** NF; **b** FF ground motions

6 Conclusions

The seismic performance of the 3D three-story BRB and the SE-SMA buildings subjected to NF and FF ground motion characteristics is evaluated. The following conclusions can be drawn from the conducted study.

Although there is no significant difference in the 84th percentile IDR demand of the SE-SMA building and the BRB building under the NF earthquake set, the SE-SMA material's self-centering capability mitigates the RIDR by a factor of 1.6 compared to the BRB building.

The ground motion selection had less effect on the beams because the brace strength bounds the axial load demand. Both buildings' base columns failed under the NF ground motions, suggesting either retrofitting or strengthening the base columns by providing additional reinforcement plates.
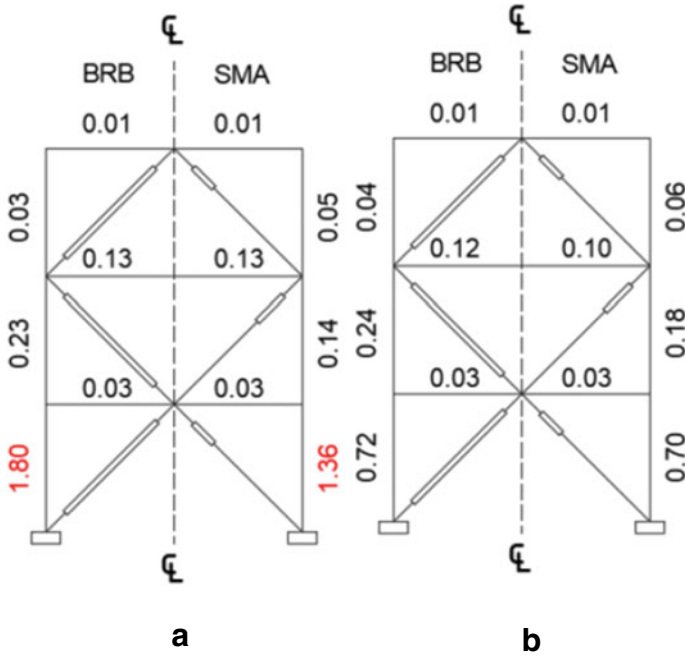
Fig. 7 Beams' and columns' deformation response under different ground motion selections for:
a NF; **b** FF

The maximum brace axial deformation of the BRB building occurred on the first floor and the second floor under NF ground motion sets, whereas the SE-SMA braces successfully passed the assessment criteria with a small margin, which is related to the large yield strength and area of SE-SMA material compared to the BRB one.

Eventually, the present study is limited to the selected SE-SMA material and brace configuration.

References

1. Auricchio F, Fugazza D, Desroches R (2006) Earthquake performance of steel frames with nitinol braces. J Earthquake Eng 10(spec01):45–66
2. Abraik E, Asteetah A (2022) Parametric analysis of slotted concrete shear walls reinforced with shape memory alloy bars. Case Studies Construct Mat 16:e00806
3. Abraik E, Assaf J (2021) Impact of ground motion duration on concrete shear walls reinforced with different types of shape memory alloy rebars. Struct 33:2739–2754
4. Abraik E, Youssef MA (2021) Ductility and overstrength of shape-memory-alloy reinforced-concrete shear walls. Eng Struct 239:112236
5. Abraik E, El-Fitiany SF, Youssef MA (2020) Seismic performance of concrete core walls reinforced with shape memory alloy bars. Struct 27:1479–1489

6. Abraik E (2021) Numerical study for the impact of torsional amplification on the seismic response of self-centring braces equipped with different shape memory alloy materials. Struct 32:505–515

7. ASCE. Seismic Rehabilitation of Existing Buildings (2017) ASCE/SEI 41-17. American Society of Civil Engineers. Reston, VA

8. American Institute of Steel Construction (AISC) (2005) AISC 341-05 seismic provisions for structural steel buildings. Chicago, IL

9. American Society of Civil Engineers (ASCE) (2016) Minimum design loads for buildings and other structures, ASCE/SEI 7-16. Reston, VA.

10. American Society of Civil Engineers (ASCE) (2005) Minimum design loads for buildings and other structures, ASCE/SEI 7-05. Reston, VA

11. Asgarian B, Moradi S (2011) Seismic response of steel braced frames with shape memory alloy braces. J Constr Steel Res 67(1):65–74

12. Akkar S, Yazgan U, Gülkan P (2005) Drift estimates in frame buildings subjected to near-fault ground motions. J Struct Eng 131(7):1014–1024

13. Bruneau M, Reinhorn A (2007) Exploring the concept of seismic resilience for acute care facilities. Earthq Spectra 23(1):41–62

14. Beiraghi H, Zhou H (2020) Dual-steel frame consisting of moment-resisting frame and shape memory alloy braces subjected to near-field earthquakes. Struct Design Tall Spec Build 29(14):e1784

15. International Code Council (ICC) (2006) International Building Code (IBC). Falls Church, VA

16. FEMA (Federal Emergency Management Agency) (2018) Seismic performance assessment of buildings: volume 1-methodology, FEMA P-58-1. Washington, DC

17. Liu Y, Lu DG, Paolacci F (2015) Multivariate probabilistic seismic demand analysis of steel-concrete composite bridges under near-fault pulse-like ground motions. In: Multi-span large bridges. CRC Press, pp 1057–1068

18. Moradi S, Alam MS, Asgarian B (2014) Incremental dynamic analysis of steel frames equipped with NiTi shape memory alloy braces. Struct Design Tall Spec Build 23(18):1406–1425

19. McKenna F, Fenves G, Scott M (2013) Computer program OpenSees: open system for earthquake engineering simulation. Pacific Earthquake Engineering Center; University of California, Berkeley, CA

20. Miller DJ, Fahnestock LA, Eatherton MR (2012) Development and experimental validation of a nickel–titanium shape memory alloy self-centering buckling-restrained brace. Eng Struct 40:288–298

21. Nazarimofrad E, Shokrgozar A (2019) Seismic performance of steel braced frames with self-centering buckling-restrained brace utilizing superelastic shape memory alloys. Struct Design Tall Spec Build 28(16):e1666

22. Ozbulut OE, Silwal B (2016) Performance assessment of buildings isolated with S-FBI system under near-fault earthquakes. Smart Struct Syst 17(5):709–724

23. Sultana P, Youssef MA (2018) Seismic performance of modular steel frames equipped with shape memory alloy braces. Bull Earthq Eng 16(11):5503–5527

24. Saiidi MS, Wang H (2006) Exploratory study of seismic response of concrete columns with shape memory alloys reinforcement. ACI Mater J 103(3):436

25. Vafaei D, Eskandari R (2016) Seismic performance of steel mega braced frames equipped with shape-memory alloy braces under near-fault earthquakes. Struct Design Tall Spec Build 25(1):3–21

26. Youssef MA, Alam MS, Nehdi M (2008) Experimental investigation on the seismic behavior of beam-column joints reinforced with superelastic shape memory alloys. J Earthquake Eng 12(7):1205–1222

Seismic Response of Nuclear-Reinforced Concrete Shear Walls with High-Strength Materials

Mohamed Abouyoussef and Mohamed Ezzeldin

Abstract Recent research studies have investigated the use of high-strength materials in nuclear power plants to enhance the constructability of their massive squat-reinforced concrete shear walls. Despite the advantages of these high-strength materials, the dynamic response of such walls has not yet been fully investigated at the different damage states. To address this, the current study focuses on developing fragility functions for squat-reinforced concrete shear walls with high-strength materials to evaluate their seismic response compared to their counterparts with normal-strength materials. In this respect, a numerical OpenSees model, validated using previous experimental programs that have been conducted on reinforced concrete shear walls (i.e., with different aspect ratios, vertical and horizontal web reinforcement ratios, yield/ultimate strengths of reinforcement, and concrete compressive strengths), is used in the current study. Incremental dynamic analyses, using the 44 far-field ground motion records recommended by the FEMA P695 methodology, are then performed to develop fragility functions for reinforced concrete shear walls with normal- and high-strength materials at different damage states. These damage states are characterized by several performance indicators including cracking and crushing of concrete, residual displacements due to sliding, and reinforcement buckling/fracturing, following the FEMA P-58 guidelines. Finally, design recommendations are presented to enhance the seismic performance of squat-reinforced concrete shear walls when high-strength materials are adopted in nuclear construction practice.

Keywords Seismic response · Nuclear-reinforced concrete · Shear walls

M. Abouyoussef (✉) · M. Ezzeldin
McMaster University, Hamilton, ON, Canada
e-mail: abouyoum@mcmaster.ca

M. Ezzeldin
e-mail: ezzeldms@mcmaster.ca

1 Introduction

Reinforced concrete (RC) shear walls are the most common type of structural system in nuclear power plants [8]. These nuclear RC shear walls are much longer (i.e., from 6 to 90 m) and thicker (i.e., from 500 to 2000 mm) compared to conventional structural buildings. Also, these nuclear RC shear walls have few openings to prevent radiation leaks and enhance blast/fire protection. In addition, the aspect ratios of these walls are very low (i.e., equal to two or less), and therefore, these walls have a high stiffness with a very short fundamental mode vibration. Typically, these walls have two or more mats of large-diameter rebars [8]. The combination of squat and thick wall geometry results in high seismic shear demands. Moreover, since nuclear structures are designed to remain essentially elastic in a design-basis earthquake, the displacement ductility demands of their stiff squat RC shear walls can be very large even if they yield slightly [11]. These squat walls tend also to fail in shear as their geometrical configurations limit their bending. Therefore, it is important to investigate the behavior of these stiff squat shear walls in case they experience severe earthquake ground motions that were not considered during their design stages.

The constructability and building costs of nuclear RC structures are affected by using large amounts of normal-strength materials. Specifically, congested horizontal and vertical rebar cages used in nuclear RC walls are heavy and difficult to construct. Overall, time, labor, and materials lead to very high construction costs that are worth billions of US dollars [17]. Therefore, the use of high-strength reinforcement (i.e., specified yield strength, $f_y \geq 500$ MPa) and/or concrete (i.e., concrete compression strength, $f'_c \geq 55$ MPa) has the potential to enhance the constructability and economy of nuclear RC walls [2]. This is because, for example, high-strength reinforcement (HSR) can significantly reduce the required steel areas, thus minimizing material/fabrication costs, reducing rebar congestion, easing concrete placement, and simplifying quality control inspections.

The main objective of the current study is to develop fragility functions for squat RC shear walls with normal- and high-strength materials at different damage states. In this respect, an *OpenSees* model is used to simulate the seismic response of squat RC walls. The model is then used to perform incremental dynamic analyses and subsequently develop fragility functions for two squat RC shear walls with normal- and high-strength materials at different damage states using the 44 far-field ground motion records recommended by the FEMA P695 [12] methodology. Finally, the study evaluates the influence of high-strength materials using the seismic fragility of squat RC shear walls.

2 Numerical Model

OpenSees was utilized in several previous studies to simulate RC shear walls with flexure-dominant, shear-dominant, and flexure–shear-dominant responses [16, 19, 20, 23, 24]. The current study utilized a 3D numerical model in *OpenSees* [21] that uses the multi-layer shell element [18] available in OpenSees (i.e., ShellMITC4″ element) in order to simulate the cyclic response of squat RC shear walls with normal- and high-strength materials. This model was validated by Abouyoussef and Ezzeldin [1] and showed good agreement with the experimental test results. Therefore, the model was used in the current study to simulate the cyclic response of squat RC shear walls and subsequently generate fragility functions for two RC walls at different damage states.

3 Damage States

Based on the guidelines for repair of RC walls [e.g., FEMA 306 [5] and FEMA 308 [6]], repair of concrete [e.g., ACI 546R-04 [4]], and observations from experimental programs, three damage states were considered in the current study following the criteria presented by the FEMA P-58/BD-3.8.8 [13]. Specifically, damage state (DS-I) is defined by the yielding of either the horizontal or the vertical web reinforcement rebars. DS-I requires only epoxy injection into the cracked concrete to restore the wall strength and stiffness. Damage state (DS-II) is characterized by concrete crushing at the compression toes or initiation of crushing in the wall web or vertical cracking in the toe regions of the web. DS-II requires removing and replacing the damaged concrete/rebars (i.e., partial wall replacement). Damage state (DS-III) is characterized by shear failure or reinforcement fracture. DS-III requires a complete replacement of the wall panel.

Previous research studies (e.g., Cheng et al. [10]) showed that RC components with high-strength materials had larger crack widths than RC components with normal-strength materials, even when both components had similar strength and deformation capacities. Therefore, three damage states (DS-0.5 mm, DS-1.5 mm, and DS-3 mm) were proposed in the current study based on the crack width of the wall, where DS-0.5 mm, DS-1.5 mm, and DS-3 mm are realized when a wall has crack widths of 0.5 mm, 1.5 mm, and 3 mm, respectively. The wall crack width, W, was calculated using the developed model based on the modified compression field theory [9, 26], as presented in Eqs. (1), (2), and (3).

$$W = S_\theta \varepsilon_1, \tag{1}$$

$$S_\theta = \frac{1}{\frac{Sin\theta}{S_X} + \frac{Cos\theta}{S_z}}, \tag{2}$$

$$\tan^2 \theta = \frac{\varepsilon_x - \varepsilon_2}{\varepsilon_z - \varepsilon_2}, \tag{3}$$

where S_θ is the crack spacing, ε_1 is the principal tensile strain, θ is the inclination of the diagonal compressive stresses, S_x was taken as the vertical distance between the bars aligned in the x-direction due to the cracks in the x-direction reinforcement, S_z was taken as the horizontal distance between the bars aligned in the z-direction based on the crack control characteristics of the z-direction reinforcement which, ε_x is the longitudinal strain in the web, ε_z is the transverse tensile strain in the web, and ε_2 is the diagonal compressive strain.

4   Nonlinear Dynamic Analysis

Incremental dynamic analysis [25] was performed for the underlying walls, using the 44 far-field ground motion records recommended by the FEMA P695 [12] methodology, to generate the fragility functions at different damage states. Incremental dynamic analysis (IDA) was conducted by scaling such records to increasing intensities until the walls reached DS-III and DS-3 mm. As Huang et al. [14] recommended, a tributary seismic mass that matches a 0.15 s fundamental model vibration period was selected for the walls based on a Candu reactor prototype. At the periods of T_1 and $0.2T_1$ [22], initial stiffness-proportional Rayleigh damping of 5% was selected for all walls, where T_1 is the wall fundamental period based on eigenvalue analysis. Also, the spectral acceleration (S_T), at the fundamental period, T_1, was selected as the intensity measure because such low-rise nuclear RC shear walls are typically dominated by the first mode [25]. Reinforcement strains, concrete compressive strains, shear strains and crack widths were recorded during the IDA, where these results were then used to identify the damage states for each wall. In this respect, reinforcement yield strain was selected as 0.0024 for RC walls with normal-strength reinforcement and 0.0044 for RC walls with high-strength reinforcement. Also, the crushing strain was selected as the strain value when the stress in the post-peak linear descending reaches zero stress [15]. Finally, shear failure is defined when the shear drift/ rotation angle reaches 0.15 [15].

5   Wall Description

As shown in Table 1, walls W1-NSC-NSR and W2-HSC-HSR were used to evaluate the seismic fragility of nuclear structures when normal-strength materials were replaced by high-strength materials, where these walls were tested by Barbachyn et al. [8] under quasi-static loading protocols. Both walls have identical dimensions with 2700 mm length, 1400 mm height, and 200 mm thickness.

Table 1 Reinforcement details for analyzed walls

Wall ID	Web reinforcement ρ_h (%)	Web reinforcement ρ_v (%)	f'_c (MPa)	f_y (MPa)	Bar Size	Reinforcement spacing (mm)
W1-NSC-NSR	1.80	1.80	48	500	#6	150
W2-HSC-HSR	0.83	0.83	100	840	#4	150

6 Fragility Evaluation

Figures 1 and 2 show IDA results for walls W1-NSC-NSR and W2-HSC-HSR, where spectral acceleration (S_T) values were plotted against the wall maximum vertical reinforcement strain, compressive strain, shear strain, and crack width. Each point in each IDA represents a single nonlinear dynamic analysis, where the wall was subjected to one ground motion record scaled to one intensity level.

For both walls, fragility curves were developed based on the IDA results through a cumulative distribution function that links the probability of damage to a ground motion intensity level (S_T), as shown in Fig. 3. The median spectral intensity and the dispersion at each damage state were estimated using the maximum likelihood method to fit the IDA data into corresponding fragility curves [7].

Figures 3a–f show the fragility curves for walls W1-NSC-NSR and W2-HSC-HSR to evaluate the influence of using high-strength materials on damage states DS-I to DS-III and DS-0.5 mm to DS-3 mm. As can be seen in the figures, wall W1-NSC-NSR shows lower probability of exceedance values to all damage states at different spectral intensities (except DS-II) compared to W2-HSC-HSR. This difference is due to the higher horizontal and vertical reinforcement ratios used in wall W1-NSC-NSR (#6 at 150 mm in each direction) compared to those used in wall W2-HSC-HSR (#4 at 150 mm in each direction). Also, Fig. 3d–f demonstrate that W2-HSC-HSR has wider crack widths compared to W1-NSC-NSR due to larger reinforcement strains due to the use of reduced steel areas in the former wall.

Figure 3 shows that both walls suffer DS-0.5 mm before the yielding of their vertical reinforcement bars (DS-I). Also, both walls suffer DS-III before reaching a crack width of 3 mm. In addition, wall W1-NSC-NSR realizes DS-II before reaching 1.5 mm crack width; however, wall W2-HSC-HSR realizes DS-1.5 mm before reaching concrete crushing (DS-II). The inconsistent results for both walls between DS-II and DS-1.5 mm clearly show that fragility curves for RC walls with high-strength materials should be developed considering a wide range of performance indicators in order to identify the appropriate methods of repair.
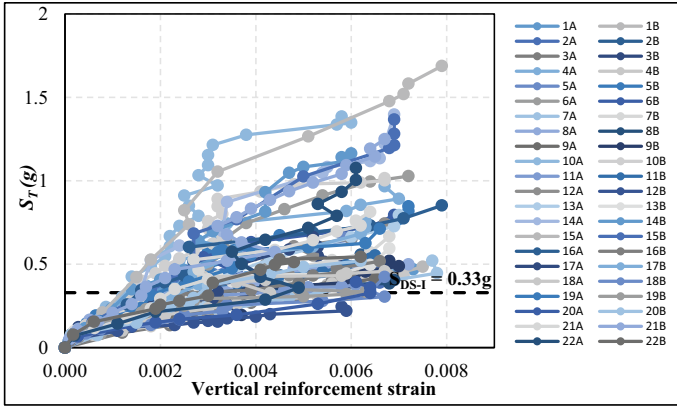
(a)Vertical reinforcement strain
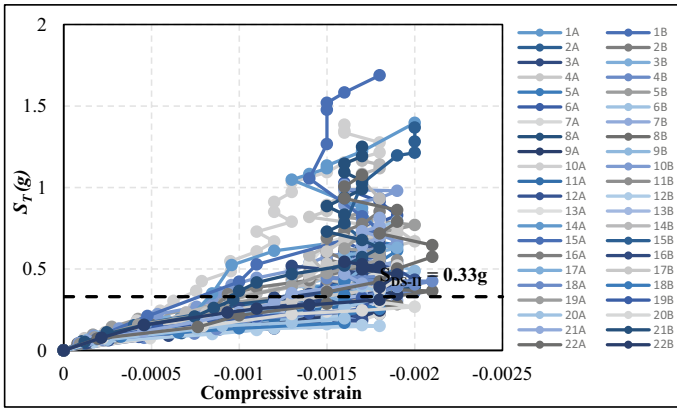
(b) Compressive strain
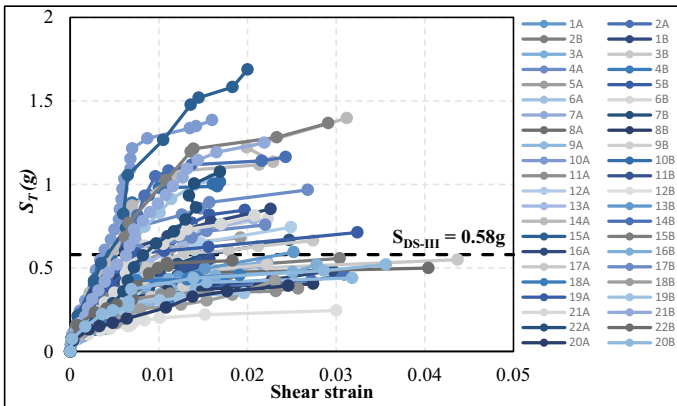
(c) Shear strain

Fig. 1 IDA response plot for wall W1-NSC-NSR
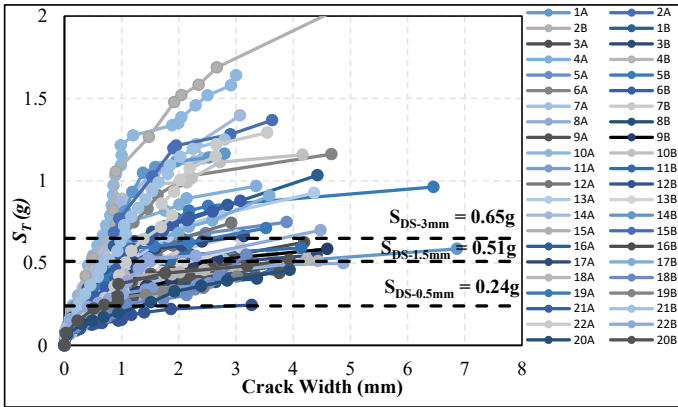
(d) Crack width

Fig. 1 (continued)

7 Conclusions

The current study evaluated the influence of high-strength materials on the seismic fragility of squat RC shear walls. In this respect, incremental dynamic analyses were performed using an *OpenSees* model through the 44 far-field ground motion records recommended by the FEMA P695 methodology. Fragility functions for RC shear walls with normal- and high-strength materials were subsequently developed at different damage states. Following the FEMA P-58 guidelines, several performance indicators were used to define such damage states. Two walls were used to quantify the seismic fragility of squat RC shear walls with normal- and high-strength materials at different damage states.

The results showed that the wall with high-strength materials had higher probability of exceedance values at most of the damage states compared to the wall with normal-strength materials due to the lower horizontal and vertical web reinforcement ratios used in the former wall. The analyses focused on squat RC shear walls with high-strength materials with specific geometrical configurations. Additional future studies are still needed to quantify the seismic fragility of such walls when different aspect ratios, different axial load levels, different spacing between horizontal and vertical reinforcement and material strengths (e.g., ultra-high-performance concrete) are utilized.
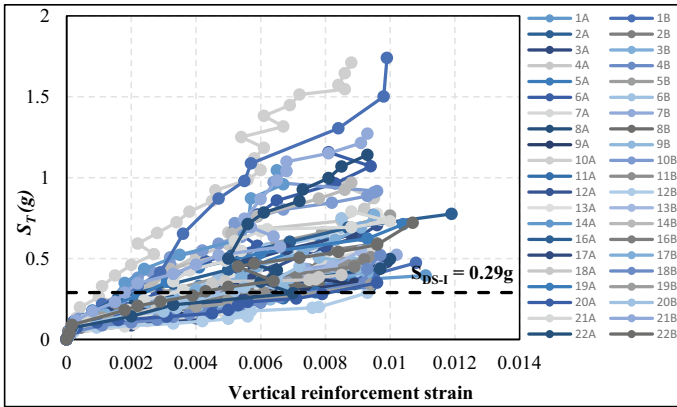
(a)Vertical reinforcement strain
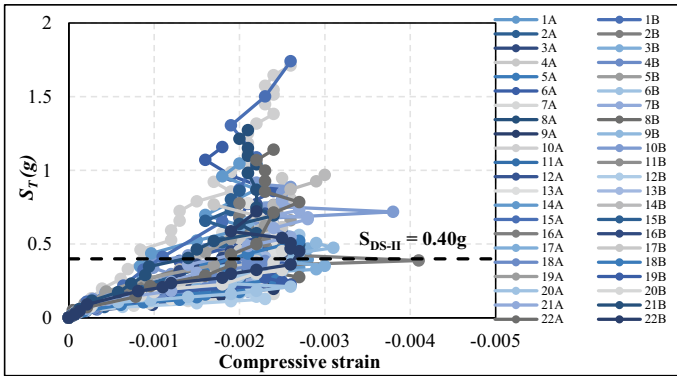
(b) Compressive strain
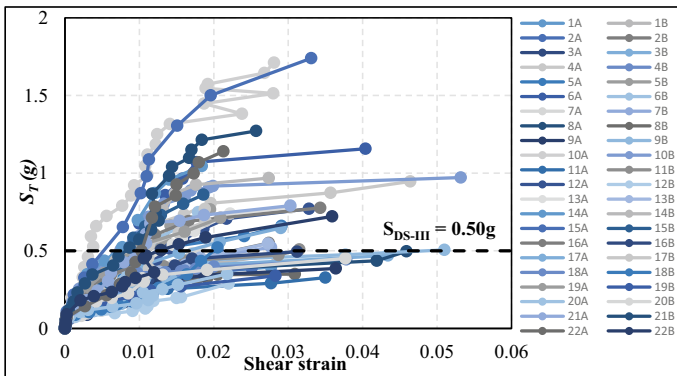
(c) Shear strain

Fig. 2 IDA response plot for wall W2-HSC-HSR
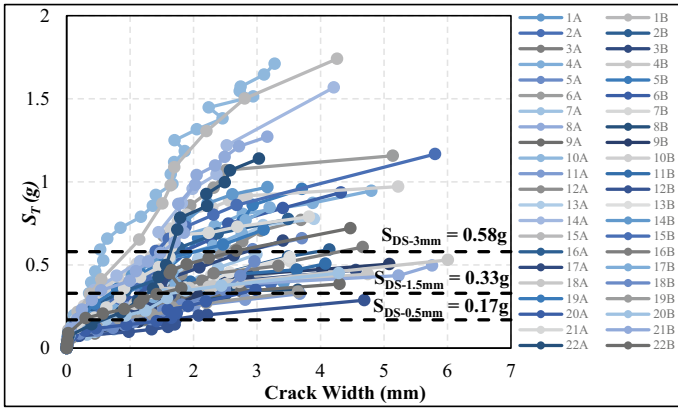
(d) Crack width

Fig. 2 (continued)

(a) DS-I

(b) DS-II

(c) DS-III

(d) DS-0.5mm

(e) DS-1.5mm

(f) DS-3mm
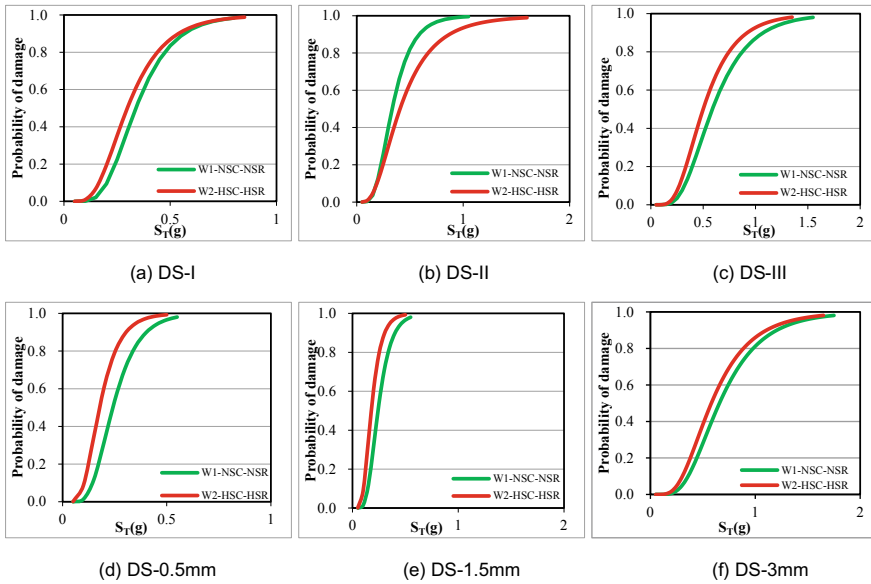
Fig. 3 Fragility curves for walls W1-NSC-NSR and W2-HSC-HSR

References

1. Abouyoussef M, Ezzeldin M (2021) Numerical modelling of reinforced concrete walls in nuclear and industrial structures under seismic loading. In: Canadian Society for Civil Engineering Annual Conference, Niagara Falls, ON, Canada
2. Abouyoussef M, Ezzeldin M (2023) Fragility and economic evaluations of high-strength reinforced concrete shear walls in nuclear power plants. J Struct Eng. https://doi.org/10.1061/JSENDH/STENG-11397
3. ACI (2014) Code requirements for nuclear safety-related concrete structures and commentary. ACI 349–13. Farmington Hills, MI
4. ACI (2004) *Concrete repair guide (*ACI 546R-04). American Concrete Institute, Farmington Hills, MI
5. ATC (1998a) Evaluation of earthquake damaged concrete and masonry buildings basic procedures manual (FEMA 306). Washington, DC
6. ATC (1998) Evaluation of earthquake damaged concrete and masonry wall buildings: technical resources
7. Baker JW (2015) Efficient analytical fragility function fitting using dynamic structural analysis. Earthq Spectra 31(1):579–599
8. Barbachyn SM, Devine RD, Thrall AP, Kurama YC (2020) Behavior of nuclear RC shear walls designed for similar lateral strengths using normal-strength versus high-strength materials. J Struct Eng 146(11):04020252
9. Bentz EC, Vecchio FJ, Collins MP (2006) Simplified modified compression field theory for calculating shear strength of reinforced concrete elements. ACI Struct J 103(4):614
10. Cheng MY, Wibowo LS, Giduquio MB, Lequesne RD (2021) Strength and deformation of reinforced concrete squat walls with high-strength materials. ACI Struct J 118(1)
11. Chopra AK (2007) Dynamics of structures: theory and applications to earthquake engineering, Prentice Hall, Englewood Cliffs. NJ, New Jersey
12. FEMA (2009) Applied technology council. In: Quantification of building seismic performance factors. US Department of Homeland Security
13. FEMA (2009) Damage states and fragility curves for low aspect ratio reinforced concrete walls (FEMA P-58/BD-3.8. 8). Federal Emergency Management Agency, Washington, DC
14. Huang YN, Whittaker AS, Kennedy RP, Mayes RL (2013) Response of base-isolated nuclear structures for design and beyond-design basis earthquake shaking. Earthquake Eng Struct Dynam 42(3):339–356
15. Gogus A, Wallace JW (2015) Seismic safety evaluation of reinforced concrete walls through FEMA P695 methodology. J Struct Eng 141(10):04015002
16. Kolozvari K, Tran TA, Orakcal K, Wallace JW (2015) Modeling of cyclic shear-flexure interaction in reinforced concrete structural walls. II: experimental validation. J Struct Eng 141(5):04014136
17. Lovering JR, Yip A, Nordhaus T (2016) Historical construction costs of global nuclear power reactors. Energy Policy 91:371–382
18. Lu X, Xie L, Guan H, Huang Y, Lu X (2015) A shear wall element for nonlinear seismic analysis of super-tall buildings using OpenSees. Finite Elem Anal Des 98:14–25
19. Massone LM, Orakcal K, Wallace JW (2009) Modelling of squat structural walls controlled by shear. ACI Struct J 106(5)
20. Massone LM, Orakcal K, Wallace JW (2006) Shear-flexure interaction for structural walls. Special Publication 236:127–150
21. McKenna F, Fenves GL, Scott MH (2000) Open system for earthquake engineering simulation. University of California, Berkeley, CA
22. NIST (National Institute of Standards and Technology) (2010) Evaluation of the FEMA P695 methodology for quantification of building seismic performance factors. NIST GCR 10-917-8. Gaithersburg, MD
23. Orakcal K, Wallace JW (2006) Flexural modeling of reinforced concrete walls-experimental verification. ACI Mater J 103(2):196

24. Sanchez LMM (2006) RC wall shear-flexure interaction: analytical and experimental responses. University of California, Los Angeles
25. Vamvatsikos D, Cornell CA (2002) Incremental dynamic analysis. Earthquake Eng Struct Dynam 31(3):491–514
26. Vecchio FJ, Collins MP (1986) The modified compression-field theory for reinforced concrete elements subjected to shear. ACI J 83(2):219–231

Numerical Evaluation of Self-Centering Buckling-Restrained Braces with Prestressed Iron-Based Shape Memory Alloy Tendons

Wilson Carofilis, Eugene Kim, Donghyuk Jung, and Johanna Pinargote

Abstract Society is moving toward resilience-oriented communities, encouraging engineers to adopt resilience-based philosophies in design. For example, in earthquake prone regions, these philosophies are aimed at regaining a building's functionality in a relatively short time compared to traditional design criteria. This study examines a dual-tube self-centering buckling-restrained brace (BRB) prestressed with iron-based shape memory alloy (Fe-SMA) tendons. Self-centering bracing systems can accommodate large deformations and limit residual effects. These devices allow structural systems to undergo large displacement without severe structural damage while providing stable energy dissipation and self-centering action. Although Fe-SMA does not possess the superelastic property as nickel–titanium (Ni–Ti) SMA, the heat-activated shape memory effect can be exploited to provide effective self-centering capabilities at a fraction of the cost of Ni–Ti SMA. The low cost and high recovery stress characteristics of Fe-SMA make it a promising alternative for self-centering and other structural engineering applications. In this study, the BRB is conceptualized in OpenSees and implemented in a 2D moment-resisting steel frame. The structural system is subjected to nonlinear time history analyses to assess its seismic performance. The re-centering capabilities of the Fe-SMA BRB demonstrate the potential for reduced post-earthquake repairs, thereby improving the seismic resilience of structures.

Keywords Fe-SMA prestressing · Self-centering · Seismic resilience · Buckling-restrained brace

W. Carofilis (✉) · E. Kim · J. Pinargote
Department of Civil and Environmental Engineering, University of Waterloo, Waterloo, ON, Canada
e-mail: wcarofil@uwaterloo.ca; wilson.carofilis@iusspavia.it

D. Jung
Department of Architectural Engineering, Pusan National University, Busan, South Korea

1 Introduction

Seismic design and assessment of buildings have traditionally focused on protecting the lives of occupants. Under the life-safety principle, however, considerable damage may be sustained by the structural and non-structural components, affecting the building functionality. Significant ground shaking can very easily leave structures unusable for several months and even for more than a year which also increments indirect economic losses (i.e., downtime, lost business, temporary and/or permanent migration, etc.). On the other hand, resilience-based philosophies complement seismic design criteria to ensure that structures can recover normal operation in a relatively short period of time after an earthquake. Seismic resilience can be measured by the rate in which a structure regains functional recovery after an extreme seismic event [9]. To achieve a seismic resilience target, a coordinated effort in planning, resource management, and seismic retrofitting are required. Nevertheless, when a structure suffers from large permanent deformations, which are considered as an important reparability metric [1], the seismic resilience of that building is severely affected. Moreover, the building is at higher risk of collapse in aftershocks. It is worth pointing out that even if a building survives a major earthquake without collapsing, if large permanent deformations are present, it is generally more economical to demolish and rebuild the structure [1]. Thus, lateral resisting systems with the ability to restore structures to their original undeformed configuration can offset these collateral earthquake's impacts.

Buckling-restrained braced frames (BRBFs) have been gaining popularity as an alternative for improving the seismic resilience of structures because they provide better ductile behavior than regular bracing systems [20]. Furthermore, self-centering buckling-restrained braced frames (SCBRBFs) can further improve the resilience of the BRBF structures by introducing self-centering action (i.e., ability to return to the pre-loading state) through pre-tensioned components (e.g., steel or composite tendons) or the use of smart materials. Shape memory alloys (SMAs) are a class of smart materials that has gained significant relevance in the field of seismic design and retrofitting due to their unique thermomechanical properties known as superelasticity and the shape memory effect. This study conceptualizes a new self-centering buckling-restrained brace (SCBRB) which incorporates low-cost iron-based SMA (Fe-SMA) tendons to achieve self-centering and examines its performance under seismic excitation.

2 Buckling-Restrained Bracing Systems

Typical BRBs are comprised of two main components: a steel core and exterior restraining tube. The steel core is the only element that carries axial forces and dissipates energy through yielding. On the other hand, the main function of the restraining tube is to prevent the steel core from buckling under compression. The tube can also
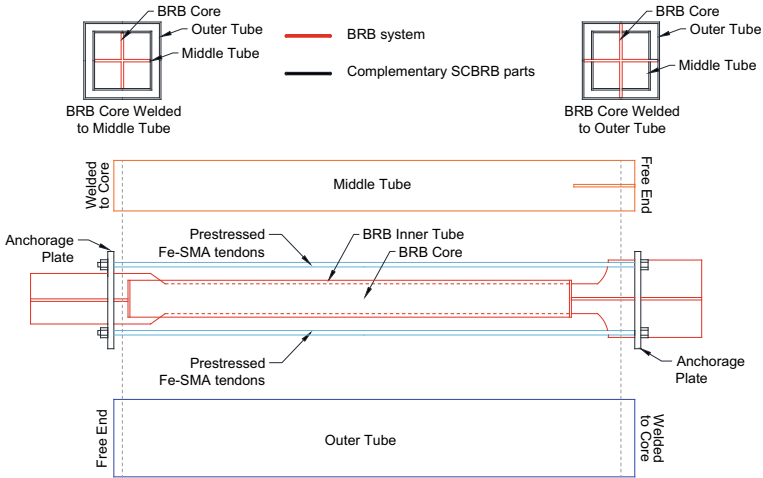
Fig. 1 SCBRB configuration

be filled with concrete to increase the buckling-restrained capacity of the brace. The steel core can yield both in tension a compression, and the yielding generates a stable hysteretic behavior with much higher ductility compared to traditional bracing systems. Figure 1 illustrates a general configuration for a BRB system.

The application of BRBFs have become more common in Canada as a replacement for standard steel bracing [21]. BRBFs were first introduced in the 2009 CSA 16 Steel Design Manual and in the 2010 National Building Code of Canada. NIST [21] states that while there is a variety of buckling-restrained braces (BRBs) in the market, the force–deformation relation is expected to be the same despite different detailing properties and applications. BRBs are expected to axially yield in compression and in tension without buckling due to confinement of the steel core (e.g., concrete filling or dual tubes). Experimentally, BRBs have been found to have significant cyclic ductility and dissipation of energy, leading to strain hardening [21]. However, the deformation of the BRB has been proved to be connected to the residual drifts of a structure [21].

3 Shape Memory Alloys (SMAs)

SMAs possess two unique properties, superelasticity and the shape memory effect, which make it an excellent material for seismic retrofitting applications. These properties are derived from phase transformations triggered by thermomechanical loading. In its austenite phase, SMAs display stress-induced superelastic behavior

which allows it to undergo large deformations but return to its original configuration with no plastic deformation upon unloading. In its martensite phase, the heat-activated shape memory effect allows the material to recover plastic strains and to return to original shape. Several studies have already investigated the use of superelastic SMA in self-centering applications [18, 22]. Eatherton et al. [12] incorporated superelastic nickel–titanium (Ni–Ti) SMA rods in BRBs and found that the braces do not lead to concentrated story drifts since the SMA produces an additional hardening effect and provides self-centering.

Ni–Ti SMAs are the most widely available commercially [10], but its high cost limits its use in seismic retrofitting applications. Fe-SMAs are a relatively new development and only possess the shape memory effect, but at a fraction of the cost of Ni–Ti SMAs, it is more practical for civil engineering applications [24]. Various researchers have exploited the shape memory effect of SMAs in structural engineering including as prestressing [18, 22] and confinement [6, 11]. As a prestressing element, it can be used to reduce residual drifts and can be easily applied on large-scale construction projects without the need for jacking tools [24]. The level of recovery stress (prestressing stress) that can be attained with Fe-SMA depends on the heating temperature and the amount of martensite present in the alloy. Shaverdi et al. [25] indicates that an initial pre-straining of 2.0% is adequate to reach recovery stress close to 300 MPa in Fe-SMA with an ultimate tensile strength of 1000 MPa and strain at failure of more than 40%. Similar values were observed in initial tests conducted on the Fe-SMA used in this study. Despite its proven potential, Fe-SMA prestressing has not been exploited in self-centering applications. This study aims to demonstrate numerically the use of Fe-SMA prestressing as a self-centering element in BRBs.

4   Self-Centering Fe-SMA BRB

SCBRBFs are efficient ductile seismic resisting systems for dissipating energy without significant structural damage and connection localized failure [18, 21]. The self-centering capability and energy absorption of SCBRBF systems can considerably reduce the damage to other structural elements [18]. High-strength steel is generally used for prestressing applications but under cyclic loading the tension in the steel rods may deteriorate and lead to deformations in the system [8]. Therefore, other materials such as composite and/or high-tensile materials have also been used for prestressing application in SCBRBF [8, 16].

The SCBRB conceptualized in this study relies on the shape memory effect of Fe-SMA bars to prestress the brace and provide the self-centering effect. To achieve the prestressing, plastically deformed (pre-strained) fs are anchored to the brace then heat is applied to trigger the shape memory effect. Since the ends of the Fe-SMA tendons are anchored, restraining the tendons from deforming back to their original shape, stress is developed which is transferred into the brace. Figure 1 shows the design of the Fe-SMA SCBRB adopted from [18].

The Fe-SMA SCBRB consists of two concentric steel tubes that act as compression struts while the Fe-SMA tendons act as tension ties. The pre-tensioned tendons are connected to the BRB through free-floating end plates on the concentric steel tubes. These anchorage plates have cruciform shape slots that enable the BRB core and tubes to move freely since the plates are not connected (welded) neither to the BRB core nor tubes. When the BRB is under compression, the steel tubes push against the anchor plates and causing tension in the Fe-SMA tendons. This allows the brace to self-center in cyclic axial loadings [18]. Similar to the superelastic SMA BRB developed by Miller et al. [18], it is expected that the BRB core itself will provide most of the seismic energy dissipation with the primary role of the Fe-SMA being inducing self-centering.

5 Numerical Analysis

5.1 Case Study Building

A three-story 2D moment-resisting steel frame was selected to analytically test the effectiveness of the Fe-SMA BRB. The assumptions and numerical model were adopted from the study of Chalarca [5] and FEMA 440 [13]. The building is composed of three bays in the north–south direction and six bays in the east–west direction and consists of brittle beam-column joint connections typical of the pre-Northridge seismic designs. Figure 2 shows the steel sections and geometry for the frame in the north–south direction which was modeled and used for subsequent analyses. The fundamental period of the moment-resisting steel frame with and without the Fe-SMA SCBRBs is 0.37 s and 0.79 s, respectively. The numerical model was developed in OpenSees [17]. To capture the inelastic behavior of the structural elements (i.e., beams and columns) the command element beam with hinges was used. Likewise, the beam-column joints were modeled as panel zones to represent the nonlinear behavior of these elements.

5.2 Dimensioning of Fe-SMA SCBRB

The effective length of the braces was taken as 70% of the work-point-to-work-point distance as recommended in NIST GCR 10–917-8 [20]. FEMA P795 [15] suggests that the effective stiffness of the brace can be represented as the in-series sum of the individual element stiffnesses, consisting of the steel core (yielding portion), stiffness of the connection portions, and the stiffness of the transition portions. However, Nippon Steel Engineering proposed a simplified relationship (Eq. 1) to approximate the total stiffness of a BRBs solely based on the stiffness of the steel core [15].
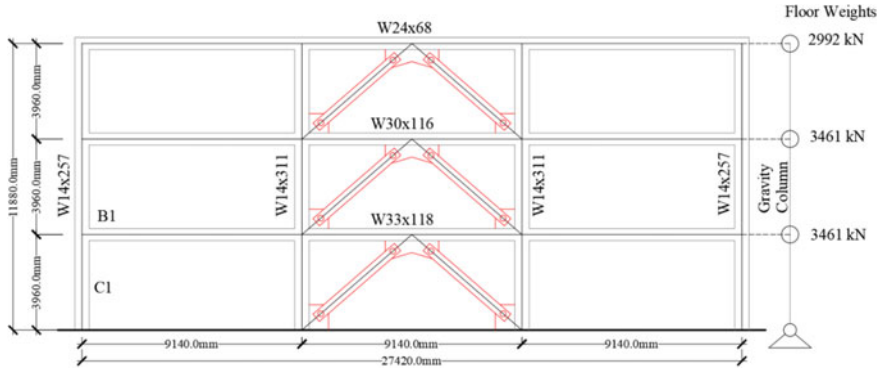
Fig. 2 General configuration of the 2D moment-resisting steel frame used as the case study building

$$K_{\text{brace}} \cong 0.83 \frac{A_y E}{L_y} \tag{1}$$

where A_y represents the cross-sectional area of the BRB steel core, L_y is the yielding length, and E is the steel modulus of elasticity. The force–displacement plots in Fig. 3 illustrate the hysteretic behavior and self-centering ability of the SCBRB. The self-centering ability comes primarily from the pretension of the Fe-SMA tendons while the energy dissipation is provided by yielding of the steel core.

As described in the preceding section, the relative movement between the middle and outer tubes results in the Fe-SMA tendons always acting in tension even when the brace is under compression. The seismic design force for the brace system was estimated by a preliminary structural analysis using the equivalent lateral force procedure and methodology defined by ASCE 7-16 [3]. For this, the fundamental period of the braced structure was estimated according to the period equations proposed by ASCE 7-16, and a reduction factor of $R = 6$ was adopted.

Once the design forces were determined, the design of the SCBRB sections was conducted according to the framework developed by Miller et al. [18]. The force in the brace was related to the contribution of the BRB steel core yielding force (P_{ysc}) and initial SMA prestressing force ($P_{i\text{-SMA}}$) using Eq. (2).
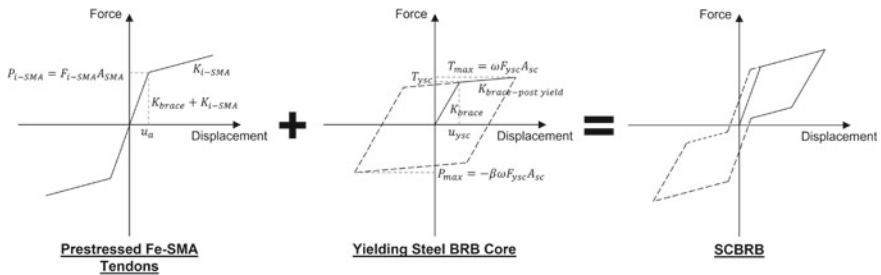
Fig. 3 SCBRB hysteretic behavior

$$\phi P_n = \phi\left(P_{\text{ysc}} + P_{i-\text{SMA}}\right) = 0.9\left(F_{\text{ysc}} A_{\text{sc}} + F_{i-\text{SMA}} A_{\text{SMA}}\right) \tag{2}$$

where F_{ysc} is the yielding stress of the steel core, $F_{i\text{-SMA}}$ is the prestressing stress in the SMA bars, A_{sc} is the cross-sectional area of the steel core, and A_{SMA} is the total area of the SMA tendons. The steel core yielding force and SMA pretension force can be related through the following equations based on the ANSI/AISC 341-16 seismic provisions [2].

$$F_{i-\text{SMA}} A_{\text{SMA}} = \alpha_{\text{sc}} \beta \omega F_{\text{ysc}} A_{\text{sc}} \tag{3}$$

$$A_{\text{sc}} = \frac{P_u}{F_{\text{ysc}}(1 + \alpha_{\text{sc}} \beta \omega)} \tag{4}$$

$$A_{\text{SMA}} = \frac{\alpha_{\text{sc}} \beta \omega F_{\text{ysc}} A_{\text{sc}}}{F_{i-\text{SMA}}} \tag{5}$$

The parameter α_{sc} defines the separation between the initial SMA pretension force and the strain hardened BRB steel core force, β is the compression strength adjustment factor for the BRB steel core, and ω is the strain hardening adjustment factor for the BRB steel core. The parameters β and ω are illustrated in Fig. 3 (Plot 2) which relates the maximum force acting in the brace and its nominal material strength [2].

Miller et al. [18] state that it is desirable for the initial SMA pretension force to be greater than the yield force of the steel core to achieve full self-centering behavior. Consequently, the α_{sc} should be set as at least one. Furthermore, Miller et al. [18] recommend typical values of $\beta = 1.20$ and $\omega = 1.35$ which were also adopted in this study.

5.3   Fe-SMA SCBRB Numerical Modeling

Several authors point out that the hysteresis curve for a SCBRB does not follow a traditional bilinear flag-shape but a trilinear shape due to the residual deformation of the brace when this is unloaded [16, 26, 27]. To attain this more realistic behavior, a SCBRB element can be represented by combining in parallel the elastoplastic energy dissipation behavior of a BRB and bilinear elastic restoring force of a self-centering system. Therefore, the dual-tube SCBRB used in this study can be conceived as two uniaxial materials combined in parallel as illustrated in Fig. 3 (Plot 3). An ElasticBilin uniaxial material was used in OpenSees to represent the self-centering system (i.e., Fe-SMA prestressing action and brace system) and a Steel01 uniaxial material was adopted for the elastoplastic behavior of the steel core. The Fe-SMA SCBRB was modeled as a two Node Link element with the resulting parallel material (Plot 3).
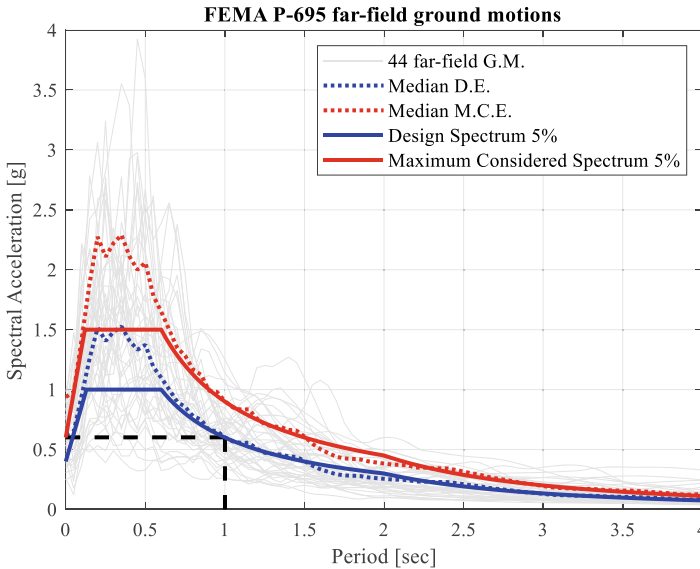
Fig. 4 5% damping acceleration response spectra (FEMA P-695 far field) and design acceleration spectra (ASCE 7-16)

5.4 Seismic Demand

The FEMA P-695 far-field ground motion set is composed of 44 individual records that represent the seismicity of western USA. This set includes strong-motion records (i.e., records with PGA > 0.2 g and PGV > 15 cm/sec) from all large-magnitude (M > 6.5) events in the Pacific Earthquake Engineering Research Center (PEER) Next-Generation Attenuation (NGA) database [14]. The records were scaled such that the median spectral acceleration at a period of one second matches the ASCE 7–16 design spectrum for the city of Los Angeles with a soil type Dmax. The acceleration response spectra for all ground motion records in the suite are shown in Fig. 4 along with the median spectra and the design spectra for the design and maximum considered earthquakes (i.e., DE and MCE). Key ground motion parameters are summarized in Table 1.

6 Analysis and Results

After running the nonlinear time history analyses for all 44 far-field ground motions, the outputs were postprocessed to obtain the median values of different demand parameters. The median values from the Fe-SMA SCBRB frame were compared to those of the bare frame (BF). Figure 5 compares the peak floor accelerations, peak

Table 1 Characterization of the 44 far-field ground motions

Parameter	Minimum value	Median value	Maximum value
Frequency content[a] (Hz)	0.19	1.42	8.05
Duration[b] (s)	20.0	40.0	99.9
Bracketed duration[c] (s)	13.3	21.7	89.7
Significant duration[d] (s)	4.3	11.1	51.1

Note
[a] Frequency content, determined through the Fast Fourier Transform
[b] Duration, defined as the interval of the ground motion action, free vibration is not considered
[c] Bracketed duration, measured the interval between two points in time where the acceleration amplitude at the first and last point exceeds a prescribed value (e.g., 0.05 g) [7]
[d] Significant duration, time required to build up from 5 to 95% of the areas intensity [7]

story drift, and residual drift for DE and MCE intensities. These demand parameters are important metrics since they influence the expected economic losses and relate to the level of damage experience by the building.

The addition of the Fe-SMA BRB resulted in increased floor acceleration in all storeys. This is somewhat expected as the Fe-SMA SCBRB provides a higher stiffness to the steel building. The Fe-SMA SCBRB system yields a linear profile of floor accelerations for both DE and MCE intensities which indicates that the building does not undergo inelastic behavior unlike the BF for which peak floor accelerations are lower but do not follow a linear trend. The floor accelerations in the top storey of the Fe-SMA SCBRB is approximately 1.7 times larger than that of the BF. It is worth noting that large peak floor accelerations can lead to more severe damage in non-structural components, particularly for acceleration sensitive components such as ceiling systems, piping systems, electrical and mechanical components, among others. However, a detailed assessment of the effects on non-structural elements is outside of the scope of this research.
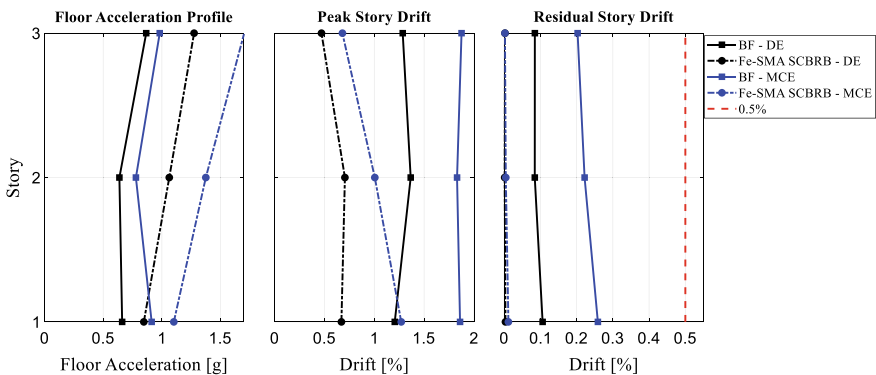
Fig. 5 Comparison of seismic demand parameters for DE and MCE

In contrast to the floor acceleration, peak story drifts are reduced by nearly 50% in the Fe-SMA braced frame compared to the BF. Furthermore, residual drifts for both the DE and MCE intensities are negligible compared to the bare frame, demonstrating the efficacy of the Fe-SMA SCBRB. It should be noted, however, that under the strong motions considered in the current study, residual drifts of the bare frame are still under the maximum limit of 0.5% which is a commonly adopted threshold for post-earthquake demolition. The effect of Fe-SMA SCBRB is noticeable and highlights its advantages over other seismic force resisting systems.

Figure 6 shows the typical hysteretic behavior of the structural components in the case study building under an MCE level ground motion. The base shear versus roof displacement plot shows narrower hysteresis for the frame with the Fe-SMA BRB but a higher lateral force capacity and lower lateral displacement in comparison with the bare frame. The Fe-SMA SCBRB more than doubles the lateral capacity of the building with a maximum roof displacement that is approximately one-third that of the unbraced configuration. However, the narrow hysteretic loops do point to the fact that the absorbed energy is much lower for the Fe-SMA SCBRB and the frame remained nearly elastic overall. Nonetheless, it is clear in Fig. 6 that the braces undergo much larger hysteresis than the beams and columns. As a result, the damage in the main structural elements can be expected to be minimal with negligible inelastic deformations.

From a seismic performance standpoint, the Fe-SMA SCBRBs show great promise, but more research is needed to validate its behavior and develop design guidelines. The performance of Fe-SMA under environmental loads (e.g., corrosion,
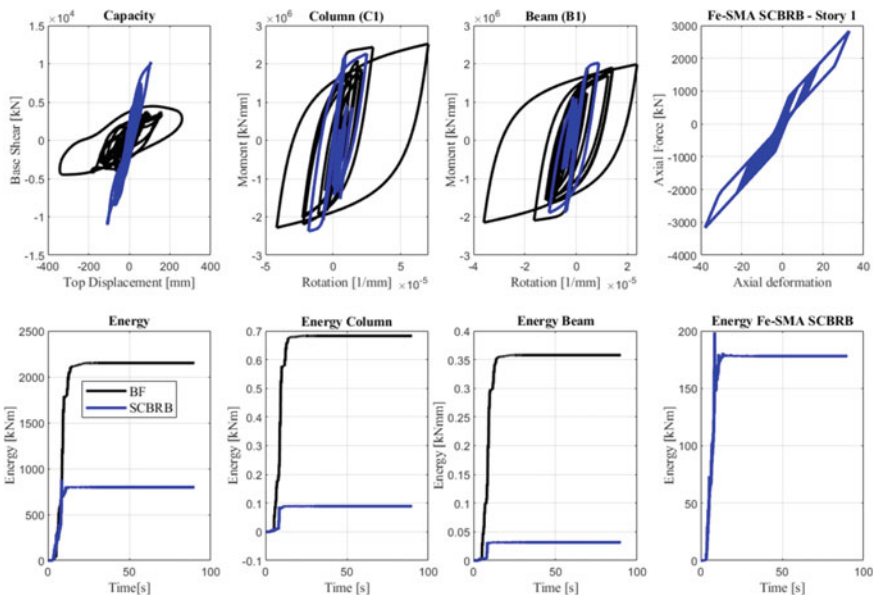
Fig. 6 Hysteresis curves of MCE intensity for one ground motion from the set of records

freeze–thaw) is an area that needs to be investigated. Additionally, Fe-SMA relaxation (ratio of actual stress to maximum stress) can be an issue if this is not controlled. Shahverdi et al. [25] examined the stress relaxation behavior of Fe-SMA strips and found relaxation ratios lower than 10%, but the effect of relaxation on the behavior of SCBRBs has not been investigated.

7 Conclusions

This study demonstrates the potential for using iron-shape memory alloys (Fe-SMAs) as the self-centering component in self-centering buckling-restrained braces (SCBRBs). A three-storey steel frame building was used to examine the energy dissipation capacity and self-centering action a novel iron-based SMA SCBRB prototype through nonlinear time histories analyses. Overall, the SCBRBs yielded considerable advantages over an unbraced steel moment frame, significantly increasing lateral stiffness and lateral load capacity. The Fe-SMA SCBRB reduced peak storey drifts by half compared to an unbraced frame and reduced residual deformations in the case study building to nearly zero showing that the Fe-SMA prestressing could be an effective self-centering option.

Despite the peak floor accelerations are increased due to the much larger lateral stiffness, this issue can be addressed by improving the seismic performance of acceleration sensitive non-structural components so that the building functionality and seismic resilience are not compromised. Likewise, any prestressing loss of relaxation of the iron-based SMA bar can be controlled by limiting not only the pre-straining before heating activation of the material but also the maximum stress in the reloading stage. These two relevant topics need special attention and thereby further research, and subsequent studies could explore these aspects.

References

1. Almufti I, Willford M (2013) REDi rating system, resilience-based earthquake design initiative for the next generation of buildings. Version 1.0.
2. ANSI/AISC 341-16 (2016) Seismic provisions for structural steel buildings, American Institute of Steel Construction, Chicago, Illinois, USA
3. ASCE (2017) Minimum design loads and associate criteria for buildings and other structures, ASCE/SEI 7–16, American Association of Civil Engineering. United States.
4. Black C, Makris N, Aiken I (2002) Component testing, stability analysis and characterization of buckling-restrained unbonded braces, PEER Report 2002/08. University of California, Berkeley, Pacific Earthquake Engineering Research Center
5. Chalarca B (2022) Implementation of fluid viscous dampers as a seismic protection system and its effects on the structural and nonstructural seismic response, Doctoral thesis, University School for Advanced Studies IUSS Pavia, Italy.

6. Chen Q, Andrawes B (2014) Experimentally validated modelling of concrete actively confined using SMA reinforcement, Tenth U.S. National Conference on Earthquake Engineering, Anchorage, Alaska.
7. Chen WF, Scawthorn C (2003) Earthquake engineering handbook. Hawaii University.
8. Christopoulos C, Tremblay R, Kim HJ, Lacerte M (2008) Self-centering energy dissipative bracing system for the seismic resistance of structures: development and validation. ASCE J Struct Eng 134(1):96–107
9. Cimellaro GP, Reinhorn AM, Bruneau M (2010) Seismic resilience of a hospital system. Struct Infrastruct Eng 6(1–2):127–144. https://doi.org/10.1080/15732470802663847
10. Czaderski C, Shahverdi M, Michels J (2021) Iron based shape memory alloys as shear reinforcement for bridge girders. Constr Build Mater 274:121793. https://doi.org/10.1016/j.conbuildmat.2020.121793
11. Dommer K, Andrawes B (2012) Thermomechanical characterization of NiTiNb shape memory alloy for concrete active confinement applications. J Mater Civ Eng ASCE 24(10):1274–1272. https://doi.org/10.1061/(ASCE)MT.1943-5533.0000495
12. Eatherton M, Fahnestock LA, Miller DJ (2014) Computational study of self-centering buckling-restrained braced frame seismic performance. Earthquake Eng Struct Dynam 43:1897–1914. https://doi.org/10.1002/eqe.2428
13. FEMA (2005) Improvement of nonlinear static seismic analysis procedures, FEMA 440, Federal Emergency Management Agency. United States
14. FEMA (2009) Quantification of building seismic performance factors, FEMA P-695, Federal Emergency Management Agency. United States
15. FEMA P-795 (2011) Quantification of building seismic performance factors: component equivalency methodology, prepared by Applied Technology Council for the Federal Emergency Management Agency, Washington, DC
16. Liu L, Zhao J, Shuang L (2018) Nonlinear displacement ratio for seismic design of self-centering buckling-restrained braced steel frame considering trilinear hysteresis behavior. Eng Struct 158:199–222. https://doi.org/10.1016/j.engstruct.2017.12.026
17. McKenna F, Scott MH, Fenves GL (2010) Nonlinear finite-element analysis software architecture using object composition. J Comput Civ Eng 24(1):95–107
18. Miller DJ, Fahnestock LA, Eatherton MR (2012) Development and experimental validation of a Nickel-Titanium shape memory alloy self-centering buckling-restrained brace. Eng Struct 40:288–298. https://doi.org/10.1016/j.engstruct.2012.02.037
19. Nippon Steel Engineering, Unbonded brace: basic design information. Nippon Steel Engineering Co. Ltd., Building Construction and Steel Structures Div., Undated
20. NIST GCR 10-917-8 (2010) Evaluation of the FEMA P-695 methodology for quantification of building seismic performance factors, prepared by NEHRP Consultants Joint Venture for the U.S. Department of Commerce
21. NIST (2015) Seismic design of steel buckling-restrained braced frames: a guide for practicing engineers, GCR 15-917-34, NEHRP Seismic Design Technical Brief No. 11, produced by the Applied Technology Council and the Consortium of Universities for Research in Earthquake Engineering for the National Institute of Standards and Technology, Gaithersburg, MD
22. NourEldin M, Naeem A, Kim J (2019) Life-cycle cost evaluation of steel structures retrofitted with steel slit damper and shape memory alloy-based hybrid damper. Adv Struct Eng 22(1):3–16
23. Otsuka K, Wayman CM (1998) Shape memory materials. Cambridge University Press, United Kingdom
24. Rojob H, El-Hacha R (2018) Performance of RC beams strengthened with self-prestressed Fe-SMA bars exposed to freeze-thaw cycles and sustained load. Eng Struct 169:107–118
25. Shahverdi M, Michels J, Czaderski C, Motavalli M (2018) Iron-based shape memory alloys strips for strengthening RC members: material behavior and characterization. Constr Build Mater 173:586–599

26. Xhahsya A, Kahraman S, Girgin SC (2019) Flexural based energy dissipative device in self-centering braces. Latin Am J Solid Struct 16(8):e231. https://doi.org/10.1590/1679-78255807
27. Zhou Z, Xie Q, Lei XC, He XT, Meng SP (2015) Experimental investigation of the hysteretic performance of dual-tube self-centering buckling-restrained braces with composite tendons. J Compos Constr 19(6):04015011–04015021. https://doi.org/10.1061/(ASCE)CC.1943-5614.0000565

Parameters Controlling the Spalling of Concrete Cover in RC Columns During Seismic Activities

Murad M. Ilomame, Maged A. Youssef, and Salah F. El-Fitiany

Abstract Building codes have been moving toward performance-based design (PBD). Although the performance criteria would be ideally linked to the level of damage, research quantifying the expected level of seismic damage is scarce. This paper focuses on assessing one of the forms of seismic damage, which is the spalling of the concrete cover in the columns. First, a comprehensive literature review was conducted, which revealed discrepancies regarding the effects of different parameters on the spalling length. A parametric study, which involved analyzing 25,920 columns, was then conducted to examine the effects of the axial load, aspect ratio, confinement, transverse steel, and longitudinal steel on the spalling length. The results helped identifying the significant parameters influencing the spalling length.

Keywords Performance-based design · Damage · Cover spalling length · Nonlinear analysis

1 Introduction

Performance-based design (PBD) in earthquake engineering equips engineers with the ability to design structures to achieve different performance levels when subjected to various seismic demands [5]. FEMA 356 [11] defined three performance levels: immediate occupancy (IO), life safety (LS), and collapse prevention (CP), and linked them to the building maximum inter-story drift (1% for IO, 2% for LS, and 4% for CP). However, linking the performance levels to the level of damage can be more advantageous, as it allows owners to make critical decisions based on the expected repair cost and expected distributions to the building operations. Therefore, application of PBD should extend to include the damage level and corresponding

M. M. Ilomame (✉) · M. A. Youssef · S. F. El-Fitiany
Civil and Environmental Engineering, Western University, London, ON N6A 5B9, Canada
e-mail: milomame@uwo.ca

S. F. El-Fitiany
Structural Engineering, Alexandria University, Alexandria, Egypt

cost of repair [4, 5]. Seismic damage can take many forms including buckling of longitudinal reinforcement, spalling of cover concrete, flexural damage, and shear damage [5]. Out of these forms, spalling of the concrete cover is expected to happen regardless of the seismic design standard and the seismic performance level.

Regarding reinforced concrete (RC) columns, Table 1 shows the correlation between the different parameters (axial load ratio, aspect ratio, drift ratio, confinement, and longitudinal reinforcement ratio) and the spalling length. Clearly, the literature is presenting conflicting opinions. The literature is also not unified on the value of the concrete compressive strain at the onset of spalling. This strain was proposed to be **0.004** [2, 15, 16, 17, 21, 22, 23, 26], **0.0045** [12], **0.0048** [13], **0.005** [1, 3, 5, 8, 14, 24], and **0.0065** [9, 16]. Instead of specifying a specific value, Berry and Eberhard [6] proposed an equation to estimate this strain which is function of the transverse reinforcement ratio, the concrete compressive strength, and the yield stress of the steel bars.

Several numerical models were developed to predict the spalling length during seismic activities. However, they reflect the same conflicting opinions about the values for the strain defining spalling as well as the parameters affecting the spalling length. Based on the equilibrium of potential energy, Suda and Masukawa [25] developed analytical models to predict the concrete spalling in flexural elements. Berry and Eberhard [5] and Berry et al. [7] proposed an equation to estimate the drift at which the cover spalling initiates using the database of the Pacific Earthquake Engineering Research Center (PEER database), which contains the experimental results of approximately 470 columns. The equation was a function of the axial load, length

Table 1 Parameters affecting spalling length

Parameter	Correlated	Not correlated
Axial load ratio	• Berry and Eberhard [5] • Wu et al. [27] • Xiong et al. [28]	• Lehman et al. [16] • Chen et al. [9]
Aspect ratio	• Berry and Eberhard [5] • Lehman et al. [16] • Chen et al. [9] • Wu et al. [27]	• Xiong et al. [28]
Drift ratio	• Chen et al. [9]	
Confinement	• Jiang et al. [14]	• Berry and Eberhard[5] • Chen et al. [5] • Lehman et al. [9] • Wu et al. [16] • Wu et al. [27] • Xiong et al. [28]
Longitudinal reinforcement ratio	• Chen et al. [9]	• Berry and Eberhard[5] • Lehman et al. [16]

of the column, and dimensions of the column. Xiong et al. [28] proposed empirical formulas to estimate the spalling characteristics, which were based on experimental tests on 16 columns and data for 21 columns from the PEER database.

The literature review has revealed that there is a lack of a rigorous study to understand the effects of the different parameters on concrete spalling. This paper addresses this issue by presenting a comprehensive parametric study that identifies the parameters affecting the spalling length.

2   Parametric Study

A parametric study was conducted to examine the spalling length in seismically damaged RC columns. The parameters considered are the lateral drift, compressive strength, axial load ratio, column dimensions, aspect ratio, steel reinforcement ratio, and confinement coefficient. Table 2 provides the values considered for each of the considered parameters, where L is the length of the column and P is the column axial load.

2.1   Numerical Model

Figure 1 shows schematic of the numerical model. Each of the examined columns was modeled as a cantilever using the finite element software OpenSees [19]. Each cantilever was discretized into 20 displacement-based beam-column elements, as recommended by Neuenhofer and Filippou [20]. Because nonlinearity was expected to be concentrated at the base, the discretization was increased at this location. Although the number of the integration points is not a significant factor in improving the local response accuracy [20], it is critical for this research as it allows estimating

Table 2   Values for the considered parameters

Parameter	Symbol	Unit	Values
Drift ratio	D	%	1, 2, 3, 4, 5
Concrete compressive strength	f_c'	MPa	30, 40, 50
Axial load ratio $[P/(W \times H \times f_c')]$	A_x	–	0.1, 0.2, 0.3, 0.4
Column depth	H	mm	300, 750, 1000, 1500
Column width	W	mm	300, 750, 1000, 1500
Aspect ratio	L/H	–	6, 8, 10
Longitudinal steel ratio	ρ_L	%	1, 2, 3
Confinement factor	K	–	1.50, 1.75, 2.0
Yield strength	f_y	MPa	400
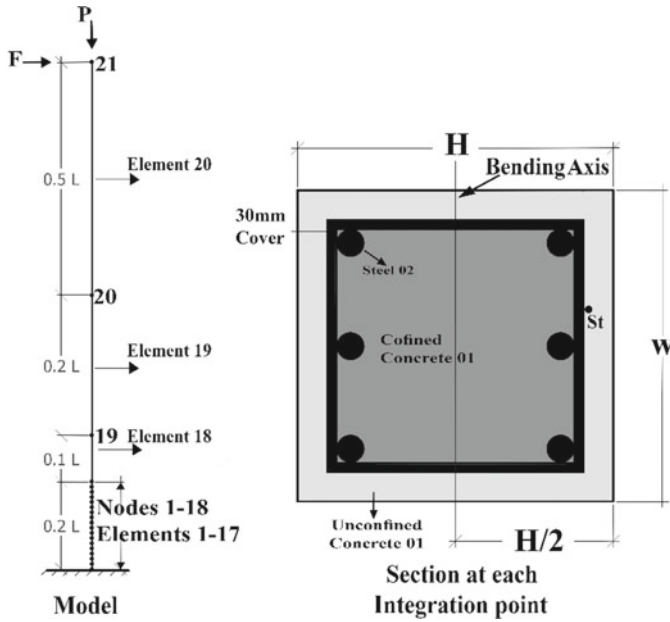
Fig. 1 Numerical model

the variation of the concrete strains along the element length. Ten Newton–Cotes integration points were utilized for each element.

Concrete 01 and Steel 02 materials, from the OpenSees library [19], were used to define the constitutive models for the unconfined concrete, confined concrete, and steel. The value of concrete strain (ε_{cc}), corresponding to the maximum confined concrete compressive strength (ε_{cc}) was calculated using Eq. (1), which was proposed by Mander et al. [18].

The model was loaded by the known axial load P and an incrementally increasing lateral force F. The concrete strains were recorded at the inner point of the concrete cover at each integration point (location St in Fig. 1). Concrete spalling was assumed to start at a compressive concrete strain of 0.004, as a conservative assumption. Analysis was terminated when the confined concrete strain reaches a value of 0.02, which defines a conservative estimate for concrete crushing [23].

$$\varepsilon_{cc} = 0.002 \times [1 + 5(k - 1)] \tag{1}$$

(a) Global response

(b) concrete strain at height of 180 mm
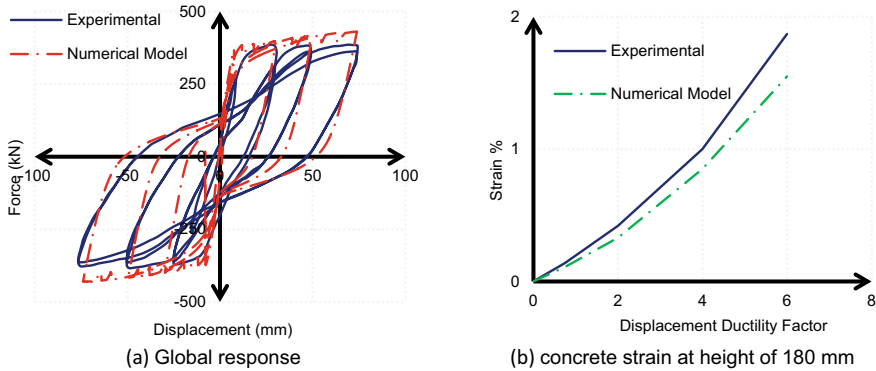
Fig. 2 Experimental results by Tanaka [26] versus predictions of the numerical model

2.2 Validation

The model is validated using the experimental results of Tanaka [26]. A column with dimensions of 550 mm width, 550 mm depth, and 1650 mm length was chosen for the validation. The column was reinforced with 12–20 mm longitudinal bars. The transverse bars were 12 mm in diameter and spaced at 110 mm. The global responses of the experimental and numerical models are shown in Fig. 2a. The model was able to capture the global response with good accuracy. Figure 2b shows the variation of the strain at the surface of the concrete core at a height 180 mm from the base with the displacement ductility. The results indicate that the model underestimates the strains by about 15–20%, which is considered relatively good accuracy. This difference could be due to the extra-confining effect provided by the concrete foundation, as explained by Lehman et al. [16].

2.3 Parametric Study Results

While presenting the results, a normalized spalling length (l_{sp}/L) is used in the discussion, where l_{sp} is the spalling length of the concrete cover.

Figure 3 shows the effect of the concrete compressive strength ($f_c^{'}$) on the normalized spalling length at low/medium drift ratios (≤3%) and high drift ratios (≥4%), considering different axial load ratios. Figure 3a indicates that the effect of $f_c^{'}$ depends on both the axial load ratio and the drift ratio. $f_c^{'}$ has no effect on the normalized spalling length at relatively low axial load ratios (≤0.2). This observation is regardless of the fact that increasing $f_c^{'}$ will lead to an increase in the applied axial load for a given axial load ratio. As such increase will not be contributing to spalling of the concrete cover, as the flexural effect is more dominant at small axial load ratios.
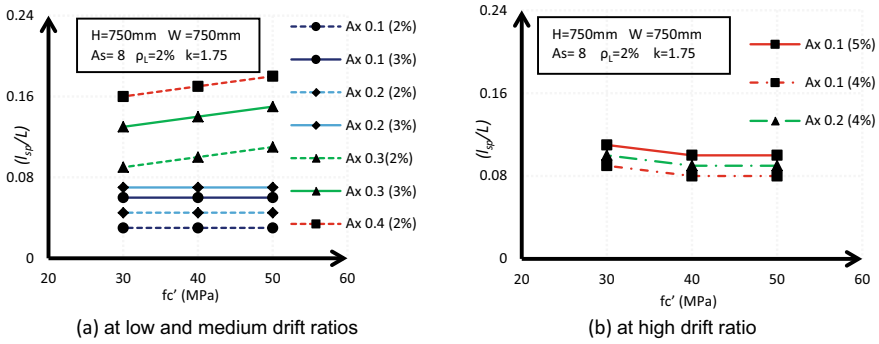
Fig. 3 Effect of the concrete compressive strength on the normalized spalling length

For high drift ratios, Fig. 3b does not show the curves for higher axial load ratios as the confined concrete core failed before achieving the desired drift.

Figure 4 shows the impact of the axial load ratio on the normalized spalling length at different drift ratios. It indicates that the axial load ratio has a significant effect, which is magnified at higher axial load ratios due to the corresponding increase in the stresses in the concrete cover. The missing point, for the curve at 5% drift, indicates that the column failed.

Figure 5 shows the effect of the column depth on the normalized spalling length at different drift ratios. For axial load ration of 0.2, Fig. 5a shows that increasing the column depth increases the spalling length, as such increase requires higher lateral load to reach the specified drift level. This effect vanishes at higher axial load ratios, Fig. 5b, as the axial stresses in the section become more effective.

Figure 6 presents the influence of the column width on the normalized spalling length at different drift ratios. It shows that the column width has a minimal effect. Although, the increase in the column width would increase the axial load, it will also distribute this load over a larger area. It should be noted that the missing point in
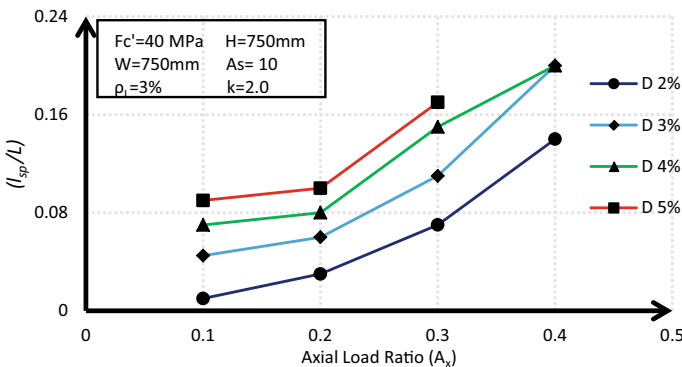
Fig. 4 Effect of axial load ratio on the normalized spalling length at different drift ratios

(a) At low axial load ratio   (b) At high axial load ratio
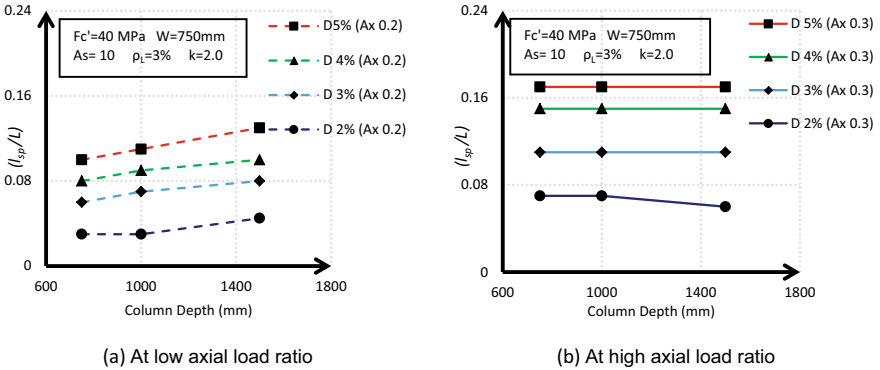
Fig. 5 Effect of the column depth on the normalized spalling length at different drift ratios

Fig. 6, for width of 350 mm, indicates that the column has failed before reaching a drift of 4%.

Figure 7 shows the effect of the aspect ratio (*L/H*) on the normalized spalling length at various drift ratios. It indicates that increasing the column aspect ratio reduces the spalling length. The reduction is due to the associated decrease in the lateral force required to cause the specified lateral deformation. It should be noted that the column with aspect ratio of 6 has collapsed at drift ratio less than 4%.

Figure 8 shows the effect of the longitudinal reinforcement ratio (ρ_L) on the normalized spalling length at different drift ratios. The figure shows that the effect is linked to the axial load ratio. Figure 8a indicates that the longitudinal reinforcement ratio at an axial load ratio of 0.2 does not affect the spalling length. In contrast, at axial load ratio of 0.3, increasing ρ_L reduces the spalling length, as shown in Fig. 8b. This might be attributed to the fact that spalling becomes affected by the axial load
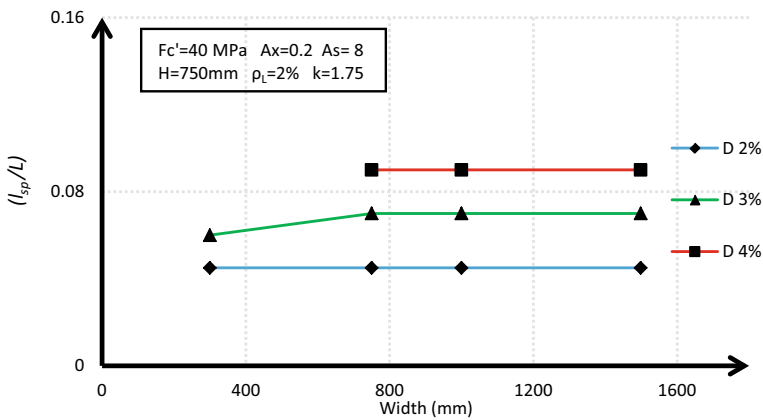
Fig. 6 Effect of column width on the normalized spalling length at different drift ratios
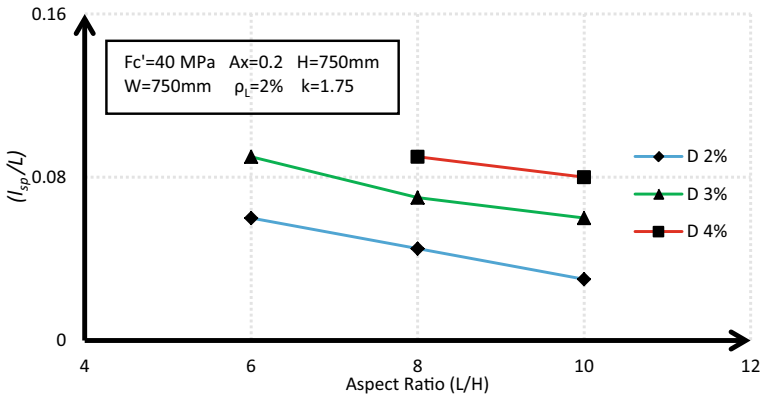
Fig. 7 Effect of column aspect ratio on the normalized spalling length at different drift ratios

when it increases above 0.3. Thus, the increase in ρ_L will contribute to reducing the concrete stresses due to axial load.

Figure 9 shows the effect of the confinement factor (k) on the normalized spalling length at different drift ratios. It shows that the effect of k becomes noticeable at higher axial load and drift ratios. Increasing the confinement has increased the spalling length. This increase can be explained by the increase of stiffness the confined section, which requires a higher lateral force to reach the specified lateral deformation. It should be noted that the column with k of 1.5 failed before reaching at drift ratio of 4% at axial load ratio of 0.2, and at a drift of 3% at axial load ratio of 0.3.

(a) At axial load ratio of 0.2

(b) At axial load ratio of 0.3
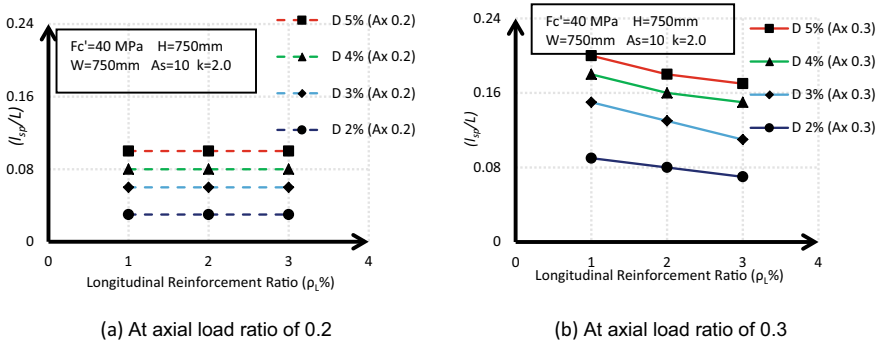
Fig. 8 Effect of longitudinal reinforcement ratio on the normalized spalling length

(a) At axial load ratio ≤ 0.2   (b) At axial load ratio ≥ 0.3
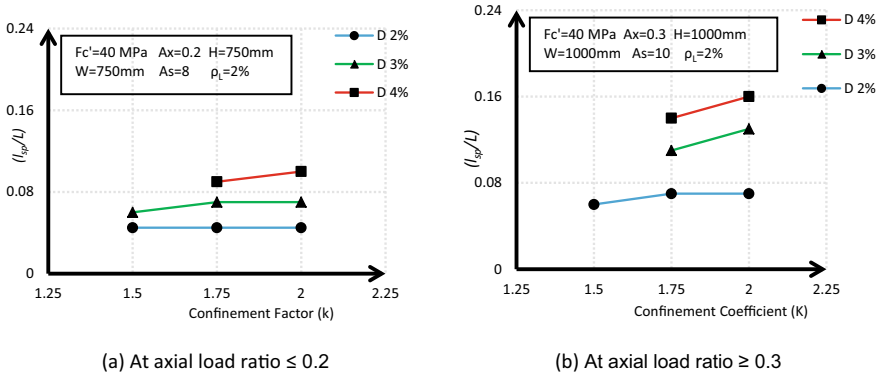
Fig. 9 Effect of column confinement factor on the normalized spalling length at different drift ratios

3 Conclusions

Based on the conducted parametric study, it was concluded that some parameters have a direct effect on the spalling length in RC columns, while others have an indirect effect. This can explain the contradiction found in the literature. Specific conclusions about the effects of different parameters on the cover spalling length are given below.

- The axial load ratio has a considerable direct impact on the spalling length. This impact is magnified for axial load ratios higher than 0.2.
- fc' has a direct effect on the spalling length at high axial load ratios. However, the effect vanishes at low and medium axial load ratios.
- The spalling length is directly proportional to the column depth at axial load ratios of 0.2 or less. However, it is independent from the column depth for higher axial load ratios.
- The column aspect ratio is inversely proportional to the spalling length.
- The longitudinal reinforcement ratio has no effect on the spalling length for axial load ratios less than 0.2. In contrast, the longitudinal reinforcement ratio is inversely proportional to the normalized spalling length at higher axial load ratios.
- The confinement factor significantly affects the spalling length at high axial load ratios and high drift ratios. On the other hand, at low axial load ratios and drift ratios, the confinement factor becomes insignificant.
- The column width has a marginal impact on the spalling length.

References

1. AASHTO (2011) Guide specifications for LRFD seismic bridge design. American Association of State Highway and Transportation Officials, Washington, DC
2. Applied Technology Council (ATC) (1996) Improved seismic design criteria for California bridges: Provisional recommendations. Rep.#ATC-32, Redwood City, CA
3. Babazadeh A, Burgueño R, Silva PF (2015) Use of 3D finite-element models for predicting intermediate damage limit states in RC bridge columns. J Struct Eng 141(10):04015012
4. Berkeley University (n.d) Pacific earthquake engineering research center: mission and goals. Accessed March 14, 2022. https://peer.berkeley.edu/about/mission-and-goals
5. Berry MP, Eberhard MO (2003) Performance models for flexural damage in reinforced concrete columns, Pacific Earthquake Engineering Research Center Report 2003. University of California, Berkeley
6. Berry MP, Eberhard MO (2006) Performance modeling strategies for modern reinforced concrete bridge columns 67(11)
7. Berry M, Parrish M, Eberhard M (2004) PEER structural performance database user's manual (version 1.0). University of California, Berkeley
8. Caltrans (2013) Caltrans seismic design criteria, Version 1.7, California Department of Transportation, Sacramento, CA
9. Chen L, Lu X, Jiang H, Zheng J (2009) Experimental investigation of damage behavior of RC frame members including non-seismically designed columns. Earthq Eng Eng Vib 8(2):301–311
10. Da Silva P (2000) Effect of concrete strength on axial load response of circular columns. McGill University, PhD diss.
11. FEMA 356 (2000) Federal emergency. Prestandard and commentary for the seismic rehabilitation of buildings. FEMA Publication No. 356
12. Goodnight JC, Kowalsky MJ, Nau JM (2013) Effect of load history on performance limit states of circular bridge columns. J Bridg Eng 18(12):1383–1396
13. Goodnight JC, Kowalsky MJ, Nau JM (2016) Strain limit states for circular RC bridge columns. Earthq Spectra 32(3):1627–1652
14. Jiang H, Lu X, Kubo T (2010) Damage displacement estimation of flexure-dominant RC columns. Adv Struct Eng 13(2):357–368
15. Kowalsky MJ (2000) Deformation limit states for circular reinforced concrete bridge columns. J Struct Eng 126(8):869–878
16. Lehman D, Moehle J, Mahin S, Calderone A, Henry L (2004) Experimental evaluation of the seismic performance of reinforced concrete bridge columns. J Struct Eng 130(6):869–879
17. Li L, Luo G, Wang Z, Zhang Y, Zhuge Y (2021) Prediction of residual behaviour for post-earthquake damaged reinforced concrete column based on damage distribution model. Eng Struct 234:111927
18. Mander JB, Priestley JN, Park R (1988) Theoretical stress-strain model for confined concrete. J Struct Eng 114(8):1804–1826
19. Mazzoni S, McKenna F, Scott MH, Fenves GL, Jeremic B (2006) Open system for earthquake engineering simulation. User Command-Language Manual, Pacific Earthquake Engineering Research Center, Berkeley, CA
20. Neuenhofer A, Filippou FC (1997) Evaluation of nonlinear frame finite-element models. J Struct Eng 123(7):958–966
21. Perdomo C, Monteiro R (2020) Simplified damage models for circular section reinforced concrete bridge columns. Eng Struct 217:110794
22. Priestley MJN, Kowalsky MJ (2000) Direct displacement-based seismic design of concrete buildings. Bull N Z Soc Earthq Eng 33(4):421–444
23. Priestley MJN, Calvi GM, Kowalsky MJ (2007) Direct displacement-based seismic design of structures. In: NZSEE conference, pp 1–23
24. Su J, Dhakal RP, Wang J (2017) Fiber-based damage analysis of reinforced concrete bridge piers. Soil Dyn Earthq Eng 96:13–34

25. Suda K, Masukawa J (2000) Models for concrete cover spalling and reinforcement buckling of reinforced concrete. In: 12th WCEE, vol 1437
26. Tanaka H (1990) Effect of lateral confining reinforcement on the ductile behaviour of reinforced concrete columns
27. Wu B, Xiong W, Liu F (2017) Fire behaviours of concrete columns with prior seismic damage. Mag Concr Res 69(7):365–378
28. Xiong W, Wu B, Wen B (2016) Spalling of concrete cover of cyclically loaded columns and fire behaviour of columns with concrete spalling. Struct Infrastruct Eng 12(12):1537–1552

Seismic Isolation of Low-Rise Residential Structures

Nolan Stratton, Niel Van Engelen, and Rajeev Ruparathna

Abstract Despite the advances in structural engineering made in the last century, earthquakes continue to pose a major risk to the lives and livelihoods of many communities in Canada. Generally, single-family wood frame residential structures are fairly resilient to seismic effects, however, the aftermath of several earthquakes has demonstrated that while life safety was acceptable, the high economic losses were not. To protect against this danger to life and livelihood, the National Building Code of Canada (NBCC) provides several methodologies to design structures for seismic events. One of the most promising is an emergent technology known as base isolation. Base isolators are specially designed structural components that effectively act as a suspension system, isolating the structure from the ground motion effects. While this technology has proven effective at protecting structures and their occupants, the current methodology requires costly custom designs and comprehensive engineering. Thus, the application of this technology is likely to be expensive for common single-family residential structures. To eliminate this cost barrier to widespread application in low-rise residential structures, software was developed to perform the engineering seismic isolation design for structures designed according to Part 9 (Housing and Small Structures) of the NBCC. Currently, the NBCC does not provide a methodology to design base isolated structures, and so the program adapts the American Society of Civil Engineers equivalent lateral force procedure to NBCC requirements. The design and analysis of the base isolated structure is performed using pre-certified isolators whose properties have been previously verified, the structural characteristics and geometry, and site data. This allows the designer to augment a low-rise residential structure with a seismic isolation system without engineering involvement, providing an economical path for seismic isolation to become the rule in low-rise residential structures.

N. Stratton · N. Van Engelen (✉) · R. Ruparathna
Department of Civil and Environmental Engineering, University of Windsor, Windsor, ON, Canada
e-mail: niel.vanengelen@uwindsor.ca

N. Stratton
e-mail: stratton@uwindsor.ca

1 Introduction

Despite the engineering achievements of the last century, earthquakes continue to be a serious threat to the lives and livelihoods of many communities. Since 1970, approximately 360 damaging earthquakes have claimed over one million lives worldwide [3]. In Canada there are approximately 4000 earthquakes yearly, mainly concentrated in regions of high seismicity. British Columbia is well-known as a region at risk from seismic hazards. However, significant seismic risk extends to Canadians across the country, for example, on 23 June 2010, a 5.2 magnitude earthquake rocked a small Quebec town 60 km north of Ottawa [9]. The threat posed to Canadians is further magnified due to the concentration of roughly 40% of the national population within areas of high seismicity [10]. In Quebec, 70% of the population lives in active seismic regions and three of the largest cities in eastern Canada–Montreal, Ottawa and Quebec City—are all located in earthquake-prone regions [14]. In British Columbia, the threat is even greater where over 80% of the population lives are in active seismic regions [5].

The National Building Code of Canada (NBCC) contains two main sections pertaining to the seismic design of structures: Part 4 Structural Design and Part 9 Housing and Small Buildings. Part 4 requires engineering involvement and can be applied to all structures while Part 9 applies only to structures with total plan areas of 600 m^2 or less and three storeys or less in height [17]. For common single-family dwellings typically referred to as a house, a prescriptive design methodology within Part 9 is generally employed to ensure the structure will be resilient enough to withstand the applied load conditions, including region-specific seismic loads. In Canada the dominant majority of modern single-family residential structures are composed primarily of wood members due to their relatively high strength to weight ratio. When subjected to seismic loads these structures typically perform well relative to masonry due to the flexibility of these structures; and the system redundancy of the members [21].

In recent years, the performance of wood frame residential structures has come under scrutiny due to the aftermath of several seismic events near urban centres. The traditional measure of disaster intensity is generally the casualty figures, which for many events in North America in recent years have been low compared with other events around the world, especially in developing countries. However, the economic losses and people left homeless remain shockingly high for moderate and strong events, such as the 1994 Northridge earthquake [7]. The Northridge earthquake was a M6.7 event that occurred in the Los Angeles area of California. This event is notable due to the magnitude as well as its proximity to an urban centre which resulted in 57 fatalities and between $25–40 billion USD in losses [8, 23]. Of the 57 fatalities, 25 casualties were a result of building damage and 24 of those occurred in wood frame residential structures with half of the $40 billion in property damages being from

wood frame structures [8]. The inflicted losses from this event, even for superficial damage, were quite high, averaging $64,500 CAD at the time, which is greater than the current yearly median provincial household income of Canadians [6]. The potential loss of over a year's worth of income, or the potential loss of their home, which is the largest single asset of many Canadians, would be a catastrophic loss for the affected individuals.

Significant economic losses may also be incurred as a result of the deformation of the structure or damage to the structures contents. Damage to structures can be categorized as either damage due to excessive inter-storey drift, or damage due to excessive floor accelerations. Drift-sensitive components, such as drywall and wall studs, can be compromised if the inter-storey drift becomes too significant leading to cracking. Acceleration-sensitive components are possessions that are not fixed to the structure, such as small appliances or other unfixed furnishings, which may become damaged when exposed to strong accelerations. In addition to the direct economic losses, the need to potentially seek temporary accommodations while repairs are underway may result in a substantial disruption to affected people's lives and additional expenses.

One method available within the NBCC that significantly improves the performance of structures during seismic events is the emergent technology known as seismic isolation. Currently base isolation requires additional capital and maintenance costs to design and implement making it less appealing to part 9 designers. To eliminate the cost barriers preventing widespread adoption of base isolation for Part 9 single-family residential structures, research is being conducted to develop a program to perform the design of the base isolated structure based on a catalogue of pre-certified and tested isolators tailored for use in residential structures. This will remove the need to conduct a comprehensive engineering design of the structure, and eliminate the costly custom testing and design of the base isolators by designing based on existing and well-understood isolators.

2 Background

2.1 Seismic Isolation

Seismic isolation is an anti-seismic technology that has been successfully used to prevent structural damage for a variety of superstructure types. Seismic isolation reduces the seismic loads on the superstructure by decoupling the structure from strong ground motions [13]. The decoupling is achieved by creating an intentionally soft horizontal layer that enables the base of the structure to displace laterally, which favourably alters the superstructures dynamic response as shown in Fig. 1. The decoupling significantly reduces the transfer of forces from the ground motion to the overlying structure, protecting the structure and its occupants from harm even

Fig. 1 Fixed base and base isolated structure
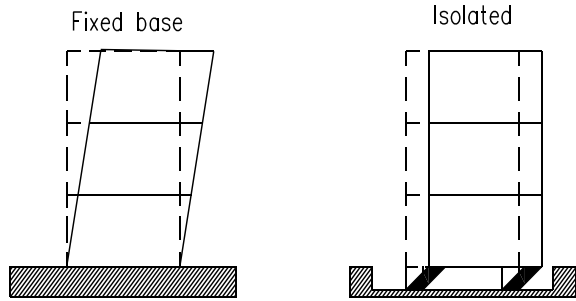
during large earthquakes [15, 16]. The properties of base isolation, and its demonstrated efficacy [2, 11] make it a suitable candidate to protect economically vulnerable single-family residential structures.

While this technology has proven effective at protecting structures, its use has been mainly limited to large high-importance structures. Currently no simplified method for the design of base isolated structures exists in the NBCC in Part 4 or Part 9 [18]. A lack of prescriptive Part 9 related requirements for the design of a base isolated residential structure means that inclusion of a base isolation system would require the involvement of an engineer familiar with base isolation. Additionally, Part 4 requires a rigorous series of tests to verify the properties of base isolators before they can be certified for use in a structure. The custom base isolator design process and comprehensive engineering requires a significant capital expenditure making the application of this technology currently cost prohibitive for single family residential structures.

There are several types of isolator units that can be fitted to provide this soft isolation layer. One type that shows promise for Part 9 structures specifically is fibre-reinforced elastomeric isolators (FREIs) which consist of layers of elastomer with fibre mesh layers interspersed between the elastomeric layers as shown in Fig. 2.

The layers of elastomer provide a relatively low horizontal stiffness, while the fibre reinforcement restrains the lateral bulging of the nearly incompressible elastomeric layers, providing a high vertical stiffness as shown in Fig. 1. This allows the structure to augment the traditional footings with elastomeric bearings, as they are
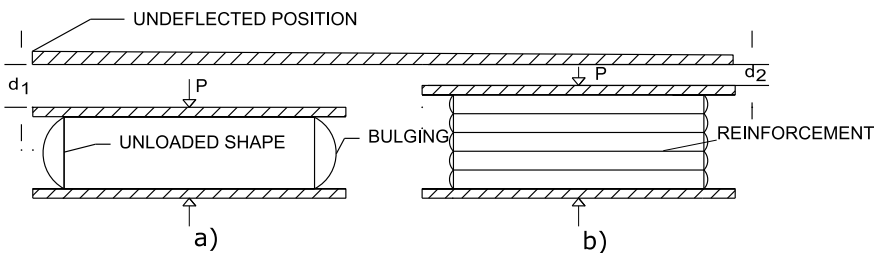
Fig. 2 **a** Unreinforced elastomeric bearing **b** Reinforced elastomeric bearing

capable of carrying the overlying structure's gravity loads while also providing the capacity for horizontal displacement. It has been suggested that FREIs could be more suitable for Part 9 structures than the traditional steel-reinforced elastomeric isolators (SREIs), due to the relatively lower bearing weight and the potential for bearings to be manufactured in larger scales more economically [12]. Due to the relatively smaller axial load deviation within a Part 9 structure's foundation, it is desirable to utilize a single type of elastomeric isolator uniformly across the isolation layer, which is not always possible in larger structures due to the large variations in axial load. This would allow designers to order a single type of bearing for the design, and would also allow for bearings of similar types to be produced in larger quantities and applied by multiple designers to structures of relatively similar requirements. This is more economically desirable than the alternative of producing smaller quantities of customized bearings, which are only applicable to structures or loadings whose properties match very closely.

2.2 Existing Base Isolation Standards and Design Methodologies

To create a program capable of producing a simplified base isolation design and analysis for a Part 9 structure, the existing standards on the subject are needed to be adapted to this purpose. While the NBCC does not currently provide any simplified design methods for the design of seismically isolated structures, it does contain several prescriptive requirements regarding performance and validation. The main requirements of note from Clause 4.1.8.20 are [17]:

1. The period of the isolated structure shall be greater than three times the fixed base period.
2. The isolation system shall produce a restoring force to prevent residual displacements.
3. The stiffness and damping characteristics of the isolation system must be validated by testing at least two full-size specimens of each predominant type and size of isolator, and a representative sample of the isolator units to be installed shall be validated by tests prior to their installation.
4. A lateral load carrying diaphragm, or horizontal structural elements located above the isolation interface, shall transmit forces due to non-uniform ground motions from one part of the structure to another.
5. All structural framing elements shall be designed to remain elastic but must also be capable of ductile action to prevent collapse in extreme scenarios.

ASCE 7–16 [1] provides a simplified analysis and design methods for isolated structures. The equivalent lateral force (ELF) procedure is the simplest method presented as it does not require detailed modelling. However, to ensure the results

produced by this procedure will be representative of the real base isolated response, the following criteria are imposed:

1. The structure is located on a site class A, B, C, or D.
2. The effective period of the isolated structure at the maximum displacement is less than or equal to 5.0 s.
3. The structure above the isolator interface is less than or equal to 19.8 m in height.
4. The effective damping of the isolation system at the maximum displacement is less than or equal to 30%.
5. The effective period of the isolated structure is greater than three times the elastic fixed base structure above the isolation system.
6. The structure above the isolation system does not have any structural irregularities.
7. The isolation system meets the following requirements:

   a. The effective stiffness of the isolation system at the maximum displacement is greater than 1/3 of the effective stiffness at 20% of the maximum displacement.
   b. The isolation system is capable of producing a restoring force.
   c. The isolation system does not limit the maximum displacement to less than the total maximum displacement, D_{TM}.

Both NBCC and ASCE requirements focus on ensuring first mode dominance, (i.e. that the displacements are concentrated at the isolation layer). This is crucial as the ELF procedure is based on the assumption of first mode dominance, the condition that best protects the superstructure. The other NBCC and ASCE requirements, while not identical, ensure the structure is sufficiently simple for the ELF procedure to be used, and that performance of the isolation system will be validated sufficiently. The main difference between the NBCC seismic design provisions and the ASCE provisions is the construction of the response spectrum as shown in Fig. 3.

Both response spectrums are developed via similar hazard analysis methods; the NBCC uses linear segments while ASCE utilizes a piecewise function. Therefore, by employing the NBCC response spectrum and integrating the prescriptive requirements of both codes, the ELF procedure can be adapted for Canadian standards, and then be subsequently employed to analyze performance of the program's design.
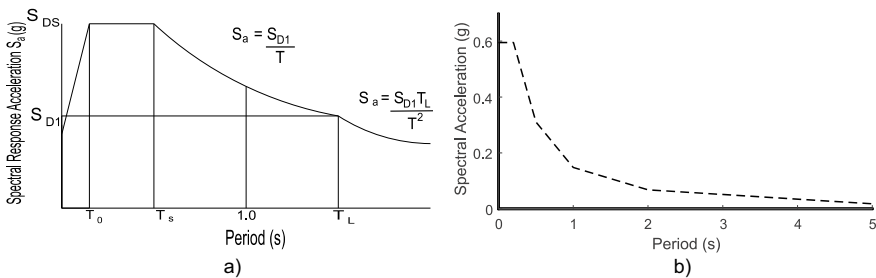
Fig. 3 **a** ASCE design response spectrum and **b** NBCC design response spectrum

3   Program Methodology

The ASCE equations presented and adapted for use by the NBCC require an iterative design process to determine several key fstructural characteristics due to the nonlinear behaviour of the isolation system. To accommodate an iterative design process, it was proposed by [4] to develop a program to analyze a seismically isolated Part 9 structure. The Government of Canada provides an online tool to generate the design response spectrum for any given location in Canada [19], and it was proposed that the developed base isolation program could be made similarly available for ease of use. It is desirable to align the online resource closely with Part 9 as base isolation is intended to augment and improve the performance of superstructure designed in compliance with NBCC Part 9 in order to minimize design changes. It is proposed that, if successful, this methodology and the relevant requirements of this method could be integrated into Part 9 to provide designers with an economical means of designing base isolated Part 9 structures.

3.1   *Key Parameters and Inputs*

The analysis of a structure requires several parameters to be extracted to ensure the performance of the structure is desirable. These parameters of interest are:

D_M: Maximum displacement of the centre of rigidity of the isolator system.
D_{TM}: Total maximum displacement of isolator units, including torsional amplification.
T_M: The fundamental period of the isolated structure at D_M.
W: Total structural weight.
V_b: Lateral forces below the isolation layer (foundation).
V_{st}: Total seismic shear within the elements above the isolator layer (ground level).
F_j: Vertical distribution of forces in the superstructure.
n: Number of isolators used in the isolation layer design.
$x_i\ y_i$: Plan coordinates of the ith isolator unit.
Δ_j: Inter-storey drifts.
a_j: Floor acceleration of the jth floor.

The ELF procedure is a simplified analysis method, and thus the required inputs are also deliberately minimized to promote accessibility and ease of use. In addition, characteristics that would normally be unknown to a non-engineer designer but that are still crucial for response analysis are approximated using information that would be readily available to a non-engineer designer. The required parameters for analysis are:

1. The storey height distribution.
2. Floor plan dimensions.

3. Structure weight class as defined by the Part 9 reference document: Canadian Wood Council Engineering Design Guide [22].
4. The damping, $\beta_M(D_M)$, and stiffness, $k_M(D_M)$, as a function of isolator displacement provided by the isolator bearing manufacturer/catalogue of isolators.
5. Foundation plan.
6. Site class.
7. Design response spectrum for site seismic conditions [19].

3.2   Isolation System Design

To design the isolation system, it is necessary for the program to evaluate the geometric and loading realities of the superstructure in order to allocate the bearings to augment the traditional footing. The program also evaluates if the bearing chosen by the designer will be sufficient to maintain structural stability under the structure's gravity loads. Many residential structures have geometries that cannot be idealized as rectangular or uniform across their height. Therefore, the program must be applicable to more complex geometries. To accommodate non-rectangular geometry the designer can choose to idealize the floor plan as either rectangular or L-shaped, and it is possible to define the geometry of each storey independently. It should be noted that structures that cannot be reasonably represented as either rectangular or L-shaped are not currently valid for analysis.

While some degree of customization is desirable, it is important to keep design input requirements to a minimum. Load distribution, storey stiffness and storey mass are all characteristics determined when designing an isolation system. To ensure ease of use, the program produces approximations of these characteristics using relevant Part 9 methods. Storey masses are determined using Part 9 distributed load averages for live loads. Part 9 superstructures are designed according to the Canadian Wood Council Engineering Design Guide (The Canadian Wood) [22] which defines a structure as either normal or heavy based on the construction practices employed. The structure's distributed dead loads can then be determined based on its weight class as shown in Table 1.

Storey stiffnesses are approximated using the structure's characteristic equation and the assumption that the ratio between individual storey stiffnesses will be proportional to the required lateral strengths of a fixed base Part 9 structure.

Table 1 CWC weight class distributed dead loads [22]

Structural component	Normal weight construction (kPa)	Heavy weight construction (kPa)
Floor	0.5	0.5–1.5
Roof	0.5	0.5–1.0
Exterior wall	0.32	0.32–1.2
Partition wall	0.5	0.5

In addition, the superstructure's design should not deviate from the normal practices of Part 9. NBCC Part 9 directs designers to design in accordance with the practices outlined in the Canadian Wood Council Engineering Design Guide [22]. The CWC guide outlines that the superstructure and the floor system must be detailed to act as a load path to enable the transfer of gravity and lateral loads to the foundation supports. These supports, typically the footings, generally connect to the superstructure at the intersecting nodes of the structural floor beams to facilitate load transfer. To comply with existing Part 9 practices, the program designs the isolation system by detailing the isolators placement to coincide with the floor system nodes. If the superstructure is designed using Part 9 methods, the load paths within the superstructure will be sufficient to transfer the relevant gravity and lateral loads onto the underlying isolation system.

A finite element approach is taken to determine the exact tributary load carried by the isolator bearing under the four relevant load cases:

$$\text{Case 1: 1.4 Dead}$$

$$\text{Case 2: 1.25 Dead} + 1.5\,\text{Live} + 1.0\,\text{Snow}$$

$$\text{Case 3: 1.25 Dead} + 1.0\,\text{Live} + 1.5\,\text{Snow}$$

$$\text{Case 4: 1.0 Dead} + 0.25\,\text{Snow} + 0.6\,\text{Storage}$$

Case 4: 1.0 Dead + 0.25 Snow + 0.6 Storage.

The individual loadings from the first to third cases are then compared with the isolator's static buckling capacity to ensure that no isolator will be loaded beyond the acceptable design static load tolerances. The fourth case is considered during the seismic analysis to ensure bearing stability is maintained under the imposed seismic shear displacement. A graphical display of the isolation layer design will then be produced for review. Additionally, the initial isolator placement automatically generated by the program can be edited by the user to account for more complex situations, although any alteration of placement from directly beneath the nodes should be done in compliance with the relevant Part 9 provisions.

3.3 Seismic Analysis

This program determines the dynamic properties of the isolated structure by iterative methods to determine the maximum lateral displacement, D_M, and the isolation period of the structure at the maximum displacement, T_M. Iterative methods are required because the isolator stiffness, k_M, and the isolator damping coefficient, B_M,

which is a function of damping, are dependent on D_M. An initial estimate of $T_M = 1$ s and $B_M = 1$ and $S_a(T_M)$ are used to begin iterations while D_M is recalculated using:

$$D_M = \frac{S_a(T_M)gT_M^2}{4\pi^2 B_{Mj}(D_M)} \tag{1}$$

New estimates of $k_M(D_M)$, $B_M(D_M)$ and T_M are produced using the isolator bearing property data provided by the bearing manufacturer and the equation:

$$T_M = 2\pi\sqrt{\frac{W}{k_M g}} \tag{2}$$

Once program converges to a period within 0.01 s of the previous iteration, the isolation layer displacement and stiffness can be used to evaluate the response of the superstructure. Response parameters of interest include:

- Floor accelerations
- Storey drifts
- Vertical force distribution
- Maximum displacements of the isolators including torsional effects.

4 Example Structure Analysis

To illustrate the abilities of the developed methodology, a case study structure has been subjected to analysis. The example structure is located in Montréal Quebec, an area of moderate seismicity, and the site class is C. The example structure is a two storey L-shaped structure comprising an L-shaped ground level formed by three conjoined 5 m × 5 m sections overlaid by an L-shaped second storey of comprising three conjoined 4 m × 4 m sections as shown in Fig. 4. Each storey is 3 m in height and the structure's Part 9 weight class is normal. The structural floor beams trace the ground floor perimeter and divide the internal spans between the three 5 m × 5 m ground floor areas as shown in Fig. 5. The storey masses, given in Table 2, and stiffnesses, given in Table 3, were calculated, and the design was completed using a theoretical square fibre-reinforced elastomeric isolator bearing tailored for use in Part 9 structures. The design characteristics of the bearing are presented in Table 4 while the properties are presented in Table 5.

The damping of the bearing is assumed constant at 10% while stiffness is approximated as a function of displacement as:

$$k_M = \frac{Ga(a - D_M)}{T_r} \tag{3}$$
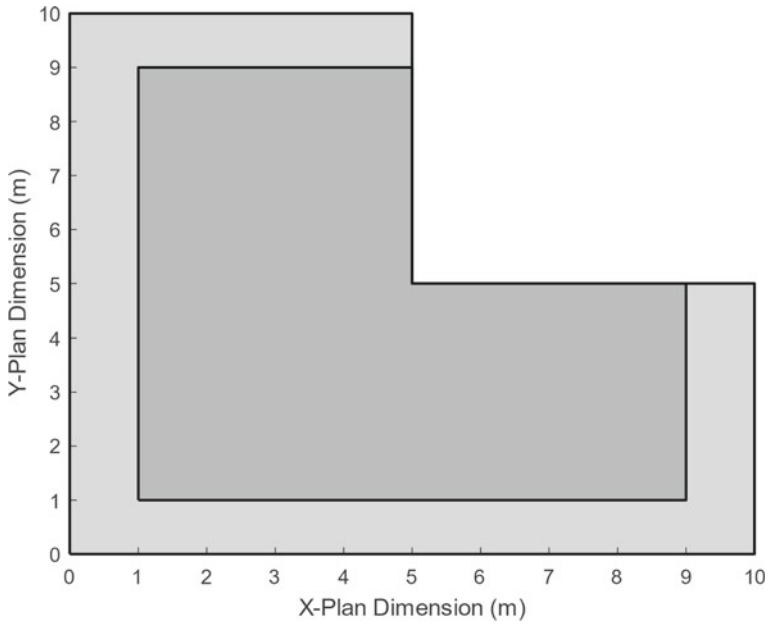
Fig. 4 First and second storey plan layout
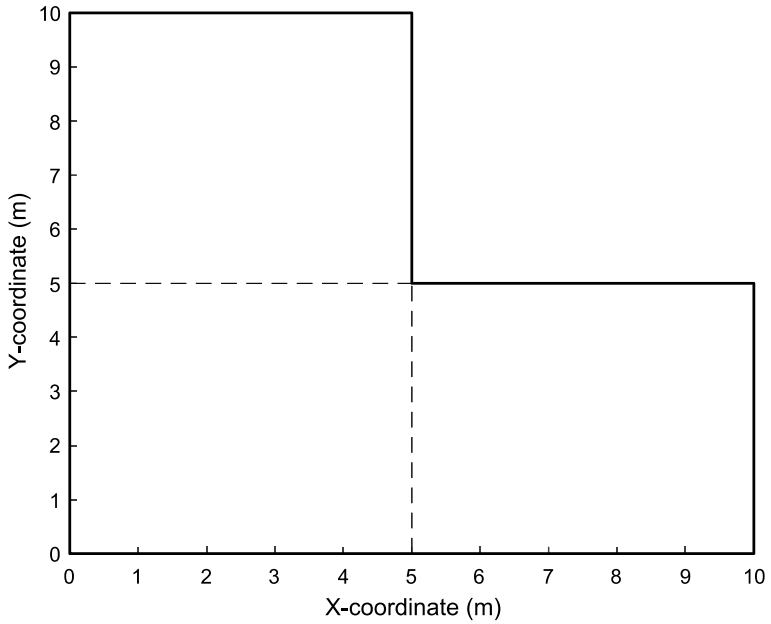
Fig. 5 Floor beam layout

Table 2 Mass and weight distribution

Storey	Mass (kg)	Weight (kN)
1 (ground)	13,425	131.7
2	12,651	124.1
3 (roof)	4746	46.6
Total	30,822	302.4

Table 3 Stiffness distribution

Storey	Stiffness (kN/mm)
1	9.71
2	4.16

Table 4 Isolator characteristics

Characteristic	Value
G (shear modulus) (MPa)	0.4
K (bulk modulus) (MPa)	2000
ζ (damping) (%)	10
a (side length) (mm)	360
t_r (layer thickness) (mm)	17
n (number of layers)	20
T_r (total thickness) (mm)	340
S (shape factor)	5.3

Table 5 Isolator properties

Property	Value
k_H (static horizontal stiffness) (kN/mm)	0.152
k_V (vertical stiffness) (kN/mm)	1.69
D_{max} (design max displacement) (mm)	80
P_{min} (design minimum seismic axial load) (kN)	15
$P_{cr}(D)$ (design maximum seismic axial load) (kN)	345
P_{cr} (design maximum static axial load) (kN)	470

The program designs the isolation system layout by placing isolators at the beam intersection nodes as shown in Fig. 6. The approximate axial loads on each individual isolator are presented for cases 1:4 in Table 6:

The first three cases constitute the static case and will govern the static buckling and rupture of the isolator bearing, while case 4 governs the buckling, rupture, and rollout stability of the bearings during seismic excitation. Isolator 5 has a static axial load of 215.2 kN and a seismic axial load of 72.4 kN. Isolator 5 is located at the approximate centre of the structure and due to local geometry carries a much greater tributary load. Both isolator 5's carried seismic and static axial loads are substantially
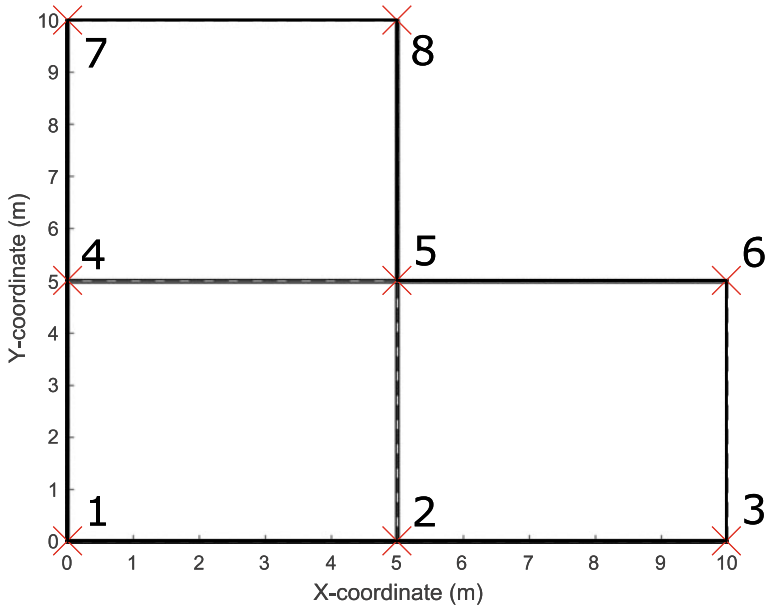
Fig. 6 Isolator layout

Table 6 Isolator axial loading (kN)

Isolator	Case 1	Case 2	Case 3	Case 4
1	38.5	77.5	70.0	29.0
2	65.3	141.4	123.2	48.8
3	31.4	63.7	57.5	23.7
4	65.3	141.5	123.2	48.8
5	97.0	**215.2**	186.3	**72.4**
6	28.8	58.2	51.9	**21.6**
7	31.4	63.7	57.5	23.7
8	28.8	58.2	51.9	**21.6**
Average	48.3	102.4	90.2	36.2

less than the isolator's critical static and seismic axial load limits of 470 kN and 345 kN, respectively. Isolator 6 and 8 have the lowest axial load at 21.6 kN making them potentially vulnerable to rollout, however their loading exceeds the 15 kN lower limit and are therefore stable so long as the design shear displacement does not exceed the maximum acceptable bearing displacement.

After the evaluation of gravity load capacity, the structural response parameters are produced to compare the fixed base response of the Part 9 structure to the isolated response. Assuming that the fixed base period falls into the 0.1–0.3 s range typical
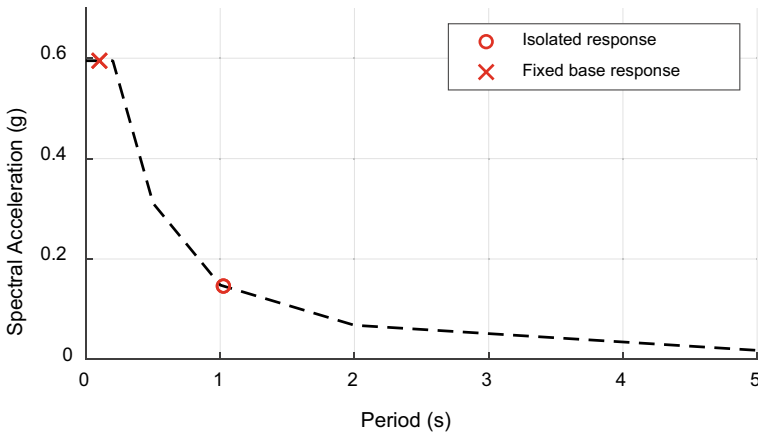
Fig. 7 Response spectrum comparison of the fixed base and isolated structure

of single-family residential structures [20] the period of the isolated structure was extended to 1.02 s and the spectral response acceleration was reduced to roughly 1/3 of the fixed base spectral acceleration. The relative reduction in spectral acceleration is highlighted in Fig. 7.

The superstructure response parameters, including the vertical force distribution, the peak floor accelerations and the relative peak storey displacements, are all substantially lower than the fixed base structure which is to be expected of an isolated structure. The peak floor acceleration was reduced from 0.310 g to 0.165 g and the peak inter-storey drifts was reduced from 0.18% to 0.079% as shown in Figs. 8 and 9. Both were reduced below the 0.25 g and 0.1% damage thresholds for acceleration-induced and drift-induced damage of wood structures, respectively [8]. Additionally the peak storey shear force was reduced from 30.5 kN to 16.5 kN as shown in Fig. 10.

The reduction in key performance indicators was achieved via a maximum translational base displacement of 31.7 mm which was increased to 36.5 mm, when including torsional amplification. The torsional amplification of individual isolators was calculated based on each isolator's local eccentricity in compliance with ASCE Clause 17.5.3.3, and are given in Table 7.

Since the calculated torsional amplification was calculated as a maximum of an 8.1%, an increase of 15% is applied instead as ASCE provisions require a minimum of 15% be considered to ensure adequate conservatism. The total maximum displacement of all isolators was determined as 36.5 mm due to the uniform 15% torsional amplification, which is less than the 80 mm displacement limit and so the stability criteria have been met. It should be noted that it is possible to extend the isolated period well beyond 1 s, however for this structure sufficient levels of superstructure protection, (i.e. no damage) can be attained without requiring a substantial period elongation and large base displacements. It is desirable that the total shear displacement of the structure be kept to the minimum value sufficient to provide the structure
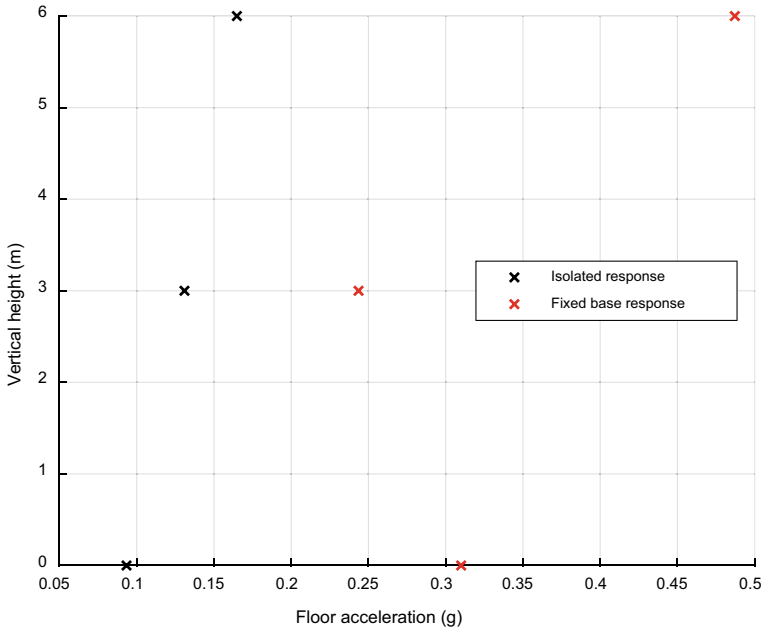
Fig. 8 Floor acceleration comparison of the fixed base and isolated structure
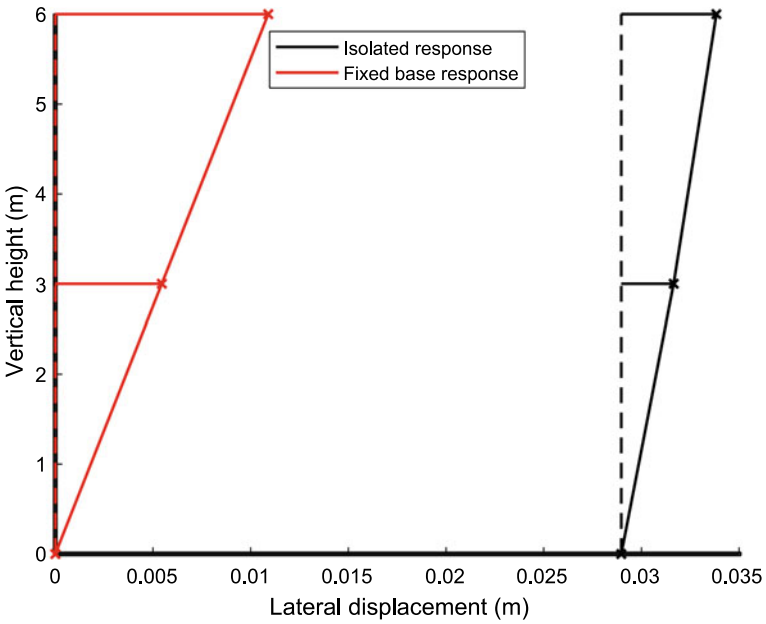
Fig. 9 Lateral displacement comparison of the fixed base and isolated structure
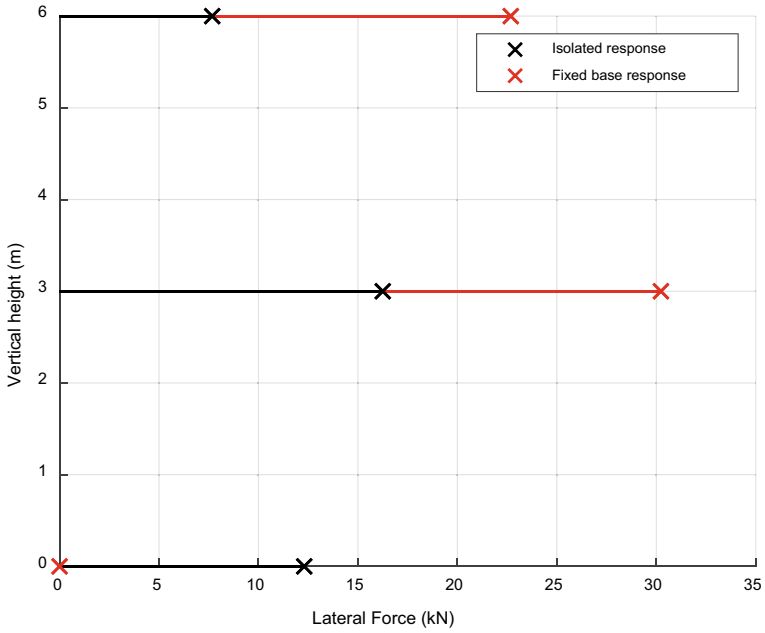
Fig. 10 Vertical force distribution comparison of the fixed base and isolated structure

Table 7 Torsional amplification

Isolator	Calculated torsional amplification	Applied torsional amplification
1	1.06	1.15
2	1.06	1.15
3	1.08	1.15
4	1.06	1.15
5	1.01	1.15
6	1.08	1.15
7	1.08	1.15
8	1.08	1.15

with a period elongation capable of protecting the superstructure. Larger displacements would require larger clearance around the structure and would increase the detailing requirements of flexible utility connections which would increase the design cost.

5 Conclusions

This paper discusses the structural seismic performance of NBCC Part 9 single-family residential structures in Canada and the economic loss potential therein. It was noted that while residential structures have performed favourably in past earthquakes from a life safety standpoint, the economic losses incurred could be substantial and financially debilitating for the owners. Seismic isolation was proposed as a means of improving performance and mitigating losses. To facilitate widespread adoption and overcome the current economic barriers, it was proposed that a program could be developed to design and analyze seismically isolated Part 9 structures based on a catalogue of pre-certified isolators.

The program method presented in this paper was used to design and analyze an isolation system for a theoretical two storey Part 9 structure using fibre-reinforced elastomeric isolators. The design conformed to the existing Part 9 gravity load design methods and was investigated under both seismic and static gravity load conditions to ensure stability. The dynamic seismic performance of the structure was also investigated to ensure that the superstructure would be sufficiently protected from acceleration and drift related damages. Parameters such as base torsion and local displacements were also considered to ensure the analysis's determined responses were conservative. The seismic performance was favourable and reduced the fixed base structural response to well below the 0.25 g floor acceleration and 0.1% inter-storey drift thresholds when damage is expected to manifest. Additionally, the structure was able to achieve favourable performance and comply with the NBCC and ASCE base isolation design performance provisions without excessive base displacement which has favourable implications regarding total design cost.

Additional validation of the method is required to ensure the expected performance matches the dynamic reality of the isolated structure's response, and to ensure the method achieves adequate structural performance for a wide range of Part 9 structures. Research is also required into the impact of base isolation on building science aspects and other areas such as utilities. However, the results are promising and indicate that base isolation can be included in Part 9 in a simplified manner.

References

1. ASCE (2017) Minimum design loads and associated criteria for buildings and other. Published by American Society of Civil Engineers, Reston
2. Aslani H, Miranda E (2004) Optimization of response simulation for loss estimation using peer's methodology. In: World Conference on Earthquake Engineering. Vancouver: The John A. Blume Earthquake Engineering Center
3. BBC News (2018) History of deadly earthquakes. https://www.bbc.com

4. Bednarek MK (2020) Seismic base isolation for residential structures in Canada. University of Windsor
5. British Columbia (2021) Population estimates—Province of British Columbia. www.gov.bc.ca
6. Canadianvisa (2021) Median household income. https://canadianvisa.org/life-in-canada/facts/household-income
7. Comerio MC (1997) Housing issues after disasters. J Conting Crisis Manag 5(3)
8. CUREE (2001) Woodframe Project Case Studies. Richmond, CUREE
9. Earthquakes Canada (2019) Earthquake Search. www.nrcan.gc.ca
10. Insurance Bureau of Canada (2013) Study of impact and the insurance an economic cost of a major earthquake in British Columbia and Ontario/Quebec. AIR Worldwide, Boston
11. Kasai K, Mita A, Kitamura H (2013) Performance of seismic protection technologies during the 2011 Tohoku-Oki earthquake. Earthquake Spect 29(1)
12. Kelly JM (1999) Analysis of fiber-reinforced elastomeric isolators. JSEE 2(1)
13. Kelly JM (1986) Aseismic base isolation: review and bibliography. Soil Dyn Earthq Eng 5(4):202–216
14. Lamontagne M, Brian F (2016) Perception of earthquake hazard and risk in the province of Quebec and the need to raise earthquake awareness in this intraplate region. Seismol Res Lett 87(6):1426–1432
15. Naeim F, Kelly JM (1999) Design of seismically isolated structures: from theory to practice. Wiley
16. Nagarajaiah S, Xiaohong S (2000) Response of base-isolated USC hospital building in Northridge earthquake. J Struct Eng 126(10)
17. National Research Council of Canada (2015) National building code of Canada 2015. Canada, Ottawa
18. National Resources Canada (n.d) Simplified seismic hazard map for Canada, the provinces and territories. http://www.seismescanada.rncan.gc.ca
19. Natural Resources Canada (2018) National building code of Canada seismic hazard values. https://earthquakescanada.nrcan.gc.ca/hazard-alea/interpolat/calc-en.php
20. Tait MJ, Drysdale RG, Toopchi-Nezhad H, Foster B, Raaf MGP (2011) Seismic isolation of residential wood frame and low-rise masonry buildings. McMaster University, Hamilton
21. Tarabia AM, ltani YR (1998) Seismic response of light-frame wood buildings. J Struct Eng 123(11):1470–1477
22. The Canadian Wood Council (2014) Engineering guide for wood frame construction. The Canadian Wood Council, Ottawa
23. Tierney KJ (1997) Business impacts of the Northridge earthquake. J Contin Crisis Manag 5(2)

Alleviation of the Oscillatory Tractions in the Extended Finite Element Method

Emre Erkmen and Daniel Dias-da-Costa

Abstract The extended finite element method (XFEM) is an efficient tool for simulating crack propagation or to tackle problems involving internal boundaries and interface discontinuities. It is known that the extended finite element method may lead to oscillations in the interface traction field, the severity of which depending on the underlying basis functions, as well as on the orientation of the embedded interface. A practical and variationally consistent strategy that alleviates oscillatory behaviour is presented. The method replaces higher-order bubble residuals with Legendre Polynomial, which creates the penalty effect. A methodology to calculate the penalty factor is proposed. Bilinear quadrilateral elements and Heaviside enrichment are used as the basis for the implementation of the extended finite element formulation. Numerical examples illustrate the efficiency and generality of the proposed approach at both element and structural levels. The developed strategy is shown to be robust for imposing Dirichlet type boundary conditions at the crack interface. The effects of numerical oscillations on the traction behaviour at the interfaces of inclusions is illustrated.

Keywords Extended finite element method · Numerical stability · Penalty method

1 Introduction

The extended finite element method (XFEM) is a practical modelling tool as it provides the ability to introduce phase changes and crack paths, independent of the underlying mesh, by embedding discontinuous functions on top of the standard

E. Erkmen (✉)

Department of Building, Civil and Environmental Engineering, Concordia University, Montreal, QC, Canada
e-mail: emre.erkmen@concordia.ca

D. Dias-da-Costa
School of Civil Engineering, University of Sydney, Sydney, NSW, Australia

polynomial-based interpolation field (e.g. [8, 23]). The idea of embedding locally suitable functions can be traced backed to Generalized Finite Element Methods (e.g. [5]). In simulating cases of material failure, modelling with XFEM can also be superior to standard FEM in avoiding numerical pathologies such as mesh dependent behaviour due to material softening (e.g. [20, 22, 33]). By virtue of the fact that the underlying regular mesh of the matrix can be kept unaltered, the XFEM is particularly efficient in introducing inclusions into the surrounding matrix and therefore has been used along with computational homogenization procedures (e.g. [9, 12, 15, 26–28, 32].

When modelling composites with inclusions, however, the interface stiffness properties may have to be significantly large to be able to impose full bond between inclusions and matrix. The XFEM has been reported to have some shortcomings with stiff interfaces, especially when used with low order elements as finite element basis. The numerical issues may manifest themselves in the form of spurious oscillations in the traction profile and influenced by the integration scheme (e.g. [2, 10, 11, 30]). The degrading effect of stiff interface conditions on the convergence characteristics has also been reported (e.g. [6, 16, 17, 21, 29]). Lagrange multiplier-based mixed variational formulations have been proposed to alleviate the numerical issues with XFEM (e.g. [25, 34]). Other strategies include bubble-stabilization method (e.g. [24]), preconditioning of the stiffness matrix (e.g. [19]), and quasi-orthogonalization of the enrichment functions (e.g. [1]). Improvement strategies based on the idea of defining alternative locations for the enrichment degrees of freedom, were also proposed (e.g. [3, 4, 18, 31]).

In the following, the stabilization scheme developed in Erkmen and Dias-da-Costa [11], which is based on a variationally consistent assumed strain-based strategy, is adopted to alleviate the oscillatory behaviour of the traction field. The paper is organized as follows: The partition of unity-based enrichment of the finite element method with discontinuity functions is shortly reviewed in Sect. 2. In Sect. 3, the mechanism for the oscillatory behaviour of the tractions is explained. Section 4 introduces the proposed stabilization strategy and a novel methodology to calculate the penalty factor. In Sect. 5, case studies are introduced to illustrate the performance of the proposed formulation. The conclusions are summarized in Sect. 6.

2 XFEM—Partition of Unity-Based Enrichment of the Fem

2.1 Kinematic Basics

According to Babuska and Melenk [5] and Belytschko and Black [7], a discontinuity is incorporated in the displacement field to capture crack opening as follows:

$$\mathbf{u} = \mathbf{Nd} + \mathscr{H}_\Gamma \mathbf{N}\beta, \tag{1}$$

where $\mathbf{u}$ is the displacement field, $\mathbf{N}$ is the array of standard finite element shape functions, $\mathbf{d}$ is the vector of displacements at finite element nodes, $\mathscr{H}_\Gamma$ is the generalized shifted Heaviside function that jumps from $-1/2$ to $1/2$ at the discontinuity Γ [14], and $\boldsymbol{\beta}$ is the vector of enriched degrees of freedom. The jump across the discontinuity interface Γ is given by:

$$[[\mathbf{u}]] = \mathbf{N}|_\Gamma\boldsymbol{\beta}. \tag{2}$$

In general, in the vicinity of a crack, the strain field $\boldsymbol{\varepsilon}$ can be expressed in term of displacements as:

$$\boldsymbol{\varepsilon} = \mathbf{B}\mathbf{d} + \mathscr{H}_\Gamma\mathbf{B}\beta + \delta|_\Gamma\mathbf{N}\beta, \tag{3}$$

where $\mathbf{B}$ is a matrix containing the derivatives of the shape functions with respect to the coordinate vector $\mathbf{x}$, i.e. $\nabla_x\mathbf{N} \to \mathbf{B}$, and $\delta|_\Gamma$ is the Dirac's delta function centred at the discontinuity.

2.2 Weak Form of Equilibrium Equations

The virtual work in terms of the unknown displacement parameters can be explicitly written as:

$$\begin{aligned}
\delta\Pi(\mathbf{d}, \boldsymbol{\beta}) = {} & \delta\mathbf{d}^T\left(\int_\Omega \mathbf{B}^T\mathbf{D}\mathbf{B}\mathrm{d}\Omega\right)\mathbf{d} + \delta\mathbf{d}^T\left(\int_\Omega \mathbf{B}^T\mathbf{D}\mathscr{H}_\Gamma\mathbf{B}\mathrm{d}\Omega\right)\boldsymbol{\beta} \\
& - \delta\mathbf{d}^T\left(\int_\Omega \mathbf{N}^T\mathrm{d}\Omega\right) + \delta\boldsymbol{\beta}^T\left(\int_\Omega \mathbf{B}^T\mathscr{H}_\Gamma\mathbf{D}\mathbf{B}\mathrm{d}\Omega\right)\mathbf{d} \\
& + \delta\boldsymbol{\beta}^T\left(\int_\Omega \mathbf{B}^T\mathscr{H}_\Gamma\mathbf{D}\mathscr{H}_\Gamma\mathbf{B}\mathrm{d}\Omega\right)\boldsymbol{\beta} + \delta\boldsymbol{\beta}^T\left(\int_\Gamma \mathbf{N}^T|_\Gamma\mathbf{t}\mathrm{d}\Gamma\right)
\end{aligned} \tag{4}$$

in which Ω refers to the analysed domain of the body, $\mathbf{q}$ is the external body load, and $\mathbf{t}$ is the traction at the interface. To derive Eq. (4), the stress field of the bulk is based on the elastic assumption that $\boldsymbol{\sigma} = \mathbf{D}\mathbf{B}\mathbf{d} + \mathbf{D}H_\Gamma\mathbf{B}\beta$, where $\mathbf{D}$ is elastic constitutive matrix. The resulting equilibrium equations can be written for a single finite element in the algebraic form of:

$$\begin{bmatrix} \mathbf{K_{FF}} & \mathbf{K_{FC}} \\ \mathbf{K_{FC}^T} & \mathbf{K_{CC}} \end{bmatrix}\begin{Bmatrix} \mathbf{d} \\ \boldsymbol{\beta} \end{Bmatrix} = \begin{Bmatrix} \mathbf{F}^{\mathrm{ext}} \\ \mathbf{0} \end{Bmatrix} \tag{5}$$

where $\mathbf{K_{FF}} = \int_{\Omega} \mathbf{B^T D B} d\Omega$, $\mathbf{K_{FC}} = \int_{\Omega} \mathbf{B^T} \mathscr{H}_{\Gamma} \mathbf{D B} d\Omega$ and $\mathbf{K_{CC}} = \int_{\Omega} \mathbf{B^T} \mathscr{H}_{\Gamma} \mathbf{D H}_{\Gamma} \mathbf{B} d\Omega + \int_{\Gamma} \mathbf{N^T}\big|_{\Gamma} \mathbf{T N}|_{\Gamma} d\Gamma$ in which the traction separation law relates the stress at the interface with opening as $\mathbf{t} = \mathbf{T N}|_{\Gamma}\boldsymbol{\beta}$, where $\mathbf{T}$ is the matrix of interface stiffness. In Eq. (5), the internal and external forces can be written as $\mathbf{F^{\mathrm{ext}}} = \int_{\Omega} \mathbf{N^T q} d\Omega$.

3 Mechanism for Numerical Instability

3.1 *Ill-Conditioning*

Ill-conditioning occurs when the interface stiffness at the discontinuity is large relative to the bulk. To illustrate this in the following, the degrees of freedom related to interface opening in Eq. (5), i.e. $\boldsymbol{\beta}$, are first condensed out:

$$\left[\mathbf{K_{FF}} - \mathbf{K_{FC}}\mathbf{K_{CC}^{-1}}\mathbf{K_{FC}^{T}}\right]\mathbf{d} = \mathbf{F^{\mathrm{ext}}} \tag{6}$$

For very stiff interfaces relative to the bulk, the nodal displacements should approach $\mathbf{d} = \mathbf{F^{\mathrm{ext}}}\mathbf{K_{FF}^{-1}}$. Eq. (5) can produce the correct result only if $\mathbf{K_{CC}^{-1}}$ becomes negligible in Eq. (6). Matrix $\mathbf{K_{CC}}$ is composed of two components, i.e. $\mathbf{K_{CC}} = \mathbf{K_{CC1}} + \mathbf{K_{CC2}}$, in which $\mathbf{K_{CC1}} = \int_{\Omega} \mathbf{B^T} \mathscr{H}_{\Gamma} \mathbf{D} \mathscr{H}_{\Gamma} \mathbf{B} d\Omega$ and $\mathbf{K_{CC2}} = \int_{\Gamma} \mathbf{N^T}\big|_{\Gamma} \mathbf{T N}|_{\Gamma} d\Gamma$. Therefore, when the components $\mathbf{K_{CC2}}$ are very large due to the stiff interface, $\mathbf{K_{CC}}$ becomes ill-conditioned since $\|\mathbf{K_{CC2}}\| \gg \|\mathbf{K_{CC1}}\|$. As illustrated in Erkmen and Dias-da-Costa [11] in the case of stiff interface, the inverse of $\mathbf{K_{CC}}$ will be unstable and contaminate the solution step while solving for $\mathbf{d}$ in Eq. (6).

4 Alleviation of Numerical Stability Issues

4.1 *Modified Variational Form for the Stabilized XFEM Formulations*

To alleviate the ill-conditioning mechanism, the methodology developed in [11] is adopted herein. Accordingly, the strain in Eq. (3) is modified as $\boldsymbol{\varepsilon} = \mathbf{B d} + \mathscr{H}|_{\Gamma} \mathbf{B}\beta + \delta|_{\Gamma}\hat{\mathbf{N}}\hat{\boldsymbol{\beta}}$, in which only the singular term is changed. The change in the strain requires the functional in Eq. (4) also to be modified accordingly as:

$$\delta\overline{\Pi}\left(\mathbf{d}, \boldsymbol{\beta}, \hat{\boldsymbol{\beta}}, \bar{\mathbf{t}}\right) = \delta\mathbf{d}^{\mathrm{T}}\left(\int_{\Omega} \mathbf{B}^{\mathrm{T}}\mathbf{D}\mathbf{B}\mathrm{d}\Omega\right)\mathbf{d} + \delta\mathbf{d}^{\mathrm{T}}\left(\int_{\Omega} \mathbf{B}^{\mathrm{T}}\mathbf{D}\mathscr{H}_{\bar{\Gamma}}\mathbf{B}\mathrm{d}\Omega\right)\boldsymbol{\beta} - \delta\mathbf{d}^{\mathrm{T}}\left(\int_{\Omega} \mathbf{N}^{\mathrm{T}}\mathbf{q}\mathrm{d}\Omega\right)$$

$$+ \delta\boldsymbol{\beta}^{\mathrm{T}}\left(\int_{\Omega} \mathbf{B}^{\mathrm{T}}\mathscr{H}_{\bar{\Gamma}}\mathbf{D}\mathbf{B}\mathrm{d}\Omega\right)\mathbf{d} + \delta\boldsymbol{\beta}^{\mathrm{T}}\left(\int_{\Omega} \mathbf{B}^{\mathrm{T}}\mathscr{H}_{\bar{\Gamma}}\mathbf{D}\mathscr{H}_{\bar{\Gamma}}\mathbf{B}\mathrm{d}\Omega\right)\boldsymbol{\beta}$$

$$+ \delta\boldsymbol{\beta}^{\mathrm{T}}\left(\int_{\Gamma} \mathbf{N}^{\mathrm{T}}\Big|_{\Gamma}\bar{\mathbf{t}}\mathrm{d}\Gamma\right) + \delta\hat{\boldsymbol{\beta}}^{\mathrm{T}}\left(\int_{\Gamma} \hat{\mathbf{N}}^{\mathrm{T}}\Big|_{\Gamma}\mathbf{t}\mathrm{d}\Gamma\right)$$

$$- \delta\hat{\boldsymbol{\beta}}^{\mathrm{T}}\left(\int_{\Gamma} \hat{\mathbf{N}}^{\mathrm{T}}\Big|_{\Gamma}\bar{\mathbf{t}}\mathrm{d}\Gamma\right) + \left(\int_{\Gamma} \delta\bar{\mathbf{t}}^{\mathrm{T}}\Big|_{\Gamma}\left(\mathbf{N}|_{\Gamma}\boldsymbol{\beta} - \hat{\mathbf{N}}\Big|_{\Gamma}\hat{\boldsymbol{\beta}}\right)\mathrm{d}\Gamma\right) = 0 \qquad (7)$$

in which the Lagrange multiplier can be approximated as $\bar{\mathbf{t}} = \mathbf{L}|_{\Gamma}\boldsymbol{\alpha}$. Upon substitution of the selected interpolation fields, the functional in Eq. (7) takes the following variational form:

$$\delta\overline{\Pi}(\mathbf{d},\boldsymbol{\beta}) = \delta\mathbf{d}^{\mathrm{T}}\left(\int_{\Omega^h} \mathbf{B}^{\mathrm{T}}\mathbf{D}\mathbf{B}\mathrm{d}\Omega\right)\mathbf{d} + \delta\mathbf{d}^{\mathrm{T}}\left(\int_{\Omega^h} \mathbf{B}^{\mathrm{T}}\mathbf{D}\mathbf{B}\mathscr{H}_{\Gamma_I}\mathrm{d}\Omega\right)\boldsymbol{\beta}$$

$$- \delta\mathbf{d}^{\mathrm{T}}\left(\int_{\Omega^h} \mathbf{N}^{\mathrm{T}}\mathbf{q}\mathrm{d}\Omega\right) + \delta\boldsymbol{\beta}^{\mathrm{T}}\left(\int_{\Omega^h} \mathscr{H}_{\Gamma_I}\mathbf{B}^{\mathrm{T}}\mathbf{D}\mathbf{B}\mathrm{d}\Omega\right)\mathbf{d}$$

$$+ \delta\boldsymbol{\beta}^{\mathrm{T}}\left(\int_{\Omega^h} \mathscr{H}_{\Gamma_I}\mathbf{B}^{\mathrm{T}}\mathbf{D}\mathbf{B}\mathscr{H}_{\Gamma_I}\mathrm{d}\Omega\right)\boldsymbol{\beta} + \delta\boldsymbol{\beta}^{\mathrm{T}}\left(\int_{\Gamma_I^h} \hat{\mathbf{N}}^{\mathrm{T}}\Big|_{\Gamma_I}\mathbf{T}\hat{\mathbf{N}}_{\Gamma_I}\mathrm{d}\Gamma\right)\boldsymbol{\beta} \qquad (8)$$

By virtue of the above functional form, we are free to select the assumed function $\hat{\mathbf{N}}\Big|_{\Gamma_I}$ as $\hat{\mathbf{N}}\Big|_{\Gamma_I} = \overline{\mathbf{N}}\Big|_{\Gamma_I} + \chi\hat{\boldsymbol{\Theta}}$, where χ is a scalar (penalty) factor, and $\hat{\boldsymbol{\Theta}}$ is a $\mathbf{T}$ quasi-orthogonal matrix function to $\overline{\mathbf{N}}\Big|_{\Gamma_I}$ according to the inner-product defined as $|\langle\mathbf{u}, \mathbf{v}\rangle| = \int_{\Gamma_I} \mathbf{u}^{\mathrm{T}}\mathbf{T}\mathbf{v}\mathrm{d}\Gamma$, i.e. $\int_{\Gamma_I^h} \overline{\mathbf{N}}^{\mathrm{T}}\Big|_{\Gamma_I}\mathbf{T}\hat{\boldsymbol{\Theta}}\mathrm{d}\Gamma = 0$.

4.2 Selection of the Assumed Jump Discontinuity Field and Stabilized XFEM Formulations

A case that satisfies the orthogonality condition was identified in Erkmen and Dias-da-Costa [11], as follows: $\hat{N}\Big|_{\Gamma_I} = \overline{\mathbf{N}}_c|_{\Gamma_I} + \chi\hat{\Theta}$, where the components of matrix $\hat{\Theta}$ are Legendre polynomials, i.e.

$$\widehat{\Theta} = \begin{bmatrix} -\widehat{\Theta}_1 - \widehat{\Theta}_2 & 0 & \widehat{\Theta}_2 - \widehat{\Theta}_3 & 0 & \widehat{\Theta}_3 + \widehat{\Theta}_4 & 0 & -\widehat{\Theta}_4 + \widehat{\Theta}_1 & 0 \\ 0 & -\widehat{\Theta}_1 - \widehat{\Theta}_2 & 0 & \widehat{\Theta}_2 - \widehat{\Theta}_3 & 0 & \widehat{\Theta}_3 + \widehat{\Theta}_4 & 0 & -\widehat{\Theta}_4 + \widehat{\Theta}_1 \end{bmatrix} \quad (9)$$

in which

$$\widehat{\Theta}_1 = \sqrt{\frac{5}{2}}\left(\frac{3}{2}s^2 - \frac{1}{2}\right) \quad (10)$$

$$\widehat{\Theta}_2 = \sqrt{\frac{7}{2}}\left(\frac{5}{2}s^3 - \frac{3}{2}s\right) \quad (11)$$

$$\widehat{\Theta}_3 = \sqrt{\frac{9}{2}}\left(\frac{35}{8}s^4 - \frac{15}{4}s^2 + \frac{3}{8}\right) \quad (12)$$

$$\widehat{\Theta}_4 = \sqrt{\frac{11}{2}}\left(\frac{63}{8}s^5 - \frac{35}{4}s^3 + \frac{15}{8}s\right) \quad (13)$$

in which $-1 \leq s \leq 1$ refers to the normalized coordinate along the discontinuity interface and

$$\overline{\mathbf{N}}_c\big|_{\Gamma_f^e} = \begin{bmatrix} \overline{N}_{\Gamma 1} & 0 & \overline{N}_{\Gamma 2} & 0 & \overline{N}_{\Gamma 3} & 0 & \overline{N}_{\Gamma 4} & 0 \\ 0 & \overline{N}_{\Gamma 1} & 0 & \overline{N}_{\Gamma 2} & 0 & \overline{N}_{\Gamma 3} & 0 & \overline{N}_{\Gamma 4} \end{bmatrix} \quad (14)$$

where

$$\overline{N}_{\Gamma 1} = \frac{1}{8}(1 - \varsigma_a)(1 - \zeta_a) + \frac{1}{8}(1 - \varsigma_b)(1 - \zeta_b)$$
$$- \frac{1}{24}(\varsigma_a - \varsigma_b)(\zeta_a - \zeta_b) \quad (15)$$

$$\overline{N}_{\Gamma 2} = \frac{1}{8}(1 + \varsigma_a)(1 - \zeta_a) + \frac{1}{8}(1 + \varsigma_b)(1 - \zeta_b)$$
$$+ \frac{1}{24}(\varsigma_a - \varsigma_b)(\zeta_a - \zeta_b) \quad (16)$$

$$\overline{N}_{\Gamma 3} = \frac{1}{8}(1 + \varsigma_a)(1 + \zeta_a) + \frac{1}{8}(1 + \varsigma_b)(1 + \zeta_b)$$
$$- \frac{1}{24}(\varsigma_a - \varsigma_b)(\zeta_a - \zeta_b) \quad (17)$$

$$\overline{N}_{\Gamma 4} = \frac{1}{8}(1 - \varsigma_a)(1 + \zeta_a) + \frac{1}{8}(1 - \varsigma_b)(1 + \zeta_b)$$
$$+ \frac{1}{24}(\varsigma_a - \varsigma_b)(\zeta_a - \zeta_b) \quad (18)$$

in which $-1 \leq \varsigma \leq 1$ and $-1 \leq \zeta \leq 1$ are the auxiliary coordinates of the parent isoparametric bilinear Quadrilateral element. The coordinates at the two element edges within the parent element are shown with (ς_a, ζ_a) and (ς_b, ζ_b). This formulation is referred to as S-XFEM3 in Erkmen and Dias-da-Costa [11] and we call it S-XFEM herein. Accordingly, the equilibrium equations in Eq. (6) becomes:

$$\begin{bmatrix} \mathbf{K}_{FF} & \mathbf{K}_{FC} \\ \mathbf{K}_{FC}^{T} & \overline{\mathbf{K}}_{CC} \end{bmatrix} \begin{Bmatrix} \mathbf{d} \\ \beta \end{Bmatrix} = \begin{Bmatrix} \mathbf{F}^{ext} \\ 0 \end{Bmatrix} \tag{19}$$

in which, the difference between Eqs. (5) and (19) is due to the modification in $\overline{\mathbf{K}}_{CC} = \mathbf{K}_{CC1} + \overline{\mathbf{K}}_{CC2}$. In Eq (19), the matrix $\mathbf{K}_{CC1}$ is the same as before however, $\overline{\mathbf{K}}_{CC2}$ can now be written as:

$$\overline{\mathbf{K}}_{CC2} = \int_{\Gamma_I^h} \overline{\mathbf{N}}^{T}\Big|_{\Gamma_I} \mathbf{T}\overline{\mathbf{N}}\Big|_{\Gamma_I} d\Gamma + \chi^2 \mathbf{I}_d \tag{20}$$

in which $\mathbf{I}_d$ is assemblage of element matrices $\mathbf{I}_d^e = \int_{\Gamma_I^e} \widehat{\mathbf{\Theta}}^{T} \mathbf{T}\widehat{\mathbf{\Theta}} d\Gamma$.

4.3 Penalty Factor Calculation

As discussed in Sect. 3, to stabilize the behaviour of the XFEM, we aim to improve the condition number of $\mathbf{K}_{CC2}$, which is the positive scalar $|\kappa| = \|\mathbf{K}_{CC2}\|\|\mathbf{K}_{CC2}^{-1}\|$, relative to condition number $\mathbf{K}_{CC1}$, which is the positive scalar $|\iota| = \|\mathbf{K}_{CC1}\|\|\mathbf{K}_{CC1}^{-1}\|$. The matrix norms are herein selected based on the spectral norm. Thus, the condition numbers of matrices are calculated using $|\lambda_{max}|/|\lambda_{min}|$, where λ_{max} and λ_{min} are the maximum and minimum eigenvalues of the matrix, respectively. It can be verified that the orthogonality properties of Legendre polynomials lead to matrices that are generally more narrowly banded. Therefore, addition of $\mathbf{I}_d$ generally better conditions the matrix in Eq. (16), however, a rule of thumb for the penalty factor was not provided in Erkmen and Dias-da-Costa [11].

Here we assume $\mathbf{I}_d = k\mathbf{I}$, where k is the interface stiffness factor and we take it as the norm of $\mathbf{I}_d$. In the case of $\mathbf{I}$ being an identity the shift in the eigenvalue λ of matrix $\mathbf{K}_{CC2}$ due to addition of a diagonal matrix $\chi^2 k\mathbf{I}$ is $\overline{\lambda}_i = \lambda_i + \chi^2 k\mathbf{v}_i^T\mathbf{v}_i$ where $\mathbf{v}_i$ is the ith eigenvector of $\mathbf{K}_{CC2}$ and $\overline{\lambda}_i$ is the ith eigenvalue of $\overline{\mathbf{K}}_{CC2} = \mathbf{K}_{CC2} + \chi^2 k\mathbf{I}$. Therefore, the condition of the matrix $\mathbf{K}_{CC2}$ is improved as $\max(\overline{\lambda}_i)/\min(\overline{\lambda}_i) = \max(\lambda_i + \chi^2 k\mathbf{v}_i^T\mathbf{v}_i)/\min(\lambda_i + \chi^2 k\mathbf{v}_i^T\mathbf{v}_i) \leq \max(\lambda_i)/\min(\lambda_i)$. Although, $\mathbf{I}_d$ is generally not a diagonal matrix as it is dependent on the orientation of the interface discontinuity, it is very narrowly banded. Penalty conditions are generally introduced with a purpose to improve the stability and often without and exact prediction for the penalty factor χ^2 to insert into our stabilization scheme, we treat $\mathbf{I}_d$ as an identity matrix for the rest of the calculations, acknowledging that the penalty χ^2 will not be

exact but will provide an approximate range. The performance of the predicted χ^2 will then be tested in the upcoming section of case studies.

For that purpose, we first express the nodal enrichment vector in terms of the eigenvectors as

$$\boldsymbol{\beta} = \sum_i^N \alpha_i \mathbf{v}_i \tag{21}$$

in which α_i is the contribution of each of the N modes. As a result, the twice strain energy of the crack interface can be calculated as $\boldsymbol{\beta}^{\mathrm{T}} \mathbf{K}_{CC2} \boldsymbol{\beta} = \sum_i^N \lambda_i \alpha_i^2 \mathbf{v}_i^{\mathrm{T}} \mathbf{v}_i$. After the addition of the $\chi^2 k \mathbf{I}$ term, twice strain energy becomes

$$\overline{\boldsymbol{\beta}}^{\mathrm{T}} \overline{\mathbf{K}}_{CC2} \overline{\boldsymbol{\beta}} = \sum_i^N \left(\lambda_i + \chi^2 k \mathbf{v}_i^{\mathrm{T}} \mathbf{v}_i\right) \overline{\alpha}_i^2 \mathbf{v}_i^{\mathrm{T}} \mathbf{v}_i \tag{22}$$

in which the change in the solution after the condition improvement is considered. Thus, the nodal enrichment vector is

$$\overline{\boldsymbol{\beta}} = \sum_i^N \overline{\alpha}_i \mathbf{v}_i \tag{23}$$

in which $\overline{\alpha}_i$ is the contribution of each mode in the stabilized solution. Note that the eigenvectors remain the same as in Eq. (21), in which however, the oscillatory behaviour can be attributed to the contributions of the higher modes and thus large values of α_i when $i > N_c$. We refer to N_c as a threshold number.

On the otherhand, after condition improvement as the oscillatory behaviour is alleviated, we expect that $\overline{\alpha}_i \ll \alpha_i$ when $i > N_c$. For example, if one aims a behaviour such that the modes higher than N_c are negligible after stabilization we can aim a solution as

$$\overline{\boldsymbol{\beta}} \approx \sum_i^{N_c} \overline{\alpha}_i \mathbf{v}_i \tag{24}$$

When the formulation is stabilized the contribution of the higher to the strain energy will also diminish. Accordingly, the twice strain energy can be written as

$$\overline{\boldsymbol{\beta}}^{\mathrm{T}} \overline{\mathbf{K}}_{CC2} \overline{\boldsymbol{\beta}} = \sum_i^{N_c} \left(\lambda_i + \chi^2 k \mathbf{v}_i^{\mathrm{T}} \mathbf{v}_i\right) \overline{\alpha}_i^2 \mathbf{v}_i^{\mathrm{T}} \mathbf{v}_i \tag{25}$$

By equating the strain energies before and after stabilization, we obtain

$$\sum_{i=1}^{N_c} \left(\lambda_i + \chi^2 k \mathbf{v}_i^{\mathrm{T}} \mathbf{v}_i \right) \overline{\alpha}_i^2 \mathbf{v}_i^{\mathrm{T}} \mathbf{v}_i = \sum_{i=1}^{N} \lambda_i \alpha_i^2 \mathbf{v}_i^{\mathrm{T}} \mathbf{v}_i \tag{26}$$

from which, the stabilization factor can be extracted as

$$\chi^2 = \left(\sum_{i=1}^{N} \lambda_i \alpha_i^2 - \sum_{i=1}^{N_c} \lambda_i \overline{\alpha}_i^2 \right) \mathbf{v}_i^{\mathrm{T}} \mathbf{v}_i \Big/ \left(\sum_{i=1}^{N_c} k \left(\overline{\alpha}_i \mathbf{v}_i^{\mathrm{T}} \mathbf{v}_i \right)^2 \right) \tag{27}$$

To simplify the equation we can assume that $\alpha_i \approx \overline{\alpha}_i$ for the first N_c modes, i.e. for when $i \leq N_c$. Accordingly, one obtains

$$\chi = \sqrt{\sum_{i=N_c+1}^{N} \lambda_i \alpha_i^2 \mathbf{v}_i^{\mathrm{T}} \mathbf{v}_i \Big/ \sum_{i=1}^{N_c} k \left(\alpha_i \mathbf{v}_i^{\mathrm{T}} \mathbf{v}_i \right)^2} \tag{28}$$

Here we assumed that the difference in the two solutions is only due to contribution factors of the higher modes, i.e. $\alpha_i \gg \overline{\alpha}_i$ when $i > N_c$. Aiming for the same strain energy equivalence is an assumption unjustified at this point. However, as we are aiming for a range for the penalty factor rather than an exact number and based on our observations that the energy calculations based on the nodal values stay around the same order before and after stabilization, we use Eq. (28) in the following case studies.

5　Case Studies

5.1　Inclusion in Composite Materials—Representative Volume Element Analysis

In this section, we assess the performance of the proposed methodology by computing the homogenized effective elastic properties of a composite material with inclusions (Fig. 1a). We also illustrate the effect of the penalty factor in alleviating the oscillatory tractions. WE have analysed two cases shown in Fig. 1b, c. By imposing the displacements of all points at the boundary according to the given total macrostrain, the Representative Volume Element (RVE) is analysed under the assumption of uniform displacement gradient. This type of boundary condition is considered for both cases analysed herein.

Under the assumption of isotropy, the two selected cases of straining below, are sufficient to determine the homogenized Young's and Shear Moduli, referred to as $\widehat{E}$ and $\widehat{G}$, respectively, i.e. The Young's modulus and Poisson ratio of the bulk matrix are taken as $E_m = 3 \times 10^3$ N/mm^2 and $\nu_m = 0.35$, respectively. For the inclusions the Young's modulus and Poisson ratio are taken as $E_i = 70 \times 10^3$ N/mm^2 and
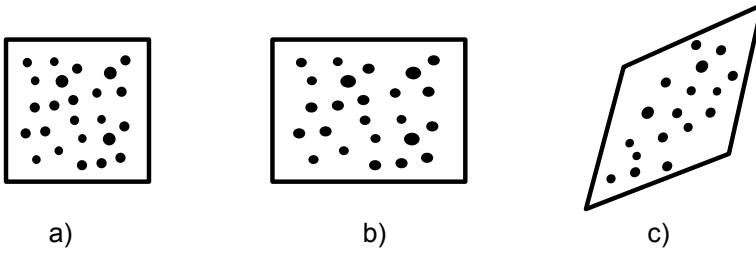
Fig. 1 **a** RVE with inclusions **b** Case 1−RVE under $\varepsilon_x = 1$ **c** Case 2−RVE under $\gamma = 1$

$v_i = 0.2$, respectively. Interface stiffness coefficients are high to impose perfect bond assumption. To illustrate the effect of interface stiffness relatively high and very high numbers are used for the coefficients, i.e. $k_t = k_n = 10^{20}$ N/mm³ and $k_t = k_n = 10^{10}$ N/mm³.

$$
\begin{bmatrix} \hat{\sigma}_{11}^1 & \hat{\sigma}_{11}^2 \\ \hat{\sigma}_{22}^1 & \hat{\sigma}_{22}^2 \\ \hat{\sigma}_{12}^1 & \hat{\sigma}_{12}^2 \end{bmatrix} = \begin{bmatrix} \hat{E} & \hat{e}_{1122} & \hat{e}_{1112} \\ \hat{e}_{1122} & \hat{e}_{2222} & \hat{e}_{2212} \\ \hat{e}_{1112} & \hat{e}_{2212} & \hat{G} \end{bmatrix} \begin{bmatrix} \text{case 1} & \text{case 2} \\ \varepsilon_x = 1 & 0 \\ 0 & 0 \\ 0 & \gamma = 1 \end{bmatrix} \tag{29}
$$

RVE size is considered as 100×100 mm². Two different distributions with a significantly different number of inclusions and with the same volume ratio $V_i = 0.196$ are analysed as shown in Fig. 2. In both cases, 30×30 and 50×50 element meshes and the 4×4 Gauss–Legendre quadrature rule are adopted for the bulk. Along the cracks 10 integration points are used.

Table 1 shows the calculated penalty factors according to Eq. (28). Two different values for the penalty factor χ was calculated for each Mesh shown in Fig. 2. In each case, the threshold value for the cut-off mode number $Nc1$ and $Nc2$ was taken as 3/4 and 15/16 of the total number degrees of freedom of the enrichment N, respectively. We have also fixed $\chi_3 = 0.1$ for a third case.

5.1.1 Analysis with Single Inclusion within the RVE

In the Tables 2 and 3, XFEM-based effective modulus predictions are compared with those based on S-XFEM with alternative penalty factors. Only, one inclusion is considered and the interface stiffness coefficients used in the analysis are very high, i.e. $k_t = k_n = 10^{20}$ N/mm³. Table 2 results are based on the 30×30 element mesh (Fig. 2a), while Table 3 results are based on the 50×50 element mesh (Fig. 2c). It can be verified that the mesh refinement influences the results only within 1% and thus the 50×50 element mesh is deemed sufficient. Figure 3 shows the distribution of stress σ_{xx} and τ_{xy}, respectively for cases 1 and 2 within the RVE based on 50×50 element mesh.

a) Mesh a1 - 30x30 Elements -1 inclusion

b) Mesh b1 - 30x30 Elements -16 inclusion

c) Mesh a2 - 50x50 Elements -1 inclusion

d) Mesh b2 - 50x50 Elements -16 inclusion
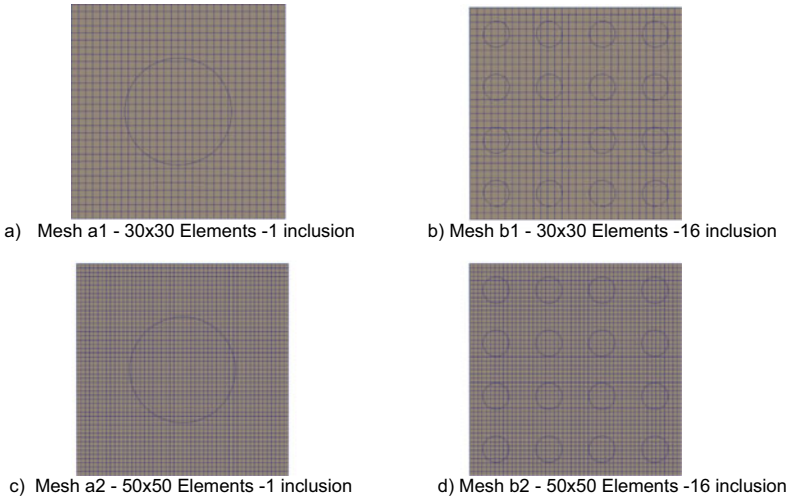
Fig. 2 RVEs used in the analyses

Table 1 Penalty factors for $k_t = k_n = 10^{20}$ N/mm^3

Mesh	N	$Nc1$	χ_1 for $Nc1$ from Eq. (28)	$Nc2$	χ_2 for $Nc2$ from Eq. (28)	χ_3
a1	240	180	0.87	225	0.38	0.1
a2	400	300	0.66	375	0.24	0.1
b1	960	720	0.80	900	0.48	0.1
b2	1536	1152	0.61	1440	0.25	0.1

Table 2 Mesh a1—effective stiffness in GPa—$k_t = k_n = 10^{20}$ N/mm^3

Analysis type	$\widehat{E}$	$\widehat{G}$
XFEM	4.80	1.59
S-XFEM $\chi = 0.1$	4.80	1.59
S-XFEM $\chi = 0.38$	4.80	1.59
S-XFEM $\chi = 0.87$	4.80	1.59

Table 3 Mesh a2—effective stiffness in GPa—$k_t = k_n = 10^{20}$ N/mm^3

Analysis type	$\widehat{E}$	$\widehat{G}$
XFEM	4.75	1.57
S-XFEM $\chi = 0.1$	4.75	1.57
S-XFEM $\chi = 0.38$	4.75	1.57
S-XFEM $\chi = 0.87$	4.75	1.57

367 | 4867 | 9366 | 13866 | 18365 | 22865

a)   Stress field σ_{xx} - Case 1 – Mesh a2

144 | 1638 | 3132 | 14626 | 6120 | 7614

b)   Stress field τ_{xy} - Case 2 – Mesh a2
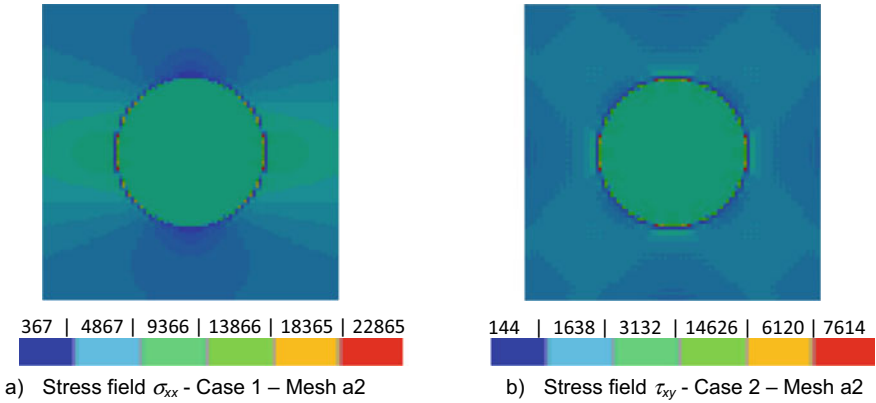
Fig. 3 Stresses for XFEM and S-XFEM for $k_t = k_n = 10^{20}$ N/mm^3

Table 4 Mesh a2—effective stiffness in GPa—$k_t = k_n = 10^{10}$ N/mm^3

Analysis type	$\widehat{E}$	$\widehat{G}$
XFEM	4.75	1.57
S-XFEM $\chi = 0.1$	4.75	1.57
S-XFEM $\chi = 0.24$	4.75	1.57
S-XFEM $\chi = 0.66$	4.75	1.57

The stress distributions shown in Fig. 3 are identical based on both XFEM and S-XFEM formulations.

When the interface stiffness values are dropped to $k_t = k_n = 10^{10}$ N/mm^3, there are no changes in the homogenized effective stiffness parameters up to two decimal points as shown in Table 4 for XFEM and S-XFEM, which implies that using $k_t = k_n = 10^{20}$ N/mm^3 is sufficient to enforce full bond between the inclusion and the matrix.

The interface tractions in normal and tangential directions are shown in Fig. 4. The tractions based on standard XFEM as well as S-XFEM without penalty show excessive oscillations, which are in the range of 10^6 N/mm^2. Therefore, standard XFEM results are not shown in Fig. 4.

It can be verified that the stabilized formulation is capable of eliminating the oscillations in the interface traction field while keeping the average properties practically unaffected. The oscillations in the interface traction field are completely avoided when S-XFEM formulation is used with a penalty factor χ corresponding to $N_c = 3/4$ N.

a) Interface normal traction for mesh a1

b) Interface tangential traction for mesh a1

c) Interface normal traction for mesh a2

d) Interface tangential traction for mesh a2
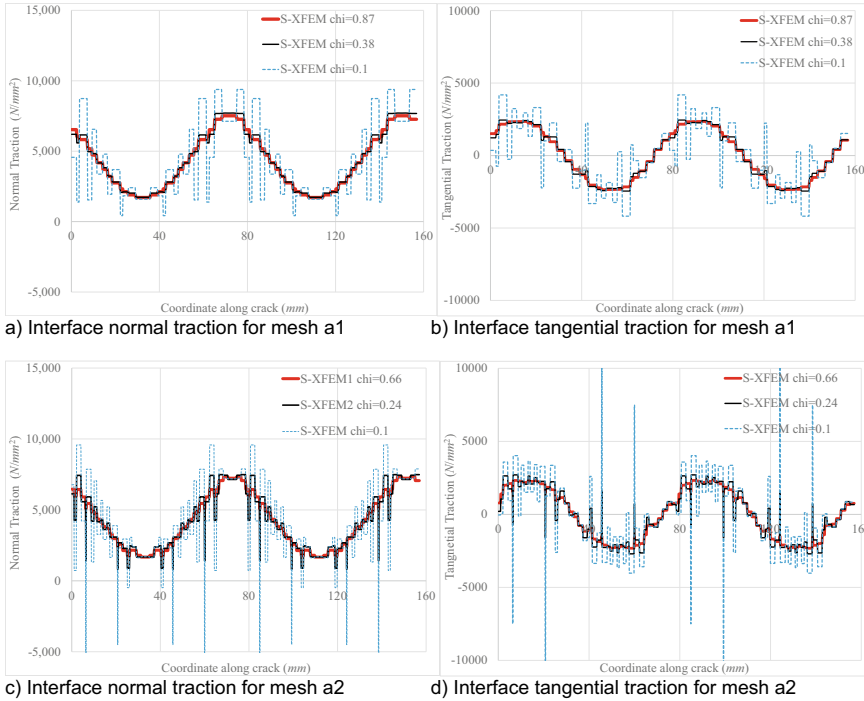
Fig. 4 Interface tractions for S-XFEM formulations for $k_t = k_n = 10^{20}$ N/mm^3

5.1.2 Analysis with 16 Inclusions Within the RVE

Tables 5 and 6 show the results of XFEM, as well as S-XFEM, based RVE analyses for very high interface stiffness. The change in the results between the 30×30 and 50×50 element mesh are within 5% and, therefore, the 50×50 element mesh is deemed sufficient.

Figure 5 shows the distribution of σ_{xx} within the RVE for Case 1, whereas Fig. 6 shows the distribution of τ_{xy} for Case 2.

In the case of the stabilized formulation, as shown in Tables 6 and 7, the effective properties are only slightly affected in comparison to those based on XFEM. On

Table 5 Mesh b1—effective stiffness in GPa—$k_t = k_n = 10^{20}$N/mm^3

Analysis type	$\widehat{E}$	$\widehat{G}$
XFEM	5.31	1.62
S-XFEM $\chi = 0.1$	5.31	1.62
S-XFEM $\chi = 0.48$	5.31	1.62
S-XFEM $\chi = 0.80$	5.31	1.62

Table 6 Mesh b2—effective stiffness in GPa—$k_t = k_n = 10^{20}$N/mm^3

Analysis type	$\widehat{E}$	$\widehat{G}$
XFEM	4.97	1.55
S-XFEM $\chi = 0.1$	4.98	1.55
S-XFEM $\chi = 0.25$	4.98	1.55
S-XFEM $\chi = 0.61$	4.98	1.55

a)   Stress field σ_{xx} - Case 1 – Mesh b2

-217 | 4720 | 9658 | 14592 | 19533 | 24470

N/mm^2

b) Stress field σ_{xx} - Case 2 – Mesh b2

-18 | 1167 | 2352 | 3538 | 4723 | 5908

Fig. 5 Stresses for XFEM and S-XFEM for $k_t = k_n = 10^{20}$ N/mm^3

a) Interface normal traction for mesh b1

b) Interface tangential traction for mesh b1

c) Interface normal traction for mesh b2

d) Interface tangential traction for mesh b2
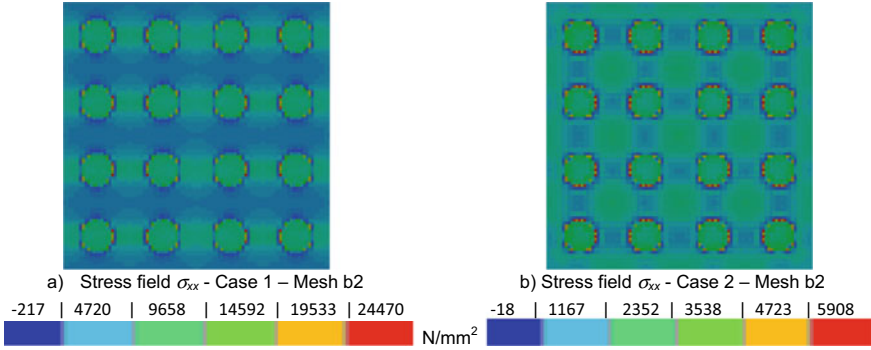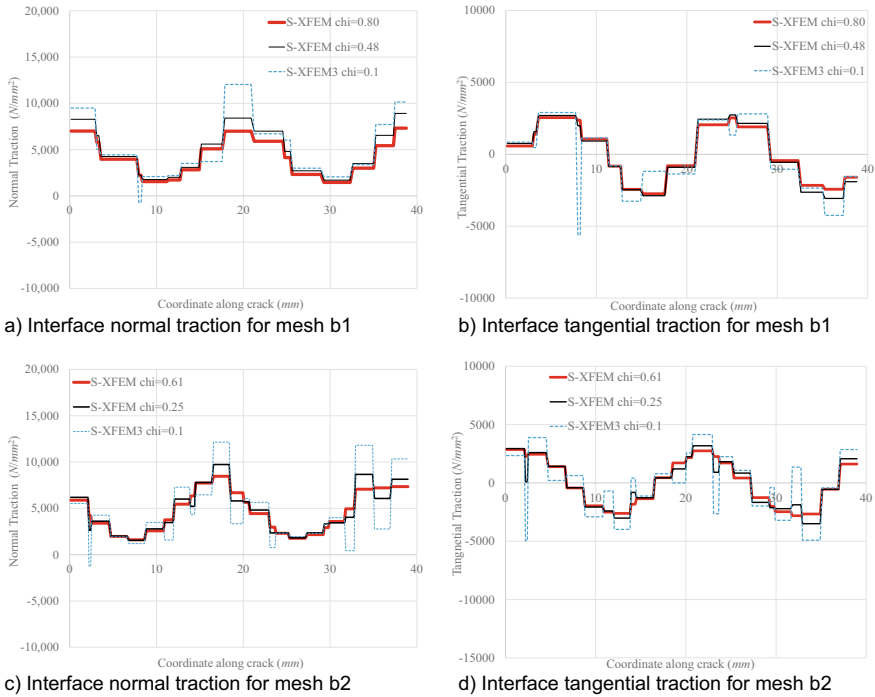
Fig. 6 Interface tractions for S-XFEM formulations for $k_t = k_n = 10^{20}$ N/mm^3

Table 7 Mesh b2—effective stiffness in GPa—$k_t = k_n = 10^{10}$ N/mm^3

Analysis type	$\widehat{E}$	$\widehat{G}$
XFEM	4.97	1.55
S-XFEM $\chi = 0.1$	4.98	1.55
S-XFEM $\chi = 0.25$	4.98	1.55
S-XFEM $\chi = 0.61$	4.98	1.55

the other hand, the effective homogenized elastic properties based on S-XFEM are identical in both Tables 6 and 7.

For Case 1 strain, Fig. 6 shows the interface tractions in both normal and tangential directions around the inclusion at the bottom left corner of the RVE in Fig. 2d. The results are shown for S-XFEM and $k_t = k_n = 10^{20}$ N/mm^3 is used for the interface stiffness. Again, it is important to note that in XFEM as well as S-XFEM without penalty, i.e. $\chi = 0$ the oscillations in the interface traction fields are excessive. Therefore, standard XFEM results are not shown in Fig. 6.

It can be verified from Table 7 that the stabilized formulation eliminates the oscillations in the interface traction field while keeping the average properties are only slightly affected or practically unaffected. Figure 6 shows that the oscillations in the interface traction field are completely avoided when S-XFEM formulation is used with a penalty factor χ corresponding to $Nc = 3/4$ N.

6 Conclusions

The mechanism of the oscillatory behaviour observed in XFEM-based models for stiff embedded interfaces was explained and a variationally consistent stabilisation strategy was proposed. The proposed modification strategy falls into the assumed strain/B-bar method and introduces a penalty effect via a certain arrangement of Legendre polynomials. An approximate method for the penalty factor calculation was proposed. The results confirm the improved performance such that an oscillation-free solution can be achieved We have employed the proposed oscillation-free formulations and compared with XFEM results in computational homogenization procedures to illustrate the effects of oscillations in determining effective properties of heterogeneous materials with inclusion. To simulate perfect bond between inclusions and the matrix, stiff interface assumption was assumed. In our tests, when the interface stiffness was increased to excessively large values, the effective stiffness properties based on the XFEM results were only very slightly influenced. The proposed formulation was shown to avoid the influence of the excessively large interface stiffness on the prediction of the effective stiffness properties, while eliminating oscillatory tractions.

References

1. Agathos K, Bordas SPA, Chatzi E (2019) Improving the conditioning of XFEM/GFEM for fracture mechanics problems through enrichment quasi-orthogonalization. Comput Methods Appl Mech Eng 346:1051–1073
2. Ahmed A, Sluys LJ (2013) Anomalous behavior of bilinear quadrilateral finite elements for modeling cohesive cracks with XFEM/GFEM. Int J Numer Meth Eng 94:454–472
3. Aragón AM, Liang B, Ahmadian H, Soghrati S (2020) On the stability and interpolating properties of the hierarchical interface-enriched finite element method. Comput Methods Appl Mech Eng 362:112671
4. Aragón AM, Simone A (2017) The discontinuity-enriched finite element method. Int J Numer Meth Eng 112:1589–1613
5. Babuška I, Melenk JM (1997) The partition of unity method. Int J Numer Meth Eng 40:727–758
6. Bechet E, Moes N, Wohlmuth B (2009) A stable Lagrange multiplier space for stiff interface conditions with the extended finite element method. Int J Numer Meth Eng 78:931–954
7. Belytschko T, Black T (1999) Elastic crack growth in finite elements with minimal remeshing. Int J Numer Meth Eng 45:601–620
8. Belytschko T, Moes N, Usui S, Parimi C (2001) Arbitrary discontinuities in finite elements. Int J Numer Meth Eng 50:993–1013
9. Bosco V, Kouznetsova VG, Geers MGD (2015) Multi-scale computational homogenization—localization for propagating discontinuities using X-FEM. Int J Numer Meth Eng 102:496–527
10. Dias-da-Costa D, Alfaiate J, Sluys LJ, Júlio ENBS (2010) A comparative study on the modelling of discontinuous fracture by means of enriched nodal and element techniques and interface elements. Int J Fract 161:97–119
11. Erkmen RE, Dias-da-Costa D (2021) Stabilisation of the extended finite element method for stiff embedded interfaces and inclusions. Int J Numer Meth Eng 122:7378–7408
12. Erkmen RE, Malek S, Ayranci C (2020). An XFEM based computational homogenization framework for thermal conductivity evaluation of composites with imperfectly bonded inclusions. Eng Res Exp 2
13. Fries T-P (2008) A corrected XFEM approximation without problems in bending elements. Int J Numer Meth Eng 75:503–532
14. Fries T-P, Belytschko T (2010) The extended/generalized finite element method: an overview of the method and its applications. Int J Numer Meth Eng 84:253–304
15. Gal E, Suday E, Weisman H (2013) Homogenization of materials having inclusions surrounded by layers modeled by the extended finite element method. Int J Multiscale Comput Eng 11:239–252
16. Giner E, Tur M, Tarancon JE, Fuenmayor FJ (2010) Crack face contact in X-FEM using a segment-to-segment approach. Int J Numer Meth Eng 82:1424–1449
17. Ji H, Dolbow J (2004) On strategies for enforcing interfacial constraints and evaluating jump functions. Int J Numer Meth Eng 61:2508–2535
18. Latifaghili A, Bybordiani M, Erkmen RE, Dias-da-Costa D (2022) An extended finite element method with polygonal enrichment shape functions for crack propagation and stiff interface problems. Int J Numer Meth Eng 123:1432–1455
19. Menk A, Bordas SP (2011) A robust pre-conditioning technique for the extended finite element method. Int J Numer Meth Eng 85:1609–1632
20. Mergheim J, Kuhl E, Steinmann P (2005) A finite element method for computational modelling of cohesive cracks. Int J Numer Meth Eng 63:276–289
21. Moes N, Bechet E, Tourbier M (2006) Imposing Dirichlet boundary conditions in the extended finite element method. Int J Numer Meth Eng 67:1641–1669
22. Moes N, Belytschko T (2002) Extended finite element method for cohesive crack growth. Eng Fract Mech 69:813–833
23. Moes N, Dolbow J, Belytschko T (1999) A finite element method for crack growth without remeshing. Int J Numer Meth Eng 46:131–150

24. Mourad HM, Dolbow J, Harari I (2007) A bubble-stabilized finite element method for Dirichlet constraints on embedded interfaces. Int J Numer Meth Eng 69:772–793
25. Mueller-Hoeppe DS, Wriggers P, Loehnert S (2012) Crack face contact for hexahedral-based XFEM formulation. Comput Mech 49:725–734
26. Nguyen TN, Erkmen RE, Sanchez LFM, Li J (2020) Computational modeling of concrete materials—stiffness degradation of concrete due to ASR: a computational homogenization approach. ACI Mater J 117:65–78
27. Norouizi E, Li B, Erkmen RE, Dias-da-Costa D (2022). Stabilisation of the extended finite element method for stiff embedded interfaces and inclusions. Comp Geotech 144
28. Patil RU, Mishra BK, Singh IV (2010) A new multiscale XFEM for the elastic property evaluation of heterogenous materials. Int J Mech Sci 122:277–287
29. Sadaba S, Romero I, Gonzales C, Llorca J (2015) A stable X-FEM for cohesive transition from closed to open crack. Int J Numer Meth Eng 101:540–570
30. Simone A (2004) Partition of unity-based discontinuous elements for interface phenomena: computational issues. Commun Numer Methods Eng 20:465–478
31. Soghrati S, Aragón AM, Duarte AC, Geubelle PH (2012) An interface-enriched generalized fem for problems with discontinuous gradient fields. Int J Numer Meth Eng 89:991–1008
32. Svenning E, Fagerstrom M, Larsson F (2016) On computational homogenization of micro-scale crack propagation. Int J Numer Meth Eng 108:76–90
33. Wells GN, Sluys LJ (2001) A new method for modelling cohesive cracks using finite elements. Int J Numer Meth Eng 50:2667–2682
34. Zilian A, Fries T-P (2009) A localized mixed-hybrid method for imposing interfacial constraints in the extended finite element method (XFEM). Int J Numer Meth Eng 79:733–752

Finite Element-Based Studies on Shear Connector Failure of Prestressed Concrete Multi-Girder Bridges

Jiadaren Liu, John Alexander, and Y. Li

Abstract Multi-girder prestressed concrete (PC) bridges represent an integral part of the transportation network in Canada and play an important role toward the socioeconomic development. They were conventionally constructed using precast PC girders erected adjacent to each other and typically connected in the field by steel shear connectors. However, deteriorations and failure of shear connectors were widely observed for these bridges during regular inspections and raised concerns on the functionality and safety of the bridge system. To study the effects of shear connector failure, this paper developed an efficient analysis tool using finite element (FE) modeling for multi-girder PC bridges. For the sake of computational efficiency, 1D fiber beam element was adopted to model each girder, and 1D spring element was adopted to model the shear connectors between adjacent girders to transfer vertical loads. To obtain the load-deformation relationship of shear connectors as an input of spring elements, a 3D continuum-based FE model was developed to simulate the behavior of shear connectors during load transfer. In the end, the influence of shear connector failure was studied by using a nine-girder bridge in Alberta under truck load as a case study. The obtained conclusion can serve as potential guidance for the maintenance and rehabilitation of multi-girder PC bridges.

Keywords Finite element · Shear connector deterioration · Prestressed concrete · Multi-girder bridges

J. Liu (✉) · Y. Li
Department of Civil and Environmental Engineering, University of Alberta, Edmonton, AB, Canada
e-mail: jiadaren@ualberta.ca

Y. Li
e-mail: yong9@ualberta.ca

J. Alexander
Alberta Ministry of Transportation, Edmonton, AB, Canada
e-mail: john.alexander@gov.ab.ca

1 Introduction

Multi-girder prestressed concrete (PC) bridges have been extensively used across Canada due to their great stiffness, ease of fabrication, fast construction, and expected high durability. It was reported that PC girder bridges constitute more than 50% of the bridge inventory in North America [4]. Many of these bridges conventionally consist of multiple shear connected girders, where the shear connectors provide load transfer between adjacent girders to form the bridge superstructure. Although this system ensures a monolithic behavior for the bridge by enabling the lateral distribution of dead/live loads, the durability of shear connectors still concerns engineers for load evaluation of bridges. Decades of experience have proven that the filed-cast shear connector is a weak link in the system, which can lead to the substandard performance of the overall bridge system [6, 12].

Several studies have been devoted to investigating the behavior of shear connectors between adjacent PC girders. Yuan et al. [15] experimentally evaluated the performance of shear connectors using ultra-high-performance concrete (UHPC) and transverse posttensioning under simulated traffic and thermal loads. Hanna et al. [5] proposed and tested two novel non-posttensioned transverse connections between adjacent box girders that can eliminate end and intermediate diagrams to simplify the production. Hussein et al. [7] studied the optimal UHPC shear key shape based on finite element (FE) modeling to obtain a desired balance between economy and strength effects. These studies mainly focused on the shear connectors at the component level.

In spite of the preceding efforts, studies on the influence of shear connectors to the bridge system behavior are limited, especially when deterioration or failure of shear connectors is involved, which is a critical problem in Canada with the wide use of deicing salt. To this end, this paper first developed an efficient FE model for multi-girder PC bridges for a representative short-span bridge in Alberta. Based on this model, the influence of shear connector failure on the bridge system behavior was studied. It was shown that shear connector failure can reduce the load-carrying capacity of bridge girder systems significantly.

2 Bridge Description

A 27-year-old (in service from 1990 to 2017) single-span bridge, called Tiger Lily bridge located near Barrhead in central Alberta, Canada was decommissioned after failing a safety inspection. The bridge consisted of nine, 11 m long, precast PC voided girders (referred to as G1–G9) without additional wearing surface, (e.g., concrete or asphalt overlay). They are tied to each other using five shear connectors located along the span between adjacent girders as shown in Fig. 1. This bridge can be considered as a typical representative of multi-girder PC bridges for short and intermediate spans in Alberta among all archived drawings [2]. Deterioration on shear connectors

was observed for this bridge and raised concerns of its influence on bridge safety. Thus, based on this bridge, the system's structural behavior and the influence of shear connector failure were studied in this paper to better guide the maintenance and rehabilitation of PC bridges for short and intermediate spans in Alberta.

The interior and exterior girders are of type SM-510 [2] with the cross section as shown in Fig. 2a, b. Compared with the standard drawings, the girders were additionally reinforced with four 25 M bars to reduce long-term camber, which were discovered during the forensic examination after the bridge decommissioning. The material properties were also tested during the forensic examination and summarized in Table 1.
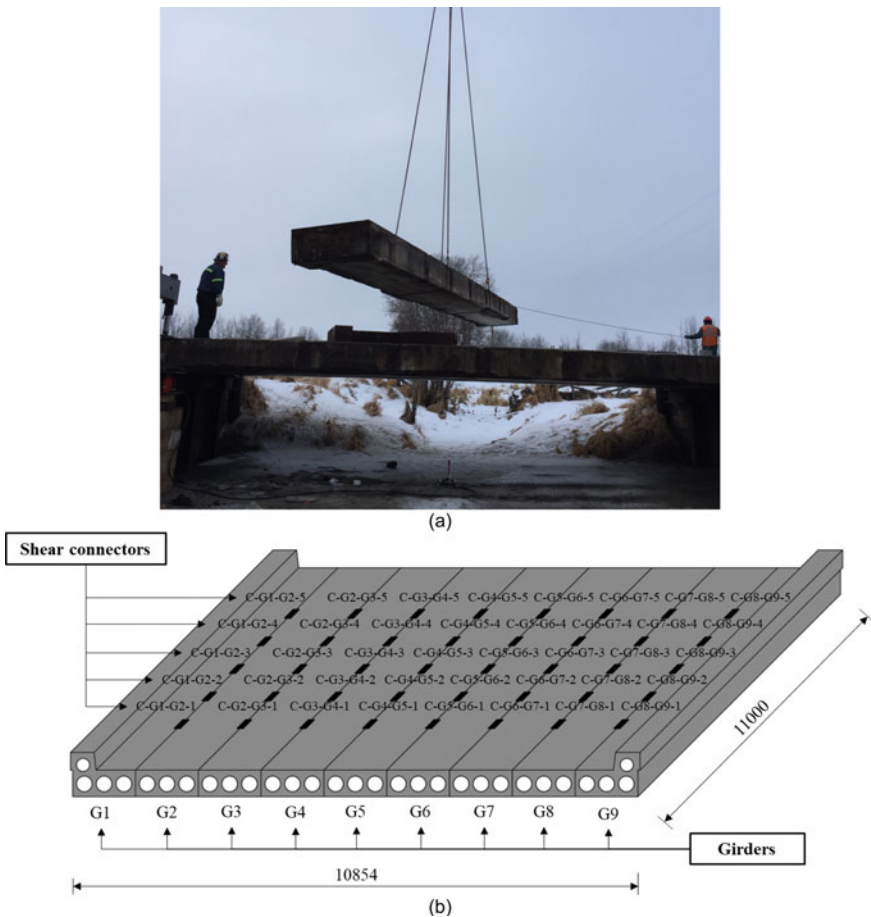
Fig. 1 Tiger Lily bridge: **a** Demolition process; **b** Schematic diagram (dimension in mm)
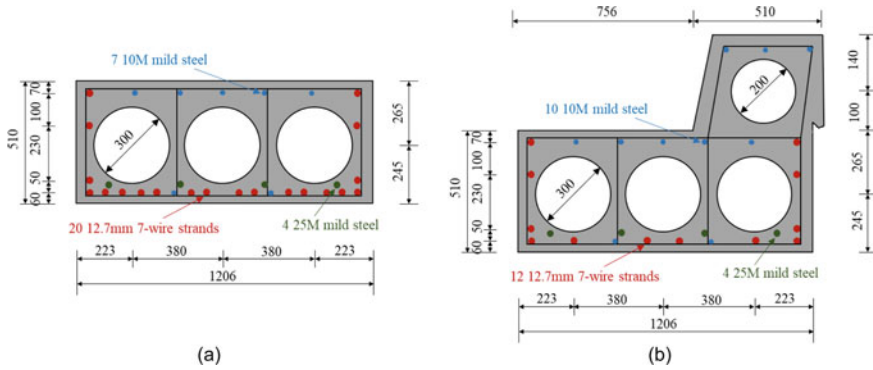
Fig. 2 Cross sections of **a** Interior girders, and **b** Exterior girders (dimension in mm)

Table 1 Tested material properties based on steel and concrete coupons

Material	Parameter	10 M	25 M	Strands
Steel	Yield strength (MPa)	417	413	1676.5
	Ultimate strength (MPa)	670	640	1860
	Elastic modulus (GPa)	198	203	196.5
Concrete	Compressive strength (MPa)	55.5		
	Ultimate compressive strain (MPa)	20.3		
	Strain at compressive strength	0.0027		
	Ultimate strain	0.0042		
	Density (kN/m^3)	1980		

3 Finite Element Model

To study the system structural behavior and the effects of shear connector failure, an efficient analysis tool based on FE is developed as shown in Fig. 3. One-dimensional (1D) fiber beam elements, (i.e., the *dispBeamColumn* element in *OpenSees*) are adopted to model each girder due to its well-received computational efficiency with adequate accuracy [14], and macro elements denoted by 1D springs, (i.e., the *zeroLength* element in *OpenSees*) are adopted to model the shear connectors between adjacent girders to transfer vertical loads.

3.1 Girder Modeling

Each girder was meshed into 50 *dispBeamColumn* elements with five Gauss–Legendre integration points for each element. The cross-section was discretized into concrete fibers with an average mesh size of 10 mm × 10 mm and steel fibers
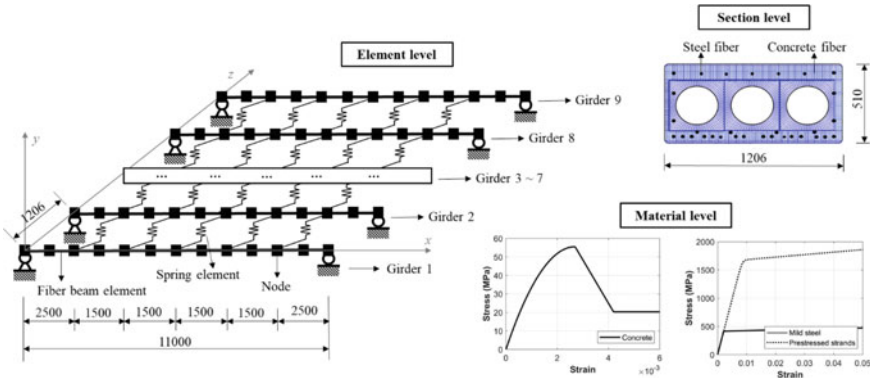
Fig. 3 FE modeling for the Tiger Lily bridge (dimension in mm)

to represent the longitudinal steels including both non-prestressed mild steel and prestressed strands. Note that the mesh size employed in this paper was determined based on convergence analysis. The *Concrete02*, *Steel01,* and *Steel02* were assigned to concrete, non-prestressed mild steel, and prestressed strands layers, respectively, with the tested material properties as summarized in Table 1. Note that the performance of the fiber beam element on simulating flexural behavior of single SM-510 girders has already been verified to be satisfactory in previous studies compared with experimental tests [11]. This paper also focusses on the flexural behavior of girder bridges, which are conventionally designed to be flexural dominated in engineering practice.

3.2　Shear Connector Modeling

In this bridge, adjacent girders were connected together as a bridge system by shear connectors consisting of two ¾ A325 bolts and A36 connector pockets as shown in Fig. 4.

To obtain the load-deformation relationship of shear connectors as an input of macro spring elements, a 3D continuum-based FE model was developed to simulate the behavior of shear connectors during load transfer based on ABAQUS [1]. The eight-node brick element *C3D8R* was adopted in this paper to model the bolts and connector pockets, since it has been extensively and successfully used in previous numerical simulations of bolted connections [9]. Figure 5a shows the finite element mesh of the developed model which is based on convergence analysis. Mesh area was divided into two, including one part around the bolt holes (90 mm area from the top of the connector pocket) with the size of 2 mm × 2 mm × 2 mm and the remaining another part with the size of 5 mm × 5 mm × 5 mm. Figure 5b summarized the boundary condition. Note that the reference point was fixed in all other directions
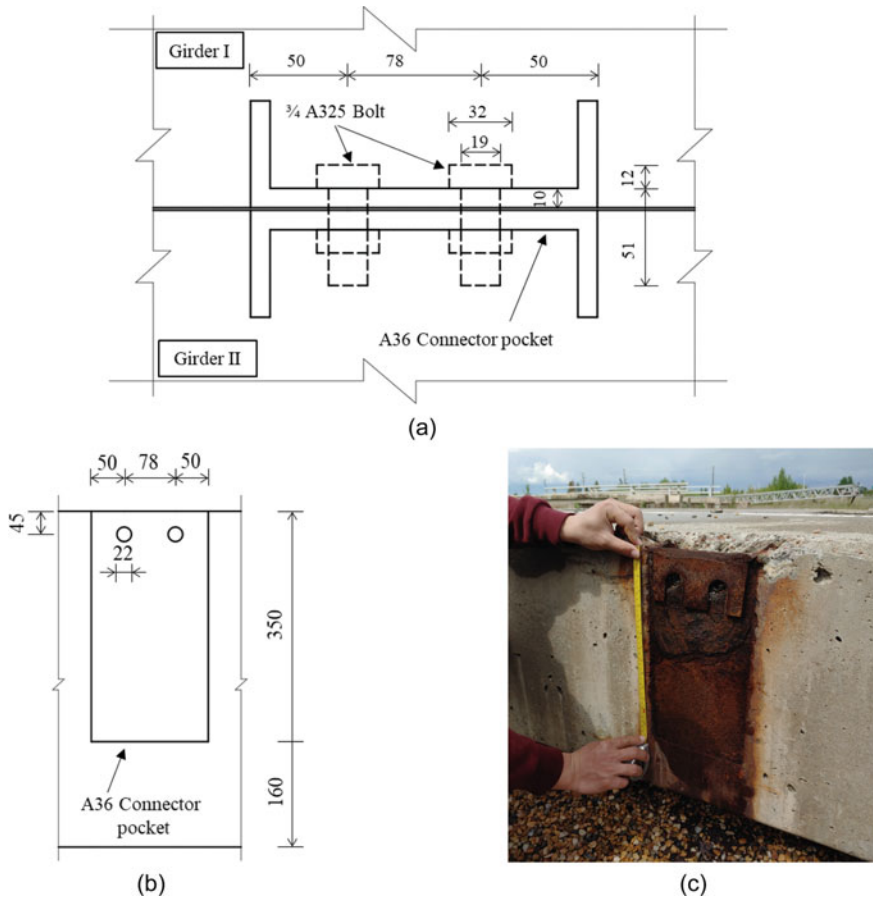
Fig. 4 Shear connectors in: **a** Plan view, **b** Front view, and **c** Engineering practice (deteriorated) (dimension in mm)

except the direction of load, (i.e., u_y). The 'general contact' in *ABAQUS* was adopted to define contacts between all components that are expected to interact with each other. The normal behavior was defined by the hard contact, while the tangential behavior was defined through the penalty approach with a friction coefficient of 0.2 [8].

It is worth mentioning that the concrete was not modeled explicitly but considered in the boundary conditions as shown in Fig. 5b to restrict the out-of-plane deformation of steel plates. This is to simulate the real boundary conditions of steel pockets in engineering practice, i.e., the curling of thin-walled steel pockets will be restricted by the surrounding concrete. The material constitutive models for A325 bolt and A36 plate were the plasticity model with Mises yield surface, where the uniaxial stress–strain curves were obtained from the test results of other researchers [10, 13]
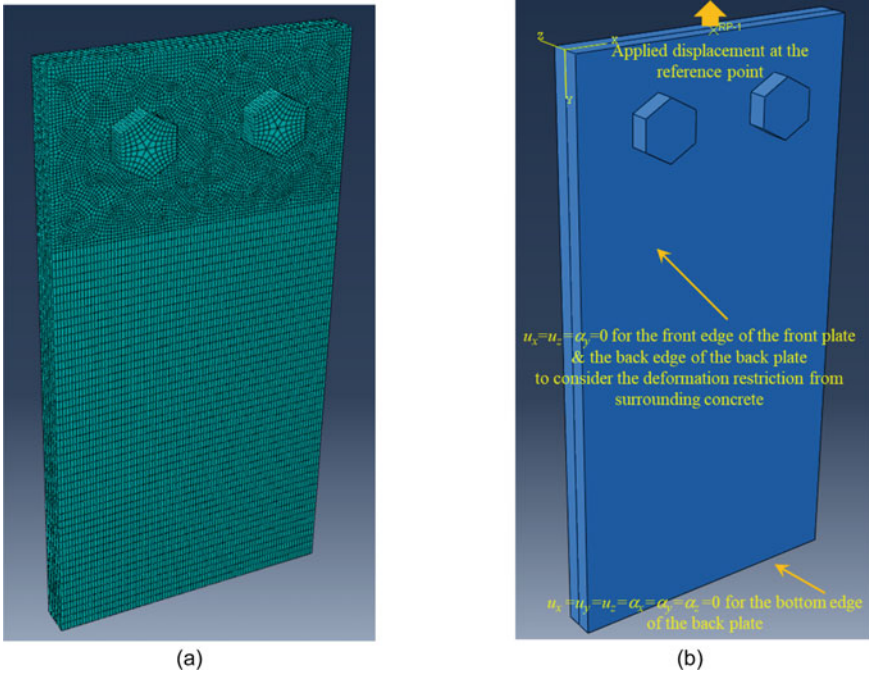
Fig. 5 3D FE model of shear connector: **a** Finite element mesh, and **b** Boundary condition

as shown in Fig. 6. Ductile damage properties were not considered in this manuscript and may need further studies in the future. In the end, the general solver was adopted to conduct nonlinear analysis on the developed model.
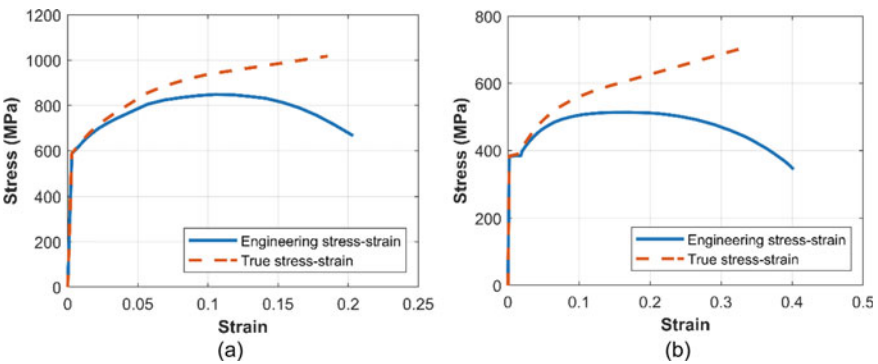
Fig. 6 Stress–strain curves of: **a** A325 bolt, and **b** A36 steel

The obtained load-deformation relationship of the shear connector is shown in Fig. 7 based on the developed 3D FE model, where the load is the total reaction force at the reference point and the deformation is the relative displacement of the bolt between the two A36 plates. A new material model to work with the macro spring element was implemented in *OpenSees* for the shear connectors considered, with the obtained load-deformation relationship analytically described by the fitted curve based on Eq. (1).

$$
y = \begin{cases}
\left(b_1 \dfrac{x}{x_1} + \dfrac{(1 - b_1)\frac{x}{x_1}}{\left[1 + \left| \frac{x}{x_1} \right|^{R_1} \right]^{1/R_1}} \right) y_1 & \leq x_0 \\[3ex]
\left(b_2 \dfrac{x}{x_2} + \dfrac{(1 - b_2)\frac{x}{x_2}}{\left[1 + \left| \frac{x}{x_2} \right|^{R_2} \right]^{1/R_2}} \right) y_2 + h & x > x_0
\end{cases}
\tag{1}
$$

where y is the load in kN, x is the displacement in mm, $x_1 = 0.157$, $x_2 = 2.54$, $y_1 = 250.667$, $y_2 = 254$, $b_1 = 0.0625$, $b_2 = 0$, $R_1 = 3$, $R_2 = 8$, $x_0 = 1.365$, and $h = 235$.
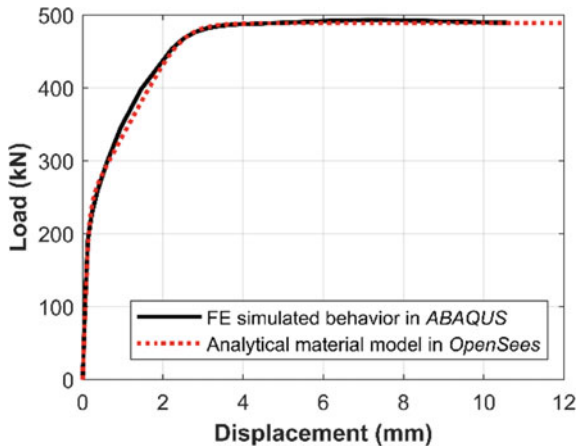
Fig. 7 Obtained load-deformation relationship

4   Structural Analysis

With the developed FE model for multi-girder bridges, the bridge system behavior and the influence of shear connector failure were studied in this section based on the Tiger Lily bridge under the combination of dead load and CL-625 truck load from CSA S6:19 [3]. The dead load of self-weight was first applied to each girder with the tested concrete density of 1980 kN/m^3. The CL-625 truck load was then applied to the bridge with each of the wheel loads located at on Girder #2 and Girder #3, respectively, as a single lane loading case. The longitudinal position of truck loading is shown as in Fig. 8. This longitudinal position will cause maximum moment effects for one single girder based on the influence line analysis. Then the CL-625 truck load was increased proportionally by a load multiplier until the bridge girder failed. The FE analyses were all carried out in displacement control using Newton-Raphson algorithm to solve nonlinear algebraic equations. The *RelativeNormDispIncr* in *OpenSees* was utilized to determine if convergence has been reached with a tolerance of 0.01. Note that no safety factors were considered in this study.

   The obtained load-midspan displacement, (i.e., displacement of Girder #2) curve is plotted in Fig. 9 and compared with the load-midspan displacement curve from one single interior girder under one wheel of the CL-625 truck with the same longitudinal position. It is shown that the bridge system capacity is significantly higher than the single girder, which is attributed to the load transferring system of shear connectors. The total load transferred by each line of shear connectors during the loading process is also summarized as shown in Fig. 10, which shows the lateral load distribution. It can be seen that the connectors between Girder #3 and Girder #4 transferred the highest load among all lines of connectors. The plateau stage near the end of loading process in Fig. 10 indicates that all shear connectors between Girder #3 and Girder #4 entered yield plateau, resulting in that afterwards no more loads can be transferred from Girder #3 to Girders #4 ~ #9.
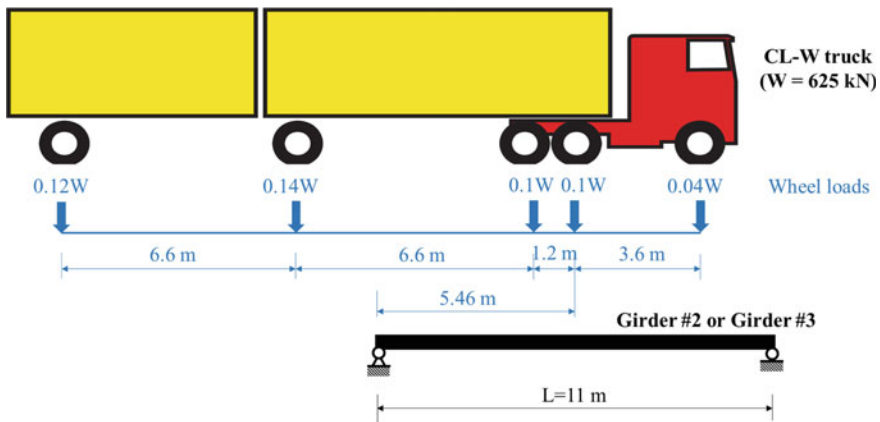
Fig. 8   Longitudinal position of the CL-625 truck load
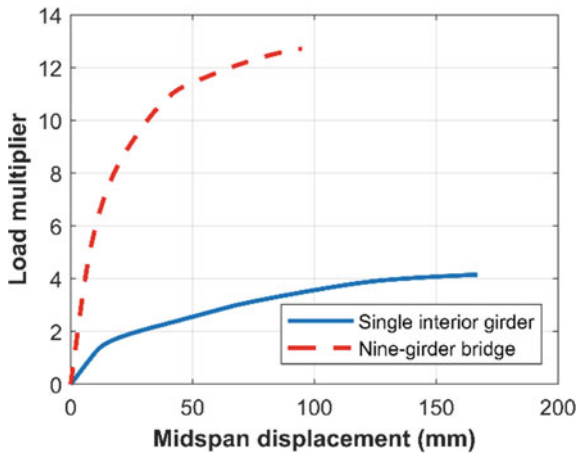
Fig. 9 Load-midspan displacement curves
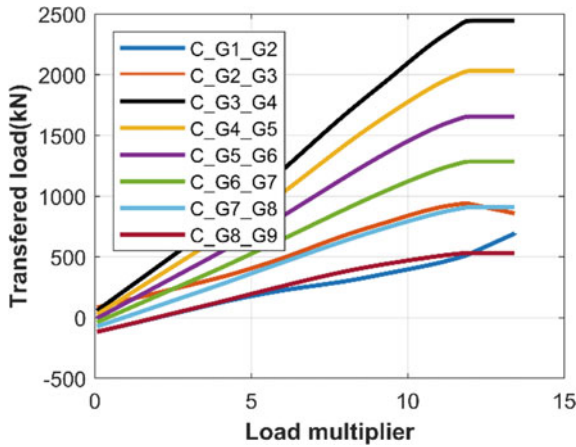
Fig. 10 Load transferred by each line of shear connectors

Since the connectors between Girder #3 and Girder #4 were shown to be critical in the system behavior of the nine-girder bridge for the loading scenario considered, the effects of single shear connector failure were studied by assuming that the five connectors between G3 and G4 failed one at a time. The obtained ultimate load multiplier and capacity loss percentage compared with the intact bridge for each cases were summarized in Table 2. It can be seen that one single shear connector failure can result in a capacity loss between 7.47% and 14.32%. This indicates that shear connectors can play an important role in the load bearing and transferring system of girder bridges. The effects of failure of two, three, and four shear connectors between G3 and G4 were also studied and summarized in Tables 3, 4, and 5, respectively. It

can be seen that the maximum capacity reduction due to two, three, and four shear connector failures are 26.01%, 37.06%, and 44.42%, respectively. Given the fact that deterioration and failure of shear connectors were widely observed for bridges during regular inspections, the potential safety issues resulted from shear connector failures should raise attentions for bridge evaluations.

Table 2 Effects of complete loss of a single shear connector between G3 and G4

Capacity	Intact	I.D. of the failed connectors of C-G3-G4-#				
		1	2	3	4	5
Ultimate load multiplier	13.42	12.42	11.79	11.50	11.95	12.53
Capacity loss percentage (%)	–	7.47	12.16	14.32	10.93	6.64

Table 3 Effects of complete loss of two shear connectors between G3 and G4

Capacity	I.D. of the failed connectors of C-G3-G4-#									
	1&2	1&3	1&4	1&5	2&3	2&4	2&5	3&4	3&5	4&5
Ultimate load multiplier	10.61	10.57	10.97	11.51	9.93	10.37	10.91	10.02	10.59	11.04
Capacity loss percentage (%)	20.94	21.26	18.22	14.19	26.01	22.71	18.72	25.36	21.05	17.74

Table 4 Effects of complete loss of three shear connectors between G3 and G4

Capacity	I.D. of the failed connectors of C-G3-G4-#									
	1&2&3	1&2&4	1&2&5	1&3&4	1&3&5	1&4&5	2&3&4	2&3&5	2&4&5	3&4&5
Ultimate load multiplier	8.90	9.30	9.83	9.08	9.65	10.00	8.45	9.03	9.41	9.12
Capacity loss percentage (%)	33.64	30.70	26.74	32.32	28.05	25.50	37.06	32.73	29.89	32.02

Table 5 Effects of complete loss of all four shear connectors between G3 and G4

Capacity	I.D. of the failed connectors of C-G3-G4-#				
	1&2&3&4	1&2&3&5	1&2&4&5	1&3&4&5	2&3&4&5
Ultimate load multiplier	7.46	8.00	8.34	8.12	7.54
Capacity loss percentage (%)	44.42	40.35	37.82	39.48	43.84

5   Conclusion

This paper studied the system behavior of multi-girder PC bridges and the influence of shear connector failure based on a representative nine-girder PC bridge in Alberta as a case study. Firstly, an efficient analysis tool using FE modeling for multi-girder PC bridges was developed. One-dimensional (1D) fiber beam element was adopted to model each girder and 1D spring element was adopted to model the shear connectors between adjacent girders. To obtain the load-deformation relationship of shear connectors as an input of spring elements, a 3D continuum-based FE model was developed to simulate the behavior of shear connectors during load transfer. In the end, the developed FE model was applied to simulate the structural behavior of the nine-girder bridge. It was shown that the shear connectors and load transferring system play an important role in the bearing capacity of multi-girder bridges. One single shear connector failure can result in a capacity loss up to 14.32%. The insights gained from this study can help better guide the maintenance and rehabilitation of multi-girder PC bridges.

References

1. ABAQUS (2014) ABAQUS analysis user's manual, Version 6.14. Dassault Systems Simulia Corp, Providence, RI, USA
2. Alberta Transportation (2019) Bridge standard drawings. Edmonton, AB, Canada
3. CSA (Canadian Standards Association) (2019) Canadian highway bridge design code. CSA S6:19. Ottawa, ON, Canada
4. Dunker KF, Rabbat BG (1993) Performance of prestressed concrete bridges in the United States—the first 40 years. PCI J 37(3):48–64
5. Hanna KE, Morcous G, Tadros MK (2011) Adjacent box girders without internal diaphragms or posttensioned joints. PCI J 56(4)
6. Huckelbridge AA, El-Esnawi H, Moses F (1995) Shear key performance in multibeam box girder bridges. J Perform Construct Facilities, ASCE 9(4):271–285
7. Hussein HH, Sargand SM, Steinberg EP (2018) Shape optimization of UHPC shear keys for precast, prestressed, adjacent box-girder bridges. J Bridge Eng, ASCE 23(4):04018009
8. Jiang K, Zhao O, Tan KH (2020) Experimental and numerical study of S700 high strength steel double shear bolted connections in tension. Eng Struct 225:111175
9. Kim TS, Kuwamura H (2007) Finite element modeling of bolted connections in thin-walled stainless steel plates under static shear. Thin-Walled Struct 45(4):407–421
10. Kodur V, Kand S, Khaliq W (2012) Effect of temperature on thermal and mechanical properties of steel bolts. J Mater Civ Eng 24(6):765–774
11. Liu J, Huang L, Wu Z, Tomlinson D, Cruz-Noguez C, Alexander J, Li Y (2021) Development of enhanced fiber beam element with multi-axial material constitutive models for reinforced/prestressed concrete beams. Eng Struct 248:113289
12. Russell HG (2011) Adjacent precast concrete box-beam bridges: state of the practice. PCI J 56(1):75–91

13. Sajid HU, Kiran R (2018) Influence of high stress triaxiality on mechanical strength of ASTM A36, ASTM A572 and ASTM A992 steels. Constr Build Mater 176:129–134
14. Spacone E, Filippou FC, Taucer FF (1996) Fibre beam–column model for non-linear analysis of R/C frames: Part I. Formulation. Earth Eng Struct Dynam 25(7):711–725
15. Yuan J, Graybeal B (2016) Full-scale testing of shear key details for precast concrete box-beam bridges. J Bridge Eng, ASCE 21(9):04016043

Dynamic Response of Multi-tiered Buckling-Restrained Braced Frames in High Seismic Regions of Canada

Moad Bani and Ali Imanpour

Abstract This paper aims to examine the seismic response of multi-tiered buckling-restrained braced frames (MT-BRBFs) with a focus on two- and three-tiered frames using the nonlinear dynamic analysis method. The prototype frames are part of a single-storey building located in Victoria, British Columbia, and Canada. The frames are designed according to the current Canadian steel design standard and their performance is examined under scaled ground motion accelerations. The results of the numerical simulations indicate that appreciable in-plane moments are imposed on the MT-BRBF columns due to the non-uniform distribution of frame inelastic deformations caused by asymmetric BRB hardening in tension and compression. This moment demand in combination with high axial compression forces led to yielding of the columns and should be considered in the design of MT-BRBF columns.

Keywords Buckling-restrained braced frames · High-seismic regions

1 Introduction

Steel multi-tiered braced frames (MT-BFs) consist of multiple bracing panels (or tiers) stacked vertically along a storey height, i.e. between out-of-plane support locations. MT-BFs are commonly used in North America as lateral load-resisting systems in tall single-storey buildings such as sports facilities, airplane hangars, warehouses, and industrial buildings. These frames are also used in multi-storey buildings with tall storey heights such as convention centres and auditoriums. A multi-tiered configuration is favoured when the use of a single-braced panel within a storey height becomes uneconomical or impractical. MT-BF columns are often wide-flange members oriented such that out-of-plane wind loading induces strong-axis bending. Intermediate horizontal struts are typically used between tiers to achieve a robust lateral load path under seismic loading while bracing the columns in the plane

M. Bani (✉) · A. Imanpour
University of Alberta, Edmonton, AB, Canada
e-mail: moad@ualberta.ca
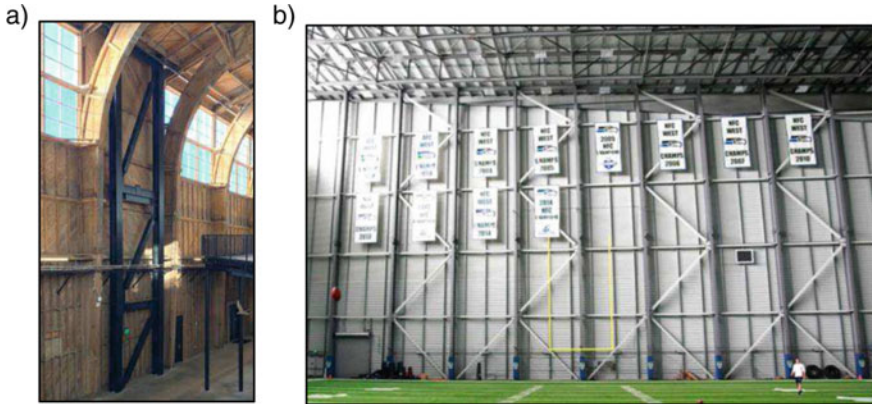
Fig. 1 Multi-tiered buckling-restrained braced frames: **a** Three-tiered BRBF in a retrofit project in Los Angeles, CA (*Courtesy of* Maren Dougherty); **b** Five-tiered BRBFs in a sports facility in Seattle, WA (*Courtesy of* Michael Lawrie)

of the frame. Although concentrically braced frames (CBFs) are often used in the multi-tiered configuration, the use of high-performance buckling-restrained braces (BRBs) can offer an attractive alternative, particularly in high-seismic regions by translating the inherent ductility of steel into system ductility, controlling the response of the structure to severe earthquakes [25, 27–29]. Figure 1 shows two examples of multi-tiered buckling-restrained braced frames (MT-BRBFs).

Buckling-restrained braces were introduced in North America in the late 1990s as an alternative to conventional steel braces [6, 8, 26]. Typical BRBs consist of a steel plate (referred to as the core), encased in a grout- or mortar-filled steel tube. A proprietary unbonding material is used to decouple the steel core and the grout such that the entire axial load is resisted by the steel core while the grout-filled tube prevents it from buckling. BRBs are designed to concentrate the inelastic action along the yielding length of the core while the end connection regions remain elastic. Under a major seismic event, the core is expected to yield in tension and compression resulting in a stable hysteretic response. BRBs under cyclic loads are expected to develop compressive forces higher than their respective tensile resistance (in the order of 1.2), due to the frictional forces developed between the core and the grout as well as Poisson's effect. Nevertheless, the nearly symmetric hysteretic behaviour of BRBs makes them an attractive alternative to their conventional counterparts, which under cyclic loading suffer from significant strength degradation due to global and local buckling or even low-cyclic fatigue fracture [24].

Design provisions for buckling-restrained braced frames (BRBFs) were introduced in the U.S. in the 2005 edition of the Seismic Provisions for Structural Steel Buildings, AISC 341-05 [1] and later in Canada in the 2009 edition of the CSA Steel Design Standard, CSA S16-09 (CSA 2009). Over the past two decades, there has been a significant body of research devoted to the mechanics and behaviour of BRBs,

seismic response and design of steel BRBFs, BRBF connections, and the development of new and more advanced BRBs. Past analytical and experimental studies confirmed the excellent seismic performance of buckling-restrained braced frames in multi-storey buildings, including higher ductility capacity, better distribution of plasticity over the frame height, and nearly identical storey shear capacity under loading reversal [23, 18, 12].

Research on MT-BFs over the past decade has mainly focused on multi-tiered concentrically braced frames (MT-CBFs) with extensive numerical studies having been conducted to examine the seismic response of low- and highly-ductile MT-CBFs in Canada and the U.S. [7, 14, 16]. The results of these studies have shown that inelastic lateral deformations under seismic loads tend to concentrate in one of the braced tiers inducing significant in-plane bending in the columns, which in the presence of large axial compression forces can lead to plastic hinging in the columns resulting in column instability. Column buckling was experimentally confirmed using hybrid simulation of a two-tiered CBF designed to the 2010 AISC Seismic Provisions [17]. Furthermore, excessive brace elongation can occur in the tier where brace tensile yielding occurs, which may result in brace low-cyclic fatigue fracture. The results of these past numerical studies resulted in the development of new seismic provisions for steel MT-BFs in Canada and the U.S. [15, 16]. These provisions mainly target the design of the columns of such frames by introducing in-plane and out-of-plane bending moments in addition to the axial compression loads induced by the inelastic response of the braces. Furthermore, a tier drift limit was prescribed to limit the inelastic deformation of braced tiers to the deformation corresponding to brace low-cyclic fatigue fracture. Finally, intermediate struts are required between braced panels to provide a vertical load path after brace yielding and buckling. Although similar performance concerns exist in MT-BRBFs, the use of BRBs is expected to provide a more uniform distribution of inelastic lateral deformations, leading to a more stable seismic response in MT-BRBF structures when compared with their conventional counterparts. The reason being is that BRBs yield in compression as they do in tension with a significant amount of strain hardening, resulting in a potentially more uniform distribution of plasticity along the frame height. However, the variation in expected BRB capacities and post-yield stiffnesses between adjacent tiers can still result in in-plane bending demands on the columns that may compromise column stability. A recent numerical study on a two-tiered BRBF located in Vancouver, BC showed that these moments can reach on average 17% of the column plastic moment capacity with more severe demands observed under ground motions produced by interface subduction earthquakes, which are one of the major sources of seismic hazard in the west coast of Canada [5].

The 2019 edition of CSA S16 [9] does not prohibit the use of MT-BRBFs, however, there are no special seismic design requirements currently available, leaving engineers without comprehensive and unified design guidelines which may lead to unsafe or uneconomical MT-BRBF designs. The latest edition of the U.S. Seismic Provisions for Structural Steel Buildings, AISC 341-16 [2] specifies design requirements for MT-BRBFs, which include provisions to design the columns under an axial compression force arising from BRB capacity forces, plus an induced in-plane bending moment

due to unbalanced forces between BRBs in adjacent tiers. Furthermore, the flexural stiffness of the column must be sufficient to limit the drift in any tier to 2%. When computing the in-plane moment, the MT-BRBF column should be treated as a simply-supported member with a length equal to the distance between points of out-of-plane supports, then a set of transverse point loads are applied corresponding to the greater of (1) the summation of frame shears from the adjusted brace strengths between adjacent tiers, and (2) a minimum notional load equal to 0.5% times the frame shear coming from the higher strength adjacent tier. Additionally, the columns should be torsionally braced at every strut-to-column connection location. Very limited research studies were performed to support the provisions prescribed in AISC 341-16 [16].

To provide insight into the seismic response of steel MT-BRBFs, this paper aims to examine the dynamic response of two- and three-tier steel BRBFs part of a tall single-storey building located in a high-seismic region of Canada (Victoria, BC). The frames were first designed as per the 2019 Canadian steel design standard. Then a detailed numerical model was developed and used to perform nonlinear time history analyses under a set of representative ground motion records. The results of the numerical simulations were finally used to evaluate the response of the frames and confirm the need for special seismic design requirements for MT-BRBFs in Canada.

2   Frames Studied

A single-storey building representing an indoor sports facility located in Victoria, BC with plan dimensions of 126 m × 70 m was selected for this study. The plan view of the prototype building is shown in Fig. 2a. The building is located on site Class C (dense soil) with a mean shear velocity, V_{s30}, between 360 to 760 m/s. The roof of the building consists of a steel deck supported by 70 m-long steel trusses that span over the full width of the building. The bay width in both principal directions of the building is equal to 7 m. The seismic force resisting system of the building consists of ductile (Type D) steel buckling-restrained braced frames (BRBFs). In total, three BRBFs along each exterior wall are used to resist lateral loads. As shown in Fig. 3b and c, two building heights were considered; 12 m for the two-tiered BRBF and 18 m for the three-tiered BRBF. The building height was equally divided between the tiers in both prototype frames. A single diagonal zig-zag bracing configuration was selected for the BRBFs. As shown in Fig. 2b and c, the selected configuration resulted in BRBs in adjacent tiers intersecting at a common joint on the columns. This configuration was selected because it limits the number of connections in the frame and creates a direct lateral load path from the roof to the foundation allowing for smaller strut sizes. Although this configuration can be seen as an efficient solution from a design and construction perspective, it is also expected to create the most critical multi-tiered response.

The roof dead load (D), live load (L), and snow load (S) are equal to 1.2, 1.0, and 1.14 kPa, respectively. The exterior cladding consists of insulated metal wall panels with a unit weight of 1.0 kPa. The seismic design base shear was determined using
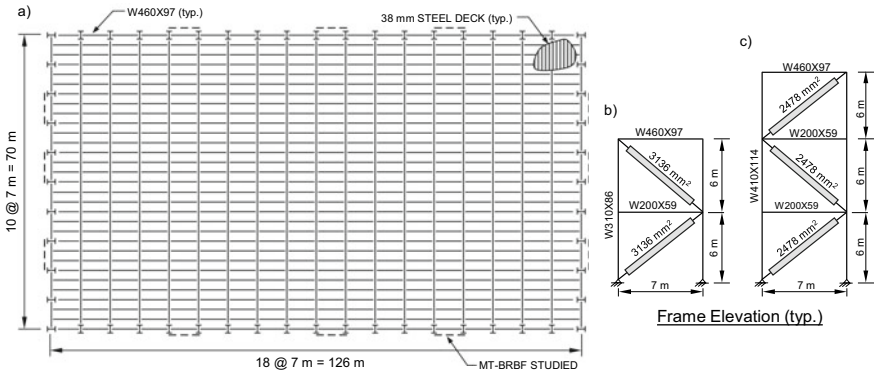
Fig. 2 **a** Plan view of the selected building; **b** Two-tiered BRBF elevation; **c** Three-tiered BRBF elevation
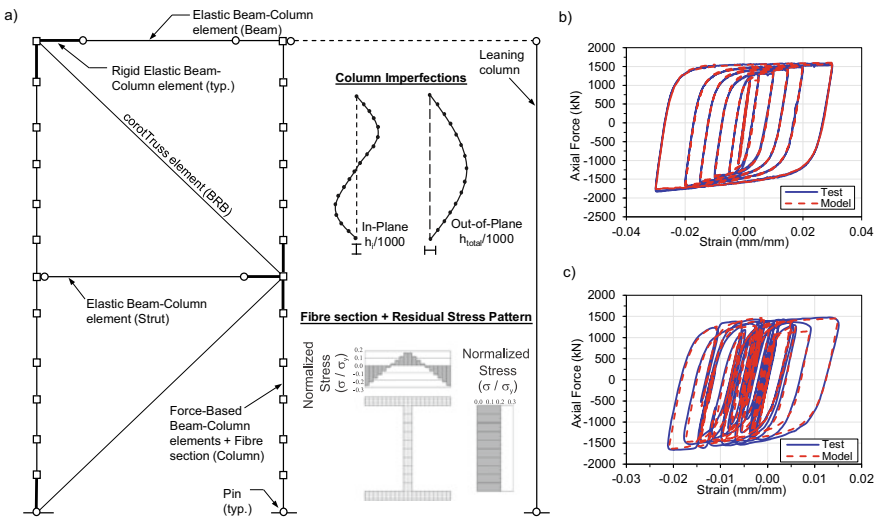
Fig. 3 **a** Fibre-based numerical model of a MT-BRBF; **b** Steel4 material calibration under a quasi-static loading protocol; **c** Steel4 material calibration under a dynamic seismic loading protocol

the equivalent static force procedure in the 2015 National Building Code of Canada (NBC) [20]. The importance factor, I_E, and the higher mode effect factor, M_v, are both equal to 1.0. For BRBFs, the ductility-related force modification factor, R_d, and the over-strength-related force modification factor, R_o, are 4 and 1.2, respectively. As permitted by NBC 2015, the design fundamental period of the building was taken as two times the empirical period (0.025 h, where h is the height of the building) for both frames. The key seismic design parameters for the frames are summarized in Table 1.

Table 1 Design parameters of frames studied

Design parameter	Two-tiered BRBF	Three-tiered BRBF
Design fundamental period, T_a, s	0.60	0.90
Analytical period, $T_{analytical}$, s	0.75	1.11
Design spectral acceleration, $S(T_a)$, g	1.07	0.78
Seismic weight per frame, W_{BRBF}, kN	2575	2771
Design base shear per frame*, V_{BRBF}, kN	620	490
Design storey drift, $R_d R_o \Delta_e / I_E$, $\%h_{Storey}$	1.36	1.44

*Including notional loads, accidental torsion, and P-delta effects

The 2015 NBC Load Combination 5 ($E + D + 0.5L + 0.25S$) was used to determine the frame design forces. The frames were designed as multi-storey BRBFs in the absence of special seismic design guidelines for MT-BRBFs in CSA S16-19. The factored column gravity load was found to be 208 kN for both frames. The BRBs were designed using a steel plate conforming to ASTM A36 with an expected yield strength, $R_y F_y$, of 290 MPa. The strain hardening adjustment factor, R_{sh}, and the friction adjustment factor, β, of the BRBs were computed as 1.42 and 1.12, using the backbone of the hysteretic response of the BRBs as discussed in Sect. 3. The probable resistances of the BRBs are $A_{sc} R_{sh} R_y F_y$ in tension and $\beta A_{sc} R_{sh} R_y F_y$ in compression, where A_{sc} is the steel core area. The roof beam, struts, and columns were sized based on a capacity design approach to resist the probable resistances of the BRBs in addition to gravity loads. Based on the distribution of axial loads along the columns (arising from BRB capacities along the frame height) effective length factors less than unity were used to obtain column in-plane and out-of-plane buckling resistances using an Eigen buckling analysis [10]. The columns, struts, and roof beam were selected from wide-flange sections conforming to ASTM A992 steel with a yield strength, F_y, of 345 MPa. The selected sections for the columns, roof beams, and struts satisfy the width-to-thickness ratio limits corresponding to Class 2 sections as specified by CSA S16-19. The selected frame member sizes are shown in Fig. 3b and c for the two-tiered BRBF and three-tiered BRBF, respectively. A stiffness modification factor of 1.24 was assigned to all BRBs in both frames to account for the added stiffness provided by the connections and the elastic regions of the BRB when calculating frame lateral deformations. The design storey drifts including inelastic effects, $\Delta R_d R_o / I_E$, were found to be lower than the maximum inter-storey drift limit of 2.5% as prescribed by 2015 NBC for normal buildings. Lastly, although it did not govern the design of the BRBFs, the lateral wind load was also considered in design.

3 Numerical Model

A fibre-based numerical model of the prototype frames was developed in the *OpenSees* programme [22] to examine the dynamic response of MT-BRBFs. Since the selected building is symmetric in plan and torsional effects can be ignored, a two-dimensional BRBF model with six degrees-of-freedom (DOFs) was used to examine the dynamic behaviour of the system. The numerical model of the MT-BRBF is shown in Fig. 3a for the two-tiered frame. The columns are pinned at the base and laterally braced in the out-of-plane direction at the top of the frame to represent lateral bracing provided by the roof truss. Multiple nonlinear force-based beam-column elements with fibre discretization of the cross section were used to model the columns. The Giuffre-Menegotto-Pinto (Steel02) material model was used to reproduce the nonlinear cyclic response of the columns considering the Bauschinger effect. The Steel02 material parameters were adapted from the calibration performed against cyclic coupon tests of G40.21-350WT steel [4]. A Young's modulus, E, of 200 GPa, and Poisson's Ratio, v, of 0.3, was assumed for all frame elements. Residual stresses were assigned to the column elements. To trigger in-plane and out-of-plane buckling, the maximum initial sinusoidal geometric out-of-straightness of the columns was set to 1/1000 times the unbraced length of the member in the plane and out of the plane of the frame. Five integration points were assumed along each element. The roof beams and struts were modelled using elastic beam-column elements. Relatively, rigid elastic elements were used at the ends of the columns, struts, and roof beam to account for the rigidity of the gusset plate connections. A corotational transformation technique was used to account for large deformations and geometric nonlinearities for all elements. An elastic element leaning column carrying the tributary gravity loads of the gravity frames was included in the model to account for P-Delta effects. The seismic masses were lumped at the top end of the columns, and the Rayleigh damping method with a mass proportional damping corresponding to 2% of critical was used in the first vibration mode of the frames to reproduce the classical viscous damping matrix.

The BRBs were modelled using corotTruss elements and assigned the Steel4 uniaxial material. This material model is an expanded definition of the Giuffré-Menegotto-Pinto Model capable of simulating the asymmetric kinematic and isotropic hardening behaviour of BRBs [30]. The Steel4 material parameters were calibrated using experimental results obtained from isolated BRB testing under a quasi-static and dynamic loading protocol [11] as shown in Fig. 3b and c, respectively. As can be seen, the BRB model is capable of adequately simulating the cyclic inelastic response of BRBs under both loading protocols. A yield strength, F_y, of 290 MPa was assumed for the BRBs, and the Young's modulus was modified by a factor of 1.24 to capture the added stiffness provided by the elastic regions of the BRBs and connections.

4 Ground Motion Selection

Ground motion records were selected and scaled in accordance with the recommendations outlined in Commentary J of 2015 NBC [21]. The uniform hazard spectra (UHS) for Victoria at a 2% probability of exceedance in 50 years was split into three seismic scenario-specific period ranges. Three sets of representative ground motions were then selected (one set for each of the potential seismic hazard sources in the west coast of Canada) and scaled within their respective scenario-specific period range. The first set of records consisted of 11 ground motions representing shallow crustal earthquakes dominating the seismic hazard for buildings with short fundamental periods. The second set consisted of 12 records featuring deep subduction in-slab earthquakes, which dominate the intermediate fundamental period range. The third set included 11 records representing large magnitude subduction interface earthquakes, which dominate for longer fundamental periods. Table 2 provides the details of the selected ground motion records including event name, selected component, year, moment magnitude, M_w, closest distance to rupture plane R_{rup}, and recording station.

The *PEER NGA-West2* database was used to select the crustal records [3] giving priority to the records included in the FEMA P695 far-field record set [13] and the *PEER NGA-Sub* preliminary flatfiles were used for the in-slab and interface records [19]. Scaling was performed in two steps. First, the individual records in each set were scaled using a factor that minimizes the mean squared error (MSE) between their 5% damped response spectra and the UHS along the scenario-specific period range. Second, all ground motions in a set were collectively scaled using a second scaling factor such that the mean response spectra of all the records in the set does not fall more than 10% below the UHS along the scenario-specific period range. The final selection of records used in this study was based on minimizing the MSE, and avoiding excessively high, i.e. greater than 5, or excessively low, i.e. less than 0.5, scaling factors. Moreover, the records with excessive spectral acceleration peaks greater than 4 g were excluded from the final sets. Figure 4a–c show the 5% damped response spectra of the scaled ground motion records for crustal, in-slab, and interface events, respectively.

5 Nonlinear Response History Analysis Results

Nonlinear response history analysis (NLRHA) was performed under the selected ground motions to evaluate the dynamic response and seismic-induced demands of the prototype MT-BRBFs. The key response parameters including the storey drift, tier drift, drift concentration ratio (DCR), column in-plane bending demand, and BRB strains are examined. The results of the single-record case studies for the two- and three-tiered BRBFs are first presented to illustrate the dynamic response of the prototype frames with an emphasis on the response of the columns and BRBs.

Table 2 Summary of selected ground motion records

Seismic source (database)	Event (component)	Year	M_w	R_{rup} (km)	Station
Crustal (PEER NGA-West2)	Imperial Valley-06 (237)	1979	6.53	15.2	Cerro Prieto
	Victoria (045)	1980	6.33	14.4	Cerro Prieto
	Loma Prieta (000)	1989	6.93	15.2	Capitola
	Landers (LN)	1992	7.28	19.7	Coolwater
	Northridge-01 (090)	1994	6.69	8.7	Arleta—Nordhoff Fire Sta
	Northridge-01 (090)	1994	6.69	10.1	Sun Valley—Roscoe Blvd
	Hector Mine (000)	1999	7.13	11.7	Hector
	Parkfield-02 (090)	2004	6.00	5.2	Vineyard Canyon
	Niigata (EW)	2004	6.63	9.5	NIGH01
	Chuetsu-oki (NS)	2007	6.80	16.1	Yoitamachi Yoita Nagaoka
	L'Aquila (TE)	2009	6.30	6.8	Aterno—Colle Grilli
In-slab (PEER NGA-Sub)	Olympia (086)	1949	6.70	47.6	OLY0
	Central America-39 (NS)	1982	7.31	60.0	2747
	Central America-38 (NS)	1992	6.51	93.1	2894
	Nisqually (180)	2001	6.80	64.6	WEK
	Nisqually (N)	2001	6.80	65.2	TKCO
	Geiyo (NS)	2001	6.83	43.6	KURE
	Pingtung Doublet-01 (E)	2006	7.02	40.7	KAU082
	Pingtung Doublet-02 (E)	2006	6.94	31.9	KAU082
	South America—2,575,090 (EW)	2007	6.74	46.4	MEJILLONE
	Ferndale (360)	2010	6.55	41.2	89,509
	Ferndale (360)	2010	6.55	36.2	Loleta
	Ferndale (090)	2010	6.55	32.9	1725
Interface (PEER NGA-Sub)	Michoacan (E)	1985	7.99	18.4	Aeropuerto Zihuatanejo
	Tokachi-oki (EW2)	2003	8.29	85.5	ASYORO-E
	Tokachi-oki (NS)	2003	8.29	92.2	SHIHORO

(continued)

Table 2 (continued)

Seismic source (database)	Event (component)	Year	M_{w}	R_{rup} (km)	Station
	Tokachi-oki (EW)	2003	8.29	61.2	47,418
	South America—2,844,986 (097)	2010	8.81	30.4	CONCEPCIÓN
	South America—2,844,986 (T)	2010	8.81	36.5	CONT
	South America—2,844,986 (T)	2010	8.81	49.8	HUAL
	Tohoku (NS)	2011	9.12	90.1	41,207
	Tohoku (NS)	2011	9.12	86.3	Taiwa
	Tohoku (NS)	2011	9.12	52.6	GN5
	Iquique (E)	2014	8.15	71.4	MNMCX
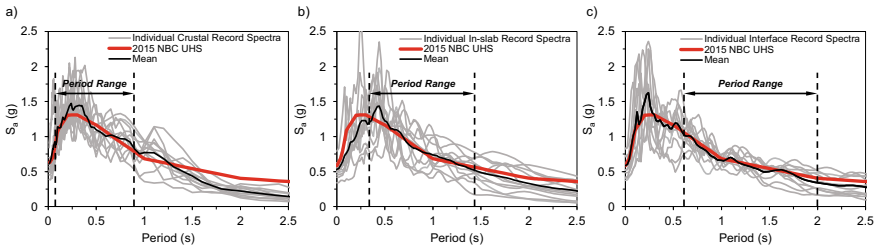
Fig. 4 Response spectra of the selected ground motion records: **a** Crustal; **b** In-slab; **c** Interface

The statistics of the selected response parameters obtained from the analyses of the prototype frames under the suite of 34 ground motions are then discussed.

5.1 Single-Record Case Studies of MT-BRBF Seismic Response

For the two-tiered BRBF, the results of the dynamic analysis under the 1999 Hector Mine earthquake are presented in Fig. 5. In the plots, the storey drift is computed as the ratio of the roof lateral displacement to the storey height h_{storey} and the tier drift is defined as the ratio of the relative lateral displacement of each tier to its tier height h_{tier}. As shown in Fig. 5a, the selected ground motion resulted in a peak positive storey drift of 1.75% at $t = 7$ s which is 1.3 times the design storey drift. The history of the tier drift is plotted in Fig. 5b. As shown, the drift tended to concentrate in Tier

1, when the frame is undergoing positive drift inducing tension in the Tier 1 BRB, making it the critical tier. The drift in Tier 1 reaches 2.73% at $t = 7$ s (Fig. 5b), which corresponds to the point where the frame experienced the maximum storey drift (Fig. 5a). A similar response but with a lower storey drift amplitude (-0.65% h_{storey} at $t = 5$ s) occurred in Tier 2 when the frame was pushed to the left inducing tension in the Tier 2 BRB earlier in the ground motion. This uneven distribution of inelastic lateral deformations through the tendency of inelastic demand to concentrate in the tier that undergoes tension is also shown in Fig. 5c. It is important to note that these observations would be different, had a different BRB configuration over the frame height been used. Figure 5d shows the BRB hysteretic response as a function of the normalized BRB force, $P_{\text{BRB}}/P_{\text{y}}$, which is the ratio of the induced axial force in the BRBs to their respective yield strength, versus tier drift. The response seen in Fig. 5d indicates that the Tier 1 BRB deformed significantly more than the Tier 2 BRB in order to carry the same base shear. Due to the asymmetric isotropic and kinematic hardening exhibited in BRBs, the BRB forces in adjacent tiers at a given time after yielding differ, resulting in different horizontal shears contributed by the BRB in each tier. Given that the storey shear in both tiers should remain the same (no inertia forces developed at the strut level), the difference in storey shears is compensated by the columns through their flexural deformations, which induces in-plane bending demands in the columns. The normalized right-hand-side (RHS) column in-plane moment demands, $M_{\text{y}}/M_{\text{py}}$, which is the ratio of the induced moment demand to the weak-axis plastic moment capacity is shown in Fig. 5e. As can be seen, these moment demands are directly related to the difference between tier drifts (Fig. 5b and c). As shown in Fig. 5e, the maximum in-plane moment demand in the RHS column at the strut level reached $0.24M_{\text{py}}$ at $t = 7$ s. The combined effect of the axial forces and induced moment demands in the columns are shown in the P-M column interaction plot in Fig. 5f. In the interaction plot, $C_{\text{f}}/C_{\text{n}}$ is the ratio of the column axial load to its nominal buckling resistance with positive values indicating compression. In the figure, the failure envelope is defined using the beam-column interaction equation in CSA S16-19. As can be seen, the RHS column is more critical with its P-M interaction, approaching the design interaction equation. Although column buckling did not occur under this ground motion, yielding was observed in the flanges of the columns. A plastic hinge formed at the middle of Tier 1, indicating that column buckling would've likely occurred had a second plastic hinge formed at the tier level.

The response of the three-tiered BRBF under the 2010 Ferndale-Loleta record is presented in Fig. 6. As shown in Fig. 6a, this record features a large drift reversal at $t = 29$ s as the frame goes from sustaining a positive storey drift of $0.76\%h_{\text{storey}}$ to a peak negative storey drift of $1.31\%h_{\text{storey}}$. The observed peak storey drift is close to the anticipated design storey drift. As shown in Fig. 6b and c, inelastic deformation concentrated in Tier 2 (critical tier) which remains in tension as the frame is pushed to the left at approximately $t = 29$ s while Tiers 1 and 3 are both in compression, and experienced nearly identical tier drifts and BRB hysteretic behaviours (Fig. 6d). The peak drift in Tier 2 reached 1.77 times the storey drift, indicating significant drift concentration has occurred in Tier 2 under negative storey drift. The observed non-uniform drift response between the tiers induced in-plane bending in the RHS
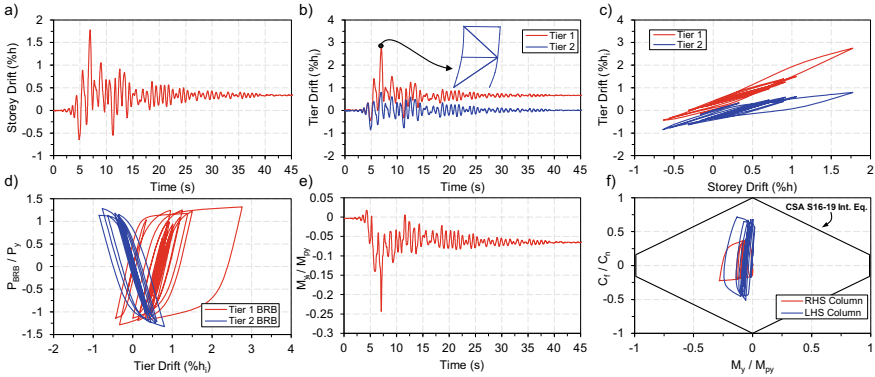
Fig. 5 Response of the two-tiered BRBF under the 1999 Hector Mine earthquake record: **a** Storey drift history; **b** Tier drift history; **c** Tier drift versus storey drift; **d** Hysteric response of BRBs; **e** RHS column in-plane moment demand history; **f** Column P-M interaction

column with a maximum value of $0.31M_{py}$ at the Tier 1 strut level and $0.27M_{py}$ at the Tier 2 strut level as shown in Fig. 6e. These moments are significant and should be considered in design. The column P-M interaction plot shown in Fig. 6f indicates that both columns remain elastic and stable without exceeding the CSA S16-19 beam-column interaction equation in tension and compression.
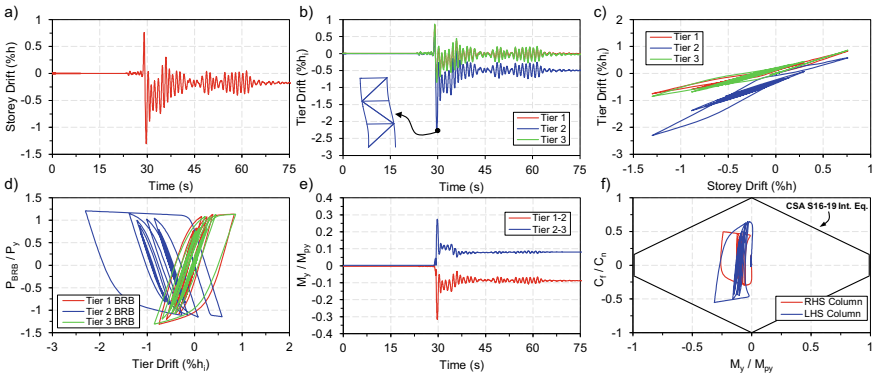
Fig. 6 Response of the three-tiered BRBF under the 2010 Ferndale-Loleta earthquake record. **a** Storey drift history; **b** Tier drift history; **c** Tier drift versus storey drift; **d** Hysteric response of BRBs; **e** RHS column in-plane moment demand history; **f** Column P-M interaction

5.2 Response Statistics

The statistics of the key response parameters including the storey drift, tier drift, drift concentration ratio (DCR), column in-plane bending demand, and BRB strains for the NLRHA are given in Table 3. The mean values presented in the table were computed for each frame by taking the maximum of means over each ground motion hazard scenario set for the peak response parameters, following the recommendations by 2015 NBC Commentary J, whereas the median (50th percentile) and 84th percentile values were calculated considering the entire suite of ground motion records analyzed. In this section, only the mean values will be discussed in detail. The median and 84th percentile results are provided to highlight the variability of seismic-induced demands in the prototype frames. For both frames, neither column nor frame instability was observed under the selected records. The storey drift in both frames was found to be close to that anticipated in design as indicated by the normalized storey drift values, $\Delta_{\text{roof}}/R_{\text{d}}R_{\text{o}}\Delta_{\text{e}}$, which are close to 1.0 for both frames. The critical tier drift in the table represents the drift in the tier which experienced the largest deformation. This value was 1.97% for the two-tiered BRBF and 1.81% for the three-tiered BRBF, which confirms the non-uniform deformation response described in the previous section. The level of non-uniform drift response is indicated by the drift concentration ratio (DCR) which is the ratio of the critical tier drift to the corresponding storey drift, with factors greater than 1.0 indicating a non-uniform distribution of lateral displacements among the tiers. For both frames, some level of drift concentration was observed in all the ground motions studied. Bending demands induced in the RHS columns were measured at the strut levels. The ratios of the induced in-plane bending demands in the columns to the plastic moment capacity, $M_{\text{y}}/M_{\text{py}}$, of the respective column section are presented in Table 3. For the two-tiered BRBF, in-plane bending reached 0.18 M_{py} in the Tier 1 strut level. Bending moments equal to 0.19 M_{py} and 0.16 M_{py} were generated in Tiers 1 and 2 for the three-tiered BRBF, respectively. These moment demands in the columns are significant and must be accounted for in design. BRB strains were found to be around 1% for all tiers in both frames. These values are well below the strain used in BRB qualification and testing as prescribed in AISC 341-16 Chapter K [2], which is around 2% for the prototype frames considered. The comparison of the response parameters among the three seismic hazard sources considered showed that in-slab earthquakes produced the largest demand in the two-tiered BRBF, whereas the long duration interface earthquakes were more critical for the three-tiered BRBF. Lastly, it is worth mentioning that in the prototype frames considered, the BRBs possessed the same yield strength and stiffness in all tiers, an assumption that may not be representative of reality; hence, the presented results represent a lower bound on the seismic demands expected in these systems. That is, a frame with non-uniform BRB properties, such as different yield strengths and stiffnesses in adjacent tiers will likely have more drift concentration and induced bending demands.

Table 3 Statistics of MT-BRBF response parameters

Response parameter	Two-tiered BRBF			Three-tiered BRBF		
	Mean	Median	84th Percentile	Mean	Median	84th Percentile
Storey drift (% h_{frame})	1.31	1.17	1.61	1.36	1.21	1.63
$\Delta_{\text{roof}}/R_{\text{d}}R_{\text{o}}\Delta_{\text{e}}$	0.96	0.86	1.18	0.95	0.84	1.13
Critical tier drift (% h_{tier})	1.97	1.64	2.60	1.81	1.64	2.22
DCR	1.49	1.45	1.63	1.37	1.28	1.61
$M_{\text{in-plane}}/M_{\text{py}}$ Tier 3–2	–	–	–	0.16	0.13	0.20
$M_{\text{in-plane}}/M_{\text{py}}$ Tier 1–2	0.18	0.14	0.25	0.19	0.16	0.24
ε_{BRB}* (%) Tier 3	–	–	–	0.99	0.74	1.25
ε_{BRB}* (%) Tier 2	1.00	0.69	1.45	0.97	0.86	1.32
ε_{BRB}* (%) Tier 1	1.07	0.93	1.47	1.02	0.72	1.29

*Assuming the yielding length is 65% of the working-point length

6 Conclusions

In this paper, the dynamic response of two- and three-tier buckling-restrained braced frames is presented. The frames are part of a building located in Victoria, BC and are designed according to the current Canadian steel design standard. A detailed numerical model was developed and used to perform nonlinear time history analyses using a suite of ground motions scaled to the building location. The response of the frames was evaluated by examining the results obtained from the numerical analyses. It was found that, although not as critical as MT-CBFs, MT-BRBFs are still prone to the concentration of inelastic demand in one or more tiers. For single-diagonal configurations, this concentration happens in the tiers undergoing tension yielding. This non-uniform drift response induced in-plane moment demands on the columns which may lead to frame instability. It was found, that the current method used in predicting BRB strain demands is conservative. Future editions of CSA S16 should require MT-BRBF columns be designed to resist the combined effects of axial forces and bending moments. Furthermore, the columns should be required to possess sufficient flexural stiffness to promote adequate yielding of the BRBs in all tiers to create a more uniform tier drift response. Future works will look at the behaviour of different frame configurations with non-uniform BRB properties as well as aim to develop comprehensive design guidelines for MT-BRBFs through experimental testing.

References

1. AISC (2005) ANSI/AISC 341-05, Seismic Provisions for structural steel buildings. American Institute of Steel Construction (AISC), Chicago, IL, USA
2. AISC (2016) ANSI/AISC 341-16, Seismic Provisions for structural steel buildings. American Institute of Steel Construction (AISC), Chicago, IL, USA
3. Ancheta TD, Darragh RB, Stewart JP, Seyhan E, Silva WJ, Chiou BSJ, Wooddell KE, Graves RW, Kottke AR, Boore DM, Kishida T, Donahue JL (2013) PEER NGA-West2 database, PEER report 2013/03, Pacific Earthquake Engineering Research Center (PEER). University of California, Berkeley, CA, USA
4. Ashrafi A, Imanpour A (2019) Seismic response of steel multi-tiered eccentrically braced frames. In: Proceedings of the 12th Canadian conference on earthquake engineering, Quebec City, QC, CAN
5. Bani M, Imanpour A (2022) Seismic performance of steel multi-tiered buckling-restrained braced frames in Canada. In: Proceedings of the 10th international conference on the behaviour of steel structures in seismic areas (STESSA), Timisoara, Romania
6. Black C, Makris N, Aiken I (2004) Component testing, seismic evaluation and characterization of buckling-restrained braces. J Struct Eng 130(6):880–894
7. Cano P, Imanpour A (2020) Evaluation of AISC seismic design methods for steel multi-tiered special concentrically braced frames. Eng J AISC 57(3):193–214
8. Clark P, Aiken I, Ko E, Kasai K, Kimura I (1999) Design procedures for buildings incorporating hysteretic damping devices. In: Proceedings of the 68th annual convention of the structural engineers association of California, vol 1. Santa Barbara, CA, USA, pp 355–371
9. CSA. 2019. CSA S16–19, Design of Steel Structures, Canadian Standards Association, Mississauga, ON, CAN.
10. Dalal ST (1969) Some non-conventional cases of column design. Eng J AISC 6(1):28–39
11. Dehghani M, Tremblay R (2016) Design and full-scale experimental evaluation of a seismically resilient steel buckling restrained brace system. Earthq Eng Struct Dynam 47(1):105–129
12. Fahnestock LA (2006) Analytical and large-scale experimental studies of earthquake-resistant buckling-restrained braced frame systems. PhD Dissertation, Lehigh University, Bethlehem, PA, USA
13. FEMA (2009) FEMA P695, quantification of building seismic performance factors. Federal Emergency Management Agency. Washington, DC, USA
14. Imanpour A, Tremblay R (2016) Seismic design and response of steel multi-tiered concentrically braced frames in Canada. Can J Civ Eng 43(10):908–919
15. Imanpour A, Tremblay R (2017) Analysis methods for the design of special concentrically braced frames with three or more tiers for in-plane seismic demand. J Struct Eng 143(4):04016213
16. Imanpour A, Tremblay R, Davaran A, Stoakes C, Fahnestock LA (2016) Seismic performance assessment of multitiered steel concentrically braced frames designed in accordance with the 2010 AISC seismic provisions. J Struct Eng 142(12):04016135
17. Imanpour A, Tremblay R, Leclerc M, Siguier R, Toutant G, Minouei YB, You S (2022) Development and application of multi-axis hybrid simulation for seismic stability of steel braced frames. Eng Struct 252(2022):113646
18. Kim J, Choi H (2004) Behavior and design of structures with buckling-restrained braces. Eng Struct 26(6):693–706
19. Mazzoni S, Kishida T, Contreras V, Ahdi SK, Kwak DY, Bozorgnia Y, Stewart JP (2021) NGA-Sub Flatfile: R211022. The B. John Garrick Institute for the Risk Sciences. Dataset. https://doi.org/10.34948/N3Z59T
20. NRC (2015) National building code of Canada. National Research Council of Canada (NRC), Ottawa, ON, CAN
21. NRC-Commentaries (2015) User's guide—NBC 2015 structural commentaries (part 4 of division B). Associate Committee on the National Building Code, Ottawa, ON, CAN

22. PEER (2021) Open system for earthquake engineering simulation (OpenSees). Pacific Earthquake Engineering Research Center (PEER), University of California, Berkeley, CA, USA. Available from: http://opensees.berkeley.edu
23. Sabelli R, Mahin S, Chang C (2003) Seismic demands on steel braced frame buildings with buckling-restrained braces. Eng Struct 25(5):655–666
24. Tremblay R (2002) Inelastic seismic response of steel bracing members. J Constr Steel Res 58(5–8):665–701
25. Tremblay R, Bolduc P, Neville R, DeVall R (2006) Seismic testing and performance of buckling-restrained bracing systems. Can J Civ Eng 33(2):183–198
26. Tremblay R, Degrange G, Blouin J (1999) Seismic rehabilitation of a four-storey building with a stiffened bracing system. In: Proceedings of the 8th Canadian conference on earthquake engineering, Vancouver, BC, CAN
27. Tsai K, Lai J, Hwang Y, Lin S, Weng C (2004) Research and application of double-core buckling restrained braces in Taiwan. In: Proceedings of the 13th world conference on earthquake engineering, Vancouver, BC, CAN. Paper No. 2179.
28. Uang CM, Nakashima M, Tsai KC (2004) Research and application of buckling-restrained braced frames. J Steel Struct Korean Soc Steel Constr 4(4):301–313
29. Watanabe A, Hitomi Y, Saeki E, Wada A, Fujimoto M (1988) Properties of brace encased in buckling-restraining concrete and steel tube. In: Proceedings of the 9th world conference on earthquake engineering, Tokyo-Kyoto, Japan
30. Zsarnóczay Á (2013) Experimental and numerical investigation of buckling restrained braced frames for eurocode conform design procedure development. PhD Dissertation, Budapest University of Technology and Economics, Budapest, Hungary

Dynamic Characterization and Assembly Methods of Full-Scale Aluminum Plate-Based Tensegrity Structure

Heather Gathman and Ann C. Sychterz

Abstract Tensegrity structures are a type of bar and cable structure that have a high strength-to-weight ratio and can easily be built into modular and adaptive structures. Plate-based tensegrity structures introduce a plate as a third element type. In addition to previously performed static analysis, there are still several design considerations which must be assessed in order to enable full-scale construction of a plate-based tensegrity structure. Namely, self-stress state determination to ensure a stable configuration, dynamic characterization to ensure resistance to vibrations induced by wind and seismic activity, and practical assembly methods must be established. A full-scale aluminum plate-based tensegrity structure is planned to be constructed over several bike racks on the University of Illinois Urbana-Champaign's campus. A finite element model has been created of this full-scale bike parking canopy. From this, the first five mode shapes and eigenfrequencies are obtained to characterize the dynamic response of the canopy structure and plate tensegrity roof. It is reasonable to truncate the analysis at mode five as the increasingly higher eigenfrequencies contribute less to the overall structural response. Results show that eigenfrequencies are sufficiently high to be beyond the risk of resonance for wind and seismic activity. The number of self-stress states for a single module and full-scale roof is also determined through the construction of the equilibrium matrix. The existence of multiple self-stress states indicates a stable configuration of the structure. Lastly, possible solutions for the joints needed to construct plate-based tensegrity structures have previously been presented in literature. However, none of these proposed solutions have been tested or manufactured. Modified joint designs which are easy to fabricate are proposed in this work, and documentation for the assembly is outlined. This paper presents previously unaddressed self-stress, dynamic, and joint design considerations for plate-based tensegrity structures. Results will further advance the practical design and construction of plate-based tensegrity structures.

Keywords Aluminum plate-based tensegrity structure · Dynamic characteristics

H. Gathman (✉) · A. C. Sychterz
Civil and Environmental Engineering, University of Illinois at Urbana-Champaign, Urbana, USA
e-mail: hfg2@illinois.edu

1 Introduction

Active and lightweight structures have recently been a cutting-edge area of research in several engineering fields including mechanical, aerospace, and civil engineering. This has led to the continued development of innovative structural concepts such as tensegrity structures. Tensegrity structures are type of statically indeterminate, pin-connected structure which are composed of discrete struts in compression interconnected by cables in tension [15, 16]. The balance of the compressive and tensile forces in tensegrity structures produces a stable self-stressed configuration. While functioning to stabilize the struts, the cable elements allow the structure to have a high-strength-to-weight ratio. In addition, due to the cables' inability to resist compression, tensegrity structures can undergo both large and small shape changes when equipped with actuators, making them well-suited for active and deployable structures.

In the field of civil engineering, tensegrity structures have been studied in applications such as bridges [13, 18], towers [10], and grid shell structures [1, 14]. Many of these designs however have not been full-scale nor incorporated a surface element such as a roof covering or bridge deck, which is a necessary component of many practical civil structures. The concept of plate-based tensegrity has emerged in recent literature as a way to expand the utility of tensegrity structures. Plate-based tensegrity introduces a plate element in addition to the strut and cable elements. The plate-based tensegrity base module [3–6] consists of a strut which passes through the center of a polygonal plate. Cables extending from the strut attach to the plate edges to stabilize the plate in its plane. The base units can then be interconnected at the plate edges and through cables at the strut ends to form modular assemblies. Figure 1 shows sample base modules for hexagonal, square, and triangular plates.

One application of the modular assembly of the units shown in Fig. 1 is as a lightweight and adaptive roof structure. The topology was first proposed to be used as a pitched timber roof in a Swedish equestrian hall. Since then, the static analysis of square plate-based tensegrity assemblies has been performed using the force density
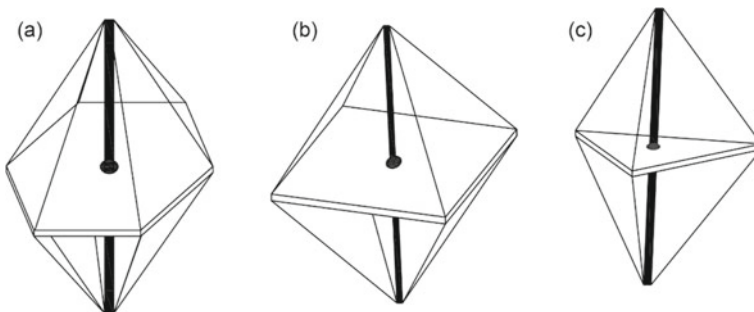
Fig. 1 Sketches of **a** hexagonal, **b** square, and **c** triangular plate tensegrity assemblies

method [5] and dynamic relaxation [8]. However, no characterization of the self-stress states or dynamics has been performed.

A key feature of tensegrity structures is that they are stabilized by self-stress. A self-stress state refers to a state where the members of a structure can be equilibrated by nonzero internal forces without the application of external loads. Therefore, for a tensegrity system to be stable, there must be at least one self-stress state [15, 19]. The existence of self-stress states can be determined from the nonzero solutions to the equilibrium equation shown in Eq. 1.

$$[\mathbf{A}]\{t\} = \{0\}, \tag{1}$$

where [**A**] is the equilibrium matrix and $\{t\}$ is the internal self-stress vector. The equilibrium matrix depends on the geometry of the structure. As defined in Moored and Bart-Smith [11], the equilibrium matrix is found by Eq. 2.

$$[\mathbf{A}] = [\mathbf{C}]\big[\tilde{\mathbf{g}}\big]\tilde{\mathbf{l}}^{-1}[\mathbf{I}]\{\tilde{\mathbf{l}}\}, \tag{2}$$

where [**C**] is the connectivity matrix, $\{g\}$ is the projection of the element lengths in each Cartesian direction, $\{1\}$ is the vector of element lengths, [**I**] is the identity matrix, and the ˜ operator refers to the block diagonal of the vector. The identity matrix has the dimension equal to the number of elements. Once the equilibrium matrix is assembled, the number of self-stress states can be solved as the number of nonzero solutions to Eq. 1. In other words, the number of self-stress states can be found by the difference between the number of elements and the rank of [**A**]. Since the conception of plate-based tensegrity, the self-stress states of the base units and assemblies have not been characterized.

Tensegrity structures are lightweight, and hence, they are sensitive to vibrations. For civil structures, it is important to ensure that the natural frequency of the structure is not close to the frequency of wind and seismic loads. Therefore, the determination of the natural frequencies and mode shapes of plate-based tensegrity structures needs to be completed before full-scale implementation. Despite their nonlinear behavior, a linearized dynamic model has been shown to be a good approximation of tensegrity structures' dynamic behavior [12]. To date, there has been no study investigating the dynamics of plate-based tensegrity structures.

Another necessary consideration for the full-scale implementation of plate-based tensegrity structures is joint design and assembly methods. In order to construct the modular assemblies, there are four primary connection types to consider: plate–strut, plate–cable, plate–plate, and strut–cable. Conceptual ideas for these connection types are described in [5]. Presented here is a turnbuckle-inspired mechanism for the strut–cable connection, a hinge between the plates, a rubber torus between the strut and plate, and a wheel or pulley system for the cables to slide over the plate. While promising starting points for the connection design, there has been no consideration for structural integrity and manufacturing.

In this paper, the self-stress states are determined for a square plate-based tensegrity module. In addition, the natural frequencies and mode shapes of a full-scale aluminum square plate-based tensegrity roof structure are determined, and joint design and assembly methods are proposed.

2 Analytical Study

2.1 Plate-Based Tensegrity Structure as a Bike Parking Canopy

The structure analyzed herein is a full-scale aluminum square plate-based tensegrity roof structure. The intended use of the structure is to provide shelter over several bike racks near Newmark Civil Engineering Building on the University of Illinois Urbana-Champaign (UIUC) campus. By constructing the bike canopy on campus, continuous monitoring of the structure in service can be performed to provide additional insight needed to inform future similar designs. The structure will also promote sustainable transportation on campus by providing a sheltered space to store bikes.

The primary construction material chosen for the structure is aluminum due to it being corrosion resistant, sustainable, and lightweight compared to other standard construction materials [9, 17]. The roof is constructed out of the square plate-based tensegrity modules presented by [3] in which the struts, plates, and columns are aluminum alloy 6061. Each module is composed of a 1-ft × 1-ft × 1/8-in. plate with a strut passing through the center of 2-ft length with a circular cross-section of 1-inch outer diameter and ¼-in. wall thickness. The cables both within the modules and interconnecting the units are stainless steel braided wire cable with a diameter of 3/32-in. The roof is composed of 8 modules by 4 modules and has an elevation change of 6-inches. The roof is supported by a 6 × 6 × 1/2 hollow square aluminum 6061 column at each corner. Dynamic relaxation (DR) has been used to check the strength and serviceability requirements of the roof [8] in accordance with the requirements outlined in the American Society of Civil Engineers' ASCE 7-16 Minimum Design Loads and Associated Criteria for Buildings and Other Structures. Figure 2 shows a preliminary dimensioned rendering of the bike parking canopy.

2.2 Generalized Equilibrium-Matrix Formulation

For a tensegrity system to be stable, there must be at least one self-stress state. Hence, the static properties of a square-plate based tensegrity system must be investigated. The equilibrium matrix is assembled using Eq. 2. To assemble the equilibrium matrix, the system must be discretized into a series of elements connected to nodes. Figure 3 displays the discretized model of the square plate tensegrity unit. Each cable is

8x4 – 1' x 1' x 1/8"
Al plates

1" OD ½" ID Al
struts

3/32" ø stainless
steel cable

Square tube Al
columns 6"x6"x1/2"

8'-0"

3'-11"
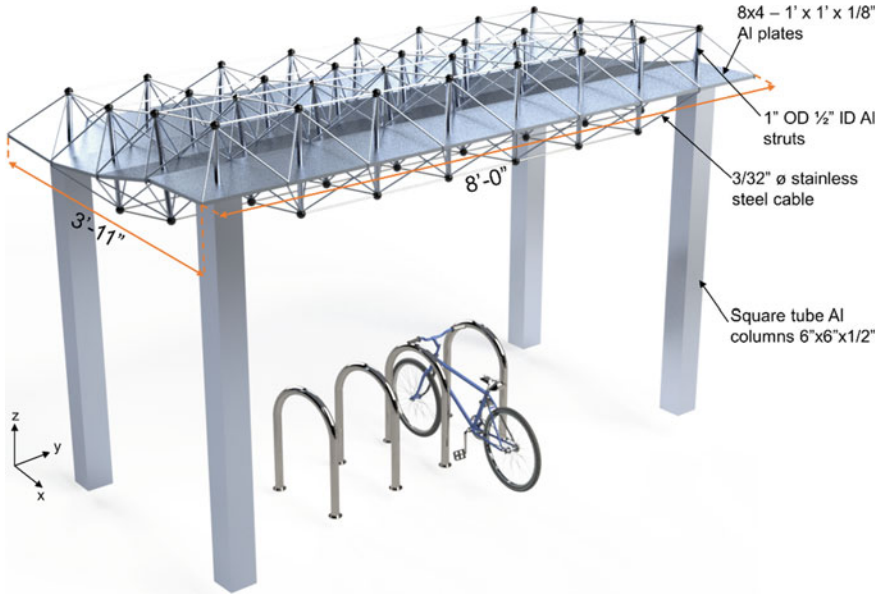
Fig. 2 Preliminary rendering of aluminum plate tensegrity structure with dimensions (NTS) and reference coordinate system

modeled as a single element, while the center strut is modeled as two elements meeting at the center of the plate. The plate is modeled using a five-node 8-bar (5N8B) bar and hinge model, which transforms the continuous plate into a series of 8 bars connected to five nodes. The bars have an adjusted area to maintain the in-plane behavior of a continuous plate [7]. The same model has been used during the DR analysis [8] and dynamic analysis described in the following section.

(a)

(b)

(c)

Idealized
node

Cable

Non-diagonal
plate strut

Diagonal
plate strut

Vertical
strut
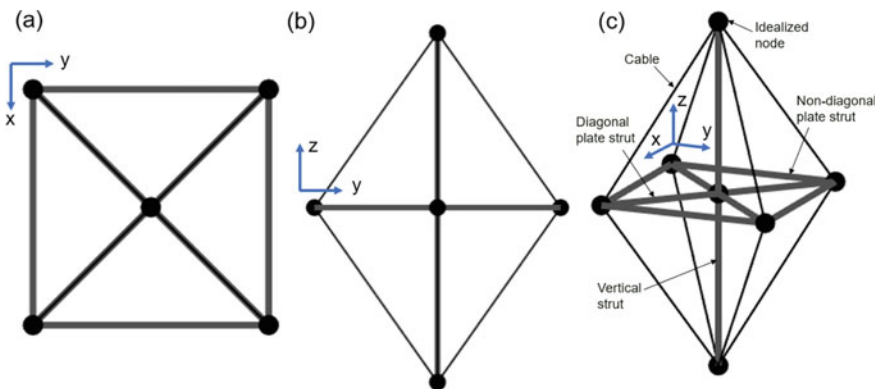
Fig. 3 Equivalent framework model of single square plate-based tensegrity module in **a** XY plane **b** YZ plane **c** 3D view labeled with element types

Table 1 Summary of self-stress states for single module and 4-module × 8-module roof

Structure	Elements (strut and cable), N_e	Nodes (joints), N_j	Equilibrium matrix rank, r_A	Self-stress states, s
Single square module	18	7	15	3
4 × 8 interconnected roof	604	192	409	195

As seen in Fig. 3, a single module is composed of seven nodes, eight cables, and ten struts for 18 elements total. The identity matrix has dimensions 18 by 18. From Eq. 2, the equilibrium matrix, [**A**], has a rank of 15. Hence, the number of independent self-stress states is 3. In addition to a single module, the equilibrium matrix is also assembled for the 4-module × 8-module interconnected roof structure. In the discretized model, there are 192 nodes, 336 cables, and 268 struts, for a total of 604 elements. The equilibrium matrix has a rank of 409, meaning that there are 195 independent self-stress states. Hence, the proposed system is able to form a stable self-stressed tensegrity structure. Table 1 summarizes the results for independent states of self-stress based on the equilibrium matrices.

2.3 Dynamic Characterization

In addition to determining the existence of self-stress states, the natural frequencies and mode shapes must be characterized in order to ensure resistance to naturally induced vibrations from wind and earthquake loads. This characterization is performed using the commercial finite element software, SOFiSTiK. The 5N8B bar-and-hinge model which has been used for the static and self-stress analysis has also been used in the dynamic model for consistency. Numerical input into the TEDDY command center was used to define the model. The vertical and plate elements have been defined as axial truss members which can resist both tension and compression. Cables have been defined as cable elements, resisting only tension, and the columns have been defined as beam elements, resisting axial loads and bending. The cable and struts are hinge connected, while the columns are fixed—fixed between the bottom supports and corner plates. The areas of the plate struts have been calculated using the equations outlined in [7] in order to maintain the stiffness and behavior of the continuous plate. Figure 4 displays the cross-section of each element type and their respective input materials. The aluminum (alloy 6061) members are assigned an elastic modulus of 10,000 ksi, Poisson's ratio of 0.33, and density of 0.098e–3 kip/in.³ [17], while the steel cables have an elastic modulus 29,000, Poisson's ratio of 0.30, and density 0.284e–3 kip/in.³ [2].

Figure 5 displays the generated model of the bike parking canopy, with the plate-based tensegrity roof supported by columns at corner plates.
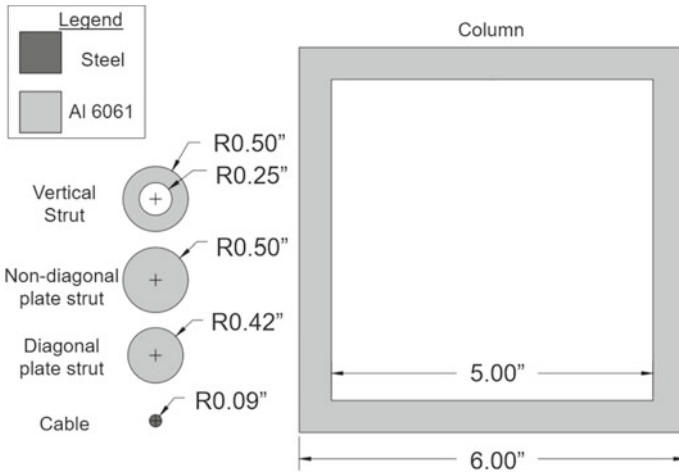
Fig. 4 Cross-section of structure member types and material assignment
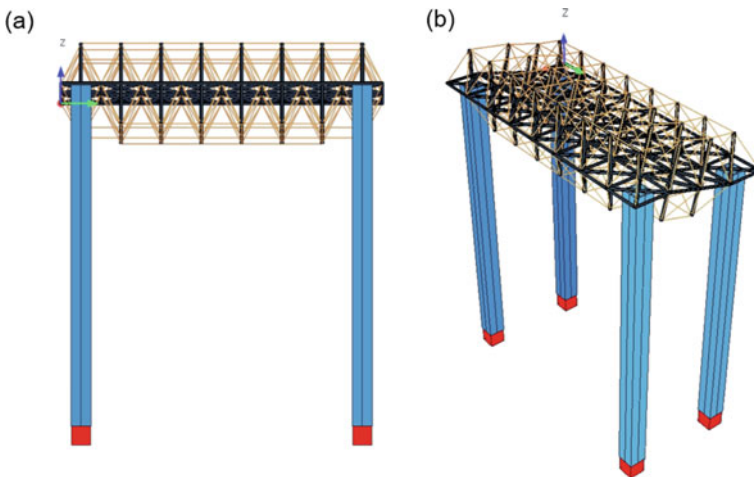
Fig. 5 Finite element model of bike canopy structure for dynamic analysis **a** view in YZ plane **b** isometric view

The first five eigenfrequencies and eigenmodes are obtained from the analysis. The first five mode shapes allowed for characterization of the overall canopy structure and first flexural and torsional modes of the plate tensegrity roof. As the higher order mode shapes contribute less and less to the overall structural response, it is reasonable to truncate the analysis at mode 5. Table 2 summarizes the eigenfrequencies and the nature of each corresponding eigenmode. As summarized in Table 2, the first three mode shapes describe vibrations of the canopy structure as whole. Mode one and two are sidesway of the canopy in the Y direction with natural frequency 14.2 Hz

Table 2 Summary of bike canopy eigenfrequencies and vibrational modes

Mode number	Eigenfrequency (Hz)	Nature of vibration
1	14.2	Canopy sidesway in Y direction
2	14.3	Canopy sidesway in X direction
3	15.6	Torsional mode of canopy
4	27.6	First vibrational mode of roof (flexure)
5	35.4	Second vibrational mode of roof (torsion)

and X direction with natural frequency 14.3 Hz, respectively. Mode three is the torsional mode of the canopy with natural frequency 15.6 Hz. Modes four and five describe the first two vibrational modes of the plate tensegrity roof. Mode four at 27.6 Hz is characterized by flexure of the roof, while mode five at 35.4 Hz is a torsional mode of the roof. As seen, the lowest eigenfrequency is 14.2 Hz. Figure 6 illustrates the motion of the mode shapes by showing the bike parking canopy at the two peaks of each vibration. As seen in Fig. 6, the resultant displacement from the first three mode shapes primarily stresses the columns, while the roof moves as a rigid body. In the fourth and fifth modes, the cables and struts of the roof undergo the most deformation, while the columns remain approximately vertical. For such a short structure, the bike-parking canopy has sufficiently high natural frequencies to be resistant to these vibrations induced by wind and seismic events.

3 Assembly Methods

3.1 Single Unit Assembly

Various architectural and structural developments have been made on the concept on plate-based tensegrity, yet a plate-based tensegrity structure is still to be constructed in full-scale. Within one base unit, there are three element types: the cables, strut, and plate which must be joined. The most complex connection to consider is the strut–cable connection, which must accommodate the four cables extending to the plate vertices and the four intermodular cables. Initially, a proposed idea for this design suggested threading the inside of the strut and having an external piece attach with wings for the cables [5]. This manufacturing method complicates alignment of the wings on the top and bottom of the strut. Instead, for the bike-parking canopy, the wings are fitted into slots which are directly milled in the strut. Eight slots are milled into each end of the strut to accommodate four cables running to the plate vertices and four cables running to adjacent modules. Each wing is 1 inch × 1 inch
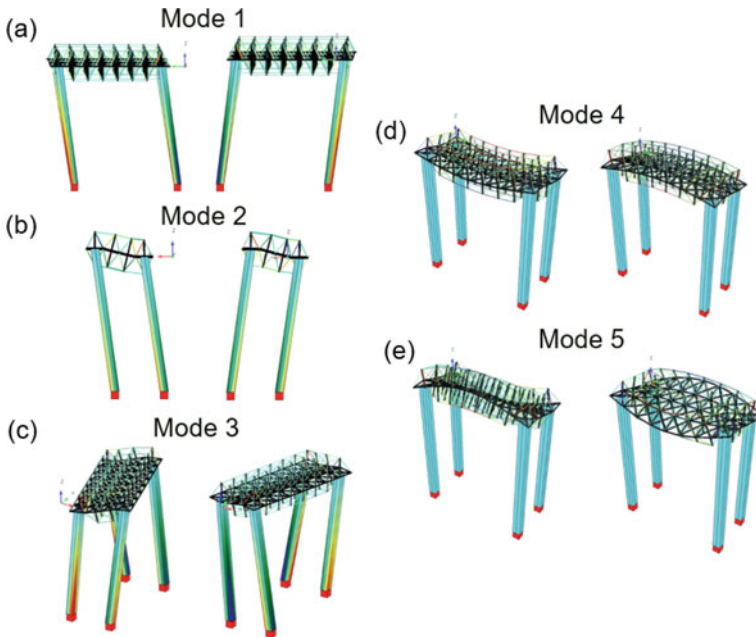
Fig. 6 Mode shapes of bike parking canopy structure for **a** mode 1 **b** mode 2 **c** mode 3 **d** mode 4 **e** mode 5

× 1/8 inch and has a 1/4 inch diameter hole in the center for the cable to be attached. From the DR analysis of different load resistance and factor designs (LRFDs) and vandalism load cases, the maximum tensile force in a cable is 148 lbs. To develop the required strength of the connection, a structural adhesive, JB WELD clear weld, is used to secure the wing into the slot. To verify that the connection could carry at least 148 lbs, a joint was manufactured and loaded until adhesive failure. The breaking strength in the adhesive exceeded 148 lbs with a 62% utilization ratio. The cables must also attach to the plate vertices. As opposed to having a continuous cable slide over the plate corners by a wheel or pulley system in which the plate could easily slip out of plane, the cables are discontinuous and loop though eye nuts at each corner on each side of the plate. Holes of ¼ inch diameter are cut in the plate corners at a distance of 5/8 inch from each edge. A threaded rod and eye nut are aligned, and the cable is looped through and crimped. A rubber grommet is used to seal the interface between the vertical strut and the center plate hole. Figure 7a shows a strut end with milled out slots, adhesively connected wing, and crimped cable. Figure 7b displays the threaded rod and eye nut assembly at the corners of the plate, while Fig. 7c shows the rubber grommet between the strut and plate.

The first step in assembling the module is to adhesively bond the aluminum wings inside the milled slots. The two-part epoxy is mixed and applied to all surfaces of the wing which will be in contact with the slot. The epoxy is applied with a thickness of approximately 1/8 in. Once inserted into the slot, elastic bands are wrapped around
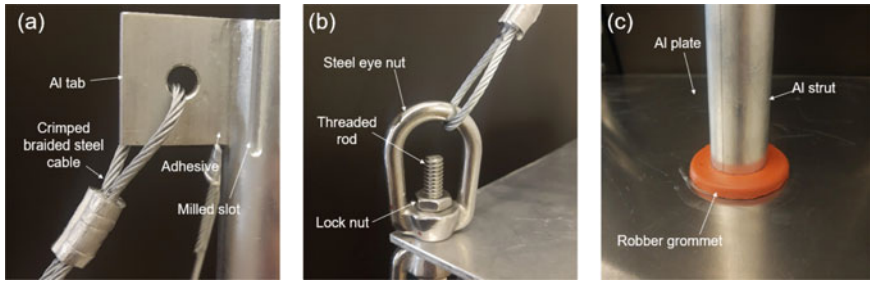
Fig. 7 **a** Strut end with milled out slots, adhesively connected wing, and crimped cable **b** threaded rod and eye nut assembly at the corners of the plate **c** rubber grommet between the strut and plate

the connection to secure the tab in place while the adhesive cures. Once all the wings are attached, the eye nuts at the plate corners are aligned such that the eye nuts are facing toward the center strut. To attach the cables, a wood stand was constructed to keep the plate level and support the plate at the proper distance while the cables are attached. The cables are cut to a length of 22 in. with a steel wire cutter. Once through the eye nut or wing, the cables are looped through an aluminum crimp sleeve and a swaging tool is used to crimp the sleeves. Dimensions of the loop were kept consistent both for aesthetic uniformity and consistent cable tightness. Weights are placed on the plate while the cables are tightened to prevent uplift of the plate. Once removed from the stand, it was checked whether the plate remained level with a ± 3-degree tolerance. Figure 8 shows the wood stand used for the assembly.

3.2 Modular Assembly

Once the individual modules are constructed, they must be assembled to form the roof structure. There are two types of connections between the modules: the plate edges and the intermodular cables which join the units by extending from the ends of the vertical strut to adjacent modules. Figure 9 shows two assembled modules connected by intermodular cables.

The plate edge connection must allow for rotation between the modules and hence must be hinge-connected. A typical hinge connection, similar to a door hinge, however, would add significant weight to structure and does not provide water proofing for the roof. Instead, a continuous carbon-Kevlar hinge can be used, which consists of rigid carbon fiber wings which are connected by a strip of flexible Kevlar. The carbon fiber wing is attached to the plate by the same structural adhesive used in the strut–cable connection. To begin the modular assembly, each of the square plate tensegrity modules are individually assembled. Then, the pre-assembled plate-based tensegrity units are modularly connected by hinges. Once the plate edges are secured by the hinge, the intermodular cables can be looped, tightened, and crimped. For the 4-module × 8-module roof structure of the bike parking canopy, modules
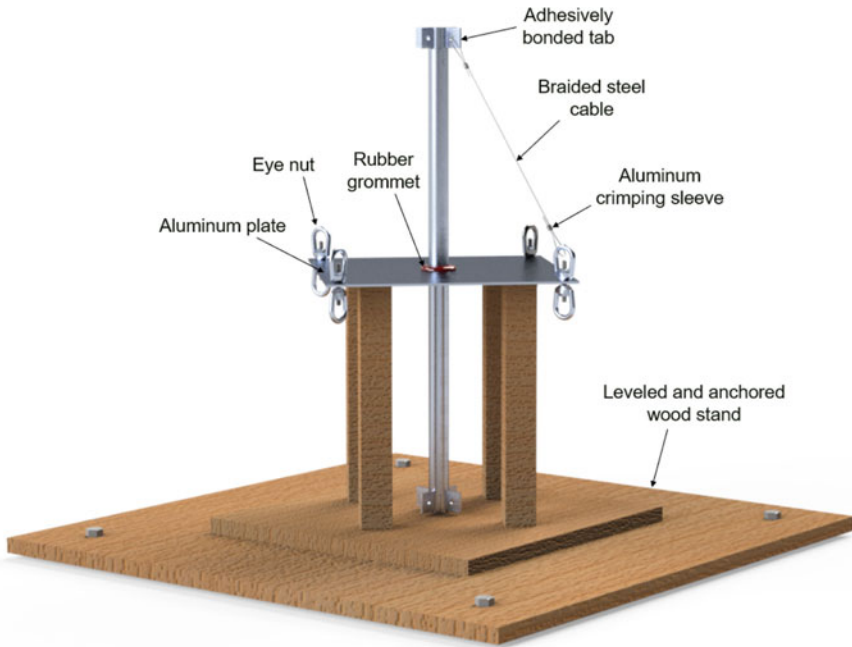
Fig. 8 Leveled wood stand used for supporting plate while cables are looped and crimped

Fig. 9 Two assembled
plate-based tensegrity
modules connected by
intermodular cables
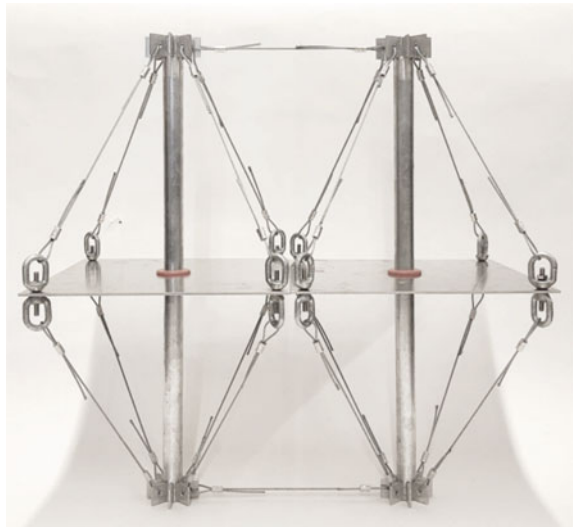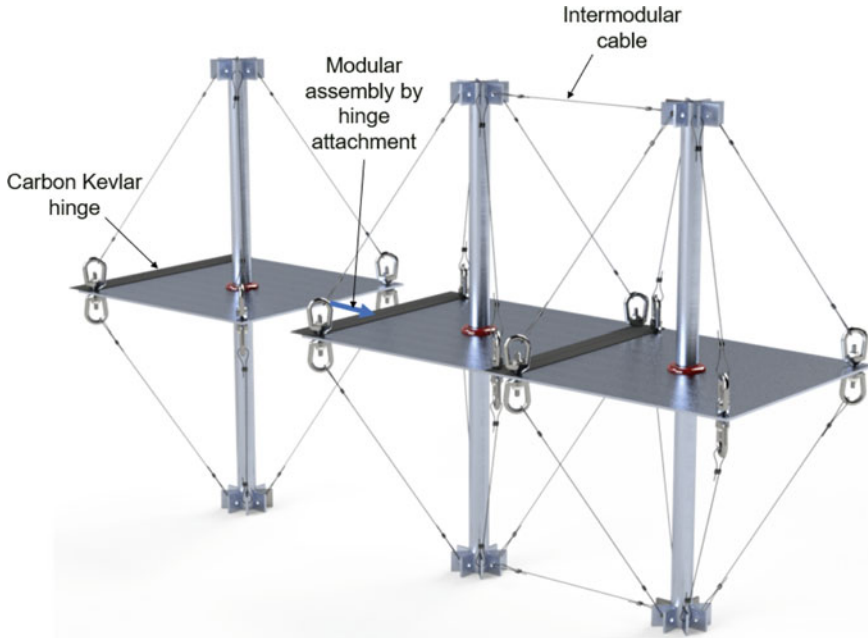
Fig. 10 Square plate-based tensegrity modules interconnected by cables and carbon Kevlar hinge

comprising the strips of the roof running parallel to the y axis can be constructed first. Once these four strips are assembled, they can similarly be connected first by the carbon Kevlar hinge at the plate edges, and then, the intermodular cables can be tightened and secured at the appropriate degree of inclination. Figure 10 illustrates the assembly of the modules in a single strip. The entire 4-module × 8-module roof structure is to be assembled flat on the ground. Once assembled, the roof structure will be lifted and connected to the supporting columns. The plates of the modules at the corner supports are to be directly welded to the aluminum columns.

4 Conclusions

Before plate-based tensegrity systems can be implemented in a full-scale civil structure, several design and analysis aspects must be considered in addition to static analysis. By using an equivalent framework model to discretize the plate, the number of self-stress states is determined for a single unit and modular assembly. The existence of multiple self-stress states indicates a stable tensegrity system. The dynamic analysis using a linearized model has allowed for the determination of the structure's natural frequencies and mode shapes. This characterization indicates that the structure has sufficiently high natural frequencies to be considered resistant to vibrations

induced by wind and seismic events. Additionally, the presented joint design and assembly techniques are simple to manufacture and can be completed without extensive labor. The modular construction method also makes it convenient to prefabricate the roof before hoisting in place, minimizing the onsite construction time.

Future work will include full assembly of the 4-module × 8-module roof structure and placement of the structure in service. Once in service, continuous structural health monitoring and use of the structure as an educational tool will be implemented.

References

1. Adriaenssens SML, Barnes MR (2001) Tensegrity spline beam and grid shell structures. Eng Struct 23(1):29–36. https://doi.org/10.1016/S0141-0296(00)00019-5
2. American Institute of Steel Construction (AISC) Steel Construction Manual (2011) 14th edn. American Institute of Steel Construction (AISC)
3. Falk A (2004) Timber-plates in tensile structures. In: IASS annual symposium: shell and spatial structures: from models to realization. Montpellier. https://doi.org/10.13140/2.1.1883.3284
4. Falk A (2006) Architectural and structural development of plate tensegrity. In: IASS annual symposium: new olympics, new shells and spatial structures. Beijing. https://doi.org/10.13140/2.1.1227.9682
5. Falk A, Tibert G (2005) Plate based tensegrity structures. In: IASS annual symposium: theory, technique, valuation, maintenance. Bucharest, pp 611–18. https://doi.org/10.13140/2.1.2931.9049
6. Falk A, Kirkegaard PH (2012) Pre-stressing timber-based plate tensegrity structures. In: IASS-APCS annual symposium: spatial structures to space structures. Seoul
7. Filipov ET, Liu K, Tachi T, Schenk M, Paulino GH (2017) Bar and hinge models for scalable analysis of origami. Int J Solids Struct 124:26–45. https://doi.org/10.1016/j.ijsolstr.2017.05.028
8. Gathman H, Sychterz AC (2021) A full-scale plate-based tensegrity structure as a bike parking canopy. In: Annual symposium of the international association for shell and spatial structures, Surrey, UK, pp 1–12
9. Georgantzia E, Gkantou M, Kamaris GS (2021) Aluminium alloys as structural material: a review of research. Eng Struct 227:111372. https://doi.org/10.1016/j.engstruct.2020.111372
10. Klimke H, Stephan S, Essrich R (2004) The making of a tensegrity tower. Stahlbau 73(2):74–79. https://doi.org/10.1002/stab.200490054
11. Moored KW, Bart-Smith H (2009) Investigation of clustered actuation in tensegrity structures. Int J Solids Struct 46(17):3272–3281. https://doi.org/10.1016/j.ijsolstr.2009.04.026
12. Motro RS, Najari S, Jouanna P (1986) Static and dynamic analysis of tensegrity systems. In: ASCE international symposium on shells and spatial structures, computational aspects
13. Motro R, Maurin B, Silvestri C (2006) Tensegrity rings and the hollow rope. In: IASS annual symposium: new olympics, new shells and spatial structures. Beijing
14. Olejníková T (2014) Geometry of prismatic tensegrity constructions composed of three and four-strut cells. Select Sci Papers J Civil Eng 9(2):47–56. https://doi.org/10.2478/sspjce-2014-0015
15. Pellegrino S (2001) Deployable structures, vol 53. Springer-Verlag Wien. https://doi.org/10.1017/CBO9781107415324.004
16. Pugh A (1976) An introduction to tensegrity. University of California Press

17. Randolph K, Ferry R (2002) Aluminum structures. A guide to their specifications and design, 2nd edn. John Wiley & Sons, Inc. New York. https://doi.org/10.1201/9781420037135.ch8
18. Rhode-Barbarigos L, Bel Hadj Ali N, Motro R, Smith IFC (2012) Design aspects of a deployable tensegrity-hollow-rope footbridge. Int J Space Struct 27(2–3):81–95. https://doi.org/10.1260/0266-3511.27.2-3.81
19. Williamson D, Skelton RE, Han J (2003) Equilibrium conditions of a tensegrity structure. Int J Solids Struct 40(23):6347–6367. https://doi.org/10.1016/S0020-7683(03)00400-1

Evaluation of a Long-Span Mass Timber Floor Under Footfall Vibration Loads

Slotboom Christian, Dickof Carla, and Tobias Fast

Abstract The following paper presents a series of footfall vibration tests run on a full-scale mock-up of the long-span floor system used in Fast+Epp's Structural Engineers' new home office. The mock-up consisted of four 3ply Cross-Laminated Timber (CLT) panels supported by glue-laminated timber (glulam) beams that span 11 m. Screws were used to connect the CLT panels to the glulam beams, and several different screw spacings were considered during testing. Two main goals were considered during vibration testing: evaluate how different spacings of screws affected the composite action between the glulam beams and CLT panels and estimate the amount of the vibration in the building floor. Measured accelerations on the floor were used to estimate its vibration performance and fundamental. It was found that the mock-up had a fundamental frequency of approximately 7 Hz and relatively high acceleration response. It was found that adding screws stiffened the system by approximately 40%, but that there were diminishing returns in stiffness increase as more screws were added.

Keywords Mass timber floor · Footfall vibration loads

1 Introduction

Footfall-induced vibration is a serviceability limit state that is important to consider for long-span floors. As pedestrians walk across a floor, the forces they impart to that floor will cause the system to accelerate. Floors that experience a large amount of acceleration from footfall forces may be uncomfortable to for occupants. A floors' vibration response is impacted by the mass, damping, and natural frequency of the system. Generally, the higher stiffness, mass, or damping, the better the perceived vibration of the system will be. The high strength-to-weight ratio of mass timber floors makes them particularly susceptible to vibration, as strength is less likely

S. Christian (✉) · D. Carla · T. Fast
Vancouver, BC Fast + Epp, Canada
e-mail: cslotboom@fastepp.com

to govern the design [3]. This is especially the case for long-span systems, which typically have lower stiffness.

To improve a floors stiffness without architectural implications, such as decreasing span lengths or increasing the member sizes, composite action is an important consideration. One common location for composite action is between floor panels and their supporting beams, allowing the panel to behave similarly to a beam flange. For mass timber systems, screws are generally used to provide a positive connection between the panel and beam. These screwed connections are typically not designed with sufficient shear strength and stiffness to provide composite action for strength and deflection. However, a greater contribution to stiffness may be present for vibration loads, which are relatively small. The US Mass Timber Vibration Guide [1] notes that the while the presence of screws can provide some composite action between the panel and beam, the amount of composite action and effective panel width are not well defined.

As part of the design process for the new home office of Fast+Epp structural engineers, a series of vibration tests were completed on a full-scale mock-up of the office floor plate. The tests were used to evaluate the general vibration response of the mock-up configuration, as well as understand the amount of composite action added by screws in the system. It is predicted that the mock-up will have a higher acceleration response than the building because it lacks non-structural elements, such as furnishings, but testing results should be roughly indicative of the building's vibration. The amount of composite action was estimated for several different configurations of the Cross-Laminated Timber (CLT) to glue-laminated timber (glulam) beam connections. Findings from the tests were used to inform later design decisions for the building.

2 Mock-Up Testing

2.1 Specimen Description

The mock-up consisted of four V2M1.1 3ply CLT (105 mm thick) panels spanning across four 24f-E grade 265×608 mm Glulam beams. The panels were oriented with their strong axis perpendicular to the beam span. The Structurlam supplied panels were 9.2 m long and 2.875 m wide; the Western Archrib supplied beams were 11.5 m long. Each beam was supported on wooden blocks with a clear span between blocks varying between 10.135 and 10.575 m. Figure 1a summarizes the geometry of the system, and an image of the mock-up can be seen in Fig. 1b.

Plywood splines were used to connect the CLT panels together at panel joints using $6\emptyset \times 220$ ASSY EcoFast screws spaced at 500 mm off center. The same ASSY EcoFast screws were also used to provide a positive connection between CLT panels to the glulam beams. Several screw spacings were considered in the experiment to
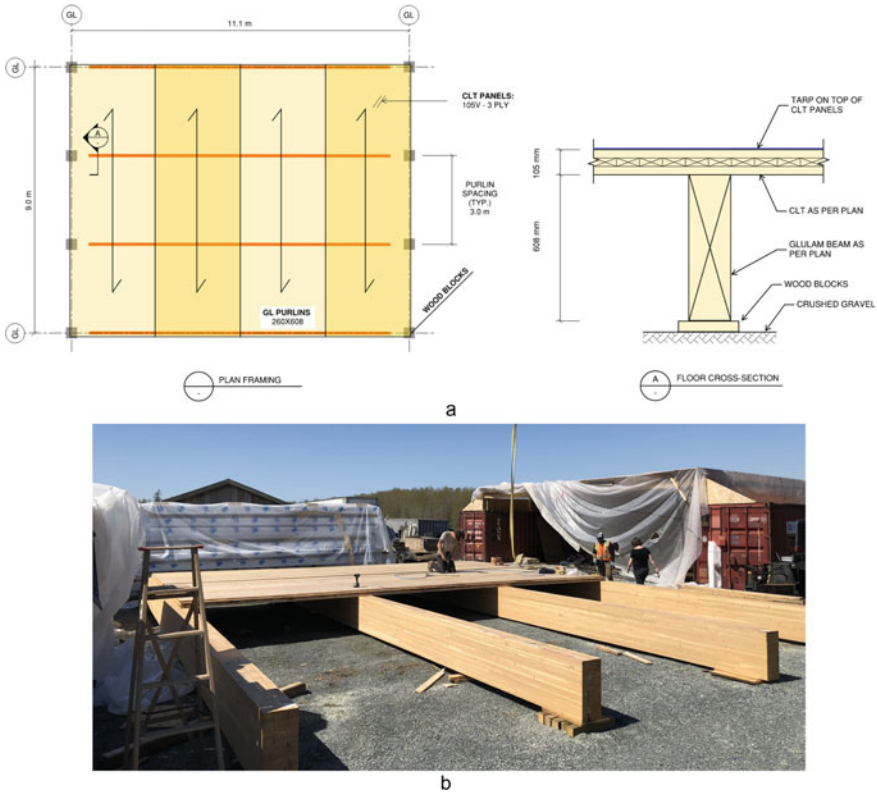
Fig. 1 Overview of **a** mock-up geometry, and **b** the mock-up during construction

Table 1 Screw spacing configurations

Test condition	Designation
No screws between panel and beam	M1
6Ø × 220 Screws spaced at 600 mm	M2
6Ø × 220 Screws spaced at 300 mm	M3
6Ø × 220 Screws spaced at 150 mm	M4

evaluate the impact of connection on the composite action in the system. The screw spacings considered are summarized in Table 1.

2.2 Testing Program

A series of heal drop and footfall vibration tests were completed for each of the screw spacings outlined in Table 1. For each screw spacing, a group set of walking tests was
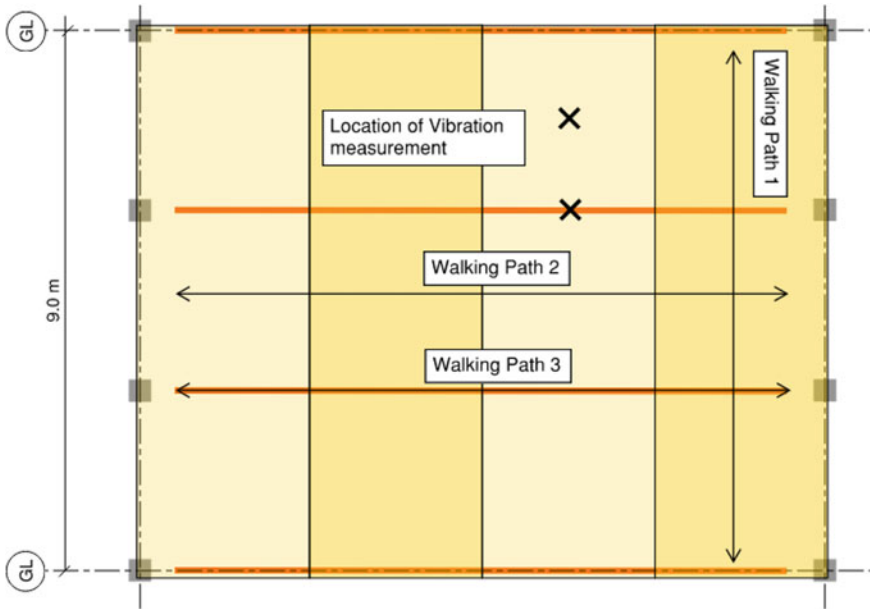
Fig. 2 Summary of walking paths and receiving locations

completed by recording the acceleration response of the floor while a single tester walked along a test path. Each set consisted of three walking paths shown in Fig. 2. For each walking path, tests were recorded at four different walking speeds: 1.25, 1.6, 1.85, and 2.1 Hz.

In each test, the panel vibrations were recorded using a Crystal instruments Spider E-20 data recorder with accelerometers placed in two locations: above an interior beam and at the midspan of the CLT between beams, as shown in Fig. 2. Each test is named according to the convention YY-ZZ-ci, where YY is the walking path used, ZZ is the walking path, and "i" is the channel. Chanel one was located at midspan of the panel, while channel two was located directly over an interior beam.

3 Results

3.1 Frequency

For each vibration test, the frequency response plots were reviewed to estimate the frequency of modes that were active at in the system. Selected normalized representative frequency response plots from testing are presented in Fig. 3. In these, the frequency response spectrum has been divided by the peak value observed, so the maximum value is one. Here, it can be observed that the first large peak in frequency

occurs at approximately 7 Hz for both testing locations; this peak was consistent for most plots. A secondary peak was observed at approximately 10 Hz, and for some tests, some higher frequency actively noted around 20 Hz. The 7 Hz peak likely corresponds to the long-span beam vibration mode, the 10 Hz peak likely applies to a higher mode activating the beams, and the 20 Hz modes mode likely corresponds to modes that activate the individual CLT panels.

The fundamental frequency of the system was estimated by measuring the frequency with the largest peak in each channel, and Figs. 4 and 5 plot the peak frequencies from each test for each screw configuration. The lowest of the two channel frequencies is used in calculating the median fundamental frequency, shown with a dashed line in the plots. For the cases where a test shows a peak frequency significantly higher than the median fundamental frequency, the peak corresponded to a response from a higher mode. Consistently higher fundamental frequencies were noted for faster F4. Table 2 summarizes the median fundamental frequency observed in each test designation.
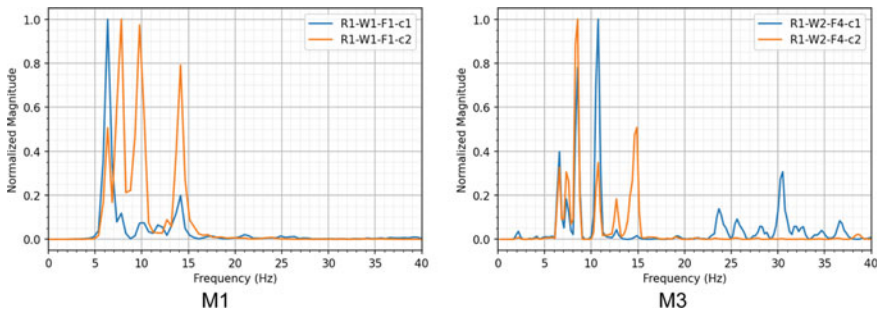
Fig. 3 Sample frequency response plots for channel one (c1) and channel two (c2) from M1 and M3
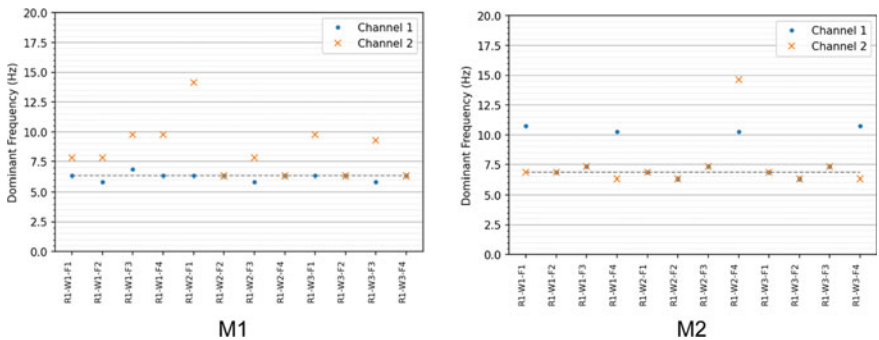
Fig. 4 Observed peak frequencies in test groups M1–M2. The median of the lowest frequencies is displayed as a dashed line
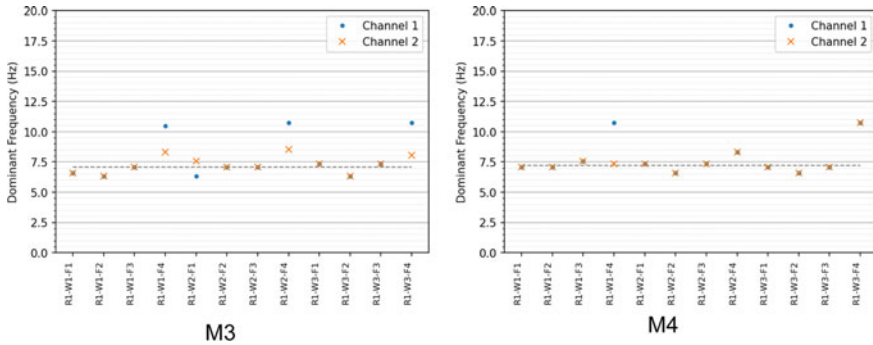
Fig. 5 Observed peak frequencies in test groups M3–M4. The median of the lowest frequencies is displayed as a dashed line

Table 2 Median fundamental frequency observed in each test group

Test designation	Median fundamental frequency (Hz)
M1	6.3
M2	6.8
M3	7.3
M4	7.4

Test results were also carried out on each individual beam before the panels were placed. Each beam was tested twice by using a hammer impact on the beam and recording accelerations near at midspan. Figures 6 and 7 show the recorded frequency spectrum for each of the four beams. The observed frequency spectra are very uniform, and the peak frequencies of all beams were found to be within a range of 10.3–11.3 Hz. The small variation is like due to changes in span length between each beam and to a lesser extent natural variations of stiffness.
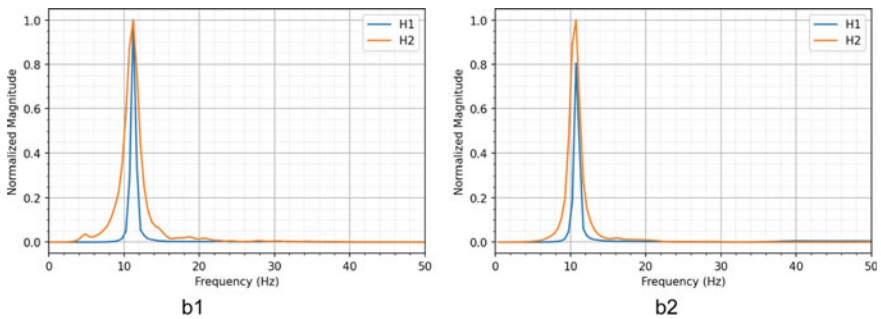
Fig. 6 Frequency response for beam one (b1) and beam two (b2) to hammer strike tests
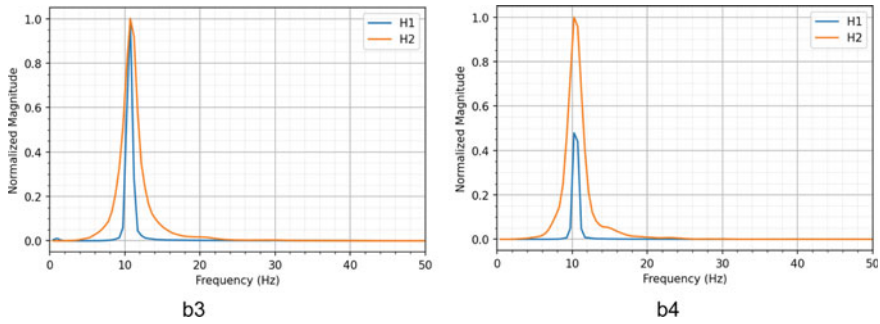
Fig. 7 Frequency response for beam three (b3) and beam four (b4) to hammer strike tests

3.2 Accelerations

Raw accelerations were recorded from each walking test, and selected raw accelerations from tests are presented with the RMS of the signal overlayed in Fig. 8. RMS accelerations have been calculated over a 1 s averaging time, according to recommendations presented in ISO 10137 (2007).

The peak RMS signal for all tests in one test group, M4, is shown in Fig. 9 as a representative sample of results. The average RMS acceleration has an R value of 15 and included as a dashed line. It can also be observed that there is an upward trend in RMS acceleration as walking speed increases from F1 to F4.
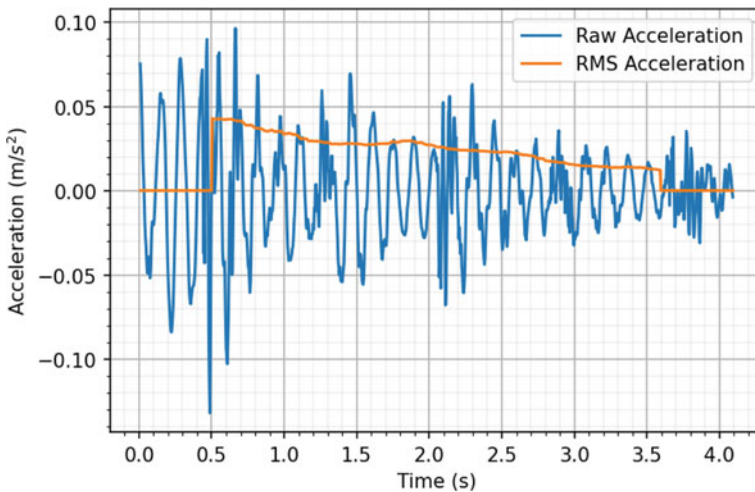
Fig. 8 Raw vibration signal and RMS of the signal for test R1-W2-F1, channel one
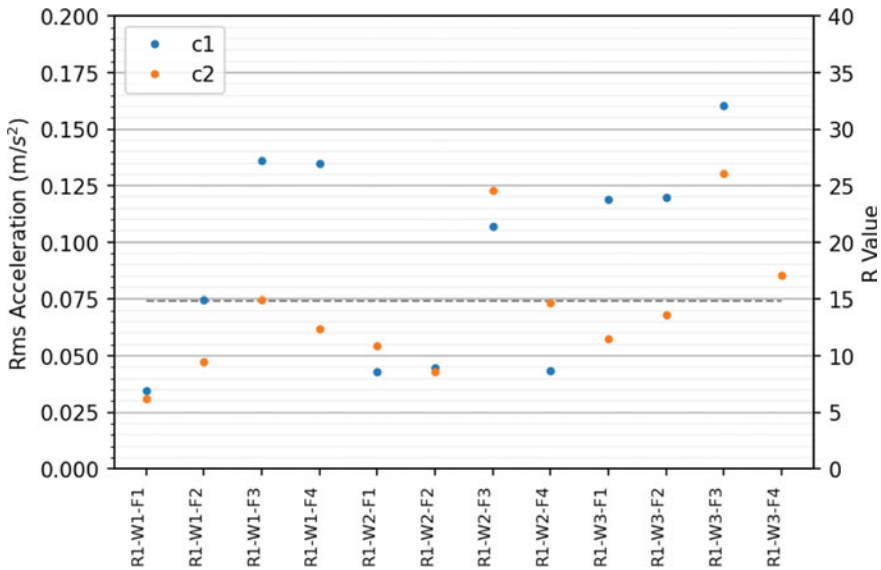
Fig. 9 Observed peak acceleration response for test group M4 for channel one (c1) and channel two (c2), with the dashed line representing the average

4 Discussions

4.1 Partial Composite Action in Mock-Up

Because the same beams and CLT panels are used for all tests, the mass and element stiffnesses are consistent across all tests. The level of composite action is the only variable impacting the stiffness of the system and thus the frequencies of each test configuration. It is observed that adding screws to the system increased by from 6.3 Hz in the bare floor to 7.4 Hz with screws at 150 mm. The fundamental frequency of the system is proportional to the square roof of the beam's stiffness, outlined in Eq. (1), and the change in stiffness added by the screws can be estimated using proportionality relationships. It is estimated that stiffness of the system was increased by approximately 40% from the baseline condition with no screws, to the final condition. Refer to Table 3 for a summary of the stiffness increase.

$$\omega_{max} \sim \sqrt{EI_{max}}, \quad \frac{EI_{max}}{EI_0} = \left(\frac{\omega_{max}}{\omega_0}\right)^2. \tag{1}$$

Predictions are also made on how much beam stiffness would increase if there was full composite action between the CLT and glulam beams. Estimates of floor stiffness are made in two states: the base state where with no composite action and a system with full composite action between the beams and CLT slab, with the CLT

Table 3 Experimentally measured changes in frequency and predicted stiffness changes

Condition	ω (Hz)	ω/ω_0	EI/EI_0
M1	6.3	1	1
M2	7	1.11	1.23
M3	7.3	1.16	1.34
M4	7.4	1.17	1.37

panel effectively functioning as a flange to the beam. Equation (2) shows the typical calculation for composite action with a specified γ factor to represent the degree of composite action [2]. Here, the area of CLT is defined as the thickness of the layers parallel to the beam span, multiplied by the effective width of the flange that is active. x_{beam} and x_{CLT} are the distance to the neutral axis from the center of the beam and CLT, respectively.

$$EI_c = EI_{beam} + EA_{beam}\overline{x_{beam}} + EI_{CLT} + \gamma E_{clt}t_{par}w_{eff}\overline{x_{CLT}}. \tag{2}$$

Note that the contribution of the CLT to the composite calculation ignores the layers of CLT perpendicular to the beam span. Table 4 summarizes the predicted mock-up effective beam stiffness, accounting for all four beams and the full width of the CLT panels. Stiffness is calculated using Eq. (2). Comparing the observed frequency change of 17% to the predicted frequency change, the beam did not achieve the stiffness of the predicted beam with full composite action. There are two explanations for this difference in stiffness: either the screws did not sufficiently increase the bond between the panel and the CLT to achieve full composite action; or sufficient stiffness was achieved to approximate a fully rigid connection, but not all of the CLT was activated as a flange due to nonlinear distributions of stress. Both options are outlined in rows three and four in Table 4. Out-of-plane effects are not considered in this assessment.

While any combination of these options is possible, it is likely that a reduced width of CLT was activated above each beam and that full composite or near full composite action was achieved. This case is considered most likely due to the diminishing change in frequency noted as additional screws were added to the system, despite a

Table 4 Predicted composite action in system

Condition	EI (MPa m^2)	Gamma factor (γ)	Activated width (%)	Stiffness ratio (EI/EI$_0$)	Frequency ratio (ω/ω_0)
No composite	249.6	0	100	1.0	1.0
Fully composite	500.6	1.0	100	2.0	1.5
Partial composite with full activated width to match in situ	350	0.4	100	1.4	1.17
Partial composite with full composite action to match in situ	350	1	32	1.4	1.17

linear increase in stiffness of the connection. Nonlinear distributions of stress causing a smaller activated width were also noted in CLT T beams in other studies [5]

4.2 Accelerations

RMS accelerations for offices are recommended to be less than 8 by the widely used CCIP floor vibration guide [6]. As noted in Fig. 9, the observed median RMS acceleration is more than double the recommended limit. This finding matched the subjective experience of the testers, who noted that the floor was the floor as "bouncy". However, the relatively high acceleration results were expected for this mock-up and not representative of the actual performance of the true floor in the building. Better performance in the building is predicted because the stiffness, mass, and damping in the true building are all expected to be higher than in the mock-up due to non-structural components. In situ floor testing on the actual building will be completed to confirm its true performance. The acceleration results from the mock-up are primarily an indication to be used for future comparisons with the actual building floor responses.

5 Conclusion

A series of vibration tests were performed on a full-scale mock-up of the long-span floor system in Fast+Epp's new home office. Testing was performed on the mock-up with no connection between the CLT slab and glulam beams, as well as screws spaced at 600 mm, 300 mm, and 150 mm, respectively. The long-span system had an estimated fundamental frequency that ranged between 6.3 Hz when there was no screws and 7.4 Hz with screws at 150 mm. This corresponded to a stiffness increased close to 40%. However, diminishing returns were noted as more screws were added, and there was no substantial change between screws at 300 mm and screws at 150 mm. Because of this, a screw spacing of 300 mm was used in the office building. It was found that the mock-up had a response factor above the limit of 8 for offices in the final mock-up condition. Future tests on the completed home office will compare to the vibration measured in the mock-up to those of the full building.

References

1. Breneman S, Zimmerman R, Gerber A, Epp L, Dickof C, Taylor A, Loasby W, Eric M, Slotboom C, McCutcheon J, Visscher R (2021) U.S. mass timber floor vibration, 1st edn. WoodWorks—Wood Products Council
2. Cuerrier-Auclair S (2020) Design guide for timber-concrete composite floors in Canada. FPInnovations
3. Ebadi MM, Doudak G, Smith I (2018) Vibration responses of glulam beam-and-deck floors. Eng Struct 156:235–242. https://doi.org/10.1016/j.engstruct.2017.11.051
4. International Organization for Standardization (ISO) (2007) ISO/TR 10137:2007—bases for design of structures—servicabiliy of buildings and walkways against vibrations, 2nd edn. International Organization for Standardization (ISO)
5. Masoudnia R, Masoudnia S (2020) Numerical investigation of effective flange width in the CLT-GLT composite T-beams. New Zealand Timber Design 27(3):7–16
6. Willford MR, Young P (2006) A design guide for footfall induced vibration of structures. In: CCIP-016. The Concrete Centre. www.concretecentre.com

Static and Dynamic Characterization of Energy-Absorbing Connections Used in Timber Assemblies Subjected to Blast Loads

Antoine Bérubé, Christian Viau, and Ghasan Doudak

Abstract This study presents the preliminary results of a research program investigating the application of energy-absorbing connections (EAC) in timber assemblies for the purpose of enhancing their energy dissipative capabilities when subjected to blast loading. Different configurations of potential EACs were designed and investigated experimentally under static and dynamic shock tube generated loading. Important blast design parameters pertaining to EACs, including yield strength, resistance curve shape, energy absorption capability and efficiency, were evaluated and quantified to assess viable and optimized EACs to be implemented into full-scale timber assemblies. An idealized model was proposed to define the load–displacement behaviour of the EAC specimens, and the applicability of the model was investigated. The research outcomes are expected to significantly improve the design and use of timber structural elements where resistance against blast loading is required.

Keywords Energy-absorbing connections · Timber assemblies · Static analysis · Dynamic analysis

1 Introduction

Past intentional and accidental explosions have highlighted the devastating effects that blast loads can have on infrastructure (i.e., 1995 Oklahoma City bombing, 2014 Lac-Mégantic rail disaster, 2020 Beirut explosion). Structures designed to resist the effects of blast explosions usually consist of reinforced concrete and structural steel structures due to their proven ability to undergo significant inelastic deformations [2, 6, 8]. Wood structures, on the other hand, are not known for their blast-resistant

A. Bérubé (✉) · G. Doudak
University of Ottawa, Ottawa, Canada
e-mail: aberu025@uottawa.ca

C. Viau
Carleton University, Ottawa, Canada

characteristic due to the material's brittle nature in flexure, shear and tension failure, and the relatively low density of the material. Recently, timber construction has gained significant momentum due to its potential to reduce the environmental impacts of the construction sector [7]. Advancements in wood manufacturing technology, accompanied by an increase in wood use in taller and larger buildings, have resulted in wood structures being at an increased risk of exposure to blast loads.

Recent research efforts have been underway to improve the performance of wood structures against blast loads by enhancing the energy dissipative capabilities. This has included typical connections such as bolts [19, 20, 15] and the use of fibre reinforced polymers [9]. However, little work has been done to enhance the energy absorption of timber structures at the connection level by using sacrificial elements such as energy-absorbing connections (EACs). The present study aims to develop and investigate the application of EACs for the purpose of increasing the blast resistance of wood assemblies. What is presented in this paper can be considered as the initial step in this process, which includes characterization of the load–displacement behaviour of selected EACs through static and dynamic testing.

2   Literature Review

2.1   Behaviour of Timber Elements Under Blast

Most of the research on timber assemblies under blast loads has focused on establishing the material properties and member behaviour under idealized boundary conditions [11, 12, 10, 17, 18] and to a lesser degree realistic boundary connections, such as bearing angles [3, 19], self-tapping screws [3, 4, 13, 15], and bolted connections [15, 20]. The behaviour of timber elements has been established as linear-elastic and brittle, with relatively low strength capacity in the post-peak region [18, 17]. Bolted connections designed to yield were shown to improve the overall performance of the timber system due to the added ductility from bolt yielding and wood crushing [20, 15]. The yielding of fasteners or angle brackets in bearing angle steel connections achieved better performance due to the significant deformation in the steel angles [3, 19]. Self-tapping screws used in floor slab-to-wall connections through end grain experienced brittle tension perpendicular to grain splitting failure and behaved poorly [3]. However, self-tapping screws used to reinforce parallel to the grain connections offered added ductility by preventing premature splitting failures [15]. In those studies, the importance of ensuring proper failure sequence was highlighted, and it was emphasized that the over-designed connections hindered energy dissipation through fastener yielding, while poorly designed connections resulted in splitting and did not allow the load-bearing elements to reach their ultimate capacity. Although adequately designed connections showed promising results in terms of improving the blast resistance of timber assemblies, the typical timber connections

tested were limited in their ability to absorb significant amount of energy, thereby highlighting the need for the current research project.

2.2 Conceptual Design of EACs in Timber Assemblies

The use of EACs to improve the performance of structural elements is not novel (e.g. [14, 16, 23]), however, its application to blast-resistant timber assemblies has not been investigated in depth prior to this study. Viau and Doudak [21] recently investigated the application of an angle EAC in heavy-timber assemblies, and successfully demonstrated the benefit of incorporating these connections in timber structural systems. The current study further investigates the effect of EAC configuration and detailing on the overall performance of the connection and assembly as a whole.

The EACs investigated as part of this study were manufactured using mild-steel top and bottom plates separated by angles or circular hollow structural sections (HSS) (Fig. 1). The dimensions of the EACs have a direct impact on their performance, and as such, they need to be selected in conjunction with the desired overall performance of the assembly. EACs can be used to connect structural elements such as beams, columns, and walls (see Fig. 1) or can be used to connect the façade to the load-bearing structural elements. The main goal of such a system is to absorb the energy from the blast loading while imparting less energy on the timber elements.

The load–displacement behaviour of EACs can be characterized by three phases, similar to those observed in foams and honeycombs under compression [5]. Figure 2 presents a general idealized tri-linear load–displacement curve for EACs depicting the three main phases of deformation. The initial region consists of elastic deformation that is typically linear up to the yield point. A load plateau ensues and extends to a displacement correlating with the onset of densification (Δ_D). Finally, the densification region occurs once contact is attained between the EAC components, where a significant increase in stiffness and load capacity occurs.

In order to achieve the intended energy dissipation in the assembly, premature failure in the EAC, as well as the primary load-bearing timber element, need to be prevented. To achieve these design objectives, the EAC is required to be designed such that its yield load (F_y) is lower than the peak capacity of the main load-bearing element. This can be achieved by employing a probabilistic capacity-based design approach, similar to that proposed by Viau and Doudak [21], where the EAC is designed for a load that is based on the nominal capacity of the timber element while using an overstrength factor representative of the inherent variability of both the connection and timber element design parameters.

An adequately designed EAC will allow for significantly greater blast energy to be absorbed prior to loading the wood member to failure. The quantity of absorbed energy prior to densification can be interpreted as the work done by the EAC (W), obtained using Eq. 1 [5]. The displacement at the onset of densification is required for this calculation and may be approximated from the relationship between the energy
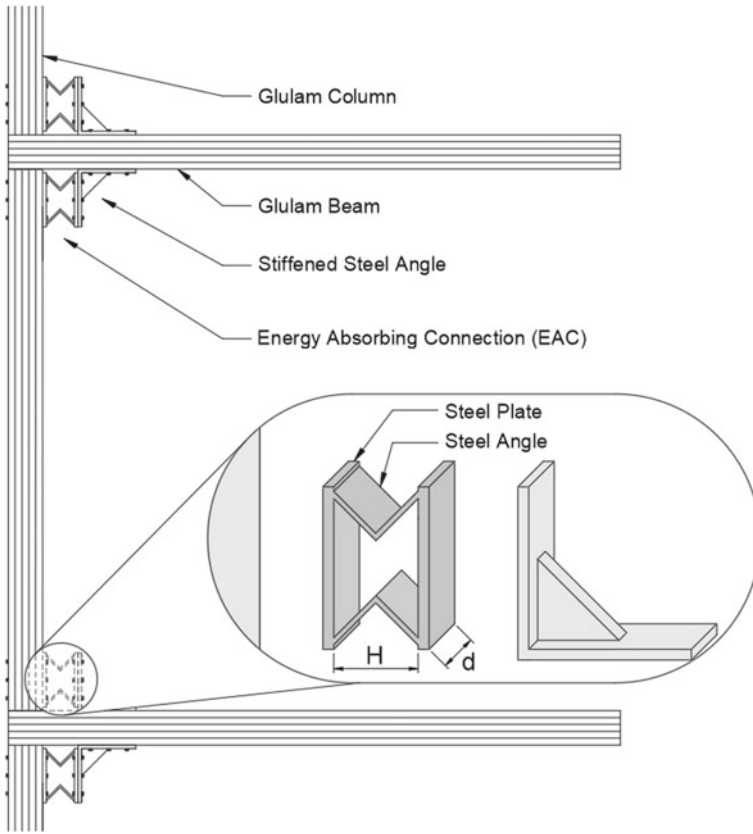
Fig. 1 Typical steel angle EAC and application within a timber assembly
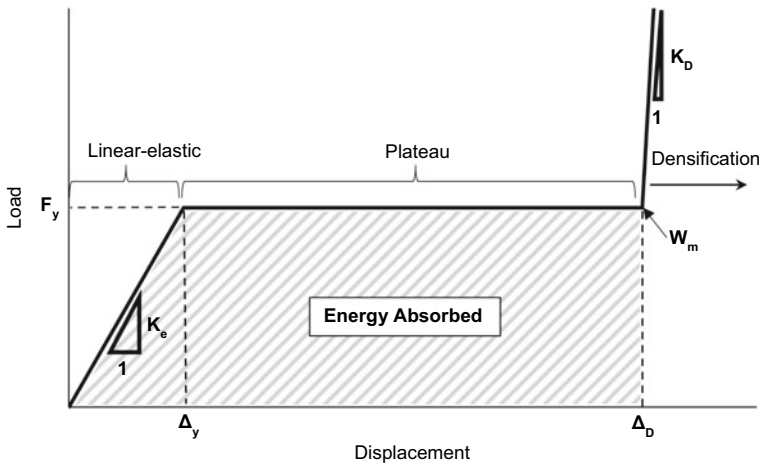
Fig. 2 Typical EAC load–displacement curve

absorption efficiency (η) and displacement. Equation 2 provides an expression to obtain the energy absorption efficiency [22].

$$W(\Delta) = \int_{0}^{\Delta_D} F(\Delta) \mathrm{d}\Delta \tag{1}$$

$$\eta(\Delta) = \frac{W(\Delta)}{F(\Delta)} \times \frac{100\%}{H} \tag{2}$$

where W is the work (energy absorbed), Δ is displacement, F is loading, Δ_D is the displacement at the onset of densification, η is the energy absorption efficiency, and H is the undeformed and maximum internal height of the EAC (see Fig. 1).

Both work and energy absorption efficiency shown in Eqs. 1 and 2 can be approximated numerically, as shown in Eqs. 3 and 4, for calculations based on tabulated experimental data.

$$W_i = W_{i-1} + F_i \times |\Delta_i - \Delta_{i-1}| \tag{3}$$

$$\eta_i = \frac{W_i}{F_i} \times \frac{100\%}{H} \tag{4}$$

where W_i, F_i, and η_i are the work, displacement, load, and energy absorption efficiency at the ith value of displacement, Δ_i, based on the measurement protocol.

2.3 Proposed Idealized Load–Displacement Curve

Although most EACs tend to follow a load–displacement curve similar to that presented in Fig. 2, the experimental behaviour typically contains some deviation from the idealized one, as illustrated in Fig. 3. To assess the experimental load–displacement curve, an idealized tri-linear load–displacement curve is proposed, including the following parameters: elastic stiffness (K_e), yield displacement (Δ_y), yield load (F_y), displacement at the onset of densification (Δ_D), maximum absorbed energy up to densification (W_m), and densification stiffness (K_D). K_e can be estimated by calculating the initial stiffness defined by the line connecting the points corresponding to 10 and 40% of the peak load. Ideally, this stiffness would represent a line connecting the initial point of the graph with the yield point; however, as can be observed in Fig. 3, the yield point may not always be well-defined. Similar to K_e, the densification stiffness (K_D) can be estimated based on a line connecting the point corresponding to the onset of densification (i.e. at Δ_D) and the last measured point on the graph. The displacement at the onset of densification (Δ_D) is calculated based on the energy absorption efficiency methodology, corresponding to the local maximum of η near the densification region (η_{max}), as shown in Fig. 3. The yield
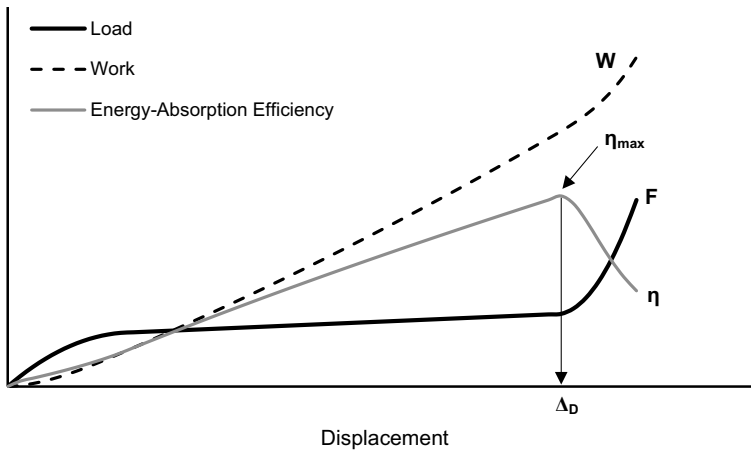
Fig. 3 Estimating Δ_D from load, work, and energy absorption efficiency displacement histories

load (F_y) and yield displacement (Δ_y) are determined such that the maximum energy absorbed by the EAC (W_m) is maintained in the idealized curve relative to the curve obtained experimentally.
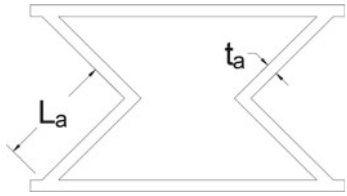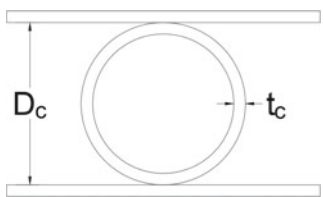
3 Experimental Program

3.1 Description of Specimens

A total of nine specimen types were selected from preliminary numerical analysis based on their load–displacement shape, level of ductility, and ability to absorb energy efficiently. Two specimen repeats were manufactured for each specimen type, resulting in a total of 36 specimens. Presented in this paper are preliminary results on tests completed on two specimen types, representing a total of eight tested specimens.

Two 300W grade, 9.525 mm thick steel plates were used for all test specimens, while varying the centre steel shapes in order to investigate the effects of EAC geometry on its load–displacement behaviour. Table 1 summarizes the specimens' dimensions and geometry. The nomenclature for the specimen repeats was designated as X–Y–Z, where X is either "A" for angular specimens or "C" for circular specimens, Y is either "S" for static tests or "D" for dynamic tests, and Z is either "1" for the 1st repeat and "2" for the 2nd repeat.

Table 1 Summary of presented test specimens

Specimen type	Description	Dimensions (mm)	Visual representation
Angular (A)	Steel angles Grade: 300W	$L_a = 76.2$ $t_a = 6.35$ $d = 50.8$	
Circular (C)	Circular HSS Grade: 1018	$D_c = 88.9$ $t_c = 6.35$ $d = 50.8$	

3.2 Static Test Setup

Compression testing of the specimens under static loading was conducted using a universal testing machine (UTM), as shown in Fig. 4. The specimens were loaded using a displacement-controlled protocol with a constant rate of 4–10 mm/min, based on the test requirement listed in ASTM E8/E8M-21 [1].

Fig. 4 Static test setup

a) Sketch · b) Example (A-D-1)
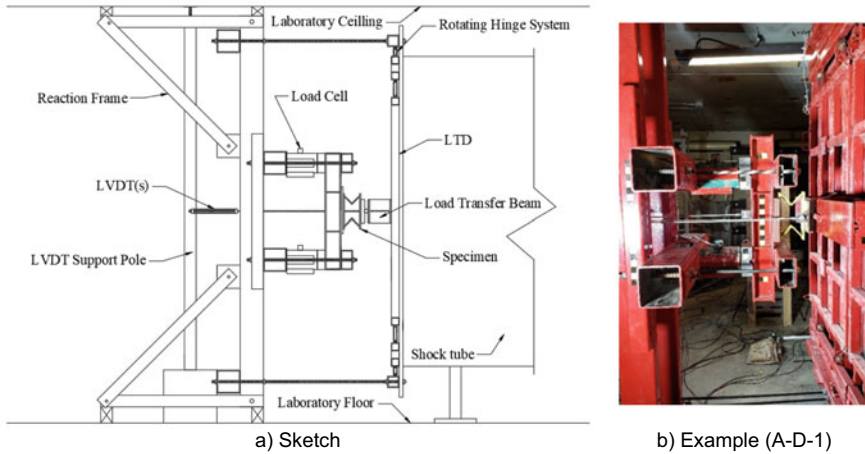
Fig. 5 Dynamic test setup

3.3 Dynamic Test Setup

The dynamic testing of the specimens was conducted using the University of Ottawa Shock Tube facility. The shock tube is a test apparatus capable of simulating the effects observed in far-field blast explosions through the generation of shock waves produced by rapidly releasing compressed air through a double diaphragm mechanism. The specimens were secured to a load-transfer device (LTD) attached at the centre of the 2032×2032 mm (80×80 in.) end frame of the shock tube (Fig. 5a and b). The LTD consists of a load-transfer beam that is capable of horizontal translation up to 200 mm through a rotating hinge system. Load cells were used to measure the reaction forces at each end of the vertical I-beams, while linear variable differential transducers (LVDT) were used to measure the translation of the vertical I-beams, specimen, and the shock tube. Two dynamic piezoelectric pressure sensors were used to measure the reflected pressure during testing. In addition, high-speed cameras were used to record and document the dynamic tests.

4 Experimental Results

The idealized parameters obtained from the load–displacement curves, using the procedure outlined in Sect. 2.2, are presented in Table 2. The experimental load–displacement curves of the angular and circular specimens are presented in Fig. 6a and b, respectively, with an example of an idealized load–displacement curve for each specimen type from the data presented in Table 2. Representative undeformed and deformed shapes of angular and circular specimens are presented in Fig. 7.

Table 2 Summary of load–displacement parameters based on experimental results

Specimen type and test	Designation	Δ_y (mm)	F_y (kN)	K_e (kN/mm)	Δ_D (mm)	W_m (J)	K_D (kN/mm)
Angle static	A-S-1	3.3	22.0	6.7	85.2	1839.1	12.0
	A-S-2	2.8	22.0	8.0	82.6	1788.6	8.2
	Average	3.0	22.0	7.4	83.9	1813.9	10.1
	CoV (%)	8.8	0.0	8.8	1.5	1.4	18.8
Angle dynamic	A-D-1	0.9	23.5	25.0	86.9	2028.9	16.6
	A-D-2	1.7	23.0	13.7	88.1	2003.5	27.0
	Average	1.3	23.3	19.4	87.5	2016.2	21.8
	CoV (%)	28.1	1.1	29.1	0.7	0.6	23.8
Circular HSS static	C-S-1	2.1	40.4	19.0	64.0	2543.9	48.6
	C-S-2	2.0	40.7	20.6	61.8	2472.4	40.1
	Average	2.1	40.6	19.8	62.9	2508.2	44.4
	CoV (%)	3.7	0.4	4.0	1.7	1.4	9.6
Circular HSS dynamic	C-D-1	1.0	30.9	30.9	57.8	1772.1	2.4
	C-D-2	1.2	32.7	26.3	59.5	1924.9	2.1
	Average	1.1	31.8	28.6	58.7	1848.5	2.2
	CoV (%)	10.7	2.8	7.9	1.5	4.1	6.5
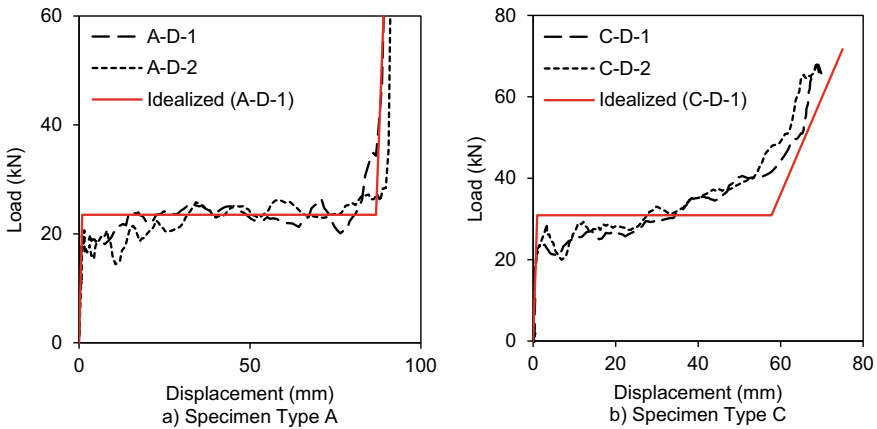
Fig. 6 Dynamic experimental load–displacement curves

a) Specimen A-S-1

b) Specimen C-S-1
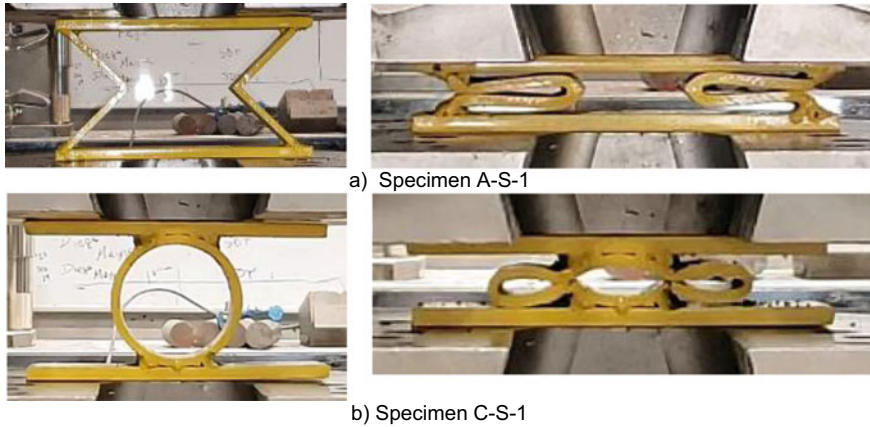
Fig. 7 Undeformed (left) and deformed shapes (right) of static specimens

5 Discussion

Based on the results from the experimental load–displacement curves, it can be observed that specimen type A had well-defined regions corresponding to the idealized behaviour outlined in this paper (see Fig. 6a). In particular, a sustained load plateau with little variation was observed for specimen type A. The static and dynamic behaviours were observed to be consistent. For specimen type C, the experimental load–displacement behaviour exhibited a more gradual increase in load following initial yield and near the densification region (see Fig. 6b). Although the idealized behaviour of specimen type C varied slightly from the observed behaviour, it captured the load–displacement behaviour for the connection reasonably well. Future analytical research studies pertaining to modelling the behaviour of EACs within a full-scale system, such as a timber assembly, will allow modelling of such connections using the idealized load–displacement curve without the need for extensive testing of EACs.

From a design perspective, the expected variation in yield strength, as observed in the experimental test results, can be quantified and used within a capacity-based design framework to develop proper overstrength factors and design methodologies, as outlined in Viau and Doudak [21]. An appropriate EAC can be selected during the design process by controlling the idealized EAC yield strength based on the EAC geometry and selecting appropriate overstrength factors that take into account the expected variations in yield strength. This process reduces the likelihood that the timber member's ultimate failure capacity is reached prior to the yielding of the EACs to an acceptable probability, thus ensuring that energy absorption occurs within the EAC.

Although the experimental results presented herein indicate that EACs can provide a large quantity of inelastic energy absorption and introduce ductility into otherwise brittle structural assemblies, further research is needed to investigate the effect of

other steel shapes and geometries on the overall behaviour. Further work is also required to demonstrate the effectiveness of EACs within full-scale assemblies.

6 Conclusions

The following conclusions can be drawn from the present study:

- Two proposed EACs were tested statically and dynamically and displayed significant potential to be used as energy-dissipating fuses.
- Specimens with angles were found to possess more consistent behaviour, when compared to the circular specimens.
- The idealized model can provide reasonable representation of the experimental load–displacement behaviour.
- When designed appropriately to account for variations in both the EAC and timber member, the use of EAC can allow for an otherwise non-ductile timber assembly to withstand greater amounts of blast energies prior to damage occurring in the timber elements.

References

1. ASTM International (2021) Standard test methods for tension testing of metallic materials. West Conshohocken, PA, USA
2. Burrell R (2012) Performance of steel fibre reinforced concrete columns under shock tube induced shock wave loading. University of Ottawa, Ottawa, ON
3. Côté D, Doudak G (2019) Experimental investigation of cross-laminated timber panels with realistic boundary conditions subjected to simulated blast loads. Eng Struct 187:444–456. https://doi.org/10.1016/j.engstruct.2019.02.009
4. Dietsch P, Brandner R (2015) Self-tapping screws and threaded rods as reinforcement for structural timber elements—a state-of-the-art report. Constr Build Mater 97:78–89. https://doi.org/10.1016/j.conbuildmat.2015.04.028
5. Gibson LJ, Ashby MF (1999) Cellular solids: structure and properties, 2nd edn. Cambridge University Place, Cambridge, UK
6. Goel MD, Matsagar VA (2014) Blast-resistant design of structures. Pract Period Struct Design Constr 19(2):04014007. Am Soc Civ Eng. https://doi.org/10.1061/(ASCE)SC.1943-5576.0000188
7. Harte AM (2017) Mass timber—the emergence of a modern construction material. J Struct Integr Maint 2(3):121–132. https://doi.org/10.1080/24705314.2017.1354156
8. Jacques E, Saatcioglu M (2020) Uncoupled compression membrane analysis of reinforced-concrete members subject to extreme loads. J Struct Eng 146(9):04020189. https://doi.org/10.1061/(ASCE)ST.1943-541X.0002736
9. Lacroix D, Doudak G (2020) Towards enhancing the post-peak performance of glued-laminated timber beams using multi-directional fibre reinforced polymers. Eng Struct 215:110680. https://doi.org/10.1016/j.engstruct.2020.110680
10. Lacroix DN, Doudak G (2015) Investigation of dynamic increase factors in light-frame wood stud walls subjected to out-of-plane blast loading. J Struct Eng 141(6):04014159. https://doi.org/10.1061/(ASCE)ST.1943-541X.0001139

11. Lacroix DN, Doudak G (2018a) Effects of high strain rates on the response of glulam beams and columns. J Struct Eng 144(5):04018029. American Society of Civil Engineers. https://doi.org/10.1061/(ASCE)ST.1943-541X.0002020.

12. Lacroix DN, Doudak G (2018b) Determining the dynamic increase factor for glued-laminated timber beams. J Struct Eng 144(9):04018160. American Society of Civil Engineers. https://doi.org/10.1061/(ASCE)ST.1943-541X.0002146

13. Lam F, Wrede MS, Yao CC, Gu JJ (2008) Moment resistance of bolted timber connections with perpendicular to grain reinforcements. In: 10th WCTE. Miyazaki, Japan

14. Lavarnway D, Pollino M (2015) Mitigation of air-blast pressure impulses on building envelopes through blast resistant ductile connectors. J Eng Archit 3(2). https://doi.org/10.15640/jea.v3n2a2

15. McGrath A, Doudak G (2021) Investigating the response of bolted timber connections subjected to blast loads. Eng Struct 236:112112. https://doi.org/10.1016/j.engstruct.2021.112112

16. Oswald C (2018) Blast testing of energy absorbing connectors for blast resistant design. Seville, Spain, pp 57–67

17. Poulin M, Viau C, Lacroix DN, Doudak G (2018) Experimental and analytical investigation of cross-laminated timber panels subjected to out-of-plane blast loads. J Struct Eng 144(2):04017197. https://doi.org/10.1061/(ASCE)ST.1943-541X.0001915

18. Viau C, Doudak G (2016) Investigating the behavior of light-frame wood stud walls subjected to severe blast loading. J Struct Eng 142(12):04016138. https://doi.org/10.1061/(ASCE)ST.1943-541X.0001622

19. Viau C, Doudak G (2019) Behaviour and modelling of cross-laminated timber panels with boundary connections subjected to blast loads. Eng Struct 197:109404. https://doi.org/10.1016/j.engstruct.2019.109404

20. Viau C, Doudak G (2021a) Behavior and modeling of glulam beams with bolted connections subjected to shock tube-simulated blast loads. J Struct Eng 147(1):04020305. https://doi.org/10.1061/(ASCE)ST.1943-541X.0002876

21. Viau C, Doudak G (2021b) Energy-absorbing connection for heavy-timber assemblies subjected to blast loads-concept development and application. J Struct Eng 147(4):04021027. https://doi.org/10.1061/(ASCE)ST.1943-541X.0002975

22. Wang Y, Pokharel R, Lu J, Zhai X (2019) Experimental, numerical, and analytical studies on polyurethane foam-filled energy absorption connectors under quasi-static loading. Thin-Walled Struct 144:106257. https://doi.org/10.1016/j.tws.2019.106257

23. Whitney MG (1996) Blast damage mitigation using reinforced concrete panels and energy absorbing connectors. Wilfred Baker Engineering Inc., San Antonio, TX

Numerical Modeling of the Bond Behavior Between Thermoplastic FRP Lattice and Concrete

A. Sabsabi, M. A. Youssef, O. El-Azizy, and M. Kamble

Abstract Replacing steel bars with fiber-reinforced polymer (FRP) bars is widely acceptable as a potential solution to eliminate the corrosion problem in reinforced concrete structures. This paper examines another option to resolve this problem, which utilizes a novel composite lattice material manufactured by WEAV3D Inc. The composite lattice is manufactured by weaving and bonding thermoplastic FRP tapes using an innovative lattice-forming process. Accurate representation of the bond between this lattice and concrete is needed to be able to utilize it in structural concrete elements. In this paper, numerical modeling of the bond between WEAV3D composite lattice and concrete is examined. The model predictions were validated using experimental data.

Keywords Thermoplastic FRP lattice · Bond behavior

1 Introduction

The thermal compatibility between concrete and steel makes steel rebars an ideal option to reinforce concrete structures. Yet, the problem of corrosion causes concerns when considering the long-term sustainability. Few alternatives were adopted by the construction industry to address this issue. Fiber-reinforced polymers (FRPs) have been the most practical option. Over the years, the continuous improvement in the

A. Sabsabi (✉) · M. A. Youssef
Civil and Environmental Engineering, Western University, London, ON N6A 5B9, Canada
e-mail: asabsabi@uwo.ca

M. A. Youssef
e-mail: youssef@uwo.ca

O. El-Azizy
Entuitive, Toronto, ON M5H 3C6, Canada

M. Kamble
WEAV3D Inc., Norcross, GA 30093, USA

Fig. 1 Composite lattice

manufacturing industry has produced wider and more economical options of FRP products (e.g., carbon, glass, basalt, etc.). A state-of-the-art lattice, produced by WEAV3D, could be a suitable concrete reinforcing alternative over traditional steel rebars. This innovative composite lattice, Fig. 1, is composed of fiber-reinforced thermoplastic tapes, which have been woven and bonded into a lattice structure using an innovative forming process.

Bond between concrete and the reinforcing material is one of the most crucial factors for reinforced concrete (RC) elements. The bond between FRP bars and concrete was found to be influenced by many factors including geometry, size, and surface conditions of the FRP rebars as well as concrete compressive strength, confinement pressure, and embedment length [13]. Bond also depends on the position of the bars and the environmental conditions [4]. An experimental study was conducted at Western University to examine the bond behavior between concrete and the composite lattice [17]. The experimental study was conducted into two stages. First, the bond behavior of single tapes, which were manufactured using different resins and fiber materials, was examined. Afterward, the bond behavior of selected composite lattices was examined. The experimental results have led to the conclusion that the bond behavior of the composite lattices is controlled by the cross-tapes. For the examined lattices, one cross-tape provided adequate anchorage for the lattices to fail in tension.

It is a common approach to model RC structures, assuming perfect bond between steel bars and concrete. However, this approach is not suitable for a new reinforcing material. Cosenza et al. [6] established that for the case of straight FRP reinforcement, the adhesion and friction components of the bond strength contribute to the pullout resistance. As the resistance due to adhesion vanishes at the instant of slipping, and mechanical interlocking was not found to have any contribution, the bond strength for this type of reinforcement is not dependent on the concrete strength. Rezazadeh et al. [16] developed a 3D FE model, using the commercial software ABAQUS [7], to simulate the bond behavior between glass FRP bars and concrete.

The bond was modeled using cohesive elements (COH3D8 element from ABAQUS library). To assess the evolution of bond damage, two damage-based approaches were introduced [16]. The model was validated using data from experimental pullout tests. A parametric study was then carried out to numerically assess the influence of critical parameters on the glass FRP bond behavior. It was concluded that concrete cover splitting failure is expected when the bars are not adequately confined by the concrete. It was also shown that increasing the concrete strength reduces the probability of having concrete cover splitting. Gooranorimi et al. [9] studied the effect of the bond action on the flexural behavior of glass FRP RC slabs. The bond behavior was defined using an experimental bond–slip relationship. It was found that a better agreement with the experimental results and more realistic predictions were obtained by incorporating the bond–slip model [9]. Another method to model the bond between reinforcing bars and concrete was explained by [10] and [18]. The bond between concrete and reinforcing bars was simulated using spring elements (i.e., translator elements from ABAQUS library). The force in the translator element was defined using Eq. 1. Results from the FE models proved that using translator elements is an efficient and simple method to model the bond behavior [10, 18].

$$F_{TR} = (C \times s \times u)/n, \tag{1}$$

where F_{TR}, C, s, u, and n are the translator force, circumference of the bars, translator spacing, bond strength, and number of translators.

The objective of the present study is to develop a reliable model to capture the bond behavior between thermoplastic FRP lattices and concrete. The following sections provide details about the developed model and its validation.

2   Material Properties

Unlike traditional FRP composites that are made of glass, carbon, aramid, or basalt fibers and thermosetting matrices (vinyl ester or epoxy resins), the proposed composite lattice utilizes thermoplastic polymers for the resin material [e.g., polypropylene, nylon, or polyethylene terephthalate glycol (PETG)]. Thermoplastic polymers are considered highly recyclable and sustainable, as they are biodegradable and can be easily reheated and remolded to form new products [3]. They have excellent corrosion resistance and are also superior to steel in terms of strength-to-weight ratio. Based on the results of single tape tests, tapes utilizing PETG resin and carbon fibers (PETG-C) were selected to from the lattice. PETG-C is a tough thermoplastic with outstanding wear properties and machinability. It also has excellent tensile and compressive strength [14]. The tapes are rectangular strips with a thickness of 0.21 mm and a width of 22 mm. According to the manufacturer data sheet, their density D is 1790 kg/m³, their tensile resistance is 1450 MPa, their Young's modulus is 101.2 GPa, and their fiber content is 38%. The concrete utilized in the experimental program by [17] had an average compressive strength of 25 MPa.

3   Finite Element Model

A finite element model was developed using ABAQUS [7] to model the bond between WEAV3D lattice and concrete. Parameters for the model were estimated based on the single tape tests, which were conducted by [17]. Then, its predictions were validated using the composite lattice tests by [17].

   Concrete was modeled using eight-node linear brick elements (C3D8R type from ABAQUS library) and the tape was modeled as a line-element (B31 type from ABAQUS library), as shown in Fig. 2. Spring translators were used to simulate bond between the tapes and the concrete. Each translator is a connector that offers a nonlinear constraint between two nodes (one on the tape and one on the concrete), which allows the two points to have different displacements in the direction parallel to the axis of the tape. A hard contact interaction was used for the direction perpendicular to the tape. Similar technique was used by [18] to model the bond between concrete and steel reinforcement in precast concrete cross-wall structures. The spring element parameters were estimated using the displacement of the unloaded sides of the single tape tests. Figure 3a shows the normalized bond stress–displacement curves for the tested PETG-C tapes, where S is the bond stress and S_u is the bond strength. These curves were simplified to a bilinear curve (Fig. 3b), with elastic and post-elastic slopes of 55 and 0.35 mm^{-1}. Based on the experimental tests, S_u can be taken equal to 1.0 MPa. This value is similar to the bond strength value for plain steel bars and smooth FRP bars [6, 8].

   The single tape tests were then analyzed to validate the assumed spring properties. Mesh sensitivity analysis was performed using four different concrete mesh sizes (elements with dimensions of 25, 15, 10, and 5 mm). The 10 mm mesh was found to be adequate. The bearing of the cylinder on the machine was modeled as a roller boundary condition (Fig. 2). The displacement readings from the experiments were applied as boundary condition at the loaded end of the tape. Figure 4 provides predictions of the ABAQUS model as compared to the experimental results. The
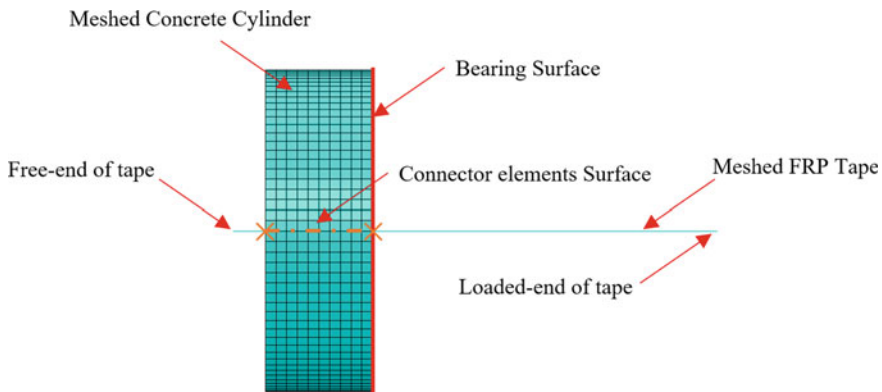
Fig. 2   Finite element model (single tape)

(a) Bond strength–slip curves

(b) Spring properties (simplified curve)
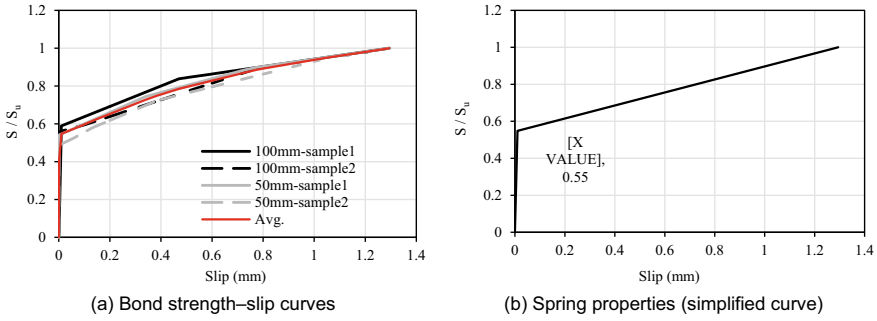
Fig. 3 Spring properties

considered tapes failed in anchorage slip and did not reach their fracture strength. Figure 5 shows the typical stress distribution in concrete at the maximum load. The principal tensile stresses in concrete are below the tensile strength of concrete, which explains the absence of cracking in the test samples [17]. Finally, the slip at the free end of the tapes was measured and compared to the values from the experiment in Fig. 6. The model has clearly predicted the bond behavior with good accuracy.

The samples with the composite lattices were then modeled, Fig. 7. The cross-tapes were assumed to be connected to the longitudinal tapes using a tie constraint. Similar to the single tape model, all tapes were connected to concrete using spring translators (from ABAQUS library). The load was applied as a displacement boundary condition at bottom tip of the tapes.

Samples with different embedment lengths and one cross-tape were selected to show the accuracy of the model. Figure 8 shows the comparison between the numerical and experimental results for these samples. The analysis was stopped when the force in the tape reached their fracture strength, as observed experimentally. It is clear that the model was able to capture the pullout behavior of the composite lattice with reasonable accuracy. The observed failure mode was tape fracture as the anchorage

(a) 100 mm embedded length

(b) 50 mm embedded length
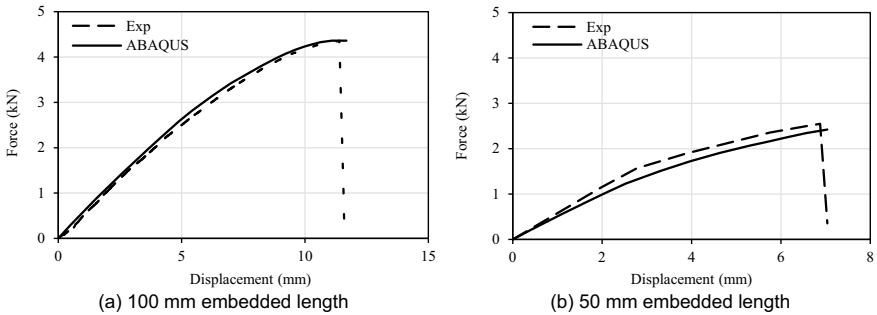
Fig. 4 Force loaded–end displacement curves
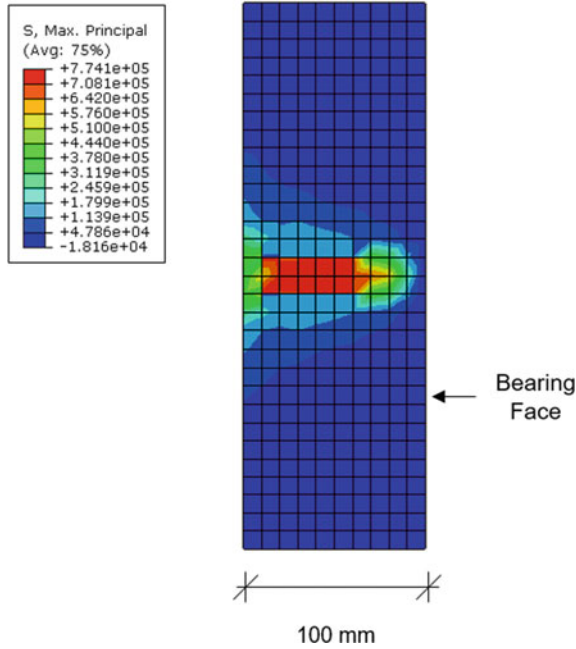
Fig. 5 Section at the middle of the cylinder showing distribution of the maximum principal stresses (Pa)
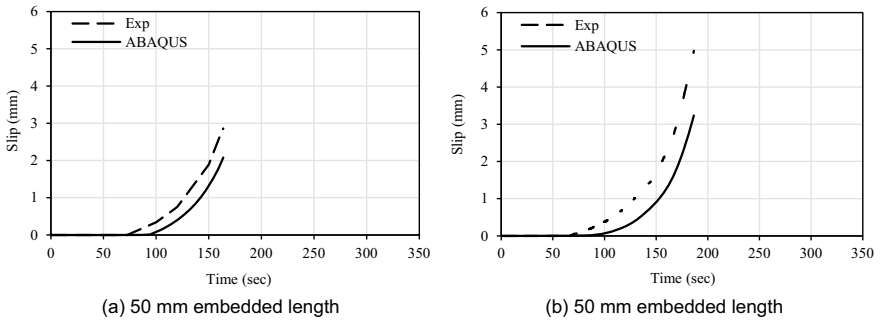
Fig. 6 Slip at the free end of the tape for the single tape tests

provided by the cross-tape prevented slippage of the tapes. Figure 9 shows a cross-section through the sample at the location of the cross-tape. It clearly shows that the tape forces are transferred to the concrete at the cross-tape location.
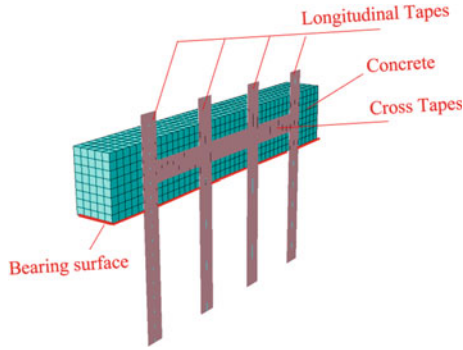
Fig. 7 Section through the FE model for the lattice test

(a) 175 mm embedded length

(b) 150 mm embedded length

(c) 100 mm embedded length
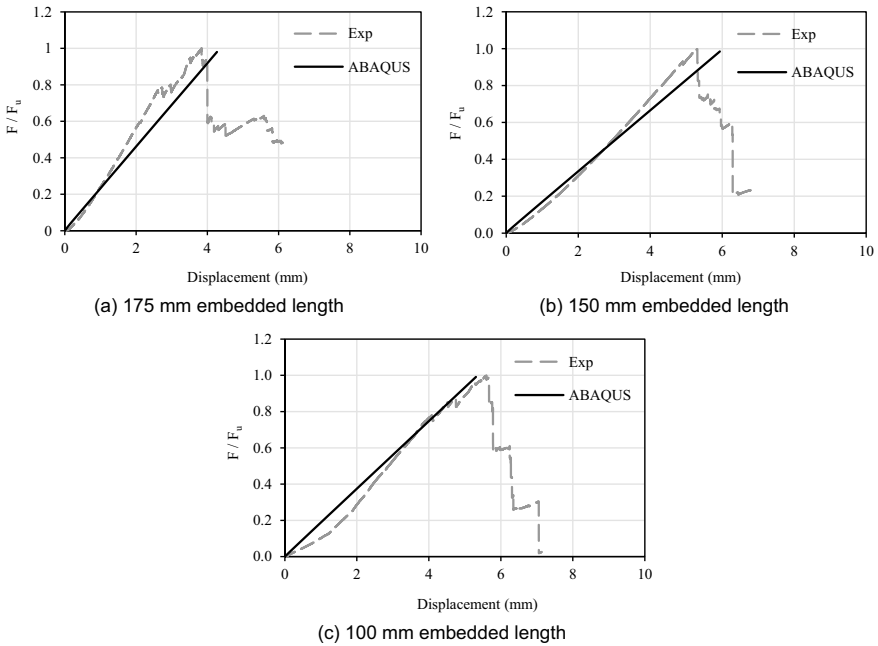
Fig. 8 Force displacement curve of the lattice samples with one cross-tape

4 Conclusions

The aim of this paper is to examine the bond between concrete and a state-of-the-art fiber-reinforced polymer (FRP) lattice developed by WEAV3D. A FE model was developed using the commercial software ABAQUS to model the bond between the FRP lattice and concrete. The model parameters were defined using results of single tape tests. The model predictions were then validated using the results of lattice-bond

Fig. 9 Maximum stresses in the concrete (Pa) at the cross-tape level
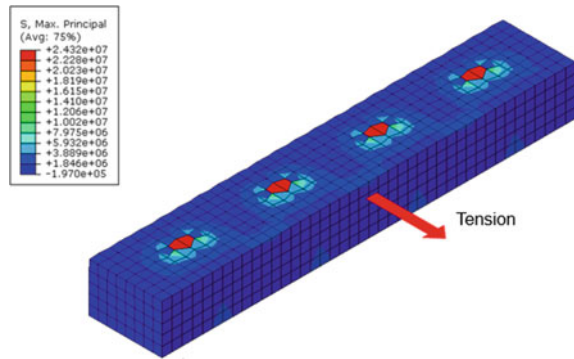
tests. The model provided reasonable accuracy in predicting the bond behavior of single and lattice pullout tests. It highlighted the role played by the cross-tapes in anchoring the lattice in the concrete samples. To confirm the model accuracy, further studies are being conducted to check the validity of the model considering different parameters and loading conditions.

References

1. ASTM International, ASTM D7913/D7913M-14 (2014) Bond strength of fiber-reinforced polymer matrix composite bars to concrete by pullout testing. ASTM International: West Conshohocken, PA, USA
2. ASTM International, ASTM C94/C94M-21b (2021) Standard specification for ready-mixed concrete. ASTM International: West Conshohocken, PA, USA
3. Baillie C, Jayasinghe R (eds) (2004) Green composites: polymer composites and the environment. Elsevier
4. Belarbi A, Wang H (2012) Bond durability of FRP bars embedded in fiber-reinforced concrete. J Compos Constr 16(4):371–380
5. Chindaprasirt P, Boonbamrung T, Poolsong A, Kroehong W (2021) Effect of elevated temperature on polypropylene fiber reinforced alkali-activated high calcium fly ash paste. Case Stud Construct Mater 15:e00554
6. Cosenza E, Manfredi G, Realfonzo R (1997) Behavior and modeling of bond of FRP rebars to concrete. J Compos Constr 1(2):40–51
7. Dassault S (2017) Abaqus 6.14 documentation. Systemes Simulia Providence, Rhode Island, US, p 1146
8. Feldman LR, Bartlett FM (2007) Bond stresses along plain steel reinforcing bars in pullout specimens. ACI Struct J 104(6):685
9. Gooranorimi O, Claure G, Suaris W, Nanni A (2018) Bond-slip effect in flexural behavior of GFRP RC slabs. Compos Struct 193:80–86
10. Issa CA, Masri O (2015) Numerical simulation of the bond behavior between concrete and steel reinforcing bars in specialty concrete. Int J Civil Environ Eng 9(6):767–774

11. Jabarin SA, Lofgren EA (1984) Thermal stability of polyethylene terephthalate. Polym Eng Sci 24(13):1056–1063
12. Kattan M, Dargent E, Ledru J, Grenet J (2001) Strain-induced crystallization in uniaxially drawn PETG plates. J Appl Polym Sci 81(14):3405–3412
13. Lin X, Zhang YX (2014) Evaluation of bond stress-slip models for FRP reinforcing bars in concrete. Compos Struct 107:131–141
14. Marcauteanu C, Stoica ET, Bortun C, Negrutiu ML, Sinescu C, Tudor A (2014) Advantages of a polyethylene terephthalate glycol-modified coated with a thermoplastic polyurethane as an occlusal appliance material. Rev Chim (Bucharest) 65:734
15. Rachtanapun P, Selke SEM, Matuana LM (2004) Effect of the high-density polyethylene melt index on the microcellular foaming of high-density polyethylene/polypropylene blends. J Appl Polym Sci 93(1):364–371
16. Rezazadeh M, Carvelli V, Veljkovic A (2017) Modelling bond of GFRP rebar and concrete. Constr Build Mater 153:102–116
17. Sabsabi A, Youssef MA, Oberste C, Hasan A (2022) Experimental assessment of the bond behaviour between thermoplastic FRP lattice and concrete. In: Proceedings of the 11th international conference on short and medium span bridges, Toronto, July 19–22, 2022
18. Tohidi M, Janby A (2020) Finite-element modeling of progressive failure for floor-to-floor assembly in the precast cross-wall structures. J Struct Eng 146(6):04020087

Numerical Evaluation of the Cyclic Response Parameters of Steel–Concrete Composite Shear

Masoumeh Asgarpoor, Ali Gharavi, Siamak Epackachi, and Ali Imanpour

Abstract Steel–concrete (SC) composite shear walls consist of infill concrete attached to two steel faceplates using tie rods and shear studs as connectors. Despite past efforts to validate the cyclic response of SC walls numerically, there is a lack of a comprehensive numerical study to propose a unique element modeling, steel and concrete material modeling, and contact definition to simulate the seismic response of all SC walls with different geometrical shapes and loading condition accurately. This paper numerically investigates the response of a wide variety of tested SC walls available in the literature. Ten SC wall specimens are modeled in the finite element-based software LS-DYNA and subjected to combined lateral cyclic loading and constant axial loading. The results show that the hysteretic response of the simulated walls, including initial stiffness, peak strength, and post-peak strength degradation, is in good agreement with experimental test results.

Keywords Cyclic response · Steel–concrete composite shear

1 Introduction

Steel–concrete composite (SC) shear walls are gaining popularity in high-rise buildings because of their lighter wall thickness compared to that of traditional reinforced concrete (RC) walls; elimination of the need for rebars and framework for concrete, fast construction procedure; and the possibility of modular off-site construction. These walls are expected to have high performance under seismic loading due to

M. Asgarpoor · A. Gharavi
Sharif University of Technology, Tehran, Iran

S. Epackachi (✉)
Amirkabir University of Technology, Tehran, Iran
e-mail: Epackachis@aut.ac.ir

A. Imanpour
University of Alberta, Alberta, Canada

eliminating disadvantages of traditional steel and concrete shear walls, including early cracking of RC shear walls and buckling of steel plate shear walls through composite action between steel and concrete.

To date, extensive experimental studies have been conducted to investigate the seismic behavior of SC walls with a wide range of design variables. Takeda et al. tested seven in-plane SC walls under cyclic lateral loading to study the effects of steel faceplate thickness, presence or absence of shear studs, and the number of partitioning webs on the global response of SC walls [23]. Ozaki et al. experimentally investigated the influence of axial load and the presence of an opening on the overall response of SC walls under cyclic lateral loading [19]. Epackachi et al., Chang et al., and Kurt conducted experiments on rectangular low-aspect-ratio walls [8, 11, 14]. Despite the low height-to-depth ratio of tested SC walls, their behavior was governed by flexure. Alzeni tested rectangular SC walls with half-circular HSS endplates and full-circular HSS boundary elements [3]. Circular boundary elements were used to avoid stress concentration and welding fracture at the connection between rectangular web and barbells or flanges of SC walls. Nie et al. tested twelve SC walls with box boundary elements using high-strength concrete and high axial load [17]. They used stiffeners and batten plates as connectors between steel faceplates. Cho et al. and Luo et al. tested a series of rectangular SC walls to estimate their seismic capacity [9, 16]. Eom et al. performed a comparative study among isolated and coupled, rectangular, T-shaped, and flanged SC walls using different strengthening methods at the wall base to relocate the plastic hinge formation [10].

Some efforts have been made to propose a robust model for the simulation of the seismic behavior of SC walls. A set of nonlinear finite-element models on I-shaped SC walls of nuclear power plants were developed by Ali et al. using ABAQUS [1]. Rafiei et al. numerically investigated the monotonic behavior of rectangular SC walls, focusing on the effect of material strength and steel–concrete interaction parameters on the behavior of these walls [21]. Epackachi et al. numerically studied the seismic behavior of low-aspect-ratio SC walls in LS-DYNA [12]. Polat and Bruneau simulated the SC walls tested by Alzeni [3] in ABAQUS in detail and could capture the overall behavior of the walls [20]. Asgarpoor et al. numerically investigated the behavior of different concrete constitutive models in simulating the seismic behavior of RC and SC walls [4, 5, 13]. There is a lack of comprehensive numerical analyses of SC walls and proposing a robust model with specific material models and element formulations to capture all important features of these walls under cyclic loading, including pre-peak, peak, and post-peak behavior and pinching. To investigate the validity of the finite element-based model, 10 SC walls with different geometrical shapes and loading conditions are selected and modeled in LS-DYNA. The force–displacement behavior and failure modes of these walls are compared to the test observations.

2 Past Experimental Programs on SC Walls and Numerical Model

A comprehensive set of SC walls, as representatives of a wide range of tested walls, are selected for numerical validation in this study. Elevation and cross-sectional views and dimensions of tested SC walls are illustrated in Fig. 1.

The numerical model of SC walls is developed in the finite-element program LS-DYNA. A plasticity model, combined with a smeared crack constitutive model, known as Winfrith, is used for concrete modeling. Plasticity formulation is based on the Ottosen theory [18], and the smeared crack approach is developed by Broadhouse [6], which considers strength reduction in concrete after it cracks in tension. Winfrith has elastic-perfectly plastic behavior under compression, linear behavior until the peak tensile strength and linear or bilinear post-peak tensile strength reduction if strain rate effects are ignored or not, respectively. In a quasi-static loading protocol, representing the cyclic nature of seismic loads, strain rate effects are not included. Hence, a linear post-cracking response for concrete in tension is used in numerical analysis. The crack width, which is required as an input parameter to the Winfrith model, can be calculated by setting the area of the post-peak tensile curve equal to fracture energy using the CEB-FIP Model Code [7]. The minimum principal strain is assumed to be the failure strain of concrete elements under compression. Once the
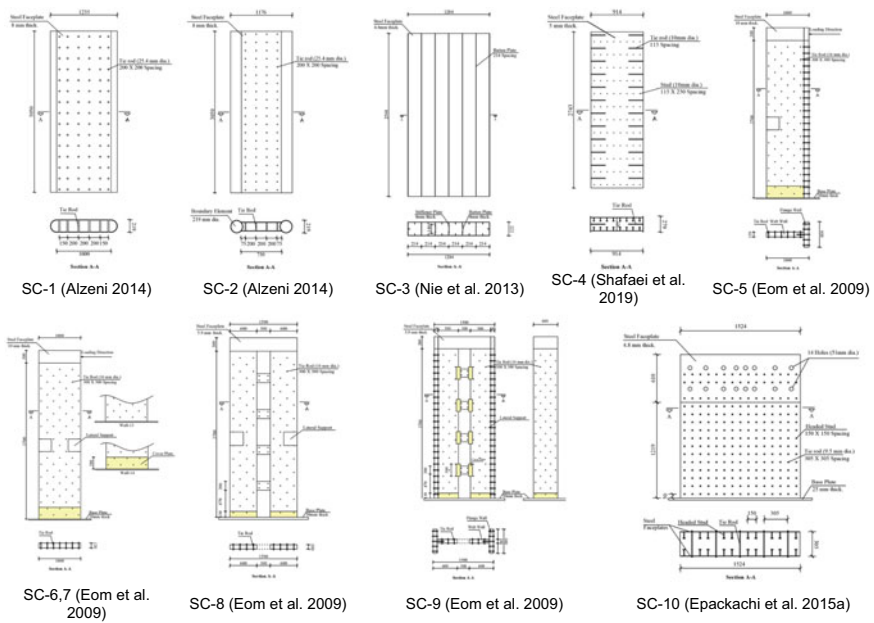
Fig. 1 Elevation and cross-sectional views of SC walls (all values in mm)

minimum principal strain of one concrete element reaches the threshold value, the element erodes and no more contributes to the strength and stiffness of the structure.

An elastic-plastic model, known as plastic kinematic material, is used for steel modeling. Both kinematic and isotropic hardening rules are available by setting the value of parameter β equals 0 or 1, respectively, or a value between 0 and 1 for the mixed hardening rule (LS-DYNA 2013). Young's modulus and tangent modulus are two other input parameters for the plastic kinematic material model. The effective plastic strain at which the steel element loses its strength can be specified as failure strain (FS). It contributes to the post-peak strength degradation observed in force–displacement results of experiments.

Concrete and baseplate elements are modeled using eight-noded solid elements with reduced integrated (RI) formulation, which considers average stress in the mid-point of the elements. Zero energy deformation modes that might be produced in elements with RI formulation need to be prevented using proper hourglass type and coefficient (LS-DYNA 2013). In this study, Flanagan–Belytschko hourglass (type 5) with a coefficient value of 0.05 is applied to all solid elements. Steel elements are modeled using four-noded shell elements with Belytschko–Tsay formulation (LS-DYNA 2013). Connectors, including tie rods and shear-headed studs, are modeled using beam elements with Hughes–Liu formulation (LS-DYNA 2013).

An automatic-surface-to-surface contact is defined between the concrete and steel faceplates to prevent any penetration of nodes into each other and enable the force transfer according to friction coefficient. Also, the shell nodes at the wall base are tied to the nodes of the baseplate elements to consider the rigid connection between steel faceplates and baseplate. Full bonding is assumed between the connector and concrete elements using Constraint Lagrange in Solid technique.

3 Validation Study

The numerical model is validated using 10 SC walls subjected to cyclic loading. The force–displacement responses of FE model are compared to experimental results (Test) in Fig. 2. The predicted responses are in good agreement with the test results, which indicates that the numerical procedure works well for modeling different types of SC walls, including rectangular and T shaped, with and without endplates or boundary elements, isolated and coupled walls. The initial stiffness of SC walls significantly depends on the type of wall base to foundation connection. The initial stiffness of the numerical model is calibrated to test data using vertical linear springs with a constant stiffness at the base of walls in which uplift is observed in test specimens. Pinching due to the opening and closing of concrete cracks at different load stages can be reasonably predicted by numerical simulations.

The failure modes of tested SC walls and their corresponding numerical models are illustrated in Fig. 3. Steel faceplate buckling and fracture and concrete cracking and crushing are the most common failure modes of SC walls. Plastic hinges are concentrated over a region near the base of the walls, as shown in both test specimens

SC-1

SC-2

SC-3

SC-4

SC-5

SC-6

SC-7

SC-8

SC-9

SC-10
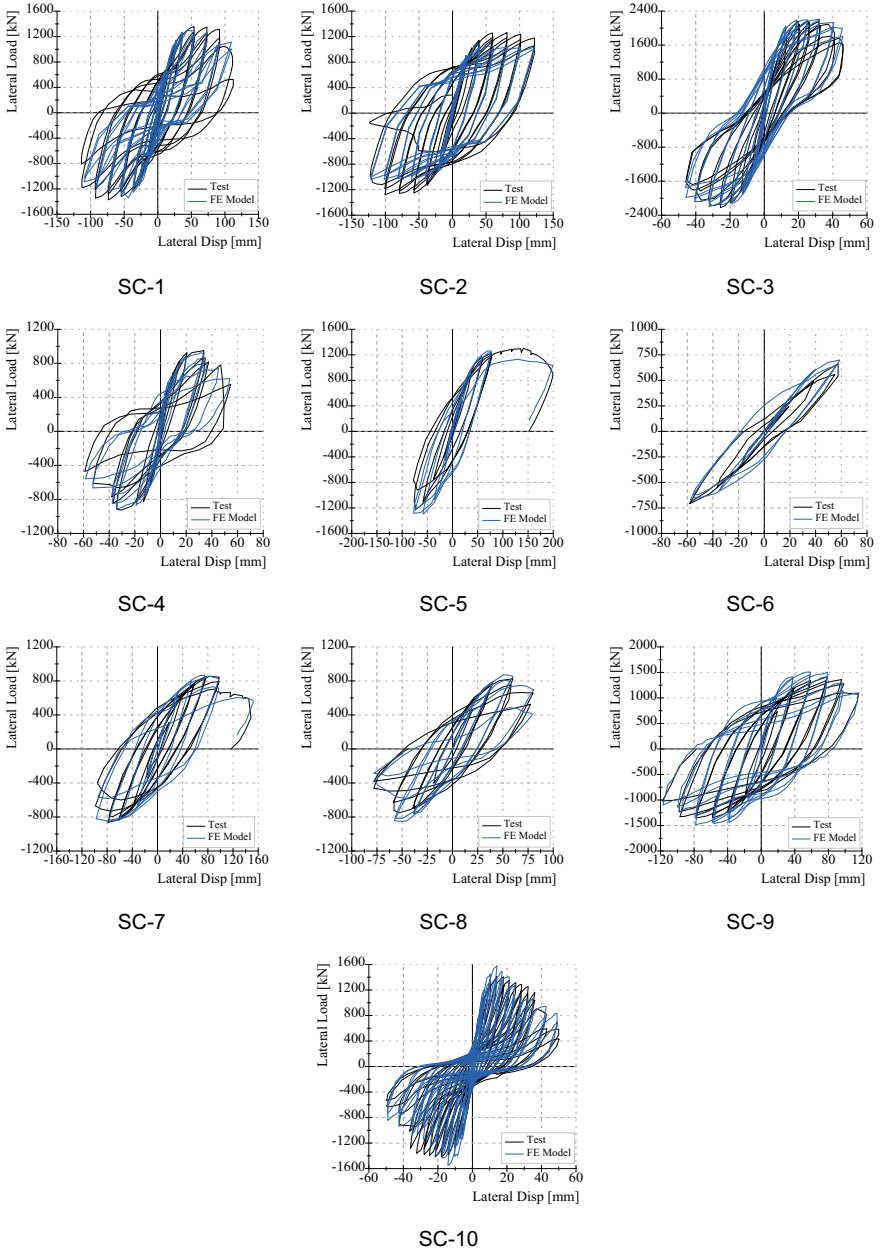
Fig. 2 Test versus predicted force–displacement cyclic response

and numerical models. Shell elements used for modeling the steel faceplates can reasonably simulate the buckling of steel faceplates and fail once the effective plastic strain of elements reaches the specified values. Winfrith's concrete model is capable of showing crack patterns on deformed shaped elements, which is a unique feature of this material model and is not implemented in other concrete material models in LS-DYNA.
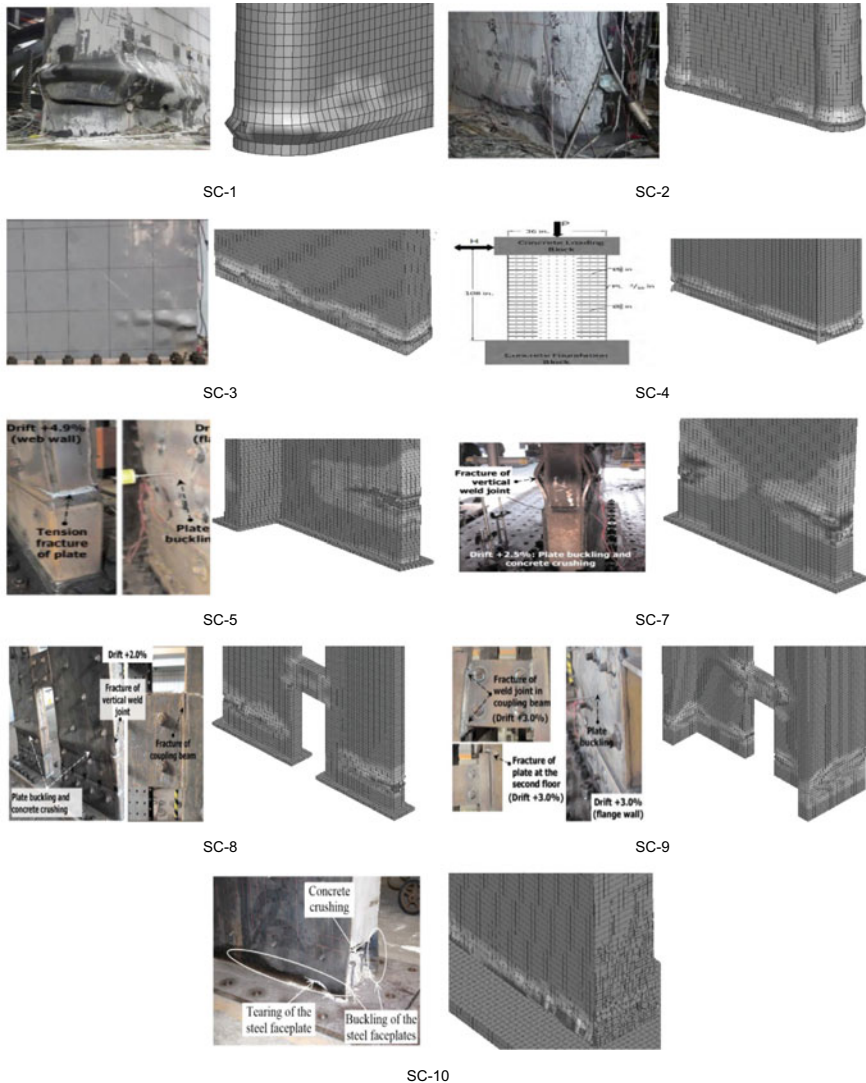
Fig. 3 Test versus predicted failure modes

4   Conclusions

A large set of SC walls, including rectangular, T-shaped, and flanged walls, isolated and coupled walls, with and without endplates and boundary elements, were numerically modeled in the finite element-based program LS-DYNA. The cyclic response parameters and failure modes of the SC wall models were presented and discussed. The results were in good agreement with those obtained from experimental testing of identical walls, which suggests the capability of the numerical modeling technique used here to predict the cyclic response of SC walls.

References

1. Ali A, Kim D, Cho SG (2013) Modeling of nonlinear cyclic load behavior of I-shaped composite steel-concrete shear walls of nuclear power plants. Nucl Eng Technol 45:89–98
2. Alzeni Y (2014) Cyclic inelastic behavior of concrete filled sandwich panel walls subjected to in-plane flexure. State University of New York at Buffalo
3. Alzeni Y, Bruneau M (2014) Cyclic inelastic behavior of concrete filled sandwich panel walls subjected to in-plane flexure. Technical Rep MCEER 14:9
4. Asgarpoor M, Gharavi A, Epackachi S (2021a) Investigation of various concrete materials to simulate seismic response of RC structures. In: Structures. Elsevier, pp 1322–51
5. Asgarpoor M, Gharavi A, Epackachi S, Mirghaderi SR (2021b) Finite element analysis of rectangular and flanged steel-concrete shear walls under cyclic loading. Struct Design Tall Spec Build 30:e1863
6. Broadhouse BJ (1986) DRASTIC: a computer code for dynamic analysis of stress transients in reinforced concrete. UKAEA Atomic Energy Establishment
7. CEB-FIP (2010) Model code 2010. Comite Euro-International du beton
8. Cheng C, Zhou D (2015) Experimental study on seismic behavior of composite concrete and double-steel-plate shear walls with binding bars. In: 6th International conference on advances in experimental structural engineering and 11th international workshop on advanced smart materials and smart structures technology, August 1–2. University of Illinois Urbana-Champaign, United States
9. Cho SG, Park W-K, So G-H, Yi S-T, Kim D (2015) Seismic capacity estimation of steel plate concrete (SC) shear wall specimens by nonlinear static analyses. KSCE J Civ Eng 19:698–709
10. Eom T-S, Park H-G, Lee C-H, Kim J-H, Chang I-H (2009) Behavior of double skin composite wall subjected to in-plane cyclic loading. J Struct Eng 135:1239–1249
11. Epackachi S, Nguyen NH, Kurt EG, Whittaker AS, Varma AH (2015a) In-plane seismic behavior of rectangular steel-plate composite wall piers. J Struct Eng 141:04014176
12. Epackachi S, Whittaker AS, Varma AH, Kurt EG (2015b) Finite element modeling of steel-plate concrete composite wall piers. Eng Struct 100:369–384
13. Gharavi A, Asgarpoor M, Epackachi S (2022) Evaluation of plasticity-based concrete constitutive models under monotonic and cyclic loadings. Struct Design Tall Spec Build 31:e1919
14. Kurt E, Whittaker A, Varma A, Booth P (2013) SC wall piers and basemat connections: numerical investigation of behavior and design. In: Transactions, SMiRT-22. San Francisco, California
15. LS-DYNA, LSTC (2013) Keyword user's manual. Livermore Software Technology Corporation, vol II
16. Luo Y, Guo X, Li J, Xiong Z, Meng L, Dong N, Zhang J (2015) Experimental research on seismic behaviour of the concrete-filled double-steel-plate composite wall. Adv Struct Eng 18:1845–1858

17. Nie JG, Hu HS, Fan JS, Tao MX, Li SY, Liu FJ (2013) Experimental study on seismic behavior of high-strength concrete filled double-steel-plate composite walls. J Construct Steel Res 88:206–19

18. Ottosen NS (1977) A failure criterion for concrete. Am Soc Civil Eng, J Eng Mech Div 103:527–35

19. Ozaki M, Akita S, Osuga H, Nakayama T, Adachi N (2004) Study on steel plate reinforced concrete panels subjected to cyclic in-plane shear. Nucl Eng Des 228:225–244

20. Polat E, Bruneau M (2017) Modeling cyclic inelastic in-plane flexural behavior of concrete filled sandwich steel panel walls. Eng Struct 148:63–80

21. Rafiei S, Hossain KMA, Lachemi M, Behdinan K, Anwar MS (2013) Finite element modeling of double skin profiled composite shear wall system under in-plane loadings. Eng Struct 56:46–57

22. Shafaei S, Kizilarslan Bruneau M, Varma EA, Broberg M, Seo J (2019) R-factors for coupled composite plate shear walls/concrete filled (CC-PSW/CF). Prepared for Charles Pankow Foundation and American Institute of Steel Construction

23. Takeda T, Yamaguchi T, Nakayama T, Akiyama KZ, Kato YZ (1995) Experimental study on shear characteristics of a concrete filled steel plate wall. In: Transactions, SMiRT-13. Brazil

Amplification of Seismic Loads on Cold-Formed Steel Mid-Rise Podium Structures

Daniel Lahey and Lei Xu

Abstract Increasingly, cold-formed steel framing (CFS) is appended to reinforced concrete or structural steel podiums, forming structures with a vertical combination of seismic force-resisting systems (SFRS). These systems are vertically irregular and so often must be analysed dynamically according to National Building Code of Canada (NBCC) provisions. Amplification may occur in the CFS structure such that static methods underestimate the upper structure's seismic base shear. However, while simplified methods such as the ASCE 7 two-stage analysis procedure may apply in certain cases, NBCC 2015 provides no simplified methods for irregular structures more than 20 m in height. This paper investigates the two-stage assumption as applied to these structures. The results are generalized using an equivalent 2DOF model and quantified in terms of amplification factor α_U. Two examples are developed satisfying the ASCE 7–16 two-stage procedure using NBCC 2015 design parameters. The applicability of the two-stage procedure is discussed, and it is proposed that the ratio of α_U in an MDOF and a 2DOF model, $\alpha_{U,MDOF}/\alpha_{U,2DOF}$, may be used to gauge the applicability of the two-stage procedure.

Keywords Seismic loads · Cold-formed steel mid-rise podium structures

1 Introduction

For both new construction and retrofit, designers often look to irregular forms to achieve design objectives. In the case of mid-rise, mixed-use development, podium-tower structures featuring different seismic force-resisting systems (SFRS) in the tower and podium are increasingly common. In residential-commercial mixed-use, a cold-formed steel (CFS) tower with a reinforced concrete (RC) podium is common—whereas RC allows large spans and higher capacity for commercial uses, CFS frames are lighter and less costly (and therefore ideal for residential units). However, North

D. Lahey · L. Xu (✉)

University of Waterloo, Waterloo, Canada

e-mail: lxu@uwaterloo.ca

American seismic codes have long recognized the challenge posed by vertical irregularities of mass and stiffness, which can reduce the accuracy of the National Building Code of Canada (NBCC) 2015 equivalent static force procedure (ESFP) [12]. Still, podium-tower structures with a much stiffer podium (relative to the tower) may be designed statically in certain scenarios. To do so, designers must distinguish between three cases characterized by [6]: (1) where the base predominates, (2) where the tower segment predominates and (3) intermediate scenarios where amplification may occur due to modal interaction as the tower becomes more dominant. The first case is relevant—where the base is sufficiently dominant, a static, two-stage procedure may be applicable.

Designers familiar with ASCE 7–16 may know its two-stage procedure, first introduced in 1988 Uniform Building Code (UBC)/1988 Structural Engineers Association of California (SEAOC) Blue Book and later incorporated into ASCE 7 [3, 10, 13]. Provided the podium is 10 times stiffer than the tower and that the tower's first mode period is almost that of the full structure ($T_1 \leq 1.1T_U$), ASCE 7 allows a designer to perform static calculations for the tower and podium separately and then combine the loads for design purposes. Likewise, while not in the code body, the commentary of NBCC 2015 mentions a similar possibility in the context of wood shear wall frames atop stout RC structures [11]. Thus, Canadian designers may be tempted to mimic the ASCE 7 approach. However, while the phenomenon exists, the conditions underlying it are not explicit. To apply such a method is to assume that modes are well-separated, and that the upper structure's base shear is not amplified (i.e. the lower structure is rigid enough to act as a fixed base for the upper structure).

However, there are no conclusive two-stage criteria. The ASCE's limit is simple but anecdotal, with no apparent research background. Instead, Yuan and Xu [15–18] and [7] argue that a more stringent limit characterized by the overall stiffness and mass ratios between the upper and lower structures should be applied, particularly in the context of the NBCC 2015 design spectrum. In conjunction with challenges to the interpretation of ASCE clauses and modelling discussed by [1], the potential for a higher-than-expected amplification of base shears on the upper structure is increased. The two-stage concept is a fragile one, and this paper discusses several key parameters of the assumption, their implications on the ASCE 7 criteria, and other research on the topic, using the amplification factor proposed by [18] to characterize the amplification effect.

2 Formulation of Two-Stage Requirement

2.1 Model Assumptions

To discuss the ASCE 7 two-stage analysis procedure, it is advantageous to express the podium-tower structure using a simplified, more general model. First, the structure is expressed as a multiple-degree of freedom (MDOF) lumped-mass system with storey

stiffness k_U and mass m_U at each of the N_U storeys of the upper structure, and storey stiffness k_L and mass m_L at each of the N_L storeys of the lower structure. With these definitions, storey stiffness ratio $r_k = k_L/k_U$ and storey mass ratio $r_m = m_L/m_U$ can be defined. This MDOF system can be further simplified, with the upper structure and lower structure each concentrated into a single degree of freedom, producing the 2DOF model shown in Fig. 1 with parameters defined as follows [16]:

$$M_U = m_U N_U \tag{1}$$

$$K_U = \left(\overline{\omega}_{1U}\sqrt{k_U/m_U}\right)^2 M_U \tag{2}$$

$$M_L = m_L N_L \tag{3}$$

$$K_L = \left(\overline{\omega}_{1L}\sqrt{k_L/m_L}\right)^2 M_L \tag{4}$$

$$R_m = M_L/M_U = r_m N_L/N_U \tag{5}$$

$$R_k = K_L/K_U = r_k(N_L/N_U)(\overline{\omega}_{1L}/\overline{\omega}_{1U})^2, \tag{6}$$

where R_k and R_m are the overall stiffness and mass ratio (analogous to r_k and r_m), and M_U, K_U, M_L and K_L are the equivalent masses and stiffnesses associated with the upper and lower DOFs. $\overline{\omega}_{1L}$ and $\overline{\omega}_{1U}$ are the normalized first mode circular frequencies of an N_L (or N_U) DOF structure. For a structure having equal mass and equal stiffness at each DOF, the value of the stiffness and mass can be factored out of the eigenvalue problem for free vibration by assuming that the nth-mode circular frequency can be expressed as ($\omega_n = \overline{\omega}_n\sqrt{k/m}$). $\overline{\omega}_1$, the first eigenvalue corresponding to a structure with unit mass and stiffness at each DOF can therefore be used to determine ω_1 of any uniform structure. The first 12 values appear in Table 1.

It is also assumed for any general conclusions that $1 \leq r_m \leq 5$ and $1 \leq r_k \leq 20$, $N_L + N_U \leq 12$ and that the first mode period of a single storey of the upper

Fig. 1 MDOF and simplified 2DOF model of podium-tower structure [16]

(a) MDOF model　　　(b) 2DOF model
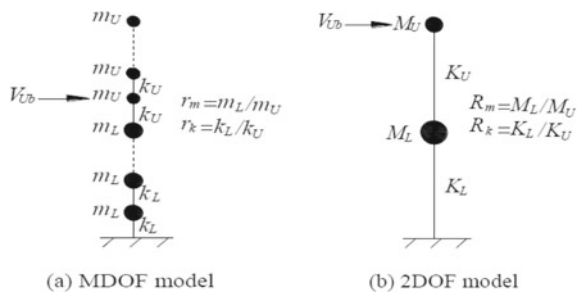
Table 1 Normalized first mode circular frequency of uniform structures

N	1	2	3	4	5	6	7	8	9	10	11	12
$\overline{\omega}_1$	1	0.618	0.445	0.347	0.285	0.241	0.209	0.185	0.165	0.150	0.137	0.126

structure, $T_{\text{singU}} = 2\pi\sqrt{k_U/m_U} \leq 0.22$ seconds for any conclusions. As $S_a(T_U)$ is used to define the spectral acceleration, the results correspond to soil class C defined by NBCC 2015.

2.2 Definition of Upper Structure Amplification

Having established the MDOF and 2DOF models, the base shear of the upper structure and corresponding amplification factor can be expressed as in [18]:

$$V_{Ub} = \alpha_U m_U N_U S_a(T_U)/(R_d R_o) \tag{7}$$

$$\alpha_U = V_{Ub}/(m_U N_U S_a(T_U)) \tag{8}$$

$$T_U = 2\pi\sqrt{M_U/K_U} = (2\pi/\overline{\omega}_{1U})\sqrt{k_U/m_U} \tag{9}$$

$$T_L = 2\pi\sqrt{M_L/K_L} = (2\pi/\overline{\omega}_{1L})\sqrt{k_L/m_L}, \tag{10}$$

where V_{Ub} is the base shear of the upper structure, α_U is the base shear amplification factor for the upper structure and T_U and T_L are the first mode periods of the upper and lower structures. These equations are defined per the NBCC 2015 spectral relationship $S_a(T)$, and inelastic modification factors for ductility and overstrength, R_d and R_o. As written, α_U is defined similarly to the higher-mode amplification factor, M_v, specified in NBCC 2015, albeit exclusively applied to the base shear of the upper structure.

In the 2DOF representation, the dynamic characteristics lend themselves to further simplification (2015):

$$T_{1,2DOF} = \sqrt{\frac{8\pi^2 R_m}{R_k + R_m + 1 - \sqrt{(R_m - R_k - 1)^2 + 4R_m}}\left(\frac{M_U}{K_U}\right)} \tag{11}$$

$$T_{2,2DOF} = \sqrt{\frac{8\pi^2 R_m}{R_k + R_m + 1 + \sqrt{(R_m - R_k - 1)^2 + 4R_m}}\left(\frac{M_U}{K_U}\right)} \tag{12}$$

$$\phi_{L1} = \left[R_m - R_k - 1 + \sqrt{(R_m - R_k - 1)^2 + 4R_m}\right]/[2R_m] \tag{13}$$

$$M_{U1} = (R_m \phi_{L1} + 1)/(R_m \phi_{L1}^2 + 1) \qquad (14)$$

$$M_{U2} = 1 - M_{U1} \qquad (15)$$

$$\alpha_{U,2DOF} = \sqrt{(M_{U1} S_a(T_1)/S_a(T_U))^2 + (M_{U2} S_a(T_2)/S_a(T_U))^2}, \qquad (16)$$

where $T_{1,2DOF}$ and $T_{2,2DOF}$ are the first and second mode periods of the 2DOF model, M_{U1} and M_{U2} are the effective modal masses of the upper structure in the first and second modes, normalized with respect to M_U, and ϕ_{L1} is the first mode shape ordinate at the lower DOF where the other DOF is taken as unity. These parameters are derived from the 2DOF model eigenvalue problem using the definitions of R_m and R_k and in combination are used to calculate $\alpha_{U,2DOF}$, the 2DOF value of the upper base shear amplification factor via square-root-sum-of-squares (SRSS). $\alpha_{U,MDOF}$ therefore analogously describes the value considering all modes in the MDOF model.

2.3 Physical Interpretation of Two-Stage Scenario and Existing Limits

While included for many years as a part of the UBC, SEAOC Blue Book and in ASCE 7–16, the two-stage procedure's period and stiffness limits historically appear without discussion of the expected dynamic behaviour characterizing podium structures [3, 10, 13]. The premise that the stiffness requirement corresponds to a stiff lower structure has been made explicit in the recent SEAOC Blue Book [14], but the period requirement is not explicitly discussed.

The criteria set out in ASCE 7–16 are interpreted herein as follows:

1. The stiffness requirement ensures that the lower structure is sufficiently stiff, such that the upper structure acts as though fixed at its base, consistent with SEAOC commentary [14].
2. Where the fundamental periods of the upper structure and the full structure are approximately equal, the upper structure is dominated by the first mode as assumed by equivalent static procedures.

In the context of the factor α_U, the premise of the two-stage assumption is that $\alpha_U \approx 1$. This implies that the upper structure acts as if it is fixed directly to the ground. In other words, there is no modal interaction between the lower and upper structures when the two-stage criteria are satisfied. However, previous research by Yuan and Xu [15–18] and [7] suggests that the limits of ASCE 7–16 may lead to unconservative designs in certain cases. Per [7], this is also true of the more limited scenario for wood-RC combinations discussed by NBCC 2015's commentary.

In place of the ASCE 7–16 criteria, both Yuan and Xu and Chen and Ni specify a similar lower bound on R_k in terms of R_m, despite a different approach. As culminating in [16], the Yuan and Xu approach is based on the lumped-mass models shown in Fig. 1 and employs code-specified linear modal response spectrum analysis (MRS) to identify the bounds on dynamic parameters corresponding to the two-stage scenario. Rather than working with specific materials, the model is characterized in terms of stiffness and mass. Conversely, [7] begin with a set of wood frames designed according to NBCC 2015's static procedure. These frames are appended to a set of concrete structures, and the combined structures are analysed with nonlinear dynamic analysis. Each then proposes an empirical two-stage requirement: Yuan and Xu's is based on a theoretical solution satisfying ASCE 7–16's limits and assumed limits on modal mass, and Chen and Ni base theirs on the satisfaction of an interstorey drift objective.

The ASCE 7 [3], Yuan and Xu [15–18] and [7] limits can all be expressed in terms of R_k and R_m as in Eqs. (17a), (17b), (19) and (20), while the NBCC criteria (18) are expressed in terms of r_k and only applicable to wood-RC structures in which the lower structure is not more than two storeys tall (NRCC, 2015a). Owing to the limitations of the NBCC criteria, they are not discussed further in this paper.

$$\begin{cases} T_1/T_U \leq 1.1 \\ R_k \geq 10 \end{cases} \tag{17a}$$

$$\cong R_k \geq \max(0.826R_m + 4.76, 10) \tag{17b}$$

$$r_k \geq 3 \text{ and } N_L \leq 2 \tag{18}$$

$$R_k \geq 10R_m \tag{19}$$

$$R_k \geq \begin{cases} 1.637R_m + 9.07 & R_m \leq 1.23 \\ 11.029R_m - 2.5 & R_m > 1.23 \end{cases} \tag{20}$$

In the above, R_k, R_m, r_k and N_L are defined as in Sect. 2.1, and the ASCE 7 period criterion has been interpreted in terms of R_k and R_m as in [15] and [16] for comparison to the other methods. This is demonstrated in Appendix 1.

The limits shown in Fig. 2 can be divided into two groups—the ASCE 7–16 limits and those proposed by [18] and [7]. Using NBCC linear modal response spectrum analysis to assess the response of the MDOF model for various configurations, the [17] and [7] limits correspond to the following conditions in addition to those related to ASCE 7:

- $\alpha_{U,2DOF} \leq 1.15$ and $0.85 \leq \alpha_{U,MDOF}/\alpha_{U,2DOF} \leq 1.15$, indicating low amplification caused primarily by the first two modes of vibration.

Fig. 2 Comparison of existing two-stage criteria
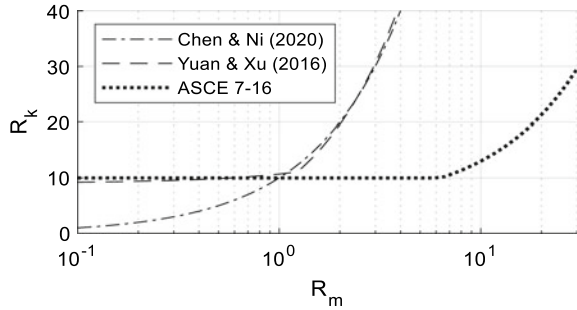
- $|M_{U2}/M_{L2}|$ and $|M_{L1}/M_{U1}| \leq 0.1$, implying the first and second modes are dominated by the modal mass of the upper and lower structures, respectively.
- $T_U \geq 3T_L$, implying the upper and lower structures' modes of vibration are well-separated.

M_{U1} and M_{U2} are the first and second normalized effective modal masses of the upper structure and M_{L1} and M_{L2} are analogous for the lower structure. The modal masses are normalized with respect to the mass of the DOF they correspond to (i.e. M_{U1} and M_{U2} are normalized with respect to M_U).

Therefore, by neglecting the mass irregularity the ASCE 7–16 limits may permit structures in which the first and higher modes of the structure interact and produce an upper base shear amplification. By incorporating the mass ratio, [17] and [7] implicitly enforce that the upper and lower structures' periods are well-separated such that the upper structure's fundamental mode period approximately matches the full structure's, while the lower structure's is similar to the full structure's second mode period. It can be demonstrated using the 2DOF model that the ratio of T_U/T_L is equal to the root of R_k/R_m:

$$\frac{T_U}{T_L} = \frac{(2\pi/\overline{\omega}_{1U})\sqrt{k_U/m_U}}{(2\pi/\overline{\omega}_{1L})\sqrt{k_L/m_L}}$$

$$= \frac{(N_L/N_U)(\overline{\omega}_{1L}/\overline{\omega}_{1U})\sqrt{r_k}}{(N_L/N_U)\sqrt{r_m}} = \sqrt{\frac{R_k}{R_m}} \qquad (21)$$

3 Design Examples

To illustrate the flaws with the ASCE 7–16 criteria, two examples are presented. Both feature mid-rise podium structures with a moderately ductile reinforced concrete moment-resisting frame (MRF) SFRS ($R_d R_o = 3.5$) for the lower structure and CFS framing with oriented strand board (OSB) sheathed shear walls ($R_d R_o = 3.4$) as the SFRS of the upper structure. Rather than a specific case study, each is hypothetical,

created to demonstrate the applicability of the ASCE 7–16's two-stage procedure and the limits proposed by [17] and [7]. In the first example, both the upper and lower structures are 3 storeys tall, while in the second example a more typical 2-storey podium with a 4-storey tower is adopted. Each are designed to the ASCE 7–16 criteria, and the second example is also designed to the [17] and [7] criteria for comparison's sake. The minimum value of $R_dR_o = 3.4$ is adopted per NBCC requirements, and the importance factor is taken as one. Interstorey heights are 3 m. Detailing is neglected, as the focus is on the overall structural behaviour.

That said, it is important to note some differences between the NBCC-based procedure here and the ASCE 7–16 two-stage procedure verbatim. Namely: (1) ASCE 7 requires that the absolute sum (ABSSUM) method be used for calculation of the lower structure's storey shears—instead, square-root-sum-of-squares (SRSS) is used here; (2) ASCE 7 uses a redundancy factor with no equivalent in the NBCC code—here, it is omitted; and (3) ASCE 7 uses different combinations of inelastic modification factors (equivalently, R_dR_o) based on the relative overstrength and ductility of the upper and lower structures—here, per NBCC recommendation, the minimum R_dR_o of the two is used. The goal is to match the intent of the two-stage provisions in NBCC application rather than the provisions themselves, particularly owing to different assumptions in defining force modification factors and design spectra in the two codes.

Both examples are located near St. Catharine's, Ontario, as the sharp difference between $S_a(0.2)$ and $S_a(5.0)$ exacerbates the amplification effect (consistent with M_v in NBCC 2015), therefore (Table 2).

The parameters of each frame are selected from MRS analysis results based on a target r_m and T_{singU}, the satisfaction of the ASCE criteria and the [17] and [7] criteria, and the calculated α_U in the lumped-mass MDOF and 2DOF models ($\alpha_{\mathrm{U,MDOF}}$ and $\alpha_{\mathrm{U,2DOF}}$). These models are then adapted into an equivalent design based on the assumed configuration of a 4 by 4 grid of columns spaced at 4.5 m for the concrete moment frame and the assumed characteristics of the CFS framing with OSB-backed shear walls.

Each concrete MRF is designed per CSA A23.3–19 [9], and the CFS shear walls are designed according to AISI S400-15 [2] with OSB panel properties obtained from the American Wood Council [4, 5] and CFS stud properties obtained from Clark-Dietrich specifications [8]. For both examples, the concrete columns are assumed to be non-sway, non-slender square columns with an effective moment of inertia specified by A23.3–19 Clause 21.2.5, with the compressive strength and column dimensions varied to achieve the desired stiffness. For the CFS framing, the stiffness is calculated based on AISI S400-15 Eq. E1.4.1.4-1, with the total wall length adjusted to achieve the desired stiffness. The chord members are back-to-back 800S300-97

Table 2 Spectral Acceleration for St. Catharine's, Ontario, per NBCC 2015 [12]

$S_a(0.2)$	$S_a(0.5)$	$S_a(1.0)$	$S_a(2.0)$	$S_a(5.0)$	$S_a(10.0)$
0.319	0.155	0.071	0.032	0.0076	0.0028

studs in combination with 48/24 rating, 23/32″ (18.26 mm) OSB panels with shear modulus of 921 MPa. It is further assumed that the maximum fastener spacing is 75 mm and the allowable vertical deformation of the anchorage is 3 mm. To estimate the shear demand, the shear force from the MRS analysis is used, and to estimate the column load, the mass based on the specified dead load is used. Finally, the length of each shear wall segment is assumed to be 4880 mm.

3.1 Example 1

The first example is assumed to have a 3-storey lower structure ($N_L = 3$) and a 3-storey upper structure ($N_U = 3$), $r_m = 3$ and $r_k = 10.81$, with 35 MPa, 500 mm by 500 mm columns for the concrete MRF and 8–4880 mm segments (total 39.0 m) of CFS shear wall on each storey of the upper structure. Following the procedure described in Sect. 3, it is calculated that each column provides a stiffness of 3.12×10^4 kN/m and collectively $k_L = 5.00 \times 10^5$ kN/m, whereas $k_U = 4.63 \times 10^4$ kN/m. Based on an assumed specified dead load of 3 kPa for each storey of the upper structure, the load is $63 \times r_m = 9$ kPa for the lower structure. In total, the resulting storey masses are $m_U = 55{,}734$ kg and $m_L = 167{,}202$ kg. The equivalent 2DOF parameters, calculated using Eqs. (1)–(6) are: MU = 167,202 kg, $M_L = 501{,}606$ kg, $K_U = 2.70 \times 10^4$ kN/m, $K_L = 2.92 \times 10^5$ kN/m, $R_k = 10.81$ and $R_m = 3.00$. The theoretical $T_{1,2DOF}$, T_{singU}, T_U and T_L per Eqs. (9)–(11) are 0.52, 0.22, 0.49 and 0.26 s. $T_1/T_U = 1.06 \leq 1.1$ and $R_k \geq 10$, so the ASCE 7–16 limits are satisfied, but neither the [7] nor the [17] criteria are satisfied.

Since the focus is to inspect the validity of the two-stage assumption rather than investigate the period calculation itself, the period based on the MDOF model is used to calculate storey shears for each of the linear MRS analysis, the ASCE 7 two-stage procedure and equivalent static force procedure (ESFP) defined in NBCC are illustrated in Fig. 3. In this case, the ESFP is not strictly applicable—the theoretical period is 0.52 s rather than the 0.5 s limit specified by the NBCC. The ESFP is nonetheless used as a lower bound on linear MRS analysis and is therefore included for comparison. In addition, the ESFP is included using both the period estimates for moment-resisting frames and general structures per the NBCC, designated as ESFP (MRF) and ESFP (Other) in Fig. 3, respectively.

In this example, despite satisfying the ASCE-7 stiffness and period requirements, the two-stage procedure underestimates the upper structure's base shear by 15%. This error is directly inverse to the $\alpha_{U,MDOF}$ of 1.19 (= 1/0.85), and to $\alpha_{U,2DOF}$, which is 1.32. While the MDOF result is closer due to considering the 3rd and higher mode, the α_U values are a useful shorthand to compare the error of various approaches. However, the largest errors of this two-stage example are not in the upper structure's base shear but in the top storey and the bottom storey. At the top, the shear is underestimated by 30%, at the bottom it is overestimated by 40%. The increasing error towards the top indicates a mismatch between the shape of the two-stage force distribution and that calculated by MRS. In the NBCC, a top storey shear is added to
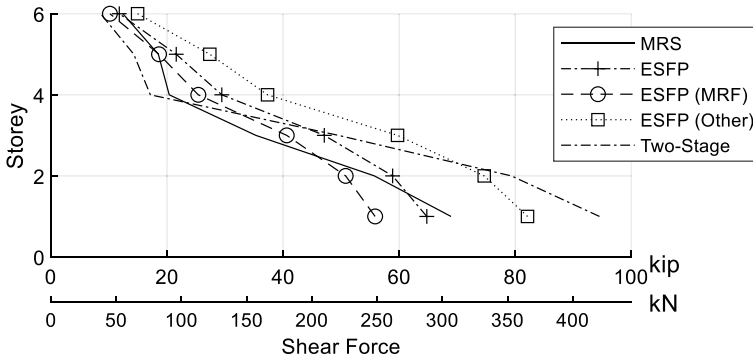
Fig. 3 Example 1 shear force

alleviate this, and in the ASCE an exponent is applied to the force distribution, but for T_1 so close to 0.5 s, either distribution is essentially the same—no top storey shear is added. Likewise, the bottom storeys are overestimated, indicating that the ABSSUM rule used by ASCE 7–16 can be overly conservative. While these errors may exist following ASCE 7–16's two-stage criterion, α_U is nonetheless a prerequisite for the two-stage procedure's efficacy. It does not correspond to the ESFP distribution as the loads are distributed considering the full structure. In any event, a designer wishing to reduce the amplification factor in this example could reduce the mass ratio r_m or increase the stiffness ratio r_k.

One final consideration is the empirical period specified by the NBCC. In this example, the height $h_n = 18$ m and therefore $T_a = 0.075(h_n)^{3/4} = 0.66$ s for the NBCC MRF calculation and $T_a = 0.05(h_n)^{3/4} = 0.44$ s for the shear wall/other calculation. In this case, the other category period is sufficiently low such that it is conservative, but this is not always the case—where T_U is lower owing to the dynamic properties of the frame, α_U will underestimate the potential error occurring at the base of the upper structure as shown in Fig. 3. In addition, [1] note that it is inappropriate to use the higher period (i.e. MRF) for calculation of the base shears— if used, the errors will be much higher than predicted otherwise. Ultimately, such period calculations are empirical and intended for regular structures, and so their application poses challenges for irregular structures outside the current scope.

3.2 Example 2

In the second example, $N_L = 2, N_U = 4, r_k = 15.08$ and $r_m = 4$, with 30 MPa, 550 mm by 550 mm columns for the concrete MRF and 12–4880 mm segments (total 58.6 m) of CFS shear wall on each storey of the upper structure. Each column provides a stiffness of 4.31×10^4 kN/m and therefore $k_L = 6.89 \times 10^5$ kN/m, whereas $k_U = 4.57 \times 10^4$ kN/m. With a specified dead load of 3 kPa for each storey of the upper

structure, the load is 12 kPa for the lower structure. In total, $m_U = 55,734$ kg and $m_L = 222,936$ kg. The equivalent 2DOF parameters are: $M_U = 222,936$ kg, $M_L = 445872$ kg, $K_U = 1.84 \times 10^4$ kN/m, $K_L = 5.27 \times 10^5$ kN/m, $R_k = 23.88$ and $R_m = 2.00$. The theoretical $T_{1,2DOF}$, T_{singU}, T_U and T_L are 0.67, 0.22, 0.63 and 0.28 s. $T_1/T_U = 1.06 \leq 1.1$ and $R_k \geq 10$, so all of the ASCE 7–16, [17] and [7] criteria are satisfied.

Unlike before, the results shown in Fig. 4 are not strictly applicable per the NBCC, because the theoretical T_U and T_1 are both larger than 0.5 s. Therefore, the theoretical results are outside the bounds of the NBCC. This is not consequential, for two reasons: (1) the period if the other systems category approximation is used (as otherwise required) is lower and therefore conservative and (2) the emphasis here is on the relative behaviour—T_U and T_1 could be reduced by designing a stiffer shear wall or lower dead load than used here. The two-stage, ESFP and MRS results appear in Fig. 4, including the code-specified period calculation as before.

Here, $\alpha_{U,MDOF}$ and $\alpha_{U,2DOF}$ are approximately 1.08, and so $\alpha_{U,MDOF}/\alpha_{U,2DOF}$ is approximately 1, This is expected as R_k is increased to satisfy the stricter [17] and [7] criteria, indicating that the two-stage amplification effect is adequately captured by the 2DOF model, and therefore that their proposed criteria are justified. Compared to Example 1, R_k and R_m satisfy all the criteria and therefore the example exhibits improved accuracy. Despite the variance in error between Examples 1 and 2, the ASCE 7–16 criteria are met in both cases. The same conclusions regarding top storey shear, ABSSUM and α_U still apply as they did in Example 1, as do those regarding the code period calculations, aside from the error of using the MRF period calculation being lower than before due to the increased T_U. Key, however, is the observation that the ASCE limits appear unable to predict if a large amplification is possible.
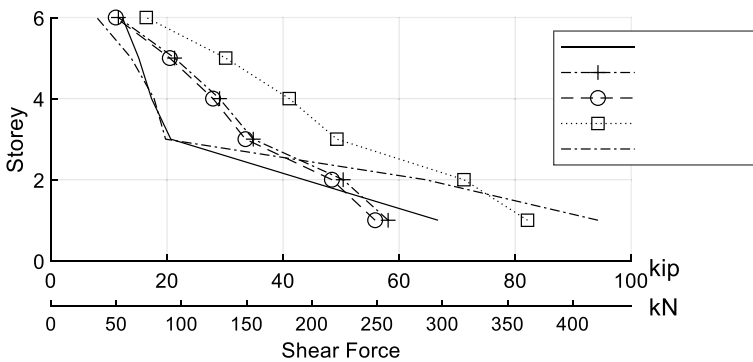
Fig. 4 Example 2 shear force

4   Conclusions

Given design trends in both Canada and the USA, it is inevitable that some will attempt to use the two-stage analysis procedure specified by ASCE 7–16 for design, even in the context of the NBCC 2015 provisions. Despite this, research suggests that such analysis warrants careful consideration of problem characteristics, as the criteria of ASCE 7–16 may be unconservative under certain scenarios. Although the ASCE 7–16 criteria ensure that the lower structure is stiff and that the upper structure's fundamental period is approximately the same as the full structure, research suggests that the criteria may not adequately ensure that the upper structure base shear is not amplified or that the modes of the upper and lower structures are well-separated. α_U is introduced to characterize this amplification effect, and the ratio of the MDOF and 2DOF results, $\alpha_{U,MDOF}/\alpha_{U,2DOF}$, is proposed as an indicator of two-stage applicability.

Two examples are presented to demonstrate the potential inadequacy and applicability of applying the ASCE 7–16 criteria to NBCC 2015 design. It is demonstrated that following the ASCE 7 criteria does not ensure either low amplification or accurate storey shear distribution. Instead, stiffness in excess of ASCE 7 requirements may be needed—[17] and [7] propose alternatives which ensure that $\alpha_{U,MDOF}/\alpha_{U,2DOF}$ is approximately 1, in which event a 2DOF model is adequate to characterize the two-stage effect. Nonetheless, current two-stage procedures as applied to the NBCC overestimate shears in the lower structure and underestimate shears in the upper structure. Further investigation needs to be conducted to evaluate the upper structure load amplification effect when considering capacity-based design and detailing procedures.

Appendix 1—Nomenclature

Variable	Description
k_L	Storey stiffness of lower structure, kN/m
K_L	Overall stiffness of lower structure, kN/m
k_U	Storey stiffness of upper structure, kN/m
K_U	Overall stiffness of upper structure, kN/m
m_L	Storey mass of lower structure, kg
M_L	Total mass of lower structure, kg
M_{Li}	Normalized effective modal mass of lower structure in ith mode

(continued)

(continued)

Variable	Description
m_U	Storey mass of lower structure, kg
M_U	Total mass of lower structure, kg
M_{Ui}	Normalized effective modal mass of upper structure in ith mode
M_v	NBCC factor to account for higher-mode effect on base shear
N_L	Storey count of lower structure
N_U	Storey count of upper structure
R_d	NBCC ductility-related force modification factor
r_k	Storey stiffness ratio
R_k	Overall stiffness ratio
r_m	Storey mass ratio
R_m	Overall mass ratio
R_o	NBCC overstrength-related force modification factor
$S_a(T)$	NBCC 5% damped spectral acceleration for period T, g
$T_{1,2DOF}$	Fundamental mode period for 2DOF model, derived by [16], s
T_L	Fundamental mode period of lower structure, s
T_{singU}	Period of single storey of upper structure
T_U	Fundamental mode period of upper structure, s
V_{ub}	Base shear of upper structure, kN
α_U	Upper structure base shear amplification factor
$\alpha_{U,2DOF}$	Upper structure base shear amplification factor, 2DOF model
$\alpha_{U,MDOF}$	Upper structure base shear amplification factor, MDOF model
ϕ_{L1}	First mode shape of the lower structure in the 2DOF model
$\overline{\omega}_1$	Normalized fundamental circular frequency of n-DOF structure having unitary mass and stiffness for each DOF

Appendix 2—Derivation of T_1/T_U Equivalent Stiffness Requirement

Using the definitions of $T_{1,2DOF}$ and T_U given in Eqs. (11) and (9), the limit of $T_1/T_U \leq 1.1$ can be expressed as a function of R_k and R_m [17]:

$$T_1/T_U = \sqrt{2R_m / \left[R_m + R_k + 1 - \sqrt{(R_m - R_k - 1)^2 + 4R_m} \right]} \leq 1.1 \qquad (22)$$

Since R_m and R_k are real-valued, positive and nonzero, the inequality can be squared and rearranged to produce a quadratic:

$$R_m(0.5739R_m - 0.6944R_k + 2) \le 0 \tag{23}$$

$$0.826R_m + 2.880 \le R_k \tag{24}$$

As R_m is greater than zero, Eq. (23) can be simplified and solved for a limit on R_k that is approximately equivalent to the period criterion of ASCE 7–16, which appears in [15].

References

1. Allen M, Chung NC, Tran A, Zepeda D (2013) Two stage analysis: implementation challenges. Struct Congr 2013:2192–2202. https://doi.org/10.1061/9780784412848.192
2. American Iron and Steel Institute (AISI) (2015) AISI S400–15: North American standard for seismic design of cold-formed steel structural systems
3. American Society of Civil Engineers (ASCE) (2017) ASCE 7–16: minimum design loads and associated criteria for buildings and other structures
4. American Wood Council (AWC) (2017) NDS: national design specification for wood construction: 2018 edition. American Wood Council
5. American Wood Council (AWC) (2018) Manual for engineered wood construction: 2018 edition, 1st edn. American Wood Council
6. Blume JA, Knox MT, Lindskog E (1960) Appendix C: report on setbacks. In: Recommended lateral force requirements and commentary, 1st edn. Structural Engineers Association of California
7. Chen Z, Ni C (2020) Criterion for applying two-step analysis procedure to seismic design of wood-frame buildings on concrete podium. J Struct Eng 146(1)
8. Clark D (2017) Cold-formed structural framing products: technical design guide
9. CSA Group (2019) CSA A23.3:19 design of concrete structures
10. International Conference of Building Officials (ICBO) (1988) Uniform building code
11. National Research Council of Canada (NRCC) (2015a) Commentary J: design for seismic effects. In: Structural commentaries user's guide—NBC 2015: Part 4 of division B. National Research Council of Canada
12. National Research Council of Canada (NRCC) (2015b) National building code of Canada 2015. National Research Council of Canada
13. Seismology Committee Structural Engineers Association of California (SEAOC) (1988) Recommended lateral force requirements and tentative commentary, 5th edn.
14. Seismology Committee Structural Engineers Association of California (SEAOC) (2019) SEAOC blue book: seismic design recommendations 2019
15. Xu L, Yuan XL (2015) A simplified seismic design approach for mid-rise buildings with vertical combination of framing systems. Eng Struct 99:568–581. https://doi.org/10.1016/j.engstruct.2015.05.019
16. Yuan XL (2016) A simplified seismic design approach for mid-rise buildings with vertical combination of framing systems. University of Waterloo
17. Yuan XL, Xu L (2016) An improved two-stage seismic analysis procedure for mid-rise buildings with vertical combination of cold-formed steel and concrete framing. In: International specialty conference on cold-formed steel structures, pp 853–867
18. Yuan XL, Xu L (2014) Simplified seismic design for mid-rise buildings with vertical combination of cold-formed steel and concrete framing. In: International specialty conference on cold-formed steel structure, pp 617–631

Analysis of Pedestrian-Induced Floor Vibrations Based on Monitoring Durations

Negar Bouzari, Niel Van Engelen, and Shaohong Cheng

Abstract Pedestrian-induced vibration (PIV) is often recognized as the most persistent floor serviceability issue for buildings. This type of vibration can cause discomfort for the occupants and can also have a negative impact on the performance of sensitive equipment residing on the floor. Resolving floor vibration problems in built structures often requires costly remedial measures. The response of a built floor to PIV can be evaluated by monitoring techniques. The purpose of long-term floor monitoring is to have a comprehensive insight into the vibration levels. However, it is relatively rare due to the associated costs and challenges. Short-term monitoring and controlled walking tests may not reflect the actual vibrations of the floor but are easier to perform. This research aims to estimate the percentiles of the long-term floor response distribution based on a sample of short-term measurement by Confidence Interval (CI) analysis. For this purpose, the minimum monitoring duration (MD) required to accurately reflect the long-term distribution and the appropriate percentile to evaluate the floor performance is investigated. In this research, two methods are considered to determine what percentile should be selected to evaluate floor performance. The minimum monitoring duration is obtained based on CI analysis. The results of this research are expected to provide a more realistic assessment of floor vibration performance.

Keywords Pedestrian · Floor vibrations · Monitoring durations

1 Introduction

Human activities are often the primary internal source of floor vibration in structures since they occur frequently and in practice cannot be isolated [19]. Among various types of loads imposed on the floor by humans, walking is the most common one [28].

N. Bouzari (✉) · N. Van Engelen · S. Cheng
Department of Civil and Environmental Engineering, University of Windsor, Windsor, Canada
e-mail: bouzarin@uwindsor.ca

With each step, a time-varying force that has components in three mutually perpendicular directions (i.e., vertical, horizontal-lateral, and horizontal-longitudinal) is applied on the floor. In particular, the vertical component of the walking force causes the greatest vibration to the floor system [31]. The response of the floor to the applied walking force can be further amplified by resonance.

Floor vibrations can be problematic if they are large enough to cause discomfort and annoyance to occupants. Furthermore, these vibrations can interfere with the function of MRIs, microscopes, and other delicate equipment [3]. There are no effective and inexpensive solutions that can reduce or eliminate PIV after construction [29]. The approaches for evaluating the PIVs of an existing floor are mostly developed based on experimental floor vibration data acquisition that are the monitoring techniques [1]. One of the common monitoring techniques for floors is by using accelerometers which can be attached to the floor for measuring PIV. The obtained data from the accelerometers can be post-processed and analyzed.

Floor vibrations can be monitored for short or long-term durations. The primary advantage of long-term monitoring is that the results better illustrate the variety of probable loads and consequent vibrations that might occur on the floor. However, long-term monitoring is rare due to the costs and challenges associated with on-site long-term measurements (i.e., installation and removal of equipment, interference with day-to-day activities of occupants, project timeline) [6]. The objective of the short-term monitoring is to measure floor vibrations under operation for a short period to provide a rapid assessment of the vibration conditions.

To properly examine PIVs, floors should be monitored for a sufficient MD to accurately reflect the conditions under regular day-to-day use. Therefore, the main objective of this research is to determine the sufficient duration for monitoring floor vibration based on evaluating available measured PIVs. The obtained MD would be considered as a representative sample of short-term measured floor vibrations. The second objective of this research is to determine the appropriate percentile(s) for evaluating floor performance provided by current design guidelines and standards for PIV.

2   Background

Available research on PIVs can be classified into two categories: deterministic and probabilistic approaches [16]. In the deterministic approach, the loads applied by humans on a floor and the floor response are assumed to be known [31]. The response of a floor to pedestrian-induced loads can be evaluated in terms of floor displacement, velocity, or acceleration, which determines whether the floor can be used in terms of structural safety, occupant comfort, and operation of delicate equipment [17].

Guidelines [9, 17, 27] are available for evaluating the response of a floor to pedestrian-induced applied loads. Based on the guidelines, a comparison is made between the obtained maximum floor response and the code-specified threshold to determine whether the floor is serviceable or not. Although the deterministic studies

and the guidelines are essential tools for civil engineers to address the serviceability issues of floors due to vibrations, they have some drawbacks. This type of approach typically assumes that the excitation source is stationary, the induced vibration is perfectly periodic, and a single pedestrian is often the only loading scenario. These assumptions may overestimate or underestimate the loads and the floor response, depending on the situation [16].

Since walking loads applied on a floor has a random nature, the response of the floor to these applied loads would be more appropriate to be defined in a statistical sense. An alternative to the deterministic method is the probabilistic method that considers the stochastic nature of the loads induced by humans on the floor. The logic of this approach is that the floor's response to pedestrian loads cannot be precisely determined due to its random parameters [24]. The probabilistic approach does not have a defined solution for evaluating floor vibrations. The lack of research on these methods is a consequence of the complexity of the human-structure dynamic interaction problems. Most of the research which contains probabilistic methods are developed based on the vibration measurements from a specific floor [30].

To determine the vibration serviceability of floors, most studies utilized existing metrics, including R factors, root-mean-square acceleration (RMS), and vibration dose values (VDV) [20]. Despite this, the maximum value of these measures tends to only appear relatively infrequently and is unrepresentative compared to the actual response [10, 25]. By measuring PIV and generating a response distribution, multiple studies have provided a more realistic insight into the RMS or R factor response of the office floor over a long-term measurement [6, 21]. As previously mentioned, performing long-term monitoring is challenging. Research is needed in this area to predict the floor response to pedestrian-induced loads based on short-term vibration monitoring durations.

In addition, limits for the probability of exceedance that reflect an actual structural response to vibrations need to be defined [4, 11]. However, in most investigations the selected limitation is defined arbitrarily and there is no consensus about the choice of probability of exceedance across different structural environments [28]. Some investigations [5, 28] state that an absolute probability of exceedance should not be defined since the results could not be correlated with how people would perceive vibrations. Therefore, the selected criteria for evaluating floor vibrations based on probabilistic approaches may define the level of the risk of exceeding certain level of floor response considered for vibrations on the floor. The acceptable risk depends on many factors, such as the significance of the structure itself, its purpose, and costs.

3 Method

3.1 PIV Sampling

This research is conducted based on analyzing the measured long-term and short-term pedestrian-induced floor vibration datasets, which are respectively known as the population dataset and the sample of data points in statistics. Statistical analysis has two main focuses, descriptive statistics, and inferential statistics. Descriptive statistics summarizes datasets. It is used to identify relationships and patterns in datasets but cannot be used to obtain any conclusions beyond the available datasets. Inferential statistics methods provide conclusions beyond the available dataset. The definition of inference is the process of concluding parameters of the population dataset based on a sample of data points taken from the population [2]. In this research, the representative PIV samples were analyzed based on inferential statistical methods to estimate the percentiles of the population dataset. There is uncertainty about how well a given sample of data points can represent the population dataset. Generally, the sample of data points taken from a population will never be a perfect representation of the population. Therefore, a method is proposed in the current study to remove samples that are truly not representative and might affect the results.

Measurements were conducted on the office floor of an engineering consulting firm located in Guelph, ON. The office building has hollow-core prestressed concrete floors supported on steel framing. In this investigation, confidence interval (CI) analysis of measured short-term PIV samples (i.e., a few minutes of measurement) is conducted to estimate the percentiles of the long-term PIV dataset (i.e., assumed to be 7 days of measurement based on the available data). The amplitude of PIV is expressed by calculating 1-s root-mean-square (RMS) velocity (μm/s). The measured PIV is filtered into 1/3 octave frequency bands to obtain its frequency content. The sampling analysis is performed in the natural logarithm scale to obtain normal distributions since the raw dataset is skewed and lognormally distributed. The results are expressed in the units of measurement (μm/s).

The start and end time of the sample measurement is within the office hours (i.e., from 8:30 AM to 5:00 PM) and the MD is extended from 5 to 100 min in 5-min intervals. Sampling is performed every 6 min starting at 8:30 AM regardless of the monitoring duration provided the measurement ends before or at 5:00 PM. The sampling examination is therefore representative of the site measurement conditions. Although this method for getting samples may be biased toward mid-day measurements, it is true for actual site measurements (i.e., measurements are more likely to be done during the day and less likely to contain the start or end of the day within the measurement.).

The first type of unqualified sample is the noise-only sample. Sensor noise in each 1/3 octave frequency band is estimated by combining measurements taken from 2:00 to 4:00 AM from the days of measurement included in the long-term dataset. In this study, the samples having a mean greater than $\mu + \sigma$ where μ and σ are, respectively, the mean and the standard deviation of noise distribution, are
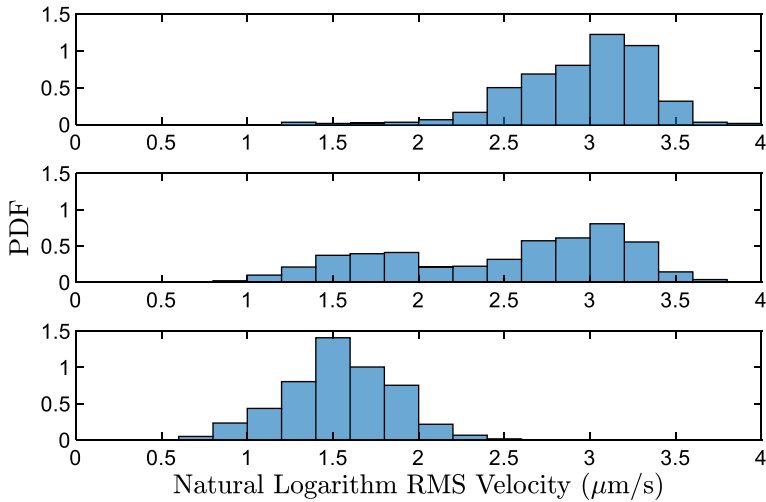
Fig. 1 PIV samples showing the unimodal sample (top), bimodal sample (middle), and the noise-only sample (bottom)

considered to represent actual vibrations. To avoid losing PIV samples, one standard deviation from the mean of the noise is experimentally considered as the threshold. Hence, if the sample's mean exceeds the threshold, it is retained for further analysis; otherwise, it is discarded as noise only.

The second consideration is to evaluate the mixture of modes in the samples. The PIV samples based on the dataset used in this research can be unimodal or bimodal. The PIV measured from the corridor where the sensor was located might be affected by the noise from the sensor or the PIV recorded were from multiple walking paths. The bimodal samples need to be separated into two distributions. In the case of bimodal samples, if both means are below the noise threshold, the sample case is ignored, and if a mean is equal to or greater than the threshold, the distribution with the greater mean is passed on for further analysis to assess the worst-case scenario. Analyzing the modality of the sample's distribution is done according to an investigation by Robertson and Fryer [22]. Each sample is subjected to a Gaussian Mixture Model (GMM) in MATLAB (MATLAB—MathWorks—MATLAB and Simulink) to obtain its parameters (i.e., sample means, standard deviations, and mixing parameter) for applying the modality test. Figure 1 illustrates the probability density function (PDF) of typical sample distributions.

3.2 Selection of a Percentile for Evaluation of Measured PIV

Two methods are proposed for selecting a percentile for performing CI analysis based on the definitions in the current guidelines to compare the floor performance

against available vibration criteria. In the first method, a percentile is selected that matches the probability of non-exceedance (PONE) used in the considered guideline's methodology. The current guidelines use a deterministic approach, but even this has some inherent probability of exceedance (POE) built into the methodology. The logic here is that if the guidelines expect the vibrations to be higher than the predicted value a percentage of the time, it is rationalized that the floor performance should be evaluated based on the same percentile. This is reinforced by the accuracy of the guidelines in identifying acceptable or unacceptable floors [18, 23]. This approach is performed based on SCI P354 [9] and CCIP-016 [27]. It should be noted that AISC Design Guide 11 does not target a specific PONE. The second approach is based on the definitions of the types of vibration according to ISO 10137 curves [13]. They are based on human exposure to continuous and intermittent vibrations. Specifically, the curves were developed by exposing people to a constant sinusoidal excitation.

3.2.1   Selection of a Percentile Based on the Inherent PONE

The PONE is developed based on the definition of the dynamic load factor (DLF) and walker's weight in the current guidelines. Assuming the DLF and walker's weight are independent [7], the POE of the vibration can be determined based on the statistical rules of conditional probability and the product rule [8]. According to SCI P354 and CCIP-016, the weight of the walker is considered respectively to be 747 N (168 lb) and 698 N (157 lb). Based on the American bodyweight distribution for men and women, the probability of having a walker weighing equal to or greater than the weight considered by the guidelines is obtained (Weight Percentile Calculator for Men and Women in the United States). Also, SCI P354 followed an Annex of EN 1990 which used parameters that for the DLF gives the POE of 15%. In the CCIP-016 the DLF is considered to have a POE of 25%. The POE for the weight and DLF based on the two mentioned guidelines are shown in Table 1. Therefore, according to CCIP-016, the PONE or the selected percentiles will be approximately the 83rd and based on SCI P354 the selected percentiles will be the 91st.

Table 1 Probability of exceedance based on guidelines

Guideline	Gender	POE			
		DLF	Weight	Vibration	Average (%)
CCIP-016	Male	0.25	0.82	0.21	17.10
	Female	0.25	0.55	0.14	
SCI P354	Male	0.15	0.73	0.11	8.80
	Female	0.15	0.44	0.07	

3.2.2 Selection of a Percentile Based on the Definitions of Vibration

Based on the ISO vibration criteria curves [13] an intermittent vibration is defined to occur more than 10 events per 24-h. It is rationalized that 4.2 events that exceed the floor classification curve may occur in a 10-hr period. Each event is assumed to have an 8-s duration as commonly assumed in design [6]. Therefore, approximately 34 s of exceedance is permitted within a 10-h period. Thus, for intermittent vibrations the selected PONE will be 99.9th percentile as proposed earlier by [6]. Again, according to the ISO curves, the continuous vibration is defined to have a duration of more than 30 min per 24 h. Therefore, the selected percentile for continuous vibration is approximately the 98th percentile [6].

3.2.3 Discussion

Several studies have acknowledged the uncertainty on how to evaluate a floor based on measurement programs and there is no consensus among researchers on considering a specific PONE for floor vibrations [5, 30, 33]. In lieu of selecting a single percentile, a range will be considered. This will confirm the applicability of the developed methodology independent of a specific percentile. It is postulated that consideration of multiple percentiles will enable the development and definition of various levels of floor performance (i.e., low, normal, high) in the future.

The selected percentiles based on the two methods considered in this research correspond well with the proposed range of percentiles from the available literature (i.e., 85th–95th percentiles) [4, 5, 10]. The 83rd and 91st percentiles are respectively close to the lower and upper bounds of this range. So, the 85th and 95th percentiles will be considered as a rounded reflection of the obtained 83rd and 91st percentiles. Whereas the 98th percentile from ISO 10137 is also considered as a conservative assessment. The 99.9th percentile is deemed to provide an over-conservative evaluation, and it will be excluded in further analysis.

3.3 Confidence Interval (CI) Bounds

To evaluate the confidence intervals for the three selected percentiles (i.e., 85th, 95th, and 98th percentiles), the selected samples are entered in the RStudio software and the two confidence intervals for the percentiles are calculated based on the "QuantCI" method in the "QuantileNPCI" package. This method was developed based on Hutson's algorithm [12] to calculate nonparametric confidence intervals for quantiles. Additional information can be found in the comprehensive paper by [12] and the RStudio documentation [14].

4 Results

4.1 Sufficient MD of Floor Vibration Measurement

This research is conducted based on the provided pedestrian-induced floor vibrations measured on an office building's floor. The governing 1/3 octave frequency band for this floor is 6.2 Hz [6]. Vibrations were measured from February 9 to 23, 2018, by a single SENSR CX1 triaxial accelerometer with a resolution of 50 μg and a sampling rate of 125 Hz. A combination of measured vibrations during office hours for 7 workdays (on February 9, 12–15, 20, and 21, 2018) is considered as the long-term measured vibrations. The representative samples are obtained and the mean of the samples with the same MD are obtained and are shown in Fig. 2. The red dashed line is the long-term percentile, and the blue and yellow line indicates the mean of the lower and upper CI bounds for samples with the same MD, respectively.

To eliminate the effect of the start-time, the mean of all samples with the same MD is evaluated. Based on Fig. 2, as the MD increases, the mean of the upper and the lower CI bounds tends toward a horizontal asymptote. So, the benefit of increasing the monitoring duration decreases. In the current study, the sufficient MD is determined based on the relative error between the CI bounds associated with two consecutive lengths of MD, which is defined by Eq. 1. According to this study, the acceptable margin of relative error is 1% or less, which is selected arbitrarily but deemed sufficiently small to minimize changes between increments of MD.
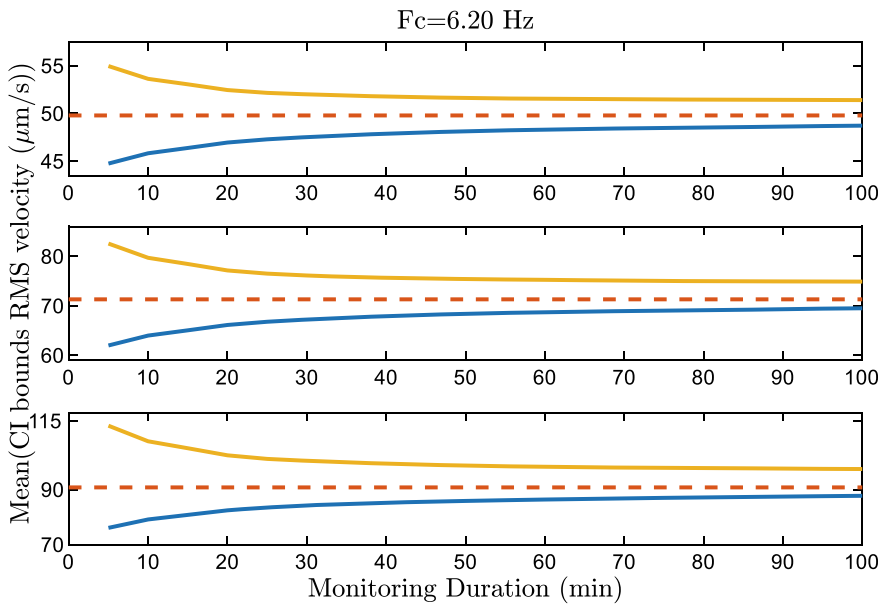
Fig. 2 CI bounds for percentiles 85th (top), 95th (middle), and 98th (bottom)
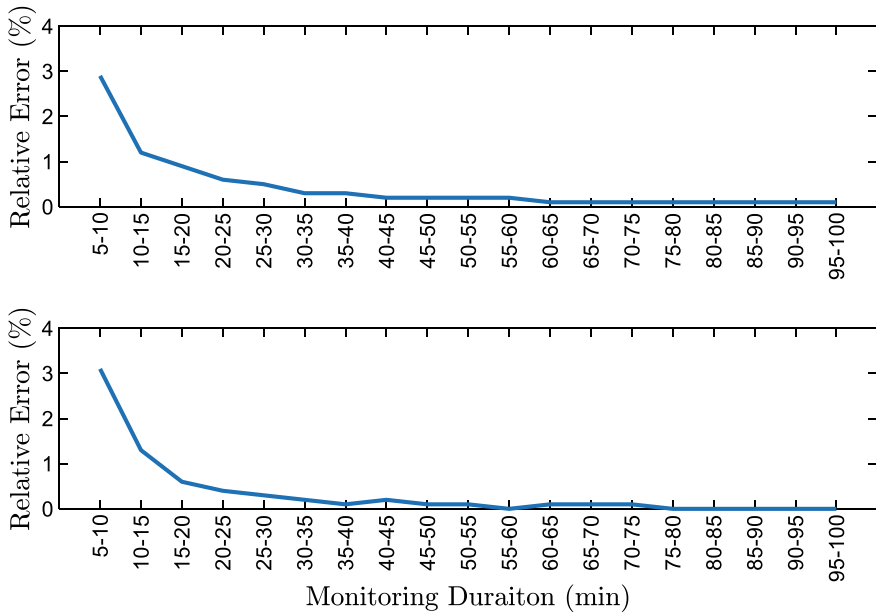
Fig. 3 Relative error based on each 5-min increase MD from the lower bound (top) and the upper bound (bottom) for the 85th percentile

Depending on the sensitivity of the analysis, the considered error criterion may be more or less than this value. Figures 3, 4, and 5 show that when the monitoring duration is 30 min, the relative error (see Eq. 1) is less than 1%. Therefore, this duration (i.e., 30 min) is considered to be the sufficient MD. Based on these figures, the error decreases with increasing MD although some exceptions occur.

$$\text{Err} = \frac{|(\text{CI})_i - (\text{CI})_{i+1}|}{(\text{CI})_{i+1}} \tag{1}$$

where i is the MD increment and Err represents the relative error.

4.2 Accuracy

A total of 567 representative samples with a duration of 30 min are obtained and the CI bounds for them are calculated. It is not expected that all the CI bounds derived from these samples would perfectly reflect the long-term percentiles. Some reasons for this expectation are summarized here. The statistical methodologies utilized in this study are mostly developed for the probabilistic studies that employ mathematical random samples. The current idea of applying these methods to the sample of PIV is new and
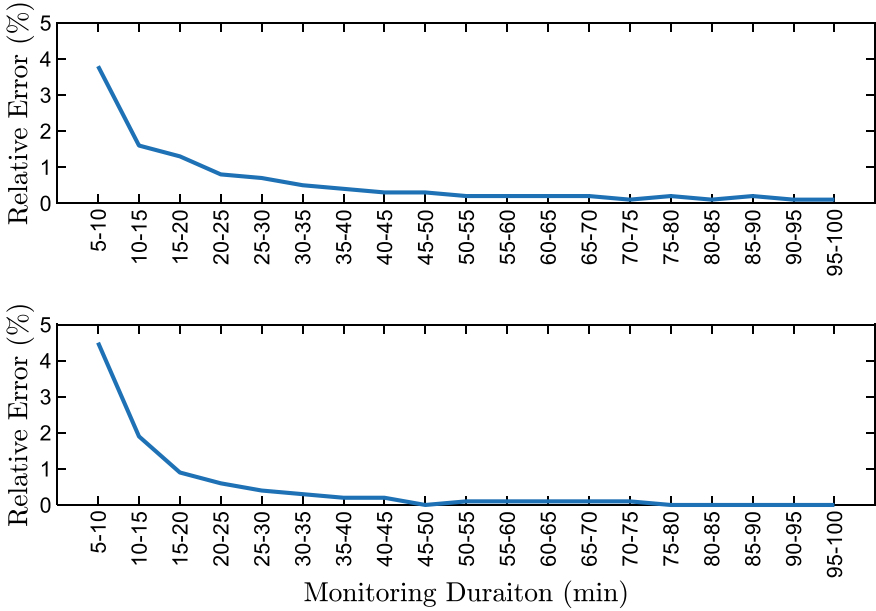
Fig. 4 Relative error based on each 5-min increase MD from the lower bound (top) and the upper bound (bottom) for the 95th percentile
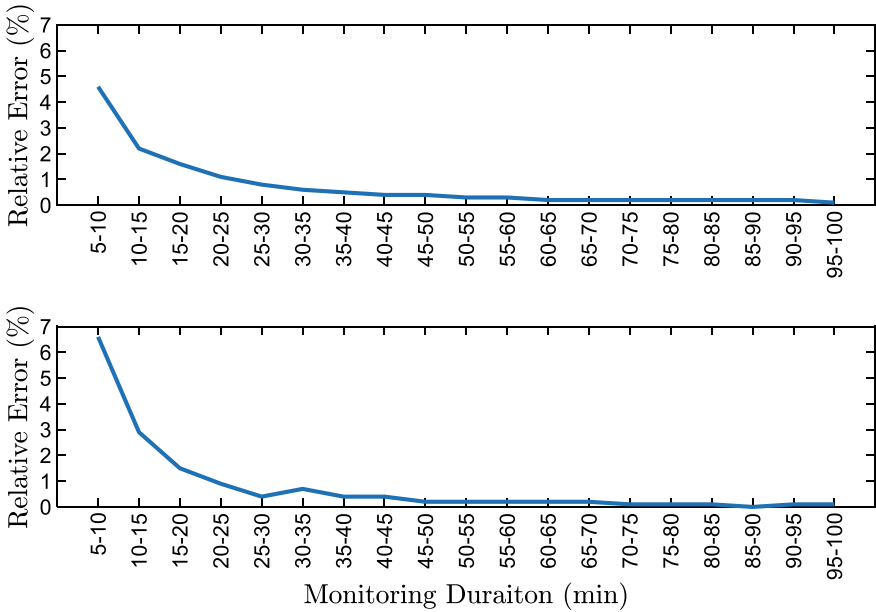
Fig. 5 Relative error based on each 5-min increase MD from the lower bound (top) and the upper bound (bottom) for the 98th percentile

should be evaluated further. Noise in a long-term dataset is often less significant than in a sample containing short-term measurements. As a result, it is possible to have a few seconds/minutes of the non-active floor data in the sample measurement, and instead of PIV, the sensor noise is measured and can be influential. Hence, the effect of sensor noise or other kinds of vibration than PIV might affect the percentiles of sample's distribution. Events in the office will also impact the results. Sometimes group meetings are held, and all occupants get up at the same time resulting in a high vibration event. Likewise, time of day has an impact (e.g., people going for lunch); this is not directly accounted for in the present methodology. It is necessary to accept a certain amount of error in order to estimate the long-term percentiles. In this research, an error of 20% from the long-term percentiles is considered as acceptable. Different classes of vibrations are estimated to be above or below each other by a factor of two based on Vibration Criteria (VC) curves [13]. So, it is reasonable to consider a 20% difference above or below the long-term percentile as this would be well within a vibration class.

The CI bounds for the samples that contain the long-term percentile or have 20% or less error from the long-term percentiles is determined. Based on that, the accuracy for the three percentiles is shown in Figs. 6, 7, and 8. According to these figures, each sample number gives a range for estimating the long-term percentiles (i.e., sample number 1 is the data collected from 8:30 to 9:00 am on February 9, and sample number 2 is from 8:36 to 9:06 am on the same day, and so on). The CI ranges containing the long-term percentiles or have a 20% or less error from long-term percentiles are shown in green, otherwise in red. Based on Figs. 6, 7, and 8, the sample number around 350–500 contain higher PIVs. These samples were measured on days February 20 and 21 around 12 PM–2:30 PM.
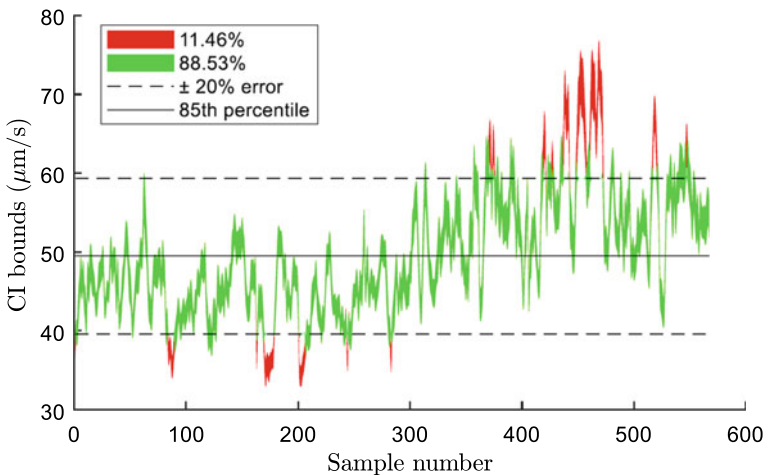
Fig. 6 The CI bounds for the samples with a 30-min MD with CI range that contain the long-term percentile or has 20% or less error from the long-term 85th percentile is shown in green and the samples that contain CI bounds outside the acceptable range are shown in red
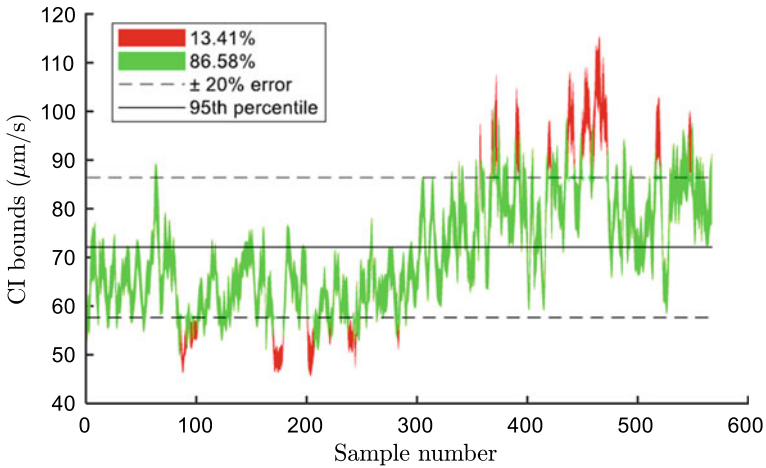
Fig. 7 The CI bounds for the samples with a 30-minute MD with CI range that contain the long-term percentile or has 20% or less error from the long-term 95th percentile is shown in green and the samples that contain CI bounds outside the acceptable range are shown in red
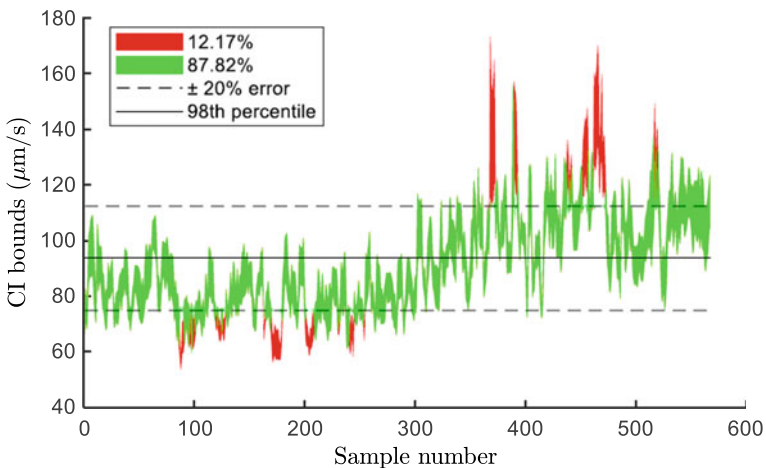
Fig. 8 The CI bounds for the samples with a 30-minute MD with CI range that contain the long-term percentile or has 20% or less error from the long-term 98th percentile is shown in green and the samples that contain CI bounds outside the acceptable range are shown in red

Table 2 column (a) shows the selected percentiles (P) and columns (b) and (c) illustrate the accuracy of CI bounds containing long-term percentiles (P_L) or having a 20% or less error from the long-term percentiles. Additionally, columns (d) and (e) respectively show the ratio of the mean of short-term (i.e., sample) percentiles (P_S) to the long-term percentiles and the ratio of the mean of CI upper bounds of short-term percentiles (P_{SU}) to the long-term percentiles. By comparing columns (d)

Table 2 Summary of results shown in Figs. 6, 7, and 8

P	CI bounds contain P_L (%)	CI bounds contain P_L or has error less than 20% from it (%)	$\frac{\text{Mean}(P_S)}{P_L}$	$\frac{\text{Mean}(P_{SU})}{P_L}$
(a)	(b)	(c)	(d)	(e)
85th	18.3	88.5	1.00	1.05
95th	19.9	86.5	0.98	1.04
98th	26.4	87.8	0.96	1.01

and (e), it can be seen that using the upper bound of the CI rather than the measured percentile values provides a more conservative, but realistic estimate of long-term percentiles on average. As a result, having confidence intervals for percentiles of samples improves the reliability of estimating long-term percentiles.

5 Conclusions

Monitoring techniques are used for evaluating the PIVs of an existing floor. The goal of this study is to determine the sufficient monitoring duration needed in order to estimate long-term percentiles of floor vibrations using a short-term sample of PIV measurements. In this research, representative PIV samples were determined by eliminating noise-only samples and analyzing the mixture modality of the samples. The selected percentiles for long-term PIV evaluation needs to be realistic and not under- or overestimate the results. This research considered that the appropriate percentiles as the 85th, 95th, and 98th. These percentiles are obtained based on considering the definition of loading to obtain vibrations in current guidelines. There is uncertainty about the selection of percentiles among available research.

The CI analysis and relative error are used to determine the sufficient MD based on the samples of measured PIV. The proposed sufficient MD based on the structure considered in this paper is at least 30 min of measurement. If the measured sample is representative according to the methodology in this paper, its CI bounds represent the long-term 85th, 95th, and 98th percentiles, or has an error of less than 20% with these long-term percentiles at a certainty level of 88.5%, 86.5%, and 87.5%, respectively. Using CI bounds of percentiles for representative samples provides a slightly more conservative estimate, which increases the reliability of estimation, compared to using the percentiles of the short-term sample. The estimation of long-term percentiles according to a short-term sample, which contains random data points, is inherently difficult, and therefore estimating errors can happen. Additional work is needed to validate the results of this paper.

References

1. Abdeljaber O, Hussein M, Avci O, Davis B, Reynolds P (2020) A novel video-vibration monitoring system for walking pattern identification on floors. Adv Eng Softw 139:102710
2. Allua S, Thompson CB (2009) Inferential statistics. Air Med J 28(4):168–171
3. Avci O, Asce M, Bhargava A, Al-Smadi Y, Isenberg J, Asce HM (2018) Vibrations serviceability of a medical facility floor for sensitive equipment replacement: evaluation with sparse in situ data. https://ascelibrary.org
4. Brownjohn J, Racic V, Chen J (2014) Universal response spectrum procedure for predicting walking-induced floor vibration. Elsevier
5. Chen J, Xu R, Zhang M (2014) Acceleration response spectrum for predicting floor vibration due to occupant walking. J Sound Vibr 333:3564–3579
6. Van Engelen NC, Graham J (2019) Comparison of prediction and measurement techniques for pedestrian-induced vibrations of a low-frequency floor. Struct Control Health Monitor 26(1):e2294
7. Graham JM, Love JS (2014) Investigating predicted floor response sensitivity to input forcing function variables. Conf Proc Soc Experiment Mech Ser 4:145–153
8. Hájek A (2003) What conditional probability could not be. Synthese 137(3):273–323
9. Hicks SJ, Devine P (2007) Design of floors for vibration: a new approach
10. Hudson EJ, Reynolds P (2013) Implications of structural design on the effectiveness of active vibration control of floor structures, vol 21, issue no 5. Wiley Online Library, John Wiley and Sons Ltd., pp 685–704
11. Hudson EJ, Reynolds P (2014) Implications of structural design on the effectiveness of active vibration control of floor structures. Struct Control Health Monitor 21(5):685–704
12. Hutson AD (1999) Calculating nonparametric confidence intervals for quantiles using fractional order statistics. J Appl Statist 26(3):343–353
13. ISO-ISO 10137:2007 (2007) Bases for design of structures—serviceability of buildings and walkways against vibrations. https://www.iso.org/standard/37070.html
14. Li M, Li Y (2019) Package 'QuantileNPCI' title nonparametric confidence intervals for quantiles
15. MATLAB—MathWorks—MATLAB and Simulink. https://www.mathworks.com/products/matlab.html
16. Muhammad Z, Reynolds P, Avci O, Hussein M (2019) Vibration review of pedestrian load models for vibration serviceability assessment of floor structures. https://mdpi.com
17. Murray TM, Allen DE, Ungar EE, Davis DB (2016) Vibrations of steel-framed structural systems due to human activity. American Institute of Steel Construction
18. Pabian S, Thomas A, Davis B, Murray TM (2013) Investigation of floor vibration evaluation criteria using an extensive database of floors
19. Pavic A, Reynolds P (2014) Vibration serviceability of long-span concrete building floors. Part 1: review of background information DynaTTB-dynamic response of tall timber buildings under service load view project-developing IMU-based wearable systems for medical-grade human movement monitoring in real-life environment (3D kinematics and kinetics) view project
20. Pavic A, Reynolds P, Waldron P, Bennett KJ (2001) Critical review of guidelines for checking vibration serviceability of post-tensioned concrete floors. Cement Concr Compos 23(1):21–31
21. Reynolds P, Pavic A (2015) Reliability of assessment criteria for office floor vibrations. In: 50th United Kingdom conference on human responses to vibration, Southampton, p 6
22. Robertson CA, Fryer JG (1969) Some descriptive properties of normal mixtures. Scand Actuar J 1969(3–4):137–146
23. Royvaran M, Avci O, Davis B (2021) An overview on floor vibration serviceability evaluation methods with a large database of recorded floor data. In: Conference proceedings of the society for experimental mechanics series, Springer, pp 91–101
24. Saul WE, Asce F, Tuan CY, Asce AM (1986) Review of live loads due to human movements
25. Shahabpoor E, Pavic A, Racic (2017) Structural vibration serviceability: new design framework featuring human-structure interaction. Elsevier

26. Weight Percentile Calculator for Men and Women in the United States. https://dqydj.com/weight-percentile-calculator-men-women/
27. Willford MR, Young P, Ceng M (2006) A design guide for footfall induced vibration of structures. Concrete Society for The Concrete Centre
28. Zivanovic S (2006) Probability-based estimation of vibration for pedestrian structures due to walking
29. Živanović S, Pavić A (2007) Probabilistic modeling of walking excitation for building floors
30. Živanović S, Pavić A (2009) Probabilistic modeling of walking excitation for building floors. J Perform Construct Facilit Am Soc Civil Eng (ASCE) 23(3):132–143
31. Živanović S, Pavic A, Reynolds P (2005) Vibration serviceability of footbridges under human-induced excitation: a literature review. J Sound Vibr
32. Živanović S, Pavic A, Reynolds P (2005) Vibration serviceability of footbridges under human-induced excitation: a literature review. Elsevier
33. Zivanoviý S (2006) Probability-based estimation of vibration for pedestrian structures due to walking

Wind Load on Structures

Comparison of Wind Tunnel Results for the Development of a New Section Model Test Rig for Bridges

Sébastien Maheux, J. Peter C. King, Ashraf El Damatty, Fabio Brancaleoni, and Mohamed AbuGazia

Abstract It has been demonstrated by mathematicians using nonlinear simplified models of suspension bridges that a vertical dynamic forcing can cause large torsional vibrations due to geometric nonlinearities of the bridge. Compared to the extensive research that has been conducted on aeroelastic instabilities in cable-supported bridges, the approach used by the mathematicians seems too simplistic, especially in terms of wind load modeling. However, they raise a point that is not considered in the wind design of cable-supported bridges, i.e., an interaction between nonlinear structural coupling and aeroelastic effects. In order to study the effect of structural geometric nonlinearities on the dynamic stability of very long cable-supported bridges, a special wind tunnel procedure was developed. Such procedure requires the development of a new experimental apparatus for section model tests of bridges that allows the representation of geometric nonlinearities and nonlinear structural coupling. Therefore, one of the first steps toward nonlinear section model tests was to design a new bridge rig for dynamic section model tests, which first needed to be validated for standard linear tests. Consequently, this paper will present a comparison of wind tunnel results for a single-box girder bridge model tested in two different wind tunnels, i.e., the main wind tunnel at the *Université de Sherbrooke* and the Boundary Layer Wind Tunnel Laboratory (BLWTL) at the University of Western Ontario. At the BLWTL, tests were conducted using the existing bridge rig and the new bridge rig designed for nonlinear tests. At first, the static aerodynamic coefficients and the flutter derivatives are compared. Then, the dynamic responses

S. Maheux (✉) · A. E. Damatty · M. AbuGazia
Department of Civil and Environmental Engineering, University of Western Ontario, London, Canada
e-mail: smaheux@uwo.ca

S. Maheux
COWI North America Ltd, Toronto, Canada

J. P. C. King
Boundary Layer Wind Tunnel Laboratory, University of Western Ontario, London, Canada

F. Brancaleoni
Dipartimento di Ingegneria Strutturale e Geotecnica, Sapienza Università di Roma, Rome, Italy

for smooth and turbulent flows obtained using the different experimental setups are analyzed. This comparison procedure allows the validation of the new bridge rig that will be used in the near future to assess the effect of structural nonlinearities on aeroelastic stability.

Keywords Wind tunnel · Test rig for bridges

1 Introduction

It is well known that long cable-supported bridges, such as suspension bridges and cable-stayed bridges, are sensitive structures to the actions of wind, especially for dynamic phenomena like flutter. Flutter, which is a self-excited instability, can lead to major structural damages and even bridge collapse. For this reason, it has been common practice in the field of long-span bridge engineering to conduct wind tunnel tests in order to verify the soundness of bridge designs with respect to aerodynamic and aeroelastic phenomena. Different wind tunnel testing procedures can be utilized for bridges. In order of increasing complexity, the most common approaches are the section model tests [7], taut-strip model tests [5], and full-aeroelastic model tests [9]. Due to their versatility, simplicity, and cost effectiveness in comparison to other testing procedures, section model tests have become the standard approach for wind tunnel tests of bridges.

Section model tests can be utilized to measure aerodynamic coefficients, measure the wind and motion-induced surface pressures and study the dynamic response of the bridge deck, especially with regard to instabilities like flutter. However, even with the improvements made in experimental apparatus over the years, section model tests still rely on the same simplifications with respect to the aerodynamic and structural behaviors. The fact that the aerodynamic contribution of the cable system is neglected is an example of such simplifications. Typically, only one vertical mode and an analogous torsional mode, which have uniform shapes, are considered in section model tests. Furthermore, the bridge structure is assumed to have a linear behavior because the modes represented in such tests are obtained considering linear structural dynamics theory.

Nevertheless, it is known that cable-supported bridges can show geometric nonlinearities [6] as well as material nonlinearities [8] and localized nonlinearities [3] in specific cases. Using advanced mathematical models of suspension bridges, mathematicians and engineers demonstrated that a dynamic vertical force can lead to large torsional oscillations due to nonlinear structural dynamic coupling [1, 4]. This coupling is caused by the intrinsic nonlinear geometric behavior of the suspension bridge system. In [4], it is mentioned that internal parametric resonance, a structural dynamic instability caused by the nonlinear structural coupling between modes of vibration, would be responsible. To the authors' knowledge, such large torsional oscillations due to nonlinear structural dynamic effects have never been witnessed on an actual bridge. Nonetheless, a transition from an antisymmetric instability mode to

a symmetric instability mode occurred for a full-aeroelastic model of a double-main-span suspension bridge [15]. Internal resonance associated with the nonlinearities of the aeroelastic system would be responsible for the phenomenon observed on this full-aeroelastic bridge model [16]. This has led to recent studies on nonlinear flutter and aerodynamic nonlinearities [14, 17]. The main focus of these studies has been on aerodynamic nonlinearities, and structural nonlinearities are only discussed in verifications that section model test rigs behave linearly. However, in the field of aeronautics, it was demonstrated using nonlinear section model tests for airfoils that a nonlinear stiffness behavior can have an influence on flutter [12, 13].

Considering that the flutter response of airfoils can be impacted by a nonlinear stiffness behavior, it is worth asking whether this can also be the case for bridges. A section model test procedure for bridges able to represent the nonlinear structural behavior would be able to answer this question. The first step toward nonlinear section model tests for bridges was to develop a numerical procedure to study the nonlinear structural vertical-torsional coupling in cable-supported bridges [11]. The procedure in [11] can also be used to determine the nonlinear structural behavior in stiffness to be considered for nonlinear section model tests. During the development of a scaling procedure for the nonlinear behavior obtained using the approach in [11], it was determined that a new section model test rig is required in order to conduct nonlinear section model tests for bridges.

Therefore, this paper presents the validation procedure of this new section model test rig in the case of standard linear tests. More specifically, a single-box girder bridge model was tested in two different wind tunnels, i.e., the main wind tunnel at the *Université de Sherbrooke* and the Boundary Layer Wind Tunnel Laboratory (BLWTL) at the University of Western Ontario. The new bridge rig of the BLWTL is validated by comparing the wind tunnel test results of the new bridge rig to those measured at the *Université de Sherbrooke* and those obtained at the BLWTL using the old bridge rig. First, the wind tunnels and section model test rigs considered in the validation procedure are presented. Then, the experimental program, which included static tests, flutter derivative tests, and dynamic tests, is discussed. Finally, a presentation of the experimental results is made, which also includes a discussion of the results.

2 Experimental Apparatuses

2.1 *Wind Tunnel at the* Université de Sherbrooke

For this validation of a new section model test rig, experimental results from two different wind tunnels are considered. The first one is the main wind tunnel at the *Université de Sherbrooke*, which is a closed-circuit wind tunnel with a maximum wind speed of 31 m/s. The 10 m-long test section is 1.83 m by 1.83 m. The mean wind speed was measured with two Pitot tubes located above and below the bridge

section model. At the test location of section models, the longitudinal and vertical turbulence intensities are approximately 1.0% under smooth flow conditions. For the turbulent flow conditions considered for some of the test runs, a grid positioned upstream of the section model was utilized. In this case, longitudinal and vertical turbulence intensities are respectively 7.1% and 5.4%.

In Fig. 1, the bridge section model test rig at the *Université de Sherbrooke* is presented. This rig is located outside the wind tunnel. As shown in Fig. 1, it can be used in two different configurations, which are a free-vibration test configuration and a force-vibration test configuration. The free-vibration configuration (Fig. 1a) can be used to measure the dynamic response of a sprung section model. Two degrees of freedom (DOF) are considered in this research, i.e., the vertical displacement and rotation. The vertical and torsional stiffnesses can be set independently for this bridge rig, and damping can be set using magnetic dampers. The free-vibration measurement of flutter derivatives is also possible in this configuration. In the forced-vibration configuration, the bridge model is attached to load cells through pretensioned cables, and dynamic hydraulic actuators are utilized to impose motion to the model (Fig. 1b). In this configuration, the test rig is typically used for a forced-vibration extraction of flutter derivatives. In both test configurations, laser displacement sensors are utilized to measure the displacements, whereas load cells are used for the forces. It is also worth noting that this test rig can also measure the static aerodynamic coefficients. More information about the experimental tests at the *Université de Sherbrooke* can be found in [10].

(a) Free-vibration tests   (b) Forced-vibration tests
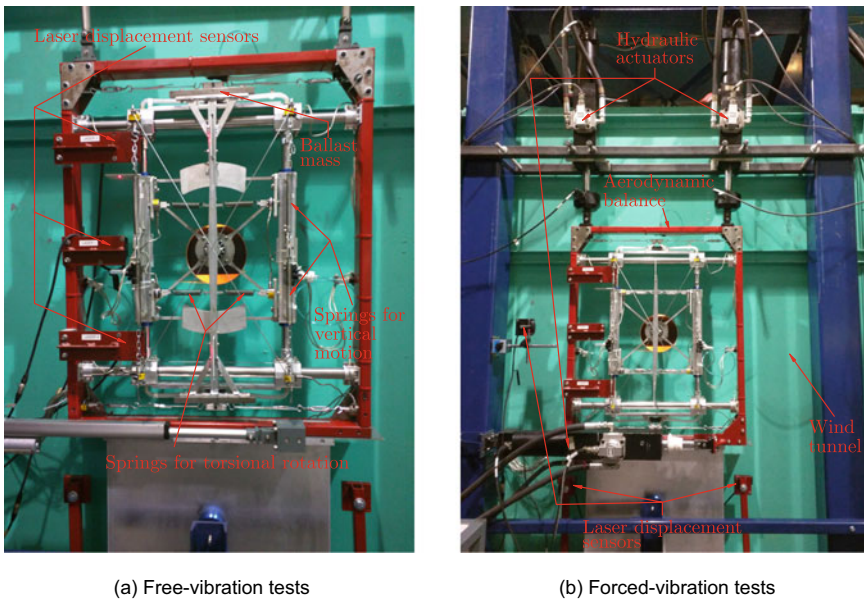
Fig. 1 Section model test rig at the *Université de Sherbrooke*

2.2 Boundary Layer Wind Tunnel Laboratory at the University of Western Ontario

Tests at the Boundary Layer Wind Tunnel Laboratory at the University of Western Ontario were conducted in the high-speed test section of the closed-circuit wind tunnel BLWT 2. For section model tests of bridges, the test rig units are installed inside two streamlined walls, one at each end of the bridge model (see Fig. 4b). Where the section model is mounted, a distance of 2.15 m between the walls is typically used, which is situated within the 3.35 m-wide test section. However, the width considered for the tests discussed herein was of 1.83 m since the bridge model considered is shorter than the models usually tested at the BLWTL. The overall height of the bridge test section is 1.77 m. The mean wind speed was measured with two Pitot tubes located above the bridge section model. The maximum wind speed achievable in the test section is 30 m/s. Smooth flow turbulence intensities are less than 0.5%. For the turbulent tests, a longitudinal turbulence intensity of 4.8% and a vertical turbulence intensity of 4.4% were obtained using the grid shown in Fig. 4b.

The section model test rigs utilized at the BLWTL are shown in Fig. 2. Both are free-vibration test rigs equipped with torsion arms on which vertical springs are attached to provide vertical and torsional stiffness to the bridge model. Therefore, two DOFs, a vertical and a rotational, are possible with these rigs. For both test rigs, the displacements and rotations of the bridge model were measured using laser displacement sensors. In the case of the old bridge rig, the lateral movement of the model is restrained using leaf springs (see Fig. 2a). Also, the damping can be adjusted using pneumatic dampers in the old rig. For the new bridge rig (Fig. 2b), the lateral movement of the bridge model is made impossible by using air bushings able to move vertically along stainless-steel shafts but restrained in the lateral direction. In the new bridge rig, a magnetic damping system is utilized to set the damping. Just like for the old rig, it is possible in the new bridge rig to adjust the horizontal position of the springs, but what differentiates the new bridge rig is that it is also possible to adjust the vertical position of the top and bottom attachment points of the springs. This is done by moving the top and bottom horizontal aluminum extrusions that are shown in Fig. 2b. This provides the flexibility to the new bridge rig that is required for a nonlinear device able to represent the nonlinear structural behavior in order to eventually conduct nonlinear section model tests for bridges.

3 Experimental Program

3.1 Bridge Section Model

The bridge section model utilized in the validation procedure of the new bridge rig is a single-box girder of a suspension bridge, which is referred herein as bridge SU2. The full-scale width of the bridge deck is 31 m. A geometric scale of $\lambda_L = 1/70$ is

(a) Old bridge rig

(b) New bridge rig
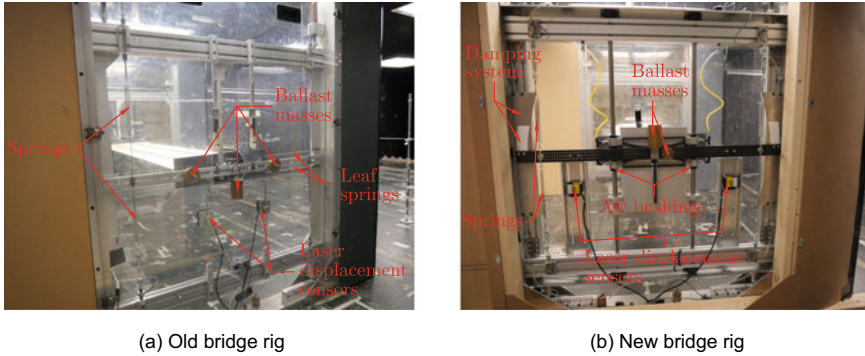
Fig. 2 Section model test rigs at the boundary layer wind tunnel laboratory

utilized, which gives a model width of 443 mm. As shown in Fig. 3, the section model consists of a carbon fiber frame that is cladded with balsa wood sheets to form the bridge-deck cross section. Using this fabrication method allows the section model to be very light with a total mass of only 1.72 kg for a model that is 1806 mm long. Having a light model is particularly important for the extraction of flutter derivatives using forced-vibration tests as it reduces the model inertial forces that are measured by the load cells. This therefore facilitates the determination of the self-excited forces needed for the extraction of flutter derivatives. Additionally, the stiffness of the carbon fiber frame combined with the lightness of the model ensure that the model vibrations are minimal for free-vibration tests as well as for forced-vibration tests. Figure 4a shows the bridge model when mounted on the section model test rig at the *Université de Sherbrooke*. The model when tested at the BLWTL is also presented in Fig. 4b.

(a) Carbon fiber frame

(b) Model in its final form
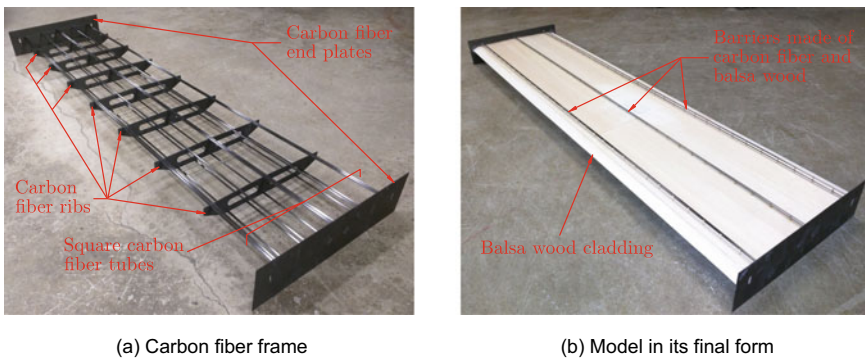
Fig. 3 Section model of bridge SU2 for $\lambda_L = 1/70$

(a) *Université de Sherbrooke*   (b) Boundary Layer Wind Tunnel Laboratory
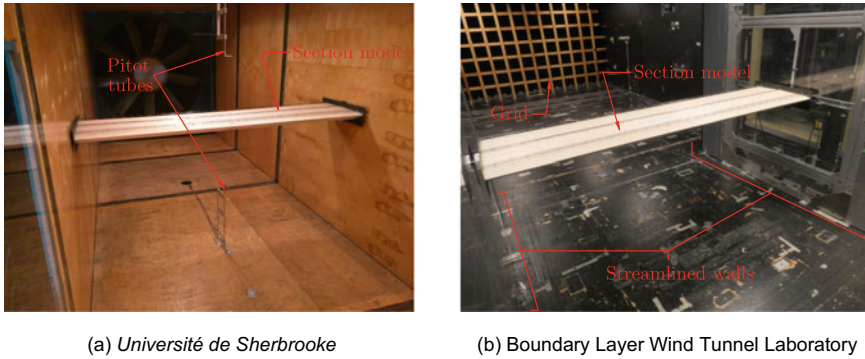
Fig. 4 Section model of bridge SU2 inside the wind tunnels

3.2 Static Tests at the Université de Sherbrooke

In order to verify that the section model of bridge SU2 was not altered from its storage and its transportation between the two universities, it was first decided to compare the static coefficients measured at the *Université de Sherbrooke* and at the BLWTL. For the static tests at the *Université de Sherbrooke*, the static coefficients were measured for an angle of attack varying from $-10°$ to $10°$. Increments of $1°$ were used for angles of attack between $-6°$ and $6°$. Otherwise, increments of $2°$ were considered. Measurements were made for three different wind speeds in order to check for potential Reynolds number effects. This was done for a smooth flow and a turbulent flow.

3.3 Static Tests at the Boundary Layer Wind Tunnel Laboratory

For the static tests at the BLWTL, the angle of attack was varied between $-10°$ and $10°$ with increments of $1°$. Static coefficients were measured for two different mean wind speeds, which correspond to the two highest wind speeds considered in the static tests at the *Université de Sherbrooke*. At an angle of attack of $0°$, the static coefficients were measured over the range of wind speeds achievable in BLWT 2. This was done to assess the Reynolds number dependence of the aerodynamic coefficients. All static tests at the BLWTL were conducted for a smooth flow as well as a turbulent flow using the static test rig presented in Fig. 5.

Fig. 5 Static test rig of the boundary layer wind tunnel laboratory
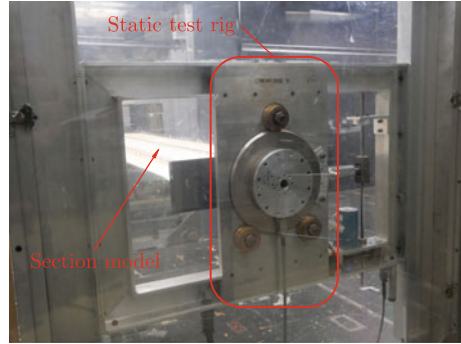
3.4 Free-Vibration Flutter Derivative Tests at the Université de Sherbrooke

The first step of the validation procedure for the new bridge rig is to compare the flutter derivatives measured using the different experimental rigs. At the *Université de Sherbrooke*, the flutter derivatives were first measured using the free-vibration procedure, which consists in measuring exponentially decaying displacement time histories of the sprung bridge model at different wind speeds. The full-scale dynamic properties of the sprung model used for these tests are shown in Table 1 (column UdeS). Flutter derivatives were measured for a smooth flow and a turbulent flow.

Table 1 Full-scale test parameters for dynamic tests of bridge SU2

Parameter	Target	UdeS		BLWTL-old		BLWTL-new	
		Value	Error	Value	Error	Value	Error
$\overline{m}_V^*$ (10^3 kg/m)	23.01	23.87	3.7%	23.54	2.3%	23.91	3.9%
$\overline{m}_\theta^*$ (10^6 kg m^2/m)	2.505	2.380	-5.0%	2.482	-0.9%	2.646	5.6%
f_{VS1} (Hz)	0.097	0.101	4.1%	0.097	0.0%	0.098	1.0%
ξ_{VS1} (%)	0.30	0.93	210%	0.31	3.3%	0.40	33.3%
$f_{\theta S1}$ (Hz)	0.279	0.279	0.0%	0.281	0.7%	0.278	-0.4%
$\xi_{\theta S1}$ (%)	0.30	0.91	203%	0.37	23.3%	0.28	-6.7%
α_s (°)	0.0	0.0	–	0.0	–	0.0	–

$\overline{m}_V^*$: mass per unit length, $\overline{m}_\theta^*$: mass moment of inertia per unit length, f_{VS1}: natural frequency of first symmetric vertical mode, ξ_{VS1}: damping ratio of first symmetric vertical mode, $f_{\theta S1}$: natural frequency of first symmetric torsional mode, $\xi_{\theta S1}$: damping ratio of first symmetric torsional mode, α_s: angle of attack

3.5 Forced-Vibration Flutter Derivative Tests at the Université de Sherbrooke

At the *Université de Sherbrooke*, the flutter derivatives were also measured using the forced-vibration procedure. For these tests, uncoupled harmonic motions were imposed to the bridge model, i.e., for one DOF at a time (vertical or torsional). By doing so for different wind speeds, it is possible to measure the corresponding self-excited forces, from which the flutter derivatives are calculated. The vertical amplitude and frequency for the vertical tests were 11 mm and 1.80 Hz. A torsional amplitude of 2.0° and a torsional frequency of 3.25 Hz were considered for the torsional tests. Smooth and turbulent flows were used for these tests.

3.6 Free-Vibration Flutter Derivative Tests at the Boundary Layer Wind Tunnel Laboratory

For the free-vibration tests at the BLWTL, the flutter derivatives were only measured for a smooth flow since turbulence did not have a significant effect on the flutter derivatives for the tests made at the *Université de Sherbrooke*. At the BLWTL, flutter derivatives tests were conducted for the old bridge rig and the new bridge rig. The full-scale dynamic properties of the sprung model considered in these tests for the old rig (column BLWTL-Old) and the new rig (column BLWTL-New) are presented in Table 1.

3.7 Dynamic Tests at the Université de Sherbrooke

As a second validation of the new bridge rig, a comparison is made for the dynamic responses of the sprung model of bridge SU2 measured using the different experimental rigs. Dynamic section model tests were performed considering the first symmetric vertical mode and first symmetric torsional mode, which are the critical modes with respect to flutter for bridge SU2. For the tests at the *Université de Sherbrooke*, the full-scale dynamic properties of the sprung model are presented in Table 1 (column UdeS). As it can be seen in this table, with the exception of the damping ratios, these dynamic parameters are close to the target values also shown in Table 1. For the UdeS damping ratios, it was required to use higher damping ratios due to limitations of the section model test rig. For these dynamic tests, time histories of the displacements of the sprung model were recorded for different mean wind speeds until the onset of flutter was reached. These tests were performed considering smooth and turbulent flows.

3.8 Dynamic Tests at the Boundary Layer Wind Tunnel Laboratory

Similar dynamic tests were conducted at the BLWTL using the old bridge rig and the new bridge rig. The full-scale dynamic properties for these tests are presented in Table 1. In this table, it can be seen that these test parameters are close to the full-scale target values. Dynamic tests at the BLWTL were also conducted for smooth and turbulent flows.

4 Results and Discussion

4.1 Results for Static Tests

First, the experimental results for the static coefficients for bridge SU2 are analyzed. Herein, the following formulation is utilized for the mean aerodynamic forces and static coefficients:

$$D_s = \frac{1}{2}\rho U^2 B C_D(\alpha_s) \quad L_s = \frac{1}{2}\rho U^2 B C_L(\alpha_s)$$

$$M_s = \frac{1}{2}\rho U^2 B C_M(\alpha_s) \tag{1}$$

where D_s, L_s, and M_s are the mean aerodynamic drag force, mean aerodynamic lift force and mean aerodynamic moment per unit length; ρ is the density of air; U is the mean wind speed; B is the bridge-deck width; C_D, C_L, and C_M are, respectively, the drag coefficient, lift coefficient, and moment coefficient; α_s is the angle of attack. The sign convention for the aerodynamic forces is shown in Fig. 6.

Fig. 6 Sign convention for displacements and forces
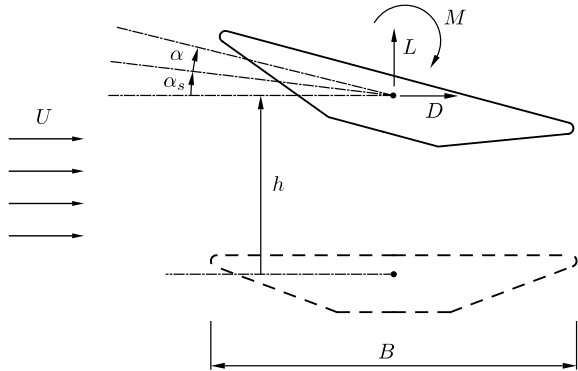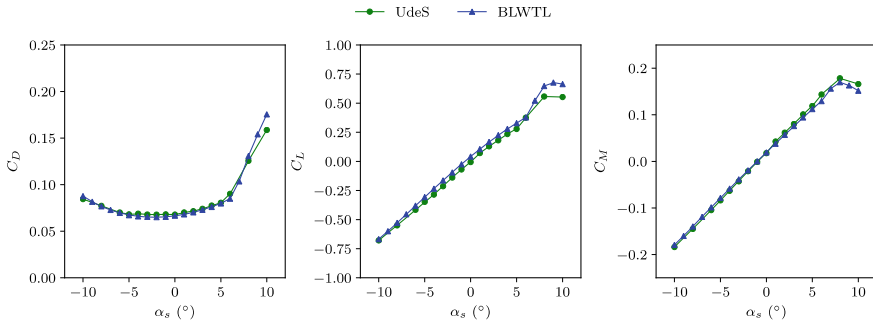
(a) Smooth flow and $Re = 3.4 \times 10^5$
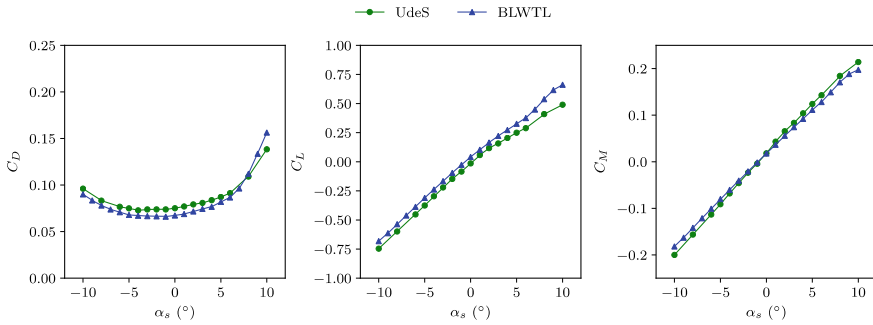
(b) Turbulent flow and $Re = 3.3 \times 10^5$

Fig. 7 Static aerodynamic coefficients of bridge SU2

Figure 7 presents a comparison of the static coefficients measured at the *Université de Sherbrooke* (UdeS) and the BLWTL for bridge SU2. Figure 7a and b show respectively the static coefficients for a smooth flow and a turbulent flow. Since it was found that the static coefficients are marginally impacted by the Reynolds number, results are only shown for a Reynolds number Re of approximately 3.4×10^5 (based on the bridge-deck width). As it can be seen in Fig. 7, there is a good agreement between the static coefficients measured from the two different wind tunnels, even though there are more noticeable discrepancies at large angles of attack. Nonetheless, it is possible to say that the section model of bridge SU2 was not altered from its storage and its transportation between the two universities.

4.2 Results for Flutter Derivative Tests

It is now of interest to examine the flutter derivatives measured using the different experimental rigs for bridge SU2. For the free-vibration tests, the flutter derivatives

were calculated using the Modified Unifying Least-Squares (MULS) method [2]. In the case of the forced-vibration tests, a linear least-squares approach was utilized to obtain the flutter derivatives from the experimental results. In this paper, the self-excited forces and flutter derivatives are defined as follows:

$$L_{se}(t) = \frac{1}{2}\rho U^2 B\left(\mathrm{KH_1^*}\frac{\dot{h}}{U} + \mathrm{KH_2^*}\frac{B\dot{\alpha}}{U} + K^2 H_3^*\alpha + K^2 H_4^*\frac{h}{B}\right) \tag{2}$$

$$M_{se}(t) = \frac{1}{2}\rho U^2 B^2\left(\mathrm{KA_1^*}\frac{\dot{h}}{U} + \mathrm{KA_2^*}\frac{B\dot{\alpha}}{U} + K^2 A_3^*\alpha + K^2 A_4^*\frac{h}{B}\right) \tag{3}$$

where $L_{se}(t)$ and $M_{se}(t)$ are the self-excited lift force and self-excited moment per unit length; t is the time; $h = h(t)$ and $\alpha = \alpha(t)$ are, respectively, the dynamic vertical displacement and dynamic rotation; $K = \omega B/U$ is the reduced frequency; $\omega = 2\pi f$ is the angular frequency of oscillation; H_i^* and A_i^* ($i = 1, \ldots, 4$) are the flutter derivatives, which are functions of the reduced velocity $U_R = U/(fB)$; f is the frequency of oscillation; the overdot denotes the time derivative. The sign convention for the forces and displacements is shown in Fig. 6.

The flutter derivatives of bridge SU2 relative to the vertical motion are presented in Fig. 8, whereas those with respect to a rotational motion are shown in Fig. 9. These results are for a smooth flow. In these figures, a comparison is made for the free- and forced-vibration results measured at the *Université de Sherbrooke* (UdeS-Free and UdeS-Forced) as well as the results measured at the BLWTL using the old bridge rig (BLWTL-Old) and the new bridge rig (BLWTL-New). As observed in Figs. 8 and 9, there is a good agreement between the different sets of flutter derivatives. This is especially the case for the flutter derivatives relative to the rotational motion. However, there are greater discrepancies for the derivatives with respect to the vertical motion. A possible explanation for this is that the aerodynamic damping is high for the vertical motion, therefore making difficult a reliable extraction of the derivatives using the free-vibration procedure. This could also be partially caused by different initial conditions considered in the free-vibration tests. Additionally, in some instances like for H_2^* in Fig. 9, the flutter derivatives measured from forced-vibration tests are different than those from free-vibration tests. This could be explained by the static rotation of the bridge model in the free-vibration tests (e.g., see Fig. 10a). Conversely, the mean angle of attack is imposed in forced-vibration tests to 0°. Nevertheless, it is possible to conclude that the new bridge rig is reliable for the measurement of flutter derivatives.

4.3   Results for Dynamic Tests

As mentioned previously, the second validation procedure of the new bridge rig consisted in comparing the dynamic response of the sprung model of bridge SU2 for the different free-vibration test rigs. Such comparisons are presented in Figs. 10
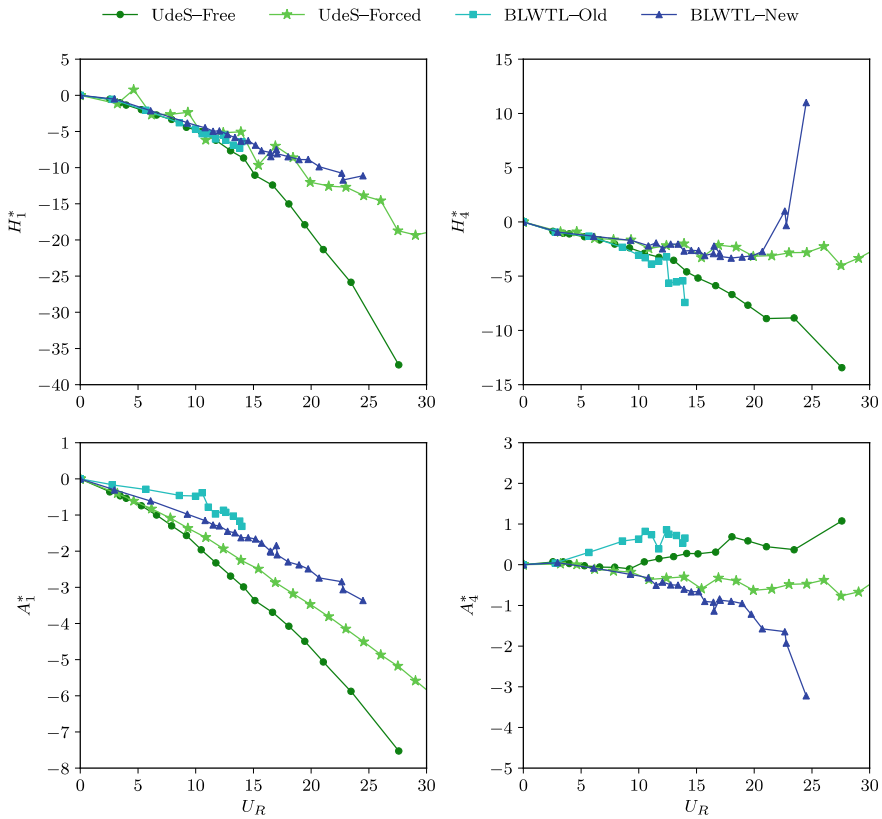
Fig. 8 Flutter derivatives of bridge SU2 for vertical motion (smooth flow)

and 11 for a smooth flow and a turbulent flow, respectively. These figures include results measured at the *Université de Sherbrooke* (UdeS) and at the BLWTL for the old bridge rig (BLWTL-Old) and the new bridge rig (BLWTL-New). Figures 10a and 11a present the mean displacements, whereas the peak displacements are shown in Figs. 10b and 11b.

In Figs. 10 and 11, it can be observed that the dynamic responses for the old and new rigs of the BLWTL agree very well. For the bridge rig of the *Université de Sherbrooke*, Figs. 10b and 11b show that the peak displacements are less than those for the BLWTL test rigs. This is attributed to the greater damping utilized for the tests at the *Université de Sherbrooke* (see Table 1). However, the larger damping for the UdeS dynamic response has a marginal effect on the onset of flutter since flutter occurs at relatively the same wind speed for the three experimental rigs. It is also worth noting that it was not always possible to measure the displacements when flutter occurred as the displacements would rapidly become very large, and the wind tunnel had to be stopped. This was the case for the results of the new BLWTL rig for a smooth flow and the old BLWTL rig for a turbulent flow. Regarding the mean
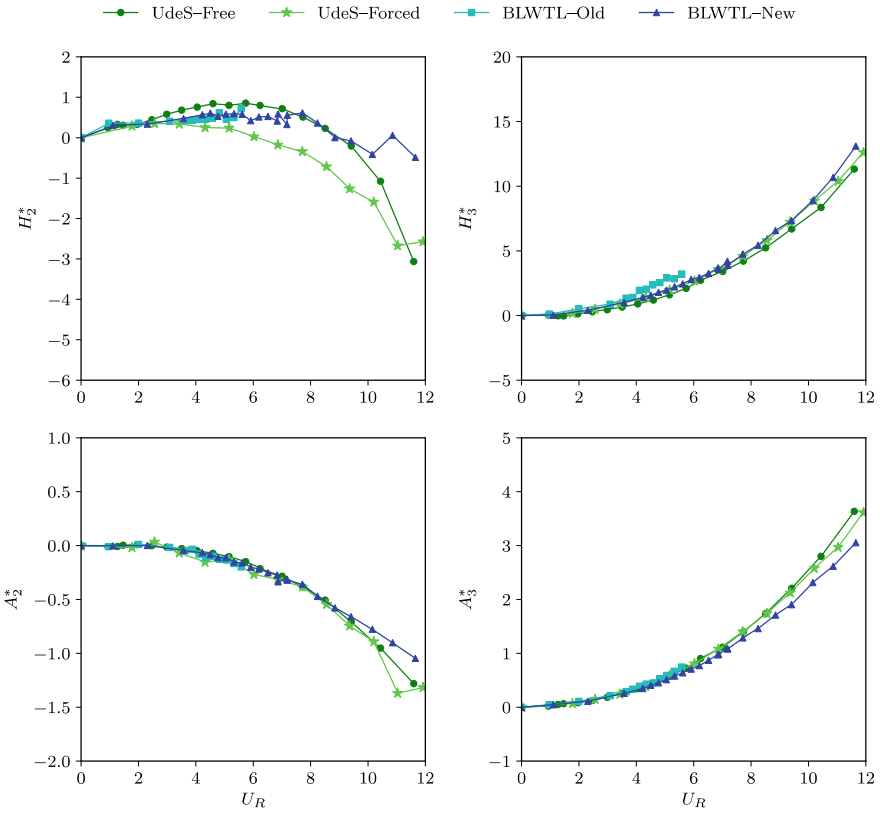
Fig. 9 Flutter derivatives of bridge SU2 for rotational motion (smooth flow)

(a) Mean displacements   (b) Peak displacements
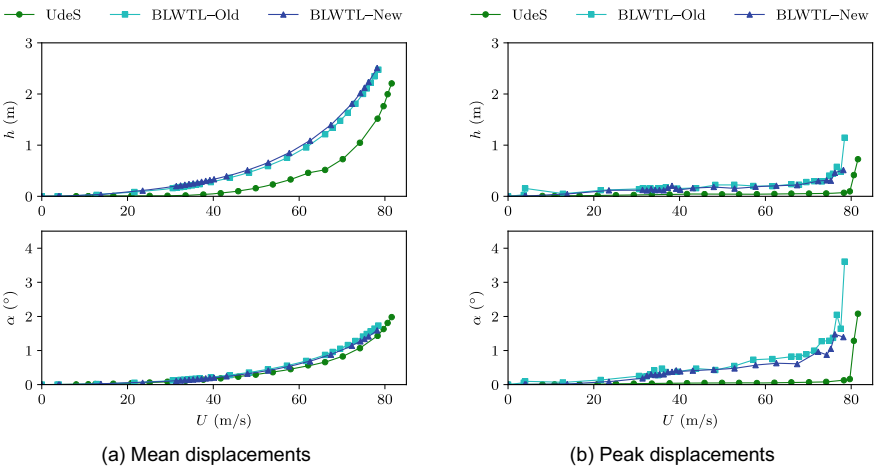
Fig. 10 Dynamic response of bridge SU2 for modes VS1 and TS1 and a smooth flow (full scale)
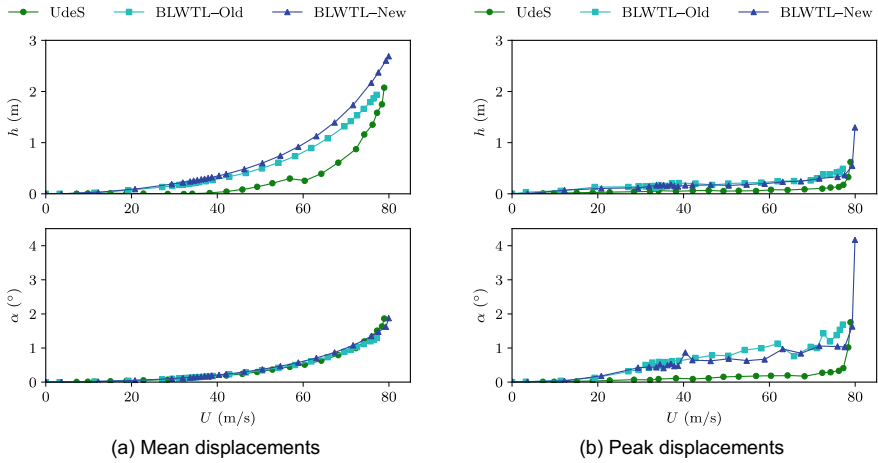
Fig. 11 Dynamic response of bridge SU2 for modes VS1 and TS1 and a turbulent flow (full scale)

displacements, the old and new BLWTL rigs have very similar results. However, in the case of the mean vertical displacement, there are discrepancies between the UdeS results and the results for the two other bridge rigs. Further investigation would be required in order to find an explanation for this behavior. This would likely require conducting additional wind tunnel tests at the *Université de Sherbrooke*. This was out of the scope of this research project since it is still possible to validate the new BLWTL rig by using the results measured for the old bridge rig of the BLWTL.

From this validation procedure based on standard linear section model tests, it is possible to conclude that the new BLWTL bridge rig is valid since it has demonstrated its reliability for the measurement of flutter derivatives and dynamic responses. The next step in this research project will be to replace the linear structural behavior by a nonlinear stiffness behavior in order to conduct nonlinear section model tests using the new bridge rig of the BLWTL. Such an experimental approach will allow an experimental investigation of the effect of structural nonlinearities on the aerodynamic and aeroelastic behavior of bridges.

5 Conclusions

Wind tunnel section model tests for cable-supported bridges are extensively used in industry and research. However, they rely on some assumptions. For example, they assume a linear structural behavior for the stiffness of the bridge. Considering theoretical demonstrations made regarding nonlinear structural dynamic phenomena in suspension bridges, it seems relevant to extend the capabilities of the section model test procedure for bridges by making such tests able to account for a nonlinear structural behavior. To achieve this, it was needed to design and fabricate a new section

model test rig able to accommodate a nonlinear device representative of the nonlinear behavior of a bridge. Before using this new bridge rig for nonlinear section model tests, it was required to validate its usage by conducting linear section model tests. The results for this new bridge rig at the Boundary Layer Wind Tunnel Laboratory of the University of Western Ontario were compared to results measured at the *Université de Sherbrooke* and results from the old bridge rig of the Boundary Layer Wind Tunnel Laboratory. This was done considering the same bridge section model. For the flutter derivatives and dynamic responses, a good agreement was obtained between the results of the different bridge rigs, therefore validating the reliability of the new bridge rig. This new bridge rig will be utilized in the near future to conduct nonlinear section model tests in order to provide an experimental assessment of the effect of structural nonlinearities on the aerodynamic and aeroelastic behavior of cable-supported bridges.

References

1. Arioli G, Gazzola F (2017) Torsional instability in suspension bridges: the Tacoma narrows bridge case. Commun Nonlinear Sci Numer Simul 42:342–357
2. Bartoli G, Contri S, Mannini C, Righi M (2009) Toward an improvement in the Identification of bridge deck flutter derivatives. J Eng Mech 135(8):771–785
3. Brancaleoni F, Diana G, Fiammenghi G, Firth IPT, Gimsing NJ, Jamiolkowski M, Sluszka P, Solari G, Valensise G, Vullo E (2010) The Messina Strait bridge: a challenge and a dream. CRC Press/Balkema, Leiden, Netherlands
4. Capsoni A, Ardito R, Guerrieri A (2017) Stability of dynamic response of suspension bridges. J Sound Vib 393:285–307
5. Davenport AG, King JPC, Larose GL (1992) Taut Strip model tests. Aerodynamics of Large Bridges, Balkema, Copenhagen, Denmark, pp 113–124
6. Gimsing NJ, Georgakis CT (2012) Cable supported bridges: concept and design, 3rd edn. John Wiley & Sons, West Sussex, UK
7. Hjorth-Hansen E (1992) Section model tests. Aerodynamics of Large Bridges, Balkema, Copenhagen, Denmark, pp 95–112
8. Hussain N, Falbe-Hansen K, Kyte S (2010) Stonecutters bridge, Hong Kong: design and construction. Arup and COWI, Hong Kong
9. Irwin PA (1992) Full aeroelastic model tests. Aerodynamics of Large Bridges, Balkema, Copenhagen, Denmark, pp 125–135

10. Maheux S (2017) Simulation Dynamique du Flottement d'un Pont Élancé à l'Aide de Coefficients Instationnaires Temporels. Master's Thesis, Université de Sherbrooke, Sherbrooke, QC, Canada
11. Maheux S, King JPC, El Damatty A, Brancaleoni F (2020) Assessment of nonlinear structural vertical-torsional coupling in cable-supported bridges. Eng Struct 219:110800
12. O'Neil T, Strganac TW (1998) Aeroelastic response of a rigid wing supported by nonlinear springs. J Aircr 35(4):616–622
13. Schwartz M, Manzoor S, Hémon P, de Langre E (2009) By-pass transition to airfoil flutter by transient growth due to gust impulse. J Fluids Struct 25(8):1272–1281
14. Skyvulstad H, Argentini T, Zasso A, Øiseth O (2021) Nonlinear modelling of aerodynamic self-excited forces: an experimental study. J Wind Eng Ind Aerodyn 209:104491
15. Zhang WM, Ge YJ (2014) Flutter mode transition of a double-main-span suspension bridge in full aeroelastic model testing. J Bridg Eng 19(7):06014004
16. Zhang WM, Quian KR, Ge YJ (2021) Research on flutter-mode transition of a triple-tower suspension bridge based on structural nonlinearity. Structures 34:787–803
17. Zhu LD, Gao GZ, Zhu Q (2020) Recent advances, future application and challenges in nonlinear flutter theory of long span bridges. J Wind Eng Ind Aerodyn 206:104307

Wind-Induced Pounding of Tall Structures in Proximity

Tristen Brown, Ahmed Elshaer, and Anas Issa

Abstract Pounding of adjacent structures under lateral loads (e.g., earthquake and wind) due to proximity has been a major cause of building damages in the past. The effects of pounding can be mitigated by providing a suitable gap distance between structures, adequate shock absorbers or by designing for the additional pounding loads. However, if not properly considered, these abnormal supplementary loads can damage the structures, notably when the attentive structure experiences a dynamic vibration in an out-of-phase order. Multiple pounding incidents have been reported to occur under lateral loads, which resulted in local and global damages. With the new generation of tall buildings, which are becoming taller and more flexible, these structures are becoming more susceptible to wind-induced pounding due to the large deflections developed during high wind problematic affairs. The present study has considered a detailed three-dimensional pounding-involved response analysis of two adjacent structures using the Finite Element Method (FEM) under nonlinear dynamic wind-induced load. This study examines the pounding between two identical tall buildings with a typical outer shape. First, the wind loads on these structures were evaluated using Large Eddy Simulations (LESs). Then, the extracted wind loads from the LES model were applied to a validated finite element model to determine the expected response (i.e., building deflections and accelerations). Different dynamic characteristics of the building and wind magnitudes were examined to assess their effects on the building responses. Results concluded that the pounding force could be correlated to building height, gap distance, and dynamic structural properties of the colliding buildings.

Keywords Wind-induced pounding · Tall structures · Proximity

T. Brown (✉) · A. Elshaer · A. Issa
Lakehead University, Thunder Bay, ON, Canada
e-mail: Tabrown3@lakeheadu.ca

A. Elshaer
e-mail: Aelshaer@lakeheadu.ca

A. Issa
e-mail: Aissa@lakeheadu.ca

1   Introduction

Buildings are continuously constructed within dense metropolitan locations to other structures in proximity. This is due to the increase in population and maximizing building use within the restricted availability of land space. The pounding of structures has become an important commodity with the design of new, tall, and slender structures when built within proximity. The term "pounding" is defined by past scholars [6, 13, 27, 30, 31] when two adjacent neighboring structures are in close proximity causing a collision when subjected to lateral loading. In addition, [23] mentioned that the pounding phenomenon occurs when different dynamic characteristics of a structure (e.g., mass and stiffness) collide due to their out-of-phase vibration from earthquake excitation. Reference [1] defined structural pounding as similar to [23], but additionally added that the out-of-phase vibrations can occur during high wind proceedings as well. The pounding phenomenon from past field evidence has ranged from light to heavy structural damages to the extent of initiating global structural failures [36]. Although most pounding cases have occurred during earthquakes causing induced ground motion and transferring to the structures, it can also be generated when structures are subjected to extreme lateral loads, such as extensive wind loads [21]. Many past scholars have extensively studied these pounding events, particularly from past earthquake occurrences [4, 5, 22, 23, 27, 28, 30, 36]. An extensive literature review focusing on structural pounding has been recently published by [7, 32].

Past scholars have demonstrated that tall and slender structures are ultimately sensitive toward lateral loading [21, 29], where wind forces are applied toward the building's exposed surfaces. Alternatively, seismic forces applied are inertial, resulting from inertial resistance of the building and distortion of the ground [34]. A study by [3] examined multi-hazards on a high-rise structure by comparing the fundamental differences between wind and earthquake demands. In their research, the same structure under wind forces can create a larger deflection and inter-storey drifts than an earthquake within the same location (i.e., up to eight times higher lateral deflection and 2.5 times inter-storey drift). The lateral loads applied can develop a high value of lateral forces, producing intensive sway movement or causing strong vibrations throughout the structure [39]. Meeting the lateral deflection requirements or controlling the extensive vibrations can be, in some cases, more challenging than meeting the strength and capacity requirements within the building [15]. Lateral deflection and structural sway in tall buildings can affect the non-structural elements (i.e., cladding and partition), the main structural elements, and possible adjacent structures [10, 34, 40]. For the adequate designs in new tall structures in proximity, extreme measures for large deflection and structural sway need to be addressed appropriately in the design.

Rigorous studies have been conducted to mitigate these safety precautions to avoid such pounding hazard phenomena. An objective in the past was to develop procedures for evaluating adequate separation distances between structures to prevent contact during extensive lateral motion events [24, 25, 33]. However, these requirements are

not correlated to the dynamic properties of the adjacent buildings or the lateral loads from such natural hazards [9]. Moreover, numerous buildings and structures were designed and built before such requirements in their codes and provisions, leading to pre-existing structural pounding failures [35]. Namely, tall structures should provide reliable analysis and a correct basis for selecting load factors in these building provisions [19]. While most building codes identify these necessities toward standards and hazards for deflection, limited cases for building codes are identified for the required minimum separation distance for structures at proximity during wind evaluations. Mitigation can be implemented for structural pounding if no or insufficient building spacing is provided. Despite past scholars regarding earthquake-induced pounding, colliding of structures (such as buildings or bridges) can be motivated by building deflections generated from their out-of-phase vibrations, depending on their dynamic structural properties. Namely, out-of-phase vibrations arise from intensive lateral loading (e.g., wind events), making the occurrence of wind affairs problematic for these specific pounding phenomena. This paper articulates a case study relating to possible structural damages which lead from the wind-induced pounding of structures at proximity. The study will consist of a numerical wind simulation to determine the problematic wind forces subjected to two tall, slender structures, leading the slender structure to have large lateral deflections. Once forces have been collected, a numerical simulation will then be used to apply the wind forces subjected to the structures to determine their structural responses. Once applied, strong forces will trigger a simultaneous pounding effect on the proximate structure due to an insufficient separation distance. Such structural forces will then be gathered from simulations with altering the separation distances between the two adjacent structures. Once results are concluded, an adequate separation distance between the two proximate structures will be determined to ultimately eliminate structural pounding, leading to no possible damages.

This paper is divided into five key sections. In Sect. 1 (this section), an introduction on past events and occurrences of structural pounding. Section 2 describes the Large Eddy Simulation (LES) modeled structure simulated through a Computational Fluid Dynamics (CFD) wind analysis. Such wind forces are then conducted and inputted in a finite element model, detailed in Sect. 3, to simulate the structures' responses, neighboring interactions when structural pounding occurs. In Sect. 4, the numerical Finite Element Method (FEM) results and discussion are provided, and comparisons are made to determine the possible pounding forces when structural pounding occurs. The conclusion is then presented in Sect. 5.

2 Numerical Modeled Structure

The focus of the present study is on the correlation to the pounding between two adjacent tall structures. To accurately model the CFD and FEM modeled simulation, all the fluid properties and structural details of the buildings must be accurately modeled.

A simplified structural analysis scheme will be conducted to reduce the computational cost without affecting the accuracy of the developed wind loading, responses, and dynamic analysis of the pounding structures. Therefore, the current study has adopted the Commonwealth Advisory Aeronautical Research Council (CAARC) structure from defining such geometric details. This structure has been an ever-continuing benchmark in several wind-related experimental and numerical studies. The full-scale building's geometric rectangular footprint has a depth of 45 m and a base of 30 m with a corresponding total height of 180 m. All aerodynamic measures and characteristics are assigned according to [14], where the structural characteristics were assigned according to [8, 20]. The wind direction is considered perpendicular to the wider side of the building (i.e., zero degree angle along the y-axis), which is identified as the most unfavorable incident wind direction and considered in the dynamic response.

2.1 Numerical Wind Model

To accurately model a numerical wind simulation, a 1:400 scaled aeroelastic LES model is considered to validate the modeled CAARC structure [12]. In addition, a 1:100 time scale is considered for the LES model. This modeled analysis has comparable results as a wind tunnel simulation [12] from the tested facility at Rowan Williams Davies and Irwin (RWID) Inc's wind tunnel.

2.1.1 Large Eddy Simulation Modeled Computational Domain and Boundary Conditions

The computational domain dimensions employed for the LES are defined based on the recommendation of [11, 16, 17] as shown in Fig. 1a. In the computational domain, a non-slip boundary condition is assigned to the ground and all walls of the structure, where the tangential velocity component is set to zero. The symmetry plane boundary condition is assigned to the sides and top faces of the computational domain, extrapolating the parallel velocity and pressure components in the adjacent cell using reconstruction gradients and developing zero shear stress at the symmetry plane. The inflow boundary condition utilizes a database for each velocity component depending on both location and time [e.g., $u_x(x, y, z, t)$], which is previously generated using the Consistent Discrete Random Flow Generator (CDRFG) technique [2, 14]. Finally, the outlet of the computational domain is defined as an outlet.

   A mean wind velocity of 10 m/s at the top of the structure's height is shown in Fig. 1b which is considered in the CFD simulated model. The LES simulations are conducted using a commercial CFD package (STAR-CCM+ v.15.04.008) with a dynamic sub-grid scale model by [18, 38]. The parameters used in the simulation to handle flow quantities and the solution method are as follows. The exposure factor for the structures is within open terrain, having an average mean wind velocity of 10 m/s
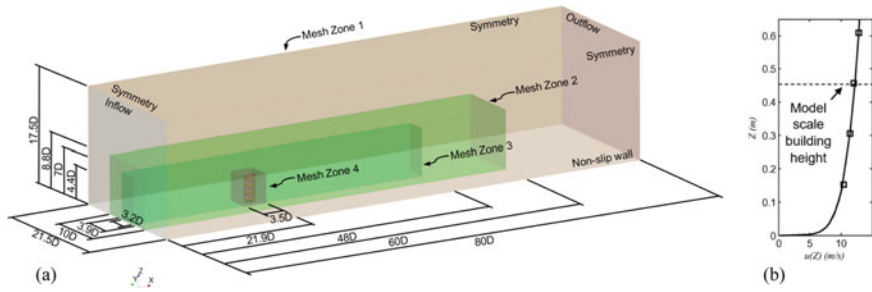
Fig. 1 **a** Computational domain dimensions and boundary conditions, **b** velocity-modeled scale at building height

corresponding to the structure's reference height equal to 0.4562 m in the modeled scale. The turbulence intensity reference in u, v, and w directions is 0.197, 0.167, and 0.145, respectively. The referenced length scale in the x, y, and z directions is 0.563 m, 0.147 m, and 0.186 m, respectively. A Courant–Friedrichs–Lewy (CFL) must be maintained less than 1.0 to maintain the wind solution's accuracy and convergence. To complete this, a time step is to be 5×10^3 s (i.e., maximum CFL = 0.5 at the top of the CAARC structure). Each simulation is resolved for 14,000 time steps representing 7.0 s in the scaled model (i.e., 11.5 min in a full-scaled model). To conduct the CFD simulations in a costly manner, the simulations are performed using the ("SharcNet," 2022) high-performance computer (HPC) facility. The duration required for the numerical simulations was on ninety-six processors, which took sixty hrs.

2.1.2 Grid Discretization

The grid discretization is considered inside the computational domain as hexahedral control volumes. The grid resolution and properties are summarized in Table 1 for the isolated CAARC structure. Each grid within the computational domain is divided into four zones, as illustrated in Fig. 2. Zone 1 is considered as the furthest zone away from the building of interest, with the grid size being the largest. Zone 4 is located closest to the building of interest with the smallest volumetric grid size. Having a decreased grid size compared to zone 1 captures essential details of flow structures in the wake zone and the from zone between the inflow boundary condition and the building. Zone 2 and zone 3 are considered between zones 1 and 3 and have a medium grid size.

2.1.3 Wind Analysis Results

To perform the structural response of the CAARC structures when subjected to intensive wind loads, a history of forces acting on each storey of the structures must

Table 1 Parameters for the generated wind flow velocity field

Grid	G1			
Grid size	Zone 1	Zone 2	Zone 3	Zone 4
	H/5	H/10	H/25	H/66
Total number of cells	1,750,000			

Computational Mesh   Surface Mesh   Fine Air Mesh
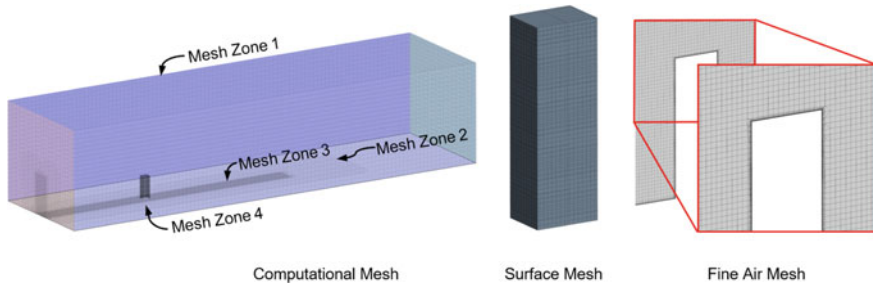
Fig. 2 Mesh grid resolution utilized in the CFD simulation for the proximate structures

be obtained from the LES simulation. In Fig. 3, the LES modeled structure is divided into two equal size structures to represent the modeled CAARC structure with no separation distance between each structure as it will cause convergent issues over time. Figure 3 shows the derived surfaces acting on the 25th storey for the first structure. Next, the two structures are divided into forty-five equal levels to represent each storey height. To average the forces acting on the floor of each structure over time, all surfaces of the structure are summed together and conducted in one acting force. Figures 4a and b show the time histories of the wind force acting on the 45th storey for each structure in the x-direction (longitudinal) in the full-scale model. It is noted that the first 50 s was not captured in the numerical simulation to allow for the initial converging.

2.2 Finite Element Model

The 180 m-tall CAARC structure conducted to assess the potential pounding phenomenon in a time-history analysis consists of 45 stories, with a 10-bay by 15-bay rectangular tubular steel skeletal framework shown in Fig. 5. Each storey height is 4 m tall, with each bay width being 3 m wide. The structure's member sizes are based on [8, 20] study, which was established based on a preliminary strength check according to the AISC steel code (2001). The selected steel columns are to be W14 shapes and for the beams to W30 shapes, which can be seen in Table 2. The ground supports are considered fixed, giving the overall building a rigid floor connection. The steel structure building has a natural frequency and modal damping ratios which
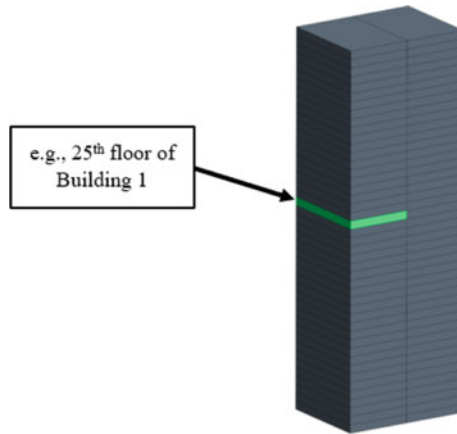
Fig. 3 Derived surfaces for both structures with the 25th storey of the first structure as highlighted
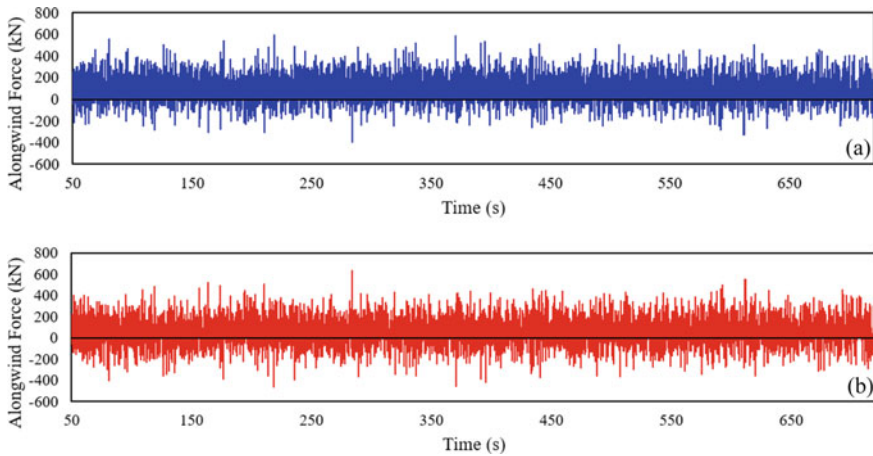
Fig. 4 Full-scale forces' time history in the along-wind direction acting on the 45th storey of **a** building 1 and **b** building 2

equal to 0.15 and 2%, respectively. The density, Young's modulus, and Poison's ratio of the structure are assigned to be $7850 \, \text{kg/m}^3$, 200, 000 MPa, and 0.25, respectively. The first, second, and third modes of the natural frequencies of the buildings were found to be 0.198, 0.281, and 0.361, respectively. Table 3 presents the along-wind and across-wind base shear forces, respectively, in addition to the torsional base torque from the wind-induced structural loads of the CAARC building.

The structure is located in a dense metropolitan within many structures close in proximity. The overall wind loading applied to the structure was obtained using a numerical LES simulation as previously mentioned in Sect. 2.1. In addition, a time-stepping method is conducted to analyze the time-history dynamic response of

Fig. 5 Framework of the
45-storey CAARC structure
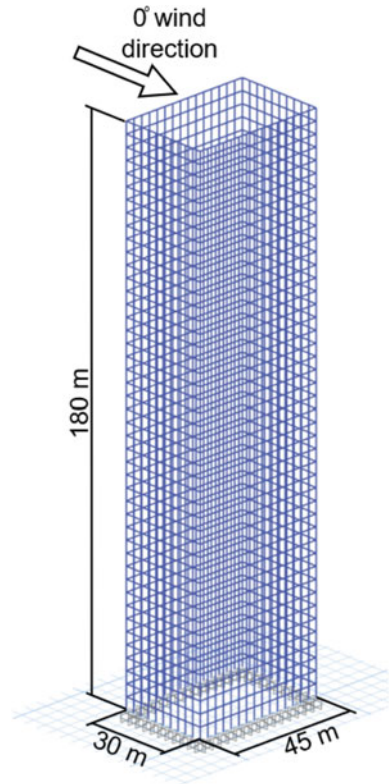
Table 2 Steel member sizes
for the 45-storey CAARC
structure framework

Storey level	Column size	Beam size
1–9	W14 × 550	W30 × 357
10–18	W14 × 500	W30 × 326
19–27	W14 × 370	W30 × 292
28–36	W14 × 257	W30 × 261
37–45	W14 × 159	W30 × 211

Table 3 Structural wind
loads for the CAARC
structure framework

Along-wind base shear (kN)	Across-wind base shear (kN)	Torsional base torque (kN m)
18,826	28,238	688,307

the CAARC structure. The x-direction (across wind) of the CAARC structure was
found to have more significant displacement and drift than the y-directional response
of the building under 0° wind angle of attack. Figure 6a shows a comparison of the
maximum top lateral deflection along the x-direction and Fig. 6b shows a comparison
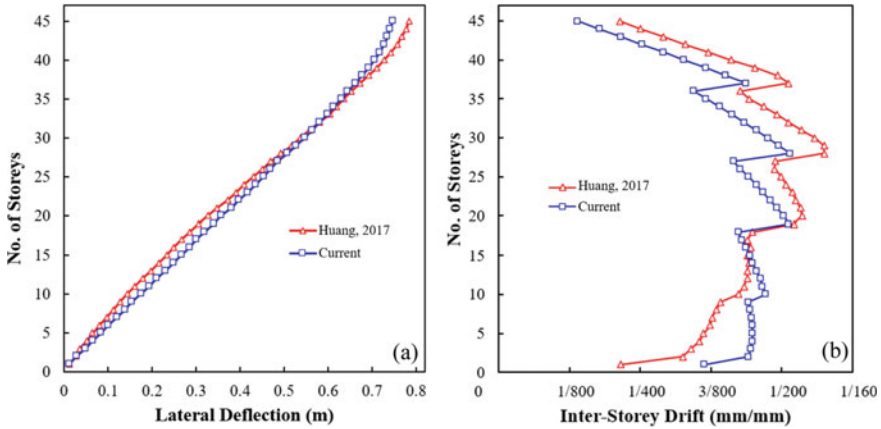
Fig. 6 a Maximum top deflection and b maximum inter-storey drift in the along-wind direction

of the maximum inter-storey drift at the most critical instant, respectively. The initial top deflection and inter-storey drift from [8, 20] study both exceeded the drift limit ratios of 1/400. It was attributed to the fact that the initial member sizes were based on the preliminary strength check and the structural system intended use was to be used in a structural optimization study for deflection strains.

3 Finite Element Pounding Model

The pounding-involved response of the two adjacent CAARC structures that are numerically simulated with their dynamic properties has been mentioned in Sect. 2.2 and has been conducted using the model structure shown in Fig. 7. The applied wind forces from the CFD analysis are extrapolated for each storey level on both structures in the x-direction (longitudinal direction) and then imported into the FEM analysis using a time-history analysis. All wind forces are scaled to full-scale wind velocities at 40 m/s in the along-wind direction (10 m/s in modeled scale), which is dependent over a period of 11.5 min. The analytical result for the longitudinal direction shows the displacement, moment, and shear force–time histories of building 1 and building 2 in Fig. 8, respectively.

3.1 Model Idealization

In this present work, the interaction of the two identical adjacent structures with comparable overall structure heights is studied. Each structure has a dynamic
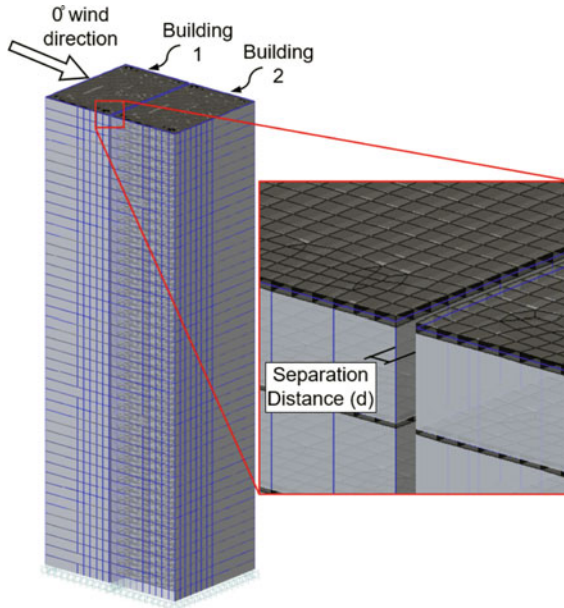
Fig. 7 Three-dimensional view of the two CAARC structures with a proximate separation distance (d)
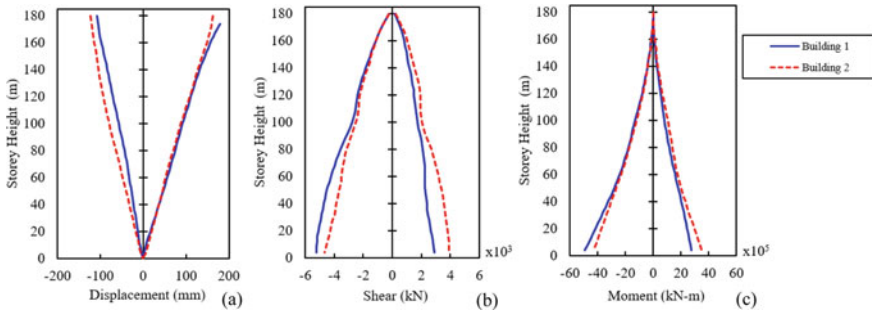
Fig. 8 Extreme **a** displacement, **b** base shear force, and **c** base moment for building 1 and building 2

response and vibrates independently. Each structure is modeled as an inelastic multi-degree-of-freedom system but only produces forces in the longitudinal direction. In comparison, one structure is considered in contact or proximity to a similar adjacent structure. When examined, if there is a gap distance between the two adjacent structures and a collision occurs, the lateral displacement of the structures must exceed the separation gap distance (d). The influence of the gap size on the pounding effect is parametrically examined in this investigation. Since the involved structures have identical storey heights and a similar overall building height, pounding, if conducted,

will occur between the storey floor diaphragms, making contact pounding at the columns and, therefore, among the storey masses.

3.2 Contact Element

Contacts points for the pounding phenomena between the studied structures are replicated using linear compression links. The contact links will only register (record compression values over time) when the contact points of the structures make the connection from the overlapping of the building frames (beams, columns, or slabs) [26]. This idealization is constant with the constructing model used and looks acceptable for analyzing the outcomes of pounding on the general structural reaction for the pounding instances through examination. As this study examines the effects of pounding (i.e., forces acting on the linear springs), the local effects on the columns and beams are not considered for the modeled structures.

The contact links will consist of three scenarios for the pounding phenomena. Firstly, the first structure will laterally deflect in a negative x-axis direction. The second structure is either stable, laterally deflects in a positive x-axis direction, or laterally deflects in a lesser negative x-axis direction than the first structure. The contact links in this scenario will allow the spring constant to produce a negative axial force, leading to no pounding. The second and third scenarios consist of the first structure to sway in a positive x-axis direction and the second structure to either be stable, move in a negative x-axis direction or a lesser positive x-axis direction than the first structure. The last two scenarios consider the separation distance (d) between both structures. The second scenario consists of the aforementioned statement, but the separation distance (d) between the two structures is greater than the summation of both structures' lateral deflections. The contact springs in this scenario will consist of a non-negative compression value; however, the contact springs will remain as non-active as no contact (pounding) between the two structures has occurred. As previously mentioned, the third and last scenarios consist of the summation of both structures' lateral deflections exceeding the separation distance (d) between both structures, conducting a pounding effect, leading to a positive compression value in the contact points (linear compression links). The separation distance (d) can also be seen in Fig. 7.

4 Results and Discussion

A parametric study has been conducted to investigate the influence of different gap distances between the adjacent CAARC structures involved in the wind-induced pounding using numerical nonlinear finite element software. In the analysis, the fundamental values of the structural model's parameters, specified in Sect. 2, have been applied. In addition, the records of the nonlinear time-history wind forces have

been used as a dynamic load applied to each floor of each structure separately in the longitudinal direction (x-direction) to investigate the pounding forces of structures in a finite element system.

4.1 Numerical Results

A comparison of the motion responses of the adjacent structures by pounding-involved and independent vibration (significant separation distance preventing contacts) displacement responses of the buildings in the longitudinal direction (x-axis) on the 45th storey of both structures is shown in Fig. 9. Additionally, the analysis results showing the pounding force–time histories on the 45th storey of both structures are presented in Figs. 10a, 11, and 12 for the top storey buildings spaced at 200 mm, 100 mm, and 0 mm, respectively.

As seen in Fig. 9, both structures spaced at 300 mm came into close contact at the time of 627 s, but no collision of structures occurred, and therefore, no force was recorded. However, the first sign of structural pounding happened when the structures were spaced out at 200 mm at the same instant of time of 627s, which can be seen in Fig. 10a. Figure 10b compares the recorded force at the time of 627 s when the two structures come into contact at the top three-storey heights. It can be seen from Figs. 11a and b when both structures have a separation distance (d) of 100 mm that both structures came into contact multiple times during the wind-induced force analysis. Figure 10a shows that after the pounding has occurred, the lateral deflection of the first and second structures is minimized in compared to both of the structures when pounding does not happen. An increase in lateral deflection can also be seen in Figs. 11a and 12a for both structures when multiple contacts occur at a short period of time. As can be noted in comparison to Figs. 10b, 11b, and 12b, as the separation distance (d) is decreased between both structures, the pounding forces increase.

As shown in Fig. 13, a comparison between the lateral displacement in the longitudinal direction for building 1 on the 45th storey when pounding is involved at the time of 627 s, spaced at 200 mm, and when the structure is independently vibrating.
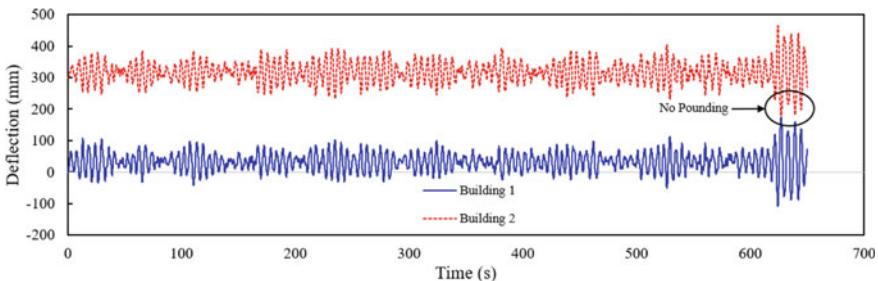
Fig. 9 Time history for the 45th storey of both buildings in the longitudinal direction at a separation distance of 300 mm for displacement without contact to the neighboring structure
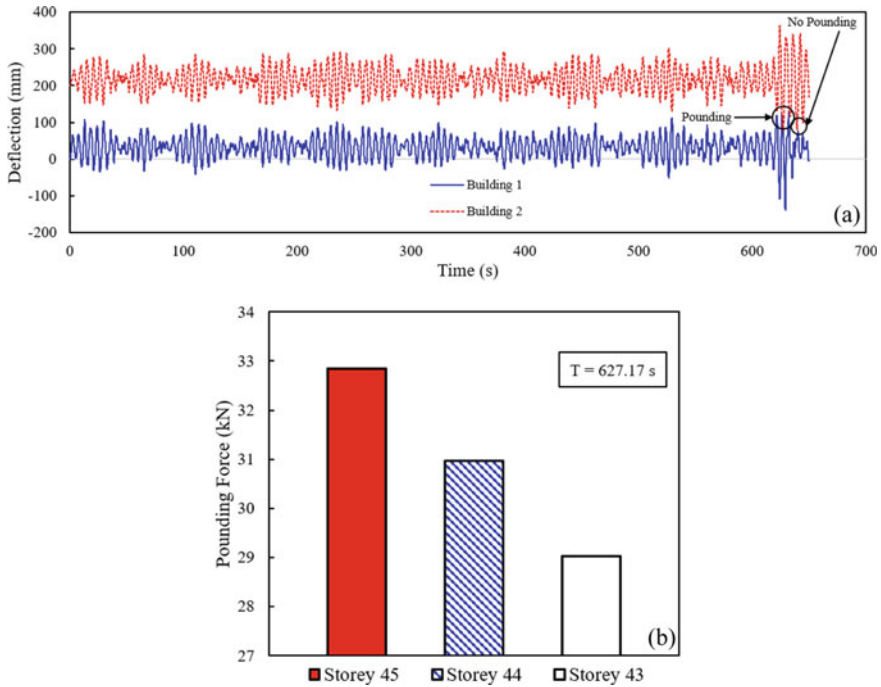
Fig. 10 Time history for both buildings in the longitudinal direction at a separation distance of 200 mm for the **a** 45th storey displacement, and **b** pounding forces on the 45th, 44th, and 43rd storey 45

A comparison is shown in Fig. 10b, which shows the results or the maximum forces acting on the 45th, 44th, and 43rd stories at the instant when pounding is presented at 627 s. The results indicate that the highest contact point (at the 45th storey) is the most critical pounding force when such contact is developed and decreases with respect to the structure height.

4.2 Separation Distance Effects Between Structures

The in-between gap distance is a crucial configuration parameter that describes neighboring buildings' spatial association. Figure 14 displays the most significant displacements of the pounding structures within the longitudinal direction received for distinctive values of this parameter. It is visible from the figures that the three-dimensional response of the first structure has a more significant variation and is more sensitive to the separation distance (d) value since the first structure is more susceptible to more vital wind-triggered forces. On the other hand, in the case of lateral deflection in the longitudinal direction for the second structure (see Fig. 14b),
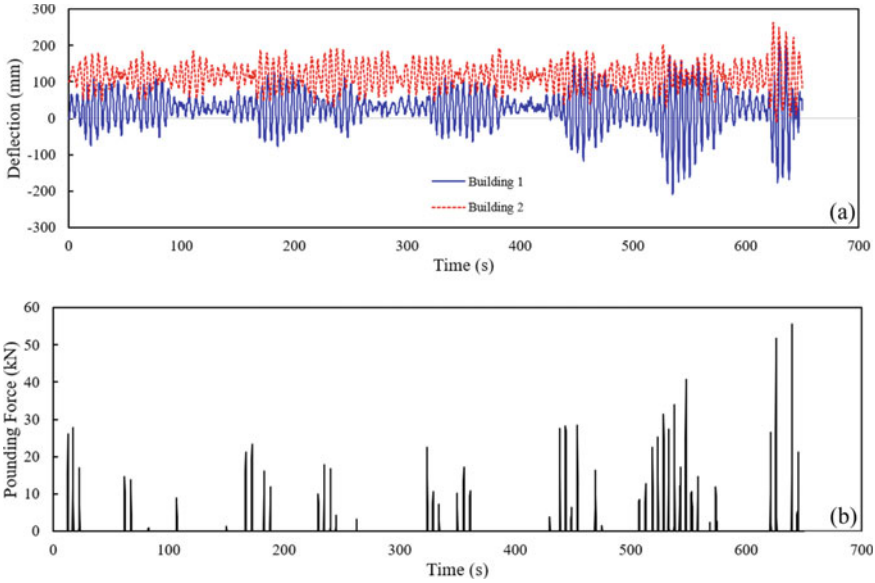
Fig. 11 Time history for the 45th storey of both buildings in the longitudinal direction at a separation distance of 100 mm for the **a** displacement, and **b** pounding forces
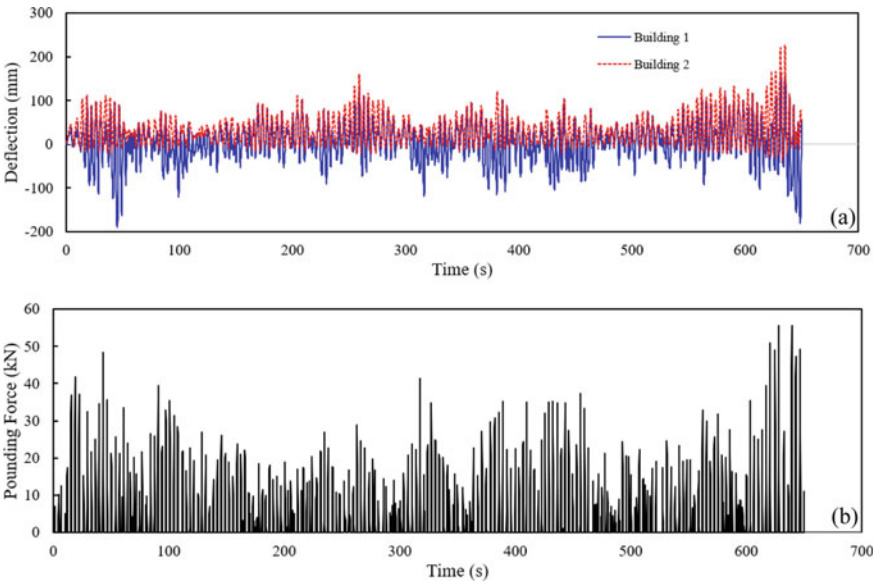
Fig. 12 Time-history for the 45th storey of both buildings in the longitudinal direction at a separation distance of 0 mm for the **a** displacement, and **b** pounding forces
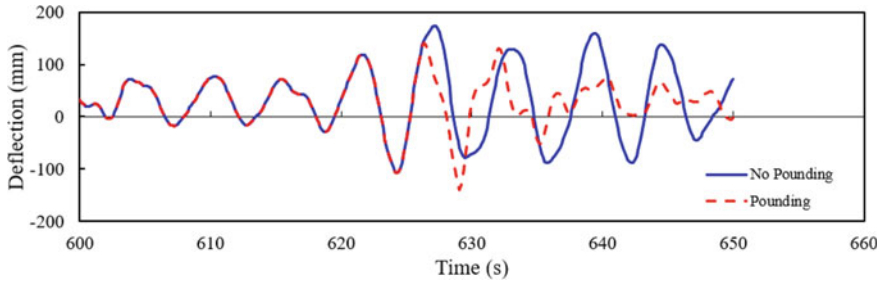
Fig. 13 Wind-induced pounding displacement and independent displacement of building one time histories of the 45th storey

a growth withinside the gap distance is related to a reduction in the top displacement. As opposed to the second structure, the reaction of the first structure is slightly more affected by the difference in the gap size, as shown in Fig. 14a. Figure 15 shows the forces gathered when the structural pounding occurs concerning the separation distance (d). It can be noted that the forces will increase when the separation distance (d) decreases. However, the pounding force will decrease when the structures are initially completely touching [0 mm separation distance (d)]. As seen in Fig. 16, the maximum inter-storey drifts are compared for both structures (see Fig. 16a for building 1 and Fig. 16b for building 2) with respect to the separation distance (d). For building 1, the storey drift decreases as the separation distance (d) decreases, whereas for building 2, the storey drift increases as the separation distance (d) decreases.

From the parametric examination of wind-triggered structural pounding, consequences can conclude that a separation distance (d) of 294.5 mm is required to prevent such pounding phenomena among similar adjoining CAARC structures under a time-history wind velocity of 40 m/s in full scale (10 m/s in modeled scale). It must be noted that the minimum separation distance (d) will rely upon many factors, such as
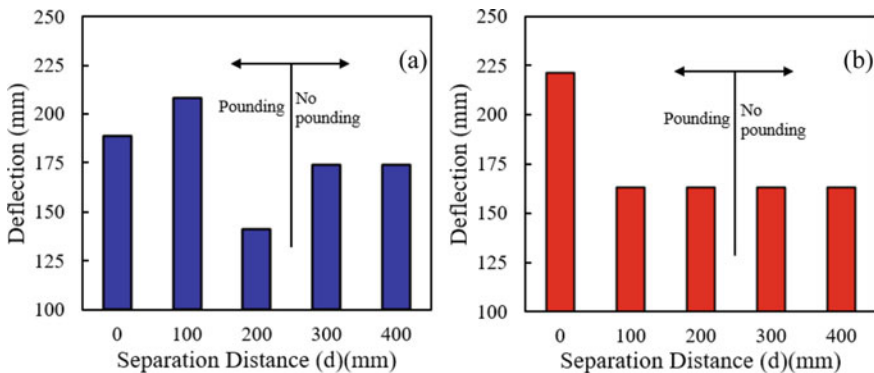
Fig. 14 Maximum deflection in the longitudinal direction with respect to the separation distance (d) between structures for **a** building 1 and **b** building 2
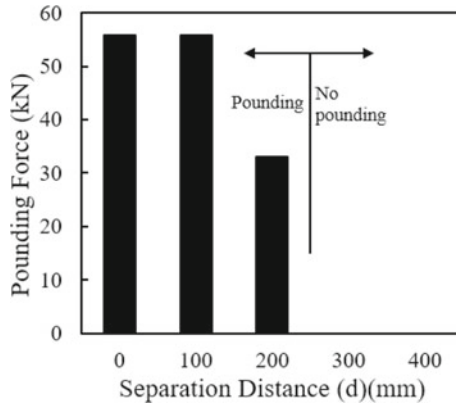
Fig. 15 Pounding force at the 45th storey of both structures for different separation distances
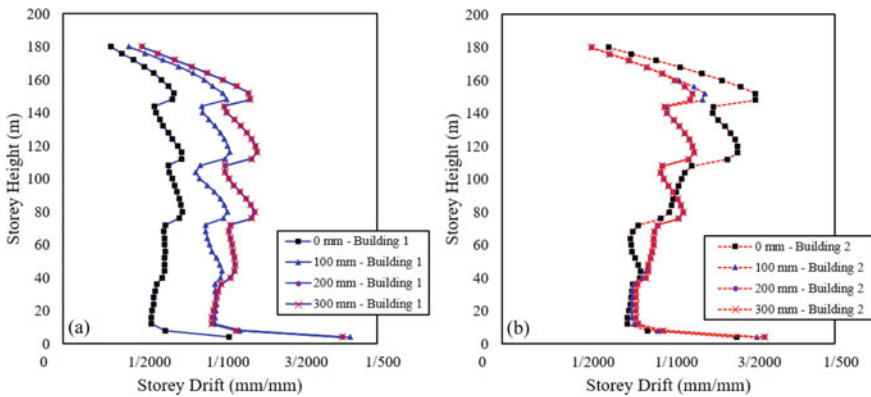
Fig. 16 Maximum storey drift at different storey heights with respect to the separation distance for **a** building 1 and **b** building 2

the dynamic structural properties, location of structures, and intensity of the wind analysis.

5   Conclusion

This study conducted a nonlinear FEM analysis to simulate a wind-induced structural pounding phenomenon between two structures of equal height. The modeled buildings are considered as an inelastic multi-degree-of-freedom skeletal steel structures that only produces pounding forces in the longitudinal direction. The pounding study has focused on the colliding forces from two typical tall structures. The investigation

results have been conducted for different values for the structural spacing, which has been presented.

The results for the studied analysis show that pounding of two adjacent structures under extreme wind loads is influenced by the structures' height, density, structures flexibility, more specifically in the longitudinal direction, and separation distance. The numerical analysis results demonstrated that the pounding forces when collisions occur depend on the structure's separation distance. The general trend for all pounding forces ultimately reveals similarities when the structures are very close, and pounding is regular. However, the pounding forces decreased when the colliding structures had more considerable separation distances and minimum number of impacts.

It was found that the lateral structural deflections on the first structure subjected to wind could have larger deflections with smaller separation distances compared to larger separation distances. Such deflections can be from both structures having similar in-phase responses when there is no separation. The findings, however, have opposing trends for the adjacent following structures. Trends show the following structure to have the most significant lateral deflection when there is no separation distance between the structures, then decreases in deflection when the separation is increased.

The studied analysis appears that particular attention must be acquired to appropriately design tall structures' built-in proximity, for which extreme wind-induced structural pounding can lead to structural failures. To prevent such failures from adjacent, proximate structures, a required separation distance is critical to achieve. For structures already built at close proximity and none of the solutions available, pounding mitigation techniques should be considered to prevent such pounding phenomena from severe wind impacts.

References

1. Abdullah MM, Hanif JH, Richardson A, Sobanjo J (2001) Use of a shared tuned mass damper (STMD) to reduce vibration and pounding in adjacent structures. Earthq Eng Struct Dyn 30:1185–1201. https://doi.org/10.1002/eqe.58
2. Aboshosha H, Elshaer A, Bitsuamlak GT, El Damatty A (2015) Consistent inflow turbulence generator for LES evaluation of wind-induced responses for tall buildings. J Wind Eng Ind Aerodyn 142:198–216. https://doi.org/10.1016/j.jweia.2015.04.004
3. AlyAM, Abburu S (2015) On the design of high-rise buildings for multihazard: fundamental differences between wind and earthquake demand. Shock Vib. https://doi.org/10.1155/2015/148681
4. Anagnostopoulos SA (1995) Earthquake induced pounding: state of the art. In: Proceedings of the 10th European conference on earthquake engineering. Rotterdam, Balkema, pp 897–905
5. Anagnostopoulos SA (1988) Pounding of buildings in series during earthquakes. Earthq Eng Struct Dyn 16:443–456. https://doi.org/10.1002/eqe.4290160311
6. Anagnostopoulos SA, Spiliopoulos KV (1992) An investigation of earthquake induced pounding between adjacent buildings. Earthq Eng Struct Dyn 21:289–302
7. Brown T, Elshaer A (2022) Pounding of structures at proximity: a state-of-the-art review. J Build Eng 48:103991. https://doi.org/10.1016/j.jobe.2022.103991

8. Chan CM, Chui JKL, Huang MF (2009) Integrated aerodynamic load determination and stiffness design optimization of tall buildings. Struct Des Tall Spec Build 18:59–80. https://doi.org/10.1002/tal.397

9. Chau KT, Wei XX (2001) Pounding of structures modelled as non-linear impacts of two oscillators. Earthq Eng Struct Dyn 30:633–651. https://doi.org/10.1002/eqe.27

10. Chenna R, Ramancharla PK (2018) Damage assessment due to pounding between adjacent structures with equal and unequal heights. J Civ Struct Heal Monit 8:635–648. https://doi.org/10.1007/s13349-018-0296-1

11. Dagnew AK, Bitsuamlak GT (2013) Computational evaluation of wind loads on buildings: a review. Wind Struct. An Int J 16:629–660. https://doi.org/10.12989/was.2013.16.6.629

12. Dragoiescu C, Garber J, Kumar KS (2006) A comparison of force balance and pressure integration techniques for predicting wind-induced responses of tall buildings. Proc Struct Congr Expo 2006:14. https://doi.org/10.1061/40889(201)14

13. Efraimiadou S, Hatzigeorgiou GD, Beskos DE (2013) Structural pounding between adjacent buildings subjected to strong ground motions. Part I: the effect of different structures arrangement. Earthq Eng Struct Dyn 42:1509–1528. https://doi.org/10.1002/eqe

14. Elshaer A, Aboshosha H, Bitsuamlak G, El Damatty A, Dagnew A (2016) LES evaluation of wind-induced responses for an isolated and a surrounded tall building. Eng Struct 115:179–195. https://doi.org/10.1016/j.engstruct.2016.02.026

15. Elshaer A, Bitsuamlak G (2018) Multiobjective aerodynamic optimization of tall building openings for wind-induced load reduction. J Struct Eng (United States) 144:1–11. https://doi.org/10.1061/(ASCE)ST.1943-541X.0002199

16. Franke J (2006) Recommendations of the COST action C14 on the use of CFD in predicting pedestrian wind environment. Recommentations of the COST action C14 use CFD prediction pedestrian winds environment, pp 529–532

17. Franke J, Hellsten A, Schlunzen KH, Carissimo B (2011) The COST 732 best practice guideline for CFD simulation of flows in the urban environment: a summary. Int J Environ Pollut 44:419–427

18. Germano M, Piomelli U, Moin P, Cabot WH (1991) A dynamic subgrid-scale eddy viscosity model. Phys Fluids A 3:1760–1765. https://doi.org/10.1063/1.857955

19. Halabian AM, El Naggar MH, Vickery BJ (2003) Reliability analysis of wind response of flexibly supported tall structures. Struct Des Tall Build 12:1–20. https://doi.org/10.1002/tal.207

20. Huang M (2017) High-rise buildings under multi-hazard environment, high-rise buildings under multi-hazard environment: assessment and design for optimal performance. Springer Singapore, Singapore. https://doi.org/10.1007/978-981-10-1744-5

21. Huang MF, Chan CM, Lou WJ (2012) Optimal performance-based design of wind sensitive tall buildings considering uncertainties. Comput Struct 98–99:7–16. https://doi.org/10.1016/j.compstruc.2012.01.012

22. Jankowski R (2012) Non-linear FEM analysis of pounding-involved response of buildings under non-uniform earthquake excitation. Eng Struct 37:99–105. https://doi.org/10.1016/j.engstruct.2011.12.035

23. Jankowski R (2009) Non-linear FEM analysis of earthquake-induced pounding between the main building and the stairway tower of the Olive View Hospital. Eng Struct 31:1851–1864. https://doi.org/10.1016/j.engstruct.2009.03.024

24. Jankowski R (2005) Non-linear viscoelastic modelling of earthquake-induced structural pounding. Earthq Eng Struct Dyn 34:595–611. https://doi.org/10.1002/eqe.434

25. Jankowski R, Mahmoud S (2015) Mitigation of pounding effects. Earthquake-Induced Struct Pound 103–132

26. Karayannis CG, Favvata MJ (2005) Earthquake-induced interaction between adjacent reinforced concrete structures with non-equal heights. Earthq Eng Struct Dyn 34:1–20. https://doi.org/10.1002/eqe.398

27. Kasai K, Maison BF (1997) Building pounding damage during the 1989 Loma Prieta earthquake. Eng Struct 19:195–207. https://doi.org/10.1016/S0141-0296(96)00082-X

28. Kaushik HB, Dasgupta K, Sahoo DR, Kharel G (2006) Performance of structures during the Sikkim earthquake of 14 February 2006. Curr Sci 91:449–455
29. Lam KM, Wong SY, To AP (2009) Dynamic wind loading of H-shaped tall buildings. In: 7th Asia-Pacific conference on wind engineering, APCWE-VII.
30. Maison BF, Kasai K (1992) Dynamics of pounding when two buildings collide. Earthq Eng Struct Dyn 21:771–786
31. Maison BF, Kasai K (1990) Analysis for a type of structural pounding. J Struct Eng 116:957–977. https://doi.org/10.1061/(ASCE)0733-9445(1990)116:4(957)
32. Miari M, Choong KK, Jankowski R (2021) Seismic pounding between bridge segments: a state-of-the-art review. Arch Comput Methods Eng 28:495–504. https://doi.org/10.1007/s11831-019-09389-x
33. Penzien J (1997) Evaluation of building separation distance required to prevent pounding during strong earthquakes. Earthq Eng Struct Dyn 26:849–858. https://doi.org/10.1002/(SICI)1096-9845(199708)26:8%3c849::AID-EQE680%3e3.0.CO;2-M
34. Rahman A, Fancy SF, Bobby SA (2012) Analysis of drift due to wind loads and earthquake loads on tall structures by programming language c. Int J Sci Eng Res 3:6–9
35. Rezavandi A, Moghadam AS (2007) Experimental and numerical study on pounding effects and mitigation techniques for adjacent structures. Adv Struct Eng 10:121–134. https://doi.org/10.1260/136943307780429752
36. Rosenblueth E, Meli R (1986) The 1985 Mexico earthquake. Concr Int 8:23–34
37. SharcNet [WWW Document] (2022) SHARCNET. Consort Coll Univ Res Inst Oper. Netw High-Perform Comput Clust Across South West Cent North Ontario. [Online]. Available www.sharcnet.ca
38. Smagorinsky J (1963) General circulation experiments with the primitive equations. Mon Weather Rev 91:99–164. https://doi.org/10.1175/1520-0493(1963)091%3c0099:GCEWTP%3e2.3.CO;2
39. Stafford Smith B, Coull A (1991) Tall building structures: analysis and design
40. Wolfgang S (1977) High-rise building structures

Innovation in Structural Engineering

Development of a Physical Model and In Situ Test for the Study of Polymer Injections in Concrete Fractures for Waterproofing

K. El Mekari, F. Duhaime, and L. Colorado

Abstract Polymer injections in concrete fractures are commonly used in practice for the waterproofing of tunnels. This paper introduces two physical models and in situ test for the study of water and polymer flow in fractures. The physical models were created by pouring on top of each other two concrete slabs separated by a plastic film. The in situ tests were performed in a tunnel concrete fracture sealed with a surface capping. Both fractures were instrumented with multiple ports for injection or pressure measurements. This paper presents the main results for the physical models and some preliminary results of the in situ tests. The parameters that were varied include the injection pressure, injection volume, fluid viscosity, and flow rate. Water and four water-glycerol mixtures were used to verify the influence of viscosity on flow. Three major parameters influenced the results: the boundary condition, the saturation level of the fracture, and the dynamic viscosity of the injected liquid. Sealed fractures and moist fractures provoked an important pressure gain inside the fracture. The highest pressure values were obtained with the most viscous liquid. The propagation of the liquid was influenced by the same three parameters. The in situ tests established the hydraulic aperture and hydraulic conductivity of the joint. This paper is intended for all professionals in the concrete structure reparation field.

Keywords Polymer injections · Concrete fractures · Waterproofing

K. E. Mekari (✉) · F. Duhaime
Department of Construction Engineering, École de Technologie Supérieure, Montreal, Canada
e-mail: khalil.el-mekari.1@ens.etsmtl.ca

L. Colorado
Société de Transport de Montréal, Montreal, Canada

1 Introduction

Water infiltration through fractures in tunnels can have important consequences such as frost damages, surfaces finishes deterioration, and rebar corrosion [1], (ITA 2011), [2]. Polymer injection is a common solution to seal concrete fractures for water-proofing or to improve the mechanical properties of concrete [3–6]. The polymers that are used in soil, rock, and concrete during injections are epoxy, polyurethane, and acrylic [1, 7, 8]. To keep the polymer inside the fracture, a surface capping product can be used on the fracture (Trout 2006). A low viscosity polymer is generally used to have a higher liquid penetrability throughout the fracture [3, 9]. A cleaning agent is sometimes used to wipe out the dust inside the fracture before the injection, but the importance of cleaning and the fluid that should be used remain a matter of debate (Trout 2006) [6].

The injection parameters for polymer injections are [1]:

- Resin type and dynamic viscosity;
- Location of the injection ports;
- Injection pressure;
- Injection duration;
- Injection volume.

Their selection is often arbitrary and it is difficult to find specifications that maximize the injection results. Available specifications are often not based on the same criteria. For example, for the injection time and epoxy type one and four based on ASTM C881 standard, [10] mentioned to inject until the port reaches a *refusal* state. This state can be achieved when the injection pressure becomes constant. Reference [6] specifies the importance of matching the injection time with the pot life.

Most of the research work done with physical models of fractures was intended to study the mechanical properties of resin [11–13]. For example, the injection of silane in the fracture before an epoxy injection improves freeze–thaw resistance of the epoxy/concrete interface [13].

Another important element to consider during a fracture injection is the hydraulic aperture. This aperture can be established from in situ tests and from the cubic law to analyze the flow and the head loss in fractures [14–16]. Many documents have been produced over the past years to establish the hydraulic aperture in rock fractures. For example, [17] designed a hydraulic test based on the hydraulic aperture to achieve a penetration length of at least 1 m in rock fracture. Those tests give quantitative information on the relationship between injection parameters and fracture characteristics such as the liquid velocity propagation or injected volume. Such tests are uncommon for waterproofing injections in concrete.

2　Objectives

This article presents the results obtained with two physical models and the development of an in situ test. The goal of this research project is to gain a better understanding of the optimal injection parameters, the fracture characteristics and improve polymer injection durability and effectiveness against water infiltration. Two specific objectives are considered in this paper:

1. Establish how boundary conditions, initial fracture saturation and liquid viscosity affect the pressure and the liquid propagation inside a fracture during injections;
2. Establish the hydraulic aperture and the hydraulic conductivity of a concrete joint with an in situ test.

　　The resin dynamic viscosity and the main injection parameters were varied during the injection tests on the physical models. One model was sealed to determine the effect of the surface capping on the pressure inside the fracture during the injections. Injections were conducted in both dry and moist fractures to characterize the pressure and liquid propagation during the injections in both environments.

　　The in situ tests were done in a concrete construction joint in a tunnel. Surface capping was applied on the joint and a single injection point was chosen to perform all the tests.

3　Methodology

3.1　Physical Models

Two physical models were developed. For both models, two concrete slabs were poured on top of each other. Plastic wrap was inserted between the two slabs to be able to separate them after the concrete curing. All-purpose concrete mix *(Bomix brand)* was used for all models. Tubing with a diameter of 6.35 mm was installed in both models before pouring the concrete for injection and pressure measurement during the tests. Table 1 shows the physical characteristics of both models.

　　For the first model, the injection point was in the middle of the model. Four pressure measurement tubes were in the corner at 30 cm from the injection point. The head loss was measured with a portable pressure gauge. After the first injection, the model was opened and a picture of the propagation area was taken. Then a second

Table 1 Physical characteristics of the physical models

Model	Size (cm)	Thickness (cm)	Ports	Boundary condition	Initial fracture saturation
#1	61 × 61	12.7	5	Not sealed	Dry and moist
#2	61 × 61	11.7	13 (7 used)	Sealed	Moist

Table 2 Pressure gauge details of the second model

Pressure gauge	Distance from IP (cm)	Description
P1	2	Injection point entry pressure
P2	10	Pressure in the flow direction P3 is also tunnel extrados pressure
P3	30	
P4	14	
P7	30	
P5	14	Tunnel intrados pressure

injection was performed and another picture was taken after the second injection. The total injection volume is the sum of two volumes. Eight tests for a total of 24 injections were done.

For the second model, the injection point was in the middle with a 45° angle to understand its influence on the results. The pressure was measured with multiple tubes. A data logger system was used to record the pressure values every second. The location of the gauges and their description with respect to a real tunnel fracture are shown in Table 2 (IP stands for injection point). Pressure gauge #6 (P6) was installed at the pump outlet to measure the injection pressure. A total weight of 159 kg was put on top of the model with metal plates and beams to prevent the fracture from opening due to pressure jacking (e.g., [18]). The second model was sealed with DAP silicon to simulate injection in a capped fracture. Figure 1 shows the second model with the added weight just before the injection.

For the first model, injections were made with an *ELDPC* pressure–volume controller from *GDS*. A constant pressure was applied depending on the injected mixture. For the second model, a *KDS410* pump from *kdScientific* was used with a constant flow rate of 2.02 mL/s.

Fig. 1 Second physical model of concrete fracture with the 159 kg load

Table 3 Test parameters for the two physical models

Model	Injected liquid	Injection pressure (kPa)	Flow rate (mL/s)	Injection time (s)	Injection volume (mL)
#1	Water, mixtures #1 and #2	From 2 to 31	From 0.55 to 1.36	From 17 to 116	20, 50, 60, 110, 120, 125, 170, and 220
#2	Mixtures #2, #3 and #4	From 5 to 157	2.02	From 23 to 52	50 and 100

Five liquids were injected. The volumetric proportions of water-glycerol mixtures are presented:

1. Water (1.01×10^{-3} Pa·s);
2. Mixture #1: 61% water and 32% glycerol (7.5×10^{-3} Pa·s);
3. Mixture #2: 22% water and 78% glycerol (8.5×10^{-2} Pa·s);
4. Mixture #3: 12% water and 88% glycerol (2.2×10^{-1} Pa·s);
5. Mixture #4: 6% water and 94% glycerol (5.2×10^{-1} Pa·s).

The [19] equation was used to calculate the dynamic viscosity (μ) based on the water-glycerol mass proportion. Dye was added in the injected liquids when the fracture was moist to distinguish them from the liquid already present in the fracture before the injection. Table 3 shows the main injection parameters.

3.2   In Situ Tests in Tunnel

In situ injections were performed in a tunnel construction joint to study the liquid flow in a real discontinuity and to design a characterization test for concrete joints in tunnels. A horizontal construction joint in a mechanical ventilation station of the Montréal Metro was chosen. Surface capping was used to seal the joint. The injection was performed on the extrados side of a water stop membrane installed when the concrete was poured during the Metro construction. A cleaning agent based on phosphoric acid (*Oxy-cem*) was injected before the tests to clean the joint. The facture was rinsed with water for 10 min to evacuate any debris and acid solution entrained in the concrete.

Figure 2 shows the joint before the injection tests and Fig. 3 shows the drilling parameters of the injection point. Multiple ports were drilled in the joint for injection point and pressure reading. Trial-and-error injections with water permitted to conclude that four ports were to be used for the tests. P11 was the injection point, while P7, P4, and P3 were the pressure reading ports. Details of all injection ports used are available in Table 4 and a conceptual model of the joint is presented in Fig. 4. A *P300* pump from *hydracell* was used with a constant flow rate. Mixtures #2, #3, and #4 were injected. The injection parameters depended on the injected liquid with flow rates between 2.61 and 3.91 mL/s, injection pressures between 7 kPa and 2.75 MPa,

Fig. 2 Injected joint for the in situ tests

injection time between 350 and 550 s, and injected volumes between 1.09 and 3.71 L. The injections were stopped when the pressure of the liquid inside the joint became constant.

4   Results and Discussion

4.1   Physical Models

For the first physical model, no pressure was noted at any pressure reading ports located 30 cm away from the injection point. The head loss was total for this distance. All the pressure was concentrated near the injection point.

Figure 5 shows the relationship between the liquid propagation and the dynamic viscosity. Figure 5a and b show the propagation surface obtained in initially dry and initially moist fractures, respectively. The propagation areas have been colored to better visualize the propagation. The injected volume is 20 mL in each case. For a dry fracture, it is possible to notice a propagation area that varies according to the dynamic viscosity. A higher dynamic viscosity resulted in a smaller propagation surface with a circular shape. A lower dynamic viscosity resulted in a larger propagation surface with a more irregular shape. For a moist fracture, the results suggest that the dynamic viscosity is less important. The shape of the propagation area is irregular irrespective of the viscosity. The propagation surface for mixture #1 shows fingering with elongated tongues of liquid that spread away from the main propagation surface (Fig. 5b).

For the second model, an important pressure gain occurred during the injections. Figure 6 shows the results for the 100 ml–0.224 Pa s injection. They are representative of the results for other injections. The relationship between pressure and injection time can be separated in two parts. The first part corresponds to the gradual saturation of the fracture. As mentioned previously, all tests for the second model were conducted with an initially moist fracture. It took between 35 and 40 s to complete

Fig. 3 Drilling parameters
for P11 [22, 23]
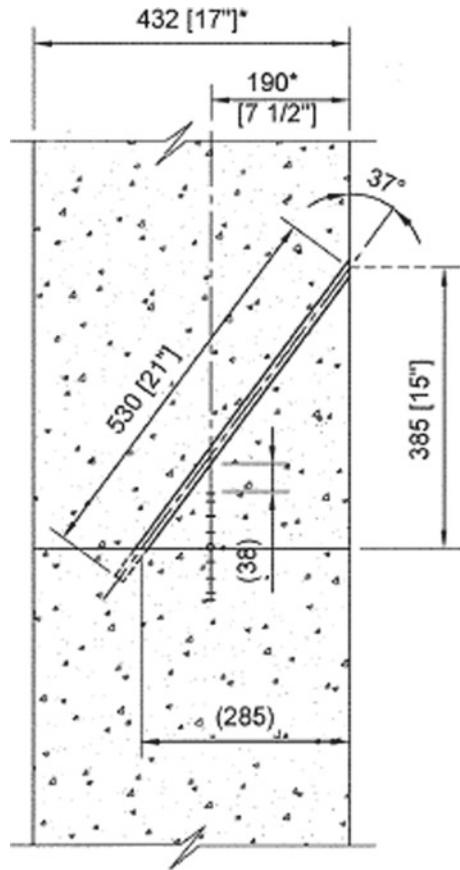
Table 4 Injection port parameters for the in situ tests

Parameter	P3	P4	P7	P11
Distance from injection port (mm)	1632	1238	900	0
Drilling distance (mm)	525	472	525	530
Drilling angle (°)	39	53	39	37

the saturation of the model and for the liquid to reach the fracture boundary and the capping. The second part is an important rise of the pressure inside the model. It can be explained by the completion of the saturation. The liquid got encapsulated because the fracture was sealed. The pressure measurements for each pressure transducers are similar. Imposing the flow in a precise direction with a 45° injection angle did not have any influence on the results.
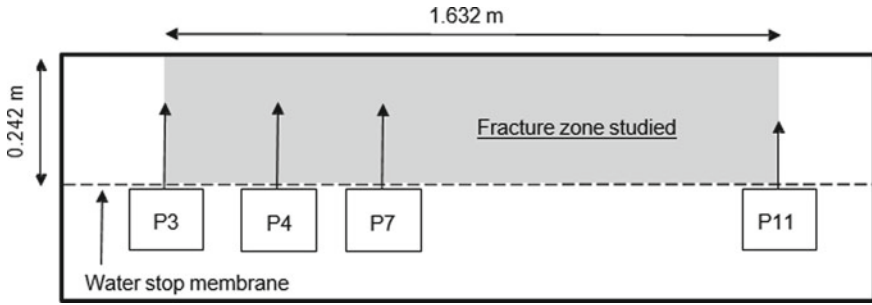
Fig. 4 Conceptual model of joint

Fig. 5 Propagation surfaces in the first model for dry and moist environment and 20 mL injected
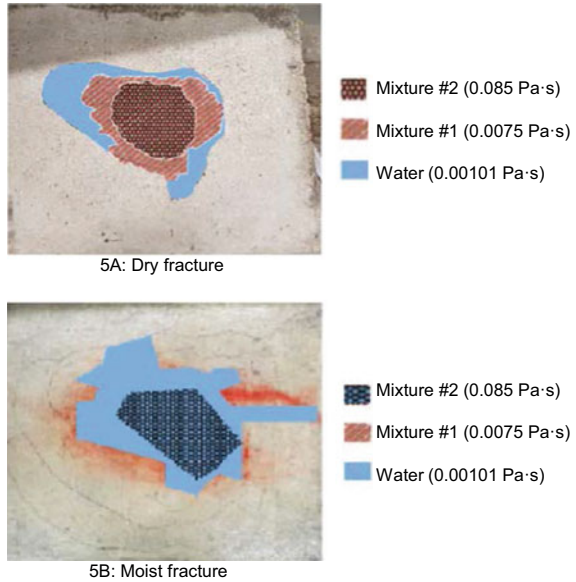
4.2 In Situ Tests in Tunnel

Figure 7 shows the relationship between pressure and injection time for pressure transducer P7. Globally, the in situ test results are similar to the results obtained with the second physical model before saturation. The second part of Fig. 6 corresponding to a more rapid pressure increase following saturation and confinement of the injected liquid was not observed. This implies that the joint was never completely saturated and that an open boundary was reached by the liquid. This can probably be explained by the presence of an open boundary for the joint at the tunnel extrados. The liquid was not confined and was able to flow out of the joint at the extrados. The highest pressures were obtained for the liquids with the highest dynamic viscosity. Figure 7 also suggests an injection time from 50 to 150 s is enough to reach a constant
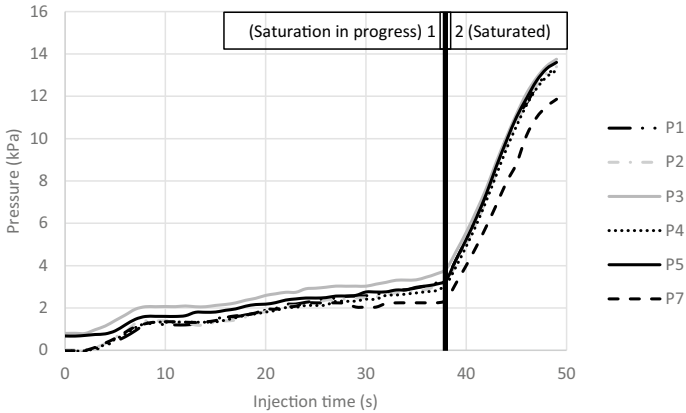
Fig. 6 Pressure readings inside the second model during the test with a volume of 100 ml and a viscosity of 0.224 Pa s

pressure for all the injected liquids. This can be considered as the optimal injection time if an open boundary is present. The optimal injection volume can be obtained by multiplying the optimal injection time by the injection flow. If 150 s is considered to be the optimal injection time, for the case of mixture #3, the optimal injection volume is 394 mL with a flow rate of 2.63 mL/s. The optimal volume is 587 and 465 mL for mixtures #2 and #4, respectively.

Figure 8 shows the pressure readings for ports P3, P4, P7, and P11 for mixtures #2 to #4 Head loss was observed for all the injection results. Mixtures #2, #3, and #4 lost, respectively, 37, 31, and 51% of their initial injection pressure when the liquid reached P3.

To establish the hydraulic aperture (b_h), the cubic law (Eq. 1) was introduced in Darcy's law (Eq. 2) to obtain Eq. (3):
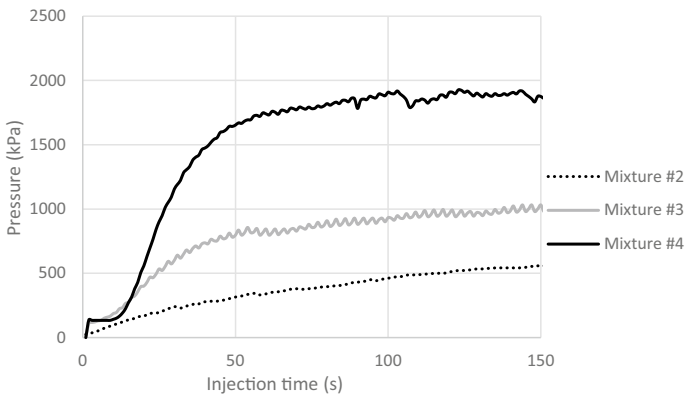
Fig. 7 Pressure according to injection time for the P7 port
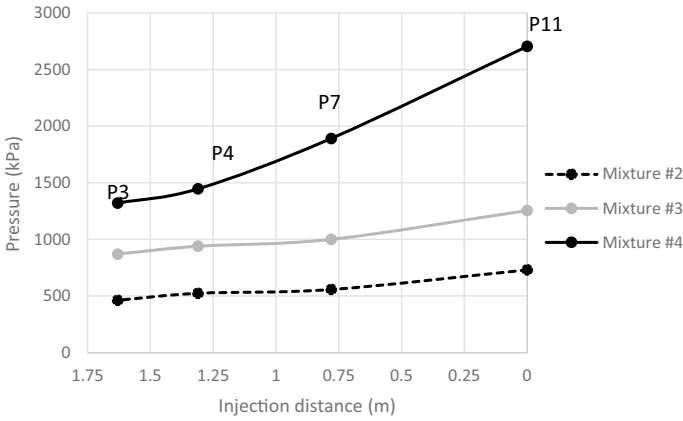
Fig. 8 Pressure according to injection distance at 150 s

$$K = \frac{\rho g b_h^2}{12\mu} \tag{1}$$

$$Q = KiA \tag{2}$$

$$Q = \frac{\rho g b_h^2}{12\mu}\frac{dh}{L}0.242b_h \tag{3}$$

where K is the hydraulic conductivity, i is the hydraulic gradient, A is the section area, g is the gravitational acceleration, ρ is the liquid density, and μ is the liquid dynamic viscosity. Section A is equal to the joint width (0.242 m) multiplied by b_h. The hydraulic gradient i is equal to the head loss (dh) divided by the injection distance (L). Darcy's law and the cubic law apply to laminar flow. The hydraulic aperture can be isolated from Eq. (3) to obtain the following equation:

$$b_h = 3.67\sqrt[3]{\frac{LQ\mu}{g\rho dh}} \tag{4}$$

The hydraulic aperture values for injection times of 50, 100, and 150 s were calculated. Table 5 shows that the hydraulic aperture varies from 0.46 and 0.51 mm.

After establishing the hydraulic aperture at 0.5 mm, it was possible to establish the hydraulic conductivity of the joint. Because each injected liquid had its own

Table 5 Hydraulic aperture (mm) depending on the injection time for mixtures #2 to #4

Injection time (s)	Mixture #2	Mixture #3	Mixture #4
50	0.49	0.49	0.46
100	0.48	0.50	0.47
150	0.46	0.51	0.46

μ and ρ, the hydraulic conductivity of the joint varies from a liquid to another. The results using Eq. (1) are, respectively, 2.83×10^{-3}, 1.11×10^{-3}, and 4.96×10^{-4} m/s for mixtures #2, #3, and #4. A higher dynamic viscosity leads to a lower hydraulic conductivity of the joint.

5   Conclusion

This article was intended to gain some fundamental knowledge on liquid flow in fractures in the context of waterproofing injections in concrete fractures. The development of physical models and an in situ test permitted to make the following observations:

1. The in situ tests permitted to conclude that the dynamic viscosity is the most important injection parameter. It influenced many aspects of the test: injection pressure, liquid propagation, hydraulic conductivity, and head loss;
2. The injection port angle did not seem to have any influence on the results.
3. The boundary conditions and the initial fracture saturation also influenced the liquid pressure inside the fracture and the propagation of the liquid. An open fracture never reached a full saturation state in both types of tests (physical models and in situ). The second pressure rise observed in sealed fracture can be used to conclude a saturation state of the fracture. A dry and sealed fracture requires a longer time for the fracture to reach a saturation state. A moist fracture simply shortened the amount of injection time needed to reach that saturation state.

It is important to mention that no polymer injections were made to confirm the results. The final step would be to perform a polymer injection and analyze samples from drilling to confirm that the injected liquid filled the joint. Also, numerical models can be developed to predict the result of an injection based on a full hydraulic characterization.

References

1. Association française des tunnels et de l'espace souterrain (AFTES) (2016) Recommandations de l'AFTES relatives aux traitements d'arrêts d'eau dans les ouvrages souterrains. (Report #257)

2. Yuan C, Li S, Li S (2011) Study on the defects characteristics of water leaking of old tunnels in cold regions. Tunnel management, emerging technologies, and innovation, pp 187–193

3. Krauss PD, Scanlon JM, Hanson MA (1995) Evaluation of injection materials for the repair of deep cracks in concrete structures. (Report REMR-CS-48). US Army engineer waterways experiment station

4. Mailvaganam NP (1991) Repair and protection of concrete structures. CRC Press, Ottawa, Canada

5. Mangum WD, Bermudez-Goldman AJ, Whitney D, Fowler D, Meyer AH (1986) Repairing cracks in Portland cement concrete using polymers. (Report 385-2F). Center for Transportation Research, The University of Texas at Austin

6. von Fay KF (2015) Guide to concrete repair, 2nd edn. U.S. Bureau of Reclamation

7. Andersson H (1999) Chemical rock grouting-an experimental study on polyurethane foams (Unpublished doctoral dissertation). Chalmers university of technology

8. US Army Corps of Engineers (2004) Grouting methods and equipment. The army technical manual of the air force manual. (Report #UFC 3-220-06)

9. Karol RH (2003) Chemical grouting and soil stabilization, revised and expanded, vol 12. CRC Press, New Jersey, USA

10. Trout J (2006) Epoxy injection in construction, 2nd edition. The Aberdeen group. Addison, USA

11. Issa CA, Debs P (2007) Experimental study of epoxy repairing of cracks in concrete. Constr Build Mater 21(1):157–163

12. Rzezniczak A-K (2013) Durability of repair techniques of fine cracks in concrete. (Doctoral dissertation, McMaster University). McMaster university repository. https://macsphere.mcm aster.ca/bitstream/11375/12912/1/fulltext.pdf

13. Wang X, Petrů M (2019) Freeze–thaw resistance of epoxy/concrete interface evaluated by a novel wedge splitting test. Constr Build Mater 210:434–441

14. Gustafson G, Stille H (1996) Prediction of groutability from grout properties and hydrogeological data. Tunn Undergr Space Technol 11(3):325–332

15. Rahmani H (2009) Estimation of grout distribution in a fractured rock by numerical modelling. (Master's thesis, University of British Columbia). UBC Theses and Dissertation. https://open. library.ubc.ca/soa/cIRcle/collections/ubctheses/24/items/1.0063121

16. Witherspoon PA, Wang JSY, Iwai K, Gale JE (1980) Validity of cubic law for fluid flow in a deformable rock fracture. Water Resour Res 16(6):1016–1024

17. Funehag J, Fransson Å (2006) Sealing narrow fractures with a Newtonian fluid: model prediction for grouting verified by field study. Tunn Undergr Space Technol 21(5):492–498

18. Rafi J, Stille H (2021) A method for determining grouting pressure and stop criteria to control grout spread distance and fracture dilation. Tunn Undergr Space Technol 112:103885

19. Cheng NS (2008) Formula for the viscosity of a glycerol-water mixture. Ind Eng Chem Res 47(9):3285–3288

20. ITA Working Group on Maintenance and Repair of Underground Structures (1991) Report on the damaging effects of water on tunnels during their working life. Tunn Undergr Space Technol 6(1):11–76

21. Lombardi G, Deere D (1993) Grouting design and control using the GIN principle. Int Water Power Dam Constr 46:15–22

22. Société de transports de Montréal (STM). 2018. Étude de perméabilité des fissures. Montréal,

23. Sun W, Liang Q, Qin S, Yuan Y, Zhang T (2021) Evaluation of groundwater effects on tunnel engineering in loess. Bull Eng Geol Env 80:1947–1962

Design and Construction of Large Diameter Storm Water Retention Shafts for the Coxwell Bypass Tunnel

Matt McGrath, Vireak Hinh, Robert Mayberry, and Rogerd Morales

Abstract The City of Toronto's Don River and Central Waterfront and Connected Projects (DRCW Project) aims to reduce Combined Sewer Overflows (CSOs) into the Lake Ontario and Don River watersheds. Once completed over the next 20 years, it will be comprised of approximately 22 km of tunnels, 12 shafts, and will intercept 27 CSOs connections in the City of Toronto. Black & Veatch in association with R.V. Anderson Associates Limited were retained to perform the detailed design and provide construction support services for phase one of the project, referred to as the Coxwell Bypass Tunnel. North Tunnel Constructors ULC is currently working to construct 10.5 km of the 7.3 m outer diameter rock tunnel, five large-diameter storage shafts, and 14 small-diameter drop shafts to allow for future diversion of CSOs. The five storage shafts range from 20-22 m in diameter and extend to depths of 58 m through both rock and soil. Key shaft features include a composite roof slab consisting of long spanning pre-cast concrete panels and a 3 m thick hemispherical concrete base slab to help resist the large hydrostatic uplift pressures applied across the slab. In addition to an overview of the structural design of these shafts, this paper will discuss the construction methods and in-field engineering solutions employed to keep the project moving forward and on schedule. The construction portion of the paper discusses the project team's construction experiences and solutions to challenges associated with shaft construction, including shoring installation and excavation, concrete reinforcement placement, pouring and monitoring temperatures of mass concrete, and construction of the shaft walls using suspended jump forms.

Keywords Water retention shafts · Coxwell bypass tunnel

M. McGrath (✉) · V. Hinh
R.V. Anderson Associates Limited, North York, Canada
e-mail: mmcgrath@rvanderson.com

R. Mayberry · R. Morales
Toronto, Canada

1 Shaft Design

The design of the 20-22 m diameter storage shafts for the Coxwell Bypass Tunnel Project presented many interesting challenges and unique features. Although similar methodologies were utilized for all five (5) shafts, the design process for each shaft individually was complicated by unique factors and requirements that had to be satisfied and taken into consideration.

Generally, the final shaft designs consisted of reinforced cast-in-place concrete wall liners ranging between 700-800 mm in thickness, heavily reinforced hemispherical concrete base slabs and composite roof slab systems. Additional features such as mass concrete benching, access stairs and baffle drop structures were also common features among the shafts. Figure 1 highlights some of the shafts' key features.

1.1 Design Considerations

The design approach for the shaft structures was developed to meet several key design objectives. Notable objectives include the following:

- Structural design to consider a minimum design life of 100-years.
- Concrete components to meet durability requirements for hydraulic structures in harsh environments.
- Shaft structure to be designed to resist hydrostatic pressure expected to be encountered during construction and throughout the service life of the shaft.
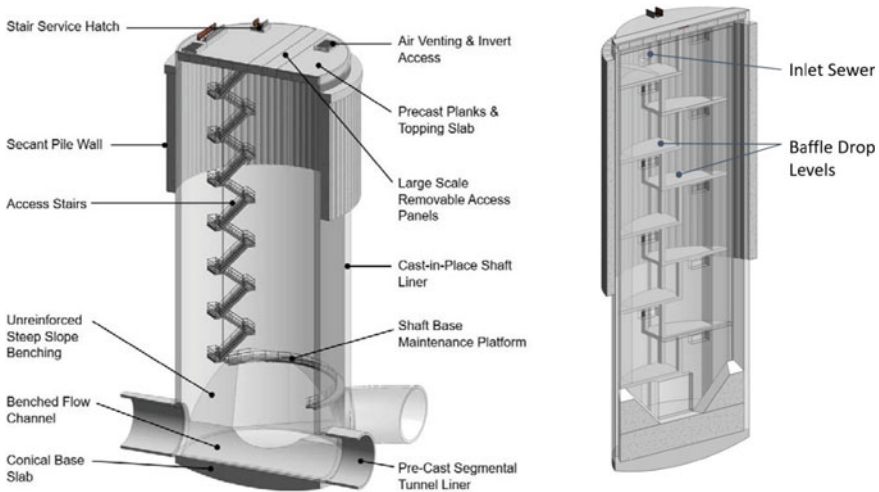
Fig. 1 Key shaft features

- Shaft structure to consider durability requirements considering additional hydraulic loading conditions due to cavitation and abrasion erosion within the baffle drop structure.
- Operational access into the shaft required for maintenance and inspection.
- Interior benching to be designed to minimize buildup of debris and sediment, reducing the maintenance and cleaning requirements within the shaft.
- Roof to be designed as a composite pre-cast panel with cast-in-place topping to simplify construction by avoiding the erection of elaborate false work inside the shaft.
- Ventilation openings in the roof to be provided to exhaust mass volumes of air during filling of the storage shafts.

The following sections provide an overview of some of the key structural design considerations and briefly summarizes the roof slab, wall, and base slab designs for the large diameter stormwater retention shafts.

1.1.1 Subsurface Conditions

All shafts extend through both soil and rock to depths of up to 58 m below grade. Due to the distances between shafts along the tunnel alignment, the subsurface soils varied dramatically in type and stratigraphy at each shaft site. While the rock elevation and profile also varied, the type was consistently Georgian Bay Shale, commonly found throughout the Greater Toronto Area. These varying ground conditions impacted the applied external pressure loads considered as part of the cast-in-place wall liner design.

Additionally, 3 of the 5 shafts are located directly within the Don River's regional flood plane, so groundwater management during shaft construction needed to be considered. Further, groundwater pressures due to a regional flood event needed to be considered during construction and throughout the service life of the structure. The unique loading conditions considered for the shaft design are discussed further in Sect. 1.1.4.

1.1.2 Functional Requirements (Operations and Maintenance)

The hydraulic requirements for each shaft had noteworthy impacts on the structural design. Ventilation openings used to exhaust the mass volumes of air during the filling of the storage shafts and tunnel during a storm event, had to be incorporated into 4 of the 5 shaft roof slab designs. Baffle drop structures used to convey water from secondary inlet sewers down to the bottom of the shafts were also structurally designed and detailed in 4 of the 5 shafts. To satisfy the City of Toronto's future maintenance requirements, access openings, emergency rescue openings, access stairways, platforms and retractable ladder systems were also accommodated within the shafts. Benching within the baffle structure and bottom of the shaft was designed

to convey the flow and minimize build-up of sediment and debris, thereby reducing operational requirements for maintenance and cleaning.

1.1.3 Unique Loading Conditions

Various loads of significant magnitude had to be taken into consideration as part of the structural design of the walls and roof slabs. Shaft #2 is located directly adjacent to a planned future development site. As a result, the shaft's walls had to be designed to resist an unbalanced soil load case of a magnitude equivalent to having excavated soil down to the top of rock elevation around any extent of its circumference. Like many of the other shafts, Shaft #2 would eventually be buried and therefore its roof slab had to be designed to resist substantial overburden soil loads in combination with vehicular traffic live loads.

On the other hand, Shafts #3, #4, and #5 are located directly within the Don River's regional flood plane, and as a result needed to be capable of resisting significant hydrostatic pressures due to a regional flood event that may occur at some point during the shaft's 100-year design service life. The roofs for these shafts were therefore designed to resist an unfactored hydrostatic water pressure of 34 kPa applied to the roof slab and were made watertight to the top of the vents 3.6 m above grade to prevent the conveyance of surface flood waters to treatment facilities downstream. Loads on the shaft walls due to time dependent rock swelling were also taken into consideration.

1.2 Design of Key Structural Components

1.2.1 Roof Slab

For structures of this size and magnitude of loading, considerations for constructability were made throughout the design process wherever possible. The shaft roof slab design utilized a composite system consisting of long spanning pre-cast concrete panels complete with a 200 mm thick cast-in place concrete topping to improve long-term durability. This option was preferable to alternatives such as having a fully cast-in-place roof slab which would have necessitated the erection of temporary scaffolding to 50 plus metre heights and in turn increased project construction costs and schedule duration. The pre-cast panel design was optimized to reduce the overall thickness and weight of the panels so that they could be lifted into place by crane. The roof slab thickness was reduced by using heavy three-bar bundled primary reinforcement, compression reinforcement and shear ties. The unfactored dead weight of the largest 2 m wide by 20 m long by 0.9 m thick precast panel at LDS-3(B) was roughly 86 metric tonnes. Additional reinforcement had to be provided near ventilation and access opening locations to resist the localized stress concentrations.

1.2.2 Walls

The governing load cases considered in the shaft wall designs consisted of internal and external water pressures in combination with a variety of unbalanced soil load cases. The impacts of time dependent rock swelling loads provided by a geotechnical subconsultant were also taken into consideration. All loads were checked under both Ultimate Limit States and Serviceability Limit States to satisfy crack control requirements. Due to the harsh exposure conditions expected in sanitary sewage and stormwater flows, crack control was limited in accordance with the *American Concrete Institute 350 Code Requirements for Environmental Engineering Concrete Structures* (ACI 350) for severe environmental exposure to maximize the long-term durability of the concrete.

Finite Element Models (FEM) were used to analyze the shaft walls under governing load cases for each shaft, applied individually and in combination. To properly model the behaviour of the walls, compression only springs were used to simulate the confinement provided by the surrounding rock mass. Both lower and upper bound rock spring stiffness coefficients were employed to capture the range of resulting impacts to the shaft walls. Results inclusive of axial forces, bending moments and shear forces at each finite element node were exported, sorted, and compared against the reinforced section capacity of the walls at that location. Hand calculations were used to verify and validate the suitability of the models' results for use. Figure 2 demonstrates the deformation and resulting stresses induced on one of the shafts as a result of an unbalance external soil pressure load.

Fig. 2 Finite element analysis model (FEM) of a shaft showing deformation (left) and stress results (right) due to unbalanced loading
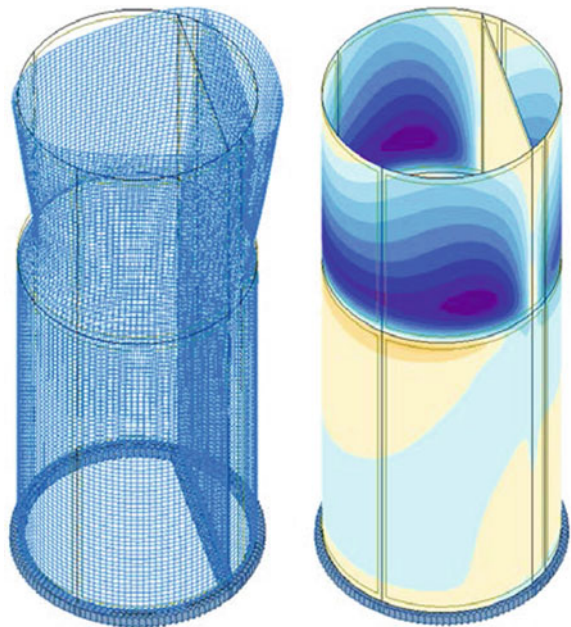
1.2.3 Base Slab

At depths of 58 m, a factored hydrostatic design uplift pressure of 850 kPa had to be applied across the 20-22 m diameter spans of the shaft base slabs. To help resist a pressure of such magnitude, a hemispherical base slab design was adopted. The introduction of shallow curvature in the shaft base slab reduced its overall cross section (compared to a conventional flat slab) and allowed for greater deformation to occur. In turn, a compression arch forms within the slab and transfers a percentage of the pure bending stresses to compressive stresses within the section. The newly introduced compressive axial force component is transferred to the surrounding rock mass through a thrust load. This compressive stress in the section counteracts the development of tensile stresses due to the large bending moment in the section, thereby allowing for an overall reduction in concrete thickness and reinforcement requirements.

The final base slab reinforcement design consisted of 2-35 M bundled bars along the top layer of the slab in both directions. Due to the heavy reinforcement requirements, the bars were detailed orthogonally as opposed to circumferentially and radially to limit congestion. Headed shear reinforcement was provided around the circumference of the slab to resist the high resulting shear stresses and provide the required capacity to the concrete section.

2 Shaft Construction

In addition to the many complexities faced during the design of the large diameter shafts, shaft construction required specific solutions to meet the design requirements. The following sections provide an overview of the various stages of construction for one of the large diameter stormwater retention shafts, and highlights some of the challenges and solutions associated with each stage.

2.1 Overburden Shoring and Excavation

The soil shoring system selected by North Tunnel Constructors ULC (NTC) to facilitate excavation of the large diameter shafts consisted of interlocking concrete secant piles that were embedded 3 m or more into sound bedrock to seal the excavation from soil and water infiltration (Fig. 3). The larger 22 m-diameter Shaft #5 required eighty (80) 1300 mm diameter by 38 m deep secant piles. The shoring system was designed to resist full soil overburden, ground water pressure, construction surcharge and crane loads. The minimum concrete strength of the caissons specified by the shoring designer was 25 MPa, and every fifth caisson was reinforced with a W460 $\times$ 52 steel beam centered in the caisson to stiffen the shoring system in the vertical direction.

Fig. 3 Looking up from bottom of shaft at concrete caisson shoring and rock support

Installation of the secant pile shoring system required accurate surveying to layout the pile locations. A guide wall was constructed to create a template for the Bauer BG-45 and BG-55 drill rigs to facilitate installation of the caissons at the correct location to achieve the required shaft diameter and caisson interlock. The guide wall was constructed by first laying out foam templates of the piles, then encasing them in concrete.

Concrete strength testing was carried out to confirm that the minimum specified design strength was achieved prior to proceeding with excavation. Once the shoring system was complete, excavation of soil overburden proceeded with the use of an excavator. The permanent structure was designed to be blind-side formed against the shoring system. Therefore, an important step during excavation was to survey the shoring wall as excavation proceeds and remove excess concrete and soil from the shoring system so that the correct shaft diameter was achieved.

Groundwater had to be managed throughout excavation. During the caisson construction, a tremie pipe and concrete pump was used to pour the caissons to mitigate segregation of the concrete and improve watertightness of the shoring system. A steel casing was used to protect the hole from water and soil migration, as concrete placement advanced the steel casing was removed.

2.2 Rock Support and Excavation

Once excavation reached the shale bedrock zone below the overburden shoring system, rock excavation was carried out using an 85-tonne excavator. Because the shaft wall would be poured against the side of the rock excavation (blind-side formed), accurate surveying and shaving of the rock face was carried out to achieve the required shaft diameter as excavation advanced.

A temporary rock support system was installed every 1–1.5 m of excavation depth and consisted of steel wire mesh bolted to the rock face with rock anchors (Fig. 3). Pull tests were performed to confirm that the rock anchors met the strength requirement.

2.3 Foundation Preparation

One of the unique features of the shaft was the hemispherical bowl shape of the subgrade and base slab. The hemispherical shaped foundation transfers the large uplift groundwater pressures on the base slab as a thrust load into the surrounding rock mass. Additionally, the base slab was 2.5-m thick at the middle and was heavily reinforced with 2-35 M bundled bars at 200 mm spacing as well as shear reinforcement. The total weight of steel reinforcement for the base slab for Shaft #3 was more than 100 metric tonnes (MT). A concrete mud slab was installed to provide a stable foundation to resist the weight of the reinforcing steel and prevent the reinforcing mat from settling prior to concrete placement.

One of the unique challenges during preparation and excavation of the foundation was achieving the specified hemispherical profile for the base slab. To achieve this, the excavation was controlled by using accurate tooling (milling head) and having accurate surveying present (Fig. 4).

2.4 Base Slab Construction

The design had to balance constructability with the design requirement for heavy reinforcement for the base slab due to the significant hydrostatic uplift pressures. Due to the circular geometry of the slab and orthogonal placement of the reinforcement, the bar lengths changed every 2–3 bars. Maintaining alignment from the bottom layer to the top layer was necessary to maintain splice lengths of the connecting side bars. Additionally, the hemispherical shape of the foundation meant that the lengths of the headed shear reinforcement in the base slab varied in the radial direction. Figure 5 shows the bottom layer of reinforcement with bars bent to the curvature of the hemispherical foundation. Figure 6 shows the top layer reinforcement consisting of 2-35 M bundled bars and headed shear reinforcement placed in a radial pattern.

Fig. 4 Hemispherical base slab foundation preparation using accurate surveying and tooling

Fig. 5 Base slab bottom layer reinforcement, bars bent to the curvature of the hemispherical foundation

Fig. 6 Base slab top mat reinforcement consisting of 2–35 M bundled bars and radially placed headed shear reinforcement

One of the main focuses when developing the concrete mix design and planning the base slab pour was controlling the temperature of the concrete. *The Canadian Standards Association A23.1 - Concrete Materials and Methods of Concrete Construction* (CSA A23.1) requires that that concrete elements more than 1000 mm in thickness shall be considered "mass concrete" and are dictated by special restrictions on concrete temperatures. This is because large concrete elements do not readily release the heat due to hydration of the cement binder during curing. This can result in differential expansion within the element. For mass concrete, the center of the element dissipates heat slower than the surface, resulting in a temperature differential across the depth of the concrete section. These temperature differentials, if not controlled, can result in significant early age cracking in the concrete element. CSA A23.1 requires that mass concrete elements be protected to limit the internal core and surface temperature differential to 20 °C and requires that the peak temperature of the concrete does not exceed a maximum temperature of 70 °C unless the concrete mix incorporates a higher percentage of supplementary cementing material (SCM) such as slag.

The shaft base slab pours ranged from 650m^3 to 1000m^3 in volume and were poured monolithically. To control the temperature of these large pours, a special concrete mix design was developed to minimize the heat released by cement hydration. The mix design used included a high SCM content. SCM replaces the cement binder content, which in turn reduces the heat generation during concrete placement and curing. Additionally, temperature probes were installed at the top, middle, and bottom of the slab to monitor the temperatures and confirm that the temperature limits prescribed by CSA A23.1 were maintained.

To control the thermal gradient across the depth of the base slab, the surface was covered with insulated tarps and portable heaters were positioned within the shaft to control the temperature of the surface of the base slab so that it did not lose too much heat relative to the peak temperatures from the middle of the slab (Fig. 7). A custom thermal control plan was developed for the project that accounted for additional cooling measures based on forecasted ambient temperatures and indicated when and how much insulation was required for the slab during curing.

The design specified low shrinkage concrete in accordance with CSA A23.1 (0.04% shrinkage limit) to minimize crack development in the shaft structure and improve durability under the design exposure conditions when the shaft is in service (storm water and combined sewer overflows). Prior to concrete placement, trial batches were performed, and various tests were carried out to verify that the compressive strength, shrinkage, and temperature requirements for the mix were met. Figure 8 shows an aerial view of the Shaft #3 site on the day of concrete placement for the base slab.

Fig. 7 Base slab curing underway with insulated tarps and portable heaters to control temperature differential of mass concrete element
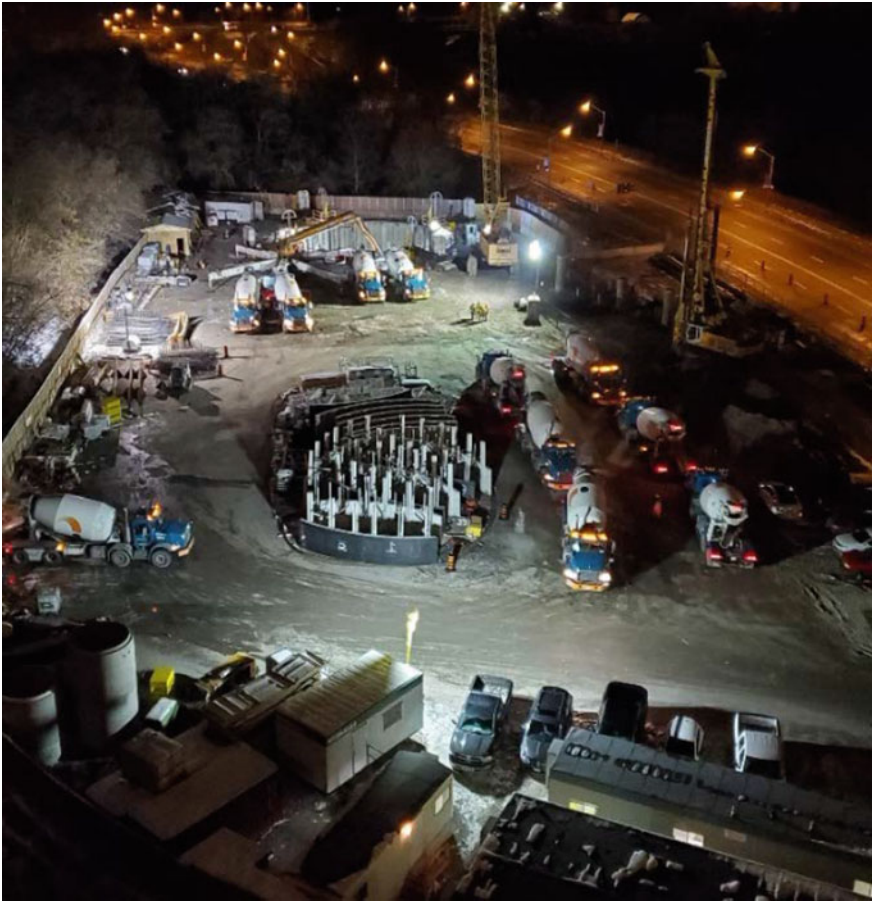
Fig. 8 Shaft site on day of concrete placement for the shaft base slab (shaft located at the back)

2.5 Tunnel Eye Box-Out

Construction of the Coxwell Bypass Tunnel was concurrent with the construction of the large diameter shafts. Tunnel excavation was ongoing during shaft construction, and as a result three out of the four shafts upstream of the launch shaft were constructed ahead of the tunnel advancement. This meant that shaft construction needed to account for future pass-through of the tunnel boring machine (TBM) once it arrived at the shaft location. The box-outs were accurately surveyed to receive the TBM based on the design tunnel alignment. It was important to provide clearance between the TBM and the shaft wall to mitigate conflict between the tunnel diameter and the shaft wall. Once the TBM passed through the shaft, the annular space between the shaft wall and the tunnel liner would be filled in with reinforced concrete complete with water stopping measures.

2.6 Shaft Wall Construction

Cast-in-place shaft walls were specified for all 5 large shafts. The wall thicknesses ranged from 700-800 mm, and the average depth was approximately 50 m. Bottom-up construction was deployed to build the shaft walls, and the walls were poured full circumference with no vertical construction joints in lifts of 3.7 m in height (Fig. 10). A steel jump form was utilized for this project and was lifted using a 4-point strand jack lifting system. Once the formwork system was lifted to the correct elevation, the formwork was supported by the previous concrete wall pour via folding brackets that were installed into pre-formed pockets in the concrete wall (Fig. 9).

Due to the size of the shaft diameters, it was not sufficient to design the formwork system to resist the concrete pressures relying on hoop confinement alone. As such, the formwork was treated as a series of straight panels. Cantilevered folding leg brackets were used to contain the concrete form pressure, and spuds were installed into the rock face to control deflection of the formwork. Rebar installation was performed by a combination of pre-tying panels at grade and installing the panels by crane, or by tying the rebar in place. To achieve the correct spacing and required lap splices, the rebar panels were tied using a template that was constructed at grade to the required shaft radius. Figure 9 shows a typical rebar panel assembly at the bottom of the shaft.

Fig. 9 View of typical rebar panel assembly for the first wall pour at the base of the shaft

Fig. 10 View of completed shaft walls poured full circumference with no vertical construction joints

3   Closure

The design and construction of the large diameter stormwater retention shafts for the Coxwell Bypass Tunnel required several unique solutions to project-specific challenges including performance criteria and in-situ conditions. Continual coordination between all members of the construction team has resulted in successful shaft construction. The City of Toronto's Wet Weather Flow Master Plan provides further information on the DRCW project and can be found in the references at the end of this paper.

References

1. City of Toronto. "The City's Wet Weather Flow Master Plan." https://www.toronto.ca/services-payments/water-environment/managing-rain-melted-snow/the-citys-wet-weather-flow-master-plan/ (accessed May 26, 2021)

2. Canadian Standards Association. 2014. Concrete Materials and Methods of Concrete Construction/Methods of Test and Standard Practices for Concrete (CAN/CSA Standard No. A23.1/A23.2).
3. American Concrete Institute Committee 350. 2006. Code Requirements for Environmental Engineering Concrete Structures (ACI Code 350–06).

External Post Tensioning Evaluation Using Vibration Response Measurements

Emilie Pellerin, Serge Desjardins, and Donald McGinn

Abstract External post-tensioning tendons (EPTTs) are commonly used in concrete box girder bridges constructed using the balanced cantilever methods. Bridge managers and operators are increasingly interested in novel means of determining the health of these important structural components as traditional visual inspections provide little to no information on their state. Due to inferior grouting, corrosion of prestressing strands within some existing bridges have required replacement of EPTTs. Monitoring the structural vibration responses of EPTTs can provide a means to determine the remaining tension which provides crucial information on their state. The basic equations to determine the stress from the vibration responses are based on vibrating string theory. Many of the important parameters in the classical equations are difficult to precisely determine in the field (stiffness, length, support conditions, etc.) due to construction variability. The basic equations have been the foundation for the development of more complex equations that attempt to account for these variabilities. These theoretical equations have rarely been tested under uncontrolled conditions, such as for the evaluation of existing in-operation EPTTs. This paper will present the practical application of three theoretical equations presented in literature that have been developed for determining the tension in EPTTs. The equations make use of modal frequencies from eight different EPTTs of varying lengths in an existing concrete box girder bridge (the Confederation Bridge in eastern Canada). The aim of this study is to develop a testing methodology based on vibration monitoring that provides reliable results and that is more efficient than the static deflection technique currently used by bridge managers/operators. Results show that the monitoring of structural vibration responses is an efficient and reliable way of determining the tension in external post-tensioning tendons.

Keyword Post tensioning evaluation · Vibration response

E. Pellerin (✉) · S. Desjardins
Université de Moncton, Moncton, Canada
e-mail: eep8468@umoncton.ca

D. McGinn
Strait Crossing Bridge Limited, Borden-Carleton, Canada

919

1 Introduction

Over the past twenty-five years, the field of structural health monitoring has received increasing attention from researchers and infrastructure managers. The motivation for research in SHM is to increase infrastructure safety by identifying faults or damages more quickly and saving on long-term structural maintenance costs. Structural health monitoring takes many forms; from automated and continuous long-term monitoring systems that aim to analyze the condition of the whole structure to short duration monitoring programs to identify or address specific issues in structural components. In the case of vibration based SHM, the recorded vibration responses are used to deduce structural conditions.

In existing concrete box girder bridge structures, the external post-tensioning tendons (EPTT) of the pre-stressed system are critical structural components. They are typically encased over most of their length, hiding defects and signs of deterioration. An indicator of damage when cables are not visible is the unexpected loss of tension. Several methods are described in the literature to determine the cable tension of an existing structure such as liftoff testing and static deflection testing with strain gauges [6, 10]. An approach that is gaining popularity for its efficiency is the estimation of cable tensile stresses by vibration analysis [2, 8, 10–14]

The EPTTs of the Confederation Bridge are periodically tested using a static deflection method [10]. This method is time-consuming, and the accuracy of the results depend greatly on the precision of a bracket installation. This study's goal is to develop a novel test method based on vibration response measurements that will be efficient and produce more accurate results which will be less susceptible to evaluator errors.

The studies on estimating cable tensile stresses by vibration analysis all compute the tension by relating it to the measured natural frequencies. Written in its simplest form, the tension can be estimated from Eq. (1):

$$T = 4 \, \mathrm{mL}^2 \left(\frac{f_n}{n} \right)^2$$

(1)

where T is the tension in kN, m is the cable linear weight in kg/m, L is the cable length in meters and f_n is the recorded frequency of the nth mode.

Equation (1) does not consider rigidity that can be important for structural members such as EPTTs. Equation (2) takes into consideration the bending stiffness of the cable as presented by [7]. This equation is based on the vibration of a tension beam with simple supports. This second equation includes the same parameters as Eq. (1) with the addition of the bending stiffness of the cable, EI in kN*m^2. The equation is developed and used for cables with simple and non-embedded supports. These conditions ensure that the effective length is equal to the cable length.

$$T = 4 \, \mathrm{mL}^2 \left(\frac{f_n}{n} \right)^2 - \frac{\mathrm{EI}}{\mathrm{L}^2} (n\pi)^2$$

(2)

The results from the formulas presented above depend on the accuracy of the parameters used in the calculations. For existing structures, most of the parameters such as the linear mass and rigidity can be determined through construction records or by direct measurements. The effective vibration length is, however, not as easy to determine when the end conditions are not hinged.

As demonstrated by ref. [9], the natural frequencies under clamped support conditions increase compared to a chord of the same length with hinged condition. Their study, however, demonstrated that there is a decrease in variation as the cables increase in length and have higher tension. Although under relatively high tension, the EPTT are relatively short cables, therefore it is important to consider the support conditions to determine the effective length of the cables.

Reference [14] proposes a method that allows the use of a single sensor to determine cable tension through vibrations. The formula makes it possible to neglect the rigidity of the cable by using two recorded frequencies instead of only one. The method is based on initially known support conditions, but it is developed to be used when the conditions are not known with certainty. By superimposing the modal shapes of the same cable for a variety of support conditions, Yu demonstrates that the modal shapes only vary near to the supports. They remain unchanged in the centre of the cables.

Using two frequencies, Yu proposes to estimate the tension of a cable by:

$$T = 4 \, \rho A L^2 \left[\frac{p^2 f_n^2 - n^2 f_p^2}{n^2 p^2 \left(p^2 - n^2 \right)} \right] \tag{3}$$

where ρ represents the density of the cable in kg/m^3, A is the cross-sectional area in m^2 and the second frequency considered is f_p, of the pth mode. Yu stated that even if the effect of the supports does not change the mode shape, the natural frequencies and the effective lengths are affected.

According to Wu et al. [12] and Wen-Hwa et al. [11], the most difficult parameter to determine with accuracy is the effective vibration length, especially with EPTTs which often pass-through intermediate diaphragms to deviate the cable direction. In their studies, several sensors are necessary to determine the modal shape of the natural frequencies, especially in the vicinity of the supports. The expected sinusoidal mode shapes are plotted and associated with the maximum amplitude ratio of each sensor, for the mode in question. For the first mode, the sinusoidal shape has only one vertex, the second mode has two and so on. An offset parameter is introduced to adjust the effective length of the cable in question according to the locations of the sensors and the amplitude values recorded. Their approach suggests concentrating all the sensors on one of the halves, close to the support, and adding a sensor at the other end to confirm where the effective length of the sinusoidal shape ends. Since the centre of the effective length is not necessarily at the centre of the span if the end conditions are not symmetrical, the optimal positioning of the sensors is close to the supports to determine the effective length. This method is intended to allow

the determination of the tension when only one of the ends of the cables is easily accessible for the installation of the sensors.

A combination of the above methods is used in this study to develop a test that will determine the tension of EPTTs through vibration. Results using the three formulas above will be compared to determine the best formula to use for the conditions at the Confederation Bridge and a different sensor layout will be proposed to properly capture the vibrating mode shapes. The AI-FSI method will be used to extract the modal properties (frequency, mode shapes and damping ratios) of the EPTT as per Desjardin and Lau [5].

2 Site Testing

This section will provide an overview of the structure that is the subject to the current study and the steps taken to assess of the tensile stresses of the existing EPTT.

3 Bridge Characteristics

With 43 main spans of 250 m each and a 100-year design life, the 12.9 km long Confederation Bridge was the world's longest prestressed concrete box girder bridge built over salt water [3]. The crossing consists of 21 approach spans, 2 transition spans and 43 main spans at a typical height of 40 m above the mean sea level (60 m at the navigation spans) as shown in Fig. 1. The main-spans portion of the bridge is comprised of 22 repetitive structural frame modules of 500 m length each. Each frame module is a 440 m portal frame made up of a 250 m center span and two 95 m overhangs, one on each side of the center span, plus a 60 m simply supported drop-in expansion span, as shown in Fig. 2. The portal frame is constructed of four types of prefabricated component units, pier base, pier shaft, main girder and fixed drop-in span girder. The connections between the different units of the portal frame are made continuous by post tensioning and grouting. The bridge girders are single trapezoidal cell box girders with section depth varying from 14 m above the piers to 4.5 m at mid-span of the drop-in girder, and a cross-section width varying from 5.0 m at the bottom to 7.0 m at the top, with 2.5 m deck overhangs.

The concrete box girder bridge was constructed using the balanced cantilever method. Six EPTT run the length of every drop-in span (hinged and fixed) between the cantilevered sections. Each tendon consists of a 111 mm diameter HDPE conduit filled with 20–15.4 mm steel strands and grout. During construction, the tendons were stressed to 72% UTS by jacking method. The EPTTs in the drop in spans measure about 16.5 to 16.9 m whereas the ones in the continuous span are in the range of 7.9 m. Figure 2 illustrates the main bridge components with a typical cross section of the concrete box girder.
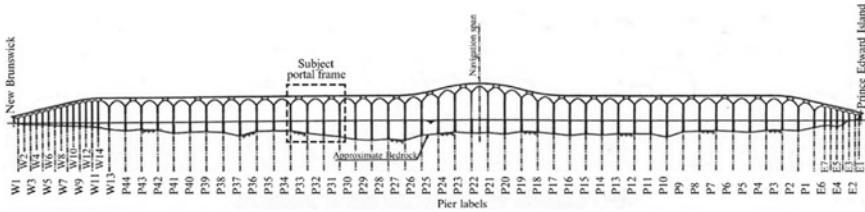
Fig. 1 Bridge spans
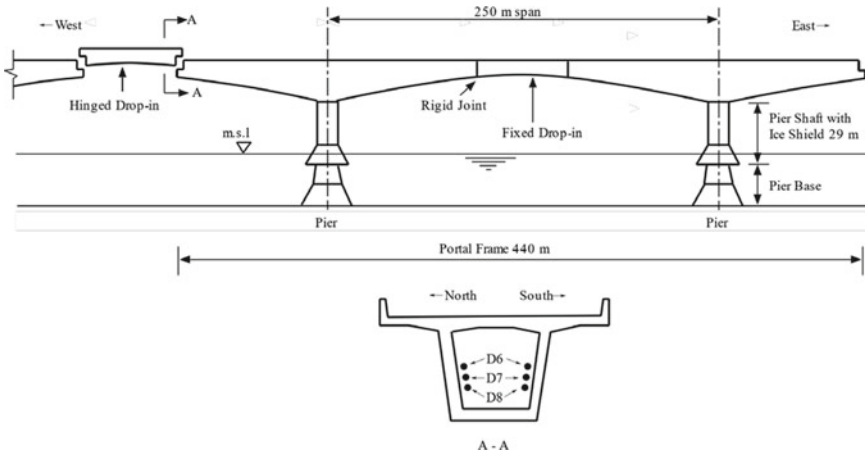
Fig. 2 Typical bridge components

In this study eight tendon segments from the same hinged drop-in span are tested: tendons D7NE, D7NW, D7SE, D7SW, D8NE, D8NW, D8SE and D8SW. The 'N' and 'S' indices refer to the north and the south side of the box girder. The 'E' and 'W' indices indicate the east and west end of the drop in span (see Fig. 2). One of the tested tendons, D7N had been replaced and has 19 tendons instead of 20.

4 Equipment and Installation

The EPTT vibrations are recorded using G-Link-200-8G LORD Microstrain tri-axial accelerometers. Mounting plates are designed and fabricated to ensure the accelerometers are properly secured to the EPTT. Figure 3 shows the accelerometers and mounting plates secured to an EPTT with metal hose clamps. The sensors are mounted on top of the EPTT and aligned. Each sensor records vibrations in three directions, in line with the tendons and in both directions perpendicular to the tendons.

Fig. 3 Sensor installation on tendon

Since the formulas rely on the mode number, *n*, it is crucial to confirm that the extracted frequencies are associated with the expected mode shapes. When estimating mode shapes from vibration responses, a higher number of sensors provides better mode shape resolution. However, a primary goal of the current study is to design a testing methodology that is fast and efficient, thus requiring the fewest number of sensors. A balance must be established from these considerations when choosing the number of sensors.

For this study, the sensors are strategically placed where peaks from the first, second and third mode shapes are expected. For a homogenous section along the tendon length with relatively symmetrical end conditions, the expected mode shapes are symmetrical about the tendon's midpoint. For the experimental phase, one sensor is placed on the second half of the cable, three on the first half and one at the centre as illustrated by the Xs in Fig. 4. The two sensors adjacent to the centre line will help determine the vibration midpoint.

5   Test Procedure

The tests are performed over two non-consecutive days. On the first day, eight tendon segments from the same hinged drop-in span are tested. On the second day, two tendons that were tested the first day (D7NW and D8NW) are retested to demonstrate repeatability.
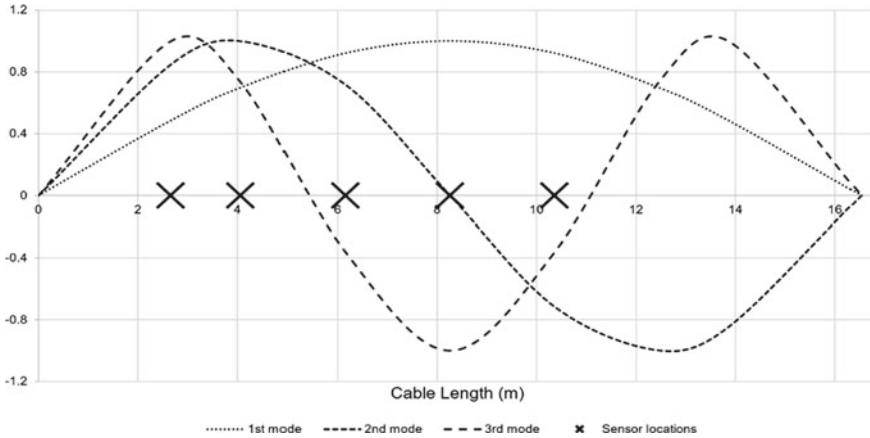
Fig. 4 Approximate sensor locations along length of cable

The EPTTs are excited by manually by pulling at the centre span with a sacrificial cable. The cable is pulled until a 3 N force is reached and then cut to create a free vibration response. The vibrations are recorded for 60 s after each pull test with a sampling rate of 128 Hz. Between five and eleven pull tests are executed for each cable. A custom script validates data synchronicity between each wireless sensors at the end of each recording. If the data becomes unsynchronized during the recording phase, the evaluator is informed, and an additional pull test is performed. The data is then saved for post processing and analysis.

6 External Factors

When recording frequencies of structural components on in-operation structures such as bridges, one must be aware that external factors can affect the vibrations. The accelerometers mounted on the EPTTs do not differentiate between the vibrations of the overall structure created by the wind and traffic and the tendon's free vibrations. Advanced system identification techniques are therefore required to effectively extract the modal estimates of the EPTT. It should be noted that the winds were very calm on the first day of recording and the traffic was moving slowly and in one direction as one lane was closed above the span where testing was completed. On the second day, there were wind gusts of 60 km/h and the traffic was free flowing in both directions during testing.
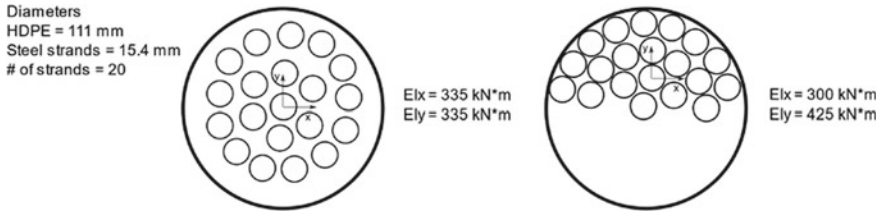
Fig. 5 Tendon sections—steel strand layouts

7 Analysis

The recorded vibration responses in *g*'s are stored in data tables containing 15 channels (three channels per sensor, one for each of the measured directions). The recorded data are pre-processed to confirm synchronicity, to purge any duplicate values and to patch gaps, as required. The data are also translated from ASCII to binary for faster import into the MATLAB® environment.

8 Mass and Rigidity Estimates

To estimate the tension, the mass and the rigidity of each EPTT need to be determined. The tendon linear mass is calculated using the density of the HDPE, the documented construction grout mixture density with an estimated 6% entrained air content and the listed strand mass per meter.

The rigidity was estimated by modifying the steel strand layouts inside the tendon duct. Two possible layouts are illustrated in Fig. 5. The tendon on the left shows the ideal section, where all strands are distributed symmetrically. The tendon on the right shows the strands gathering on one side of the tendon. The bending rigidity (*EI)* in each direction about the sections' center of mass is also indicated in Fig. 5.

It should be noted that the mass and rigidity estimates for the replacement tendon (D7N) were obtained by considering 19 strands instead of 20 strands.

9 Modal Analysis

Several methods exist to identify frequencies from the measured vibration responses of structural systems. For this study, two methods were considered, the first is the simple peak picking from FFT spectrum and the second is a novel operational modal analysis technique called automated inline full space identification (AI-FSI). Developed by Desjardins and Lau [5], AI-FSI is a variant of the established system identification technique known as SSI (stochastic subspace identification).

9.1 Peak Picking

The first method used to identify frequencies is peak picking. A fast Fourier transform (FFT) is applied to the recorded data to convert the vibration response in the time domain into the frequency domain. The first important peak is identified as the possible first structural mode. The first mode peak is typically evident but as the modes increase the peaks are less prominent. Each sensor tends to have a slightly different peak which makes it difficult to choose a single frequency for each mode. Peaks can also appear where a certain frequency is present in the signal but does not necessarily represent a proper structural mode of the EPTT. This is a significant shortcoming of the peak picking method. While not a proper system identification technique, peak picking usually allows the quick identification of the natural frequency which helps to validate the tension estimates and the AI-FSI results.

9.2 Operational Modal Analysis (AI-FSI)

To overcome the shortcomings of the peak picking method and to ensure that the identified frequencies are actual structural modes, an output only system identification technique is employed to obtain the modal parameters of the EPTT. Output-only techniques, or operational modal analysis methods, are used when the excitation force cannot be exactly quantified. Although a manual pull and release method with a known (albeit variable) input force is employed in this study to excite the EPTT, it is believed that an output-only technique will allow a greater flexibility to the evaluator and that the variability of the pull force and direction will be inherently considered and reflected in the results.

The AI-FSI method is therefore applied to estimate the modal parameters with the help of SPPLASH, a signal processing platform for the analysis of structural health developed in 2004 by Desjardins et al. [4] and updated in 2022 [5]. With the AI-FSI method now integrated in SPPLASH, the modal parameters are automatically extracted, and the mode shapes are animated allowing confirmation that the first, second and third modes are properly and consistently identified. Mode shape comparisons are calculated using the modal assurance criterion (MAC) [1]. Automated modal parameter estimations (MPE) are carried out on each 60 s dataset. Then, the integrated mode tracking algorithm effectively groups matching modes from multiple datasets by the recursive reduction of the MAC matrix. For a more detailed description of the AI-FSI method with integrated MPE and mode tracking, the reader is directed to [5].

Since EPTT are essentially unidimensional, and since responses are measured in three dimensions, two orthogonal mode shapes are extracted for every mode. The orientations of the plane of the mode shapes are generally perpendicular (orientation no.1) and parallel (orientation no.2) to the pull direction. The modal frequencies of each orthogonal mode-pair are very similar (as shown in Table 1), but not equivalent.

Theoretically, for a perfectly symmetrical section, the orthogonal mode pairs should have the same modal frequency to reflect the same cable tension. This variability can be attributed to the flexural rigidity of the tendon which is slightly different in each orientation since the cables inside the tendon tend to gather on one side of the tendon as opposed to being perfectly centred. Other sources of variability include the support conditions (which may not exhibit the same behavior in all directions), the external factors (wind, temperature, and traffic loads) and the sensor installation.

9.3 Effective Vibration Length

Curve fitting with least squares method is applied to determine an effective vibration length. The mode shapes of the selected modes are drawn with the normalized maximum amplitude of each sensor. With one sensor on each side of the measured length centreline, the vibration centreline is determined by interpolating their locations and their maximum amplitude. Based on the new vibration centre line, a theoretical curve is drawn, and the length adjusted to best fit the experimental data. With the sensors installed where the peaks from the first, second and third modes are expected, the vibration length for each mode can be corrected. The centreline and the length are corrected until the smallest sum of least squares is achieved. The adjusted lengths are taken as the effective vibration lengths. Figures 6a–c illustrate the experimental, theoretical, and adjusted curves for a representative tendon (D8NW) for all three mode shapes. Three cables (D7SE, D8SE and D8NE) are difficult to curve fit for the third mode in a single orthogonal direction. The resulting curve fitted lengths are slightly longer than the other lengths for those cables. Each mode in each direction has varying vibration lengths. Results are shown in Table 1.

10 Tension Estimates

The three formulas presented above are used to calculate the tension using the frequency estimates and the estimated mass, rigidity and effective length parameters described above. The first formula is based on basic vibrating string theory, the second considered the section rigidity and the third combined two modes to ignore the rigidity parameter. The same linear weight, frequencies and lengths are applied in each formula. The length considered is the vibration length obtained through curve fitting for each mode shape obtained from AI-FSI. For the second formula, the section rigidity is estimated for both orthogonal mode-pair orientations assuming the steel strands are not perfectly centred inside the tendon. With the curve-fitted lengths, the bending rigidity estimates (EI) are estimated by adjusting the strand distribution for each cable to lower the variability between the two mode-pair directions for all modes. The estimated rigidity values for each cable are therefore limited to the range of EI estimated between the idealistic symmetrical section and a section where all

Table 1 Cable properties and frequency estimates

Cable ID	Linear mass (kg/m)	Measured length (m)	# of pull tests	Peak picking Mode 1		Operational modal analysis (A1-FSI)					Effective length (m)	Rigidity (kN*m²)
				Avg. freq. (Hz)	CV (%)	Mode-pair orientation	Mode	Avg. frequency (Hz)	% matched modes	Coefficient of variation (%)		
D7NE	32.3	16.83	11	9.270	0.35	1	1	9.212	91	0.58	17.00	425
							2	18.368	82	0.07	16.80	
							3	28.163	100	0.06	16.85	
						2	1	9.335	82	0.23	16.75	300
							2	18.497	91	0.36	16.60	
							3	28.427	55	0.01	16.50	
D7NW	32.3	16.87	9	9.219	0.20	1	1	9.226	78	0.41	16.80	325
							2	17.877	67	0.04	17.25	
							3	27.440	100	0.12	17.00	
						2	1	9.364	67	0.70	16.65	375
							2	18.031	100	0.25	17.10	
							3	27.757	100	0.02	16.85	
D7NW Day 2	32.3	16.87	6	9.203	0.10	1	1	9.588	70	4.30	16.90	325
							2	17.751	33	2.21	17.45	
							3	27.459	100	0.04	17.30	
						2	1	None found	0	–	–	375
							2	17.829	50	1.10	17.32	

(continued)

Table 1 (continued)

Cable ID	Linear mass (kg/m)	Measured length (m)	# of pull tests	Peak picking Mode 1		Operational modal analysis (A1-FSI)					Effective length (m)	Rigidity (kN*m²)
				Avg. freq. (Hz)	CV (%)	Mode-pair orientation	Mode	Avg. frequency (Hz)	% matched modes	Coefficient of variation (%)		
							3	27.768	67	0.02	17.10	
D7SE	33.2	16.83	5	9.999	0.30	1	1	9.938	100	0.85	16.35	300
							2	20.035	100	0.05	16.55	
							3	30.218	100	0.01	16.50	
						2	1	10.517	100	3.45	16.32	425
							2	20.230	100	0.06	15.90	
							3	30.542	100	0.08	17.08	
D7SW	33.2	16.86	5	10.098	0.24	1	1	9.961	100	0.65	16.25	300
							2	20.157	80	0.01	16.50	
							3	30.366	100	0.03	16.00	
						2	1	10.216	80	1.49	16.10	425
							2	20.302	100	0.05	16.20	
							3	30.621	100	0.01	16.20	
D8NE	33.2	16.52	5	10.140	0.00	1	1	10.102	100	0.67	16.25	300
							2	20.345	80	0.06	16.10	
							3	30.698	100	0.09	16.05	

(continued)

Table 1 (continued)

Cable ID	Linear mass (kg/m)	Measured length (m)	# of pull tests	Peak picking Mode 1		Operational modal analysis (A1-FSI)					Effective length (m)	Rigidity (kN*m^2)
				Avg. freq. (Hz)	CV (%)	Mode-pair orientation	Mode	Avg. frequency (Hz)	% matched modes	Coefficient of variation (%)		
						2	1	10.271	100	0.21	15.95	425
							2	20.600	100	0.02	15.90	
							3	31.165	100	0.02	16.70	
D8NW	33.2	16.51	6	10.190	0.24	1	1	10.116	100	1.02	16.00	300
							2	20.377	83	0.18	16.20	
							3	30.740	100	0.16	15.95	
						2	1	10.230	100	0.32	16.00	400
							2	20.529	83	0.08	15.96	
							3	30.997	100	0.02	15.89	
D8NW Day 2	33.2	16.51	6	10.183	0.24	1	1	10.118	83	0.42	16.06	300
							2	20.411	100	0.01	16.20	
							3	30.779	100	0.04	15.95	
						2	1	10.295	83	0.58	16.00	400
							2	20.541	83	0.12	16.15	
							3	31.007	100	0.03	15.95	
D8SE	33.2	16.49	6	10.270	0.50	1	1	10.160	100	0.80	16.15	300

(continued)

Table 1 (continued)

Cable ID	Linear mass (kg/m)	Measured length (m)	# of pull tests	Peak picking Mode 1		Operational modal analysis (AI-FSI)					Effective length (m)	Rigidity (kN*m²)
				Avg. freq. (Hz)	CV (%)	Mode-pair orientation	Mode	Avg. frequency (Hz)	% matched modes	Coefficient of variation (%)		
							2	20.505	100	0.05	16.05	
							3	30.935	67	0.06	16.30	
						2	1	10.324	100	0.20	16.08	425
							2	20.746	100	0.15	15.70	
							3	31.364	100	0.09	17.50	
D8SW	33.2	16.56	5	10.290	0.34	1	1	10.137	80	2.01	16.25	300
							2	20.574	100	0.08	16.17	
							3	31.034	100	0.01	15.98	
						2	1	10.302	80	0.23	16.20	425
							2	20.711	80	0.06	15.85	
							3	31.249	100	0.02	16.15	

a : D8NW first mode

b : D8NW second mode
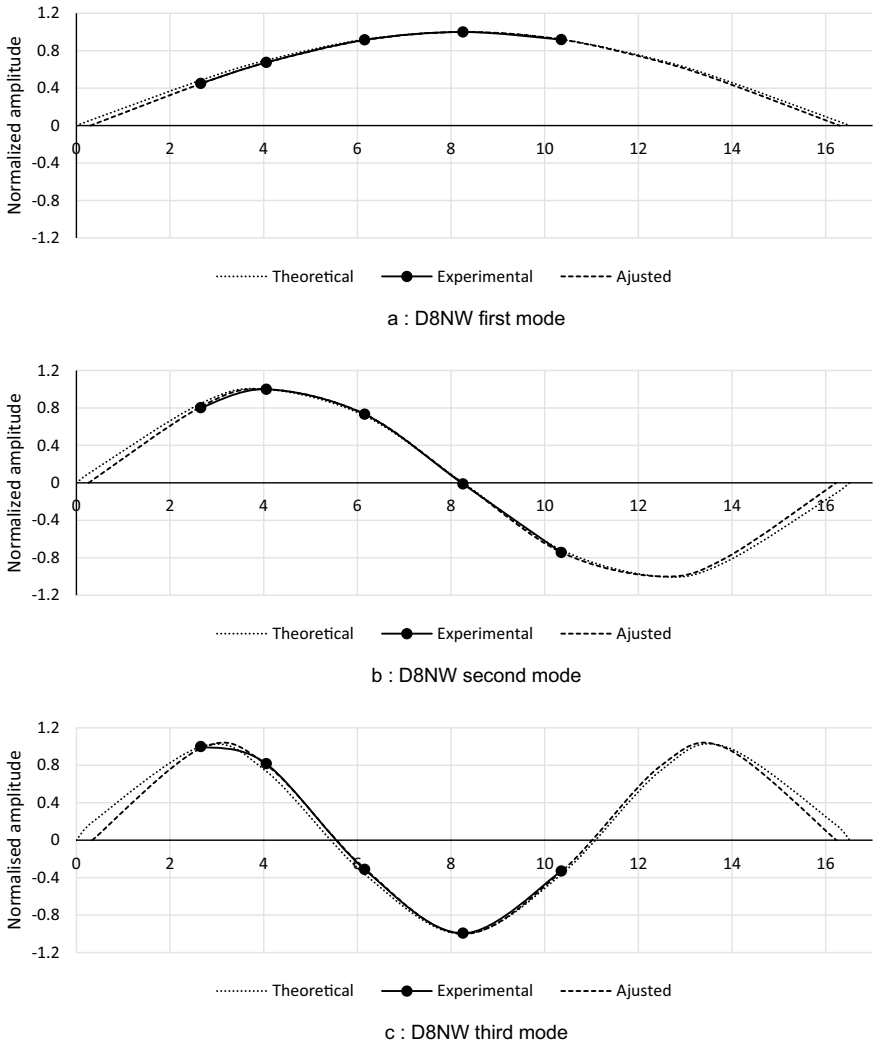
c : D8NW third mode

Fig. 6 **a** D8NW first mode, **b** D8NW second mode, **c** D8NW third mode

cables gather on one side of the tendon as shown in Fig. 5. The tension estimates are presented in Table 2.

Table 2 Tension estimates

Cable ID	Equation (1)				Equation (2)		Equation (3)	
	Mode 1 frequency (peak picking)		Mode 3-orientation 1 frequency (AI-FSI)		Mode 3-orientation 1 frequency (AI-FSI)		Mode 2 and 3-orientation 1 frequencies (AI-FSI)	
	Tension (kN)	Coeff. of var. (%)	Tension (kN)	Coeff. of var. (%)	Tension (kN)	Coeff. of var. (%)	Tension (kN)	Coeff. of var. (%)
D7NE	3145	0.70	3235	0.12	3102	0.13	2985	0.27
D7NW (day 1)	3123	0.39	3126	0.25	3026	0.26	2959	0.29
D7NW (day 2)	3113	0.19	3241	0.07	3145	0.08	2944	8.40
D7SE	3774	0.61	3665	0.01	3567	0.01	3614	0.17
D7SW	3862	0.47	3480	0.07	3376	0.07	3643	0.03
D8NE	3736	0.00	3579	0.18	3475	0.18	3527	0.23
D8NW (day 1)	3771	0.48	3544	0.32	3439	0.33	3583	0.81
D8NW (day 2)	3767	0.48	3553	0.09	3448	0.09	3596	0.08
D8SE	3823	1.01	3748	0.12	3648	0.13	3560	0.19
D8SW	3866	0.67	3626	0.02	3521	0.03	3638	0.27

11 Results

The parameter estimations and frequency results are summarized in Table 1. The calculated linear mass, the number of pull tests and the frequency estimates from both the peak picking and AI-FSI are indicated for each cable along with the associated vibration effective length and rigidity estimates. The frequency estimates obtained from the AI-FSI technique are averaged for each mode in both orthogonal directions for all pull tests. The coefficient of variation, which is the standard deviation over average in percentage, is also indicated and is useful in determining which modal frequency was most consistently identified throughout the pull tests. Not all frequencies were extracted from each pull test, the percentage of matched modes in Table 1 indicates the proportion of datasets that successfully extracted the given mode. The mode-pair orientation no.1 is generally perpendicular to the pull direction and mode-pair orientation no. 2 is generally parallel to the pull direction.

According to Table 1, the recorded frequencies for the first mode varied between 9.2 Hz and 10.9 Hz for all cables. The second and third mode were recorded at frequencies in the range of 17.8 Hz to 20.8 Hz and 27.3 Hz to 31.4 Hz respectively. When comparing the frequency estimates between different cables from Table 1, the second and third modes show standard variations between 0.01% and 2.21% compared to the first modes that vary between 0.20% and 4.30%. Another noticeable

difference between the first, second and third modes was the percentage of frequencies that could be matched between datasets. Overall, the third modes are matched in 95% of the datasets in comparison to the first and second modes that are matched in 88% of the datasets. The variation in number of pull test between cables was due to suspected unsynchronized datasets. The unsynchronized data was later adjusted during post-processing which allowed for all pull tests to be used for analysis.

Table 2 shows the tension estimates obtained from the three equations described in Sect. 1. For Eq. (1), the frequency estimates from the peak picking method and the AI-FSI technique are used. For the tension estimate using the first mode from peak picking, the measured length of the cable is considered instead as the vibration length as no mode shape is extracted from the peak picking method to allow proper estimation of the effective vibration length.

The third mode average frequency in orientation 1 obtained with the AI-FSI technique is used for Eq. (1) and (2) since it has very low coefficients of variability and is most consistently identified through the datasets. Even though the third mode second orthogonal direction variability is also low, the mode shape of three cables (D7SE, D8SE and D8NE) are difficult to curve fit in this direction resulting in effective lengths that are greater than the measured length. For this reason, results from orientation 1 were prioritized. For Eq. (3), the second and third mode average frequency in orientation 1 is used.

Equation (3), developed to ignore the rigidity component, often results in the highest standard deviation. This is due to a larger number of variables used in the formula. Typically, by using two frequencies, the variability is lower, but for this study, the opposite is true since the variability is associated with the frequency estimates. Also, only one length value is considered in the third formula even though the above results suggests that the vibration length for each mode is different. For this study, the lowest mode effective vibration length was considered in Eq. (3). The lowest overall standard deviation is consistently the results of one of the first two formulas: basic vibrating string theory and vibrating string theory with the rigidity component added. Since the variability is directly linked to the frequency, it is almost identical for both equations. The small difference can be attributed to the results of Eq. (2) being lower because of the rigidity component that lowers the estimated tension. Since the rigidity of the EPTT is a non-negligeable parameter related to cable tension, the results from Eq. (2) which includes the rigidity parameter EI are assumed to be the most accurate.

11.1 Testing Method Comparison

All cables were tested in 2016 and 2019 with a static deflection method [10]. Results from this testing method are presented in Table 3 along with the tension estimates from the current (2022) vibration analysis. The current tension estimates are those obtained from Eq. 2 calculated with the frequency estimates from AI-FSI (see Table 2). It should be noted that tension estimates from 2016 and 2019 are an average

Table 3 Cable tension summary

Cable ID	2016 (static deflection)		2019 (static deflection)		2022 (vibration)		2019 over 2016 (%)	2022 over 2019 (%)
	Tension (kN)	Coeff. of var. (%)	Tension (kN)	Coeff. of var. (%)	Tension (kN)	Coeff. of var. (%)		
D7NE	3245	1.84	3218	0.07	3102	0.13	−0.81	−3.62
D7NW	3289	2.86	3217	0.09	3026	0.26	−2.16	−5.96
D7SE	3414	2.50	3556	0.82	3567	0.01	4.17	0.31
D7SW	3504	5.05	3452	0.53	3376	0.07	−1.46	−2.21
D8NE	3577	1.12	3400	0.49	3475	0.18	−4.95	2.21
D8NW	3684	1.69	3514	0.17	3439	0.33	−4.60	−2.14
D8SE	3574	1.44	3535	0.24	3648	0.13	−1.09	3.20
D8SW	3808	7.53	3635	0.38	3521	0.03	−4.54	−3.13

of four or five measurements for each cable. The D7N tendon segments are also expected to have values different from the others because it is a replaced tendon with fewer strands.

11.2 Discussion

The main objective of the study is to design an effective vibration-based testing methodology for determining the tension in external post-tensioning tendons. For the testing stage, five sensors are used to collect data. The original assumption was that the first and second modes would be sufficient to determine the tension and that fewer sensors could be used to find reliable results. However, since the third mode showed less variability, and since all the sensors proved to be useful when curve fitting the experimental and theoretical mode shapes for the estimation of vibration length, the five-sensor setup is recommended. The two sensors adjacent to the centreline helped position the vibration midpoint and all other sensors helped curve fit around the first, second and third mode shape peaks. Furthermore, with the properly identified mode-shapes, the rigidity parameter was confirmed and shown to vary between EPTT and between mode-pair directions of the same EPTT.

Overall, the variability between pull tests is very low, with the second and third modes having the least variability in the results. To determine the tension in each tendon, the result of the mode and direction with the overall lowest variability was assumed to be most accurate; the third mode in orientation 1 in this case. Another approach considered is to use an average of the modes that show variability under a certain threshold. Effectively, this would mean an average of all second and third mode shapes. Additional analyses could help determine which approach would be best.

Results from the first day of testing show that the replacement tendons (D7N E&W) have variability in the results similar to the other tendons. It was, however, not possible to match as many modes between pull tests as the other cables. During the second day of testing, the variability of the replacement tendon was noticeably higher, and the percentage of modes matched between pulls considerably lower. Also, curve-fitting the mode shapes for this tendon revealed consistently longer vibration lengths than the measured length. These observations could indicate that the vibration test can identify tendons that have structural differences along their length or defects. When comparing the results from the first and second days of testing, tension estimates in tendon D7NW have a relative difference of 3.80%. Tension results for tendon D8NW were 3439 kN for the first day and 3448 kN for the second (0.2% relative error). More testing is required to confirm repeatability of results. The three tendon mode shapes that were difficult to curve fit (D7SE, D8SE and D8NE) should also be retested to rule out the possibility that a sensor wasn't properly installed.

Based on this study, the proposed vibration testing methodology includes five sensors, positioned as per Fig. 4. Five pull tests are suggested for each EPTT with a pull load of 3 N. The recordings are done at a sampling rate of 128 Hz for 60 s. Following these testing requirements and considering the time necessary for sensor installation by an experienced crew, the testing of one drop-in span with 12 tendons should take approximately two to three hours.

12 Conclusion

The objective of the study is to design an effective vibration-based testing methodology for determining the tension in external post-tensioning tendons that offers comparable (or better) results than the existing static deflection method.

Three formulas based on vibrating string theory that estimate the tension from the vibration frequency are considered in this study. The parameter estimates of mass, rigidity and length are determined or calculated based on construction documents and on-site measurements. Frequency estimates are obtained by peak-picking from FFT plots and by an advanced operational modal analysis technique called AI-FSI.

The tension estimates obtained from the peak-picking method and from the AI-FSI are compared in Table 2. This comparison shows the short-comings of the peak-picking method, where tension estimates are significantly higher than those obtained with the extracted frequencies from OMA. The AI-FSI method described in this study was useful in understanding the dynamic behavior of the EPTT. With the extracted mode shapes, the proper structural modes were identified, and the effective vibration length was determined for each EPTT.

From the comparison of Table 2, the second formula is chosen since it considers the EPTT rigidity and was found to offer comparable results with the previous testing method (static deflection).

The vibration analysis and the static deflection method both compute similar results. Both methods can be effective in detecting a tension loss that could indicate a

structural deficiency. The advantages of using the vibration method are its ease of use and accuracy. Another advantage is that the vibration method inherently considers many sources of variability (installation errors, differences in the pull test force and direction, environmental and operational loadings, etc.). By repeating multiple pull tests during testing, this variability can be quantified. The results of this study show that even with significant sources of uncertainty, the baseline variability of the results is very low for repeated tests under similar conditions. Since the vibration test can be easily repeated in time, temporal trends can be identified through periodic testing regimes. Any significant variability observed between measurement periods will indicate either changes in external or internal conditions. By testing multiple EPTT, trends due to external factors can be identified and removed. Any remaining variability could indicate possible deviation from a healthy state.

More tests should be done on the same cables to confirm repeatability with varying temperatures and external factors such as traffic and wind. Repeating the tests periodically should demonstrate a trend in the data. A large and sudden variation in results could indicate a structural damage that would require attention.

From preliminary calculations, the vibrations method and static deflection method take about the same amount of time to setup and test the tendons over a drop-in span. However, it is believed that with experienced evaluators and installers, and over time, the vibration method could prove to be significantly quicker. This will need to be verified and confirmed through an actual large scale testing program.

References

1. Allemang RJ (2003) The modal assurance criterion—twenty years of use and abuse. SOUND Vib. 8
2. Chen C-C, Wu W-H, Leu M-R, Lai G (2016) Tension determination of stay cable or external tendon with complicated constraints using multiple vibration measurements. Measurement 86:182–195. https://doi.org/10.1016/j.measurement.2016.02.053
3. Cheung MS, Tadros GS, Brown T, Dilger WH et al (1997) Field monitoring and research on performance of the confederation bridge. Can J Civ Eng 24:951–962
4. Desjardins SL, Londoño NA, Lau DT, Khoo H (2006) Real-time data processing, analysis and visualization for structural monitoring of the confederation bridge. Adv Struct Eng 9:141–157. https://doi.org/10.1260/136943306776232864
5. Desjardins SL, Lau DT (2022) Advances in intelligent long-term vibration-based structural health-monitoring systems for bridges. Adv Struct Eng 15. https://doi.org/10.1177/13694332221081186
6. Dinh NDTT, Hung NH (2020) Evaluating the cable tension results by lift-off and vibration method in Viet Nam. IOP conference series materials science engineering, vol 869, p 052062. https://doi.org/10.1088/1757-899X/869/5/052062
7. Fang Z, Wang J (2012) Practical formula for cable tension estimation by vibration method. J Bridge Eng 17:161–164. https://doi.org/10.1061/(ASCE)BE.1943-5592.0000200

8. Lee JK, Kang JW (2019) Experimental evaluation of vibration response of external post-tensioned tendons with corrosion. KSCE J Civ Eng 23:2561–2572. https://doi.org/10.1007/s12205-019-0735-5
9. Liu HB, Wang LL, Tan GJ, Cheng YC (2013) Effective prestressing force testing method of external prestressed bridge based on frequency method. Appl Mech Mater 303–306:363–366. https://doi.org/10.4028/www.scientific.net/AMM.303-306.363
10. Stevenson J, McGinn DJ (2018) External post-tensioning evaluation after 20 years. In: IABSE conference 2018. Presented at the engineering the past, to meet the needs of the future, Copenhagen, Denmark, p 7
11. Wen-Hwa W, Chien-Chou C, Gwolong L, Min-Ray L (2012) Determination of stay cable force based on multiple vibration measurements to consider the effects of unsymmetrical boundary constraints. 6th Eur. Workshop Struct. Health Monit. EWSHM 2012 8
12. Wu W-H, Chen C-C, Chen Y-C, Lai G, Huang C-M (2018) Tension determination for suspenders of arch bridge based on multiple vibration measurements concentrated at one end. Measurement 123:254–269. https://doi.org/10.1016/j.measurement.2018.03.077
13. Yan B, Li D, Chen W, Deng L, Jiang X (2020) Mode shape–aided cable force determination using digital image correlation. Struct Health Monit 16. https://doi.org/10.1177/1475921720952163
14. Yu C-P (2020) Tension prediction for straight cables based on effective vibration length with a two-frequency approach. Eng Struct 222:13. https://doi.org/10.1016/j.engstruct.2020.111121

High-Performance Timber Frames with Smart Braces

A. Iqbal, E. Ebrike, R. Merrikhpour, and A. Akbarnejad

Abstract As the number of stories and height of wood buildings increase, the lateral loads become significantly important in design considerations. Using moment frames in tall timber structures (i.e., buildings beyond six stories) becomes uneconomical as the member sizes have to be increased significantly to provide sufficient lateral stiffness to the structure to resist seismic load effects. A robust, yet cost-effective and practical solution to improve lateral stiffness of tall timber structures is to add a braced frame so that a novel advanced structural system is developed for practical applications. For tall timber structures in seismic regions, the concept is of considerable interest due to demand for compact arrangement and efficient lateral load-resisting system exhibiting inherent high stiffness and subsequent reduction in drifts. This paper examines the applicability of the proposed structural system in timber buildings through determination of the influential parameters on the seismic response of the proposed "Smart" system with Shape Memory Alloy (SMA) dampers used in braces. The elastic nature of SMA contributes to self-centering performance of the overall system. A robust numerical model of the frames incorporating the SMA dampers is developed and used to recommend optimized configuration practical designs.

Keywords Timber frames · Smart braces

A. Iqbal (✉) · E. Ebrike · R. Merrikhpour · A. Akbarnejad
University of Northern British Columbia, Prince George, Canada
e-mail: Asif.Iqbal@unbc.ca

E. Ebrike
e-mail: Emad.Ebrike@unbc.ca

R. Merrikhpour
e-mail: merrikhpo@unbc.ca

A. Akbarnejad
e-mail: akbarneja@unbc.ca

1   Introduction

Timber-braced frames have been investigated for seismic applications including some special braced frames with combination of timber and steel. In post-tensioned frame, the arrangement achieves self-centering due to post-tensioning while the members remain elastic. The post-tensioned timber–steel hybrid braced frame combines Glulam frame with steel braces. The system offers a high lateral stiffness due to the presence of the steel-braced frame and improved seismic performance as a result of self-centering capability of the timber structure. The connection between the timber and steel structures is detailed such that a reliable energy dissipating capacity is obtained and a proper seismic load path is provided to achieve the expected response under seismic ground motions.

2   Timber Frames with SMA Braces

In practical arrangements, replaceable ductile elements protect the structural members from serious damage through absorbing energy during seismic events [1–8]. Engineered wood products have been found to be particularly suitable for this type of applications because of their superior strength characteristics compared to rough sawn timber and the concept has been applied to different engineered wood products such as Laminated Veneer Lumber (LVL) and Glue Laminated Timber (Glulam). Researchers have been working on Smart Braces with Shape Memory Alloys for the past few years [9–15]. Extensive experimental and numerical studies have confirmed viability of this type of braces in buildings. Additionally, a preliminary study has been performed on the proposed system using the validated nonlinear numerical models, suggesting that braced frames are likely to be adoptable to timber building structures to efficiently resist seismic lateral loads. The arrangement promises to be an economical and reliable solution for timber structures in seismic regions (Fig. 1).
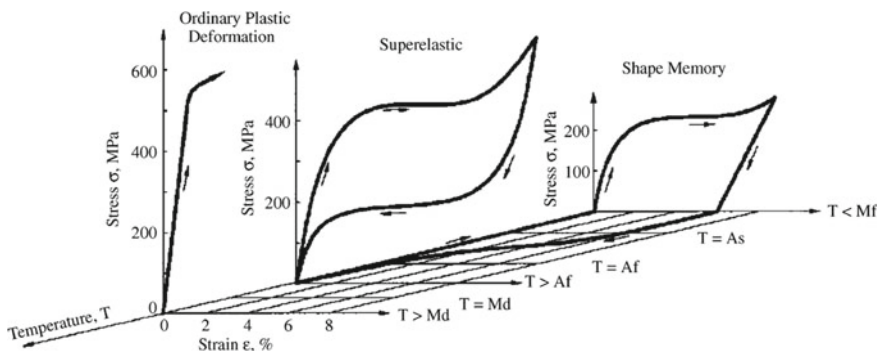
Fig. 1   Superelastic and shape memory characteristics of SMA

3 Frame and Connection Details

An extensive research program with a focus on the response evaluation of braced frame structures is currently underway at the University of Northern British Columbia. The results confirm that the numerical modeling technique developed to examine the behavior of such frames is promising [7, 8]. The project examined the applicability of the proposed structural system in timber buildings includes: determination of the influential parameters on the seismic response of the proposed "Smart" system with Shape Memory Alloy (SMA) dampers used in braces. Several configurations with typical diagonal have been considered for initial investigations (Fig. 2). In addition, inverted-V and toggle-brace arrangements (Fig. 3) have been studied. Further studies of the different types are currently ongoing.

Components of the damper have to be carefully arranged for expected performance of the damper. Three-dimensional virtual and physical models (Fig. 4) are developed to verify them. Proper anchorage details (Fig. 5) of the SMA wires in particular are critical for proper functioning of the whole assembly (Fig. 6).
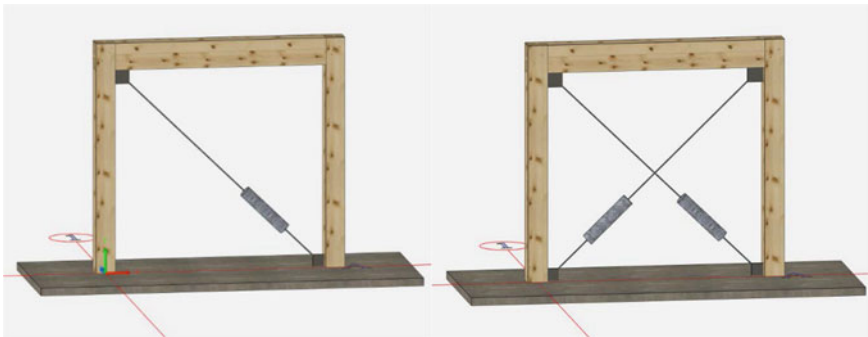
Fig. 2 Timber frames with diagonal braces
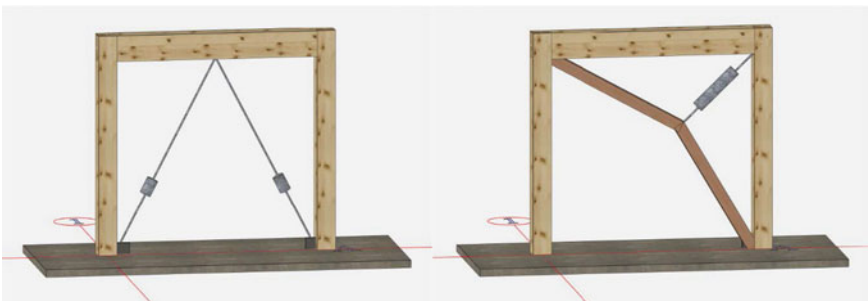
Fig. 3 Timber frames with inverted-V and toggle-brace arrangements
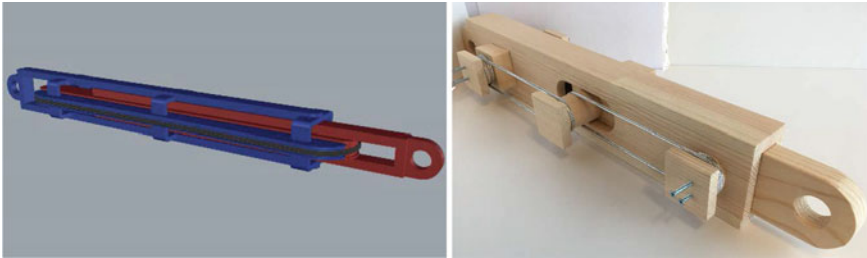
Fig. 4 Details of brace with SMA and arrangements
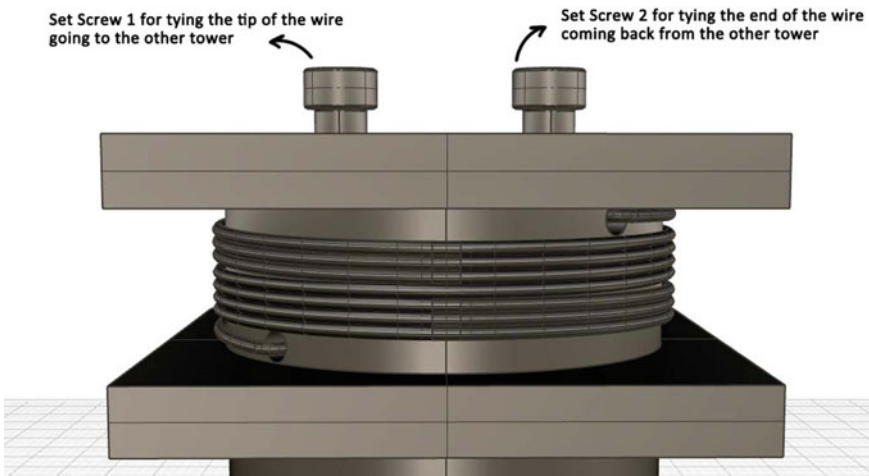
Fig. 5 View of anchorage for SMA wires

4 Numerical Modeling

Detailed numerical model of the proposed system is developed in the Open System
for Earthquake Engineering Simulation [16, 17]. A fiber-based model is used to
simulate the seismic response of the frame. Special attention is paid to the simulation
of the connections and inelastic response of bracing members. Material and geometric
nonlinearities are considered. The model was validated against previous experimental
results on timber and steel frames. This study focuses on a single- and two-storey
timber–steel-braced frames with cross0bracing configuration to evaluate the seismic
response of the proposed system. A typical force–displacement plot is shown in
Fig. 7.
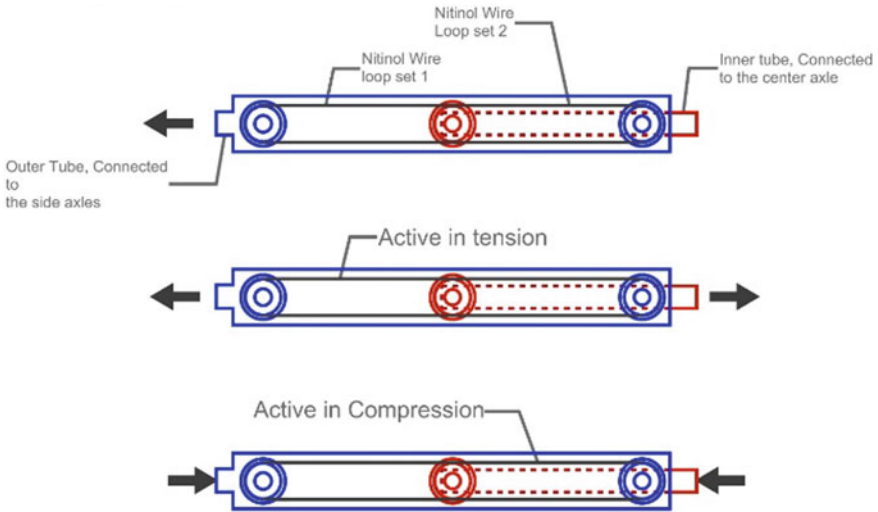
Fig. 6 Arrangement and working principle of the SMA damper

Fig. 7 Force–displacement response of braced frame
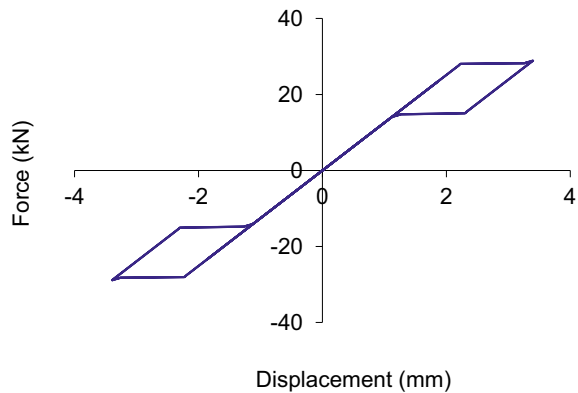
5 Conclusions

The post-tensioned braced frame solution is a novel idea that has the potential to be considered as a practical alternative for lateral load resistance systems in mid-to-high rise timber structures. As practitioners are pushing the boundary with taller timber structures, innovations such as this are required to accommodate the need for structures systems with better performance. That is particularly important for seismic applications as more and more all timber structures are planned for high-seismic regions and there is expectation from the societies to design structures that reduces economic losses as well as providing life safety.

References

1. Blomgren H (2015) Heavy timber buckling-restrained braced frames. Mass timber research workshop, Forest Products Laboratory, Madison
2. Gilbert C, Gholich R, Erochko J (2015) Nonlinear dynamic analysis of innovative hybrid timber-steel buildings. The 11th Canadian conference of earthquake engineering. Victoria, Canada
3. Gilbert C, Erochko J (2015) Adaptation of advanced high r-factor bracing systems into heavy timber frames. The 11th Canadian conference of earthquake engineering. Victoria, Canada
4. Imanpour A, Tremblay R, Davaran A, Stoakes C, Fahnestock LA (2016) Seismic performance assessment of multitiered steel concentrically braced frames designed in accordance with the 2010 AISC seismic provisions. J Struct Eng 142(12)
5. Popovski M, Prion HGL, Karacabeyli E (2003, Dec) Shake table tests on single-storey braced timber frames. Can J Civil Eng 30:1089–1100
6. Popovski M, Karacabeyli E. Force modification factors and capacity design procedures for braced timber frames. The 14th world conference on earthquake engineering
7. Wu K, Iqbal A (2020, April) Braced frame system for tall timber building. J Struct Eng Soc NZ 33(1)
8. Wu K-Y, Iqbal A, Imanpour A (2018, Aug) Seismic response of post-tensioned timber-steel hybrid braced frames. World conference on timber engineering, Seoul, Republic of Korea
9. Haque ABMR, Issa AS, Alam MS (2019) Superelastic shape memory alloy flag-shaped hysteresis model with sliding response from residual deformation: experimental and numerical study. J Intell Mater Syst Struct 30(12)
10. Issa AS, Alam MS (2019) Experimental and numerical study on the seismic performance of a self-centering bracing system using closed-loop dynamic (CLD) testing. Eng Struct 195
11. Jennings EN, van de Lindt JW (2012, Sept) Shape memory alloy dampers for response modification of light-frame wood buildings. The 15th world conference on earthquake engineering
12. Jennings EN, van de Lindt JW, Shao X, Pang W, Ziaei E (2014, July) Full-scale hybrid testing of a soft-story woodframe building seismically retrofitted using shape memory alloy devices in scissor-jack braces. The 10th US national conference on earthquake engineering
13. McCormick J, DesRoches R (2008, Oct) Characterization and optimization of shape memory alloy behavior for seismic vibration control applications in buildings. The 14th world conference on earthquake engineering
14. Speicher M, Hodgson DE, DesRoches R, Leon RT (2009, Aug) Shape memory alloy tension/compression device for seismic retrofit of buildings. J Mater Eng Perform 18(5–6)
15. van de Lindt JW, Potts A (2008, Aug) Shake table testing of a superelastic shape memory alloy response modification device in a wood shearwall. J Struct Eng, ASCE 134(8)
16. McKenna F, Fenves GL, Scott MH, Jeremic B (2000) Open system for earthquake engineering simulation (OpenSees) [Computer Software]. University of California, Berkeley, Pacific Earthquake Engineering Research Center
17. OpenSees (2014) Open system for earthquake engineering simulation, opensees.berkeley.edu/

Experimental Investigation of the Diaphragm Behavior of a New Deep Steel Deck Profile with Flange and Web Stiffeners

Milad Keshvari Ilkhechi, Ali Davaran, Charles -P. Lamarche, and Robert Tremblay

Abstract In North America, steel deck diaphragms are commonly used in low-rise commercial and industrial buildings as a roofing system to resist gravity loads. They are also used to transfer the in-plane shear forces generated by wind and seismic loads to the lateral force-resisting systems. A new 100 mm deep steel deck profile with longitudinal web and flange stiffeners, the MS100 profile, is being developed by Metal Sartigan Inc., Polytechnique Montreal, and Université de Sherbrooke. This type of deep stiffened steel deck is produced for the first time in Canada. This article describes a series of five large-scale monotonic quasi-static diaphragm test programs that was conducted on the new deep deck profile. Power-actuated fasteners were used for structural connections where self-drilling screws were used for side-lap connections. In each test, the diaphragm shear strength and stiffness were measured together with the global ductility. The measured strength and stiffness values are compared to AISI S310-20 and AISI S310-16 predictions. The results showed that MS100 steel deck diaphragms can exhibit sufficient strength for typical building applications. In the tests, it was observed that the shear strength was controlled by local buckling of the deck webs at the exterior support when closely spaced connections were used. For these specimens, the AISI S310-20 calculation method could predict reasonably well the shear strength, compared to AISI S310-16, even if the method does not account for the presence of web stiffeners. As expected, the measured diaphragm shear stiffness of such a deep deck profile is relatively low. The ductility of the tested diaphragms as measured under monotonic quasi-static loading varies from 6.95 to 11.2.

Keywords Diaphragm behavior · Deep steel deck · Flange and web stiffeners

M. K. Ilkhechi · A. Davaran · C. -P. Lamarche (✉)
Department of Civil and Building Engineering, Université de Sherbrooke, Sherbrooke, Canada
e-mail: Charles-Philippe.Lamarche@USherbrooke.ca

R. Tremblay
Department of Civil, Geological and Mining Engineering, Polytechnique Montréal, Montreal, Canada

947

1 Introduction

In North America, steel deck panels are commonly used in low-rise commercial and industrial buildings to resist gravity loads. They are also used to form a roof diaphragm collecting and transferring horizontal wind and seismic loads to the elements of the lateral force-resisting system. A new 100 mm deep stiffened steel deck profile with longitudinal web and flange stiffeners, referred to as the MS100 profile, is being developed by Metal Sartigan Inc., Polytechnique Montreal, and Université de Sherbrooke. The deck profile is illustrated in Fig. 1. This type of deep stiffened deck profile is produced for the first time in Canada. The MS100 deck panel is made of ASTM A1011, 0.76 and 0.91 mm thick steel, and intended to: (1) carry gravity loads at the roof level over spans up to 3.66 m (12 ft) to reduce the number of joists compared to traditional shallower deck profiles and (2) form a diaphragm that can efficiently resist in-plane shears induced at the roof level by wind and earthquake lateral loads.

In North America, accepted procedures exist for the elastic design of steel deck diaphragms by calculation. In Canada, the calculation and testing of steel deck are covered by the CSA S136-16 (R2021) standard—North American Specification for the Design of Cold-formed Steel Structural Members [1], which refers to the AISI S310-20—North American Standard for the Design of Profiled Steel Diaphragm Panels [2]. The design method by calculation in the AISI S310-20 standard is based on the method developed by Steel Deck Institute [3]. The method, however, is applicable only for steel decks that satisfy lower and upper limits on deck depth (12.7–178 mm), base steel thickness (0.35–1.91 mm), steel yield strength (230–550 MPa), ultimate tensile strength (310–555 MPa), and deck pitch (0–305 mm). When the deck depth exceeds 76 mm, the method applies only if the deck thickness is comprised between 0.85 and 1.91 mm. For other steel decks, the strength and stiffness of the
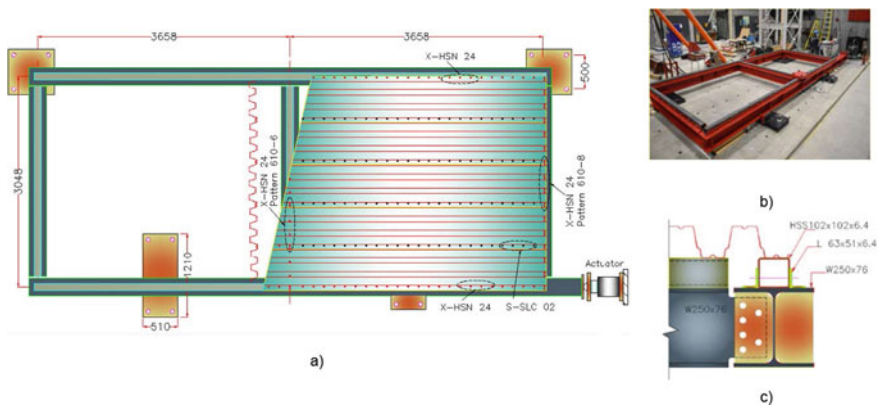
Fig. 1 Test setup: **a** schematic of the test setup and layout of connections, **b** photo of the test setup, **c** edge support (Typ.)

diaphragm must be obtained from physical testing in accordance with the AISI S907-17—Test Standard for Determining the Strength and Stiffness of Cold-Formed Steel Diaphragms by the Cantilever Test Method [4]. In AISI S310-20, a new failure mode for calculating the shear strength of diaphragms was introduced based on Nunna [5]. This failure mode is related to local web buckling of panels over exterior support. The calculation of the shear strength of the diaphragm for this failure mode involves calculating the web crippling strength using AISI S100-16 (reaffirmed in 2020)—North American Specification for the Design Cold-Formed Steel Structural Members [6]. In the case of the MS 100 deck, a longitudinal web stiffener prevents using the web crippling strength equations of AISI S100-16. Consequently, the diaphragm strength and stiffness of the MS100 deck must be evaluated experimentally.

Diaphragms with steel deck depths greater than 76 mm (3 in.), generally referred to as "deep deck diaphragms" are utilized for their increased ability to resist vertical loads for longer deck spans. However, this increased flexural resistance often comes at the cost of in-plane shear stiffness because deeper decks are more prone to lateral racking and shear distortions from in-plane forces, resulting in decreased diaphragm stiffness and strengths than decks with depths of 76 mm or less [7, 8].

This paper presents the results of the preliminary phase of a larger project that aims to characterize the elastic and inelastic behavior of the MS100 deck acting as a roof diaphragm under wind and seismic loading. Five preliminary large-scale diaphragms' tests were performed to provide insight into the elastic and the inelastic response of MS100 deck diaphragms under shear deformation: strength and failure mode, stiffness, and ductility, of steel deck roof diaphragm assemblies under monotonic quasi-static loading. The test program includes the use of two sheet thicknesses and three different combinations of deck-to-frame and side-lap fasteners. The strength and stiffness of the tested diaphragms are compared to AISI S310-16 and AISI S310-20 predictions. Although monotonic quasi-static loadings are not quite representative of the random and reversing loads experienced during an earthquake, they provide information about the ultimate strength, stiffness, ductility, and energy dissipation potential of the roof deck diaphragm under such loads.

2   Test Program

The plan view of the test setup is shown in Fig. 1a partially including deck sheets. The photo of the setup is presented in Fig. 1b. The overall size of the test setup was 7.36 m long by 3.05 m wide, with a single intermediate purlin located at mid-span of the edge support beams. The 3.05 m wide side of the setup accommodates five panels of the MS100 deck.

A cross-sectional view of the MS100 deck is presented in Fig. 2a along with the fasteners to exterior and interior beam configurations which will be discussed later in this section. All the frame corner connections, as well as the joist-to-frame connections, were Hilti H-HSN 24 power-actuated fasteners (PAF) (Fig. 2b). All the side-lap connections were Hilti S-SLC 02 size #12 self-drilling screws (Fig. 2c). The

properties of the fasteners (nominal shear strength of support connection per fastener (P_{nf}) and nominal shear strength of side-lap connection per fastener (P_{ns})), and deck steel sheets (thickness, Young's modulus (E), yield stress (F_y), and tensile strength (F_u)) are presented in Table 1. Two steel sheet thicknesses were investigated: 0.76 (gauge 22) and 0.91 mm (gauge 20). The actual length of the tested specimen sheets was 7316 mm. Structural steel equivalent to Grade 40 with a galvanized coating was used for both sheet thicknesses. The cross-sections of the bare frame beams are comprised one HSS102 × 102 × 6.4 attached to the top flange of a W250 × 73 using side-bolted angles (Fig. 1c). The yield stress values for both metal sheet thicknesses used are inferior to a 5% difference, and the test results from specimens made of different steel are therefore deemed comparable.

A 500 kN capacity MTS 244.41 was used to apply the shear load. The east-west shear deflection was measured at the southeast and southwest corners of the frame using diagonal cable transducers attached at opposite corners. The east–west and north–south deflections were measured at the northeast and northwest corners of the frame by cable transducers. Measurement of these displacements was intended to correct for support movements at these locations, thus determining the true diaphragm
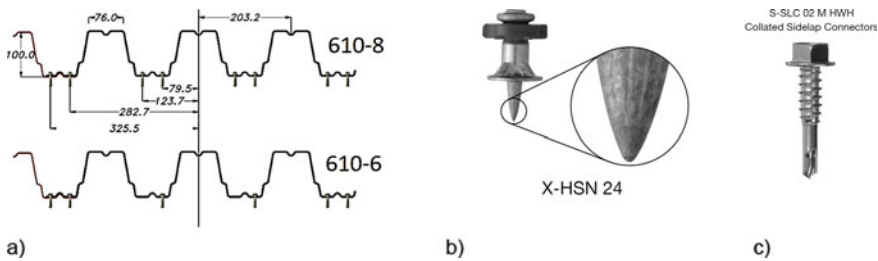
Fig. 2 **a** MS100 panel and structural connection patterns; **b** structural connector; and **c** side-lap connector

Table 1 Properties of fasteners and deck steel sheets

Fasteners				Steel sheets				
Type	Diam	P_{nf}, P_{ns}	k_s[a]	Thickness	E	F_y[a]	F_u[a]	F_u/F_y
	(mm)	(kN)	(kN/mm)	(Gauge | mm)	(GPa)	(MPa)	(MPa)	–
Hilti S-SLC 02, #12	5.36	3.21	11.04	20 | 0.91	203	335.8	409.6	1.22
Hilti S-SLC 02, #12	5.36	2.45	10.09	22 | 0.76	203	349.8	380.6	1.09
Hilti X-HSN 24	4.1	7.99	26.52	20 | 0.91	203	335.8	409.6	1.22
Hilti X-HSN 24	4.1	6.72	24.21	22 | 0.76	203	349.8	380.6	1.09

[a]: k_s is equal to $1/S_f$, where S_f is the structural flexibility of the fastener assembly according to AISI S310-20

Table 2 Characteristics of diaphragm test specimens

Test no.	Steel sheet thickness	Deck-to-frame fasteners type and distribution				Side-lap fasteners	
		PAF	Deck-to-edge supports	Exterior support	Interior support	Self-drilling screws	Spacing
	Gauge | mm	Hilti	(mm)	Pattern	Pattern	Hilti	(mm)
Test #1	20 | 0.91	X-HSN 24	152	610–8	610–6	S-SLC 02, #12	102
Test #2	20 | 0.91	X-HSN 24	152	610–8	610–6	S-SLC 02, #12	152
Test #3	22 | 0.76	X-HSN 24	152	610–8	610–6	S-SLC 02, #12	102
Test #4	22 | 0.76	X-HSN 24	152	610–8	610–6	S-SLC 02, #12	152
Test #5	22 | 0.76	X-HSN 24	305	610–8	610–6	S-SLC 02, #12	305

shear angle. All experimental measurements conform to the cantilever testing method described in AISI 907-17.

Five monotonic quasi-static tests were performed up to failure of the diaphragms using two different steel sheet thicknesses' and fasteners' configurations. The characteristics of each test specimen are presented in Table 2. A deck-to-edge support PAF spacing of 152 mm was used for all tests except Test #5 where a spacing of 305 mm was used. Two different PAF configurations were used for the exterior support and interior support. Those patterns are depicted graphically in Fig. 2a. The spacing between the side-lap screws was 102, 152, or 305 mm. Prior to initiating each monotonic diaphragm test, cyclic tests were performed on the bare test frame to assess the resistance to horizontal shear movement as specified in AISI 907-17.

3 Test Results

Three modes of failure were observed in the tests:

- FM1: local buckling of the webs at the exterior supports, corresponding to shear strength per unit length S_{nl} in AISI S310-20.
- FM2: failure of connections at interior panels, corresponding to shear strength per unit length S_{ni} in AISI S310-20.

- FM3: failure of structure connections at the corners of interior or edge panels, corresponding to shear strength per unit length S_{nc} in AISI S310-20.

  In addition, AISI S310-20 also considers two other failure modes:

- Failure of structure connections along the edge parallel to the panel span in an edge panel and located at the diaphragm reaction line, corresponding to shear strength per unit length S_{ne} in AISI S310-20.
- Out of plane buckling of deck panels, corresponding to shear strength per unit length S_{no} in AISI S310-20.

  These two modes of failure were not observed during the test program.

  The test results are presented in Table 3 along with the AISI S310-20 predictions using a resistance factor for diaphragm strength $\phi = 1$. In Table 3, S_{test} corresponds to the attainment of P_{max} (maximum applied load to the test frame) as defined in AISI S907-17. However, for Test #1 and Test #3, which exhibited an increase in shear strength after local web buckling at end support, P_{max} was taken as the load corresponding to the first local web buckling at the end support occurrence. This behavior is explained in Sect. 4. The measured and calculated strength (S) and diaphragm stiffness (G') based on AISI S310-20 are also presented in Table 3 along with tests to AISI S310-20 ratios. The measured diaphragm ductility μ as defined by AISI S400-20 is also presented in the table [11].

Table 3 Test results and AISI S310-20 predictions

Test no	Test				AISI S310-20			
	Failure	S_{test}^a	G'_{test}	μ	S_n^a	G'_{AISI}	S_{test}/S_n	G'/G'_{AISI}
	Mode	(kN/m)	(kN/mm)	–	(kN/m)	(kN/mm)	(Test/AISI)	(Test/AISI)
1	FM1	26.10	7.26	11.2	21.96	11.23	1.19	0.65
2	FM2	23.14	8.40	7.61	21.96	10.52	1.05	0.80
3	FM1	19.70	5.34	10.7	16.32	8.08	1.21	0.66
4	FM1	18.20	5.51	6.95	16.32	7.68	1.12	0.72
5	FM2 + FM3	11.28	5.55	11.1	12.83	6.81	0.88	0.81

[a] The strengths per unit of length are presented along with the experimental, and AISI S310-20 failure mode predictions, respectively

4 Analysis of Test Results

4.1 General Observations

At the beginning of each test, the diaphragms exhibited a linear elastic behavior with increasing warping deformations at the open end of the panels within the application of 40% of the ultimate load. The MS100 deck being relatively deep exhibited pronounced distortional deformations (warping) prior to attaining the peak shear load as shown in Fig. 3a, which correspond to Test #2 slightly before reaching P_{max}.

Tests #1 and #3, with the same connector configuration and different sheet thickness, exhibited similar modes of failure corresponding to local web buckling at end support. The shear load per unit of panel length vs. the shear angle measured during the tests is presented in Fig. 4a, where the end of the elastic phase corresponds to the occurrence of web bucking at the end support in one flute (Fig. 3b) initiated at a load per unit panel length S_{test} (Table 3). After all the webs under a compression force buckled due to the in-plane shear force resisted by the entire width of the deck (Fig. 3c), the diaphragm exhibited post-buckling shear strength accompanied by an increase in capacity. The behavior described herein is depicted graphically in Fig. 4a. Both tests were interrupted intentionally at a shear deformation 40×10^3 rad to avoid damaging the test setup. When the tests were interrupted, no significant damages were observed in the deck-to-frame or side-lap connections. These observations are supported by the AISI S310-20 fastener-related failure strengths' predictions presented in Table #4, where all failure modes' strengths S_{nf} have higher values than the maximum load reached during the tests. In both cases, the local
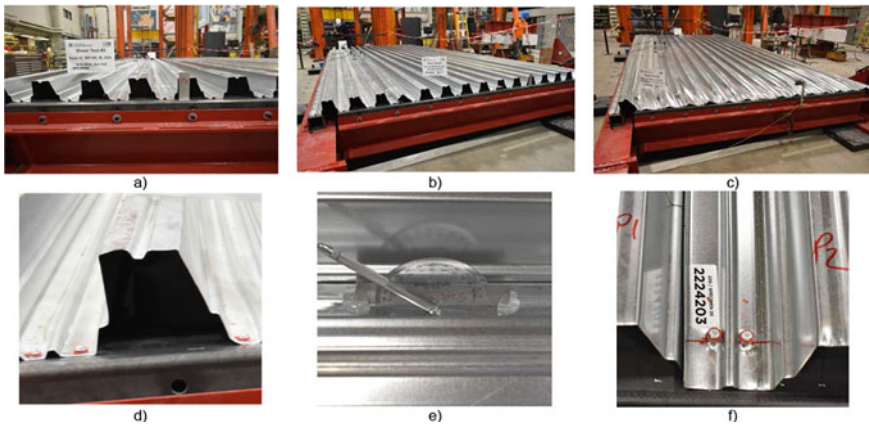
Fig. 3 **a** Distortion of the panels' sections (warping) in Test #2 before attaining P_{max}, **b** occurrence of local web buckling of one panel over exterior support in Test #4; **c** complete local web buckling of panels over exterior support in Test #3; **d** distortion of the panels' sections (warping) in Test #5, **e** tilt angle of the side-lap screws at the end of Test #5, **f** bearing failure at support connections at the corners of edge panels at the end of Test #5
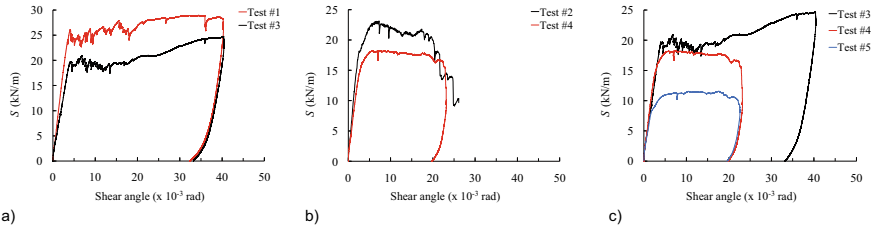
Fig. 4 Shear force per unit length of diaphragm versus shear angle: **a** Tests #1 and #3, **b** Tests #2 and #4, **c** Tests #3, #4, and #5

web buckling at end support in the experiment occurred at higher loads than those predicted by AISI S310-20 (Table 3). This is because the MS100 deck has a higher web crippling strength than the prediction equation in AISI S310-20 due to web stiffeners that are not considered in the calculation of S_{nl}. Test #1 exhibited higher strength and stiffness than Test #3 due to its thicker steel sheet material compared to Test #3.

Tests #2 and #4, with the same connector configuration and different sheet thickness, exhibited similar failure modes. The shear load per unit of panel length vs. shear angle measured during the tests is presented in Fig. 4b. At the end of the elastic regime, the failure observed in Test #2 corresponds to a combination of co-occurring panel corner connection and side-lap failures. In the case of Test #4, the same failure type was observed but was preceded by local web buckling at end support in a single flute. Once again, because the MS100 deck has a higher web crippling strength due to the presence of web stiffeners compared to flat webs as assumed in AISI S310-20, the web buckling capacity was not attained in Test #2. In Table 4, considering the added strength in the webs due to the presence of stiffeners, the failure modes S_{ni}, S_{nc}, and S_{nl} values are very close to one another, and any of these failure modes could have controlled the overall diaphragm strength. The shear capacity as a function of the shear angle degraded more rapidly in Tests #2 and #4 compared to Tests #1 and #3. The tests were terminated when the measured post-peak load dropped below $0.8P_{max}$. Test #2 exhibited higher strength and stiffness than Test #4 due to its thicker steel sheet material compared to Test #4.

In Test #5, the spacing between the side-lap screws and the spacing between the edge support fasteners was doubled compared to Tests #2 and #4. At the beginning of the test, the behavior was linear elastic until a load per unit length of deck of 8 kN/m was reached (Fig. 4c). Then, the stiffness of the deck decreased until a plateau was reached. This loss of stiffness was due to failures of side-lap connections. No local web buckling at end support was observed. The test was terminated when the measured post-peak load dropped below $0.8P_{max}$. The test was stopped before the sheets would separate. At the end of the test, the screws of the side laps were heavily tilted (more than 50 degrees with respect to the vertical (Fig. 3e)), and the capacity of the diaphragm dropped sharply. Significant bearing permanent deformations were

Table 4 Measured and calculated strengths according to AISI S310-20

Tests		S_{nf} (fastener-related strength)[a]			S_{nb} (stability)[a]	
Test no.	S_{test}	S_{ni}	S_{nc}	S_{ne}	S_{no}	S_{nl}
	(kN/m)	(kN/m)	(kN/m)	(kN/m)	(kN/m)	(kN/m)
Test #1	26.10	39.58	35.82	58.65	91.95	**21.96**
Test #2	23.14	**28.24**	**27.12**	58.65	91.95	**21.96**
Test #3	19.70	28.92	26.92	49.28	70.18	**16.32**
Test #4	18.20	**20.88**	**20.38**	49.28	70.18	**16.32**
Test #5	11.28	**12.83**	**13.12**	27.25	70.18	**16.32**

[a] Bold S_n values are potential fastener-related and potential stability-related failure modes

also observed between the PAF and deck sheet on the exterior and interior supports (Fig. 3f).

Tests #3, #4, and #5 had the same sheet thickness but different side-lap screw spacings: 102, 152, and 305 mm, respectively. As expected, the smaller spacing between the side-lap screws leads to higher strength. The measured stiffness of the three diaphragms was almost the same. It is believed to be attributable to the very high flexibility caused by distortional deformation (warping) compared to the flexibility of the connections and pure shear of the steel material (Fig. 3d). This phenomenon is less pronounced for Tests #1 and #2 because of the thicker steel sheet that was used to form the deck panels.

4.2 Comparison Between the Test Results and AISI S310-20

4.2.1 Diaphragm Shear Strength

The test versus AISI (test/AISI) diaphragm strength ratios are presented in Table 3. The diaphragm strengths are also compared in Fig. 5a. The measured strengths are comparable to standard 76 mm decks readily available on the market. The diaphragm strengths calculated with AISI S310-16 [9], which does not take into account local web buckling of panels over exterior support, are also presented in Fig. 5a. The test/ AISI-20 strength ratios varied between 0.88 and 1.21. The AISI S310-20 strength predictions are close to the test values. Only the prediction for Test #5 was not conservative. All other predictions were on the safe side. The failure modes predicted by AISI S310-20 are in good agreement with the test except for Test #2, but the multiple failure modes have very close strength values. AISI S310-20 predictions could have been closer if the calculation of the web crippling strength considered the presence of web stiffeners. Because web buckling of panels over exterior support is diaphragm strength which was observed in Tests #1, #3, and #4, the predictions using AISI S310-16 are not in good agreement with Tests #1 and #3, with the denser side-lap screw pattern. Overall, AISI S310-16 overestimates the capacity of all tests.
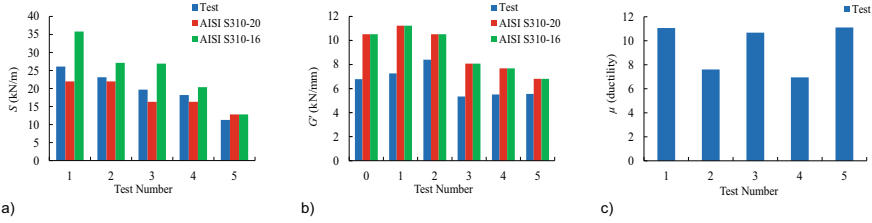
Fig. 5 Test versus AISI S310-20 and AISI S310-16: **a** diaphragm strength, **b** diaphragm stiffness, **c** diaphragm ductility

4.2.2 Diaphragm Shear Stiffness

As expected from deep decks, the MS100 diaphragm stiffnesses are relatively low. The test/AISI diaphragm stiffness ratios are presented in Table 3. The diaphragm stiffnesses are also compared in Fig. 5b along with the AISI S310-16 predictions which are the same as AISI S310-20. The AISI S310-20 prediction systematically underestimates the diaphragm stiffnesses. The test/AISI diaphragm stiffness ratios varied between 0.65 and 0.81. Similar results have been reported in the past for deep decks [7]. It is believed that this discrepancy is due to an underestimation of the shear deformations attributed to the distortion of the deck section. This matter necessitates further investigations to identify the sources of these discrepancies.

4.2.3 Diaphragm Shear Ductility

The measured global ductility of the diaphragms was evaluated based on AISI S400-20. The ductility values are presented in Table 3 and depicted graphically in Fig. 5c. Overall, the ductility ranged between 6.95 and 11.2. Due to the monotonic nature of the tests, the ductility values cannot be used in a seismic context where load reversals significantly to deteriorate the performance of the diaphragm. However, the ductility measured under monotonic loading can be used as an indicator of the potential to sustain large inelastic deformations and dissipate seismic energy [10]. In the case where the strength of the diaphragm is governed by local web buckling of panels over exterior support, the gravity load-carrying capacity of the deck might be severely impacted and therefore might not be possible to take advantage of this ductility in practice. Therefore, based on the preliminary test results presented herein, Test #5, where the strength was governed by the failure of the side laps and panel corner connections, appears to have the most potential for seismic applications.

5 Conclusions

A total of five large-scale monotonic quasi-static diaphragm tests were performed using a new deep deck profile with flange and web stiffeners. Power-actuated fasteners were used for the deck-to-frame connections and self-drilling screws were used for the deck-to-deck (side lap) connections. For each test, the diaphragm strength, stiffness, and global ductility were measured. The diaphragm strength and stiffness were also calculated according to AISI S310-20 and AISI S130-16 for comparison purposes.

Overall, the measured strengths are comparable to standard 76 mm decks readily available on the market. Three tests out of five exhibited web buckling of panels over exterior support as a mode of failure. This failure mode is not generally encountered in shallower decks with shorter webs that are less prone to buckling under compression loads. The diaphragm strengths compared well with AISI S310-20 prediction, including an equation for calculating the strength under web buckling of panels over exterior support. The predictions of AISI S310-20 for this mode of failure underestimated the measured strength because it does not consider the effect of the longitudinal web stiffener of the MS100 deck. Some research is needed to establish more accurate design equations for calculating the web crippling strength of stiffened webs. More research is also necessary to understand the impact of web buckling of panels over exterior support on the gravity load-carrying capacity of roof diaphragms, because the interaction between the gravity loads and in-plane shear loads at the end supports might prematurely trigger this mode of failure. Based on the current incomplete information on this subject, failure mode related to connections is preferable.

The shear stiffness of the MS100 diaphragm is low due to the pronounced distortion of the deck profile at the end supports. Because of that, the stiffnesses calculated with AISI S310 overestimate the actual stiffness of the diaphragms. Mechanical devices such as end closures might reduce or block the distortion of the panel. The effect of such devices on diaphragm stiffness will be studied in a future phase of the project.

The diaphragm ductility that was measured under monotonic quasi-static loading ranged between 6.95 and 11.2. It is expected that this ductility will significantly drop under reversed cyclic loading due to the degradation of the shear load-carrying capacity in the inelastic range. The behavior of MS100 roof diaphragms under cyclic loading will be investigated in a future phase of this project.

the planning and execution of the experiments. The implication of Luc St-Pierre, ing., and Stéphane Couture of Métal Sartigan is also acknowledged.

References

1. CSA (2021). CSA S136-16 (R2021), North American specification for the design of cold-formed steel structural members. Canadian Standards Association, Toronto, Ontario, Canada
2. AISI (2020a) AISI S310-20, North American Standard for the design of profiled steel diaphragm panels. American Iron and Steel Institute, Washington, DC, USA
3. Luttrell L (2015) Diaphragm design manual, 4th edn. Steel Deck Institute, Glenshaw, Pennsylvania, USA
4. AISI (2017) AISI S907-17, test Standard for Determining the Strength and Stiffness of Cold Formed Steel diaphragms by the Cantilever test method. American Iron and Steel Institute, Washington, DC, USA
5. Nunna RV (2018) Exterior support local web buckling for profiled steel diaphragms. Report No. 18-01, S. Barnes Associates
6. AISI (2016a) AISI S100-16 (R2020), North American specification for the design cold-formed steel structural members. American Iron and Steel Institute, Washington, DC, USA
7. Bagwell J, Easterling WS (2008) Deep deck and cellular deck diaphragm strength and stiffness evaluation. Report No. CEE/VPI-ST-08/03, Virginia Tech
8. O'Brien P, Eatherton MR, Easterling WS (2017) Characterizing the load-deformation behavior of steel deck diaphragms using past test data. Report No. CFSRC R-2017-02, Cold-formed steel research consortium report series, steel diaphragm innovation initiative
9. AISI (2016b) AISI S310-16, North American standard for the design of profiled steel diaphragm panels. American Iron and Steel Institute, Washington, DC, USA
10. Essa HS, Tremblay R, Rogers CA (2003) Behavior of roof deck diaphragms under quasi-static cyclic loading. J Struct Eng ASCE 129(12):1658–1666
11. AISI (2020b) AISI S400-20, North American Standard for Seismic design of cold-formed steel structural systems. American Iron and Steel Institute, Washington, DC, USA

Finite-Element Modelling of a Novel High-Performance Shear Connector for Mass Timber Structural Assemblies

K. Feujofack, V. Blériot, and Cristiano Loss

Abstract Mass timber structural systems constitute a promising building technology that can address the desire and need for larger and taller building applications in wood. However, a significant hurdle in the development of such structures is the lack of reliable and resilient connection technologies—especially for mass timber shear-wall assemblies. In this work, a novel high-performance hybrid steel-grout shear connector for cross-laminated timber (CLT) panels is presented. A 3D solid finite-element (FE) model is developed as an aid for simulating its behaviour under static loading conditions. The model is developed in the ANSYS environment and is based on the beam-on-foundation philosophy, assuming a flow of internal forces from steel to wood through an intermediate layer of grout—and conversely. The plastic behaviour of steel is accounted through a multilinear isotropic hardening model. As for the grout, its fragile behaviour is considered through the Drucker–Prager model. CLT is modelled as a cross-layered composite material, where each layer is assigned the orthotropic elastic properties of wood. The nonlinear plastic behaviour and failure of wood layers are considered through a stress-based failure criterion. The comparison with previously tested connectors shows that experimental results are in good agreement with simulated ones, pointing out the acceptability of the model.

Keyword Finite-element · Shear connector · Mass timber

K. Feujofack · V. Blériot · C. Loss (✉)
Sustainable Engineered Structural Solutions Laboratory, Department of Wood Science, University of British Columbia, Vancouver, BC, Canada
e-mail: cristiano.loss@ubc.ca

1 Introduction

1.1 Towards Sustainable Cities

There has been a fulgurant ascension of mass timber structures lately. Factors such as high sustainability of wood components, ease of hybridization, recent advances in wood manufacturing and processing, and better fire performance of mass timber products (MTPs) have motivated the relaxation of timber buildings' height limitations in many countries. In Canada, the limit has been shifted from 6 to 12 stories, as per the announced 2020 edition of the National Building Code [1].

Most of mid-rise and high-rise mass timber buildings erected to date are structural systems with cross-laminated timber (CLT) panels being used as principal bearing elements. From a construction method standpoint, such systems can be subdivided in (a) platform-type systems and (b) balloon-type systems. In a balloon structural system, load-bearing vertical elements (walls, columns) run for two storeys or more without interruption [2–4]; and floor diaphragms hang on the flank of continuous those walls. Balloon systems enable to build taller while avoiding the compression perpendicular to the grain in the CLT panels. However, building taller implies that higher level of forces must be sustained by systems. Therefore, there is a need for the development of high-performance connection and hold-down technologies for balloon-type CLT systems.

1.2 Hold-Down Connections for Mass Timber Construction

Conventional connection technologies for CLT shear walls consist of metal-shaped hold-downs and bracket-type devices. Hold-downs are usually designed to prevent uplifts in shear-wall segments, while brackets provide equilibrium against shear forces at their base. In CLT balloon-type lateral force-resisting systems, CLT walls behave as giant cantilevered beams—generating a high concentration of shear forces and bending moments in the joints. Dowelled slotted-in plates connections (DSSP) can be designed to endure a high level of forces and moments [5]. Such connections are constituted of predrilled steel plates slotted into the timber elements and are mechanically fastened using bolts, threaded rods or dowels. Conceived as a dissipative device, slip-friction joints are based on traditional dowelled slotted-in plate timber connections. Friction is generated through the steel-to-steel contact surfaces of the plates. The slippage of plates along the slotted holes is enabled by spring washers installed on both sides of the bolts [6]. Resilient slip-friction joints (RSFJs) are innovative connectors that emerged from slip-friction joints [7, 8] lately. Like in symmetric slip-friction joints, RSFJs are made of two principal parts: the plates and the bolting systems. Two cap plates and two slotted plates assure an elastic–plastic behaviour of the joint, while the bolts assure the integrity of the system. Belleville washers are used to create a controlled pressure between the plates. Pinching-free

connectors (PFC) are based on doweled connections. PFC works as a ratcheting system that ensures a perpetual contact between the fastener and wood throughout the deformation [9]. In general, for connection technologies aforementioned, groups of fasteners inevitably intersect a large volume of wood; a situation that can result under high stress. There is thus a potential of brittle failure of wood in such contact areas: this situation often forces engineers to under-design steel components in order to avoid brittle failures—what results in low-performance connections.

1.3 Glued-in Connections in Timber Construction

For decades, adhesives have been used in timber construction for jointing purposes, reaching its apogee in the early twentieth century with the introduction of glued-laminated timber [10]. A prior application of hybrid adhesive-based connections in timber construction includes glued-in rods. Solid rods are used as jointing elements with adhesive filling the cavities between the rods and wood elements. Common rod materials include metals and composites (especially fibre-reinforced polymers (FRP)). When axially loaded, glued-in rods can provide timber joints with high stiffness [11].

Grout-filled joints are an alternative to common glued-in rod joints, where a fine-grained polymer concrete is used to fill the gap between rods and grooves in timber elements. Early applications of polymer-concrete grouted joints in timber construction include butt joints developed for longer beams by Cepelka and Malo [12]. Polymer-concrete grouts can also be used in external connecting device applications as proposed by Schober et al. [13], where precast polymer-concrete connecting devices are used to join round-timber elements [14]. In general, grout-based timber joints provide designers with connections with a substantially high strength resistance, stiffness and level of reliability. Using a thick layer of grout around a steel fastener produces a large-diameter connector that can spread loads more efficiently [15], thus reducing stress concentration in the wood underneath the fastener.

1.4 Numerical Modelling of Doweled Timber Connections

The behaviour of dowelled timber connections is investigated numerically adopting a simplified approach where a stick model simulates the connection behaviour. In the stick-based approach, dowels are modelled with infinitely rigid sticks, with several yielding points. Yielding points are modelled with rotational springs, according to the bending parameters of dowels. Embedment in wood is modelled with linear springs, connected to the infinitely rigid sticks representing dowels [16].

Reference [17] developed a three-dimensional model of nailed connections—featuring the concept of beam-on-foundation. They showed that using a nonlinear foundation material, with different properties than the wood member, around the

dowel yielded better estimates of the embedment behaviour in wood. Such concept was then used to model the load-slip behaviour of nailed connections loaded laterally. The results showed a high accuracy of the model, with simulation results closely matching experimental ones. Beam-on-foundation models can be used to capture the load-slip behaviour of dowelled slotted-in steel plate connections, as demonstrated by Roncari and Loss [5] and Roncari et al. [18].

1.5 *Aim and Scope*

This work aims at simulating the load-slip behaviour a novel hybrid steel-grout shear connector for cross-laminated timber (CLT) panels under monotonic loading, through a 3D solid finite-element model. The results from the simulation are compared to the experimental data obtained via monotonic push-out shear tests of the connector. The model developed in this work enables to predict the following mechanical parameters: initial stiffness, yield capacity and the ultimate capacity of the connector under monotonic loading.

2 Proposed Hybrid Shear Connector

The hybrid shear connector modelled in this work consists of a threaded steel rod embedded into cross-laminated timber (CLT) through a thick layer of epoxy-based grout mixture. With specific reference to Fig. 1, basic connector components include

- a steel threaded rod, which ensures the transfer of loads from external bodies to the connector and conversely,
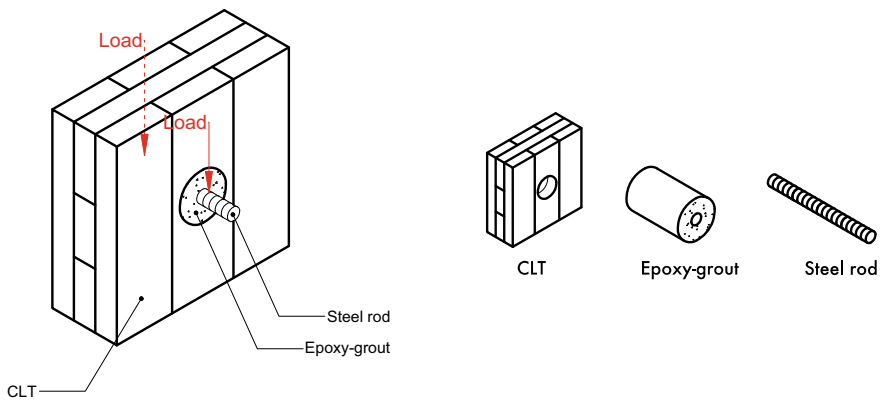
Fig. 1 Hybrid steel-grout connector (left); individual components (right)

- an intermediary thick layer of epoxy-based grout, which enables to embed the threaded rod into the CLT panel (wood) and
- wood (from the CLT panel) located in the vicinity of the grout layer.

The role of the intermediary layer of grout is paramount in this connector, as it enables a more uniform repartition of stresses on wood, preventing both yielding and brittle failure of wood to a great extent, as shown by Shulman [19]. Results from an extensive study on the monotonic behaviour of the connection by Shulman [19] provided further understanding of the actual structural performance of such connectors. The results of one variant of connectors tested by Shulman [19] were used to validate the model developed in this work. The variant used was the connector made of E-graded CLT, 24 M class 8.8 steel rods, and a grout diameter equivalent to 4 times the rod diameter.

3 Finite-Element Modelling

3.1 Materials and Mechanical Properties

E1M5 CLT made of 3 35-mm-thick spruce-pine-fir lumber plies was used in this work. The face layers of the CLT consist of machine stress-rated spruce-pine-fir lumber (MSR 2100 1.8E SPF), while the internal minor layer consists of visually graded SPF lumber #2 or better grade. A three-component mix high-performance epoxy-based grout, produced by Hilti, was used during experimental tests. Lastly, 8.8 strength-class M24 fully threaded steel rods were used in building the specimens tested in Shulman [19].

In Table 1, the elastic properties of the wood material used to model CLT are shown. Those properties were obtained with a procedure starting from the modulus of elasticity in the grain direction of wood (E_L) [20]. Then, the elastic ratios for the Spruce Engelmann species—from the Wood Handbook [21]—were used calculate the remaining five elastic constants of lumber as follows:

$$\frac{E_T}{E_L} = 0.059; \ \frac{E_R}{E_L} = 0.128; \ \frac{G_{LR}}{E_L} = 0.124; \ \frac{G_{LT}}{E_L} = 0.120; \ \frac{G_{RT}}{E_L} = 0.010, \quad (1)$$

where E_i represents the modulus of elasticity in the ith direction and G_{ij} represents the shear modulus in the ij plane. The Poisson's ratio values are taken from the

Table 1 Wood material elastic properties

Properties	E_x	E_y	E_z	G_{xy}	G_{yz}	G_{zx}
Values (MPa)	1587.2	12,400	731.6	1537.6	1488	124
Poisson's ratios	$\nu_{xy} = 0.083$		$\nu_{yz} = 0.462$		$\nu_{zx} = 0.255$	
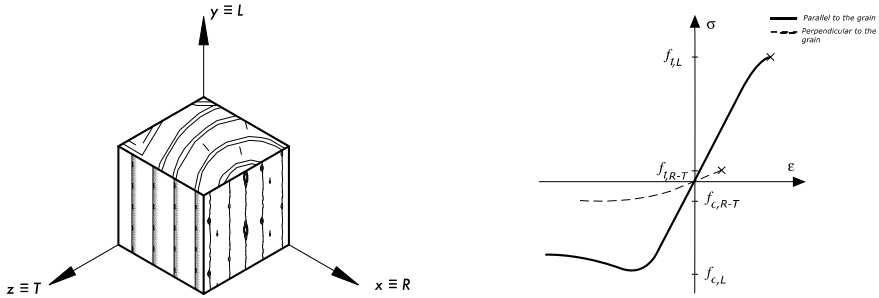
Fig. 2 Wood material coordinate system (left); stress–strain curve of clear wood exposed to tensile [*t*] and compressive stresses [*c*] *(Adapted from* Blaß & Sandhaas, 2017*)* (right)

Table 2 Material properties for steel components

Component	Grade/Class	E (GPa)	F_{pr} (MPa)	F_y (MPa)	F_u (MPa)	a (%)	Reference
Side plate	A572 Gr50	200	–	345	450	2	ASTM A572
Threaded rod	8.8 Class	210	600	660	830	35	ISO 898-1
Nuts	Class 8	210	1075	1075	–	–	ASTM A563

Wood Handbook [21]. Following the diagram in Fig. 2 (left), directional mechanical properties of wood are translated from the (R, L, T) coordinate system to a direct (x, y, z) coordinate system.

In addition to 8.8 strength-class fully threaded rods, steel side plates of ¾″ thickness were used to apply the displacement-type load on the threaded rods during experiments (Fig. 4). Further, hexagonal nuts of class-strength 8 were used to prevent the lateral movement of side plates during testing. The mechanical properties of all steel components in the model are provided in Table 2.

Pertaining epoxy-based grout, uniaxial compressive tests have been conducted on small-scale samples as per ASTM C579-18. At 28-day curing time, epoxy-based grout displayed a compressive strength of 135 MPa and an initial modulus of elasticity of 25 GPa.

3.2 Material Models

3.2.1 Cross-Laminated Timber

CLT was modelled as a cross-laminated composite material through the module ACP (ANSYS composite pre- and post-processing). Each layer (laminate) was assigned

Table 3 Hill's criterion constants

F	G	H	L	M	N
$\frac{1}{2}\left(\frac{1}{R_{yy}^2}+\frac{1}{R_{zz}^2}-\frac{1}{R_{xx}^2}\right)$	$\frac{1}{2}\left(\frac{1}{R_{zz}^2}+\frac{1}{R_{xx}^2}-\frac{1}{R_{yy}^2}\right)$	$\frac{1}{2}\left(\frac{1}{R_{xx}^2}+\frac{1}{R_{yy}^2}-\frac{1}{R_{zz}^2}\right)$	$\frac{3}{2R_{yz}^2}$	$\frac{3}{2R_{zx}^2}$	$\frac{3}{2R_{xy}^2}$

the properties of the lumber used in manufacturing the CLT. A similar approach was adopted in the modelling of CLT panels in a work by Martínez-Martínez et al. [22]. Individual laminates were assigned an orthotropic behaviour following the elastic material constants of wood given in Table 1. Beyond the elastic range, the behaviour of wood was handled through a plastic theory. In what follows, the yield criterion used in modelling wood is described.

Unlike isotropic materials, the yielding in anisotropic materials such as wood cannot be modelled by shear-stress criteria such as Tresca or von Mises criteria. An extension to the von Mises yield criterion, which can handle anisotropic materials such as wood, was proposed by Hill [23]. Hill's criterion accounts for anisotropicity through six parameters specifying the state of anisotropicity in the modelled material (Table 3). One major limitation of Hill's criterion is that it does not discriminate between tensile and compressive strengths [24, 25]. Nevertheless, Hill's criterion has been extensively and successfully used to model the yielding in wood [26–29]. Thus, in this study, the Hill's criterion (Eq. 2) was adopted and coupled with bilinear kinematic hardening in the FE software ANSYS.

$$F\left(\sigma_{yy}-\sigma_{zz}\right)^2 + G(\sigma_{zz}-\sigma_{xx})^2 + H\left(\sigma_{xx}-\sigma_{yy}\right)^2$$
$$+ 2L\sigma_{yz}^2 + 2M\sigma_{zx}^2 + 2N\sigma_{xy}^2 - \sigma_r^2 = 0 \tag{2}$$

From in Table 3,

$$R_{ij} = \begin{cases} \frac{f_i}{\sigma_r}, \text{ for } i = j \\ \frac{f_{ij}}{\tau_r}, \text{ for } i \neq j \end{cases} \text{ and } \quad \tau_r = \frac{\sigma_r}{\sqrt{3}} \tag{3}$$

The initial Hill's (yield) criterion was developed for anisotropic metals [23], where f_i represent the tensile yield stresses in the principal anisotropic directions, while f_{ij} represent the yield stresses in shear respective to the principal anisotropic axes. In the case of wood, the tensile and compressive yield stresses vary greatly from one direction to another (Fig. 2–right). Therefore, the minimum of tensile and compressive yield stress in each direction was selected.

3.2.2 Epoxy-Based Grout

Due to the similarity between concrete and the epoxy-based grout used in this project, this latter has been modelled based on the literature on concrete material models.

Research has shown that the Drucker–Prager (DP) model is capable of modelling the stress–strain response of confined concrete and concrete structural members [30, 31]. Therefore, DP constitutive equations were used in the epoxy-based grout material model for this study. The yield function for the linear DP model reads as follows [32]:

$$f = \alpha J_1 + J_2^{1/2} = k \qquad (4)$$

where α and k are positive constants at each point of the material.

$$J_1 = \sigma_1 + \sigma_2 + \sigma_3 \qquad (5)$$

J_2 is the second invariant of the stress deviation:

$$J_2 = \frac{1}{6}\left[(\sigma_1 - \sigma_2)^2 + (\sigma_2 - \sigma_3)^2 + (\sigma_1 - \sigma_3)^2\right]. \qquad (6)$$

The parameters α and k can be determined by plotting triaxial tests results in the $(J_1, \sqrt{J_2})$ space [33]. Given that the DP failure criterion is an approximation of the Mohr–Coulomb (MC) criterion, the two constants α and k can also be expressed in terms of the Mohr–Coulomb parameters S_0 (cohesion intercept) and Φ_f (internal friction angle) [33, 34]—by matching two particular points to those of MC in the principal stress space. Thus, the following equations can be obtained:

$$\alpha = \frac{2\sin\phi_f}{\sqrt{3}(3 - \sin\phi_f)}; k = \frac{6S_0\cos\phi_f}{\sqrt{3}(3 - \sin\phi_f)}. \qquad (7)$$

Experimental tests on epoxy-based grout specimens also enabled to extract the Mohr–Coulomb parameters S_0 and Φ_f, which were used in Eq. (7) to determine the Drucker–Prager parameters α and k.

3.2.3   Steel

A multilinear hardening model was used for each steel component following the models proposed by Bahaari and Sherbourne [35]. For the plate element, a strain hardening of 2% was assumed beyond the yield point ($E_t = 0.02E$) up to a strain of $11\epsilon_y$, and then the ultimate stress is reached at $21\epsilon_y$. For bolts, a first plastic hinge is considered to occur when the bolt reaches its proof stress [35]. Then, a line connects the proof stress of the component to its yield stress—at strain of 0.006. The last line connects the yield stress and the ultimate stress at a strain of $8\epsilon_p$. These models have been successfully used to predict the behaviour of bolted steel connections [36, 37]. Pertaining to nuts, a strain hardening of 1% was assumed beyond the proof stress.

The stress–strain behaviours of all steel elements are plotted in Fig. 3. For all steel elements, the ubiquitous von Mises yield criterion has been used.
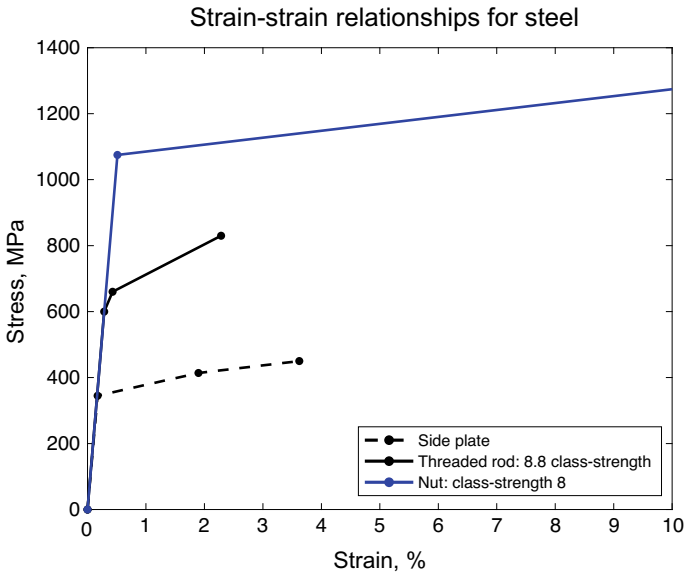
Fig. 3 Stress–strain steel plates, rods, and nuts
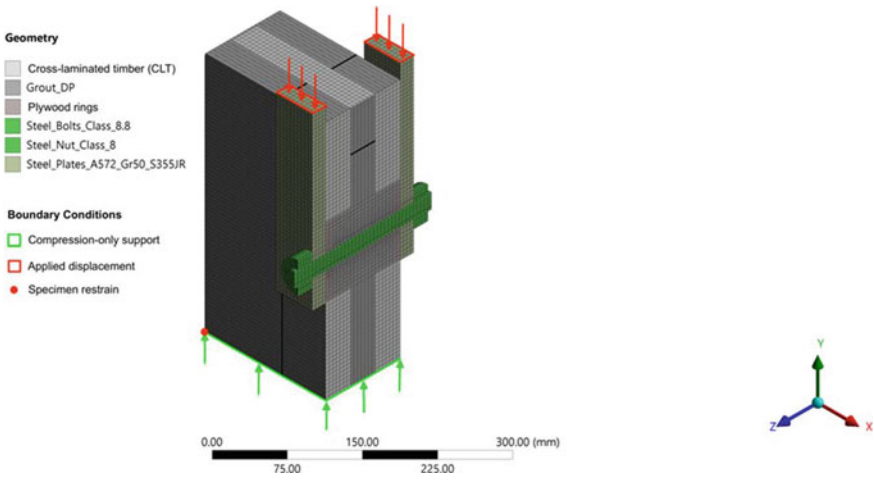
Fig. 4 Cross section of the finite-element model

3.3   Geometry

The as-built finite-element model is shown in Fig. 4. It consists of a 340×340 mm CLT block with a hybrid connector at the centre. The thick layer of grout is used to embed a 24 M fully threaded rod into CLT. The grout external diameter was set to 4 times the diameter of the rod: this specimen configuration corresponds to the variant 24 M-8E-4 $\times$ tested by Shulman [19]. A 3D modelling approach using ANSYS Mechanical was adopted. The CLT material was modelled using ACP (ANSYS composite pre- and post-processing) and was imported into ANSYS Mechanical and merged to other components in the model. CLT, epoxy-based grout, and steel components were modelled using SOLID 186 elements.

3.4   Boundary Conditions and Loading

The model was set to lay on compression-only support on its bottom face (Fig. 4). To avoid instability and the horizontal sliding of the specimen, one lower corner was restrained in X- and Z-direction, while the adjacent corner was restrained in Z-direction only.

A friction coefficient was defined for each contact pair where bodies were in friction. Additionally, a normal stiffness factor was defined for certain contacts to account for the penetration in target bodies. To account for the effect of threads from the steel rod, a "bolt thread" contact geometry correction was applied to the rod, where values for the pitch diameter, pitch distance, and thread angle for 24 M rods were defined.

Considering that nuts used to fasten the specimen to the side plates of the test set-up were hand tighten, a frictionless contact was defined between the side plate and each face of the CLT. The contact between the steel side plate and the rod was set to rough, which prevents lateral sliding but allows for normal displacement. The contact between rods and nuts was set "rough", which prevents any lateral sliding. Table 4 lists the contact properties used in the model.

The loading of the connector was executed by applying a controlled displacement on the top faces of side plates—conformably to experimental tests conducted by Shulman [19].

Table 4 Contact properties

Contact–target bodies	Type of contact/ behaviour	Friction coefficient	Normal stiffness factor
Rod–grout	Frictional/ symmetric	0.4	0.4
Rod–plywood ring	Frictional/ symmetric	0.4	0.1
Rod–nut	Rough/symmetric	–	–
Grout–plywood ring	Frictional/ symmetric	0.5	–
Side plate–plywood ring	Frictionless/ symmetric	–	–
Side plate–nut	Frictionless/ symmetric	–	–
Side plate–rod	Rough/symmetric	–	–
Grout–CLT	Bonded/symmetric	–	0.2
Plywood ring–CLT	Frictional/ symmetric	0.375	0.1

4 Results and Discussion

4.1 Collapse Mechanism and Failure Propagation

Figure 5 provides the maximum stress maps in all the bodies at the end of the simulation, corresponding to a slip of 10 mm. It can be observed that the steel rod yields in three main zones: (i and ii) at locations where the load is applied (through side plates) and (iii) in the middle of the specimen—where the contact reaction from the grout creates a high bending in the rod. Concerning the grout layer, high-stress zones are located on both edges, beneath the rod. More importantly, it can be seen that the grout reduces the stress from 169.15 MPa (stress in the grout near the rod) to only 64.40 MPa (stress in the grout near wood): implying a stress reduction of about 60% as a result. Lastly, the principal stress plot on CLT shows that the transversal lamella beneath the grout is fully compressed, while longitudinal layers are only partially compressed: this can be attributed to the higher compressive strength of wood in the direction parallel to the grain.

4.2 Load-Slip Curve

Figure 6 shows the simulated load-slip curve of the connector, plotted using the reaction force probed at the bottom of the CLT block and the relative slip of the side plate. The experimental curves obtained by Shulman [19] for the connector variant

Equivalent stress – whole connection

Equivalent stress – Steel rod

Equivalent stress – Grout

Equivalent stress – CLT

Maximum principal stress – Grout

Maximum principal stress – CLT
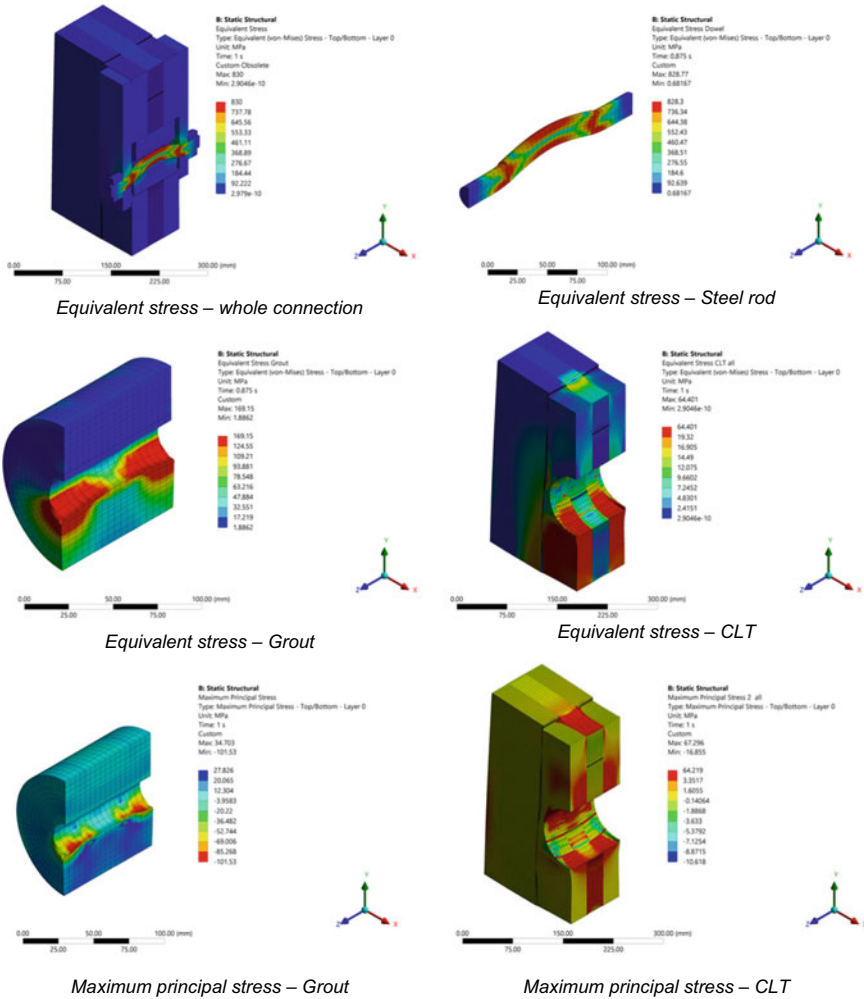
Fig. 5 Stress states

24 M-8E-4x (seven replicates) are also plotted. In Table 5, structural performance parameters in terms of initial stiffness, yield load, and ultimate load are reported.

The slip (δ) of the connector was evaluated as the relative slip of the side plate at a position of (¾) the height of the CLT panel—conformably to experimental tests conducted by Shulman [19]. The stiffness of the connector was evaluated using the using the formula provided in [38, p. 68].

$$K_{El} = (0.4F_{max} - 0.1F_{max})/(\delta_{40\%,max} - \delta_{10\%,max}), \qquad (8)$$
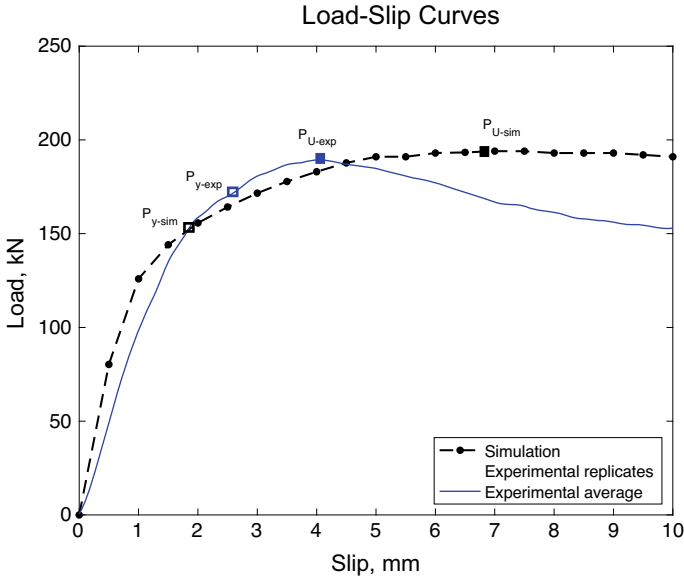
Fig. 6 Load-slip curve of the connector (experimental versus simulation)

Table 5 Comparison of mechanical properties: experimental versus simulation

Property/ parameter	Experimental average	Simulation	Error (%)
Initial stiffness (kN/mm)	110.82	125.91	13.62
Yield load–P_y (kN)	176.02	155.70	11.54
Ultimate load–P_U (kN)	189.47	193.99	2.39
Load mobile-error analysis			
Slip range (mm)	Average error between experimental-average load and simulated load (%)		
$\delta \in [0, 2.5]$	12.50		
$\delta \in [2.5, 5]$	4.49		
$\delta \in [5, 7.5]$	14.51		
$\delta \in [7.5, 10]$	18.03		

where F_{max} is the ultimate load of the connector and $\delta_{10\%,max}$ and $\delta_{40\%,max}$ are the slips corresponding to 10% and 40% of the ultimate load, respectively.

A mobile-error analysis is presented in Table 5. It is observed that the average error in the elastic range ($\delta \in \sim [0, 2.5]$mm) is 12.5%. This can be largely attributed to the overlooked friction between the side plates and the faces of the CLT panel. In the

range from the yield point to the ultimate load ($\delta \in \sim$ [5, 7.5]mm), the average error regressed to 5%. This can be attributed to the consolidation of the connector after the loading in the elastic phase, leading to a lower discrepancy between experimental and simulated values. The post-peak zone ($\delta > 5$mm) displays an even larger error. In this phase, all deformations are plastic—in all parts of the connector. Thus, the error can be attributed to the approximation of plastic behaviours in material models. Plus, failure of the connector is driven by the crushing of wood (high level of damage) underneath the grout.

Overall, the model is able to capture the load-slip behaviour of the connector fairly well up to a slip of 5 mm, as confirmed by the load mobile-error analysis between experimental and simulated load values given in Table 5.

5   Conclusion

A finite-element modelling approach for simulating the monotonic push-out response of a novel hybrid steel-grout connection technology was presented in this study. The following conclusions can be drawn:

- The modelling of CLT as a composite material with crossed layers, as presented in this work, proves to provide acceptable results under elastic-level deformations.
- When loaded laterally, the deformation mechanism in the connector flows from rod bending to CLT crushing and densification.
- The model proves to be able to capture the load-slip behaviour of the connector fairly well up to a slip of 5 mm.
- With an overall error below 15% between experimental and simulated loads throughout the slip domain, the simulated load-slip behaviour of the connector can be assumed to be in good agreement with the experimental one, indicating the acceptability of the model.
- The results from the simulation validate the assumption that the grout layer enables to reduce the stress level from the rod to the CLT: a stress reduction of up to 40% is observed in this case.
- The model can be further improved by using a yield criterion that takes into account the difference in tensile and compressive loading for wood. Further, an advanced plastic flow rule and a damage evolution model for wood can help improve the accuracy of the FE model in the post-peak zone. Lastly, further research is needed in order to adequately define the contact properties between the pairs epoxy-based grout–steel and epoxy-based grout–wood.

References

1. Mohammad M, Tourrilhes J, Coxford R, Williamson M (2019) Canadian mass timber demonstration projects initiatives. Modular and offsite construction (MOC) summit proceedings. 51–58. https://doi.org/10.29173/mocs76

2. Anderson LO (1970) Wood-frame house construction: 1956–1960. US Department of agriculture

3. Bell P (1983) The balloon frame myth. J Aust Stud 7(12):53–66

4. De Araujo VA, Cortez-Barbosa J, Gava M, Garcia JN, de Souza AJD, Savi AF, Morales EAM, Molina JC, Vasconcelos JS, Christoforo AL (2016) Classification of wooden housing building systems. BioResources 11(3):7889–7901

5. Roncari A, Loss C (2020) Cross-laminated timber buildings equipped with ductile multiple shear slotted-in steel plates connections: proof of concept. In: World conference on timber engineering. August 2020 p

6. Loo WY, Quenneville P, Chouw N (2014) A new type of symmetric slip-friction connector. J Constr Steel Res 94:11–22. https://doi.org/10.1016/j.jcsr.2013.11.005

7. Hashemi A, Masoudnia R, Quenneville P (2016) Seismic performance of hybrid self-centring steel-timber rocking core walls with slip friction connections. J Constr Steel Res 126:201–213. https://doi.org/10.1016/j.jcsr.2016.07.022

8. Hashemi A, Zarnani P, Masoudnia R, Quenneville P (2017) Seismic resistant rocking coupled walls with innovative resilient slip friction (RSF) joints. J Constr Steel Res 129:215–226. https://doi.org/10.1016/j.jcsr.2016.11.016

9. Chan N, Hashemi A, Zarnani P, Quenneville P (2021) Pinching-free connector for timber structures. J Struct Eng 147(5):04021036. https://doi.org/10.1061/(ASCE)ST.1943-541X.0002982

10. Vallée T, Tannert T, Fecht S (2017) Adhesively bonded connections in the context of timber engineering—a review. J Adhes 93(4):257–287. https://doi.org/10.1080/00218464.2015.1071255

11. Tannert T, Zhu H, Myslicki S, Walther F, Vallée T (2017) Tensile and fatigue investigations of timber joints with glued-in FRP rods. J Adhes 93(11):926–942. https://doi.org/10.1080/00218464.2016.1190653

12. Cepelka M, Malo KA (2017) Moment resisting splice of timber beams using long threaded rods and grout-filled couplers—experimental results and predictive models. Constr Build Mater 155:560–570. https://doi.org/10.1016/j.conbuildmat.2017.08.089

13. Schober K-U, Becker W, Negrão JH (2018) Grouted joints for modern round wood bridge truss structures. Portguese J Struct Eng 7:55–64

14. Schober K-U, Kuechler M (2014) Pre-tensioned timber-truss pedestrian bridges an innovative bio-hybrid design approach using round-timber. In: COST timber bridge conference–CTBC 2014. 2014, p 73

15. Jahreis M, Rautenstrauch K (2016) High efficient joint system for timber engineering with casted-in connectors. In: Paper 71 in proceedings of world conference on timber engineering (WCTE), Vienna 2016, p 2016

16. Izzi M, Rinaldin G, Polastri A, Fragiacomo M (2018) A hysteresis model for timber joints with dowel-type fasteners. Eng Struct 157:170–178. https://doi.org/10.1016/j.engstruct.2017.12.011

17. Hong J-P, Barrett D (2010) Three-dimensional finite-element modeling of nailed connections in wood. J Struct Eng 136(6):715–722. https://doi.org/10.1061/(ASCE)ST.1943-541X.0000160

18. Roncari A, Feujofack K, Loss CBV (2021) Modal response spectrum analysis of cross-laminated mid-rise timber buildings equipped with multiple shear slotted-in steel plates connections. In: 1st Croatian conference on earthquake engineering. 2021 Zagreb, Croatia, pp 449–459. https://doi.org/10.5592/CO/1CroCEE.2021.25
19. Shulman S (2021) A deconstructable grout-reinforced hybrid shear connector for tall cross-laminated timber buildings
20. CSA Group (2019) CSA O86-19. Engineering design in wood. Toronto, Ontario, Canada: CSA Group
21. Ross RJ (2010) Wood handbook: wood as an engineering material. USDA forest service, forest products laboratory, general technical report FPL-GTR-190, 2010: 509, vol 190, p 1
22. Martínez-Martínez JE, Alonso-Martínez M, Rabanal FPÁ, del Díaz JJ C (2018) Finite element analysis of composite laminated timber (CLT). Proceedings 2(23):1454. https://doi.org/10.3390/proceedings2231454
23. Hill R (1948) A theory of the yielding and plastic flow of anisotropic metals. Proceedings of the royal society of London. Series A. Math Phys Sci 193(1033):281–297. https://doi.org/10.1098/rspa.1948.0045
24. Chen Z, Ni C, Dagenais C, Kuan S (2020) Woodst: a temperature-dependent plastic-damage constitutive model used for numerical simulation of wood-based materials and connections. J Struct Eng 146(3):04019225
25. Eslami H, Jayasinghe LB, Waldmann D (2021) Nonlinear three-dimensional anisotropic material model for failure analysis of timber. Eng Fail Anal 130:105764
26. François P (1992) Plasticité du bois en compression multiaxiale: application à l'absorption d'énergie mécanique. Bordeaux 1
27. He M, Sun X, Li Z (2018) Bending and compressive properties of cross-laminated timber (CLT) panels made from Canadian hemlock. Constr Build Mater 185:175–183
28. He M, Sun X, Li Z, Feng W (2020) Bending, shear, and compressive properties of three-and five-layer cross-laminated timber fabricated with black spruce. J Wood Sci 66(1):1–17
29. Kharouf N, McClure G, Smith I (2003) Elasto-plastic modeling of wood bolted connections. Comput Struct 81(8):747–754. https://doi.org/10.1016/S0045-7949(02)00482-0
30. Jiang J-F, Wu Y-F (2012) Identification of material parameters for Drucker-Prager plasticity model for FRP confined circular concrete columns. Int J Solids Struct 49(3–4):445–456. https://doi.org/10.1016/j.ijsolstr.2011.10.002
31. Karabinis AI, Rousakis TC (2002) Concrete confined by FRP material: a plasticity approach. Eng Struct 24(7):923–932
32. Drucker DC, Prager W (1952) Soil mechanics and plastic analysis or limit design. Q Appl Math 10(2):157–165
33. Alejano LR, Bobet A (2012) Drucker-Prager criterion. Rock Mech Rock Eng 45(6):995–999. https://doi.org/10.1007/s00603-012-0278-2
34. Yi X, Valkó PP, Russell JE (2005) Effect of rock strength criterion on the predicted onset of sand production. Int J Geomech 5(1):66–73. https://doi.org/10.1061/(ASCE)1532-3641(2005)5:1(66)
35. Bahaari MR, Sherbourne AN (2000) Behavior of eight-bolt large capacity endplate connections. Comput Struct 77(3):315–325. https://doi.org/10.1016/S0045-7949(99)00218-7
36. Dessouki AK, Youssef AH Ibrahim MM (2013) Behavior of I-beam bolted extended end-plate moment connections. Ain Shams Engineering Journal. 4:685–699
37. Kontolati K (2018) Numerical investigation of weak axis i profile connections. Master's thesis, University of Thessaly, Greece
38. ISO (1983) ISO 6891:1983 Timber structures—joints made with mechanical fasteners—general principles for the determination of strength and deformation characteristics. https://www.iso.org/cms/render/live/en/sites/isoorg/contents/data/standard/01/34/13413.html
39. Blaß HJ, Sandhaas C (2017) Timber engineering-principles for design. KIT Scientific Publishing. https://doi.org/10.5445/KSP/1000069616

Thin-Walled Beam Formulations with Cross-Sectional Deformation

Emre Erkmen

Abstract Thin-walled beams are widely used in steel construction with various restraint arrangements and sizes. Due to the slenderness of their cross-section thin-walled beams are prone to distortional behaviour as a result of web bending. Web bending is a major concern in thin-walled buckling behaviour especially when the top flanges are restraint as in highway bridge construction of girders. Web distortion also gains significance with slender webs, stocky flanges, and/or shorter spans. This paper evaluates the performance of beam-type Finite Element formulations that are capable of capturing the deformation modes involving web distortion in thin-walled beam behaviour by contrasting the analysis results against shell element-based models. In the selected case studies elastic buckling load predictions and corresponding first mode shapes of steel girders with various sizes and restraining conditions is illustrated.

Keywords Thin-walled beam · Deformation

1 Introduction

Open-section thin-walled steel beams are extensively used in the civil engineering industry. Relative slenderness of open-section thin-walled beams makes them prone to various elastic buckling modes depending on their size and restraint conditions. One of the prevalent buckling modes of failure in thin-walled beams is lateral-torsional buckling by which an unconstrained steel beam subjected to vertical transverse loads tends to move laterally and twists. Lateral-torsional buckling may occur in steel building frames and roofs due to lack of sufficient lateral restraint. In bridge girders of steel–concrete composite beams, steel sections are prone to web distortions

E. Erkmen (✉)

Department of Building, Civil and Environmental Engineering, Concordia University, Montreal, QC, Canada

e-mail: emre.erkmen@concordia.ca

under continuous restraint of the top flange. Distortional behaviour also gain significance in girder beams with slender and deep webs, stocky flanges, and/or shorter spans. Modelling approaches that capture necessary buckling modes of deformation are required for accurate analyses of thin-walled beams. Beam-type finite element approaches that capture the required modes of deformations offer an efficient option for modelling and analysis.

There has been a vast amount of work on the lateral-torsional buckling analysis of thin-walled beams, including the early works of [1–3] and most recent works by refs. [4–8] investigated the effect of pre-buckling deformations on lateral-torsional buckling of thin-walled beams. On the other hand, web distortions have been captured in shell element-based the modelling approaches developed by Schafer and Pekoz [9]. Finite strip methods have also been used to capture the distortional effects in the buckling behaviour of thin-walled beams by refs. [10, 11]. However, beam-type FE formulations with nodes only at the ends of their longitudinal axis are generally computationally most efficient as model sizes and accordingly computational time, as well as modelling effort can be kept relatively small compared to shell and finite strip-type modelling approaches. Furthermore, beam behaviour is easier to interpret as the dominant modes of behaviour can be more easily identified in reduced size models. In fact, beam formulations can be sufficiently equipped to capture any predetermined modes of deformations including web distortions as in the generalized beam theory (e.g. [12]). Reference [13] and Pezeshky and Mohareb [14] developed beam-type Finite Element (FE) formulations that can capture web distortion. For the buckling analysis of thin-walled beams FE formulations based on the generalized beam theory were developed by ref. [15].

Recently, [16] developed a family of distortional beam formulations and presented comparisons between the results based on alternative kinematic assumptions involving the rotation tensor, Poisson ratio effects as well as the second order strains. In this paper, we modify the beam formulation in [16] by introducing additional degrees-of-freedoms within the plane of the web. As a result of the new formulation introduced herein, strains and stress changes within the web as well as the load position effects can be captured. Alternative kinematic assumptions can be imposed as special cases of the beam formulation introduced herein. We illustrate the effect of alternative kinematic assumptions when used for the analysis of a steel bridge girder. For that purpose, we have modelled a 40-m span, 1.5-m deep steel thin-walled beam girder under alternative restraint conditions. Results of the beam formulations are also compared with those based on shell element models.

The paper is organized as follows; Methodology used in the distortional thin-walled beam formulation and the equilibrium equations of the linearized buckling analyses are presented in Sect. 2. In Sect. 3, the descriptions of the finite element solution procedure are presented. Case studies are introduced in Sect. 4, and conclusions are drawn in Sect. 5.

2 Methodology

2.1 Kinematic Assumptions Considered in the Beam Formulations

The methodology follows [16] and more details can be found therein. As shown in Fig. 1, a Cartesian coordinate system is adopted where z- and y-axes are along the directions of the beam axis and web height, respectively. For a thin-walled beam, the horizontal component of the displacement vector at any point on the cross-section is a function of y and z only, i.e.

$$u(y, z) = \bar{u} + \int_{a_{Gy}}^{y} \dot{u} \, dy \tag{1}$$

where $\bar{u}(z)$ is defined at the shear centre $\left(a_{Gx}, a_{Gy}\right)$ and generally, $\left(^{-}\right)$ indicates values at the shear centre. In Eq. (1), the superimposed dot $(\cdot)$ indicates derivative along the web direction, i.e. with respect to y. The angle of twist around the z-axis $\phi(y, z)$ is also a function of both y and z, and it is related to the horizontal displacement as $\phi_z(y, z) = -\dot{u}(y, z)$. The web is allowed to bend about the longitudinal axis z due to change in the twist angle along the web; however, the flanges stay rigid within the plane of the cross-section, therefore the twist angle is constant on the flanges. The vertical displacement at any point on the cross-section can be written as

Fig. 1 Displacement field of an open thin-walled beam
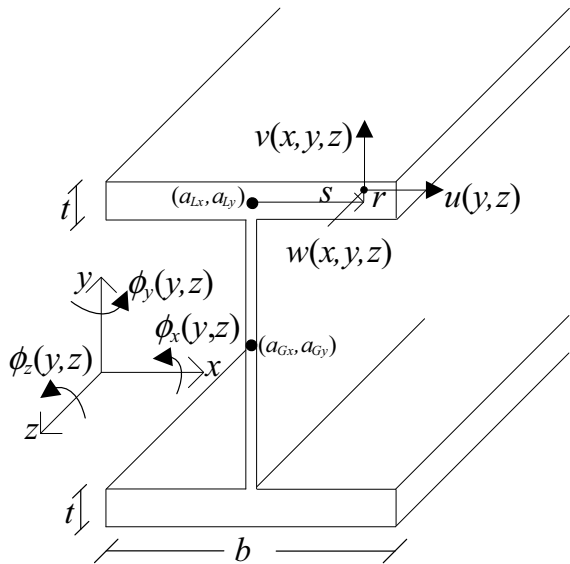
$$v(x, y, z) = \hat{v}(y, z) + \int_{a_{Gx}}^{x} \phi_z \mathrm{d}x \tag{2}$$

where $\hat{v}(y, z)$ is the vertical deflection of the mid-surface of the web at $x = a_{Gx}$. Following the discussions [16], the axial displacement of a point on the cross-section can be written as

$$w(x, y, z) = \overline{w} - x\phi_y + y\hat{\phi}_x - \hat{\omega}\phi_z' - \beta x\hat{v}'\phi_z + \beta y\overline{u'}\phi_z \tag{3}$$

in which $()'$ indicates derivative along the axial z direction and $\hat{\omega}$ is the local warping function due to St. Venant's uniform torsion. From the St. Venant's elasticity solution under uniform torsion assumption, in the limit case of thin segments, the local warping function simplifies to $\hat{\omega} = sr$, where s is the distance from the centre of the segment along the contour direction and r is along the thickness (see Fig. 1). In Eq. (3), $\beta = 0$ can be used to omit second order rotation terms, $\beta = 0.5$ can be used when the Euler-Rodriguez rotation tensor (e.g. [17]) is employed, or $\beta = 1$ can be used when the rotation tensor (e.g. [7]) is employed.

2.2 Strains

From [16], the non-zero first order strains of the beam formulation can be written as:

$$\varepsilon_{zz} = \overline{w}' - x\overline{\phi}'_y + y\hat{\phi}'_x - \hat{\omega}\overline{\psi}' + \tilde{\omega}\frac{\chi'}{6}\left(y^2 + a_{Gy}y - 2a_{Gy}^2\right) - \tilde{\omega}\frac{c'}{2}\left(y - a_{Gy}\right) \tag{4}$$

$$\varepsilon_{yy} = \dot{\hat{v}} - r\dot{\phi}_z \tag{5}$$

$$\varepsilon_{xz} = 0.5\left(\overline{u}' - \int_{a_{Gy}}^{y} \phi'_z \mathrm{d}y - \overline{\phi}_y + `\tilde{\omega}\overline{\phi}_y + \int_{a_{Gy}}^{y}\left(\int_{a_{Gy}}^{y}\dot{\psi}\mathrm{d}y\right)\mathrm{d}y - `\hat{\omega}\phi'_z\right) \tag{6}$$

$$\varepsilon_{yz} = 0.5\left(\hat{v}' + \int_{a_{Gx}}^{x}\phi'_z\mathrm{d}x + \hat{\phi}_x + \dot{\tilde{\omega}}\overline{\phi}_y + x\int_{a_{Gy}}^{y}\dot{\psi}\mathrm{d}y - \dot{\hat{\omega}}\phi'_z - \hat{\omega}\dot{\phi}'_z\right) \tag{7}$$

in which $`()$ indicates derivative along the x direction. The shear strain can be determined as

$$\gamma = 2\varepsilon_{xz}\cos\alpha + 2\varepsilon_{yz}\sin\alpha \tag{8}$$

where α is 0 for the flanges and $\pi/2$ for the web. The second order strains can be written as

$$e_{zz} = 0.5\left(u'^2 + \hat{v}'^2\right) - a_{Gx}\hat{v}'\phi'_z - \beta x\hat{v}''\phi_z + (1 - \beta)x\hat{v}'\phi'_z + \beta y\left(\overline{u}''\phi_z + \overline{u}'\phi'_z\right)$$

$$+ 0.5(x - a_{Gx})^2 \phi_z'^2 \tag{9}$$

$$e_{yy} = 0.5\left(\phi_z^2 + \hat{\phi}_x^2\right)\mu \tag{10}$$

In the above equations, $\ddot{\psi}(y, z) = -\chi(z)$ was assumed constant in y direction and accordingly the relation $\dot{\psi} = \int \ddot{\psi} dy + c = -\chi(z)y + c(z)$ was used in which $c(z)$ is the integration constant provided in [16]. The rotation tensor is selected using the β parameter in Eq. (9). Also, the second order strains were optionally included within the web direction based on a switch parameter, i.e. $\mu = 0$ excludes while $\mu = 1$ includes the contribution of second order strain e_{yy} in Eq. (10), in the buckling analysis.

2.3 Constitutive Relations

The constitutive matrix relating three non-zero components of the stress tensor $\boldsymbol{\sigma} = \left\langle \sigma_{zz} \ \sigma_{yy} \ \tau \right\rangle^{\mathrm{T}}$ to the corresponding strain components, respectively to normal strain in z, normal strain in y and non-zero shear is written herein in two alternative forms, i.e.

$$\mathbf{E}_a = \frac{E}{\left(1 - \upsilon^2\right)} \begin{bmatrix} 1 & \upsilon & 0 \\ \upsilon & 1 & 0 \\ 0 & 0 & \frac{(1-\upsilon)}{2} \end{bmatrix} \tag{11}$$

and

$$\mathbf{E}_b = \begin{bmatrix} E & 0 & 0 \\ 0 & E & 0 \\ 0 & 0 & G \end{bmatrix} \tag{12}$$

in which E is the Elasticity modulus and υ is the Poisson's ratio. It will be shown later that the selection between Eqs. (11) and (12) may have significant effect on the buckling load predictions.

2.4 Linearized Buckling Analysis

For the analyses conducted in case studies, the pre-buckling deformations are neglected. Accordingly, the equations of the linearized buckling analysis can be obtained in the form

$$\mathbf{K}_e \delta \mathbf{d}_b - \lambda \mathbf{K}_g \delta \mathbf{d}_b = 0 \tag{13}$$

in which $\mathbf{K}_e$ is the elastic stiffness matrix without the pre-buckling deformation effects, and $\mathbf{K}_g$ is the geometric stiffness matrix. In obtaining, Eq. (13) virtual work principle and the strain displacement relations in discrete form is to be used. Discrete strain displacement relations depend on the interpolated displacement field and thus, both matrices $\mathbf{K}_e$ and $\mathbf{K}_g$ depend on the interpolation scheme. In Eq. (13), λ is the buckling load factor and $\delta\mathbf{d}_b$ is the corresponding eigenvector.

3 Finite Element Formulations

3.1 Interpolation Scheme

A new beam-type finite element formulation with end nodes is developed. As a result of the adopted interpolation scheme, the formulation differs from the one presented in [16] due to the following modifications:

- The vertical deflection component $\hat{v}$ is a linear function of the position along the web direction. Therefore, web is extensible along the y direction and produce additional ε_{yy} strains (see Eq. (5)).
- Top or bottom flange load position effects of the vertical loads can be captured as a result of the locations of the vertical degrees-of-freedoms at the beam ends.

The element's nodal displacement vector $\tilde{\mathbf{d}}$ contains twenty-six terms, thirteen of which are defined at the front end as shown in Fig. 2, and the other thirteen are defined at the back end. We label this element as the distortional beam formulation (DBF) herein. In the nodal displacement vector $\tilde{\mathbf{d}}$ of DBF, the components are collected in the order of axial, vertical, bottom flange lateral, bottom flange twist, top flange lateral, and top flange twist related terms, respectively, i.e.

$$\tilde{\mathbf{d}} = \left\langle \mathbf{w} \,\middle|\, \mathbf{\Omega}_B \,\middle|\, \mathbf{\Lambda}_B \,\middle|\, \mathbf{\Gamma}_B \,\middle|\, \mathbf{\Omega}_T \,\middle|\, \mathbf{\Lambda}_T \,\middle|\, \mathbf{\Gamma}_T \right\rangle^{\mathrm{T}} \tag{14}$$

in which

$$\mathbf{w} = \left\langle w_1 \; w_2 \right\rangle^{\mathrm{T}}, \tag{15}$$

$$\mathbf{\Omega}_B = \left\langle v_{B1} \; \phi_{xB1} \; v_{B2} \; \phi_{xB2} \right\rangle^{\mathrm{T}}, \tag{16}$$

$$\mathbf{\Lambda}_B = \left\langle u_{B1} \; \phi_{yB1} \; u_{B2} \; \phi_{yB2} \right\rangle^{\mathrm{T}}, \tag{17}$$

$$\mathbf{\Gamma}_B = \left\langle \phi_{zB1} \; \psi_{B1} \; \phi_{zB2} \; \psi_{B2} \right\rangle^{\mathrm{T}}, \tag{18}$$

$$\mathbf{\Omega}_T = \left\langle v_{T1} \; \phi_{xT1} \; v_{T2} \; \phi_{xT2} \right\rangle^{\mathrm{T}}, \tag{19}$$
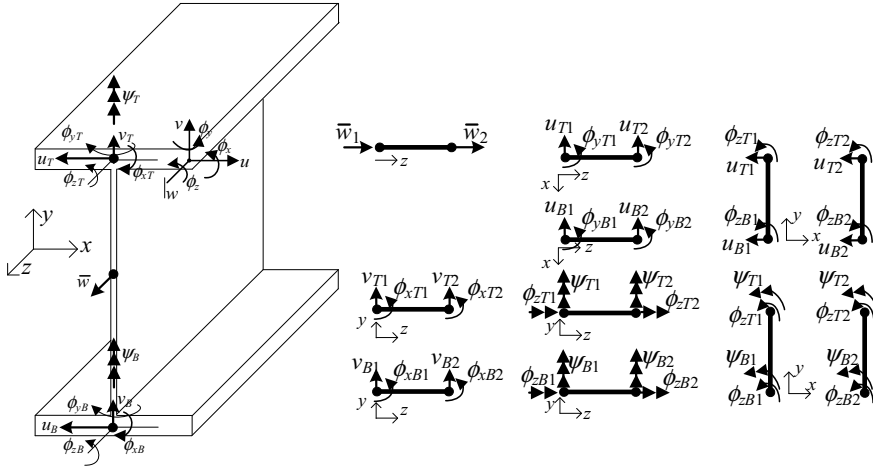
Fig. 2 Degrees-of-Freedom of the proposed beam element

$$\boldsymbol{\Lambda}_T = \left\langle u_{T1}\ \phi_{yT1}\ u_{T2}\ \phi_{yT2} \right\rangle^{\mathrm{T}} \tag{20}$$

and

$$\boldsymbol{\Gamma}_T = \left\langle \phi_{zT1}\ \psi_{T1}\ \phi_{zT2}\ \psi_{T2} \right\rangle^{\mathrm{T}}. \tag{21}$$

Accordingly, element displacement field vector becomes

$$\begin{aligned}
\mathbf{u} &= \left\langle \overline{w}(z)\ v(y,z)\ \phi_x(y,z)\ u(y,z)\ \phi_y(y,z)\ \phi_z(y,z)\ \psi(y,z) \right\rangle^{\mathrm{T}} \\
&= \tilde{\mathbf{N}}(y,z)\tilde{\mathbf{d}}
\end{aligned} \tag{22}$$

The matrix of shape functions In Eq. (22) can be written as

$$\tilde{\mathbf{N}}(y,z) = \begin{bmatrix}
\mathbf{N} & \mathbf{0} & \mathbf{0} & \mathbf{0} & \mathbf{0} & \mathbf{0} & \mathbf{0} \\
\mathbf{0} & \widehat{N}_1 \mathbf{L} & \widehat{N}_2 \mathbf{L} & \mathbf{0} & \mathbf{0} & \mathbf{0} & \mathbf{0} \\
\mathbf{0} & \widehat{N}_1 \mathbf{M} & \widehat{N}_2 \mathbf{M} & \mathbf{0} & \mathbf{0} & \mathbf{0} & \mathbf{0} \\
\mathbf{0} & \mathbf{0} & \mathbf{0} & \widehat{H}_1 \mathbf{L} & \widehat{H}_2 \mathbf{L} & \widehat{H}_3 \mathbf{L} & \widehat{H}_4 \mathbf{L} \\
\mathbf{0} & \mathbf{0} & \mathbf{0} & \widehat{H}_1 \mathbf{M} & \widehat{H}_2 \mathbf{M} & \widehat{H}_3 \mathbf{M} & \widehat{H}_4 \mathbf{M} \\
\mathbf{0} & \mathbf{0} & \mathbf{0} & \dot{H}_1 \mathbf{L} & \dot{H}_2 \mathbf{L} & \dot{H}_3 \mathbf{L} & \dot{H}_4 \mathbf{L} \\
\mathbf{0} & \mathbf{0} & \mathbf{0} & \dot{H}_1 \mathbf{M} & \dot{H}_2 \mathbf{M} & \dot{H}_3 \mathbf{M} & \dot{H}_4 \mathbf{M}
\end{bmatrix} \tag{23}$$

In Eq. (23), the axial displacement field in z direction is interpolated by using usual linear functions. Thus, the components of the vector $\mathbf{N}$ in Eq. (23) can be explicitly

written as

$$N_1 = (L - z)/L \tag{24}$$

and

$$N_2 = z/L \tag{25}$$

For the transverse and vertical displacement fields, and the rotation field in z direction, Hermitian polynomials are used along the beam span and thus, the components of the vector $\mathbf{L}$ in Eq. (23) can be explicitly written as

$$L_1 = 1 - 3z^2/L^2 + 2z^3/L^3, \tag{26}$$

$$L_2 = z - 2z^2/L + z^3/L^2, \tag{27}$$

$$L_3 = 3z^2/L^2 - 2z^3/L^3, \tag{28}$$

$$L_4 = z^3/L^2 - z^2/L \tag{29}$$

Components of the vector $\mathbf{M}$ can be obtained from the z-derivatives of the components in Eq. (26–29), respectively, which is consistent with the assumption that $\bar{u}' = \overline{\phi}_y$, $\hat{v}' = -\hat{\phi}_x$, and $\overline{\psi} = \overline{\phi}'_z$. In Eq. (23), the interpolation along the web is based on linear functions for the in-plane deformations, i.e.

$$\underset{1}{\widehat{N}} = 1 - (y - y_B)/h_w \tag{30}$$

and

$$\underset{2}{\widehat{N}} = (y - y_B)/h_w \tag{31}$$

and based on Hermitian functions for lateral deformations, i.e.

$$H_1 = 1 - 3(y - y_B)^2/h_w^2 + 2(y - y_B)^3/h_w^3, \tag{32}$$

$$H_2 = (y - y_B) - 2(y - y_B)^2/h_w + (y - y_B)^3/h_w^2, \tag{33}$$

$$H_3 = 3(y - y_B)^2/h_w^2 - 2(y - y_B)^3/h_w^3, \tag{34}$$

$$H_4 = -(y - y_B)^2/h_w + (y - y_B)^3/h_w^2 \tag{35}$$

where $h_w = y_T - y_B$. The components of the vector $\widehat{H}_i$ in Eq. (23) can be written as

$$\widehat{H}_i = H_i - \kappa(y - 0.5h_w)\dot{H}_i(y_0), \tag{36}$$

where $i = 1, 2, 3, 4$ and $y_0 = (y_T + y_B)/2$.

For alternative modelling purposes and validation, we also used a Shell Element Formulation (SEF) which has 6DOFs per node and it is formed by combining plate and membrane elements. Its interpolation scheme is a combination of Discrete Kirchhoff Plate developed in [18] and the membrane with drilling degrees-of-freedom developed in [19], where of SEF, 2×2 Gauss integration is used for numerical integration. Further details about the SEF element can also be found in [16]. Both DBF and SEF formulations have been implemented in an in-house structural analysis programme coded by the author in Fortran Programming Language.

3.2 Element Designations

To be able to collect various analysis options under a unified DBF formulation, as mentioned in Sect. 2, a β parameter was introduced for the selection of the rotation tensor and a μ parameter to switch on/off the contribution of the second order strains within the web direction. Table 1 provides the list of the combinations used in the analysis with the DBF. The labelling shown as DBF11a, DBF11b, etc. are later to be used in referencing the buckling load predictions under different assumptions. It should be noted that results based on the alternative constitutive matrices in Eqs. (11) and (12) are collected in separate tables.

Table 1 DBF analysis options and designation

	$\beta = 0 \ \mu = 0$	$\beta = 0.5 \ \mu = 0$	$\beta = 1 \ \mu = 0$	$\beta = 0 \ \mu = 1$	$\beta = 0.5 \ \mu = 1$	$\beta = 1 \ \mu = 1$
Non-extensible web and Mid-web Loading	DBF11a	DBF11b	DBF11c			
Extensible Web And Top Flange Loading	DBF13a	DBF13b	DBF13c	DBF13d	DBF13e	DBF13f

4 Case Studies

4.1 Description of the Girder Model and the Applied Conditions

The depth and the span of the girder is 1.5 m and 40 m, respectively, as shown in Fig. 3 along with the loading boundary conditions, and section dimensions. The same Figure also shows the alternative restraint conditions (Cases A, B, and C) used in the assessment. In Case A, the beam is under fixed-pinned condition which allows for lateral movements. In Case B, to create the effect of resistance provided by the bridge deck, lateral restraints are added in the middle of the top flange continuously along the span. In Case C, to create the effect of lateral bracings, lateral restraints in the middle of the bottom flange are added at every 5 m along the span.

Figure 3 shows the alternative restraint conditions applied to the analysed girder beam when Shell Element-based modelling is used and effectively same conditions are imposed on the DBF models. The uniformly distributed load of 1N/mm is applied in two alternative ways; in the middle of the web and at the centre of the top flange, which are labelled in the presented results as mid-web load (MWL) and top flange load (TFL), respectively. For the steel material, the modulus of elasticity and Poisson ratio are taken as $E = 200$ GPa and $\nu = 0.3$, respectively. When possible, two alternative meshing were used for both SEF and DBF models. For SEF modelling, the web is always divided into 4 elements, and each flange is always modelled with one element, however, along the span alternatively 32 and 64 elements are used.
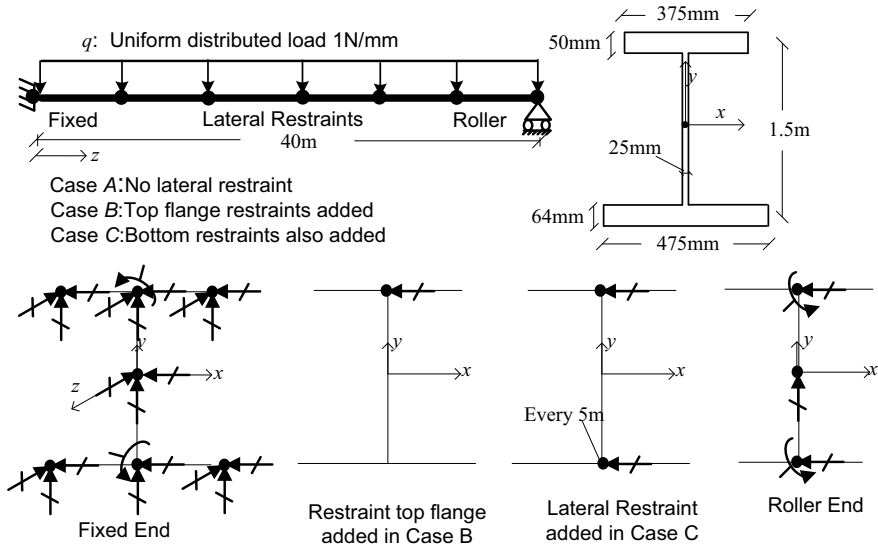
Fig. 3 Alternative boundary conditions applied to the analysed girder beam

DBF require meshing only along the beam span and for DBF alternatively 32 and 64 elements are used.

The following sub-sections present the results under alternative conditions imposed on the girder. Buckling load predictions of 4 of the first modes are shown in Tables for two alternative meshes. The negative modes indicate the loading in the opposite direction. The lower value for the load prediction in each mode corresponds to the finer mesh results. Deformed shapes of the girder based on the first buckling mode are also shown based on a 3D view. The deformed shape figures are based on the most refined mesh presented in the tables. In Sects. 4.2 to 4.4, DBF11 was used and in Sects. 4.5 to 4.6, DBF13 was used. DBF11 can only consider mid-web load, whereas DBF13 can consider top flange load as indicated in Table 1. Also note that DBF11 results with $\mu = 1$ are not presented (i.e. DBF11d, DBF11e, and DBF11f do not exist) because when the web is not extensible, the pre-buckling stresses in y direction can only exist due to Poisson ratio effect. This is to say, 30% of the axial stresses in z direction are produced in the y direction as a result of the Poisson ratio effect. The interaction of axial stresses with the second order strain e_{yy} cause overly conservative results as reported (e.g. [16]). On the other hand, when $\mathbf{E}_b$ in Eq. (12) is used, pre-buckling stresses in y direction vanish and therefore, DBF11d, DBF11e, and DBF11f results would be identical to those predicted by DBF11a, DBF11b, and DBF11c, respectively.

4.2 Case a Under Mid-Web Load–Analyses with DBF11

In Table 2 below, the buckling load predictions for Case A are presented. DBF results are obtained under mid-web load and the constitutive matrix $\mathbf{E}_b$ in Eq. (12) was used. It can be verified that DBF11c agrees the best with SEF (MWL) results. The effect of the selection of the rotation tensor is also significant as DBF11a as well as DBF11b predict significantly higher loads than that of DBF11c.

Figure 4 below shows the first buckling mode shapes of the girder.

Table 2 Case A–DBF11 analysis with $\mathbf{E}_b$

	DBF11a	DBF11b	DBF11c	SEF (MWL)
Mode 1	49.10	35.32	25.20	26.36
	49.10	35.32	25.19	26.23
Mode 2	71.04	64.51	57.71	61.27
	71.03	64.50	57.70	60.70
Mode −2	−121.62	−111.91	−94.74	−99.58
	−121.58	−111.89	−94.72	−98.21
Mode −1	−74.24	−51.65	−35.50	−37.22
	−74.23	−51.64	−35.49	−36.98

a) DBF11a   b) DBF11b   c) DBF11c   d) SEF (MWL)
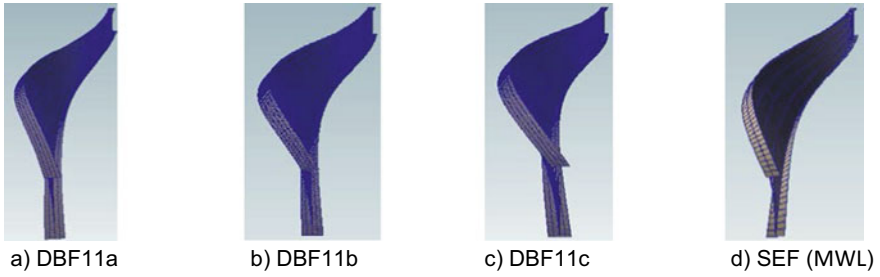
Fig. 4 Deformed shapes based on the first mode in Case A Table 2

4.3   Case B Under Mid-Web Load–Analyses with DBF11

In Table 3 below, the buckling load predictions for Case B are presented. Again, the results are contrasted with SEF (MWL) results. DBF results are obtained under mid-web load and the constitutive matrix $\mathbf{E}_b$ in Eq. (12) was used. Figure 5 shows the first mode shapes.

Table 3 Case B–DBF11 analysis with $\mathbf{E}_b$

	DBF11a	DBF11b	DBF11c	SEF (MWL)
Mode 1	262.75	331.83	315.99	357.51
	262.48	331.62	315.53	342.55
Mode 2	755.18	729.13	529.63	599.36
	753.96	728.11	527.99	567.93
Mode −2	−136.25	−120.66	−107.32	−114.05
	−136.26	−120.66	−107.31	−112.92
Mode −1	−94.87	−65.59	−47.56	−49.53
	−94.88	−65.58	−47.55	−49.27

a) DBF11a   b) DBF11b   c) DBF11c   d) SEF (MWL)
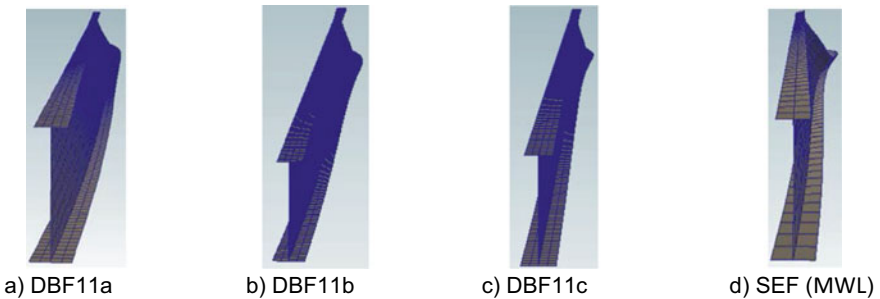
Fig. 5 Deformed shapes based on the first mode in Case B Table 3

Table 4 Case C–DBF11 analysis with $\mathbf{E}_b$

	DBF11a	DBF11b	DBF11c	SEF (MWL)
Mode 1	852.56	847.24	647.26	610.42
	848.10	842.07	642.56	569.17
Mode 2	935.02	936.70	682.91	657.28
	919.62	920.25	676.16	570.57
Mode −2	−685.56	−664.39	−498.22	−608.00
	−584.24	−579.06	−485.23	−388.81
Mode −1	−626.77	−577.92	−458.67	−466.46
	−559.74	−538.27	−448.34	−319.43

a) DBF11a   b) DBF11b   c) DBF11c   d) SEF (MWL)
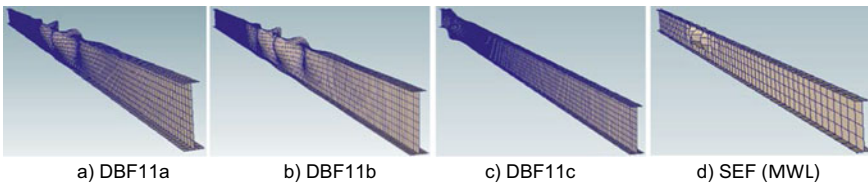
Fig. 6 Deformed shapes based on the first mode in Case C Table 4

From Tables 2 and 3, it can be observed that the differences between DBF11c and SEF (MWL) results are relatively more pronounced comparison to Case A. It can be verified, however, that for the smallest buckling load (i.e. Mode −1), DBF11c provides the closest results to SEF (MWL) comparison to DBF11a or DBF11b.

4.4 Case C Under Mid-Web Load–Analyses with DBF11

Table 4 below shows that when bracings are added in Case C, DBF11a or DBF11b predictions are significantly different than those of the SEF (MWL) results, while DBF11c still provides good predictions comparison to SEF (MWL). DBF results are obtained under mid-web load and the constitutive matrix $\mathbf{E}_b$ in Eq. (12) was used. Figure 6 shows the first mode shapes.

4.5 Case a Under Top Flange Load–Analyses with DBF13

Table 5 below includes the results based on the newly proposed element DBF13 under top flange loading. SEF results under top flange loading are also provided for comparisons. Constitutive matrix $\mathbf{E}_b$ in Eq. (12) was used in DBF analysis. It can be verified that DBF13f agrees the best with SEF (TFL) results. The effect of the

selection of the rotation tensor is also significant as DBF11d as well as DBF13e predict significantly higher loads than that of DBF13f. It can also be verified that when the effects of the second order strain are removed as in DBF13a, b, c, the buckling load predictions are upper bounds to those of DBF13d, e, f. In particular, DBF13f agrees with SEF better than DBF13c. The agreement of the first mode shapes can also be verified from Fig. 7. It can be verified from Fig. 7 that the first mode shape is a lateral-torsional buckling mode.

Table 6 is the repetition of Case A under top flange load except that constitutive matrix $\mathbf{E}_a$ in Eq. (11) was used in DBF analysis. It can be seen that DBF13a, b, c are almost identical to those in Table 5 because $\mu = 0$ and thus second order strain e_{yy} are not considered in their formulation. Whereas drops in DBF13d, e, f are significant as $\mu = 1$ were used in their formulation. It should be noted that although DBF13 allows web extensibility, the interpolation used for that purpose is linear which results with constant strains in y direction. Considering this low order of interpolation and looking at the results of DBF13f with respect to SEF, use of matrix $\mathbf{E}_a$ is still not recommended even in the DBF13 formulation. Mode shapes are not presented when constitutive matrix $\mathbf{E}_a$ is used. First mode shapes are presented in Fig. 8.

Table 5 Case A–DBF13 analysis with $\mathbf{E}_b$

	DBF13a	DBF13b	DBF13c	DBF13d	DBF13e	DBF13f	SEF (TFL)
Mode 1	49.10	35.32	25.20	33.75	24.96	19.22	20.14
	49.09	35.32	25.19	33.75	24.95	19.21	20.05
Mode 2	71.04	64.51	57.71	60.68	55.68	50.52	53.71
	71.03	64.50	57.70	60.67	55.676	50.51	53.24
Mode −2	−121.65	−111.91	−94.75	−135.68	−131.28	−109.38	−117.34
	−121.59	−111.89	−94.73	−135.67	−131.27	−109.35	−115.69
Mode −1	−74.23	−51.65	−35.50	−86.26	−70.34	−46.31	−49.57
	−74.23	−51.64	−35.49	−86.25	−70.33	−46.30	−49.26

a) DBF13a   b) DBF13b   c) DBF13c   d) DBF13d   e) DBF13e   f) DBF13f   g) SEF (TFL)
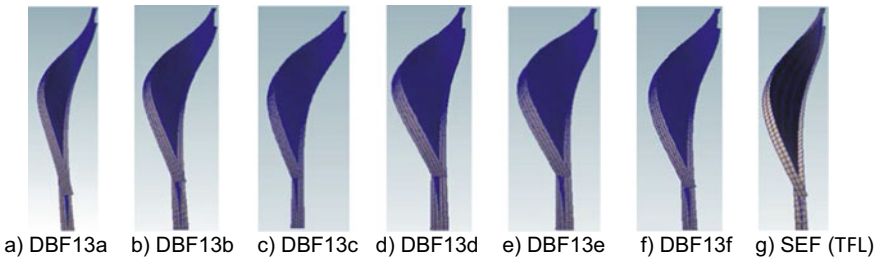
Fig. 7 Deformed shapes based on the first mode in Case A Table 5

Table 6 Case A–DBF13 analysis with $\mathbf{E}_a$

	DBF13a	DBF13b	DBF13c	DBF13d	DBF13e	DBF13f	SEF (TFL)
Mode 1	49.18	35.37	25.23	15.17	14.06	12.79	20.14
	49.18	35.37	25.22	15.17	14.05	12.79	20.05
Mode 2	71.21	64.67	57.86	38.19	37.27	35.93	53.71
	71.21	64.66	57.85	38.18	37.26	35.92	53.24
Mode −2	−121.91	−112.17	−95.00	−74.34	−77.79	−75.03	−117.34
	−121.84	−112.15	−94.96	−74.29	−77.78	−75.02	−115.69
Mode −1	−74.39	−51.73	−35.55	−28.71	−27.50	−25.12	−49.57
	−74.38	−51.72	−35.54	−28.71	−27.49	−25.12	−49.26

a) DBF13a b) DBF13b c) DBF13c d) DBF13d e) DBF13e f) DBF13f
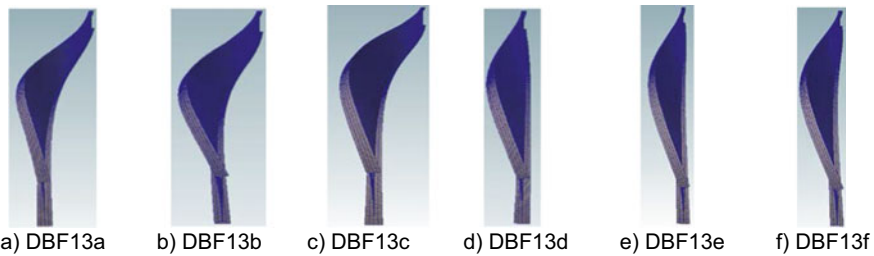
Fig. 8 Deformed shapes based on the first mode in Case A Table 6

4.6 Case B Under Top Flange Load–Analyses with DBF13

Table 7 below includes the results for Case B based on the newly proposed element DBF13 as well as SEF under top flange loading. It can be verified that DBF13b still agrees the best with SEF and QTS8 results are significantly lower than those of SEF. From Fig. 9, it can be observed that the first mode shapes are in good agreement between SEF and DBF13f. It can be verified from Fig. 9 that in all cases, the first mode shape is a distortional buckling mode as the top flange is laterally restraint.

Table 8 is the repetition of Case B under top flange load except that constitutive matrix $\mathbf{E}_a$ in Eq. (11) was used. Corresponding mode shapes are given in Fig. 10. Similar to the previous case, DBF13a, b, c are almost not affected, however, the drop in DBF13d, e, f suggest that $\mathbf{E}_b$ should be used in DBF analysis and otherwise the buckling load predictions can be very conservative even comparison to the SEF solution.

4.7 Case C Under Top Flange Load–Analyses with DBF13

To evaluate the performance of the proposed element DBF13, Case C results are presented in Table 9 below along with SEF. Constitutive matrix $\mathbf{E}_b$ in Eq. (12)

Table 7 Case B–DBF13 analysis with $\mathbf{E}_b$

	DBF13a	DBF13b	DBF13c	DBF13d	DBF13e	DBF13f	SEF (TFL)
Mode 1	262.70	332.00	318.75	88.68	143.96	202.23	223.59
	262.46	331.83	318.43	88.64	143.89	202.04	218.07
Mode 2	755.00	733.08	548.53	506.72	541.99	466.89	543.41
	753.90	732.19	547.61	506.18	541.51	466.16	510.83
Mode −2	−136.26	−120.67	−107.33	−183.00	−155.34	−132.76	−142.77
	−136.26	−120.66	−107.31	−183.00	−155.33	−132.74	−141.30
Mode −1	−94.88	−65.59	−47.56	−157.52	−130.78	−94.51	−100.02
	−94.88	−65.58	−47.55	−157.52	−130.78	−94.48	−99.39

a) DBF13a   b) DBF13b   c) DBF13c   d) DBF13d   e) DBF13e   f) DBF13f   g) SEF (TFL)
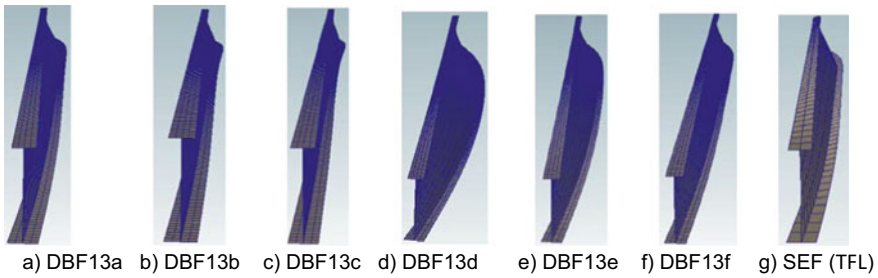
Fig. 9 Deformed Shapes based on the first mode in Case B Table 7

Table 8 Case B–DBF13 analysis with $\mathbf{E}_a$

	DBF13a	DBF13b	DBF13c	DBF13d	DBF13e	DBF13f	SEF (TFL)
Mode 1	263.45	334.63	324.07	21.70	23.88	26.33	223.59
	263.27	334.61	324.00	21.69	23.88	26.33	218.07
Mode 2	756.89	740.42	561.16	97.06	104.88	112.66	543.41
	756.22	739.96	560.60	97.016	104.84	112.62	510.83
Mode −2	−136.73	−121.14	−107.85	−81.74	−79.77	−77.60	−142.77
	−136.73	−121.13	−107.83	−81.74	−79.77	−77.59	−141.30
Mode −1	−95.16	−65.79	−47.72	−29.77	−27.86	−25.99	−100.02
	−95.16	−65.78	−47.71	−29.76	−27.805	−25.99	−99.39

was used in DBF analysis. DBF13f is the most accurate solution among all DBF alternatives comparison to SEF. The mode shapes are presented in Fig. 11. Table 10 is the repetition of Case C under top flange load except that constitutive matrix $\mathbf{E}_a$ in Eq. (11) was used in DBF analysis. Mode shapes corresponding to Table 10 results are presented in Fig. 12.

From Fig. 11, it can be observed that mode shapes are more of local buckling type due to the bottom restraints preventing the lateral movements. From Table 9, it

a) DBF13a　　b) DBF13b　　c) DBF13c　　d) DBF13d　　e) DBF13e　　f) DBF13f
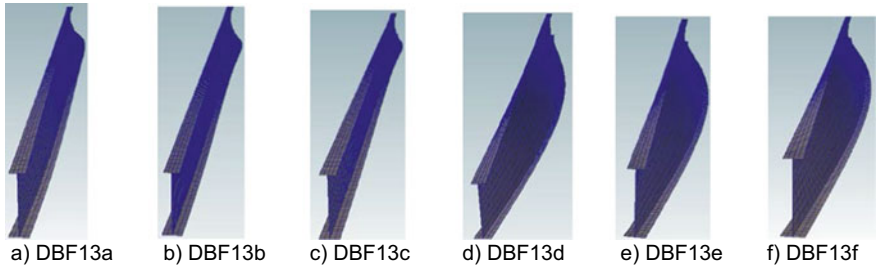
Fig. 10 Deformed shapes based on the first mode in Case B Table 8

Table 9 Case C–DBF13 analysis with $\mathbf{E}_b$

	DBF13a	DBF13b	DBF13c	DBF13d	DBF13e	DBF13f	SEF (TFL)
Mode 1	851.25	838.40	688.85	838.85	825.9	665.89	591.25
	849.14	837.40	686.11	838.32	826.49	663.57	559.58
Mode 2	934.14	933.43	797.38	929.64	922.08	746.90	633.65
	921.77	921.56	795.25	920.85	919.51	745.39	561.76
Mode −2	−684.94	−645.79	−576.81	−690.94	−651.44	−585.74	−626.62
	−585.07	−577.59	−542.62	−585.32	−577.93	−543.56	−394.73
Mode −1	−625.38	−606.92	−534.62	−627.60	−609.98	−540.16	−476.87
	−559.69	−555.85	−523.49	−559.79	−555.98	−526.42	−321.62

a) DBF13a　　　　　b) DBF13b　　　　　c) DBF13c

d) DBF13d　　　e) DBF13e　　　f) DBF13f　　　g) SEF (TFL)
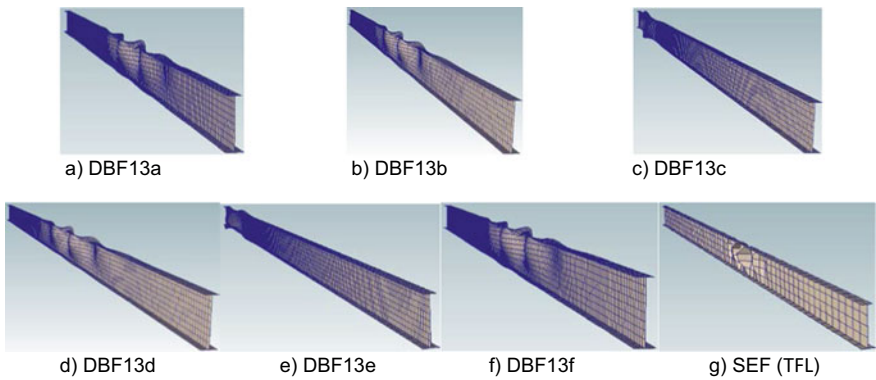
Fig. 11 Deformed shapes based on the first mode in Case C Table 9

can also be observed that the difference between DBF13f and the reference solution SEF are increasing comparison to previous cases and DBF13f is becoming a clear upper bound to SEF. This can be attributed to the fact that DBF13 is not sufficiently flexible to be able to capture local buckling modes.

Table 10 Case C–DBF13 analysis with $\mathbf{E}_a$

	DBF13a	DBF13b	DBF13c	DBF13d	DBF13e	DBF13f	SEF (TFL)
Mode 1	863.61	851.015	702.03	327.15	332.28	336.86	591.25
	861.34	849.39	700.07	327.04	332.16	336.63	559.58
Mode 2	942.54	941.92	823.26	379.15	384.32	385.31	633.65
	928.28	928.09	821.79	379.03	384.19	382.55	561.76
Mode −2	−693.46	−654.15	−596.93	−393.20	−401.63	−397.58	−626.62
	−588.19	−578.56	−542.49	−393.06	−401.50	−393.06	−394.73
Mode −1	−633.97	−593.77	−504.60	−350.57	−330.19	−304.68	−476.87
	−567.03	−557.96	−507.01	−346.19	−327.59	−303.25	−321.62

a) DBF13a   b) DBF13b   c) DBF13c

d) DBF13d   e) DBF13e   f) DBF13f
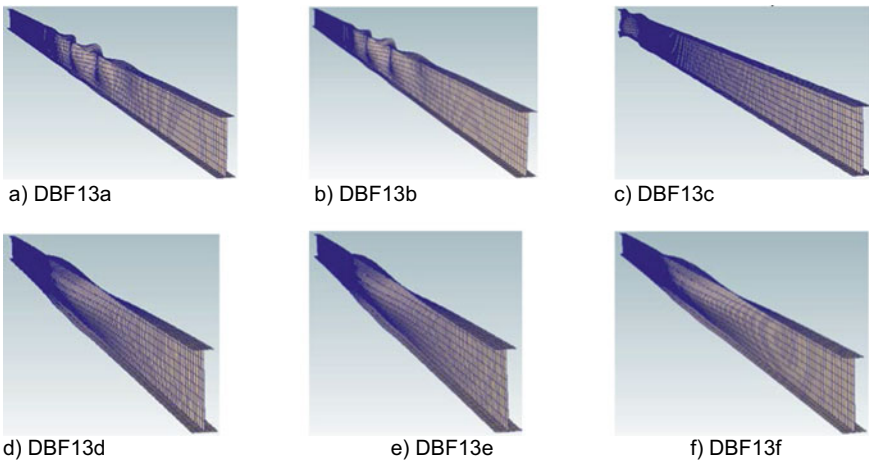
Fig. 12 Deformed shapes based on the first mode in Case C Table 10

5 Conclusions

For the elastic distortional buckling analysis of thin-walled members, a family of 13 Degree-Of-Freedom per node Beam Finite Element formulation (DBF13) was proposed. The performance of the distortional beam formulation was evaluated by comparisons with shell element-based models and beam element. Effect of various assumptions, such as the selection of the rotation tensor, strains, and the constitutive matrix were shown to be significant. The applicability of the developed beam formulation was illustrated on practical case studies where web bending mode is the dominant buckling mode. It was shown that assumptions on rotation tensor and strains may have very significant effect on the results. One member of the family DBF13f shows very good agreement with those of the shell element SEF-based models, especially for the cases that involve lateral-torsional and distortional buckling behaviour. It was shown however that, as the local buckling modes start to govern, the proposed

beam formulation may become overly stiff comparison to the shell element-based models.

References

1. Barsoum RJ, Gallagher RH (1970) Finite element analysis of torsional and torsional–flexural stability problems. Int J Numer Meth Eng 2:335–352
2. Bazant ZP, El-Nimeri M (1973) Large-deflection spatial buckling of thin-walled beams and frames. J Eng Mech Div 99(6):1259–81
3. Krajcinovic D (1969) A consistent discrete elements technique for thin wall assemblages. Int J Solids Struct 5:639–662
4. Alsafadie R, Hjiaj M, Battini J-M (2010) Corotational mixed finite element formulation for thin-walled beams with generic cross-section. Comput Methods Appl Mech Eng 199:3197–3212
5. Erkmen RE, Attard MM (2011) Lateral-torsional buckling analysis of thin-walled beams including shear and pre-buckling deformation effects. Int J Mech Sci 53:918–925
6. Roberts TM, Azizian ZG (1983) Instability of thin-walled bars. J Eng Mech, ASCE 109:781–794
7. Pi Y-L, Trahair N, Rajasekaran S (1992) Energy equations for beam lateral buckling. J Struct Eng ASCE 118:1462–1479
8. Wu L, Mohareb M (2012) Finite element formulation for the lateral torsional buckling of plane frames. J Eng Mech, ASCE 139:512–524
9. Schafer BW, Pekoz T (1998) Computational modeling of cold-formed steel: characterizing geometric imperfections and residual stresses. J Constr Steel Res 47:193–210
10. Adany S, Schafer BW (2008) A full modal decomposition of thin-walled, single-branched open cross-section members via the constrained finite strip method. J Constr Steel Res 64:12–29
11. Hancock GJ (1978) Local, distortional, and lateral buckling of I-beams. J Struct Div 104:1787–1798
12. Davies JM, Leach P (1994) Second order generalized beam theory. J Constr Steel Res 31:221–241
13. Roberts TM, Jhita PS (1983) Lateral, local and distortional buckling of I-beams. Thin-Walled Struct 1:289–308
14. Pezeshky P, Mohareb M (2018) Distortional lateral-torsional buckling of beam-columns including pre-buckling deformation effects. Comput Struct 209:93–116
15. Camotim D, Silvestre N, Gonçalves R, Dinis PB (2004) GBT analysis of thin-walled members: new formulations and applications. In: Loughlan J (ed) Thin-walled structures: recent advances and future trends in thin-walled structures technology. Canopus Publishing, Bath, pp 137–168
16. Erkmen RE (2022) Elastic buckling analysis of thin-walled beams including web-distortion. Thin-Walled Struct 170
17. Teh LH (2005) Spatial rotation kinematics and flexural-torsional buckling. J Eng Mech, ASCE 131:598–605
18. Batoz J-L, Tahar MB (1982) Evaluation of a new quadrilateral thin plate bending element. Int J Numer Meth Eng 18:1655–1677
19. Ibrahimbegovic A, Taylor RL, Wilson EL (1990) A robust quadrilateral membrane finite element with drilling degrees of freedom. Int J Numer Meth Eng 30:445–457

Machine Learning and AI in Strucrural Engineering

Elastic Lateral Torsional Buckling Resistance for Continuous Beams Using Artificial Neural Networks

Amin Iranpour and Magdi Mohareb

Abstract Elastic lateral torsional buckling (ELTB) is a mode of failure that tends to govern the capacity of long-span laterally unsupported steel beams with open cross sections bent about their major axis. The ELTB design provisions in structural steel design standards are primarily intended for flexural members with a single laterally unbraced segments and offer no specific guidance for treating multiple-segment continuous beams. Analysis and design methods for determining the ELTB resistance of multiple-span members available in the literature range from omitting interactions between spans, to iterative analytical techniques for hand calculations, to finite element modeling and thus range from the simple but overly conservative to the elaborate but potentially overly complex in a design environment. There is a need to develop simple design-oriented equations for routine design. Within this context, a large database of finite element runs was generated to determine the elastic critical moments of two-span beams based on eigenvalue buckling models using a Vlasov-type thin-walled beam element. The results show that while standard-based equations reasonably predict the ELTB resistance of single-segment members, they can grossly underestimate the critical moments when applied to two-span continuous members. The study then develops a design equation for predicting the ELTB resistance of two-span beams by integrating finite element results with artificial neural network techniques, culminating in an equation that accurately characterizes the critical moments for two-span continuous beams under uniformly distributed load.

Keywords Lateral torsional buckling · Finite element analysis · Wide flange sections · Continuous beams · Artificial neural network

A. Iranpour (✉) · M. Mohareb
University of Ottawa, Ottawa, Canada
e-mail: Amin.iranpour@uottawa.ca

1 Introduction and Literature Review

Elastic lateral torsional buckling (ELTB) is a mode of failure that tends to govern the capacity of long-span laterally unsupported steel beams with open cross sections bent about their major axis. The ELTB design provisions in structural steel design standards (e.g., [1, 2]) are primarily intended for flexural members with a single laterally unbraced segments and offer no specific guidance for treating multiple-span continuous beams. Analysis and design methods for determining the ELTB resistance of multiple-span members available in the literature range from omitting interactions between spans [3], to iterative analytical techniques for hand calculations (e.g., [4, 5] and [6]), to finite element (FE) modeling [7] and range from the simple but overly conservative to the elaborate but complex. Existing iterative procedures are reported to be conservative in most cases [8]. However, in cases of high moment gradients, they can overestimate the LTB capacity.

None of the previous studies developed a simple design-oriented equation for routine design. Within this context, using a series of elastic FE eigenvalue buckling models based on a Vlasov-type thin-walled beam element [9, 10], the present study shows that while standard-based equations reasonably predict the ELTB resistance of single-span members in most cases, they can lead to inaccurate predictions for the ELTB resistance of two-span continuous members. The present study thus develops a design equation for predicting the ELTB of two-span beams by integrating finite element results with artificial neural network (ANN) techniques.

ANN has successfully been employed to develop mathematical models to predict various types of structural behavior in steel elements such as welded flange plate connections [11], single-plate shear connections [12], frames [13], and cellular beams [14]. Some studies specifically investigated the buckling of steel beams using ANN (e.g., [15] and [16]). Reference [16] reported that ANN presents more accurate LTB capacities for castellated steel beams than those predicted by current design equations (e.g., [1]), which may overpredict the capacity.

2 Finite Element Background

The LTB-UO program [17] is used for the FE investigation. This program is developed based on the formulation by Barsoum and Gallagher [9] (referred to subsequently as the BG element) and computes the elastic LTB capacity of beams under general transverse loading for beams with general boundary conditions.

The FE formulation of the element is developed based on the total potential energy Π functional of a beam during buckling. The simplest form of Π that omits the effects of shear deformation, distortion, pre-buckling deformation and load height effects is

$$\Pi = \frac{1}{2} \int_L \left(E I_y U''^2 + E C_w \theta''^2 + G J \theta'^2 + 2\lambda M \theta U'' \right) dx \tag{1}$$
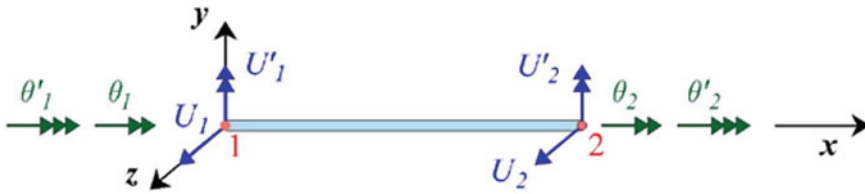
Fig. 1 Degrees of freedom of the BG element employed in the LTB-UO program

in which E is the modulus of elasticity, G is shear modulus, I_y is the weak axis moment of inertia, J is the Saint–Venant torsional constant, C_w is the warping constant, $U = U(x)$ is the lateral displacement, $\theta = \theta(x)$ is the angle of twist, λ is a buckling load multiplier to be determined from an eigenvalue analysis, $M = M(x)$ is the bending moment distribution within the member under the applied transverse loads. Within the finite element, it is obtained adopting linear interpolation over the element length L_e, i.e.,

$$M(x) = -M_1\left(1 - x/L_e\right) + M_2\left(x/L_e\right) \tag{2}$$

in which, M_1 and M_2 are bending moment values at element ends and are obtained from the pre-buckling analysis. The BG element is a two-node thin-walled beam element with four buckling degrees of freedom per node including lateral displacement U, rotation about weak axis U', angle of twist θ and warping θ' (Fig. 1).

The functions of lateral displacement $U(x)$ and twist $\theta(x)$ are related to the vector of degrees of freedom $\mathbf{d}^{\mathbf{T}} = \left(U_1\ U_1'\ U_2\ U_2'\ \theta_1\ \theta_1'\ \theta_2\ \theta_2' \right)$ through

$$U(x) = \mathbf{H_U^T d}, \quad \theta(x) = \mathbf{H_\theta^T d} \tag{3a-b}$$

in which the vectors of shape functions are defined by

$$\begin{aligned}
\mathbf{H_U^T} = \mathbf{H_U^T}(x) &= \left(H_1\ -H_2\ H_3\ -H_4\ 0\ 0\ 0\ 0 \right) \\
\mathbf{H_\theta^T} = \mathbf{H_\theta^T}(x) &= \left(0\ 0\ 0\ 0\ H_1\ H_2\ H_3\ H_4 \right) \\
\left\langle H_1, H_2, H_3, H_4 \right\rangle &= \left(1 - 3\zeta^2 + 2\zeta^3,\ L_e\zeta(1 - \zeta)^2,\ 3\zeta^2 - 2\zeta^3,\ L_e\zeta^2(\zeta - 1) \right), \\
\zeta &= x/L_e
\end{aligned} \tag{4a-b}$$

From Eqs. (3a-b), by substituting into the variational principle in Eq. (1) and evoking the stationarity conditions $\left(\partial \Pi/\partial \mathbf{d}\right)\delta \mathbf{d} = 0$, one obtains the linearized eigenvalue problem that yields λ corresponding to the state of onset of buckling, i.e.,

$$\left(\mathbf{k_E} - \lambda \mathbf{k_G}\right)_{8\times 8}\mathbf{d}_{8\times 1} = \mathbf{0}_{8\times 1} \tag{5}$$

in which, $\mathbf{k_E}$ is the elastic stiffness matrix and $\mathbf{k_G}$ is the geometric matrix.

3   Validation Study

The BG element has been extensively used to determine the elastic critical moments for laterally unbraced beams. Comparisons against the predictions of FEA models based on thin-walled beam elements with advanced features (e.g., [7, 18–21]), shell elements (e.g., [22–24]), and 3D solid elements (e.g., [25]) established the validity of the model predictions for a wide range of cross sections, spans, loading patterns, and boundary conditions.

To further investigate the accuracy of the BG element, this study compares the results obtained using the BG element with those predicted using CAN/CSA-S16 [2] and ANSI/AISC360 [1]. For this purpose, a beam of span 6 m with W310 × 45 cross section is considered. The beam is simply supported relative to lateral displacement (i.e., $U = 0$ and $U' \neq 0$) and relative to twist (i.e., $\theta = 0$ and $\theta' \neq 0$) at both ends. By performing a mesh sensitivity analysis, it was found that using eight elements along the span is adequate to achieve convergence. A variety of loading conditions is investigated (Fig. 2). In beams under uniform moment (Fig. 2a) only Pin-Pin boundary condition relative to transverse displacement (i.e., transverse displacement $V = 0$ and in-plane rotation $V' \neq 0$ at both ends) is considered, but different values of end moments (M, αM) are applied by adjusting the value of α, where $\alpha = 1$, 0.5, 0, −0.5, −1 (runs #1–5 in Table 1). In other loading configurations (Fig. 2b–f), three Transverse Boundary Conditions (TBCs) are considered: (1) Pin-Pin, (2) Fix-Pin, and (3) Fix-Fix, in which Fix means $V = V' = 0$ and Pin means $V = 0$ and $V' \neq 0$. Column 3 in Table 1 summarizes the TBC for each case.

The moment distributions normalized to the absolute value of the peak moment are presented in Column 4 of Table 1. These figures also include the normalized bending moments at quarter point, mid-span, and third-quarter point. Using these values, one can obtain the moment gradient factor from CAN/CSA-S16 [2] ω_{2-CSA} and ANSI/AISC360 [1] ω_{2-AISC}:

$$\omega_{2-CSA} = \frac{4M_{\max}}{\sqrt{M_{\max}^2 + 4M_{1/4}^2 + 7M_{1/2}^2 + 4M_{3/4}^2}},$$
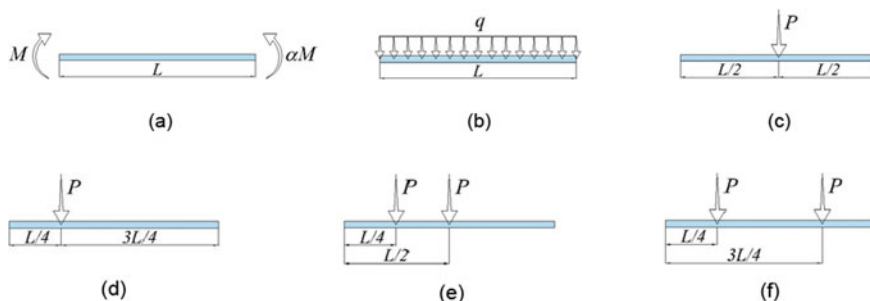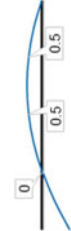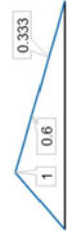
Fig. 2 Loading configurations investigated

Table 1 Comparison of moment gradient factors of FEA, CAN/CSA-S16 [2] and ANSI/AISC360 [1]

#	Load	TBC[a]	Normalized bending moment distribution	ω_{2-FEA}	ω_{2-CSA}	ω_{2-AISC}	$\frac{\omega_{2-CSA}}{\omega_{2-FEA}}$	$\frac{\omega_{2-AISC}}{\omega_{2-FEA}}$
(1)	(2)	(3)	(4)	(5)	(6)	(7)	(8)	(9)
1	Figure 2a	Pin-Pin[b]		1.00	1.00	1.00	1.000	1.000
2	Figure 2a	Pin-Pin		1.32	1.29	1.25	0.981	0.948
3	Figure 2a	Pin-Pin		1.84	1.75	1.67	0.951	0.908
4	Figure 2a	Pin-Pin		2.55	2.29	2.17	0.895	0.852
5	Figure 2a	Pin-Pin		2.72	2.31	2.27	0.849	0.836
6	Figure 2b	Pin-Pin		1.14	1.13	1.14	0.989	0.993
7	Figure 2b	Fix-Pin[c]		2.30	2.07	2.08	0.898	0.905

Table 1 (continued)

#	Load	TBC[a]	Normalized bending moment distribution	ω_{2-FEA}	ω_{2-CSA}	ω_{2-AISC}	$\dfrac{\omega_{2-CSA}}{\omega_{2-FEA}}$	$\dfrac{\omega_{2-AISC}}{\omega_{2-FEA}}$
(1)	(2)	(3)	(4)	(5)	(6)	(7)	(8)	(9)
8	Figure 2b	Fix-Fix[d]	0.125 0.5 0.125	2.70	2.36	2.38	0.875	0.883
9	Figure 2c	Pin-Pin	0.5 1 0.5	1.36	1.26	1.32	0.929	0.966
10	Figure 2c	Fix-Pin	−0.0833 0.833 0.417	1.82	1.56	1.70	0.856	0.936
11	Figure 2c	Fix-Fix	0 1 0	1.72	1.41	1.92	0.821	1.116
12	Figure 2d	Pin-Pin	1 0.6 0.333	1.47	1.37	1.36	0.929	0.926
13	Figure 2d	Fix-Pin	0.393 0.262 0.131	3.79	2.72	2.44	0.717	0.644
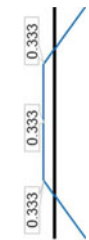
(continued)

Table 1 (continued)

#	Load	TBC[a]	Normalized bending moment distribution	ω_{2-FEA}	ω_{2-CSA}	ω_{2-AISC}	$\dfrac{\omega_{2-CSA}}{\omega_{2-FEA}}$	$\dfrac{\omega_{2-AISC}}{\omega_{2-FEA}}$
(1)	(2)	(3)	(4)	(5)	(6)	(7)	(8)	(9)
14	Figure 2d	Fix-Fix		3.69	2.60	2.47	0.706	0.670
15	Figure 2e	Pin-Pin		1.23	1.17	1.19	0.948	0.968
16	Figure 2e	Fix-Pin		2.52	2.09	2.07	0.831	0.821
17	Figure 2e	Fix-Fix		2.60	2.08	2.18	0.799	0.838
18	Figure 2f	Pin-Pin		1.04	1.00	1.00	0.962	0.962
19	Figure 2f	Fix-Pin		2.41	2.06	1.96	0.855	0.811

(continued)

Table 1 (continued)

#	Load	TBC[a]	Normalized bending moment distribution	ω_{2-FEA}	ω_{2-CSA}	ω_{2-AISC}	$\dfrac{\omega_{2-CSA}}{\omega_{2-FEA}}$	$\dfrac{\omega_{2-AISC}}{\omega_{2-FEA}}$
(1)	(2)	(3)	(4)	(5)	(6)	(7)	(8)	(9)
20	Figure 2f	Fix-Fix		3.11	2.45	2.14	0.787	0.688
			Average:				0.879	0.884
			Standard deviation:				0.0831	0.115

In all cases, the beam is simply supported relative to lateral displacement (i.e., $U = 0$ and $U' \neq 0$) and relative to twist (i.e., $\theta = 0$ and $\theta' \neq 0$) at both ends. However, different BCs relative to transverse displacement are adopted.

[a] TBC: Transverse Boundary Condition

[b] Pin-Pin: $V(0) = V(L) = 0$, $V'(0) \neq 0$ and $V'(L) \neq 0$

[c] Fix-Pin: $V(0) = V'(0) = V(L) = 0$ and $V'(L) \neq 0$

[d] Fix-Fix: $V(0) = V'(0) = V(L) = V'(L) = 0$.

$$\omega_{2-AISC} = \frac{12.5 M_{\max}}{2.5 M_{\max} + 3 M_{1/4} + 4 M_{1/2} + 3 M_{3/4}} \tag{6a-b}$$

in which $M_{\max}$, $M_{1/4}$, $M_{1/2}$, and $M_{3/4}$ are the absolute value of the peak moment, and moments at the quarter, mid-span, and third-quarter points of the unbraced segment, respectively.

In each case, the FEA value for the moment gradient factor ω_{2-FEA} is obtained by dividing the critical moment as predicted by the BG model by that of the basic case, in which the beam is subjected to uniform moment (i.e., run #1). The obtained values of ω_{2-FEA} are provided in Column 5 of Table 1 and predicted values of moment gradient factor using Eq. (6a-b) are presented in Columns 6 and 7. The ratios $\omega_{2-CSA} \big/ \omega_{2-FEA}$ and $\omega_{2-AISC} \big/ \omega_{2-FEA}$ are provided in Columns 8 and 9. In all cases, the FEA predictions closely match the moment gradient factors predicted by Canadian and American moment gradient equations, with an average $\omega_{2-CSA} \big/ \omega_{2-FEA}$ ratio of 0.88 and a standard deviation of 0.083 and an average $\omega_{2-AISC} \big/ \omega_{2-FEA}$ ratio of 0.88 and a standard deviation of 0.12. The difference between the predictions of FEA and standard-based quarter point moment gradient factors is attributed to the fact that standard-based equations intend to provide relatively simple solutions that err, for the most part, on the conservative side.

4   Statement of the Problem

A two-span prismatic beam with a doubly symmetric wide flange section is restrained at both ends, points A and C, and at an intermediate point B, relative to the transverse and lateral displacements and relative to twist (Fig. 3a). The supports are assumed to provide no restraints against warping nor weak axis rotation. The beam is subjected to a uniformly distributed load (UDL) acting at the shear center axis of the beam. Given that the beam is prismatic, the longer span is more prone to LTB than the shorter span. As such, when the longer span attempts to buckle, the shorter span restrains, to some extent, the weak axis rotation and warping deformation at intermediate support B and delays the buckling of the longer span and resulting in a larger elastic critical moment for the system. The accurate determination of the elastic critical moment of the system must account for the interaction between both spans and can be performed from the FE modeling described under Sect. 2. Alternatively, a lower bound solution that omits the beneficial span interaction effect can be obtained by disregarding the shorter span while applying the moment M_e equal to the bending moment at the intermediate support B, resulting in the simplified idealized system depicted in Fig. 3b. It is required to develop a model that accurately predicts the elastic critical moment of the two-span beam by accounting for the beneficial interaction effect between both spans.
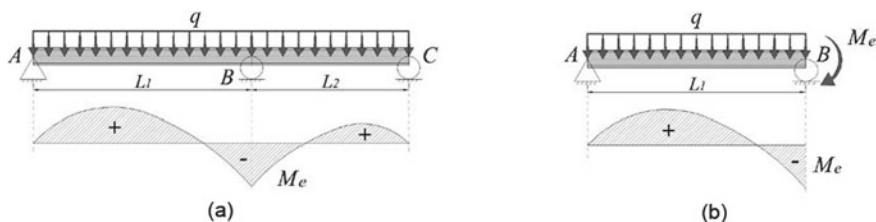
Fig. 3 Cases investigated **a** Case 1: Two-span system including span interaction effect and **b** Case 2: Idealized system-long span alone omitting span interaction effect

5 Parameters to Be Investigated

To quantify the span interaction effect on the LTB capacity, two sets of analyses are conducted: (1) a two-span beam under UDL on both spans (Fig. 3a) and (2) a single-span beam of span L_1 (i.e., the short span is removed) subjected to UDL and a concentrated moment M_e at point B (Fig. 3b). This concentrated moment tends to produce a moment distribution identical to the one generated in Case 1 and hence leads to an identical moment gradient factor as the latter. The moment magnification due to span interaction effect is defined as $m = M_{cr1}/M_{cr2}$, in which M_{cr1} denotes the critical moments for the two-span system depicted in Fig. 3a, and M_{cr2} is the critical moment for the idealized representation depicted in Fig. 3b. The value of critical moment M_{cr} is a function of seven parameters, i.e., $M_{cr} = f_1(E, G, I_y, J, C_w, L_1, L_2)$. For steel, E and G are constant values, and hence, the critical moment depends only on five parameters $M_{cr} = f_2(I_y, J, C_w, L_1, L_2)$. Using the Buckingham Pi theorem, one can express m as a function of four dimensionless parameters $m(\rho_1, \rho_2, \rho_3, \rho_4)$, in which

$$\rho_1 = \frac{L_2}{L_1}, \rho_2 = L_2\sqrt{\frac{I_y}{C_w}}, \rho_3 = \frac{I_y}{J}, \rho_4 = \frac{C_w^{2/3}}{J} \qquad \text{(7a-d)}$$

The span ratio ρ_1 is taken as 0.2, 0.4, 0.6, and 0.8. The long span to depth ratio L_1/d is taken as 15, 20, 25, and 30. Beam cross sections were selected to cover all 281 W sections available in the handbook of steel construction database [26]. Hence, ρ_2 was taken to vary between 6 and 61, ρ_3 was taken to range from 3 to 90, and ρ_4 was taken to range between 3 to 399, leading to 4496 cases/FEA runs.

6 Special Case of Equal Spans

The case of equal spans $(L_2/L_1 = 1)$ was not considered in the database of runs, since equal spans with identical cross sections, boundary conditions, and loading tend to attain their elastic buckling critical moment simultaneously. Figure 4 depicts the
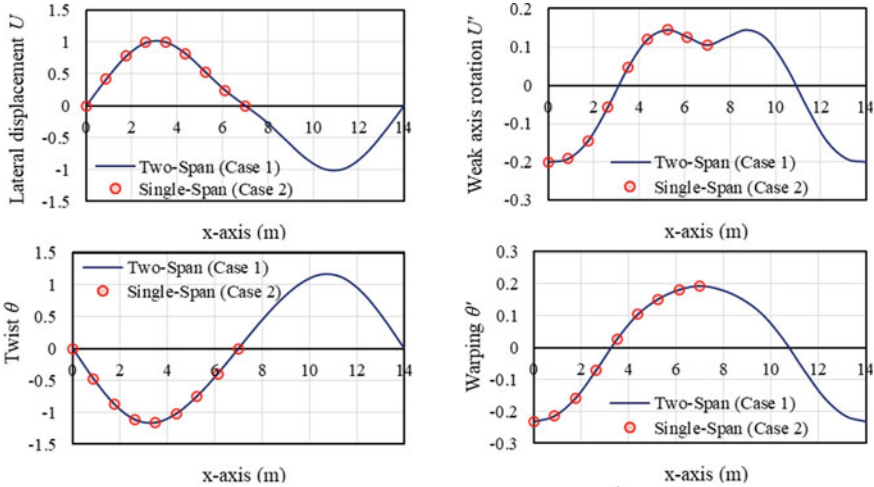
Fig. 4 Mode shapes for example when $L_2/L_1 = 1$

mode shape for $L_2/L_1 = 1$. In this case, both spans buckle identically on opposite sides (Fig. 4, U and θ), and no magnification is obtained by incorporating the effect of span L_2 into the FEA model. In fact, in this case, the critical moment corresponding to Case 1 in Fig. 3a is found identical to that of the critical moment corresponding to the idealized model of Case 2 in Fig. 3b. Thus, when $L_2/L_1 = 1$, it is evident that $m = 1$.

7 Evaluation of Critical Moments Predicted by Canadian Standard

As discussed, two cases are considered for each run (Fig. 3). To observe the difference between the FE-predicted critical moments and those predicted by CAN/CSA-S16 [2], the critical moments M_{cr1} and M_{cr2} were normalized relative to critical moments M_{CSA} as determined from CAN/CSA-S16 [2]:

$$M_{CSA} = \omega_{2-CSA} \frac{\pi}{L} \sqrt{EI_y GJ + \left(\frac{\pi E}{L}\right)^2 I_y C_w} \tag{8}$$

Figure 5 shows the normalized FE-predicted critical moments for both cases for all 4496 runs. As shown, Canadian standard predictions are slightly conservative when the short span is discarded from the model. The small difference between FEA predicted results and those based on CAN/CSA-S16 [2] is attributed to the approximate nature of the quarter point moment gradient factor adopted by the Canadian
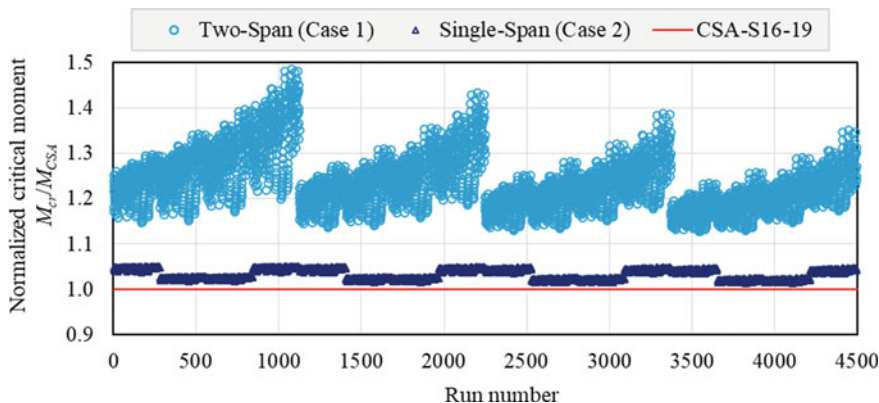
Fig. 5 Comparison between the FE results and those predicted by CAN/CSA-S16 [2] for all runs

standards. However, when the effect of span interaction is captured by modeling both spans (Fig. 3a), the predictions of CAN/CSA-S16 [2] become overly conservative as they do not account for the beneficial span interaction effect.

8 Effects of Input Parameters on ELTB

To investigate the effect of parameter $\rho_1 - \rho_4$ on the critical moment magnification factor m separately, a reference case is considered ($\rho_1 = 0.6$, $\rho_2 = 25$, $\rho_3 = 50$ and $\rho_4 = 200$). Each dimensionless parameter is then varied one at a time while maintaining the remaining three parameters constant and the resulting magnification factor m is plotted versus the varied parameter. As depicted in Fig. 6, the magnification factor m is found to increase with ρ_3, but to decrease with ρ_2. Given that ρ_4 does not affect m (Fig. 6d), it was removed from the input parameters when performing the regression analysis in the next section.

9 Artificial Neural Network

In total, 4496 FE runs were done and the corresponding magnification factors m (hereafter called target values or actual outputs) were obtained. Using the neural network toolbox in [27], a supervised ANN is employed to use the FE results and derive an empirical equation to predict m. The network architecture used in this paper consists of three layers: an input layer, a hidden layer, and an output layer (Fig. 7).

As Fig. 7 shows, there are three inputs that are fed into the network. Each input includes 4496 data points X. To increase the speed of learning process and achieve a more reliable network, input parameters X_i were first scaled to X_n using the *mapstd*
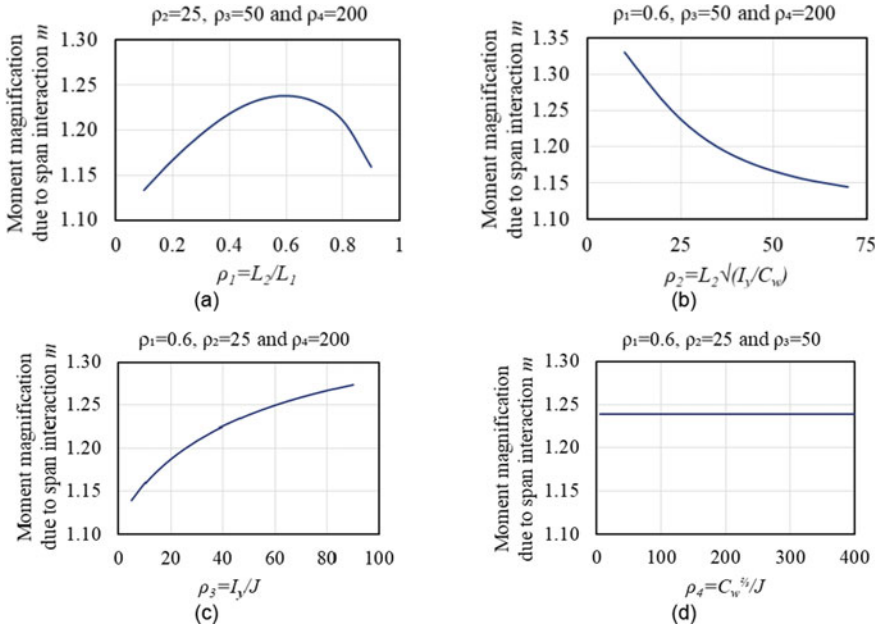
Fig. 6 Moment magnification due to span interaction m versus **a** ρ_1, **b** ρ_2, **c** ρ_3, and **d** ρ_4
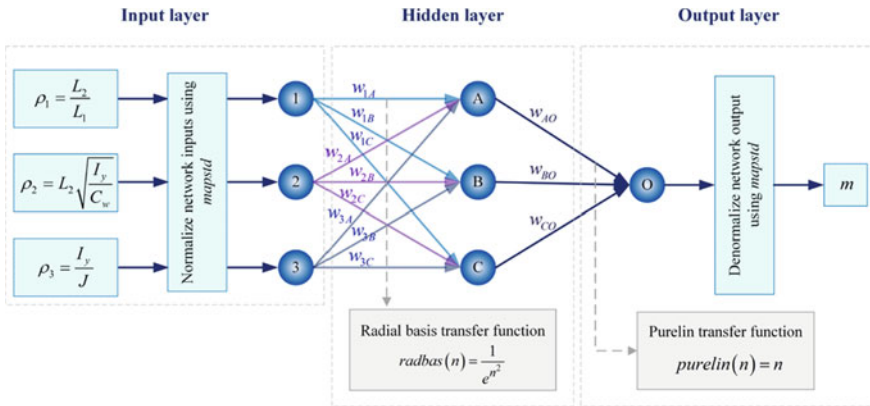
Fig. 7 Network architecture

function (Eq. 9). This function normalizes the inputs and output so that they have zero mean $\overline{X}$ and unity standard deviation X_{SD}.

$$X_n = \frac{X_i - \overline{X}}{X_{SD}} \tag{9}$$

A feedforward network was employed to map the inputs to the outputs. This network reduces the computational effort and the required memory capacity to store the weights [28]. To train the network, the Levenberg–Marquardt back-propagation algorithm was employed. The back-propagation algorithm uses the target and predicted values to adjust the connection weights. The Levenberg–Marquardt algorithm is very efficient for training networks that have up to a few hundred weights [15, 29]. To train, validate and test the network, 70%, 15%, and 15% of the data were selected randomly.

It has been shown that the number of neurons (or nodes) within the hidden layer significantly affects the accuracy of the output. The optimum value of this parameter was determined by a trial-and-error procedure to reach an adequate network performance. The performance of the network is examined through the correlation factor (R), Average Absolute percentage Error (AAE), and Maximum Absolute percentage Error (MAE):

$$R = \frac{\sum_{i=1}^{N}\left(Y_i - \overline{Y}\right)\left(T_i - \overline{T}\right)}{\sqrt{\sum_{i=1}^{N}\left(Y_i - \overline{Y}\right)^2 \times \sum_{i=1}^{N}\left(T_i - \overline{T}\right)^2}} \tag{10}$$

$$\text{AAE} = \frac{1}{N}\sum_{i=1}^{N}\left|\frac{Y_i - T_i}{T_i}\right| \times 100 \tag{11}$$

in which, Y_i is the predicted output, T_i is the actual output obtained from the FE analysis, $\overline{Y}$ is the average of the predicted outputs, $\overline{T}$ is the average of the actual outputs, and N denotes the number of samples.

For example, when 10 nodes were used in the hidden layer, the network was very efficient and AAE and MAE were reduced to 0.039% and 0.402%, respectively. However, having a large number of nodes in the hidden layer leads to more complex predictive equations which are difficult to use. By trial and error, it was found that using three nodes leads to a network with an acceptable level of accuracy. Figure 7 illustrates the architecture of the network in this study. Different transfer functions were used in the hidden and output layers, and the results were compared to identify the most efficient ones. It was found that both the Tan-Sigmoid and Radial basis functions can work very well in the hidden layer, and they lead to approximately the same performance. However, the Radial basis function gives a simpler appearance to the final predictive equation for m and hence was selected in the hidden layer. For the output layer, a linear transfer function was employed. Equation (12) provides the equation to predict the proposed m. For this equation, $R = 0.995$, $AAE = 0.367\%$, and $MAE = 2.54\%$. The actual and predicted values of m in training, validation, and testing sets are shown in Fig. 8.

$$m = 1.14 - \frac{1800}{e^{\beta_1^2}} + \frac{6500}{e^{\beta_2^2}} + \frac{0.104}{e^{\beta_3^2}}$$

$$\beta_1 = \left(98.9\frac{L_2}{L_1} + 2.18L_2\sqrt{\frac{I_y}{C_w}} + 4.74\frac{I_y}{J} + 2990 \right) \times 10^{-3}$$

$$\beta_2 = \left(280\frac{L_2}{L_1} - 22.8L_2\sqrt{\frac{I_y}{C_w}} + 0.915\frac{I_y}{J} - 3180 \right) \times 10^{-3}$$

$$\beta_3 = \left(1710\frac{L_2}{L_1} + 17.7L_2\sqrt{\frac{I_y}{C_w}} - 3.21\frac{I_y}{J} - 1030 \right) \times 10^{-3} \quad \text{(12a-d)}$$

In order to determine the importance of each input parameter, Garson's algorithm [30] was employed. The algorithm uses all weights connecting a specific input to the output variable, passing through the hidden layer. The process of quantifying the importance of input parameters using Garson's algorithm is summarized into the following four steps:

1. Forming the matrix containing input-hidden-output neuron connection weights (Fig. 7) of the trained network (Table 2).
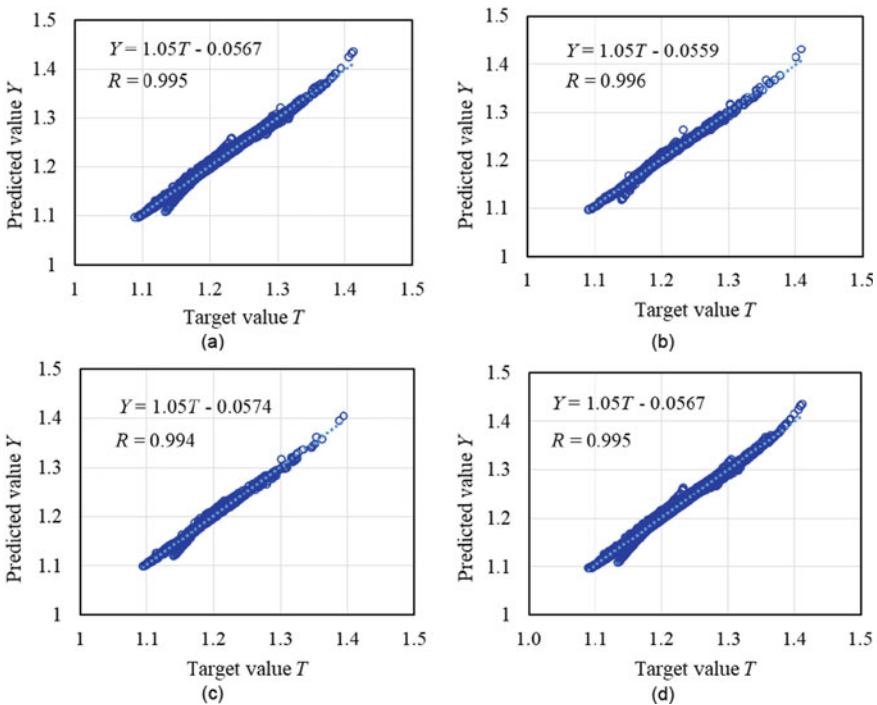
Fig. 8 Actual versus predicted values of m **a** training data, **b** validation data, **c** testing data, and **d** all data

Table 2 Connection weights

	Hidden A	Hidden B	Hidden C
Input 1	$w_{1A} = -0.0221$	$w_{1B} = 0.0627$	$w_{1C} = 0.381$
Input 2	$w_{2A} = -0.0275$	$w_{2B} = -0.287$	$w_{2C} = 0.223$
Input 3	$w_{3A} = -0.0808$	$w_{3B} = 0.0156$	$w_{3C} = -0.0547$
Output	$w_{AO} = -32757$	$w_{BO} = 118139$	$w_{CO} = 1.88$

Table 3 Contribution of inputs to the output through each hidden neuron

	Hidden A	Hidden B	Hidden C
Input 1	$c_{1AO} = 724$	$c_{1BO} = 7407$	$c_{1CO} = 0.716$
Input 2	$c_{2AO} = 901$	$c_{2BO} = -33906$	$c_{2CO} = 0.419$
Input 3	$c_{3AO} = 2647$	$c_{3BO} = 1843$	$c_{3CO} = -0.103$
Sum	4272	43156	1.24

Table 4 Relative contribution of inputs to the outgoing signal of each hidden neuron

	Hidden A	Hidden B	Hidden C	Sum
Input 1	$r_{1AO} = 0.169$	$r_{1BO} = 0.172$	$r_{1CO} = 0.578$	$S_1 = 0.919$
Input 2	$r_{2AO} = 0.211$	$r_{2BO} = 0.786$	$r_{2CO} = 0.339$	$S_2 = 1.34$
Input 3	$r_{3AO} = 0.620$	$r_{3BO} = 0.0427$	$r_{3CO} = 0.0830$	$S_3 = 0.746$

2. Determining the contribution of each input to the output via each hidden neuron as the product of the input-hidden connection and hidden-output connection, e.g., $c_{1AO} = w_{1A} \times w_{AO} = -0.0221 \times -32757 = 724$ (Table 3)
3. Determining the relative contribution of each input to the outgoing signal of each hidden neuron, e.g., $r_{1AO} = |C_{1AO}| / (|C_{1AO}| + |C_{2AO}| + |C_{3AO}|) = 724 / (724 + 901 + 2647) = 0.169$ and the sum of input contributions, e.g., $S_1 = r_{1AO} + r_{1BO} + r_{1CO} = 0.169 + 0.172 + 0.578 = 0.919$ (Table 4).
4. Obtaining the relative importance of each input variable, e.g., $RI_1 = S_1 / (S_1 + S_2 + S_3) \times 100 = 0.919 / (0.919 + 1.34 + 0.746) \times 100 = 30.6\%$

According to the above algorithm, the importance of parameters ρ_1, ρ_2, and ρ_3 are 30.6%, 44.5%, and 24.9%, respectively.

10 Design Example

This section provides an example to illustrate the process of considering the span interaction effect by using Eq. (12). Figure 9 shows the geometry of the example. Cross-sectional properties for the built-up wide flange beam investigated (Fig. 9b) are $I_z = 2.83 \times 10^8 \text{mm}^4$, $I_y = 3.13 \times 10^7 \text{mm}^4$, $J = 3.56 \times 10^5 \text{mm}^4$, and $C_w = 1.25 \times 10^{12} \text{mm}^6$. By omitting the span interaction effect, the critical moments of both
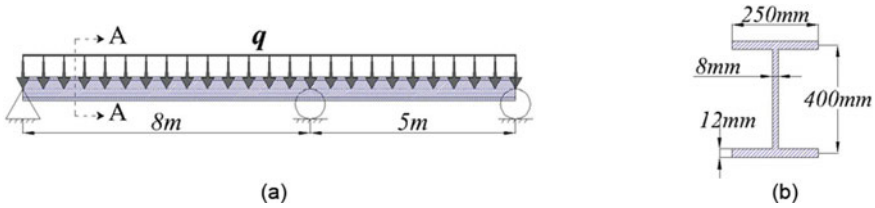
Fig. 9 Design example (1) spans and loading and (2) cross-sectional geometry (Section A-A)

spans are obtained from Eq. (8) as 359.2 kNm for the long span and 1758 kNm for the short span. The FEA predicted critical moment which accounts for span interaction is $M_{cr-FEA} = 469.4$ kNm, which lies between the critical moment of the short and long span, as expected.

In this example, the geometric dimensionless parameters are $L_2 / L_1 = 0.625$, $L_2\sqrt{I_y / C_w} = 25.0$, and $I_y / J = 87.7$. By using Eq. (12), one obtains $\beta_1 = 3.52$, $\beta_2 = -3.49$, $\beta_3 = 0.200$, and the critical moment magnification factor due to span interaction effect is $m = 1.27$. By multiplying the critical moment of the long span with m, one obtains the critical moment for the system $M_{cr-m} = 1.27 \times 359.2 = 456.2$ kNm, which is in close agreement with the corresponding FEA predicted value since $M_{cr-m} / M_{cr-FEA} = 0.97$. The 3% difference is appropriate for design purposes and is attributed, for the most part, to the approximation involved in the moment gradient factor equation provided by CSA-S16 (Eq. 6a) for single segments.

A more accurate value for the moment gradient factor can be obtained using FEA results in three steps: (1) isolating the span of interest and conducting an eigenvalue analysis to determine the critical moment for span under the moment distribution corresponding to the loading acting on the continuous system, (2) re-analyzing the isolated span under the action of uniform moments to obtain the uniform critical moment, and (3) dividing the critical moment obtained from step 1 by that from step 2. For the longer span in this example, the above procedure yielded a moment gradient factor of 1.47. This value compares to 1.42 based on CSA-S16 Eq. (6a) and is 1.45 based on the AISC360 moment gradient Eq. (6b).

It can be verified that the AISC360 moment gradient equation gives a closer prediction of the critical moment in this example. By substituting the value $\omega_{2-AISC} = 1.45$ into Eq. (8), the critical moment for the long span is obtained as 366.5 kNm and $M_{cr-m} = 1.27 \times 366.5 = 465.5$ kNm, which very closely matches that predicted by FEA as $M_{cr-m} / M_{cr-FEA} = 0.99$.

11   Summary and Conclusions

The present study developed a large database of finite element runs to characterize the critical moments for two-span beams that account for span interaction effects. Beam geometries were carefully selected to be representative of practical design situations and cross-sectional geometries. The critical moments were normalized with respect to the critical moment estimates based on the idealized condition which omits interaction effects. Using dimensional analysis, the normalized critical moment was postulated to depend on four dimensionless parameters, of which only three parameters turned out to be influential on the predicted normalized critical moments. The finite element analysis database was then used in conjunction with artificial neural network techniques to develop an accurate expression for computing the normalized critical moment as a function of the three dimensionless parameters. The proposed equation enables designers to quantify the critical moment of two-span beams under uniformly distributed load without resorting to iterative nor to finite element analysis.

References

1. ANSI/AISC360 (2016) Specification for structural steel buildings (ANSI/AISC 360-16). American institute of steel construction, Chicago-Illinois
2. CAN/CSA-S16 (2019) CSA S16: 19, design of steel structures, Toronto, Canada. Canadian standards association
3. Salvadori MG (1955) Lateral buckling of I-beams. Trans Am Soc Civ Eng 120(1):1165–1177
4. Nethercot D, Trahair N (1976) Lateral buckling approximations for elastic beams. Struct Eng 54(Analytic)
5. Trahair N (1977) Lateral buckling of beams and beam-columns. Theory Beam-columns 2:71–157
6. Trahair NS, Bradford MA (1988) The behaviour and design of steel structures. Chapman & Hall, London
7. Sahraei A, Pezeshky P, Mohareb M (2017) Lateral torsional buckling analysis and design of steel beams with continuous spans. In: Proceedings of the 6th international conference on engineering mechanics and materials
8. Ziemian RD (2010) Guide to stability design criteria for metal structures. Wiley
9. Barsoum RS, Gallagher RH (1970) Finite element analysis of torsional and torsional–flexural stability problems. Int J Numer Methods Eng 2(3):335–352
10. Vlasov V (1961) Thin-walled elastic beams. Jerusalem, Israel, Israel program for scientific translations
11. Hedayat AA, Jazebi E, AsadAbadi S, Iranpour A (2017) Flexural strength prediction of welded flange plate connections based on slenderness ratios of beam elements using ANN. Advances in civil engineering, 2018
12. Iranpour A, Hedayat AA, Afzadi EA (2019) Rotational demand and capacity of conventional single-plate shear connections subjected to gravity loading. Eng Struct 184:384–405

13. Hedayat AA, Afzadi EA, Kalantaripour H, Morshedi E, Iranpour A (2019) A new predictive model for the minimum strength requirement of steel moment frames using artificial neural network. Soil Dyn Earthq Eng 116:69–81
14. Limbachiya V, Shamass R (2021) Application of artificial neural networks for web-post shear resistance of cellular steel beams. Thin-Walled Struct 161:107414
15. Tohidi S, Sharifi Y (2015) Neural networks for inelastic distortional buckling capacity assessment of steel I-beams. Thin-Walled Struct 94:359–371
16. Hosseinpour M, Sharifi Y, Sharifi H (2020) Neural network application for distortional buckling capacity assessment of castellated steel beams. Elsevier, Structures
17. Sahraei A, Iranpour A, Mohareb M (2020) User manual for LTB-UO V3.0 (LTB-UO is a computer program for lateral torsional buckling analysis of beams/beam-columns, written at the University of Ottawa), University of Ottawa
18. Arizou R, Mohareb M (2022) Finite element formulation for distortional lateral buckling of I-BEAMS. Engineering structures. In press
19. Pezeshky P, Sahraei A, Mohareb M (2017) Effect of bracing height on lateral torsional buckling resistance of steel beams. In: Proceedings, 6th international conference on engineering mechanics and materials CSCE. Montreal, QC, Canada: Canadian Society for Civil Engineering
20. Sahraei A, Wu L, Mohareb M (2015) Finite element formulation for lateral torsional buckling analysis of shear deformable mono-symmetric thin-walled members. Thin-Walled Struct 89:212–226
21. Wu L, Mohareb M (2011) Buckling formulation for shear deformable thin-walled members—II. Finite element formulation. Thin-Walled Struct 49(1):208–222
22. Pezeshky P, Sahraei A, Mohareb M (2019) Distortional lateral torsional buckling analysis of beams with overhangs. J Struct Eng 145(3):04018266
23. Pezeshky P, Sahraei A, Rong F, Sasibut S, Mohareb M (2020) Generalization of the Vlasov theory for lateral torsional buckling analysis of built-up monosymmetric assemblies. Eng Struct 221:111055
24. Xie W, Mohareb M (2022) Elastic critical moment for monosymmetric beams under linear moment gradients. Can J Civ Eng 99(999):1–15
25. Pham PV, Mohareb M, Fam A (2018) Lateral torsional buckling of steel beams strengthened with GFRP plate. Thin-Walled Struct 131:55–75
26. CISC (2021) Handbook of steel construction, 12th edn. Canadian institute of steel construction
27. MATLAB (2020) The mathworks Inc., Natick, Massachusetts, United States, 488
28. Malinowski A, Cholewo TJ, Zurada JM (1995) Capabilities and limitations of feedforward neural networks with multilevel neurons. In: Proceedings of ISCAS'95-international symposium on circuits and systems, IEEE
29. Marquardt DW (1963) An algorithm for least-squares estimation of nonlinear parameters. J Soc Ind Appl Math 11(2):431–441
30. Garson DG (1991) Interpreting neural network connection weights

Gusset Plate Compression Capacity Prediction Using Ensemble Machine Learning Models

Palisa Arafin and A. H. M. Muntasir Billah

Abstract Gusset plates have a vital role in aspect of stability and behaviour of bracing system and truss bridges, especially under compression, where the strength of the gusset plate connections is highly depended on boundary conditions and plate geometry. Even with an extensive amount of existing study and analysis, due to the complexity of the stress distribution mechanism in the connection area a high amount of uncertainty still remains in compressive strength design methods. With the growing interest of machine learning (ML) approach in performance evaluation of a structure, this study aims to develop a gusset plate compressive strength prediction model using the regression and ensemble machine learning techniques named support vector regression (SVR), decision tree regression (DT), XGBoost (XB), CATBoost (CB) and AdaBoost (AB), while avoiding the crude assumptions and complex calculations. These ensemble models are performed on a database of 68 experimental and 184 numerical datasets. In terms of performance evaluation, XB and CB have outperformed compared to the conventional design practice and empirical solutions, with an accuracy of 96% and 95%, respectively. To explain the models' feature importance and performance evaluation, Shapley Additive exPlanations (SHAP) is used. After analysis with the existing empirical equations—Thornton (Eng J 21(3):139–148, [1]) and Chou et al. (Earthq Eng Struct D., 41(7):1137–1156, [2]), it is found that CB has shown the best performance in predicting the compressive strength of gusset plate with the lowest mean absolute error of 50.76 kN and Nash–Sutcliffe model efficiency coefficient of 0.984 compared with the existing methods, where the Modified Thornton method has achieved the highest accurate prediction among the existing methods with mean absolute error and Nash–Sutcliffe model efficiency coefficient of 227.22 kN and 0.872, respectively.

Keywords Gusset plate · Compression capacity · Machine learning

P. Arafin · A. H. M. M. Billah (✉)
Department of Civil Engineering, Lakehead University, Thunder Bay, ON, Canada
e-mail: habillah@lakeheadu.ca

P. Arafin
e-mail: parafin@lakeheadu.ca

1   Introduction

In seismic-prone areas, especially in North America, concentrically braced frames (CBFs) and buckling restrained braced frames (BRBFs) are considered to be a better solution to resist the seismic lateral forces. Considering the capacity-based design, CBFs and BRBFs are designed as such that the brace members are expected to experience plastic deformation, whereas the components, like columns, beams and connections, between the members show elastic behaviour. Conventionally, gusset plates are used to strengthen these connections between the bracing members and the framing elements, and also to link the truss members of the bridges at conjunction points. Keeping the high seismic loading in mind, detail gusset plate design is required to withstand any brittle failure while indulging significant inelastic deformation [3–5]. In most cases, gusset plates in the BRBF structure fail in buckling mode, as these plates experience a high range of compressive forces in its lifetime [6, 7]. Typically, under compression various parameters like gusset plate dimension and boundary conditions affect the behaviour of gusset plate. Among all the forces, gusset plate's connection with CBFs is most vulnerable when the bracing system faces tension forces. In view of design concepts, bracing components and gusset plates are designed considering the compressive strength and have adverse effect under tension [8]. In previous studies, the adversity of these connections under seismic occurrences is studied in depth. From the post-earthquake investigation and the experimental studies, it is observed that inadequate detailing can result in premature brittle failure and inelastic deformation [1, 9]. Accommodating the complex behaviour of internal stress distribution of gusset plate is not quite easy, which has lead the designers to follow a more straightforward design method. One conventional assumption in gusset plate design is the apprehension of the buckling capacity of gusset plate equivalent to column buckling capacity. However, this simplified approach results in higher inaccuracy. Therefore, for steel-framed structures it is required to develop a robust technique to design a reliable and durable gusset plate connection.

Previously, many researchers conducted experimental and numerical studies on the behaviour of gusset plate. Ref. [10] experimentally studied the two most important features of the gusset plate connection—the compressive behaviour and the ultimate strength. They observed sway buckling failure and a significant amount of yielding before reaching the ultimate capacity. Ref. [11] did a numerical analysis using finite element (FE) software ABAQUS to understand the interconnection relation between brace members and the gusset plate. The authors concluded that the best simulation of gusset plate under cyclic loading can be achieved by using an elastic-perfectly plastic material model while considering some initial imperfections.

In case of designing the gusset plate, [12] used the AISC column curves to recommend a design procedure with the equivalent column analogy method (also known as the effective length factor method). The primary assumptions of this study were: taking the gusset plate compressive strength equal to Whitmore width [13] and Thornton buckling length. Unfortunately, later on, this study was proved inaccurate and highly conservative. To improve this existing Thornton method, [14] advanced

to modified Thornton method to recall the inaccuracies. The improvements were: firstly to calculate the Whitmore width they considered a dispersion angle 45° and then validated analysis excrementally showing less conservative buckling capacity estimations [10, 15]. Among many other studies, [6] proposed an improvement on Thornton method by using Euler column buckling curve, and it gave a more conservative prediction.

Previously several studies have investigated the behaviour of gusset plate under different loading criteria to solve the complicated measures in order to predict the gusset plate compressive strength more precisely [4, 16, 17]. A nonlinear model of gusset plate in connection with truss bridge members was suggested by ref. [18] and resulted effective in global analysis of connection performance. Fang et al. [12] studied the connection of gusset plate and single-sided splice members numerically, analytically and experimentally. This study provided the information on different failure modes of eccentrically loaded gusset plates and suggested a design solution for each of that failure modes.

With the extensive previous studies on gusset plate, machine learning (ML) techniques have opened a new window towards reliable prediction of structural behaviour. Researchers have already implicated ML in determination of structural capacities and failure mode [18–20]. Feng et al. [18] used interpretable XGBoost model to predict the shear capacity of squat reinforced concrete walls with an accuracy of 97%. Reference [21] showed that support vector regression (SVR) and artificial neural network (ANN) models have made successful predictions on resistance of steel columns in fire. In case of seismic analysis for steel moment frame buildings and bridges, data-driven methods have achieved a great potentiality in current times [19, 22, 23]. Unfortunately, the conventional ML models have interpretability issue, whereas ensemble learning ML models like boosting trees (XGBoost, AdaBoost and CatBoost) mitigate these issues and provide a more robust and accurate results [18]. Finally, it can be stated that the robustness of the ensemble learners as powerful ML models is bringing popularity in the structural engineering and design community.

For gusset plate compressive strength analysis, most of the previous studies adopted simplified approaches and consequently are unable to identify all the complex relations among material properties, geometric properties and boundary conditions. Therefore, the predictions of compression capacity are restrained in many ways. This study aims to develop a comprehensive ML technique, taking account of complex interactions between different parameters, to predict the compressive strength of the gusset plate with a higher precision avoiding the oversimplified assumptions. The developed ML models take account of different parameters, such as geometric and material properties and boundary conditions to interpret the in-depth relation between these parameters. Here, Shapley Additive exPlanations (SHAP) is used to discuss the interpretability of the results with the variables. Consequently, a comparison of ML results is done with the existing empirical equations.

2   Database for Gusset Plate Compressive Strength Analysis

To develop a comprehensive ML technique with high prediction accuracy and to identify the most important features, a detailed and extensive database is the primary requirement. For this study, 252 experimental and validated numerical data is collected, from the previous study conducted from 1987 to 2016. Most of the experimental data is taken from the testing conducted at University of Alberta [5, 6, 24, 25]. Remaining dataset is built with results from validated numerical analysis results (184) considering a variety of parameters, like gusset plate material and geometric properties [12, 14, 16, 17, 26, 27]. Finite element (FE) simulation can provide a thorough understanding and flexible modelling scope when analysing the structure with a vast range of parameters reducing the extensive labour and cost of experiments. Moreover, some literatures have identified that these numerical results help in creating a complex database for ML model development, which ultimately increase the fidelity of the model performance [19, 21, 26, 28, 29].

This study aims on predict the ultimate compressive strength of gusset plate considering the buckling failure mode, and the dataset only includes the results of buckling failure. While performing the ML simulations, ultimate strength of gusset plate (Pu) is taken as output feature, whereas the input features consist of steel yield strength (F_y), gusset plate thickness (t), plate cantilever length (C), connection length (L_c), fastener distance perpendicular to the axis of braces (S) and plate buckling length (L). These input parameters are considered to have the most influence on predicting the compressive strength of gusset plate in the past researches [7, 12, 26]. Figure 1a and b demonstrates the various input variable of gusset pate for both welded and bolted connection, respectively. Figure 2 illustrates the effects of input parameters on the compressive strength of gusset plate. From Fig. 2a, it is observed that with the increment in F_y, the compressive buckling capacity of gusset plate increased. Also, the buckling capacity increased with the increase of plate thickness up to 12 mm (Fig. 2b) compiling with the findings of [10] and [30], whereas the Pu has a boost when the parameter L decreased (Fig. 2c). Again, the buckling capacity has taken a rise with the increment of Lc (Fig. 2e), which actually aligns with the study of [7].

3   Overview of ML Models

ML method is well known for its state-of-the-art performance and has gained a lot of attraction from researchers. For this study, five ML techniques are developed to make a comparison of the performance of these models and identify the best performed model in predicting the compressive capacity of the gusset plate. The five ML techniques are: decision tree (DT), support vector regression (SVR), XGBoost (XG), AdaBoost (AB) and CatBoost (CB). Here, DT is a flow chart-like tree structure algorithm which uses a decision tool from training data of various variables to predict the output result. For SVR, simple class separation technique works to find the least error
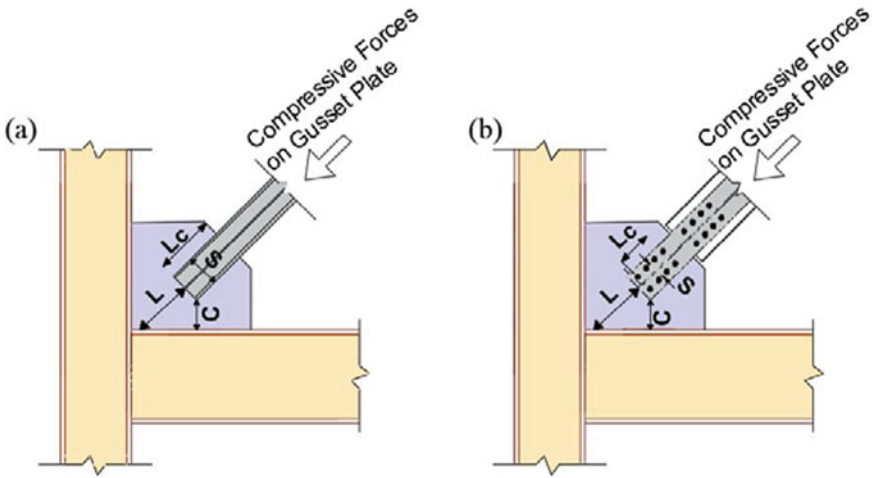
Fig. 1 Schematic diagram of **a** welded and **b** bolted gusset plates used in model development
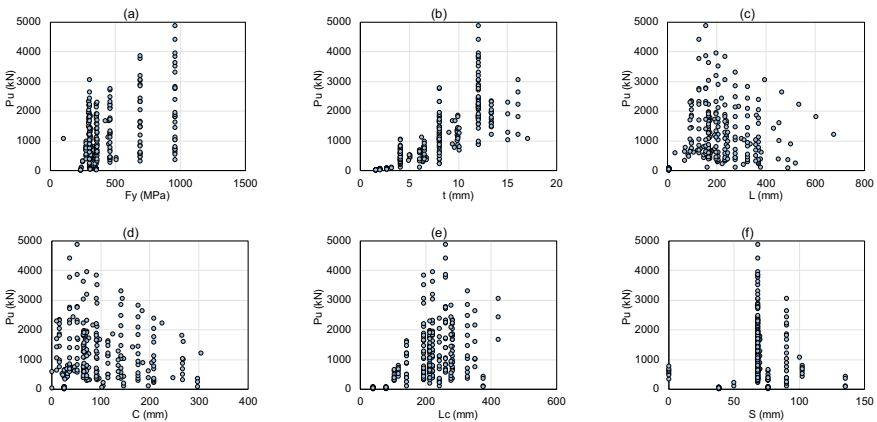
Fig. 2 Effect of input parameters on compressive strength of gusset plates

prediction based on the comparison of new data and training dataset. This study used three types of boosting framework with different boosting features—XG, AB and CB. XG is based on decision tree algorithm combining with a gradient descent algorithm helping the model to minimize the error. AB has an adaptive boosting feature that combines weak learning algorithm in order to achieve the best performance. CB algorithm consists of two important features—category and boosting. Both these features create an oblivious tree by building a rule to make all the predictions maintaining all the nodes at same level. This paper has sufficiently considered few fundamental types of ML methods to comprehend the models outcome satisfactorily.

3.1   SHAP for Feature Importance Analysis

To analyse the relationship between the input parameters and output result, this study implemented the interpretable ML modelling system. Interpretability can be defined as the user-friendly model-agnostic technique that helps understanding the significance of a particular output from a given model [22]. SHAP, an extensive state-of-the-art algorithm for ML model explanation system, gives interpretability to input and output results and ranks the importance of the features. This study used the Global Interpretability feature of the SHAP to compare the importance of various features on the prediction, and to explain the contribution of the parameters either positive or negative. Here, for Global Interpretability the "summary.plot" system is used to explain the outperformed prediction model. It is to be mentioned that using interpretable ML models to explain the complex phenomena of input and output features is important for understanding the feature importance [15, 18, 21, 30, 31], and therefore, the result of this study can provide confidence in reliable prediction of gusset plate compressive capacity.

3.2   K-Fold Cross-Validation

To ensure the robustness of the model's performance, cross-validation is performed that uses a resampling procedure which evaluates the accuracy of the model on a limited randomly selected dataset. Here, *k*-fold represents the number of splits done to the original train dataset. In cross-validation, the training dataset is sub-divided into training and validation set, and the model is trained on the majority of the data, whereas the validation set is used to evaluate the performance. This study used tenfold cross-validation, dividing the training dataset into 10 subsets. Within these 10 subsets, only one is used to validate the performance, while the rest works as test set, and this process continues till each subset is considered for cross-validation. Finally, the average of all the results from cross-validation is taken as the final output.

4   Interpretation of Results

To start the ML model analysis, the database is divided into two sets—training dataset and testing dataset, where the training dataset is used to train the model to learn from the features and the testing dataset is used to predict the output value based on the prior learning. This study has followed the common adoption of dividing the dataset into 80% for training purpose, and the rest 20% is used as testing dataset. Previously, [15, 19, 21, 32] have adopted 80/20 test/train ratio for their study and achieved high accuracy in model development. After the data processing, the training dataset is further analysed to get the optimized values of the hyper-parameters for the best

Table 1 List of hyper-parameters

Model	Hyper-parameters	Value
SVR	a. C	5
	b. Degree	1
DT	a. Random State	5000
RF	a. Random State	2
	b. Number of Estimators	1
XGB	a. Number of Estimators	100
	b. Learning rate	0.1
AdaB	a. Random State	30
	b. Number of Estimators	50
CatB	a. Iterations	700
	b. Learning Rate	0.02
	c. Eval_metric	RMSE
	d. Random_seed	23

fitting performance. Table 1 shows the summary of the hyper-parameters applied in this study for all the ML models.

4.1 Summary of ML Model Results Using k-fold Cross-Validation

A boxplot diagram in Fig. 3 illustrates the final results of all the ML models after the cross-validation, where the boxes represent the interquartile range, and the mid-straight line shows the median values. The top and bottom whiskers represent data 1.5 times higher of the difference between the first and third quartiles, respectively. For all the model, the maiden accuracy varies from 50% for SVR to 92% for CB. After analysing the summary of the final cross-validation results of all the models, CB has achieved the highest maiden accuracy of 92% and has the least difference between first and third quartile. Subsequently, XB has the second highest maiden accuracy of 88%, having a similar range of difference between first and third quartile as CB. To further explore the results of the ML models, some evaluation metrics–coefficient of determination (R^2), root mean squared error (RMSE), mean absolute error (*MAE)*, Nash–Sutcliffe model efficiency coefficient (NSE), and index of agreement (*d*) are used (Table 2). The complete performance evaluation results of ML models after tenfold cross-validation are summarized in Table 3. Table 3 shows that XB and CB have got the best R^2 score of 0.935 and 0.941, respectively. On the other hand, SVR has the lowest R^2 score (0.606). In case of metrics MAE and RMSE, XB has the lowest value of 113.409 kN and 170.94 kN, respectively. It is also observed that
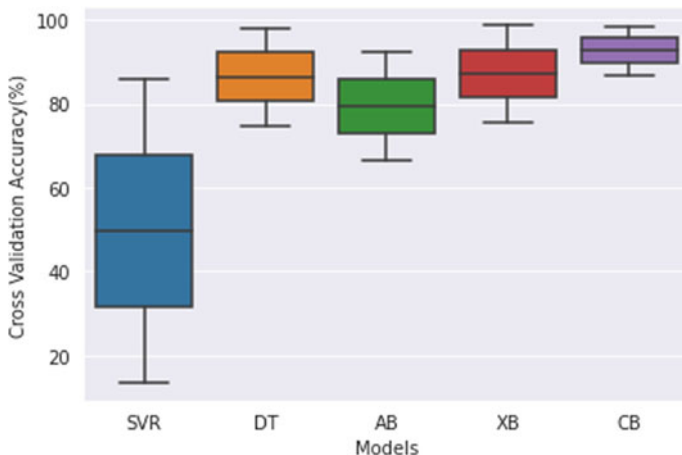
Fig. 3 Cross-validation accuracy results for ML models

Table 2 Formulas for the evaluation metrics

Performance measure	Notation	Formula
Coefficient of determination	R^2	$R^2 = 1 - \frac{\sum_{i=1}^{m}(P_i - A_i)^2}{\sum_{i=1}^{m}(P_i - \overline{A})^2}$ Here, A_i denotes as actual data and P_i as the predicted; $\overline{A}$ denotes the average value of actual data; $i = 1, 2, 3 \ldots m$ indicates the number of samples
Root mean squared error	RMSE	$\text{RMSE} = \sqrt{\frac{\sum_{i=1}^{m}(P_i - A_i)^2}{m}}$
Mean absolute error	MAE	$\text{MAE} = \frac{\sum_{i=1}^{m}|P_i - A_i|}{m}$
Nash–Sutcliffe model efficiency coefficient	NSE	$\text{NSE} = 1 - \frac{\sum_{i}^{m}(A_i - P_i)^2}{\sum_{i}^{m}(A_i - \overline{A})^2}, \; -\infty < \text{NSE} \leq 1$
Index of agreement	d	$d = 1 - \frac{\sum_{i}^{m}(A_i - P_i)^2}{\sum_{i}^{m}(|A_i - \overline{A}| + |P_i - \overline{A}|)^2}, \; 0 < d \leq 1$

CB has the second-best performance with MAE and RMSE score 125.72 kN and 184.88 kN, respectively.

4.2 Interpretation of XB and CB Models Result with SHAP Vales

Using the Global Interpretability, the input features importance for XB and CB is shown in Fig. 4a and b. On the plot, Y-axis represents the input features ranked from

Table 3 Performance measures of train and test dataset

Model	Training data (80%)			Testing data (20%)			Tenfold Cross-Validation
	RMSE (kN)	R^2	MAE (kN)	RMSE (kN)	R^2	MAE (kN)	Mean R^2
SVR	543.461	0.656	304.591	666.456	0.522	344.287	0.606
DT	51.610	0.997	16.797	278.733	0.916	196.329	0.895
[a]**XB**	**84.568**	**0.992**	**60.744**	**170.939**	**0.969**	**113.409**	**0.935**
AB	256.844	0.923	218.248	299.131	0.904	214.776	0.842
[a]**CB**	**86.788**	**0.991**	**63.036**	**184.882**	**0.963**	**125.723**	**0.941**

[a] Best Performed Model

top to bottom in order of highest to lowest importance, whereas along the horizontal lines each red point and blue point indicates high impact and low impact, respectively. For both cases, gusset plate thickness (t) is the most importance feature, and fastener distance perpendicular to the brace axis (S) is the least important feature. In case of thickness (t), the red points have positive SHAP value indicating that higher the thickness gives more compressive strength to the gusset plate. Previously in parametric studies, it is discovered that with the increase in gusset plate thickness, the buckling capacity also increased and vice versa [7, 12, 25].

Following the thickness, for both models the second and third most important features are steel yield strength (F_y) and the connection length (L_c). With the increment of F_y and L_c, the SHAP values have also increased in positive direction, implying that the gusset plate buckling capacity increases with the higher range of F_y and L_c.
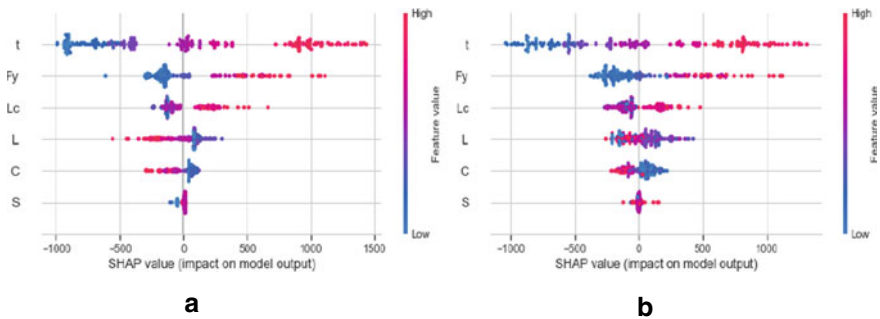
Fig. 4 SHAP summary plot for **a** XB and **b** CB models

4.3   Comparison of Empirical Equations with ML Models Results

To monitor the proficiency of the ML models developed in this study, three existing design methods [12], Chou et al. [1] results are compared, and the formulas are presented in Table 4. Later on, a verification of empirical equations and best-performed ML models is done on the predicted buckling capacity (P_{pred}) versus experimental buckling capacity (P_u) graph using a 1:1 diagonal line (Fig. 5). The points above the 45° line indicate the unsafe prediction, whereas the points below the line represent the safe design. It is observed that [12] has the most points below the diagonal line indicating a conservative solution, whereas the has less conservative nature as most of the points are staying along the diagonal line. Among all the empirical equations Chou et al. [1] have the most points under the diagonal line, resulting to have the most conservative solution. This finding is also mentioned where Chou et al. [1] were mostly conservative in nature. On the other hand, the XB and CB have predicted the results most accurately adhering the data points close to the diagonal line. This indicates that the ML models outperformed the existing empirical methods.

Figure 6a and b shows the result of root-mean-squared error (RMSE), mean absolute error (MAE), index of agreement (*d*) and Nash–Sutcliffe model efficiency coefficient (NSE). Also, a summary of the existing methods performance and best-performed ML models from this study is given in Table 5. According to the performance standard, the developed ML models for this study should have a low value of RMSE and MAE, and NSE and *d* values close to 1.00. For NSE and index of agreement (*d*), 1.00 represents the absolute compliance of the experimental values and predicted values, whereas 0 indicates no correlation. Figure 6 shows that in case of empirical methods Modified Thornton method achieved the lowest RMSE and MAE score (335.587 kN and 227.217 kN, respectively), followed by the highest value of *d* (0.973) and NSE (0.872). Figure 6 also illustrates that both the lowest value of RMSE and MAE and the highest value of NSE and *d* are achieved by the ML model CB, proving that CB has outperformed all the empirical methods and other ML models. CB has shown RMSE and MAE score 119.37 kN and 50.76 kN, respectively, with the highest score of NSE (0.984) and *d* (0.996).

4.4   Variation in Prediction to Experimental Compression Capacity Ratio

The variation of predicted to experimental ratio in terms of the dataset for all the existing empirical methods and the best-performed ML models of this study is summarized in Table 6 and Fig. 7. Here different parameters like- mean, standard deviation (SD), and coefficient of variance (CoV) of predicted to experimental capacities are mentioned. The higher *CoV* implies the higher dispersion in the mean of available data points, therefore accuracy goes downward. Among all the existing

Table 4 Equations for the existing methods adopted for comparison

Model	Equation	Column curve	Effective width	Length	Effective length factor
Thornton Method [2]	$r = \frac{t}{\sqrt{12}}$ $\lambda_c = \frac{kL}{\pi r}\sqrt{\frac{F_y}{E}}$ $P_{cr1} =$ $0.658^{\lambda_c^2} F_y b_e t$, when $\lambda_c < 1.5$ $P_{cr2} = \frac{0.877}{\lambda_c^2} F_y b_e t$, when $\lambda_c > 1.5$	AISC	Whitmore $\theta = 30°$	Average Thornton	0.65
	$r = \frac{t}{\sqrt{12}}$ $\lambda_c = \frac{kL}{\pi r}\sqrt{\frac{F_y}{E}}$ $P_{cr1} =$ $0.658^{\lambda_c^2} F_y b_e t$, when $\lambda_c < 1.5$ $P_{cr2} = \frac{0.877}{\lambda_c^2} F_y b_e t$, when $\lambda_c > 1.5$	CAN/ CSA-S16.1-M89	Whitmore $\theta = 45°$	Splice plate end to beam/column	0.65
[6]	$r = \frac{t}{\sqrt{12}}$ $\lambda_c = \frac{kL}{\pi r}\sqrt{\frac{F_y}{E}}$ $P_{cr1} =$ $0.658^{\lambda_c^2} F_y b_e t$, when $\lambda_c < 1.5$ $P_{cr2} = \frac{0.877}{\lambda_c^2} F_y b_e t$, when $\lambda_c > 1.5$	AISC	Whitmore $\theta = 30°$	Average Thornton	2.0

method [6] has the highest *CoV* of 1.334, with a mean of 0.305 and *SD* of 0.420 indicating the poor performance. On the other hand, has the lowest *CoV* (0.557) implicating the conservative nature. Out of the developed ML models in this study, CB and XB has showed a mean ratio very close to 1.00. In comparison with XB, CB model's data points are less scatted with $SD = 0.146$ and $CoV = 0.147$, whereas XB has showed a little higher value of *SD* (0.235) and *CoV* (0.232) than CB. So it is evident that CB is the best performed model compare to the existing methods and ML models.
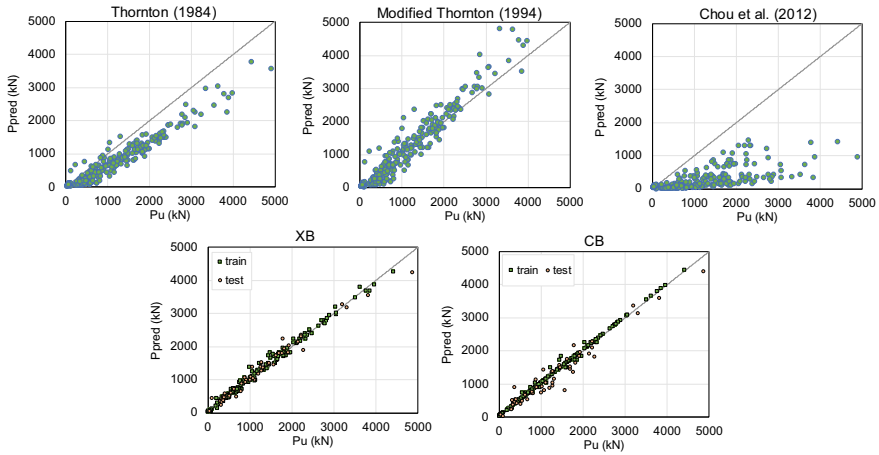
Fig. 5 Comparison between experimental and predicted results of gusset plate based on empirical equation and ML models
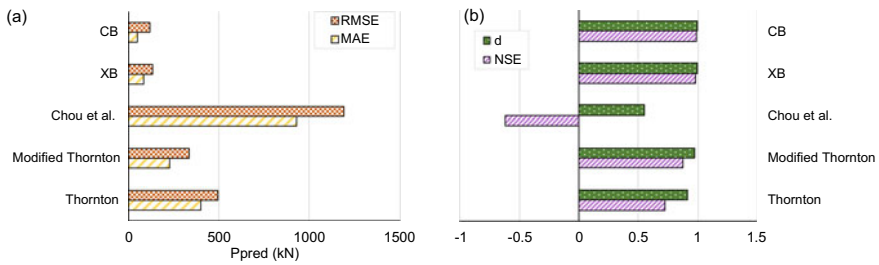
Fig. 6 Comparison between experimental and predicted results based on **a** MAE and RMSE **b** NSE coefficient and d

Table 5 Summary of the existing methods performance and best-performed ML models

Methods	MAE	RMSE	NSE	d
[12]	401.153	495.197	0.721	0.913
	227.217	335.587	0.872	0.973
[6]	927.030	1192.545	−0.620	0.546
XGB (Current study)	86.396	136.026	0.980	0.995
[a]CatB (Current study)	**50.759**	**119.369**	**0.984**	**0.996**

[a] Best Performed Model

Table 6 Statistical measure of predicted to experimental capacity ratio for the existing methods and current study

Method	P_{pred}/P_u		
	Mean	SD	CoV
[12]	0.735	0.418	0.569
	1.133	0.631	0.557
[6]	0.305	0.407	1.334
XB (current study)	1.013	0.235	0.232
CB (current study)	0.991	0.146	0.147
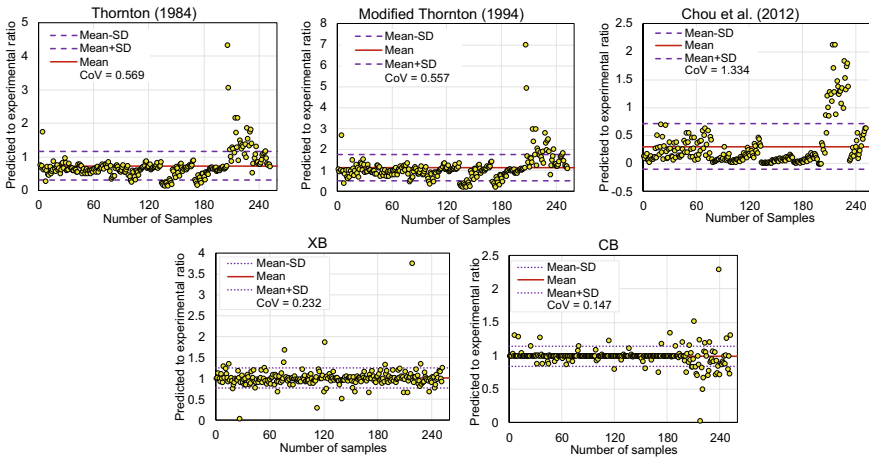
Fig. 7 Variation in predicted to experimental gusset plate compressive strength ratio

5 Conclusion

The primary aim of this study is to develop ML models with higher accuracy for prediction of compressive strength of gusset plate. To develop the ML models, the database is created with experimental and numerical results from previous literature. The dataset incorporates various parameters including- steel yield strength, gusset plate thickness, plate cantilever length, connection length, fastener distance perpendicular to the axis of braces, and plate buckling length. This database is then used in five machine learning techniques- support vector regression (SVR), decision tree regression (DT), XGBoost (XB), AdaBoost (AB) and CatBoost (CB) to identify the specific ML model with the highest accuracy. To achieve the best accuracy various hyper-parameters and tenfold validation technique is imposed. After developing the models SHaply Additive exPlanations is used to make the ML models interpretable by ranking the effect of the input features on the output. To evaluate the performance of the ML models with high confidence, this study also explored some existing empirical design methods- Thornton method [2] (the most commonly used design

method) and method by Chou et al. [6]. Following is the summary of the comparison between the empirical equation results and ML models results:

- With the hyper-parameter tuning and tenfold validation it has came forth that CB has significantly outperformed all the other developed ML models. After CB, XB has ranked as the second best-performed model to predict the compressive strength of gusset plate.
- The parametric study conveys that gusset plate buckling capacity increases with the increment in plate thickness, and also one of the most important input feature to positively affect the capacity. Also, the SHap value has recognized the plate thickness (t) as the most important feature for both XB and CB, followed by steel yield strength and connection length.
- The comparison among the empirical equations has provided more conservative results, and out of these equations modified Thornton method performed best. This method has achieved the least mean absolute and root mean squared error of 227.22 kN and 335.59 kN, respectively. Also it has the highest agreement index and Nash–Sutcliffe model efficiency coefficient (0.973 and 0.872, respectively).
- Considering the mean value of XB and CB based on the predicted to experimental ratio, both models have acquired a ratio of 1.00. Within these two models CB has the lowest standard deviation (0.146), least mean absolute and root mean squared error of 50.759 kN and 119.369 kN, respectively with an agreement score and Nash–Sutcliffe model efficiency coefficient close to 1.0.

References

1. Davaran A, Tremblay R, Beland T, Fahnestock LA, Hines E (2014) Experimental behavior of low-ductility brace connection limit states. Struct Congr 2014:2429–2441
2. Hadianfard MA, Khakzad AR (2016) Inelastic buckling and post-buckling behavior of gusset plate connections. Steel Compos Struct 22(2):411–427
3. Lehman DE, Roeder CW, Herman D, Johnson S, Kotulka B (2008)Improved seismic performance of gusset plate connections. J Struct Eng 134(6):890–901
4. Sabelli R, Saxey B, Li C-H, Thornton WA (2021) Design for local web shear at brace connections: an adaptation of the uniform force method. Eng J 58(4):223–265
5. Tremblay R, Castonguay P, Guilini-Charette K, Koboevic S (2010) Seismic force demand on brace connections of conventional construction braced steel frames designed according to Canadian seismic provisions. Struct Congr 2010:1361–1372
6. Chou CC, Liu JH, Pham DH (2012) Steel buckling-restrained braced frames with single and dual corner gusset connections: seismic tests and analyses. Earthq Eng Struct D 41(7):1137–1156
7. Wong A, Too V, Colunga SV, Lee C (2019) Buckling capacity of gusset plates derived from stability functions. In: 2019 Pacific conference on earthquake engineering, New Zealand Society for Earthquake Engineering. SkyCity, Auckland, New Zealand

8. Naghipour M, Abdollahzadeh G, Shokri M (2013) Analysis and design procedure of corner gusset plate connection in BRBFs. Iran J Energy Environ 4(3)
9. Tremblay R, Filiatrault A, Timler P, Bruneau M (1995) Performance of steel structures during the 1994 Northridge earthquake. Can J Civ Eng 22(2):338–360
10. Yam MC, Cheng J (1993) Experimental investigation of the compressive behavior of gusset plate connections. Structural engineering report no. 194. University of Alberta. Edmonton, Alberta, Canada
11. Walbridge SS, Grondin GY, Cheng J (1998) An analysis of the cyclic behaviour of steel gusset plate connections. Structural engineering report no. 225. Edmonton, Alberta, Canada. University of Alberta
12. Thornton WA (1984) Bracing connections for heavy construction. Eng J 21(3):139–148
13. Rahman J, Ahmed KS, Khan NI, Islam K, Mangalathu S (2021) Data-driven shear strength prediction of steel fiber reinforced concrete beams using machine learning approach. Eng Struct 233:111743
14. Yam MCH, Cheng J (1994) Analytical investigation of the compressive behavior and strength of steel gusset plate connections. Structural engineering report no. 207. University of Alberta. Edmonton, Alberta, Canada
15. Yam MC, Cheng J (2002) Behavior and design of gusset plate connections in compression. J Constr Steel Res 58(5–8):1143–1159
16. Cheng J, Hu S (1987) Compressive tests of gusset plate connections. In: Proceedings of the 1987 annual technical session, structural stability research council, (SSRC)
17. Guan X, Burton H, Shokrabadi M, Yi Z (2021) Seismic drift demand estimation for steel moment frame buildings: from mechanics-based to data-driven models. J Struct Eng 147(6):04021058
18. Crosti C, Duthinh D (2014) A nonlinear model for gusset plate connections. Eng Struct 62:135–147
19. Almustafa M, Nehdi M (2020) Machine learning model for predicting structural response of RC slabs exposed to blast loading. Eng Struct 221:111109
20. Cheng J, Rabinovitch JS (1993) Cyclic behavior of steel gusset plate connections. Structural engineering report no. 191. University of Alberta. Edmonton, Alberta, Canada
21. Tong Q, Couto C, Gernay T (2021) Predicting the capacity of slender steel columns at elevated temperature with finite element method and machine learning. Applications of structural fire engineering. Ljubljana, Slovenia
22. Molnar C (2020) Interpretable machine learning. A Guide for making black box models explainable. Accessed 14 Oct 2021. https://christophm.github.io/interpretable-ml-book/
23. Naser M, Thai S, Thai H-T (2021) Evaluating structural response of concrete-filled steel tubular columns through machine learning. J Build Eng 34:101888
24. Deliktas B, Mizamkhan A (2014) Modeling nonlinear behavior of gusset plates in the truss based steel bridges. Struct Eng Mech: Int J 51(5):809–821
25. Sheng N, Yam C, Iu V (2002) Analytical investigation and the design of the compressive strength of steel gusset plate connections. J Constr Steel Res 58(11):1473–1493
26. Feng D-C, Fu B (2020) Shear strength of internal reinforced concrete beam-column joints: intelligent modeling approach and sensitivity analysis. Advan Civil Eng
27. Nast TE (1999) Cyclic behavior of stiffened gusset plate-brace member assemblies. Master's Thesis, University of Alberta
28. Fu F (2020) Fire induced progressive collapse potential assessment of steel framed buildings using machine learning. J Constr Steel Res 166:105918
29. Zarringol M, Thai H-T, Naser M (2021) Application of machine learning models for designing CFCFST columns. J Constr Steel Res 185:106856

30. Cheng R, Xu L, Jin S, Shi Y (2016) Compressive behavior of gusset plates connected with single-angle members. J Struct Eng 142(3):04015161
31. Zhao X, Lovreglio R, Nilsson D (2020) Modelling and interpreting pre-evacuation decision-making using machine learning. Autom Constr 113:103140
32. Fang C, Yam MC, Cheng JR, Zhang Y (2015) Compressive strength and behaviour of gusset plate connections with single-sided splice members. J Constr Steel Res 106:166–183

Machine Learning Driven Shear Strength Prediction Model for FRP-Reinforced Concrete Beams

Mohammad Rezaul Karim, Kamrul Islam, A. H. M. Muntasir Billah, and M. Shahria Alam

Abstract The shear strength prediction of a fiber-reinforced polymer (FRP)-reinforced concrete (RC) beam is a difficult undertaking that is influenced by several design variables. While the usage of FRP bars has emerged as a viable alternative in reducing corrosion problems associated with steel reinforcement in an extreme environment, a precise and reliable method of shear strength prediction is required to assure cost-effective material use and optimum design. Several design provisions and optimized design equations are now available in the current literature; nevertheless, when these equations are used, a significant variation between the experimental and the predicted shear strength of FRP-RC beams is observed. This study utilised the power of data-driven modelling techniques for enhanced prediction capability of such a complex phenomenon. The objective of the current study is to develop a data-driven shear strength prediction model for FRP-RC slender beams using the extreme gradient boosting (XGBoost) algorithm. A large database of 302 tests of RC beams longitudinally reinforced with FRP bars without stirrups was collected from the available literature. The performance of the proposed ML model is compared with the existing standards, codes, guidelines, and optimized shear strength equation. The results reveal that the XGBoost model outperformed the existing shear strength provisions and has a high level of prediction accuracy.

Keywords FRP-reinforced concrete beams · Shear strength · Machine learning

M. R. Karim (✉)
Department of Civil and Environmental Engineering, University of Alberta, Edmonton, AB, Canada
e-mail: mrkarim1@ualberta.ca

K. Islam
Department of Civil, Geological and Mining Engineering, Polytechnique Montreal, Montreal, QC, Canada

A. H. M. M. Billah
Department of Civil Engineering, Lakehead University, Thunder Bay, ON, Canada

M. S. Alam
The School of Engineering, The University of British Columbia, Kelowna, BC, Canada
e-mail: shahria.alam@ubc.ca

1 Introduction

Fiber-reinforced polymer (FRP) has a variety of mechanical properties that differ from mild steel. FRP is lighter and stronger than steel, as well as more resistant to corrosion, creep, and fatigue [1]. Thereby, despite certain shortcomings such as a lower elastic modulus (for most FRPs), a linear stress–strain relationship, and ruptures without yielding, FRPs are gaining popularity in the construction industry due to their better mechanical performances compared to mild steel rebars. It is typically assumed when designing and predicting shear resistance that an FRP-RC beam will exhibit a mechanism similar to that exhibited by mild steel reinforcement in concrete beams, where the sum of the shear capacity of concrete (V_c) and the shear capacity of FRP shear reinforcement $\left(V_f\right)$ will be the total nominal shear capacity of an FRP-reinforced beam (V_n) [2]. In an RC beam, typically, the shear force is a combination of six forces or stresses [3], outlined as follows:

- Shear friction depends on the aggregate type, crack dimensions, and concrete strength. Shear friction has a more significant effect in the case of larger aggregate and narrower cracks. However, if the concrete strength is high, then crack propagation through the aggregate and shear friction will have less effect [3, 4].
- Dowel action of the longitudinal steel rebar across cracks is an important component of the overall shear resistance of RC beams. However, in the case of FRP, it is negligible [4].
- Concrete also transfers shear forces to the support through the arching phenomenon. However, in the case of a slender beam (a/d > 2.5), the arching action is negligible [4].
- Concrete strength and the depth of the compressive zone also contribute to the shear force. With the decrease in concrete strength, the shear strength decreases, and it also decreases as the un-cracked compression zone becomes shallower [3, 4].
- Residual tension carries substantial shear strength for small concrete cracks (i.e., less than 0.15 mm in width) (ACI-ASCE 445 1998). However, for wider cracks, the share of shear strength tends toward zero.
- The crack shear force is borne by the transverse reinforcement, as illustrated by the truss model (ACI-ASCE 445 1998).

Existing empirical or semi-empirical models for shear strength prediction of FRP-RC members have been established by simply modifying the methods available for steel-RC members and based on limited test data [5–9]. This causes a wide scatter in the prediction when compared to experimental data, and it tends to be conservative, demanding a large amount of FRP and making FRP applications less cost-effective [10–12]. Nevertheless, there has been a recent tendency among researchers to enhance the amount of data used in their study, and numerous recent studies have used machine learning (ML) approaches to estimate the shear resistance of slender and deep reinforced concrete beams. For example, [8] retrieved 150 experimental data of FRP-RC beams to see if an ANN-based model could be used to

predict nominal shear capacity. They also used this database to assess the validity of the JSCE [13], ACI 440.1R-03 (ACI 2003), and CSA S806-02 for shear strength calculations of FRP-RC beams (CSA 2002). In comparison to conventional design specifications, suggested ANN-based model exhibited enhanced accuracy in estimating shear capacity. However, while using the ML model in applied field it is important to understand that ML algorithms actively 'learn' information from data using computational methods, rather than relying on a pre-existing equation. The performance of the algorithms adapts as the number of samples available for training rises. As a result, feeding new experimental data is a constant process to enhance forecast accuracy. Since existing codes, standards, guidelines for designing FRP-RC beams have notable limitations in predicting shear strength for FRP-RC beams, ML can be useful in many situations where empirical or semi-empirical equations have become outdated. In this context, the current work intends to establish an updated data-driven boosting ML model known as extreme gradient boosting (XGBoost) to predict the shear strength of FRP-RC slender beams more precisely.

2 Experimental Databases for FRP-RC Beams

A comprehensive experimental database of 302 FRP-RC slender beams without shear reinforcement is developed from existing literatures [3, 4, 10, 12, 14–40]. The studies show that the shear strength of FRP-RC beams depends on the width (b_w) and effective depth (d) of the beam, shear span to depth ratio (a/d), concrete strength $\left(f_c'\right)$, longitudinal reinforcement ratio (ρ_f), and modulus of elasticity of rebar (E_f). A schematic diagram showing different geometric parameters of a tested beam under flexural loading is shown in Fig. 1.

The experimental results compiled are the shear strength values of FRP-RC slender beams without stirrups. The database contains FRP-RC beams having a slenderness ratio (a/d) greater or equal to 2.5. Four different FRP rebars, namely CFRP, GFRP, BFRP, and AFRP are considered along with concrete strength ranging
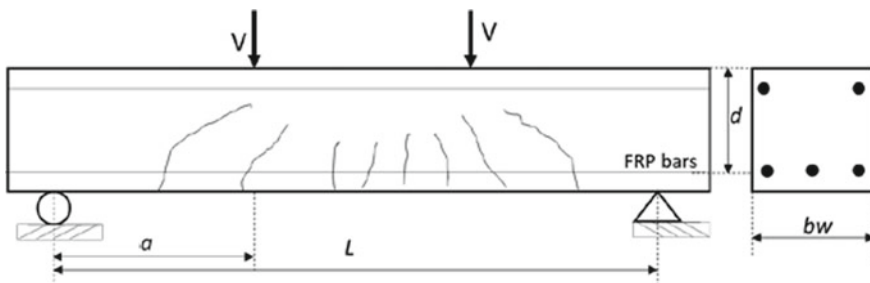
Fig. 1 Geometric properties of FRP reinforced concrete beam

Table 1 Statistical range of the parameters in the database

Parameter	Min value	Max value	Mean	Std deviation
a/d	2.50	12.50	3.82	1.33
$\rho_f\ (\%)$	0.12	4.36	1.11	0.70
f'_c (MPa)	19.20	93.00	42.60	16.00
d (mm)	73.00	938.00	278.00	160.00
b_w (mm)	89.00	1000.00	271.00	177.00
E_f (GPa)	26.50	192.00	70.00	43.00
$V_{\exp}$ (kN)	9.80	263.00	58.00	47.50
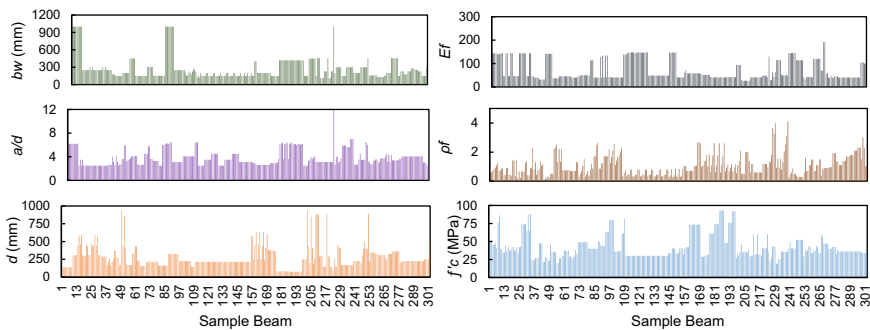
Fig. 2 Statistical summary of the database of experimental results

from low to high. The statistical range of the design parameters and summary of the database are listed in Table 1 and shown graphically in Fig. 2 respectively.

3 Overviews of Existing Models and Design Provisions

For evaluating the shear strength of FRP-RC beams, most codes, standards, and recommendations employed a method like that used for Steel-RC beams. However, due to the variations in material characteristics between FRP and steel reinforcement, certain equations proposed specific adjustment parameters to account for these variances. The proposed ML model is compared to shear design equations (listed in Table 2) for FRP-RC beams with or without stirrups as prescribed by ACI 440.1R-15 [41], JSCE [13], CSA S806-12 [46], and BISE-1999 [42]. In addition, this work also considers two other shear strength prediction equations presented by Reineck [43], Gao and Zhang [6] as indicated in Table 2.

Table 2 Shear design equations of FRP-RC beams

Code/equation	Year	Equation
ACI 440.1R-15	2015	$V_c = \left(\frac{2}{5}\right)\sqrt{f_c'}\,b_w c$, $c = kd$, $k = \sqrt{2p_f n_f + (p_f n_f)^2} - p_f n_f$, $p_f = A_f/(b_w d)$, $n_f = E_f/E_c$
JSCE [13]	1997	$V_c = \beta_d \beta_p \beta_n f_{vcd} b_w d/\gamma_b$; $f_{vcd} = 0.2(f_c')^{1/3} \le 0.72$ N/mm^2; $\beta_d(1000/d)^2 \le 1.5$; $\beta_p((100\rho_{f1}E_{f1})/E_s)^{1/3} \le 1.5$ $\beta_n = 1.0$ for sections without the axial force, γ_b = member safety factor, $\gamma_b = 1.3$
CSA S806-12	2012	$0.11\sqrt{f_c'}\,b_w d \le V_c = 0.05 k_m k_r k_a k_s (f_c')^{\frac{1}{3}} b_w d \le 0.22\sqrt{f_c'}\,b_w d$; $k_m = (d/a)^{\frac{1}{2}} \le 1.0$ $k_r = 1 + (E_f \rho_f)^{\frac{1}{3}}$, $1.0 \le k_a = \frac{2.5d}{a} \le 2.5$, $k_s = \frac{750}{450+d} \le 1.0$
BISE [42]	1999	$V_c = 0.79\left(100\rho_f \frac{E_f}{E_s}\right)^{1/3}\left(\frac{d}{400}\right)^{1/4}\left(\frac{f_{cu}'}{25}\right)^{1/3} b_w d$
[43]	2017	$V_c = 7.5\lambda\left(\rho_f \frac{f_c'}{d}\right)^{1/3} b_w d$
Gao and Zhang [6]	2020	$V_c = k_{fad} k_d \sqrt{f_c'}\,bd$, $k_d = 1.35 - \frac{d}{100} \ge 0.75$, $k = \sqrt{2p_f n_f + (p_f n_f)^2} - p_f n_f$, $k_{fad} = \frac{1-\frac{a}{d}}{1+\frac{a}{d}} + 2(k+0.1)\left(\frac{a}{d}\right)$, when $\frac{a}{d} \le 1$, $k_{fad} = \frac{K+0.1}{\frac{a}{d}-0.5}$, when $1 < \frac{a}{d} \le 3$, $k_{fad} = 0.4(k+0.1)$ when $3 < \frac{a}{d} \le 6$, $k_{fad} = \frac{2.4(k+0.1)}{\frac{a}{d}}$ when $\frac{a}{d} > 6$

3.1 Extreme Gradient Boosting (XGBoost) Machine Learning Algorithm

XGBoost is a scalable end-to-end tree boosting technique that is the most powerful and quickest approach in ensemble learning. It builds an arbitrarily accurate strong predictor by merging several weak learners, much like the other boosting approach, and improves prediction accuracy. The boosting ML method usually consists of two stages. The initial stage is to use individual learning algorithms to generate a group of base learners. The learning methods used for base learners might be homogeneous (identical) or heterogeneous, depending on the ensemble. The outputs of the different learners are sent on to another group of learning algorithms in the second stage, which creates the predictive model. The dataset in this study has defined input parameters and their associated goal outputs; hence, this ML is a supervised learning issue. A detailed description on XGBoost ML workflow can be found in

[44]. The performance of various guidelines, codes, and optimized equations were compared with the XGBoost model outcomes.

4 Results and Discussions

While analysing the performance of the existing equations of FRP-RC Beams, it is critical to use a big dataset, such as the one obtained in this work. The performances of the proposed ML model are evaluated by comparing the test results to all the specified codes, standards, guidelines, and models in estimating the shear strengths of FRP-RC beams. To assess the performances, two generally used statistical model parameters, namely coefficient of determination R^2, and root mean square error (RMSE) are utilised. The R^2 score indicates how well the suggested equation can predict experimental results consistently. The RMSE, which indicates the total errors relative to the experimental database, is also used to assess the goodness of fit and accuracy of the created models. The equivalent values of R^2 will be one in an ideal situation, and RMSE will be zero. According to [45], when the squared root of the R^2 value is more than 0.80 and the discrepancy between experimental and projected outcomes is the smallest, the model has attained excellent performance. The performances of the evaluated design provisions, optimized equations and XGBoost are presented in Fig. 3a–g that show the relationship between measured versus predicted shear strength. For FRP-RC beams without shear reinforcement, Table 3 compares the performance of existing shear design codes, standards, and equations to that of XGBoost. The present design specifications and equations for calculating the shear strength of FRP-RC beams are shown to differ greatly and provide considerable amounts of dispersed data. The higher mean values of V_{exp} /V_{cal}, which are 1.85 and 1.35, respectively, show that ACI-440.1R-15 [41] and JSCE [13] provided more cautious results in computing the shear strength. The mean value of CSA S806-12 was less than 1.0, resulting in more dispersion in prediction.

When compared to the existing design provisions, optimized equations performed better with higher R^2, and reduced RMS. It's worth noting that the optimized equations are evaluated with a larger number of samples now than they were while the researcher has formulated them. In current study, the authors used the most typical dataset division: 80/20 train/test ratio to analyse the relative model performance of XGBoost. The training set is used to create the model, whereas the test set is used to assess the accuracy of the prediction. The XGBoost model had the greatest performance of all the models, with R^2 values of 0.998 and 0.957 for the train and test sets, respectively. the RMSE of the XGBoost train and test sets are (1.102) and (8.905), respectively, which are also quite low when compared to the other models. The XGBoost algorithm's mean value and SD of test data are 1.00 and 0.14, respectively, which are also the lowest. Overall, our findings suggest that XGBoost can outperform all other models in terms of accuracy and performance in predicting the shear strength.

(a) XGBoost

(b) ACI 440.1R-15 (ACI 2015)

(c) CSA S806-12

(d) JSCE 1997

(e) BISE 1999

(f) Gao and Zhang (2020) optimized equation

(g) Reineck (2017) optimized equation
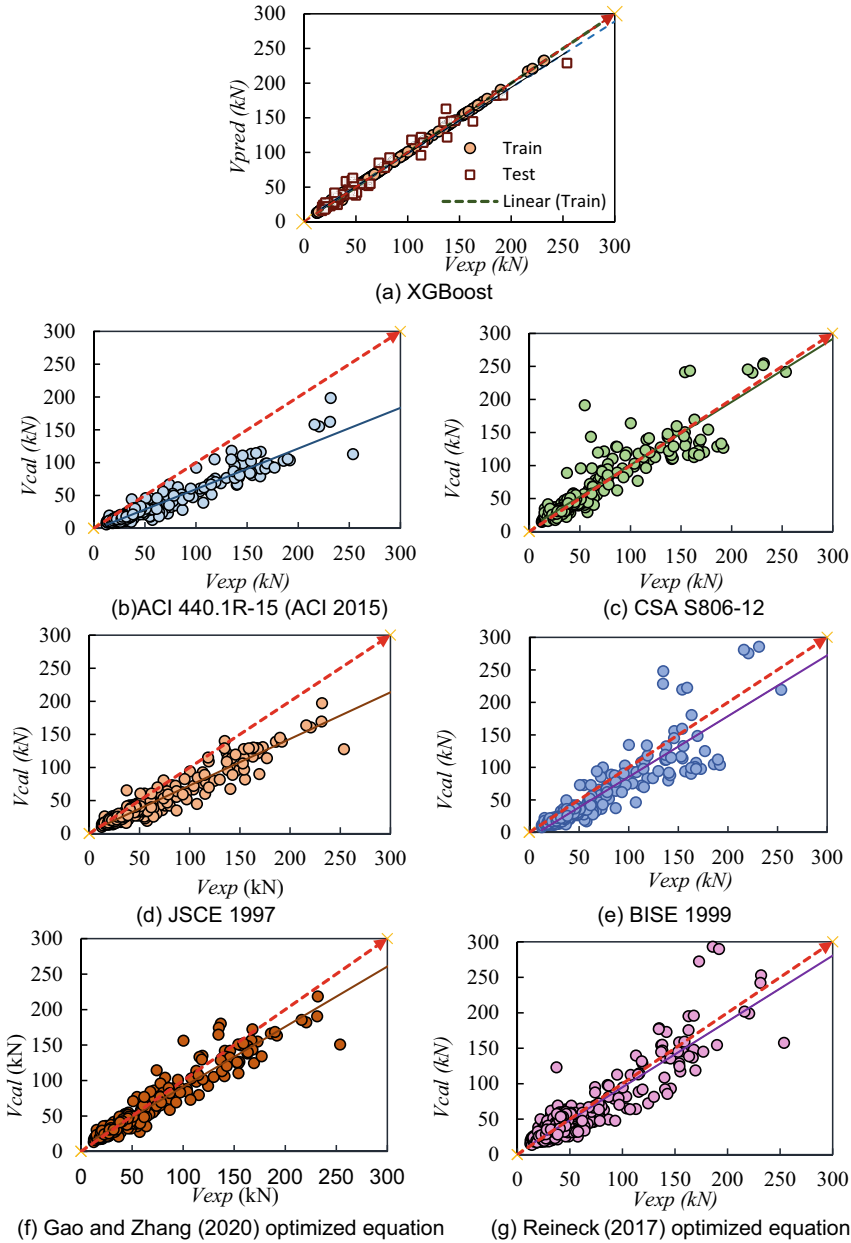
Fig. 3 Experimental versus predicted/ calculated shear strength in **a** XGBoost, **b** ACI 440.1R-15, **c** CSA S806-12 **d** JSCE [13], **e** BISE [42], **f** Gao and Zhang [6], **g** Reineck [43]

Table 3 Performance evaluation of codes, guidelines, equations, and model

Design provision/equation	Mean V_{exp}/V_{cal}	SD	R^2	RMSE
ACI 440.1R-15	1.85	0.47	0.912	32.27
CSA-S806-12	0.97	0.22	0.785	24.25
JSCE [13]	1.35	0.31	0.919	23.09
BISE [42]	1.43	0.38	0.803	25.49
[43]	1.07	0.32	0.828	20.72
Gao and Zhang [6]	1.03	0.20	0.923	14.15
XGBoost Train	1.00	0.03	0.998	1.012
Test	1.00	0.14	0.957	8.905

5 Effects of Shear Strength Parameters

Precise shear strength prediction of FRP-RC beams and determining which features are most important in effectively predicting overall shear resistance is difficult. Feature importance analyses were performed to identify the key design parameters. Figure 4a–d depicts the influence of changing four critical design parameters (f'_c, b_w, d, and E_f) on the shear strength value for four distinct models analysed in this work. In this scenario, input parameters were determined based on an approximation of the average value of the complete dataset utilised in this study: $f'_c = 42$ MPa, $b_w = 250$ mm, $d = 400$ mm, $a/d = 3.5$, $\rho_f = 0.01$, and $E_f = 72$ GPa. While determining the effect of a given parameter, ten intermediate values were chosen from the range of that parameter's maximum and minimum values while keeping the other parameters constant. The shear strength of FRP-RC beams calculated using ML algorithms shows that all four factors display a significant impact on the slender RC beams' shear strength. Based on the results, it can be concluded that the developed ML model XGBoost yielded shear capacities greater than the ACI 440.1R-15 in all cases and intersected or merged nonlinearly with the other three models at various values.

XGBoost, like all other optimized equations and algorithms, exhibited a rise in shear strength as f'_c was increased, although at varying rates. The shear strength of the XGBoost model rises in three segments of the f'_c value: less than 30 MPa, 30 to 60 MPa, and more than 60 MPa, as shown in Fig. 4a. The influence of f'_c on shear strength, as shown in design codes and standards equations, may be attributed to the rise in shear strength depending on segments. According to previous research, shear strength varies with the cubic root or the square root of f'_c.
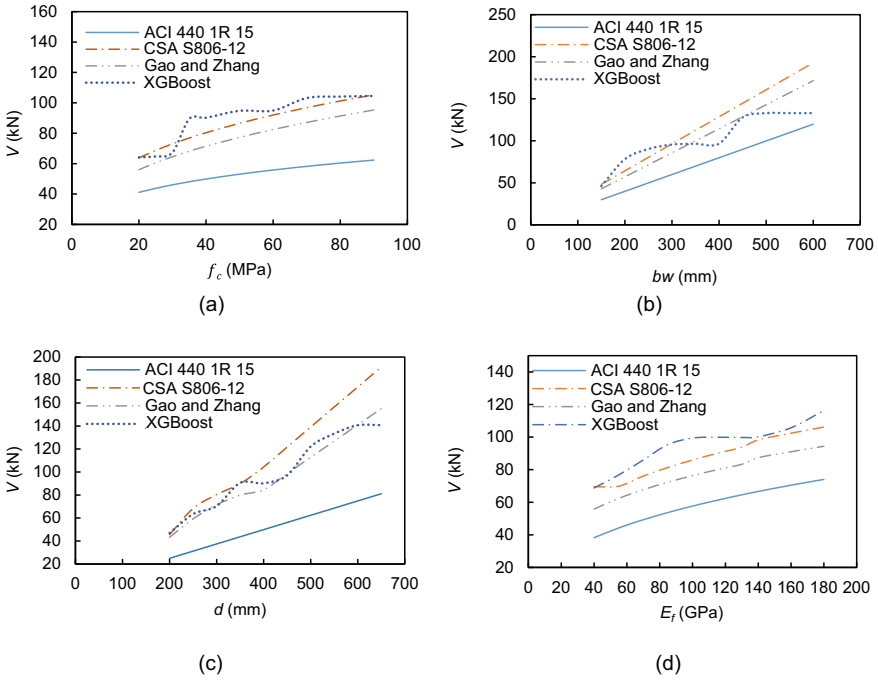
Fig. 4 Effects of **a** concrete strength $\left(f_c'\right)$, **b** beam width (b_w), **c** effective depth (d), and **d** modulus of elasticity $\left(E_f\right)$ of FRP rebars on shear strength of FRP-RC beams

6 Conclusions

This study developed prediction models using the XGBoost ML technique to derive improved and alternative methods of predicting the shear strength of slender FRP-RC beams. A large database consisting of available test results of 302 FRP-RC beams without stirrups subjected to shear strength tests was developed to investigate the performance of four existing codes and guidelines and two proposed equations with that of XGBoost ML model. From the analysis of the study following conclusions can be drawn:

- Existing codes and earlier proposed or modified equations reveals that the prediction results exhibit significant variations when dealing with a new dataset. Each code or method tends to take its own approach, with dissimilarities in input parameters and their influences.
- The overall findings of the present study shows that the optimized equation proposed by Gao and Zhang [6] significantly improved performance with higher R^2 (0.923) value and lower RMSE (14.15) than that of other earlier design provisions. XGBoost ML algorithms outperform Gao and Zhang's [6] equation and also perform better than any of the other traditional codes displaying the most

consistent results with with R^2 values of 0.998 (train) and 0.957 (test), RMSE valued of 1.012 (train) and 8.905 (test), and a Mean V_{exp}/V_{cal} of 1.00 for both cases. Overall, it can be concluded that the XGBoost ML model is a promising alternative for dealing with complex structural applications and predicting the design shear strength that can outperform all other models in terms of accuracy and reliability.

- Finally, it should be noted that future study needs to focus on collecting new test results to improve the existing FRP-RC slender beam database that will eventually increase the ML model prediction capability. Moreover, the current study only performed feature importance analysis to interpret the ML model outcomes. To make the ML model output interpretable, future research should focus on partial dependency analyses and Shapley Additive Explanations (SHAP) based feature importance analyses.

References

1. Chaallal O, Benmokrane B (1996) Fiber-reinforced plastic rebars for concrete applications. Compos B Eng 27(3–4):245–252
2. Machial R, Alam MS, Rteil A (2012) Revisiting the shear design equations for concrete beams reinforced with FRP rebar and stirrup. Mater Struct 45:1593–1612
3. Razaqpur AG, Isgor BO, Greenaway S, Selley A (2004) Concrete contribution to the shear resistance of fiber reinforced polymer reinforced concrete members. J Compos Constr 8(5):452–460
4. Razaqpur AG, Shedid M, Isgor B (2011) Shear strength of fiber-reinforced polymer reinforced concrete beams subject to unsymmetric loading. J Compos Constr 15
5. Shah AM, Gazder U (2020) Shear strength prediction of FRP reinforced concrete members using generalized regression neural network. Neural Comput Appl 32(10):6151–6158
6. Gao D, Changhui Z (2020) Shear strength prediction model of FRP bar-reinforced concrete beams without stirrups. Mathematical problems in engineering, 2020
7. Lee S, Lee C (2014) Prediction of shear strength of FRP-reinforced concrete flexural members without stirrups using artificial neural networks. Eng Struct 61:99–112
8. Nehdi M, El Chabib H, Saïd A (2006) Evaluation of shear capacity of FRP reinforced concrete beams using artificial neural networks. Smart Struct Syst 2(1):81–100
9. Shahnewaz M, Robert Machial M, Alam S, Rteil A (2016) Optimized shear design equation for slender concrete beams reinforced with FRP bars and stirrups using genetic algorithm and reliability analysis. Eng Struct 107:151–165
10. El-Sayed AK, El-Salakawy EF, Benmokrane B (2006) Shear capacity of high-strength concrete beams reinforced with FRP bars. ACI Struct J 103(3):383–389
11. Naderpour H, Poursaeidi O, Ahmadi M (2018) Shear resistance prediction of concrete beams reinforced by FRP bars using artificial neural networks. Meas: J Int Meas Confederation 126(June):299–308
12. Tomlinson D, Fam A (2015) Performance of concrete beams reinforced with basalt FRP for flexure and shear. J Compos Constr 19(2)
13. Japan Society of Civil Engineers, Tokyo, Japan (1997) Recommendation for design and construction of concrete structures using continuous fiber reinforcing materials (JSCE-1997). Tokyo, Japan, Japan Society of Civil Engineers
14. Abdulsalam B, Farghaly A, Benmokrane B (2013) Evaluation of shear behavior for one-way concrete slabs reinforced with carbon-FRP bars. In: CSCE general conference, GEN 243-1-11

15. Alam MS, Hussein A (2017) Relationship between the shear capacity and the flexural cracking load of FRP reinforced concrete beams. Constr Build Mater 154:819–828
16. Ashour AF (2006) Flexural and shear capacities of concrete beams reinforced with GFRP bars. Constr Build Mater 20(10)
17. Ashour AF, Kara IF (2014) Size effect on shear strength of FRP reinforced concrete beams. Compos Part B: Eng 60(April)
18. Bentz, Evan C., Laurent Massam, and Michael P. Collins. (2010) Shear strength of large concrete members with FRP reinforcement. J Compos Constr 14(6)
19. Caporale A, Luciano R (2009) Indagine Sperimentale e Numerica Sulla Resistenza a Taglio Di Travi Di Calcestruzzo Armate Con Barre Di GFRP. In XXXVIII Convegno Nazionale AIAS. Turin, Italy: XXXVIII Convegno Nazionale AIAS
20. Cholostiakow S, Benedetti MD, Guadagnini M, Gowda C, Barros J, Zappa E (2018) Experimental and numerical study on the shear behaviour of geometrically similar FRP RC beams. In: Proceedings of the 8th international conference on fibre-reinforced polymer (FRP) composites in civil engineering (CICE 2016), February
21. Deitz D, Harik I, Gesund H (1999) One-way slabs reinforced with glass fiber reinforced polymer reinforcing bars. Spec Publ 188:279–286
22. Duranovic N, Pilakoutas K, Waldron P (1997) Tests on concrete beams reinforced with glass fibre reinforced plastic bars. In: Proceedings of the cird international symposium on non-metallic (FRP) reinforcement for concrete structures (FRPRCS-3). Sapporo, Japan, pp 479–86
23. Gross S, Yost J, Dinehart D, Svensen E, Liu N (2003) Shear strength of normal and high strength concrete beams reinforced with GFRP bars. High performance materials in Bridges
24. Jin MH, Jang HS, Kim CH, Baek DI (2009) Concrete shear strength of lightweight concrete beam reinforced with FRP bar. In: AsiaPacific conference on FRP in structures (APFIS 2009). Seoul, Korea, pp 203–7
25. Johnson DT, Sheikh SA (2016) Experimental investigation of glass fiber-reinforced polymer-reinforced normal-strength concrete beams. ACI Struct J 113(6)
26. Kaszubska M, Kotynia R, Barros JAO (2017) Influence of longitudinal GFRP reinforcement ratio on shear capacity of concrete beams without stirrups. Procedia Eng 193
27. Kilpatrick AE, Dawborn R (2006) Flexural shear capacity of high strength concrete slabs reinforced with longitudinal GFRP bars. In: FIB. Naples, Italy, pp 1–10
28. Massam L (2001) The behaviour of GFRP reinforced concrete beams in shear. University of Toronto, Thesis, Canada
29. Matta F, Nanni A, Hernandez TM, Benmokrane B (2008) Scaling of strength of FRP reinforced concrete beams without shear reinforcement. In: Proceedings of the 4th international conference on FRP composites in civil engineering, CICE 2008, no. July
30. Mizukawa Y, Sato Y, Ueda T, Kakuta Y (1997) A study on shear fatigue behavior of concrete beams with FRP rods. In: International symposium; 3rd, non-metallic (FRP) reinforcement for concrete structures, vol 2. Japan Concrete Institute, pp 309–16
31. Nakamura H, Higai T, Higai T (1995) Evaluation of shear strength of the concrete beams reinforced with FRP. In: Proceedings of Japan society of civil engineers. Ghent, Belgium, pp 89–97
32. Olivito RS, Zuccarello FA (2010) On the shear behaviour of concrete beams reinforced by carbon fibre-reinforced polymer bars: an experimental investigation by means of acoustic emission technique. Strain 46(5)
33. El Refai A, Abed F (2016) Concrete contribution to shear strength of beams reinforced with basalt fiber-reinforced bars. J Compos Constr 20(4)
34. Steiner S, El-Sayed AK, Benmokrane B, Matta F, Nanni A (2008) Shear strength of large-size concrete beams reinforced with glass FRP bars. In: Proceedings of the 5th international conference on advanced composite materials in bridges and structures. Winnipeg, Canada
35. Swamy N, Aburawi M (1997) Structural implications of using GFRP bars as concrete reinforcement. In: Proceedings of 3rd international symposium, FRPRCS. Sapporo, Japan, pp 503–10

36. Tariq M, Newhook J (2003) Shear testing of FRP reinforced concrete without transverse reinforcement. In: Proceedings, annual conference—Canadian society for civil engineering 2003 (January), pp 1330–39
37. Tottori S, Wakui H (1993) Shear capacity of RC and PC beams using FRP reinforcement. ACI Symposium Publication 138. https://doi.org/10.14359/3944
38. Tureyen AK, Frosch RJ (2002) Shear tests of FRP-reinforced concrete beams without stirrups. ACI Struct J 99(4):427–434
39. Yost JR, Gross SP, Dinehart DW (2001) Shear strength of normal strength concrete beams reinforced with deformed GFRP bars. J Compos Constr 5(4)
40. Zhao W, Maruyama K, Suzuki H (1995) Shear behaviour of concrete beams reinforced by FRP rods as longitudinal and shear reinforcement. In: Proceedings of the 2nd international RILEM symposium on non-metallic (FRP) reinforcement for concrete structures. Ghent, Belgium, pp 352–59
41. ACI Committee 440 (2015) Guide for the design and construction of concrete reinforced with fiber rienforced polymers (FRP) Bars (ACI 440.1R-15). Farmington Hills, MI, USA: ACI Committee
42. BISE (British Institution of Structural Engineers) (1999) Interim guidance on the design of reinforced concrete structures using fiber composite reinforcement. London
43. Reineck K-H (2017) Proposal for ACI 318 shear design. Concr Int 39(9)
44. Feng D-C, Wang W-J, Mangalathu S, Taciroglu E (2021) Interpretable XGBoost-SHAP machine-learning model for shear strength prediction of squat RC walls. J Struct Eng 147(11):04021173
45. Smith GN (1986) Probability and statistics in civil engineering: an introduction. Collins Professional and Technical Books, London
46. Canadian Standards Association (2012) Design and construction of building structures with fibre-reinforced polymers (CSAS806-12). Mississauga, Canada, Canadian Standards Association
47. CSA (Canadian Standards Association) (2002) Design and construction of building components with fibre-reinforced polymers. CSA S806-02. Mississauga, ON, Canada
48. Rammant J-P, Smith I (1999) Integrated information technology for structural engineers. Struct Eng Int 9(1):54–56

Real-Time Structural Inspection Using Augmented Reality

Jack Peplinski, Premjeet Singh, and Ayan Sadhu

Abstract Most existing infrastructure, such as bridges, buildings, dams, and culverts, is approaching the end of their service lives due to age, increased operational load, and adverse weather. According to a recent infrastructure report card, North America's infrastructure is assessed as "at-risk." This impaired infrastructure threatens nation's ability to grow its population, quality of life, and economy. Despite advancements in structural health monitoring (SHM) technology, there are several implementation challenges, including prolonged closure of the facility, expensive and time-intensive sensor installation, and access to instrumentation. To eliminate accessibility issues with sensor placement during normal operations or post-disaster inspection, an Augmented Reality (AR)-based SHM strategy is explored in this study. The AR headset is made of an RGB camera, depth imager, IMUs, microphones, onboard processing, and wireless communication links. It captures high-resolution and 3D measurements that are free of human errors and ambiguity and creates a 3D map of surrounding images with accurate distance measurements. It enables tracking and visualizing the position and motion of the user and devices as well as mapping the environmental and surrounding objects and structures. In this paper, the AR device is programmed to inspect cracks and their severity in civil structures. It is shown how this device is used to detect the severity of cracks in various structures, such as bridges and buildings.

Keywords Structural inspection · Augmented reality

J. Peplinski
Department of Electrical and Computer Engineering, Western University, London, Canada

P. Singh · A. Sadhu (✉)
Department of Civil and Environmental Engineering, Western University, London, Canada
e-mail: asadhu@uwo.ca

1 Introduction

Most existing civil infrastructure in North America was built in the post-World War II era and is close to the end of its useful life. The American infrastructure report card of 2021 [2] indicated that one-third of America's infrastructure is at risk of rapid deterioration. Canada's infrastructure is also assessed to be "at-risk" and needs improvements in structural maintenance. Traditional structural health monitoring (SHM) and infrastructure management techniques face significant challenges under adverse weather and busy operational conditions in North America. These challenges include prolonged closures of structures, dense instrumentation, the need for numerous images of damage from inaccessible areas, and an asynchronous mode of data collection. Considering the abundance of aging infrastructure (i.e., bridges, culverts, highways, and pavements) in North America, such asynchronous collection of big data and associated decision-making becomes a laborious and time-intensive process, resulting in billions of dollars of annual maintenance budget for the government and infrastructure owners. This paper proposes augmented reality devices to enhance real-time visualization of structural inspection of large-scale infrastructure.

Built assets can be continuously monitored using SHM systems using a network of sensors. Structural performance and damage identification can be assessed using a wide range of sensors by measuring various parameters. These parameters are generally related to the structural loads and their responses. Visual inspections have been used as a conventional method for detecting surface damages such as spalling, corrosion, cracks, and partially failed members. This method can be limited in detecting embedded and minor damages, and particularly delamination. Additionally, this manual approach can be labor-intensive, time-consuming, and subjective in nature. The reduced costs of sensing technologies have allowed for the widespread installation of SHM systems in numerous construction projects. SHM has emerged as a powerful solution for inspectors and operators with the recent advancements in transducers, data acquisition, and signal processing techniques. Infrastructure owners and decision-makers have recognized this need to improve SHM and have developed technologies, including contact [13] and non-contact sensing [1, 22] to eliminate outdated visual inspection practices. Examples of recent hardware technologies that have been used in SHM include cameras, LiDAR, drones, ground-based robots, and smartphones. These hardwares have been combined with new software technologies to enable the Internet-of-things (IoT) devices and digital twins (DT) systems for improved communication and visualization of SHM data. The large amounts of data collected from these technologies are often referred to as "Big Data," which can be analyzed using artificial intelligence (AI), computer vision, and data science to further inform these decisions [9]. Various tools have also been developed to display the big data of various disciplines [6], including augmented reality (AR), virtual reality (VR), and mixed reality (MR) as illustrated in Fig. 1.
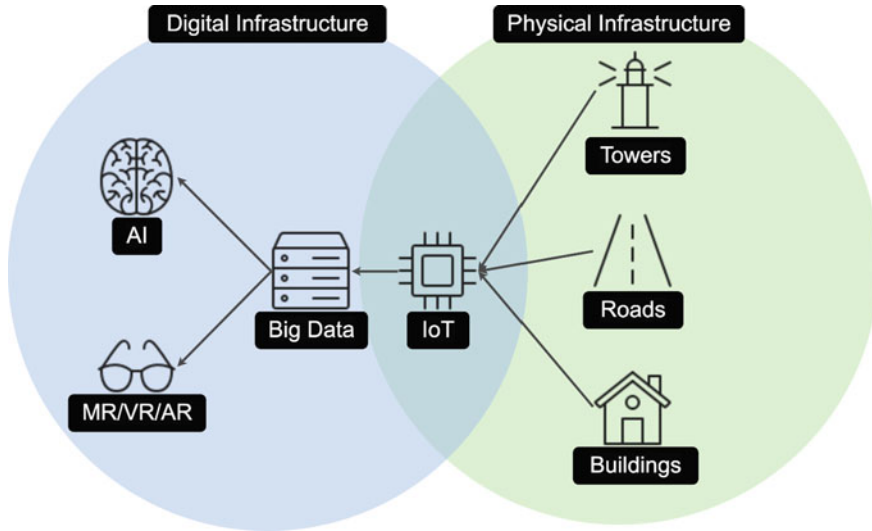
Fig. 1 Illustration of improved visualization of SHM data and decision-making

2 Recent Developments of Mixed Reality in SHM

Interest in MR-enabled SHM has increased over the past few years in part due to the increased accessibility and decreased cost of MR hardware and software, such as the Microsoft HoloLens, which was first released for development use in 2016. A variety of different head-mounted displays (HMD) are featured in Fig. 2. According to Milgram's Taxonomy of MR Visual Displays, AR and VR are subsets of MR. VR involves merging real and virtual worlds by replacing a user's field of view with a virtual environment displayed on a screen, whereas AR involves merging real and virtual worlds by replacing the user's entire view with a real environment, that may be augmented with virtual objects using a screen. MR does not replace the user's view with a screen but instead allows the user to see the real environment directly with virtual objects superimposed on the real environment [16].

Proper use of MR technologies can yield significant SHM insights and benefits the inspection and surveying operation in structural and construction engineering. For example, Kamat and El-Tawil [11] proposed an AR and GPS-based post-earthquake damage assessment for buildings. The distance between the post-earthquake building stories was compared to pre-earthquake measurements to determine a damage index for the building. Shin and Dunston [20] analyzed the potential to use AR to complete a variety of construction tasks, including a structural inspection. Shin and Dunston [21] analyzed the tilt of steel columns in a laboratory using AR. This AR approach delivered faster results than traditional manual inspection. Similar to Kamat and El-Tawil [11], Dong et al. [8] proposed an AR-based post-earthquake damage assessment for buildings by measuring inter-story drift. The authors proposed an autonomous system

(a)

(b)

(c)

(d)

(e)

(f)

(g)

Fig. 2 Typical AR HMDs: **a** Google Glass Explorer 1, **b** Epson Movario BT-300 Smart Glass, **c** Microsoft HoloLens (1st generation), **d** Magic Leap 1, **e** Microsoft HoloLens 2, **f** Google Glass Enterprise Edition, **g** Eyesight Raptor

that allowed inspectors visualization of the inter-story drift. Bernasconi et al. [5] used AR to measure crack lengths in structures which allowed to compare crack length and strain data simultaneously. Glisic et al. [9] reviewed nearly 150 articles primarily related to AR/VR-based SHM visualization techniques, including the current uses of AR/VR in SHM and future research directions. Behzadan et al. [4] reviewed the

existing challenges in AR and listed spatial registration, visual occlusion, and integrations with open-access software as well as challenges preventing more adoption of AR in AEC industries. In recent studies, Moreu et al. [17] proposed a structural inspection tool using AR. A railway bridge was displayed and tested in an AR environment.

Napolitano et al. [18] proposed a workflow for organizing and integrating SHM data with VR technologies. In another recent study, Napolitano et al. [18] used MR to visualize building models and superimposed these models in the real world. Attard et al. [3] proposed a mobile robot capable of creating 3D models of underground infrastructure. These underground 3D models were displayed with VR. Palmarini et al. [19] reviewed multiple articles about the use of AR to support maintenance operations and found that interoperability of hardware and software components was a primary inhibitor of wider adoption. Dang and Shim [7] developed a bridge maintenance system using AR and 3D bridge models. The HoloLens was used to edit and view the 3D model for over a year. Mascarenas et al. [15] proposed a quantitative visual inspection tool using AR to capture 3D measurements of critical infrastructure. For example, the tool was used to measure the geometry of irregularly shaped sidewalks. Maharjan et al. [14] proposed an infrastructure interface for structural inspection and monitoring. The HoloLens was used to display real-time strain data using sensors. In another recent study, Wang et al. [23] proposed an AI algorithm that automated damage detection, analysis, and visualization using the Epson BT-300 glasses. Kilic and Caner [12] used non-destructive testing to determine the position of rebar and defects in a bridge, and using AR, the position of the rebar and defects could be visualized. Xu and Moreu [24] reviewed recent articles on AR use in multiple civil engineering fields and ranked 16 HMDs by their applicability. The authors also compared different features of each HMD, including camera resolution, RAM, memory, battery life, working temperature and humidity ranges, safe dropping distance, weight, the field of view, and whether the HMD had head and eye-tracking and depth perception.

3 Description of the AR Device

The HoloLens is a MR-HMD developed by Microsoft. When used for the first time, the user powers on the device and places it on their head with the transparent visor in front of their eyes. The user is then presented with a few user-friendly calibration steps and a tour of how to use the device through holographic illusions projected by the HoloLens onto the transparent visor. The user interacts with these holograms by "touching" them with their finger. The HoloLens maps this touch to the holographic illusion and responds. The HoloLens also has eye-tracking capable of identifying commands and can receive some voice commands. The HoloLens uses a modified version of Windows 10 called Windows Holographic OS, has four head-tracking cameras, two eye-tracking cameras, a camera for taking videos or photos, Wi-Fi and Bluetooth connectivity, and an adjustable head strap. When using an HMD,
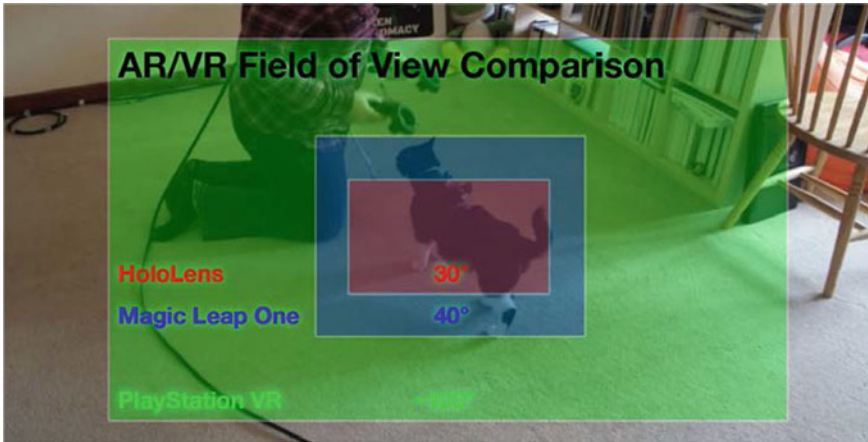
Fig. 3 Field of view of the HoloLens (first generation) and other AR/VR headsets [10]

an important feature is the field of view (FOV). FOV is the angle at which the user can see the holograms. Any holograms outside this FOV will not be visible. The HoloLens 2 has a FOV of 52º, which is higher compared to many other existing HMD. A comparison of the HoloLens' (first generation) FOV to other popular HMDs is presented in Fig. 3. New applications for the HoloLens are being developed and discussed by Microsoft and the HoloLens community.

4 Demonstration of the AR-Based Structural Inspection

4.1 Details of the Preliminary Setup

To explore AR applications related to SHM, the HoloLens 2 and other hardware and software components were combined and tested. In addition to the HoloLens 2, a MXChip AZ3166 IoT DevKit was purchased. The MXChip included the following sensors: a microphone, two clickable physical buttons, a magnetometer, and pressure, motion, humidity, and temperature sensors. The MXChip was also capable of connecting to Wi-Fi or a computer through a micro-USB port and displaying a variety of status and sensor information through six light sources (i.e., one infrared light bulb and five LEDs) and one non-touch OLED screen. The MXChip is specially configured for connection to Microsoft's Azure cloud services. A consumer-grade laptop, the Acer Aspire E5-574 running Microsoft Windows 10, was also used to interact with the HoloLens and MXChip using multiple software applications as shown in Fig. 4.

The HoloLens 2, MXChip, and Microsoft Windows 10 laptop constituted the hardware are used to explore AR-SHM applications. Multiple software applications
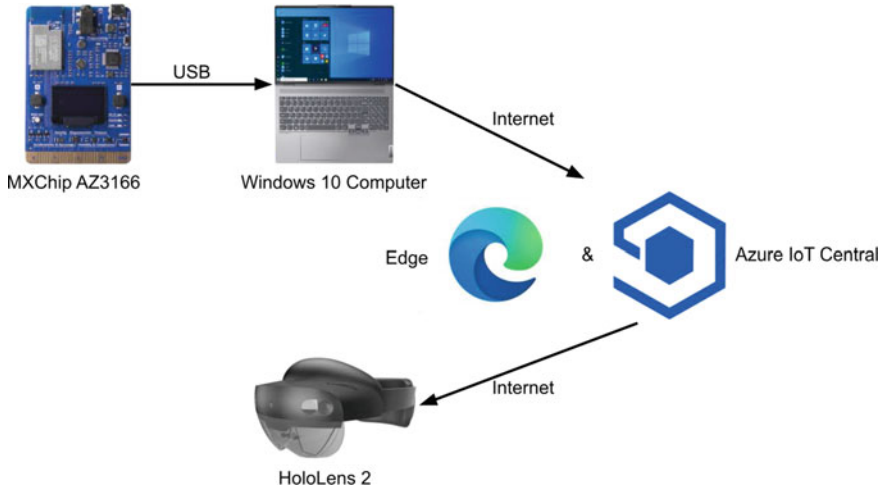
Fig. 4 Typical configuration of hardware and software used for AR applications

were used to further explore AR-based SHM. The software used included: Unity, a game logic and design software with emerging enterprise applications; Azure IoT Central and Azure IoT Hub, cloud services for connecting to Internet-connected devices; Visual Studio Code, a code editor; Google Draw and diagrams.net, diagram illustration software; Trimble Connect, a construction app for the HoloLens; and Git/ Github, a version control software.

One functionality of Trimble Connect is to measure distances. By utilizing "measure" mode, the user is presented with a white dot in their FOV. The user can move the white dot by moving their hand and can set the white dot in place by tapping their index and thumb fingers together. Once the first white dot is set in place, a second white dot will appear in the user's FOV. By moving the white dot with their hand and then tapping their index and thumb fingers together, the user can set the position of the second white dot. After the second white dot is in place, a distance is calculated.

4.2 Case Study for IoT Sensor

Accurately displaying data from SHM devices is an emerging problem as the amount of data increases. In this case study, a solution for displaying data using the HoloLens and MXChip is presented. Originally, Unity and Azure IoT Hub were used to create a custom interface display for temperature data from the MXChip; however, after further exploration of the MXChip's integrations, Azure IoT Central was selected to be used for further development because it provides many more ready-to-use functionalities that would have to be built from scratch if Unity and Azure IoT Hub were used. In Fig. 5, the Azure IoT Central interface is displayed using the HoloLens
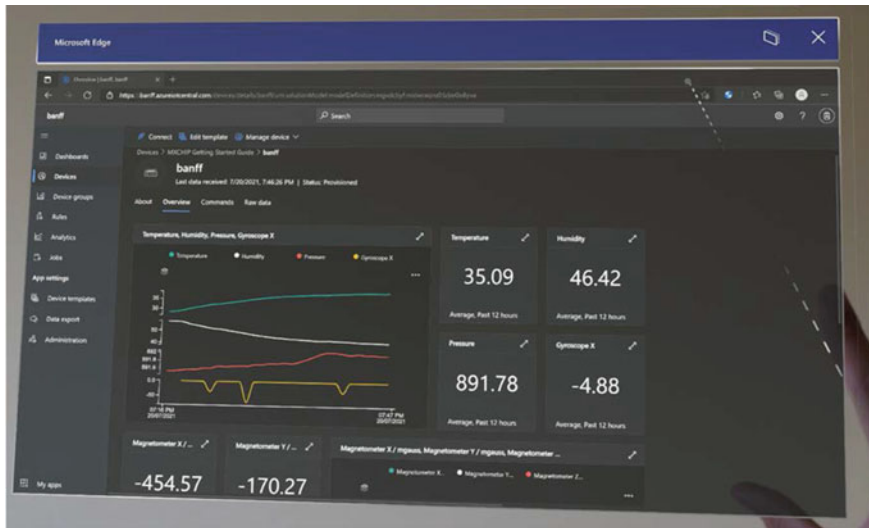
Fig. 5 Azure IoT central interface accessed through the HoloLens' Edge browser

Edge browser. The data displayed are also accessible through mobile and desktop devices with modern browser capabilities.

To display these data, the MXChip was connected to Wi-Fi and the laptop; the laptop was used solely as a power source for the MXChip—all data were transmitted through the device's own Wi-Fi capabilities. The data were then sent to an Azure IoT Central API endpoint which displayed the data. Azure IoT Central has a customizable interface that can be used to present data in a variety of formats. Displaying data using the HoloLens is potentially useful as it can allow workers to move the window to a comfortable position they can refer to or pin the window to move with the view all while keeping the worker's hands free to focus on other tasks.

4.3 Case Study for Crack Inspection in Lab Models

This section demonstrates the linear measurement capabilities of the HoloLens device. Figure 6 shows the measurements for a scaled lab concrete beam model. The dimensions of the beam are $14'' \times 3'' \times 3''$. The length of the beam is measured twice in Fig. 6a with varying degrees of accuracy. The depth of the beam or the crack depth is measured in Fig. 6b. Furthermore, Fig. 7 shows the measurements of a concrete cylinder specimen taken with HoloLens. The dimensions of the concrete cylinder are $4'' \times 8''$. Figures 7a and b show the height and diameter of the concrete cylinder measured with the HoloLens device. The measurement of crack depth is shown in Fig. 7c. This approach is further developed and applied to a full-scale structure in the next section.
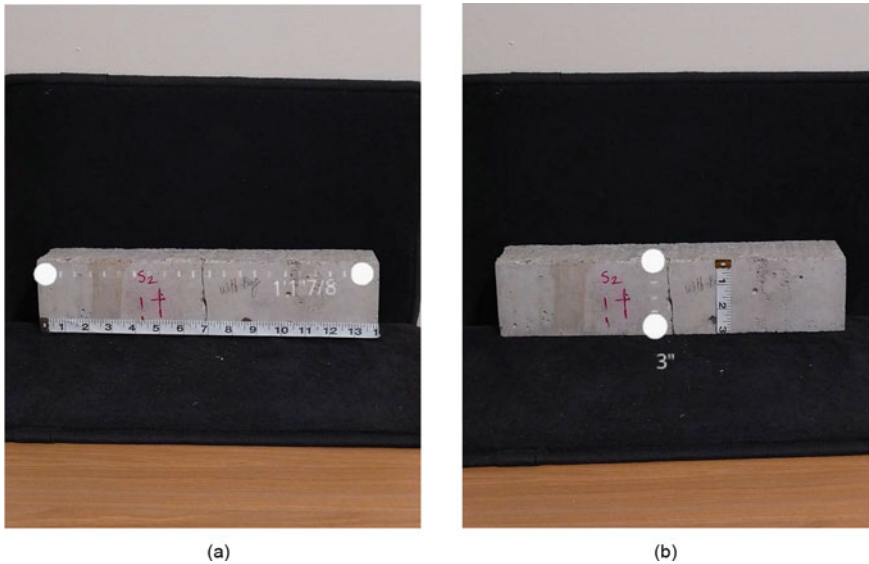
Fig. 6 Measurements of a concrete beam; **a** beam length, and **b** crack depth

4.4 Case Study for Crack Inspection in Full-Scale Structure

Measuring crack lengths in existing structures is a common inspection strategy for SHM; however, such an exercise can be difficult due to accessibility issues. For example, inspectors may measure the same crack differently, and cracks sometimes cannot be accessed easily (e.g., a crack on the underside of the bridge). In this case study, a solution for measuring crack length using the HoloLens and Trimble Connect is demonstrated. An example of two measurements is shown in Fig. 8.

Pictures of the measurement can be taken easily using the HoloLens built-in camera. Taking a photo of the measurement solves the first example problem because inspectors could compare images and crack length measurements. The HoloLens ability to superimpose images at a distance also solves the second example problem. As shown in Fig. 9, two measurements are made on the underside of a pedestrian overpass that would have been physically awkward to make otherwise.

5 Conclusions

This paper proposed the use of an AR device called HoloLens for the purpose of structural inspections. Multiple software applications were used in this study to explore AR-based SHM. Apart from visualizing the data using an IoT sensor, the device could perform crack detection in a lab environment and a full-scale structure.
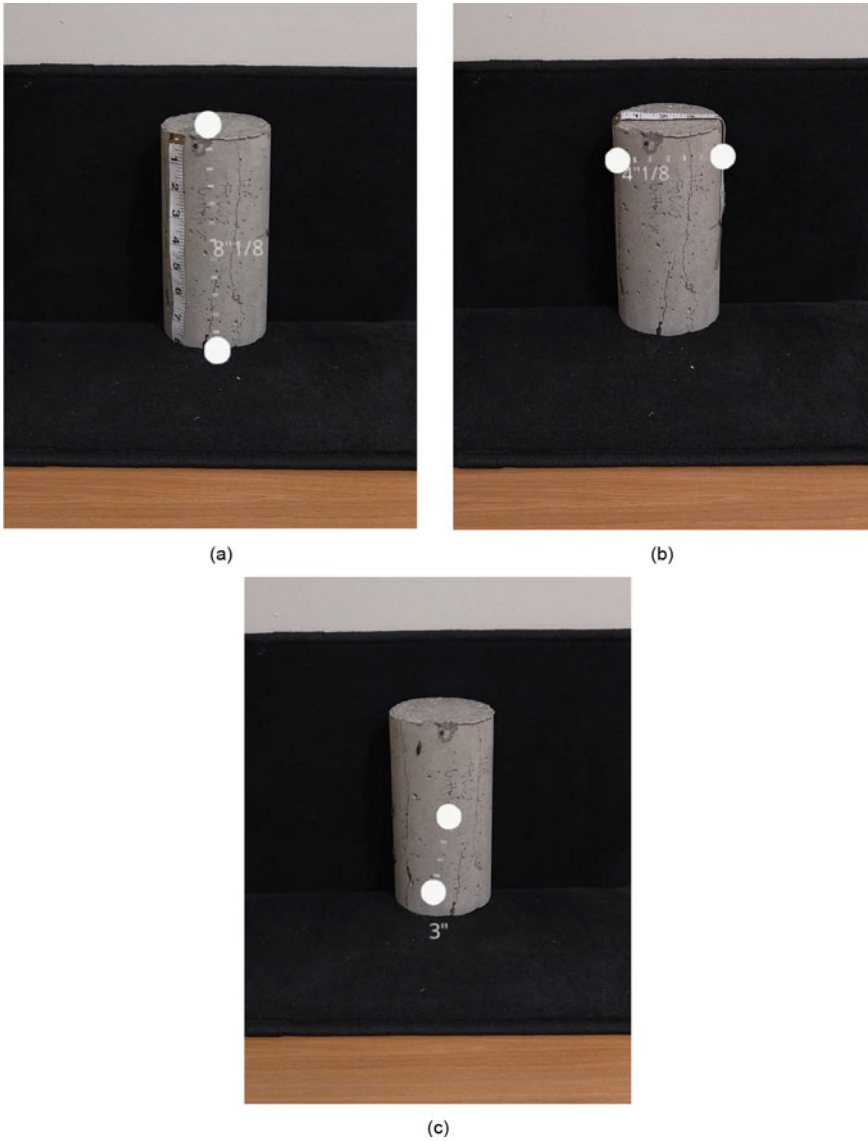
Fig. 7 Measurements of a concrete cylinder; **a** cylinder height, **b** cylinder diameter, and **c** cylinder crack length

Both tasks explored in this study using HoloLens can enhance the decision-making capabilities of the stakeholders by providing them with real-time SHM information. With huge amounts of data generated from SHM systems, the visualization of such endless streams of data can be challenging. This issue was resolved by using Azure IoT central as a user interface to interact and visualize the collected data. The data

Fig. 8 Top: measurements on a retaining wall; bottom: exterior view of the measurement

could also be accessed through mobile or desktop devices with browsing capabilities. Secondly, the HoloLens device was used for damage detection by detecting cracks in a full-scale structure. The measurement capabilities of the device were first tested in the lab environment with concrete beam and cylinder specimens. Afterward, the crack measurements were taken on a full-scale pedestrian bridge. The pictures of crack measurements, superimposed over the structure, can be taken using the device and shared instantaneously with remote participants. This device has the potential to significantly change conventional structural inspections. The application of this device can be further enhanced by using sophisticated coding and programming, which will be part of a future study.
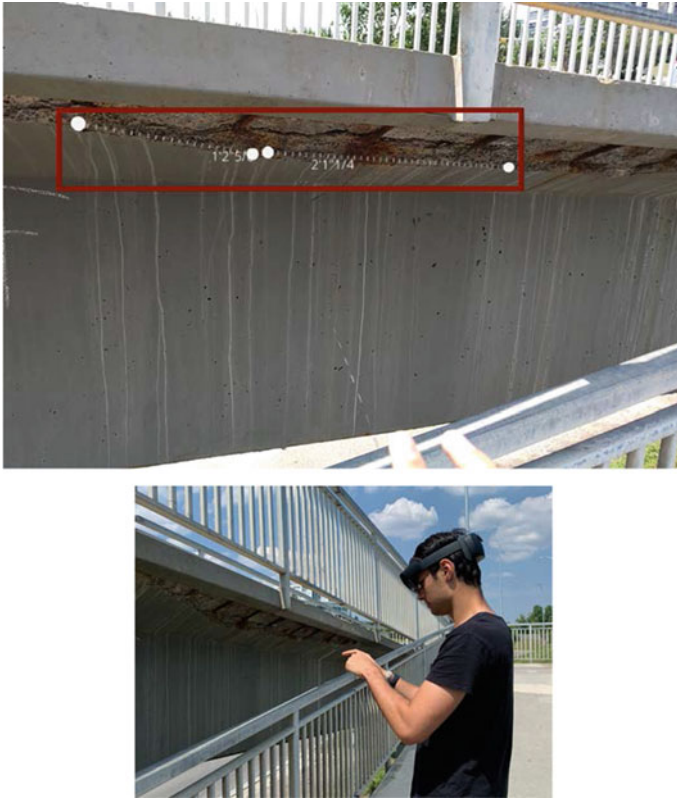
Fig. 9 Top: two measurements on the underside of a pedestrian bridge; bottom: exterior view of the measurement

References

1. Agnisarman S, Lopes S, Madathil KC, Piratla K, Gramopadhye A (2019) A survey of automation-enabled human-in-the-loop systems for infrastructure visual inspection. Autom Constr 97:52–76
2. ASCE (2021) A comprehensive assessment of America's infrastructure. https://infrastructurer eportcard.org/wp-content/uploads/2020/12/National_IRC_2021-report.pdf
3. Attard L, Debono C, Valentino G (2018) A comprehensive virtual reality system for tunnel surface documentation and structural health monitoring. In: IEEE international conference on imaging systems and techniques

4. Behzadan A, Dong S, Kamat V (2015) Augmented reality visualization: a review of civil infrastructure system applications. Adv Eng Inf 29
5. Bernasconi A, Kharshiduzzman M, Anodio LF, Bordegoni M, Re GM, Braghin F, Comolli L (2014) Development of a monitoring system for crack growth in bonded single-lap joints based on the strain field and visualization by augmented reality. J Adhesion
6. Bouchlaghem D, Shang H, Whyte J, Ganah A (2020) Visualization in architecture, engineering and construction (AEC). Autom Constr 14:287–295
7. Dang NS, Shim CS (2020) BIM-based innovative bridge maintenance system using augmented reality technology. CIGOS 2019 Sustain Infrastruct 54:1217–1222
8. Dong S, Feng C, Kamat V (2013) Sensitivity analysis of augmented reality-assisted building damage reconnaissance using virtual prototyping. Autom Constr 33:24–36
9. Glisic B, Yarnold M, Moon F, Aktan A (2014) Advanced visualization and accessibility to heterogenous monitoring data. Comput-Aided Civil Infrastruct Eng 29(5):1–17
10. Hills-Duty R (2018) Magic leap one field of view leaked. GMW3. https://www.vrfocus.com/wp-content/uploads/2018/08/ARVRFOV1.jpg
11. Kamat V, El-Tawil S (2007) Evaluation of augmented reality for rapid assessment of earthquake-induced building damage. J Comput Civil Eng 21
12. Kilic G, Caner A (2020) Augmented reality for bridge condition assessment using advanced non-destructive techniques. Struct Infrastruct Eng
13. Li H, Yi T, Ren L, Li D, Huo L (2014) Reviews on innovations and application in structural health monitoring. Struct Monit Maintenance 1(1):1–45
14. Maharjan D, Agüero M, Mascarenas D, Fierro R, Moreu F (2020) Enabling human–infrastructure interfaces for inspection using augmented reality. Struct Health Monit
15. Mascareñas DD, Ballor JP, McClain OL, Mellor MA, Shen CH, Bleck B, Morales J, Yeong LM, Narushof B, Shelton P, Martinez E, Yang Y, Cattaneo A, Harden T, Moreu F (2020) Augmented reality for next-generation infrastructure inspections. Struct Health Monit
16. Milgram P, Kishino F (1994) A taxonomy of mixed reality visual displays. IEICE Trans Inf Syst 12(12):1321–1329
17. Moreu F, Bleck B, Vemuganti S, Rogers D, Mascarenas D (2017) Augmented reality tools for enhanced structural inspection. Struct Health Monit
18. Napolitano R, Blyth A, Glisic B (2018) Virtual environments for visualizing structural health monitoring sensor networks, data, and metadata. Sensors 18
19. Palmarini R, Erokiyuncu JA, Roy R, Torabmostaedi H (2018) A systematic review of augmented reality applications in maintenance. Robot Comput-Integr Manuf 49:215–228
20. Shin DH, Dunston PS (2008) Identification of application areas for Augmented Reality in industrial construction based on technology suitability. Autom Constr 17:882–894
21. Shin DH, Dunston PS (2009) Evaluation of Augmented Reality in steel column inspection. Autom Constr 18:118–129
22. Sony S, Laventure S, Sadhu A (2019) A literature review of next-generation smart sensing technology in structural health monitoring. Struct Control Health Monit 26(3):e2321
23. Wang S, Zargar SA, Yuan FG (2020) Augmented reality for enhanced visual inspection through knowledge-based deep learning. Struct Health Monit 20(1):426–442
24. Xu J, Moreu F (2021) A review of augmented reality applications in civil infrastructure during the 4th industrial revolution. Front Built-Up Environ 7

Design of Ground Structures

Effects of Design Provisions on the Response of RC Frame Structures to Foundation Settlements

Abdelmoneim El Naggar, Maged A. Youssef, and Hany El Naggar

Abstract Differential settlements may occur due to a nearby excavation, consolidation, liquefaction, vibration, or other natural causes. In some cases, buildings are not designed for the conditions imposed by these settlements, which can lead to a structural damage. Certain components of the Canadian design provisions, such as seismicity requirements, could influence the performance of a structure under foundation settlements. Current seismic provisions contain ductility requirements that ensure the development of plastic hinges within the beams, thereby dissipating the seismic energy. Understanding the effects of such provisions on the performance of a building experiencing differential settlement is important in developing comprehensive structural assessments and enhancing current design standards. In this study, the performance of reinforced concrete-framed structures, designed considering different seismic categories, is assessed from strength and serviceability points of view. Three settlement cases are considered, namely prescribed settlement of a center-intermediate column, intermediate column, and edge column. The study provides a critical assessment of the effectiveness of seismic provisions in preventing the loss of structural functionality due to settlement.

Keywords Differential settlement · Strength · Serviceability · Plastic hinge development

1 Introduction

Differential settlements could develop due to several reasons, including inappropriate foundation design and the failure to account for the soil's bearing capacity, consolidation effects, vibration due to seismic activity or machinery, and nearby

A. El Naggar (✉) · M. A. Youssef
Civil and Environmental Engineering, Western University, London, ON, Canada
e-mail: Aelnagg3@uwo.ca

H. El Naggar
Civil and Resource Engineering, Dalhousie University, Halifax, NS, Canada

excavation. Uneven relaxation within the soil results in a non-uniform settlement of the underlying stratum. This settlement imposes a new stress scenario for the over-lying foundations, which may lead to a several structural problems, including tilting, cracking, or severe damage. Thus, the primary function of the structure could be compromised, resulting in financial and social losses.

The developed structural damage depends on the nature of the settlements. For instance, when the soil deforms to form a curved surface, the resulting negative concavity may leave the building supported at its ends and unsupported at the middle region. This would create a loading scheme analogous to that of a simply supported beam experiencing compression at its top portion while tensioned at the lower part [23]. In this situation, the suspended structural members lose bearing, and the load demand increases at the ends.

Early researchers tried to qualitatively assess the effects of differential settlements on existing structures. Damage criteria were developed to assess the effect of foun-dation settlement on the of lateral and angular distortions of buildings. Meyerhof [18] established that a relatively small uneven foundation settlement could result in increased stresses, especially in the external joints of the lower stories. Skempton and MacDonald [22] summarized the results of a survey involving 98 buildings subjected to settlements, 40 of which suffered damage. From this survey, damage limits in terms of angular distortion were established. Likewise, Polshin and Tokar [20] analyzed the settlements of various structures on different soils in over 100 sites and proposed more appropriate distortion limits for different soil conditions and structures. It was noted that constructing box-section reinforced concrete slabs underneath a structure could decrease the non-uniform settlements at the supports and prevent crack propagations within the superstructure.

As research progressed, critical strains for various types of buildings were studied, and Burland and Wroth [6] and Burland et al. [7] introduced a damage classifica-tion system based on limiting the tensile strains in structural members. Boscardin and Cording [5] linked these proposed damage categories to field observations and analyt-ical studies and found that the tolerance of a building to ground settlement is depen-dent on its ability to resist lateral forces. Likewise, it was concluded that increasing the number of stories enhances the shear stiffness of a structure, making it less vulnerable to distortions and more vulnerable to tilting actions. As the number of bays increases, however, the building's vulnerability to distortion increases. Techniques correlating the ground elongation strain, member's bending strains, shear strains, and maximum member slope have been developed. These techniques followed a stepwise method [3, 4].

Numerical studies have been conducted to provide a more accurate quantitative assessment of the vulnerability of a building to foundation settlements. For instance, Lin et al. [15] investigated the stresses induced in a typical ten-storey reinforced concrete building subjected to excessive differential settlement. It was shown that the building behaved elastically up to an uneven settlement of 25 mm, 5 mm more than the limit proposed by American Concrete Institute concrete design guidelines [1]. Similarly, Fotopoulou et al. [10] assessed the vulnerability of low moment-resisting reinforced concrete frames (MRF). Shear failure was observed more dominant for

the low code high-rise MRF buildings subjected to liquefaction-induced settlements including vertical settlements and lateral spreading. Other researchers studied the effects of height and length of structural elements and its impact on the overall member stiffness and performance under differential settlements [2, 8, 13, 14]. The effect of seismic provisions on the performance of a low-rise building subjected to differential settlement was discussed by Desbrousses [9]. Limited research, if any, exists however considering the vulnerability of medium rise buildings to such settlements. Likewise, the literature lacks a concrete consideration for the material nonlinearity and damage propagation occurring within a reinforced concrete frame subjected to differential settlements. Hence, in this study, the effects of the Canadian seismic design provisions on the behavior of RC frames during ground settlement are investigated, while considering material nonlinearity and damage propagation. The following sections provide detail about the modeling technique and analysis associated with this study.

2 Finite Element Model

The fiber element-based nonlinear finite element program, Seismostruct [21], has been utilized to model the examined RC frames. The program accounts for the effects of geometric and material nonlinearities. RC frame elements are modeled using the distributed plasticity approach. The sectional stress–strain state of the elements is obtained via integration of the nonlinear uniaxial stress–strain response of their individual fibers. The spread of inelasticity along the member length is then estimated using inelastic cubic formulation [11].

The beam and column elements were modeled using displacement-based inelastic frame elements. The cross-sections of the structural members were divided into concrete and steel fibers (300×300 fiber elements), where the concrete fibers had confined fibers for the core region and unconfined fibers for the cover region. Two integration gauss points per fiber element are used for the numerical integration. The constitutive relationship for the concrete material is calculated based on the relationship proposed by Mander et al. [16], while the steel reinforcement fibers are modeled using the constitutive relationship proposed by Menegetto and Pinto [17].

The proposed modeling technique was validated against the beam column joint tested by Youssef et al. [24], shown in Fig. 1a. The concrete had an average compressive strength of 53.5 MPa, a split tensile strength of 3.5 MPa. The 4-20M longitudinal rebars had a yield strength of 520 MPa and Young's modulus of 198 GPa. The 10 M stirrups had a yield strength of 422 MPa. The idealized beam column joint is shown in Fig. 1b. The beam tip is subjected to a displacement controlled cyclic loading, with a maximum amplitude of 72 mm. The nature of the loading is shown in Fig. 1c. As shown in Fig. 1d, there is a good agreement between the experimental data and the results obtained from the Seismostruct simulation.

(a) Joint tested by Youssef et al. (2008)

(b) idealization

(c) beam tip cyclic load

(d) Load-deflection diagram
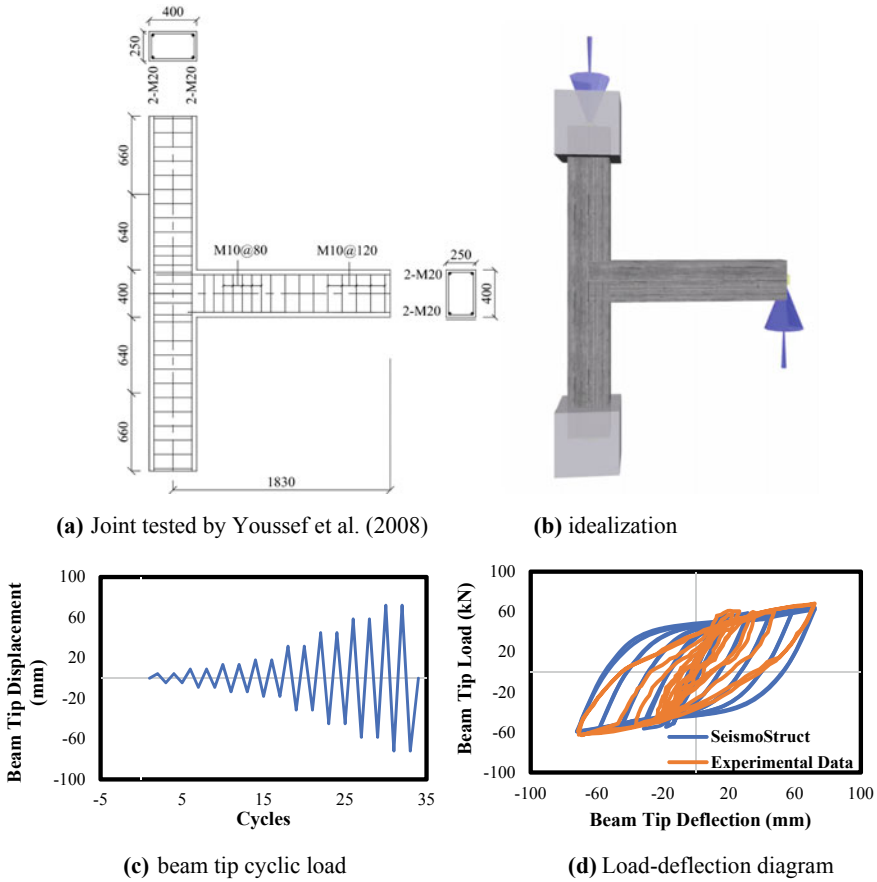
Fig. 1 Validation of the used modeling approach

3 Steel RC Frame Design and Modeling

Three RC frame buildings were designed to study the effects of seismic design provisions on the performance of RC structure subjected to differential settlement. The three buildings represent a symmetric six-storey residential apartment building, which is located in Victoria (high seismic hazard area), Montreal (moderate seismic hazard area), or Winnipeg (low seismic hazard area). The buildings are designed to satisfy the requirements of the National Building Code of Canada [19]. The design spectra corresponding to these regions are shown in Fig. 2. A site class "C" was assumed, as it represents reference ground condition.

The lateral load-resisting system for the three buildings is composed of moment-resisting frames. The concrete compressive strength was taken 30 MPa and the steel yielding stress was 400 MPa. The dead loads included the weight of the structural
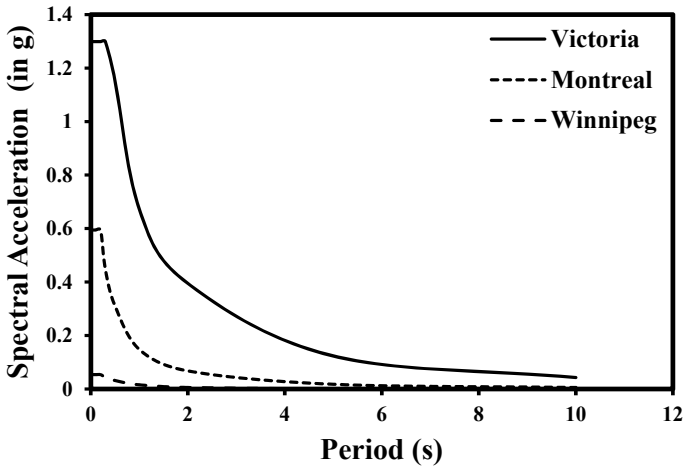
Fig. 2 Design spectra for Victoria, Montreal, and Winnipeg

elements in addition to a superimposed dead load of 1.5 kPa. The live load was 1.9 kPa as per NBCC [19]. The geometry of the moment frames and typical details for a beam are shown in Fig. 3. The cross-section dimensions and reinforcement details of the frame are summarized in Tables 1 and 2.

Due to the symmetry of the designed buildings, only one moment-resisting frame is selected for the analysis. The beams and columns are modeled using cubic elasto-plastic elements, where the beams are divided into six displacement-based inelastic frame elements, while the columns are modeled using three elements to match the distribution of the reinforcements and monitor the progress of the local damage, as recommended by Youssef and Elfeki [25]. The beam elements were modeled using T-sections, with an effective flange width equal to the beam width plus 14% of the clear span, as recommended by Jeong and Elnashai [12].

4 Analysis and Results

Differential settlement occurs due to in situ stress relaxation and the irregular movement of the ground profile. This movement would result in the settlement of a column relative to one another within a structure, resulting in a change of load distribution within the structure, affecting the overall performance of a building. To simulate the ground movement and potential loss of load bearing capabilities for a given column, the column was modeled to be supported by a vertical spring. The spring stiffness was incrementally reduced to induce the differential settlement until the column, experiencing settlement, cannot contribute to resisting the vertical loads. Each of the three designed frames were first exposed to differential settlement of middle-intermediate column, Fig. 4.

(a) plan view

(b) elevation view

(c) typical beam detail
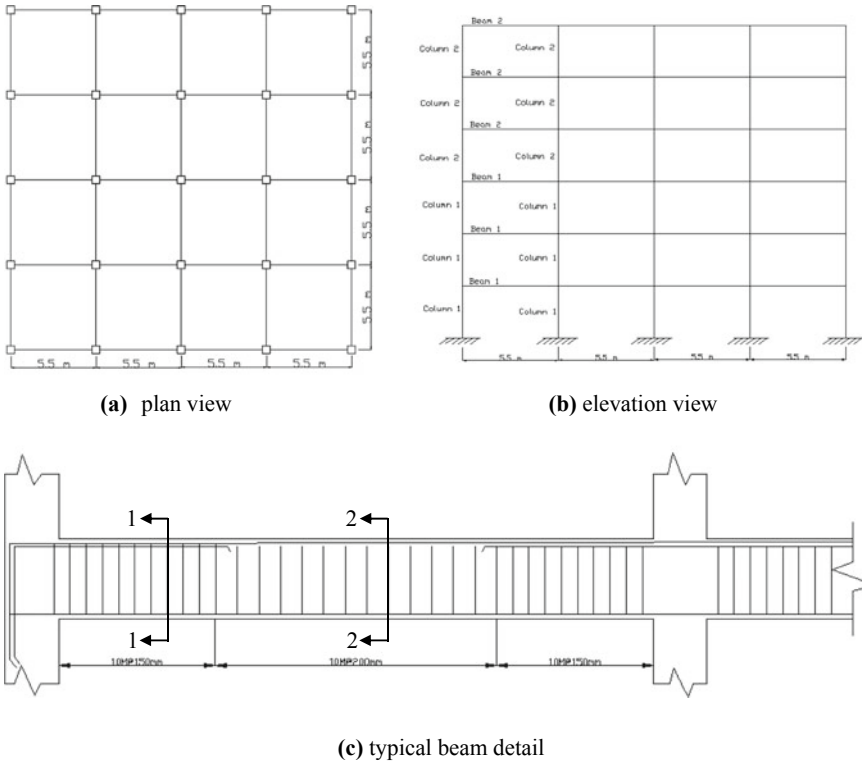
Fig. 3 RC frame

Table 1 Beam geometry and reinforcement details

Beam ID	Beam 1		Beam 2	
Section number	Top reinforcement	Bottom reinforcement	Top reinforcement	Bottom reinforcement
Victoria				
	650 × 350		550 × 350	
1-1	3-25M + 2-15M	3-25M	3-25M + 2-15M	3-25M
2-2	3-25M	3-25M	3-25M	3-25M
Montreal				
	500 × 300		400 × 250	
1-1	2-20M + 2-15M	2-20M	2-20M + 2-15M	2-20M
2-2	2-20M	2-20M	2-20M	2-20M
Winnipeg				
	450 × 250		425 × 250	
1-1	2-15M + 2-10M	2-15M	2-15M + 2-10M	2-15M
2-2	2-15M	2-15M	2-15M	2-15M

Table 2 Column geometry and reinforcement details

Column ID	Column 1		Column 2	
	Top reinforcement	Bottom reinforcement	Top reinforcement	Bottom reinforcement
Victoria				
Dimensions (mm)	600 × 600		500 × 500	
Reinforcement	8-35M		8-35M	
Montreal				
Dimensions (mm)	400 × 400		350 × 350	
Reinforcement	8-25M		8-20M	
Winnipeg				
Dimensions (mm)	350 × 350		300 × 300	
Reinforcement	8-20M		8-15M	

Fig. 4 Differential settlement case of a middle-intermediate column
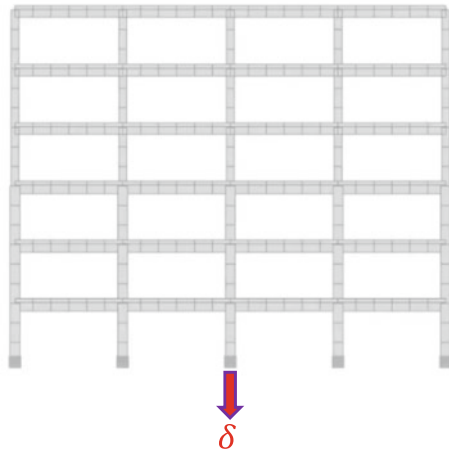
The differential settlement has resulted in a change of the load propagation path within the frames. Figure 5 shows the changes in axial load and maximum moment of the intermediate column adjacent to the middle-intermediate column, which experienced settlement. At the maximum considered settlement, the axial loads for the frames in Victoria, Montreal, and Winnipeg increased by about 58%. This increase was associated with moments of 81, 52, and 50 kN m for the three cities. Figure 6 shows the changes in axial loads and maximum moments in the next column, which is the edge column. Even though the developed moments were observed to increase, the axial loads decreased, as the middle column settlement caused uplift forces in the edge column.

It is evident, however, that seismic provisions have a profound effect on the magnitude of differential settlement that the building could experience when a loss of

(a) Axial Force (b) Bending Moment
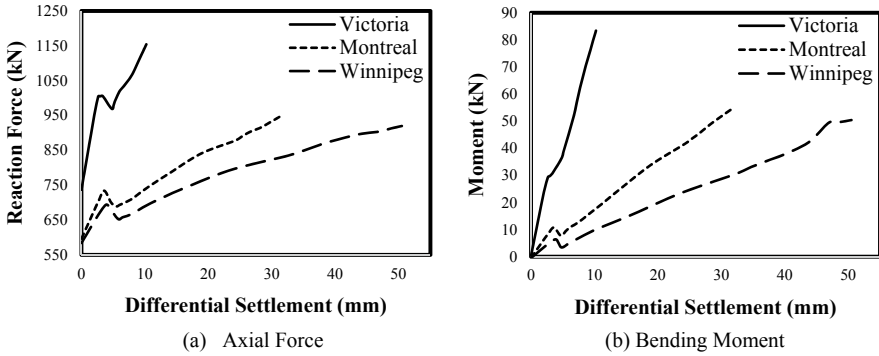
Fig. 5 Axial force and moment in the column adjacent to the column experiencing settlement

(a) Axial Force (b) Bending Moment
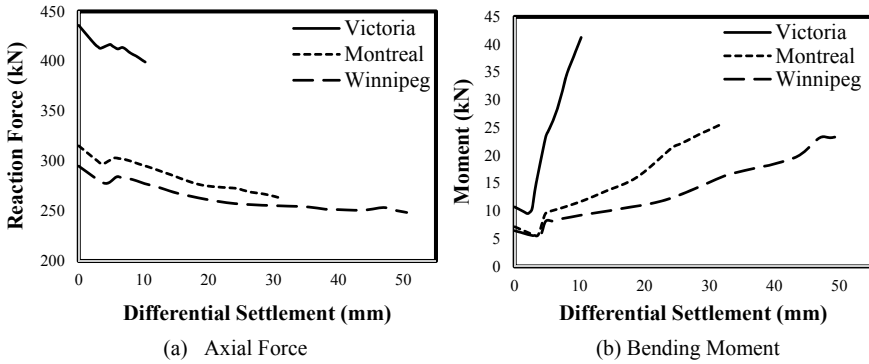
Fig. 6 Axial force and moment in the edge column

support happens. For instance, structures designed for high seismic hazard regions experienced a settlement of about 10 mm, while structures designed for low seismicity regions experienced a settlement of around 50 mm. The maximum settlements experienced by the middle column for the three frames, due to loss of support, are shown in Fig. 7. These settlement values were associated with damage in the form of yielding of the steel bars in the frame located in the low seismicity region of Winnipeg.

To assess the influence of foundation settlement location on the overall structural performance, the frame in Winnipeg was subjected to two additional settlement cases, settlement of an intermediate column and edge column, as shown in Fig. 8.

The maximum support settlement with respect to the location of the settled column is shown in Fig. 9. The greatest resistance to differential settlement was exhibited by the building when the center column was allowed to settle. At total loss of support, the center column settled 50 mm. When the edge column lost its support, a settlement of about 83 mm occurred. Figure 10 shows the variation of the axial force in the column located next to the settled column with the settlement value. Even though the graphs
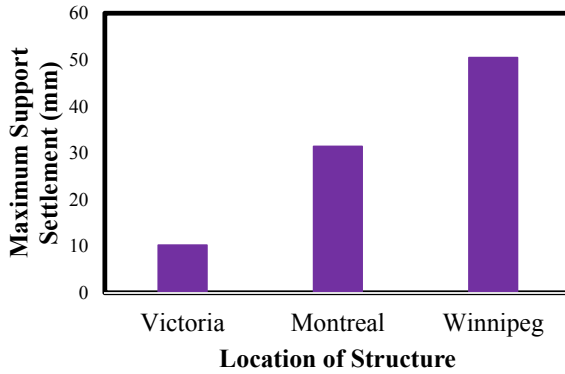
Fig. 7 Maximum settlement experienced by the frames for total support loss

(a) At Intermediate Column   **(b)** At Edge Column
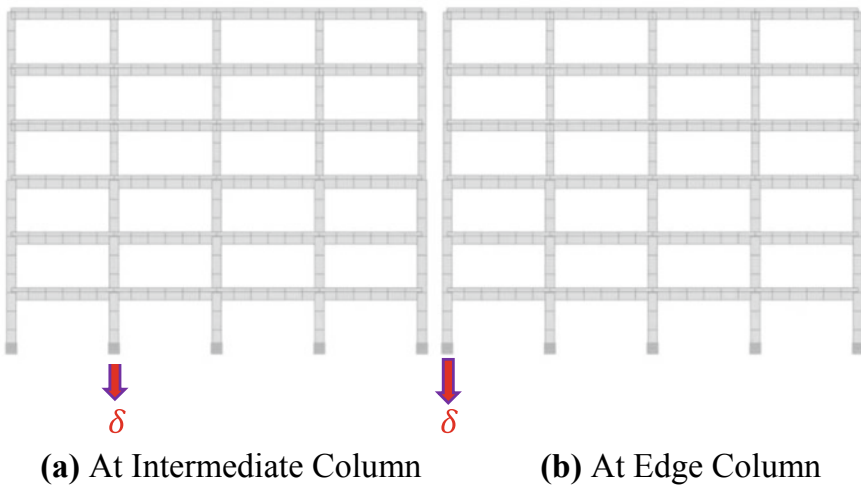
Fig. 8   Additional settlement loading scenarios for frame in Winnipeg

follow the same trend, the increase in the force demand varies with respect to the location of the settling column. For instance, the force demand increased by 57% when the center column lost its load bearing ability. When the intermediate column lost its functionality, the demand increased by 62%. The largest increase in load demand was experienced when the edge column lost its load bearing capabilities, where a 77% increase was observed.

Fig. 9 Maximum settlement of the support at each of the three locations investigated
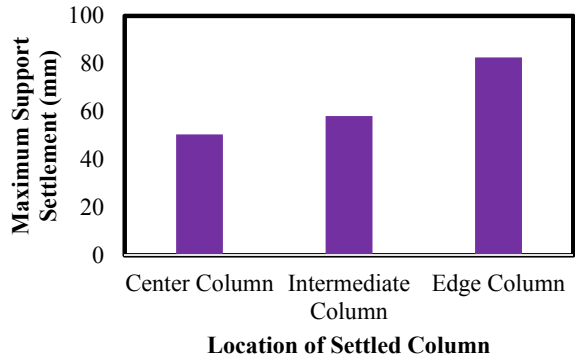
Fig. 10 Axial force developed in columns adjacent to the column exposed to settlement, shown in the legend
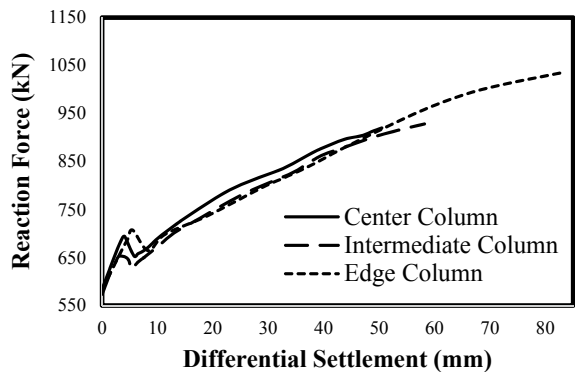
5 Conclusion

Foundation settlements could result in serious damage to structures, due to the increase in stresses and distortions. Such damage could eventually threaten the integrity of the structure, creating catastrophic failures. Hence, comprehensively understanding the effects of such settlements on the overall structural performance is important to prevent unfortunate events. In this study, it was deduced that buildings designed to withstand higher seismic hazard zones are able to provide a greater resistance to support loss and foundation settlements as compared to buildings located in low seismicity areas.

References

1. ACI (1992) Building code requirements for reinforced concrete—ACI 318-89. American Concrete Institute, Detroit, MI

2. Boldini D, Losacco N, Bertolin S, Amorosi A (2016) Modelling of reinforced concrete framed structures interacting with a shallow tunnel. Procedia Eng 158:176–181
3. Boone SJ (1996) Ground-movement-related building damage. J Geotech Eng 122(11):886–896
4. Boone SJ, Westland J, Nusink R (1999) Comparative evaluation of building responses to an adjacent braced excavation. Can Geotech J 36(2):210–223
5. Boscardin MD, Cording EJ (1989) Building response to excavation-induced settlement. J Geotech Eng 115(1):1–21
6. Burland JB, Wroth CP (1974) Settlement of buildings and associated damage. Proceedings, Conference on settlement of structures. Pentech Press, London, England, pp 611–654
7. Burland JB, Broms BB, De Mello VF (1978) Behaviour of foundations and structures
8. Chen W (2020) Structural response of multi-story buildings subjected to foundation differential settlements. Doctoral dissertation, Concordia University
9. Desbrousses RLE, Lin L (2021) Enhancing building resistance to differential settlement with Canadian seismic design provisions. Pract Period Struct Des Constr 26(2):04021011
10. Fotopoulou S, Karafagka S, Pitilakis K (2018) Vulnerability assessment of low-code reinforced concrete frame buildings subjected to liquefaction-induced differential displacements. Soil Dyn Earthq Eng 110:173–184
11. Izzuddin BA (1991) Nonlinear dynamic analysis of framed structures. Ph.D. Thesis, Imperial College, University of London, London
12. Jeong SH, Elnashai A (2005) Analytical assessment of an irregular RC frame for full-scale 3D pseudodynamic testing part I: analytical model verification. J Earthq Eng 9(1):95–128
13. Lahri A, Garg V (2015) Effect of differential settlement on frame forces. Int J Res Eng Technol 4(9):453–464. https://doi.org/10.15623/ijret.2015.0409083
14. Lin L, Hanna A, Sinha A, Tirca L (2015) Structural response to differential settlement of its foundations. J Civ Eng Res 5(3):59–66. https://doi.org/10.5923/j.jce.20150503.02
15. Lin L, Hanna A, Sinha A, Tirca L (2017) High-rise building subjected to excessive settlement of its foundation: a case study. Int J Struct Integrity
16. Mander JB, Priestley MJ, Park R (1988) Theoretical stress-strain model for confined concrete. J Struct Eng 114(8):1804–1826
17. Menegotto M, Pinto PE (1973) Method of analysis for cyclically loaded R.C. plane frames including changes in geometry and non-elastic behaviour of elements under combined normal force and bending. In: Symposium on the resistance and ultimate deformability of structures acted on by well defined repeated loads. International Association for Bridge and Structural Engineering, Zurich, Switzerland, pp 15–22
18. Meyerhof GG (1947) The settlement analysis of building frames. The Structural Engineer, September, pp 370–409
19. NBCC (2015) National Building Code of Canada. Institute for Research in Construction, National Research Council of Canada, Ottawa
20. Polshin DE, Tokar RA (1957) Maximum allowable non-uniform settlement of structures. In: Fourth international conference on soil mechanic and foundation engineering, pp 402–405
21. SeismoSoft S (2021) A computer program for static and dynamic nonlinear analysis of framed structures. Disponível online em: http://www.seismosoft.com
22. Skempton AW, MacDonald DH (1956) Allowable Settlement of Buildings. Proc Insyn Civ Eng Pt III 5:727–768
23. Wang S, Fu J, Zhang C, Yang J (2021) Ground deformation and its effects on the environment. Shield Tunnel Eng. https://doi.org/10.1016/B978-0-12-823992-6.00011-4
24. Youssef MA, Alam MS, Nehdi M (2008) Experimental investigation on the seismic behavior of beam column joints reinforced with superelastic shape memory alloys. J Earthq Eng 12(7):1205–1222
25. Youssef MA, Elfeki MA (2012) Seismic performance of concrete frames reinforced with superelastic shape memory alloys. Smart Struct Syst 9(4):313–333

Assessment of Pullout Stiffness of Grillage Foundations in Lattice Tower Structures

Majid Bahari, Sébastien Langlois, and Simon Prud'homme

Abstract Traditionally and based on the common design codes, the foundation of lattice tower structures has been considered as a fixed base, regarding no soil–structure interaction or foundation flexibility. As the lattice tower structures are subjected to complex dynamic loads and also specific nonlinear behavior, the foundation performance and consequently overall tower response under static and dynamic loads are dependent on the stiffness and damping characteristics of the foundation. To predict the foundation rigidity in different directions in numerical modeling methods, the analytical equations have been suggested in the literature in the form of impedance functions. However, the relations are generally for concrete foundations and more importantly do not include the pullout stiffness. In this study, experimental pullout tests of grillage foundations, performed by Hydro-Québec, in three different soil types including sand, clay and crushed gravel have been investigated to calculate and predict the pullout stiffness of soil-foundation system in each soil type. Exploring theoretical expressions in calculating pullout resistance of grillage foundations and tests results, the closer results to experimental values were presented. Developing a numerical code, a curve fitting has been performed for all tests of the same soil type to reproduce the normalized force–displacement curves, representing elastic, elasto-plastic and plastic behaviors of the soil-foundation system under tension forces. The results are normalized load–displacement curves, suggesting three normalized stiffnesses and two normalized displacements for clay (cohesive soils), sand and crushed gravel (non-cohesive soils) which could be implemented in prediction of the foundation pullout rigidity with an arbitrary geometry and depth of embedment. The normalized curves are compared to available analogous results in the literature.

Keywords Lattice tower structures · Grillage foundations · Pullout stiffness · Three-linear force–displacement curves

M. Bahari (✉) · S. Langlois
Département de Génie Civil et de Genie du Bâtiment, Université de Sherbrooke, Sherbrooke, Canada
e-mail: baha1704@usherbrooke.ca

S. Prud'homme
Hydro-Québec, Montréal, Canada

1 Introduction

The reliability and safety of electrical transmission line lattice tower structure are in high importance due to the demand of a resilient infrastructure to enhance the stability of energy supply system [13, 19, 20]. The interaction between lattice tower structures and foundation-soil system could significantly affect the whole structure behavior under different loading conditions [2]. However, in practice and based on common design codes, the foundation of lattice towers is considered as a fixed base, regarding no soil–structure interaction [2, 9, 13]. That is, the foundation-soil system is separated from the tower and is considered as a rigid body, representing a fixed or pinned support for the tower structure. This approach would be questionable and not realistic as the interaction among structure, foundation and soil medium could alter the actual behavior of the structure [3] and is important in the field of structural engineering [1, 18] such as seismic engineering and dynamic loads conditions [5, 8].

One approach to consider the soil–structure interaction is to define impedance functions [1, 3], which introduces springs and dashpots as interface elements between structure and foundation-soil system. Equations for impedance functions based on the foundation geometry and soil parameters have been suggested and reported in the literature in various research works such as [5, 6, 15, 17]. However, it seems that they have been developed more generally for typical concrete foundations and more importantly do not contain equations for pullout stiffness of the foundation-soil system. As the grillage foundations are widely used in lattice tower structures, it is essential to have realistic estimation of these foundations' pullout rigidity under tension forces which the tower could experience under loads such as wind or conductor breakage. This research work focuses on the evaluation and development of the uplift stiffness of an arbitrary grillage foundation of lattice tower structures in different soil types by exploring available theoretical equations for pullout resistance, soil parameters, embedment depth of the foundation and experimental pullout test results of full-scale grillage foundations.

2 Pullout Tests

The pullout experiments of grillage foundations in granular and cohesive soils have been performed by Hydro-Québec [7] on the full-scale grillage foundations of lattice towers in different sites and soil types. Figure 1 shows a sample of the conducted tests.

The foundations geometry and soil parameters of each test category have been summarized in the following subdivisions.

2.1 Granular Soils

Twenty tests in granular soils have been performed, in which sixteen tests are in sand soils and four tests in crushed gravel. Tables 1 and 2 present foundations geometry and soil parameters of each individual test for each soil type.

L and B are length and width of the grillage foundation, as shown in Fig. 2, and D is depth of the soil on top of the grillage. γ' and ϕ' are respectively volumetric weight and angle of friction of the soil in drained condition.

Table 1 Foundation geometry and soil parameters for sand soil tests

Tower	L (m)	B (m)	D (m)	γ' (kN/m^3)	ϕ' (°)
4-2	1.473	1.372	2.642	9.5	29
4-4	1.473	1.372	2.950	9.5	29
6-2	1.473	1.372	2.705	9.5	29
6-4	1.473	1.372	2.667	9.5	29
17-3	0.457	0.737	1.803	9.5	29
17-4	0.457	0.737	2.108	9.5	29
18-3	0.457	0.737	1.727	12.0	29
18-4	0.457	0.737	2.133	12.0	29
71-A	1.219	0.686	2.388	10.5	30
71-B	1.219	0.686	2.388	10.5	30
72-1	1.473	1.372	2.997	9.5	30
72-2	1.473	1.372	3.048	9.5	30
73-1	1.473	1.372	2.972	9.5	30
73-3	1.473	1.372	2.972	9.5	30
89-1	1.295	0.914	3.124	9.5	30
89-3	1.295	0.914	3.136	9.5	32

Table 2 Foundation geometry and soil parameters for crushed gravel tests

Tower	L (m)	B (m)	D (m)	γ' (kN/m^3)	ϕ' (°)
IREQ-A-1	1.295	0.914	3.100	13.0	42
IREQ-A-3	1.295	0.914	2.718	13.0	40
IREQ-B-1	1.295	0.914	2.800	13.0	40
IREQ-B-3	1.295	0.914	2.700	13.0	40

Fig. 2 Typical geometry of grillage foundation
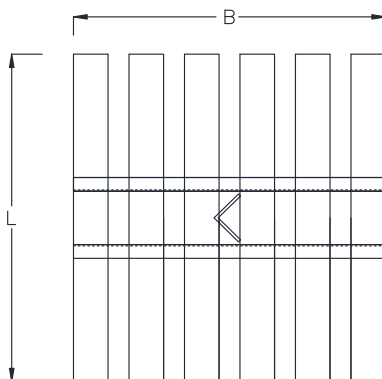
2.2 Cohesive Soils

Similarly, the foundation geometry and soil parameters of fifteen tests conducted in cohesive soils have been summarized in Table 3.

$C_{u,\text{ave}}$ is average cohesion parameter of the native soil, and $C_{u,\text{grillage}}$ is the cohesion parameter of the back fill soil on the top of the grillage.

3 Theoretical Expression for Pullout Resistance and Interpretation of Experimental Results

Various methods have been studied and suggested in literature to calculate the uplift resistance of shallow and deep foundations, such as the works of Kulhawy [10, 12]. A critical review of the methods which are more applicable for metallic foundations of lattice towers has been provided in the [7]. Based on the interpreted experimental resistance and investigated theoretical calculations, the applicable method which has closer results to experimental tests, introduced in previous section, has been determined. Accordingly, the best-match method for each soil type would be implemented in calculating and predicting foundation pullout stiffness. The following sections briefly explain the available theoretical methods in calculation of pullout resistance of grillage foundations for the two general types of granular and cohesive soils.

Table 3 Foundation geometry and soil parameters for cohesive soil tests

Tower	L (m)	B (m)	D (m)	$C_{u,\text{ave}}$ (kPa)	$C_{u,\text{grillage}}$ (kPa)	γ_{Sat} (kN/m^3)
27-1	1.295	0.914	2.845	23	32	15.6
27-4	1.295	0.914	2.794	32	48	14.6
49-3	1.905	1.219	3.048	29	32	16.4
50-3	1.905	1.219	3.100	34	42	15.8
54-4	1.905	1.219	3.100	31	20	15.5
57-1	1.905	1.219	2.997	42	37	16.6
58-2	1.295	0.914	2.845	30	37	16.9
74-B	1.219	0.686	2.388	36	14	16.2
80-A	1.219	0.686	2.388	42	14	16.1
80-C	1.219	0.686	2.388	38	15	16.1
90-1	1.295	0.914	2.959	24	21	16.0
90-2	1.295	0.914	2.921	19	17	15.8
96-1	1.295	0.914	2.743	48	48	15.9
96-4	1.295	0.914	2.642	27	84	18.9
110-1	1.295	0.914	3.050	29	37	17.7

3.1 Granular Soils

Four methods to calculate pullout resistance of the grillage foundations in granular soils have been investigated, in which the details are available in [7]. The comparison among the results of investigated theoretical methods and experimental results clarifies that the method of Kulhawy [10] for granular soils has more realistic prediction of the uplift resistance. Therefore, this method has been used in this study for the definition of theoretical resistance for granular soils, which would be used in prediction of foundation stiffness. Table 4 summarizes the other methods and the average of 'm' factor in each method for all tests. The 'm' factor has been defined as the ratio between measured experimental rupture force (Q_m) and theoretical calculated resistance force (Q_c) in each method. Q_m has been determined using the tangents method, which will be presented later.

The methods mentioned in Table 4 have been explained in the report of Hydro-Québec [7]. The method of Kulhawy which is applicable for granular soils in drained conditions is defined as follows [10]:

Table 4 The m values of different methods in calculation of uplift resistance for sand soils [7]

Average m for sand soils	Method of cone ($\alpha = 10°$)	Method of cone ($\alpha = 15°$)	Method of SN-40.1 HQ	Method of Kulhawy	Method of Meyerhof & Adams
m_{ave}	0.89	1.21	1.23	1.05	1.82

$$Q_c = W_f + W_s + Q_{su} + Q_{tu} \tag{1}$$

W_f and W_s are respectively weight of the foundation and weight of the soil on the top of the grillage. Q_c is the calculated theoretical resistance of the foundation, and Q_{su} is the shear resistance of the soil which is defined in Eq. (2). Q_{tu} is the suction resistance under the grillage.

$$Q_{su} = 2 \times (B + L) \times \sum_{n=1}^{N} \sigma'_{vn} \times K_n \times \tan \phi'_n \times d_n, \tag{2}$$

in which:

N is the total number of soil layers, K_n is horizontal soil pressure coefficient of layer n, ϕ'_n is angle of friction for layer n, d_n is thickness of soil layer (in m), and σ'_{vn} is the effective vertical stress of layer n (in kPa). Equation (1) has been used in estimation of pullout resistance of the foundation of tests in granular soils.

On the other hand, to interpret and determine the measured rupture resistance (Q_m) from experimental force–displacement curves, different strategies have been suggested in the literature. Nevertheless, the transition border between elastic and elastoplastic/plastic deformation zones in the force–displacement curve of the foundation under uplift force is not always easy to identify. Besides, the rupture force could not be considered as the ultimate (Q_u) force in the curve, as it has less practical use in engineering works, since it is associated to the large displacements of foundation.

The interpretation methods could be listed such as hyperbolic model, log–log method, parabolic method, method of intersection of tangents, slope-tangent method and fixed-displacement method. Definition and details of the mentioned methods could be found in [4]. Reviewing the literature such as [4, 7, 10, 11], the method of intersection of tangents, especially for granular soils, to define the rupture force and margin of elastic and nonelastic displacement zones, is the preferred one. Therefore, this method has been used in this study to evaluate the rupture resistance for granular soils. The value of Q_m of each test, determined based on the intersection of tangents method, is listed in Table 5 along with calculated theoretical value. Figure 3 shows an example of application of the tangents method to a curve of sand soil. In this method, as illustrated in Fig. 3, two lines are defined in which the first (tg1) is tangent to the elastic part of the curve and the second (tg2) is tangent to the plastic part of the curve. The intersection of the two lines corresponds to rupture resistance.

3.2 Cohesive Soils

Similar to granular soils, different methods to calculate and predict the rupture resistance from experimental force–displacement curves of cohesive soils under uplift loads have been suggested in the literature. Four methods have been explored and

Table 5 Theoretical resistance versus experimental resistance in sand soils

Tower	Theoretical resistance, Q_c (Kulhawy method) (kN)	Experimental resistance, Q_m (intersection of tangents) (kN)
4-2	118	145
4-4	139	174
6-2	178	202
6-4	172	202
17-3	36	45
17-4	47	39
18-3	47	47
18-4	64	69
71-A	77	53
71-B	77	65
72-1	192	179
72-2	193	130
73-1	155	121
73-3	155	138
89-1	160	153
89-3	170	178
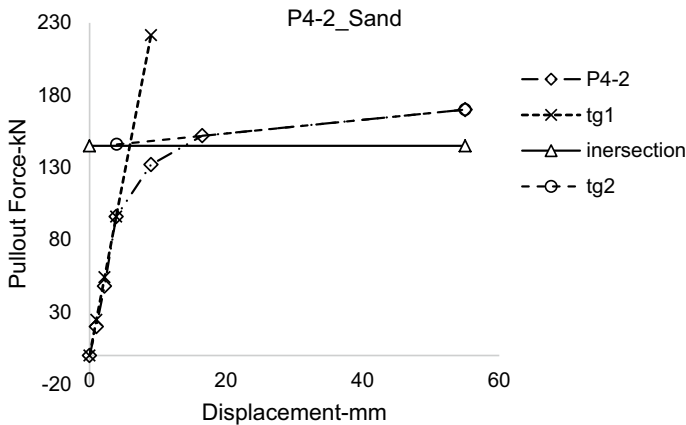
Fig. 3 Interpretation of experimental uplift resistance in sand soils with tangents method

results compared to experimental resistance. The evaluation of the experimental resistance will be presented at the end of this section. The comparison between different methods and experimental results shows that the shear method [16, 21] gives closer estimation to experimental results. The investigated method and '*m*' factor for each equation are summarized in Table 6.

Table 6 The m values of different methods in calculation of uplift resistance for cohesive soils [7]

Average m for sand soils	Method of cone ($\alpha =$ 10 °)	Method of cone ($\alpha =$ 15 °)	Method of SN-40.1 HQ	Shear method	Method of Meyerhof & Adams
m_{ave}	0.80	1.12	1.32	1.06	1.60

The general form of shear method is defined in Eq. (3). The concept of the method which is similar to method of Meyerhof and Adams [14] has been defined and suggested by both Turner [21] and Ontario-Hydro (now Hydro One) [16].

$$Q_c = S_v \times \omega \times 2 \times (B + L) \times D + W_f + W_s, \tag{3}$$

in which:

Q_c is theoretical calculated uplift resistance (in kN), D is depth of grillage foundation (in m), and B and L are width and length of the foundation (in m). W_f and W_s are respectively weight of the foundation and that of the soil, and ω is dynamic amplification factor for short-duration tests. S_v is the shear resistance along the vertical rupture face of the soil on top of foundation, which is a function of $C_{u,ave}$, soil cohesion (in kPa):

$$S_v = \Psi \times C_{u,ave}, \tag{4}$$

where Ψ is the ratio between mobilized shear resistance and the average of shear resistance of the soil in undrained conditions which is usually considered as 0.2 [16].

Like for granular soils, it is needed to define the pullout resistance based on the experimental results. Comparing the general shape of force–displacement curves in granular and cohesive soils, change between the slopes of the elastic and inelastic parts of the curve happens more gradually in cohesive soils. That is, differentiation between these two zones is more challenging in cohesive soils, as the transformation between the phases occurs smoothly. Besides, the ultimate resistance in cohesive soils corresponds to a larger displacement in comparison with sand soils. Consequently, and according to [7] suggestion, the experimental rupture uplift resistance of cohesive soils has been established based on the maximum value of intersection of tangents methods and the value equivalent to a fixed displacement of 25 mm. Figure 4 illustrates a sample curve of cohesive soil test in which the uplift resistance is evaluated. Table 7 summarizes the calculated theoretical resistance based on the shear method versus experimental interpretation of uplift resistance.
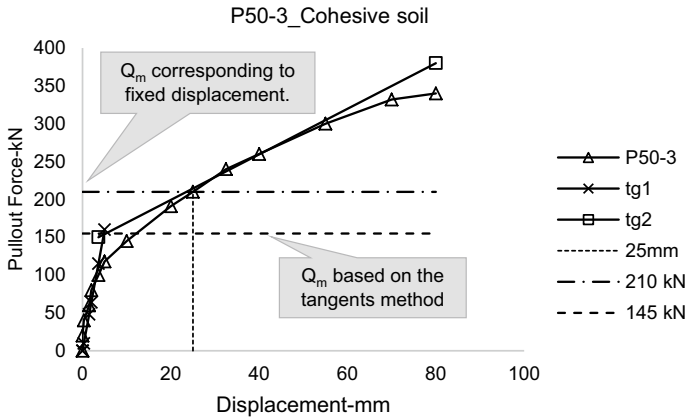
Fig. 4 Interpretation of rupture resistance in a sample of cohesive soil

Table 7 Theoretical resistance versus experimental resistance in cohesive soils

Tower	Theoretical resistance (shear method) (kN)	Experimental resistance (maximum of the two methods) (kN)
27-1	113	150
27-4	130	250
49-3	230	253
50-3	247	210
54-4	199	191
57-1	278	162
58-2	136	102
74-B	51	56
80-A	51	50
80-C	55	60
90-1	122	95
90-2	106	85
96-1	183	200
96-4	125	132
110-1	149	122

4 Normalization of the Force–Displacement Curves

When force–displacement points from all available tests for the same soil type are plotted in one graph, a scattered cloud of points appears. The following figures demonstrate this graph for each soil type (Figs. 5, 6 and 7).
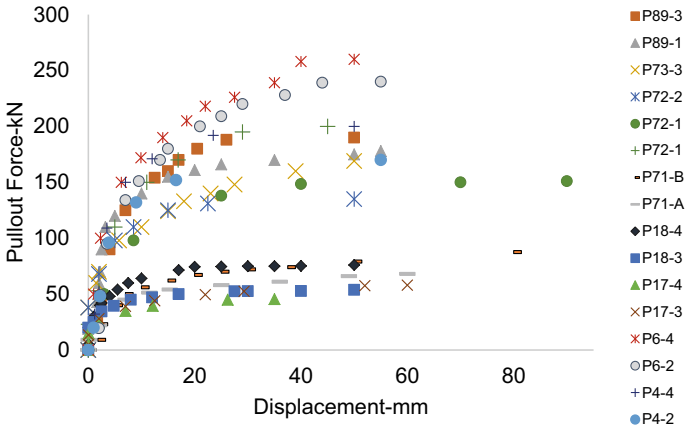
Fig. 5 Force–displacement results of all pullout tests of foundation in sand soils
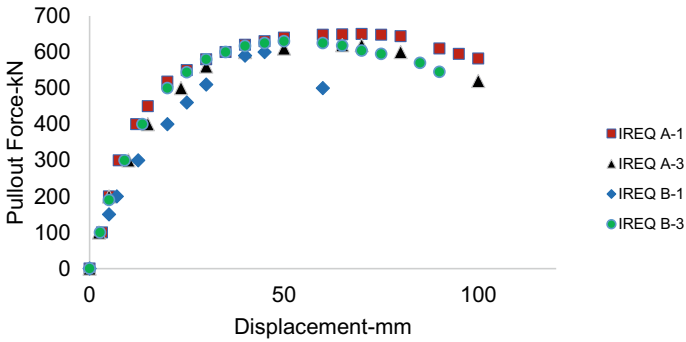
Fig. 6 Force–displacement results of all pullout tests of foundation in crushed gravel
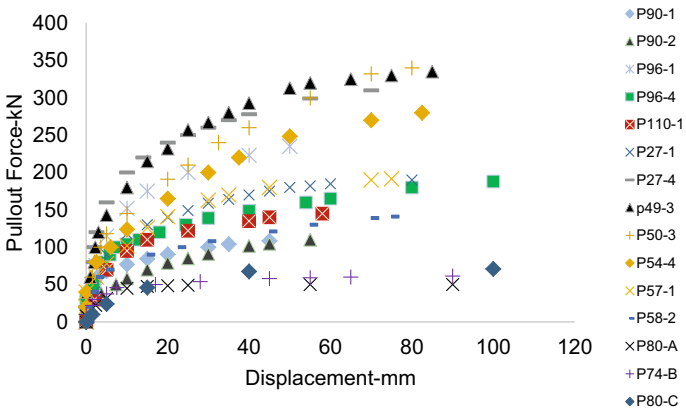
Fig. 7 Force–displacement results of all pullout tests of foundation in cohesive soils

Therefore, to regroup all available data and also to consider soil properties and foundation geometry, a normalization has been performed for both the displacement and the force axes of the curve. The displacement is normalized by the depth of the foundation (z/D), where z is the vertical displacement from experiment and D is the depth of the soil on top of the foundation. Similarly, the force is normalized by the measured rupture resistance (Q/Q_m), where Q is the vertical force applied in experiment and Q_m is the measured rupture resistance, calculated in Sect. 3. This normalization is in accordance with the one presented in [11]. Figures 8, 9 and 10 show the results of normalization for the three soil types. It is observed that the normalized data points are now regrouped and share similar tendency.
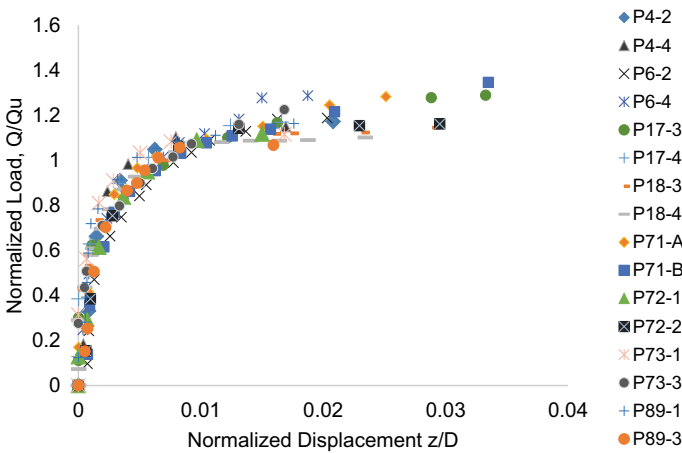
Fig. 8 Normalized force–displacement curve of all pullout tests of foundation in sand soils
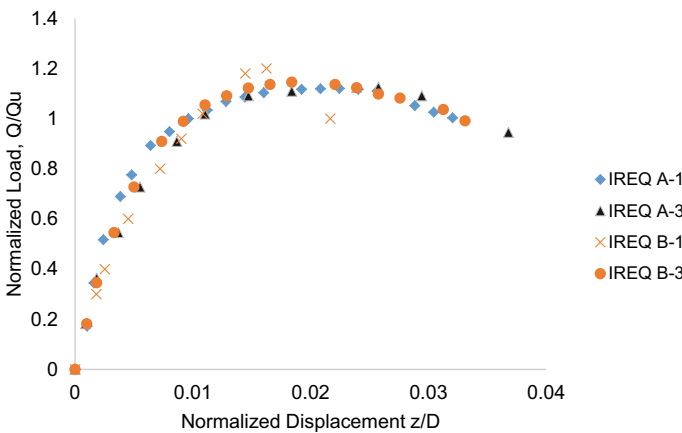
Fig. 9 Normalized force–displacement curve of all pullout tests of foundation in crushed gravel
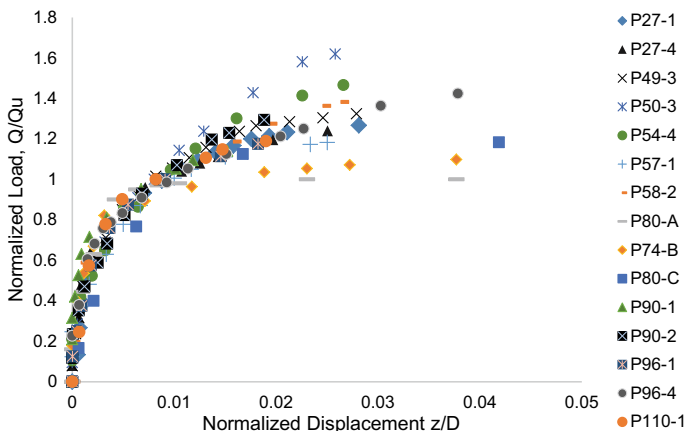
Fig. 10 Normalized force–displacement curve of all pullout tests of foundation in cohesive soils

5 Definition of Normalized Three-Linear Force–Displacement Curves

The purpose of this research work is to estimate the uplift stiffness of grillage foundations under pullout axial forces in different soil types and foundation properties. To do so, normalized experimental force–displacement curves have been replicated with a three-linear curve, representing three different behavioral phases of the soil-foundation system under uplift force: elastic, elastoplastic and plastic.

5.1 Curve Fitting for Three-Linear Curves

Three uplift rigidities representing elastic, elastoplastic and plastic deformation of a grillage foundation, for three types of soils, have been characterized through curve fitting of three-linear functions. Illustrated in Fig. 11, k_1^* is the first slope of the normalized curve, starting from zero normalized displacement until Δ_1^*. k_2^* starts from the end of k_1^* until Δ_2^*. And k_3^* continues k_2^* up to the maximum point of the measured normalized displacement corresponding to a measured maximum force. The values after the maximum force have been removed from raw experimental data, as the measured force decreases after this point by increasing in displacement.

Developing a Python code, a curve-fitting evaluation has been performed for the normalized experimental data for each soil type, and five parameters including k_1^*, k_2^*, k_3^*, Δ_1^* and Δ_2^* have been calculated. The following figures illustrate final normalized three-linear curves of normalized force–displacement test results. These five normalized parameters are listed in Table 8 (Figs. 12, 13 and 14).
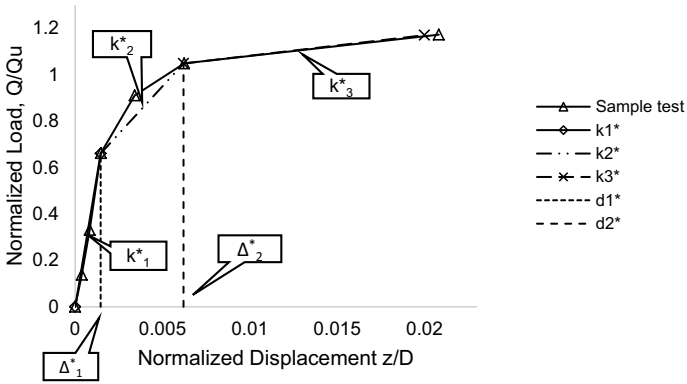
Fig. 11 Three-linear normalized curve for a sample test in sand soils

Table 8 Normalized parameters for each soil type

Soil type	k_1^*	k_2^*	k_3^*	Δ_1^*	Δ_2^*
Sand	499.339	65.360	8.950	0.00141	0.00677
Crushed gravel	189.194	66.434	6.098	0.00304	0.01045
Clay (cohesive soil)	535.104	55.426	6.258	0.00109	0.01137
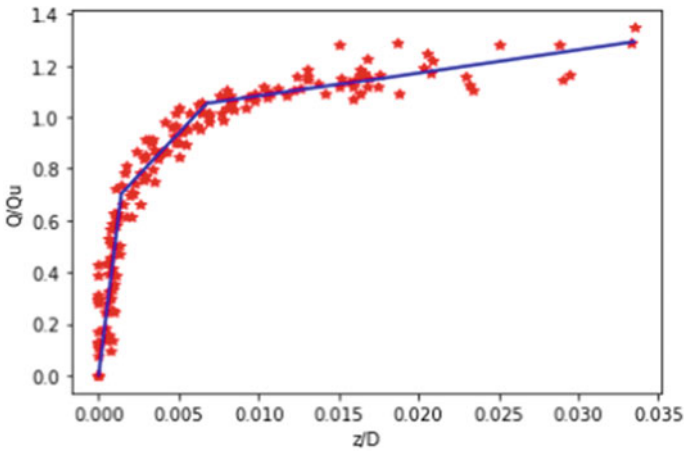
Fig. 12 Three-linear normalized curve of all sand tests
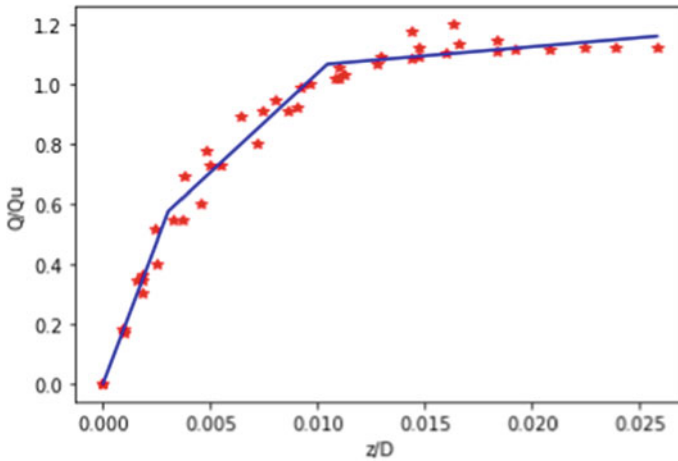
Fig. 13 Three-linear normalized curve of all gravel tests
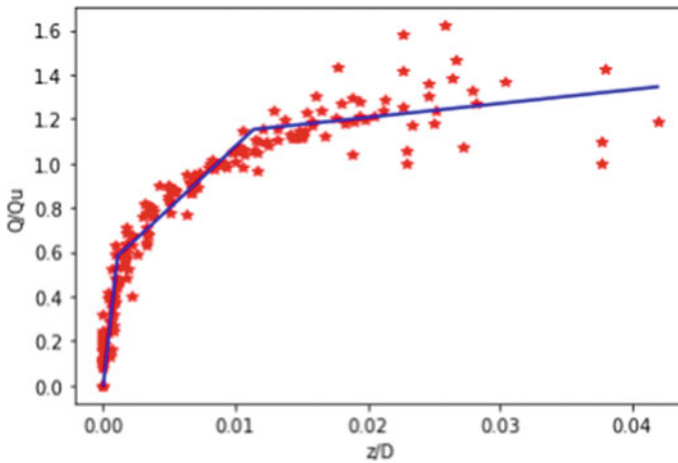
Fig. 14 Three-linear normalized curve of all cohesive tests

6 Discussion

Knowing the installation depth and calculating the Q_m theoretically, the three-linear force–displacement curve of an arbitrary grillage foundation under pullout force could be generated using values from Table 8. To calculate Q_m (Q_c), as discussed and verified in Sect. 3, the Kulhawy method for granular soils and shear method for cohesive soils give the more realistic estimations and could be implemented in calculation of each k. Once Q_m (Q_c) is calculated, k^* must be multiplied by Q_c/D
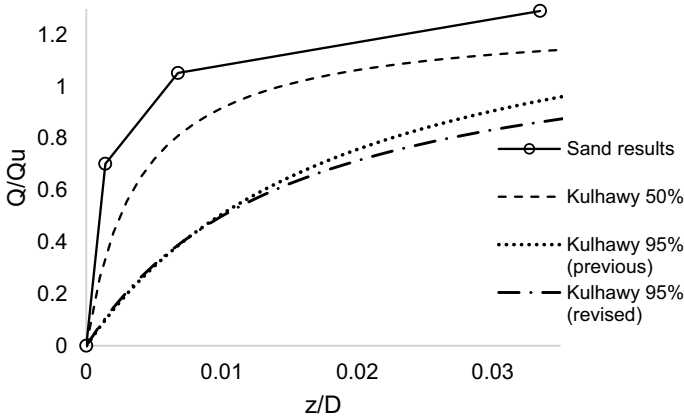
Fig. 15 Comparison of different normalized curves in sand soils

and Δ^* multiplied by D in order to calculate the specific pullout force–displacement curve of the foundation.

In the literature, a normalized curve has also been suggested by Kulhawy [11] through investigation of eight full-scale tests only for granular soils. The study suggests a revised equation of normalized curve for 95% confidence limit. The 50% (median) confidence limit curve is also defined, which is compared in Figs. 15, 16 and 17 to the curve fitting of the normalized experimental data for each soil type. As the results show, the normalized force–displacement curves are dependent on the soil type and characteristics. Accordingly, since the Kulhawy's curve is based only on the granular soils, it might be normal to obtain differences in the comparison figures of different soil types. More information about compaction of the backfill soil and its geotechnical parameters such as SPT number, angle of friction and cohesion resistance in Kulhawy's tests and comparison to soil parameters of this study tests might lead to more clarifications in the differences.

As expected, a general comparison in each soil type shows that the provided three-linear curves are close to Kulhawy 50% confidence curves rather than 95% confidence ones, especially in crushed gravel. However, the first and second estimated slopes (stiffnesses) in each three-linear curve are larger than those of Kulhawy 50% curve, especially in sand and cohesive soils. Meanwhile, it could be inferred that the third slope of each three-linear curve is almost parallel to the analogous part of Kulhawy's curve. Overall, it could be said that the stiffnesses obtained in this research study are found to be in a general accordance with those of previously presented by Kulhawy.
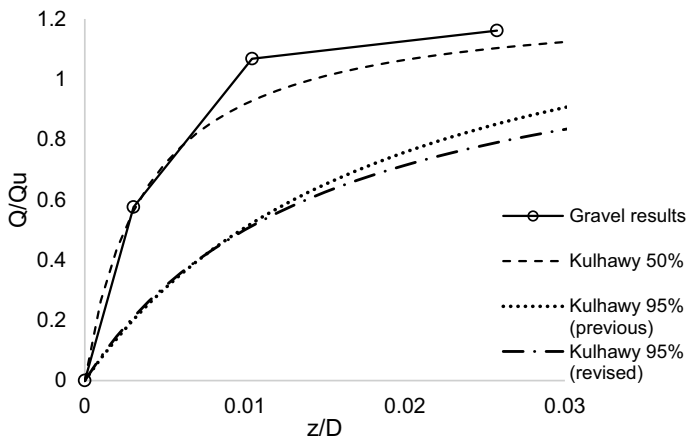
Fig. 16 Comparison of different normalized curves in crushed gravel
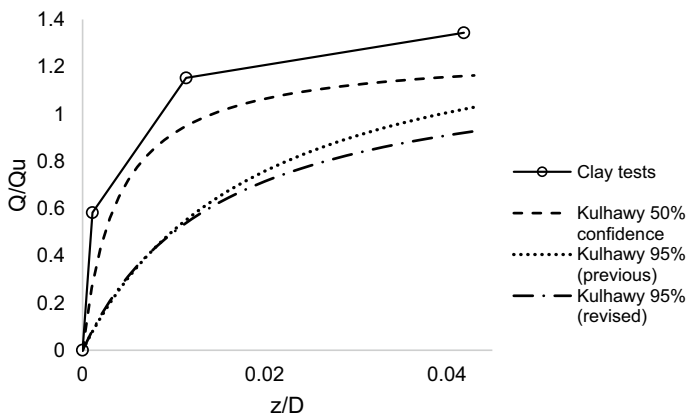
Fig. 17 Comparison of different normalized curves in cohesive soils

7　Summary and Conclusion

As grillage foundations are widely used in lattice tower structures, it is essential to estimate the soil-foundation system stiffness in order to evaluate its effect on overall tower behavior under different loading conditions. This paper explored the uplift stiffness of grillage foundations in different soil types for three deformation phases of load–displacement curves. To do so, the uplift force–displacement experimental results of fifteen grillage foundations in cohesive soils, sixteen tests in sand soils and four foundations in crushed gravel, which were performed by Hydro-Québec, were presented and analyzed. Pullout rupture resistance of each individual test was interpreted from experimental load–displacement curves and was compared to results

of different theoretical methods. Comparing the experimental test results, the best-match theoretical method in calculation of pullout resistance of grillage foundations in granular and cohesive soils was reviewed and presented.

Using the approach of [11], the force–displacement curves were normalized. Developing a Python code, a three-linear normalized force–displacement curve was fitted, and consequently, three normalized stiffnesses and two normalized displacements were extracted for each soil type. The three normalized stiffnesses represent respectively elastic, elastoplastic and plastic behaviors of soil-foundation system under uplift force. Employing three normalized stiffnesses, resulting from this study, knowing the embedment depth of the foundation and calculating rupture resistance theoretically, three uplift stiffnesses for three behavioral phases of the grillage foundation could be estimated. To calculate theoretical resistance, Kulhawy method for granular soils and shear method for cohesive soils have closer results to experimental values. Similarly, applying two normalized displacements for each soil type and knowing the depth of embedment of foundation, two displacements corresponding to the elastic and elastoplastic deformation limits could be evaluated.

The normalized three-linear curves were compared to the normalized curve of Kulhawy, which has been suggested only for granular soils. A general comparison between all three-linear normalized curves and Kulhawy's results shows that the three-linear curves are close to 50% confidence curves, rather than 95% ones. Besides, in cohesive and sand soils, the first and second slopes of the provided curves are greater than Kulhawy's estimations. Generally, as the results demonstrate, the normalized force–displacement curves are dependent on the soil types, and more geotechnical data of soil tests in Kulhawy's work might explain the differences.

More tests in each soil type with different degree of resistance and compaction might provide more insight and generality of the provided three-linear curves. The same procedure could be performed for concrete foundations to estimate pullout stiffness for concrete ones, as the impedance functions in the literature do not comprise uplift stiffness. The comparison in results of concrete and grillage foundation might result in the accurate use of available impedance functions for grillage foundation and accordingly the comparison of overall tower behavior with grillage and concrete foundations under different loading conditions.

References

1. Anand V, Kumar SR (2018) Seismic soil-structure interaction: a state-of-the-art review. Structures 16:317–326
2. CIGRE (2020) Conseil International des Grands Réseaux Électriques, B2. Dynamic loading effects on overhead lines: impacts on foundations. CIGRE B2, Overhead lines, Reference 788

3. Dutta SCh, Roy R (2002) A critical review on idealization and modeling for interaction among soil–foundation–structure system. Comput Struct 80:1579–1594
4. EPRI (1983) Transmission line structure foundations for uplift-compression loading. Electric Power Res. Inst. EL-2870. Project 1493-1
5. Gazetas G (1991) Formulas and charts for impedances of surface and embedded foundations. J Geotech Eng 117(9):1363–1381
6. Gazetas G, Anastasopoulos I, Adamidis O, Kontoroupi T (2013) Nonlinear rocking stiffness of foundations. Soil Dyn Earthq Eng 47:83–91
7. Hydro-Québec (2005) Amélioration de la Robustess des Lignes de Tarnsport. Resistance en Soulevement des Fondations Existantes de Type Grillage Metallique. LCG-39.DOC-18
8. Jendoubi A, Legeron F (2013) Effect of the dynamic soil-structure interaction on rigid transmission line towers subjected to wind and impulse loads. In: Electrical transmission and substation structures. ASCE, pp 250–261
9. Jendoubi A (2015) Effet de l'interaction dynamique linéaire et non-linéaire sol-structure: application aux pylônes de transport d'énergie. Ph.D. thesis, Université de Sherbrooke, Québec, Canada
10. Kulhawy FH (1988) Tension behavior of foundations in soil, an overview. Cross Canada Lecture
11. Kulhawy FH, Stewart HE (1994) Uplift load-displacement behaviour of grillage foundations. In: Foundation and embankment deformations, pp 233–244
12. Kulhawy FH, Stewart HE, Trautmann CH (2003) On the uplift behaviour of spread foundations. Fondations superficielles. Magnan et Droniuc. Presses de l'ENPC/LCPC, Paris, pp 327–334
13. Kyung D, Choi Y, Jeong S, Lee J (2015) Improved performance of electrical transmission tower structure using connected foundation in soft ground. Energies 8:4963–4982
14. Meyerhof G, Adams G (1968) The ultimate uplift capacity of foundations. Can Geotech J 5(4):225–244
15. Mylonakis G, Nikolaou S, Gazetas G (2006) Footings under seismic loading: analysis and design issues with emphasis on bridge foundations. J Soil Dyn Earthq Eng 26:824–853
16. Ontario-Hydro (1979–1981) Transmission design methods. Recueil des pratiques d'Ontario-Hydro
17. Pais A, Kausel E (1988) Approximate formulas for dynamic stiffnesses of rigid foundations. J Soil Dyn Earthq Eng 7(4):213–227
18. Roesset JM (1980) A review of soil-structure interaction, Soil-structure interaction: the status of current analysis methods and research. J.J. Johnson. Report, US. Regulatory Commission and Lawrence Livermore Laboratory
19. Savory E, Parke GAR, Disney P, Toy N (2008) Wind-induced transmission tower foundation loads: a field study-design code comparison. J Wind Eng Ind Aerodyn 96(8):1103–1110
20. Shu Q, Huang Z, Yuan G, Ma W, Ye Sh, Zhou J (2018) Impact of wind loads on the resistance capacity of the transmission tower subjected to ground surface deformations. Thin-Walled Struct 131:619–630
21. Turner EA (1962) Uplift resistance of transmission tower footings. J Power Div 88(2)

Damage Mitigation for Precast Concrete Column-to-Pile Shaft Member Socket Connections

Haifeng He and Cancan Yang

Abstract Designing precast concrete substructure connections, which adjoin a column to its foundation/cap beam, for satisfactory seismic performance is a daunting challenge to deploy Accelerated Bridge Construction in seismic regions. Among various connection types, member sockets feature the ease of construction due to their ability to provide large installation tolerances. However, their seismic application is limited, because resisting earthquake-induced loading often requires the column adjoining member sizes that exceed those in cast-in-situ construction. The member socket connection provides flexural load resistance mainly through prying action. Ultra-high-performance concrete (UHPC), a fiber-reinforced cementitious material with exceptional tensile properties, offers substantial potential in mitigating the prying action-induced damage to the pile shaft. This research aims to analytically investigate if and to what extent the pile shaft size can be reduced due to the excellent damage control ability of UHPC. To this end, a nonlinear finite element approach is first developed to simulate the behavior of precast concrete column-to-pile shaft member socket connections under a combination of axial and reversed cyclic loads. The modeling approaches are validated by comparing the predicted behavior with the prior laboratory test results. The verified finite element model is then used to evaluate the behavior of member sockets with different UHPC shaft diameters. Analysis results show that UHPC plays an effective role in reducing prying action-induced damage. Using UHPC for casting the shaft within the connection region presents a feasible solution to reduce the pile shaft size without compromising the connection's ability to sustain prying-induced inelastic action.

Keywords Damage mitigation · precast concrete · Column-to-pile shaft member · Connections

H. He (✉) · C. Yang
McMaster University, Hamilton, Canada
e-mail: heh36@mcmaster.ca

1   Introduction

Accelerated bridge construction (ABC) has been widely accepted as an efficient technique due to its advantages over cast-in-place bridge systems [5]. Besides improving site constructability and material quality, ABC can help to reduce traffic disruptions and minimize environmental impacts [1]. In ABC, prefabricated bridge elements are joined through special connectors to form the bridge system. Therefore, reliable connections between these components are essential to achieving satisfactory structural behavior. In recent studies, various connection types including mechanical bar couplers, grouted ducts, pocket, and member socket connections have been proposed and investigated [2]. Among these connections, member socket connections offer much larger installation tolerances. However, their field application is quite limited in moderate-to-high seismic regions due to the lack of understanding of their seismic performance [4].

In general, the precast column-to-pile shaft member socket connection provides flexural resistance through prying action [1]. The concrete tensile strength of the shaft and shaft transverse reinforcement are the two major sources to provide confinement for pile shafts to resist prying action. Tran [7] tested three column-to-pile shaft socket connections under quasi-static loads and found that insufficient transverse reinforcement could lead to premature failure of the pile shaft. In the meanwhile, the test results also showed that more transverse reinforcement was required if the size of the pile shaft was reduced. Therefore, column-to-pile shaft member socket connections usually require the pile shaft with a larger geometric size compared with a cast-in-place system, and enough amount of transverse reinforcement must be provided to avoid prying action failure. This will lead to the increasing cost and hamper their practical application. UHPC is a fiber-reinforced cementitious material with exceptional tensile properties [8], thereby offering great potential to minimize prying action-induced damage, therefore reducing the required pile shaft size. However, the effect of UHPC on the seismic performance of column-to-pile shaft member socket connections has been rarely investigated.

Thus, this study aimed to unlock the potential of UHPC in improving the seismic performance of column-to-pile shaft member socket connections. Firstly, the test results in the previous studies were used to validate the numerical modeling methodologies for column-to-pile shaft member socket connections and UHPC. Then, UHPC was used to replace the pile shaft concrete in the numerical model and the dimension of the pile shaft with UHPC was changed. At last, the numerical results obtained for cases with varying dimensions of UHPC pile shaft were discussed to understand the effective role played by UHPC in controlling seismic damage for column-to-pile shaft member socket connections. The analysis results also shed light on the potential of UHPC to reduce the required size of pile shafts while maintaining satisfactory seismic performance.

2 Numerical Modeling for Member Socket Connections

2.1 Test Specimens

The test specimens in Tran's study [7] were used as the benchmark column-to-pile shaft member socket connections in this study as shown in Fig. 1a. It can be seen that the specimens DS-1 and DS-2 shared the same column details including the diameter of 508 mm, longitudinal reinforcement ratio of 1%, and transverse reinforcement ratio of 0.8%. The diameter and longitudinal reinforcement ratio of the pile shaft for the two different specimens were 762 mm and 0.9%. The embedment of the column had an octagonal shape with an intentionally roughed surface and the embedment length was 711 mm. The only difference between the specimen DS-1 and DS-2 is the transverse reinforcement ratio in the pile shaft. The amount of transverse reinforcement of DS-1 was two times that of DS-2. The objective to do so was to induce prying action failure at the connection region for DS-2. The two specimens were tested under the constant axial load of 707 kN and quasi-static loads until ultimate limit states were reached. The test results showed that the plastic hinge occurred at the bottom of the column for DS-1 and failure was caused by the rupture of longitudinal reinforcement near the interface between the column and pile shaft. However, the failure of DS-2 was caused by the rupture of transverse reinforcement in the pile shaft while the damage to the column was not very severe.
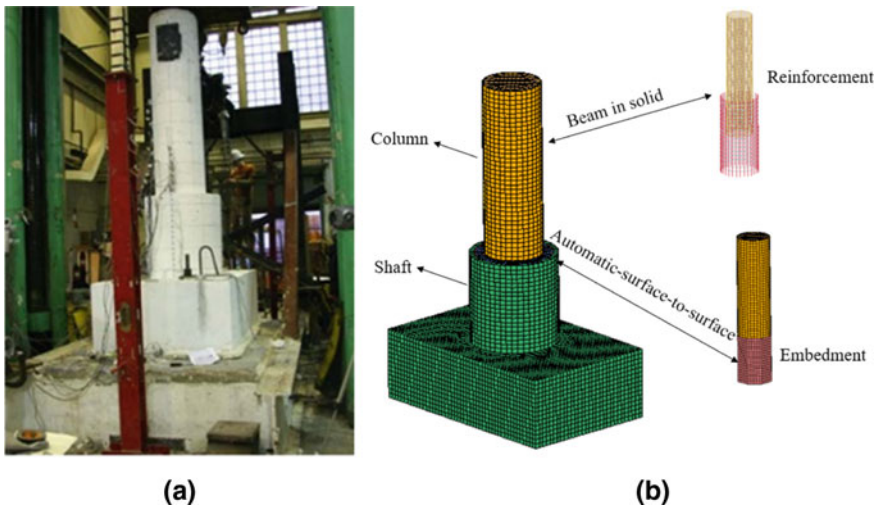
Fig. 1 a Tested specimen [7]; **b** finite element model in LS-DYNA

2.2 Numerical Modeling

The finite element models for the two specimens were created in the LS-DYNA software. As shown in Fig. 1b, the concrete of the column and shaft was modeled by solid elements and its material properties were captured by the concrete damage plasticity model, which has been proved to be capable of providing more accurate concrete behavior compared with other material models [9, 10]. In the CDP model, an exponential stress–nonlinear strain relationship was used to reflect the compressive responses and the inelastic strain ε_{fc} should be defined to describe the strain-softening behavior of concrete under compression. According to Zhao et al. [9, 10], the parameter ε_{fc} was defined as 0.005 for unconfined concrete and 0.01 for confined concrete, respectively. For the tensile response, a bilinear damage model was employed and the tensile threshold parameter w_f should be defined to describe the strain-softening behavior of concrete under tension. The parameter w_f can be expressed as follows [3]:

$$w_f = \frac{4.444 G_f}{f_t'} \tag{1}$$

in which G_f is tensile fracture energy and f_t' is the tensile strength of concrete. These two parameters can be calculated as [6, 9, 10]:

$$G_f = 73 f_c'^{0.18}, \tag{2}$$

$$f_t = 0.53\sqrt{f_c'} \tag{3}$$

in which f_c' is the compressive strength of the concrete. In this study, the compressive concrete strength for the column and pile shaft was 53.6 MPa and 49.4 MPa, respectively. The longitudinal reinforcement in the column and pile shaft was modeled by the "Piecewise-Linear-Plasticity" material in LS-DYNA using the uniaxial stress–strain relationship from material tests. The transverse reinforcement for the column and shaft was modeled by "Plastic-Kinematic" material due to the lack of measured stress–strain relationship. The "Beam-in-solid" command was used to reflect the interaction between the concrete and reinforcement. In this study, the perfect bond was considered for the reinforcement in the column, pile shaft, and base. The automatic surface-to-surface command was used to model the contact between the embedment of the column and pile shaft. Due to the intentionally roughed surface for the embedment, a friction coefficient of 2.0 was defined in the contact model to reflect the interlocking phenomenon between the column and pile shaft.

2.3 Validation for the Numerical Model

The loading history in the literature was used as input to conduct quasi-static tests for the specimens DS-1 and DS-2. The global force–displacement relationships predicted from the numerical models were compared with those obtained from the experiments. As shown in Fig. 2, the numerical model could provide a reasonable prediction for the stiffness, strength and energy dissipation capabilities of the test specimens. Moreover, the damage condition of the column-to-pile shaft member socket connections can be analyzed based on the maximum principal strain distribution in the column and pile shaft as shown in Fig. 3. DS-1 failed due to the severe damage that occurred at the bottom of the column. DS-2 experienced significant damage within the connection region, while the column remained intact. From the maximum principal strain distribution, it can be seen that specimen DS-2 marks significantly higher strains in the concrete of the pile shaft, as compared to DS-1. The concrete principal tensile direction of the pile shaft is perpendicular to the vertical axis, which well explains the vertical cracking observed in specimen DS-2. Finite element analysis results also show that the transverse reinforcement reached the fracture strain before the occurrence of column flexural failure. These are consistent with the observations from the experiments. Thus, the numerical model is capable of predicting different damage modes for the column-to-pile shaft member socket connections.

The undesirable pile shaft damage that occurred to specimen DS-2 is strongly associated with the fewer amount of transverse reinforcement in the shaft. Therefore, the transverse reinforcement played an important role in providing confinement for the pile shaft. It should be carefully proportioned to ensure that the column-to-pile shaft member socket connection is able to sustain earthquake-induced inelastic action, enabling the plastic hinge to be formed in the column.
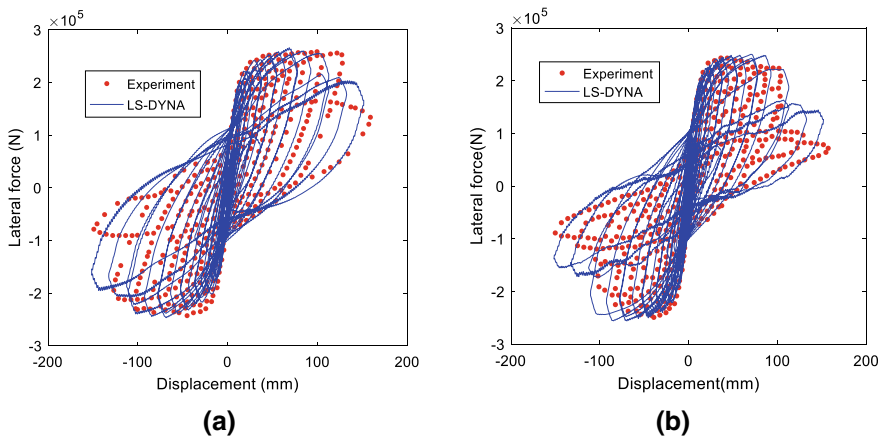
Fig. 2 Hysteresis responses of: **a** DS-1; **b** DS-2
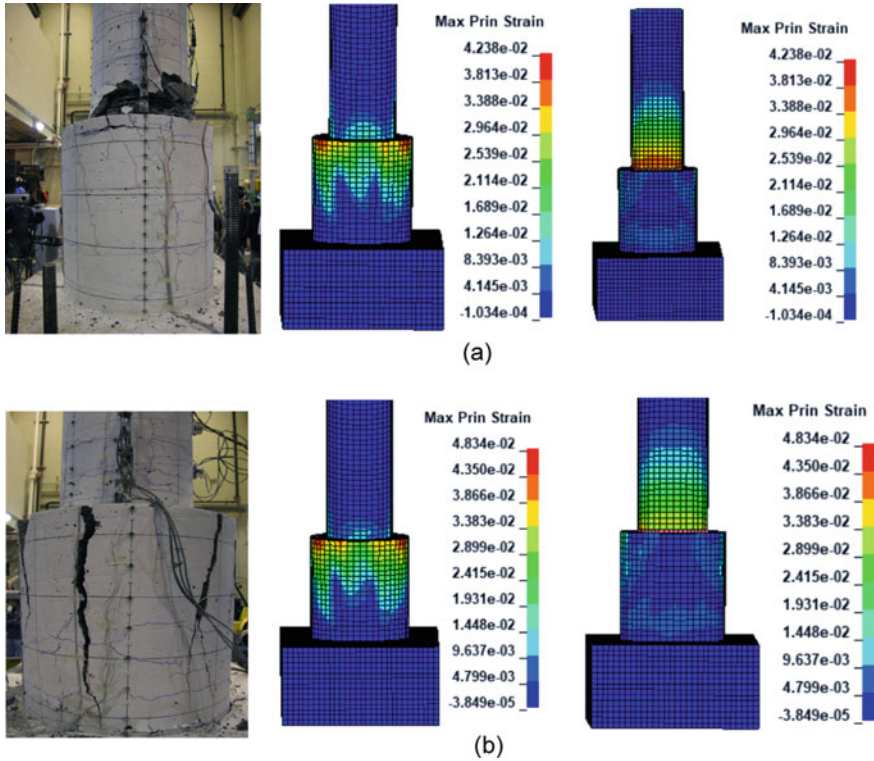
Fig. 3 Reactions in concrete for **a** DS-1; **b** DS-2

3 Numerical Modeling for UHPC

3.1 UHPC Column Modeling

To investigate the effect of UHPC on the seismic performance of column-to-pile shaft member socket connections, the numerical modeling technique for UHPC should be developed and validated first. For this purpose, the test specimen in the work of [11] was selected as the example UHPC column. As shown in Fig. 4a, the example column consisted of UHPC with a length of 610 mm and normal concrete for the remaining portion of the column. The compressive strength of the UHPC and normal concrete was 151.7 MPa and 50.9 MPa, respectively. The diameter of the cross-section was 305 mm. The longitudinal reinforcement ratio was 1.6% with 16-10M bars in the cross-section. The diameter of the transverse reinforcement was 4.9 mm with a spacing of 32 mm along the column height. The yield stress for the longitudinal and transverse reinforcement was 414 MPa. The numerical model of the UHPC column was established by LS-DYNA software. Both the UHPC and normal concrete were modeled by a constant-stress solid element with the CDP material. The material
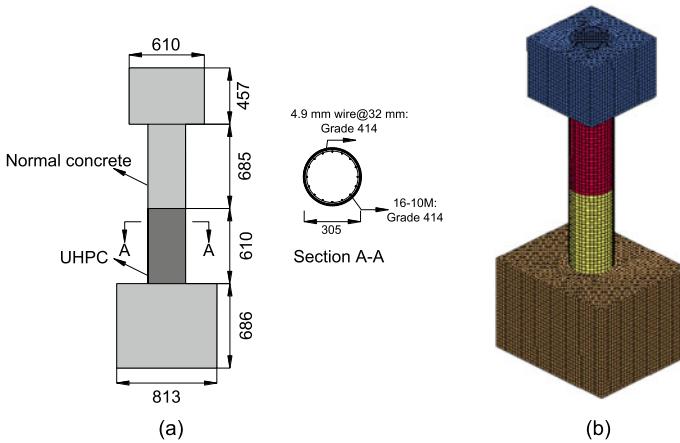
Fig. 4 **a** Geometry of the UHPC column (Unit: mm) [11], **b** numerical model in LS-DYNA

properties for the normal concrete were calculated using the formulas in Sect. 2. For the UHPC, the parameters ε_{fc} and w_f could be different from those for normal concrete. Thus, the effect of the two parameters on the structural performance of the UHPC column will be discussed in the following section. The reinforcement was modeled by "Plastic-Kinematic" material with the yield stress of 414 MPa. The "Beam-in-solid" command was employed to model the interaction between the reinforcement and concrete, while the bond slip was not considered in this study.

3.2 Results and Discussion

The parameters ε_{fc} and w_f needed as the input of the CDP model were calibrated to enable valid structural performance prediction of the UHPC column. In this regard, monotonic pushover analyses were first conducted to obtain the global-level force–displacement relationship for cases with varying ε_{fc} and w_f. As shown in Fig. 5, the lateral stiffness and strength of the UHPC column increase with the increasing value of w_f. The value of w_f for the normal concrete was 0.1 in this study. Using the same value of w_f would underestimate the lateral strength of the UHPC column. This study also investigated using w_f of 0.5 and 1, and the case with w_f of 0.5 was able to produce the global-level lateral stiffness and strength that were comparable with experimental results. The effect of ε_{fc} on the lateral stiffness and strength of the UHPC column was negligible, and its value was maintained the same as that for the normal concrete.

Then, the cyclic displacement-controlled loading protocol used in the test was adopted in the numerical model to analyze the UHPC column. Figure 6 plots the comparison between the experimentally measured and numerically predicted
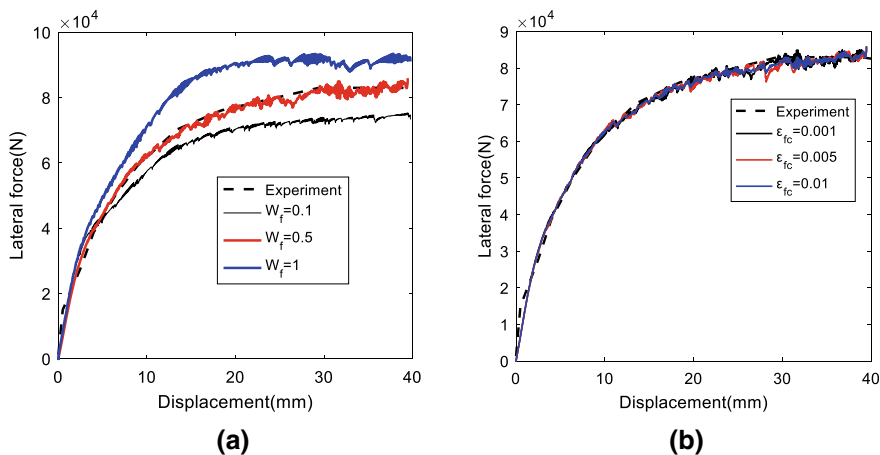
Fig. 5 Effect of: **a** w_f; **b** ε_{fc}

hysteretic responses for the tested UHPC column. It can be seen that the lateral stiffness and strength can be predicted with acceptable accuracy using the finite element model. However, the energy dissipation capability was overestimated by the current numerical model.

Fig. 6 Hysteretic response of the UHPC column
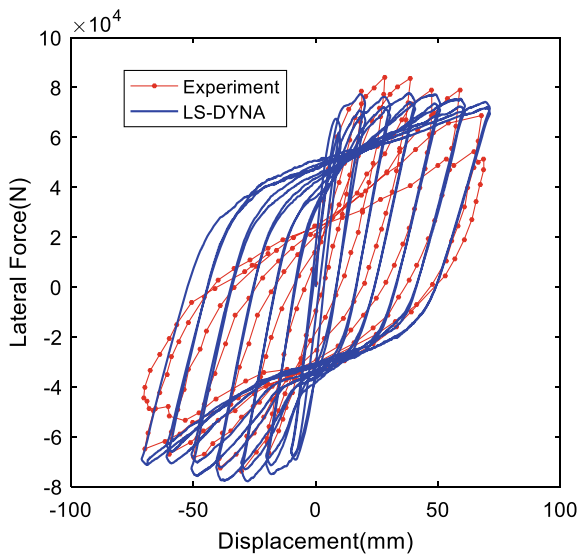
4 Effect of UHPC

After verifying the numerical modeling methodology of UHPC, the normal concrete of the pile shaft for specimen DS-2 was replaced with UHPC to investigate the potential of UHPC in improving the seismic performance of column-to-pile shaft member socket connections. Three different diameters (762 mm, 711 mm, and 660 mm) of the UHPC pile shaft were considered in this study. The transverse reinforcement size and spacing were both kept the same as that for the pile shaft for the specimen DS-2. Quasi-static analyses were conducted for the cases with different UHPC pile shaft diameters and their skeleton curves were obtained for comparison. Notably, the diameter of the normal concrete pile shaft for specimen DS-2 was 762 mm. As shown in Fig. 7, the cases with the UHPC shaft diameter of 762 mm and 711 mm were able to develop higher stiffness and lateral strength than those for specimen DS-2. When the diameter of the UHPC shaft was reduced to 660 mm, the lateral strength of the member socket connection with UHPC was comparable to that for the specimen DS-2. Thus, using UHPC can potentially reduce the pile shaft by 7–13% without compromising the lateral stiffness and strength of the column-to-pile shaft member socket connections.
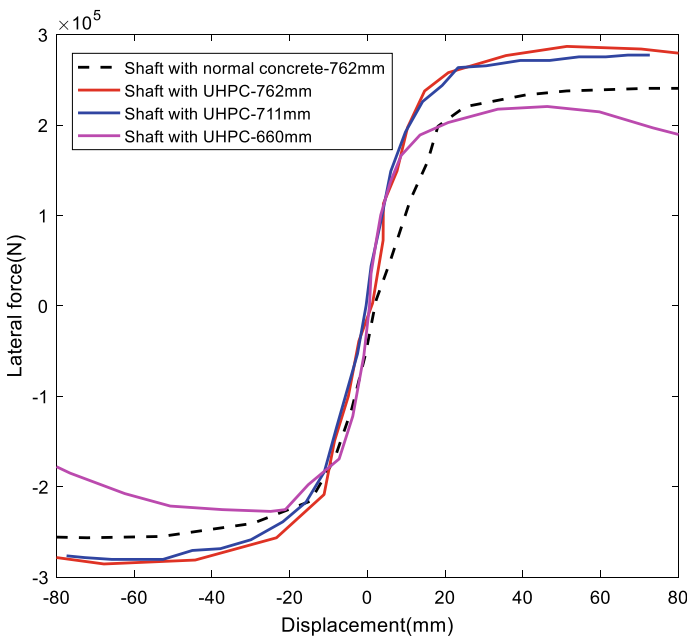
Fig. 7 Effect of UHPC on the seismic performance of the member socket connection

5 Conclusion

This study aimed to investigate the role played by UHPC in mitigating earthquake-induced damage to precast concrete column-to-pile shaft member socket connections. The numerical modeling techniques for the member socket connection and UHPC were validated using the previous experimental results. The effect of change in the dimension of the UHPC pile shaft on the seismic performance of member socket connections was discussed. The main conclusions were listed as follows:

1. The developed numerical model for the column-to-pile shaft member socket connection was capable of predicting global hysteretic response and damage mechanism with acceptable accuracy.
2. The CDP material model is feasible to simulate the behavior UHPC column under combined axial and lateral loads. The lateral stiffness and strength of the UHPC column could be reasonably captured, whereas the energy dissipation capability was overestimated.
3. Analysis results show that UHPC plays an effective role in reducing prying action-induced damage. Using UHPC for casting the shaft within the connection region presents a feasible solution to reduce the pile shaft size without compromising the connection's ability to sustain prying-induced inelastic action.

It should be mentioned that only one UHPC column test was used to validate the numerical modeling methodology in this study. Notably, the response mechanism of UHPC in column-to-pile shaft member socket connections can be quite different from that for cast-in-place construction. Thus, an experimental study is underway to investigate the particular damage conditions of precast concrete column-to-UHPC pile shaft member sockets.

References

1. Cheng Z, Sritharan S (2019) Side shear strength of preformed socket connections suitable for vertical precast members. J Bridg Eng 24(5):04019025
2. Cheng Z, Liu D, Li S, Wang J, Zhang J (2021) Performance characterization and design recommendations of socket connections for precast columns. Eng Struct 242:112537
3. Grassl P, Xenos D, Nyström U, Rempling R, Gylltoft K (2013) CDPM2: A damage-plasticity approach to modelling the failure of concrete. Int J Solids Struct 50(24):3805–3816
4. He Z, Zhong T, Fu G, Li H, Wang W (2021) Review on seismic behavior of precast bridge column with socket connections. J Phys Conf Ser 1838(1):012043

5. Saiidi MS, Mehraein M, Shrestha G, Jordan E, Itani A, Tazarv M, Sanders D, Murphy TP, Reno ML, Pohll MN, Pohll MN (2020) Proposed AASHTO seismic specifications for ABC column connections (No. Project 12-105)
6. Stewart MG (2012) Spatial and time-dependent reliability modelling of corrosion damage, safety and maintenance for reinforced concrete structures. Struct Infrastruct Eng 8(6):607–619
7. Tran HV, Stanton JF (2015) Drilled shaft socket connections for precast columns in seismic regions. Doctoral dissertation, Department of Civil and Environmental Engineering, University of Washington
8. Yang C, Okumus P (2017) Ultrahigh-performance concrete for post-tensioned precast bridge piers for seismic resilience. J Struct Eng 143(12):04017161
9. Zhao MZ, Lehman DE, Roeder CW (2021) Modelling recommendations for RC and CFST sections in LS-Dyna including bond slip. Eng Struct 229:111612
10. Zhao MZ, Lehman DE, Roeder CW (2021) Analytical investigation of a new direct Column-to-Cased shaft connection. Eng Struct 245:112909
11. Zohrevand P, Mirmiran A (2012) Cyclic behavior of hybrid columns made of ultra high performance concrete and fiber reinforced polymers. J Compos Constr 16(1):91–99

Analysis and Design of Bridges

Simplified Framework for Preliminary Estimates of Bridge Bearing Demands and Fatigue Loading

Ahmed M. Abdelmaksoud, Minesh K. Patel, Tracy C. Becker, and Georgios P. Balomenos

Abstract While bridge bearings are ubiquitous, there is minimal information available on their performance lifespan bringing uncertainty to bridge rating and maintenance. The assessment of the life expectancy of bridge bearings requires proper estimation of the bearing demands under working conditions. These demands can vary significantly depending on the loading type (e.g., temperature, traffic, or seismic events), bridge configuration (e.g., geometry of pier, deck, superstructure, etc.), and bearing properties (e.g., horizontal stiffness). Hence, it can be quite challenging to predict the appropriate timing for bearing replacement. To aid authorities in decision-making, this study proposes a simplified regression-based framework for preliminary prediction of the annual demands of elastomeric bearings. First, Monte Carlo simulation, combined with Latin Hypercube Sampling, is used to generate random bridge configurations as well as random temperature profiles, earthquake records, and traffic loading scenarios. The displacement demands are evaluated for each simulation using a nonlinear OpenSees model, and then, the demands are related to the bridge design parameters via regression analysis. Based on the predicted demands, a parameterized fatigue loading protocol is proposed which can be used for testing and rating sample bearings. The results from the simplified method are then compared to those derived using a more detailed method. The comparison reveals that the proposed simplified method is a good alternative for rough and quick estimates before the application of the detailed method.

Keywords Bridge bearing · Fatigue loading

A. M. Abdelmaksoud (✉) · M. K. Patel · G. P. Balomenos
McMaster University, Hamilton, Canada
e-mail: abdela33@mcmaster.ca

T. C. Becker
University of California—Berkeley, Berkeley, CA, USA

1 Introduction

Bridge bearings have a vital role in reducing the design forces of bridges due to the bearings' ability to accommodate the deformation of the superstructure under various loading conditions. As such, the performance of bridge bearings can have a significant impact on the safety and functionality of bridges. Similar to any other bridge component, bearings experience time-based degradation in their performance with aging [4] and accumulated loading cycles [9, 18], which can potentially result in structural damages to bridges. A clear example is the Birmingham Bridge in Pennsylvania, USA, which suffered from a partial collapse in its deck due to the undetected deterioration of the supporting rocker bearings, resulting in $8 million in damages [12]. Also, field investigations of concrete bridges in Maryland, USA, revealed that several bridges are susceptible to structural damage due to their aging and fatigued elastomeric bearings [4]. Despite the above examples, still there is no clear and reliable policy for scheduling bearing replacements. To date, bearing replacement decisions continue to be based on engineering judgment.

Scheduling and budgeting of bearing replacement require reliable estimation of the life expectancy of the bearing. This can be done by testing sample bearings with loading protocols representative of the lifetime displacement demands experienced on-site. Such loading protocols should consist of a mixture of (1) numerous cycles with low displacement amplitudes, simulating temperature fluctuations, and traffic loads and (2) a few cycles with large displacement amplitudes, simulating rare events such as earthquakes. To date, the loading protocols specified in design codes [1, 7] do not represent the lifetime loading with its amplitude-variant pattern. This pattern is also not considered in several analytical and experimental studies on the fatigue life of elastomeric bearings subjected to cyclic compression or shear loading [19, 24, 28, 31].

To address this issue, Noade and Becker [26] recently proposed an amplitude-variant loading protocol for elastomeric bearings based on elastic analysis of the Chemin des Dalles Bridge, located in Quebec City, under temperature, traffic, and seismic loading. The protocol was derived based on the observed attributes of the displacement demands (i.e., cycle amplitudes and cycle counts) in the analysis. This framework was generalized by Abdelmaksoud et al. [2] to account for a range of bridge superstructure types (e.g., deck on concrete girder and deck on steel girder systems), geometric parameters (e.g., number of spans, stiffness of pier and deck, etc.), bearing properties (e.g., horizontal stiffness), and possible nonlinearities in the deck and piers due to traffic and seismic loads, respectively. Based on the nonlinear analysis, Abdelmaksoud et al. [2] proposed parameterized prediction models for the cumulative and maximum bearing demands in the longitudinal direction of a bridge. Then, they provided detailed procedures to derive the attributes of the bearing demands and to construct the loading protocol in the longitudinal direction.

During the preliminary bridge design, it may be useful to provide a quick and rough estimation of the bearing demands to compare and select few possible bearing alternatives. However, at this design stage, several bridge design alternatives may

still be under consideration. Also, many of the bridge design parameters that affect the bearing demands, such as the bearing stiffness and column cross-sections, may not be yet known. As such, using the detailed procedures in Abdelmaksoud et al. [2] may prove time-consuming at this design stage. The current work proposes a simplified version of the procedures in Abdelmaksoud et al. [2] to provide rough and quick estimates of the bearing demands given the general or limited bridge information available in the preliminary design stage [33]. The bearing demand uncertainties arising from the lack of detailed knowledge about the relevant bridge design parameters are also discussed. Finally, additional provisions are proposed to derive bearing loading protocols in the vertical direction.

2 Bridge Model in OpenSees

The Chemin des Dalles Bridge is one of the most studied bridges in Canada. The bridge's original structural properties and site conditions can be found from literature [29, 30, 32] and are briefly illustrated herewithin. The bridge superstructure has three spans each with length of 35.5 m, a concrete deck with thickness of 165 mm, and 6 AASHTO Type-V precast prestressed concrete girders with depth and spacing of 1.6 m and 2.2 m, respectively. The bridge substructure has two piers and two abutments. Each pier has three circular columns with a diameter of 900 mm and a height of 6 m, connected by a bent beam with cross-section of 1.25 m × 1.25 m. The superstructure is supported on four lines of elastomeric bearings at the piers and abutments. Each line has six bearings located directly below the six girders. Only the abutment bearings are allowed to displace horizontally, whereas the others allow for rotation only.

Abdelmaksoud et al. [2] used OpenSees [22] to construct and validate a nonlinear model of the Chemin des Dalles Bridge (Fig. 1). The first mode for the model was in the transverse direction with a period of 0.43 s, a near match to the findings of Tavares et al. [32]. Afterward, five more bridge configurations were derived based on the original model while varying the number of spans and superstructure type. The same six models are used in the current study and are briefly described herewithin. The models have either a deck on concrete girder or a deck on steel girder system with either 1, 2, or 3 spans. In all models, the deck, columns, and girders were modeled using nonlinear displacement-based beam–column fiber elements. The only exception was the prestressed concrete girders which are typically designed to be uncracked; hence, they were modeled using elastic beam–column elements [29]. The elastomeric bearings were modeled as zero length elements. The vertical stiffness of the bearing was modeled as a linear spring and the rotational stiffness was computed based on the work of Kelly and Konstantinidis [16]. For the abutment bearings, the shear behavior was modeled using a bilinear model with low yield strength. The current work conducts a parametric study using the six described models to establish the simplified procedures for rough estimating the bearing demand and its attributes.
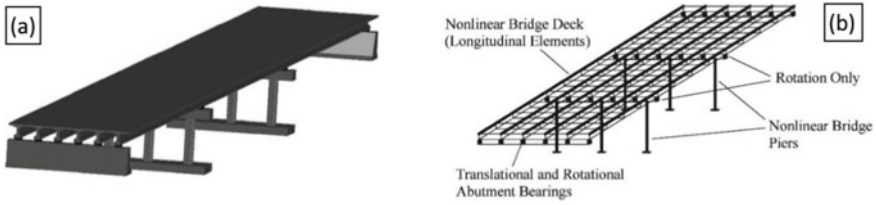
Fig. 1 **a** Three-dimensional view of Chemin De Dallas Bridge and **b** OpenSees model

3   Bridge Loading

This study investigates three primary load types: temperature, traffic, and seismic loads. The details of loading conditions can be found in Abdelmaksoud et al. [2] and are briefly summarized herewithin.

3.1   Temperature Loads

Bearing demands are related to the thermal deformations of the superstructure which include: (1) uniform expansion/contraction, due to daily fluctuations in the average bridge temperature, and (2) end rotations, due to the vertical thermal gradient across the depth. The all-year-round daily fluctuations in average bridge temperature were projected from random air temperature profiles, generated based on data from ECCC [10], using the Emerson method [11] (Fig. 2a and b). The minimum daily bridge temperature was predicted given the air temperature in the preceding day(s). Next, the maximum daily temperature was computed by adding a range function of the material, season, and cloud cover (Table 1).
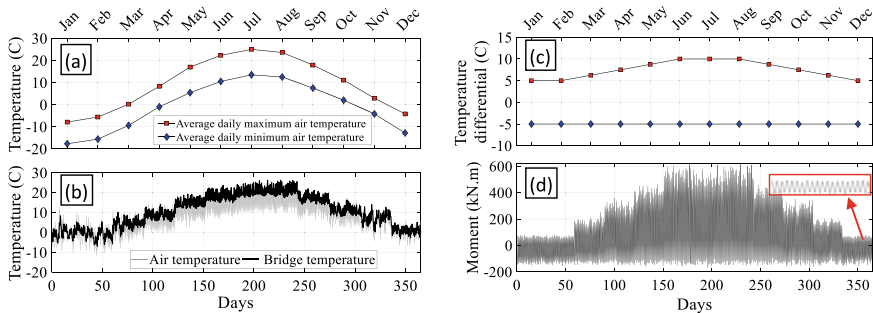
Fig. 2 **a** Sample air temperature data from ECCC [10], **b** random annual air and bridge temperature profiles, **c** annual ΔT profile for concrete bridges (CSA S6-19), and **d** random annual moment profile

Table 1 Bridge temperature ranges (°C) for different seasons and levels of cloud cover

	Deck on concrete girders			Deck on steel girders		
	Thick (°C)	Partial (°C)	Clear (°C)	Thick (°C)	Partial (°C)	Clear (°C)
Winter	0–2	2–4	4	0–4	4–8	8
Spring/Autumn	0–2.5	2.5–5	5	0–6	6–12	12
Summer	0–3	3–6	6	0–7	7–14	14

Vertical temperature gradients over the superstructure depth result in moments (M) at the end of the deck which induce longitudinal bearing displacement. The value of M is equivalent to

$$M = EI\alpha(\Delta T)/h, \tag{1}$$

where EI, α, and h are the bending rigidity, coefficient of thermal expansion, and depth of the superstructure, respectively. ΔT is the temperature differential between the top and soffit of the superstructure. The annual profile of ΔT was adopted from CSA S6-19 [7, 8] and Kennedy and Soliman [17] for the deck on concrete girder and deck on steel girder systems, respectively (Fig. 2c). To account for any uncertainties in ΔT [15], the adopted ΔT profiles were treated as averages and were superimposed with a coefficient of variation of 10%. Random ΔT profiles were then generated and converted into moment profiles (Fig. 2d) using (1) which were then inputted into the OpenSees model to evaluate the bearing demands. The bearing demand histories from both components of thermal deformation were then summed up to get the total demand history in the longitudinal direction.

3.2 Traffic Loads

In practice, bearings can experience numerous traffic loading scenarios depending on the number of traffic lanes and traffic trends. Hence, a general methodology was developed to allow for the modeling of any investigated traffic loading scenario. Consider the horizontal and vertical bearing displacement profiles caused by an axle load j located at a random location (Fig. 3). The displacements of bearing i (D_i) are expressed as a percentage (p_{ij}) of the maximum possible displacements (D_{max}) that occur when the axle load is directly above the bearing. Then, the total bearing displacement in any given traffic loading scenario can be computed by summing up the displacements caused by all axles. Furthermore, the horizontal displacements are amplified using an impact factor (IF) to account for the braking forces that a bridge might experience if located on or near an exit/entrance ramp. As such, for any given loading scenario, the horizontal and vertical displacements of bearing i are expressed as follows:

$$D_{hi} = \text{IF} * D_{h\text{-}\max} * P_h, \quad \text{where } P_h = \sum_{j=1}^{j=m} p_{ij-h}, \tag{2}$$

$$D_{vi} = D_{v\text{-}\max} * P_v, \quad \text{where } P_v = \sum_{j=1}^{j=m} p_{ij-v}. \tag{3}$$

Simplified expressions are proposed in this work to estimate the values of the parameters in (2) and (3) given the target number of traffic lanes, general information about the superstructure, and few braking force parameters (e.g., deceleration rate). These expressions are developed while using the axle load of the CL-625 truck which is the heaviest truck load in the provisions of CSA S6-19 [7].

3.3 Seismic Loads

During seismic events, bearings experience few displacement cycles with large magnitudes that can potentially cause the bearing to exceed its design displacement. To explore the variation in bearing demands with the various types of seismic records, 59 eastern and 55 shallow crustal records were extracted from the PEER strong motion database [6]. Also, 46 Cascadia subduction records were extracted from the NGA-subduction database [5]. The records were selected based on the seismic hazard deaggregation values at several sites in Canada for the 2% probability of exceedance in 50 years [13].

The eastern and shallow crustal records were scaled to match the expected range of design spectra in the east and west of Canada [25] within a period range of 0.2 $\times T_{1-\min}$ to 1.5 s [8], where $T_{1-\min}$ is the minimum first mode period from all possible bridge configurations, whereas the subduction records were scaled to match the expected range of design spectra in the Cascadia zone [25] within a period range of 0.5–1.5 s [13]. Site class C is assumed during the analysis.
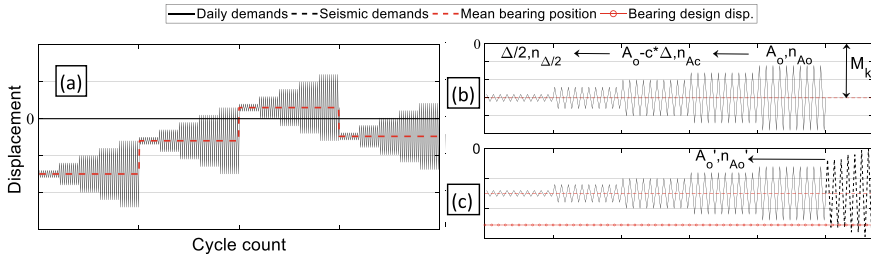
Fig. 4 **a** Loading protocol in the horizontal direction, **b** modeling parameters of the proposed loading protocol, and **c** seismic cycles added to the horizontal loading protocol

4 Methodology

4.1 Loading Protocol Variables

Figure 4a shows the annual loading protocol in the horizontal direction with its modeling variables in Fig. 4b and c. To capture the seasonal mean position of the bearing, the protocol is divided into four segments per year each with a mean position M_k, where $k = 1$ to 4 (Fig. 4b). For each segment, a stepped amplitude function is used (Fig. 4b) where A_o is the maximum amplitude from either traffic or temperature loading, Δ is a user-specified amplitude increment, and n_{A_c} is the cycle count for a given amplitude A_c. Optionally, few seismic cycles can be also added to the protocol (Fig. 4c) to test how fatigued bearings behave during seismic events. Only the seismic cycles that displace the bearing beyond its design displacement are included. The maximum seismic cycle amplitude is A_o' and the corresponding cycle count is n_o'. The loading protocol in the vertical direction is described by Fig. 4b only. For the vertical direction: (1) A_o is computed solely based on the traffic demands, (2) M_k is constant throughout the year and is equal to the expected static vertical deformation under gravity loads, and (3) seismic cycles are neglected.

4.2 Formulation of Prediction Models

To investigate the trends in the loading protocol variables with various loading conditions and bridge design parameters, Monte Carlo simulations were used with Latin Hypercube Sampling [21]. For each of the six bridge configurations, 150, 300, and 450 simulations were carried out for the temperature, traffic, and seismic loads, respectively. The same bridge design parameters and their range of values in Abdelmaksoud et al. [2] were used to generate random bridge models for the nonlinear OpenSees analysis. The loading protocol variables were then evaluated and related to the design and loading parameters via regression analysis while retaining 20%

of the simulation results for validation. However, not all of the design parameters, used in the OpenSees analysis, were considered for the regression analysis. As this work is intended for the preliminary design stage, only the design parameters that are likely to be known [33] or can be easily estimated at this stage were included. Design parameters, such as the bearing stiffness, deck thickness, and pier cross-sections, are not expected to be known at this design stage and hence were excluded from the regression analysis. Naturally, this lack of knowledge about some of the design parameters, which is typical for the preliminary design stage, leads to high uncertainty and scatter in the demand predictions. To address this uncertainty, the regression models are formulated for a 90% prediction interval for the demand observations. This conservatism is assumed to be acceptable for the purpose of comparing and selecting potential design alternatives for the bearing.

5 Results

5.1 Loading Protocol in the Horizontal Direction

This section introduces the prediction models for A_{oh}, $n_{\text{Ac-}h}$, and $M_{k\text{-}h}$ at a 90% prediction interval for the demand observations. First, the maximum amplitude (A_{oh}) is evaluated as follows:

$$A_{oh} = \max(A_{\text{max-temp}}, A_{\text{max-traffic-}h}),\tag{4}$$

where $A_{\text{max-temp}}$ and $A_{\text{max-traffic-}h}$ are the maximum amplitudes due to temperature and traffic loads, respectively. For temperature loads, the annual bearing displacement history due to the uniform expansion/contraction and the vertical thermal gradient is evaluated for each simulation (Fig. 5a). Then, the maximum annual amplitude about the mean bearing position is computed. For traffic loads, the maximum displacements typically occur in traffic scenarios with braking forces and are determined from the displacement histories of such scenarios (Fig. 5b).

For temperature loads, $A_{\text{max-temp}}$ is expressed as
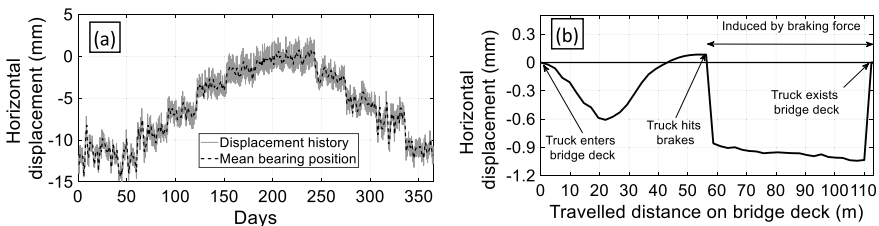
Fig. 5 Sample horizontal displacement histories due to **a** temperature loads and **b** traffic loads with braking force

$$A_{\text{max-temp}} = 13.2 + 0.04 * L + 0.31 * \frac{I * (\Delta T^+ - \Delta T^-)_{\text{avg}}}{h} - 3.56 * N_{\text{ubs}} - 6.5 * \text{MF}, \tag{5}$$

where $A_{\text{max-temp}}$ is in (mm), L is the bridge length (m), I is the inertia of one girder and a portion of the deck (m^4), h is the depth of the superstructure (m), $(\Delta T^+ - \Delta T^-)_{\text{avg}}$ is the annual average fluctuation of temperature differentials, N_{ubs} is the number of unrestricted bearing supports in the horizontal direction, and MF is a material factor equal to 1 and 0 for concrete and steel girders, respectively.

The value of L is determined based on the general bridge layout, whereas h can be estimated based on the common depth-to-span ratios for a given structural system. The inertia I is typically not known at this stage; however, an empirical equation is proposed herewithin to roughly estimate I given the depth h. This equation was calibrated for two standard types of girder sections: AASHTO I-girders [27] and W-steel sections [3]. The value of I can be estimated as $c_o * h^{c_1}$, where c_o and c_1 are empirical factors equal to 0.06 and 3.35 for AASHTO I-girders and 0.01 and 3.57 for W-steel sections. The annual average of $(\Delta T^+ - \Delta T^-)$ can be estimated from the available design profiles. For example, $(\Delta T^+ - \Delta T^-)_{\text{avg}}$ is equal to 12.5 °C for concrete girders (Fig. 2c) and 21 °C for steel girders with a concrete deck [17]. N_{ubs} is typically equal to 1 for single-span bridges and 2 for multi-span bridges.

For traffic loads, $A_{\text{max-traffic-}h}$ is expressed as

$$A_{\text{max-traffic-}h} = \text{IF} * D_{\text{max-}h} * P_h \tag{6}$$

and

$$\text{IF} = -4.55 + 4.22 * a + 62.4 * \tfrac{h}{s} + 0.32 * h_{\text{pier}} \geq 1, \quad \text{if braking on multi-span bridges}$$
$$= 1.5, \qquad\qquad\qquad\qquad\qquad\qquad\qquad \text{if braking on single span bridges}$$
$$= 1, \qquad\qquad\qquad\qquad\qquad\qquad\qquad\quad \text{if braking is not considered}$$

$$D_{\text{max-}h} = 5.11 - 55 * \frac{h}{s} + 0.04 * \text{GS} - 1.6 * N_{\text{ubs}} + 0.33 * N_s + 0.71 * \text{MF}$$
$$P_h = 375 - 71 * \text{GS} + 118 * N_L - 141 * N_{\text{ubs}} + 40 * N_s + 115 * \text{MF}$$

where $A_{\text{max-traffic-}h}$ and $D_{\text{max-}h}$ are in (mm), P_h is a percentage, a is the deceleration in units of g, h/S is the depth-to-span ratio, h_{pier} is the pier height (m), GS is the girder spacing (m), N_s is the number of spans, N_L is the number of traffic lanes, and MF is a material factor equal to 1 and 0 for concrete and steel girders, respectively. The value of a can be taken as 0.25–0.75 [20], whereas the other parameters can be estimated from the bridge's general layout and structural system [33].

Figure 6a plots the actual IF values against the predictions of the average model (equation is not presented). A fair correlation can be observed, RMSE-to-mean = 60% based on Abdelmaksoud et al. [2], which shows that the average model fairly captures the trends of IF. However, as expected the scatter in the predictions is relatively wide when including only the design parameters available at the preliminary
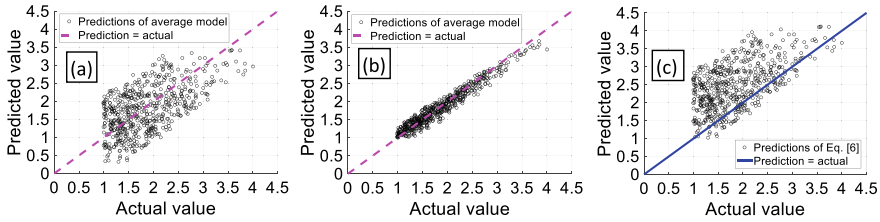
Fig. 6 Actual IF versus IF predictions from **a** an average model with only the preliminary design parameters, **b** an average model with all design parameters [2], and **c** the proposed simplified model at 90% prediction interval for the demand observations

Fig. 7 Distribution of normalized cycle amplitudes
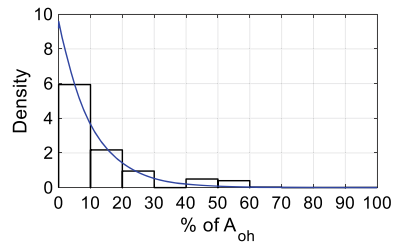
stage. Parameters such as the bearing horizontal stiffness and pier cross-section have an impact on IF [2] but can only be known at the final design stage. If such parameters are considered, a smaller scatter can be observed for the average model (Fig. 6b), RMSE-to-mean = 15%. To ensure an adequate safety level in presence of uncertainty, only the models at 90% prediction interval are presented herewithin (Fig. 6c). Similar trends were observed for the other loading protocol variables.

The next step is to compute the cycle count ($n_{A_{c\text{-}h}}$) for a given amplitude $A_{c\text{-}h}$. The displacement histories due to temperature loads (about the mean position) and traffic loads (Fig. 5) were normalized using A_{oh}. Then, the statistical distribution of the normalized cycle amplitudes is established (Fig. 7).

The distribution is of exponential type, and thus, $n_{A_{c\text{-}h}}$ can be estimated as

$$n_{A_{c\text{-}h}} = \frac{e^{-\frac{A_{c-h}-0.5*\Delta}{z}} - e^{-\frac{A_{c-h}+0.5*\Delta}{z}}}{1-e^{-\frac{100}{z}}} * N_{\text{annual}} \tag{7}$$

and

$$A_{c\text{-}h} = A_{oh} - c * \Delta, \quad (\text{expressed as a } \%A_{oh})$$
$$z = 20 - 3.65 * N_{\text{ubs}} - 1.65 * N_s + 2.85 * \text{MF}$$

where c is a counting variable for the amplitude steps (Fig. 4b), Δ is the user-specified amplitude increment (expressed as $\%A_{oh}$), z is the distribution parameter, and MF is a material factor equal to 1 and 0 for concrete and steel girders, respectively. N_{annual}

is the annual number of cycles from temperature and traffic loads which can be estimated as

$$N_{\text{annual}} = N_{\text{annual-temp}} + N_{\text{annual-traffic}} \tag{8}$$

and

$$N_{\text{annual-temp}} = 365$$
$$N_{\text{annual-traffic}} = \sum \frac{\ell_s * V_{\text{annual}}}{V_s} * n_s,$$

where ℓ_s is the likelihood of a traffic scenario, V_{annual} is the annual truck volume passing the bridge, V_s is the number of trucks per scenario, and n_s is the number of bearing displacement cycles per scenario occurrence. V_{annual} can be determined from traffic volume databases (e.g., [23]), whereas ℓ_s is typically measured from traffic surveys at the planned bridge location. If such surveys are not available, then the following empirical formula can be used instead to estimate $N_{\text{annual-traffic}}$

$$N_{\text{annual-traffic}} = 1.23 * V_{\text{annual}} * (1 + 1.07 * \text{CF} + 0.71 * \text{LF} - 0.087 * N_{\text{L}}), \tag{9}$$

where CF is a continuity factor equal to 1 and 0 for multi-span and single-span bridges, respectively, and LF is a location factor equal to 1, 0.5, and 0 for bridges located on, near, and away from a highway exit/entrance ramp, respectively. This formula employs the following assumptions: (1) the likelihood ℓ_s follows a Poisson distribution with a distribution parameter λ computed based on [14], (2) the likelihood of a truck braking/accelerating is discretized into three values (indicated by LF) and is assumed to be proportional to the relative location of the bridge with respect to the nearest highway exit/entrance ramp, (3) the worst case traffic loading scenario is defined as the trucks per scenario (V_s) being equal to the number of bridge lanes (N_{L}), and (4) the value of n_s is taken from [2].

The final variable for the loading distribution in the horizontal direction is the mean position $M_{k\text{-}h}$. This position is computed as the thermal expansion/contraction of the bridge due to the difference between the average seasonal bridge temperature ($T_{\text{season-}k}$) and the effective construction temperature (T_{const})

$$M_{k\text{-}h} = \alpha * L * (T_{\text{season-k}} - T_{\text{const}})/N_{\text{ubs}}, \tag{10}$$

where T_{const} can be assumed equal to 15 °C, and $T_{\text{season-}k}$ can be estimated from the average seasonal air temperature ($T_{\text{air-season-k}}$) at the bridge location [10] using the Emerson method [11]

$$T_{\text{season-k}} = c_2 * T_{\text{air-season-k}} + c_3 + c_4, \tag{11}$$

where c_2 is equal to 1.14 and 1.13 for concrete and steel girders, respectively, c_3 is equal to -0.7 and -2.1 for concrete and steel girders, respectively, and c_4 is equal to half the temperature range (Table 1) corresponding to the season under consideration and an assumed cloud clover.

5.2 Loading Protocol in the Vertical Direction

This section introduces the prediction models for A_{ov}, $n_{A_{c\text{-}v}}$, and $M_{k\text{-}v}$ at a 90% prediction interval for the demand observations. These parameters were driven using similar steps to those used for the horizontal direction. For the vertical direction, the maximum amplitude (A_{ov}) is identified from the vertical displacement histories due to traffic loads and is expressed as

$$A_{ov} = D_{\max\text{-}v} * P_v \tag{12}$$

and

$$D_{\max\text{-}v} = 0.48 - 0.84 * \frac{h}{s} + 0.16 * \text{GS} + 0.0275 * N_s - 0.05 * \text{MF}$$
$$P_v = 316 - 75 * \text{GS} + 18.1 * N_\text{L},$$

where A_{ov} and $D_{\max\text{-}v}$ are in (mm), P_v is a percentage, MF is a material factor equal to 1 and 0 for concrete and steel girders, respectively. To get the number of cycles ($n_{A_{c\text{-}v}}$) for a given amplitude $A_{c\text{-}v}$, the vertical displacement histories of the traffic demands were normalized using the computed A_{ov}. Then, the statistical distribution of the normalized cycle amplitudes is evaluated. The distribution is of exponential type, thus, $n_{A_{c\text{-}v}}$ can be estimated as

$$n_{A_{c\text{-}v}} = \frac{e^{-\frac{A_{c\text{-}v} - 0.5*\Delta}{z}} - e^{-\frac{A_{c\text{-}v} + 0.5*\Delta}{z}}}{1 - e^{-\frac{100}{z}}} * N_{\text{annual-traffic}} \tag{13}$$

and

$$A_{c\text{-}v} = A_{ov} - c * \Delta, \quad (\text{expressed as a } \% A_{ov})$$
$$z = 39 - 8.9 * N_s,$$

where $N_{\text{annual-traffic}}$ can be computed from (9). Finally, the mean vertical displacement ($M_{k\text{-}v}$) is evaluated as the static vertical gravity deformation. In each simulation, the bearing size was selected based on the horizontal thermal deformation of the superstructure and checked for vertical load capacity [34]. Then, the corresponding vertical stiffness was determined, and the gravity deformation was evaluated as

$$M_{k\text{-}v} = (1085 + 15 * L - 559.1 * N_{\text{ubs}} + 6.65 * W + 9.24 * S_{\text{ext}}$$
$$- 8.81 * N_{\text{b}} + 14.2 * \text{MF}) * 10^{-3}, \tag{14}$$

where $M_{k\text{-}v}$ is in (mm), W is the bridge width (m), S_{ext} is the length of the exterior span (m), N_{b} is the number of bearings on a single abutment, and MF is a material factor equal to 1 and 0 for concrete and steel girders, respectively. Note that (14) has parameters related to the magnitude of vertical loads (W, S_{ext}, and N_{b}) and to the horizontal bearing demand (L and N_{ubs}). This is due to the fact that both of the vertical and horizontal properties of standard elastomeric bearings are related to the bearing size. Thus, even if the bearing size selection was governed by horizontal demand, the vertical displacement will be indirectly affected.

5.3 Seismic Cycles in the Horizontal Direction

This section introduces the prediction models for A_{o}' and n_{o}' at a 90% prediction interval for the demand observations. The maximum seismic amplitude (A_{o}') is expressed as follows:

$$A_{\text{o}}' = -6.7 + 2.1 * \text{Sa}(0.2) + 25.4 * \text{Sa}(1.0) + 2.96 * h_{\text{pier}} + 0.0047 * \text{DA}$$
$$- 2.36 * \text{CF} + \text{SR} + 1.16 * \text{MF}, \tag{15}$$

where A_{o}' is in (mm), Sa(0.2) and Sa(1.0) are the spectrum accelerations at periods 0.2 s and 1 s in units of g, h_{pier} (m) is the pier height for multi-span bridges and is taken as 0 for single-span bridges, DA refers to the deck area (m^2), CF is a continuity factor taken as 1 and 0 for multi-span and single-span bridges, respectively, SR is a seismic record factor taken as -2.45, 0, and 4.3 for eastern, shallow crustal, and subduction earthquakes, and MF is a material factor equal to 1 and 0 for concrete and steel girders, respectively. In this work, the DA and MF are used as indicators of the seismic weight of the structure. Larger deck areas and concrete systems tend to have higher seismic weights and displacements. Also, CF and h_{pier} are indicators of the geometry of the super- and substructure. Finally, Sa(0.2), Sa(1.0), and SR are indicators of the impact of the seismic properties of bridges and records on the bearing displacements.

The number of seismic cycles to be included in the loading protocol of the horizontal direction can be taken from Abdelmaksoud et al. [2]. Only the larger amplitudes are of interest as they may force the bearing to exceed its design displacement. Note that bearings experience higher cycle counts in single-span bridges given their high longitudinal stiffness. Also, bridges in subduction regions tend to exhibit larger cycle counts.

6   Comparison with the Detailed Method

To examine how the proposed simplified method performs against the detailed method presented in Abdelmaksoud et al. [2], the same case study bridge was investigated. The layout of the bridge is described in Abdelmaksoud et al. [2], and the design parameters required for the simplified method are shown in Table 2. Using the simplified method, a loading protocol was created in the horizontal direction and was compared to that of the detailed method in terms of (1) maximum amplitudes about the mean position, (2) cycle counts, and (3) cumulative displacements.

Using the simplified method, the maximum amplitude due to temperature ($A_{\text{max-temp}}$) is about 25% higher than that of the detailed method (5 and 4 mm, respectively), whereas the maximum amplitude due to traffic loads ($A_{\text{max-traffic}}$) is similar in both methods (10 mm). This indicates that if the bearing demands are dominated by the traffic loads (e.g., large braking forces), the prediction of the absolute maximum horizontal amplitude (A_{oh}) from the simplified or detailed method may not be significantly different. However, the simplified method may be more conservative if the temperature loads are dominant (e.g., no braking events). For the maximum seismic amplitude (A_{o}'), the simplified method is about 35% more conservative than the detailed method (19.2 and 14.1 mm, respectively).

In terms of cycle count, the simplified method's prediction is in agreement with that of the detailed method (about 1.2×10^6 cycles/year). However, the simplified method overestimates the cycle count at the higher amplitude range (Table 3). The cycle count in Table 3 indicates an annual cumulative displacement demand of 1672 m and 1327 m for the simplified and detailed methods, respectively. Thus, the simplified method is 26% more conservative in terms of cumulative demand. One reason to this difference in predictions is that the detailed method develops separate cycle amplitude distributions for each of the temperature and traffic cycles, whereas the simplified method provides an approximate unified cycle amplitude distribution.

Table 2 Design parameters for the case study bridge

	Parameter	Value	Parameter	Value	Parameter	Value
Geometric properties	Ns	3	L	120 m	DA	1584 m^2
	N_{UBS}	2	I/h	0.21 m^3	GS	2.2 m
	System	Concrete girders	h	2 m	N_{L}	2 lanes
	h_{pier}	6 m	h/S	0.05	Location	Near ramp
Loading properties	$(\Delta T^+ - \Delta T^-)_{\text{avg}}$	12.5 °C	Deceleration	0.5g	Sa(0.2)	0.49g
	V_{annual}	445,300	Record type	Eastern	Sa(1.0)	0.13g

Table 3 Annual cycle counts for the simplified method versus the detailed method

Method	Amplitude range (mm)					Total cycle count	Cumulative demands (m)
	0–2	2–4	4–6	6–8	8–10		
Simplified	1,046,142	158,550	24,030	3642	552	1.233×10^6	1672
Detailed	1,134,107	53,630	5203	718	137	1.194×10^6	1327

7 Conclusions

The current study proposes a simplified method that provides rough and quick estimates of the bearing demands during the preliminary bridge design stage. Such method can aid bridge designers when comparing between multiple preliminary design alternatives for bridges and bridge bearings. The proposed simplified method takes into account the uncertainty faced by the designers when not all of bridge design parameters affecting the bearing demands are known. Prediction models are proposed for the bearing demand attributes (i.e., cycle amplitudes and cycle counts) at a 90% prediction level and function of the typically available design parameters at the preliminary design stage.

The proposed simplified method was shown to result in more conservative estimates of the bearing demands compared to the detailed method. For a case study bridge, the demand predictions from the simplified method were 25–35% higher than those estimated while having full knowledge of the final design parameters' values. In particular, the method yielded conservative estimates of the maximum amplitude in case of temperature and seismic loads, but was less so in case of traffic loads. The proposed simplified method well predicted the total annual cycle count, but it overestimated the cycle count at the higher amplitude range, resulting in a 26% increase in the cumulative demands. Getting a better grasp on how much conservative is the method requires testing for other bridge configurations. However, the results of this paper reveal that the simplified method can provide preliminary estimates of the bearing demands with a safety factor on the magnitude of 1.25–1.35 which is considered acceptable at the preliminary design stage. And then, if needed, the demands can be further assessed more accurately using the detailed method when the final bridge design parameters are determined. The prediction intervals can be also adjusted to achieve target safety factors for the loading protocol variables. Future work will extend the proposed method to include other bridge configurations such as multi-span simply supported bridges.

References

1. AASHTO (2017) LRFD bridge design specification. Washington, DC.
2. Abdelmaksoud AM, Patel MK, Becker TC, Balomenos GP (2022) Parameterized models for prediction of lifetime bearing demands. Eng Struct 252:113649
3. AISC American Institute for Steel Construction (2015) AISC Shapes Database v15.0

4. Angelilli C (2007) Surveillance of the performance of elastomeric bearings in Maryland's concrete bridges. Doctoral Dissertation, University of Maryland, College Park, Maryland, United States

5. Bozorgnia Y, Kishida T, Abrahamson NA, Ahdi SK, Ancheta TD, Archuleta RJ, Atkinson G, Boore DM, Campbell KW, Chiou B (2018) NGA-Sub research program. In: Proceedings, 11th US national conference on earthquake engineering, pp 25–29

6. Chiou B, Darragh R, Gregor N, Silva W (2008) NGA project strong-motion database. Earthq Spectra 24(1):23–44

7. CSA (Canadian Standards Association) (2019a) Canadian Highway Bridge Design Code. CSA S6-19. Toronto, Canada

8. CSA (Canadian Standards Association) (2019b) Commentry on CSA S6-19, Canadian Highway Bridge Design Code. CSA S6-19. Toronto, Canada

9. Deng P, Warn GP (2016) Modeling the compression stiffness degradation in circular elastomeric bearings due to fatigue. J Eng Mech 142(1):4015057

10. ECCC (Environment and Climate Change Canada) (2019) 1981–2010 Canadian climate normals and averages. Accessed 26 Oct 2018. Available from: https://climate.weather.gc.ca/climate_normals/index_e.html

11. Emerson M (1976) Bridge temperatures estimated from the shade temperature. TRRL Report SR 696, Department of Transport, Crowthorne, England

12. Grata J (2008) Birmingham bridge report confirms rocker bearing failure. Available from: https://www.post-gazette.com/breaking/2008/07/01/Birmingham-Bridge-report-confirms-rocker-bearing-failure/stories/200807010159. Accessed July 2020

13. Halchuk S, Adams J, Kolaj M, Allen T (2019) Deaggregation of NBCC 2015 seismic hazard for selected Canadian cities In: Proceedings of the 12th Canadian conference on earthquake engineering, Quebec City, QC, Canada, pp 17–20

14. Harman D (1985) Multiple presence surveys of commercial vehicles in Ontario 1981 and 1982. Ministry of Transportation and Communication: Research and Development Branch—Research Report SRR-84-10, Faculty of Engineering Science, University of Western Ontario, London, Ontario

15. Hedegaard BD, French CEW, Shield CK (2013) Investigation of thermal gradient effects in the I-35W St. Anthony Falls Bridge. J Bridge Eng 18(9):890–900

16. Kelly JM, Konstantinidis D (2011) Mechanics of rubber bearings for seismic and vibration isolation. Wiley

17. Kennedy JB, Soliman MH (1987) Temperature distribution in composite bridges. J Struct Eng 113(3):475–482

18. Kumar R, Gardoni P, Sanchez-Silva M (2009) Effect of cumulative seismic damage and corrosion on the life-cycle cost of reinforced concrete bridges. Earthquake Eng Struct Dynam 38(7):887–905

19. Mars WV, Fatemi A (2002) A literature survey on fatigue analysis approaches for rubber. Int J Fatigue 24(9):949–961

20. Martins J, Fénart M-A, Feltrin G, Dumont A-G, Beyer K (2016) Deriving a load model for the braking force on road bridges: comparison between a deterministic and a probabilistic approach. In: Developments in international bridge engineering. Springer, pp 27–39

21. McKay MD, Beckman RJ, Conover WJ (2000) A comparison of three methods for selecting values of input variables in the analysis of output from a computer code. Technometrics 42(1):55–61

22. McKenna F, Scott MH, Fenves GL (2010) Nonlinear finite-element analysis software architecture using object composition. J Comput Civ Eng 24(1):95–107

23. MTO (Ministry of Transportation Ontario) (2019) MTO iCorridor: Historical Provincial Highways Traffic Volumes. Available from: http://www.maps.mto.gov.on.ca/icorridor/index.html. Accessed October 2020

24. Muhr AH (2006) Fracture of rubber-steel laminated bearings. In: Elastomers and components. Elsevier, pp 209–226

25. NBCC (2015) National Building Code of Canada 2015. National Research Council of Canada, Ottawa, NRCC 56190 Vol 1 & 2
26. Noade BM, Becker TC (2019) probabilistic framework for lifetime bridge-bearing demands. J Bridg Eng 24(7):4019065
27. PCI Bridge Design Manual Steering Committee (2014) Precast prestressed concrete bridge design manual. MNL-133-14, 3rd edn. PCI, Chicago, IL
28. Roeder CW, Stanton JF, Taylor AW (1990) Fatigue of steel-reinforced elastomeric bearings. J Struct Eng 116(2):407–426
29. Roy N, Paultre P, Proulx J (2010) Performance-based seismic retrofit of a bridge bent: design and experimental validation. Can J Civ Eng 37(3):367–379
30. Siqueira GH, Tavares DH, Paultre P (2014) Seismic fragility of a highway bridge in Quebec retrofitted with natural rubber isolators. Revista IBRACON de Estruturas e Materiais 7:534–547
31. Suryatal B, Phakatkar H, Rajkumar K, Thavamani P (2015) Fatigue life estimation of an elastomeric pad by ε-N curve and FEA. J Surface Eng Mater Adv Technol 5(2):85
32. Tavares DH, Suescun JR, Paultre P, Padgett JE (2013) Seismic fragility of a highway bridge in Quebec. J Bridg Eng 18(11):1131–1139
33. Troitsky MS (2019) Conceptual bridge design. In: Bridge engineering handbook, chap 1. CRC Press
34. Z-Tech G (2010) Elastomeric bearings. Québec

Life Estimation of Canadian Roadway Bridges Considering Effect of Damage on Fatigue Limit

Ali Chehrazi, Michelle Y. X. Chien, and Scott Walbridge

Abstract Fatigue failure is a significant design consideration for bridge elements. In design codes, fatigue design of a bridge element involves passing a code truck over a model of the bridge and then calculating the stress range for the element of interest. For the infinite life design of Canadian bridges, the code stress range multiplied by a correction factor should be lower than the fatigue limit of the element. This correction factor accounts for the differences between the code truck and the trucks in the real traffic. As the truck weights in the real traffic can significantly vary, a small percentage of real traffic stress ranges can be over the fatigue limit and damage the bridge elements. This can also happen due to overload trucks or trucks that cross the bridge simultaneously. Therefore, the actual life of components that are designed based on the current infinite life design procedure may not be infinite. However, their lives can still be very long. This work evaluates the fatigue life of bridge elements based on damage from the stress ranges that are over the fatigue limit. Two traffic databases from the Ontario Ministry of Transportation, obtained in 1995 and 2012, are employed in this work. Miner's sum is used to determine the damage due to stress ranges that are over the fatigue limit of the component. The results of this study show that the current infinite life design criteria in CSA S6 can be unconservative for bridge elements with long influence lines.

Keywords Roadway bridges · Fatigue limit · Life estimation

1 Introduction

Fatigue failure is a major problem for bridge components that are subjected to cyclic loading. In several bridge design codes, fatigue design of an element starts with passing a code truck over a model of the bridge and then determining the design stress range in the element of interest. This stress range is then modified by a correction

A. Chehrazi (✉) · M. Y. X. Chien · S. Walbridge
University of Waterloo, Waterloo, Canada
e-mail: achehrazi@uwaterloo.ca

1123

factor, which accounts for the differences between the design or code truck and the trucks in the real traffic. The modified design stress range is then compared with the fatigue resistance of the component. An appropriate code truck model and correction factor are critical in this design method. Given the possible changes in gross vehicle weight (GVW) histogram of the trucks in the real traffic over time, regular calibration of the correction factors is required.

Typically, two fatigue limit states are employed in bridge design codes: one for finite life and another for infinite life design [1]. Finite life correction factors can be determined employing a methodology developed by Hirt et al. [8]. The required inputs for this method are a code truck, a real traffic database, and a bridge model. Coughlin and Walbridge [4] employed this method to evaluate the finite life correction factors in North American bridge design codes for welded aluminum structures and showed the effect of overload trucks on these correction factors. Fischer [6] and Walbridge et al. [12] showed that simultaneous truck crossing can significantly affect the correction factors for bridges elements with long influence lines, especially at the locations with a high volume of traffic where multiple trucks can be on the bridge at the same time. Chehrazi et al. [3] evaluated Canadian Highway Bridge Design Code, CSA S6, correction factors for bridge elements with very short influence lines.

The fatigue limit of a component is a stress range below which infinite life is practically assumed. It is established with constant amplitude loading fatigue tests, based on runout data (tests that did not lead to failure). In real bridge structures, however, the components experience variable amplitude cyclic loading. Designing the components with a very conservative factor that ensures all the stress ranges are below the fatigue limit can be very costly and inefficient. Therefore, typically, the correction factors can be determined so that only a very small percentage of cycles, e.g., 0.01%, will be over the fatigue limit [9, 11]. The fatigue life of components designed based on the infinite fatigue life criteria is thus not truly infinite, as a few stress ranges are over the fatigue limit and damage the component. However, the fatigue life can still be much more than the typical design life of a bridge (e.g., 75 years). With this background, this paper aims to estimate the actual fatigue life of bridge components designed based on the infinite life criteria in CSA S6. To do this, traffic databases from 1995 and 2012 are used to examine the effect of changes in the GVWs of real traffic on the fatigue life of bridge components.

2   CSA S6 Infinite Fatigue Life Design Criteria

According to CSA S6, the code stress range (f_{sr}) modified by the code correction factor (λ_1) shall be lower than the fatigue resistance of the component (F_{sr}):

$$\lambda_1 \cdot f_{sr} < F_{sr} \tag{1}$$

The code stress range can be determined by passing the code truck model over the bridge model or the influence line of the component of interest and then recording

the stress range (maximum minus minimum stress) in that component. λ_1 is 0.52 for all structural elements except components in bridge decks and 0.62 for expansion joints and components in bridge decks, except stringers and floor beams. The fatigue resistance of the component is calculated using the following equations:

$$F_{sr} = \left(\frac{\gamma}{N_c}\right)^{\frac{1}{3}} \tag{2}$$

$$\text{If } F_{sr} = \left(\frac{\gamma}{N_c}\right)^{\frac{1}{3}} < F_{srt} \text{ then } F_{sr} = \left(\frac{\gamma'}{N_c}\right)^{\frac{1}{5}} \geq \frac{F_{srt}}{2} \tag{3}$$

where N_c is the expected number of code stress ranges during the design life of the bridge, γ and γ' are the fatigue constants, and F_{srt} is the fatigue limit for the detail category of interest.

Based on Eqs. 1–3, the infinite life design equation can be written as follows:

$$\lambda_1 \cdot f_{sr} < \frac{F_{srt}}{2} \tag{4}$$

To determine the correction factor for infinite life design, similar to λ_1 for finite life design, Eq. 4 can be written as follows:

$$\lambda_2 \cdot f_{sr} < F_{srt} \tag{5}$$

where λ_2 is the infinite life correction factor and is equal to $(2\lambda_1)$. Therefore, the infinite life correction factor is equal to 1.04 for all structural elements except the components in bridge decks and 1.24 for expansion joints and the components in bridge decks, except stringers and floor beams. The purpose of rewriting the equation was to simplify the comparisons made in the rest of this paper. This also allows comparison with [1], which employs an infinite life design limit state similar to Eq. 5.

3 Methodology

In constant amplitude fatigue tests, the fatigue threshold is defined as the stress range below which a component can be practically assumed to have an infinite life. However, bridge components experience a wide variation in actual stress ranges during their design life. Employing a correction factor that ensures the fatigue resistance is always higher than these variable stress ranges is not economical and over-conservative. Therefore, the current infinite life correction factor allows a very small percentage (e.g., 0.01%) of real stress ranges to be over the fatigue limit. These stress ranges over the fatigue limit damage the components. Consequently, the life of the components is not infinite, but it still can be considerably higher than the design

life of the bridge (e.g., 75 years). The initial methodology that was employed in the current study for estimating damage and consequently fatigue life is shown in Fig. 1.

The steps of this methodology are as follows:

1. The code truck model is passed over the influence line of the element of interest to determine the code truck load effect range, ΔF_{code}.
2. A factor is required to relate the code load effect range to the code stress range ($f_{sr} = k \cdot \Delta F_{code}$). To consider the worst-case scenario in infinite life design, this factor is determined so that the code stress range multiplied by the correction factor equals the fatigue limit of the detail of interest:

$$k = \frac{F_{srt}}{\lambda_2 \cdot \Delta F_{code}} \tag{6}$$

3. The trucks in the real traffic database are passed over the influence line of the element of interest, and the load effect history is recorded.
4. The k factor determined in Step 2 is multiplied by the load effect history, and the stress history is calculated.
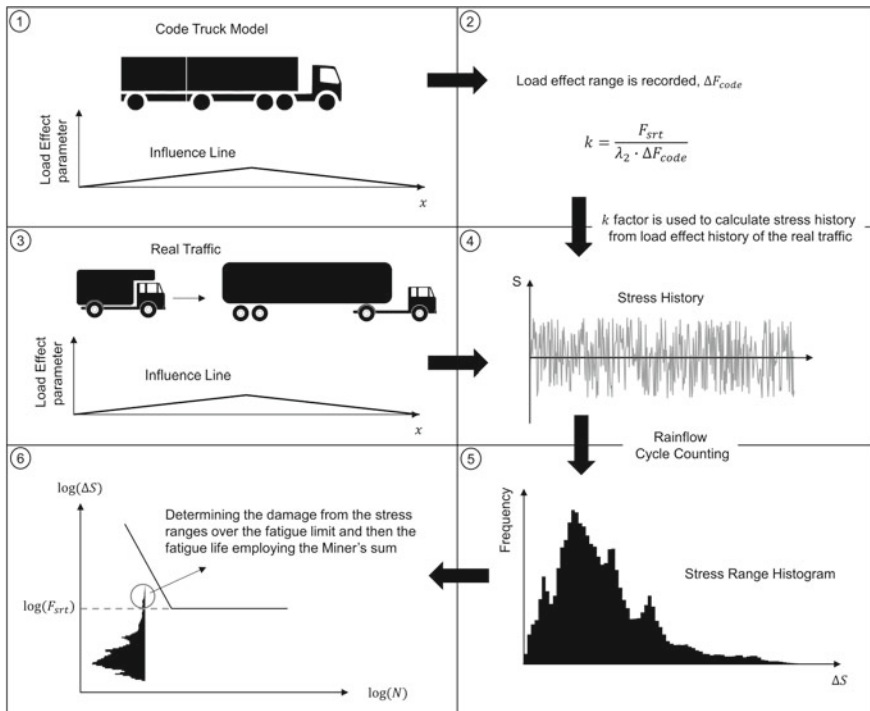
Fig. 1 Fatigue life estimation methodology

5. A rain flow cycle counting method is used to determine the stress range histogram of the real traffic database. In this study, the method by Downing and Socie [5] is employed.
6. The Miner's sum is used to determine the fatigue life of the components:

$$D = \frac{\sum n_i}{\sum N_i} \tag{7}$$

where n_i is the frequency of each stress range and N_i is the number of cycles at each stress range which can be determined using the following equation:

$$\mathrm{Log}_{10}(N) = \mathrm{Log}_{10}(M) - m\mathrm{Log}_{10}(\Delta S) \tag{8}$$

where m is the slope of the S–N curve, N is the fatigue life of the component, ΔS is the stress range, and M is the horizontal intercept of the S–N curve.

4 Damage Effect on Fatigue Limit

Constant amplitude fatigue tests typically can be fitted to a 1-slope S–N curve and a cut-off limit at the fatigue threshold (see Fig. 2a). With this curve, it is assumed that the fatigue life for stress ranges below the fatigue limit is infinite, and these stress ranges do not cause any damage to the components. This has been proven to be valid for many cases in constant amplitude fatigue tests. For variable amplitude fatigue loading, however, the problem gets more complicated. In variable amplitude conditions, a percentage of stress ranges can be over the fatigue limit and damage the component. The damaged component can then be affected by stress ranges below the initial fatigue limit, since cracks are affected by smaller and smaller stress ranges as they grow. In other words, the fatigue limit decreases because of damage from the stress ranges that are over the fatigue limit. Therefore, employing the original S–N curve and Miner's sum without considering the decrease in the fatigue limit is not acceptable.

Several works have evaluated possible methods to present S–N curves for variable amplitude fatigue loadings. Haibach [7] presented a 2-slope S–N curve with an initial slope of m up to the fatigue limit and a shallower second slope of $2m - 1$ below it. This approach has been used in several studies and has been adopted in some international design codes—particularly in Europe. Usually, a cut-off limit is used for the 2-slope S–N curves as well. The current paper employs this method with an initial slope of 3, based on CSA S6, a second slope of 5, and a cut-off limit equal to 50% of the constant amplitude fatigue limit. This 2-slope S–N curve has a similar shape to the typical CSA S6 design curve for steel (see Fig. 2a).

Kunz and Hirt [10] presented another method for considering the effect of damage on the fatigue limit. Based on this method, the fatigue limit of a damaged component can be updated as follows:
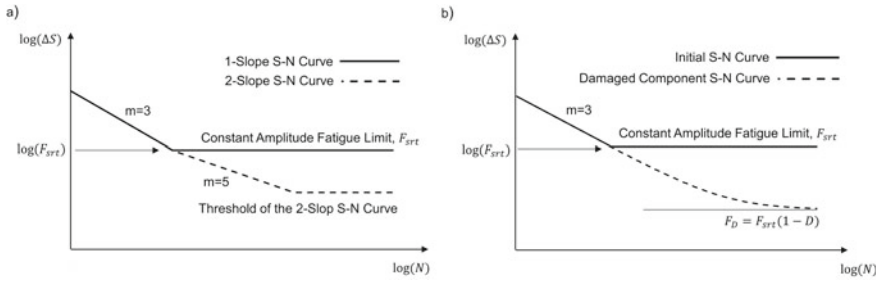
Fig. 2 Modified 2-slope S–N curve presented by Haibach [7] (**a**), S–N curve based on Kunz and Hirt [10] (**b**)

$$F_D = F_{srt} \cdot (1 - D) \tag{9}$$

where F_{srt} is the constant amplitude fatigue threshold or the initial threshold, D is the total damage of the component, which can be determined based on the Miner's sum, and F_D is the fatigue limit of the damaged component. In this method, a reference point should be assumed on the initial line with the slope of $m = 3$, and the damage at the points below the reference point and the new threshold, F_D, can be determined using the following equation:

$$d_i = \frac{\Delta S_i^3 - F_D^3}{\Delta S_R^3 - F_D^3} \cdot \frac{1}{N_R}$$

where ΔS_i are stress ranges between the initial and the damaged fatigue limit, ΔS_R and N_R are the reference stress range and corresponding life of the reference stress range, and F_D is the fatigue limit of the damaged component. In this study, the reference stress range was considered at the initial fatigue limit point.

5 Traffic Simulation Parameters

Figure 3 shows the gross vehicle weight, GVW, histograms of the real traffic databases employed in the current study. These GVW databases were obtained by the Ontario Ministry of Transportation, MTO, in 1995 and 2012, using stationary weigh scales. They include axle weights and the spacing between the axles of the trucks. The MTO 1995 and 2012 databases include 10,198 and 45,192 trucks, respectively.

The CSA S6 code truck model, CL-625, was employed in the current study. This five-axle truck model has a GVW of 625 kN. The axle spacing and individual axle weights of this design truck can be seen in Fig. 4a. According to CSA S6, the dynamic load allowance, DLA, changes for different structural elements. (For example, DLA is 0.25 when three or more axles of the truck model are affecting the component.) However, as this parameter is assumed to be constant for the code truck model and
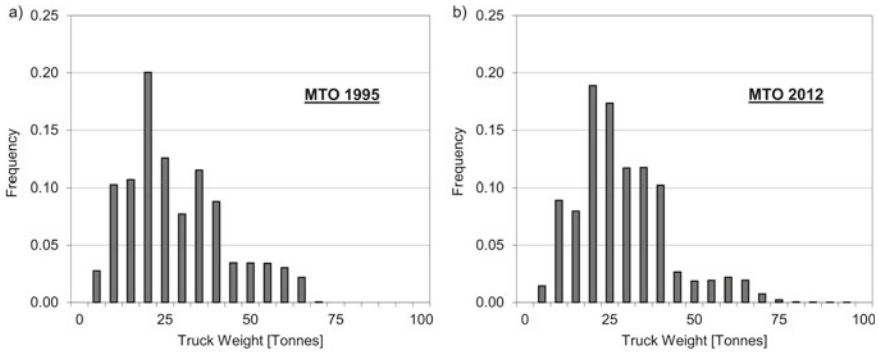
Fig. 3 GVW histograms of the real traffic databases

the trucks in the real traffic database for the current study, this parameter does not affect the results.

Two influence line types, shown in Fig. 4b, were employed for the current study. To evaluate the effect of span on the fatigue life, several spans, namely: 0.1, 0.2, 0.5, 1, 2, 5, 10, 15, 25, 50, and 100 m, were used in this study. Three different detail categories, A, C, and E, from CSA S6 were employed. The fatigue constants and constant amplitude fatigue threshold of these details are listed in Table 1.
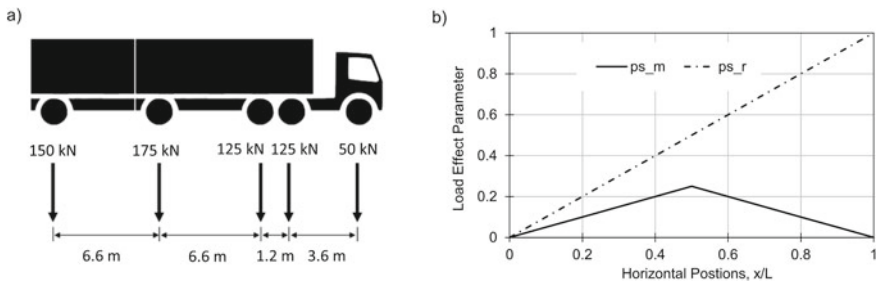
Fig. 4 CSA S6 code truck model (**a**), investigated influence lines (**b**)

Table 1 Fatigue properties of the studied detail categories (CSA S6)

Detail category	F_{srt} (MPa)	γ	γ'
A	165	8190×10^9	223×10^{15}
C	69	1440×10^9	6.86×10^{15}
E	31	361×10^9	0.347×10^{15}

6 Fatigue Life Estimations

The first analysis was done to evaluate the effect of the discussed S–N curves on the damage calculation and consequently the fatigue life. The analysis was done for a Category A detail, with an ADTT, average daily truck traffic, of 4000 and a ps_m influence line. Figure 5 compares the results for the MTO 1995 and 2012 databases. It can be seen that the 2-slope S–N curve results are always lower than Kunz's method results. For the 2-slope curve, a threshold less than the fatigue limit (50% of the fatigue limit in this study) is assumed. With this assumption, the stress ranges over 50% of the fatigue limit are assumed to damage the component during the whole life of the component. However, this assumption can be very conservative. In some cases, the stress ranges over the fatigue limit are very few. The damage to the component can be very limited in these cases. Therefore, the required time for the fatigue threshold to reach 50% of its initial value can be very long. Kunz's method, however, directly considers the stress ranges over the fatigue threshold and uses the damage from those stress ranges to decrease the fatigue threshold. Kunz's method seems to be more logical, especially for research purposes. For design purposes, however, a 2-slope S–N curve is probably easier to implement. With this in mind, the rest of the results are only based on Kunz's method.

One of the steps of Kunz's method is periodically updating the fatigue threshold for the damaged component. To evaluate the possible effect of fatigue threshold updating frequency on the fatigue life predictions, three frequencies of 6, 12, and 24 months were used. The results for the Category A detail, ps_m influence line, and ADTT of 4000 are shown in Fig. 6. No significant difference is seen between the results. As the results are presented in years, a frequency of once per year was employed for the rest of the paper as a practical assumption.

Figure 7 shows fatigue life predictions for the full range of studied parameters. First, it can be seen that the fatigue life results based on MTO 2012 database are lower than the results based on MTO 1995. Looking at the histograms of these databases in Fig. 3, it can be seen that the MTO 2012 database has more heavy trucks. These heavy trucks cause higher stress ranges and can cause more damage to the components,
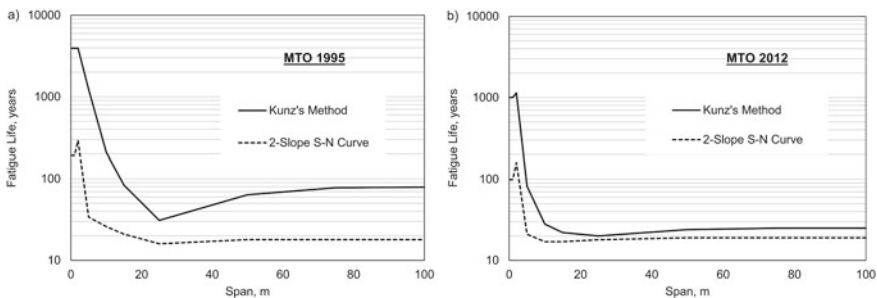
Fig. 5 Kunz's method versus 2-slope S–N curve results for Category A detail, ps_m influence line, and an ADTT of 4000
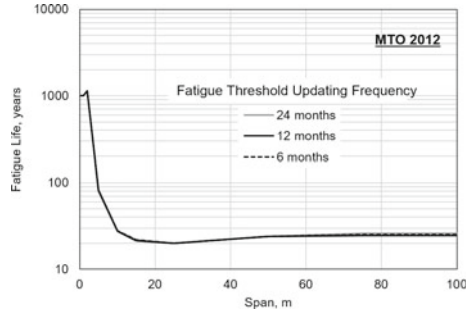
and consequently, the fatigue life predictions based on this database are lower than the predictions based on MTO 1995 database. Looking at the results for the different detail categories, it can be seen that the Category E detail was not critical in any cases. The fatigue life of Category C detail was slightly lower than 75 years when the MTO 2012 database and ps_m influence line were employed. Category A detail was the most critical detail category, and it seems that the code is not conservative for this detail category, especially for bridges with long spans.

The higher fatigue life for Category E may seem counter-intuitive. Normally, if details are subjected to the same nominal stress history, Category E detail will have the lowest life, and Category A detail will have the longest. In this analysis, it should
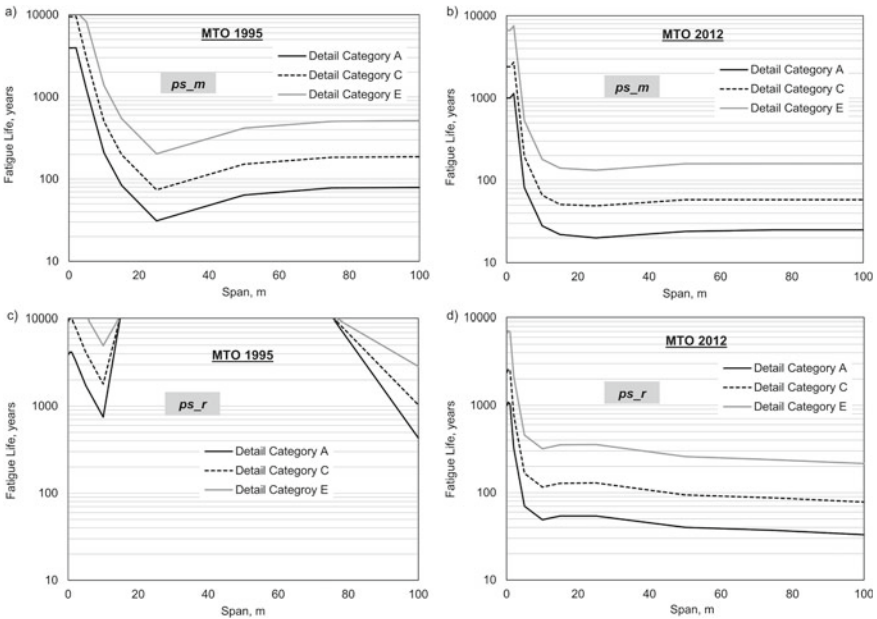
Fig. 7 Fatigue life predictions for the studied detail categories, influence lines, and databases

be noted that the stress levels are not the same for each category—rather, they have been set to ensure a nominal stress range just below that required to ensure "infinite life" according to the existing design provisions. The reason the present analysis gives a higher life for Category E has to do with the location of the transition point between finite and infinite life design, which occurs at a higher number of cycles, N, for Category E.

Another observation from these results is that the elements with short influence lines, or spans less than 10 m, are not critical, while the most critical components are the ones with long influence lines. This can be explained by the way the code stress range is determined for elements with short and long influence lines. For components with short influence lines, Axle 4, 175 kN, of the code truck determines the design stress range. Only 0.01% and 0.02% of the trucks in the MTO 1995 and 2012 databases, respectively, have a heavier axle than Axle 4 of the code truck. For components with long influence lines, however, the GVW of the truck is more effective rather than the individual axle weights. In the MTO 1995 and MTO 2012 databases, 0.77% and 1.87% of the trucks have a GVW higher than the code truck. Therefore, for elements with long influence lines, the design stress range is lower in comparison with the maximum real stress ranges. Consequently, a shorter fatigue life is expected.

The results in this paper showed that the current correction factor can potentially be unreliable for some detail categories, especially for components with longer influence lines. It should be noted that in this analysis, the trucks in the real traffic database were passed over the bridge one at a time. Simultaneous truck crossing, when trucks follow each other closely or cross the bridge side by side, can worsen the situation for elements that carry the loads from multiple lanes or elements with long influence lines, as discussed in Walbridge et al. [12]. Also, the traffic databases showed that the trucks are getting heavier over time and having more heavier trucks means lower fatigue life. Therefore, regular calibration of the correction factors is essential. It should be noted that further studies are required to consider the effect of other factors that can affect the bridge life such as corrosion attacks due to de-icing and marine salts and environmental pollutants.

7 Conclusions

Based on the results of this paper, the following conclusions can be drawn:

1. Fatigue life prediction based on the 2-slope S–N curve can be very conservative. Therefore, an iterative approach for considering the effect of damage on the fatigue limit can be a more logical approach in variable amplitude loading conditions.

2. The current infinite life design criteria of CSA S6 are reliable for elements with short influence lines. However, the results based on the MTO 2012 database show that the design criteria can be unconservative for some detail categories, especially for elements with long influence lines.
3. The code stress range for elements with short influence lines is very reliable, as the maximum axle weight of the code truck (175 kN) is very heavy in comparison with the axle weights of the trucks in the real traffic databases.
4. The code stress range for elements with long influence lines is not conservative, as there are more heavier trucks in the databases, especially MTO 2012 database. These trucks can damage the components and consequently decrease their fatigue lives.
5. The GVW histogram of the real traffic can significantly affect the results. Therefore, regular monitoring of the real traffic and calibration of the code correction factors are required.

References

1. AASHTO (American Association of State Highway and Transportation Officials) (2017) AASHTO LRFD bridge design specifications. AASHTO, Washington, D.C.
2. CSA (Canadian Standards Association) (2019) Canadian highway bridge design code. CAN/CSA-S6. CSA, Mississauga, ON, Canada
3. Chehrazi A, Chien MYX, Walbridge S (2022) Assessment of fatigue design provisions for bridge elements with very short influence lines. In: Canadian Society of Civil Engineering annual conference. Springer, Singapore
4. Coughlin R, Walbridge S (2011) Fatigue correction factors for welded aluminum highway structures. Can J Civ Eng 38(10):1082–1091
5. Downing SD, Socie DF (1982) Simple rainflow counting algorithms. Int J Fatigue 4(1):31–40
6. Fischer V (2012) Effect of simultaneous vehicle crossings on the North American fatigue correction factors. Master's thesis report, École Polytechnique Fédérale de Lausanne, Lausanne, Switzerland
7. Haibach E (1970) Modifizierte lineare Schadensakkumulations-hypothese zur Berücksichtigung des Dauerfestigkeitsabfalls mit fortschreitender Schädigung. Laboratorium für Betriebsfestigkeit
8. Hirt MA, Bez R, Nussbaumer A (2006) Traite de génie civil, vol. 10: Construction métallique—Notions fondamentales et méthodes de dimensionnement. Presses Polytechniques et Universitaires Romandes, Lausanne, Switzerland
9. Kulicki JM, Wasser WG, Mertz DR, Nowak AS (2015) Bridges for service life beyond 100 years: service limit state design. Transportation Research Board, Washington, DC
10. Kunz P, Hirt MA (1993) Reliability analysis of steel railway bridges under fatigue loading. IABSE Colloquium Copenhagen 1993 on Remaining Structural Capacity, IABSE Report 67

11. Russo FM, Mertz DR, Frank KH, Wilson KE (2016) Design and evaluation of steel bridges for fatigue and fracture–reference manual. Rep. FHWA-NHI-16-016, Federal Highway Administration, Washington, DC
12. Walbridge S, Fischer V, Maddah N, Nussbaumer A (2013) Simultaneous vehicle crossing effects on fatigue damage equivalence factors for North American roadway bridges. J Bridg Eng 18(12):1309–1318

Data-Driven Models for Predicting Drift Ratio Limits of Segmental Post-tensioned Precast Concrete Bridge Piers

Chanh Nien Luong, Cancan Yang, and Mohamed Ezzeldin

Abstract Segmental post-tensioned precast concrete (SPPC), an important technique of Accelerated Bridge Construction (ABC), has been proven its advantages over monolithic cast-in-place concrete in rapid bridge rehabilitation and construction. To deploy its implementation in bridge substructures for seismic applications, proposing performance-based design specifications is much needed. However, one main challenge of achieving this goal stems from defining quantitative criteria for a series of damage states that are associated with different performance levels, in relation to the functionality of the bridge. In recent years, data-driven models have been recognized as a powerful tool for making rational predictions in several structural engineering applications. Multiple linear regression (MLR) offers great potential to develop equations that are capable of identifying the maximum drift ratio limits for the four performance levels (i.e., immediate service, limited service, service disruption, and life safety) for SPPC piers. In this respect, based on a database generated from validated finite element models, MLR with stepwise backward elimination is performed in the current study using key design parameters, including concrete strength, aspect ratio, gravity load ratio, post-tension force, post-tension strand ratio, and energy dissipation bar ratio. For each damage state, a predictive equation for the threshold drift ratio is developed by seeking a balance between accuracy and simplicity. Sensitivity analysis is also performed to evaluate the effect of design parameters on the variability of the predicted drift ratio limits.

Keywords Drift ratio limits · Bridge piers

C. N. Luong (✉) · C. Yang · M. Ezzeldin
McMaster University, Hamilton, Canada
e-mail: luongcn@mcmaster.ca

1 Introduction and Literature Review

Over the past two decades, growing attention has been given to the development and application of precast concrete bridge elements and systems in seismic regions [22]. As a critical component of the bridge system, segmental post-tensioned precast concrete (SPPC) bridge pier has been studied and shown satisfactory seismic performance. To enhance the resilience of infrastructure, performance-based seismic design (PBSD) has rapidly gained recognition over force-based seismic design (FBSD). This is because PBSD assists engineers and owners in decision making by directly connecting engineering demand parameters (EDP), including drift ratios and residual drifts, to decision variables, such as replacement cost, casualty rate, and downtime [6]. With tremendous research efforts [4, 19, 21, 23, 32], PBSD for RC piers was adopted in highway bridge design codes, such as CSA S6-19 [11], New Zealand Bridge Manual [27], and Caltrans 2016 [7]. However, there are limited research has been devoted to developing PBSD procedures for SPPC piers.

In PBD, a well-defined EDP that quantifies structural damage degree is foremost important [25]. By comparing the predicted EDP for a given seismic hazard level to the EDP limits, engineers can estimate whether the performance objective is met. In the current CSA S6-19, material strains, including concrete and steel rebar, are used to evaluate damage states. Although the strain is a direct measure of structural damage, it is not common to assess strains during a seismic event. Thus, several other EDPs have been proposed and used by researchers in PBD for monolithic cast-in-place columns, including drift ratio and residual displacement [3, 4, 17, 31]. However, these EDP limits cannot be directly applied to SPPC piers, which have different seismic response mechanisms and damage types, such as concentrated concrete crushing at rocking toe, and significant elongation of post-tensioning strand (PT strand) and energy dissipation bar (ED bar) due to joint opening. To address this research gap, several studies have been conducted to develop EDP limits for SPPC [14, 20, 36]. However, some limitations remain and require further investigation, including (1) the EDP limits were established for SPPC piers with inadequate design space; and (2) the definition of EDP was inconsistent.

To link the drift ratios to material strain limits, a finite element (FE) model was adopted in the current study to generate the database for the development of the data-driven model. In general, FE models have proven their outstanding capability in predicting global seismic responses (e.g., force–displacement relationship), as well as capturing structural damages [8, 14, 35]. Multiple linear regression (MLR) models are widely implemented by researchers to derive prediction expressions on plastic hinge length [5], and column's effective stiffness [33], which are based on fitting different experimental results. Due to its simplicity and reasonably high accuracy in structural engineering applications, MLR is still one of the most accepted statistical models in the field [26]. As such, MLR models have been utilized in the current study to develop drift ratio limit equations for corresponding damage states.

The primary objectives of the current study include (1) establishing material strain-based criteria that are associated with the performance levels specified in CSA S6

for SPPC piers; (2) developing drift ratio prediction equations for four damage states using MLR; (3) evaluating the effect of different design parameters on the drift ratio-based limit states for SPPC piers.

2 Damage Limit State

In the current CSA S6, four damage states have been specified for PBSD of monolithic cast-in-place piers [11]. To adapt the PBSD of CSA S6 to the design of SPPC piers, one of the foremost components to implement PBSD for SPPC piers is to establish a set of well-defined damage states and the associated criteria. In addition, a good selection of EDP, which serves as a measure of the structure's performance, is also required. Researchers have employed several EDP limits, including material strains, displacement ductility ratios, plastic rotations, and residual drift ratios, to quantify structural damage. However, such EDPs have their limitations when adapted to SPPC pier. For example, material strains are not typically obtained during an earthquake event. Plastic rotations and residual drifts may not be also effective damage indicators for SPPC piers due to their superior self-centering capacity. Therefore, in this study, the drift ratio limit was selected as a quantitative measure for SPPC piers. Moreover, previously proposed damage states and criteria for SPPC piers in the literature have two main drawbacks, which might not be suitable to be used in CSA S6. First, the number of performance levels is not adequate [14, 20]. Second, the criteria that define damage states are not consistent [14]. As a result, a modified set of material strain-based damage criteria, which is presented in Table 1, was proposed by [22] to match the current code provision. In this study, the abovementioned set of damage criteria is adopted.

3 Finite Element Model

A 3D nonlinear SPPC pier FE model was developed using the commercial software ABAQUS/Standard [13]. This software has been extensively used by several researchers and has proven its outstanding ability in simulating the seismic response and local damage of SPPC piers [14, 23, 35]. Figure 1 shows the SPPC pier assembly created in ABAQUS. The model consists of a cap beam, precast concrete column segment, foundation, PT strand, ED bar, discontinuous mild steel, confinement steel, and PVC duct.

Table 1 Proposed performance criteria

Service	Damage (CSA S6-19 Table 4.16)	Proposed damage (SPPC piers)
Immediate Bridge shall be fully serviceable for normal traffic and repair work does not cause any service disruption	**Minimal damage** • General: Bridge shall remain essentially elastic with minor damage that does not affect the performance level of the structure • Concrete compressive strains shall not exceed 0.006 • Reinforcing steel strains shall not exceed 0.01	**Minimal damage** • General: Bridge shall remain essentially elastic with minor damage that does not affect the performance level of the structure • Concrete compressive strains shall not exceed spalling strain • Energy dissipation bar tensile strains shall not exceed yield strain
Limited Bridge shall be usable for emergency traffic and be repairable without requiring bridge closure. At least 50% of the lanes, but not less than one lane, shall remain operational. If damaged, normal service shall be restored within a month	**Repairable damage** • General: Some inelastic behavior and moderate visible damage, such as spalling of concrete at the rocking toe, might occur. However, primary members shall not need to replace, shall be repairable in place, and shall be capable of supporting the dead load plus live load corresponding to the service performance criteria during repairs • Reinforcing steel tensile strains shall not exceed 0.025	**Repairable damage** • General: Some inelastic behavior and moderate visible damage, such as spalling of concrete at the rocking toe, might occur. However, primary members shall not need to replace, shall be repairable in place, and shall be capable of supporting the dead load plus live load corresponding to the service performance criteria during repairs • Energy dissipation bar tensile strains shall not exceed 0.025 • Confined core concrete shall not exceed 30% of its ultimate confined concrete strain limit
Service disruption The bridge shall be usable for emergency traffic after inspection. The bridge shall be repairable. Repairs to restore the bridge to full service might require bridge closure	**Extensive damage** • General: Inelastic behavior is expected. Members might have extensive damage, but strength degradation shall not occur. Members shall be capable of supporting the plus one lane of live load, including P-delta effects, without collapse • Concrete spalling is permitted, but the confined core concrete shall not be exceeded 80% of its ultimate confined strain limit • Reinforcing steel tensile strains shall not exceed 0.05	**Extensive damage** • General: Inelastic behavior is expected. Members might have extensive damage, but strength degradation shall not occur. Members shall be capable of supporting the plus one lane of live load, including P-delta effects, without collapse • Concrete spalling is permitted, but the confined core concrete shall not exceed 80% of its ultimate confined concrete strain limit • Post-tensioning strand tensile strain shall not exceed 0.0085

(continued)

Table 1 (continued)

Service	Damage (CSA S6-19 Table 4.16)	Proposed damage (SPPC piers)
Life safety The structure shall not collapse and it shall be possible to evacuate the bridge safely	**Probable replacement** • General: Bridge column shall remain in place, but the bridge might be unusable and might have to be extensively repaired or replaced • Damage does not cause crushing of the confined concrete core • Reinforcing steel tensile strains shall not exceed 0.075, except that for steel reinforcing of 35 M or larger the strains shall not exceed 0.06	**Probable replacement** • General: Bridge column shall remain in place, but the bridge might be unusable and might have to be extensively repaired or replaced • Damage does not cause crushing of the confined concrete core • Energy dissipation bar tensile strains shall not exceed 0.09 • Post-tensioning strain tensile strains shall not exceed 0.01
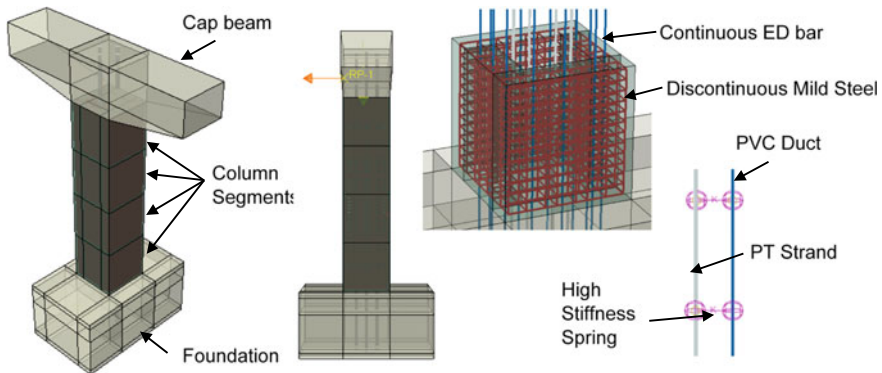
Fig. 1 Typical SPPC bridge pier assembly in ABAQUS

3.1 Material Constitutive Modeling

Young's modulus of concrete was calculated as per ACI 318-19 [1]. To define the inelastic compressive stress–strain relationship, Popovic's unconfined concrete constitutive model was used [30]. The limit of elasticity for concrete compression was assumed to be 45% of the design strength as stated in ACI 318-19. Concrete damaged plasticity (CDP) was selected to model the nonlinearity of concrete in ABAQUS. In addition, tension softening behavior was defined as a function of crack opening as per [15].

Mander's nonlinear tensile constitutive model [24] for steel was used for non-continuous and ED bars. Young's modulus and Poisson's ratio for steel were selected

to be 200,000 MPa and 0.3, respectively, while the fracture strain limit was set to be 0.09 as per ASTM A615-20 [2].

The constitutive model for the PT strand was defined by Yang [34]. This model considers the prestress loss due to anchorage wedge-seating and strand inelasticity. The ultimate design strain for the PT strand was set to be 0.01 considering premature failure due to stress concentration at anchorage [34].

3.2 Constraints, Boundary, and Loading Condition

Both cap beam and foundation were defined as a rigid body, except for a small region of the foundation near the rocking surface. Embedded constraints were used to bond PVC ducts, discontinuous, and ED bars to the surrounding concrete. To simulate the unbonding behavior of PT strands, only a small portion of the strand was embedded into the foundation and cap beam. In addition, high stiffness springs were used to connect PT strand and PVC ducts at several discrete points along its length. Surface-to-surface contact was used between concrete segments with a constant friction coefficient of 0.5 in the tangential direction and hard contact behavior in the normal direction. Fixed-end constraints were set to the foundation to avoid any translational and rotational movements. Gravity load was applied at the top of the cap beam in the form of point loads, while lateral displacement was applied: (1) at a height based on the corresponding experimental program used for model validation; and (2) at mid-height of the cap beam during the analysis.

3.3 Model Validation

The developed FE model was validated in the current study using two specimens from [28, 29] to examine its accuracy in simulating SPPC pier's behavior and local damage such as concrete spalling and ED bar fracture. Table 2 shows the summary of the two tested specimens with their design parameters.

Figure 2 shows the comparison between the model and experimental results for the lateral force-drift ratio relationship. The FE models over-predicted the lateral strength of the SPPC pier in both cases with an error of about 17%. This overestimation might be attributed to the uncertainties of material properties, and also the static pushover analysis performed on the FE model did not account for the accumulated damages due to cyclic loading.

Generally, the developed FE was capable of simulating the damage conditions of SPPC piers reasonably well. Concrete spalling and ED bar fracture were defined by material strain limit in the numerical analysis. Concrete spalling was recorded when the ultimate unconfined concrete strain was reached, which was corresponding to the strain when compression stress decreases to 50% in the softening portion [34], while the ultimate strain for the ED bar was set to be 0.09. Using this method,

Table 2 Summary of design parameters used in the tested specimens

References	Designation	Compressive strength of concrete	Aspect ratio	Gravity load	Initial PT force ratio	PT strand ratio	ED bar ratio	Yield Strength of ED bar	Transverse volumetric reinforcing ratio
		f_c'	L/D	$P/f_c'A_g$	$f_{pu}A_{pt}$			$f_{y,ED}$	ρ_v
		MPa	–	%	%	%	%	MPa	%
Ou et al. [28, 29]	C0C	22	4.2	12.5	55	0.276	0	–	2.46
Ou et al. [28, 29]	C5C	55	4.2	5	47	0.276	0.5	434	2.46
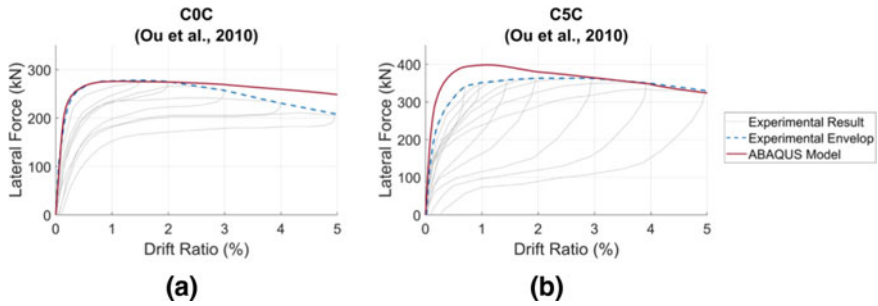
Fig. 2 Lateral force versus drift ratio for validated SPPC piers: **a** C0C and **b** C5C

Table 3 Summary of local damages with associated drift ratio for SPPC piers

Specimen	Damage	Experimental observation (%)	FE model result (%)
C0C [28, 29]	Concrete spalling	4	3.8
C5C [28, 29]	Concrete spalling	4	3.5
	ED bar fracture	5	5.4

the concrete spalling occurred at drift ratios of 3.8% and 3.5% in the FE model for specimens C0C and C5C, respectively, while experimental observation reported concrete spalling happened at a drift ratio of 4%. Both FE models and experiments showed that the spalling of concrete occurred at the bottom column segment near the rocking toe. In addition, for specimen C5C, the first ED fracture was recorded at a drift ratio of 5% during the experiment, and the FE analysis predicted ED fracture at 5.4% drift based on material strain limit. This difference might be due to fatigue failure of ED bar due to cyclic loading during the experiment test. Table 3 presents the drift ratios associated with the damages in the experiment and FE model simulation.

The developed FE model in this section was used to generate a database for the development of a regression model in a later section.

4 Drift Ratio Prediction Equation Development

This section describes in detail the implementation of MLR to develop four drift ratio prediction equations, corresponding to four damage limit states, for SPPC pier using a dataset generated from FE models.

Table 4 Summary of three-level value used in data generation

Design parameter	Post-tensioning strand ratio	Initial post-tensioning stress ratio	Aspect ratio	ED bar ratio	Gravity load ratio
	(%)	(%)	–	(%)	(%)
Level 1	0.31	35	3.84	0.22	2
Level 2	0.43	42.5	4.80	0.62	5
Level 3	0.59	50	5.76	1.58	8
Design parameter	Yield Strength of ED Bar	Transverse volumetric reinforcement ratio		Compressive Strength of concrete	
	(MPa)	(%)		(MPa)	
Level 1	280	1.47		30	
Level 2	350	2.05		50	
Level 3	420	2.64		70	

4.1 Data Generation

316 sample models were created using the developed FE model with different design parameter combinations. Table 4 presents three-level values for eight common design parameters for SPPC piers, namely PT strand ratio (A_{PT}/A_g), initial PT stress ratio (f_{ini}/f_u), the aspect ratio (L/D), ED bar ratio (A_{ED}/A_g), gravity load ratio ($P/A_g f_c'$), transverse volumetric reinforcing ratio (ρ_v), concrete compressive strength (f_c'), and yield strength of ED bar (f_y). The drift ratios associated with four damage states were documented based on the material strain limits proposed in the damage limit state section. The obtained drift ratio dataset will be used as input for MLR models.

4.2 Variable Normalization, Data Splitting, and Analysis Approach

Although MLR has proven its popularity in obtaining prediction equations, particular attention should be paid to the physical units when deriving mathematical equations. Such unawareness can lead to biased outputs. As a result, two input parameters, including concrete's compressive strength $\left(f_c'\right)$ and yield strength of ED bar $\left(f_y\right)$, were transformed into unitless input variables by dividing by reference values. The reference concrete strength was taken to be 30 MPa, corresponding to the minimum concrete strength for precast concrete per CSA A23.4-16 [10], and the reference yield strength of steel was taken as 400 MPa, corresponding to the yield strength of Grade 400R steel per CSA G30.18-21 [12].

To avoid overfitting, the developed drift ratio equations were validated using a set of unseen data. In this respect, the input dataset was split into training and testing
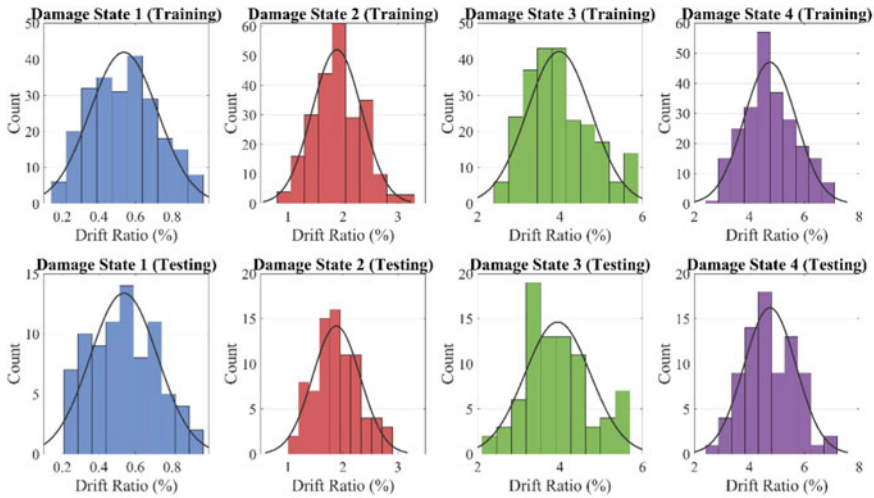
Fig. 3 Summary of split data for training and testing

subsets with ratios of 75% and 25%, respectively. Furthermore, the training and testing subsets were randomly selected four times, so that the output variable (drift ratio) follows the normal-like distribution, as shown in Fig. 3. This procedure is essential to guarantee critical samples at two tails of the distribution are presented in both training and testing subsets, hence enhancing the accuracy and generalization of the developed equations.

MLR is a regression technique commonly used by researchers to obtain a mathematical equation that predicts an output variable with multiple explanatory variables. The backward stepwise elimination technique was also used to eliminate the least significant variables in order to minimize the required computational demands while developing the predictive equations.

4.3 Performance Evaluation Measures and Validation Approach

In this study, the squared correlation coefficient (R^2) and normalized root-mean-square error (NRMSE) were chosen to evaluate the performance of developed drift ratio equations. R^2 indicates the linear correlation between observed and predicted values, while NRMSE measures the distance, which is also known as residual error. A perfect prediction model results in R^2 equal 1.0 and NRMSE equal 0 [9, 18]. Equations 1 and 2 present the mathematical expression of R^2 and NRMSE:

$$R^2 = \left[\frac{n\left(\sum_{i=1}^n y_i y_i'\right) - \left(\sum_{i=1}^n y_i\right)\left(\sum_{i=1}^n y_i'\right)}{\sqrt{n\sum_{i=1}^n y_i^2 - \left(\sum_{i=1}^n y_i\right)^2}\sqrt{n\sum_{i=1}^n y_i'^2 - \left(\sum_{i=1}^n y_i'\right)^2}} \right]^2 \quad (1)$$

$$\text{NRMSE} = \frac{\sqrt{\frac{1}{n}\sum_{i=1}^n \left(y_i - y_i'\right)^2}}{\overline{y}}, \quad (2)$$

where n = number of data samples; y = actual values; y' = predicted values; and $\overline{y}$ = mean of actual values.

In addition, the fitness function was also used for another layer of performance evaluation. The fitness function contains both R^2 and NRMSE to provide a powerful performance measure, which is capable of capturing both linear correlation and residual error [18]. A higher fitness value indicates a more accurate prediction model, with smaller NRMSE and larger R^2 values. Equation 3 presents the mathematical expression of the fitness function:

$$\text{Fitness} = \frac{1}{R^2} + \text{NRMSE} \quad (3)$$

4.4 Final Drift Ratio Prediction Equations

MLR analysis was conducted to obtain the simplified prediction equation for drift ratio limits, Eqs. 4 to 7, for damage states 1 to 4, respectively, when eight design parameters are considered.

$$\begin{aligned} DR = {}&-0.178 - 6.765PTR + 0.092AR + 20.479EDR \\ &- 0.406GLR - 0.064CSR + 0.279YSR \end{aligned} \quad (4)$$

$$\begin{aligned} DR = {}&1.125 - 85.182PTR - 0.679IPTSR + 0.204AR + 5.299EDR \\ &- 4.171GLR + 44.468TRR - 0.269CSR + 0.177YSR \end{aligned} \quad (5)$$

$$\begin{aligned} DR = {}&4.921 - 53.606PTR - 4.676IPTSR + 0.276AR - 13.688EDR \\ &- 7.223GLR + 58.621TRR - 0.450CSR \end{aligned} \quad (6)$$

$$\begin{aligned} DR = {}&5.311 - 135.452PTR - 3.242IPTSR + 0.282AR - 18.168EDR \\ &- 8.314GLR + 76.873TRR - 0.762CSR + 0.412YSR \end{aligned} \quad (7)$$

where DR = drift ratio (%); PTR = PT strand ratio; IPTSR = initial PT stress ratio; AR = aspect ratio; EDR = ED bar ratio; GLR = gravity load ratio; TRR =

transverse volumetric reinforcement ratio; CSR = concrete's compressive strength ratio; and YSR = ED bar's yield strength ratio.

5 Equation Performance Evaluation

The analysis result for the training data subset is presented in Fig. 4a and Table 5. From the NRMSE values, it is observed that the residual errors for all four damage states are relatively small. However, the R^2 values of damage states 1 and 2 are higher than the values of damage states 3 and 4. This indicates that the observed and predicted drift ratios are more correlated in damage states 1 and 2. As a result, damage states 3 and 4 have higher fitness values. Moreover, the predicted-to-actual drift ratios (DR_{MLR}/DR_{FEM}) were also calculated. The mean and median values of all four damage states are closed to 1.0 implying the MLR models have good predictions on the drift ratio limits. The maximum and minimum values illustrate the overprediction and underprediction of the MLR models. Damage state 1 has the greatest overprediction and underprediction values, indicating although the drift ratio prediction equation has good overall performance, it also has over- and underprediction issues in some specific cases.

The developed drift ratio prediction equations using MLR were validated against the unseen testing data subset. The analysis result is presented in Fig. 4b and Table 5. As expected, the performance values of the equations are slightly lower compared to the training data subset. However, by evaluating the developed equations using a dataset that the MLR models have not trained before, it can confirm that the drift ratio prediction equation for damage state 2 has the best performance among the four
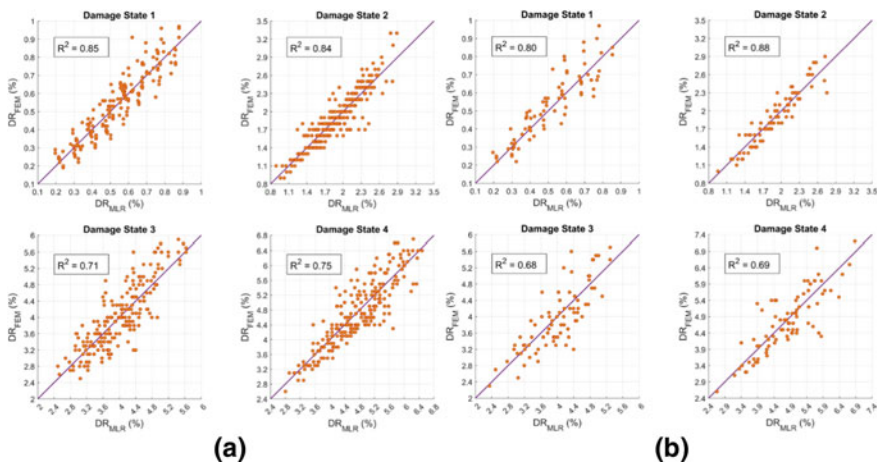
Fig. 4 Correlation between predicted values and FEM results for: **a** training set; **b** testing set for the four damage states using MLR model

Table 5 Performance evaluation on training and testing set for four damage states

Statistical indicator (DR_{MLR}/DR_{FEM})	DS1	DS2	DS3	DS4
Minimum	0.68 (0.72)	0.73 (0.82)	0.75 (0.78)	0.69 (0.73)
Maximum	1.47 (1.47)	1.39 (1.20)	1.37 (1.37)	1.33 (1.36)
Mean	1.02 (0.98)	1.01 (1.01)	1.01 (1.03)	1.01 (1.02)
Median	1.01 (0.97)	1.00 (1.01)	1.00 (1.02)	1.01 (1.03)
Standard deviation	0.15 (0.15)	0.10 (0.08)	0.11 (0.11)	0.09 (0.11)
COV	0.15 (0.15)	0.09 (0.08)	0.11 (0.11)	0.09 (0.11)
Performance evaluation measure	**DS1**	**DS2**	**DS3**	**DS4**
Accuracy (%)	88.44 (87.78)	92.94 (93.46)	91.51 (90.77)	92.76 (91.52)
R^2	0.85 (0.80)	0.84 (0.88)	0.71 (0.68)	0.75 (0.69)
NRMSE	0.13 (0.16)	0.09 (0.08)	0.11 (0.11)	0.10 (0.11)
$1/R^2 + \text{NRMSE}$	1.30 (1.40)	1.28 (1.22)	1.52 (1.58)	1.44 (1.55)

Note Values in parentheses indicate values for the testing subset

damage states. Damage state 2 has the greatest accuracy, R^2 value, and the lowest NRMSE, fitness value.

6 Sensitivity Analysis

To understand the impact of the design parameters on the variability of predicted drift ratio limits, sensitivity analysis was conducted using Eqs. 8 and 9 [16].

$$N_i = \text{DR}_{\max}(x_i) - \text{DR}_{\min}(x_i) \tag{8}$$

$$S_i = \frac{N_i}{\sum_{i=1}^{n} N_i} \times 100, \tag{9}$$

where N_i = difference between maximum and minimum of predicted drift ratio of ith input design parameter; S_i = sensitivity percentage of ith input design parameter; $\text{DR}_{\max}(x_i)$ and $\text{DR}_{\min}(x_i)$ are, respectively, the maximum and minimum of predicted drift ratio obtained from the ith input design parameter.

The sensitivity analysis result for the developed drift ratio equations is presented in Fig. 5. In damage state 1, ED bar ratio and aspect ratio have the greatest impact on the output drift ratio, while PT strand ratio has the least effect in determining drift ratio limit. Damage state 2 is mainly driven by volumetric transverse reinforcement ratio, aspect ratio, and concrete compressive strength. ED bar ratio and its yield strength have also a minimal effect only accounting for 3.6% and 3.1%. In damage state 3,
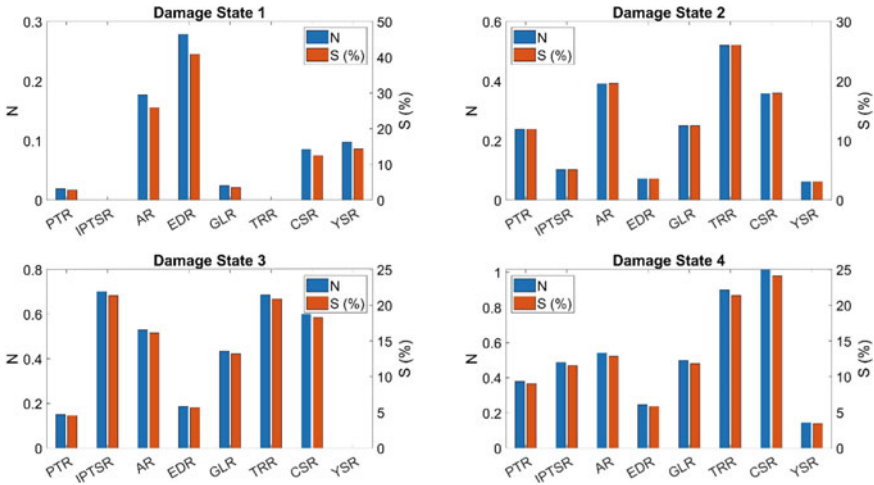
Fig. 5 Sensitivity analysis of input design parameters in developed drift ratio equations

the contributions of design parameters that were included in the prediction equation are quite even, except for the PT strand ratio and ED bar ratio. Concrete parameters, including concrete compressive strength and volumetric transverse reinforcement, are the main factors controlling the drift ratio of damage state 4. Except for the yield strength of the ED bar, all other design parameters have a moderate effect on the drift ratio, where their contributions are from 6 to 13%.

7　Conclusion and Future Work

The current study proposed a new set of damage criteria for SPPC piers that are associated with four damage states currently adopted in CSA S6. Next, 316 samples were generated using a FE model to serve as input data for MLR models. MLR was used to derive drift ratio limit prediction equations using a set of training data. Finally, the developed equations were validated against testing data to evaluate their performance, and sensitivity analyses were subsequently conducted to understand the impact of different design parameters on the predicted drift ratio limits. The main conclusions are as follows:

- The MLR-based drift ratio equations perform reasonably well in predicting the drift ratio limits for four damage states for the considered design parameter ranges.
- The sensitivity analysis shows that damage state 1 is driven by yielding of ED bar and damage states 2 and 4 are mainly affected by core concrete damage, while the damage of PT strand and core concrete define drift ratio limits for damage state 3.

- However, although MLR models show promising results in deriving the drift ratio limit prediction equations, it does not consider the interaction between the input variables. Therefore, other data-driven techniques are still recommended to improve the accuracy and generalization of the prediction equations.

References

1. ACI 318-19 (2019) Building code requirements for structural concrete (ACI 318-19). In: 318-19 building code requirements for structural concrete and commentary. American Concrete Institute. https://doi.org/10.14359/51716937
2. ASTM A615/A615-20 (2020) Standard specification for deformed and plain carbon-steel bars for concrete reinforcement. https://doi.org/10.1520/A0615_A0615M-20
3. Berry MP, Marc EO (2005) Practical performance model for bar buckling. J Struct Eng 131(6):946–955. https://doi.org/10.1061/(ASCE)0733-9445(2005)131
4. Billah AHMM, Alam MS (2016) Performance-based seismic design of shape memory alloy–reinforced concrete bridge piers. I: Development of performance-based damage states. J Struct Eng 142(12):04016140. https://doi.org/10.1061/(asce)st.1943-541x.0001458
5. Billah AHMM, Shahria Alam M (2016) Plastic hinge length of shape memory alloy (SMA) reinforced concrete bridge pier. Eng Struct 117:321–331. https://doi.org/10.1016/j.engstruct.2016.02.050
6. Caldwell PJ, Kennedy RP, Rojahn C, Hamburger RO, May PJ, Moehle JP, Phipps MT, Traw J, Holmes WT, Abrams DP, Beck DB, Berdine R, Borcherdt RD, Brothers J, Bruneau M, Dooley T, Ettouney M, Gillengerten J, Petak WJ et al (2004) ATC-58 project task report phase 2, Task 2.3 Engineering demand parameters for nonstructural components. www.ATCouncil.org
7. Caltrans (2016) Caltrans seismic design specifications for steel bridges. www.dot.ca.gov
8. Chou CC, Chang HJ, Hewes JT (2013) Two-plastic-hinge and two dimensional finite element models for post-tensioned precast concrete segmental bridge columns. Eng Struct 46:205–217. https://doi.org/10.1016/j.engstruct.2012.07.009
9. Chou J-S, Ngo N-T, Pham A-D (2016) Shear strength prediction in reinforced concrete deep beams using nature-inspired metaheuristic support vector regression. J Comput Civ Eng 30(1):04015002. https://doi.org/10.1061/(asce)cp.1943-5487.0000466
10. CSA.(2016) Precast concrete—materials and construction. Canadian Standards Association
11. CSA (2019. Canadian Highway Bridge Design Code. Canadian Standards Association
12. CSA (2021) Carbon steel bars for concrete reinforcement. Canadian Standards Association
13. Dassault Systèmes Simulia (2018) ABAQUS/Standard
14. Dawood H, ElGawady M, Cofer W (2011) Seismic behavior and design of segmental precast post-tensioned concrete pier (Issue 64)
15. FIB (2010) fib model code for concrete structures 2010. International Federation for Structural Concrete. https://doi.org/10.16309/j.cnki.issn.1007-1776.2003.03.004
16. Gandomi AH, Yun GJ, Alavi AH (2013) An evolutionary approach for modeling of shear strength of RC deep beams. Materials and Structures/Materiaux et Constructions 46(12):2109–2119. https://doi.org/10.1617/s11527-013-0039-z
17. Ghobarah A (2001) Performance-based design in earthquake engineering: state of development. In: Engineering structures, vol 23. www.elsevier.com/locate/engstruct

18. Gondia A, Ezzeldin M, El-Dakhakhni W (2020) Mechanics-guided genetic programming expression for shear-strength prediction of squat reinforced concrete walls with boundary elements. J Struct Eng 146(11):04020223. https://doi.org/10.1061/(asce)st.1943-541x.000 2734

19. Kim TH, Kim YJ, Kang HT, Shin HM (2007) Performance assessment of reinforced concrete bridge columns using a damage index. Can J Civ Eng 34(7):843–855. https://doi.org/10.1139/ L07-003

20. Kwan W-P, Billington SL (2003) Unbonded posttensioned concrete bridge piers. I: Monotonic and cyclic analyses. J Bridge Eng 8(2):92–101. https://doi.org/10.1061/(asce)1084-0702(200 3)8:2(92)

21. Lehman D, Moehle J, Mahin S, Calderone A, Henry L (2004) Experimental evaluation of the seismic performance of reinforced concrete bridge columns. J Struct Eng 130(6):869–879. https://doi.org/10.1061/(ASCE)0733-9445(2004)130

22. Luong CN, Yang C, Ezzeldin M (2023) Genetic programming–based drift ratio limit models for segmental posttensioned precast concrete piers. J Bridge Eng 28(2). https://doi.org/10.1061/ JBENF2.BEENG-5786

23. Mackie KR, Stojadinovic B (2007) Performance-based seismic bridge design for damage and loss limit states. Pacific Conf Earthq Eng 36(13):1953–1971. https://doi.org/10.1002/eqe

24. Mander JB (1983) Seismic design of bridge piers. University of Canterbury, New Zealand

25. Marsh ML, Stringer SJ (2013) Performance-based seismic bridge design (No. 400). Transportation Research Board

26. Moustapha M, Bourinet J-M, Guillaume B, Sudret B (2018) Comparative study of kriging and support vector regression for structural engineering applications. ASCE-ASME J Risk Uncertainty Eng Syst 4(2):10. https://doi.org/10.1061/ajrua6.0000950

27. NZT (2016) New Zealand bridge manual. Transit New Zealand

28. Ou YC, Wang PH, Tsai MS, Chang KC, Lee GC (2010) Large-scale experimental study of precast segmental unbonded posttensioned concrete bridge columns for seismic regions. J Struct Eng 136(3):255–264. https://doi.org/10.1061/(ASCE)ST.1943-541X.0000110

29. Ou Y-C, Tsai M-S, Chang K-C, Lee GC (2010) Cyclic behavior of precast segmental concrete bridge columns with high performance or conventional steel reinforcing bars as energy dissipation bars. Earthq Eng Struct Dyn 39:1181–1198. https://doi.org/10.1002/eqe.986

30. Popovics S (1973) A numerical approach to the complete stress-strain curve of concrete. Cement Concr Res 3(5):583–599. https://doi.org/10.1016/0008-8846(73)90096-3

31. Reza SM, Alam MS, Tesfamariam S (2014) Lateral load resistance of bridge piers under flexure and shear using factorial analysis. Eng Struct 59:821–835. https://doi.org/10.1016/j.engstruct. 2013.12.009

32. Sheikh MN, Tsang HH, McCarthy TJ, Lam NTK (2010) Yield curvature for seismic design of circular reinforced concrete columns. Mag Concr Res 62(10):741–748. https://doi.org/10. 1680/macr.2010.62.10.741

33. Wang Z, Wang J, Tang Y, Gao Y, Zhang J (2019) Lateral behavior of precast segmental UHPC bridge columns based on the equivalent plastic-hinge model. J Bridg Eng 24(3):04018124. https://doi.org/10.1061/(asce)be.1943-5592.0001332

34. Yang C (2019) Reducing earthquake-induced damage to precast concrete bridge piers. University at Buffalo, The State University of New York

35. Yang C, Okumus P (2017) Ultrahigh-performance concrete for posttensioned precast bridge piers for seismic resilience. J Struct Eng (United States) 143(12):1–13. https://doi.org/10.1061/ (ASCE)ST.1943-541X.0001906

36. Zhang Q, Alam MS (2020) Drift-based design criteria for reinforced concrete columns and hybrid rocking columns. In: IABSE-JSCE joint conference on advances in bridge engineering

Effect of Isolation Bearing Types on the Seismic Response of Base-Isolated Bridges Subjected to Mainshock-Aftershock Sequences

Vahid Aghaeidoost and A. H. M. Muntasir Billah

Abstract One of the most critical infrastructures of the transportation systems is highway bridges. Damaged bridges during a seismic event cause a crisis and irreparable losses on the transportation networks. Therefore, performance assessment of damaged bridges is a crucial part of post-earthquake response and recovery. Furthermore, aftershocks can further disrupt the performance of bridges due to their high rate of occurrence over a period of time after the mainshocks and bridges' structural integrity due to their reduced bearing capacity in the mainshocks. Efficient seismic protection systems should be used to reduce economic losses and casualties during seismic and post-seismic events. One of the most effective seismic protection systems is the base-isolation system. Therefore, assessing the vulnerability of base-isolated bridges equipped with various types of isolation bearings subjected to sequential mainshock-aftershocks is crucial for an efficient assessment of bridge performance. Therefore, two widely used seismic isolation systems, lead rubber bearings and friction pendulum bearings, have been used in this study to evaluate the performance of base-isolated bridges. This study investigates the effect of isolation system types on the seismic performance of bridges considering curved reinforced concrete bridges. Seismic vulnerability models of the bridges have been developed through finite element analysis under a sequence of mainshock-aftershocks. The comparison between lead rubber bearing and friction pendulum bearing isolation systems of bridges reveals that the friction pendulum bearing isolated bridge is more vulnerable under both mainshock-only and mainshock-aftershock sequences.

Keywords Isolation bearing types · Seismic response · Base-isolated bridges

V. Aghaeidoost (✉) · A. H. M. M. Billah
Department of Civil Engineering, Lakehead University, Thunder Bay, Canada
e-mail: vaghaei@lakeheadu.ca

1 Introduction

Bridges are an integral part of transportation infrastructure, and the mobility of emergency responders is highly dependent on the functionality of the transportation network during a seismic event. The post-earthquake response and recovery process depend on evaluating the damaged bridges' structural integrity and functionality after seismic events. Since aftershocks typically occur within a short period after the mainshock, they could complicate the effort to restore functionally of damaged bridges and, in addition, damage their structural integrity once the mainshock reduces their load-carrying capacities. In many cases, an earthquake is followed by several aftershocks, which can be severe and cause more damage to the bridge and increase their seismic demand.

HAZUS [11] classifies the bridge seismic damage based on their ability to operate after the seismic event as slight, moderate, extensive, and complete damage states. To evaluate a bridge's seismic vulnerability based on the damage level under various ground motions, fragility curves must be developed [1]. Therefore, the precise assessment of highway bridges under sequential seismic events is crucial.

It has become increasingly popular to evaluate how bridges perform after being exposed to multiple sequences of mainshock-aftershock [1, 8]. Research on mainshock-aftershock effects on the seismic performance of base-isolated bridges is limited. Previous studies found that aftershocks would make highway bridges significantly more vulnerable [8, 12]. Although these studies developed fragility curves for irregular bridges, for example, skewed bridges were found to be more vulnerable to earthquake damage than straight bridges [15]. Despite this, there is no research on the seismic assessment of curved base-isolated bridge equipped with different isolation systems subjected to mainshock-aftershock sequences. Moreover, the different isolation systems in the isolated bridge significantly affect the bridge damage level. As part of the seismic protection of bridges, lead rubber bearings (LRBs) and friction pendulum bearings (FPBs) are among the most popular isolation systems. There have been many experimental and numerical studies [9] that illustrate the effectiveness of these two isolation systems. However, the seismic vulnerability of base-isolated bridges under the mainshock-aftershock seismic sequence is a gap in the current literature.

This study compares the LRB and FPB isolated multi-span curved bridge fragility curves under mainshock-only and mainshock-aftershock sequences. The fragility curves based on the cloud method are developed for base-isolated curved bridges subjected to mainshocks-aftershocks considering different component demand parameters. The outcomes of this study will help practitioners in selecting suitable isolation systems for bridges susceptible to mainshock-aftershock ground motions.

2 Methodology

A seismic assessment of isolated bridges equipped with different isolation systems is performed using damage state-dependent fragility analysis. Figure 1 presents the framework used for the seismic assessment of a bridge using fragility curves subjected to mainshock-aftershock sequences. The mainshock fragility curves are developed by performing the incremental dynamic analysis (IDA) using the mainshock records, while the aftershock fragility curves are developed by performing IDA on the mainshock damaged bridge. The seismic demand resulting from different suits of mainshock-aftershock ground motions, and the corresponding damage exceedance probability is investigated through fragility curves developed using IDA results.

Billah and Alam [6] performed an in-depth evaluation of various bridge seismic vulnerability assessment approaches. Seismic fragility models estimate the conditional probability of damage state (DS) exceedance given the occurrence of a seismic event with a specific intensity measure level IM $= y$, as indicated by:

$$\text{Fragility}_{\text{DS}}(y) = P[\text{DM} \geq \text{DS}|\text{IM} = y] \tag{1}$$

To decrease the computational cost [4], the probabilistic seismic demand model (PSDM) using the scaling approach [3] is used to establish the correlation between parameters which is obtained from IDA (engineering demand parameter (EDP) and intensity measure (IM)). In this method, a nonlinear time history analysis is performed
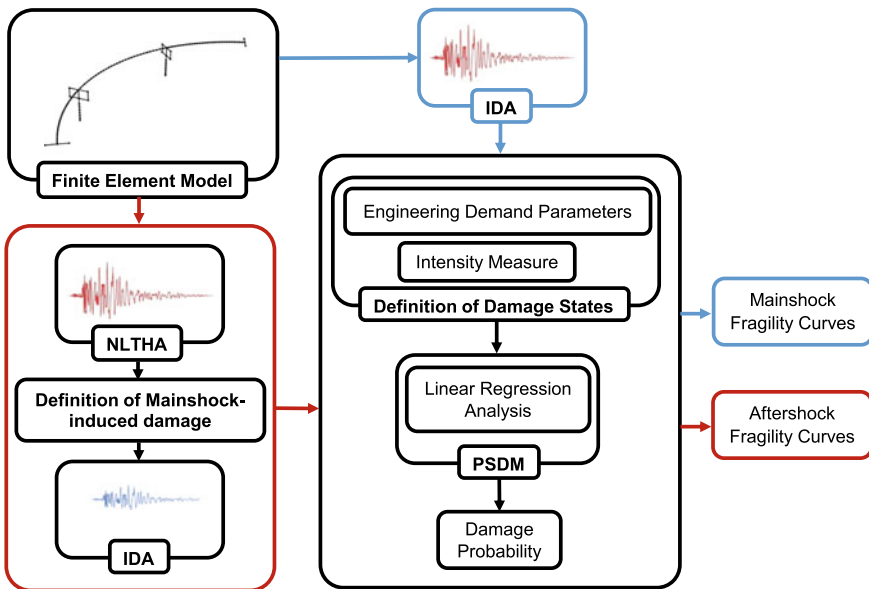
Fig. 1 Methodology flow diagram

for each distinct scaling factor for each ground motion record scaled from low to high IM values to extract sufficient IM-EDP pairs for establishing PSDMs and developing fragility curves. Isolation systems shear strain and pier displacement ductility are nominated as the EDPs. Also, spectral acceleration (S_a) is utilized as the IM. The EDP and IM are correlated in a log-transformed space to define the demand model:

$$\ln(\text{EDP}) = \ln(a) + b \ln(\text{IM}) \tag{2}$$

The regression coefficients are defined as a and b. The demand dispersion $\beta_{D|IM}$ is estimated by:

$$\beta_{\text{EDP|IM}} = \sqrt{\frac{\sum_{i=1}^{N}\left(\left(\ln(\text{EDP}) - \ln\left(a\text{IM}^b\right)\right)^2\right)}{N-2}} \tag{3}$$

The number of numerical simulations is defined as N. The following conditional probability is used to generate fragility curves:

$$P[\text{DS|IM}] = \phi\left[\frac{\ln(\text{IM}) - \ln(\text{IM}_n)}{\beta_{\text{comp}}}\right] \tag{4}$$

The median value of the IMs for the specific damage states, the dispersion component, and the standard normal cumulative distribution function is indicated by $\text{IM}_{n,}$ β_{comp} and $\phi[.]$, respectively. The following equations represent them:

$$\ln(\text{IM}_n) = \frac{\ln(S_c) - \ln(a)}{b} \tag{5}$$

$$\beta_{\text{comp}} = \frac{\sqrt{\beta_{\text{EDP|IM}}^2 + \beta_c^2}}{b}, \tag{6}$$

where β_c and S_c are the dispersion and median values for a specific damage state of each component.

$$\beta_c = \sqrt{\ln\left(1 + \text{COV}^2\right)} \tag{7}$$

According to Nielson [14], the coefficient of variation (COV) is assumed to be 0.25 and 0.5 for slight, moderate damage states and extensive, complete damage states, respectively.

The system-level fragility analysis is calculated as follows:

$$\max_{i=1}^{n}[P(F_i)] \leq P\left(F_{\text{system}}\right) \leq 1 - \prod_{i=1}^{n}[1 - P(F_i)] \tag{8}$$

Table 1 Damage states of bridge components [2]

Bridge components	Demand parameter	Damage state			
		Slight	Moderate	Extensive	Complete
System-level	Physical phenomenon	Cracking and spalling	Moderate cracking and spalling	Degradation without collapse	Failure leading to collapse
Bridge pier	Displacement ductility μ_d	$\mu_d > 1.0$	$\mu_d > 1.2$	$\mu_d > 1.76$	$\mu_d > 4.76$
Isolation bearing	Shear strain γ (%)	$\gamma > 100$	$\gamma > 150$	$\gamma > 200$	$\gamma > 250$

The $P(F_i)$ and $P(F_{\text{system}})$ are the component and system-level probability of exceedance, respectively.

A PSDM and limit state model are also used to develop fragility curves for isolated bridges under aftershock events. Nonetheless, the conditional likelihood of damage is described by mainshock fragility curves based on the mainshock intensity. The fragility curve of aftershock is developed as a conditional probability based on the intensity measure of the aftershock and the initial damage state corresponding to the mainshock record. Aftershock fragility of isolated bridges is developed according to mainshock fragility curves (Eqs. (1) and (8)).

Capacity models of structural components must be defined to assess seismic fragility. These capacities are determined by the expected component damage and the post-event service level for highway bridges. The HAZUS [11] damage levels are used in this study (slight, moderate, extensive, and complete). Also, two different EDPs, pier displacement ductility and isolation Bearing's shear strain, are examined to develop the fragility curves [2]. The qualitative and quantitative capacity limits for different demand parameters used in this study are listed in Table 1.

3 Bridge Description and Finite Element Modelling

This study considers a curved three-span composite steel I-girder isolated bridge to evaluate base-isolated bridges' seismic fragility (Fig. 2). The curved bridge's configuration and characteristics and more details about the design and geometric details can be found in Monzon [13]. Based on the superstructure loads and forces, FPBs are designed to achieve an isolation period similar to the isolation period of the LRB isolated bridge. The isolation period of the LRB and FPB isolated bridges are 0.68 s and 0.67 s, respectively. The superstructure consists of three steel girders with a spacing of 1.37 m topped with an 83 mm concrete slab. The centreline radius, width, and lengths of the spans are 24.4 m, 3.66 m, 12.8 m, 18.6 m, and 12.8 m, respectively, with a total length of 44.2 m. The diameter and height of columns are assumed to be 0.61 m and 2.44 m, respectively. The detailed numerical model and dimension

of the bridge are shown in Fig. 2. A706 steel rebar is used to reinforce the mono-column piers, having a yield strength of 490 MPa, a steel ratio of 1% longitudinally and transversely, and a concrete compression strength of 44 MPa. The total weight of the bridge is 1486 kN which is distributed along with the longitudinal nodes of the deck. In order to verify the accuracy of the numerical model, experimental results of the scaled base-isolated bridge equipped with LRB under the 1940 Imperial Valley earthquake at the Sylmar station are used [13] as shown in Fig. 2. The result shows reasonable accuracy with only a 9% error in terms of energy dissipation. The numerical simulation is conducted using OpenSees, where concrete07 and steel02 represent the confined and unconfined behaviour of concrete and the behaviour of reinforcement, respectively. The superstructure is considered as an elastic element, and the piers and isolation bearing systems (LeadRubberX and singleFPBearing elements in OpenSees) are modelled using nonlinear beam-column elements and link elements respectively. The details of the finite element model of various bridge components are presented in Fig. 2.
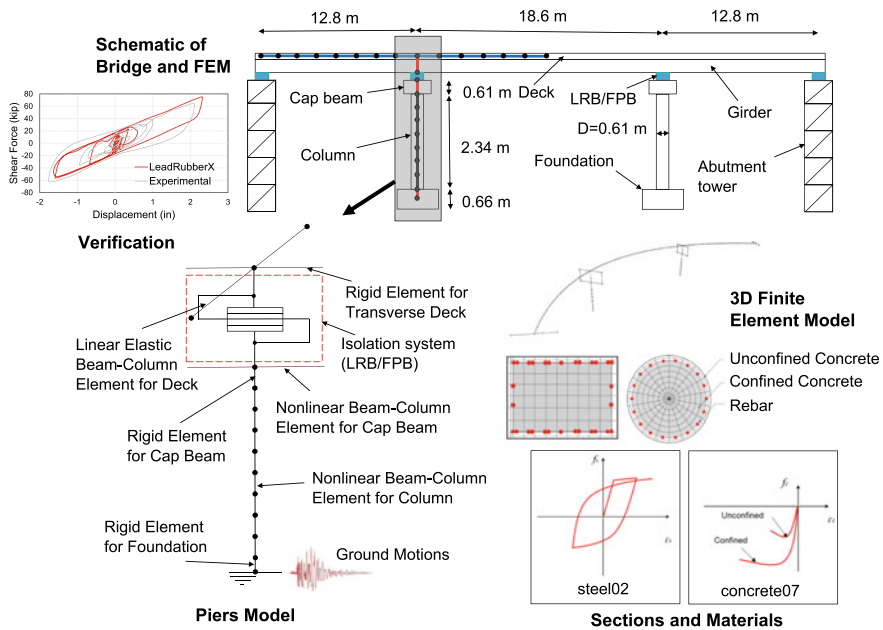
Fig. 2 Geometry of the isolated curved bridge and finite element model schematic representation

4 Sequential Ground Motions Selection

The ground motions are selected according to the bridge location (soil class C in Vancouver, British Columbia, Canada) to generate the seismic fragility curves. Cascadia subduction events with shallow crustal, sub-crustal, and mega-thrust characteristics have various ground motion characteristics due to the various paths and sources and are essential for the seismicity of Vancouver [10]. Therefore, to estimate the corresponding seismic hazard of Vancouver for interface, in-slab, and crustal earthquake scenarios, a conditional mean spectrum (CMS) is developed. CMS for three different seismic sources is developed following the procedure suggested by Baker et al. [5]. For this study, 30 ground motion suites are selected as presented in Table 2.

5 Results and Discussion

In this study, to assess the seismic performance of LRB and FPB isolated bridges subjected to mainshock-aftershock records, the seismic fragility curves are generated based on the data obtained from IDA. Pier displacement ductility and isolation bearing's shear strain are considered as the EDP, and spectral acceleration (S_a) is considered as the IM. EDP-IM relationship is modelled using linear regression to determine slope, intercept, and dispersion. Two sample PSDMs are shown in Fig. 3. The mainshock fragility curves for the LRB and FPB isolation bearing systems are developed, as shown in Fig. 4. Due to space limitations, the component fragility curves for the piers and isolation bearings are not presented here. Comparing the vulnerability of the LRB and FPB isolated bridges revealed that the isolated bridge equipped with FPB isolation system is more vulnerable along with the slight, moderate, extensive, and complete damage states. These differences between two isolation systems in slight and moderate damage states are less than in the extensive and complete damage states. The likelihood of damage in the FPB isolation system is significantly higher than in the LRB isolation system, along with the four damage states. The probability of damage in the LRB isolated bridge is less than in the FPB isolated bridge. The probability of damages calculated for the LRB isolated bridge at S_a corresponding to the 1.0g is 34% for slight and 5% for moderate damage states, while those calculated for the FPB isolated bridge are 68% and 24%, respectively. The difference in the likelihood of damage is also more evident in moderate, extensive, and complete damage states than in slight damage for system level.

IDA is also performed for mainshock damaged isolated bridges using sequential mainshock-aftershock records. While the intensity of the mainshock is constant and unchanged, the aftershock record is scaled from low to high until the bridge collapses. Different scenarios for damage accumulation during the mainshock event are investigated to evaluate the influence of the aftershocks. This study considers the following mainshock-induced damage corresponding to Table 1: intact (DS0), slight

Table 2 Selected mainshock-aftershock ground motion records [7]

Event ID	RSN	No	Seismic event				PGA (g)
			M	Type	Name	Source	
127	953	1	6.69	Crustal	Northridge	PEER	0.46
138	1602	2	7.14	Crustal	Duzce, Turkey	PEER	0.72
158	1787	3	7.16	Crustal	Hector mine	PEER	0.31
50	169	4	6.53	Crustal	Imperial Valley	PEER	0.28
136	1158	5	7.51	Crustal	Kocaeli, Turkey	PEER	0.30
125	900	6	7.28	Crustal	Landers	PEER	0.21
118	752	7	6.93	Crustal	Loma Prieta	PEER	0.48
144	1633	8	7.37	Crustal	Manjil, Iran	PEER	0.52
137	1485	9	7.62	Crustal	Chi Chi, Taiwan	PEER	0.47
129	1106	10	6.90	Crustal	Kobe, Japan	PEER	0.71
368	27,538	11	6.80	In-slab	Tohoku, Japan	K-KIK	0.85
368	27,451	12	6.80	In-slab	Tohoku, Japan	K-KIK	0.48
368	27,454	13	6.80	In-slab	Tohoku, Japan	K-KIK	0.48
184	9813	14	7.00	In-slab	Tohoku, Japan	K-KIK	0.75
184	9837	15	7.00	In-slab	Tohoku, Japan	K-KIK	0.72
184	9831	16	7.00	In-slab	Tohoku, Japan	K-KIK	0.58
294	20,480	17	6.00	In-slab	Tohoku, Japan	K-KIK	0.15
285	19,650	18	6.20	In-slab	Tohoku, Japan	K-KIK	0.14
148	6306	19	6.80	In-slab	Tokachi-oki, Japan	K-KIK	0.41
141	6267	20	6.80	In-slab	Tokachi-oki, Japan	K-KIK	0.39
276	19,085	21	7.00	Interface	Tokachi-oki, Japan	K-KIK	0.66
276	19,004	22	7.00	Interface	Tokachi-oki, Japan	K-KIK	0.34
194	11,026	23	7.90	Interface	Tokachi-oki, Japan	K-KIK	0.56
194	11,025	24	7.90	Interface	Tokachi-oki, Japan	K-KIK	0.38
301	21,598	25	7.10	Interface	Tokachi-oki, Japan	K-KIK	0.38
–	169	26	9.00	Interface	Tohoku, Japan	K-KIK	1.75
–	175	27	9.00	Interface	Tohoku, Japan	K-KIK	0.96
–	237	28	9.00	Interface	Tohoku, Japan	K-KIK	0.90
–	323	29	9.00	Interface	Tohoku, Japan	K-KIK	0.67
–	168	30	9.00	Interface	Tohoku, Japan	K-KIK	0.62

(DS1), moderate (DS2), extensive (DS3), and complete (DS4) damage. The IDA has been performed for each pair of aftershock records, and EDPs were monitored. To develop a PSDM for each isolated bridge, a lognormal distribution of seismic demand is taken into account. The fragility curves of aftershocks are derived using PSDMs and damage states. The fragility curves of aftershock for LRB and FPB isolated bridges considering five different initial damage states are presented in Fig. 5.
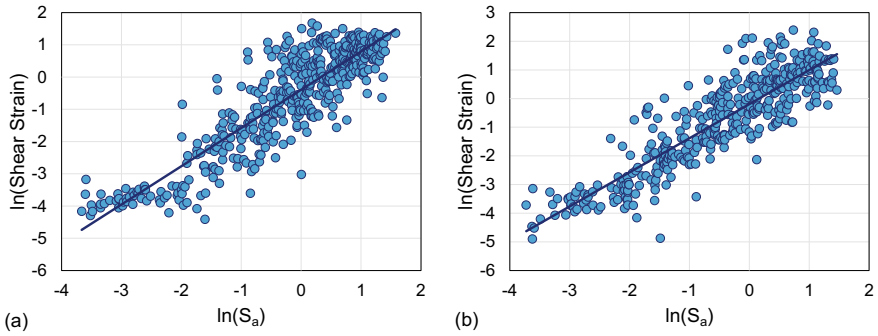
Fig. 3 PSDMs for pier bearing of **a** LRB and **b** FPB isolated bridges
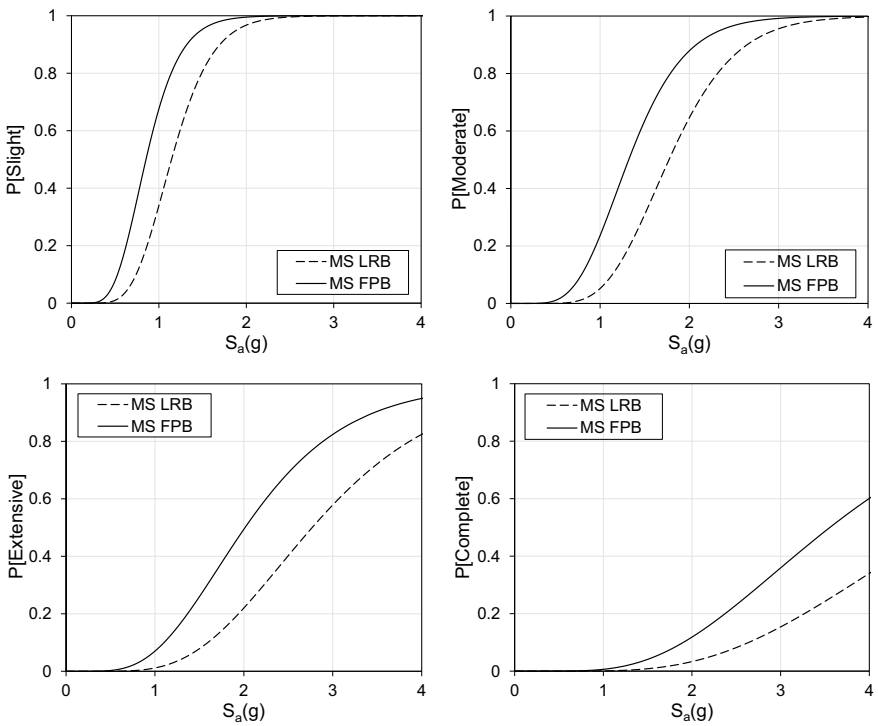
Fig. 4 Mainshock fragility curves for slight, moderate, extensive, and complete damage states of LRB and FPB isolated bridges

The aftershock fragility curves show the increased vulnerability of bridges because of the damages accumulated during the mainshock events. The fragility curves of aftershock take on a steeper slope for LRB and FPB isolated bridges, as shown in Fig. 5. For example, the comparison of intact (DS0) and damaged (DS4) LRB isolated
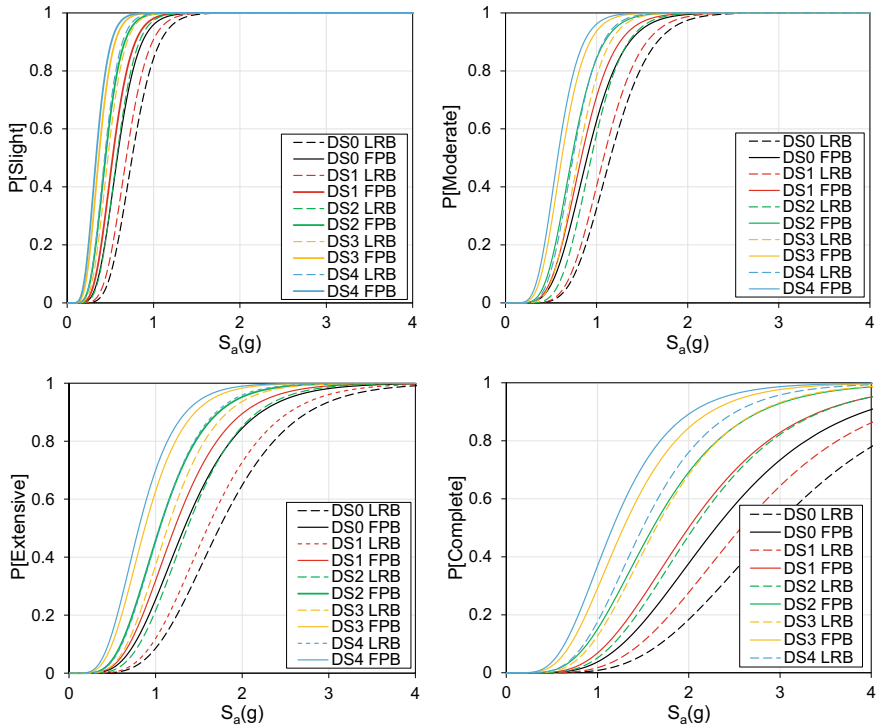
Fig. 5 Aftershock fragility curves for FPB and LRB isolated bridges for slight, moderate, extensive, and complete damage states

bridge fragility curves at S_a corresponding to 1.0g of aftershock motions reveals a 37% increased likelihood of damage for extensive damage state, which is 45% for FPB isolated bridge. The fragility curves of aftershock for a mainshock damaged bridge for a specific IM have more likelihood of damage resulting in increased vulnerability of bridge subjected to sequential ground motions. The increased vulnerability for different initial damage scenarios (DS0, DS1, DS2, DS3, and DS4) is higher in LRB isolated bridges than FPB isolated bridges. This may be due to the strength degradation of the lead core due to heating under the repetitive cycle of sequential ground motions. The aftershock fragility curves illustrate that the LRB isolated bridge is less vulnerable to aftershock as compared to FPB isolated bridge. The probability of collapse when exposed to only aftershocks (DS0) for LRB and FPB isolated bridges at S_a corresponding to 1.0g for extensive damage state is 9% and 26%, respectively. LRB and FPB isolated bridges with moderate mainshock damage (DS2) have a 58% and 84% probability of damage when subjected to aftershock, respectively.

6 Conclusion

The fragility curves are developed for two isolated bridges equipped with lead rubber bearing and friction pendulum bearing in this paper. The sequential mainshock-aftershock earthquakes are sourced from the sub-crustal, crustal, and subduction zone events. The mainshock-only and mainshock-aftershock PSDMs are derived considering the spectral acceleration as IM and pier displacement ductility, and the isolation bearing's shear strain as EDPs. The PSDMs showed that the greater the initial damage sustained by a bridge, the greater the seismic demand during subsequent earthquakes. Moreover, the PSDMs of aftershocks, as well as limit states, are utilized to generate and compare fragility curves of aftershocks based on different initial damage states. It reveals that when the bridge is subjected to similar aftershock records, the seismic demand is increased when the initial damage to a bridge is greater. The following conclusions could be drawn from comparing fragility curves for the LRB and FPB isolated bridge:

– Because of the previous mainshock damage to bridges, LRB and FPB isolated bridges are more vulnerable during aftershocks than the mainshocks.
– Aftershock vulnerability is influenced by the level of damage caused by mainshock events. When mainshock damage accumulation increases, the likelihood of damage rises subjected to aftershocks.
– In both mainshock-only and mainshock-aftershock sequences, the FPB isolated bridge is more prone to collapse.
– The increased vulnerability for mainshock damage scenarios is higher in LRB isolated bridges because of the strength degradation of the lead core due to heating subjected to the mainshock-aftershock sequence.

References

1. Abdelnaby AE (2018) Fragility curves for RC frames subjected to tohoku mainshock-aftershocks sequences. J Earthquake Eng 22(5):902–920. https://doi.org/10.1080/13632469.2016.1264328
2. Aghaeidoost V, Billah AM (2021) Effect of lead rubber bearing (LRB) modeling technique on the seismic response of base-isolated bridges. Eccomas Proceedia, 3930–3941. https://doi.org/10.7712/120121.8757.18899
3. Alam MS, Bhuiyan MAR, Billah AHMM (2012) Seismic fragility assessment of SMA-bar restrained multi-span continuous highway bridge isolated by different laminated rubber bearings in medium to strong seismic risk zones. Bull Earthq Eng 10(6):1885–1909. https://doi.org/10.1007/s10518-012-9381-8
4. Bakalis K, Vamvatsikos D (2018) Seismic fragility functions via nonlinear response history analysis. J Struct Eng 144(10):04018181. https://doi.org/10.1061/(ASCE)ST.1943-541X.0002141

5. Baker JW (2011) Conditional mean spectrum: tool for ground-motion selection. J Struct Eng 137(3):322–331. https://doi.org/10.1061/(ASCE)ST.1943-541X.0000215

6. Billah AHMM, Alam MS (2015) Seismic fragility assessment of highway bridges: a state-of-the-art review. Struct Infrastruct Eng 11(6):804–832. https://doi.org/10.1080/15732479.2014.912243

7. Billah AHMM, Todorov B (2020) Mainshock-Aftershock damage assessment of concrete bridge reinforced with shape memory alloy rebar. 17WCEE, 2d-0051-1–11

8. Dong Y, Frangopol DM (2015) Risk and resilience assessment of bridges under mainshock and aftershocks incorporating uncertainties. Eng Struct 83:198–208. https://doi.org/10.1016/j.engstruct.2014.10.050

9. Eröz M, DesRoches R (2013) A comparative assessment of sliding and elastomeric seismic isolation in a typical multi-span bridge. J Earthquake Eng 17(5):637–657. https://doi.org/10.1080/13632469.2013.771589

10. Goda K, Atkinson GM (2011) Seismic performance of wood-frame houses in south-western British Columbia. Earthquake Eng Struct Dynam 40(8):903–924. https://doi.org/10.1002/eqe.1068

11. Hazus MH (2011) Multi-hazard loss estimation methodology: earthquake model hazus-MH MR5 technical manual. Federal Emergency Management Agency, Washington, DC, USA

12. Kumar R, Gardoni P (2014) Effect of seismic degradation on the fragility of reinforced concrete bridges. Eng Struct 79:267–275. https://doi.org/10.1016/j.engstruct.2014.08.019

13. Monzon EV (2013) Seismic performance of curved steel plate girder bridges with seismic isolation. https://scholarworks.unr.edu//handle/11714/3004

14. Nielson BG (2005) Analytical fragility curves for highway bridges in moderate seismic zones [Georgia Institute of Technology]. https://smartech.gatech.edu/handle/1853/7542

15. Zakeri B, Padgett JE, Ghodrati Amiri G (2015) Fragility assessment for seismically retrofitted skewed reinforced concrete box girder bridges. J Perform Constr Facil 29(2):04014043. https://doi.org/10.1061/(ASCE)CF.1943-5509.0000502

A Spatial Assessment of Corrosion Initiation Risks of Bridge Decks Across North America

M. Xu, Y. Liu, and C. Yang

Abstract The temperature and humidity are recognized as the major environmental drivers that increase corrosion risks of reinforced concrete (RC) bridge decks under chloride ingress. The report released by the Intergovernmental Panel on Climate Change (IPCC) in 2021 sounded an alarm again on the 'irreversible' climate change impact. This study conducts a holistic spatial assessment of corrosion-induced damage risks for RC bridge decks across North America. The areas with cold winter, where chlorides come from de-icing salts, were classified into 16 climate regions. For each region, 30 representative bridge locations were selected to perform a spatial time-dependent reliability analysis to quantify corrosion damage risks of RC bridge decks under both historical and future climate scenarios. The analysis results formed a data collection for training artificial neural network (ANN) models, which were subsequently incorporated with the coordinated regional climate change projection to unveil the relationship between climate data and the concerned corrosion damage index for bridge decks across North America. Finally, a series of corrosion risk maps were generated to reveal the spatial patterns of corrosion initiation risks. The likelihood of corrosion initiation of bridge decks by 2100 varied considerably by region, from nearly 0% for the northern areas to 92.1% for the south. In general, the decks in northern regions were more strongly impacted by climate change than those in southern regions due to the more notable change in climate conditions. The outcomes will assist transportation agencies to make informed decisions for bridge management with consideration of future climates.

Keywords Corrosion · Bridge decks · North America

M. Xu (✉) · C. Yang
Department of Civil Engineering, McMaster University, Hamilton, ON L8S 4L7, Canada
e-mail: xum94@mcmaster.ca

Y. Liu
Ministry of Transportation, London, ON, Canada

1 Introduction

The report released by the Intergovernmental Panel on Climate Change (IPCC) in 2021 made it clear that the climate change impact is 'irreversible' [1]. Climate change can accelerate structural deterioration, creating additional risks for the serviceability and safety of highway bridges. Among different ageing issues, chloride-induced corrosion is the major threat to RC bridges in Canada due to the extensive use of de-icing salts in winter. Climate change is expected to alter the environmental factors that are known to influence the chloride-induced corrosion process, further compromising the durability of RC bridges [3].

To develop and facilitate effective adaptation strategies to counteract the adverse climate change impact, it's required to first quantify to what extent the performance of bridges will be affected by climate change. The commonly used method to evaluate the climate change impact on structure deterioration is to factor climatic conditions (mainly temperature and relative humidity) into deterioration models and compare the predicted service life of bridges under different climate scenarios. For example, Bastidas-Arteaga et al. [3] investigated the effects of climate change on the durability of an RC bridge girder by utilizing a series of mechanistic-based models which can take into account the change in temperature, relative humidity and carbon dioxide concentrations due to global warming. The results showed that global warming can cause up to 31% reduction in the time to failure for moderate levels of aggressiveness. Shirkhani et al. [23] analysed the interaction between climate change-induced increase in temperature and the onset of corrosion of RC decks in seven different Canadian cities by using a Fickian diffusion model. The results indicated that the increase in temperature projected from global climate models can reduce the time to the onset of corrosion of ordinary Portland cement concrete bridge decks, on average, by 33%. The analysis also illustrated the regional variations in the climate change impacts. Guest et al. [10] also adopted mechanistic-empirical deterioration models to incorporate the effects of climate change on the durability of bridge decks across five major cities in Canada. It was found that a nonstationary climate could significantly affect the service life of a bridge deck.

Previous studies indicate that it's applicable to use deterioration models that incorporate climate data as inputs to estimate the climate change impacts on the deterioration of bridge structures. However, such an approach is only suitable for assessing a particular city or a few cities, as it will become inefficient when dealing with tens of thousands of climatic conditions for assessment at the provincial scale or the national scale. The abovementioned studies have proven that the extent to which the corrosion-induced damage of RC bridges is affected by climate change varies between different locations due to different weather and exposure conditions. As such, it is necessary to extend the assessment to a larger scale to understand the spatial patterns of climate change impacts.

To this end, this study proposes the use of a machine learning-based approach to carry out the spatial assessment of corrosion-induced RC deck deterioration risks due to its great efficiency. By reviewing the literature, it's believed that this study

makes the first attempt to conduct a holistic spatial assessment of RC deck deterioration across North America. To be specific, artificial neural networks (ANNs) were selected to serve as the functional mapping tool between the climate data and the concerned deterioration condition index for bridge decks. The training and testing datasets required for the development of ANNs were generated by a probabilistic assessment framework for corrosion-induced serviceability risks for RC decks which combined mechanistic models, random field analysis and Monte Carlo simulation. The developed ANN models were incorporated with the coordinated regional climate change projection to assess the corrosion risks for bridge decks across North America. The results were mapped out by generating a series of 'corrosion hazard maps' at a regional scale (grid size = 50×50 km^2) to visualize the spatial patterns of deck deterioration rates. These maps can potentially contribute to the formulation of region-based climate change adaptation solutions.

2 Probabilistic Modelling of Corrosion-Induced Serviceability Risks of RC Bridge Decks

A hierarchical two-level framework was developed to estimate the corrosion-induced damage severity and extent over the deck. First, a mechanistic model at the local deck element level was used to simulate the deterioration process as a function of material/structural properties and environmental parameters. Corrosion due to chloride ingress can be characterized by three key phases: 'corrosion initiation', 'crack initiation' and 'crack propagation' [18]. The time to corrosion initiation is determined as the time it takes for the chloride concentration near steel bars to reach a critical threshold value, after which an electrochemical reaction starts, followed by a reduction in bar diameter, formation of rust and cracking. Since the corrosion initiation stage typically accounts for the largest proportion of the entire corrosion process, this study only focuses on the modelling and prediction of the corrosion initiation stage. Fick's second law of diffusion was used to describe chloride ingress based on the assumption that ionic diffusion is the dominant transport process of chloride into concrete. The chloride diffusion coefficient D was determined as the multiplication of the reference diffusion coefficient (D_{ref}) and a series of modification factors, as shown in Eq. 1. The reference diffusion coefficient (D_{ref}) was obtained for a given environmental condition (i.e. temperature and humidity) [8] (Eq. 2). The modification factors $f(T)$, $f(h)$ and $f(t)$ were set to account for the effects of temperature, relative humidity and concrete age, respectively, and their mathematical expressions are presented in Eqs. 3 to 6 [15, 21, 25].

$$D = D_{\text{ref}} f(T) f(h) f(t) \tag{1}$$

$$D_{\text{ref}} = 10^{(-12.06+2.4*w/c)} \tag{2}$$

$$f(T) = \exp\left[\frac{E}{R}\left(\frac{1}{T_{\text{ref}}} - \frac{1}{T}\right)\right] \tag{3}$$

$$f(h) = 1 \left/ \left[1 + \left(\frac{1-h}{1-h_c}\right)^4\right]\right. \tag{4}$$

$$f(t) = \left(\frac{t_{\text{ref}}}{t}\right)^m \text{ when } t \leq t_{\text{lim}} \text{ years} \tag{5}$$

$$f(t) = \left(\frac{t_{\text{ref}}}{t_{\text{lim}}}\right)^m \text{ when } t > t_{\text{lim}} \text{ years,} \tag{6}$$

where w/c is the water–cement ratio of concrete; E is the activation energy for the diffusion process (KJ/mol); R is the gas constant (8.314 J/mol K); T_{ref} and t_{ref} are the reference temperature (293 K) and the reference time (28 days) at which the reference diffusion coefficient D_{ref} has been evaluated, respectively; h_c is critical humidity (0.75); $m = 0.2$ and t_{lim} is 30 years.

The results obtained from the element were then implemented into a global-level two-dimensional spatial time-dependent reliability method to estimate the corrosion-induced damage severity and extent over the deck. This global-level prediction was based on random field analysis and MCS to model the random spatial variability of deck material and design parameters. As a result, the deterioration condition of a bridge deck can be expressively illustrated as the proportion of surface subject to corrosion initiation.

Concrete cover and exposure conditions typically vary spatially over an RC deck due to many influential factors including material properties, workmanship as well as the environment [26]. In this study, the spatial variability of concrete cover and surface chloride concentration were considered by using random field analysis. In a random field analysis, the RC bridge deck was discretized into a number of elements of size Δ and a random variable was used to represent the random field over each element. These random variables were statistically correlated and the correlation between them can be defined by correlation functions. The mid-point method was selected for this study to model the random fields, meaning that the value at the centroid of each element represented the entire element. The Gaussian correlation function was used to define the spatial correlation between elements:

$$\rho(\tau) = \exp\left[-\left(\frac{|\tau_x|^2}{d_x^2}\right) - \left(\frac{|\tau_y|^2}{d_y^2}\right)\right], \tag{7}$$

where τ_x and τ_y are the distances between the centroid of correlated elements in the x- and y-directions, respectively; $d_x = \theta_x/\sqrt{\pi}$ and $d_y = \theta_y/\sqrt{\pi}$, where θ_x and θ_y are the scales of fluctuation in the x- and y-directions, respectively, referring to the distance within which correlation exists in the random field. In this study, an element size $\Delta = 0.5$ m was chosen based on the state-of-practice bar spacing

in bridge decks. The scales of fluctuation for concrete cover and surface chloride concentration were taken as 2 m based on prior studies [20].

At the element level, the deterioration state of each element was predicted at each time interval. Accordingly, the extent of corrosion initiation of the deck was quantified at daily time increments for a design life span of 80 years. For each MCS run, the extent of RC deck elements that have been corrosion initiated at a given time t can be calculated using Eq. 8:

$$p(t) = \frac{n[t \geq T]}{k} \times 100\% \, , \tag{8}$$

where k is the total number of elements and T denotes the time required for corrosion initiation. The abovementioned method was coded in MATLAB.

3 Deck Design and Climate Change Considerations

The RC bridge deck considered in this study was 10 m × 10 m, consisting of ordinary Portland concrete and black carbon steel. The concrete cover depth over the reinforcing steel was 70 mm according to the durability design requirement specified in Canadian Highway Bridge Design Code [6]. Distributions for the probabilistic inputs used in the MCS are shown in Table 1.

Two climate scenarios were considered in this study to investigate the effect of climate change on RC deck deterioration under chloride attack: (1) Historical Climate Database: this climate scenario used the climate data (annual average temperature and relative humidity) of a historical period (1991–2020); (2) Climate Change Projection: this climate scenario used the climate change projections (annual average temperature and relative humidity) of a future period (2021–2100). Climate data was obtained from the Canadian Regional Climate Model (CanRCM4) developed by the Canadian Centre for Climate Modelling and Analysis [22]. IPCC [19] has defined four RCP scenarios of future greenhouse gas (GHG) emissions, including RCP2.6, RCP4.5, RCP6.0 and RCP8.5, which means that the radiative force will reach 2.6, 4.5, 6.0 and 8.5 W/m2 by 2100, respectively. This study intended to take into account the

Table 1 Statistical parameters of random variables for probabilistic analysis

Variable	Distribution	Parameters	References
Concrete cover c	Normal	$\mu = 70$ mm cov = 0.25	Lounis and Daigle [14]
Surface chloride concentration C_s	Lognormal	$\mu = 4.57$ kg/m^3 cov = 0.5	Morcous and Lounis [16]
Chloride threshold level C_{th}	Lognormal	$\mu = 1.2$ kg/m^3 cov = 0.2	Guest et al. [10]

climate change effects for the worst scenario, therefore the projected climate change (temperature and relative humidity) was characterized using CanRCM4 driven by the Second Generation Canadian Earth System Model (CanESM2) under the RCP8.5 scenario.

4 Development of ANN Algorithms

To reveal the spatial patterns of deck deterioration rates, the developed framework needed to be implemented at a regional scale (grid size = 50 × 50 km^2) across North America, thus requiring prohibitively large computational time. A machine learning-based approach was implemented to tackle this concern. In particular, ANN algorithms were developed to serve as functional mapping tools between the climate data and the concerned deterioration condition index for bridge decks. A schematic of the methodology adopted in this step is shown in Fig. 1.

4.1 Data Generation and Division

The training and testing datasets required for the development of ANN algorithms were generated by the probabilistic deck damage assessment framework introduced
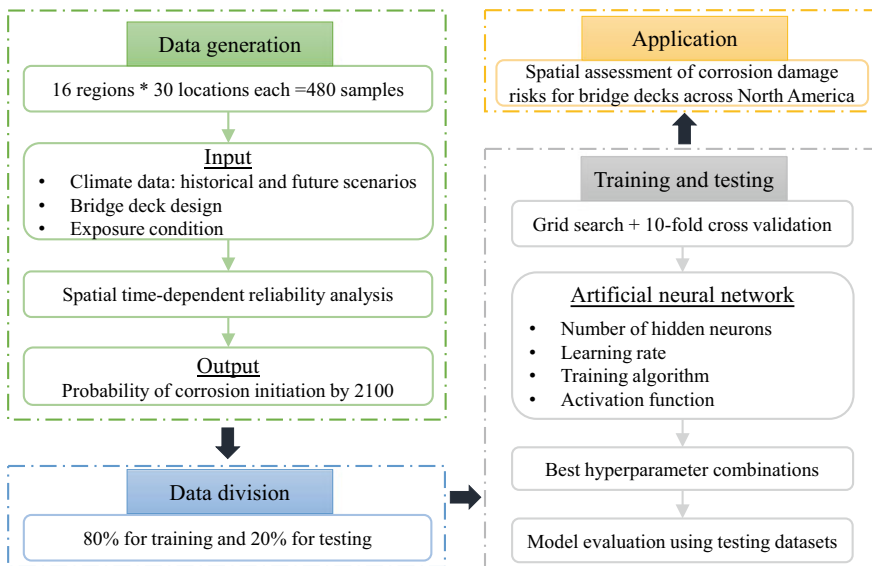

Fig. 1 A schematic of the methodology for corrosion hazard map generation

in Sect. 2. The input of the framework includes climate data, exposure condition and deck design parameters. The climate data constitutes temperature and relative humidity, which are known as the two most influential climate factors affecting corrosion progress. They were extracted from the regional climate model-CanRCM4 according to the coordinates of bridge locations. The spatial assessment only covered the topographic locations that have cold winter with snowfalls, in which the corrosion of RC decks is caused by the application of de-icing salts. Other sources of external chlorides (e.g. seawater exposure) were out of the scope of this study. As such, the surface chloride concentration was assumed to be constant within the considered domain. A constant durability design shown in Table 1 was assumed for decks in different locations.

To assure the ability of the developed machine learning algorithms to tackle a variety of climatic conditions, the data generation shall be based on bridge locations evenly distributed within different climate regions across North America. The sampling of bridge locations was conducted in each climate region. For the USA, the Koppen–Trewartha maps [28] as an improved version of the Koppen-Geiger maps [9, 13] were used for climate region classification. In this climate classification system, the climate is divided into six categories as per temperature or precipitation amounts. They are A (tropical), B (dry), C (subtropical), D (temperate), E (boreal) and F (Polar). These main six categories can then be further broken down into 13 climate types, which are represented by small letters after the capital A-E, as shown in Fig. 2. The regions above the boundary line between D and C roughly represent where the temperature will fall below 0 °C and snowfall could be expected. Referring to Fig. 2, a total of five climate regions that are enclosed in red lines (H-highland, BSk-temperate semiarid, Dc-temperate continental, E-boreal and Ft-tundra) were considered for data generation in the USA. For Canada, a total of 11 categories of climate were classified by the Climate Research Branch of Environmental Canada based on temperature and precipitation conditions (Fig. 3). In summary, the North American areas with cold winter, where chlorides come from de-icing salts, were classified into 16 climate regions. The CanRCM4 model provides climate projection results at a resolution of about 50 km, and these data are interpolated into 155×130 grids across the considered domain. For each climate region, 30 representative bridge locations were selected to perform the spatial time-dependent analysis to quantify corrosion damage risks of RC bridge decks under both historical and future climate scenarios. Sensitivity analysis has been performed to confirm the adequacy of this selected sample size. Random location sampling was used to select sample grids for each climate region. The numerical coordinate of each sampling location was recorded and used to extract climate data.

Two ANN algorithms were trained for historical and future climate scenarios, respectively. At each location, the historical climate scenario was defined by 60 input climate variables (i.e. annual average temperature and relative humidity over the time period from 1991 to 2020), whereas the future climate scenario was defined by 160 input climate variables (i.e. annual average temperature and relative humidity over the time period from 2021 to 2100). These climatic variables were then fed into
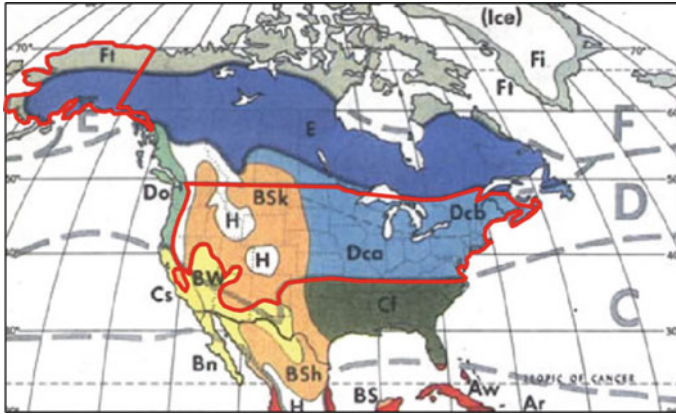
Fig. 2 The US climate regions under consideration (https://kkh.ltrr.arizona.edu/kkh/climate/trewartha_maps.htm)

the corrosion damage assessment framework to generate the deck condition index probability of corrosion initiation by 2100.

The analysis results for all sampling bridge locations were compiled to form a data collection, which was subsequently partitioned into 80% (384 deck locations) as a training dataset, 20% (96 deck locations) as a test dataset. Such a division ratio of 80, 20% was commonly used in previous studies [2]. These two datasets were used for ANN model development and verification, respectively.

4.2 Hyperparameter Determination

ANN is considered as one of the most powerful machine learning techniques as it can map the complex functional relationship between input and output data [11]. Previous studies have demonstrated the effectiveness of using ANN to solve complicated nonlinear engineering problems, such as structural degradation [4, 5, 7, 27, 29]. The network structure of an ANN model consists of the input layer, one or multiple hidden layers and output layer [12]. The neurons in the input layer receive external signals and transfer them to all neurons in the hidden layer. After processing the input signals, the hidden layer passes the information to the output layer [17].

The performance of an ANN model is highly influenced by its network architecture and settings, i.e. number of neurons in each layer, number of hidden layers, activation function, training algorithm and learning rate [2]. The number of neurons in the input layer is equal to the number of input variables, which is related to the climate scenarios as mentioned before (60 for historical climate scenarios and 160 for future climate scenarios). There is only one output variable which is the predicted value of the probability of corrosion initiation. As such, a three-layer ANN (one hidden layer)

Source(s): Environment Canada, Atmospheric Environment Service, Climate Research Branch, 1998, *Climate Trends and Variations Bulletin for Canada*, Ottawa.

Fig. 3 Canadian climate regions (statcan.gc.ca)

structure was adopted in this study due to its better generalization capabilities and computational efficiency compared with multiple hidden layer ANNs [16]. Previous studies also showed the adequacy of using a three-layer ANN is sufficient to handle most of the engineering problems [24].

Other network setting parameters, including the number of neurons in the hidden layer, learning rate, activation function and training algorithm, were determined through trial and error. The grid search method was used in this study to find the best combinations of the values of these parameters to optimize the performance of ANN models. The investigated values for each parameter are presented in Table 2. It is worth mentioning that the values considered for each parameter didn't cover all possible values. Nevertheless, the model evaluation section justifies the adequacy of

Table 2 ANN hyperparameters considered in the grid search

Hyperparameters	Investigated values
Hidden neurons	5, 10, 20, 30, 40
Activation function	Log-Sigmoid, Tan-Sigmoid, Positive Linear
Learning rate	0.1, 0.01, 0.001
Training algorithm	Levenberg–Marquardt, BFGS Quasi-Newton

these investigated values for ensuring a satisfactory prediction performance of ANN models. The development of ANN models was realized using the MATLAB neural network toolbox. The training and activation functions utilized for grid search are available in this toolbox.

The grid search method and tenfold cross-validation were performed on the training dataset to select optimal hyperparameters for ANN models. The 'Mean Squared Error' (MSE) was used as the index to measure the performance of ANN models. Learning curves were used to monitor the performance of ANN algorithms and early stopping was adopted to avoid overfitting or underfitting. The average values of the performance evaluation index obtained from 10 iterations were calculated and used as the basis to select the best hyperparameter combination. The results of grid search in terms of the best combination of hyperparameters for ANN algorithms are shown in Table 3. The best ANN model for the probability of corrosion initiation under historical climate scenario corresponded to 40 neurons in the hidden layer, a learning rate of 0.001, BFGS Quasi-Newton training algorithm and tan-sigmoid activation function with a mean cross-validation MSE of 0.00016. The best ANN model for the probability of corrosion initiation under future climate scenarios had 10 neurons in the hidden layer, a learning rate of 0.1, BFGS Quasi-Newton training algorithm and tan-sigmoid activation function with a mean cross-validation MSE of 0.000086.

Table 3 Optimal hyperparameter combinations of ANN models

Climate scenarios	Number of hidden neurons	Learning rate	Training algorithm	Activation function	Mean cross-validation MSE
Historical	40	0.001	BFGS Quasi-Newton	Tan-sigmoid	1.6e−4
Future	10	0.1	BFGS Quasi-Newton	Tan-sigmoid	8.6e−5

4.3 Model Evaluation

The ANN models were developed based on the optimal hyperparameters displayed in Table 3. In this section, they were evaluated on the previously unseen 20% test dataset for examining their predictive capability. The performance metrics include 'Person Correlation Coefficient' (r), 'Mean Absolute Percentage Error' (MAPE) and 'Mean Squared Error' (MSE).

$$r = \frac{n \sum y \cdot y' - (\sum y)(\sum y')}{\sqrt{n(\sum y^2) - (\sum y)^2}\sqrt{n(\sum y'^2) - (\sum y')^2}} \tag{9}$$

$$\text{MAPE} = \frac{100\%}{n} \sum \frac{|y - y'|}{y} \tag{10}$$

$$\text{MSE} = \frac{1}{n} \sum |y - y'|^2, \tag{11}$$

where n is the total number of samples in the training or testing dataset, y is the value calculated from the probabilistic mechanistic models (regarded as actual value), $\overline{y}$ represents its mean and y' is the predicted value. r is a measure of the linear relationship between the actual and predicted values, ranging from -1 to 1. MAPE and MSE indicate how well the predicted value approximates the actual value. The smaller the MAPE and MSE of the prediction from the actual value, that is, the better the performance. The performance of the developed machine learning algorithms was evaluated for the training and test datasets using the abovementioned performance evaluation metrics, and the results are shown in Table 4. It can be noticed that the training and testing performances were similar, which indicated no overfitting in the ANN models. The accuracy of developed ANN models in this study on predicting the chloride-induced deck deterioration of RC bridge decks in relation to climate condition was considered acceptable. This can be reflected by the low MSE (< 0.00012) and low MAPE ($< 2.34\%$) for predicting the probability of corrosion initiation.

Table 4 Performance of the best ANN models

Climate scenarios	MSE		r		MAPE	
	Training	Testing	Training	Testing	Training	Testing
Historical	6.8e−5	1.2e−4	0.9990	0.9985	1.92	2.34
Future	2.1e−5	6.6e−5	0.9995	0.9988	1.05	1.08

5 Mapping Out the Projected Adverse Impact of Climate Change

The developed ANN models were incorporated with the coordinated regional climate data to conduct a holistic spatial assessment of corrosion-induced damage risks for RC bridge decks across North America. Consequently, a series of cartographic expressions (corrosion hazard maps) were generated to reveal the spatial patterns of deck deterioration rates. Figure 4 presents the predicted probability of corrosion initiation by 2100 under both historical and future climate scenarios.

The likelihood of corrosion initiation varied considerably by region, from nearly 0% for the northern areas to 92.1% in the south. In other words, RC decks located in the northern areas were less likely to corrode, as compared to those in the south. A noticeable exception was the lower left part of the considered domain on the map, where the corrosion initiation probability was lower than other regions at the same latitude. This was mainly because this region was on the periphery of the desert and the lack of moisture led to a very low chloride diffusion rate.

The climate change impact on the probability of corrosion initiation of bridge decks can be observed by comparing Fig. 4a and b. In general, bridge decks in northern regions were more vulnerable to climate change than those in southern regions due to the more notable change in climate conditions (mainly temperature). More efforts (e.g. effective adaptation strategies implemented during design, construction or in-service) need to be made for bridges in northern regions to counteract the more remarkable climate change impact.
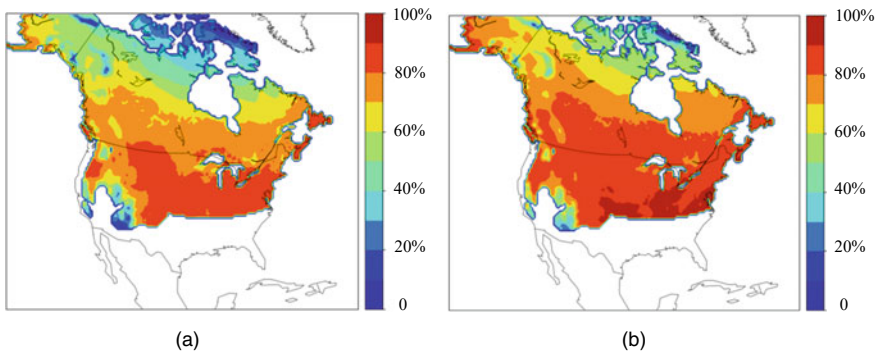

(a)   (b)

Fig. 4 Probability of corrosion initiation by 2100: **a** under historical climate scenario and **b** under future climate scenario

6   Conclusions

This study attempted to conduct a holistic spatial assessment of corrosion-induced damage risks for RC bridge decks across North America in a changing climate. For this purpose, machine learning algorithms (ANN) were employed to serve as functional mapping tools between the climate data and the concerned corrosion damage index (probability of corrosion initiation) for bridge decks. Probabilistic mechanistic models based on the integration of mechanistic deterioration models, random field analysis and Monte Carlo simulation were used to generate the training and testing datasets for ANN algorithms. Incorporated with the coordinated regional climate data, the developed ANN models were applied to predict the probability of corrosion initiation for bridge decks across North America under both historical and future climate scenarios. All the predicted results were mapped out to reveal the spatial patterns of deck deterioration rates as well as the climate change impacts. The main findings of this study are summarized as follows:

- The developed ANN models can predict the probability of corrosion initiation of RC bridge decks with sufficient accuracy and great efficiency. The trained ANN algorithms achieved the following (testing) performances: MSE < 0.00012 (MAPE < 2.34%).
- This study produced a series of cartographic expressions (corrosion risk maps) to reveal the spatial patterns of RC deck deterioration. These maps could serve as visual tools to assist transportation agencies to make informed decisions for bridge management with due consideration of future climates.
- The likelihood of corrosion-induced damage varied considerably by region. This finding demonstrated the need for 'corrosion hazard maps' to determine the region-based corrosion risks for the cases with and without considering climate change.
- In general, the decks in northern regions were more strongly impacted by climate change than those in southern regions due to the more notable change in climate conditions (mainly temperature). The irregular pattern observed on the map that projected the impact of climate change on the corrosion behaviour could be attributed to the complex interaction among changes in warming, relative humidity and weather fluctuation.

7   Future Studies

This study has taken the necessary first step to characterize the corrosion-induced damage and the reduction in serviceability for RC bridges at different locations, which are affected by climate change to various degrees. However, it did not consider spatially varying exposure conditions, nor did it predict the variation of climate change-exacerbated corrosion effects among different components of

bridges. Notably, the chloride exposure conditions are not the same for different locations and different bridge components. For example, chloride exposure of concrete surfaces arises from de-icing salts applied directly to the decks, whereas from traffic splash from roads to the piers. Leaking from joints contributes to increased surface chloride concentrations on soffits, and the soffit is less likely to be attenuated by rainwater. The corrosion maps that we generated so far are only suited to decks and do not account for the variation of chloride exposure conditions for different locations. To further address this limitation, we will upgrade the developed corrosion maps, particularly for Ontario by incorporating the effects of traffic and weather on the chloride concentration levels.

References

1. Allan RP, Hawkins E, Bellouin N, Collins B (2021) IPCC, 2021: summary for policymakers
2. Assaad R, El-adaway IH (2020) Bridge infrastructure asset management system: comparative computational machine learning approach for evaluating and predicting deck deterioration conditions. J Infrastruct Syst 26(3):04020032
3. Bastidas-Arteaga E, Schoefs F, Stewart MG, Wang X (2013) Influence of global warming on durability of corroding rc structures: a probabilistic approach. Eng Struct 51:259–266
4. Bonagura M, Nobile L (2021) Artificial neural network (ANN) approach for predicting concrete compressive strength by SonReb. Struct Durab Health Monit 15(2):125
5. Cai R, Han T, Liao W, Huang J, Li D, Kumar A, Ma H (2020) Prediction of surface chloride concentration of marine concrete using ensemble machine learning. Cem Concr Res 136:106164
6. Canadian Standards Association (CSA) S6:19 (2019) Canadian Highway Bridge Design Code, Canadian Standards Association, Rexadle, ON, Canada
7. Ding L, Rangaraju P, Poursaee A (2019) Application of generalized regression neural network method for corrosion modeling of steel embedded in soil. Soils Found 59(2):474–483
8. Gao X-J, Wang X-Y (2017) Impacts of global warming and sea level rise on service life of chloride-exposed concrete structures. Sustainability 9(3):460
9. Geiger R (1954) Landolt-börnstein–Zahlenwerte Und Funktionen Aus Physik, Chemie, Astronomie, Geophysik Und Technik, Alte Serie Vol. 3. Ch. Klassifikation Der Klimate Nach W. Köppen. Springer, Berlin, pp 603–607
10. Guest G, Zhang J, Atadero R, Shirkhani H (2020) Incorporating the effects of climate change into bridge deterioration modeling: the case of slab-on-girder highway bridge deck designs across Canada. J Mater Civ Eng 32(7):04020175
11. Hornik K, Stinchcombe M, White H (1989) Multilayer feedforward networks are universal approximators. Neural Netw 2(5):359–366
12. Kewalramani MA, Gupta R (2006) Concrete compressive strength prediction using ultrasonic pulse velocity through artificial neural networks. Autom Constr 15(3):374–379
13. Koppen W (1936) Das Geographische System Der Klimat. Handbuch Der Klimatologie 46

14. Lounis Z, Daigle L (2008) Reliability-based decision support tool for life cycle design and management of highway bridge decks. In: Annual conference of the Transportation Association of Canada, pp 1–19
15. Martın-Pérez B, Pantazopoulou SJ, Thomas MDA (2001) Numerical solution of mass transport equations in concrete structures. Comput Struct 79(13):1251–1264
16. Morcous G, Lounis Z (2005) Prediction of onset of corrosion in concrete bridge decks using neural networks and case-based reasoning. Comput-Aided Civil Infrastruct Eng 20(2):108–117
17. Negnevitsky M (2005) Artificial intelligence: a guide to intelligent systems. Pearson Education
18. Nickless K, Atadero RA (2018) Mechanistic deterioration modeling for bridge design and management. J Bridg Eng 23(5):04018018
19. Pachauri RK, Allen MR, Barros VR, Broome J, Cramer W, Christ R, Church JA et al (2014) Climate change 2014: synthesis report. Contribution of Working Groups I, II and III to the fifth assessment report of the Intergovernmental Panel on Climate Change. IPCC
20. Peng L (2015) Spatial time-dependent reliability analysis of carbonation induced corrosion damage to RC structures under a changing climate and cost-benefit analysis of climate adaptation strategies
21. Saetta AV, Scotta RV, Vitaliani RV (1993) Analysis of chloride diffusion into partially saturated concrete. Mater J 90(5):441–451
22. Scinocca JF, Kharin VV, Jiao Y, Qian MW, Lazare M, Solheim L, Flato GM, Biner S, Desgagne M, Dugas B (2016) Coordinated global and regional climate modeling. J Clim 29(1):17–35
23. Shirkhani H, Zhang J, Lounis Z (2020) Ensemble analysis of climate-change impacts on design-service life of reinforced concrete bridge decks across Canada. Nat Hazard Rev 21(3):04020030
24. Simpson PK (1996) Neural networks theory, technology, and applications. IEEE
25. Song H-W, Shim H-B, Petcherdchoo A, Park S-K (2009) Service life prediction of repaired concrete structures under chloride environment using finite difference method. Cement Concr Compos 31(2):120–127
26. Stewart MG (2006) Spatial variability of damage and expected maintenance costs for deteriorating RC structures. Struct Infrastruct Eng 2(2):79–90
27. Taffese WZ, Sistonen E (2017) Machine learning for durability and service-life assessment of reinforced concrete structures: recent advances and future directions. Autom Constr 77:1–14
28. Trewartha GT, Horn LH (1980) An introduction to climate. McGraw-Hill, New York, 416 pp
29. Ukrainczyk N, Ukrainczyk V (2008) A neural network method for analysing concrete durability. Mag Concr Res 60(7):475–486

Existing Structures and Study Cases

Commonalities in the Degradation of Two Reinforced Concrete Structures Constructed in the Early Twentieth Century in Southern Alberta

Alireza Rouhi and Nigel Shrive

Abstract Brooks Aqueduct is a 3.2 km long reinforced concrete elevated flume built by the Canadian Pacific Railway (CPR) near the city of Brooks in southeast Alberta starting in 1914. The aqueduct was constructed to supply water to irrigate 50,000 ha of land and thus had a significant effect on the economy of that region for a long time. The structure is now a National Historic Site. Various types of damage have been observed over the years, some from very early in the use of the flume. In contrast, the Greenhill mine primary rotary tipple structure is a Provincial Historic Site. It is one of the few remaining structures from the mining that used to occur in the Crowsnest Pass area of southwest Alberta and is the most important building at the Greenhill site. The structure consists of a 40 m long, 9 m wide concrete frame supporting a steel superstructure. This type of construction was quite innovative at the time of its development in 1914 and was thus considered state of the art because of the use of new methods and materials such as steel and reinforced concrete. The mining company was not in the same league as the CPR in terms of the funds it could place towards construction and the supposed quality of what was done. The structure has also suffered from damage and deterioration. The various types of damage are compared and can be seen to result from similar causes—a lack of knowledge at the time about issues related to the durability of reinforced concrete (e.g. cover for the steel, freeze–thaw) and the need for certain levels of precision in construction (e.g. aggregate gradation, location of reinforcement, splice length).

Keywords Reinforced concrete · Degradation · Southern Alberta

A. Rouhi · N. Shrive (✉)
Department of Civil Engineering, University of Calgary, Calgary, Canada
e-mail: ngshrive@ucalgary.ca

1   Introduction

The two structures examined are the Brooks Aqueduct in southeast Alberta, a 3.2 km long elevated flume built by the Canadian Pacific Railway (CPR) near the city of Brooks, and the Greenhill mine tipple structure in the Crowsnest Pass area of the southwest of the province. Brooks Aqueduct was constructed entirely of reinforced concrete, whereas the Greenhill mine structure consists of a steel superstructure supported on a reinforced concrete frame and slab. The CPR could afford to do the best at the time, whereas West Canadian Collieries could not. Each structure is introduced before comparing the deterioration that both structures have suffered over time.

1.1   Brooks Aqueduct

Brooks Aqueduct was constructed to supply water to irrigate 50,000 ha of land and thus had a significant effect on the economy of that region for a long time. The aqueduct (Fig. 1a) also had a noticeable role in the CPR's efforts to settle Western Canada and played an important role in the growth of farming in southeast Alberta. The aqueduct was commissioned in 1914 to transfer water at a volume of 25.5 cubic metres per second over a valley 3.2 km wide and 20 m deep [1]. A typical segment of the aqueduct is 24 m between expansion joints, involving five equally spaced columns, each supporting one side of the flume. The only variable in this arrangement along the length of the aqueduct is the height of the columns. The Eastern Irrigation District operated and maintained the aqueduct after 1935. The aqueduct was abandoned in 1979 after 65 years of service and was replaced with a larger earthen canal built to the south of the aqueduct. Brooks Aqueduct is a significant civil engineering achievement because of its design, materials and large size, being now recognized as both a National and Provincial Historic Site. An interpretative centre has been constructed, and while a small part of the aqueduct has been removed to improve access for the public, more than 3 km still remains. Various problems exist with the concrete—cracking and spalling in the frames and some patches missing from the flume [1, 2]. Indeed, the concrete in the aqueduct was subject to significant damage and deterioration almost from the beginning of operation. The damage is developed mostly due to the poor quality of the concrete with respect to durability issues, poor design and a lack of proper workmanship, all stemming from the paucity of knowledge about these issues at the time of construction. The flume itself is a shell (the top part of the structure seen in Fig. 1a) in the shape of a "hydrostatic catenary" (Fig. 1b). This geometric shape is supposed to place the flume under direct axial tension with no moment or shear when the flume is filled to the design level. However, finite element analysis shows that the fixation of the flume to the rigid longitudinal beams at the top of the flume induces moments in the cross-section when the flume is modelled with water at the design depth [3].
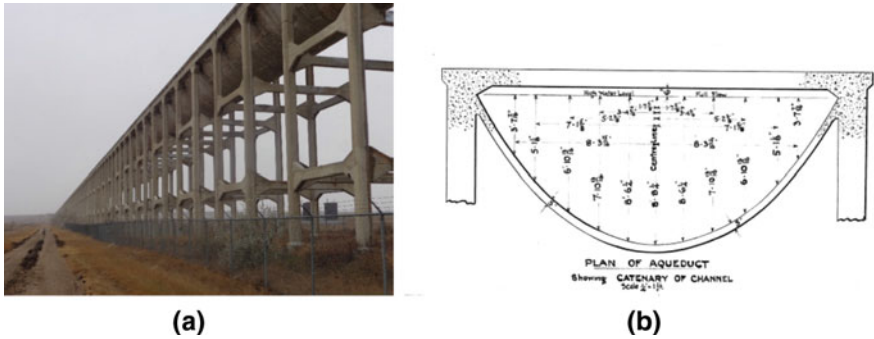
Fig. 1 **a** View of the aqueduct stretching across the valley. **b** Cross section of the flume showing the catenary shape (Eastern Irrigation District Archives)

Construction of the aqueduct (Fig. 2) allowed the irrigation of a region of Southern Alberta called "the Eastern Irrigation District". The aqueduct is a remarkable product of Canadian engineering and one of the largest aqueducts of its kind in the world [1]. Brooks Aqueduct would be considered a significant construction project even on today's scales. Despite the flaws that have been observed during its century of existence, the people who built this structure deserve high respect for their innovation and work [1].

Fig. 2 Superstructure forms and construction, July 18, 1914 (Manz et al. [1], from the Glenbow Alberta Institute Archives NA-2622-65)
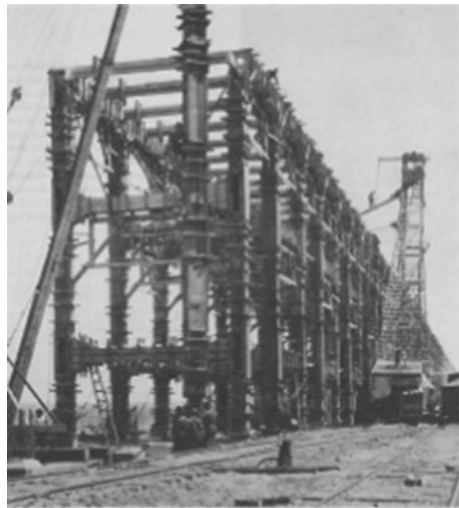
1.2 Greenhill Mine Tipple Structure

Coal mining was a major activity of the Crowsnest Pass area of southwest Alberta during the first half of the twentieth century, with the Greenhill mine complex being one of several active coal mining operations in the area. This mine complex is located north of Highway 3 next to the town of Blairmore. Operated by West Canadian Collieries, the mine began service in 1914. Like the other mining activities in the area, the Greenhill mine suffered from rapid changes in coal prices during its time of operation. The introduction of diesel engines by the Canadian Pacific Railway in the early 1950s resulted in mining operations at Greenhill ceasing in 1957. The site was abandoned but is now a Registered Historical Resource under jurisdiction of the Province of Alberta in recognition of the significance of coal mining to the Crowsnest Pass region culturally and economically in the first half of the twentieth century.

   The primary rotary tipple structure is considered to be the most important building at the Greenhill site. Views of the tipple building from the front and rear are shown in Fig. 3. The structure consists of a 40 m long, 9 m wide reinforced concrete frame supporting a reinforced concrete slab on which there is a steel superstructure. The use of what were relatively new methods and materials in 1914 such as steel and reinforced concrete made this type of construction innovative and viewed as state of the art at the time. Various types of damage and deterioration are visible, typically to the exterior columns and beams of the frame and the sheathing of the steel superstructure.

   There are no records of the design, construction, any alterations or maintenance of the tipple structure. What can now be seen is that the reinforced concrete moment frame (300 × 300 mm columns and beams) supports the 200 mm thick reinforced concrete slab and the steel superstructure. This superstructure consists of Fink trusses at the roof built from double-angle chords, single-angle web members and channel purlins: some trusses have been altered to accommodate changing requirements over the working life of the structure (Fig. 3). The columns are built-up members of channels and angles. Single-angle braces located at two bays on each side of the building provide lateral load resistance in the longitudinal direction. Some parts of the braces were also removed at unrecorded times in the past. No lateral load-supporting system exists in the short direction of the superstructure, and it is not clear if any bracings existed originally in that direction. As a result, only moment frame action of the steel columns provides lateral resistance in the short direction of the superstructure. Thus, it may well be that to ensure the stability of the superstructure in future, additional bracings will have to be provided in the short direction. In the concrete frame, the beams and columns are each reinforced with at least four round rebars of 20 mm diameter. Bars of different dimensions and sections were used with what would now be deemed inadequate lap splicing (e.g. see Fig. 4).

Fig. 3 Views of the Greenhill mine tipple structure from the front and rear above, with a complete roof truss and one missing part of the bottom chord below

Fig. 4 Round bar overlapped with a square bar in a beam, near a beam-column connection

Fig. 5 Lack of proper cover for concrete—the reinforcing bars must have been touching the formwork in these parts of the Brooks Aqueduct

2 Common Features in Construction

2.1 Lack of Cover—Placement of Steel Reinforcing Bars in Formwork

The need for concrete cover to protect the steel reinforcing bars from rusting was not recognized in the reinforced concrete parts of either structure. As may be seen in Fig. 5, bars clearly ended up lying against the formwork in parts of the Brooks Aqueduct, and in Fig. 6, inconsistent placement of bars becomes evident in addition to the bars sometimes being too close to the formwork and thereby not providing sufficient cover for the steel. At the Greenhill mine, the minimal amount of cover for the steel in some locations can be observed with examples from beams in the tipple frame, as shown in Fig. 7. Reinforcing bars are only visible where concrete has spalled, indicating that in this structure, all bars were held off the formwork, but that the cover was minimal.

2.2 Splices and Stirrups

Splices for reinforcement in 1914 were not as they are now. At the Greenhill mine site, the splice shown in Fig. 4 is about 50 mm (2 inches) long with the square bar not tied to the round one. The bar in the column shown in Fig. 8 is not spliced to a starter bar from the foundation, if there is one, and the stirrups in a crossbeam are widely spaced (Fig. 8). Note also that the stirrups are not tied to the longitudinal bar.

Reinforcement at a column head where there is an expansion joint in the Brooks Aqueduct is shown schematically in Fig. 9, but cracks in some of the beams at expansion joints are difficult to reconcile with the supposed arrangement (if the stirrups were as in modern construction). It is quite possible the stirrups are single leg in the middle or on the flume side of the beam. In Fig. 10, we show two examples,

Fig. 6 Inconsistent placement of steel reinforcing bars, Brooks Aqueduct. Top left, a bar right at the front of a column head: top right, three bars all with virtually no cover in a column head: bottom left, a bar exposed at the rear of a column head: and bottom right, bars in a beam where it joins to a column—note the bars are not parallel

Fig. 7 Crossbeams in the frame supporting the Greenhill mine tipple structure—the minimal cover (about 10 mm) for the steel in the beams can easily be seen

one where there are no visible stirrups and a second where a wide crack crossing where the steel should restrain such opening. Cracking and spalling of the beams where they meet at expansion joints are seen in many such locations, whereas cracks in the beams where they are continuous across a column are rare. This would suggest that leaks at the expansion joints (a well-documented seemingly frequent occurrence) were involved in the deterioration seen there. It is interesting that stirrups are not

Fig. 8 Reinforcement in a column not spliced to a starter bar in the foundation and shear stirrups in a beam much more widely spaced than one would expect from a modern design

Fig. 9 Schematic of the reinforcement details at the end of the beams meeting at an expansion joint—note the layer of tar paper to be placed between the column head and the base of the beam to reduce friction to accommodate movement (Eastern Irrigation District Archives)
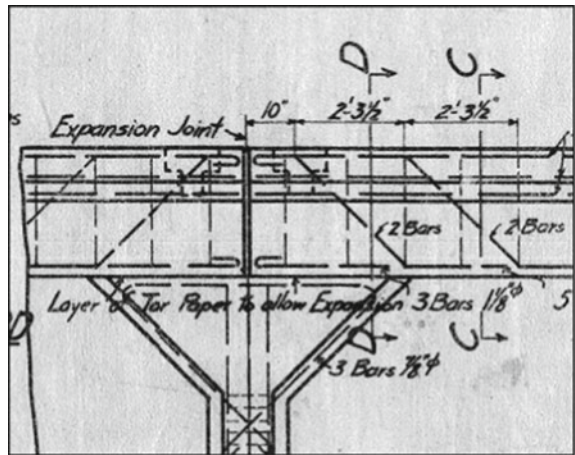
observed in areas of degradation. Leaks were first recorded in 1915, after a year of operation accompanied soon after by deterioration of the concrete in the vicinity, both in the longitudinal beams and the tops and sides of the local crossbeams of the structural frame. Changing the type of joint helped somewhat but did not eliminate the problem.

2.3   The Concretes

The concrete mixes for Brooks Aqueduct were volume-based [1]. The mix used for the pedestals had proportions of 1:3:6 (1 portion of cement to 3 portions of sand and six portions of coarse aggregate) with a maximum aggregate size of 40 mm. The superstructure and shell were built with a 1:2:4 mix with 20 mm maximum aggregate size for the shell and 40 mm maximum aggregate size for the rest of

Fig. 10 Beams meeting at an expansion joint: the one on the left has been repaired at least once before, but there is a lack of stirrups holding the rusting longitudinal bar at the bottom of the beam: similarly in the beam on the right, the length and direction of the crack suggest that the stirrups and the angled longitudinal reinforcing bar were not placed as suggested in the schematic

structure. Washed gravel was supplied from Keith, 220 km to the west, by rail. The quantity of water used in the mix was not recorded which is not surprising as the relationship between the water–cement ratio and strength was not known at the time of construction. Similarly, there is no record if any tools were used for vibrating the concrete or the forms or tamping of the fresh concrete. The clean finish of the concrete with no honeycombs would suggest that the concrete was fluid with high slump, or that something was done to compact it, or both. The aggregate contained 40–50% sand and had a void ratio of 20–23%. The cement passed the specifications of the Canadian Society of Civil Engineers for that time.

The concrete used at the Greenhill mine site was distinctly different. There are no records available for the design of the structure, nor for the concrete mix, nor of any procedure in placement. It would appear that the company simply went to the local river and extracted river gravel. Large aggregate pieces are visible in many parts of the structure (Fig. 11), with a quarter (about 25 mm) next to a piece of aggregate with a visible dimension of about 100 mm. A 95 mm core cut from the slab reveals another large stone (Fig. 11, stone with dimension greater than 100 mm) with the core failing as it was removed. Such large pieces of aggregate are generally not observed in the beams (Figs. 4, 7 and 8), so different mixes could have been used for different parts of the structure. As with the aqueduct, the water–cement ratio is an unknown as are all mix proportions.

Fig. 11 Views of the surface of the slab at the Greenhill mine tipple building on the left, with a quarter for size, and part of a large stone occupying a large proportion of the area of a 95 mm core on the right

3 Causes of Degradation

3.1 Brooks Aqueduct

Brooks Aqueduct suffered problems from very early. Finch [2] notes problems with the flume and column bases in 1921 and 1927, respectively (Fig. 12). Similar problems still exist as shown in Fig. 13. There are several sites where concrete is missing from the flume and numerous columns with damage at the base. Damage to the flume was extensive (Fig. 14), such that repairs were frequently made. Some of the forms are shown in Fig. 14. Care to align the forms with the original structure was not always taken (Fig. 14).

The problem with the flume, columns and crossbeams is the lack of freeze–thaw resistance of the concrete. The concrete in the flume would be saturated from the water in the flume. The expansion joints are noted to have leaked frequently, so

Fig. 12 Loss of concrete in the flume of Brooks Aqueduct (May 1921) and a footing (1927) as noted by Finch [2]

Fig. 13 Hole in the flume on the left and the base of a column showing loss of concrete on the right

Fig. 14 Length of repaired flume is extensive as may be seen top left. Lots of forms were required with some shown top right. A geometric mismatch of the repair with the original flume is seen bottom left. Damage to the top and bottom of a crossbeam under an expansion joint is shown bottom right

water ended up soaking the crossbeams near the expansion joints. Crossbeams away from the expansion joints are in much better condition than those under or close to expansion joints. Many column bases show degradation with spalling and cracking of the concrete similar to failure under freeze–thaw conditions, much more so than typical failure from alkali-aggregate reaction. Both failures would develop from

moisture rising in the column from the ground. There also appear to be cold joints in the frames, but these have typically not resulted in failures.

3.2 Greenhill Mine

The failure of the concrete at the Greenhill mine also appears to be mainly due to a lack of freeze–thaw durability. The flaking seen in Fig. 15 is again more reminiscent of freeze–thaw than of alkali-aggregate reaction. The fact that a lot of the initial damage is seen on the top of beams is consistent with moisture sitting on these members and soaking in. However, freeze–thaw is difficult to explain as the cause of the complete loss of concrete in the beam fully under the slab as shown in Fig. 15. The cold joint shown has also not seen much damage, presumably because water has not penetrated the joint as it is well exposed and can dry easily.

Fig. 15 Damage at the Greenhill mine tipple. Top left—flaking and spalling of a beam and the adjoining column. Damage to the top rather than the bottom of a beam (top right). Bottom left, complete loss of concrete in a beam under the slab where the coal was poured and a cold joint with minimal damage bottom right

4 Discussion

There are several common features in the damage to the two structures. This is not surprising as we have learned a lot about how to produce more durable concrete structures over the last century. The first issue is the damage due to freeze–thaw. The need for air entrainment in concrete to relieve the stresses induced by water freezing was recognized during the 1930s, but it took to the 1950s to introduce the topic into standards. At the Brooks site, numerous repairs have been implemented over the years, and failure in both the flume and the base of piers is an ongoing problem. Some repaired columns are doing well, and repairs to others are prioritized on the extent to which the column is damaged.

The second issue is the lack of sufficient cover for the steel. At Brooks, the inconsistent placement of the reinforcing bars led to the bars touching the formwork in some places and thus no cover at all. At the Greenhill site, the bars were placed more consistently, but the cover was very small compared to modern requirements. In general, the low level of cover has led to rusting of the reinforcement and consequent cracking and spalling of the concrete. For some of the cracks in the Brooks aqueduct, the relationship between the visible damage and the rusting of the reinforcing bars is distinct. In others (e.g. Fig. 10 right), the relationship is not so clear. However, we performed many structural analyses using finite element modelling to determine if those cracks were due to a structural or mechanical problem [3, 4], including friction during thermal expansion/contraction between the column head and the beam but found nothing to develop the stress levels to cause the observed cracking. Thus, we concluded that this cracking was also due to rusting of embedded reinforcing bars.

The vast majority of cracking and degradation in the Brooks Aqueduct is clearly associated with the expansion joints and the leaking of water therefrom. This has compounded what would now be seen to be errors in construction and the concrete. However, we have to recognize that the structure was very innovative for its time, and the "errors" are simply the lack of knowledge of certain issues at the time of construction. The same can be said of the Greenhill mine tipple structure. The lack of cover and the subsequent spalling of concrete have revealed clearly the lack of knowledge of the time of what would now be considered an appropriate splice length. However, the loading in the frame has not been large enough for this to be a problem. One could therefore argue that longer splice lengths are not necessary for a structure like the frame at the site.

There are no records for the Greenhill mine structure—no structural calculations, no design drawings and no record of the concrete mix(es). We do not know how the mix was decided, nor how the concrete was placed and compacted. Nevertheless, for the most part, the concrete is still there in sufficient quantity for the structure to remain standing. Some columns are in need of repair, but the estimate of the concrete strength [3] and the remaining net area indicates that while overloading should not yet have occurred, repair is needed to stop further deterioration and to avoid the potential of structural failure. The concretes at Brooks involved shipping in aggregates, but again the important issues of water–cement ratio and compaction technique are unknown.

As with Greenhill, the loading can be carried by the current structure, but further deterioration needs to be stopped and the worst columns repaired.

5   Conclusions

From the observations above, we can conclude that reinforced concrete structures constructed in the early twentieth century are likely to suffer from what would now be seen as several deficiencies. The concrete might well not have a mix design based on well-graded aggregate, and the water–cement ratio is probably unknown. There would be no air entrainment, so susceptibility to freeze–thaw degradation will be high. As alkali-aggregate reaction was also an unknown at that time, problems due to that possibility in sulphate-rich soils also need to be considered. Whether the beams and columns were designed to have the steel reinforcement at specific locations, during construction, certainly at Brooks, quality control on placement was not tight, so actual positioning of bars might not reflect drawings as well as one would like. Lastly, splices will not be of the length required today, and the bars are unlikely to be tied together: indeed, there may not even be an overlap of bars. Thus, assessment of early reinforced concrete structures needs to be done with recognition of what was known at the time of construction. It is unrealistic to expect and apply modern standards.

References

1. Manz DH, Loov RE, Webber J (1989) Brooks Aqueduct. Can J Civ Eng 16(5):684–692
2. Finch D (1988) The Brooks Aqueduct, A technological and engineering history 1912–79. Environment Canada, Canadian Parks Service
3. Rouhi A (2018) Historic reinforced concrete in Alberta: analysis and conservation of two structures. Ph.D. Thesis, University of Calgary
4. Rouhi A, Shrive NG (2020) Structural evaluation and maintenance of Brooks Aqueduct historic site. In: Proceedings, 12th international conference on the structural analysis of historical constructions. Barcelona, Spain, pp 168–179

Evaluation of the Load-Carrying Capacity of the Superstructure Elements of an 80-Year-Old Railway Bridge

Poulad Daneshvar, Armin Sadeghian, and Munzer Hassan

Abstract Load capacity assessment can lead to a more accurate and effective evaluation of the serviceability of a bridge. This is particularly the case for older railway bridges that have been in service for over half a century. This paper focuses on an open-deck five-span steel railway bridge which has been in service for about 80 years. The load-carrying capacity assessment of the bridge based on the most recent code-based conditions and requirements and the current condition of the superstructure elements is presented. Through considering the history of the traffic passing over the bridge, the paper also investigates the fatigue-related condition of the superstructure elements for the next 30 years. The analyses revealed that important fatigue-related concerns are to be expected in the girders of the shorter spans in the case that the bridge will be in service for another 30 years. For longer spans, fatigue-related issues were observed in the secondary members. Accordingly, replacement and repair activities are proposed to keep the bridge in service for the near future.

Keywords Load-carrying capacity · Superstructure elements · Railway bridge

1 Introduction

Railway networks are key elements of transportation systems all around the globe. Railway bridges play a major role in efficiency of such networks and thus their satisfactory performance and their ability to carry the required loads is of utmost importance for the safety of those crossing *(it)* them and for an economy that partly or fully relies on transportation of goods. For example, temporary rerouting which is a common solution for dealing with bridge repairs or replacements, is much more

P. Daneshvar (✉) · A. Sadeghian
CIMA+, Montreal, Canada
e-mail: poulad.daneshvar@cima.ca

M. Hassan
ETS, University of Quebec, Quebec City, Montreal, Canada
e-mail: munzer.hassan@etsmtl.ca

complicated and costly for railway networks in general, than it is for other means of transportation. This could contribute to the fact that, in comparison to highway bridges, railway bridges are designed to have a longer service life [3] and therefore, there are still several bridges in service which were built close to or even more than a century ago. Examples of such bridges include Victoria Bridge [9] in Quebec and Whirlpool Rapids Bridge [4] in Ontario built in 1859 and 1897, respectively. Such long lifespans increase the possibility and the number of times of exposure to extreme weather as well as minor or major incidents. Accordingly, given the risks associated with railway bridge failures, the frequency of inspections followed by load-carrying capacity evaluations increases as these bridges age. Fatigue analysis and the corresponding remaining life of the bridge components, based on the number of cycles to which they have been exposed, comprise an important section of the railway bridge evaluation process.

This paper focuses on the load-carrying capacity assessment of a bridge that extends over a body of water. The analyses are based on the most recent code-based conditions and requirements and the current condition of the superstructure elements. The bridge is an open-deck five (5)-span steel railway bridge which has been in service for about 80 years. Furthermore, through considering the history of the traffic passing over the bridge, the paper also investigates the fatigue-related condition of the superstructure elements for the next 30 years. Based on the obtained results, replacement and repair activities are proposed to keep the bridge in service for the desired extended life of the bridge.

2 Bridge Studied

The studied bridge is a five-span open-deck steel girder bridge which was built in 1941. It has a skew angle of about 45°. The deck for all five spans consists of a wooden deck (ties) resting on longitudinal steel girders. The girders of the middle spans (Spans 2, 3, and 4) are supported by transverse steel beams at each end. The girders of the approach span (Spans 1 and 5) rest on reinforced concrete abutments on one side and on transverse beams on the other side. None of the spans share the same transverse beam. The transverse beams of the middle spans are built up box girders sitting on two bearings while those of the approach spans are deep built up I-section girders supported by a bearing in the middle and two columns at the extremities. The role of the transverse beams is the transfer of loads to the support units (and columns) and then to the intermediate piers.

The width of the deck is about 9 m and the vertical clearance under the structure (relative to the water level) is about 3.2 m. The bridge carries two tracks with continuous rails along the bridge and over the spans. The spacing between the rails of the same track is 1.5 m and the two tracks are placed 4 m apart (centre to centre). According to the information on the original drawings, the design live load for the bridge was the Cooper E60 locomotive as described in the Manual for Railway Engineering [2]. Table 1 summarizes the information concerning the studied bridge. All

Table 1 Summary of the information regarding the studied bridge

Item	Detail
Construction year	1941
Bridge type	Open-deck bridge
Number of spans	5
Skew angle	45°28′
Total length (m)	107.3
Bridge width (m)	9
Foundation type at extremities	Reinforced concrete abutment
Foundation type at piers	Reinforced concrete pile bent
Foundation pile diameter (m)	2.6
Design live load	Cooper E-60

the connections for the built up girders as well as the secondary members of the super-structure of the bridge are riveted. Four catenary support structures are connected to the structure at the exterior girders. Two of them are installed at spans 1 and 5 and the other two are at the two ends of span 3. The catenary support structures are no longer in use.

2.1 Spans 1 and 5

Spans 1 and 5 have similar configurations. They are approximately 11 m in length from centre to centre of the bearings each of which have two (West and East) sections as shown in Fig. 1. Each section consists of four simply supported built up plate girders approximately 0.72 m deep carrying one track on timber ties. For each girder, guided metal plates (two per bearing) serve as bearings which are placed on the abutment and the transverse beam. This configuration results in a short cantilever (approximately 1 m long) for each girder beyond the transverse beam, which makes the total length of the girders about 12 m. The translational movement of the eight bearings on the abutment is blocked by means of dowels placed on each side of the girder. The dowels go through the bottom flange as well as both bearing plates and into the abutment seat. On the transverse beam, the bearing plates are attached to the top flange of the transverse beam by bolts that go through the bottom flange and the bearing plates on each side of the girder. For these bearings, the bolts are aligned so that there is one bolt on each side of the transverse beam. While the bearings are fixed at the abutment, the bolts in the bearings on the transverse beam go through slotted holes to accommodate the longitudinal movement of the girders and form expansion bearings. The girders in each section are connected through four rows of internal diaphragms installed perpendicular to the beams. There are also two rows of end diaphragms that are aligned in the direction of the skew, that is, along the
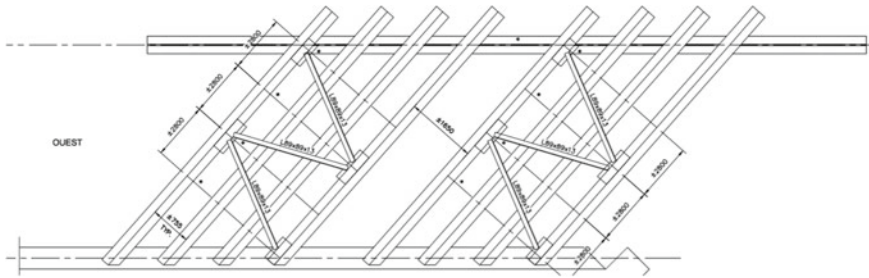
Fig. 1 Plan view of span1 (Span 5 has a similar configuration)

abutment and the transverse beam. In addition, in each section of the span, the upper flanges of the beams are braced with a single angle as shown in Fig. 1.

2.2 Spans 2 and 4

Spans 2 and 4 have an identical geometry consisting of four steel plate girders approximately 3 m deep with a span length of a bit shorter than 37 m. Each track is carried by two girders and is positioned between the two. There is a reduction of section height in the girders at supports forming an inverted step where the shallower section sits on the previously mentioned steel transverse beams. There is a steel plate acting as a shoe plate between the bottom flange of the girders and the top flange of the box-shaped transverse girder all of which are connected through rivets. The span is fixed at one end and is free to move longitudinally as it relies on the transverse beam and its bearings and connections to the side columns to accommodate movements due to temperature change or the passage of live load over the bridge. Each two girders carrying the same track are connected at the top and the bottom through horizontal X-braces. There is also vertical X-bracing between the two girders. The two middle girders are also connected through top and bottom horizontal k-type braces as well as vertical X-bracing. In addition, there are end diaphragms between the pairs of girders carrying the tracks at both ends of the span over the supports. The configuration of spans 2 and 4 is illustrated in Fig. 2. It should be noted that the bottom flange of the deeper section of the girders was originally connected to the bottom flange of the transverse beam. However, currently, almost all the plates connecting the two members are cracked and practically of no influence on the behaviour of the bridge.

2.3 Span 3

Span 3 consists of four built up steel girders approximately 1.3 m deep with a span length of 11.5 m. The girders rest on a steel transverse beam at each end. The
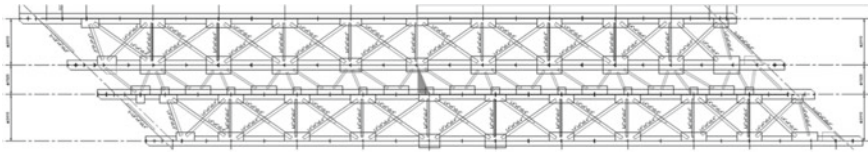
Fig. 2 Plan view of span 2 (Span 4 has a similar configuration)
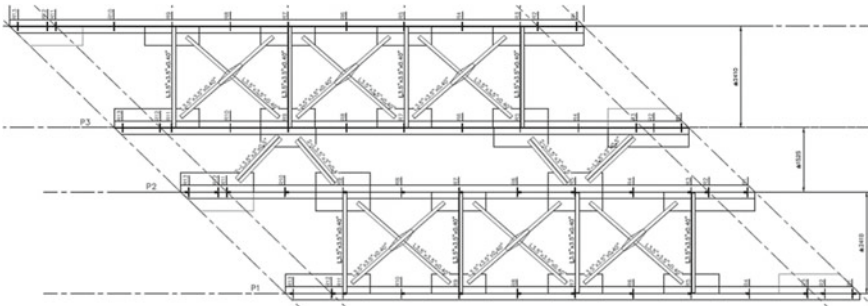
Fig. 3 Plan view of span 3

connections between the girders and the transverse beam resemble those of spans 2 and 4. The transfer beams are similar to those of spans 1 and 5. Similar to spans 2 and 4, each two girders carry one track in which the rails are positioned between the two girders. Each pair of girders carrying the track are connected to each other with top and bottom horizontal as well as vertical X-braces. Only four horizontal braces connect the middle girders at the bottom. Figure 3 shows the configuration of span 3.

3 Inspection

A detailed structural inspection activity was conducted with a focus on the condition of the bridge components as well as a dimensional survey to obtain the missing information on certain elements. In addition to some corrosion and loss of section in the bottom flanges of the girders and also the secondary elements, the inspection activity revealed that there was a loss of contact between the shoe and the base plates of two of the bearings of the girders at the transverse girder end in span 1. The gap corresponding to the exterior girder was measured to be 10 mm. The second gap was for the adjacent interior girder and was about 3 mm. It was observed that the gaps closed and re-opened continuously as the train axles moved along the span. For spans 2 and 4, most of the damage observed was caused by corrosion of the steel elements. Section losses were noted in the lower and upper flanges of the girders. Perforations were observed in the webs, stiffeners, gusset plates, and braces.

Cracks were also reported in the gusset plates connecting the bottom flange of the girders to that of the transverse girder. Span 3 showed fewer signs of damage in comparison to the other spans. Minor section losses were observed for top flanges of the girders. Relatively more severe corrosion as well as perforation were reported for the secondary elements. The observed damages and loss of sections were then considered in the evaluation of the load-carrying capacity of the spans.

4   Numerical Model

Numerical models of the spans were developed to analyse and eventually evaluate the superstructure of the bridge. The main objective of numerical modelling was to understand the distribution of loads between the main elements of these spans considering the particularities of the structure such as the skew. CSiBridge 2019 v.21.2.0 [5] was used to model the spans. Girders, transverse beams, interior and end diaphragms, and the braces were modelled using frame elements. For spans 2 and 4, the end diaphragms were modelled using shell elements to have a more realistic assessment of the particular configuration at girder ends. The bearings were represented by link elements with different properties to represent their fixed and expansion states. Permanent loads were determined from the defined properties of materials in the software as well as added loads to account for those bridge elements that were not modelled (e.g. rails, ties, cable conduit, and catenary support structure). Considering the configuration of the deck (i.e. absence of ballast, open-deck, and girders being supported laterally), based on AREMA MRE [2] the live load could be distributed evenly among the girders. Therefore, lanes for the moving live load were defined on each beam and the portion of the appropriate load, based on the position of the rails relative to the girders, was assigned to them. To verify the developed numerical models, the bending moments due to the live load obtained from the models were compared with those provided in Table 15-1-16 of AREMA MRE [2] for single spans. The provided values were modified to represent the Cooper E60 live load used in the analyses. Such a comparison is considered valid as no significant change in the maximum bending moments is foreseen with the introduction of a skew to an open-deck bridge with wooden ties. Agreement was observed between the obtained and the provided bending moment values and thus the models were validated. Figures 4, 5 and 6 demonstrate the constructed numerical models.

The models were first constructed using the as built condition of the structure as presented on the original drawings. If necessary, the models were then updated to include particular damages or changes in the superstructure members based on the observations during the inspection activity. For example, for spans 1 and 5, to produce the lack of support observed between the bearing plates, the supports at the corresponding girders were modelled using gap elements. These elements functioned as springs with zero axial stiffness as long as the displacement in the bearing was less than the size of the observed gaps. As soon as the displacements exceeded the value of the observed spaces and the gaps were closed, the springs would function as normal
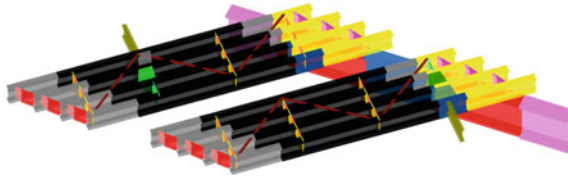
Fig. 4 Numerical model (rendered) of span 1 constructed in CSiBridge including the cantilever beams connecting the catenary support to the exterior girders

Fig. 5 Numerical model (rendered) of section of span 2 constructed in CSiBridge
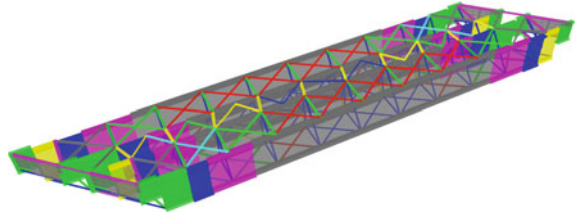
Fig. 6 Numerical model (rendered) of span 3 constructed in CSiBridge
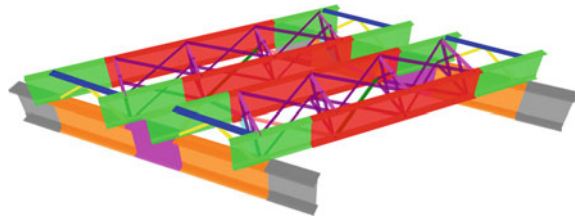
supports, i.e. having a very high axial rigidity. Nonlinear analyses were run to analyse this model. In the case of spans 2 and 4, a few damaged braces were removed to study the impact on the load distribution among the rest of the members of the span. The cracked plates connecting the bottom flanges of the girders to the transverse beam were not included in the model as the extent of cracking had practically disconnected the two elements.

5 Evaluation of Load-Carrying Capacity

The objective of the load-carrying capacity assessment was to determine whether the structure in its current condition can safely withstand the loads to which it is currently subjected and if its remaining fatigue life is sufficient for it to remain in service for an additional 30 years. It would also determine whether future repair work, other than the recommendations following the inspection activity, was required. The evaluation was carried out on the main elements of the steel structure, namely the girders and the transverse beams. The evaluation of the transverse beams is not included in this

paper. The assessment of the timber ties, assemblies, gussets, piers, abutments, and the foundation units was out of the scope of this work. Both the as built and the damaged states of the spans were considered in the evaluation of the load-carrying capacity of the spans. The allowable stress method based on AREMA MRE [2] was adopted for the evaluation process. Although a speed limit is imposed on the trains going over the bridge, the present study considered speed ranges from 10 to 60 mph in assessing the load-carrying capacity of the bridge.

5.1 *Loads*

The main load types considered for this study were (i) Dead load; (ii) Live load; and (iii) Impact load. Wind load and longitudinal forces were considered in the evaluation of braces. The dead load consisted of the weight of the girders, braces, diaphragms, ties, rails, and the cable conduit. Where applicable, the load from the catenary support structure was also added to the dead loads. For the analyses, the weight of the steel structure was increased by 10% to take into account the gusset plates, stiffeners, and rivets. According to the original plans of the existing structure, the design live load for the bridge is the Cooper E60. The same load was used in the evaluation process. Two other trains were also considered in the analyses: (i) ALP45DP locomotive with four 325 kN axles; and (ii) ALP46A locomotive with four 225.6 kN axles. These loads would best represent the current live load on the bridge. The locomotives used in the analyses are shown in Fig. 7. The impact load is determined as a combination of direct impact and rocking impact. In other words, the total impact is the sum of the vertical (direct) effect and the tipping effect. The determined value for impact load is applied to the locomotive live load as a percentage of the vertical load applied to the top of each rail. AREMA MRE [2] provides equations to determine the direct impact for the case of an open-deck bridge without ballast for equipment running without a hammer blow (diesel or electric locomotives). It also specifies rocking impact as a vertical torque resulting from the rotation of the train relative to its centreline and transmitting the forces to the rails. This impact load can be taken as 20% of the wheel load, without impact, acting on the rail as a force couple. Furthermore, for existing bridges, AREMA MRE [2] allows a reduction in the determined vertical impact load for train speeds below 60 mph. Table 2 shows the calculated impact factors for the evaluated spans.

5.2 *Allowable Stress*

AREMA MRE [2] specifies two types of rating to be assigned to a bridge: (i) Normal and (ii) Maximum. The Normal rating represents the load-carrying capacity of the bridge in its expected service life whereas the Maximum rating is the load level the bridge can carry at infrequent intervals. In cases where the Normal rating is higher
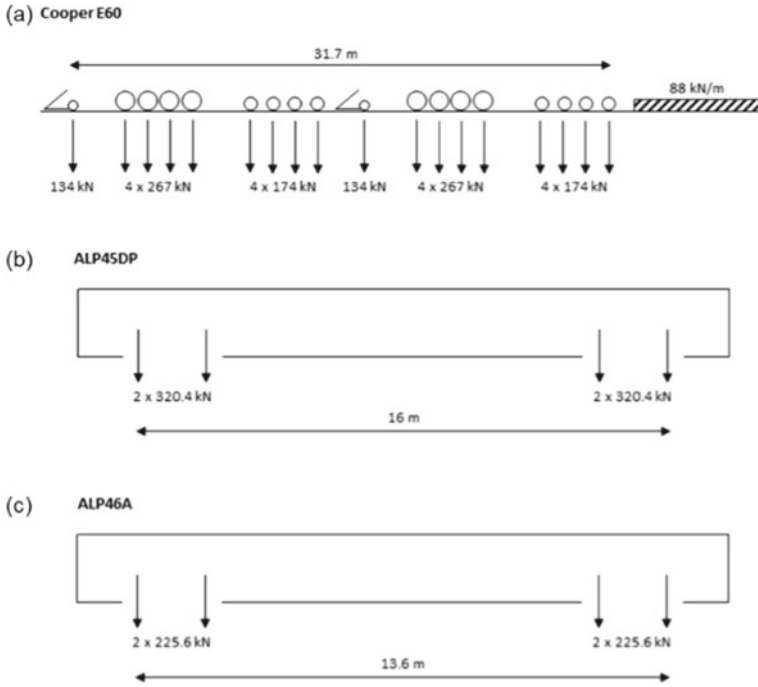
Fig. 7 Live load used in the evaluation process: **a** Cooper E60; **b** ALP45DP locomotive; and **c** ALP46A locomotive

Table 2 Impact loads factors used in the analyses determined based on the considered train speeds

Span	Speed (mph)					
	10	20	30	40	50	60
1/5	1.28	1.39	1.47	1.53	1.57	1.58
2/4	1.11	1.17	1.22	1.26	1.28	1.29
3	1.17	1.28	1.36	1.42	1.45	1.46

than the Maximum one, the lower one has to be considered. AREMA MRE [2] prescribes two different sets of stress limits for the two rating types.

5.3 Fatigue

The number of experienced stress cycles, the stress range amplitude, and the detail category associated with the member under study are the main factors governing the fatigue life of a bridge [2, 7, 10]. Changes in the live load passing over the bridge and its frequency as well as deterioration of bridge elements are influential in the

life span of a bridge [1]. Therefore, knowing the traffic history of the bridge would be an asset in determination of the required parameters for fatigue evaluation. In the absence of such data, AREMA MRE [2] provides a simplified method for evaluation of fatigue life of bridge components. This is based on a study considering 60, 110-car trains passing daily over a bridge during a period of 80 years. The number of cycles (i.e. either equal to 2 million or more than 2 million cycles) to be considered is provided based on span length and/or the number of loaded tracks. Allowable fatigue stress ranges are provided based on the proposed detail categories of the bridge elements and the stipulated number of cycles. It is noted that AREMA MRE [2] considers only a percentage of the live load mean impact factor for fatigue design and evaluation. In this study, the simplified approach was first adopted to evaluate the fatigue condition of the bridge elements. However, the parameters of the study that formed the basis of AREMA's simplified approach are quite penalizing for some old bridges as the traffic might have not been as severe. This issue and the fact that the objectives of this work also included the determination of the remaining fatigue life of the bridge prompted an investigation of the history of the traffic on the studied bridge. Numerous consultations with historians as well as examination of various documents resulted in the traffic history provided in Table 3. It was concluded that, for the detailed fatigue analyses, the trains going over the bridge between 1941 and 1957 could be represented by the Cooper E60 Locomotive pulling 12 waggons. Every other pair of waggons was considered to be empty. The authors note that due to the lack of comprehensive data, particularly those corresponding to the early years of the exploitation of the bridge, there is uncertainty associated with some of the information provided in Table 3.

For each of the trains mentioned in Table 3, the stress time-histories of the components being evaluated are determined. The tensile bending stresses in the girders were calculated based on the net section area through increasing the stresses by 15%, an approximate factor determined after calculating the stresses considering the net sections at different locations along the girders. The rain-flow method [6] was used to determine the stress ranges and the number of the associated stress cycles. For each stress range, the total number of cycles in the period of presence of each train was calculated according to the information provided in Table 3. The diagrams presenting the stress limits as a function of the number of cycles to which an element is subjected (i.e. S–N curves) prescribed by AREMA MRE [2] were consulted to

Table 3 History of the trains going over the bridge as used in the detailed fatigue evaluation

Train	E60 + 12 Waggons		ALP46A + 10 Waggons			ALP45DP + 10 Waggons		
Presence	1941 to 1953	1953 to 1957	1957 to 1969	1969 to 1986	1986 to 2011	2011 to 2018	2018 to 2020	2020 to 2050
Trains/ day	60	34	40	17	20	20	17	17
Duration (yr)	12	4	12	17	25	7	2	30

Fig. 8 Stress range versus number of cycles for fatigue detail category D from AREMA MRE [2]
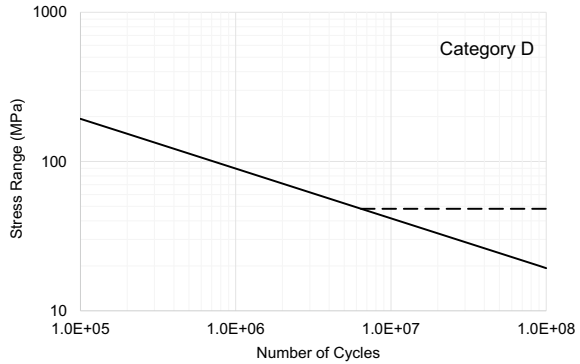
determine the limit for number of cycles. All the connections on the flanges and the webs of the studied girders are riveted. Therefore, the fatigue detail category D [2] was selected for the evaluation and the corresponding S–N curve, reproduced in Fig. 8, was adopted. Subsequently, the corresponding percentage of damage for each case was calculated as the ratio of the total number of cycles to which the element had been subjected to the limit for the number of cycles taken from the S–N curve. A ratio over 1 corresponded to the damaged status of the element under the considered cycles, load, or stress range. The sum of these ratios represented the status of the element under consideration. A similar approach was adopted by Jaworski et al. [8].

5.4 Analyses Results

5.4.1 Load-Carrying Capacity

To determine the condition of the bridge components in term of load-carrying capacity, the load combinations and the corresponding allowable stress limits prescribed by AREMA MRE [2] were considered, as shown in Table 4.

The capacity factor for each analysed element was determined using Eq. 1:

$$\text{Capacity Factor} = (A - DWL)/LI \tag{1}$$

where A is the allowable stress determined based on the type of stress and the component under study; DWL is the stress induced due to either the dead load, wind force, the longitudinal force or a combination of them, and LI is the stress due to the passage of the train including the impact factor. In the following sections, the capacity factors determined for the components of each span are presented. For brevity, only those associated with Normal rating are included.

Table 4 Load combinations and allowable stress factors used in the evaluation process

Span	Component	Load combination[a]	Allowable stress factor (%)
1/5	All	DL + LL + I	100
2/4	All	DL + LL + I	100
2/4	Braces	DL + LL + I + WF + LF	125
3	All	DL + LL + I	100
3	Braces	DL + LL + I + WF + LF	125

[a] *DL* Dead Load; *LL* Live Load; *I* Impact Load; *WF* Wind Force; *LF* Longitudinal Force

Table 5 Capacity factors for girders (G5 to G8) considering lack of contact in bearings of span 1

Stress type	Live load	Speed = 10 (mph)				Speed = 30 (mph)			
		G5	G6	G7	G8	G5	G6	G7	G8
Bending	Cooper E60-AB[a]	1.36	1.47	1.43	1.31	1.34	1.27	1.25	1.14
	Cooper E60	1.33	1.21	1.38	1.51	1.15	1.05	1.20	1.31
	ALP45DP	2.25	2.08	2.09	2.53	1.96	1.81	1.82	2.20
	ALP46A	3.13	2.88	2.49	3.47	2.72	2.50	2.16	3.02
Shear	Cooper E60-AB[a]	1.61	1.82	1.76	1.66	1.18	1.58	1.53	1.44
	Cooper E60	1.81	0.79	1.41	2.35	1.57	0.69	1.23	2.04
	ALP45DP	2.67	1.24	2.04	3.67	2.32	1.08	1.77	3.19
	ALP46A	3.93	2.00	2.52	5.00	3.42	1.74	2.19	4.35

[a] Cooper E60-AB: As built state of the span (i.e. there is no damage or lack of contact)

Span 1

As previously mentioned in Sect. 3, spans 1 and 5 have the same geometry and since the components of span 1 had shown relatively more severe deterioration, only the results for span 1 are presented. The inspection had revealed a lack of contact at two bearings of span 1 (Girders G5 and G6). As the investigation of this issue was given high priority, a model of only the problematic part of span 1 was constructed to evaluate the girders and the diaphragms affected by the lack of contact. It consisted of four girders (G5 to G8) and the corresponding braces and diaphragms. The transverse girder was not modelled. Table 5 presents the capacity factors for the girders corresponding to (i) all the three live load types while there was lack of contact; and (ii) Cooper E60 for the case where the lack of contact did not exist.

The results show that the loss of contact at the supports did not significantly affect the capacity of G5. In fact, its shear capacity factor increased. This is mainly due to the redistribution of forces following the lack of support at one end of G5. Thus, the demand was reduced on this beam, resulting in higher shear capacity

Table 6 Capacity factors for interior diaphragms close to the bearings considering lack of contact in bearings of span 1

Stress type	Live load	Speed = 10 (mph)	Speed = 30 (mph)
Bending	Cooper E60-AB[a]	5.08	4.41
	Cooper E60	0.79	0.69
	ALP45DP	1.15	1.00
	ALP46A	1.52	1.32
Shear	Cooper E60-AB[a]	7.25	6.30
	Cooper E60	1.78	1.54
	ALP45DP	2.66	2.31
	ALP46A	3.61	3.14

[a] Cooper E60-AB: As built state of the span (i.e. lack of contact does not exist)

factors. The redistribution resulted in G6 also taking a part of the load from G5 and consequently, not having sufficient load-carrying capacity in shear and at speeds higher than 30 mph in bending when considering the design load. Table 5 shows that load redistribution also affected G7, however, with a less significant magnitude than G6. G7 demonstrated sufficient capacity even if there were two cases of loss of contact in the adjacent girders. The capacity reserve of G8 increased when there was lack of contact in the bearings of G5 and G6 girders. This could be attributed to the fact that G5 and G6 were pushed downwards as the train passed over the span, a slight lift occurred on the side of G8 since the four beams in span 1 were connected by diaphragms. This counteracted some of the forces on G8 and resulted in higher capacity factors. It is noted that the girders had sufficient capacity for the passage of the current trains on the bridge. Nevertheless, the shear capacities of G6 were barely sufficient at train speeds exceeding 30 mph.

Table 6 shows the capacity factors determined for the interior diaphragms close to the damaged bearings. It can be seen that these diaphragms did not have sufficient capacity, under the design load, in the absence of contact at the bearings as they played the role of supports for the G5 and G6 girders. This resulted in the diaphragms undergoing bending moments for which they were not designed, hence the dramatic decrease in the capacity factors. Shear capacity factors, although still acceptable, are significantly reduced due to the lack of support contact. Table 6 and the analyses results also indicate that the diaphragms did not have the required capacity under the current train loads for speeds greater than 30 mph.

It is noted that the loss of contact in bearings could also affect the live load impact. The impact factors such as those used in this work (see Sect. 5.1) are generally defined for normal track conditions, bridges in good condition, and bridges with conventional types of damage such as loss of section for elements. These factors are not appropriate in cases where the bridge has suffered specific types of damage such as the loss of contact in bearings of span 1 of the studied bridge. The fact that two

Table 7 Capacity factors for girders of span 1 with damage but loss of contact in bearings neglected

Stress type	Live load	Speed = 30 (mph)							
		G1	G2	G3	G4	G5	G6	G7	G8
Bending	Cooper E60-AB[a]	1.20	1.37	1.41	1.32	1.34	1.42	1.37	1.23
	Cooper E60	0.94	1.08	1.12	1.05	1.06	1.12	1.08	0.97
	ALP45DP	1.55	1.78	1.87	1.75	1.75	1.84	1.82	1.66
	ALP46A	2.19	2.47	2.58	2.44	2.51	2.63	2.66	2.55
Shear	Cooper E60-AB[a]	1.31	1.60	1.49	1.46	1.48	1.67	1.60	1.29
	Cooper E60	1.13	1.37	1.28	1.26	1.28	1.44	1.38	1.11
	ALP45DP	1.86	2.01	1.72	2.19	2.32	2.45	2.42	2.05
	ALP46A	2.47	2.86	2.36	2.96	3.17	3.67	3.20	2.70

[a] Cooper E60-AB: As built state of the span (i.e. there is no damage or lack of contact)

of the beams are suspended at one end can give rise to impact factors much higher than those calculated using the equations given by AREMA MRE [2]. Adoption of higher impact factors would result in even lower capacity factors as was observed for a hypothetical case of a 25% increase in these factors.

The next series of capacity factors for span 1 was determined assuming that the damaged bearings had been repaired. The analyses were performed using a numerical model consisting of all the eight girders as well as the transfer girder. The observed damages due to corrosion were considered in the analyses. Table 7 presents the determined capacity factors for the girders considering a train speed of 30 mph. The calculated factors showed that the girders had enough reserve capacity for shear at all speeds. However, the bending capacity factors for the four exterior girders (i.e. G1, G4, G5, and G8) were not satisfactory at higher speeds, particularly for G5 and G8 due to the observed damages. It is noted that the as built factors are slightly different than those presented in Table 5 as the models used for the analyses were not identical. The analyses also showed that the diaphragms in both as built and damaged conditions had sufficient capacity under the design load.

Spans 2 and 4

Spans 2 and 4 were evaluated using the results of the numerical analyses of the model described in Sect. 4. Although the two spans are similar, since they comprise the main spans of the bridge, the results for both spans are presented. Tables 8 and 9 contain the capacity factors corresponding to speeds of 10 mph and 30 mph for spans 2 and 4, respectively. Based on the obtained capacity factors, it was concluded that all the girders of spans 2 and 4 had sufficient bending and shear capacity even in their damaged condition under the design and the current live loads.

The load-carrying capacity was also assessed for the horizontal and vertical bracings between the girders. The analysis was not carried out on all the elements and only

Table 8 Capacity factors for the girders (G1 to G4) of span 2

Stress type	Live load	Speed = 10 (mph)				Speed = 30 (mph)			
		G1	G2	G3	G4	G1	G2	G3	G4
Bending	Cooper E60-AB[a]	1.62	1.66	1.66	1.62	1.47	1.50	1.50	1.47
	Cooper E60	1.48	1.56	1.55	1.50	1.34	1.42	1.41	1.36
	ALP45DP	3.03	3.67	3.65	3.07	2.74	3.32	3.30	2.78
	ALP46A	4.02	5.50	5.46	4.07	3.64	4.98	4.95	3.69
Shear	Cooper E60-AB[a]	1.81	2.08	2.08	1.81	1.63	1.88	1.88	1.63
	Cooper E60	1.58	1.36	1.36	1.59	1.43	1.23	1.23	1.43
	ALP45DP	3.07	2.64	2.64	3.08	2.78	2.39	2.39	2.79
	ALP46A	4.05	3.70	3.70	4.06	3.67	3.35	3.35	3.68

[a] Cooper E60-AB: As built state of the span (i.e. there is no damage)

Table 9 Capacity factors for the girders (G1 to G4) of span 4

Stress type	Live load	Speed = 10 (mph)				Speed = 30 (mph)			
		G1	G2	G3	G4	G1	G2	G3	G4
Bending	Cooper E60-AB[a]	1.62	1.66	1.66	1.62	1.47	1.50	1.50	1.47
	Cooper E60	1.47	1.54	1.53	1.49	1.33	1.39	1.39	1.35
	ALP45DP	3.00	3.60	3.59	3.04	2.72	3.26	3.25	2.75
	ALP46A	3.98	5.40	5.38	4.04	3.60	4.89	4.87	3.65
Shear	Cooper E60-AB[a]	1.81	2.08	2.08	1.81	1.63	1.88	1.88	1.63
	Cooper E60	1.54	1.36	1.31	1.54	1.39	1.23	1.19	1.40
	ALP45DP	2.99	2.64	2.54	3.00	2.71	2.39	2.30	2.71
	ALP46A	3.94	3.70	3.56	3.95	3.57	3.35	3.23	3.57

[a] Cooper E60-AB: As built state of the span (i.e. there is no damage)

Table 10 Capacity factors (damaged state) for the horizontal (H) and vertical (V) bracings between the girders of spans 2 and 4 corresponding to a speed of 30 mph

Live load	V[a]	Top H[a]	Bot. H[a]
Cooper E60	1.11	1.11	1.16
ALP45DP	2.37	2.12	2.47
ALP46A	3.18	2.92	3.31

[a] Factors correspond to the worst cases

certain more critical elements were evaluated. These elements were either subjected to great stress or were relatively more severely damaged. Table 10 presents the capacity factors determined for these elements. The factors show that the vertical and horizontal braces between the girders had sufficient capacity to support the design load as well as the current loads.

Table 11 Capacity factors for the girders (G1 to G4) of span 3

Stress type	Live load	Speed = 10 (mph)				Speed = 30 (mph)			
		G1	G2	G3	G4	G1	G2	G3	G4
Bending	Cooper E60-AB[a]	1.78	1.80	1.82	1.82	1.54	1.55	1.57	1.58
	Cooper E60	1.78	1.80	1.82	1.82	1.54	1.55	1.57	1.58
	ALP45DP	2.98	2.98	3.07	3.06	2.58	2.57	2.65	2.65
	ALP46A	4.12	4.27	4.31	4.28	3.56	3.68	3.72	3.70
Shear	Cooper E60-AB[a]	1.45	1.58	1.46	1.54	1.25	1.37	1.26	1.33
	Cooper E60	1.45	1.58	1.46	1.54	1.25	1.36	1.26	1.33
	ALP45DP	2.32	2.37	2.35	2.63	2.00	2.04	2.03	2.27
	ALP46A	3.26	3.73	3.11	3.31	2.81	3.22	2.69	2.86

[a] Cooper E60-AB: As built state of the span (i.e. there is no damage)

Span 3

Span 3 was also evaluated using the results of the numerical analyses of the model described in Sect. 4. Table 11 shows the load-carrying capacity factors determined for the girders of span 3.

The obtained capacity factors revealed that all girders in span 3 had sufficient capacity in bending and shear for both the design and the current live load. The deterioration of the girders of this span was relatively small which explains the minor difference between the capacity factors of the two states of the girders.

The load-carrying capacity of the horizontal and vertical braces between the girders of span 3 was also investigated. Similar to spans 2 and 4, the analyses were not carried out for all the elements and only certain more critical elements were evaluated. The results showed that the vertical and horizontal braces between the girders had sufficient capacity to support the design load as well as the current live loads.

5.4.2 Fatigue

The simplified method mentioned in Sect. 5.3 was first used to investigate the condition of the components of each span. As expected, this approach resulted in very conservative factors placing most of the superstructure components at the end of their fatigue life. Table 12 shows examples of factors obtained through this approach. The factors represent the ratio of the determined allowable stress range from AREMA MRE [2] to the applied stress under the considered live load. A factor below 1 shows that the state of the member is not acceptable, i.e. it has passed its acceptable fatigue life.

As the simplified approach does not consider the variation in the live load, to obtain fatigue factors which better correspond to the traffic history of the bridge, the detailed fatigue evaluation approach explained in Sect. 5.3 was next adopted.

Table 12 Fatigue factors for girders under the design load based on the simplified approach

Stress type	Live load	Speed = 10 (mph)				Speed = 30 (mph)			
		G1	G2	G3	G4	G1	G2	G3	G4
1/5[a]	Cooper E60-AB[b]	0.51	0.54	0.54	0.50	0.44	0.47	0.47	0.43
	Cooper E60	0.47	0.50	0.50	0.46	0.41	0.44	0.43	0.40
2/4	Cooper E60-AB[b]	0.70	1.02	1.02	0.70	0.67	0.98	0.98	0.67
	Cooper E60	0.64	0.95	0.95	0.65	0.62	0.92	0.92	0.62
3	Cooper E60-AB[b]	0.66	0.67	0.67	0.68	0.57	0.58	0.58	0.59
	Cooper E60	0.66	0.67	0.67	0.68	0.57	0.58	0.58	0.59

[a] Only the results for G1 to G4 are presented
[b] Cooper E60-AB: As built state of the span (i.e. there is no damage or lack of contact)

Table 13 presents the factors obtained from the detailed approach for train speeds of 10 mph and 30 mph. The presented values are for the most critical sections.

The presented fatigue factors for the as built state of spans 1 and 5 showed that there were sections in the girders of spans 1 and 5 that might have reached the end of their theoretical fatigue life. It was seen that even at speeds as low as 10 mph the fatigue condition of the girders was not satisfactory. It is needless to mention that considering damages to the spans would decrease the obtained factors. The short span length, the heavy live load in the early decades of the bridge being in service, and the number of cycles to which the girders were subjected played an important role in such low fatigue factors for spans 1 and 5.

The results of the simplified method, as presented in Table 12, seemed too conservative for the longer spans, i.e. spans 2 and 4. Therefore, the detailed fatigue analysis was also performed for these spans. Table 14 contains the fatigue factors for the most critical case, i.e. the exterior girder of span 2 with the highest stress value.

These results showed that the girders of spans 2 and 4 had sufficient capacity to maintain the structure in service until 2050. Table 15 shows the fatigue factors

Table 13 Fatigue factors for spans 1 and 5 (as built state) determined based on the detailed approach

Fatigue factor	Speed = 10 (mph)				Speed = 30 (mph)			
	G1	G2	G3	G4	G1	G2	G3	G4
At present	0.94	0.98	0.94	0.76	0.87	0.89	0.86	0.70
By 2050	0.81	0.85	0.81	0.66	0.75	0.77	0.75	0.60

Table 14 Fatigue factors for spans 2 and 4 based on the detailed approach (worst-case scenario)

Span	Fatigue factor	Speed = 30 (mph)
		G1
2	At present	5.59
	By 2050	5.23

Table 15 Fatigue factors for span 3 based on the detailed approach

Fatigue factor	Speed = 10 (mph)				Speed = 30 (mph)			
	G1	G2	G3	G4	G1	G2	G3	G4
At present	1.62	1.65	1.71	1.73	1.50	1.49	1.46	1.58
By 2050	1.36	1.38	1.47	1.49	1.29	1.29	1.26	1.36

obtained for the girders of span 3 based on the detailed fatigue analysis approach for train speed of 10 mph and 30 mph. The presented values correspond to the most critical sections of each girder.

The detailed fatigue analysis showed that the girders of span 3 had sufficient fatigue capacity to maintain the structure in service until 2050 considering the observed damage.

Detailed fatigue analysis was also performed for vertical and horizontal braces between the girders. The analysis was not performed on all elements, but only on some more critical elements subjected to higher stress. It was concluded that, for span 3, there was sufficient fatigue life associated with these elements to keep them in service until 2050. Concerning the braces of spans 2 and 4, a number of vertical and horizontal bracings did not have sufficient fatigue capacity to remain in service until 2050. It should be noted that the failure of these secondary components would not hinder the structure's remaining in service. Given the high redundancy of the bracings, their failure would result in a redistribution of forces in the adjacent braces which showed sufficient capacity to carry the additional load.

Comparing the results obtained for each of the spans, it was observed that the longer spans demonstrated a better fatigue life expectancy. This was expected as, in general, under the same load, shorter spans are subjected to more stress cycles.

6 Conclusion

Railway bridges are vital elements of railway transportation networks. These bridges are usually built to have very long lifespans resulting in increases in the probability of them being impacted by incidents as well as their experiencing more occurrences of severe weather conditions. Therefore, evaluation of the load-carrying capacity of railway bridge components deems necessary as they age. It is also necessary to verify the fatigue condition in such components to confirm their satisfactory performance while in service. In this study, a five-span steel railway bridge was evaluated using the results of a previous inspection activity. Numerical models of different spans representing the as built and the damaged states of the superstructure were constructed. The considered elements were evaluated for load-carrying capacity and fatigue under the design and current train loads.

The results showed that the lack of contact observed in two of the bearings of span 1 led to a dramatic reduction of the load-carrying capacity for one of the interior

girders as the redistribution of loads added to the magnitude of loads sustained by this girder. The analyses showed that the girder did not have the required capacity in shear for all train speeds and in bending for higher train speeds. The lack of contact also affected the capacity of the adjacent interior diaphragms as they played the role of supports for the affected girders. The shear capacity of the interior diaphragms was determined as insufficient. As a result, an immediate repair of the damaged bearings was recommended. It was proposed that steel shim plates be used to fill the gap between the bearing plates. The use of any sort of grout was not advised as the configuration of the bearings and the traffic schedule on the bridge would not allow for sufficient setting of the grout.

Taking account of other damages in span 1 and assuming that the lack of contact in bearings was fixed, the load-carrying capacity was re-evaluated. The obtained shear capacity factors were acceptable. However, the exterior girders, particularly at higher train speeds, showed insufficient bending capacity. The superstructure components of spans 2, 3, and 4 (girders and braces) demonstrated satisfactory load-carrying capacity under the design and the current loads.

The fatigue evaluation was conducted using a simplified and a detailed method. As the simplified method indicated that the majority of the superstructure elements had passed their fatigue life, the detailed method that considered a load history more similar to what the bridge had experienced was adopted. The detailed approach improved the fatigue factors obtained for all the spans. However, for spans 1 and 5 the results still demonstrated that there was not sufficient fatigue capacity in the girders. Based on the obtained results, spans 2, 3, and 4 had the capacity to remain in service for the next 30 years. While there was no fatigue problem with the braces of span 3, there were some braces in spans 2 and 4 that had insufficient fatigue life. Although these elements were not critical for the continued service of the bridge for the next 30 years, it was recommended that they be replaced.

Loss of contact between bearing plate, insufficient bending capacity particularly at higher train speeds, and the theoretically finished fatigue life suggested replacing spans 1 and 5. This recommendation also took into account the amount of work and the difficulty associated with it due to the number of elements involved in the repair process as well as time constraints.

References

1. Alampalli S, Lund R (2006) Estimating fatigue life of bridge components using measured strains. J Bridg Eng 109(6):725–736
2. AREMA MRE (2020) Manual for railway engineering. American Railway Engineering and Maintenance-of-Way Association, Lanham, MD, USA

3. AREMA PGRE (2003) Practical guide to railway engineering. American Railway Engineering and Maintenance-of-Way Association, Lanham, MD, USA
4. Buck RS (1898) The Niagara Railway Arch. Trans Am Soc Civ Eng 40:125–177
5. CSiBridge (2019) CSiBridge v.21.2.0, Computer and Structures, Inc., Berkeley, CA, USA
6. Endo T, Mitsunaga K, Takahashi K, Kobayashi K, Matsuishi M (1974) Damage evaluation of metals for random or varying loading—three aspects of rain flow method. In: Proceedings of the symposium on mechanical behavior of materials, Kyoto, August 21–24
7. Fisher JW, Kulak GL, Smith FC (1998) A fatigue primer for structural engineers. National Steel Bridge Alliance, Chicago, IL, USA
8. Jaworski J, Hassan M, Pietraszek T, Daneshvar P, Gagné M-È (2021) Étude de la Fatigue des Poutres en Acier du Pont Ferroviaire au-dessus de la Rue Saint-Maurice, Centreville de Montréal. 28e Colloque sur la progression de la recherche québécoise sur les ouvrages d'art, Université Laval, 4–6 mai 2021
9. Legge C (1860) A glance at the victoria bridge and the men who built it. John Lovell, Montreal, QC, Canada
10. Russo FM, Mertz DR, Frank KH, Wilson KE (2016) Design and evaluation of steel bridges for fatigue and fracture. Federal Highway Administration, Technical Report No. FHWA-NHI-16-016